Lecture Notes in Earth System Sciences
LNESS

Lev Eppelbaum
Izzy Kutasov
Arkady Pilchin

Applied Geothermics

Springer

Lecture Notes in Earth System Sciences

For further volumes:
http://www.springer.com/series/10529

Lev Eppelbaum · Izzy Kutasov
Arkady Pilchin

Applied Geothermics

Springer

Lev Eppelbaum
Geophysics, Atmospheric and Planetary Sciences
Tel Aviv University
Tel Aviv
Israel

Izzy Kutasov
BYG Consulting Co.
Boston, MA
USA

Arkady Pilchin
Universal Geoscience and Environment Consulting Company
Willowdale, ON
Canada

ISSN 2193-8571 ISSN 2193-858X (electronic)
ISBN 978-3-642-34022-2 ISBN 978-3-642-34023-9 (eBook)
DOI 10.1007/978-3-642-34023-9
Springer Heidelberg New York Dordrecht London

Library of Congress Control Number: 2014936038

Printed on acid-free paper

Springer is part of Springer Science+Business Media (www.springer.com)

Contents

Summary

This book describes the origin and characteristics of the Earth's thermal field, thermal flow propagation, and some thermal phenomena in the Earth. Description of thermal properties of rocks and methods of thermal field measurements in boreholes, underground, at near-surface conditions enables to understand the principles of temperature field acquisition and geothermal model development. Processing and interpretation of geothermal data are shown on numerous field examples from different regions of the world. The book warps, for instance, such fields as analysis of thermal regime of the Earth's crust, evolution and thermodynamic conditions of the magma-ocean and early Earth atmosphere, thermal properties of permafrost, thermal waters, geysers and mud volcanoes, methods of Curie discontinuity construction, quantitative interpretation of thermal anomalies, examination of some nonlinear effects, and integration of geothermal data with other geophysical methods.

This book is intended for students and researchers in the field of Earth Sciences and Environment studying thermal processes in the Earth and in the subsurface. It will be useful for specialists applying thermal field analysis in petroleum, water and ore geophysics, environmental and ecological studies, archaeological prospection, and climate of the past.

Introduction

Geothermics is an area of geophysics that studies the thermal state and history of the interior of the Earth. Solar heat penetrates only into the topmost layers of the Earth's crust. Diurnal soil temperature variations extend to a depth of 1.2–1.5 m; annual variations, to 10–20 m. The heat associated with solar radiation does not penetrate further, although a regular increase in temperature with increasing depth has been established, indicating the existence of sources of heat inside the Earth. Heat flows continuously from the depths to the surface of the Earth and is scattered into surrounding space. The density of the heat flow is given by the product of the geothermal gradient and the coefficient of thermal conductivity. A considerable part of the heat flow is radiogenic heat—that is, heat involved in the breakdown of radioactive elements present in the Earth.

The temperature of the Earth's interior within the boundaries of dry land is determined directly in shafts and boreholes by means of electric thermometers. Instruments for recording the thermal gradient are used for measurements on the ocean floor. Laboratory measurements are made to determine the thermal conductivity of rocks, and show that the change in temperature with depth at various places varies from 0.006 to 0.15 °/m. The density of heat flow is more constant and is closely connected with the tectonic structure. Very rarely does it extend beyond the limits of 0.025–0.1 W/m^2; individual values attain 0.3 W/m^2. Precambrian crystalline shields are characterized by low values (up to 0.04 W/m^2); platforms, by medium values (0.05–0.06 W/m^2); and technically active regions (midocean ridges, rifts, and regions of modern orogenesis), by high values (0.07–0.1 W/m^2). On average, oceans and continents yield the same values; about 0.05 W/m^2; however, this figure is not very reliable, since most of the Earth's surface has not yet been examined.

The Earth's temperature may be measured directly to a depth of only a few kilometers. Below that, the temperature is estimated indirectly from the temperature of volcanic lavas and from certain geophysical data. At depths of over 400 km, only probable temperature limits can be obtained.

The energy of the total heat flow coming from the Earth is about 2.5×10^{13} W, which is about 30 times greater than that of all the electric power stations in the world but 4,000 times less than the amount of heat the Earth receives from the Sun. Consequently, the heat coming from the Earth's interior does not affect the regional climate.

An explanation of the Earth's thermal history requires data about the original content of radioactive material of the various shells of the Earth, their shifts from one geosphere to another, energies and rates of decomposition, the Earth's age, the amount of heat received by the planet during its formation, and the amount of heat involved and absorbed in the various mechanical, physical, and chemical processes in the Earth's interior. The coefficients of thermal conductivity, the specific heat of the material of the interior, and the temperature and pressure at various depths and on the Earth's surface should also be taken into account.

Geothermic research is of great theoretical significance for various types of Earth studies. Its role is particularly important in constructing and evaluating tectonic hypotheses. For example, geothermic data contradict the thermal contraction hypothesis and other hypotheses that postulate that the Earth's heat loss is much greater than the observed values. Geothermic measurements are also used practically; they assist in prospecting for oil and minerals and in preparation for using the Earth's heat for industrial and domestic purposes.

The purpose of this book is to present methods of utilizing the data of temperature surveys in deep boreholes as well as the results of field, laboratory, and analytical investigations in geothermics in a clear and concise form to environment science engineers, petroleum reservoir and drilling/production engineers, geophysicists, and geologists. Although some aspects of this book have been discussed in a number of monographs including Lubimova 1968b; Kappelmeyer and Hänel 1974; Cheremensky 1977; Gretener 1981; Jessop 1990; Somerton 1992; Kutasov 1999; Beardsmore and Cull 2001 among others and numerous papers, no comprehensive monographs are available to Earth scientists/petroleum engineers. This volume also incorporates the main results of publications by the authors in the last 20 years.

It is obvious that many geothermal problems (propagation of thermal waves in complex media, glaciation cycles, dangerous geodynamic events at a depth, etc.) are nonlinear. Therefore, some attention has been paid to the possible ways of solving these problems.

The objective of this book is to present the state of the art and predictions of downhole and formation temperatures during well drilling, well completion, shut-in, and production. Our intent is to reach drilling engineers (impact of elevated temperatures on well drilling and completion technology, arctic drilling); production engineers (temperature regime of production, injection, geothermal wells, and arctic production); reservoir engineers (temperature field of reservoirs, thermal properties of formations and formation fluids); well logging engineers (interpretation of electrical resistance, mud density, and temperature logs); geophysicists and geologists (interpretation of geophysical data, calculation of the terrestrial heat flow, reconstruction of the past climate). The authors also hope that this volume can be used as a textbook for senior and graduate geologists, geophysics, environmental as well as petroleum engineering students.

The potential applications of the data presented in this book are listed below.

Well drilling and oil/gas production: (1) Prediction and control of downhole mud properties; (2) Designing deep well cementing programs; (3) Evaluation of thermal stresses in casings and around borehole formations; (4) Logging tool design and log interpretation; (5) Determination of the physical properties of reservoir fluids; (6) Prediction of permafrost thaw and refreezing around the wellbore; (7) Determination of the gas hydrate prone zone; (8) Hole enlargement control in permafrost areas; and (9) Well planning in arctic areas (determination of the surface casing shoe depth, selection of low-temperature cements, design of safe casing strings to avoid pipes buckling during the freezeback).

This book will be useful for geophysicists interested in: (1) Searching hydrocarbon, ore and other economic deposits by the use of thermal methods; (2) Calculation of the terrestrial heat flow; (3) Extrapolation of temperatures to greater depths in the crust and the upper mantle; (4) Determination of the dynamics of the permafrost zone by comparing the values of heat flow in the frozen and unfrozen zones; (5) Forecasting of possible dangerous geodynamic events at a depth by the use of thermal monitoring in subsurface and deep wells; and (6) Integrated analysis of thermal and other geophysical fields.

This book will be useful for geologists interested in: (1) Calculation of the regional heat flow for various tectonic structures; (2) Preparation of regional temperature gradient maps; (3) Evaluation of geothermal energy resources; (4) Evaluation of the rates of erosion and sedimentation from temperature profiles; and (5) Studying underground water movement using the difference in vertical heat in water recharge and discharge areas.

This book will be useful for experts in geodynamics and tectonics interested in: (1) Formation and evolution of the magma-ocean; (2) Early Earth atmosphere; (3) Dynamic interactions of the asthenosphere and lithosphere; and (4) Interrelationship between the thermal regime and tectonic processes.

This book will be useful for specialists in environmental sciences interested in: (1) Reconstruction of the past climate from the temperature profiles; (2) Localization of archaeological targets by near-surface temperature survey; (3) Revealing karst terranes and other dangerous environmental features by temperature field analysis; and (4) Computation of water flow geodynamics in stratified liquids.

References

Beardsmore GR, Gull JP (2001) Crustal heat flow: A guide to measurement and modelling. Cambridge, Cambridge University Press

Cheremensky GA (1977) Applied geothermics. Nedra, Leningrad (in Russian)

Gretener PE (1981) Geothermics: Using temperature in hydrocarbon exploration. AAPG, Short Course Notes 17

Jessop AM (1990) Thermal geophysics. Developments in solid earth geophysics, No 17 Elsevier, Amsterdam

Kappelmeyer O, Hänel R (1974) Geothermics with special reference to application. Gebruder Borntrargen, Berlin–Stutgart
Kutasov IM (1999) Applied geothermics for petroleum engineers. Elsevier, Amsterdam
Lubimova EA (1968b) Thermics of the earth and moon. Nauka, Moscow (in Russian)
Somerton WH (1992) Thermal properties and temperature related behavior of rock/fluid systems. Developments in petroleum science, 37. Elsevier, Amsterdam

Chapter 1
The Thermal Field of the Earth

The Earth is about 4.6 billion years old (Anderson 2007). In terms of its thermal regime, the planet is in the process of cooling. However, to have reached its current state, the Earth and the other objects making up the Solar System went through a number of stages such as the accretion of the planet from dust of the solar nebula, the formation of the magma-ocean, stratification of matter by density, solidification of the magma-ocean, formation of the lithosphere which is taking place today, periods of increased volcanic and metamorphic activity, numerous tectonic processes with global and regional significance (obduction, subduction, orogeny, etc.), heat production by short-lived and long-lived radioisotopes, and numerous other features and processes related to thermodynamic and temperature conditions.

All of these features and processes are related to heat: some led to the accumulation of heat (accretion, heat produced by radioactive decay, stratification of the magma-ocean, etc.), whereas others were involved in the transfer of heat energy to the surface (volcanism, obduction, formation of orogeny, hot springs, etc.) or the transfer of colder matter to greater depths (subduction, immersion, penetration of water through fractures to deeper layers within the crust and upper mantle). A number of features and processes prevent the Earth from cooling quickly. These include the Sun's radiation, heat production by long-lived radioactive isotopes, different chemical reactions, amongst others. All these processes are tightly related and have been influenced by the ever-changing thermal regime of the Earth at every step of its evolution, and are associated with or represent essential components of geothermics. All these features and processes therefore warrant special attention and analysis to paint a complete picture of the thermal evolution and conditions of planet Earth.

1.1 Hypotheses Concerning the Origin of the Solar System Throughout History

Throughout the nineteenth century an increasing amount of geological data began to conflict with religious beliefs concerning the origin of the Earth. The main controversies had to do with (1) the formation of the Solar System and Earth,

L. Eppelbaum et al., *Applied Geothermics*, Lecture Notes in Earth System Sciences,
DOI: 10.1007/978-3-642-34023-9_1, © Springer-Verlag Berlin Heidelberg 2014

(2) the age of Earth, and (3) the composition and conditions of Earth at the time of its formation. All these are factors that dictate the Earth's thermal regime, thermal gradient, the depth of the Curie discontinuity and many other geothermal factors.

The first scientific theory of planetary formation was the "vortex theory" put forward in 1644 by Descartes (Brandner 2006). Descartes believed that the universe was filled with vortices of swirling particles, and that the Sun was condensed from a particularly large vortex that somehow contracted, while the planets and satellites were formed from smaller vortices.

The nebular hypothesis was introduced in the eighteenth century. It was first proposed in 1734 by Swedenborg (1734), but later apparently presented independently as a complete model by both Kant (1755) and Laplace (1799–1825). This hypothesis, known as the Kant-Laplace theory, constituted a turning point in our scientific understanding of the formation of the Solar System and the Universe. The nebular hypothesis proposed by Kant (1755) is qualitative and includes such details as the slow rotation of nebulae, their gradual condensing and flattening due to gravity, and eventually the formation of stars and planets. By contrast, Laplace (1799–1825) based his hypothesis on a solid mathematical and physical foundation. In his work Laplace also proved the dynamic stability of the Solar System.

Even though the nebular hypothesis is generally the most widely accepted model of the formation of the Solar System and Earth, it faced strong criticism related to its supposed conflict with the angular momentum of the system (e.g., Woolfson 2000). This led some astronomers at the end of the nineteenth and early twentieth century to introduce the 'near-collision' hypothesis, which states that the planets were formed by the passage of another star close to the Sun. This was thought to have drawn massive amounts of matter away from our Sun, as well as from the passing star, thus forming the planets of the Solar System (Woolfson 2000). During this same time frame several other new approaches were put forward to explain the formation of the Solar System as alternatives to the Kant-Laplace hypothesis. One was the 'planetesimal theory' developed by Chamberlin and Moulton in about 1901–1905 (Chamberlin 1916; Brush 1977; Woolfson 2008). Around 1916, Jeans suggested a new version of the 'near-collision' hypothesis known as the 'tidal theory' (Woolfson 2000). The main idea was that the body of the Sun was strongly and tidally influenced by a massive passing star, creating a tide so great that it drove away some material from the Sun and eventually formed planets. However, both of these 'near-collision' models by Chamberlin-Moulton and Jeans were strongly criticized by Jeffreys (1929) and Woolfson (2000) and Whipple (2007). Instead, Jeffreys propounded the 'collisional hypothesis' (Jeffreys 1929; Whipple 2007) which posited that an approaching star actually brushed against or made contact with the Sun.

In 1944, Schmidt (Woolfson 2000; Schmidt 2001) argued that the Sun in its present form passed through a dense interstellar cloud, from which the planets were later formed. This solved the angular momentum problem for the Kant-Laplace theory. In 1961 Lyttleton (Woolfson 2000) modified Schmidt's hypothesis, which became known as the Schmidt-Lyttleton 'accretionary theory'. In 1960, McCrea put forward a 'proto-planet theory' (McCrea 1960; Woolfson 2000)

which states that because a collision between cosmic bodies is not elastic, collisions lead to a gradual buildup of greater cosmic bodies which continue to accumulate, and larger aggregates continue to grow by capturing smaller bodies and increasing their diameter, and hence their gravity. This theory thus attempts to explain the simultaneous formation of the Sun and the planets.

The most recent and best accepted theory of the formation of the Solar System—the Solar Nebular Disk Model or the Solar Nebular Model—was first described in publications by Safronov (1969), Cameron and Pine (1973) and Cameron (1973, 1978). It posits that the Solar System was formed from a cloud of gas that collapsed under its own gravity. The gaseous cloud was first flattened into a disk known as the accretion disk, with all of the matter in the system in constant rotation about the center. During the accretion process—resulting from growth through the collision and coalescence of entities—objects of different sizes were formed. The largest objects initially formed in the accretion disk are called planetesimals (bodies 1–10 km in size). Collisions between planetesimals led to the formation of planetary embryos or protoplanets (exceptionally large planetesimals). Planetary embryos then continued to grow to full scale planets, accreting planetesimals and other entities of the protoplanetary disk colliding with them.

Thus overall, the Kant-Laplace model of the formation of the Solar System is still considered valid and has remained the main cosmogony theory for the past 250 years.

1.1.1 Formation of Star Systems and Planets

There is a general consensus that the Solar System was formed from the Solar Nebula (dust cloud). But where did this dust cloud and the matter composing it come from? It is obvious that it existed prior to the formation of the Sun and planets of the Solar System. According to Solar Nebula Theory (Nebular hypothesis) the starting point of planetary formation was a disk of mostly gaseous composition with about 1–2 % solid material and a temperature that increased with its proximity to the center (Woolfson 2000). A nebula initially takes a spherical form, since gravity is a centric field, with a more or less even distribution of gas and solid matter, and its initial temperature is thought to have been about 10–30 K. Figure 1.1 shows the directions of the force of gravity applied to an entity located in different parts of the nebula.

It is known that a mutual force of gravity is generated between any two entities within a nebula. The direction and speed of movement of an entity is dependent on the net force of gravity applied to it. Figure 1.1 shows that the gravitational force on a gas or dust entity outside or at the edge of a nebula (1, 2) would draw it inwards, such that the net force would direct it to the nebular center of gravity. Likewise, though an entity inside the nebula (3) would have forces of gravity pulling it in other directions, those originating from the center of gravity would overpower the others, again causing it to move towards the center. However, an

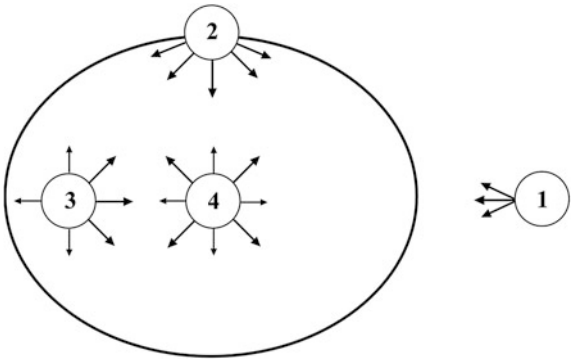

Fig. 1.1 Directions of the force of gravity applied to an entity in different parts of the star-forming nebula

entity which is already located in the gravitational center of the nebula (4) would have forces of gravity drawing it away from the center in all directions of the nebula, effectively cancelling each other out and producing a net gravity force of zero. These entities would then remain in the center of gravity. It is clear that the gravitational collapse of the nebula is inevitable, leading to the concentration of the nebula's mass at its center of gravity. This growing mass in the center would apply a gravity force F on any entity within the nebula according to Newton's law of gravity:

$$F = G\frac{Mm}{r^2}. \tag{1.1.1}$$

where G is the universal gravitational constant (6.67×10^{-11} $m^3/kg\ s^2$), M is the mass of the center of gravity of the nebula, m is the mass of an entity in the nebula, and r is the distance between the entity and the center of gravity.

From Eq. (1.1.1) it is obvious that the force of gravity increases with the increase in the central mass M and the decrease of the distance r. The central mass gets larger by absorbing and accumulating the mass of the entities in the nebula drawn into the center, and represents the mass of the growing star. The rates at which the entities in a nebula are drawn into its center are dependent on both the strength of the force of gravity [see Eq. (1.1.1)] and the acceleration g created by this force:

$$g = \frac{GM}{r^2}. \tag{1.1.2}$$

Any central gravity field can be characterized by its gravity potential, which is generated by its mass. The difference in gravitational potential ΔU between any two points is:

$$\Delta U = -\int g * dr. \tag{1.1.3}$$

The gravitational potential for a body with a constant mass (for example, the Earth) is:

$$\frac{GM_e}{r}, \tag{1.1.4}$$

where M_e is the mass of the Earth.

It is also clear that the collapse of a nebula is caused by the gravitational potential generated by the central mass of the forming star, and the gravity applied by this mass on all other objects within the nebula. The rate of collapse is proportional to the value of the acceleration due to the gravity created by the central mass. The gravitational potential, force of gravity, and acceleration due to gravity increase with the increase of the central mass M. This collapse of the nebula with increasing central mass (leading to a star) is called accretion. The accreting central mass obviously causes a cycle where the rate at which entities are drawn into it increases, thereby increasing its mass, and therefore cumulatively increasing its power to collapse the remaining entities in the nebula. This process causes the first and fastest stage of star growth, which has been dubbed "runaway" accretion. Potentially all entities within a nebula can collapse to the center and contribute to forming the star, creating a system without any planets. However, the presence of planets such as in our Solar System shows that this is not always the case. In order to escape being dragged into the center of gravity, an object must revolve around it, and its speed (v) should correspond to this equation:

$$\frac{GMm}{r^2} = \frac{mv^2}{r}. \tag{1.1.5}$$

In other words, the value of the centripetal force applied to an object by its revolution about the center of gravity should be equal to the force of gravity applied to it by the central mass. Equation (1.1.5) also shows that the minimal speed of revolution for an object to avoid collapsing into the center of gravity is:

$$v = \sqrt{\frac{GM}{r}}. \tag{1.1.6}$$

This means that if the speed of an entity within the nebula is less than the value determined by Eq. (1.1.6), it will be drawn into the center of gravity; if its speed is equal to the value, it will continue its revolution around the center in its current orbit; and if its speed is greater than this value, it will move to a higher orbit (with greater r) within the nebula or possibly even escape from the nebula. It is clear from Eq. (1.1.6) that the increasing mass of a growing star requires objects to move at greater speeds to prevent collapsing into the center. This means that all

entities that are not revolving around the center of gravity or that are slower than the minimum speed as defined by Eq. (1.1.6) will be drawn into the forming star during the first stage of accretion. By the end of this stage, which is the shortest, the accretionary disk is formed around the developing star: disks of dust surrounding some stars have actually been observed (Beckwith et al. 1990). During the initial stages of accretion, objects can revolve around the central mass in any direction, but movement in opposite directions can cause a high rate of collisions, resulting in a loss of speed for the colliding entities and their subsequent collapse into the center of gravity. Thus eventually only objects revolving in one primary direction survive. For the same reason, the forming disk is flattened. After the formation of a flat accretionary disk, the rate of further growth of the central mass (protostar) decreases significantly.

During all stages of the forming protostar, its matter is gradually differentiated, leading to the accumulation of density in its core. Both the accretion of matter and the differentiation of the protostar cause the release of significant amounts of energy, thus greatly increasing the temperature of the forming protostar and in turn the temperature within the accretionary disk. The level of energy released during these two processes is dependent on the latent energy of each entity involved. Any object within a nebula can have potential energy (E_P) depending on its position relative to the nebular center of gravity, the kinetic energy of its speed (E_K), and the kinetic energy of its rotation (E_{KR}) if it rotates on its own axis. The amount of each kind of energy can be calculated using the following equations:

$$E_P = mgr, \tag{1.1.7}$$

where m is the mass of an object, g is acceleration due to gravity, and r is the distance from the nebular center of gravity.

$$E_K = \frac{1}{2}mv^2, \tag{1.1.8}$$

where v is the velocity of the object.

$$E_{KR} = \frac{1}{2}I\omega^2, \tag{1.1.9}$$

where I is the moment of inertia and ω is the object's angular speed of rotation on its own axis.

The amount of energy released during stellar accretion can be tremendous. For example, the release of potential energy by an object with a mass of 1 kg falling onto the Sun from the distance of Pluto would be about 6.1×10^6 J. The amount of energy released if this same object had a speed of roughly 5 km/s would be about 1.25×10^7 J. The kinetic energy of the Earth's rotation on its axis is about 1.3×10^{28} J.

Our Sun is a low-mass star, and therefore cannot generate all elements. Its ability to produce elements heavier than helium is limited and its core temperature is not high enough for the helium burning process to begin. At the same time, ninety-two elements on the Periodic Table naturally exist on the Earth and in meteorites, and nearly a third of the Earth's mass is represented by iron (Pilchin and Eppelbaum 2006) which has no chance of being produced in our current Solar System. Because the Sun was formed from the same nebula as all the planets and moons of the Solar System, the matter making up the nebula existed before the formation of the Solar System began. In other words, the material of the Solar System and other nebulas in the galaxy was produced by stars of a previous generation, which most likely exploded, releasing the very matter composing these nebulae, which was then recycled into a new generation of stars.

The Earth and the other planets of the Solar System were formed from the same accretion disk as the Sun. That is why this disk is also known as the protoplanetary disk. The fact that so many elements are naturally found on Earth and the rest of the Solar System whereas the Sun is only capable of hydrogen burning processes indicates that all these elements were present within the initial protoplanetary disk. From the beginning of accretion, entities in the nebula began to cohere as a result of electrostatic forces, van der Waals forces, collisions, etc. The effect of electrostatic forces formed during the exchange of charges between grains of matter, grains and gas, and the generation of electric dipoles leading to the rapid formation of dust aggregates is discussed in (Marshall and Cuzzi 2001). Pilchin (2011) also discussed the role of magnetic forces in the initial coalescence of entities. These processes led to a significant increase in mass of many entities in the evolving nebula. When the size and mass of certain entities increased to a substantial value, they began to attract smaller entities by the force of gravity. Recall that to avoid being drawn into the center, the objects must revolve around it within the protoplanetary disk. From the beginning of nebular collapse, accretionary processes took place throughout the entire nebula. These processes include the accretion of the Sun, the planets of the Solar System, planetesimals, etc. The density of the matter in a nebula determines the rate of accretion, but unfortunately direct observations of planetary growth are next to impossible, which makes modeling the processes related to planet formation the main technique for studying them. However, to model planetary growth, scientists use different physical conditions, assumptions, initial conditions, and different mathematical descriptions of planetary growth (Nakazawa et al. 1993).

1.1.2 Temperatures in the Protoplanetary Disks

The temperature rises during accretion and differentiation of the Sun and terrestrial planets, as well as during decay of short-lived and long-lived radioactive isotopes.

Studies of the stability of rocks and minerals, as well as certain oxides such as iron (Pilchin and Eppelbaum 2006; Pilchin 2011) during the early stages of

Table 1.1 Estimated values of iron content in the mantle and core of terrestrial planets (after Pilchin and Eppelbaum 2006)

Planet	Mass of planet (kg)	Mass of iron in crust and mantle (kg)	Mass of iron in core (kg)
Mercury	3.30×10^{23}	0	2.09×10^{23}
Venus	4.87×10^{24}	5.52×10^{22}	1.31×10^{24}
Earth	5.97×10^{24}	2.1×10^{23}–2.8×10^{23}	1.73×10^{24}
Mars	6.42×10^{23}	1.07×10^{23}	5.50×10^{22}

Table 1.2 Content of iron in the Sun and the terrestrial planets (after Pilchin and Eppelbaum 2006)

Body	Mass (kg)	Iron content	
		wt%	kg
Sun	1.99×10^{30}	0.1792	3.566×10^{26}
Mercury	3.30×10^{23}	63.32	2.09×10^{23}
Venus	4.87×10^{24}	28.02	1.36×10^{24}
Earth	5.97×10^{24}	31.00–33.68	$(1.85–2.01) \times 10^{24}$
Mars	6.42×10^{23}	25.26	1.62×10^{23}

formation and evolution of the Sun and planets of the Solar System can yield important insights into the processes of the formation of rocks and minerals, their differentiation, and their thermal conditions. It was shown (Pilchin and Eppelbaum 2007; Pilchin 2011) that a number of processes can be used as indicators of certain thermal conditions at different stages of nebular evolution, as well as at different stages in the formation and evolution of the planets. For instance, Tables 1.1 and 1.2, show that the iron content of the terrestrial planets is extremely high, and is mostly concentrated within their iron cores.

This shows that the different processes and chemical reactions involving iron, iron oxides and other rocks and minerals containing iron are fundamental to any study of the formation and evolution of the terrestrial planets, as well as the meteorites and asteroids in this part of the protoplanetary disk. Data (Pilchin and Eppelbaum 2006, 2009) indicate that one of the main indicators of the thermal conditions of iron oxides and iron-containing rocks and minerals is the transformation of ferric to ferrous iron (TFFI), which takes place under the following reaction conditions (Pilchin and Eppelbaum 2006, 2009):

$$4\mathrm{FeO} \rightarrow \mathrm{Fe_3O_4} + \mathrm{Fe}. \tag{1.1.10}$$

The distribution of heat in the protoplanetary disk is concentrated in the central star, with a reducing thermal gradient leading away to the outer edges of the disk. However, the accretion of planets also generates local increases of temperature stemming from the center of the forming planet, and likewise gradually decreasing towards the edges of planetary accretion disk from which it was formed, though this disk is present within the larger protoplanetary disk.

Table 1.3 Temperature in the solar nebula in terms of the distance of the planets from the Sun, and current day surface (or cloud-top) temperatures of the planets

Planet	Temperature in solar nebula at the distance of the planets (K)			Current day average surface (or cloud-top) temperature (K)
	After Kaufmann (1994)	After Kaufmann and Freedman (1999)	After Kaler (1994)	
Mercury	~1,400	~1,200	1,400	700 (day side) 100 (night side)
Venus	~750	~750	800–850	740
Earth	~650–700	~650–700	600	290
Mars	~450–460	~500	500	240
Jupiter	~170	~170	150	125
Saturn	~90–95	~90–95	85	95
Uranus	~50	~50	50	60
Neptune	~40	~40	45	60
Pluto	~30	~30	30	40

Table 1.4 Temperature and pressure distribution in the inner part of the solar nebula

Distance from Sun (AU)	Temperature (K)	Pressure (MPa)	References
0.01	7,600	7×10^{-2}	Lewis (1974)
1	600	1×10^{-5}	
0.01	2,200	3×10^{-3}	Cameron (1995)
1	470	4×10^{-6}	
0.01	1,500	4×10^{-4}	Willacy et al. (1998)
1	600	1×10^{-6}	

Estimates of initial temperatures in the solar nebula are presented in Tables 1.3 and 1.4.

Different models show that the temperatures in the nebula during accretion in terms of the distance of the Earth from the Sun (1 AU) could have reached values of 900–1,400 K (Deming 2002) and 1,400 K (Humayun and Cassen 2000). Boss (1998) showed that in his model, temperatures in the inner part of the proto-planetary disk were in the range of 500–1,500 K. Another study (Woolum and Cassen 1999) indicated that the midplane temperatures of 26 stellar nebulae at 1 AU from the center are in the range of 200–800 K, and decrease to 100–400 K by 2.5 AU. Kerridge (1977) suggested that the distribution of iron among planets and meteorites can be adequately modeled by condensation and fractionation under equilibrium conditions above ~700 K. Analysis of these temperature data in the solar nebula showed that the temperature at the distance of the Earth from the Sun (1 AU) in only one model was near the lower limit (~470 K) of the conditions needed for the transformation from ferrous to ferric iron [Eq. (1.1.10)] to take place, whereas for all the other models in Table 1.4 (see also Pilchin and Eppelbaum 2006) it was squarely within the temperature interval of TFFI.

However, given that magnetite could have been formed in the solar nebula from native iron at temperatures of ~370 K (Fegley 2000), iron oxides in all the models referenced above were within the temperature range of TFFI through reactions right before the start of the formation of the Earth [Eq. (1.1.10)].

Magnetite and the thermal conditions of its formation are fundamental to many features and processes taking place throughout the evolution of the Earth (Pilchin and Eppelbaum 2006; Pilchin 2011). Moreover, magnetite may have played a crucial role in the initial adhesion of entities within the solar nebula before they had sufficient gravitational force, hence leading to the formation of larger entities, eventually planetesimals, and finally planets (Pilchin 2011). This means it is crucial to analyze the content of magnetite and iron in meteorites to assess the similarity between the features and processes on Earth and other objects in the Solar System at the beginning of accretion.

All of the above suggests that data on the iron oxide content in the material used to form the Earth is crucial (Pilchin and Eppelbaum 2006), as well as the temperature conditions during its early formation and evolution. At the same time, further research on iron oxides content can yield additional information about the existence and role of TFFI through reactions [Eq. (1.1.10)] during the early stages of the evolution of the Solar System. Previous studies have shown that most meteorites contain FeO but only a few contain Fe_2O_3 (McCall 1973); the content of iron and stony-iron meteorites is respectively 5 and 1 % of all meteorites, and the initial temperature in the solar nebula in terms of the distance of the terrestrial planets from the Sun was relatively high (see Table 1.3).

The presence of enormous quantities of metallic iron in the cores of terrestrial planets and some moons in the Solar System is a sign of reduction conditions during the formation of these cores. It was shown based on the density distribution of iron, iron oxides and iron-containing minerals (Pilchin and Eppelbaum 2006), that native iron would likely have had a greater concentration closer to Sun (where Mercury is located), whereas iron oxides, iron sulfides and iron silicates are likely to have had higher concentrations corresponding to the location of Mars. These concentrations would then be somewhat balanced for the Earth and Venus. This is consistent with the known reducing conditions at the location of Mercury, the presence of temperatures above the reaction (1.1.10) limit, and the presence of an almost entirely metallic iron core in Mercury with almost a complete absence of iron-containing minerals in its mantle. At the same time, at the location of Mars, where the temperature in the nebula was near the lower limit but still within the temperature range for reaction (1.1.10), the content of native iron is minimal, whereas that of the iron-containing minerals in the mantle is the maximum of all the terrestrial planets. This is also in line with the fact that Martian soil contains 18 % Fe_2O_3 (Anderson 1989). Our Moon also has an elevated content of iron oxides in its crust and mantle (Pilchin and Eppelbaum 2006).

The data presented in (Pilchin and Eppelbaum 2006) show the abovementioned trends in iron content in the core, the crust and the mantle of terrestrial planets. The Earth has the maximum content, which may have been in the region of greatest

concentration of both iron oxides and iron-containing minerals. Since the mass of the Earth's metallic iron core makes up a much greater percentage of the Earth's mass than that of iron in iron and stony-iron meteorites (Pilchin and Eppelbaum 2006), there must have been some process of extracting native iron from compounds during the evolution of the Earth. The distribution of iron in terrestrial planets is also suggestive of the possibility that the higher temperature in the inner part of the solar nebula may have led to the condensation of most Fe in native form, with very little oxidation to iron(II) or iron(III) (Cox 1990). The transformation from ferrous to ferric iron (reaction 1.1.10) could obviously have played a significant role in the reduction of iron. This coincides with the fact that all the main iron-containing minerals mentioned in (Pilchin and Eppelbaum 2006) (native iron, ferrous iron oxide, ferric iron oxide, magnetite, pyrite, troilite, pyrrhotite, fayalite, almandine, and ferrosilite), are known to be found on the Earth and meteorites. Iron-rich garnet (almandine) is a very common mineral in kimberlites (Schulze et al. 2000), and almandine-rich garnet is very common in regions of orogenic belts. Such garnets have been found in the Aegean region (Mposkos and Perraki 2001; Perraki and Mposkos 2001), New Zealand (White 1996), La Ronge domain of the Trans-Hudson Orogen (Yang et al. 1998), North Jay Pluton in Maine (Dutrow et al. 1999), Gualala basin of California (Schott and Johnson 2001), the Branisko Mts. in the Western Carpathians (Faryad 1999), Bårdsholmen, WGR, Norway (Engik et al. 2000), Dabie Shan, China (Schmid 2000), the Qaidam eclogite belt, NW China (Song et al. 2003), Bahia, Brazil (Osako et al. 2001), the Maksyutov Complex, S. Ural Mountains (Leech and Ernst 2000), the Mozambique belt, Tanzania (Johnson et al. 2003), the Sanbagawa metamorphic belt, etc. Almandine-rich garnet has also been found in micro-diamond-bearing regions (Dobrzhinetskaya et al. 1995).

Estimates of the combined value of energy generated during planetary accretion, including the gravitational settling of Earth's metallic core, decay of short- and long-lived radioactive isotopes, meteorite impacts, and possible collision with a Mars-size body shows that it was sufficient to melt the entire Earth (Lubimova 1968a, b; Halliday 2000; Valley et al. 2002; Walter and Trønnes 2004, etc.). In geothermal research (MacDonald 1962; Lubimova 1968a, b, etc.) there are two hypotheses concerning the earliest temperature conditions on the Earth and the Moon: the first presupposes a hot origin of the Earth (the planet was completely molten initially) whereas the second argues for a cold/warm origin (the planet was hot but not completely molten). Other authors indicate that at the time of core formation, the Earth (and possibly Venus and Mars) may have been entirely molten (Jakosky 1999; Walter and Trønnes 2004). Under these conditions any free iron would have been heavy enough to sink through the layers of molten rock. Birch (1965) also showed that in order for Earth's iron core to form, the temperature of the Earth's layers had to be above that of the melting point of iron at some point in the past. Other studies have suggested that at some point in its early evolution the Earth was covered by a magma-ocean (Safronov 1978; Abe 1997; Pollack 1997; Solomatov 2000; Walter and Trønnes 2004; Pilchin and Eppelbaum

2012, etc.) that was at least a few hundred kilometers deep (Safronov 1978; Walter and Trønnes 2004, etc.). Magma-oceans also formed on other terrestrial planets (Condie 1989a; McSween 1993; Lauretta et al. 2006), the Moon (McSween 1993, 1999; Bennett et al. 2004), and the asteroid Vesta (Righter and Drake 1997a). Some scientists believe that such a magma-ocean could have existed for only about 1–10 million years (Davies 1990; Spohn and Schubert 1991; Franck 1992; Sleep et al. 2001), while others believe that it could have remained for 100–200 million years (Abe 1997; Pollack 1997), or even longer (Solomatov 2000). This is the prime controversy as regards the Earth's thermal regime after the Hadean, since some investigators believe that the Earth cooled down in no time at all on a geological scale, and others consider that it took a very substantial amount of time.

It is obvious that if there were a magma-ocean, ferric iron was unlikely to emerge. In other words, ferric iron could only be formed through TFFI, when the Earth's surface cooled to below 843–723 K. This also means that any mineral containing iron (III) is only secondary in origin. This is consistent with the abovementioned results showing that magnetite and ferric iron oxide (Nagatha 1961; Bagin et al. 1969; Pechersky et al. 1975), as well as magnetite in meteorites (McCall 1973) are of secondary origin. Since the atmosphere during the early period of the Earth's evolution was essentially anoxic (Holland 1984), there was no other way for ferric iron to form.

It is also evident that the duration of the solidification of the magma-ocean and the cooling of the Earth's surface and upper crustal layers was crucial for the development of many important processes including the origin of the water ocean and the formation of rock magnetism. Unfortunately, some researchers do not take into account such features as the length of time necessary for the Earth's differentiation, cooling rates, or release of energy in their calculation of the decay of short- and long-lived radioactive elements. For instance, an analysis of geothermal data shows that the energy released by long-lived radioactive elements alone would create a massive heating of the Earth's interior (Lubimova 1968b), which would be enough to melt the entire planet. This is consistent with the formation of komatiite magmas at the end of the Archean, which indicates a temperature maximum in the mantle. Calculations presented by Birch (1965) and Lubimova (1968a) indicate that the temperature inside the Earth could have increased to the melting point of iron during the first half a billion to billion years after the accretion of the Earth. None of this supports the hypothesis that the Earth's layers cooled quickly.

The cooling rate of the mantle ranges from 0.03 K/Ma (Peck et al. 2001) to 0.20 K/Ma (Condie 1989b) depending on the nature of different researchers' estimates. Estimates of the cooling rates of magmatic and metamorphic formations and regions of Earth differ considerably and go from 0.2 K/Ma to hundreds of K per Ma, but in most cases the values are in single units of K per Ma (Pilchin and Eppelbaum 2009). It is highly unlikely that the cooling rate of the magma-ocean covering the entire Earth would be higher or even equal to the cooling rates of

small regional or local magmatic bodies, or metamorphic or orogenic belts. Interestingly, estimates of the cooling rates of Mars and Venus are 0.25 and 0.10 K/Ma, respectively (van Thienen et al. 2005). At the same time, estimates of the cooling rate in the Adirondack Highlands vary from very fast >200.0 K/Ma (Storm and Spear 2005) to slow 4.0 K/Ma (Johnson et al. 2002), or even very slow 0.5–1.0 K/Ma (Mezger et al. 1989). Many authors have noted that the cooling rates are faster for high temperatures and much slower for lower temperatures (Zeck 1996; Christoffel et al. 1999; Okudaira et al. 2001; Meert et al. 2003; da Silva Schmitt et al. 2004; Zhao et al. 2004).

A comparison of the cooling of any size of magmatic effusive or intrusive complex, metamorphic complex, or orogenic belts with the cooling of a magma-ocean covering the entire planet that was a few hundred kilometers deep suggests that the rate of cooling for the magma-ocean should be thousands, or even millions of times slower (Pilchin and Eppelbaum 2009). Importantly, in contrast to any local structure, the magma-ocean could not lose heat energy by any other means than radiating that energy into space and through contact with the atmosphere.

After the start of planetary accretion and prior to the time Earth's surface cooled to below 843–723 K, there was no chance for any significant amounts of ferric iron oxide to exist on Earth. It is therefore possible that the time of the first formation of magnetite (banded iron formation - BIF) marks the point in the Earth's evolution at which the surface temperatures dropped to and below 843–723 K. The only other mineral that can obtain its ferric iron before the formation of magnetites is biotite, one of the main rock-forming minerals of the Early and Middle Precambrian. This means that the appearance of first Algoma-type BIF indicates the point in time when the surface temperature cooled below the upper limit of the temperature range of TFFI. It is also very likely that during the formation of every BIF, the surface temperatures in the area were within the temperature range of TFFI. This is congruent with the well-known fact that both Algoma- and Superior-type BIFs are characterized by positive Europium anomalies, which are indicative of high-temperature alteration of volcanic rocks (Graf 1978; Derry and Jacobsen 1990; Klein and Beukes 1992; Huston and Logan 2004). Research also shows (Huston and Logan 2004) that Algoma-type BIFs have notably larger Europium anomalies (over 1.8) than Superior-type BIFs. This could point to higher surface temperatures during periods of the earliest BIF deposition. Although the Earth's surface temperature was not necessarily within the temperature range of TFFI throughout the entire period of BIF deposition from 3.85 Ga until 1.85–1.80 Ga, at the time of BIF deposition it most certainly would have been within this temperature range. It is also possible that the first BIFs were the earliest in which the rocks contained in them acquired magnetism since the start of planetary accretion. The possibility of high regional or local surface temperatures is also supported by well-known facts such as the relatively widespread komatiite magmatism in the Late Archean, picrite magmatism in the Early Proterozoic, and the Late Archean global magmatic event that took place on all Archean cratons (Pilchin and Eppelbaum 2006, 2009).

1.1.3 History of Geothermics

In this section we look at the chronological evolution of geothermic theories. René Descartes (1644) first proposed that the Earth was initially a small star that subsequently cooled from a molten state, and as such had a certain amount of internal heat. Kircher (1665) mentioned the subterranean heat that was felt at the bottom of mines which he attributed to subterranean fires. Leibniz (1749), in his *Protogaea* written in 1691–1693 and first published in 1749 (Wolf and Dannemann 1935), proposed that the Earth had cooled through time from a molten state, and that during the cooling process a universal ocean gradually condensed from vapor.

The earliest measurements of underground temperature were probably made in 1740 in the mines of Alsace, France by De Gensanne (de Buffon 1778; Radau 1880; Prestwich 1886). In 1783, de Lavoisier installed a thermometer for monitoring temperatures in Paris in the deep caverns below street level which are famous for displaying a constant temperature of 11.86 °C (285.01 K) at all seasons, which interestingly still remain unchanged (Gillispie 2004). de Buffon (1778) proposed the existence of heat originating within the Earth. They estimated the time of the Earth's cooling, based on the cooling rate of iron, to have been about 75,000 years. Toward the end of the 18th century, de Saussure found the increment rate of temperature with depth to be 1° for 37 m in the salt mines of Bex (Radau 1880). Von Buch (1802) provided indications of the rate of temperature change by 1 °F with depth. Cordier (1827) was probably one of first scientists to calculate the average geothermal gradient, and concluded that the value was about 20–25 °C/km.

Some of the earliest reports of thermal measurements can be found in the publications of l'Abbé Chevalier (1782), de Saussure (see in Cordier 1827), d'Aubuisson de Voisins (1801, 1802, 1806), von Buch (1802, 1806), von Humboldt (1817, 1820), Arago (1820), Fox (1822, 1827), Forbes (1822), and d' Aubuisson de Voisins (1830). The first crucial milestone in the evolution of geothermics, however, dates to Alexander von Humboldt (1817) when he introduced isothermal lines (isotherms), which also played an important role in the evolution of cartography (Robinson and Wallis 1967).

During the 19th century problems related to thermal measurements, the calculation of the rate of increase of temperature with depth, and other thermal characteristics used in contemporary geothermics were formulated (Arago 1820; Cordier 1827; d'Aubuisson de Voisins 1830; Daubeny 1837; Bakewell 1838; De La Beche 1853; Arago 1857; Fox 1858; von Humboldt 1868; Radau 1880; Lebour 1882; Everett 1883; Prestwich 1884, 1886). During this time scientists abandoned the high-temperature liquid Earth interior model (circa 1790) and began to support a high-temperature solid Earth interior model (circa 1840) (Zemtsov 2005).

Another crucial milestone was the development of the mathematical foundation of geothermics by Fourier (1824), who presented a mathematical theory of heat conduction. Fourier (1824) was also the first scientist to suggest that gases in the atmosphere can increase the surface temperature of the Earth, which would later lead to the development of the greenhouse effect theory. de Beaumont (1830)

published his theory on the origin of mountains, which he believed was caused by the cooling of the Earth's crust.

Bischof (1836) reported results of temperature measurements in hot and thermal springs, and came to the conclusion that the temperature rose towards the center of the Earth. He showed that as a general rule the temperature in mineral springs more or less exceeded the mean temperatures of the region (average annual temperature), based on analysis of temperatures in numerous springs in Germany, France, Austria, Switzerland, Moravia, Hungary, Transylvania, Slovenia, Croatia, Bohemia, the Caucasus, the Alps, the Pyrenees, and in some other regions. He also reported measurements made at levels significantly above sea level (up to about 2,700 m) and in the vicinity of glaciers. He also came to the conclusion that the temperatures of spring water do not correspond to those of the soil. Daubeny (1837) also surveyed temperature in the mineral and thermal waters of Germany, Austria, France, Spain, Portugal, Greece, Iceland, Turkey, Venezuela, the Alps, the Carpathians, the Pyrenees, and the Cordilleras. He showed that the data supported the theories of Humboldt and others that the temperature in springs was higher than that of the atmosphere and increases with latitude.

Thermal measurements by Arago and Walferdin (Walferdin 1837; De La Beche 1853; Knight 1866; Everett 1883) in an artesian well in Grenelle, near Paris were very important for the evolution of geothermics. These measurements showed that the increase in heat with depth takes place at a rate of 1° per 32.3 m (De La Beche 1853). From the beginnings of thermal research, scientists have been using the mean of annual temperatures of regions in their calculations (Fox 1827; Everett 1883; Prestwich 1886), which were collected by a number of scientists (Quetelet 1837, 1839, 1840; Carpenter 1843; Adie 1863; Quetelet 1875). The rate of increase of depth for the increment of a single degree of temperature was sometimes calculated from the surface, and at other times by assuming a *mean invariable surface-temperature* to lie at a certain depth. Based on an analysis of the annual fluctuations of temperatures at shallow depths in areas surrounding Edinburgh and Greenwich, Prestwich (1886) showed that to reach the lower limit of the temperature range or the plane of uniform annual temperature in these latitudes, the temperatures would have to be measured at a depth of about 50–60 ft. (15.2–18.3 m), which is very close to the mean invariable surface-temperature of 18–21 m accepted today (Lubimova 1968a). He also indicated that in future observations it would be crucial to calculate the temperature at this depth, or where the first instance of uniform temperature occurred, and to find the rate of increase of temperature with depth from that point.

Numerous studies on the thermal conditions within mines, and artesian and mineral springs were conducted in the mid-19th century (Adie 1854; Thomson 1860 and others). Scientists paid close attention to such problems as the change of temperature in a horizontal direction within mines (Fox 1822; Prestwich 1886), seasonal (monthly) variations in temperature (Fox 1827; Everett 1883; Prestwich 1886), variation in the rate of increase of depth in different places for each degree of temperature, called by some the 'thermometric gradient' (Prestwich 1886), the influence of surface relief on temperature (Everett 1883; Stapff 1883;

Prestwich 1886), different causes of seasonal and annual changes in temperature in different places (Prestwich 1886), etc. Different conditions causing seasonal and annual variations in measured temperatures in different geological structures led some researchers (Everett 1883; Prestwich 1884, 1886) to classify the data on underground thermal conditions into four groups: (1) metallic mines (2) coal mines (3) wells and wet borings, and (4) tunnels.

The average rate of depth change with an increase of temperature of 1 °F was calculated (Radau 1880; Everett 1883; Prestwich 1886) to be between 30–37 m in most cases, and it was commonplace to take a mean rate of 1° for every 30 m (Prestwich 1886), which is almost equal to the value of the average geothermal gradient accepted for continents (Lubimova 1968b). Measurements taken in a borehole in La Chapelle St. Denis, Paris showed a rate of increase of 39 ft. per 1 °F for the first 100 m, but a rate of 1 °F for 84 ft. at a depth of 660 m (Prestwich 1886), which shows a decrease in the geothermal gradient with depth.

There were several attempts by Walferdin (see Knight 1866), Fairbairn (1861), and Radau (1880) to estimate temperatures at great depths using the estimated rates of depth change with a temperature increase of 1°. Walferdin used his calculations to predict the temperature at a depth not yet reached at the time, which would later turn out to be very close to the actual temperature measured (see Knight 1866). Fairbairn (1861) predicted temperatures of 212 °F at a depth of 2.5 miles and 3,000 °F at 40 miles. However, he went on to further state that if the conductivity of the lower rocks was twice as great as the strata in which the observations were made, a temperature of 3,000 °F should be found at depths of 80–100 miles. Radau (1880) suggested that if the rate of temperature increase of 1 °C with a depth of 30 m was constant, temperatures should reach the boiling point of water at a depth of 2,700 m, and would exceed 1,873 K at 50 km.

Everett (1883) showed that it was better not to use the number of feet per degree in calculations, but its reciprocal—the increase in temperature per foot. He also suggested that to obtain an approximation of the rate at which heat escapes annually from the Earth, it should be converted to degrees centigrade per centimeter of depth (see also Prestwich 1886). He also argued that to calculate the rate of escape of heat, the geothermal gradient should be multiplied by the conductivity, and provided an approximation of the heat escaping annually from every square centimeter of the Earth's surface. Similar estimates were also made by Kelvin (1866). At around the same time, a number of researchers were working on the thermal conductivities of rocks (Kelvin 1866; Everett 1883; Prestwich 1886), the temperature variation of the thermal conductivity of rocks (Kelvin and Murray 1885a, b; Weber 1895), and thermal diffusivity (Everett 1875; Thomson 1878).

Towards the middle of the 19th century thermodynamics and problems related to the origin of solar heat attracted enormous scientific attention (Williams 1897; James 1982; Olby 1996). Mayer (1848, 1867) hypothesized that the Sun's heat and luminosity were generated and supported by falling meteorites. A similar theory was also put forward by Waterston (1853). Some later von Helmholtz posited that the Sun's heat and luminosity were generated by its gravitational contraction (von Helmholtz 1856). William Thompson (Lord Kelvin) initially supported Mayer's

meteorite theory, but later decided in favor of von Helmholtz's gravitational contraction hypothesis (Smith and Wise 1989). It was known that gravitational contraction with the release of heat indeed plays a crucial role in the accretion process of stars and planets. It heats stars to temperatures permitting them to begin fusion processes and leads to the rise in temperature between nuclear burning processes.

Lord Kelvin used geothermal methods to calculate the age of the Earth, which are described in a number of his publications (Thomson 1862, 1890; Kelvin 1863, 1864, 1895, 1899) and discussed in many others (Richter 1986; Hallam 1989; Stacey 2000; Dalrymple 2004; England et al. 2007). Since temperature increases with increases in depth, Lord Kelvin concluded that the Earth was slowly cooling, and he decided to use thermal conduction to calculate the time required for the Earth to cool from its initially molten state. He assumed the temperature of Earth's core to be that of molten rocks, and took into account the temperature gradient with regards to the depth below the surface and the thermal conductivity of the rocks. In 1862, Kelvin estimated that the Earth was about 100 million years old, with lower and upper limits caused by uncertainties in the data to be in the range of about 20 million and 400 million years, respectively. He also concluded that the Sun could sustain its present rate of radiation for no longer than about 100 million years.

All of the above shows that prior to the discovery of radioactivity, scientists had a very good analytical picture of the thermal conditions of the underground layers, and had a firm grasp of many methods used today in geothermics. With the discovery of radioactivity by Becquerel (1896), one of the main sources of the Earth's internal heat was identified (Détraz 1999). The problems related to radioactivity were analyzed by a number of early researchers (Curie 1898; Curie and Curie 1898; Curie et al. 1898; Crookes 1900; Becquerel 1901; Rutherford 1903, etc.). Curie and Laborde (1903) reported results of experiments showing that radium and its compounds produced significant amounts of heat. Their ensuing experiments also supported the claim that radioactive elements generate heat (Curie and Laborde 1906). Wilson (1903) came to the conclusion that the radiation of heat by radium might be the source of energy in the Sun and stars. By 1905, most physicists believed that radioactive energy was responsible for the energy output of the Sun (Stinner 2002).

Strutt was among the first researchers to analyze the content of radioactive elements in rocks and minerals (Strutt 1906, 1910), and their role in the formation of internal heat. However, Lord Kelvin initially rejected the idea that radioactivity could emit significant heat, and never accepted it as the primary source of the Earth's internal thermal energy (Lewis 2000). Holmes published a series of papers (e.g., Holmes 1915, 1916, 1925) on the role of radioactivity in the thermal history of the Earth. It was later shown that the concentrations of thorium, uranium, and potassium, the main radioactive elements within the Earth, increase considerably as they come closer to the Earth's surface (Holmes 1915; Jeffreys 1924, 1952, 1970; Urey 1952).

Carslaw (1906, 1921) and Carslaw and Jaeger (1946, 1959) made a significant contribution to geothermics by suggesting a mathematical theory of the conduction of heat in solids and its applications to numerous problems. Joly (1909) proposed a mantle convection current hypothesis, based on the idea that the decay of radioactive elements in the mantle should lead to its heating and subsequently trigger the convection process. Wegener (1912) put forward the continental drift hypothesis, which revised version hypothesis was published in 1929. The main weakness in the initial version of the hypothesis was the absence of any description of forces capable of causing a continental drift. Later supporters of the hypothesis (Holmes 1925, 1930; van Waterschoot et al. 1928) proposed upper mantle convection as a possible cause of this drift. However, from the outset both the continental drift and the convection hypotheses faced virulent opposition from scientists in Europe and America. In Europe the strongest criticism of the continental drift hypothesis came from Lake (1922) and Jeffreys 1924, 1929 (see also Stewart 1990). Jeffreys remained opposed to the theory until 1970s (Jeffreys 1970; Stewart 1990).

The continental drift hypothesis was finally tested by European scientists and reported in 1923 (Stewart 1990) and in 1926 (van Waterschoot et al. 1928; Stewart 1990). In the US, opponents included such prominent geologists as Chamberlin (van Waterschoot et al., 1928), Bucher (1933), Simpson (1943), and Willis (1944). It should be noted that Bucher (1933) hypothesis about the geodynamic pulsation character of the Earth's evolution was theoretically supported by Aleinikov et al. (2001). Holmes (1930, 1931) was one of the first to accept the role of convection in continental drift. He suggested that the differential heating of the Earth's interior, generated by the decay of radioactive elements, caused the convection of the mantle, which generates forces sufficient to drag continents. However, his ideas failed to attract much support at that time (Hellman 1998; Hallam 1989; Oreskes 1999; Lewis 2002) and in fact faced strong opposition (Adams 1924; Jeffreys 1930). Adams (1924) tried to find the initial temperature of the Earth from its original molten condition, and showed that convection would continue until the crust cooled so much that either its viscosity would become so great that movement would be impossible, or it would become totally solid. He also compared the adiabatic temperature gradient of about 0.5 K/km, which is necessary for the crust to stay liquid, with the gradient necessary to keep viscosity constant ($\sim$1–10 K/km) and the gradient corresponding to the melting temperature of rocks ($\sim$2.5–5 K/km), and came to the conclusion that convection would cease from the bottom. He concluded that heat conduction was the key factor. However, other researchers continued to work on mantle cooling by convection (see for example Pekeris (1935), Hales (1936), Griggs (1939)). Apparently the theory of mantle convection was not initially accepted because it was associated with Wegener's continental drift hypothesis, which was initially rejected by virtually all scientists at that time.

The next key milestone in the evolution of geothermics was the recording of heat flow values in different areas. This took time, since to determine the heat flow density, both the geothermal gradient and heat conductivity of the same place need to be known (NRC 1964). Anderson (1934) made the first estimates of heat flow in

England from temperature gradients measured in boreholes and the thermal conductivity of the main rock sections. However, the first actual measurements of heat flow in continents were only reported in 1939 (NRC 1964; Stein 1995) by Bullard for South Africa (Bullard 1939) and Benfield (1939) for Great Britain. Davis and Elderfield (2005) note that Petterson (1949) was the first to measure the geothermal gradient in a sea, but that the heat flux in oceans was first measured by Revelle and Maxwell (1952) and Bullard (1954).

Tikhonov (1937) published results of fundamental research in which for the first time a full theoretical analysis of the thermal regime of Earth's crust was established for conditions with stationary and non-stationary thermal heat flow using layered models. In this article, a solution to the non-homogeneous stationary heat conduction equation for one- and two-layered models was used with the hypothesis that radioactive elements are concentrated in one or several layers near the Earth's surface. He also analyzed the problem of estimating the non-stationary component of temperature using his non-homogeneous non-stationary equation of heat conduction. Tikhonov's ideas were further developed by his disciple Lubimova (1953, 1955, 1958, 1967, 1968a, b). Most researchers at this time assumed (Condie 1981; Saltzman 1984) that conduction was the major means of heat transfer (Lubimova 1958; MacDonald 1959).

However, starting from the mid-1960s, most researchers began to consider the idea that thermal convection was the dominant mechanism of heat transfer in the interior of the Earth (Condie 1981; Saltzman 1984). This shift in perspective was prompted by the publications of Tozer (1965, 1967, 1972), Turcotte and Oxburgh (1967), Turcotte et al. (1973), Schubert et al. (1979) amongst others. At this point, though, researchers were still split between support for the main models of mantle convection (Basu et al. 1986; Anderson 1989; Christensen 1989; Wen and Anderson 1997; Schubert et al. 2001; Turcotte et al. 2001, etc.); namely whole mantle convection, or layered mantle convection. In addition, the subduction of slabs was now considered one of the main causes of cooling of the crust-mantle transition layer (see, for example, Kröner et al. 2001; Foulger and Jurdy 2007; Omori and Komabayashi 2007).

Thus, over the last 400 years, knowledge and understanding of geothermics has developed and expanded enormously.

1.2 Sources of Thermal Energy in the Earth's Interior

Flood basalts, volcanoes, hot springs, geysers, earthquakes, and many other such natural features point to the presence of significant amounts of heat energy in the interior of the Earth. This is clearly shown by the fact that temperature increases with depth. However, heat energy must have a source. This makes research on the sources of heat energy within the Earth crucial for investigating the evolution of the planet, its geothermal resources, the thermodynamic processes within the

planet, and many other processes taking place during the evolution of the Earth that rely on or are related to heat.

There is a general consensus that the main sources of heat energy on Earth are the release of gravitational energy during planetary accretion, gravitational energy during differentiation, the contraction of the planet and its separation into its core, mantle and crust, radioactive energy by short- and long-lived radioactive isotopes, the energy of solar radiation, energy from a possible collision between the Earth and a Mars-sized body, which could also have formed the Moon, lunar tidal energy, kinetic energy infalling cosmic objects (planetesimals, asteroids, comets, meteorites, etc.), and many other less powerful sources. At the same time, there are also different losses of energy. These include the constant radiation of heat by the Earth into outer space and escaping matter (e.g. hydrogen). Obviously the equilibrium of thermal energy on the Earth relies on the amount of heat generated from within the planet, received by the planet (from the Sun and falling objects), and lost by the planet. Depending on which outweighs the other, the planet is either in a process of heating or cooling.

The sources of heat energy on the Earth, as well as those of any other planet, can be divided into two groups: sources that generated heat energy in the past (accretion, overall differentiation of the planet, decay of short-lived radioactive isotopes) resulting in the accumulation of much of that energy within the planet, and sources of perpetual and ongoing generation of heat energy (radiogenic heat from the decay of long-lived radioactive isotopes, ensuing differentiation, tidal energy, chemical reactions, etc.).

The amounts of energy released by different features and processes over the course of the Earth's evolution estimated by different researchers are presented in Table 1.5.

No matter how you look at it, Table 1.5 clearly shows that the greatest amount of heat delivered to the Earth is from solar radiation. The second largest amount of heat was generated by the conversion of gravitational energy into heat during the accretion, differentiation, separation of the core, mantle and crust, and the contraction of the Earth. In order of descending magnitude the other sources of heat are the bombardment of the surface by cosmic objects after planetary accretion, the possible collision of Earth with a Mars-sized body with the subsequent formation of the Moon, and the decay of short-lived and long-lived radioactive isotopes. The other heat sources are much less important.

The main external source of thermal energy, solar radiation, is about 4,000 times greater than the heat flux from Earth's surface today (Sorokhtin and Ushakov 2002). Even though solar radiation is the greatest source of heat for the Earth, its role in heating the deeper layers is not clear, since the resulting changes in temperature take place only on a thin surface layer 0.9–1.2 m in thickness for daily variations, and about 18–21 m for yearly variations in temperature (see for example Lubimova 1968b). However, this heat does protect the Earth's interior from cooling rapidly, since the Earth's surface re-releases solar radiation rather than radiating significant amounts of its own energy. The fact that the Earth's surface temperatures in different regions are more or less stable shows that the heat

Table 1.5 Energy released by the main sources within the Earth (in Joules)

Source of energy	Energy released during the lifespan of the Earth, according to author						
	Monin (1977)	Adushkin and Vityazev (2007)[a]	Orlyonok (1980, 2000)	Sorokhtin and Ushakov (2002)	Sorokhtin and Ushakov (2002)[b]	Pollack (1997)	Hancock and Skinner (2000)
Accretion				2.32×10^{32}		2.24×10^{32}	2.49×10^{32}
Planet differentiation	1.61×10^{31}	1.5×10^{31}	$1.5–5 \times 10^{31}$	1.684×10^{31}			
Core separation				1.403×10^{31}		1.493×10^{31}	1.61×10^{31}
Bombard-ment		2.0×10^{32}					
Short-lived isotopes		10^{30}					
Long-lived isotopes	0.9×10^{31}	4.0×10^{30}	$(0.6–1.2) \times 10^{31}$	4.33×10^{30}	1.6×10^{30}		8.0×10^{30}[c]
Elastic contraction		10^{30}	1.2×10^{31}				
Tidal dissipation		10^{30}	3.6×10^{30}	$4–5 \times 10^{30}$	2.04×10^{30}		$2–3 \times 10^{30}$
Chemical reactions and phase transitions		10^{30}	1.7×10^{30}				
Solar radiation		2.5×10^{34}					
Collision with Mars-sized body						4.48×10^{31}	

[a] Energy released during first 500 Ma of the Earth's evolution
[b] Energy released during first 600 Ma of the Earth's evolution
[c] Radiogenic heat

from solar radiation, inconsistent since it depends on latitude, times of day and year, and weather conditions, is not substantial enough to heat the Earth's surface and upper layers.

The amount of gravitational energy released during the accretion of the Earth was so immense that if that alone were used to heat the Earth, the temperature of the planet would reach 30,000 K (Sorokhtin and Ushakov 2002), 35,000 K (Pollack 1997) or even 37,500 K (Schubert et al. 2001). Anderson (2007) also showed that temperatures in the upper mantle were in excess of the melting temperatures of rocks for most of the planet's accretion. However, most of this energy was radiated by the Earth out into space. Hills (1973) indicated that the maximum temperature of the Earth at the end of accretion would have been about 3,000 K. Calculations show (Safronov 1969; Safronov and Kozlovskaya 1977) that from the moment the accreting Earth reached about 10 % of its present mass, the temperatures at depths of about 1,000 km increased to those capable of melting its matter.

Estimates by Sorokhtin and Ushakov (2002) show that out of the gravitational energy generated during the accretion of the Earth (2.324×10^{32} J), about 2.00×10^{32} J were converted into heat, 1.929×10^{32} J of which were lost by the radiation of heat from the Earth. If we accept a period of 100 million years for the accretion of the Earth, such heat radiation would have a power of about 6.11×10^{16} J/s, which is about 1,420 times greater than that of the present heat flow from the Earth's surface (Sorokhtin and Ushakov 2002). They also estimated that the initial heat accumulated by the Earth was roughly 7.12×10^{30} J, and increased to about 1.674×10^{31} J by the end of the Archean, and gradually dropped to the Earth's current remaining accumulated heat energy of about 1.59×10^{31} J. This would mean that throughout its existence, the Earth has been heated on average by 1,650 K (Sorokhtin and Ushakov 2002), even though it has been cooling as of the Archean.

The energy released by the formation of the core was sufficient to raise the average temperature of the Earth by about 2,300 K (Birch 1965; Flasar and Birch 1973; Pollack 1997). Hancock and Skinner (2000) showed that almost all the gravitational energy in the formation of the core translated as heat energy and raised the Earth's temperature by about 3,000 K. Lubmiova (1968b) claimed that the heat energy released by short-lived radioactive isotopes (^{26}Al, ^{36}Cl, ^{60}Fe) would have been sufficient to melt the entire planet. Some estimates show that over the 4.6 Ga of the Earth's existence, the gravitational differentiation and decaying of long-lived radioactive elements has generated about 2.5×10^{31} J of heat energy (Monin 1977) accumulated inside the planet. Similar calculations by Lubimova (1968b) yielded a value of about 2.0×10^{31} J.

The magnitude of heat energy needed to melt the entire Earth is estimated to be on the order of about 3.2×10^{38} J (Lubimova 1968b; Monin 1977). Comparing this amount with the amount of heat collected by the Earth indicates that the Earth was never entirely molten (Lubimova 1968b; Monin 1977). It should be noted that Lubimova (1968b) came to this conclusion on the basis of a model of the Earth's formation introduced by Schmidt (1949), who argued that the Earth was formed from a cold cloud with no initial heat energy (Rezanov 2002). Estimates by

Sorokhtin and Ushakov (2002) showed that from the start of the Earth's formation until the beginning of the Archean, about 1.16×10^{30} J was released by radioactive isotopes, while during the Archean this source of energy generated about 1.67×10^{30} J of heat. They also claimed that the energy released by the gravitational differentiation of the Earth (1.685×10^{31} J), the decay of radioactive isotopes (4.33×10^{30} J), and tidal friction (2.24×10^{30} J) would have been enough to heat the entire Earth by 4,400 K (Sorokhtin and Ushakov 2002).

The possible collision of the Earth with a Mars-sized body would have vastly affected the conditions on and around the Earth, generating a mean temperature of over 4,000 K out to about 8 Earth radii, and in excess of 2,000 K out to about 20 Earth radii (Cameron 1997). Estimates by Stevenson (2008) also show that such an impact would have resulted in a mean rise in the temperature of Earth by 4,000 K, whereas others claim it would have led to an average temperature increase on the order of 7,500 K (Melosh 1990; Pollack 1997).

The amount of heat loss due to outward radiation by the Earth during the entire lifetime of the planet is evaluated to be about 0.45×10^{31} J (Monin 1977). Similar estimates by Lubimova (1968) yielded amounts no greater than about 0.74×10^{31} J. The heat radiated from the Earth's surface was estimated by Sorokhtin and Ushakov (2002) to have the power of about 3.39×10^{13} J/s, but to have been about 4.833×10^{14} J/s at the end of the Archean (about 2.7 Ga), and about 1.033×10^{14} J/s in the beginning of the early Proterozoic. The Earth radiated about 1.03×10^{30} J of thermal energy into space before the start of the Archean, 6.7×10^{30} J during the Archean, and 5.69×10^{30} J over the entire period since the end of the Archean (Sorokhtin and Ushakov 2002).

The differences in the modelling of temperature conditions of the formation of the Earth and the other planets and the objects in the Solar System depend on which model is selected for the origin of the formation of the Solar System. The model that assumes the simultaneous formation of the Sun and the other objects of the Solar System from same nebula would lead to high initial temperatures within the protoplanetary disk when the Earth and other planets began forming. By contrast, in the "cold" formation models of the Earth (for example Schmidt's 1949 hypothesis) the initial temperature within the nebula would have been very low. These different models of the Earth's formation are discussed in Sect. 1.1.

It should be pointed out that the most complete model from a thermal point of view is in fact Schmidt's (1949) cold model, which was further expanded by his followers E. A. Lubimova and V. S. Safronov. Of course, this does not mean that this model is the right one. Even the fact that the main components of the cosmogonic model developed by Safronov (1969) are now widely accepted does not mean that the model of the thermal evolution of Earth upon which it is based is correct.

According to Safronov's model (Safronov 1959, 1969) after the accretion of Earth, which took about 100 million years, the central layers of Earth had temperatures below 1,000 K, with a surface temperature of about 300–400 K, about 350–400 K at depths of 2,000 km, and a peak temperature of about 1,500 K at depths of 300–500 km. Later attempts to modernize Safronov's thermal model (Vityazev and Pechernikova, 1996) took into account the early differentiation of

Earth and led to a significant increase in the amount of heat initially accumulated, and hence to much greater temperatures in the center of the planet. The thermal model put forward by Lubimova (1968b) assumes that the Earth was initially cold and gradually heated during its evolution through the energy released by radioactive isotopes. The initial conditions for Lubimova's thermal model (Lubimova 1955) were temperatures of about 300–400 K in the center and near the surface of the Earth, with a maximum temperature of about 1,500–2,000 K at depths of 2,500–3,000 km.

The main problem with the cold Earth models is the fact that it would take a very long time for radiogenic heat sources to heat the Earth's layers to the melting point of rocks. Calculations by Lubimova (1968) showed that the temperature of the melting point of iron from radioactive heat generation could have been reached on the Earth during the first 0.5–1.0 billion years, and over a shorter period on the Moon. At the same time, similar calculations by Levin and Mayeva (1960) determined that up to 1.5–2.0 billion years would be necessary to accumulate enough radiogenic heat to melt silicates. Lubimova and Mayeva (1982) suggested that the released radioactive energy could have raised the Earth's temperature to about 2,273 K during the first few billion years, and continued heating it by a few hundred degrees every billion years.

However, the fact that the Moon was originally hot was one of the main reasons Rezanov (2002) claimed that Schmidt's hypothesis of an initially cold formation of the Earth was ultimately wrong. Numerous findings show that the Earth and Moon were initially hot. These include the partial melting of plagioclase on the Moon starting from 4.6 Ga (Hays and Walker 1975), the possible existence of a magma-ocean on the Moon at about 4.5–4.4 Ga (Warren 1990; Norman et al. 2003; Elkins-Tanton and Parmentier 2004; Boyet and Carlson 2007); the Hadean magma-ocean on the Earth (Ringwood 1960; Caro et al. 2005; Lee et al. 2006), calculations of the energetics of terrestrial accretion indicating that the Earth was extensively molten prior to 4.46 Ga (Caro et al. 2005), the presence of magmatic zircons dating back 4.4 billion years (Valley et al. 2005; Valley 2006), among others. These facts clearly show that gigantic amounts of melted matter existed on Earth and the Moon long before the energy released by radioactive elements could have melted these rocks and minerals. All these strongly suggest that the hypothesis of a cold origin of the Earth and the Moon should be rejected.

Nevertheless, there are models challenging the "hot" origin of the Earth and the Moon (Lewis 1974; Kaler 1994; Cameron 1995; Pollack 1997; Boss 1998; Willacy et al. 1998; Kaufmann and Freedman 1999; Humayun and Cassen 2000; Deming 2002, and many others). Some of these models show that the initial thermal conditions at a distance of the Earth from the Sun (1 AU) in the solar nebula were relatively high, about 650–700 K (Kaufmann and Freedman 1999), or 600 K (Kaler 1994) (see also Tables 1.3, 1.4). The calculations of the temperature in the solar nebula during planetary accretion 1 AU from the Sun in other models yield values as high as 900–1,400 K (Deming 2002) and 1,400 K (Humayun and Cassen 2000). Boss (1998) claimed that the temperatures within the inner part of the protoplanetary disk were in the range of 500–1,500 K for his model.

Analysis of type B coarse-grained calcium-aluminum-rich inclusions (CAIs), the oldest known remaining materials to have formed in the Solar System, shows that once their precursors condensed from the solar nebula, they were reheated to 1,523–1,723 K (Richter et al. 2006). Other evidence supporting the significant increase in temperature during planetary accretion is that meteorites of types 4–6 underwent heating of 900–1,300 K (Scott and Krot 2005). From all of the above, it seems incontestable that the hot origin of Earth is much more likely than the cold one, since the initial temperatures within the solar nebula before the start of accretion were already high.

Ascertaining how long it took for planetary accretion is crucial to determining the initial conditions of the Earth's evolution as a planet. Different models of planetary accretion suggest various time intervals for the accretionary process ranging from $\sim$1 to $\sim$100 million years (Lubimova 1968a, b; Safronov 1969; Halliday 2000; Anderson 2002a, b; Kleine et al. 2002; Valley et al. 2002; Walter and Trønnes 2004; Jacobsen 2005; Wood et al. 2006). Some models of a cold origin suggest an even shorter time frame for the formation of the Earth and the planets of about 10^5–10^6 years (Lubimova and Mayeva 1982). However, regardless of whether there was a rapid or relatively slow accretion, there is a general consensus that the energy released was sufficient to melt the entire planet. The release of the same quantity of energy over a different period of time results in different initial temperatures of the planetary matter at all depths within the planet, since during rapid accretion the amount of energy radiated out into space would be much smaller, and matter making up the planet would also be heated to much greater temperatures than during a period of relatively slow accretion. At the same time, in both cases the melting points of different rocks and minerals originally composing the planet at the end of the accretion period may correspond to the absolute minimum temperatures of the Earth's layers and its surface at that time. The real temperatures of the matter in these layers could have been much greater than their melting points, and would most certainly affect the cooling process of the planet after accretion. Higher initial temperatures would require a longer cooling time, and would take longer to reduce their temperature to equal or below their solidus temperature.

Studies have shown that at some point of its early evolution Earth was entirely covered by a magma-ocean (Ringwood 1960; Jeffreys 1962; Ohtani 1985; Spohn and Schubert 1991; Li and Agee 1996; Abe 1997; Pollack 1997; Righter and Drake 1997b; Solomatov 2000; Sleep et al. 2001; Sukumaran 2001; Rubie et al. 2004; Walter and Trønnes 2004; Valley et al. 2006; Labrosse et al. 2007; etc.), which was up to 1,000 km deep (Ohtani 1985; Labrosse et al. 2007) or even deeper (Righter and Drake 1997b; Rubie et al. 2004). Some scientists believe that such a magma-ocean could have only existed for about 1–10 million years (Spohn and Schubert 1991) or less (Davies 1990; Franck 1992; Sleep et al. 2001). Davies (1990) argued that the solidification of a thin surface layer of the magma-ocean would only take a few years. However, other authors believe that this magma-ocean could have remained for 100–200 million years (Abe 1997; Pollack 1997) and even longer (Solomatov 2000).

The estimated surface temperature of the magma-ocean (Abe 1997) varies from 1,500 to 4,700 K, depending on the density of the nebula, the abundance of dust grains, and the chemical interaction between material at the surface of the proto-Earth and the atmosphere. Brown and Mussett (1993) also showed that the initial temperature of the Earth's surface would have been very high and that the surface temperature of the magma-ocean could have reached a few thousand degrees Kelvin. The maximal temperature estimates of the Earth's surface immediately after accretion may have been much higher (Pollack 1997). In addition, the heat from short-lived radio-isotopes alone could have generated a surface temperature in the range of 1,200–1,700 K (Pollack 1997).

Safronov (1978) and Kaula (1979) emphasized the important role of the impact of large bodies in heating the upper layers of the Earth (to a depth of up to 1,200 km) to the melting point during the last stage of the Earth's formation (Safronov 1978). It is generally accepted that the inner planets of the Solar System experienced heavy bombardment by debris during planetary formation, which lasted from $\sim$4.5 to 3.8 Ga (Lubimova 1968a; Kaula 1979; Lubimova and Mayeva 1982; Chyba 1990; Tonks and Melosh 1993; Abe 1997; Righter and Drake 1997b; Bennett et al. 2004; Anderson 2007), and could have led to additional heating of the Earth's crust and mantle, as well as the formation of local magma-oceans. Some evidence derived from lunar rocks also points to intense 'late heavy bombardment' at about 3.85–3.9 Ga (Koeberl 2006; Marty and Meibom 2007). This suggests that during the Hadean and the beginning of the Archean, the surface temperature of the Earth was very high and the surface was made up of either a planet-wide ocean or local oceans of magma for a significant part of these time periods. Vacquier (1998) suggested that events such as runaway accretion, the formation of the Moon, and the impact that tilted the Earth's axis of rotation could possibly have created conditions such that the Earth could have melted and solidified three times.

Results (Pilchin and Eppelbaum 2008a, b) show that during the formation of the magma-ocean, the melts formed stratified magmatic layers in ascending order of their density and iron content. This differentiation of the Earth's layers began with the start of planetary accretion and continued until the solidification of the magma-ocean. Anderson (1989, 2006, 2007) also reported on the differentiation and stratification of rocks within the magma-ocean.

1.3 Initial Surface Temperature of the Earth

Most scientists agree that even though at some point the Earth was covered by a magma-ocean, it cooled fairly quickly in terms of geological time. Some authors suggest that the Earth was cold even in the Hadean (Mukhin and Pimenov 2002) and that it is even possible that Earth's surface was frozen at $\sim$4.6 Ga (Mukhin and Pimenov 2002). Certain other investigators think that the Earth's internal heat sources could not have maintained its surface temperature for any significant

Table 1.6 Estimates of the Earth's surface temperature in the early and middle Precambrian

Time (Ga)	Surface temperature (K)	References
4.4	$<\sim 473$	Valley et al. (2002)
3.5–3.2	343 ± 15	Lowe and Tice (2004)
After 2.9	<333	Lowe and Tice (2004)
During the pre-Archean	573 ± 100	Valley et al. (2006)
Late Archean–early proterozoic	30 K less than now	Eyles and Young (1994)
3.5–3.2	328–358 (ocean water)	Knauth (2005), Knauth and Lowe (2003)
Most geological time	5 K higher than now	Kuhn et al. (1989)
Archean hydrosphere	343	Lambert (1982)
~0.2 after the Earth's formation	~373	Mackenzie (1998)
4.3	373	Morse and Mackenzie (1998)
3.8	343	Morse and Mackenzie (1998)
4.2	373	Mojzsis et al. (2001), Sleep et al. (2001)
Hadean	90 % of surface <0	Mukhin and Pimenov (2002)

period of time. For instance, Sleep et al. (2001) believe that the available internal heat within the Earth could have maintained surface temperature conditions of about 373 K for at most several million years and more likely for much less than 1 million years. Some examples of estimates of the Earth's surface temperature in the early Precambrian are presented in Table 1.6.

Most scientists agree that the initial surface temperature of Earth right after accretion and the rate of its cooling depend to a great extent on the thickness of the early Earth's atmosphere. The devolitalization and rise in temperature associated with impacts generated a hot, dense atmosphere that served to trap solar radiation and maintain a very hot surface temperature by insulating it from outer space (Anderson 2007). Pollack (1997) showed that the massive proto-atmosphere formed during the Earth's accretion, which was mostly composed of water vapor could have created a surface temperature in the range of 1,200–1,700 K. The Abe and Matsui (1985) model predicted that the Earth accreted from the mass of the Moon to its present mass with a ~1,500 K molten H_2O-rich basalt surface layer. In the case of a blanketing effect of the atmosphere, the estimated surface temperature of the magma-ocean could have exceeded 2,100 K (Abe 1997). Other researchers suggest that the lack of craters on the Earth's surface can be explained by the disintegration of falling bodies that contributed to its extremely dense and thick atmosphere (e.g., Rezanov 2002). Results of numerous studies show that Earth preserved part of its hydrogen layer after accretion (Marakushev 1999; Rezanov 2002; Voytov 2002; Gilat and Vol 2005), which is supported by the ongoing escape of hydrogen from great depths even today (Voytov 2002; Gilat and Vol 2005); the same can also be said of helium (Gilat and Vol 2005).

A number of other studies also point to the possible presence of significant amounts of hydrogen in deep layers of the Earth and especially in the core (Yagi and Hishinuma 1995; Okuchi 1997, 1998; Williams and Hemley 2001; Antonov et al. 2002; Ohtani et al. 2005; Righter et al. 2006). Since it is well known that hydrogen, helium and water have the greatest specific heat capacities of all the elements and compounds on Earth at 14.304, 5.193, and 4.187 kJ/(kgK) respectively (e.g., Lide 2005), it is self-evident that such a thick atmosphere could contain gigantic amounts of heat and still keep the average temperature of the atmosphere relatively low and at the same time prevent a rapid loss of heat by radiation. This also implies that the escape of substantial amounts of hydrogen from the Earth would result in a significant heat energy loss. Given that heat capacity increases sharply with increases in temperature (Lide 2005; Gilat and Vol 2005), it can be surmised that the amount of heat stored by the thick early atmosphere of the Earth could have been simply gigantic (see for example Table 3 in Gilat and Vol 2005). The composition and possible P-T conditions in the early Earth's atmosphere will be discussed in Sect. 2.8.

The results of reverse-integrating (Korenaga 2006) a global heat balance equation (Christensen 1985) from the present-day mantle temperature of 1,623 K with the Urey ratio of 0.15–0.3 and activation energy of 300 kJ/mol shows that the internal temperature quickly rises and diverges toward infinity before reaching 2 Ga (Korenaga 2006). This paradox in reconstructing Earth's cooling history is known as the 'thermal catastrophe' and is related to the belief that mantle temperatures were lower than about 2,073 K in the Archean (Korenaga 2006), even though clear-cut data such as the widespread formation of significant amounts of komatites in the Archean characterize the conditions at the time, with temperatures during their formation of about 2,073 K for dry melting and about 1,773 K for wet melting (Grove and Parman 2004). At the same time, the 'thermal catastrophe' places certain limitations on the role of convection in the thermal evolution of the mantle.

1.4 Heat Flow from the Sun and Heat Radiation

Most of the energy received by the Earth is radiant heat energy from the Sun. Almost all of the radiation of the Sun that reaches the Earth is reflected or re-radiated by the Earth's surface and the atmosphere. The best indication of this process is the average annual temperatures in different places, which are more or less stable over geological scale time intervals. There are daily and yearly fluctuations of temperature which take place over a thin layer at the surface, at a thickness of about 0.9–1.2 m for daily fluctuations, and about 18–21 m for yearly fluctuations (e.g., Lubimova 1968b). However, at greater depths the temperature remains practically unchanged (is constant for long periods of time) and is independent of the changes taking place on the surface under the influence of solar radiation although the average temperature of the Earth's surface is determined primarily by the Sun's radiation. This means that the Sun's radiation is neither

capable of heating the deeper layers of the Earth nor raising the Earth's surface temperatures for significant periods of geological time.

It should be pointed out that the solar constant has a magnitude of 1.37 kW/m^2 according to the ISO standard, and 1.35 kW/m^2 according to the CIE standard (Benenson et al. 2002). Other sources assign the power of solar radiation (solar irradiance) a value of 1,366.1 W/m^2 (Tobiska and Nusinov 2000), and 1,367 W/m^2, or 342 W/m^2 when averaged over the entire surface of the Earth, including the dark side (Hancock and Skinner 2000). However, the value for the solar constant used in this book, as calculated by the authors, is 1,389.8 W/m^2. The slight difference in the values of the solar constant has to do with methods of calculation; i.e., using curved area corresponding to the sphere with a radius the distance between Earth and the Sun (1 AU) rather than the area (πR^2) of Earth's cross-section straight through its center.

Numerous researchers have discussed the so-called "faint young Sun paradox" (Sagan and Mullen 1972; Newman and Rood 1977; Gough 1981; Lenton 1998; Shaviv 2003, and many others). These studies suggest that the young Sun had a luminosity that was 25 % (Newman and Rood 1977; Sagan and Chyba 1997; Lenton 1998) to 30 % (Sagan and Mullen 1972; Shaviv 2003) lower than at present. This theory attempts to account for the apparent contradiction between investigations indicating the presence of liquid water early in the Earth's history, and the prediction that the Sun's output was only 70–75 % as intense during the early Earth's evolution as it is now. For such low brightness at about 4.0–4.5 Ga, if we were to use the present concentration of the content of greenhouse gases in Earth's atmosphere at that time, any liquid water exposed to the surface would simply freeze, but there are no signs of glaciation in that era. This is important to point out since the greenhouse effect is what is usually cited to explain this paradox (Newman and Rood 1977; Walker 1985; Sagan and Chyba 1997; Pavlov et al. 2000; Shaviv 2003). Issues concerning the thermal characteristics of terrestrial planets as they relate to the greenhouse effect are discussed in detail in Bennett et al. (2004), along with estimates of 'no greenhouse' average surface temperatures, actual average surface temperatures, and global warming due to the greenhouse effect.

It is obvious that for the cooling of the Earth's surface and its upper layers to take place, a significant amount of heat energy must have been removed or transferred away. In physics, there are only three main kinds of heat transfer: heat conduction, heat convection, and heat radiation. In the case of the Earth's upper slabs, the rocks composing them have very small heat conduction coefficient values; therefore only convection (in the atmosphere, the ocean, or circulating underground waters) and heat radiation could provide a significant mode of heat transfer. At the same time, each planet is isolated from the other matter making up the Solar System by space, which does not contain any matter capable of supporting either the transfer or the convection of heat away from Earth. This implies that the only ways for the Earth to give off heat energy is through heat radiation and the escape of some matter from the Earth, such as hydrogen. Since hydrogen can absorb significant amounts of heat (its specific heat capacity is $\sim$14,300 J/(kg K),

see Sect. 1.2), it could have been a very important agent of heat escape after the decomposition of water from UV rays and certain other causes (Kasting and Donahue 1981; Zahnle et al. 1988).

Processes related to heat radiation from the Earth's surface have been studied extensively (Chandrasekhar 1935; Lubimova 1968b; Kappelmeyer and Hänel 1974; Davies 1980; Barkstrom and Smith 1986; Ramanathan et al. 1989; Kaufmann 1994; Loaiciga et al. 1996; Kaufmann and Freedman 1999; Sertorio and Tinetti 2001; Sleep et al. 2001; Bennett et al. 2004; etc.). Typically authors (Chandrasekhar 1935; Barkstrom and Smith 1986; Ramanathan et al. 1989; Sertorio and Tinetti 2001; Sleep et al. 2001; etc.) use the Stefan-Boltzmann law for a black body to analyze the cooling process of the Earth's surface and upper layers. This analysis indicates that their rate of cooling is either fast or very fast in terms of geological time. To investigate problems of heat radiation, the values of heat energy radiated by some planets and the Moon were calculated using known astronomical and physical parameters, and constants published in (Kaler 1994; Kaufmann 1994; Kaufmann and Freedman 1999; Bennett et al. 2004; etc.), and are presented along with certain parameters and constants in Tables 1.7 and 1.8. Table 1.7 shows the results of thermal radiation calculations for terrestrial planets using the Stefan-Boltzmann law along with related characteristics, and the thermal radiation, and the corresponding characteristics for the Moon are presented in Table 1.8.

First, to avoid the influence of the greenhouse effect, we analyze the thermal radiation processes on Mars, Mercury and the Moon, which have no atmosphere or a negligible atmosphere in the case of Mars. Table 1.7 shows that there are clear-cut difficulties in applying the Stefan-Boltzmann law. Since Mercury does not have a real atmosphere, there is no likelihood of observing a greenhouse effect, yet the radiation from its surface on its day side is even more powerful than the Sun's radiation reaching Mercury's orbit. At the same time, the radiation from its night side is so low that this vast difference between the two cannot be accounted for by Mercury's internal heat flow. Astoundingly, Mercury's average surface temperature is $\sim$100 K on its night side and $\sim$700 K on its day side (Bennett et al. 2004). It is obvious that the solar radiation energy first has to heat up the planet's surface on its day side by $\sim$600 K, at which point the rest of the solar energy that is not reflected would be absorbed and re-radiated from Mercury's surface into space. In other words, after reflection of part of the solar radiation, the remaining energy is spent on drastically heating Mercury's surface, which would be accomplished in a very short span of time since the Sun's radiation at that distance is considerable. However, when using the Stefan-Boltzmann law to calculate the radiation emitted by Mercury and that of the Sun to Mercury's orbit, the results indicate that the radiation from Mercury is significantly greater than that of the solar radiation. The ratio of the energy radiated by the Sun onto Mercury to the energy radiated by Mercury's day-side is 0.303 (see Table 1.7). This certainly seems strange.

Similarly, if we accept that the Moon emits heat from an area of $2\pi R^2$ representing its day side, as well as from the same area representing its night side, but that the Sun's radiation only affects an area of πR^2, a value that should be further

Table 1.7 Thermal radiation of terrestrial planets and related characteristics calculated using the Stefan-Boltzmann law for a black body

Name	Radius (km)	Distance from Sun (10^6 km)	Sun's radiation at planet orbit (W m^{-2})	Planet's radiation (W m^{-2})	Ratio of Sun's radiation to planet's	Planet's albedo (%) (after Bennett et al. 2004)	Real Sun's radiation at planet's orbit[b] (W m^{-2})	Real ratio of Sun's radiation to planet's[b]	Ratio of real Sun's radiation to 4 times ($4\pi R^2$) of planet's radiation
Mercury									
Day side	1,440	57.9	9,278.3	13,613.7	0.682	11	8,257.7	0.607	0.303[a]
Night side				5.67					
Venus	6,051	108.2	2,656.9	17,002.4	0.156	72	743.9	0.044	0.011
Earth	6,378	149.6	1,389.8	401.0	3.466	36	889.5	2.218	0.445
Mars									
Average			598.9	188.1	3.184	25	449.2	2.388	0.597
Max	3,397	227.9	598.9	417.88		25	449.2	1.075	0.537[a]
Min			598.9	17.74					

[a] Value calculated for a planet's radiation from day side only (half of a planet's surface area, $2\pi R^2$)
[b] Takes into account the albedo (reflectivity) effect

Table 1.8 Thermal radiation and related characteristics of the Moon, calculated using the Stefan-Boltzmann law for a black body

Characteristic	Value
Closest distance from Sun	149,215,600 km
Farthest distance from the Sun	149,984,400 km
Average distance from Earth	384,400 km
Albedo (reflectivity)	7 %
Temperature of day side	125 °C (398 K)
Temperature of night side	−175 °C (98 K)
Radius of the Moon	1,738 km
Moon's radiation from day side	1,422.7066 W m^{-2}
Moon's radiation from night side	5.229827 W m^{-2}
Sun's radiation at closest distance to the Moon	1,396.97 W m^{-2}
Sun's radiation at farthest distance from the Moon	1,386.24 W m^{-2}
Real (average) Sun's radiation on the Moon including reflectivity	1,294.10 W m^{-2}
Earth's radiation on the Moon's orbit	0.11 W m^{-2}
Ratio of real Sun's radiation to 2 times the Moon's day side radiation	0.455

reduced by the Moon's albedo (7 %), it would seem that the Moon emits heat energy 2.22 times greater than the amount it absorbs from the Sun (see Table 1.8). However, this is impossible since the values of heat radiation from the night side of the Moon show that it does not have sources of heat capable of strong radiation. Even the difference of 128.61 W m^{-2} between the Moon's radiation from its day side (Table 1.8: 1,422.71 W m^{-2}) and the Sun's radiation of the Moon with reflectivity taken into account (Table 1.8: 1,294.10 W m^{-2}) cannot be accounted for by the Moon's internal sources of heat. This would suggest that the Stefan-Boltzmann law of radiation for a black body cannot be applied to the Moon or to Mercury. The ratio of the energy radiated by the Sun on the Moon to the energy radiated by the day side of the Moon is 0.455 (see Table 1.8). Nevertheless the results show that this is incorrect and that the Stefan-Boltzmann law does not apply here.

There is also a problem with the ratio of the Sun's radiation to the radiation of other terrestrial planets (see Table 1.7). The ratio of the energy radiated by the Sun onto Mars to that radiated by the day side of Mars is 0.537. The ratios for Earth and Venus are 0.445 and 0.011, respectively. To equilibrate these values, the average temperature of the Earth's surface would have to be ∼266 K, and Venus's surface would need to be ∼465.1 K. Clearly, that these values conflict with the actual average surface temperatures for Earth and Venus, which are 288 and 743 K (Bennett et al. 2004), respectively. Hence the Stefan-Boltzmann law does not work in these cases either. However, in the case of the Earth and Venus, scientists usually explain such discrepancies between the solar and planetary radiations by the greenhouse effect, since both Venus and Earth have an atmosphere. If we accept that both Earth and Venus have ongoing greenhouse effects, and the Earth's surface temperature is less than that expected for equilibrium with the Sun's

radiation, the greenhouse effect accounts for this by adding the temperature difference. We can then expect the greenhouse effect on Venus to do the same and supplement the temperature difference. However, the surface temperature of Venus is already much greater than that required to achieve this equilibrium with the Sun's radiation. This is a major contradiction, since if these discrepancies were caused by the greenhouse effect it should indeed have the same effect of increasing the temperature on both planets.

Venus is cooling the fastest of all the terrestrial planets, because the ratio of the Sun's radiation striking the planet to four times Venus's radiation (in terms of total surface area) is the smallest of all the planets. It is also evident that in the past, when Venus had a much higher surface temperature, the cooling rate was much greater. However, if that were the case, why has Venus not yet cooled and is still very hot? All these facts show that the Stefan-Boltzmann law should not be used for terrestrial planets. In other words, if the question is 'does the planet's surface radiate heat?' the answer is of course yes, but if the question is 'does this radiation satisfy the Stefan-Boltzmann law?' the answer would have to be 'no'.

A number of definitions and formulas in physics can help clarify this problem. Marshall et al. (1967, p. 445) defined a black body in the following way: "In considering radiant heat, a perfect absorber, i.e., a surface that absorbs all the radiation falling on it, whatever the wavelength, is called a 'black body'." In terms of the Kirchhoff and Stefan-Boltzmann laws of radiation, Marshall et al. (1967, p. 448) state: "It is perfectly true to say that $e_{BB} \propto \theta^4$, it is not necessarily true that $e \propto \theta^4$ for anybody at all." Here, e stands for the radiation per unit area per unit of time, e_{BB} is the radiation per unit of area per unit of time for black body, and θ is the temperature (Marshall et al. 1967).

A comparison of the intensity of sunlight over a wide range of wavelengths with the intensity of radiation of a black body at a temperature of 5,800 K shows (see Fig. 5–9 in Kaufmann 1994; Fig. 5–11 in Kaufmann and Freedman 1999) that both curves on the graph are very similar, but there are some differences, mostly for wavelengths smaller than 1 μm. The Sun's intensity is lower for these wavelengths than that of the black body, except for a portion of the visible light spectrum, but the intensity of the black body over a large range of wavelengths is significantly greater for wavelengths shorter than visible light. This means that even using the Stefan-Boltzmann law for sunlight can lead to significant errors in estimating the Sun's radiation intensity and its energy over a long period of time. Consequently, the Sun itself can be defined as a black body with significant model-specific approximations. Therefore, it would be a mistake to view the Earth or Venus, which reflect 36 and 72 % of radiation, respectively, as black bodies. Kaler (1994) also argued that neither stars nor planets are perfect black bodies. All of the above shows that statements suggesting that in Kirchhoff's Law of spectral analysis ($q = \varepsilon\sigma T^4$, where q is the radiating energy, ε is emissivity, σ is the Stefan-Boltzmann constant, and T is temperature in degrees Kelvin), emissivity ε is very close to 1 (Sertorio and Tinetti 2001) should be considered false. Hence the Stefan-Boltzmann law can only be used for extremely rough estimates of surface temperature, which in no way should be used as the foundation for any hypothesis or

theory. The major problem this creates when estimating the cooling rates of a planet's surface is that since estimates for any given moment are erroneous, any estimate made for a prolonged period of time will drastically increase the magnitude of error.

When considering heat radiation from the surface of a planet, it is important to keep in mind that if the radiation is greater than that received by the planet from the Sun (see Table 1.8), there must be a mechanism of heat transfer from the planet's interior to the surface which accounts for the difference. In the case of the Earth, it is clear that conductive heat transfer could not support such significant heat loss, as suggested in Table 1.7. Thus the cooling of Earth's surface during its early evolution must have been much slower than the results calculated using the Stefan-Boltzmann law or Kirchhoff's law of radiation.

During accretion, planetesimal collisions and differentiation, the temperature of Earth was rising and the planet was possibly completely or almost completely molten, which also resulted in the formation of Earth's iron core as the dense iron sank to the center. Over the course of the Earth's evolution as a planet, there were different sources of heat (bombardment of the surface by heavy bodies, radioactive decay, solar radiation, etc.), as well as sinks of heat (heat radiation and escape of light elements, especially hydrogen). It should be stressed that heat radiation did and does act, but it does not correspond to the Stefan-Boltzmann law. Because the ancient atmosphere of the Earth was even denser than the present atmosphere of Venus, it is obvious that the reflection of the Sun's radiation by the early Earth's atmosphere could have been even greater than it now is on Venus (>72 %). Hence the early Earth was very different indeed from a black body, and therefore the Stefan-Boltzmann law cannot be used to estimate the cooling rate of the early Earth. At some point in its evolution, the Earth was covered by a magma-ocean hundreds of km deep. At that time, the main sources of energy were the radioactive decay of long-lived radioactive isotopes and radiation from the Sun. The atmosphere began to play an increasing role in the Earth's cooling, which itself cooled down first before proceeding to cool the Earth's surface. The cooling of the atmosphere is also a result of heat radiation and the escape of light elements.

One of the most famous applications of the heat radiation is the 'greenhouse effect' theory, which was developed to explain the difference between the expected temperatures of the Earth's surface calculated using the Stefan-Boltzmann law and the actual measured temperatures of the surface. Since it was shown above that the Stefan-Boltzmann law cannot be used for the terrestrial planets or the Moon, the expected temperatures calculated using this law may be incorrect. Certain other publications (see, for example, Gerlich and Tscheuschner 2009) also show that the Stefan-Boltzmann law is not applicable to the Earth.

Thus overall, the Stefan-Boltzmann law cannot be applied to the terrestrial planets or the Moon and the fundamentals of the greenhouse effect need to be revised (see also Gerlich and Tscheuschner 2009).

1.5 Geothermal Gradient

The temperature regime of sedimentary formations is influenced by many topographical and geological factors (constant terrain, sedimentation, erosion, lateral conductivity contrasts, underground water movement), past climate, and by the heat flow from the Earth's interior which is known as the terrestrial heat flow. As a result, the formula for the temperature field of formations is time (t) dependent and three dimensional,

$$T = T(x, y, z, t). \tag{1.5.1}$$

The time dependence of the temperature is mainly caused by changes in the Earth's surface temperature conditions (past climate) or by the changes in the value of the terrestrial heat flow (q). Calculations based on several models of the Earth's thermal history have shown that for the crust, the value of q has hardly changed over several million years. The impact of the past climate on the subsurface temperatures is usually limited to several hundred meters. Thus, for deep depths (>300–500 m) we can assume that

$$T = t(x, y, z). \tag{1.5.2}$$

Most temperature surveys are conducted in boreholes. The total vertical depth of the boreholes (<10 km) is small in comparison to the radius of the Earth (6,371 km) and for this reason the curvature of the Earth's surface can be neglected.

It is known that the formation temperature increases with depth. The temperature only reduces with depth in some offshore-onshore transition areas and permafrost regions at shallow depths (several hundred meters). The rate of the temperature increase is determined by the geothermal gradient (Γ). In the general case the geothermal gradient has three components,

$$\Gamma = \sqrt{\Gamma_x^2 + \Gamma_y^2 + \Gamma_z^2}, \quad \Gamma_x = \frac{\partial T}{\partial x}, \quad \Gamma_y = \frac{\partial T}{\partial y}, \quad \Gamma_z = \frac{\partial T}{\partial z}. \tag{1.5.3}$$

For several (N) layers with negligible heat production, the geothermal gradient—the coefficient of thermal conductivity product is a constant,

$$\lambda_1 \Gamma_1 = \lambda_2 \Gamma_2 = \cdots = \lambda_N \Gamma_N \tag{1.5.4}$$

and low values of the geothermal gradient correspond to high thermal conductivity formations (Fig. 1.2).

In some cases is convenient to use the reciprocal of the geothermal gradient parameter—geothermal step $C = 1/\Gamma$. The change of the geothermal step with the depth for one wellbore is shown in Fig. 1.3.

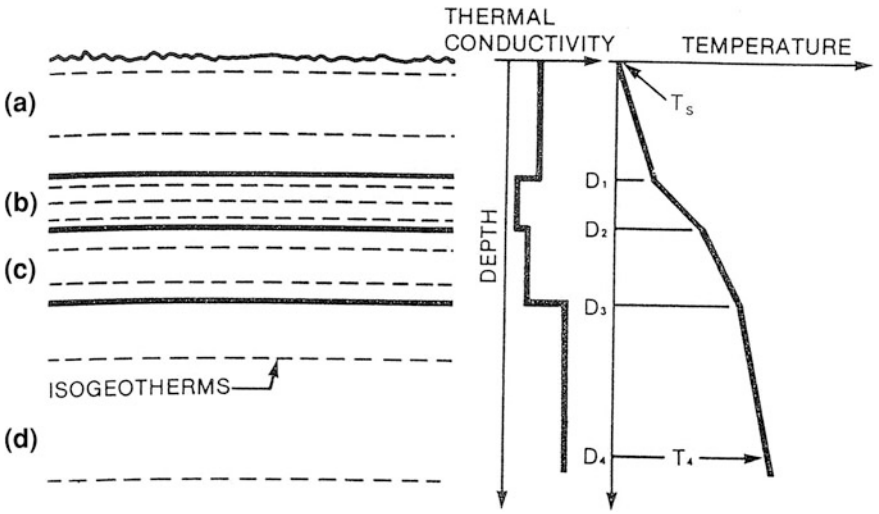

Fig. 1.2 Isogeotherms and formation temperature/depth profile in a hypothetical rock sequence (after Jorden and Campbell 1984)

1.5.1 Conductivity Contrasts

Consider a region of flat relief with a constant heat flow density q. When the lithological profile of a wellbore consists of n uniform horizontal layers, the formation temperature will be a function of the vertical depth alone. The geothermal gradient for any formation layer (Γ_n) can be calculated from the formula: $\Gamma_n \cdot \lambda_n = q$.

Let us assume that the area of the given region is A; then the total amount of heat per unit of time transferred to the Earth's surface will be $Q = Aq$. Suppose now that near the wellbore a body of anomalous thermal conductivity such as a salt dome was discovered. In this case an increase in the heat flow density (HFD) above the salt dome will occur. At the same time a corresponding reduction of HFD will occur at some distance from the salt dome (Fig. 1.4).

It is clear that the presence of a salt dome can only change the temperature field of formations but the value of Q will remain constant. The effect of lateral thermal conductivity contrasts due to the impact of the anomalously high thermal conductivity of rock salt on the temperature field of formations near salt domes has been discussed in the literature (Guyod 1946; Kappelmeyer and Hänel 1974; Cheremensky 1977; Gretener 1981). The value of HFD in salt domes and salt anticlines is high and causes anomalously high temperature gradients (Fig. 1.5).

Guyod (1946) showed that the temperature gradients can reach 0.072 °C/m over the Humble dome (Texas, USA) with salt at 380 m. Gradients from 0.067 to 0.100 °C/m (2–3 times the regional average) were recorded in diapiric salt at 150–250 m below the sea floor (Gretener 1981). Interesting results based on

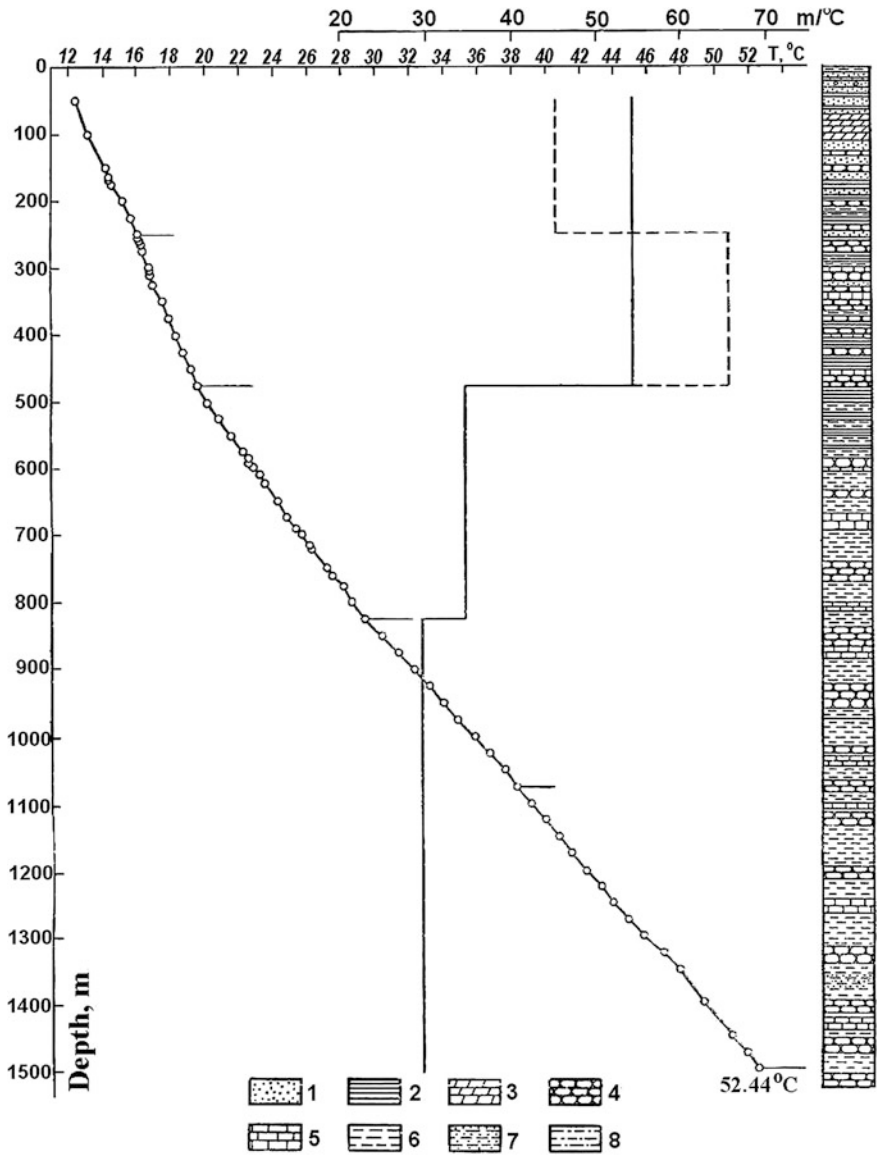

Fig. 1.3 Temperature profile and geothermal step, Well #1, Poltava region, Ukraine (Lubimova et al. 1964). (*1*) sand, (*2*) clay, (*3*) marl, (*4*) sandstone, (*5*) chalk and limestone, (*6*) shale, (*7*) siltstone, (*8*) claystone and shale

numerical modeling were presented by Gretener (1981). He calculated the anomalies of the geothermal gradient and temperature at 150 m below the surface (at different distances from center of the salt dome) for salt rising from 13 km to

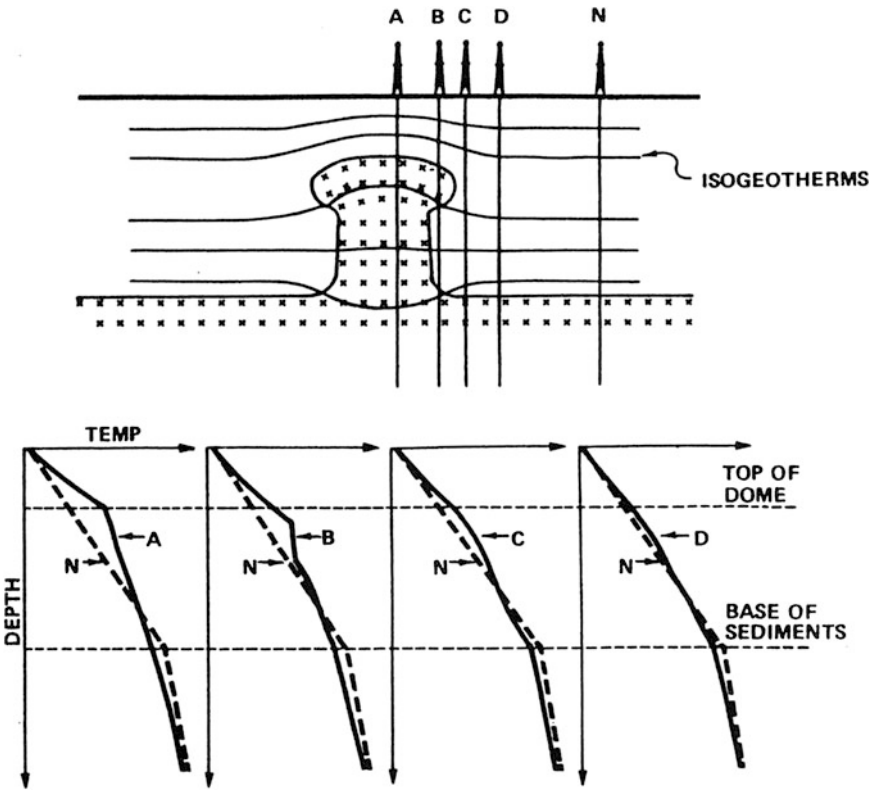

Fig. 1.4 Temperature-depth profiles near a salt dome (after Guyod 1946)

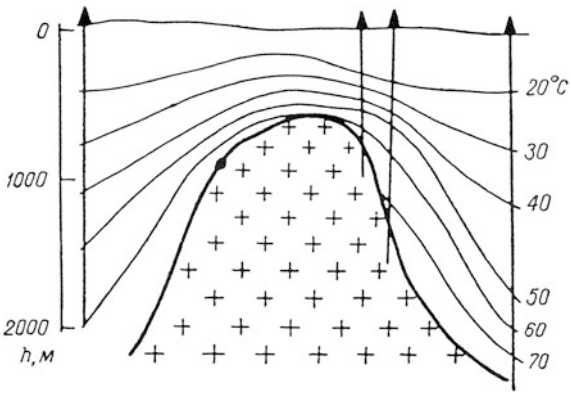

Fig. 1.5 Isogeotherms near a salt dome (after Cheremensky 1977)

various depths. The strong dependence of thermal conductivity on temperature (depth) was taken into account in the calculations. The well-known solutions (Carslow and Jaeger 1959) for a spherical, cylindrical, or an ellipsoidal body of

thermal conductivity λ^* immersed in a medium of thermal conductivity λ, in which the undisturbed geothermal gradient is Γ, can often be used for crude estimates of the effect of the lateral thermal conductivity contrasts on a reservoir's temperature field. Below we present solutions for two cases.

The region within the sphere $0 \leq r < a$ (radius of the sphere) has a conductivity λ^* and the region outside has a conductivity λ. The temperature T tends to $T_0 + \Gamma z$ at great distances. The temperatures T^* inside, and T outside the sphere are

$$T = T_0 + \Gamma z + \frac{\Gamma a^3(\lambda - \lambda^*)z}{r^3(2\lambda + \lambda^*)}, \tag{1.5.3}$$

$$T^* = T_0 + \frac{3\Gamma\lambda z}{2\lambda + \lambda^*}. \tag{1.5.4}$$

The cylinder $0 \leq r < a$ has a conductivity λ^* and its axis is perpendicular to the z-axis. The region outside has a conductivity λ and a temperature $T_0 + \Gamma z$ at great distances. The temperatures T^* inside and T outside the cylinder are

$$T^* = T_0 + \frac{2\Gamma\lambda z}{\lambda + \lambda^*}, \tag{1.5.5}$$

$$T = T_0 + \Gamma z - \frac{\Gamma a^2(\lambda - \lambda^*)z}{\mathrm{r}^2(\lambda + \lambda^*)}. \tag{1.5.6}$$

1.5.2 *Effect of Non-uniform Surface Temperature on Temperature Profiles*

Observed temperature profiles may be altered by the nonuniform surface temperature effect. Such effects occur for instance when the drilling sites of boreholes are located within or near deep lakes. To calculate these effects a method based on the utilization of the Laplace equation with nonuniform boundary conditions was developed (Balobaev et al. 2009). This method makes it possible to estimate the maximum effect of deep lakes on the borehole temperature profiles. It can be assumed that the lake (or another disturbing quasi-constant factor) has existed for an infinitely long period of time. In this case the solution to the Laplace equation with nonuniform boundary conditions can be used to describe the steady temperature field of formations beneath the lake and estimate the maximum effect (based on the assumption that the lake has existed for an infinitely long period of time) of lakes on borehole temperature profiles. This method is presented in detail in Sect. 11.3.

Table 1.9 Calculation of heat flow density (HFD), drill site WSR-1 at Woodside, on the Colorado Plateau (after Bodell and Chapman 1982)

Depth interval	Thermal gradient	Sample type	Thermal conductivity	HFD	Mean value
45–105	15.0 ± 1.0	Core	3.96 ± 0.23	60 ± 5	
105–245	18.0 ± 1.0	Core	3.43 ± 0.15	62 ± 4	
245–320	24.8 ± 0.7	Core	2.75 ± 0.14	68 ± 4	65 ± 4
320–455	16.0 ± 0.4	Core	4.18 ± 0.15	67 ± 3	
455–515	17.2 ± 0.5	Core	4.20 ± 0.14	72 ± 3	
515–575	16.5 ± 0.6	Core	3.86 ± 0.09	64 ± 3	

Depth interval in m, gradient in mK m^{-1} , conductivity in W m^{-1} K^{-1} , heat flow density in mW m^{-2}

1.6 Density of Heat Flow

The value of the heat flow density (HFD) determines the amount of heat per unit of area and per unit of time which is transmitted by heat conduction from the Earth's interior. For isotropic and homogeneous formations where the coefficient of thermal conductivity (λ) is a constant, the value of HFD can be calculated from the Fourier's law:

$$\mathbf{q} = -\lambda \operatorname{grad} T = -\lambda \nabla T. \tag{1.6.1}$$

Here the values of q and grad T are vectors. The minus sign shows that heat flows from points with high temperatures to points with lower temperatures. For anisotropic rocks, where the coefficient of thermal conductivity at a given point depends on direction, the corresponding equation for HFD is

$$\mathbf{q} = (q_x, q_y, q_z), \tag{1.6.2}$$

In an isotropic and homogeneous layer, where $\lambda_x = \lambda_y = \lambda_z = \lambda$ and $\Gamma_x = \Gamma_y = 0$, $\Gamma_z = \Gamma$, the absolute value of HFD is

$$q = \lambda \Gamma. \tag{1.63}$$

Thus to calculate the HFD we need to estimate the value of the static (undisturbed) geothermal gradient (Γ) and to measure the thermal conductivity of the formation.

Two methods that combine thermal conductivity and temperature gradient data are used: the interval method and the Bullard method (Powell et al. 1988). It is assumed that the effect of climate changes, relief, underground water movement, subsurface conductivity variations on the temperature gradient (G) have been estimated and the corrected value of G is close to the value of Γ. In the interval method, for each depth interval a temperature gradient is combined with the representative value of formation thermal conductivity. An example of HFD calculation by the interval method is presented in Table 1.9.

Bullard's method can be used for one dimensional conductive heat flows in a flat layered medium. The following expression is used to process the temperature-thermal conductivity data

$$T(z) = T_0 + q_0 \sum_{i=1}^{N} \frac{\Delta z_i}{\lambda_i}, \tag{1.64}$$

where T_0 is the extrapolated surface temperature, q_0 is constant heat flow density, and λ_i is the thermal conductivity at the depth interval Δz_i.

The average value of HFD over continents is about 60 mW m^{-2} (Kappelmeyer and Hänel 1974; Davies 1980). For years it was believed that the average values of HFD over continents and oceans were practically the same. Today, taking the non-conductivity component (hydrothermal circulation in the oceanic crust) into account, the average oceanic HFD is estimated to be about 100 mW m^2 (Uyeda 1988).

1.7 Regional Patterns of Heat Flow

As discussed above, one of the key parameters in geothermics is heat flow density (HFD), which is the amount of heat transferred through a unit of surface area during a unit of time. The value of HFD (Q or q) can be expressed as the product of multiplying the heat conductivity coefficient (λ) by the geothermal gradient (Γ), $Q = \lambda\Gamma$. HFU is the HFD unit, and its value is thought to be 41.84 mW m^{-2} (1 HFU = 41.84 mW m^{-2} = 1 × 10 $^{-6}$ cal $cm^{-2}s^{-1}$). It is clear from the definition of heat flow density that its value cannot be measured directly, and can only be calculated by identifying the corresponding values of heat conductivity and the geothermal gradient. HFD is used to characterize the geothermal regime of a region, but it is important to determine its values through the surface of continents and the ocean floor, because they represent the amount of heat energy being lost by the Earth. Heat flow density can also be used to analyze how much heat different areas are losing compared to others to determine which average HFD values for a region should be applied. Various researchers have determined the average values of HFD for continents and for oceans (see Table 1.10).

As is clear from Table 1.10 the average values of heat flow density, especially for oceans, are calculated primarily by using certain models determining the heat lost by the Earth from magmatic activity and the discharge of hot fluids. Thus most of these values can only be used to get rough estimates, and do not represent actual values. The average HFD for the entire Earth was estimated to be about 80 mW m^{-2} by Davies (1980) and 87 mW m^{-2} by Pollack et al. (1993).

Determining the HFD in different continental areas became popular in the 1960s, 1970s and 1980s. This was related to the search for sources of geothermal energy, analysis of the thermal conditions in oil and gas fields, use of geothermal

Table 1.10 Average HFD for continents and oceans from different published sources

Average heat flow density (mW m^{-2})		References
Continents	Oceans	
61	61	Lee (1970)
61	93	Williams and von Herzen (1974)
53	62	Chapman and Pollack (1975)
61	87	Langseth and Anderson (1979)
53	100	Davies (1980)
55	95	Davies (1980)
57	99	Sclater et al. (1980)
64.4[a]	71.8[a]	Čermák (1984)
65	101	Pollack et al. (1993)
65	101	Stein (1995)
79.7[b]	117.6[b]	Hofmeister and Criss (2005)
66[c]	70[c]	Hofmeister and Criss (2005)
65	94	Jaupart et al. (2007)
67	100	Clauser (2009)
70.9	105.4	Davies and Davies (2010)

[a] For continental Europe and seas only
[b] All data with Q up to 4,183 mW m^{-2}
[c] data with $Q > 200$ mW m^{-2} omitted

methods for geological (primarily tectonic) modelling, etc. The data collected on heat flow density in different regions are discussed in numerous reviews (Lee and Uyeda 1965; Lubimova 1968a, b; Chapman and Pollack 1975; Pollack and Chapman 1977b; Čermák and Rybach 1979, 1991; Pollack et al. 1979, 1993; Sclater et al. 1980; Pollack 1980, 1982; Duchkov 1985; Nyblade and Pollack 1993; Stein 1995; Jaupart and Mareschal 2003, 2007, and many others). These studies showed that there are numerous causes that can create variations in HFD values in different regions. These include surface relief, lithology, the presence of underground water, the presence of thermal water, proximity to centers of young volcanism, differences in radiogenic heat production content, heat flow from the lower crust and mantle, the cooling effects of rapid sedimentation, basement structure, tectonic activity, time of borehole stabilization before taking temperature measurements, and others.

Analysis of available information shows that the heat flux data exhibit a large scatter, and most areas and regions are characterized by a mosaic of local maxima and minima dispersed around the average heat flow (Čermák and Bodri 1995). Examples of these scattered HFD values for some regions are presented in Table 1.11.

It is clear from Table 1.11 that HFD values differ significantly even over small areas. For example, the HFD for such a small area as the Marmara Sea are within the range of 35–115 mW m^{-2}. Interestingly, among the first 12 heat flow densities determined for the Red Sea (Girdler 1970), the lowest value was about 46 mW m^{-2}, and the highest was about 3,307 mW m^{-2}. It is obvious that under

Table 1.11 Heat flow density range in some regions

Country or region	HFD range (mW m^{-2})	References
Austria	43–127	Čermák (1984)
Bulgaria	8–132	Čermák (1984)
Cyprus	41–185	Čermák (1984)
France	45–176	Čermák (1984)
Eastern Germany	26–172	Čermák (1984)
Western Germany	21–168	Čermák (1984)
Greece	30–105	Čermák (1984)
Hungary	52–139	Čermák (1984)
Iceland	63–281	Čermák (1984)
Israel	7–93	Čermák (1984)
Italy	17–143	Čermák (1984)
Romania	19–118	Čermák (1984)
Spain	29–189	Čermák (1984)
USSR (European part)	19–142	Čermák (1984)
Greenland and Norwegian Seas	14–268	Čermák (1984)
Reykyjanes range	2–343	Čermák (1984)
Ranges of the Atlantics	0–282	Čermák (1984)
Other regions of the Atlantics	11–90	Čermák (1984)
Mediterranean near Spain	55–155	Čermák (1984)
Mediterranean West of Sardinia	33–132	Čermák (1984)
Tyrrhenian Sea, Mediterranean	30–173	Čermák (1984)
Adriatic Sea, Mediterranean	36–104	Čermák (1984)
Aegean Sea, Mediterranean	47–114	Čermák (1984)
Ionic and Eastern Mediterranean Seas	10–74	Čermák (1984)
Black Sea	8–91	Čermák (1984)
Caspian Sea	40–99	Čermák (1984)
Alaskan interior	42–130	Williams et al. (2006)
Egypt	42–175	Morgan and Swanberg (1978)
Marmara Sea	35–115	Pfister et al. (1998)
Baltic Shield	25–70	Kukkonen et al. (1998)
Kura Depression, Azerbaijan	12–105	Pilchin (1983)
Cordillera, South America	25 to >160	Hamza and Muñoz (1996)
Brazilian platform	30 to >100	Hamza and Muñoz (1996)
Altiplano, Cordillera	50–180	Springer and Förster (1998)
Oregon Cascade Range, USA	40–100	Blackwell et al. (1980)
Pannonian basin	50–130	Lenkey et al. (2002)
Deccan basalt province, India	33–73	Kumar et al. (2007a)
Mesozoic Luangwa and Zambezi rifts	44–110	Nyblade et al. (1990)

such circumstances, the determination of any average HFD for an area is sample-dependent. At the same time, HFD changes significantly with depth, even within the same borehole. Some examples of HFD changes within boreholes at shallow depths are presented in Tables 1.12 and 1.13.

Table 1.12 HFD differences in shallow boreholes for some areas of the United States (after Costain et al. 1986; Lachenbruch et al. 1985)

Area	Borehole	Depth interval (m)	Heat flow (mW m^{-2})
Petersburg, VA	CL1	113.4–171.4	114.7
		188.2–195.4	131.6
Palmetto, GA	PM1	89.5–148.5	37.5
		149.5–160.0	37.3
		161.4–205.0	41.9
State Farm, VA	SF1	50.0–92.5	37.0
		185.0–192.5	44.4
		197.5–207.5	38.8
Southport, NC	C14A	200.8–206.4	53.6
		361.6–371.3	54.9
		478.2–545.4	53.7
Kinston, NC	C16A	81.0–87.1	26.3
		174.7–180.8	71.2
Eatontown, NJ	C40	230.2–237.8	33.1
		292.2–303.4	51.5
Princess Anne, MD	C52	212.2–223.4	51.1
		300.1–310.2	59.6
Snow Hill, MD	C53	234.4–242.6	45.0
		297.0–306.7	53.7
Eastville, VA	C56	118.1–124.7	55.5
		121.1–125.7	62.0
Salton trough, CA	ERQU	38.0–59.0	43.0
		56.0–59.0	77.0
Salton Trough, CA	GSLN	46.0–145.0	84.0
		152.0–239.0	89.0
Salton trough, CA	ORCA	30.0–69.0	109.0
		70.0–122.0	112.0
Salton trough, CA	DSRT	46.0–85.0	57.0
		85.0–162.0	61.0
Salton trough, CA	PALN	61.0–122.0	106.0
		128.0–177.0	112.0
Salton trough, CA	RIVM	46.0–114.0	74.0
		122.0–175.0	81.0

It is obvious from Tables 1.12 and 1.13 that in some boreholes the scatter of the HFD data is substantial. Analysis of geothermal data from the Michigan Basin (Speece et al. 1985) shows that within a cross section of Mississippian-Cambrian deposits, the HFD values cover a range from about 0 to 260 mW m^{-2}. The fact that HFD changes with depth means that average HFD values for an area depend substantially on the depths at which individual values of HFD are determined. This makes any average value of HFD for an area extremely ambiguous.

Tables 1.11, 1.12, 1.13 show that heat flow density values can vary significantly in both the horizontal (by area) and the vertical (with depth) directions. This makes

Table 1.13 HFD values differ in shallow boreholes for some areas (after Lubimova and Firsov 1966; Kutas and Gordienko 1971)

Region	Borehole	Depth interval (m)	Heat flow (mW m^{-2})
Ukrainian Shield	Perga 2	60–120	23.5
		220–600	27.3
Ukraine	Belaya Tserkov 349	30–50	19.1
		70–105	35.1
Ukraine	DDV 47	25	21.0
		150	48.0
Ukraine	Stariy Krym 106	131–167	28.1
		167–246	45.2
Kazakhstan	Chatirkul 590	17–59	26.2
		382–394	46.4
Kirghizstan	Orgachevskaya	100	66.0
		196	73.2

any measured value of HFD dependent on both the point within the area and depth chosen for geothermal measurements, in addition to the impact of the area within the greater region investigated. All the causes noted above can influence the outcome of these measurements.

Hofmeister and Criss (2005) noted that most of the continental measurements of HFD come from localities in the United Sates and returned heat flux values mostly above 200 mW m^{-2}. This is important since vast regions in Africa, South America, the former Soviet Union, and Antarctica remain unprobed, whereas some high-flux localities of particular interest tend to be over-sampled. They further show that the mean HFD value depends on whether the sample selection includes or excludes high or extremely high values. Neumann et al. (2000) estimated that 90 % of all HFD measurements are from three continents: Europe, North America and Africa. Jaupart and Mareschal (2007) pointed out that despite many decades of measurements, many geological continental provinces and large parts of the oceans remain poorly sampled. Clearly there is unbalanced and inadequate sampling such that much of the world is not represented. Jaupart and Mareschal (2003) emphasized that sampling problems lead to inaccurate determination of local, regional and especially global HFD averages. They came to the conclusion that this sampling bias can be diminished or removed by weighing the data by area. In other words, to determine any average HFD value, the average values for equal areas of longitude and latitude (1° × 1°, 5° × 5°, etc.) should be obtained first. However, calculating the average using this method faces two obstacles.

First, few continental and oceanic regions have been measured or the measurements are inaccurate. For example, in mountain regions it is very difficult and sometimes virtually impossible to drill boreholes to take geothermal measurements because of the uneven landscape. Even in areas such as these where boreholes can be drilled, they are too shallow to get good measurements. Unfortunately measurements taken in shallow holes in an area where climatic conditions may be of

significant impact up to depths of several hundred meters cannot be considered reliable. The same can be said of deep oceanic regions, because to take readings from such regions, on top of the problems mentioned for mountain areas it is also necessary to have equipment that can withstand the massive water pressures.

The second obstacle is that high heat flow regions in continents that cover a small surface are always oversampled (Hofmeister and Criss 2005; Jaupart and Mareschal 2007). This is because the main areas of interest in geothermics are related to geothermal energy resources (thermal waters, regions of young magmatism, etc.), and oil and gas fields, which are usually located within anticline structures characterized by elevated geothermal parameters. Obviously such measurements are biased towards higher HFD values, higher geothermal gradients, and overall higher temperatures at given depths. In addition, if values of HFD are only measured from a limited number of continental and oceanic regions, would any calculated average value of HFD represent the real average value for continents and oceans? Furthermore, there is always the problem of determining values of geothermal parameters for areas of the globe where geothermal measurements have not been made. To solve this particular problem there have been attempts to look for relationships between heat production rate values and general tectonic settings, lithological types, and the primary composition and petrophysical properties of rocks. For instance, Kukkonen and Peltoniemi (1998) tried to find an association between thermal conductivity, the heat production rate and other petrophysical properties (density, magnetic susceptibility, intensity of remanent magnetization, *P*-wave velocity), which they investigated empirically in roughly 2,700 drill core samples from the Finish Precambrian bedrock. Among the relationships proposed by the authors, three were accepted by a number of researchers for practical use. These are the relationships between heat generation and seismic velocity, heat generation and surface HFD, and HFD and the geological age of a region. These three relationships are examined in greater detail below.

1.7.1 Seismic Velocity and Heat Production

Radioactive heat production A in rocks depends on their uranium, thorium and potassium content. Originally this was measured in heat generation units (HGU: 1 HGU $= 10^{-13}$ cal/(cm^3 s) $= 0.4184$ μW m^{-3}). Parameter A varies across rock types by several orders of magnitude and reflects geochemical conditions during rock formation. Since the concentration of long-lived radioactive elements (U, Th, and K) in all rocks differs in both its horizontal and vertical distribution, the value of A for an area is sample-dependent. Consequently there is no way to make accurate estimates of A for depths at which samples have not been collected or are unfeasible (areas with no boreholes, deep layers within the crust, etc.). This makes the problem of determining the portion of the heat flow density generated within the crust by decaying radioactive elements excessively complicated. To overcome this problem, researchers have looked for relationships between heat production

and certain other physical parameters, in an analogy to Birch's law (Birch 1960, 1961; Anderson 1967) which describes the relationship between seismic velocity v_p and density σ. One of the most prominent attempts was made by Rybach (1976, 1978), who proposed relationships between heat generation and seismic velocity or density to determine the distribution of heat generation with depth. Based on the high correlation of A with density and compressional wave velocity v_p that was obtained, he showed that an empirical $A(v_p)$ relationship exists for the v_p range of 5.0–8.0 km/s for crustal rocks at different pressures, which follows the exponential law:

$$A(v_p) = a \exp(-bv_p), \tag{1.7.1}$$

where the numerical factors a and b are dependent on pressure.

At the same time, Rybach (1976) showed experimentally that there is no correlation between the heat production rate A and thermal conductivity λ in igneous and metamorphic rocks, as was believed earlier. Given that heat generation exhibits considerable variation across rock types as well as with their geological age, this correlation was split into two, one for Phanerozoic rocks and the other for Precambrian rocks (Rybach and Buntebarth 1982, 1984). This relationship has been used in many studies (see for example: Kutas 1979; Rybach and Cermák 1987; Čermák 1989; Čermák et al. 1990) to determine the distribution of the heat production rate with depth within the continental crust.

This relationship was also heavily criticized (Fountain 1986; Čermák 1989; Kern and Siegesmund 1989; Kukkonen and Peltoniemi 1998; Kukkonen and Lahtinen 2001, etc.). Fountain (1986) argued that since there is no correlation between the heat production rate and seismic velocity for rock samples from the Pikwitonei granulite domain and the Sachigo granite-greenstone subprovince of the Superior Province, relationships between these parameters cannot be reliably predicted. Čermák (1989) indicated that because of the highly variable value of the pressure derivative of v_p in the uppermost crust, using an $A - v_p$ relationship is problematic in this depth range. Kukkonen and Lahtinen (2001) showed that for 1,150 outcrop samples from Finland in the central Fennoscandian Shield, well-defined systematic relationships of heat production rate values with either SiO_2 content, density, or P-wave velocity could not be found. They further demonstrated that the correlations were weak and dispersed and sometimes were reversed in plutonic, metavolcanic, and metasedimentary rocks. Kern and Siegesmund (1989) indicated that laboratory data do not convincingly fit the proposed relationships between heat generation rate and seismic velocity, or that of heat generation rate and density. Other results based on the analysis of roughly 2,700 drilled core samples from the Finish Precambrian bedrock also suggested that there were no well-defined relationships between thermal properties and other petrophysical properties which were expected for crystalline rocks, and that the coefficients of correlation were not substantial, with data points scattered in cross-correlation diagrams (Kukkonen and Peltoniemi 1998).

Ultimately, some researchers have claimed that there is no tangible relationship between seismic velocity and heat production rate, because seismic velocity depends on the crystal properties of the major minerals in the rock, whereas the heat production rate results from radiogenic components which are largely concentrated in accessory minerals (Fountain 1986; Kern and Siegesmund 1989). Given the evidence, this argument seems compelling, since seismic velocity and the heat generation rate are indeed two different properties of a rock that have no apparent relationship between them.

1.7.2 Changes in Radioactivity with Depth

The first observation of a linear relationship between heat flow and radioactive heat generation of plutonic rocks was made by Francis Birch (Blackwell and Thakur 2007) and reported by Birch et al. (1968). The relationship states that for a given area, the measured HFD Q varies linearly with the near-surface radioactive heat production rate A. This correlation is also sometimes termed Birch's Law (Blackwell and Thakur 2007) and can be expressed by:

$$Q = q_0 + DA_0. \tag{1.7.2}$$

Here Q is the heat flow on the surface, A_0 is the heat generation of surface rocks, q_0 is the reduced heat flow (Roy et al. 1968; Čermák 1982a) (the heat flow if there are no radiogenic heat sources), and parameter D represents the thickness of a near surface heat-producing layer usually smaller than 10 km (Jaupart and Mareschal 2003). Initially it was suggested that D represents a slab of uniform heat production (Roy et al. 1968; Stein 1995).

Lachenbruch (1968) described a similar relation in the Sierra Nevada. This linear relationship between heat flow and the heat generation rate observed for plutonic rocks was interpreted by Lachenbruch to require an exponential depletion of radioactive elements with depth (Lachenbruch 1968; Albarede 1975) which could be expressed as:

$$A(z) = A_0 \exp\left(\frac{-z}{D}\right), \tag{1.7.3}$$

where the value of the constant D ranges from 7.5 to 10 km (Blackwell 1971). For some models (Čermák 1982b) the values of $A_0 = 2\ \mu\text{W m}^{-3}$ and $D = 10$ km.

Both the linear relationships between surface heat flow and the heat generation rate, and the exponential decline of A with depth have been widely discussed in the scientific literature (Lachenbruch 1970, 1971; Blackwell 1971; Pollack and Chapman 1977a, b; Costain et al. 1986; Vigneresse 1988; Stein 1995; and many others), and used to determine the thermal parameters within the crust.

However, this relationship between heat flow and heat generation has also been challenged by many studies. Vigneresse (1988) reported that the linear relationship was not maintained over large regions, and showed that data from Scotland do not fit with data from the Southern and Central United Kingdom. Rybach and Cermák (1987) demonstrated that the dependence of A on depth does not follow a simple exponential law [Eq. (1.7.3)]. Jaupart and Mareschal (2003) showed that measurements of heat production in deep boreholes have not revealed that the concentration of heat sources systematically decreases with depth. They pointed out that in the Abitibi subprovince (the Superior Province) and the Flin Flon belt (Trans-Hudson Orogen) the upper crust consists of depleted mafic volcanics and intrusives that overlay a more radiogenic basement. This relationship is also weak for data from the large Precambrian provinces of India, Canada, and South Africa; notably a linear correlation between surface heat flow and heat production for areas of the Precambrian of North America is completely absent (Jaupart and Mareschal 2003). Later they concluded Jaupart and Mareschal (2007) that there is no universal law that relates crustal heat production to surface heat flux, nor one defining the distribution of vertical heat production.

Jaupart and Mareschal (2003) also showed that the correlation between local values of surface heat flow and heat production are only found in exposed plutons enriched in radioactive elements, but even within a single pluton the concentration of radioelements can be highly variable in both the vertical and horizontal distribution. For example, in the Bohus granite of Sweden, concentrations of relatively immobile thorium varied by a factor of 5 over horizontal distances as small as a few dozen meters (Landstrom et al. 1980). Ashwal et al. (1987) found that there was relatively large variation in heat production among the silicic plutonic rocks of the Superior Province of the Canadian Shield, and that an apparently linear heat flow to heat production relationship previously calculated for the Kapuskasing area of the Superior Province did not correspond to the distribution of heat production with depth.

Similarly, there are a number of studies showing that the exponential depletion of radioactive elements with depth described by (1.7.3) does not hold. These studies revealed that the heat production in rocks from the lower crust is not negligible. Analyses of xenoliths prompted Rudnick and Fountain (1995) to accept a global average heat production of 0.28 $\mu W\ m^{-3}$ for the lower crust. Jaupart and Mareschal (2007) claimed that data from exposed rocks of the lower crust points to heat production in the range of 0.4–0.5 $\mu W\ m^{-3}$. The heat production values of samples from a large exposure of granulite facies terranes of the Superior Province were reported to be $\approx$ 0.4 $\mu W\ m^{-3}$ (Jaupart et al. 2007). Kutas (1979) stated that heat generation is at a constant of about 0.3 $\mu W\ m^{-3}$ at depths greater than 8 km in the Ukrainian Shield. Certain other researchers (Ashwal et al. 1987; Fountain et al. 1987; Ketcham 1996; Jaupart and Mareschal 2007) suggested that even though for exposed crustal sections a general trend of decreasing heat production with depth is valid, this trend is not represented by a monotonic function. In fact, more recent analyses even for the Sierra Nevada batholith, for which Lachenbruch (1968) initially proposed the exponential model (1.7.3) have shown (Brady et al. 2006)

that the heat production does not decrease exponentially with depth, but rather even increases in the upper layers before beginning to decrease. Furthermore, sampling in superdeep boreholes [Kola (Russia), and KTB (Germany)] demonstrates that heat production does not exhibit the systematic variation with depth required by the linear relationship (Jaupart et al. 2007; Jaupart and Mareschal 2007). In the Kola superdeep SG-3 borehole, the Proterozoic supracrustal rocks (top 4 km) produce less heat (0.4 $\mu W\ m^{-3}$) than the Archean basement (1.47 $\mu W\ m^{-3}$) (Kremenentsky et al. 1989). In the KTB superdeep borehole, heat production decreases with depth at shallow levels, reaching a minimum between 3 and 8 km, and then increases again (Jaupart et al. 2007; Jaupart and Mareschal 2007).

In the articles criticizing the two relationships described in (1.7.2) and (1.7.3), cases such as the simple increase of heat flow density with depth were overlooked by most researchers. In fact, if the heat flow increases with depth there cannot be a linear relationship between surface heat flow and heat generation, or a contradictory exponential decrease of heat production with depth. Analysis data from the deep Vorotilovo borehole, from the Puchezh-Katunk impact structure of the East European Platform, show that HFD is 22–31 $mW\ m^{-2}$ down to a depth of 1.2 km, 34–42 $mW\ m^{-2}$ in the 1.2–1.9 km interval, and 40–56 $mW\ m^{-2}$ in the 1.9–5.3 km interval (Popov et al. 1998). There is a significant increase in heat flow at a depth of 34–36 $mW\ m^{-2}$ to 55–58 $mW\ m^{-2}$ in the top 2 km of the SG-3 superdeep Kola borehole with a maximum HFD at a depth of about 3 km (Mottaghy et al. 2005). Another study carried out in the Kola superdeep borehole SG-3 showed (Popov et al. 1999) that the average value of HFD is even greater, and reaches about 63 $mW\ m^{-2}$, in the 5.2–7.5 km interval. HFD was also reported to increase in the Ural superdeep SG-4 borehole from about 20 $mW\ m^{-2}$ at a depth of 500 m to about 55 $mW\ m^{-2}$ at 2,500 m (Kukkonen et al. 1997). Analysis of data for the Superdeep borehole SG-1 Saatly (Azerbaijan) shows (Pilchin 1983) that HFD in SG-1 increases from 18 $mW\ m^{-2}$ at depths of 800–2,150 m to 51.1 $mW\ m^{-2}$ at 3,500–4,400 m, and then further to 96.7 $mW\ m^{-2}$ at 4,400–5,000 m. The increase in HFD with depth was also found for the superdeep SG-1 Aralsor borehole in the Precaspian Depression of Russia in a depth range of 2,790–5,250 m (Pilchin 1983). Likewise, it was found to increase in the Ukrainian Shield in the Krivoy Rog—8,500 borehole (9.2–14.6 $mW\ m^{-2}$ at depths of 675–925 m to 27.3 $mW\ m^{-2}$ at depths of 925–1,425 m) (Lubimova et al. 1964) and Gorokhov-1 (25.8 $mW\ m^{-2}$ at 450–670 m to 37.6–50.2 $mW\ m^{-2}$ at 1,080–2,300 m) (Kutas and Gordienko 1971). In almost the entire territory of the Ukrainian Shield, HFD values at depths of 100–150 m are lower by 10–15 % and in some areas by 20–30 %, and usually remain relatively stable down to 300–350 m (Kutas et al. 1979).

Data on heat flow density in some boreholes of the Red Sea also show increased values with depth. A significant increase in HFD was observed in the Durvara 1 and Durvara 2 boreholes (110 $mW\ m^{-2}$ at depths of 0–2 km and 143 $mW\ m^{-2}$ at depths of 2–3.5 km) on the western margin of the Red Sea, while a small increase in HFD was recorded in the Mansiyah 1 (110 $mW\ m^{-2}$ at depths of 1–2 km and 113 $mW\ m^{-2}$ at depths of 2–3.5 km) on the eastern margin of the Red Sea, and

Amber 1 (121 mW m^{-2} at depths of 0.917–2.567 km and 123 mW m^{-2} at depths of 2.567–3.551 km) boreholes on the southwestern margin of the Red Sea (Girdler 1970). Numerous instances of HFD increase with depth (heat absorption) are further discussed in Sect. 7.4.

1.7.3 Heat Flow and Geological Age

The lack of geothermal data for numerous continental regions of the Earth prompted scientists to search for yet another universal law capturing the relationship between HFD and the geological age of a region. The aim was simple: if such a universal relationship were found, a corresponding average value of HFD could be attributed to a region with a known geological age without having to make any geothermal measurements. Numerous studies have been carried out, the results of which are still highly controversial. For example, Rao et al. (1982), who actually criticized the relationship, also stated that extensive use of empirical correlations of heat flow for a given age in the field of thermal studies indicates that the basic concept is deeply entrenched.

Lee and Uyeda (1965) were among the first researchers to suggest that continental heat flow was age dependent (Stein 1995). However, the first statistical analysis of the problem on the dependence of HFD on geological age of a region was carried out by Polyak and Smirnov (1968). The relationship between surface heat flow and geological age was later discussed in (Hamza and Verma 1969; Chapman and Furlong 1977; Vitorello and Pollack 1980; Čermák 1982b; Rao et al. 1982; Stein 1995; Jaupart and Mareschal 2003, 2007; Mareschal 2010; and many others).

Čermák (1982b) came to the conclusion that there are few variations of surface heat flow with age in the Precambrian tectonic units (30–40 mW m^{-2}), and that most of the increase in surface heat flow activity (from 40 to 80 mW m^{-2}) has taken place within the last 500 million years. Sclater et al. (1980) showed that the heat flow in continents is generally high in younger regions and decreases to a constant value (46 mW m^{-2}) after 800 Ma, whereas the nonradiogenic component reaches an equilibrium value (a constant of 21–25 mW m^{-2}) after about 200–400 Ma. They also indicated that in well-sedimented areas, HFD decreases from about 250 mW m^{-2} for crusts younger than 4 Ma to about 46 mW m^{-2} for crusts aged about 120–140 Ma, and for crusts older than 200 Ma the HFD reaches an equilibrium value of about 38 mW m^{-2}. The low heat flow of about 40 mW m^{-2} in the ca. 65 Ma Deccan traps region (Roy and Rao 2000) is one of the most unusual findings on HFD in the world. The average HFDs determined for different geological periods are presented in Table 1.14.

Table 1.14 shows that the values for HFD relative to age put forward by Chapman and Furlong (1977) show some discrepancies from the HFD increase pattern, since the mean HFD value for the Late Proterozoic (54 mW m^{-2}) is

Table 1.14 HFD for regions with different geological ages from published data

Geological age	Average HFD (in mW m^{-2}) for regions with different geological ages			
	McLaren et al. (2002)	Stein (1995)	Pollack et al. (1993), Nyblade and Pollack (1993)	Chapman and Furlong (1977)
Archaean	41–46	51.5	41	41
Proterozoic	49–54	58.3	48	51–54[b]
Phanerozoic[a]	50–70			
Paleozoic		57.7–61.0	58	52–61[c]
Mesozoic		63.1–64.2	64	73
Cenozoic		63.9–97.0	Up to 97	71

[a] HFD values estimated as average for Phanerozoic (Paleozoic to present) age
[b] 51 mW m^{-2} for Early Proterozoic and 54 mW m^{-2} for late Proterozoic
[c] 52 mW m^{-2} for Early Paleozoic and 61 mW m^{-2} for late Paleozoic

Table 1.15 Statistical estimates of HFD (after Hofmeister and Criss 2005)

Region	Area characteristics	Mean HFD (mW m^{-2})
Continents	All data with Q up to 4,183 mW m^{-2}	79.7
	Data U.S. and data with $Q > 904$ mW m^{-2} omitted	65.8
	Data with $Q > 400$ mW m^{-2} omitted	69
	Data with $Q > 200$ mW m^{-2} omitted	66
Oceans	All data with Q up to 8,910 mW m^{-2}	117.6
	Data with $Q > 400$ mW m^{-2} omitted	86.2
	Data with $Q > 200$ mW m^{-2} omitted	70

slightly higher than that for the Early Paleozoic (52 mW m^{-2}), and the mean HFD value for the Mesozoic (73 mW m^{-2}) is slightly higher than that for the Cenozoic (71 mW m^{-2}).

Table 1.15 shows that high HFD values significantly increase the mean (average) values of HFD for both continents and oceans. It is also obvious that for cases with such huge HFD values, determining the average value of HFD can be a considerable problem. For example, data reported for the Lake Baikal Basin show (Lysak and Sherman 2002) the presence of HFD values as high as 200 to over 1,000 mW m^{-2}, and even greater than 6,000–8,000 mW m^{-2} within an area with average heat flow density values of about 78 ± 36 to 87 ± 10 mW m^{-2}, but these extremely high values of HFD were not taken into consideration when the average heat flow value was estimated. In Tables 1.16, 1.17, 1.18, 1.19 HFD values for the Archean, the Proterozoic and Paleozoic periods are presented for different regions.

It is clear from Tables 1.16, 1.17, 1.18, 1.19 that the values are highly dispersed for each geological period, which would suggest that there is not a clear relationship between the HFD and geological age of a region. In addition there are numerous cases of abnormally low HFDs and abnormally high HFDs for every geological period (see Tables 1.20, 1.21).

Table 1.16 Mean heat flow in different Archean provinces

Region	Mean heat flow (mW m^{-2})	References
Superior Province	42	Mareschal and Jaupart (2006)
Superior Province, excluding Abitibi	45	Mareschal and Jaupart (2006)
Abitibi GSB (Superior Province)	37	Mareschal and Jaupart (2006)
Western Australian Craton	39	Mareschal and Jaupart (2006)
Yilgarn block	39	Mareschal and Jaupart (2006)
Pilbara block	43	Mareschal and Jaupart (2006)
Kaapvaal granite domes, S. Africa	33	Mareschal and Jaupart (2006)
Witwatersrand	45	Mareschal and Jaupart (2006)
Lesotho	61	Mareschal and Jaupart (2006)
Siberian Shields	38	Mareschal and Jaupart (2006)
Baltic Shield	34	Mareschal and Jaupart (2006)
Ukrainian Shield	36	Mareschal and Jaupart (2006)
Dharwar Craton, India	36	Roy and Rao (2000)
Slave Craton, Canada	54	Lewis et al. (2003)
Zimbabwe (S. Africa)	47	Jones (1987)
Slave Craton, Canada	50	Mareschal et al. (2004)
Wyoming (USA)	48	Decker et al. (1980)
Niger	20	Morgan (1985)
Ukrainian Shield	37	Morgan (1985)
Superior Province	34	Morgan (1985)
Baltic Shield	36	Morgan (1985)
Kalahari Craton	47	Nyblade et al. (1990)
Tanzania Craton	34	Nyblade et al. (1990)
E. Finland-S. Estonia	<30	Kukkonen and Jõeleht (1996)
São Francisco Craton	41	Hamza and Muñoz (1996)

In several parts of the Canadian Shield, heat flow values as low as 22 mW m^{-2} have been measured, and similar values have also been reported for the Norwegian Shield, and Western Australia (Jaupart and Mareschal 2003).

It should also be mentioned that most of the good boreholes in which geothermal measurements have been taken are related to gas and oil fields and areas of oil and gas prospecting. However, such regions are present exclusively in depressional areas with a significant thickness of sedimentary and cap rocks. Such areas are known to be characterized by extremely low HFD values, especially in young sedimentary basins. For example, the oil and gas fields of the Middle Kura and Lower Kura Depressions are mostly filled with Cenozoic-Quaternary sediments and their mean HFD values are in the range of 33.5–50.2 mW m^{-2} and 16.7–29.3 mW m^{-2}, respectively (Pilchin 1983). It is worth noting that the thickness of younger sediments (as young as the Pliocene age) is greater in the Lower Kura Depression. In the sedimentary layers of the super-deep borehole SG-1 Saatly, in Azerbaijan, the HFD values are within the range of 11.3–23 mW m^{-2}, but in the deeper magmatic portion the HFD values increase to 36.4–96.7 mW m^{-2}. In the Dnieper-Donets Depression of the Ukraine, the HFD in

Table 1.17 Regional variations of the heat flow in some Archean Cratons

Province, Craton	HFD range (mW m^{-2})	References
Superior Province	22–48	Mareschal and Jaupart (2006)
Australian Cratons	34–54	Mareschal and Jaupart (2006)
Baltic Shield	15–39	Mareschal and Jaupart (2006)
Siberian Shields	18–46	Mareschal and Jaupart (2006)
Anabar Shield	15–25	Duchkov (1991)
Ukrainian Shield	30–50	Galushkin et al. (1991)
Karelia, Baltic Shield	35–40	Slagstad et al. (2009)
Dharwar Craton, India	25–51	Roy and Rao (2000)
eastern Dharwar Craton, India	33–73	Kumar et al. (2007a)
Karelian and Belomorian prov., Baltic Shield	20–30	Shwartsman (2001)
Belomorian Belt, Baltic Shield	20–30	Čermák et al. (1993)
Karelia and Kola Peninsula, Baltic Shield	<20–35	Čermák et al. (1993)
Laponian supracrustals	20–30	Čermák et al. (1993)

sedimentary layers is minimal (15–31 mW m^{-2}) at depths ranging 25–50 m and they approach values of 33–46 mW m^{-2} at greater than 1,000 m (Kutas et al. 1979). The Black Sea Basin, where the total thickness of Cretaceous-Quaternary sediments in the central areas reaches 14–18 km, is also characterized by a low HFD of less than 20–30 mW m^{-2} (Kutas et al. 1998). This evident presence of low heat flow density values in sedimentary basins is typical and is considered by some to be an effect of sedimentation. Jones et al. (1988) also reported low HFD values (less than 40 mW m^{-2}) in the Beaufort-Mackenzie Basin and Rapid Depression, both of which are areas of thick successions of Cretaceous and Tertiary clastic sedimentary strata. This significant lowering of HFD values in sedimentary basins is related to heat absorption and is discussed in detail in Sect. 7.4.

Based on a physical model of the continents, Mareschal (2010) showed that there is no simple relationship between HFD and age, and that the relationship proposed by Polyak and Smirnov (1968) between heat flux and rock age is based only on a very weak statistical trend. He further pointed out that there is a negative correlation between heat flux and age for a young crust in a transient thermal regime, and that age cannot be used to predict heat flux in poorly sampled regions. Morgan (1985) also argued that the relationship was weak for the Paleozoic and older ages. Rao et al. (1982) showed that there is no correlation between a particular geological age and a specific characteristic heat flow value, and concluded that any relationship between the two should be rejected because it is not supported by available continental heat flow data.

Table 1.18 Regional mean heat flows in different Proterozoic regions

Region	HFD, average or range (mW m^{-2})	References
Australian Proterozoic terrains	83 ± 18	McLaren et al. (2002)
Karasjok–Kautokeino GSB, Baltic Shield	30	Slagstad et al. (2009)
Egersund anorthosite complex, Baltic Shield	30	Slagstad et al. (2009)
Granites in southern Norway	60–80	Slagstad et al. (2009)
Karelia, Baltic Shield	50–55	Slagstad et al. (2009)
Aravalli province, India	68	Roy and Rao (2000)
Central Shield (Australia)	78	Cull (1991)
Baltic Shield	31	Čermák (1993)
Ukrainian Shield	32	Čermák (1993)
Trans-Hudson Orogen, Canada	42	Rolandone et al. (2002)
Wopmay orogen, Canada	90	Lewis et al. (2003)
Grenville Province, Canada	41	Mareschal et al. (2000a)
North China Massif	50	Hu et al. (2000)
Upper Yangtze Block (China)	53	Hu et al. (2000)
Tarim Block (China)	44	Hu et al. (2000)
Qaidam Basin (China)	52	Hu et al. (2000)
Thomson Belt, Canada	53	Jaupart and Mareschal (2003)
Zimbabwe (S. Africa)	61	Jones (1987)
Gawler Craton (Australia)	94	Cull (1991)
Sao Francisco Craton (Brazil)	42	Vitorello et al. (1980)
Brazilian mobile belt (Brazil)	55	Vitorello et al. (1980)
Ukrainian Shield	36	Kutas (1984)
Voisey Bay, Labrador	22	Mareschal et al. (2000b)
Mozambique Belt	47	Nyblade et al. (1990)
E. Finland-S. Estonia	35–55	Kukkonen and Jõeleht (1996)
Gawler craton, Australia	~90	Cull (1982)
Adelaide Fold Belt, Australia	92	Neumann et al. (2000)
Lapland Granulite Belt, Baltic Shield	30–40	Čermák et al. (1993)
Pechenga-Varzuga Belt, Baltic Shield	~32–42	Čermák et al. (1993)
Svecofennian crust	<30–70	Čermák et al. (1993)
Transscandinavian Granite Porphyry Belt	52 to >70	Čermák et al. (1993)
Southwest Scandinavian Domain	50 to >60	Čermák et al. (1993)
Eastern Fold Belt, Brazil	67	Hamza and Muñoz (1996)
Northern Fold Belt, Brazil	87	Hamza and Muñoz (1996)
Western Fold Belt, Brazil	81	Hamza and Muñoz (1996)

Table 1.19 Regional mean heat flows in different Paleozoic regions

Region	Average HFD (mW m^{-2})	References
The Appalachians	57	Jaupart and Mareschal (1999)
Mainland United Kingdom	54	Lee et al. (1987)
Dnieper aulacogen, the Ukraine	45	Čermák (1993)
Pripyat Depression, Belorussia	66	Čermák (1993)
Russian Platform	68	Čermák (1993)
Caledonian	~50	Čermák et al. (1993)
Hercynian	~70	Čermák et al. (1993)
Altay-Ergula Belt (China)	60	Hu et al. (2000)
Junggar-Higgan Belt (China)	47	Hu et al. (2000)
The Urals	30	Kukkonen et al. (1997)
Ural Foredeep[a]	29	Kukkonen et al. (1997)
West Ural Folded Zone[a]	28	Kukkonen et al. (1997)
Central Ural Uplift[a]	24	Kukkonen et al. (1997)
Tagil-Magnitogorsk Zone[a]	14	Kukkonen et al. (1997)
East Ural Uplift[a]	18	Kukkonen et al. (1997)
East Ural Depression[a]	27	Kukkonen et al. (1997)
Trans-Ural Uplift[a]	20	Kukkonen et al. (1997)
Tyumen-Kustanay Depression[a]	26	Kukkonen et al. (1997)

[a] Different regions of the Urals

Since the relationship between geological age and HFD for different regions is very weak, rather than put forward a direct relationship between the two characteristics, there have been attempts to associate surface geothermal activity and the age of the last tectonothermal event (Čermák 1982b). This is also problematic since in such regions of high tectonic activity as the Lower Kura Depression, Apsheron, and the South Caspian Depression, which has hundreds of mud volcanoes, many of which are still active volcanoes, the heat flow is abnormally low. Interestingly, it was shown (Pilchin 1985) that the main cause for the formation of mud volcanoes is high thermal activity in their epicenters (see Sect. 4.3).

Many authors try to avoid making strong statements about the geological age-HFD relationship and may instead implicitly say that the heat flow within a given continent generally decreases with age (Sclater et al. 1980; Jaupart and Mareschal 2003). However, as it is stated in (Jaupart and Mareschal 2003) this trend only appears to be valid in global terms and does not apply to individual continents. Jaupart and Mareschal (2007) surmised that for stable continents, the very wide range of average heat fluxes within each age group (Archean, 36–50 mW m^{-2}; Proterozoic, 36–94 mW m^{-2}; Paleozoic: 30–57 mW m^{-2}) implies that age is not a proxy for heat flux.

All the above clearly imply that accepting a HFD value for a region of specific age without geothermal measurements leads to significant error.

Table 1.20 Abnormally low HFD values for some areas

Region	Values of HFD as low as (mW m^{-2})	References
Coastal Cordillera, South America	25	Hamza and Muñoz (1996)
Mesozoic Espirito Santos Basin, Brazil	26	Hamza and Muñoz (1996)
Continental part of Barents Sea region	20	Shwartsman (2001)
Drill holes, Kamennye Lakes, Eastern Karelia	2.4–11.6	Kukkonen et al. (1998)
Black Sea Basin	<20	Kutas et al. (1998)
Coastal Cordillera	20	Springer and Förster (1998)
Sierra Nevada Mountains, USA	<20	Blackwell et al. (1991)
Middle Rocky Mountains	30	Blackwell et al. (1991)
Canadian Shield	22	Mareschal et al. (2000b)
Mesozoic of Iberia abyssal plain, Galicia	47.5	Louden et al. (1997)
Pleistocene deposits, Gulf of Mexico	~20	Nagihara and Jones (2005)
The Urals	<20	Kukkonen et al. (1997)
East Ural Uplift	18	Kukkonen et al. (1997)
Transylvanian Depression	30	Şerban et al. (2001)
Outer Dinarides	<30	Lenkey et al. (2002)
Magadi, Late Archean Closepet Granite, India	25	Roy et al. (2008)
Ushachi, Belorussia	5	Zuy (2007)
Sudilovochi, Belorussia	4–10	Zuy (2007)
Kosari, Belorussia	3–7	Zuy (2007)
Kozlovka, Belorussia	3–6	Zuy (2007)
Senno, Belorussia	2–4	Zuy (2007)
Deccan basalt province, India	33	Kumar et al. (2007a)
Middle Kura Depression, Azerbaijan	11–12	Pilchin (1983)
Lower Kura Depression, Azerbaijan	12–16	Pilchin (1983)
Krivoy Rog, Ukrainian Shield	9.2–14.6	Lubimova et al. (1964)
Staraya Mazesta, Russia	15.9	Lubimova et al. (1964)
Sukhokumskaya, North Caucasus	8–12	Amirkhanov et al. (1975)
Dchevskaya, Saratov Province, Russia	1.3	Pilchin (1983)
Astrakhan Province	8.3	Suyetnov et al. (1980)

1.7.4 Heat Generation and Geological Age

It was mentioned earlier (see Sect. 1.2) that researchers supporting models of a 'cold' origin of Earth believe that after the formation of the Earth the main source of heat energy was the decay of the radioactive elements ^{238}U, ^{235}U, ^{232}Th and ^{40}K (Urey 1955; Birch 1965; Lubimova 1968b; Safronov 1969, etc.). As was also mentioned, most scientists believe that during the Earth's formation and differentiation the main radioactive elements were concentrated in a thin layer within the upper crust (see Sect. 1.7.2).

Table 1.21 Abnormally high HFD values for some areas

Region	Values of HFD as high as[a] (mW m^{-2})	References
Central Valley, Cordillera	158	Hamza and Muñoz (1996)
Patagonian Cordillera	160	Hamza and Muñoz (1996)
Altiplano, Cordillera	180	Springer and Förster (1998)
Yellowstone, USA	>120	Blackwell et al. (1991)
Salton Trough, USA	>120	Blackwell et al. (1991)
Northeast German Basin	91	Norden et al. (2009)
North Caucasus, Russia	205	Suyetnov (1963)
Saratov province, Russia	267.5	Pilchin (1983)
Astrakhan Province, Russia	193	Suyetnov et al. (1980)
Baikal rift zone, Russia	≥200	Lysak and Sherman (2002)

This would then mean that the main sources of the Earth's heat flow are the energy from radioactive decay within the upper crustal layers and the secular cooling of Earth (release of the heat energy accumulated during accretion). Thus analyzing the sources of heat generation and cooling rates within the crust and mantle, as well as the impact of each of these components on surface heat flow, is crucial. For this purpose, available data on sources of heat generation within the crust and mantle will be discussed in this section, while cooling rates within the crust and mantle and estimates of mantle heat flow in various regions by different authors are discussed in Sect. 1.7.5.

Since neither the Earth nor the Sun is capable of synthesizing radioactive elements, it is clear that all the radioactive elements present within the Earth came from the accretion process and since then have been decaying, thus releasing heat. This means that there is no renewable source of such elements and their present abundance on Earth depends on their initial quantities and half-life periods. For this reason all radioisotopes are divided into two groups: short-lived radioactive elements with short half-lives that mostly decayed during the early periods of the Earth's evolution, and long-lived radioactive elements (^{238}U, ^{235}U, ^{232}Th and ^{40}K), with half-lives of a few billion years whose initial quantity has only fractionally decayed since the formation of the Earth.

The issues related to heat generation in the Hadean and Archean are discussed in a number of studies (e.g., Urey 1955, 1956; Lubimova 1968b; Lambert 1976; Burke and Kidd 1978; Watson 1978; England 1979; Bott 1982; Turcotte and Schubert 1982; Holm and Hennet 1992; Pollack 1997; Bjørnerud and Austrheim 2004; Korenaga 2006; Jaupart and Mareschal 2007; Michaut et al. 2009). They suggest that the results of estimates of heat generation by radioisotopes in rocks depend to a great extent on which geochemical model of the Earth and the composition of the Earth's layers is used. However, since radioisotopes/nuclides are constantly decaying, only long-lived radioactive isotopes can still be found in rocks, and their present abundances represent a mere fraction of those at the time of accretion, in the Hadean, Archean, Proterozoic, Paleozoic, etc. Hence, since all

nuclides have different half-life constants, they all preserve different relative fractions of their original quantity. We can therefore extrapolate the abundance of each radioisotope for every period of geological time and estimate the amount of heat it would have released based on its half-life, heat production, and present concentration.

Even though parameters such as the half-life of radioisotopes ^{238}U, ^{235}U, ^{232}Th, ^{40}K and their heat production are constants, estimates of the amount of heat generation in rocks and rock layers still depend considerably on the abundance of these radioisotopes/nuclides within rocks. Since the content of thorium (Th) and uranium (U) on the planet is relatively well-established, a key task is determining the level of potassium (K) in silicate rocks (see for example Wasserburg et al. 1964; Jochum et al. 1983; Arevalo et al. 2009). K acts as a volatile species and its content in silicates on the Earth is usually determined as a function of the terrestrial K/U ratio (Wasserburg et al. 1964; Jochum et al. 1983; Arevalo et al. 2009). As indicated in a review in (Arevalo et al. 2009) and recent data presented there, the K/U ratio depends on the kind of magmatic rocks analyzed (Mid Ocean Ridge Basalts, Ocean Island Basalts, etc.) as well as on the sampling region. As a function of the data available for analysis, various researchers have reported different values for the K/U ratio, ranging from 6,000–7,000, to even more than 20,000 (see review and data presented in Arevalo et al. 2009). Naturally, any study should utilize calculations of abundances of long-lived radioisotopes in rocks from the area under study. Since most geothermal data indicate a clear concentration of the absolute majority of long-lived radioisotopes within the upper crust layers, which are mostly composed of felsic and intermediate magmatic rocks, it is these kinds of rocks that should be probed when determining the K/U ratio, rather than different kinds of basalts as was done in (Arevalo et al. 2009). For example, data from (Pollack 1982) shows the average K/U ratio to be 9,000 for granites and rhyolites, 11,000 for granodiorites and dacites, 7,000 for diorites and andesites, 8,000 for gabbro and basalts, and 3,000 for peridotites and dunites.

Estimates of the abundances of the main long-lived radioisotopes ^{238}U, ^{235}U, ^{232}Th and ^{40}K, their relative content, the relative heat produced by a unit of the radioisotope, and the relative total heat produced per unit during the entire span of the Earth's evolution from $\sim$4.6 Ga to the present are presented in Tables 1.22 and 1.23. For these estimates, the current values of the relative concentration of these radioisotopes were normalized to the abundance of total U, according to the ratio U:Th:K = 1:4:(1.27×10^4), where ^{238}U/U = 0.9927, ^{235}U/U = 0.0072, and ^{40}K/K = 1.28×10^{-4}; and all Th as ^{232}Th is accepted, after (Korenaga 2006). The half-life and heat production values of these radioisotopes are similar to those accepted by (Turcotte and Schubert 1982). Since these kinds of estimates are extremely model dependent, the abundance of U is accepted as a unit. Clearly the results presented in Tables 1.22 and 1.23 are only relative estimates and should not be used for any precise calculations.

It is clear from Tables 1.22 and 1.23 that the relative content of long-lived radioactive isotopes (U^{238}, U^{235}, Th^{232}, and K^{40}) was about four times greater at the time of accretion than it is currently, and that the energy released by them was

Table 1.22 Relative abundance of long-lived radioisotopes and their radiogenic heat production throughout the Earth's evolution

Isotope	Half-life, Ga	Heat production (μW/kg)	Relative abundances of radioisotopes in:					
			0 Ga	1 Ga	2 Ga	3 Ga	4 Ga	4.6 Ga
^{238}U	4.47	94	0.9927	1.159	1.354	1.581	1.846	2.026
^{235}U	0.704	570	0.0072	0.019	0.052	0.138	0.370	0.667
^{232}Th	14.00	26.6	4.0	4.203	4.416	4.641	4.876	5.023
^{40}K	1.25	27.9	1.6256	2.830	4.928	8.580	14.939	20.836

Table 1.23 Relative heat production by different long-lived radioisotopes

Age (Ga)	Relative content of radioisotopes	Relative heat produced per unit of radioisotope (relative concentration · heat production)				Relative total heat produced per unit	No. of times present value of heat was produced
		^{238}U	^{235}U	^{232}Th	^{40}K		
0	6.6255	93.314	4.104	106.400	45.354	249.172	1.00
1	8.204	108.946	10.830	111.780	78.957	310.509	1.25
2	10.750	127.276	29.640	117.466	137.491	411.873	1.65
3	14.940	148.614	78.660	123.451	239.382	590.106	2.37
4	22.031	173.524	210.900	129.702	416.798	930.924	3.74
4.6	28.552	190.444	380.190	133.612	581.324	1,285.570	5.16

about five times higher than it is now. It is well known that the Proterozoic content of long-lived radioactive isotopes and their heat generation was significantly greater than it is today (Attoh 2000; McLaren et al. 2003, etc.).

Analysis of data on heat generation by radioactive elements shows that it varies significantly by lithological composition, area, age, depth, and other parameters. It was mentioned above that during the evolution of the early Earth short-lived radioisotopes could have been involved in the generation of heat. Based on analysis of short-lived radionuclides, Urey (1955) came to the conclusion that only two radioisotopes ^{26}Al and ^{36}Cl could have played a significant role in the thermal regime of the early Earth. ^{26}Al has a half-life in the range of 7.05×10^5 (Norris et al. 1983) to 7.38×10^5 (Kohman 1997) years with an accepted value of 7.16×10^5 (Norris et al. 1983). ^{36}Cl has a half-life of 3.01×10^5 years (Daillant et al. 2009). These half-life values show that both these radioisotopes could only have been important for heat generation for the first ten or few tens of millions of years, and quite possibly only during accretion of the planet.

There is much debate on how to estimate the proportion of crustal radiogenic heat production in the surface heat flows. For instance, Rudnick and Fountain (1995) estimated that in Archean regions, 50–85 % of the heat flowing from the surface of Earth was generated within the crust. Turcotte (1980) believed that 83 % of the present heat flow can be attributed to the decay of radioactive isotopes and 17 % to the cooling of the Earth. Schubert et al. (1980) stated that radiogenic heat production would only be 65–85 % of the surface heat flow. Thakur and

Table 1.24 Heat generation (A) in rocks of the crust and upper mantle

Rock types	Heat generation A ($\mu W\ m^{-3}$)		
	After Vinogradov (1962)	After Tilton and Reed (1963)	After Pollack (1982)
Granites	2.5100	2.3900	2.500
Intermediate magmatic rocks	1.2600	1.2600	1.100–1.500
Basalts	0.5000	0.5400	0.300
Peridotites	–	0.0040	0.010
Dunites	0.0050	0.0008	0.002
Sedimentary	1.7000	–	–
Chondrites	0.0190	0.0170	–

Table 1.25 Heat generation (A) in different layers of crust and upper mantle (after Smyslov 1974)

Layer	Heat generation A ($\mu W\ m^{-3}$)
Sedimentary	1.39
Granite-metamorphic	2.57
Diorite-trachiandesite	1.31
Basalt	0.47
Upper mantle	0.13

Blackwell (2008) showed that only 16–24 % of the total heat-producing elements are in the crust. Vacquier (1998) estimated the radiogenic heat production lost as only 41% of the total heat lost by the Earth. His estimates also indicate that 70 % of the worldwide mantle heat flowing through very old ocean floors is radiogenic, and only 30 % of it is from secular cooling.

There is a general consensus that radioactive heat production A decreases from acidic to basic compositions (Rybach 1978). The heat production (A) values for various rocks and layers of the crust and mantle are presented in Tables 1.24, 1.25, 1.26, 1.27, 1.28.

Tables 1.24, 1.25, 1.26, 1.27, 1.28 show that heat generation varies greatly in rocks as a function of different lithological compositions and different areas, but in general it decreases from acidic to basic rocks and with depth. It is also obvious that the heat generation of the middle and lower crust, as well as upper mantle, is not negligible and cannot be ignored in geothermal analyses of the conditions within the crust and upper mantle. Interestingly, gneisses, which are among the oldest kinds of rock in the world, are characterized by very high values of heat production in the Kerala Khondalite Block of the Southern Granulite Province of India (see Table 1.26). In fact, in the Kerala Khondalite Block garnet biotite gneisses are known to contain high levels of Th and U, with mean values of 60 and 3 ppm, respectively (Ray et al. 2008). The high heat production of this region's granulites contrasts with the relatively low heat production of the Late Archean granulites of the Northern Block of the Southern Granulite Province of India (Ray et al. 2008). Ray et al. (2003) reported that in the Northern Block of the Southern

Table 1.26 Heat generation for rocks of the upper, middle and lower crust and the upper mantle in some regions

Area	Lithology described	Heat generation ($\mu W\ m^{-3}$)	References
Archean	Bulk crust	0.65	McLennan et al. (2006)
Arabian plate	East of the Dead Sea Fault	0.83	Förster et al. (2007)
Crust	Bulk radioactivity	0.50	Thakur and Blackwell (2008)
Iberian Peninsula	Granitic rocks	2.50–3.50	Fernàmdez et al. (1998)
Iberian Peninsula	Metasediments	1.00–2.50	Fernàmdez et al. (1998)
Australia, Proteroz.	Granites, granitic gneisses	4.60	McLaren et al. (2003)
Eastern Ghats Belt	Charnockites, gneisses	2.5–2.9	Kumar et al. (2007b)
Eastern Ghats Belt	Intermediate granulites	0.60–1.10	Kumar et al. (2007b)
Eastern Ghats Belt	Mafic granulites	0.30	Kumar et al. (2007b)
Galicia	Granodiorites	1.67	Louden and Mareschal (1996)
Galicia	Metamorphosed gabbros	0.21	Louden and Mareschal (1996)
Galicia	Serpentinized peridotites	< 0.01	Louden and Mareschal (1996)
Deccan Province	Basalts (tholeiite)	0.39	Kumar et al. (2007a)
S. Scandinavia	Granulite	0.40	Pinet and Jaupart (1987)
S. Scandinavia	Amphibolite facies rocks	1.60	Pinet and Jaupart (1987)
S. Scandinavia	Granites	2.70	Pinet and Jaupart (1987)
Lower crust	Granulites	0.40	Hasterok and Chapman (2007)
Lower crust	Mafic xenoliths	0.13	Hasterok and Chapman (2007)
Upper mantle	Cratonic xenoliths	0.019	Hasterok and Chapman (2007)
Continental margin	Mid-lower crust	0.30	Shi et al. (2000)
Altiplano plateau	Upper crust	1.00–1.50	Muñoz (2005)
Altiplano plateau	Middle crust	0.60–0 .80	Muñoz (2005)
Altiplano plateau	Lower crust	0.20–0.50	Muñoz (2005)
Altiplano plateau	Upper mantle	0.02	Muñoz (2005)
Eastern Desert, Egypt	Basalt	0.11	Abbady et al. (2006)
Eastern Desert, Egypt	Granite	Up to 9.53	Abbady et al. (2006)
Eastern Desert, Egypt	Serpentinite	0.28	Abbady et al. (2006)
Eastern Desert, Egypt	Metagabbro	0.91	Abbady et al. (2006)

(continued)

Table 1.26 (continued)

Area	Lithology described	Heat generation ($\mu W\ m^{-3}$)	References
Eastern Desert, Egypt	Amphibolites	0.40	Abbady et al. (2006)
Anabar Province	Middle crust	0.56	Glebovitskiĭ (1997)
Himalaya	Granites and gneisses	3.93–6.52	Kumar et al. (2009)
KKB[a], India	Garnet–biotite gneiss	5.50	Ray et al. (2008)
KKB[a], India	Granitic gneisses	4.60	Ray et al. (2008)
KKB[a], India	Khondalite	2.70	Ray et al. (2008)
KKB[a], India	Charnockite	2.20	Ray et al. (2008)
KKB[a], India	Granites	2.60	Ray et al. (2008)
KKB[a], India	Leucogranites	3.40	Ray et al. (2008)
KKB[a], India	Syenites	1.40	Ray et al. (2008)
Oslo Rift	Granites	5.00	Slagstad (2006)

[a] KKB—the Kerala Khondalite Block, Southern Granulite Province, India

Table 1.27 Heat generation in clays and sands of Tertiary deposits of some areas of Azerbaijan (after Pilchin 1983)

Area	Heat generation A in clays		Heat generation A in sands	
	Number, n	A ($\mu W\ m^{-3}$)	Number, n	A ($\mu W\ m^{-3}$)
Precaspian-Kuba region	19	4.83	6	2.28
Apsheron archipelago	11	4.50	32	1.25
Baku Archipelago	40	3.56	6	1.94

Table 1.28 Heat generation in crystalline rocks (after Mekhtiev et al. 1971; Pilchin 1983)

Rock types	Acidic	Intermediate	Basic
Heat generation A ($\mu W\ m^{-3}$)	1.80	0.80	0.67

Granulite Province of India, a two-layer granulitic crust of Late Archean charnockites and gneisses is present. They indicated that the heat production in the upper (roughly 7–10 km thick) metasomatized granulitic layer ranges from 0.2 to 0.75 $\mu W\ m^{-3}$ (with a mean of 0.5 $\mu W\ m^{-3}$); and this layer overlies granulites of the second layer, which is depleted of radioelements, with a very low heat production ranging from 0.14 to 0.2 $\mu W\ m^{-3}$ (with a mean of 0.16 $\mu W\ m^{-3}$). Observations from exposed granulite terranes indicate values of heat generation in the range of 0.15–2.0 $\mu W\ m^{-3}$ with a median value of 0.4 $\mu W\ m^{-3}$ (Hasterok and Chapman 2007). Since it is believed that granulites compose a significant portion of the lower crust of Archaean cratons, the heat production of lower crustal rocks may be considerable. At the same time, analysis of available data on heat generation shows that there is a clear increase in the value of heat production the younger the region of formation. The average heat generation for regions formed in different geological periods are presented in Table 1.29.

Table 1.29 Estimates of the bulk continental crust heat production from heat flux data (after Jaupart and Mareschal 2003, 2007; Jaupart et al. 2007)

Geological age	Heat generation (A) ($\mu W\ m^{-3}$)
Archaean	0.56–0.73
Proterozoic	0.73–0.90
Phanerozoic	0.95–1.21

It is clear from Table 1.29 that regions formed mostly during the Archaean have the lowest heat generation values. Jaupart and Mareschal (2003) also determined the average heat generation for the Precambrian crust ($0.77 \pm 0.08\ \mu W\ m^{-3}$) and for the Phanerozoic crust ($1.03 \pm 0.08\ \mu W\ m^{-3}$). These values contradict the common belief that radioactive heat sources were collected within the crust during the differentiation of the early Earth.

Even though the heat flow is slightly lower in the Yilgarn block than in the Pilbara block of the Western Australian craton (39 and 43 $mW\ m^{-2}$, respectively), the average surface heat generation is high for the Yilgarn block ($2.5\ \mu W\ m^{-3}$), with some extremely high local values of up to $8\ \mu W\ m^{-3}$ (Cull 1991). These facts clearly disconfirm any relationship between HFD and heat generation. The high heat flux in the Paleozoic Appalachians is mostly accounted for by the high heat production ($3\ \mu W\ m^{-3}$) at shallow depths (Jaupart and Mareschal 2007). Morgan (1985) showed that on average, the abundance of potassium, uranium, and thorium is low in the surviving Archean crust relative to the younger continental crust. Jaupart and Mareschal (2007) also pointed out that on average, the Archean crust of today is associated with fewer heat-producing elements than the younger crust. Kukkonen and Lahtinen (2001) reported an increase in the heat production rate from Archean to Proterozoic rocks in an E–W direction within the central Fennoscandian Shield. Up to 5 km thick regional-scale Late- to Post-Sveconorwegian granites with average heat production rates of about $5\ \mu W\ m^{-3}$ were reported in the area of the Oslo Rift (Slagstad 2006). Attoh (2000) showed that during Penokean metamorphism in northern Michigan, heat generation was $\sim 10.6\ \mu W\ m^{-3}$, whereas it was $\sim 3.7\ \mu W\ m^{-3}$ in the Archean basement. Heat generation values of about $4.8\ \mu W\ m^{-3}$ were reported for the Proterozoic Wopmay orogen of Canada (Jaupart and Mareschal 2003). High values of heat production of about $3.6\ \mu W\ m^{-3}$ were also reported for the Proterozoic Gawler craton of Central Australia (Heier and Lambert 1978). Mesoproterozoic gneisses and granites of the Mount Painter Province in the northern Adelaide Fold Belt of South Australia yielded an area-integrated mean heat production of $9.9\ \mu W\ m^{-3}$ (Neumann et al. 2000). Even greater values of heat generation for Proterozoic granites and granite gneisses from the Mount Painter Province of up to $16.1\ \mu W\ m^{-3}$ were reported by McLaren et al. (2006) as the average heat production for the region, with individual lithology yielding heat production in excess of $60\ \mu W\ m^{-3}$. Rybach and Buntebarth (1984) indicated that Precambrian rocks exhibit significantly lower heat generation than that of Phanerozoic rocks (only about one third).

All these data show that in many cases heat generation in Proterozoic regions is much greater than in regions adjacent to the Archean crust. Taking into account that heat generation is the highest in granitic rocks (see Tables 1.24, 1.25, 1.26, 1.28) and that the thickness of granites is maximal in the Archean lithosphere, this distribution of heat generation with the age of a region is somewhat unexpected. The content of radioactive elements in rocks and rock layers depends on their initial distribution and subsequent re-distribution in the rock layers. If radioactive elements have been concentrated in a thin layer in the upper crust since the differentiation of the Earth's layers (most likely during the formation, cooling and solidification of the magma-ocean) and there are no new sources of radioactive elements, how is it possible that in more recent time periods the Earth's crust has acquired higher concentrations of radioactive elements?

Another point is the obvious increase in the proportion of basic magmas formed since the Proterozoic, which contain much smaller amounts of radioactive elements and are characterized by much lower values of heat generation (see Tables 1.24, 1.25, 1.26, 1.28). In addition, the depths from which magmas are formed increase with the recency of the magmatic event, which is also confirmed by the known increase in iron-content in these younger magmas (Pilchin and Eppelbaum 2009). Thus where do such significant additional amounts of radioactive elements come from? If radioactive elements are concentrated within a thin layer near the surface, rising magmas cannot have brought radioactive elements to the surface. One possible answer to such an unusual distribution of heat generation values with age is related to the formation of sediments, known as the second highest source of heat generation after granitic rocks (see Tables 1.24, 1.25, 1.27). Another reason for this distribution of radioactive elements may be the formation of layers within the magma-ocean, which is stratified by differences in density and consequently prevented from active exchange of matter between layers (Pilchin and Eppelbaum 2009). In this case, radioactive elements would be concentrated at the top of each layer and magma rising to the surface could bring them up as well. Magma passing through several such layers would be more highly enriched in radioactive elements, and could deliver them to the surface. It is also possible that the higher surface heat flow in Proterozoic than in Archean regions, and heat flows that are higher in Phanerozoic regions than in Proterozoic ones are related to differences not in the heat generation within the crust of these areas, but to mantle heat flow which is greater in younger regions. This is because the lower crust and upper mantle of these younger regions are more permeable to heat transfer to the upper crust and surface. This is consistent with (Cull 1982) who provided two possible explanations for the considerable variation in heat flow between the central Proterozoic and western Archean terranes of Australia: either the mantle heat flow is greater in central Australia, or higher crustal heat production in the central Proterozoic terrane causes the variation.

Another method of characterizing the thermal regime of the Earth's strata is based on the use of the Urey ratio, which is the ratio of heat production to heat loss. This ratio shows the proportion of heat production associated with radioisotopes in the heat balance of the Earth. This value is also strongly model

dependent, and different estimates yield values from 0.15–0.30 (Korenaga 2006) and 0.21–0.49 (Labrosse and Jaupart 2007) to values as high as 0.70 (Korenaga 2006; Labrosse and Jaupart 2007) and 0.65–0.85 (Schubert et al. 1980). It is obvious that such significant differences in the ratio lead to substantial ambiguity in interpretations.

1.7.5 Mantle Heat Flow

Surface heat flow is the amount of heat that escapes through the Earth's surface, and is the result of radiogenic heat production and secular cooling (Jaupart and Mareschal 2003). On the other hand, mantle heat flow represents the flow of heat from the mantle into the crust. Together with the heat generated within the crust, mantle heat flow combines into HFD at any depth within the crust. This means that the surface heat flow has two main components: heat generated by radioactive sources within the crust and heat entering the crust from the mantle and transferred by conduction through the crust to the surface (Jaupart and Mareschal 2003). Jaupart and Mareschal (2003) showed that for stable continents, crustal heat production and mantle heat flow are the main properties of the thermal regime. The value of the mantle heat flow can be obtained by subtracting the crustal contribution to the heat flow from the surface heat flow (Mareschal and Jaupart 2006). In other words, to estimate a component of heat flow from the mantle (Q_M), the amount of heat generated within the crust (Q_C) should first be determined and subtracted from surface heat flow (Q_S) measured near the surface ($Q_M = Q_S - Q_C$).

Since estimates of the component of crustal heat flow cannot be based on direct measurements at any level within the crust, it is clear that the estimates for Q_C and Q_M are model dependent. In order to make such estimates, we first have to determine the approximate distribution of heat generation with depth within the crust, and then calculate the heat generated within the crust by radioactive decay alone. For example, to determine the crustal and mantle heat flow components, a model of radioactivity exponentially decreasing with depth was used in (Čermák 1982b); in (Rybach and Cermák 1987) a model of the conversion of compressional seismic velocity into heat production was used; similar models were also used in (Kutas 1979), etc. These models were discussed in Sect. 1.7.1. Using these models is controversial as they can lead to highly ambiguous estimates, the accuracy of which is difficult or even impossible to verify. For instance, when employing these models, the mantle heat flow for the Baltic Shield has been estimated to be high (20–30 mW m^{-2}, Arshavskaya 1979, and <30 mW m^{-2}, Čermák and Bodri 1995), low (5–7 mW m^{-2}, Hänel et al. 1979), intermediate (16–17 mW m^{-2}, Balling 1976) and as low- to- intermediate (7–15 mW m^{-2}, Kukkonen and Peltonen 1999).

The results of estimates of the crustal contribution to surface heat flow by different authors are presented in Sect. 1.7.4. These estimates also suggest that the mantle component of the surface heat flow can be as low as 15–17 %, and up to

76–84 %. McLaren et al. (2002) claimed that out of the global mean heat flow value for the continental crust of 65 ± 1.6 mW m^{-2}, about 30 mW m^{-2} is a consequence of radiogenic heat production within the crust. This would suggest a possible percentage of the mantle component in surface heat flow of about 35 %. Gornov et al. (2009) reported dome-shaped features in the crust which correlate upwards at the top of the asthenosphere and are marked by high heat flows of about 60–90 mW m^{-2}, with a greater contribution of heat from the mantle than the crust (about 30–60 mW m^{-2} mantle component to 20–30 mW m^{-2} crustal component), making the proportion of mantle heat flow in these structures about 50–67 %. They also detailed how the mantle component of heat flow is significantly higher than the radiogenic component in such structures as the Upper Zeya Basin, the Central Zeya Basin, the Songliao Basin, the Tokko Basin, the Liaodong uplift, and the Zhangguangcailing terrane, in which the mantle heat flow contribution is about 69, 64, 65, 64–71, 62, and up to 72 %, respectively. Data reported by Blackwell (1983) show that the mantle component of the heat flow in the Northern Basin and Range Province is about 69 % of the mean heat flow. Čermák and Bodri (1995) reported values of heat flow as high as up to about 40 mW m^{-2} for the Norwegian Caledonides, 50 mW m^{-2} for the Hercynides, 60 mW m^{-2} for the Alps, 90 mW m^{-2} for the Tyrrhenian Sea, and 70 mW m^{-2} for Tunisia.

Sclater et al. (1980) estimated the values of the mantle heat flow beneath the ocean at equilibrium and beneath an old stable continent to be between about 25–38 and 17–31 mW m^{-2}), respectively. Majorowicz (1978) estimated the mantle heat flow to be as low as 8.4–12.6 mW m^{-2} for the Precambrian Platform and as high as 31–40.2 mW m^{-2} for Paleozoic orogenic areas. Čermák (1982b) estimated the value of the mantle heat flow for the Pannonian Basin to be as high as about 61 mW m^{-2}. He also estimated the values of mantle heat flow beneath the European shields to be 15–20 mW m^{-2}, and for the platform areas, Paleozoic folded units, and in Cenozoic mountain belts to vary from 20–25 to 30–35 mW m^{-2}. The mantle heat flow estimated for the Thompson Early Proterozoic metasedimentary belt of the Trans-Hudson Orogen of Canada is as low as of 11–12 mW m^{-2} (Rolandone et al. 2002). Estimates of the mantle heat flow for some cratons are in the following ranges: 7–15 mW m^{-2} beneath the Baltic Shield (Kukkonen and Peltonen 1999); 17–25 mW m^{-2} for the Kalahari craton, South Africa (Rudnick and Nyblade 1999); 15–20 mW m^{-2} for European Shields (Čermák 1982b); 11–18 mW m^{-2} for the Canadian Shield (Jaupart and Mareschal 2003); 11–16 mW m^{-2} for the Dharwar Craton of India (Ray et al. 2003); 23–32 mW m^{-2} for Late Archean Southern granulite province of India, and 12–24 mW m^{-2} for the Slave Craton of Canada (Russell and Kopylova 1999).

Unfortunately, the results of all these estimates of mantle heat flow values are not completely model dependent, and neither the heat flow going through the Moho into the crust, nor its proportion within surface heat flow can be independently verified.

It should be pointed out that there is an enormous difference between heat flow from the mantle (HFD entering the crust from the mantle) and the mantle

component of surface heat flow (part of surface heat flow coming from the mantle via conduction through the crust and exiting from the surface). Both of these heat flows are referred to as "mantle heat flow" in the scientific literature and one should be careful not to confuse them. For example, some researchers mention heat flow at the Moho (Kutas 1979; Čermák 1982b; Čermák and Bodri 1995; Vosteen et al. 2003; Kumar et al. 2007a, and many others), which in fact represents the heat flow entering the crust from the mantle. Conversely, the mantle heat flow determined by subtracting the heat flow rising from the Earth's crust from the surface heat flow (Pollack and Chapman 1977b; Ray et al. 2003), as well as the mantle heat flow component discussed in (Lenardic et al. 2000) definitely refer to the proportion of mantle heat flow contributed by surface heat flow. It should also be taken into account that according to the standard model of heat production that assumes radioactive decay alone (see for example Lubimova 1968b) the radiogenic crustal component of heat flow drops from a maximum near the surface to zero at the Moho; hence the mantle component should be at a maximum at the Moho and a minimum near the surface. This is related to the fact that since the Earth's crust is not transparent and not a vacuum, the heat flow entering the Earth's crust through the Moho from the mantle cannot be immediately released from the surface (see Sect. 7.4), and is instead either partially or completely absorbed by the crustal layers, to later be gradually re-transferred to the upper layers until it reaches the surface. Part of the heat flow generated by radioactive decay within the crust would also be absorbed by the crustal layers before being transmitted to the surface. This means that the value of HFD released at any given moment from the surface does not necessarily equal the value of HFD released within the crust or entering the crust from the mantle at the same moment. It is incorrect to expect that heat released at the core-mantle interface would reach the surface within a short time interval. If, as most scientists believe, radioactive elements are concentrated in the crust and primarily distributed within a thin layer near the surface, the heat flow from the mantle into the crust would lead to cooling of the mantle. The characteristics of mantle cooling, and the cooling rates of the mantle estimated by different researchers are presented in Table 1.30. The cooling rates of some magmatic and metamorphic formations within the crust are presented for purposes of comparison of these rates with the estimated mantle cooling rates in Table 1.31.

1.7.6 Temperature Distribution Inside the Earth

It is well known that calculation of temperature field distribution inside the Earth is one of the most sophisticated geophysical problems (e.g., Stacey 1992). Development of the deep temperature models by the use of thermal conductivity equations is based on the suggestion of presence of stationary thermal flows at the vertical boundaries of the considered area as well as knowledge of temperature (thermal flows) values at the upper and lower boundaries (Ollinger et al. 2010; Spichak and Zakharova 2013). Application of nonstationary approaches

Table 1.30 Cooling rates of the Earth's mantle estimated by different authors or calculated using their data (modified after Pilchin and Eppelbaum 2012)

Mantle cooling rate (K/Ma)	References
0.04	Jarvis and Campbell (1983)
0.06	Kröner (1982)
0.10–0.12	Dickson and Fanelli (2004)
0.13	Takahashi (1990)
~0.16	Richter (1985)
~0.03 (for continents)	Galer and Mezger (1998)
~0.06 (for no continents)	Galer and Mezger (1998)
0.08	Hamilton (1998)
0.09	De Smet and van den Berg (2000)
~0.04 (today's cooling rate)	Turcotte (1980)
0.05 (mean for last 3 Ga)	Turcotte (1980)
0.20 (today's cooling rate)	Condie (1989a)
~0.12–0.15 (Archean mean cooling rate)	Pollack (1997)
~0.08–0.09 (post-Archean mean cooling rate)	Pollack (1997)
~0.08–0.09 (at mantle-core border)	Yukutake (2000)
0.04–0.10 (for South African lithosphere)	Bedini et al. (2004)
0.03–0.09	Peck et al. (2001)
0.14	Richter (1985)
0.10	van den Berg and Yuen (2002)
0.04–0.06	Cook and Turcotte (1981)
0.04–0.05	Abbott et al. (1994)
0.05–0.10	Schubert et al. (1980)
0.04–0.06	Michaut et al. (2009)
0.03–0.12	Slichter (1941)

(e.g., Alexidze et al. 1993) enables to compute more appropriate models. At the same time for construction of such models a knowledge of important physical-geological conditions (past volcanic events, lithology, age of geological formations, etc.) are necessary. Absence of insufficient knowledge of these geological-geophysical data complicates development of nonstationary geothermal models (Spichak and Zakharova 2013). The temperature distribution inside the Earth may be computed on the basis of several different approaches which are generalized in Fig. 1.6.

1.8 Geothermal Maps

One of the crucial milestones in geothermal mapping was the introduction of isothermal lines (isotherms) by von Humboldt (1817), which would also play an important role in the evolution of cartography (Robinson and Wallis 1967). Some of the first geothermal maps recorded the average annual temperatures of different

Table 1.31 Cooling rates of some magmatic and/or metamorphic complexes from published data (modified after Pilchin and Eppelbaum 2012)

Complex, area	Cooling rate (K/Ma)	Reference
Halls Creek Orogen, W. Australia	1.4–1.5	Bodorkos and Reddy (2004)
Mazury complex, NE Poland	~2.0	Dörr et al. (2002)
Las Termas Belt, NW Argentina	3.0–4.0	Höckenreiner et al. (2003)
Cherry Valley, New York	0.38	Johnsson (1985)
Ruhr Basin, Germany	0.1–0.2	Karg et al. (2005)
Grenville Province, W. Québec	6.0	Martignole and Reynolds (1997)
Central and Eastern Pyrenees	3.7	Morris et al. (1998)
Witwatersrand Basin, South Africa	1.4	Omar et al. (2003)
Four orogenic belts of India	0.2–25.0	Sharma et al. (1980)
Urach, SW Germany	1.0	Zaun and Wagner (1985)
Adirondack Highlands, New York	4.0	Johnson et al. (2002)
Grenville Province	1.0–3.0	Peck et al. (2003)
Grenville Province	1.0–3.0	Mezger et al. (1991)
Proterozoic Adirondack terrane	0.5–1.0	McKenzie (1978)
Pikwitonei granulite domain, Canada	0.5	McKenzie (1978)
Lowlands and the Highlands, Adirondacks	1.0–2.0	Streepey et al. (2000)
Metamorphism in the W Canadian Shield	~1.0	Baldwin et al. (2004)
Manzano Mountains, New Mexico	1.0	Heizler et al. (1997)
Meteorites	1.0	Shen et al. (1996)
Asteroids	1.0	Rubin and Mittlefehldt (1993)

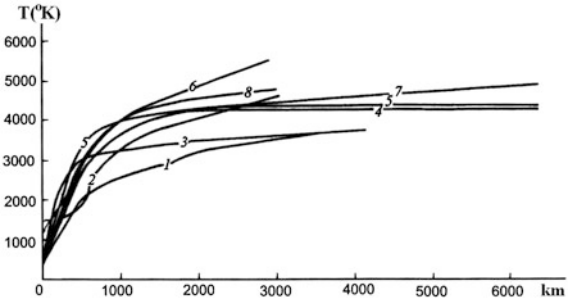

Fig. 1.6 Temperature distribution inside the Earth (Dmitriev et al. 1975; Spichak and Zakharova 2013): (*1*) average temperature with calculation of convection effect in the Earth's mantle (Stacey 1992), (*2*) temperature behavior with calculation of convection (Tozer 1959), (*3*) oceanic model without calculation of convection effect, (*4*) temperature behavior according to Zharkov et al. (1971), (*5*) temperature behavior by constant thermal conductivity (Lubimova 1968b), (*6*) temperature behavior computed by the seismic wave analysis (Zharkov 1958), (*7*) thermal behavior computed by the reference point method (Zharkov et al. 1971), (*8*) thermal behavior computed by the electric conductivity data (Tozer 1959)

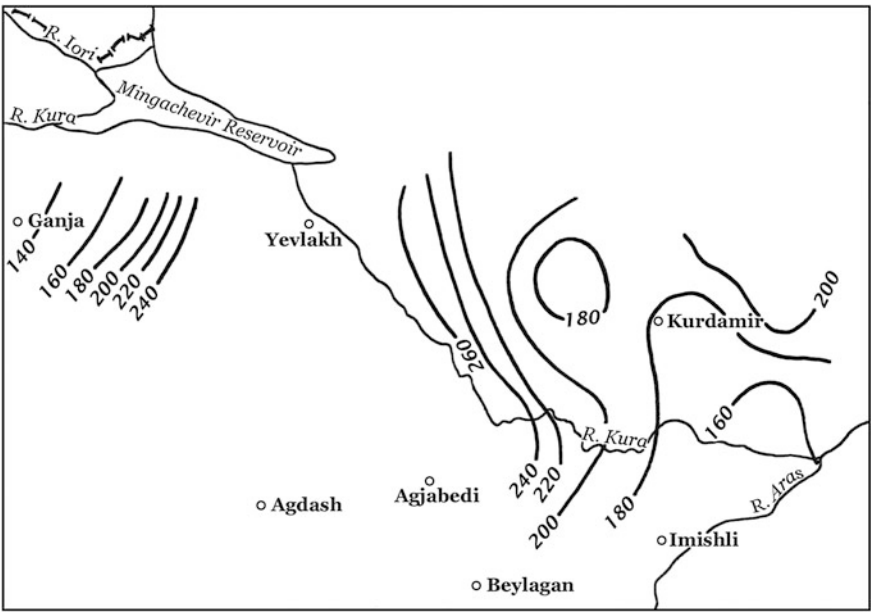

Fig. 1.7 Temperature values (in °C; for conversion 1 °C = 273.15 K) at the top surface of Mesozoic deposits in the Middle Kura Depression

areas (see Sect. 1.1.4), which greatly expanded the fields of geothermics and meteorology. Isotherms, along with similar lines for other thermal parameters (geothermal gradient, heat flow, etc.), can also be used for compiling cross-sections corresponding to a region, by showing the distribution of these geothermal parameters in the horizontal and vertical directions. For instance, in many cases, in order to determine heat absorbing and heat releasing intervals within a region, the information derived from geothermal cross-sections may be even more important than from geothermal maps. Compiling a number of such cross-sections for a region yields a three-dimensional picture of the distribution of geothermal parameters in the region.

Different geothermal maps are compiled to meet varying purposes and aims. They can depict the distribution of heat flow in an area or region (near the surface, at the Moho discontinuity, etc.), the distribution of a specific temperature (Curie point, 200, 400, 600 °C, etc.) at depths, the temperature at a specific geological surface/boundary (the Moho, consolidated crust, "basaltic" layer, "granitic" layer, surface of Jurassic deposits, surface of Mesozoic rocks, etc.), the distribution of geothermal gradients (both vertical and horizontal) over an area or region (near the surface, on the Moho, etc.). The main purpose of geothermal mapping is to show and analyze the relationships between the geological structures of a region and the temperature conditions throughout these structures. Geothermal mapping is also important for estimating the possible depths at which certain processes take place

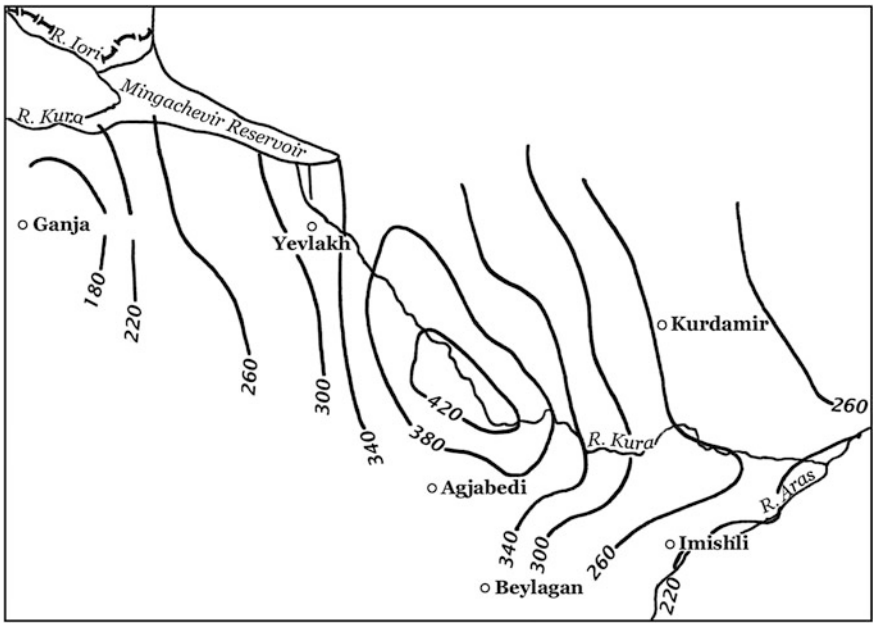

Fig. 1.8 Distribution of temperatures (in °C) at the surface of the consolidated crust in the Middle Kura Depression

(metamorphism, decomposition of rocks and minerals, transformation of ferrous to ferric iron, etc.), and specific conditions and/or states of matter (critical or supercritical state of water, melting point of rocks and minerals, maximum overpressure in porous fluids, etc.). One of the main applications of geothermal mapping is to search for geothermal sources of energy by evaluating regions and identifying depth intervals with abnormally high temperatures and heat flow.

In many cases to accurately compile a geothermal map for a region, especially in cases involving geothermal parameters at depths greater than those at which measurements were and can be taken, requires specific methods of calculation and specific models of the composition of the Earth's layers (for example multi-layered models and multi-dimensional models). Methods of calculating thermal parameters at great depths are discussed in Sect. 1.7. Examples of different geothermal maps for the Kura Depression region are presented in Figs. 1.7, 1.8, 1.9, 1.10, 1.11.

Numerous maps of the distribution of heat flow at the surface have been compiled (e.g., Čermák et al. 1976; Čermák and Hurting 1979; Čermak and Hänel 1988; Hurtig et al. 1992; Čermák and Bodri 1998, etc.). More complex and informative maps can also be generated. For example, a very detailed geothermal map of the Caucasus region at a scale of 1:1,000,000 was published by Kerimov et al. (1989), which includes such regions as Azerbaijan, Armenia, Georgia, Krasnodar province, Stavropol province, Chechnya, Dagestan, Ingushetiya,

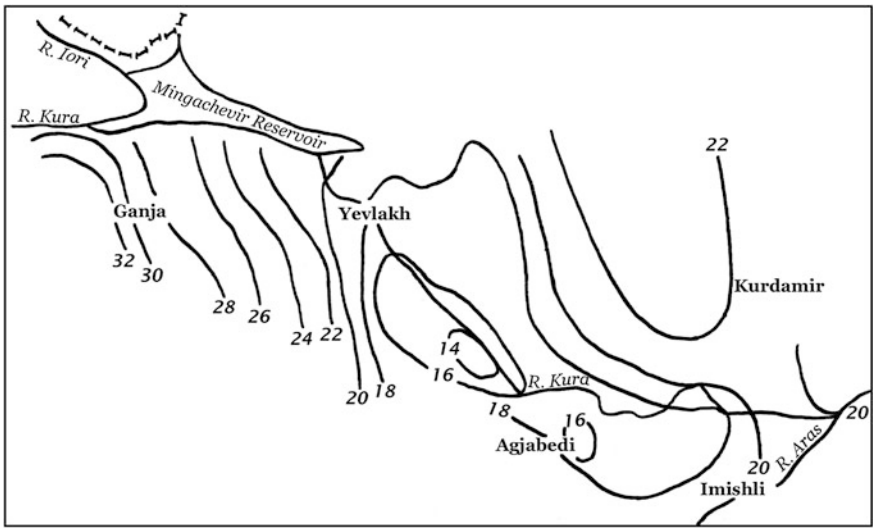

Fig. 1.9 Distribution of the vertical geothermal gradient (in K/km) at the base of the sedimentary layer in the Middle-Kura Depression

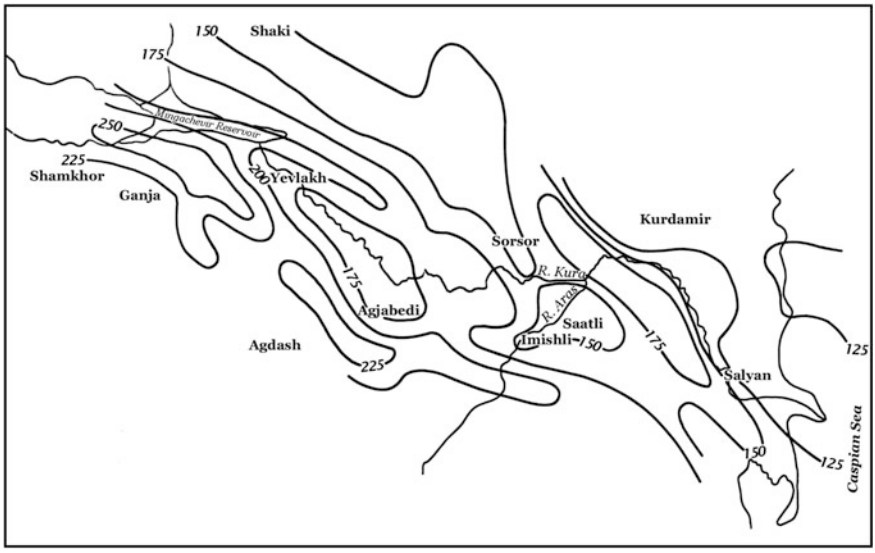

Fig. 1.10 Schematic map of the distribution of temperature (in °C) at a depth of 7,000 m in the Kura Depression

adjoining regions of the Caspian and Black Seas, and certain other areas. It shows the distribution of the geothermal gradient at a depth of 2 km and the distribution of temperatures at depths of 4 and 6 km for the entire Caucasus region. The

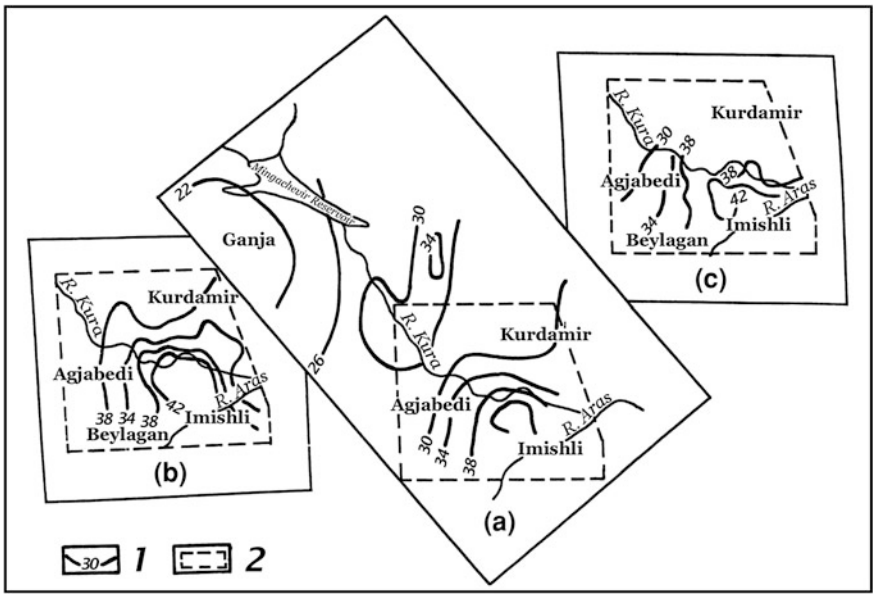

Fig. 1.11 Schematic map of the depth of the Curie point (in km) in the central part of the Kura Depression. Calculations were made using following assumptions: **a** and **b** are 3-layered models; **c** is 5-layered model; (*1*) depth isolines; (*2*) area of calculations made using models **a** and **c**

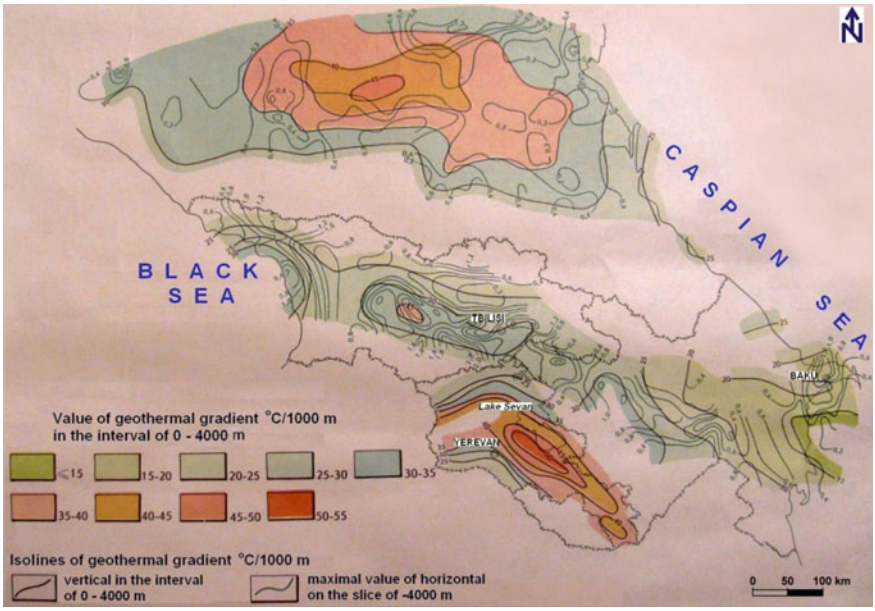

Fig. 1.12 Values of vertical and horizontal geothermal gradients at depths of 0–4,000 m in the Caucasian region (after Kerimov et al. 1989)

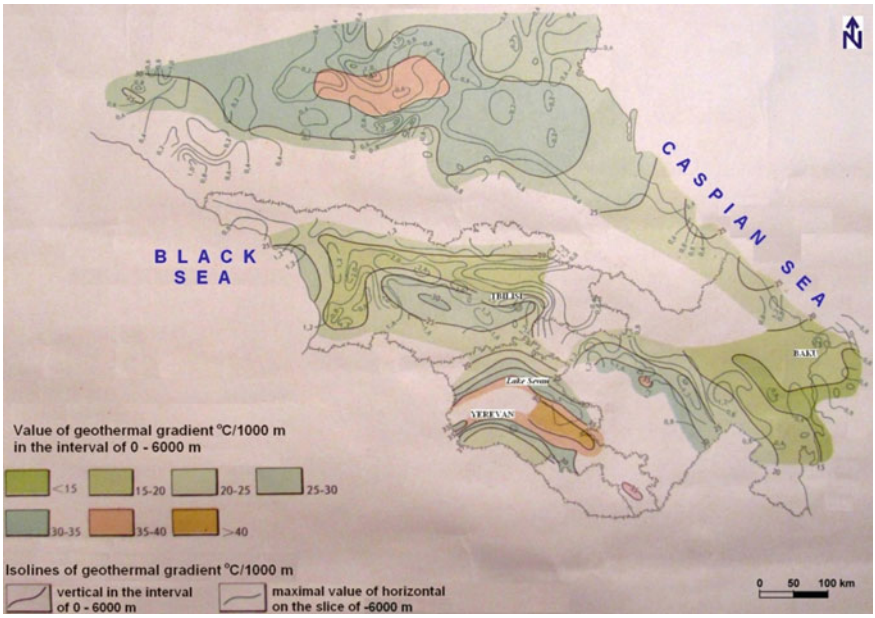

Fig. 1.13 Values of vertical and horizontal geothermal gradients at depths of 0–6,000 m in the Caucasian region (after Kerimov et al. 1989)

publication also included two smaller maps (scale 1:4,000,000) of the region with a comparison of vertical and horizontal geothermal gradients at depths of 4 and 6 km (Figs. 1.12, 1.13).

References

Abbady AGE, El-Arabi AM, Abbady A (2006) Heat production rate from radioactive elements in igneous and metamorphic rocks in Eastern Desert, Egypt. Appl Radiat Isot 64(1):131–137

Abbott D, Burgess L, Longhi J (1994) An empirical thermal history of the Earth's upper mantle. J Geophys Res 99:13835–13850

Abe Y (1997) Thermal and chemical evolution of the terrestrial magma ocean. Phys Earth Planet Int 100(1–4):27–39

Abe Y, Matsui T (1985) The formation of an impact-generated H_2O atmosphere and its implications for the early thermal history of the earth. J Geophys Res 90:C545–C559

Adams LX (1924) Temperatures at moderate depths within the earth. J Wash Acad Sci 459–472

Adie R (1854) On the temperature of running streams during periods of frost. Edinb Phil J LVI:224–229

Adie R (1863) On the mean annual temperature of Western Europe, compared with other climes. Brit Meteor Soc Proc I:303–306

Adushkin VV, Vityazev AV (2007) Origin and evolution of Earth: present view. Vestnik Russ Acad Sci 77(5):396–402 (in Russian)

Albarede F (1975) The heat flow/heat generation relationship: An interaction model of fluids with cooling intrusions. Earth Planet Sci Lett 27(1):73–78
Aleinikov AL, Belikov VT, Eppelbaum LV (2001) Some Physical Foundations of Geodynamics. Kedem Printing-House, Tel Aviv, Israel (in Russian, contents and summary in English)
Alexidze MA, Gugunava GG, Kiria DK, Chelidze TL (1993) A three-dimensional stationary model of the thermal and thermoelastic fields of the Caucasus. Tectonophysics 227(1–4):191–203
Amirkhanov KhI, Rovnin LI, Suyetnov VC, Gaurbekov KhA, Baykov AM (1975) Experience of oil and gas thermal research. Makhachkala, Russia (in Russian)
Anderson EM (1934) Earth contraction and mountain building. Gerlands Beiträge zur Geophisik 42:133–159, 43:1–18
Anderson DL (1967) A seismic equation of state. Geophys J Roy Astron Soc 13:9–30
Anderson DL (1989) Theory of the Earth. Blackwell Science, Oxford
Anderson DL (2002a) The case for irreversible chemical stratification of the mantle. Int Geol Rev 44(2):97–116
Anderson DL (2002b) The inner inner core of Earth. Proc Natl Acad Sci USA 99(22):13966–13968
Anderson DL (2006) Speculations on the nature and cause of mantle heterogeneity. Tectonophysics 416(1–4):7–22
Anderson DL (2007) New theory of the earth. Cambridge University Press, Cambridge
Antonov VE, Baier M, Dorner B, Fedotov VK, Grosse G, Kolesnikov AI, Ponyatovsky EG, Schneider G, Wagner FE (2002) High-pressure hydrides of iron and its alloys. J Phys Condens Matter 14:6427–6445
Arago DFJ (1820) Sur la temperature de l'interieur du globe. Ann Chim, XIII, pp 183–211
Arago F (1857) Sur l'état thermométrique du globe terrestre. In: Notices Scientifiques, Oeuvres Complètes, 2ème éd. tome cinquième, Paris, Legrand, Pomey et Crouzet, pp 148–646
Arevalo R Jr, McDonough WF, Luong M (2009) The K/U ratio of the silicate Earth: insights into mantle composition, structure and thermal evolution. Earth Planet Sci Lett 278:361–369
Arshavskaya NI (1979) On the linear relationship between heat ffow and heat generation in the shields. In: Experimental and theoretical studies of heat flow. Nauka, Moscow, pp 177–194 (in Russian)
Ashwal LD, Morgan P, Kelley SA, Percival J (1987) Heat production in an Archean crustal profile and implications for heat flow and mobilization of heat producing elements. Earth Planet Sci Lett 85:439–450
Attoh K (2000) Contrasting metamorphic record of heat production anomalies in the Penokean Orogen of Northern Michigan. J Geol 108:353–361
Bagin VI, Brodskaya SY, Petrova GN, Pechersky DM (1969) Study on the ferromagnetic fractions in basalts. Izv Acad Nauk USSR Ser Phys Earth (11):66–76 (in Russian)
Bakewell R (1838) An introduction to geology: intended to convey a practical knowledge of the science, and comprising the most important recent discoveries; with explanations of the facts and phenomena which serve to confirm or invalidate various geological theories. Longman, Orme, Brown, Green, and Longmans, London
Baldwin JA, Bowring SA, Williams ML, Williams IS (2004) Eclogites of the Snowbird tectonic zone: petrological and U-Pb geochronological evidence for Paleoproterozoic high-pressure metamorphism in the western Canadian Shield. Contrib Mineral Petrol 147(5):528–548
Balling NP (1976) Geothermal models of the crust and uppermost mantle of the Fennoscandian shield in south Norway and the Danisch Embayment. J Geophys 42:237–256
Balobaev VT, Kutasov IM, Eppelbaum LV (2009) The maximum effect of deep lakes on temperature profiles – determination of the geothermal gradient. Earth Sci Res J 13(1):54–63
Barkstrom BR, Smith GL (1986) The Earth radiation budget experiment: science and implementation. Rev Geophys 24:379–390
Basu AR, Ongley JS, Macgregor ID (1986) Eclogites, pyroxene geotherm, and layered mantle convection. Science 233(4770):1303–1305

Beckwith SVW, Sargent AI, Chini RS, Guesten R (1990) A survey for circumstellar disks around young stellar objects. Astron J 99:924–945

Becquerel H (1896) Sur les radiations émises par phosphorescence. Comptes rendus de l'Académie des Sciences, Paris 122:420–421 (in French)

Becquerel H (1901) Sur la radioactivitie de l'uranium. Comptes Rendus de Seances de l'academie de Sciences 83:977–978 (in French)

Bedini R-M, Blichert-Toft J, Boyet M, Albarède F (2004) Isotopic constraints on the cooling of the continental lithosphere. Earth Planet Sci Lett 223(1–2):99–111

Benenson W, Harris JW, Stocker H, Lutz H (eds) (2002) Handbook of physics, 4th edn. Springer, New York

Benfield AE (1939) Terrestrial heat flow in Great Britian. Proc R Soc Lond A 173:428–450

Bennett J, Donahue M, Schneider N, Voit M (2004) The cosmic perspective, 3rd edn. San Francisco Pearson Education Inc. publ. as Addison Wesley, 844 p

Birch F (1960) The velocity of compressional waves in rocks to 10 kilobars. Part I. J Geophys Res 65:1083–1102

Birch F (1961) The velocity of compressional waves in rocks to 10 kilobars. Part 2. J Geophys Res 66:2199–2224

Birch F (1965) Energetics of core formation. J Geophys Res 24(70):6217–6221

Birch F, Roy RF, Decker ER (1968) Heat flow and thermal history in New York and New England. In: Zen E, White WS, Hadley JB, Thompson Jr JB (eds) Studies of appalachian geology: Northern and maritime. Interscience, New York, pp 437–451

Bischof G (1836) On, the cause of the temperature of hot and thermal springs; and on the bearings of this subject, as connected with the general question regarding the internal temperature of the Earth. Edinb Phil J XX(XL):329–375

Bjørnerud MG, Austrheim H (2004) Inhibited eclogite formation: the key to the rapid growth of strong and buoyant Archean continental crust. Geology 32(9):765–768

Blackwell DD (1971) The thermal structure of the continental crust. In: Heacock JD (ed) The structure and physical properties of the Earth's crust. Geophys Monogr Ser 14:169–184. AGU, Washington, DC

Blackwell DD (1983) Heat flow in the Northern Basin and Range Province. In: Geothermal Resources Council (ed) The role of heat in the development of energy and mineral resources in the Northern Basin and Range Province, Special Report 13, pp 81–93

Blackwell DD, Thakur M (2007) Birch's crustal heat production-heat flow law: key to quantifying mantle heat flow as a function of time. In: Preoceedings of the American Geophysical Union Fall Meeting 2007, Abstract T22B-07

Blackwell DD, Steele JL, Brott CA (1980) The terrain effect on terrestrial heat flow. J Geophys Res 85(B9):4757–4772

Blackwell DD, Steele JL, Carter LC (1991) Heat flow patterns of the North American continent: a discussion of the Dnag geothermal map of North America. In: Slemmons DB, Engdahl ER, Zoback MD, Blackwell DD (eds) Neotectonics of North America, Boulder, Colorado, Geological Society of America, Decade Map volume 1

Bodell JM, Chapman DS (1982) Heat flow in the North-Central Colorado Plateu. J Geophys Res 87:2869–2884

Bodorkos S, Reddy SM (2004) Proterozoic cooling and exhumation of the northern central Halls Creek Orogen, Western Australia: constraints from a reconnaissance $^{40}Ar/^{39}Ar$ study. Aust J Earth Sci 51(4):591–609

Boss AP (1998) Temperatures in protoplanetary disks. Ann Rev Earth Plan Sci 26:53–80

Bott MHP (1982) The interior of the Earth: its structure, constitution, and evolution, 2nd edn. Elsevier, New York, 403 p

Boyet M, Carlson RW (2007) A highly depleted moon or a non-magma ocean origin for the lunar crust? Earth Planet Sci Lett 262(3–4):505–516

Brady RJ, Ducea MN, Kidder SB, Saleeby JB (2006) The distribution of radiogenic heat production as a function of depth in the Sierra Nevada batholith, California. Lithos 86:229–244

Brandner W (2006) Planet formation: theory, observations and experiments. Cambridge University Press, Cambridge
Brown GC, Mussett AE (1993) The inaccessible Earth. Chapman & Hall, London
Brush SG (1977) The origin of the planetesimal theory. Orig Life Evol Biosph 8(1):3–6
Bucher WH (1933) The deformation of the Earth's Crust. Princeton University Press, Princeton
Bullard EC (1939) Heat flow in South Africa. Proc R Soc Lond A 173:474–502
Bullard EC (1954) The flow of heat through the floor of the Atlantic Ocean. Proc R Soc Lond A 222:408–429
Burke KC, Kidd WSF (1978) Were Archean continental geothermal gradients much steeper than those of today? Nature 272:240–241
Cameron AGW (1973) Accumulation processes in the primitive solar nebula. Icarus 18(3):407–450
Cameron AGW (1978) The primitive solar accretion disk and the formation of planets. In: Dermot SF (ed) The origin of the Solar System. Willey, New York, pp 49–74
Cameron AGW (1995) The first ten million years in the solar nebula. Meteoritics 30:133–161
Cameron AGW (1997) The Origin of the Moon and the Single Impact Hypothesis V. Icarus 126(1):126–137
Cameron AGW, Pine MR (1973) Numerical models of the primitive solar nebula. Icarus 18:377–406
Caro G, Bourdon B, Wood BJ, Corgne A (2005) Trace-element fractionation in Hadean mantle generated by melt segregation from a magma ocean. Nature 436:246–249
Carpenter WM (1843) Some remarks on the methods in common use of obtaining the mean temperature of places, and on the supposed difference between temperature of the air and that of the Earth. Am J Sci Arts 44:50–54
Carslaw HS (1906) Introduction to the mathematical theory of the conduction of heat in solids. Dover Publications, London
Carslaw HS (1921) Introduction to the mathematical theory of the conduction of heat in solids, 2nd edn. Completely revised. Macmillan and Co., Ltd, London
Carslaw HS, Jaeger JC (1946) Conduction of heat in solids. Oxford University Press, Oxford
Carslow HS, Jaeger JC (1959) Conduction of heat in solids, 2nd edn. Oxford University Press, Oxford
Čermák V (1982a) A geothermal model of the lithosphere and a map of the thickness of the lithosphere on the territory of the USSR. Izv Acad Sci USSR Phys Earth 18(1):18–27
Čermák V (1982b) Crustai temperature and mantle heat flow in Europe. Tectonophysics 83:123–142
Čermák V (1989) Crustal heat production and mantle heat flow in Central and Eastern Europe. Tectonophysics 159(3–4):195–215
Čermák V (1993) Lithospheric thermal regimes in Europe. Phys Earth Planet Int 79:179–193
Čermák V, Bodri L (1995) Three-dimensional deep temperature modelling along the European geotraverse. Tectonophysics 244(1–3):1–11
Čermak V, Hänel R (1988) Geothermal maps. In: Hänel R, Rybach L, Stegena L (eds) Handbook of terrestrial heat flow density determination. Kluwer Academic Publishers, Dordrecht, pp 261–300
Čermák V, Hurting E (1979) Heat flow map of Europe, 1:5,000,000. In: Čermák V, Rybach L (eds) Terrestrial heat flow in Europe. Springer, Berlin
Čermák V, Rybach L (eds) (1979) Terrestrial heat flow in Europe. Springer, Berlin
Čermák V, Rybach L (eds) (1991) Terrestrial heat flow and the lithosphere structure. Springer, Berlin
Čermák V, Bodri L, Rybach L, Buntebarth G (1990) Relationship between seismic *velocity and heat production*: comparison between two sets of data and test of validity. Earth Planet Sci Lett 99(1–2):48–57
Čermàk V, Balling N, Kukkonen IT, Zui VI (1993) Heat flow in the Baltic Shield—Results of the lithospheric geothermal modelling. Precambr Res 64:53–65

Čermák V (1984) Heat flow and deep structure of Europe. In: Proceedings of 27th international geological congress, vol 8, Moscow, pp 94–110
Čermák V, Bodri L (1998) Heat flow map of Europe revisited. In: Clauser C (ed) Mitteilungen DGG, Sonderband II/1998, pp 58–63
Čermák V, Lubimova EA, Stegina L (1976) Geothermal mapping in Central and Eastern Europe. In: Development and use of geothermal resources, vol 1. Transactions of the 2nd UN symposium, San Francisco. US Government Printing Office, Washington, pp 47–57
Chamberlin TC (1916) The origin of the earth. The University of Chicago Press, Chicago
Chandrasekhar S (1935) The radiation equilibrium of the outer layer of a star with special reference to the blanquening effect of the reverse layer. Mon Not R Astron Soc 95:21
Chapman DS, Furlong KP (1977) Continental heat flow-age relationships (abstract). EOS Trans 58:1240
Chapman SS, Pollack HN (1975) Global heat flow: a new look. Earth Planet Sci Lett 28:23–32
Cheremensky GA (1977) Applied Geothermics. Nedra, Leningrad (in Russian)
Chevalier l'abbé (1782) Observations et remarques sur la température tic l'hiver de l'année 1782. Mémoires de l'Académie impériale et royale de Bruxelles IV:271–275
Christensen UR (1985) Thermal evolution models for the Earth. J Geophys Res 90:2995–3007
Christensen UR (1989) Models of mantle convection: one or several layers. Phil Trans R Soc Lond A 328:417–424
Christoffel CA, Connelly JN, Åhäll K-I (1999) Timing and characterization of recurrent pre-Sveconorwegian metamorphism and deformation in the Varberg-Halmstad region of SW Sweden. Precambr Res 98(3–4):173–195
Chyba ChF (1990) Impact delivery and erosion of planetary oceans in the early inner Solar System. Nature 343:129–133
Clauser Ch (2009) Heat transport processes in the Earth's crust. Surv Geophys 30:163–191
Condie KC (1981) Archean greenstone belts. Elsevier, Amsterdam
Condie KC (1989a) Origin of the Earth's crust. Global Planet Change 1(1–2):57–81
Condie KC (1989b) Plate tectonics and crustal evolution, 3rd edn. Pergamon Press, New York
Cook FA, Turcotte DL (1981) Parameterized convection and the thermal evolution of the Earth. Tectonophysics 75(1–2):1–17
Cordier PLA (1827) Essai sur la température de l'intérieur de la terre. In: Mémoires de l'Académie des Sciences, pp 473–556 (in French)
Costain JK, Speer JA, Glover L III, Perry L, Dashevsky S, McKinney M (1986) Heat flow in the Piedmont and Atlantic Coastal Plain of the southeastern United States. J Geophys Res 91(B2):2123–2136
Cox PA (1990) The elements: their origin, abundance, and distribution. Oxford University Press, New York
Crookes W (1900) Radio-activity of uranium. Proc R Soc Lond 66:409–422
Cull JP (1982) An appraisal of Australian heat flow data, BMR. J Aust Geol Geophys 7:11–21
Cull JP (1991) Heat flow and regional geophysics in Australia. In: Cermak V, Rybach L (eds) Terrestrial heat flow and the lithosphere structure. Springer, New York, pp 486–500
Curie M (1898) Rays emmitted by compounds of uranium and thorium. Comptes Rendus de Seances de l'academie de Sciences 126:1101–1103 (in French)
Curie P, Curie M (1898) Sur une nouvelle substance radioactive, contenue dans la pechblende. Comptes Rendus de Seances de l'academie de Sciences 127:175–178 (in French)
Curie P, Laborde A (1903) On the heat spontaneously released by the salts of radium. Comptes Rendus de Seances de l'academie de Sciences 86:673
Curie P, Laborde A (1906) Sur la radioactivité des gaz qui proviennent de l'eau des sources thermales. Comptes Rendus de Seances de l'academie de Sciences 142:1462–1465
Curie P, Curie M, Bemont G (1898) Sur une nouvelle substance fortement radioactive, contenue dans la pechblende. Comptes Rendus de Seances de l'academie de Sciences 127:1215–1217 (in French)
d'Aubuisson de Voisins JF (1801) Extrait d'une lettre contenant quelques observations thermometriques faites a la mine de Beschert-Gliick. J Min XI:1801–1802, 517–520

d'Aubuisson de Voisins JF (1802) Sur la temperature dans les mines de Freyberg. J Min, XIII, pp 113–122
d'Aubuisson de Voisins JF (1806) Notices sur la Temperature de la terre. J Phys LXIL:443–461 (in French)
d'Aubuisson de Voisins JF (1830) Mernoire sur la temperature de la terre. Mem Acad II:102–107 (Toulouse) (in French)
da Silva Schmitt R, Trouw RAJ, Van Schmus WR, Pimentel MM (2004) Late amalgamation in the central part of West Gondwana: new geochronological data and the characterization of a Cambrian collisional orogeny in the Ribeira Belt (SE Brazil). Precambr Res 133(1–2):29–61
Daillant OR, Bernollin A, Josset M, Fifield KL (2009) Potential of lichens for monitoring iodine-129 and chlorine-36. J Radioanal Nucl Chem 281(2):241–245
Dalrymple GB (2004) Ancient earth, ancient skies: the age of the earth and its cosmic surroundings. Stanford University Press, Stanford, 247 p
Daubeny C (1837) Report on the present state of our knowledge with respect to mineral and thermal waters. Report: 6th meeting of the British Association for the advancement of science, vol V. John Murray, London, pp 1–96
Davies GF (1980) Thermal histories of convective Earth models and constraints on radiogenic heat production in the Earth. J Geophys Res 85:2517–2530
Davies GE (1990) Heat and Mass transport in the early Earth. In: Jones JH, Newsom HE (eds) The origin of the Earth. Oxford University Press, Oxford, pp 151–174
Davies JH, Davies DR (2010) Earth's surface heat flux. Solid Earth 1:5–24
Davis EE, Elderfield H (eds) (2005) Hydrogeology of the oceanic lithosphere. Cambridge University Press, Cambridge
de Beaumont JBALLE (1830) Recherches sur quelques-unes des revolutions de la surface du globe. Crochard (in French)
de Buffon G-L (1778) Les époques de la nature. In: Histoire naturelle, vol XII. De L'Imprimerie Royale, À Paris (in French)
De La Beche HT (1853) The geological observer, 2nd edn. Longman, Brown, Green, and Longmans, London
De Smet J, van den Berg NJ (2000) Early formation and long-term stability of continents resulting from decompression melting in a convecting mantle. Tectonophysics 322(1–2):19–33
Decker ER, Baker KR, Bucher GJ, Heasler HP (1980) Preliminary heat flow and radioactivity studies in Wyoming. J Geophys Res 85:311–321
Deming D (2002) Origin of the ocean and continents: a unified theory of the Earth. Int Geol Rev 44(2):137–152
Derry LA, Jacobsen SB (1990) The chemical evolution of Precambrian seawater: evidence from REEs in banded iron formation. Geochim Cosmochim Acta 54:2965–2977
Descartes R (1644). Principia Philosophiae, Amsterdam
Détraz C (1999) The discovery of radioactivity: a one-hundred year heritage. Nucl Phys A 654(1–2):C12–C18
Dickson MH, Fanelli M (2004) What is geothermal energy?. Istituto di Geoscienze e Georisorse, CNR, Pisa
Dmitriev VI, Rotanova NM, Zakharova OK (1975) Construction of mathematical models of distribution of electric conductivity and temperature inside the Earth. In: Analysis of space-temporary structure of geomagnetic field. Nauka, Moscow, pp 111–129
Dobrzhinetskaya LF, Eide EA, Larsen RB, Sturt BA, Trønnes RG, Smith DC, Taylor WR, Posukhova TV (1995) Microdiamonds in high-grade metamorphic rocks of the Western Gneiss region, Norway. Geology 23(7):597–600
Dörr W, Belka Z, Marheine D, Schastok J, Valverde-Vaquero P, Wiszniewska J (2002) U-Pb and Ar–Ar geochronology of anorogenic granite magmatism of the Mazury complex, NE Poland. Precambr Res 119(1–4):101–120

Duchkov AD (ed) (1985) Catalog of heat flow data from Siberia (1966–1984). Institute of Geology and Geophysics, Siberian Branch of the Academic Science of the USSR, Novosibirsk (in Russian)
Duchkov AD (1991) Review of Siberian heat flow data. In: Cermak V, Rybach L (eds) Terrestrial heat flow and the lithosphere structure. Springer, New York, pp 426–443
Dutrow BL, Foster CT Jr, Henry DJ (1999) Tourmaline-rich pseudomorphs in sillimanite zone metapelites: demarcation of an infiltration front. Am Mineral 84:794–805
Elkins-Tanton LT, Parmentier EM (2004) Consequences of high crystallinity for the evolution of the lunar msgma ocean: trapped plagioclase. Lunar Planet Sci XXXV:1678
Engik AK, Austrheim H, Andersen TB (2000) Structural, moneralogical and petrophysical effects on deep crustal rocks of fluid-limited polymetamorphism, Western Gneiss Region, Norway. J Geol Soc Lond 157:121–134
England PC (1979) Continental geotherms during the Archaean. Nature 277:556–558. doi:10.1038/277556a0
England P, Molnar P, Richter F (2007) John Perry's neglected critique of Kelvin's age for the Earth: a missed opportunity in geodynamics. GSA Today 17(1):4–9
Everett JD (1875) Illustrations of the centimeter-gram-second (C.G.S.) system of units. Phys Soc Lond
Everett JD (1883) Underground Temperature Committee, summary of results contained in the first fifteen reports of the, by Prof. Everett. Report of the 52 meeting of the British Association for the advancement of science, Held at Southampton. John Murray, London, pp 74–90
Eyles N, Young GM (1994) Geodynamic controls on glaciation in Earth history. In: Deynoux M, Miller JMG, Domack EW, Eyles N, Fairchild IJ, Young GM (eds) International geological correlation program Project 260: Earth's glacial record. Cambridge University Press, Cambridge, pp 1–28
Fairbairn W (1861) On the temperature of earth's crust, as exhibited by thermometrical observations obtained during the sinking of the Deep Mine in Dukinfield. Edinb Phil J XIV(New series):163–164
Faryad SW (1999) Exhumation of the Meliata high-pressure rocks (Westerm Carpathians): petrological and structural records in blueschists. Acta Monstanistica Slovaca Ročnik 4(2):137–144
Fegley B Jr (2000) Kinetics of gas-grain reactions in the solar nebula. Space Sci Rev 92:177–200
Fernàmdez M, Marzám I, Correia A, Ramalho E (1998) Heat flow, heat production, and lithospheric thermal regime in the Iberian Peninsula. Tectonophysics 291:29–53
Flasar FM, Birch F (1973) Energetics of core formation: a correction. J Geophys Res 78:6101–6103
Forbes J (1822) On the temperature of mines. Trans R Geol Soc Cornwall 2:159–217
Förster A, Förster H-J, Masarweh R, Masri A, Tarawneh K, DESERT Group (2007) The surface heat flow of the Arabian Shield in Jordan. J Asian Earth Sci 30(2):271–284
Foulger GR, Jurdy DM (eds) (2007) Plates, plumes, and planetary processes. Geological Society of America, New York
Fountain DM (1986) Is there a relationship between seismic velocity and heat production for crustal rocks? Earth Planet Sci Lett 79(1–2):145–150
Fountain DM, Salisbury MH, Furlong KP (1987) Heat production and thermal conductivity of rocks from the Pikwitonei-Sachigo continental cross-section, central Manitoba: implications for the thermal structure of Archean crust. Can J Earth Sci 24:1583–1594
Fourier J (1824) Remarques Générales Sur Les Températures Du Globe Terrestre Et Des Espaces Planétaires. Ann Chim Phys 27:136–167
Fox RW (1822) On the temperature of mines. Trans R Geol Soc Cornwall 2:14–28
Fox RW (1827) Some further observations on the temperature of mines. Trans R Geol Soc Cornwall 3:313–328
Fox RW (1858) Report on the temperature of some deep mines in Cornwall. Report of the 27th meeting of the British Association for the advancement of science. John Murray, London, pp 11, 96–101

Franck S (1992) Olivine flotation and crystallization of a global magma ocean. Phys Earth Planet Int 74(1–2):23–28
Galer SJG, Mezger K (1998) Metamorphism, denudation and sea level in the Archean and cooling of the Earth. Precambr Res 92(4):389–412
Galushkin YI, Kutas RI, Smirnov YB (1991) Heat flow and analysis of the thermal structure of the lithosphere in the European part of the USSR. In: Cermak V, Rybach L (eds) Terrestrial heat flow and the lithosphere structure. Springer, New York, pp 206–237
Gerlich G, Tscheuschner RD (2009) Falsification of the atmospheric CO_2 greenhouse effects within the frame of physics. Int J Mod Phys B 23(3):275–364
Gilat A, Vol A (2005) Primordial hydrogen-helium degasing, an overlooked major energy source for internal processes. *HAIT* (Holon Academic Institute of Technology, Israel). B, **2**. J Sci Eng 2(1–2):125–167
Gillispie CC (2004) Science and polity in France: the end of the old regime. Princeton University Press, Princeton
Girdler RW (1970) A review of Red Sea heat flow. Phil Trans R Soc Lond A 267:191–203
Glebovitskiĭ VA (1997) The early precambrian of Russia. CRC Press
Gornov PY, Goroshko MV, Malyshev YF, Podgornyi VY (2009) Thermal structure of lithosphere in Central Asian and Pacific belts and their adjacent cratons, from data of geoscience transects. Russ Geol Geophys 50:485–499
Gough DO (1981) Solar interior structure and luminosity variations. Sol Phys 74:21–34
Graf JL Jr (1978) Rare earth elements, iron formations and seawater. Geochim Cosmochim Acta 42:1845–1863
Gretener PE (1981) Geothermics: using temperature in hydrocarbon exploration. Short course notes, No 17. AAPG, 156 p
Griggs DT (1939) A theory of mountain building. Am J Sci 237:611–650
Grove TL, Parman SW (2004) Thermal evolution of the Earth as recorded by komatiites. Earth Planet Sci Lett 219:173–187
Guyod H (1946) Temperature well logging. Oil Wkly 123(7):1–42
Hales AL (1936) Convection currents in the Earth. Mon Not Roy Soc Geophys Suppl 3:372–379
Hallam A (1989) Great geological controversies. Oxford University Press, New York
Halliday AN (2000) Terrestrial accretion rates and the origin of the Moon. Earth Planet Sci Lett 176:17–30
Hamilton WB (1998) Archean magmatism and deformation were not products of plate tectonics. Precambr Res 91(1–2):143–179
Hamza VM, Muñoz M (1996) Heat flow map of South America. Geothermics 25(6):599–621
Hamza VM, Verma RK (1969) The relationship of heat flow with the age of basement rocks. Bull Volcanol 33:123–152
Hancock P, Skinner BJ (eds) (2000) The Oxford companion to the Earth. Oxford University Press, Oxford
Hänel R, Grcnlie G, Heier KS (1979) Terrestrial heat flow determination in Norway and an attempted interpretation. In: Čermák V, Rybach L (eds) Terrestrial heat flow in Europe. Springer, Berlin, pp 232–240
Hasterok D, Chapman DS (2007) A reference heat generation model for the continental lithosphere constrained by heat flow and elevation. AGU Transactions, Fall Meeting, Abstract #T22B-04
Hays JF, Walker D (1975) Igneous lunar rocks and origin of Moon. In: Cosmochemistry of Moon and Planets, transaction of the Soviet-American conference on cosmochemistry of the Moon and Planets, 4–8 June 1974, Moscow. Nauka, Moscow (in Russian)
Heier KS, Lambert IB (1978) A compilation of potassium, uranium and thorium abundances and heat production of Australian rocks. Technical report, Research School of Earth Science, Australian National University, Canberra
Heizler MT, Ralser S, Karlstrom KE (1997) Late Proterozoic (Grenville?) deformation in central New Mexico determined from single-crystal muscovite $^{40}Ar/^{39}Ar$ age spectra. Precambr Res 84(1–2):1–15

Hellman H (1998) Great feuds in science: ten of the liveliest disputes ever. Wiley, New York
Hills JG (1973) On the process of accretion in the formation of the planets and comets. Icarus 18(3):505–522
Höckenreiner M, Söllner F, Miller H (2003) Dating the TIPA shear zone: an early Devonian terrane boundary between the Famatinian and Pampean systems (NW Argentina). J South Am Earth Sci 16(1):45–66
Hofmeister AM, Criss RE (2005) Earth's heat flux revised and linked to chemistry. Tectonophysics 395:159–177
Holland HD (1984) The chemical evolution of atmosphere and oceans. Princeton University Press, Princeton
Holm NG, Hennet RJ-C (1992) Chapter 2 Hydrothermal systems: their varieties, dynamics, and suitability for prebiotic chemistry. Orig Life Evol Biosph 22(1–4):15–31
Holmes A (1915) Radioactivity and the Earth's thermal history. Part II. Radioactivity and the Earth as a cooling body. Geol Mag 6:102–112
Holmes A (1916) Radioactivity and the Earth's thermal history. Part III. Radioactivity and isostasy. Geol Mag 6:265–274
Holmes A (1925) Radioactivity and the earth's thermal history. Part. IV. A criticism of Parts I, II and III. Geol Mag 62:504–515
Holmes A (1930) Radioactivity and geology. Trans Edinb Geol Soc 12:281–283
Holmes A (1931) Radioactivity and earth movements. Nature 128:496
Hu S, He L, Wang J (2000) Heat flow in the continental area of China: a new data set. Earth Planet Sci Lett 179:407–419
Humayun M, Cassen P (2000) Processes determining the volatile abundances of the meteorites and terrestrial planets. In: Canup RM, Righter K et al (eds) Origin of the Earth and Moon. University of Arizona Press, Tucson, pp 3–23
Hurtig E, Schrötter J, Grosswig S, Kühn K, Harjes B, Wieferig W (1992) Temperaturmessungen in Bohrlöchem mit Hilfe optischer Fasern. In: Forum für Zukunftsenergien e.V., Geothermische Vereinigung e.V., Geothermische Fachtagung 1992, Tagungsband, Bonn, pp 311–324
Huston DL, Logan GA (2004) Barite, BIFs and bugs: evidence for the evolution of the Earth's early hydrosphere. Earth Planet Sci Lett 220:41–55
Jacobsen SB (2005) The Hf-W isotopic system and the origin of the Earth and Moon. Ann Rev Earth Planet Sci 33:531–570
Jakosky BM (1999) Atmospheres of the terrestrial planets. In: Beatty JK, Petersen CC, Chaikin A (eds) The new Solar System, 4th edn. Cambridge University Press, Cambridge, pp 175–191
James FAJL (1982) Thermodynamics and sources of solar heat, 1846–1862. Brit J Hist Sci 15:155–181
Jarvis GT, Campbell IH (1983) Archean komatiites and geotherms—Solution to an apparent contradiction. Geophys Res Lett 10:1133–1136
Jaupart C, Mareschal J-C (1999) The thermal structure of continental roots. Lithos 48:93–114
Jaupart C, Mareschal J-C (2003) Constraints on crustal heat production from *heat flow* data. In: Rudnick R (ed) Treatise of geochemistry, vol 3, The Crust. Elsevier, New York, pp 65–84
Jaupart C, Mareschal J-C (2007) Heat flow and thermal structure of the lithosphere. In: Schubert G (ed) Treatise of geophysics, vol 6. Elsevier, Oxford, pp 217–252
Jaupart C, Labrosse S, Mareschal JC (2007) Temperatures, heat and energy in the mantle of the Earth. In: Bercovici D, Schubert G (eds) Treatise on geophysics, vol 7, Mantle dynamics, Chap 7.06. Elsevier, Amsterdam, pp 253–303
Jeffreys H (1924) The Earth, its origin, history and physical constitution. Cambridge University Press, Cambridge
Jeffreys H (1929) The early history of the Solar System on the collision theory. Mon Not R Astron Soc 89:731–739
Jeffreys H (1930) The instability of a compressible fluid heated below. Proc Camb Philos Soc 26:170–172
Jeffreys H (1952). The Earth: its origin, history and physical constitution, 3rd edn. Cambridge University Press, Cambridge

Jeffreys H (1962) The Earth: its origin, history and physical constitution, 4th edn. Cambridge University Press, Cambridge
Jeffreys H (1970) The Earth: its origin, history and physical constitution, 5th edn. Cambridge University Press, Cambridge
Jochum KP, Hofmann AW, Ito E, Seufert HM, White WM (1983) K, U and Th in mid-ocean ridge basalt glasses and heat production, K/U and K/Rb in the mantle. Nature 306:431–436
Johnson EA, Rossman GR, Dyar MD, Valley JW (2002) Correlation between OH concentration and oxygen isotope diffusion rate in diopsides from the Adirondack Mountains, New York. Am Mineral 87:899–908
Johnson SP, Cutten HNC, Muhongo S, De Waele B (2003) Neoarchaean magmatism and metamorphism of the western granulites in the central domain of the Mozambique belt, Tanzania: U-Pb shrimp geochronology and PT estimates. Tectonophysics 375:125–145
Johnsson MJ (1985) Late paleozoic-middle Mesozoic uplift rate, cooling rate and geothermal gradient for south-central New York State. Nucl Tracks Radiat Meas 10(3):295–301
Joly J (1909) Radioactivity and geology: an account of the influence of radioactive energy on terrestrial history. Archibald Constable & Co., Ltd, London
Jones MQW (1987) Heat flow and heat production in the Namaqua mobile belt, South Africa. J Geophys Res 92:6273–6289
Jones FW, Majorowicz JA, Dietrich J (1988) The geothermal regime of the northern Yukon and Mackenzie delta regions of northwest Canada—Studies of two regional profiles. Pure Appl Geophys 127(4):641–658
Jorden JR, Campbell FL (1984) Well logging I—Rock properties, Borehole Environment, Mud and Temperature Logging. Monograph Ser 9. SPE of AIME, New York, Dallas
Kaler JB (1994) Astronomy!. HarperCollins College Publications, New York
Kant I (1755) Allgemeine Naturgeschichte und Theorie des Himmels. Johann Friederich Petersen, Königsberg und Leipzig
Kappelmeyer O, Hänel R (1974) Geothermics with special reference to application. Gebruder Borntrargen, Berlin, Stutgart
Karg H, Carter A, Brix MR, Littke R (2005) Late- and post-Variscan cooling and exhumation history of the northern Rhenish massif and the southern Ruhr Basin: New constraints from fission-track analysis. Int J Earth Sci 94(2):180–192
Kasting JF, Donahue TM (1981) Evolution of oxygen and ozone in the Earth's atmosphere. In: Billingham J (ed) Life in the universe. MIT Press, Cambridge, pp 149–162
Kaufmann WJ III (1994) Universe, 4th edn. Freeman & Co., New York
Kaufmann WJ III, Freedman RA (1999) Universe, 5th edn. Freeman & Co., New York
Kaula WM (1979) Thermal evolution of the Earth and Moon growing by planetesimal impacts. J Geophys Res 84:999–1008
Kelvin WT (1863). On the secular cooling of the Earth. Phil Mag 25(Series 4):1–14
Kelvin WT (1864) On the secular cooling of the Earth. Excerpt. Trans R Soc Edinb, XXIII, pp 167–169
Kelvin WT (1866) The "Doctrine of Uniformity" in geology briefly refuted. Proc R Soc Edinb 5:512–513
Kelvin WT (1895) On the age of the earth. Nature 51:438–440
Kelvin WT (1899) The age of the earth as an abode fitted for life. J Trans Victoria Inst 31:11–35
Kelvin WT, Murray JR (1885a) On the temperature variation of the thermal conductivity of rocks. Science 2(31):129–130
Kelvin WT, Murray JRE (1885) On the temperature variation of the thermal conductivity of rocks. Proc R Soc Lond 58:162–167
Kerimov KM, Pilchin AN, Gadzhiev TG, Buachidze GY (1989) Geothermal map of the Caucasus, Scale 1:1,000,000. Baku, Cartographic Plant No. 11 (in Russian)
Kern H, Siegesmund S (1989) A test of the relationship between seismic velocity and heat production for crustal rocks. Earth and Planet Sci Lett 92(1):89–94
Kerridge JF (1977) Iron: whence it came, where it went. Space Sci Rev 20(1):3–68

Ketcham RA (1996) Distribution of heat-producing elements in the upper and middle crust of southern and west central Arizona: evidence from the core complexes. J Geophys Res 101:13611–13632

Kircher A (1665) Mundus Subterraneus in XII Libros Digestus. Joanne Jansson et Elize Weyerstraten, Amsterdam

Klein C, Beukes NJ (1992) Time distribution, stratigraphy, sedimentologic setting, and geochemistry of Precambrian iron-formations. In: Schopf JW, Klein C (eds) The proterozoic biosphere. Cambridge University Press, Cambridge, pp 139–146

Kleine T, Münker C, Mezger K, Palme H (2002) Rapid accretion and early core formation on asteroids and the terrestrial planets from Hf-W chronometry. Nature 418(6901):952–955

Knauth LP (2005) Temperature and salinity history of the Precambrian ocean: implications for the course of microbial evolution. Palaeogeogr Palaeoclimatol Palaeoecol 219(1–2):53–69

Knauth LP, Lowe DR (2003) High Archean climatic temperature inferred from oxygen isotope geochemistry of cherts in the 3.5 Ga Swaziland Supergroup, South Africa. GSA Bull 115(5):566–580

Knight C (ed) (1866) The English cyclopaedia, vol 1. Bradbury and Evans, London

Koeberl Ch (2006) Impact processes on the early Earth. Elements 2(4):211–216

Kohman TP (1997) Aluminum-26: a nuclide for all seasons. J Radioanal Nucl Chem 219(2):165–176

Korenaga J (2006) Archean geodynamics and the thermal evolution of Earth. In: Benn K, Mareschal J-C, Condie KC (eds) Archean geodynamics and environments. Geophys Monogr Ser 164:7–32. AGU, Washington, DC

Kremenentsky AA, Milanovsky SY, Ovchinnikov LN (1989) A heat generation model for the continental crust based on deep drilling in the Baltic Shield. Tectonophysics 159:231–246

Kröner A (1982) Archaean to early Proterozoic tectonics and crustal evolution: a review. Rev Bras Geociências 12:15–31

Kröner A, Collins AS, Hegner E, Muhongo S, Willner AP, Kehelpannala KVW (2001) Has the East African orogen played any role in the formation and breakup of the Supercontinent Rodinia and the amalgamation of Gondwana? New evidence from field relationship and isotopic data. Gondwana Res 4(4):669–671

Kuhn WR, Walker JC, Marshall HG (1989) The effect on Earth's surface temperature from variations in rotation rate, continent formation, solar luminosity, and carbon dioxide. J Geophys Res 94(D8):11129–11136

Kukkonen IT, Jõeleht A (1996) Geothermal modelling of the lithosphere in the central Baltic Shield and its southern slope. Tectonophysics 255:25–45

Kukkonen IT, Lahtinen R (2001) Variation of radiogenic heat production rate in 2.8–1.8 Ga old rocks in the central Fennoscandian Shield. Phys Earth Planet Int 126(3–4):279–294

Kukkonen IT, Peltoniemi S (1998) Relationships between thermal and other petrophysical properties of rocks in Finland. Phys Chem Earth 23(3):341–349

Kukkonen IT, Peltonen P (1999) Xenolith-controlled geotherm for the central Fennoscandian Shield: implications for lithosphere–asthenosphere relations. Tectonophysics 304:301–315

Kukkonen IT, Golovanova YV, Druzhinin VS, Kosarev AM, Schapov VA (1997) Low geothermal heat flow of the Urals fold belt: Implication of low heat production, fluid circulation or paleoclimate. Tectonophysics 276:63–85

Kukkonen IT, Gosnold WD, Safanda J (1998) Anomalously low heat flow density in eastern Karelia, Baltic Shield: a possible palaeoclimatic signature. Tectonophysics 291:235–249

Kumar PS, Menon R, Reddy GK (2007a) Crustal geotherm in southern Deccan basalt province, India: The Moho is as cold as adjoining cratons. GSA Spec Papers 430:275–284

Kumar PS, Menon R, Reddy GK (2007b) The role of radiogenic heat production in the thermal evolution of a Proterozoic granulite-facies orogenic belt: Eastern Ghats, Indian Shield. Earth Planet Sci Lett 254(1–2):39–54

Kumar PS, Menon R, Reddy GK (2009) Heat production heterogeneity of the Indian crust beneath the Himalaya: insights from the northern Indian Shield. Earth Planet Sci Lett 283(1–4):190–196

Kutas RI (1979) A geothermal model of the Earth's crust on the territory of the Ukrainian Shield. In: Cermak V, Rybach L (eds) Terrestrial heat flow in Europe. Springer, Berlin, pp 309–315
Kutas RI (1984) Heat flow, radiogenic heat production, and crustal thickness in southwest USSR. Tectonophysics 103:167–174
Kutas RI, Gordienko VV (1971) Heat flow of the Ukraine. Naukova Dumka, Kiev (in Russian)
Kutas RI, Bevzyuk MI, Vigovsky VF, Mikhaylyuk SF (1979) Investigation of geologic origin of heat field heterogeneities. Report on problem No 39-76-102/3. Institute of Geophysics, Ukrainian Academy of Science, Kiev (in Russian)
Kutas RI, Kobolev VP, Tsvyashchenko VA (1998) Heat flow and geothermal model of the Black Sea depression. Tectonophysics 291:91–100
Labrosse S, Jaupart C (2007) The thermal evolution of the Earth: Long term and uctuations. Earth Planet Sci Lett 260(3–4):465–481
Labrosse S, Hernlund JW, Coltice N (2007) A crystallizing dense magma ocean at the base of the Earth's mantle. Nature 450:866–869
Lachenbruch AH (1968) Preliminary geothermal model for the Sierra Nevada. J Geophys Res 73:6977–6989
Lachenbruch AH (1970) Crustal temperature and heat production: Implications of the linear beat-flow relation. J Geophys Res 75:3291–3300
Lachenbruch AH (1971) Vertical gradients of heat production in the continental crust. Theoretical detectability from nearsurface measurements. J Geophys 17:3842–3851
Lachenbruch AH, Sass JH, Galanis SP Jr (1985) Heat flow in Southernmost California and the origin of the salton trough. J Geophys Res 90:6709–6736
Lake P (1922) Wegener's displacement theory. Geol Mag 59(8):338–346
Lambert RSJ (1976) Archean thermal regimes, crustal and upper mantle temperatures, and a progressive evolutionary model for the Earth. In: Windley BF (ed) The early history of the Earth. Wiley, London, pp 363–373
Lambert IB (1982) Early geobiochemical evolution of the Earth. Rev Bras Geociências 12:32–38
Landstrom O, Larson SA, Lind G, Malmqvist D (1980) Geothermal investigations in the Bohus granite area in southwestern Sweden. Tectonophysics 64:131–162
Langseth MG, Anderson RN (1979) Correction. J Geophys Res 84:1139–1140
Laplace PS (1799–1825) Traite de Mecanique Celeste. 5 volumes (vols I–II, 1799, vol III, 1802, vol IV, 1805, and vol V, 1825), Bachelier, Paris
Lauretta DS, Nagahara H, Alexander CM O'D (2006) Petrology and origin of ferromagnesian silicate chondrules. In: Lauretta DS, McSween Jr HY (eds) Meteorites and the Early Solar System II. University of Arizona Press, Tucson, pp 431–459
Lebour GA (1882) On the present state of our knowledge of underground temperature. Trans Engl Inst Min Mech Eng 31:59–71
Lee WHK (1970) On the global variations of terrestrial heat-flow. Phys Earth Planet Int 2:332–341
Lee WHK, Uyeda S (1965) Review of heat flow data. In: Lee WHK (ed) Terrestrial heat flow. Geophys Monogr 8:87–190. AGU, Washington, DC
Lee MK, Brown GC, Webb PC, Wheildon J, Rollin KE (1987) Heat flow, heat production and thermotectonic setting in mainland UK. J Geol Soc Lond 144:35–42
Lee C-TA, Lenardic A, Thiagarajan N, Agranier A, O'Neill CJ, Yin Q-Z (2006) Remnant iron oxide/sulfide mattes from a Hadean magma ocean at the core–mantle boundary: Insights from a small scale post-Archean analog. Geochim Cosmochim Acta 70(18, Suppl. 1):A347
Leech ML, Ernst WG (2000) Petrotectonic evolution of the high- to ultrahigh-pressure Maksyutov Complex, Karayanova area, south Ural Mountains: structural and oxygen isotope constraints. Lithos 52:235–252
Leibniz GW (1749) Protogaea. I.G. Schmidii. Goettingae, Sumptibus Ioh. Guil. Schmidii
Lenardic A, Guillou-Frottier L, Mareschal J-C, Jaupart C, Moresi L-N, Kaula WM (2000) What the mantle sees: the effects of continents on mantle heat flow. In: Richards MA, Gordon RG, Van Der Hilst RD (eds) The history and dynamics of global plate motions. Geophys Monogr 121:95–112. AGU, Washington, DC

Lenkey L, Dövényi P, Horváth F, Cloetingh SAPL (2002) Geothermics of the Pannonian basin and its bearing on the neotectonics. EGU Stephan Mueller Spec Publ Ser 3:29–40
Lenton TM (1998) Gaia and natural selection. Nature 394(6692):439–447
Levin BYu, Mayeva SV (1960) About thermic history of the Earth. Izv Acad Sci USSR Ser Geophys 2:243–252
Lewis JS (1974) The temperature gradient in the solar nebula. Science 186:440–443
Lewis CL (2000) The dating game: one man's search for the age of the Earth. Cambridge University Press, Cambridge
Lewis CLE (2002) Arthur Holmes' unifying theory: from radioactivity to continental drift. Geol Soc Lond Spec Publ 192:167–183
Lewis TJ, Hyndman RD, Fluck P (2003) Heat flow, heat generation and crustal temperatures in the northern Canadian cordillera: thermal control on tectonics. J Geophys Res 108:B6. doi:10.1029/2002JB002090
Li J, Agee CB (1996) Geochemistry of mantle-core differentiation at high pressure. Nature 381:686–689
Lide DR (ed) (2005) CRC handbook of chemistry and physics, 86th edn
Loaiciga HA, Valdes JB, Vogel R, Garvey J, Schwarz H (1996) Global warming and the hydrologic cycle. J Hydrol 174:83–127
Louden KE, Mareschal J-C (1996) Measurements of radiogenic heat production on basement samples from sites 897 and 9001. In: Whitmarsh RB, Sawyer DS, Klaus A, Masson DG (eds) Proceedings of the Ocean drilling program, scientific results, vol 14, p 44
Louden KE, Sibuet J-C, Harmegnies F (1997) Variations in heat flow across the ocean—continent transition in the Iberia abyssal plain. Earth Planet Sci Lett 151(3–4):233–254
Lowe DR, Tice MM (2004) Geologic evidence for Archean atmospheric and climatic evolution: Fluctuating levels of CO_2, CH_4, and O_2 with an overriding tectonic control. Geology 32(6):493–496
Lubimova EA (1953) Role of diffusivity in heat regime of Earth. Izv Acad Sci USSR Ser Geophys (6)
Lubimova EA (1955) About heating of Earth's deeps during the process of Earth formation. Izv Acad Sci USSR Ser Geophys 5:416–424 (in Russian)
Lubimova EA (1958) Thermal history of the earth with consideration of the variable thermal conductivity of the mantle. Geophysics 1:115–134
Lubimova EA (1967) Theory of thermal state of the Earth's mantle. In: Gaskell TF (ed) The Earth's mantle. Academic Press, London, pp 231–323
Lubimova EA (1968a) Thermal history of the Earth. In: The Earth's crust and upper mantle. Geophys Monogr Ser 13:63–77. American Geophysical Union, Washington, DC
Lubimova EA (1968b) Thermics of the Earth and Moon. Nauka, Moscow (in Russian)
Lubimova EA, Firsov FV (1966) Determination of heat flow in some areas of Middle Asia. In: Chitarov NI (ed) Problems of deep heat flow. Nauka, Moscow, pp 88–105 (in Russian)
Lubimova EA, Mayeva SV (1982) Models of the thermal evolution of the Earth. Izv Acad Sci USSR Ser Geophys (6):83–93
Lubimova EA, Lusova LN, Firsov FV (1964) Basics of heat flow from Earths depths determination and results of measurements. In: Geothermal researches, Nauka, Moscow, pp 5–103 (in Russian)
Lysak SV, Sherman SI (2002) Terrestrial heat flow in areas of dynamic influence of faults in the Baikal rift zone. EGU Stephan Mueller Spec Publ Ser 2:153–160
MacDonald GJF (1959) Calculations on the thermal history of the Earth. J Geophys Res 64:1967–2000
MacDonald GJF (1962) The Moon and its interior. Astronautics 7(7):14–18
Mackenzie FT (1998) Our changing planet: an introduction to earth system science and global environmental change. Prentice-Hall, Englewood Cliffs
Majorowicz J (1978) Mantle heat flow and geotherms for major tectonic units in central Europe. Pure Appl Geoph 117(1–2):109–123

Marakushev AA (1999). The origin of Earth and Nature of its endogenic activity. Moscow (in Russian)
Mareschal J-C (2010) Interactive comment on "Earth's surface heat flux" by JH Davies and DR Davies. Solid Earth Discuss 1:C7–C9
Mareschal J-C, Jaupart C (2006) Archean thermal regime and stabilization of the cratons. Geophys Monogr 164:61–73
Mareschal J-C, Jaupart C, Gariépy C, Cheng L-Z, Guillou-Frottier L, Bienfait G, Lapointe R (2000a) Heat flow and deep thermal structure near the edge of the Canadian Shield. Can J Earth Sci 37:399–414
Mareschal JC, Poirier A, Rolandone F, Bienfait G, Gariéepy C, Lapointe R, Jaupart C (2000b) Low mantle heat flow at the edge of the North American continent, Voisey Bay, Labrador. Geophys Res Lett 27(6):823–826
Mareschal JC, Nyblade A, Perry HKC, Jaupart C, Bienfait G (2004) Heat flow and deep lithospheric thermal structure at Lac de Gras, Slave Province, Canada. Geophys Res Lett 31:L12611
Marshall J, Cuzzi J (2001) Electrostatic enhancement of coagulation in protoplanetary nebulae. Transaction of the 32nd Lunar Planetary Science Conference, Houston, Texas, Abstract 1262
Marshall JS, Pounder ER, Stewart RW (1967) Physics. Macmillan of Canada, Toronto
Martignole J, Reynolds P (1997) $^{40}Ar/^{39}Ar$ thermochronology along a western Québec transect of the Grenville Province, Canada. J Metamorph Geol 15(2):283–296
Marty B, Meibom A (2007) Noble gas signature of the Late Heavy Bombardment in the Earth's atmosphere. eEarth 2:43–49
Mayer JR (1848) Beiträge zur Dynamik des Himmels in populärer Darstellung. Heilbronn, Landherr
Mayer JR (1867) Die Mechanik der Wärme in gesammelten Schriften. Stuttgart Cotta
McCall GJ (1973) Meteorites and their origins. Wiley, New York
McCrea WH (1960) The origin of the Solar System. Proc R Soc Lond A 256:245–266
McKenzie DP (1978) Active tectonics of the Alpine-Himalayan Belt: the Aegean Sea and surrounding regions. Geophys J Roy Astron Soc 55:217–254
McLaren S, Sandiford M, Hand M, Neumann N, Wyborn N, Bastrakova I (2002) The hot southern continent: heat flow and heat production in Australian Proterozoic terranes, Chap 12, vol 22. Geological Society of Australia Special Publication, pp 151–161
McLaren S, Sandiford M, Hand M, Neumann N, Wyborn N, Bastrakova I (2003) The hot southern continent: heat flow and heat production in Australian Proterozoic terranes. GSA Spec Pap 372:157–167
McLaren S, Sandiford M, Powell R, Neumann N, Woodhead J (2006) Palaeozoic intraplate crustal anatexis in the Mount Painter Province, South Australia: timing, thermal budgets and the role of crustal heat production. J Petrol 47(12):2281–2302
McLennan SM, Taylor SR, Hemming SR (2006) Composition, differentiation, and evolution of continental crust: constraints from sedimentary rocks and heat flow. In: Brown M, Rushmer T (eds) Evolution and differentiation of the continental crust. Cambridge University Press, Cambridge, pp 92–134
McSween HY Jr (1993) Stardust to planets. St. Martin's Griffin, New York
McSween HY (1999) Meteorites and their planet parents, 2nd edn. Cambridge University Press, Cambridge
Meert JG, Nédélec A, Hall C (2003) The stratoid granites of central Madagascar: paleomagnetism and further age constraints on neoproterozoic deformation. Precambr Res 120(1–2):101–129
Mekhtiev ShF, Mirzajanzadeh AKh, Aliyev SA (1971) Geothermal investigation of oil and gas fields. Nedra, Moscow (in Russian)
Melosh HJ (1990) Giant impacts and the thermal state of the early Earth. In: Newsom H, Jones J (eds) Origin of the Earth. Oxford University Press, Oxford, pp 69–83
Mezger K, Hanson GN, Bohlen SR (1989) High-precision U-Pb ages of metamorphic rutile: application to the cooling history of high-grade terranes. Earth Planet Sci Lett 96(1–2):106–118

Mezger K, Rawnsley CM, Bohlen SR, Hanson GN (1991) U-Pb garnet, sphene, monazite, and rutile ages: Implications for the duration of high grade metamorphism and cooling histories, Adirondack Mts, New York. J Geol 99:415–428
Michaut Ch, Jaupart C, Mareschal J-C (2009) Thermal evolution of cratonic roots. Lithos 109:47–60
Mojzsis SJ, Harrison TM, Pidgeon RT (2001) Oxygen-isotope evidence from ancient zircons for liquid water at the Earth's surface 4.300 Myr ago. Nature 409:178–181
Monin AS (1977) History of the Earth. Nauka, Leningrad (in Russian)
Morgan P (1985) Crustal radiogenic heat production and the selective survival of ancient continental crust. J Geophys Res 90(Suppl):C561–C570
Morgan P, Swanberg ChA (1978) Heat flow and the geothermal potential of Egypt. Pure Appl Geophys 117:213–226
Morris RG, Sinclair HD, Yelland AJ (1998) Exhumation of the Pyrenean orogen: implications for sediment discharge. Basin Res 10:69–85
Morse JW, Mackenzie FT (1998) Hadean Ocean carbonate geochemistry. Aquat Geochem 4(3–4):301–319
Mottaghy D, Schellschmidt R, Popov YA, Clauser C, Kukkonen IT, Nover G, Milanovsky S, Romushkevich RA (2005) New heat flow data from the immediate vicinity of the Kola super-deep borehole: Vertical variation in heat flow confirmed and attributed to advection. Tectonophysics 401:119–142
Mposkos E, Perraki M (2001) High pressure Alpine metamorphism of the pelagonian allochton in the Kastania area (Southern Vermion), Greece. Bull Geol Soc Greece V:XXXIV/3, 939–947
Mukhin LM, Pimenov KYu (2002) Impact hot spots on the cold surface of the early Earth. Planet Space Sci 50(1):41–43
Muñoz M (2005) Approaches to the relatively hot Altiplano plateau. In: Proceedings of the 6th international symposium on Andean geodynamics, Barcelona, pp 544–547
Nagatha T (1961) Rock magnetism. Maruzen Co., Tokyo
Nagihara S, Jones KO (2005) Geothermal heat flow in the northeast margin of the Gulf of Mexico. AAPG Bull 89(6):821–831
Nakazawa K, Ida S, Ohtsuki K (1993) Elementary processes in planetary accretion. In: Oya H (ed) Primitive solar nebula and origin of planets. Terra Scientific Publishing Company, Tokyo, pp 265–280
Neumann N, Sandiford M, Foden J (2000) Regional geochemistry and continental heat flow: implications for the origin of the South Australian heat flow anomaly. Earth Planet Sci Lett 183(1–2):107–120
Newman MJ, Rood RT (1977) Implications of solar evolution for the Earth's early atmosphere. Science 198:1035–1037
Norden B, Förster A, Balling N (2009) What causes the increased heat flow of the Northeast German Basin? EGU General Assem. 2009, Geophys Research Abstracts, vol 11, EGU2009-8358
Norman MD, Borg LE, Nyquist LE, Bogard DD (2003) Chronology, geochemistry, and petrology of a ferroan noritic anorthosite clast from Descartes breccia 67215: clues to the age, origin, structure, and impact history of the lunar crust. Meteor Planet Sci 38:645–661
Norris TL, Gancarz AJ, Rokop DJ, Thomas KW (1983) Half-life of Al-26. J Geophys Res 88(Suppl):B331–B333
NRC—National Research Council (1964) Solid-earth geophysics: survey and outlook. National Research Council (U.S.). Panel on solid earth problems, Washington, National Academy of Science Publications, No. 1231
Nyblade AA, Pollack HN (1993) A global analysis of heat flow from Precambrian terrains: implications for the thermal structure of Archean and Proterozoic lithosphere. J Geophys Res 98(B7):12207–12218
Nyblade AA, Pollack HN, Jones DL, Podmore F, Mushayandebvu M (1990) Terrestrial heat flow in East and Southern Africa. J Geophys Res 95(B11):17371–17384

Ohtani E (1985) The primordial terrestrial magma ocean and its implication for stratification of the mantle. Phys Earth Planet Int 38:70–80
Ohtani E, Hirao N, Kondo T, Ito M, Kikegawa T (2005) Iron-water reaction at high pressure and temperature, and hydrogen transport into the core. Phys Chem Minerals 32(1):77–82
Okuchi T (1997) Hydrogen partitioning into molten iron at high pressure: implications for Earth's core. Science 278:1781–1784
Okuchi T (1998) The melting temperature of iron hydride at high pressures and its implications for the temperature of the Earth's core. J Phys Condens Matter 10:11595–11598
Okudaira T, Hayasaka Y, Himeno O, Watanabe K, Sakurai Y, Ohtomo Y (2001) Cooling and inferred exhumation history of the Ryoke metamorphic belt in the Yanai district, south-west Japan: Constraints from Rb–Sr and fission-track ages of gneissose granitoid and numerical modelling. I Arc 10(2):98–115
Olby RC (1996) Companion to the history of modern science. Routledge, London
Ollinger D, Baujard C, Kohl T, Moeck I (2010) Temperature inversion derived from deep borehole data in the Northeastern German Basin. Geothermics 39:46–58
Omar GI, Onstott TC, Hoek J (2003) The origin of deep subsurface microbial communities in the Witwatersrand Basin, South Africa as deduced from apatite fission track analyses. Geofluids 3(1):69–80
Omori S, Komabayashi T (2007) Subduction zone: the water channel to the mantle. In: Yuen DA, Maruyama S, Karato S-I, Windley BF (eds) Superplumes: beyond plate tectonics, Part II. Springer, New York, pp 113–138
Oreskes N (1999) The rejection of continental drift: theory and method in American Earth Science. Oxford University Press, Oxford
Orlyonok VV (1980) Physical basics of Earth's perispher evolution. Leningrad State University, Leningrad (in Russian)
Orlyonok VV (2000) Foundations of geophysics. Kaliningrad (in Russian)
Osako M, Ito E, Yoneda A (2001) Thermal diffusivity and thermal conductivity of olivine and garnet under pressures up to 8 GPa and at temperatures up to 1000 K. In: Proceedings of the conference "Transport of materials in the dynamic Earth", Kurayoshi, Japan, 3.17, pp 83–85
Pavlov AA, Kasting JF, Brown LL, Rages KA, Freedman R (2000) Greenhouse warming by CH4 in the atmosphere of early Earth. J Geophys Res 105(E5):11981–11990
Pechersky DM, Bagin VI, Brodskaya SY, Sharonov ZV (1975) Magnetism and conditions of generation for igneous mountainous rocks. Nauka, Moscow (in Russian)
Peck WH, Valley JW, Wilde SA, Graham CM (2001) Oxygen isotope ratios and rare earth elements in 3.3 to 4.4 Ga zircons: ion microprobe evidence for high $\delta^{18}O$ continental crust and oceans in the Early Archean. Geochim Cosmochim Acta 65(22):4215–4229
Peck WH, Valley JW, Graham CM (2003) Slow oxygen diffusion rates in igneous zircons from metamorphic rocks. Am Mineral 88(7):1003–1014
Pekeris CL (1935) Thermal convection in the interior of the Earth. Mon Not R Astron Soc Geophys Suppl 3:343–367
Perraki M, Mposkos E (2001) New constraints for the Alpine HP metamorphism of the Ios basement, Cyclades, Greece. Bull Geol Soc Greece XXXIV/3:977–984
Petterson H (1949) Exploring the bed of the ocean. Nature (4168):468–470
Pfister M, Rybach L, Simsek S (1998) Geothermal reconnaissance of the Marmara Sea region (NW Turkey): surface heat flow density in an area of active continental extension. Tectonophysics 291:77–89
Pilchin A (1983) Geothermal regime of Earth's crust of the Kura depression and its influence on pressure distribution in it. PhD Thesis, Institute of Geophysics of the Georgia Academy of Sciences, Tbilisi (in Russian)
Pilchin AN (1985) On the origin of mud volcanoes. Sov Geol (Sovetskaia Geologiya) 10:78–81 (in Russian)
Pilchin AN (2011) Magnetite: the story of the mineral's formation and stability. In: Angrove DM (ed) Magnetite: structure, properties and applications, Chap 1. Nova Science Publishers, New York, pp 1–99

Pilchin AN, Eppelbaum LV (2006) Iron and its unique role in earth evolution. In: Monograph, vol 9. Mexican Geophysical Society

Pilchin AN, Eppelbaum LV (2007) Stability of iron oxides in the Earth and their role in the formation of rock magnetism. Acta Geofis 55(2):133–153

Pilchin AN, Eppelbaum LV (2008a) Iron content of magmatic rocks as a marker of mantle heterogeneity. Transactions of the 33rd international geological conference, Oslo, Norway, EID05421P

Pilchin AN, Eppelbaum LV (2008b) Some causes of initial mantle heterogeneity. Transactions of the 33rd international geological conference, Oslo, Norway, EID05422P

Pilchin AN, Eppelbaum LV (2009) The early earth and formation of the lithosphere. In: Anderson JE, Coates RW (eds) The lithosphere: geochemistry, geology and geophysics, Chap 1. Nova Science Publishers, New York, pp 1–68

Pilchin A, Eppelbaum L (2012) The early Earth formation and evolution of the lithosphere in the Hadean–Middle Archean. In: Sato F, Nakamura S (eds) Encyclopedia of earth science research, vol 1, Chap 1, pp 1–93

Pinet C, Jaupart C (1987) The vertical distribution of radiogenic heat production in the Precambrian crust of Norway and Sweden: geothermal implications. Geophys Res Lett 14(3):260–263

Pollack HN (1980) The heat flow from the earth: a review. In: Davies PA, Runcorn SK (eds) Mechanisms of continental drift and plate tectonics. Academic Press, London, pp 183–192

Pollack HN (1982) The heat flow from the Continents. Ann Rev Earth Planet Sci 10:459–481

Pollack HN (1997) Thermal characteristics of the Archaean. In: de Wit MJ, Ashwal MD (eds) Greenstone belts. Clarendon Press, Oxford, pp 223–232

Pollack HN, Chapman DS (1977a) On the regional variation of heat flow, geotherms and the thickness of the lithosphere. Tectonophysics 38:279–296

Pollack HN, Chapman DS (1977b) Mantle heat flow. Earth Planet Sci Lett 2:174–184

Pollack HN, Chapman DS, Cermak V (1979) Global heat flow with special reference to the region of Europe. In: Cermak V, Rybach L (eds) Terrestrial heat flow in Europe. Springer, Berlin, pp 41–48

Pollack HN, Hurter SJ, Johnson JR (1993) Heat flow from the Earth's interior: analysis of the global data set. Rev Geophys 31(3):267–280

Polyak BG, Smirnov YA (1968) Relationship between terrestrial heat flow and the tectonics of continents. Geotectonics 4:205–213

Popov YA, Pimenov VP, Pevzner LA, Romushkevich RA, Popov EY (1998) Geothermal characteristics of the Vorotilovo deep borehole drilled into the Puchezh-Katunk impact structure. Tectonophysics 291:205–223

Popov YA, Pevzner SL, Pimenov VP, Romushkevich RA (1999) New geothermal data from the Kola superdeep well SG-3. Tectonophysics 306(3–4):345–366

Powell WG, Chapman DS, Balling N, Beck AE (1988) Continental heat-flow density. In: Hänel R, Rybach L, Stegena L (eds) Handbook of terrestrial heat-flow density determination. Kluwer Academic Publishers, Dordrecht, pp 167–222

Prestwich J (1884) On underground temperatures, with observations on the conductivity of rocks, on the thermal effects of saturation and imbibition, and on a special source of heat in mountain ranges. Proc R Soc Lond 38:161–168

Prestwich J (1886) On underground temperatures, with observations on certain causes which influence the conductivity of rocks, on the thermal effects of saturation and imbibition, and on a source of heat in mountain ranges. Proc R Soc Lond 41(246):1–116

Quetelet A (1837) Sur les variations des températures de la terre (1er mémoire). Mémoires de l'Académie impériale et royale de Bruxelles X:88

Quetelet A (1839) Résumé des observations météorologicues el des observations sur les températures de la Terre laites en 1838 à l'Observatoire royal de Bruxelles. Mémoires de l'Académie impériale et royale de Bruxelles XII:1–12

Quetelet A (1840) Sur les variations annuelles de la température de la Terre à différentes profondeurs (2e mémoire). Mémoires de l'Académie impériale et royale de Bruxelles XIII:1–52
Quetelet E (1875–1876) Sur la température de l'air à Bruxelles, 1833–1872 (supplément). Mémoires de l'Académie impériale et royale de Bruxelles XLI(Part II):1–52
Radau R (1880) The interior of the earth. Popular Sci Mon (July):289–303
Ramanathan V, Barkstrom BR, Harrison EF (1989) Climate and the earth's radiation budget. Phys Today 42(5):22–32
Rao RUM, Rao GV, Reddy GK (1982) Age dependence of continental heat flow—Fantasy and facts. Earth Planet Sci Lett 59:288–302
Ray L, Senthil KP, Reddy GK, Roy S, Rao GV, Srinrvasan R, Rao RUM (2003) High mantle heat flow in a Precambrian granulite province: evidence from southern India. J Geophys Res 108:B2, ETG6.1–ETG6.13
Ray L, Roy S, Srinivasan R (2008) High radiogenic heat production in the Kerala Khondalite Block, Southern Granulite Province, India. Int J Earth Sci 97(2):257–267
Revelle RR, Maxwell AE (1952) Heat flow through the floor of the Eastern North Pacific Ocean. Nature 170:199–202
Rezanov IA (2002) History of the cosmogonic hypothesis of O. Yu. Shmidt. Probl Hist Sci Tech (4) (in Russian)
Richter FM (1985) Models for the Archean thermal regime. Earth Planet Sci Lett 73:350–360
Richter FM (1986) Kelvin and the age of the Earth. J Geol 94:395–401
Richter FM, Mendybaev RA, Davis AM (2006) Conditions in the protoplanetary disk as seen by the type B CAIs. Meteor Planet Sci 41(1):83–93
Righter K, Drake MJ (1997a) A magma ocean on Vesta: core formation and petrogenesis of eucrites and diogenites. Meteorit Planet Sci 32:929–944
Righter K, Drake MJ (1997b) Metal-silicate equilibrium in a homogeneously accreting earth: new results for Re. Earth Planet Sci Lett 146(3–4):541–553
Righter K, Drake MJ, Scott E (2006) Compositional relationships between meteorites and terrestrial planets. In: Lauretta DS, McSween Jr HY (eds), Meteorites and the early Solar System II (Space Science). University of Arizona Press, Tucson
Ringwood AE (1960) Some aspects of the thermal evolution of the Earth. Geochim Cosmochim Acta 20(3–4):241–259
Robinson AH, Wallis HM (1967) Humboldt's map of isothermal lines: a milestone in thematic cartography. Cartogr J 4(2):119–123
Rolandone F, Jaupart C, Mareschal J-C, Gariépy C, Bienfait G, Carbonne C, Lapointe R (2002) Surface heat flow, crustal temperatures and mantle heat flow in the Proterozoic Trans-Hudson Orogen, Canadian Shield. J Geophys Res 107(2341):1–19
Roy S, Rao RUM (2000) Heat flow in the Indian shield. J Geophys Res 105:25587–25604
Roy RF, Blackwell DD, Birch F (1968) Heat generation of plutonic rocks and continental heat flow provinces. Earth Planet Sci Lett 5:1–12
Roy S, Ray L, Bhattacharya A, Srinivasan R (2008) Heat flow and crustal thermal structure in the Late Archaean Closepet Granite batholith, south India. Int J Earth Sci 97(2):245–256
Rubie DC, Gessmann CK, Frost DJ (2004) Partitioning of oxygen during core formation on the Earth and Mars. Nature 429:58–61
Rubin AE, Mittlefehldt DW (1993) Evolutionary history of the mesosiderite asteroid: a chronologic and petrologic synthesis. Icarus 101(2):201–212
Rudnick RL, Fountain DM (1995) Nature and composition of the continental crust: a lower crustal perspective. Rev Geophys 33(3):267–309
Rudnick RL, Nyblade AA (1999) The thickness and heat production of Archean lithosphere: constraints from xenolith thermobarometry and surface heat flow. In: Fei Y, Bertka CM, Mysen BO (eds) Mantle petrology: field observations and high pressure xperimentation: a tribute to Francis R. (Joe) Boyd. The Geochemical Society, pp 3–12

Russell JK, Kopylova MG (1999) A steady-state conductive geotherm for the north central Slave, Canada: inversion of petrological data from the Jericho Kimberlite pipe. J Geophys Res 104:7089–7101
Rutherford E (1903) Radioactive change. Phil Mag 5:576–591
Rybach L (1976) Radioactive heat production in rocks and its relation to other petrophysical parameters. Pure Appl Geophys 114(2):309–317
Rybach L (1978) The relationship between seismic velocity and radioactive heat production in crustal rocks: An exponential law. Pure Appl Geophys 117(1–2):75–82
Rybach L, Buntebarth G (1982) Relationships between the petrophysical properties density, seismic *velocity*, heat generation, and mineralogical consitution. Earth Planet Sci Lett 57:367–376
Rybach L, Buntebarth G (1984) The variation of *heat* generation, density and seismic *velocity* with rock type in the continental lithosphere. Tectonophysics 103(1–4):335–344
Rybach L, Cermák V (1987) The depth dependence of heat production in the continental lithosphere, derived from seismic velocities. Geophys Res Lett 14(3):311–313
Safronov VS (1959) About initial temperature of Earth. Izv Acad Sci USSR Ser Geophys (1) (in Russian)
Safronov VS (1969) Evolution of the protoplanetary cloud and formation of the earth and the planets. Nauka, Moscow, 206 p (in Russian)
Safronov VS (1978) The heating of the Earth during its formation. Icarus 33(1):3–12
Safronov VS, Kozlovskaya SV (1977) Heating of Earth by its bombardment by forming it bodies. Isv Acad Sci USSR Phys Earth 10:3–13 (in Russian)
Sagan C, Chyba C (1997) The early faint Sun paradox: organic shielding of ultraviolet-labile greenhouse gases. Science 276(5316):1217–1221
Sagan C, Mullen G (1972) Earth and Mars: evolution of atmospheres and surface temperatures. Science 177:52–56
Saltzman B (1984). Advances in Geophysics, vol 26. Academic Press, London, 349 p
Schmid R (2000) Geology of ultra-high-pressure rocks from the Dabie Shan, Eastern China. PhD Thesis, Institut für Geowissenschaften, University of Potsdam
Schmidt OY (1949) Four lectures on the theory of the Earth's origins. Academy of Science of USSR Publishers, Moscow
Schmidt O (2001) A theory of earth's origin: four lectures. University Press of the Pacific (originally published in Russian in 1949)
Schott RC, Johnson CM (2001) Garnet-bearing trondhjemite and other conglomerate clasts from the Gualala basin, California: Sedimentary record of the missing western portion of the Salinian magmatic arc? Geol Soc Am Bull 113(7):870–880
Schubert G, Cassen P, Young RE (1979) Core cooling by subsolidus mantle convection. Phys Earth Planet Int 20:194–208
Schubert G, Stevenson D, Cassen P (1980) Whole Planet cooling and the radiogenic heat source contents of the Earth and Moon. J Geophys Res 85(B5):2531–2538
Schubert G, Turcotte DL, Olson P (2001) Mantle convection in the Earth and Planets, 2 vols. Cambridge University Press, Cambridge
Schulze DJ, Valley JW, Spicuzza KJ (2000) Coesite eclogites from the Roberts Victor kimberlite, South Africa. Lithos 54:23–32
Sclater JG, Jaupart C, Galson D (1980) The heat flow through oceanic and continental crust and the heat loss of the Earth. Rev Geophys Space Phys 18:269–311
Scott ERD, Krot AN (2005) Thermal processing of silicate dust in the solar nebula: clues from primitive chondrite matrices. Astrophys J 623:578
Şerban DZ, Nielsen SB, Demetrescu C (2001) Transylvanian heat flow in the presence of topography, paleoclimate and groundwater flow. Tectonophysics 335(3–4):331–344
Sertorio L, Tinetti G (2001) Available energy for life on a planet with or without stellar radiation. Nuovo Cimento 24 C(3):421–443
Sharma KK, Bal KD, Parshad R, Lal N, Nagpaul KK (1980) Tectonophysics 70(1–2):135–158

Shaviv NJ (2003) Toward a solution to the early faint Sun paradox: a lower cosmic ray flux from a stronger solar wind. J Geophys Res 108(A12):1437
Shen JJ, Papanastassiou DA, Wasserburg GJ (1996) Precise Re-Os determinations and systematics of iron meteorites. Geochim Cosmochim Acta 60(15):2887–2900
Shi X, Zhou D, Zhang Y (2000) Lithospheric thermal-rheological structures of the continental margin in the northern South China Sea. Chinese Sci Bull 45(22):2107–2112
Shwartsman YG (2001) Heat condition of the lithosphere and latest changes of climat on European North. In: The lithosphere and hydrosphere of European North of Russia. Ural Branch of the Russian Academy of Science, pp 130–154 (in Russian)
Simpson GG (1943) Mammals and the nature of continents. Am J Sci 241:1–31
Slagstad T (2006) Did hot, high heat-producing granites determine the location of the Oslo Rift? Tectonophysics 412(1–2):105–119
Slagstad T, Balling N, Elvebakk H, Midttømme K, Olesen O, Olsen L, Pascal Ch (2009) Heat-flow measurements in Late Palaeoproterozoic to Permian geological provinces in south and central Norway and a new heat-flow map of Fennoscandia and the Norwegian-Greenland Sea. Tectonophysics 473:341–361
Sleep NH, Zahnle K, Neuhoff PS (2001) Initiation of clement surface conditions on the earliest Earth. Proc Natl Acad Sci USA 98(7):3666–3672
Slichter LB (1941) Cooling of the Earth. Bull Geol Soc Am 52(4):561–600 Part 2
Smith C, Wise MN (1989) Energy and empire: a biographical study of Lord Kelvin. Cambridge University Press, Cambridge, 898 p
Smyslov AA (1974) Uranium and Thorium in the Earth's crust. Nedra, Leningrad, 232 p (in Russian)
Solomatov VS (2000) Fluid dynamics of a terrestrial magma ocean. In: Canup R, Righter K (eds) Origin of the Earth and Moon. University of Arizona Press, Tucson, Arizona, pp 323–338
Song S, Yang J, Liou JG, Wu C, Shi R, Xu Z (2003) Petrology, geochemistry and isotopic ages of eclogites from the Dulan UHPM Terrane, the North Qaidam, NW China. Lithos 70:195–211
Sorokhtin OG, Ushakov SA (2002) Evolution of the Earth: text book. Moscow State University, Moscow (in Russian)
Speece MA, Bowen TD, Folcik JL, Pollack HN (1985) Analysis of temperatures in sedimentary basins: the Michigan Basin. Geophysics 50(8):1318–1334
Spichak V, Zakharova O (2013) Electromagnetic Geothermometer. Scientific World, Moscow (in Russian)
Spohn T, Schubert G (1991) Thermal equilibration of the Earth following a giant impact. Geophys J Int 107:163–170
Springer M, Förster A (1998) Heat-flow density across the Central Andean subduction zone. Tectonophysics 291:123–139
Stacey FD (1992) Physics of the Earth, 3rd edn. Brookfield Press, Brisbane
Stacey FD (2000) Kelvin's age of the earth paradox revisited. J Geophys Res 105(13):13155–13158
Stapff F (1883) On some results of the observations on underground temperature during the construction of the St. Gothard Tunnel. Trans North Engl Inst Min Mech Eng, XXXIII, pp 19–30
Stein CA (1995) Heat flow of the Earth. Global Earth Physics. In: A handbook of physical constants. AGU Reference Shelf 1, pp 144–158
Stevenson DJ (2008) A planetary perspective on the deep Earth. Nature 451:261–265
Stewart JA (1990) Drifting continents and colliding paradigms: perspectives on the geoscience revolution. Indiana University Press, Bloomington, 304 p
Stinner A (2002) Calculating the age of the Earth and the Sun. Phys Educ 37(4):296–305
Storm LC, Spear FS (2005) Pressure, temperature and cooling rates of granulite facies migmatitic pelites from the southern Adirondack Highlands, New York. J Metamorph Geol 23(2):107–130
Streepey MM, van der Pluijm BA, Essene EJ, Hall CM, Magloughlin JF (2000) Late Proterozoic (ca. 930 Ma) extension in eastern Laurentia. GSA Bull 112(10):1522–1530

Strutt RJ (1906) On the distribution of radium in the Earth's crust. Proc R Soc Lond Ser A (Containing papers of a mathematical and physical character) 78(522):150–153
Strutt RJ (1910) On the radium content of basalt. Proc R Soc Lond A 84:377–379
Sukumaran PV (2001) Early planetary environments and the origin of life. Resonance 6(10):16–28
Suyetnov VV (1963) To the problem of search of structures using heat flow density. Transaction of the Institute of Geological of Dagestan Branch of the USSR Academy of Science, pp 73–76
Suyetnov VV, Savin AV, Magomedov AG-G (1980) Some peculiarities of heat flow of left bank of the Astrakhan province. Abstracts of the Conference "Present conditions of methods and eqwipment for geothermal researches". IVZ PGO "Uralgeologiya" Publishing, Swerdlovsk, pp 43–44
Swedenborg E (1734) Opera Philosophica et Mineralia, Principia, vol 1, Leipzig
Takahashi E (1990) Speculations on the Archean mantle: missing link between komatiite and depleted garnet peridotite. J Geophys Res 95(B10):15941–15954
Thakur M, Blackwell DD (2008) Systematics of crustal radioactivity distribution and implication for mantle thermal evolution through time. AAPG search and discover Article No 90087 2008 AAPG/SEG Student Expo, Houston, Texas
Thomson W (1860) On the reduction of observations of underground temperature. Trans R Soc Edinb 22:409
Thomson W (1862) On the age of the Sun's heat. Macmillan's Mag 5:388–393
Thomson W (1878) Problems relating to underground temperature. A fragment. Phil Mag 5(32):370–374
Thomson W (Lord Kelvin) (1890) On the secular cooling of the Earth. In: Mathematical and physical papers, vol III, elasticity, heat, electro-magnetism. C.J. Clay and Sons, London, pp 295–311
Tikhonov AN (1937) On influence of radioactive decay on the earth crust temperature. Izv Acad Sci USSR Ser Geogr Geophys (3):431–458
Tilton GR, Reed GW (1963) Radioactive heat production in eclogite and some ultramafic rocks. In: Gneiss J, Goldberg ED (eds) Earth science and meteoritics. North-Holland, Amsterdam, pp 31–43
Tobiska WK, Nusinov AA (2000) Status of ISO draft International Standard for determining solar irradiances (DIS 21348). Phys Chem Earth Part C Solar Terr Planet Sci 25(5–6):387–388
Tonks WB, Melosh HJ (1993) Magma ocean formation due to giant impacts. J Geophys Res 98:5319–5333
Tozer DC (1959) The electrical properties of the Earth interiors. Phys Chem Earth 3:414–436
Tozer DC (1965) Thermal history of the Earth. Geophys J Int 3(2–3):95–112
Tozer DC (1967) Towards a theory of thermal convection in the mantle. In: Gaskell TF (ed) The Earth's mantle. Academic Press, New York, pp 325–353
Tozer DC (1972) The present thermal state of the terrestrial planet. Phys Earth Planet Int 6:182–197
Turcotte DL (1980) On the thermal evolution of the Earth. Earth Planet Sci Lett 48(1):53–58
Turcotte DL, Oxburgh ER (1967) Convection in a mantle with variable physical properties. J Geophys Res 74:1458
Turcotte DL, Schubert G (1982) Geodynamics: applications of continuum physics to geological problems. Wiley, New York
Turcotte DL, Torrance KE, Hsui AT (1973) Convection in the earth's mantle. Methods Comput Phys 13:431–454
Turcotte DL, Paul D, White WM (2001) Thorium-uranium systematics require layered mantle convection. J Geophys Res 106(B3):4265–4276
Urey HC (1952) The planets. Their origin and development. Yel University Press, New Haven
Urey HC (1955) The cosmic abundances of potassium, uranium, and thorium and the heat balances of the Earth, the Moon, and Mars. Proc Nat Acad Sci USA 41:127–144
Urey HC (1956) The cosmic abundances of potassium, uranium, and thorium and the heat balances of the Earth, the Moon, and Mars. Proc Natl Acad Sci USA 42:889–891

Uyeda S (1988) Geodynamics. In: Hänel R, Rybach L, Stegena L (eds) Handbook of terrestrial heat-flow density determination. Kluwer Academic Publishers, Dordrecht, pp 317–351
Vacquier V (1998) A theory of the origin of the Earth's internal heat. Tectonophysics 291(1–4):1–7
Valley JW (2006) Early Earth. Elements 2:201–204
Valley JW, Peck WH, King EM, Wilde SA (2002) A cool early Earth. Geology 30(4):351–354
Valley JW, Lackey JS, Cavosie AJ, Clechenko CC, Spicuzza MJ, Basei MAS, Bindeman IN, Ferreira VP, Sial AN, King EM, Peck WH, Sinha AK, Wei CS (2005) 4.4 billion years of crustal maturation: oxygen isotopes in magmatic zircon. Contrib Mineral Petrol 1–20. doi:10.1007/s00410-005-0025-8
Valley JW, Cavosie AJ, Fu B, Peck WH, Wilde SA (2006) Comment on "Heterogeneous Hadean hafnium: evidence of continental crust at 4.4 to 4.5 Ga". Science 312(5777):1139
van den Berg AP, Yuen DA (2002) Delayed cooling of the Earth's mantle due to variable thermal conductivity and the formation of a low conductivity zone. Earth Planet Sci Lett 199(3–4):403–413
van Thienen P, Vlaar NJ, van den Berg AP (2005) Assessment of the cooling capacity of plate tectonics and flood volcanism in the evolution of Earth, Mars and Venus. Phys Earth Planet Int 150:287–315
van Waterschoot WAJM, der Gracht V, Willis B, Chamberlin RT, Joly J, Molengraaff GAF, Gregory JW, Wegener A, Schuchert C, Longwell CR, Taylor FB, Bowie W, White D, Singewald Jr JT, Berry EW (1928). Theory of continental drift: a symposium on the origin and movement of land masses both inter-continental and intra-continental, as proposed by Alfred Wegener. American Association of Petroleum Geologists, Tulsa, Oklahoma, USA
Vigneresse JL (1988) Heat flow, heat production and crustal structure in peri-Atlantic regions. Earth Planet Sci Lett 87(3):303–312
Vinogradov AP (1962) Average content of chemical elements in main kinds of igneous rocks of Earth crust. Geochemistry (Geokhimiya) 7:555–571 (in Russian)
Vitorello I, Pollack HN (1980) On the variation of continental heat flow with age and the thermal evolution of continents. J Geophys Res 85(B2):983–995
Vitorello I, Hamza VM, Pollack HN (1980) Terrestrial heat flow in the Brazilian highlands. J Geophys Res 85:3778–3788
Vityazev AV, and Pechernikova GV (1996) Early differentiation of the earth and problems of composition of Moon. Izv Russ Acad Sci, Phys Solid Earth 31(6):3–16
von Buch L (1802) Lettre de. Mr. De Buch à M. A., Pictet, Sur la temperature de quelques sources des environs de Neuchatel. Bibliothèque Britannique. Sci Arts 9(3):261–269
von Buch L (1806) Ueber die Temperatur von Rom. Gilbert Ann XXIV:236–241
von Helmholtz H (1856) Lecture "On the interaction of natural forces", Königsberg, 7 Feb 1854. Phil Mag 11(Series 4):489–518
von Humboldt A (1817) Des lignes isothermes et de la distribution de la chaleur sur le globe. Mémoires de Physique et de Chimie de la Société d'Arcueil 3:462–602
von Humboldt A (1820) On the temperature of the different mines in America. Printed for A. Constable (Edinburgh)
von Humboldt A (1868) Cosmos: a sketch of a physical description of the universe, vol V. Henry G Bohn, London (translated from German)
Vosteen H-D, Rath V, Clauser Ch, Lammerer B (2003) The thermal regime of the Eastern Alps from inversion analyses along the TRANSALP profile. Phys Chem Earth Parts A/B/C 28(9–11):393–405
Voytov GI (2002) To the problem of hydrogen breathing of Earth. In: Degasing of Earth: geodynamics, geofluids, oil and gas. Nedra, Moscow (in Russian)
Walferdin M (1837) Observation de la température du puits foré de Grenelle. Comptes rendus de l'Académie des Sciences 4
Walker JCG (1985) Carbon dioxide on the early earth. Orig Life Evol Biosph 16(2):117–127
Walter MJ, Trønnes RG (2004) Early Earth differentiation. Earth Planet Sci Lett 225(3–4):253–269

Warren PH (1990) Lunar anorthosites and the magma-ocean plagioclase-flotation hypothesis: importance of FeO enrichment in the parent magma. Am Mineral 75:46–58
Wasserburg GJ, MacDonald GJF, Hoyle F, Fowler WA (1964) Relative contributions of Uranium, Thorium, and Potassium to heat production in the Earth. Science 143(3605):465–467
Waterston JJ (1853) On dynamical sequences in Kosmos. Athenaeum, pp 1099–1100
Watson JV (1978) Precambrian thermal regimes. Philos Trans R Soc Lond A 288:431–440
Weber R (1895) On the temperature variation of the thermal conductivity of rocks. Nature 52:458–459
Wegener A (1912) Die Entstehung der Kontinente. Dr. A. Petermanns Mitteilungen aus Justus Perthes' Geographischer Anstalt 63:185–195, 253–256, 305–309
Wen L, Anderson DL (1997) Layered mantle convection: a model for geoid and topography. Earth Planet Sci Lett 146(3–4):367–377
Whipple FL (2007) Earth moon and planets. Whipple Press
White S (1996) Composition and zoning of garnet and plagioclase in Haast Schist, Northwest Otago, New Zealand: implications for progressive regional metamorphism. NZ J Geol Geophys 39:515–531
Willacy K, Klahr HH, Millar TJ, Henning Th (1998) Gas and grain chemistry in a protoplanetary disk. Astron Astrophys 338:995–1005
Williams HS (1897) The century's progress in physics. Harper's Mon Mag 95(566):258–259
Williams Q, Hemley RJ (2001) Hydrogen in the deep Earth. Ann Rev Earth Planet Sci 29:365–418
Williams DL, von Herzen RP (1974) Heat loss from the Earth: new estimate. Geology 2:327–328
Williams CF, Galanis SP, Grubb FV, Sass JH (2006) Heat flow and geothermal resources of the Alaskan interior. Geol Soc Am Abstr 38(5):14
Willis B (1944) Continental Drift: Ein marchen. Am J Sci 242:509–513
Wilson WE (1903) Radium and Solar Energy. Nature 68:222
Wolf A, Dannemann F (1935) A history of science, technology, and philosophy in the 16th & 17th centuries. George Allen & Unwin, London, 692 p
Wood RJ, Walter MJ, Wade J (2006) Accretion of the Earth and segregation of its core. Nature 441:825–833
Woolfson MM (2000) The origin and evolution of the solar system. Taylor & Francis, London
Woolfson MM (2008) The formation of the solar system: theories old and new. World Scientific Publishing, Singapore
Woolum DS, Cassen P (1999) Astronomical constraints on nebular temperatures: implications for planetesimal formation. Meteorit Planet Sci 34(6):897–907
Yagi T, Hishinuma T (1995) Iron hydride formed by the reaction of iron, silicate, and water: implications for the light element of the Earth's core. Geophys Res Lett 22(14):1933–1936
Yang H, Kyser K, Ansdell K (1998) Metamorphism of the MacLean Lake and Central Metavolcanic belts, La Ronge domain, Trans-Hudson Orogen: pressure–temperature variations and tectonic implications. Can J Earth Sci 35:905–922
Yukutake T (2000) The inner core and the surface heat flow as clues to estimating the initial temperature of the Earth's core. Phys Earth Planet Int 121(1–2):103–137
Zahnle KJ, Kasting JF, Pollack JB (1988) Evolution of a steam atmosphere during Earth's accretion. Icarus 74:62–97
Zaun PE, Wagner GA (1985) Fission-track stability in zircons under geological conditions. Nucl Tracks Radiat Meas 10(3):303–307
Zeck HP (1996) Betic-Rif orogeny: subduction of Mesozoic Tethys lithosphere under eastward drifting Iberia, slab detachment shortly before 22 Ma, and subsequent uplift and extensional tectonics. Tectonophysics 254(1–2):1–16
Zemtsov A (2005). Alexander von Humboldt's ideas on volcanism and their influence on Russian scientists. Humboldt Net Int Rev Humboldtian Stud VI:11, 32–38

Zhao Z-F, Zheng Y-F, Wei C-S, Gong B (2004) Temporal relationship between granite cooling and hydrothermal uranium mineralization at Dalongshan in China: a combined radiometric and oxygen isotopic study. Ore Geol Rev 25(3–4):221–236

Zharkov VI (1958) On the electric conductivity and temperature of the Earth's mantle. Izv Russ Acad Sci Phys Solid Earth 40:458–470

Zharkov VI, Trubitsin VP, Samsonenko LV (1971) Physics of the Earth and Planets. Nauka, Moscow (in Russian)

Zuy VI (2007) Structure of heat field of platform cover in Belorussia. D. Sci Thesis, Minsk

Chapter 2
Thermal Properties of Rocks and Density of Fluids

2.1 Thermal Conductivity

Thermal conductivity or the thermal conductivity coefficient of a material defines its ability to transfer heat. Consider an infinite plane wall of a certain material with a thickness of one unit in length. The sides of the wall are maintained at constant temperatures and the temperature difference is equal to 1 °C.

Let us also assume that a sensor can measure the amount of heat per unit of the area of the wall per unit of time. In this case the amount of heat measured will be numerically equal to the thermal conductivity coefficient (λ) of the given material. The dimension of this quantity in SI is J m^{-1} s^{-1} K^{-1} or W m^{-1} K^{-1}.

It was found experimentally that the amount of heat transferred through the wall (q_A) is proportional to the area (A) and to ratio of the temperature difference (ΔT) to the wall thickness (Δx). This statement is known as Fourier's law (or equation) of thermal diffusion. In the differential form, the Fourier law for a unit of area may be expressed by the formula,

$$q = -\lambda \frac{\partial T}{\partial x}, \tag{2.2.1}$$

where q is the heat flow rate in the direction of x. The negative sign is due to the fact that heat flows in the direction of lower temperatures.

Thus, the coefficient of proportionality in Eq. (2.2.1) is the thermal conductivity (in the direction of x) coefficient. In the hydrodynamics of flow of incompressible fluids through porous media, an analogous equation was suggested by Darcy. In the Darcy equation, the flow rate is proportional to the pressure gradient and the coefficient proportionality is the permeability and hydrodynamic viscosity ratio (mobility). Similarly, in electrical current conduction, according to Ohm's formula, the current is proportional to the voltage gradient. The coefficient of proportionality here is the specific electrical conductivity. Thus there is a correspondence between the thermal conductivity coefficient, mobility, and

L. Eppelbaum et al., *Applied Geothermics*, Lecture Notes in Earth System Sciences,
DOI: 10.1007/978-3-642-34023-9_2, © Springer-Verlag Berlin Heidelberg 2014

Table 2.1 Thermal conductivities[a] of some geological materials (Poelchau et al. 1997)

Material	$Wm^{-1}\ K^{-1}$	Source
Earth's crust	2.0–2.5	Mean value, Kappelmeyer and Hänel (1974)
Rocks	1.2–5.9	Sass et al. (1971)
Sandstone	2.5	Clark (1966)
Shale	1.1–2.1	Clark (1966), Blackwell and Steele (1989)
Limestone	2.5–3	Clark (1966), Robertson (1979)
Water	0.6 at 20 °C	Birch et al. (1942)
Oil	0.15 at 20 °C	Birch et al. (1942)
Ice	2.1	Gretener (1981)
Air	0.025	CRC (1974) Handbook
Methane	0.033	CRC (1974) Handbook

[a] Please take into account that measured conductivities and some other thermal properties of rocks observed in various regions (and even within the same regions) may vary due to influence of different physical-chemical factors

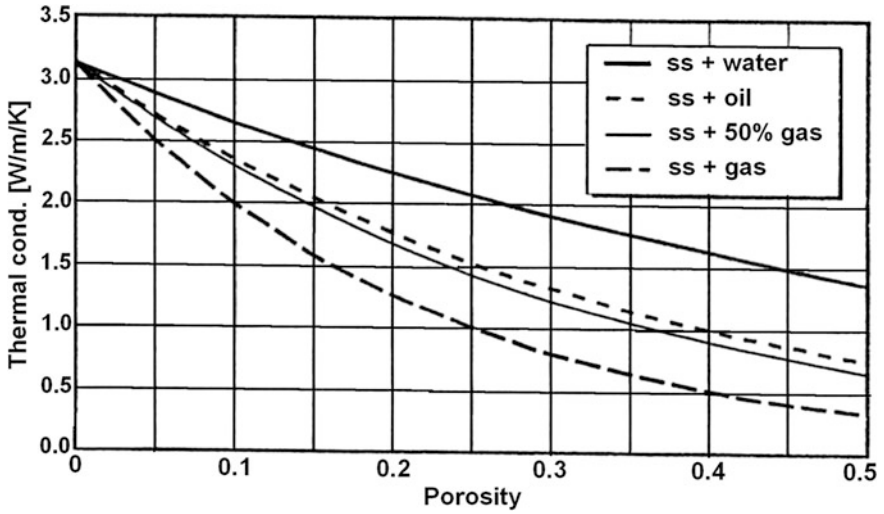

Fig. 2.1 Thermal conductivity of sandstone as a function of porosity and pore fluid at ambient temperature and pressure (Poelchau et al. 1997)

specific electrical conductivity. The thermal conductivity of formations is dependent on temperature, pressure, porosity, composition, and properties of pore-filling fluids and gases. Values of thermal conductivity coefficients range widely for rocks and pore-filling substances (Table 2.1).

All pore-filling fluids have lower λ values than rocks and this causes the overall thermal conductivity to decrease with increasing porosity (Poelchau et al. 1997). Examples of the effect of porosity are presented in Fig. 2.1.

For low porosity formations, temperature has a major effect on variation of thermal conductivity (Fig. 2.2, Table 2.2).

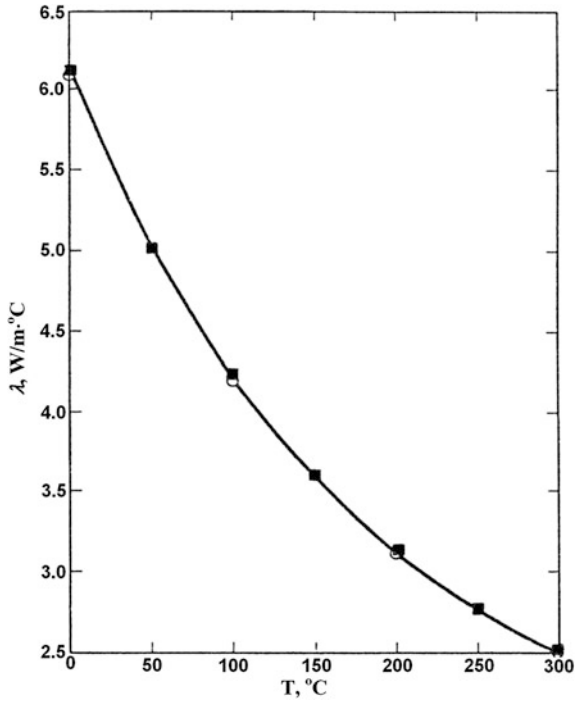

Fig. 2.2 Variation of the thermal conductivity of salt with temperature (Blesh et al. 1983)

Table 2.2 Temperature effect on thermal conductivity (values are given in 10^{-3} cal/cm s °C; 1×10^{-3} cal/cm s °C = 41.86 m Wm^{-2}) of sedimentary rocks (Kappelmeyer and Hänel 1974)

Formation	ρ (g/cm^3)	0 °C	50 °C	100 °C	200 °C	300 °C	400 °C	500 °C
Dolomite	2.83	11.9	10.30	9.30	7.95			
Limestone	2.60	7.20	6.14	5.53	4.77			
Limestone, parallel	2.60	8.24	7.55	7.04	6.54			
Limestone, perpend.	2.69	6.09	5.68	5.41				
Quartz-sandstone, parallel	2.64	13.6	11.80	10.60	9.00			
Quartz-sandstone, perpend.	2.65	13.1	11.40	10.30	8.65			
Shale			2.17	2.25	2.38	2.54	2.68	2.83
Slate, parallel	2.70	6.35	6.05	5.85	5.50	5.20	4.95	4.80
Slate, perpend.	2.76	4.83	4.40	4.23	4.08			
Calcite, parallel		27.3	22.40	19.00	15.1	12.30	10.30	
Calcite, perpend.		16.3	13.50	11.80	9.70	8.40	7.40	
Halite	2.16	14.6	12.00	10.05	7.45	5.95	4.98	

Birch and Clark (1940) suggested that the reciprocal of thermal conductivity (thermal resistivity) might be a linear function of the temperature. Blesh et al. (1983) found that the agreement between the best-fit line and experimental data for several rocks for temperatures up to 300 °C is acceptable, and does not vary by more than 3 %. Coefficients of the equation

Table 2.3 Coefficients of the least-squares fit for thermal conductivity data (Blesh et al. 1983)

Rock	a_0 (m °C/W)	$a_1 \times 10^4$ (m/W)
Salt	0.1605	7.955
Granite	0.3514	3.795
Basalt	0.8684	−6.146
$\text{Shale}_{\text{vert}}$	0.5297	2.215
$\text{Shale}_{\text{hor}}$	0.7167	2.949

$$\lambda^{-1} = a_0 + a_1 T \tag{2.1.2}$$

are presented in Table 2.3.

As shown in Table 2.3 the thermal conductivity for shale parallel to bedding is higher than the vertical thermal conductivity. For sedimentary rocks, thermal anisotropy ratios (horizontal to vertical) up to 2.5 have been reported (Kappelmeyer and Hänel 1974; Gretener 1981; Popov et al. 1995). Kutas and Gordienko (1971) proposed the following empirical formula for estimating the thermal conductivities of sedimentary formations at temperatures of up to 300 °C,

$$\lambda_T = \lambda_{20} - (\lambda_{20} - 3.3)\left[\exp\left(0.725\frac{T-20}{T+130}\right) - 1\right], \tag{2.1.3}$$

where λ_{20} is the thermal conductivity coefficient at 20 °C in 10^{-3} cal s^{-1} cm^{-1} °C.

This formula is accurate within 5–10 %. Only one value of λ_T is needed to use the latter formula. For example, let assume that the value of the thermal conductivity coefficient at $T = 50$ °C is known. Then from the equation above the value of λ_{20} is calculated. The increase in thermal conductivity with pressure (p) can be accounted for by the following equation (Kappelmeyer and Hänel 1974):

$$\lambda = \lambda_0(1 + \delta p), \tag{2.1.4}$$

where λ_0 is the thermal conductivity coefficient at normal pressure, and σ is the pressure coefficient of the thermal conductivity.

Very few experiments have been conducted to estimate the values of σ. From experiments at pressures up to 10,000–12,000 kg cm^{-2} the calculated values of σ were small: for rocksalt 3.6×10^{-5}; for dry and wet limestone with a density of 2.31 g/cm^3 9.5×10^{-5} and 1.35×10^{-5}; and for dry and wet sandstone with a density of 2.64 g/cm^3 respectively 2.5×10^{-4} and 5.7×10^{-5} kg^{-1} cm^2 (Kappelmeyer and Hänel 1974). However, at lower pressures (up to 205 kg cm^{-2}) higher values of δ were obtained (Hurtig and Brugger 1970, Table 2.4).

The average values of heat conductivity for certain rocks are presented in Table 2.5.

It should be noted that in Table 2.5 the values of heat conductivity listed for some rocks (for example for granites, gneisses, amphibolites, limestones) reproduced from Sharma (2002) are too high relative to other data. For example the average value of heat conductivity of granites is 3.07 W/(m K) and has a range of 2.3–3.6 W/(m K) (Sharma 2002) conflicts with the value of 2.2 W/(m K) presented

Table 2.4 Effect of pressure on thermal conductivity of sedimentary rocks. Thermal conductivity data (Hurtig and Brugger 1970)

Sample	λ at 0.4 kg/cm^2 (10^{-3} cal/cm s °C)	Pressure (kg/cm^2)	δ (10^{-3} kg/cm^2)
Sandstone			
No. 172	6.84	0.4–164	0.434
No. 224	5.51	0.4–164	0.612
No. 234	6.69	0.4–164	0.626
No. 286	7.50	0.4–164	0.931
No. 313	9.44	0.4–164	0.905
No. 343	8.51	0.4–41	3.43
Limestone			
No. 19	5.06	0.4–164	0.599
No. 34	4.22	0.4–164	0.185
No. 102	7.67	0.4–164	0.406
No. 260	4.33	0.4–123	0.808
No. 270	3.53	0.4–164	0.579
Dolomite			
No 103	7.62	0.4–123	1.71
No. 365	6.18	0.4–123	0.928

After Kappelmeyer and Hänel (1974)

in Lide (2005), which is completely out of the range reported by Sharma (2002). The value of heat conductivity for granites 2.5–2.6 W/(m K) presented by Côté and Konrad (2005) is also much smaller. At the same time, the average heat conductivity value for basalts presented by Sharma (2002) of 1.69 W/(m K) [with a range of 1.12–2.38 W/(m K)] appears too low compared even to the value of 2 W/(m K) presented in Lide (2005). However these discrepancies could have been caused by the local characteristics of the rocks and/or sampling dependence. For instance, the ranges of heat conductivity values for some rocks presented in Sharma (2002) are very wide [such as 1.35–4.86 W/(m K) for andesite; 1.82–4.73 W/(m K) for amphibolite, 1.63–6.26 W/(m K) for limestone], which can definitely render the average value sample-dependent.

Another explanation for these different and elevated values may be the varying degrees of water saturation in the samples. It is well established that samples saturated with water have much higher values of heat conductivity than dry samples (Pribnow et al. 1996; Cho et al. 2009; Shim et al. 2010). Porosity also significantly affects values of heat conductivity. Cho et al. (2009) reported that values of heat conductivity of dry granites range from 2.12 W/(m K) for rocks with high porosity to 3.12 W/(m K) for those with low porosity. The heat conductivity of rocks also depends on their mineralogical composition. For example, the heat conductivity of granites depends considerably on their quartz [$\sim$7.69 W/(m K)] and albite [2.14 W/(m K)] (Kim et al. 2007) content, two key components of this rock. In addition, in different localities even the same kinds of rock could have been formed under different conditions and can have significantly different heat

Table 2.5 Average values of heat conductivity λ of certain rocks [in W/(m K)]

Rock	From published data[a]		After Sharma (2002)
	No. of samples	Average heat conductivity	Average heat conductivity
Sand	1,149	1.79	1.1–2.1
Siltstone	476	1.58	–
Argillite, clay schist	783	1.67	2.09
Clay	660	1.43	0.8–1.5
Marl	217	1.78	–
Limestone	781	2.37	3.44
Chock	21	1.63	
Granite	383	2.68	3.07
Granodiorite	83	2.79	2.63
Porphyrite	137	1.74	–
Diorite	78	2.10	2.5
Andesites, andesite-basalt	81	1.87	2.26
Basalt	98	2.11	1.69
Diabase	67	2.50	2.2
Gabbro	116	2.47	2.57
Schist	181	2.55	–
Gneiss	88	2.41	2.7–3.1
Amphibolite	47	2.39	3.33
Gneiss-granite	35	2.04	–
Quartzite	–	5.00	5.03
Anhydrite	–	–	5.43
Harzburgite	106	2.69	–
Dunites	23	2.77	–
Olivine gabbro	55	2.65	–
Gabbro-norite	36	2.22	–

[a] Compiled using data from (Birch et al. 1942; Dakhnov and Dyakonov 1952; Lubimova et al. 1964; Magnitsky 1965; Clark 1966; Lubimova 1968b; Dmitriev et al. 1969; Aliev and Mekhtiev 1970; Kutas and Gordienko 1971; Mekhtiev et al. 1971, 1972, 1973; Starikova and Lubimova 1973; Lubimova and Smirnova 1974; Aliev et al. 1977; Zinger and Kotrovsky 1979; Gillis et al. 1993; Cannat et al. 1995; Kelemen et al. 2004)

conductivity values. The average heat conductivity of gabbro from the Mid-Atlantic ridge is 2.20 W/(m K) (calculated using data from Cannat et al. 1995; Kelemen et al. 2004), but its value from the East Pacific Rise is 2.58 W/(m K) (calculated using data from Gillis et al. 1993).

Such discrepancies prove that it is wise to use data obtained from local rocks to conduct geothermal calculations and analyze the geothermal regime of a region, since applying published average values not related specifically to the rocks and conditions of the target area can clearly lead to significant error.

2.2 Thermal Capacity

This parameter is defined as the amount of energy required to raise the temperature of a unit of the mass of a substance by 1°. The specific heat indicates the capability of the formations to store heat. The dimension of specific heat in the SI is: J/kg K.

The specific heat can be measured at constant pressure (c_p) or at constant volume (c_v). For an incompressible material the specific heats are equal to one another, $c(T) = c_p(T) = c_v(T)$. The $c(T)$ is a weak function of the temperature and for a wide temperature interval it can be approximated by a linear equation,

$$c(T) = c(T_i) + \beta(T - T_i), \tag{2.2.1}$$

where T_i is the initial temperature, and β is the coefficient.

From experimental data (Somerton 1958) we calculated parameters in Eq. (2.2.1) for several rocks. For the 70 °F (21 °C)–620 °F (327 °C) interval we obtained the following values for sandstone c (70 °F) = 0.197 Btu/lbm^{-1} °F^{-1} and $\beta = 1.24 \times 10^{-4}$ Btu lbm^{-1} °F^{-2}. The corresponding values of c (70 °F) and β are: 0.190 and 1.43×10^{-4} for shale; and 0.203 and 1.12×10^{-4} for siltstone. Very often a density and specific heat product (ρc)—volumetric heat capacity is used. For fluid-saturated rocks at high temperatures the effective specific heat of the reservoir (c_R) can be estimated from the following equations (Prats 1982):

$$c_R = \frac{M_R}{\rho_a} \tag{2.2.2}$$

$$\left\{ \begin{array}{l} M_R = (1-\varphi)M_\delta + \varphi(S_o M_o + S_w M_w) + \varphi S_g \\ \qquad \times \left[f M_g + (1-f)\left(\dfrac{\rho_s L_v}{\Delta T} + \rho_s C_w \right) \right], \qquad \Delta T = 1\,^\circ\mathrm{C} \end{array} \right\}, \tag{2.2.3}$$

$$\rho_a = \rho_\delta(1-\phi) + \phi\left(S_o\rho_o + S_w\rho_w + S_g\rho_g\right), \tag{2.2.4}$$

where ρ_a is the average density, M_R is the effective volumetric capacity, ϕ is porosity, f is the volume fraction of non-condensable gas in the vapor phase; M_σ, M_o, M_w, and M_g are the isobaric volumetric heat capacities of the solid, oil, water, and gas respectively; S_o, S_w and S_g are the saturation of the fluid and gas phases; L_v is the latent heat of vaporization of water; c_w is the isobaric specific heat capacity of water; ρ_s is the steam density, ρ_σ, ρ_o, ρ_w and ρ_g are the densities of the solid, oil, water, and gas phases, respectively.

Some values of the thermal capacity of typical formations have been presented in the literature (Kappelmeyer and Hänel 1974; Proselkov 1975; Somerton 1992) Some thermal properties after Proselkov (1975) are presented in Tables 2.6, 2.7.

The average values of specific heat capacity (c) for certain rocks are presented in Tables 2.8 and 2.9. Published data were used to compile Table 2.8 (Birch et al. 1942; Dakhnov and Dyakonov 1952; Lubimova et al. 1964; Magnitsky 1965; Clark 1966; Lubimova 1968b; Dmitriev et al. 1969; Aliev and Mekhtiev 1970;

Table 2.6 Thermal properties of rocks in the Romashkino oil field (Russia), after Proselkov (1975)

Formation	$\rho \times 10^{-3}$ (kg/m^3)	$a \times 10^7$ (m^2/s)	λ [W/(m °C)]	$c \times 10^{-3}$ (J/kg °C)
Dolomite	2.75	9.95	2.11	0.802
Limestone	2.70	9.6	2.2	0.851
Clayey limestone	2.65	9.05	1.96	0.844
Argillite	2.3	9.94	2.25	0.838
Siltstone	2.55	10.8	2.22	0.795
Siltstone, oil-bearing	2.3	12.9	2.8	0.88
Clayey sandstone	2.5	14.3	3.36	0.915
Sandstone, fine-grained	2.55	7.19	1.55	0.844
Sandstone, fine-grained	2.4	10.5	1.85	0.845
Sandstone, oil-bearing	2.09	12.54	2.28	0.876
Sandstone, oil saturated	2.2	11.57	1.7	0.737
Sandstone, water saturated	2.3	12.8	2.46	0.84

Table 2.7 Thermal properties of rocks (average data), after Proselkov (1975)

Formation	$\rho \times 10^{-3}$ (kg/m^3)	$a \times 10^7$ (m^2/s)	λ (W/m °C)	$c \times 10^{-3}$ (J/kg °C)
Chalk	1.810	4.73	0.82	0.959
Chalk, compacted	1.920	5.80	1.02	0.922
Marl	1.970	4.04	1.38	1.734
Dolomite	2.753	9.95	2.11	0.802
Clayey limestone	2.644	9.05	1.96	0.844
Limestone	2.714	9.60	2.20	0.851
Clay	2.080	3.21	1.42	2.127
Sandy shale	2.057	3.21	1.42	2.151
Argillite	2.555	9.94	2.25	0.838
Sandstone, oil-bearing	2.198	11.57	1.70	0.737
Clayey siltstone	2.566	10.80	2.22	0.795
Quartzite schist	2.710	18.00	4.19	0.858

Kutas and Gordienko 1971; Mekhtiev et al. 1971, 1972, 1973; Starikova and Lubimova 1973; Lubimova and Smirnova 1974; Aliev et al. 1977; Zinger and Kotrovsky 1979).

Schärli and Rybach (2001) reported values of specific heat c_p of 752 J/(kg K) for granodiorite, 775 J/(kg K) for diorite, 720 J/(kg K) for granite, and 827–855 J/(kg K) for peridotite.

2.3 Thermal Diffusivity

Under transient conditions this parameter determines how fast the temperature field of a solid changes with time. The coefficient of thermal diffusivity (a) is expressed by the formula

Table 2.8 Average values of specific heat capacity [c in 10^{-3} J/(kg K)] for some rocks

Rock	N	c
Sand	130	0.96
Siltstone	42	0.87
Argillite, clay schist	18	0.86
Clay	116	1.10
Marl	19	1.55
Limestone	108	0.89
Chock	13	1.86
Granite	87	0.95
Granodiorite	11	1.02
Porpyrite	11	0.91
Diorite	4	1.00
Basalt	12	1.23
Diabas	12	0.87
Gabbro	13	0.98
Schist	95	1.10
Gneiss	14	1.02
Amphibolite	7	1.13
Gneiss-granite	15	1.11

Table 2.9 Average values of specific heat capacity [c in 10^{-3} J/(kg K)] for some rocks (after ETB 2011)

Rock, mineral	Specific heat capacity (C_p) [kJ/(kg K)]
Augite	0.8
Basalt rock	0.84
Dolomite rock	0.92
Garnet	0.75
Granite	0.79
Hornblende	0.84
Hypersthene	0.8
Labradorite	0.8
Lava	0.84
Limestone	0.84
Sand	0.8
Sandstone	0.92
Serpentine	1.09

$$a = \frac{\lambda}{\rho c}. \tag{2.3.1}$$

The dimension of thermal diffusivity is m^2/s. In hydrodynamics, the analogous quantity is hydraulic diffusivity (the ratio of mobility to the product of porosity and total system compressibility). Some values of the thermal properties of certain formations have been presented in the literature (Birch and Clark 1940; Clark 1966; Kappelmeyer and Hänel 1974 (Table 2.10); Somerton 1992).

The average values of thermal diffusivity (a) for certain rocks are listed in Table 2.11 from published data (Birch et al. 1942; Dakhnov and Dyakonov 1952;

Table 2.10 Thermal properties of sedimentary rocks at temperature of 50 °C (Kappelmeyer and Hänel 1974)

Material	n	ρ, ρ_{aver} (g/cm^3)	λ, λ_{aver} (10^{-3} cal/cm s °C)	n	c, c_{aver} (cal/g °C)	a, a_{aver} (10^{-3} cm^2/s)
Anhydrite	7	2.65–2.91	9.80–14.50	7	–	17.00–25.7
		2.80	12.61		–	22.41
Clay	3	2.49–2.54	5.20–5.40	3	0.213–0.240	8.53–10.18
		2.52	5.30		0.223	9.50
Clay marl	7	2.43–2.64	4.14–6.15	7	0.186–0.234	8.01–11.66
		2.54	4.87		0.205	9.34
Claystone	15	2.36–2.83	4.17–8.18	9	0.197–0.223	8.24–15.80
		2.60	5.68		0.211	12.18
Dolomite	6	2.53–2.72	6.01–9.06	6	0.220–0.239	10.75–14.97
		2.63	7.98		0.228	11.17
Schistose clay	3	2.42–2.57	4.60–5.50	3	0.218–0.222	8.10–10.24
		2.49	5.13		0.220	9.37
Limestone	11	2.41–2.67	4.05–6.40		0.197–0.227	8.24–12.15
		2.55	5.28		0.204	10.54
Limestone	6	2.58–2.66	5.58–8.38	6	0.197–0.220	10.78–15.21
		2.62	6.75		0.210	12.18
Lime marl	2	2.43–2.62	4.40–5.74	2	0.200–0.227	9.04–9.64
		2.53	5.07		0.214	9.34
Marl	3	2.59–2.67	5.55–7.71	3	0.217–0.221	9.89–13.82
		2.63	6.44		0.219	11.18
Marly clay	2	2.46–2.49	4.21–4.82	3	0.183–0.236	7.17–10.72
		2.47	4.52		0.210	8.94
Clay slate		2.62–2.83	3.45–8.79	5	0.205–0.205	6.42–15.15
	5	2.68	5.13		0.205	9.26
Salt		2.08–2.28	10.7–13.7	14	–	25.20–33.80
	14	2.16	13.19		–	30.60
Salt slate		2.13–2.57	3.00–10.00	7	–	6.38–21.70
	7	2.37	6.59		–	13.90
Sandstone		2.35–2.97	5.20–12.18	31	0.182–0.256	10.94–23.62
	54	2.65	7.75		0.197	16.45

Lubimova et al. 1964; Magnitsky 1965; Clark 1966; Lubimova 1968b; Dmitriev et al. 1969; Aliev and Mekhtiev 1970; Kutas and Gordienko 1971; Mekhtiev et al. 1971, 1972, 1973; Starikova and Lubimova 1973; Lubimova and Smirnova 1974; Aliev et al. 1977; Zinger and Kotrovsky 1979).

2.4 Melting Points of Rocks and Minerals

The melting point of a substance is the temperature at which the solid and liquid phases exist in equilibrium and the substance can be transformed from one of these states into the other. Transformations of one state to another are known as the

Table 2.11 Average values of thermal diffusivity (a, in 10^{-7} m^2/s) for some rocks

Rock	N	a
Sand	154	9.57
Siltstone	45	10.28
Argillite, clay schist	23	9.76
Clay	126	7.30
Marl	26	7.53
Limestone	115	10.92
Chock	13	4.77
Granite	92	9.13
Granodiorite	16	5.15
Porpyrite	23	9.54
Diorite	10	6.38
Basalt	13	5.34
Diabas	13	9.93
Gabbro	21	9.70
Schist	106	9.60
Gneiss	15	7.98
Amphibolite	9	6.84
Gneiss–granite	18	7.24

fusion point, freezing point or crystallization point. The melting point of rocks and minerals is an extremely important feature because it characterizes the temperature at which different rocks and minerals change from a solid to a liquid and back. The process of melting and solidification of rocks and minerals can also be defined by the liquids and solidus temperatures of a substance, which together with the melting point are fundamental physical properties of every rock and mineral. The solidus temperature is the temperature (or curve on a phase diagram) below which a substance is completely solid. It quantifies the temperature at which the melting of a substance begins, while not yet completely melted. Conversely, the liquidus temperature is the temperature at which a substance is completely melted and homogeneous. No crystals can exist within the substance above this temperature. Similarly, below the liquidus temperature the crystallization of a substance begins while it is not yet completely solid.

Merely reaching the melting point temperature does not guarantee that the substance will begin melting, since the melting process requires additional heat energy to convert it from a solid to a liquid state. The amount of additional energy needed is termed the *latent heat of fusion*; i.e., the amount of energy absorbed by a substance during a change of state from a solid to a liquid. In the case of the solidification of a melt, the latent heat of fusion (crystallization) represents the amount of heat released during the conversion of the melt to a solid state at the melting point. The latent heat of fusion is also a characteristic physical parameter that varies for different rocks and minerals.

Thus, overall, the melting point, the solidus and liquidus temperatures, and the latent heat of fusion are parameters expressing the heat energy of rock and/or

Table 2.12 Melting points of some rock-forming minerals

Mineral	Melting point (K)	References
Fayalite	1,490	Hewins et al. (1996)
Fayalite	1,478	Yoder (1976)
Forsterite	2,163	Hewins et al. (1996)
Forsterite	2,163	Yoder (1976)
Forsterite	2,171	Speight (2005)
Enstatite	1,830	Speight (2005)
Clinoenstatite	1,830	Hewins et al. (1996)
Ferrosilite	1,413	Speight (2005)
Albite	1,391	Hewins et al. (1996)
Albite	1,393	Hall (1995)
Anorthite	1,830	Hewins et al. (1996)
Christobalite	1,996	Hewins et al. (1996)
Diopside	1,664	Hewins et al. (1996)
Diopside	1,665	Wenk and Bulakh (2004)
Fe metal	1,889	Hewins et al. (1996)
Wollastonite	1,813	Nikonova et al. (2003)
Augite	1,440–1,455	Thy et al. (1999)
Low-Ca pyroxene	1,386–1,426	Thy et al. (1999)
Olivine (Fo82)	1,955	Del Gaudio et al. (2009)
Olivine (Fo85)	1,993	Del Gaudio et al. (2009)
Pyrope	1,575–1,609	Van Westrenen et al. (2001)
Pyrope	1,570	Téqui et al. (1991)
K-feldspar	1,423	Best (2002)
Pure leucite	1,958	Best (2002)

mineral at the temperature when it transforms from a solid to a liquid or vice versa. These parameters are crucial for analyzing the heat capacity and level of heat transfer during the formation of magma, the uplift of magma to the surface, magma eruption, and other related processes. The melting point of different rocks and minerals is important for estimating the amount of heat energy contained within the magma-ocean, the amounts released during differentiation and solidification of the magma-ocean, the rates of cooling of different layers of the magma-ocean, the amounts of heat energy needed to form magma chambers within solid crustal layers, the amount of heat transferred by erupting magma, etc. The melting point can also reveal which mineral would be first to solidify within the magma-ocean and in what sequence others would follow within its different layers or magma chambers. The melting points of some key minerals and rocks are presented in Tables 2.12 and 2.13.

Note that the melting point of any rock or mineral increase with increases in pressure, and therefore with depth. See for example Table 2.14.

On the other hand, it is well-known that the melting point of rocks and minerals drops significantly with increases in water, carbon dioxide or iron content. For instance, at a depth of about 100 km, peridotite begins to melt at a temperature of

Table 2.13 Melting points of some rocks

Rock	Melting point (K)	References
Basalts	~1,473	Adylov and Mansurova (1999)
Basic rocks with Fe# = 0.35	~1723	Yoder (1976)
Basic rocks with Fe# = 0.50	~1,503	Yoder (1976)
Basic rocks with Fe# = 1.00	1,273	Yoder (1976)
Basalt (beginning of melting at 0.1 MPa)	1,273	Yoder (1976)
Basalt	1,343	Hall (1995)
Basalt	1,413	Hall (1995)
Basalts	1,473	Faure (2000)
Basalt, gabbro	1,473	Bayly (1968)
Rhyolite, granite	1,073	Bayly (1968)
Granites	973–1,123	Attrill and Gibb (2003)
Granite	1,173	Hall (1995)
Granite	1,223	Hall (1995)
Komatiites	2,063	Grove and Parman (2004)
Andesite	1,373	Tamura et al. (2003)
Andesite	1,343	Hall (1995)
Eclogite	1,573	Anderson (2007)
Tonalite	1,173	Hall (1995)
Tholeiitic basalt[a]	1,423–1,498	Hall (1995)
Basaltic andesite[a]	1,293–1,383	Hall (1995)
Leucite basalt[a]	1,368	Hall (1995)
Rhyolite[a]	1,008–1,163	Hall (1995)
Rhyodacite[a]	1,173–1,198	Hall (1995)
Andesite pamice[a]	1,213–1,263	Hall (1995)
Dacite[a]	1,198	Hall (1995)
Peridotite	1,363	Faure and Mensing (2007)
MORB[a]	1,516–1,624	Falloon et al. (2007)
OIB[a]	1,559–1,645	Falloon et al. (2007)

[a] Extrusion temperatures of lavas

Table 2.14 Melting point of peridotites at different pressures

Peridotite	Pressure (GPa)	Melting point (K)	References
	0	1,363	Faure and Mensing (2007)
Dry peridotite	~3	1,613	Faure and Mensing (2007)
	~13.2	1,973	Faure and Mensing (2007)
	1	1,483	Lee et al. (2009)
Dry lherzolite solidus	~3	1,713	Lee et al. (2009)
	~6	1,973	Lee et al. (2009)
Dry peridotite	0	1,400	Schubert et al. (2001)
	~3	1,700	Schubert et al. (2001)

about 1,073 K with the presence of excess water, but at the same depth, dry peridotite will start melting at about 1,773 K (Grove et al. 2006). The solidus temperature of lherzolite containing 5 % water is about 1,273 K at ~0.5 GPa, and

about 1,653 K at ~4 GPa (Lee et al. 2009). However, the solidus temperature of lherzolite containing 10 % water is about 1,273 K at 1.25 GPa, and about 1,543 K at ~4 GPa (Lee et al. 2009). At standard pressure, peridotites melt at temperatures of ~1,400 K in the absence of water and other volatiles, and their solidus increases with pressure to around 1,700 K at ~3 GPa (Schubert et al. 2001). However, even concentrations of H_2O as low as only 0.1 % reduce the standard pressure melting point to ~1,340 K, and it actually continues to decrease with pressure, reaching a minimum near 1,270 K at about 3 GPa (Schubert et al. 2001). At higher pressures and greater water content, the melting point of peridotite can drop by about 300–400 K (Schubert et al. 2001).

Experiments document that in the presence of carbon dioxide, the peridotite solidus temperature decreases by ~200 K at a depth of about 70 km, whereas at greater depths the carbon dioxide present can reduce the initial melting temperatures of a carbonated peridotite by about 450–600 K compared to the same composition devoid of carbon dioxide (Dasgupta and Hirschmann 2007). Schubert et al. (2001) also indicated that the presence of CO_2 lowers the melting point.

Lastly, the increase of iron content also significantly lowers the melting point of silicates (Kushiro et al. 1968; McCall 1973; Pilchin and Eppelbaum 2004, 2006). We can see this by comparing the melting points of Mg-rich to Fe-rich olivines (forsterite and fayalite) to orthopyroxenes (enstatite and ferrosilite). See Table 2.12, which reveals this trend.

2.5 Effect of Thermal Anisotropy

The term "anisotropy" can be defined as an observed difference when measurements are made on different axes of a given material (in our case geological rock). The thermal anisotropic properties of graphitic, coal, pyritized and other shale, stratified clays and sandstone, some types of sulphide ores, igneous (for instance, xenoliths) and metamorphic rocks were identified some years ago (Lubimova 1968a, b; Cheremensky 1977; Brigaud 1989; Clauser and Huenges 1995). Simmons (1961) underlined that the thermal conductivity calculated in a single borehole through anisotropic rock will not correspond to the thermal conductivity parallel to the borehole.

Clauser and Huenges (1995) suggested the following three-tier classification:

1. Anisotropic of minerals (microscopic scale),
2. Anisotropy of rocks (laboratory scale). However, even if rocks are composed of anisotropic minerals, the common random orientation of the crystals within the rock may affect the rock's thermal conductivity isotropically,
3. Anisotropy of rock complexes (areal or regional scale). Tectonic processes such as folding, orogeny, displacement etc., the thermal conductivity of the resulting rock formation may be either isotropic as or anisotropic.

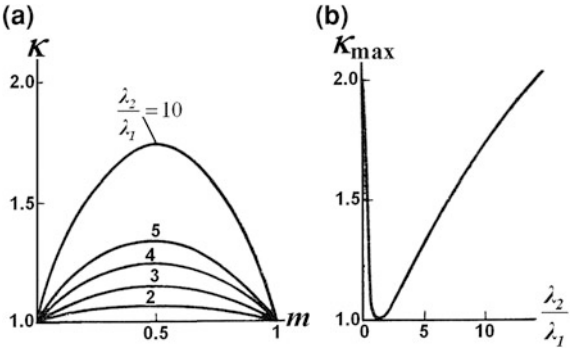

Fig. 2.3 Relationships: **a** between the coefficient of thermal anisotropy κ and parameter m, **b** between the maximal value of κ and ratio λ_2/λ_1 (after Cheremensky 1977)

It should be noted that methods of anisotropy calculation have been studied in detail in electric prospecting (e.g., Dakhnov 1972) which makes it possible to transfer the obtained solution (with necessary modifications) to thermal data analysis.

In a first approximation, anisotropic rock may be present as two-component medium consisting of interbedding of alternations with a thickness of h_1 and h_2 and thermal conductivities λ_1 and λ_2. Thus we can calculate a coefficient of thermal anisotropy κ:

$$\kappa = \sqrt{\frac{\lambda_\tau}{\lambda_n}} = \sqrt{1 + \frac{m(1-m)(\lambda_1 - \lambda_2)^2}{\lambda_1 \lambda_2}}, \quad m = \frac{h_1}{h_1 + h_2}, \tag{2.5.1}$$

where λ_T and λ_n are the longitudinal ($||$) and transversal ($\perp$) thermal conductivities, respectively. In any case $\lambda_T \geq \lambda_n$. The value of κ increases with increasing number of alterations and reaches its maximum value by $m = 0.5$ (Fig. 2.3). The relation λ_T/λ_n for claystone and limestone of Donbas (Ukraine) were found to be 1.6 and 1.4, respectively (Kutas and Gordienko 1971). Popov et al. (2003) described the significant effect of thermal anisotropy of sedimentary rocks on other physical parameters and underlined the advantage of using the component λ_T.

2.6 Effect of Temperature and Pressure on the Thermal Properties of Rocks and Minerals

Analysis of experimental data on the variance of thermal parameters with increases in temperature and pressure shows that in general, heat conductivity (λ) declines, heat capacity (C_p) increases and thermal diffusivity (a) decreases considerably with increases in temperature. Stated differently, at low and moderate temperatures (up to 573–773 K) the value of heat conductivity varies proportionally with the reciprocal of the temperature (Lubimova 1968b; Clauser and Huenges 1995, amongst others), but the actual relationships between these two

parameters are more complicated. For example, Eucken's empirical law (1911) shows that the thermal resistivity ($1/\lambda_1$) of a crystalline dielectric at $T \geq \theta$ is directly proportional to its absolute temperature (Petrunin and Popov 1995):

$$\frac{1}{\lambda_1} = \text{const} \cdot T, \tag{2.6.1}$$

which can be described by the equation (Litovsky and Shapiro 1992):

$$\lambda = (C + DT)^{-1}, \tag{2.6.2}$$

where C and D are the material-dependent constants.

To determine the thermal conductivity of most rocks in the upper crust, Čermak and Rybach (1982) used the equation:

$$\lambda = \frac{\lambda_0}{1 + cT}, \tag{2.6.3}$$

where λ_0 is the thermal conductivity at 0 °C (273.15 K) and near-surface pressure conditions, and c is a material constant (in the range of 0–0.003 $°C^{-1}$) determined through experimental studies on rock samples (for the actual study, c was assumed to be 0.001 $°C^{-1}$ for the upper crust).

Zoth and Hänel (1988) suggested that a relationship existed of the form:

$$\lambda(T) = A + \frac{B}{350 + T}, \tag{2.6.4}$$

where λ is given in W/(m K), T in °C, and the empirical constants A and B are determined from a least-squares plot of measured data for different rock types.

Experimental research on the dependence of heat conductivity on temperature by Vosteen and Schellschmidt (2003) showed that the mean values of λ drop for magmatic, metamorphic, and sedimentary rocks from 2.4, 2.6 and 2.75 $Wm^{-1}\ K^{-1}$ respectively at 273 K, to 1.5, 1.4, and 1.6 $Wm^{-1}\ K^{-1}$ respectively at 573 K. Other studies have shown (Clark 1966) that at a temperature of 473 K, the values for granite, tonalite, and syenite can drop to as low as 2.14, 2.31, and 2.09 $Wm^{-1}\ K^{-1}$, respectively. For sedimentary rocks at temperatures of up to 573 K, there is a reduction of heat conductivity by nearly a factor of two (Clauser 2006, 2009). For quartzite this decline is very rapid, by nearly a factor of three up to a temperature of ~773 K (Clauser 2009). There are some reports (Clauser and Huenges 1995; Clauser 2009) that at high temperatures the radiative component of heat conductivity appears and balances and in some cases even inverts the decreasing trend of heat conductivity with the increase in temperature at about 1,273–1,473 K. Clauser and Huenges (1995) showed that with increases in temperature up to 573 K, there is a reduction of heat conductivity by nearly a factor of two for both clastic and carbonaceous sediments, while above 573 K the decrease is much slower. They also noted that the heat conductivity of volcanic rocks decreases to about 1,173 K, at which point it is about 50 % of its value at ambient temperature, and that at temperatures

above 1,073–1,273 K the radiative component of thermal conductivity starts to rise, although they did not find a very significant radiative contribution in plutonic rocks.

At the same time, radiation only becomes a very efficient form of heat transfer above 1,473 K (Clauser 2006). Ray et al. (2008) stated that in granulites, the radiative heat transfer is negligible up to 823 K. Similarly, Kukkonen et al. (1999) failed to find a radiative heat-transfer effect to be present below 1,150 K for mafic granulites. Aronson et al. (1970) also showed that opacity significantly decreases the magnitude of radiative thermal conductivity. Another study demonstrated that radiation is more effective for rocks with a larger mean free path of radiation corresponding to smaller values of their absorption coefficient and opacity (Clauser 1988, 2006). For metamorphic rocks, the heat conductivity at ~473 K decreases by about 33 % of its value at ambient temperature, and then drops again by about an additional 33 % of its value at ambient temperature with increases in temperature to ~1,023 K (Clauser and Huenges 1995). Pribnow et al. (1996) showed that the thermal conductivity of water-saturated rocks from the KTB Pilot Hole took longer to decline with increasing temperatures than dry rocks. Differences in heat conductivity with increases in temperature for some typical rocks are presented in Fig. 2.4.

Research (Vosteen and Schellschmidt 2003) showed that the mean values and ranges of the variable specific heat capacity c_p at constant pressure for magmatic, metamorphic, and sedimentary rocks increases respectively from about 760, 770 and 810 J kg^{-1} K^{-1} at 273 K, to about 970, 970, and 1,010 J kg^{-1} K^{-1} at 573 K. Sometimes parameters such as the thermal capacity ($\sigma \cdot C_{p,}$ where σ is the density) are used to characterize the thermal properties of rocks and minerals. However, since the thermal volume expansion coefficient of rocks and minerals is very small (on the order of ~10^{-5} K^{-1}), the variable density with increases in temperature will also be extremely insubstantial and so may be ignored. The value of density can therefore be accepted as a constant (Vosteen and Schellschmidt 2003).

The thermal diffusivity, which describes the equilibration of a temperature imbalance, is a function of thermal conductivity λ, density σ, and specific heat capacity C_p at a constant pressure: $a = \frac{\lambda}{C_p \lambda}$. The temperature-dependence of thermal diffusivity is usually proportional to the reciprocal of the absolute temperature (Seipold and Gutzeit 1980). Given that with temperature increasing, the thermal conductivity decreases, the specific heat capacity increases whereas the density does not change significantly. Thus it is clear from the definition of thermal diffusivity that it will decline sharply with temperature increasing. In reality, experimental data on variable thermal parameter values with increase of temperature show that for magmatic, metamorphic, and sedimentary rocks within a temperature interval of 273–573 K, the thermal conductivity decreases by 25–44 % and the thermal diffusivity decreases by 42–54 %.

Thermal diffusivity (in mm^2/s) for all the rocks investigated in Whittington et al. (2009) went from ~1.8–2.2 at ~298 K to ~0.3–0.5 at 1,200–1,250 K. They also provide data demonstrating that it drops substantially from 1.5–2.5 mm^2/s at ambient conditions to about 0.5 mm^2/s at mid-crustal temperatures which goes to

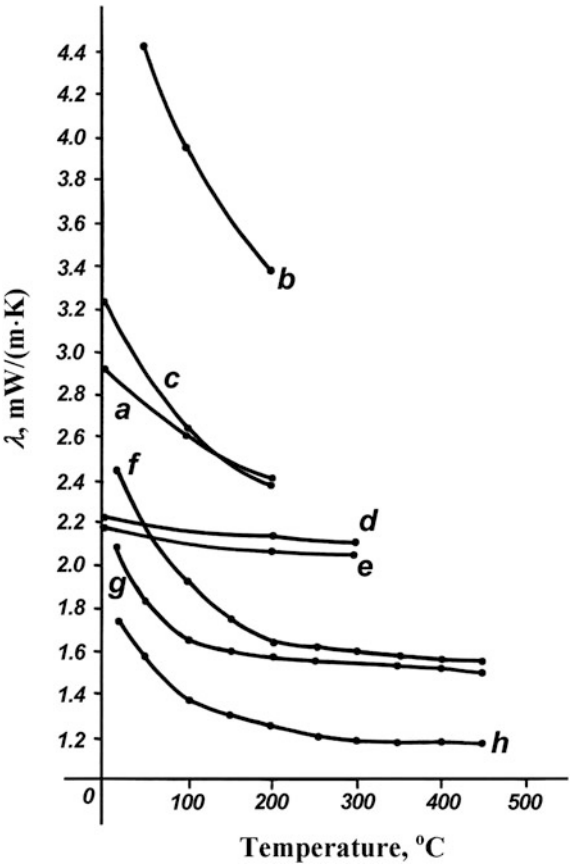

Fig. 2.4 Variable heat conductivity with increases in temperature for some rocks: *a* and *h* granites; *b* dunite; *c* limestone; *d* and *g* diabase; *e* and *f* gabbro [data for samples *a*, *b*, *c*, *d*, and *e* taken from Clark (1966); and for samples *f*, *g* and *h* taken from Dmitriev et al. (1969)]

show that the hot middle-lower crust is a very effective thermal insulator. Ray et al. (2008) reported a decrease of the thermal diffusivity of granulites and amphibolite facies gneisses of about 35–45 % with temperature increasing from 293 to 723 K. Analysis of the thermal diffusivity of rocks of different origin shows that the value varies inversely with temperature, and is 50–75 % lower at 800 K than at ambient temperature (Hanley et al. 1978). At the same time, research shows that at ambient temperature rocks saturated with water have their thermal diffusivity increased by as much as 24 % (Hanley et al. 1978). Pertermann and Hofmeister (2006) reported results showing that the substitution of ~10 % Fe for Mg in forsterite lowers the thermal diffusivity (*a*) by ~50 %, and that the *a* of olivines and olivine-rich rocks can decrease to about 20 % of its value at ambient temperature at 1,163–1,353 K. Hofmeister and Pertermann (2008) stated that thermal diffusivity decreases with increasing temperature, and approaches a constant at about 1,400 K. Their research also shows that for clinopyroxenes it decreases from ~3.9 mm^2/s at 298 K to about 0.5–0.9 mm^2/s at ~1,400 K. The variable thermal diffusivity with increase of temperature for some typical rocks is presented in Fig. 2.5.

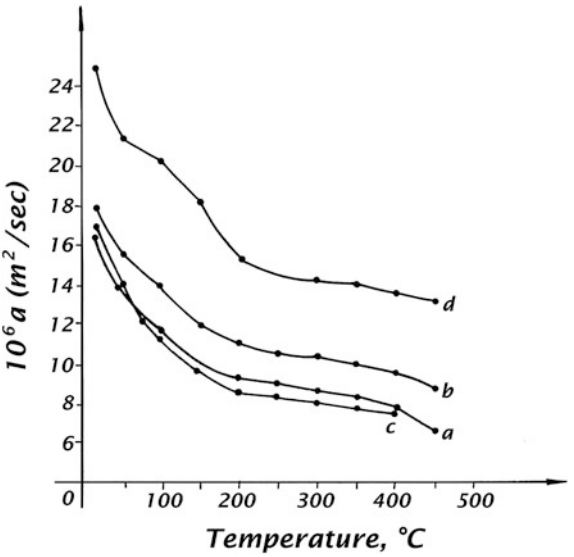

Fig. 2.5 Variable thermal diffusivity with increases in temperature for some rocks: *a* gabbro; *b* diabase; *c* granite; *d* granite-gneiss [using data from Dmitriev et al. (1969)]

Though its effect is much weaker than increases in temperature, increases in pressure lead to a general increase in heat conductivity as well. Clark (1966) also pointed out this weak influence of pressure on heat conductivity. Clauser and Huenges (1995) showed that for granite and metamorphic rocks, there is about a 10 % increase in heat conductivity over the entire range of pressures from 0 to 500 MPa, but the increase is the greatest over the first 50 MPa. The effect of pressure on the value of heat conductivity is mostly dependent on fractures, micro-cracks and porosity (Clauser 2006). Depending on the volume of space within these features, heat conductivity can increase by up to 20 %, with an increase in pressure to ~15 MPa; whereas a further increase in pressure to ~40 MPa typically does not lead to a change in heat conductivity. However, when the pressure is increased from 50 to 500 MPa it will lead to an additional increase of ~10 % (Clauser 2006). Seipold and Gutzeit (1980) showed that in many cases thermal conductivity increases linearly with rising pressure from a rate of around 10^{-5}–10^{-4} MPa^{-1}. Linear relationships between thermal transfer parameters and pressure for pressures ranging from 50 to 1,000 MPa were reported for metamorphic rocks of the Saxonian Granulite Mountains with pressure coefficients of $(0.75 \pm 0.35) \times 10^{-4}$ MPa^{-1} for thermal conductivity and $(0.61 \pm 0.22) \times 10^{-4}$ MPa^{-1} for thermal diffusivity (Seipold and Huenges 1998; Seipold 2002).

At the same time, certain researchers have suggested that the effects of pressure on the heat capacities of solids can be neglected (Waples and Waples 2004). The estimated pressure derivatives for clinopyroxenes are $\partial(\ln\ k)/\partial P = (4.2–4.7) \times 10^{-5}$ MPa^{-1} (Hofmeister and Pertermann 2008).

Durham et al. (1987) reported results showing that diffusivity in all cases rose or remained steady with increasing confining pressure, and that the effect of pressure was the strongest with the lowest pressures and vanished between 10 and

Table 2.15 Pressure derivatives of thermal conductivity for some minerals (after Hofmeister 2007)

Mineral	P_{max} (MPa)	$\lambda^{-1}\partial\lambda/\partial P$ (10^{-4} MPa^{-1})
Mg_2SiO_4	500	16.0
$Mg_{1.8}Fe_{0.2}SiO_4$	200	12.0
$Mg_{1.8}Fe_{0.2}SiO_4$	1,000	9.0–12.0
$Mg_{1.8}Fe_{0.2}SiO_4$	4,800	~4.8
$Mg_{1.8}Fe_{0.2}SiO_4$	5,600	6.0–7.0
$Mg_{1.8}Fe_{0.2}SiO_4$	5,600	5.0–6.0
$Mg_{1.8}Fe_{0.2}SiO_4$	8,300	3.2–3.8
$Mg_{1.8}Fe_{0.2}SiO_4$	9,000	5.5
$Mg_{1.8}Fe_{0.2}SiO_4$	10,000	4.4
$Mg_{0.85}Fe_{0.15}O_3$	5,600	7.0
MgO	5,000	2.0–4.0
MgO	1,200	5.0
Coesite	4,000	3.9
Coesite	5,600	1.4–4.4
$Py_{25}Al_{74}Gr_1$ (garnet)	8,300	4.6
$NaAlSi_2O_6$	3,000	4.6

100 MPa, depending on rock type. Analysis of the combined influence of pressure and temperature on the value of the heat conductivity of marl also showed that the role of temperature is dominant (Lubimova et al. 1978). The differences in relative values of heat conductivity with pressure for some minerals are presented in Table 2.15.

2.7 The Impact of High Pressures and Temperatures on Fluid Density in a Porous Space Within Rocks and Rock Layers

Of all the types of rocks in the upper crust, sedimentary rocks have the highest porosity value which can reach 45 % for some clays. For instance, the average porosity of sedimentary layers in Azerbaijan is about 25 %. Porosity is generally expressed by the porosity coefficient K_p, which is calculated as the ratio of porous volume to the total volume of rock. Porous space is usually filled with some fluid, in most cases water; but in some instances it can be filled with oil, gas, and their mixtures with water. Conversely, magmatic and metamorphic rocks usually have very low porosity unless they are located in layers with pressures under 15 MPa. Since in the great majority of cases the porous space of rock is filled with water, the normal porous pressure (P_0), known as the hydrostatic pressure, is usually calculated using the equation:

$$P_0 = 0.1\,H, \tag{2.7.1}$$

where H is depth in meters (m) and the normal hydrostatic pressure P_0 is in 100 kPa.

Thermodynamic conditions (*P-T*-conditions) regulate the density of porous fluid, and this can be used in some cases to determine and/or analyse the *P-T*-conditions present within a rock or rock layer.

It is crucial to note that in crystalline rocks the porous volume is held by the crystalline lattice, whereas in sedimentary rocks it is held by fluid-filled pores and their thermodynamic conditions. In sedimentary layers, there are conditions that allow a porous fluid to move more or less freely through the porous space (sands, sandstones, limestones, etc.), as well as conditions preventing the fluid from moving freely within the pores (sediments capped by clays, salt or frozen layers; in clays most of water is bound to clay minerals).

Knowing the lithostatic pressure value is extremely important in any study of the *P-T*-conditions of a porous fluid, since in most cases it is capable of squeezing some amount of porous fluid out of porous space, thereby reducing the space. A similar effect can take place in tectonically active regions when an external tectonic force (typically horizontal) can squeeze fluid out of porous space. This effect can cause the porous pressure to increase to the value of the lithostatic pressure to achieve an equilibrium (Pilchin 1983). Such a situation would definitely lead to the formation of pressures within a porous fluid that are greater than its hydrostatic value determined by Eq. (2.7.1), a condition usually called overpressure or abnormally high stratum pressure (AHSP). The presence of AHSP is an enormous problem for drilling wells in oil and gas fields. It should be noted that in some cases one of the hallmarks of AHSP is abnormally low porous pressures, which are usually found within the first few hundred meters from the surface, as well as in some cooling layers.

To analyze the density and/or volume of any fluid or any other matter under given *P-T*-conditions, coefficients such as volume thermal expansion (α) and compressibility (β) are usually employed:

$$\alpha = \frac{(\partial V/\partial T)_P}{V_0}, \tag{2.7.2}$$

$$\beta = \frac{(\partial V/\partial T)_T}{V_0}, \tag{2.7.3}$$

where V and V_0 are volume and initial volume, respectively.

It was shown (Pilchin 1978a; Kerimov et al. 1980; Mekhtiev et al. 1982; Pilchin and Eppelbaum 2009) that the relationship between the primary thermodynamic parameters Pressure-Temperature-Volume (*P-T-V*) for any type of matter, without any preconditions, can be described by the equation:

$$P = P_0 + \frac{\alpha}{\beta}(T - T_0) - \frac{1}{\beta}\frac{\Delta V}{V_0}, \tag{2.7.4}$$

where P is the real pressure, P_0 is the lithostatic or hydrostatic pressure, T is temperature, T_0 is the normal temperature (the normal temperature for matter is determined using the condition for the equilibrium line ($V/V_0 = 1$), as shown in

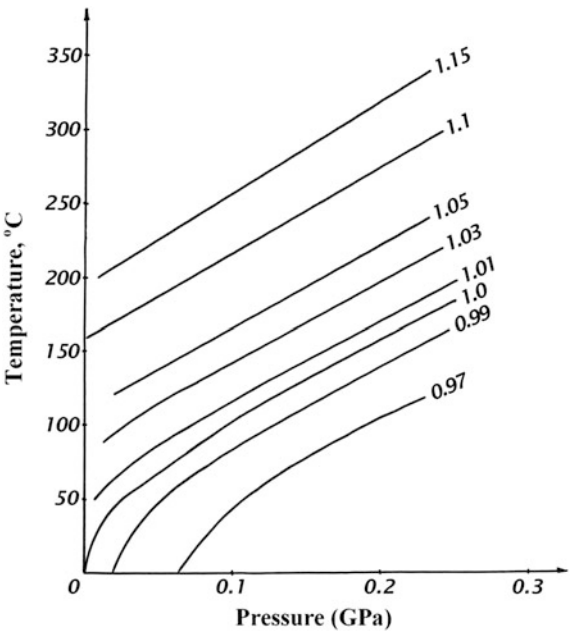

Fig. 2.6 Change in a unit of volume of water under a wide range of pressures and temperatures, calculated using data from Clark (1966)

Fig. 2.6, ΔV is the change in volume ($V - V_0$), and V_0 is the initial volume. The second term on the right side of the equation $(\alpha/\beta)(T - T_0)$ characterizes the dependence of pressure on the temperature of the rock or rock layer. It is clear that temperatures greater than T_0 will lead to an increase of pressure compared to the lithostatic or hydrostatic value, whereas temperatures lower than T_0 will lead to pressures below the lithostatic or hydrostatic value. The third term on the right side of the equation $(1/\beta) \cdot (\Delta V/V_0)$ represents pressure unloading (when $\Delta V > 0$). This unloading can take place when some porous fluid is forced out by increasing porous pressure; for instance, by pumping out water, oil, or gas during well exploitation, etc. At the same time, there are possible cases where $\Delta V < 0$, which would lead to an increase in pressure and could represent such processes as tectonic compression. There are also possible scenarios where $\Delta V = 0$; this represents a state of equilibrium and is used to determine the normal temperature T_0. For equilibrium conditions, Eq. (2.7.4) can be simplified into the following equation:

$$P = P_0 + \frac{\alpha}{\beta}(T - T_0). \tag{2.7.5}$$

A plot of the change in the volume unit of water (V/V_0) with variable P-T-conditions is presented in Fig. 2.6. The equilibrium condition $\Delta V = 0$ is represented on the graph by the line $V/V_0 = 1$; conditions with $\Delta V > 0$ are represented by lines $V/V_0 > 1$, and $\Delta V < 0$ are represented by lines $V/V_0 < 1$ respectively.

It is clear from Eq. (2.7.5) that conditions of equilibrium can only be achieved when the real pressure is equal to its lithostatic or hydrostatic value. This is used to

determine the normal temperature (T_0) for different types of matter, because a case of $P = P_0$ necessarily has $T = T_0$. Calculating the lithostatic (Pilchin and Eppelbaum 2002, 2009) or hydrostatic pressure using Eq. (2.7.1) for different depths and substituting it for P_0 in Eq. (2.7.5) can be used to find the value of the normal temperature T_0 for the rock or mineral at the depth for which P_0 was determined. It is clear that for each depth there is only one pair of P_0 and T_0 values, represented by the line of equilibrium ($V/V_0 = 1$) in Fig. 2.6.

From the definition of the density σ of matter, which is its mass (m) divided by its volume (V) (or as the mass of a unit volume of matter), it is obvious that the condition of equilibrium $\Delta V = 0$ results in:

$$\Delta\sigma = 0, \tag{2.7.6}$$

where $\Delta\sigma = (\sigma - \sigma_0)$ is the change of density of the rock, mineral, etc.

Given the relationship between variable volume and variable density (e.g., Pilchin and Eppelbaum 2009):

$$\frac{\Delta V}{V_0} = -\frac{\Delta\sigma}{\sigma}. \tag{2.7.7}$$

Equation (2.7.4) can be rewritten as:

$$P = P_0 + \frac{\alpha}{\beta}(T - T_0) + \frac{1}{\beta}\frac{\Delta\sigma}{\sigma}. \tag{2.7.8}$$

Another important relationship between the relative change in volume and relative change in density is (Pilchin and Eppelbaum 2009):

$$\frac{\Delta V}{V_0} = -\frac{\Delta\sigma/\sigma_0}{(1 + \Delta\sigma/\sigma_0)}. \tag{2.7.9}$$

It should be pointed out that the values of the coefficients of volume heat expansion (α) and compressibility (β) also depend on pressure and temperature, and these relationships are presented in Figs. 2.7 and 2.8.

These figures show that neither P_0 nor T_0 is constant, and that both are depth dependent parameters. This means that the relationship described by Eq. (2.7.4) indicates the dependence of pressure (P) not on the temperature (T), but rather on the excess temperature ($T - T_0$). The use of the P_0, T_0 pairs for each depth thus provides an opportunity to use compatible and correlated values to analyze both pressure and temperature conditions simultaneously.

Another advantage of using both P_0 and T_0 in analyzing the thermodynamic conditions of porous fluids is the elimination of the dependence on depth of such parameters as K_{aP} (coefficient of abnormality of pressure defined as $K_{aP} = P_{AHSP}/P_0$), K_{aT} (coefficient of abnormality of temperature defined as $K_{aT} = T/T_0$), the excess of pressure ($P - P_0$), the excess of temperature ($T - T_0$), etc. (Kerimov and Pilchin 1986b). In fact, both the excess of pressure and the excess of temperature could have the same values at different depths, which would obviously produce different effects and create problems in interpreting these values together. In order to avoid such problems, it was suggested (Pilchin 1983; Kerimov and Pilchin

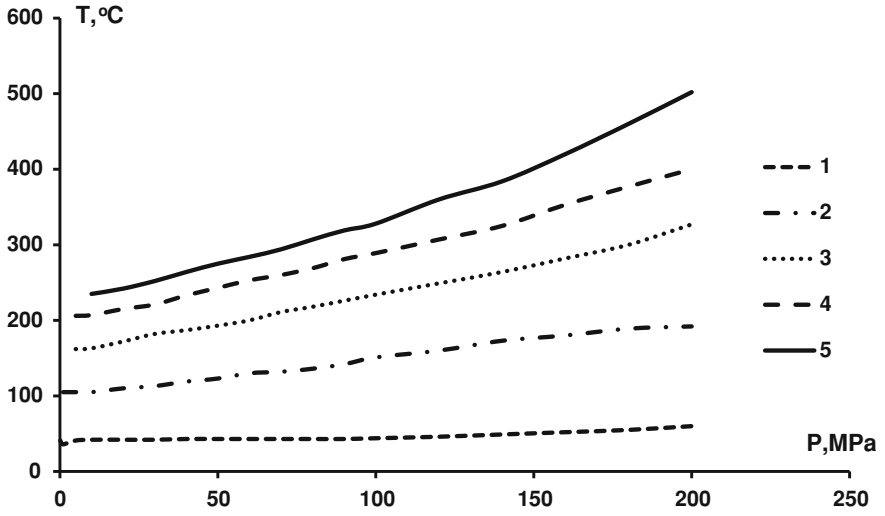

Fig. 2.7 Changes in the coefficient of volume expansion of water ($10^4 \times \alpha$, 1/°C) under a wide range of pressures and temperatures, calculated using data from Clark (1966)

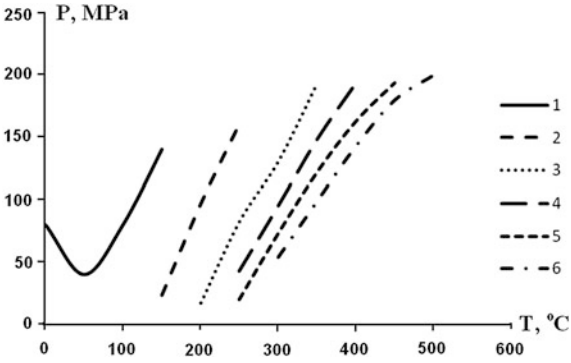

Fig. 2.8 Changes in the coefficient of compressibility of water [$10^5 \times \beta$, 1/(10^2 kPa)] under a wide range of pressures and temperatures, calculated using data from Clark (1966)

1986b) to use dimensionless relative values $(P - P_0)/P_0$ and $(T - T_0)/T_0$ for the analysis of *P*-*T*-conditions of porous fluids which are compatible for data analysis and not depth dependent. For example, the scatter plot composed of values $(P - P_0)/P_0$ and $(T - T_0)/T_0$ from measurements at various depths of the Kyurovdag area of the Lower Kura Depression presented in Fig. 2.9 shows the strong correlation for the area between these relative values, with a correlation coefficient of $r = 0.77$ ($n = 159$). However, there was no correlation found between values of $(P - P_0)$ and $(T - T_0)$.

Interestingly, a correlation between the same parameters for a number of other oil and gas areas also yielded a strong correlation coefficient of $r = 0.78$ ($n = 347$;

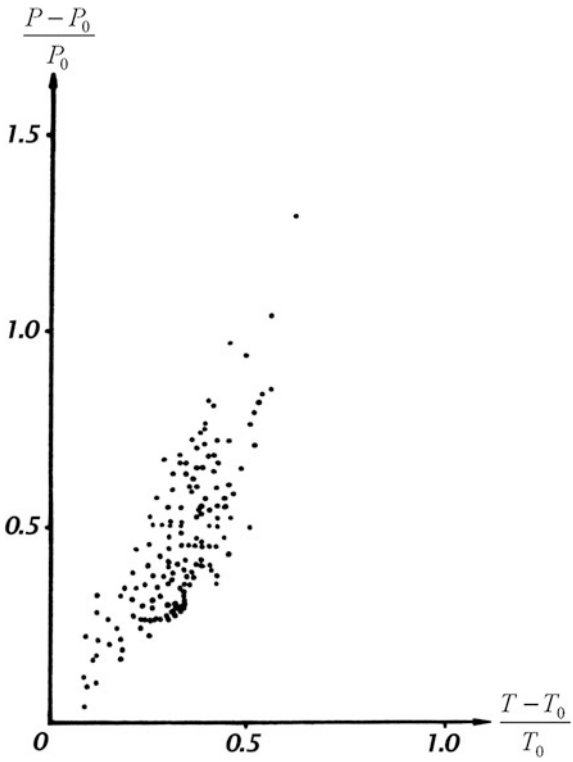

Fig. 2.9 Scatter plot of values $(P - P_0)/P_0$ versus $(T - T_0)/T_0$ for oil and gas fields in the Kyurovdag area of the lower Kura depression

Pilchin 1983). Similar analyses that have been conducted for such areas as the Sangachaly Sea—Duvanniy Sea—Bulla Island (Caspian Sea, Azerbaijan), Bragooni and Hayan Kort (Chechen and Ingush Republics) ($r = 0.78$, $n = 29$; Mekhtiev et al. 1985), Western Turkmenian Depression (Turkmenistan) ($r = 0.87$, $n = 59$; Mekhtiev et al. 1985) and Dowletabad area of Turkmenistan ($r = 0.81$ for 73 fields; Mekhtiev et al. 1985) also indicate a very high correlation between $(P - P_0)/P_0$ and $(T - T_0)/T_0$. Given the evidence, there is clearly a strong relationship between the relative excess of pressure and the relative excess of temperature. This is also consistent with Eqs. (2.7.4) and (2.7.5) showing functional relationship between these parameters. At the same time, it is obvious from Eq. (2.7.4) that the unloading of pressure can compromise this relationship, at least partially, which is demonstrated by the correlations.

In the case of $\Delta V > 0$, water contained in porous matter tends to expand, which could lead to partial unloading of pressure by moving part of the water out of the porous space. However, if such unloading cannot take place, for example when water-saturated rock is surrounded or capped by clay or a salt layer, the tendency of water to expand could in fact lead to an increase of porous pressure (Kerimov et al. 1980; Pilchin 1983) without a change in the porous volume. This thermodynamic state would be in a forced condition of equilibrium, because $\Delta V = 0$,

which corresponds to Eq. (2.7.5). In such a case, the porous pressure would be maximal under conditions without external forces, since there would be no unloading of pressure.

Let us analyze the state of porous fluid under thermodynamic conditions at great depths. Any arbitrary volume V_0 of a rock composed of a solid part and its porous space V_{P0} is characterized by the volume coefficient of porosity $K_P = V_{P0}/V_0$. The porous space is usually filled with water, in which case the solid part of the rock would have the following volume (V_s):

$$V_s = (1 - Kp)V_0. \tag{2.7.10}$$

According to Volarovich (1978), this type of rock can be treated as a two-component system, by analyzing the solid and the fluid-filled porous parts of the rock separately. Under conditions of heating ($T - T_0 > 0$), the solid part of the volume of a rock tends to expand according to the equation:

$$\Delta V_1 = \alpha_s(T - T_0)(1 - K_P)V_0, \tag{2.7.11}$$

where α_s is the coefficient of volume expansion and T_0 is the normal temperature of the solid part of the volume V_0.

Moreover, under pressure P, the solid part of the volume is under compression according to the following equation:

$$\Delta V_2 = \beta_s(P - P_0)(1 - K_P)V_0, \tag{2.7.12}$$

where β_s is the coefficient of compressibility of the solid part of the volume V_0, and P_0 is the lithostatic pressure.

At the same time, any volume of rock is surrounded by other rocks that tend to expand as well and could prevent the target volume from expanding (Pilchin 1983; Pilchin and Eppelbaum 2002). In other words, any change in the volume of the solid part of a rock can only take place at the expense of the volume of the fluid-filled porous space of the volume V_0. Possible changes to the porous space can be defined by the equation:

$$\Delta V_3 = \beta_p(P - P_{AHPP})K_P V_0, \tag{2.7.13}$$

where β_p is the coefficient of compressibility of the porous space, after Volarovich (1978), and P_{AHPP} is the value of abnormally high porous pressure (AHPP).

By the same token, the effect of temperature and pressure on the volume of water in the porous space of a rock can be defined by the following equations:

$$\Delta V_4 = \alpha_w(T - T_{w0})K_P V_0, \tag{2.7.14}$$

$$\Delta V_5 = \beta_w(P_{AHHP} - P_{w0})K_P V_0, \tag{2.7.15}$$

where α_w is the coefficient of volume expansion, βw is the coefficient of compressibility of the porous water, T_{w0} is the normal temperature of water, and P_{w0} is

the hydrostatic pressure. A state of forced equilibrium $\Delta V = 0$ for an analyzed volume of rock requires these conditions of equilibrium:

$$\Delta V_1 - \Delta V_3 = \Delta V_2,\ \Delta V_4 + \Delta V_3 = \Delta V_5. \tag{2.7.16}$$

This leads to a condition of equilibrium between the solid part of the volume and the porous water:

$$\Delta V_1 + \Delta V_4 = \Delta V_2 + \Delta V_5,\ \Delta V_4 + \Delta V_3 = \Delta V_5. \tag{2.7.17}$$

Substituting the values of ΔV_1, ΔV_2, ΔV_4 and ΔV_5 by their values from Eqs. (2.7.12–2.7.15), dividing both sides of Eq. (2.7.17) by V_0 and solving the equation for P_{AHPP} produces (Mekhtiev et al. 1982):

$$P_{AHPP} = P_{w0} + \frac{\alpha_w}{\beta_w}(T - T_{w0}) + \frac{1 - K_P}{K_P}\frac{\alpha_s}{\beta_w}(T - T_0) - \frac{1 - K_P}{K_P}\frac{\beta_s}{\beta_w}(P - P_0). \tag{2.7.18}$$

Given that α_s and β_s should be on the same order of magnitude as similar coefficients for minerals (Mekhtiev et al. 1982), their values should be around $\alpha_s \sim 10^{-6}$–10^{-5} 1/K and $\beta_s \sim 10^{-6}$–10^{-5} 1/MPa (Clark 1966). Values of similar coefficients for water are on the order of $\alpha_w \sim 10^{-4}$–10^{-3} 1/K and $\beta_w \sim 10^{-4}$–10^{-3} 1/MPa. Comparing these values and taking into consideration that the average porosity for the upper part of sedimentary cover of the Kura Depression is $K_P = 0.25$, the value of $(1 - K_P)/K_P = 3$, and that the value of lithostatic pressure is less than 2.5 times the hydrostatic pressure, it is clear that term 3 and term 4 in Eq. (2.7.18) would be negligible, yielding a result fairly similar to Eq. (2.7.5).

Another important case is when $\Delta V < 0$. If this condition were applied to the entire volume of a rock, it would mean that the rock is under the influence of external forces (e.g., tectonic forces), where according to Eq. (2.7.4) the pressure of this volume would even exceed the maximum pressure for situations devoid of external forces, as defined by Eq. (2.7.5). However, if $\Delta V < 0$ were applied to the porous fluid alone, it would mean that the pores are not completely filled with fluid and have extra space available for either fluid expansion or additional fluid. Such circumstances can exist in continental areas at depths up to 0.5–1.0 km or in some oil and gas fields with abnormally low stratum pressure (ALSP) (Pilchin 1983). Since Eqs. (2.7.4) and (2.7.5) do not require any limitations or preconditions about the type of rock, mineral, initial or border conditions, they can be used for any volume and any type of matter. For example, if the porous fluid is oil, its coefficient of compressibility β_{oil} would be in the range of 7–140 $\times$ 10^{-4} MPa^{-1} (Dortman 1976), and the coefficient of volume heat expansion α_{oil} in the temperature range of 273–323 K would be about 8.54 $\times$ 10^{-4} K^{-1} (calculated using data in Driatskaya et al. 1971, 1972). A comparison of these values to the values of similar coefficients for water (α_w, β_w) shows that the coefficient of compressibility for oil is greater on average than that of water by one order of magnitude, whereas the coefficient for volume thermal expansion remains roughly on the same order as

Table 2.16 Values of K_{aP} of pressure in collector rocks with different degrees of saturation (Azerbaijan) (after Pilchin and Kerimov 1986)

Kind of fluid in layers	Number of wells investigated	K_{aP}
Gas, condensed gas	44	0.30–1.33
Oil, oil and gas	115	0.63–1.37
Water with oil and/or gas	59	1.13–1.62
Water in collectors	49	1.22–2.11
Water in clays	68	1.47–2.23

Table 2.17 Values of K_{aP} of pressure in collector rocks with different degrees of saturation Turkmenistan ($n = 214$) and Tajikistan ($n = 217$) (after Pilchin and Kerimov 1986)

Kind of fluid in layers	K_{aP} (Turkmenistan)	K_{aP} (Tajikistan)
Gas, condensed gas	0.84–1.30	–
Oil, oil and gas	0.92–1.35	0.78–1.09
Oil	0.96–1.47	0.83–1.05
Water with oil and/or gas	1.26–1.80	1.14–2.17
Water in collectors	up to 2.00	1.20–2.41

that of water. This means that the ratio α_{oil}/β_{oil} for oil would be on average about one order of magnitude less than that of water (α_w/β_w). Therefore, according to Eqs. (2.7.4) and (2.7.5) the value of the AHPP would be greater in pores filled with water than in pores filled with oil and/or gas for the same thermal conditions. This is consistent with data obtained from measurements in the oil and gas fields of Azerbaijan (see Table 2.16), and Turkmenistan and Tajikistan (see Table 2.17).

Tables 2.16 and 2.17 show that cases with $K_{aP} < 1$ (where the pressure P is less than the hydrostatic pressure P_0) are only present in pores of sedimentary rocks filled with either gas, oil, both gas and oil, or gas and gas condensate. At the same time, K_{aP} is maximal in water-filled pores in collector rocks and clays. Moreover, K_{aP} is the highest in clays (see Table 2.16) since they contain water bound in clay minerals which cannot be easily forced out, whereas water in collector rocks can be forced out by AHSP or AHPP. It is also clear from Tables 2.16 and 2.17 that oil and gas fields containing water do not have $K_{aP} < 1$. Research also shows (Pilchin 1983; Pilchin and Kerimov 1986) that the highest values of AHSP are found in fields of PreCaucasian and Middle Asia, where the thermal regime is characterized by very high temperatures and geothermal gradients (G). By contrast, the lowest values of AHSP are found in fields characterized by low temperature values and geothermal gradients.

In numerous cases, there are signs pointing to the presence of pressures greater than the lithostatic pressure in one sector of the fields in some regions. It is obvious that in such cases AHSP played significant role in the tectonic evolution of the region. At the same time, very small values of AHSP have been found in a number of cases in active thermal fields. Such instances could be related to the fact that the values of AHSP were so high in the past that they caused an unloading of overpressure by forcing part of the porous fluid out, but subsequent cooling of

sedimentary layers in these regions led to the decline of K_{aP} under Eqs. (2.7.4) and (2.7.5), since the thermal regime in these fields was under conditions of $\Delta T < 0$. These facts show how important it is to analyze the thermodynamic regime in fields under maximum possible values of AHSP (or K_{aP}), and compare these values to the lithostatic pressure to determine the change of fluid volume ($\Delta V/V_0$), which characterizes both the unloading of pressure [see Eq. (2.7.4)] and the amount of fluid forced out of pores by AHSP. It should also be noted that the formation of AHSP exceeding the lithostatic pressure could lead to the emergence of fractures and the destruction of cap rock layers as a consequence of unloading the extremely high fluid pressure. For instance, such effects are well known in regions of mud volcano formation.

In the 1960s the stress–dilatancy relationship was put forward for some sedimentary rocks (Rowe 1962; Roscoe et al. 1963; Roscoe and Burland 1968), and later served to derive the dilatancy theory of earthquake prediction in the 1970s (Nur 1972, 1975; Anderson and Whitcomb 1973; Scholz et al. 1973; Cherry et al. 1975). Problems related to dilatancy models will be discussed in detail in Sect. 4.4; hence the role of porous fluid on dilatancy is only mentioned here briefly.

Dilatancy is the process by which the volume of rock increases under stress (during deformation). It is derived from the word dilation which refers to the volume expansion of brittle rock. It corresponds to an increase of volume caused by the opening of cracks, increases in porosity, and/or microfracturing of rocks. Sibson (1981) defined hydro-fracture dilatancy essentially as a low differential stress phenomenon. Aleinikov et al. (2000) proposed a new physical-mathematical conception describing the rock destruction process as a phase transition.

The significance of dilatancy in some physical applications was first pointed out by Reynolds (1885), but the stress-dilatancy theory/model was only introduced in 1962 for sands (Rowe 1962) and subsequently for soft clays (Roscoe et al. 1963). The theory would later be summarized by Roscoe and Burland (1968), Schofield and Wroth (1968), Chu et al. (2004), etc. The idea behind the stress-dilatancy theory/model is based on the experimentally discovered relationship between the main effect of dilatancy and shear strength (Rowe 1962), which thus links the stress ratio to the dilatancy rate.

It was found that at low confining pressures, dilatancy has a major influence on the shear strength of coarse-grained soils, and is largely influenced by stress level and the packing state of the soil particles (Charles 1991). Rowe (1962) showed that the stress-dilatancy relationship is more appropriate in the case of dense sand. Pender (1978) also suggested a plastic dilatancy relationship for over-consolidated clays which reveal the development of positive pore pressures in lightly and normally over-consolidated clays and negative pore pressures in heavily over-consolidated clays. This effect in clays is also discussed in Chu et al. (2004). Wan and Guo (2004) showed that under particular strain paths and fabric conditions, relatively dense sand can give way to instability or liquefaction under conditions other than isochoric. This phenomenon is consistent with laboratory experiments demonstrating that dilation (or compaction) can be controlled by modulating the amount of water flowing in or out of a sand specimen during shearing. Some

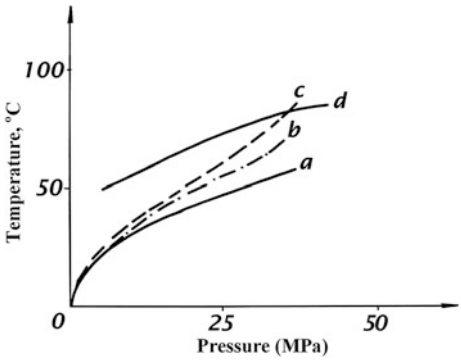

Fig. 2.10 Changes in a unit of volume of water (V/V_0) under different temperatures and pressures for well 558 of the Duvanniy Sea area: *a* curve of conditions for water at $V/V_0 = 1.00$; *b* curve of conditions in the well with unloading of layer from excess water (V_2/V_0); *c* curve of conditions in the well without unloading of layer from excess water (V_1/V_0); *d* curve of condition of water with $V/V_0 = 1.01$

studies help relate the plastic dilatancy ratio to the development of pore pressures in clay soils (Chu et al. 2004). Authors have also noted the importance of effective pressure, which is defined as the total pressure minus the porous pressure, for saturated and dry rocks (e.g., Scholz et al. 1973) in analyzing dilatancy.

From all of the above, it is clear that dilatancy is strongly related to the porosity of sedimentary rocks and porous pressure. It is also evident that Eq. (2.7.4) can be used to determine or estimate the relative volume change ($\Delta V/V_0$) that can be used to characterize dilatancy in sedimentary rocks and rock layers. From this point of view, it also seems important to analyze the variable volume ($\Delta V/V_0$) in relation to maximal porous pressure for sedimentary layers in different regions with varying thermodynamic regimes.

Equation (2.7.4) can be used to calculate the relative change of volume ($\Delta V/V_0$) of porous fluid.

In fact, solving Eq. (2.7.4) for $\Delta V/V_0$ yields:

$$\frac{\Delta V}{V_0} = \alpha(T - T_0) - \beta(P - P_0). \tag{2.7.19}$$

It is clear from Eq. (2.7.19) that it can be used to determine the amount of water forced out by AHSP/AHPP in a case where $(T - T_0) > 0$, as well as the relative reduction in fluid volume (and/or amount of porous volume available for additional fluid) in a case where (ALSP/ALPP) of $(T - T_0) < 0$. Thus if $(T - T_0) > 0$, the amount of fluid (usually water) forced out of pores by AHSP/AHPP is defined as the difference between the values V_1/V_0 and V_2/V_0 shown in Fig. 2.6 for cases where there is no fluid unloading ($\Delta V = 0$ and P_{AHPP} is maximal without unloading), and real volume conditions (with the measured value of P_{AHPP}), respectively. For example, such a determination for well 558 of the Duvanniy Sea area is presented in Fig. 2.10.

The relative change of the volume of water (ΔV_{12}) for each pair of P and T values can be determined from the equation:

$$\frac{V_{12}}{V_0} = \frac{V_1}{V_0} - \frac{V_2}{V_0}. \tag{2.7.20}$$

It should be taken into account that changes in the volume of porous water do not imply changes in the porous volume, since even though in most cases part of the water would be forced out by the AHSP/AHPP, the remaining water would fill the porous volume. However, the density of the remaining water would be different from that of the porous water prior to unloading. If under certain P-T-conditions the initial volume of water V_0 has a density σ_0, the average change in density with variable volume V would be:

$$\Delta\sigma = K_P \frac{V_0 - V}{V} \sigma_0. \tag{2.7.21}$$

Depending on the thermodynamic conditions, a volume of water could decrease, leading to an increase in its density and a positive gravity effect. Conversely, an increase in volume is also possible, which would lead to decreased density in the case of unloading of part of the water from the porous volume. Using geothermal data and Figs. 2.6 and 2.10, the change in a unit of volume (V/V_0) and the corresponding change in density ($\Delta\sigma$) for each 1 km interval to a depth of 4 km, and subsequently the average values of V/V_0 and $\Delta\sigma$ for the upper 4 km layer were calculated for some regions of the Kura Depression (Azerbaijan) and adjacent areas of the Caspian Sea (see Table 2.18). Data on variable density were also used to determine the gravity effect of such a change in density for selected oil and gas fields, as also presented in Table 2.18. A maximum depth of 4 km for the estimates was selected for the following reasons: (1) a significant distance from the surface layers below a depth of 4 km would have a very small effect on the gravity field; (2) at depths of over 4 km, porosity can be much smaller, and likewise produce a much smaller effect; (3) if the upper 4 km layer showed some significant gravity effect, including lower layers could only serve to increase this effect, whereas the purpose of these estimates is first and foremost to verify the presence of a gravity effect.

It can be seen from Table 2.18 that the values of both V/V_0 and $\Delta\sigma$ are very small, but they create quite a significant gravity effect Δg, on the same order of magnitude as the gravity effect caused by oil and gas fields, which enables the use of high definition gravity for prospecting for oil and gas fields. Note that the value of the density change of water is negative for all these areas, which points to the unloading of some water from the porous volume. However, this effect may simply be typical of the region, and not useful for further interpretation. To verify this possibility, the gravity effect caused by variable density under thermodynamic conditions was estimated for different parts (crest and slope) of anticline structures on the Muradkhanly and Kyursangya areas (Azerbaijan). The results of these estimates are presented in Table 2.19.

Table 2.18 Average changes in the density of water, and gravity effect caused by these changes under the thermodynamic conditions of some oil and gas areas of the Kura depression and adjacent areas of the Caspian sea

Area	Average change of unit of volume of water (V/V_0)	Average change of density of water [$\Delta\sigma$ (kg/m^3)]	Value of gravity effect (Δg in mGal)
Borsunly	1.030	−6.1	−1.00
Sovetlyar	1.023	−4.7	−0.73
Zardob	1.017	−3.5	−0.54
Muradkhanly	1.022	−4.5	−0.69
Sor-Sor	1.012	−2.7	−0.38
Dzharly	1.011	−2.6	−0.38
Padar	1.010	−2.5	−0.37
Kalamadin	1.006	−1.5	−0.31
Kyurovdag	1.009	−2.3	−0.36
Karabagly	1.002	−0.6	−0.13
Kyursangya	1.009	−2.3	−0.36
Sangachali Sea	1.016	−3.5	−0.54
Garadag	1.016	−3.5	−0.54
Duvanniy Sea, Bulla island	1.016	−3.5	−0.54

Table 2.19 Estimates of the gravity effect caused by changes in the density of porous water for the Muradkhanly and Kyursangya areas

Area	Average change of unit of volume of water (V/V_0)	Average change of density of water [$\Delta\sigma$ (kg/m^3)]	Value of gravity effect (Δg in mGal)
Muradkhanly			
Crest	1.023	−4.7	−0.72
NE Slope	1.015	−3.1	−0.49
Kyursangya			
Crest	1.013	−3.0	−0.49
Slope	1.005	−1.3	−0.20

Table 2.19 indicates that the gravity effect for these areas is considerable and the difference between its effect for the crest and the slope of these anticline structures is −0.23 mGal for the Muradkhanly area and −0.29 mGal for the Kyursangya area. These values are significant and can be measured with gravimeters. Moreover, these values are on the order of the gravity effect formed by oil and gas fields, and consequently in some cases anomalies in the gravity field caused by the reduction of density of water under thermodynamic conditions could be mistaken for ones caused by oil and gas fields.

From Eq. (2.7.5), accepting P_1 as the maximal possible pressure defined as the pressure without unloading (see above), P_1 can be defined as:

$$P_1 = P_0 + \frac{\alpha}{\beta}(T - T_0). \tag{2.7.22}$$

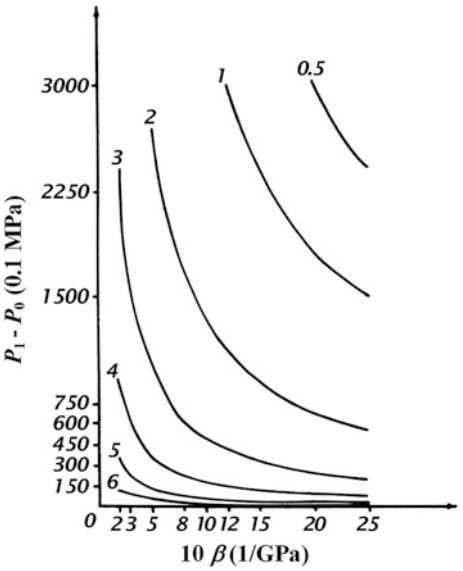

Fig. 2.11 Chart for determining the change in volume of water [in $-\lg(\Delta V/V_0)$]

Equation (2.7.22) can be written as:

$$\beta(P_1 - P_0) = \alpha(T - T_0). \tag{2.7.23}$$

Substituting $\alpha(T - T_0)$ from Eq. (2.7.23) into Eq. (2.7.19) and solving it for P gives:

$$P = P_1 - \frac{1}{\beta}\frac{\Delta V}{V_0}. \tag{2.7.24}$$

Finally, Eq. (2.7.24) can be presented as (Mekhtiev et al. 1982):

$$\frac{\Delta V}{V_0} = \beta(P_1 - P). \tag{2.7.25}$$

Equation (2.7.25) was used for compiling Fig. 2.11, which can be used to determine the $\Delta V/V_0$ of water for different P-T-conditions (Mekhtiev et al. 1982).

In order to determine the value of total possible unloading of porous volume from water caused by P-T-conditions in Eq. (2.7.24), note that P should be replaced by P_0. Determining the $\Delta V/V_0$ for both P and P_0 can serve to estimate the excess fluid (water) contained in porous volumes under the given P-T-conditions. It can also be used to estimate the quantity (reserves) of fluid/water in a layer.

Equation (2.7.24) was used to analyze the amount of unloading of layers in some oil and gas areas of West and East PreCaucasian. Research shows that in Azerbaijan, the highest values of unloading of porous volume in layers are found in areas of Middle Kura Depression (Pilchin 1983). Estimates made for 23 wells of Muradkhanly area returned a value of water volume change of $\Delta V/V_0 = 0.035$–0.070 or 3.5–7.0 % of the total porous fluid. Significantly lower $\Delta V/V_0$ values were

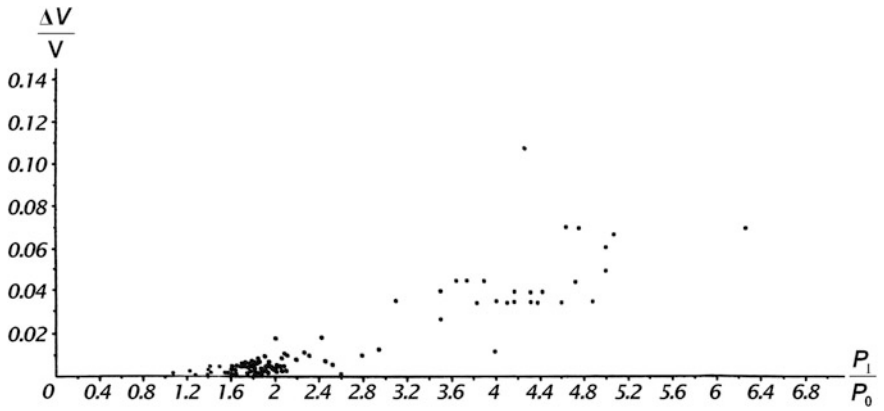

Fig. 2.12 Dependence of values of relative change in the volume $\Delta V/V_0$ on the maximal value of $K_{aP} = P_1/P_0$ for oil and gas fields of Azerbaijan

obtained for areas of the Lower Kura Depression: for 51 wells in Kyurovdag area $\Delta V/V_0 = 0.005–0.027$ (or 0.5–2.7 %); 21 wells of Kalmas area $\Delta V/V_0 = 0.003–0.011$ (or 0.3–1.1 %); 7 wells of Mishovdag area $\Delta V/V_0 = 0.0005–0.0120$ (or 0.05–1.2 %). Very low values of $\Delta V/V_0$ were found for areas of the Caspian Sea: for well 550 in the Sangachaly Sea area $\Delta V/V_0 = 0.0005–0.0050$ (or 0.05–0.5 %); well 558 in the Duvanniy Sea area $\Delta V/V_0 = 0.0023$ (or 0.23 %). Similar estimates of the unloading of porous volume from an excess of fluid for the PreCaucasian (Mekhtiev et al. 1982) yielded the following values: $\Delta V/V_0 = 0.001–0.070$ (or 0.1–7.0 %) for 21 wells of Hayan Kort area and $\Delta V/V_0 = 0.045–0.086$ (or 4.5–8.6 %) for the Braguni area. As a whole, the Western PreCaucasian (30 wells) and Eastern PreCaucasian (55 wells) values of $\Delta V/V_0$ were 0.022–0.091 (or 2.2–9.1 %) and 0.018–0.177 (or 1.8–17.7 %), respectively. These values indicate that high temperatures in the layers of the PreCaucasian force out up to 17.7 % of their normal volume from their porous space. For a better understanding of the influences of the variable volume of fluid $\Delta V/V_0$, the relationships between values of $\Delta V/V_0$ and P_1/P_0 are presented in Figs. 2.12 and 2.13 for oil and gas fields in Azerbaijan and the PreCaucasian, respectively. From the definition of P_1 (see above), it is clear that the value of P_1/P_0 represents the maximum possible value of K_{aP} in the high temperature regime in a region.

Figures 2.12 and 2.13 show that for both regions increased values of $K_{aP} = P_1/P_0$ go hand in hand with increased $\Delta V/V_0$ values.

Interestingly, for the 23 wells of the Muradkhanly area $P_1/P_0 = 3.09–6.25$, the lithostatic pressure P_{lit} at the same depths is only $\sim$2.5 times greater than the hydrostatic pressure P_0 ($P_{lit}/P_0 = 2.5$). This means that in the oil and gas fields of the Muradkhanly area, the value of P_{AHSP} could have been greater than the lithostatic pressure P_{lit}. Such a situation could have led to the formation of the types of cracks and dilatancy discussed above. This is consistent with results of studies by Sibson (1981) reporting arrays of parallel extension fractures and veins

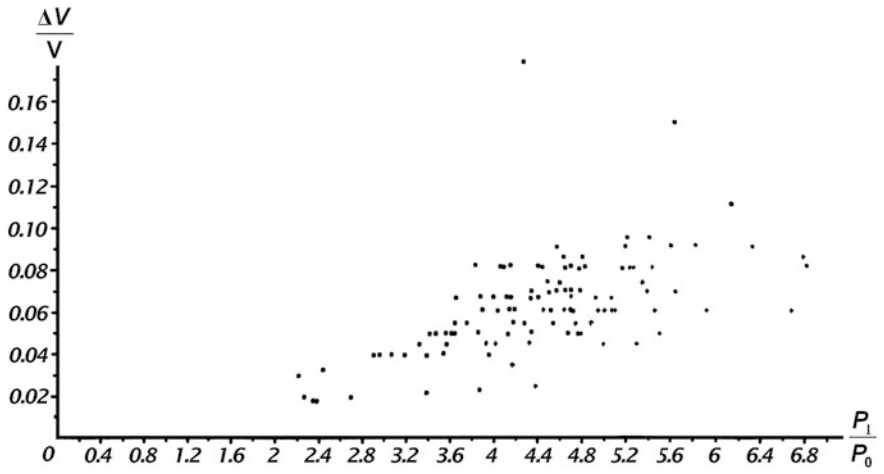

Fig. 2.13 Dependence of the value of the relative change in volume $\Delta V/V_0$ on the maximal value of $K_{aP} = P_1/P_0$ for oil and gas fields of the PreCaucasian

associated with exhumed faults that appear to be the product of repeated hydrofracturing under a shared stress regime, which can only occur in association with thrusts when fluid pressures exceed the lithostatic load. Moreover, it is clear that the highest possible value of AHSP/AHPP could have been 2.5 times greater than the lithostatic pressure. However, such high pressures could not have actually been collected prior to the start of its unloading, since porous pressure primarily generates tensile stress, whereas the tensile stress limits of any rocks and especially sedimentary rocks is very low (e.g. Clark 1966). The presence of significant pressure unloading is also proven by data from other authors (e.g., Magara 1978). The value of AHSP/AHPP would increase gradually and likewise be gradually unloaded. In other words, even though the maximal possible AHSP/AHPP could be very high it would unload throughout the entire period of evolution of the layer.

In the oil and gas fields of the Lower Kura Depression areas (Pilchin 1983), the maximum possible AHSP/AHPP is much lower, and the value of P_1/P_0 is 1.18–3.50 (for 51 wells of the Kyurovdag area); 1.42–4.00 (for 8 wells of the Mishovdag area); 1.42–2.94 (for 21 wells of Kalmas area). For well 550 in the Sangachaly Sea area, the value of P_1/P_0 is in the range of 1.55–2.11; i.e., in layers of the Sangachaly Sea area (Azerbaijan) AHSP/AHPP was never greater than the lithostatic pressure P_{Lit}. For areas of the PreCaucasian, the values of possible maximum AHSP/AHPP are very high and the value of P_1/P_0 is 2.26–6.80 for 116 readings, and values of $P_1/P_0 < 3.0$ have only been determined for 9 points. For areas of Turkmenistan (Kerimov and Pilchin 1986b), these values are Western Turkmenistan $\Delta V/V_0 = 0.0020$–0.0203, $P_1/P_0 = 1.69$–2.64 (for 24 wells); Central Turkmenistan $\Delta V/V_0 = 0.0020$–0.0263, $P_1/P_0 = 3.68$–7.79 (for 68 wells); and Eastern Turkmenistan $\Delta V/V_0 = 0.0129$–0.0610, $P_1/P_0 = 3.57$–6.53 (for 84 wells).

It should be stated that in all cases, the highest P_1/P_0 ratio and the relative change of volume $\Delta V/V_0$ are regulated by the thermal regime in the sedimentary layers. For example, in the Kura Depression the geothermal gradient is about 39–43 K/km in its westernmost part, drops to 20–30 K/km in the central part of the Middle Kura Depression, and further declines to 18–20 K/km in the eastern part of the Lower Kura Depression (Mekhtiev et al. 1985; Kerimov and Pilchin 1986a). In depression zones of the Northern Caucasus (including the Pre-Caucasian), the geothermal gradient is in the range of 25–60 K/km, and in some isolated cases even greater (Mekhtiev et al. 1985; Kerimov and Pilchin 1986a). The geothermal gradients for areas of Western Turkmenistan are within the range of 21–28 K/km, increasing in areas of the Central Turkmenistan and reaching 40–60 K/km, and then declining to 31–39 K/km in areas of Eastern Turkmenistan (Mekhtiev et al. 1985; Kerimov and Pilchin 1986a).

Thus overall, dilatancy indeed exists and has been found to take place in a wide range of regions. If the dilatancy effect were not present, the obtained pressure values in all cases would be equal to the maximum possible value of P_1. However, in fact, all these pressures were much lower than the maximum of AHSP/AHPP. Thus, unloading of pressure took place in all the cases mentioned above, and according to Eq. (2.7.4) the value of the change in volume ΔV was never zero. It is also clear that if at very shallow depths (up to 500–1,000 m, at which the zone of AHSP/AHPP usually begins) the pores were permeable all the way through to the surface, it would allow the unloading fluid flow to reach the surface without forming cracks and fractures. However, such a situation would not be possible for fluid within layers capped by impermeable layers (e.g., clay or salt layers). At the same time, most of the data used for the above analysis were taken from measurement values of temperatures and pressures in layers containing oil and gas fields, which are most certainly capped by clay layers in Azerbaijan, the Caspian Sea, Western Turkmenistan and the PreCaucasian, and capped by salt layers in Eastern Turkmenistan and Uzbekistan. Additionally, it can be seen from Tables (2.16) and (2.17) that in all cases, pressures in fields, including fields filled with water, are much lower than the maximum possible pressure under the present thermal regime. Data from other regions of Russia, Ukraine, Kazakhstan and Uzbekistan also support this trend (Table 2.20).

Such values (Table 2.20) are only possible if dilatancy took place, since in layers below the cap layer an increase in volume is possible only by forming cracks and fractures. Since the average density of the upper sedimentary layers is about 2,350 kg/m^3, it follows that the lithostatic pressure (P_{lit}) in such layers should be about 2.35 times greater than the hydrostatic pressure (P_0), and $P_{\text{lit}}/P_0 = 2.35$. At the same time, it was shown above that the maximum values of $K_{aP} = P_1/P_0$ can be as high as 7.79 for Central Turkmenistan. This means that the total possible maximum values of AHSP/AHPP (P_1) can be greater than the lithostatic pressure (P_1/P_{lat}) by up to 2.7 times for the Middle Kura Depression, 1.7 times for the Lower Kura Depression, 2.9 times for the PreCaucasian, 1.1 times for the Western Turkmenistan, 3.3 times for Central Turkmenistan and 2.8 times for Eastern Turkmenistan. Naturally, at such shallow depths the lithostatic pressure

Table 2.20 Values of K_{aP} of pressure in fields with different kinds of fluid saturation for some areas of Russia, the Ukraine, Kazakhstan, and Uzbekistan

Region	Kind of porous fluid					No. of tests
	Gas, condensed gas	Gas, oil	Oil	Hydrocarbons and water	Water	
Permian province	–	0.88–1.14	0.9–1.13	–	–	52
Bashkirtystan	–	0.55–1.03	0.74–1.35	–	–	161
Orenburg province	0.84	0.72–1.19	1.03–1.11	–	–	30
Kuybishev province	–	0.79–1.14	0.81–1.19	–	–	65
Komi republic	–	0.64–1.04	0.75–1.12	–	–	29
Stavropol province	–	0.96–1.22	0.98–1.19	–	–	38
Krasnodar province	–	0.51–1.32	0.47–1.45	–	–	60
Sakhalin Island	–	0.84–1.16	0.64–1.17	–	–	118
Napsko-Botuobinskiy	0.71–1.23	–	0.72–1.43	–	–	59
Dnieper-Donets	0.95–1.26	0.76–1.13	1.00–1.16	–	up to 1.8	106
PreCarpathian	0.81–1.49	0.44–1.12	0.67–1.52	1.31–1.61	to 2.02	67
Crimea	0.50–1.19	0.75–1.02	1.03–1.52	1.02–1.88	to 2.19	58
Precaspian	–	–	0.53–1.39	1.25–1.55	–	163
	–	1.00–1.35	–	1.21–1.46	–	17
South-Mangyshlak	1.10–1.20	0.55–1.32	0.56–1.40	1.23–1.77	–	52
Fergana						

would be unable to maintain such enormous pressures. This also means that dilatancy was in most cases caused by an increase of AHSP/AHPP.

The highest value of $\Delta V/V_0$ taken from the above results is 17.7 %. Since this is the change in the fluid part of the volume alone, for sedimentary rock with a porosity of $\sim$25 % it would yield a maximum change of the rock volume of about 4.425 %. We can then conclude that the value of dilatancy in all cases was no more than 4.425 %. At the same time, as was shown earlier, the maximal possible pressure cannot be accumulated completely until the start of its unloading, and it would continue unloading bit by bit as it was increasing. Given that this volume was growing a little at a time over millions and tens of millions of years (e.g., the Muradkhanly oil and gas field are within Mesozoic layers in Central Azerbaijan), it is obviously very difficult to measure this effect in nature. Pinpointing the dilatancy effect in depressional regions through seismological investigation is hence a very complicated task.

It was mentioned above that in the case of regional tectonic activity, the value of $\Delta V/V_0$ may be less than zero, indicating an additional pressure increase beyond its maximum possible value as a result of the thermal regime. Such cases were reported by Kerimov and Pilchin (1986b) based on water density values under layer conditions for wells 666 and 680 (at depths of 1.51 and 4.45 km, respectively) of the Starogroznenskiy area and well 503 (depth 3.35 km) of the Orliniy area of the Tersko-Sunzhensk Depression, for all of which the value of the ratio $\Delta\sigma/\sigma > 0$. This feature, in addition to the positive value of compressibility ($\beta > 0$)

in Eq. (2.7.8) points to an additional increase in pressure above and beyond the value caused solely by the thermal regime. This means that in these cases, tectonic stresses in sedimentary layers contributed significantly to the abnormal pressure values.

Kerimov and Pilchin (1986b) showed that analysis of the geothermal regime of layers at great depths can be used to identify conditions related to the presence of oil and gas in different layers. Theoretically, this problem can be solved as follows. Assume that there is a two-component field containing oil and water, characterized by a field pressure P_1, temperature T_1 and coefficients of expansion and compressibility for oil α_o, β_o and water α_w, β_w, respectively. If the thermodynamic conditions within the field were to somehow change to pressure P_2 and temperature T_2, there would be a re-distribution of the initial volumes of oil (V_{o0}) and water (V_{w0}). The relative change in volumes of oil and water respectively, would be characterized by the state equations:

$$\frac{\Delta V_0}{V_{o0}} = \alpha_o(T_2 - T_1) - \beta o(P_2 - P_1). \tag{2.7.26}$$

$$\frac{\Delta V_w}{V_{w0}} = \alpha_w(T_2 - T_1) - \beta_w(P_2 - P_1). \tag{2.7.27}$$

Under these changes to the components, the initial volumes in the field value of the total volume of both fluids would be constant:

$$V_{o0} + V_{w0} = \text{const}. \tag{2.7.28}$$

Thus, changes to one component of the fluid mixture in the field could only take place at the expense of a volume change in the other component:

$$\Delta V_o = -\Delta V_w. \tag{2.7.29}$$

Dividing Eq. (2.7.27) by Eq. (2.7.26) and taking into account the condition in Eq. (2.7.29), one gets:

$$\frac{V_{o0}}{V_{w0}} = -\frac{\alpha_w(T_2 - T_1) - \beta_w(P_2 - P_1)}{\alpha_o(T_2 - T_1) - \beta_o(P_2 - P_1)}. \tag{2.7.30}$$

Let us term the value of the ratio V_{o0}/V_{w0} the coefficient of relative oil content μ:

$$\mu = \frac{V_{o0}}{V_{w0}}. \tag{2.7.31}$$

It is clear from Eq. (2.7.31) that for $\mu = 1$, the initial volumes of oil and water are equal; for $\mu > 1$ oil has a higher volume than water in the field. In such a case, $K_o > K_w$. In particular, in a case where $\mu \to \infty$, there would be very little water content in that field. At the same time, for $\mu < 1$ the volume of water would be

greater than that of oil, and if $\mu \to 0$ the field would contain very little oil. Thus, by using the coefficient of the relative oil content, it is also possible to estimate the coefficient of the oil saturation of rocks (K_o) from:

$$K_o = \frac{1}{1 + \frac{1}{\mu}}. \tag{2.7.32}$$

2.8 Density of Fluids in the Early Earth Atmosphere

As it was discussed in Sect. 1.1, various sources generated energy during the Earth's formation and evolution, the most significant of which were planetary accretion, planetary differentiation, bombardment by huge astronomic objects (planetesimals, asteroids, etc.), and the radioactive decay of short-lived and long-lived radioisotopes (Lubimova 1968a; Pollack 1997). Estimates of the combined energy produced by these processes, even disregarding the Earth's possible collision with a Mars-sized body, show that the energy was sufficient to melt the entire planet during its accretion (Lubimova 1968a, b; Pollack 1997; Valley et al. 2002).

It is generally accepted that for some period in its early evolution, the Earth was entirely covered by a magma-ocean (Abe 1997; Li and Agee 1996; Pollack 1997; Labrosse et al. 2007; Righter and Drake 1997b; Sleep et al. 2001; Solomatov 2000; Valley et al. 2002; Pilchin and Eppelbaum 2006, 2009), which was between several hundred (Walter and Trønnes 2004) up to about 1,000 km deep (Li and Agee 1996; Labrosse et al. 2007). Some scientists believe that this magma-ocean could only have existed for about 1–10 million years (Spohn and Schubert 1991), while others argue that it could have remained for 100–200 million years (Abe 1997; Pollack 1997), and could have persisted for even a few hundred million years in the case of a thick early atmosphere (Abe 1997; Solomatov 2000). This type of magma-ocean was also present at one time on other terrestrial planets and the Moon (Matsui and Abe 1986; McSween 1993).

The content and composition of the early Earth's atmosphere above this magma-ocean would have been determined by the stability conditions of the chemical compounds existing in the solar nebula and the developing planetesimals, asteroids and other cosmic objects. Previous studies have shown that the early Earth's atmosphere was rich in carbon dioxide and water vapor (Table 2.21).

Numerous compounds (chlorides, hydrides, oxides, sulfides, sulfates, sulfites, nitrates, etc.) decompose at temperatures lower than those of the magma-ocean (Lide 2005; Speight 2005; Pilchin and Eppelbaum 2006). For example, K_2O decomposes at 623 K (Lide 2005), Na_2O at 1,445 K (Lide 2005), Ni_2O_3 at 873 K (Lide 2005), NaH at 698 K (Lide 2005), etc. This means that some compounds and even pure elements would have been in the atmosphere over the magma-ocean,

Table 2.21 Estimates of the partial pressure of carbon dioxide and water vapor in the early Earth's atmosphere

Atmosphere Component	Age	Partial pressure (MPa)	References
Carbon dioxide, CO_2	Hadean	1	Morse and Mackenzie (1998)
	After end of accretion	A few MPa	Abe (1993)
	First several hundred Ma	1–2	Kasting and Ackerman (1986)
	Early earth atmosphere	10–100	Sukumaran (2001)
	Early earth atmosphere	1	Walker (1985)
	Proto-atmosphere	10	Liu (2004)
	Early earth atmosphere	Up to 4.35	Pilchin (2011)
Water vapor, H_2O	Hadean	All water was vaporized	Pollack (1997)
	Right after accretion	20–30	Abe (1993)
	Early earth atmosphere	10–30	Zahnle et al. (1988)
	Early earth atmosphere	27	Zahnle et al. (1988)
	Proto-atmosphere	56	Liu (2004)
	Early earth atmosphere	~30	Genda and Ikoma (2008)
	Early earth atmosphere	~26	Pilchin and Eppelbaum (2009)

since they have relatively low boiling points of 1,032 K for K (potassium), 1,156 K for Na, 717.7 K for S, and 1,180 K for Zn (Lide 2005; Speight 2005).

As was discussed earlier, even though other compounds have greater temperatures of decomposition, they could still have sunk in the magma-ocean to hotter depths where they would have decomposed and released volatiles, which would once again have eventually ended up in the atmosphere. All of this means that the atmosphere above the magma-ocean was rich in all the typical atmospheric gases, volcanic gases, as well as numerous other compounds which would have existed in a gaseous state at those temperatures.

Observing gases released during different magmatic activities reveals (Hall 1995; Stoiber 1995; Textor et al. 2004) that H_2O, SO_2 and CO_2 are by far the chief components of any volcanic process. This makes an examination of the conditions of stability of carbon and sulfur compounds, as well as water, a key to any investigation of the composition of the early atmosphere.

Analyses of published experimental data show (Pilchin and Eppelbaum 2006) that none of the main carbonate rocks (limestone, dolomite, calcite, siderite, magnesite, K_2CO_3, Na_2CO_3, etc.) are stable at temperatures above 1,173–1,193 K, and that the temperatures for their stability are generally a great deal lower (Lide 2005; Speight 2005; Pilchin and Eppelbaum 2009). This means that at the time of the magma-ocean, none of these carbonates would have survived and must have decomposed, releasing CO_2.

A similar analysis of publications on the conditions of pyrite stability shows that the maximum temperature at which it is stable is about 1,016 K, and is usually

much lower (Lide 2005; Pilchin and Eppelbaum 2006; Speight 2005). Experimental data also show that pyrrhotite is unstable above ~1,463 K, and pyrite is stable below ~873 K (Lide 2005; Speight 2005). Furthermore, pyrite decomposes at temperatures of 743 K in a CO_2 atmosphere (Golden et al. 2004). As such, since neither pyrite nor pyrrhotite could have been stable within the magma-ocean, elemental sulfur would have been released into the atmosphere after their decomposition. It can be seen from data presented in (Lide 2005; Speight 2005) that a number of sulfides, sulfites and sulfates would likewise have been unstable under such conditions. For example, iron(III) sulfate decomposes at a temperature of ~1,451 K (Speight 2005) and nickel sulfate decomposes at a temperature of ~1,113 K (Lide 2005).

Analysis of the composition of magmatic gases collected from basaltic lavas during eruptions (Hall 1995) shows that their main components are H_2O, SO_2 and CO_2, and that the average content of SO_2 is second by volume to water and first by weight. Textor et al. (2004) further indicated that the dominant sulfur component of volcanic gases is sulfur dioxide (SO_2). Furthermore, given the immense temperatures, no liquid water could have existed on the Earth's surface at the time of the magma-ocean, and it all would have been in vaporous form in the atmosphere.

All of the above shows that during the formation and evolution of the magma-ocean there would have been a very dense and thick atmosphere. This corresponds to other studies showing that the primitive atmosphere and ocean appear to have been formed from gases arising from the magma-ocean (Drake 2000).

Estimates of the pressure generated by such an atmosphere indicate a minimum value of ~35 MPa (Pilchin and Eppelbaum 2006). This estimate represents the absolute minimal possible atmospheric pressure, because the amount of water used for the calculations was that of the current day ocean and subsurface underground content. For example, the partial pressure of water alone calculated using estimates of its content in the biosphere, hydrosphere and crust presented in (Holland 1984) is ~39 MPa. Estimates by Zhang and Zindler (1993) show that the amount of carbon dioxide currently bound in carbonate rocks is sufficient to generate an additional partial pressure of ~21.5 MPa. The estimated partial pressure of carbon oxides within the early Earth's atmosphere to determine the abundance of carbon presently within the crust alone indicate 2.99 MPa for carbon as CO, and 4.35 MPa for carbon as CO_2 (Pilchin 2011). Similar estimates of the partial pressure within the early Earth's atmosphere from such elements as F, Cl, and S, as well as their compounds using the abundance values of these elements within the present crust alone (Pilchin 2011) indicate minimal values of 4.35 MPa for elemental F_2, 2.72 MPa for elemental Cl_2, 2.72 MPa for elemental S^0, and 5.44 MPa for sulfur as SO_2.

Some studies have concluded that the water content on Earth at the time could have been equal to about 5–6 current Earth oceans, and even up to 50 Earth oceans [see review in Drake (2005)]. Stimpfl et al. (2004) and Drake (2005) calculated

Table 2.22 Critical properties of some fluids after (Rau et al. 1973; Reid et al. 1987; Lide 2005; Speight 2005; Yaws 2001, 2008)

Fluid	Temperature (K)	Pressure (MPa)	Density (kg/m^3)
Carbon dioxide, CO_2	304.1	7.38	468
Water, H_2O	647.3	22.12	322
Methane, CH_4	190.4	4.60	162
Hydrogen sulfide, H_2S	373.2	8.94	349
Sulfur dioxide, SO_2	430.7	7.88	525
Sulfur trioxide, SO_3	491.1	8.20	633
Oxygen, O_2	154.6	5.04	436
Carbon monoxide, CO	132.9	3.50	1,465
Carbon disulfide, CS_2	552.0	7.90	476
Chlorine dioxide, ClO_2	465.0	8.61	690
Sulfuric acid, H_2SO_4	925.0	6.40	552
Sulfur monochloride, S_2Cl_2	659.4	6.28	554
Trisulfur dichloride, S_3Cl_2	489.7	3.58	560
Carbonyl sulfide, COS	378.8	6.35	445
Chlorine, Cl_2	417.0	7.71	573
Sulfur, S_n	1,313.0	18.2	563

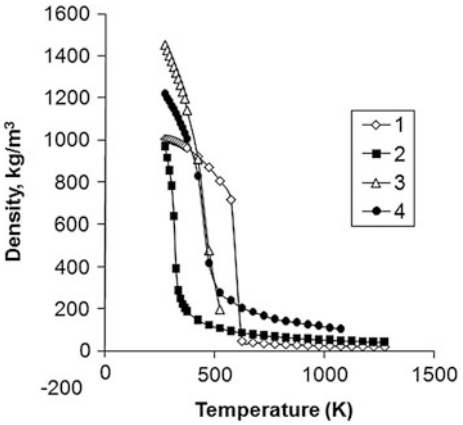

Fig. 2.14 Changes in the density of H_2O, CO_2, and SO_2 with increases in temperature under pressure of 10 MPa: (*1*) H_2O, (*2*) CO_2, (*3*) SO_2 from experimental data (Ihmels et al. 2003), (*4*) SO_2 calculated using thermodynamic methods for fluids

that the amount of water adsorbed in the Earth during accretion could have been as much as 1–3 Earth oceans. Needless to say, this would have dramatically increased the atmospheric pressure. At the same time, both the temperature and pressure within the Earth's atmosphere are variable with altitude. This means that at different altitudes within the early Earth's atmosphere there would have been different values of pressure, temperature, and therefore density. It is also important to note that the key components of the early Earth's atmosphere (H_2O, SO_2, CO_2, etc.) would have been under supercritical conditions (Table 2.22).

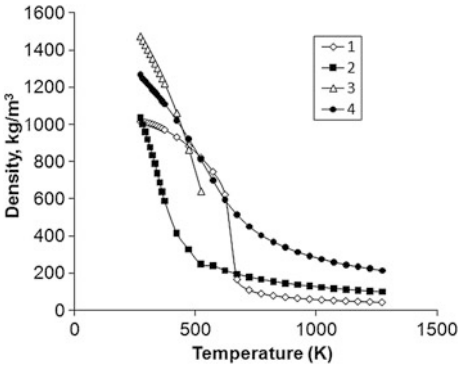

Fig. 2.15 Changes in the density of H_2O, CO_2, and SO_2 with increases in temperature under pressure of 25 MPa: (*1*) H_2O, (*2*) CO_2, (*3*) SO_2 from experimental data (Ihmels et al. 2003), (*4*) SO_2 calculated using thermodynamic methods for fluids

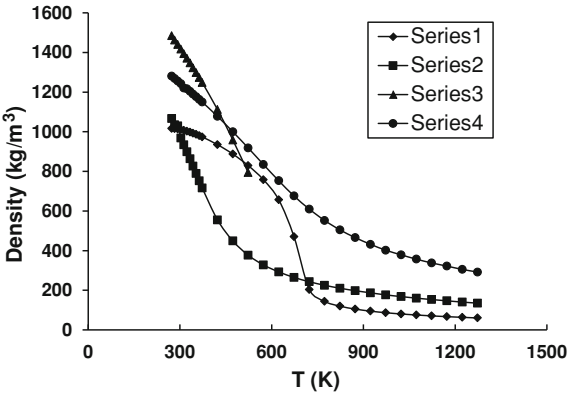

Fig. 2.16 Changes in the density of H_2O, CO_2, and SO_2 with increases in temperature under pressure of 35 MPa: (*1*) H_2O, (*2*) CO_2, (*3*) SO_2 from experimental data (Ihmels et al. 2003), (*4*) SO_2 calculated using thermodynamic methods for fluids

Table 2.23 Temperature range within which the density of water is greater or about the same as the densities of SO_2, CO and CO_2 at different pressures (adapted from Pilchin 2011)

Atmosphere component	Temperature range (in K) at pressure				
	10 MPa	25 MPa	35 MPa	50 MPa	100 MPa
SO_2, calculated	~400–600	~500–600	None[a]	None[a]	None[a]
SO_2, from experimental data	~400–?	~450–?	~500–550	–	–
CO_2	<~600	~280–650	~300–700	~315–760	360–780
Co	–	–	~415–630	–	–

[a] Below this pressure the densities of SO_2 calculated using thermodynamic methods for fluids are greater than the density of water at any temperature; however experimental data show that conditions in which the density of water is greater than that of SO_2 are possible

Naturally, not all the water in the atmosphere would have been under supercritical conditions, but rather only the portion under a pressure higher than the critical pressure of water. Since H_2O, CO_2 and SO_2 were by far the main

components of the early Earth's atmosphere, analysis of their densities has been conducted for different temperatures and pressures of 10, 25, and 35 MPa (Figs. 2.14, 2.15, 2.16). Data from (Clark 1966; Kerimov et al. 1980; Lide 2005; Speight 2005) were used to calculate the density of H_2O and CO_2, and experimental data reported in (Ihmels et al. 2003) for SO_2. Thermodynamic calculation methods were used to derive the density of SO_2 (Pilchin 2011). This analysis is important for modeling both the conditions at different levels within the atmosphere, and conditions during processes of surface cooling and decline of atmospheric pressures.

The results shown in Fig. 2.16 indicate that the density of water reaches a value of about 75.8 % of the normal density of water (NDW) at 573 K, and decreases drastically to 14.4 % of the NDW at 773 K. Along with the further increase of temperature, the density of water begins to drop much more slowly to a value of about 6 % of the NDW at 1,273 K. Figures 2.14, 2.15 and 2.16 highlight that under specific *P-T*-conditions, the density of water becomes greater than that of SO_2 and CO_2 (see Table 2.23).

Problems related to the evolution of the early Earth's atmosphere during the cooling of the Earth and the formation of the water ocean are discussed in Sect. 6.2.

References

Abe Y (1993) Physical state of the very early Earth. Lithos 30(3–4):223–235

Abe Y (1997) Thermal and chemical evolution of the terrestrial magma ocean. Phys Earth Planet Inter 100(1–4):27–39

Adylov GT, Mansurova EP (1999) The use of basalt rocks from koitashskoe ore deposit in production of building ceramics and filter materials. Glass Ceram 56(1–2):20–21

Aleinikov AL, Belikov VT, Eppelbaum LV, Nemzorov NI (2000) Mountainous rock destruction and metamorphic processes in the Earth: a view from classical physics. Sci Isr (3):65–87

Aliev SA, Mekhtiev SF (1970) Geothermics of depression zones of Azerbaijan. Report for 1964–1970. AzTGF, Baku (in Russian)

Aliev SA, Rustamov RI, Mirzababayev II, Alieva ZA (1977) Geothermal cross-section of forerunner of superdeep Saatly borehole. Izv AN Azerb SSR, Ser: Earth Sci 6:115–117 (in Russian)

Anderson DL (2007) New theory of the Earth. Cambridge University Press, Cambridge

Anderson DL, Whitcomb JH (1973) The dilatancy-diffusion model of earthquake prediction. In: Kovach RL, Nur A (eds) Proceedings of the Conference on tectonic problems of the San Andreas fault, geological sciences, vol 13, pp 417–426

Aronson JR, Bellotti LH, Eckroad SW, Emslie AG, McConnell RK, von Thüna PC (1970) Infrared spectra and radiative thermal conductivity of minerals at high temperatures. J Geophys Res 75(17):3443–3456

Attrill PG, Gibb FGF (2003) Partial melting and recrystallization of granite and their application to deep disposal of radioactive waste: Part 1—rationale and partial melting. Lithos 67(1–2):103–117

Bayly B (1968) Introduction to petrology. Prentice-Hall Inc, Englewood Cliffs, NJ

Best MG (2002) Igneous and metamorphic petrology, 2nd edn. Wiley-Blackwell, Hoboken
Birch F, Clark H (1940) The thermal conductivity of rocks and its dependence upon temperature and composition. Am J Sci 238(8):529–558, 613–635
Birch F, Schairer JF, Spicer HC (eds) (1942) Handbook of physical constants. Geological Society of America. Special papers, No. 36
Blackwell DD, Steele JL (1989) Thermal conductivity of sedimentary rocks: measurement and significance. In: Naeser ND, McCulloch TH (eds) Thermal history of sedimentary basins.Springer, New York, pp 5–96
Blesh CJ, Kulacki FA, Christensen RN (1983) Application of integral methods to prediction of heat transfer from a nuclear waste repository. Open file report ONWI-495, Battelle Memorial Institute, Columbus, OH, 12–17
Brigaud F (1989) Conductiviter thermique et champr de temperature dans les bassins serdimentaires a‘ partir des donneres de puits (Documents et Travaux, Centre Gerologique et Gerophysique de Montpellier)
Cannat M, Karson JA, Miller DJ et al. (1995) Proceedings of the ocean drilling program, initial reports, vol 153
Čermak V, Rybach L (1982) Thermal conductivity and specific heat of minerals and rocks. In: Angenheister G (ed) Landolt-Bornstein numerical data and functional relationships in science and technology. Springer, New York, pp 213–256
Charles JA (1991) Laboratory share strength tests and the stability of rockfill slopes. In: Maranha das Neves E (ed) Advances in rockfill structures. Springer, New York, pp 53–72
CRC Handbook on Chemistry and Physics, 1974. 55th Ed., CRC Press, Florida
Cheremensky GA (1977) Applied geothermics. Nedra, Leningrad (in Russian)
Cherry JTh, Schock RN, Sweet J (1975) A theoretical model of the dilatant behavior of a brittle rock. Pure Appl Geophys 113(1):183–196
Cho WJ, Kwon S, Choi JW (2009) The thermal conductivity for granite with various water contents. Eng Geol 107(3–4):167–171
Chu J, Kim SR, Oh YN, Balasubramaniam AS, Bergado DT (2004) An experimental and theoretical study on the dilatancy of sand and clays. In: Proceedings of the 9th Australia–New Zealand. Conference on geomechanics, vol 2, Auckland, New Zealand, pp 654–660
Clark SP Jr (Ed.) (1966) Handbook of physical constants (revised edition). Geological Society of America. Memoir 97, Washington, DC
Clauser C (1988) Opacity: the concept of radiative thermal conductivity. In: Hänel R, Rybach L, Stegena L (eds) Handbook of terrestrial heat flow density determination. Kluwer Academic Publication, Dordrecht, pp 143–165
Clauser C (2006) Geothermal energy. In: Heinloth K (ed) Landolt-Börnstein, group VIII: advanced materials and technologies, vol 3. Energy technologies, Subvol. C: renewable energies, Springer, Berlin, pp 493–604
Clauser Ch (2009) Heat transport processes in the Earth’s crust. Surv Geophys 30:163–191
Clauser C, Huenges E (1995) Thermal conductivity of rocks and minerals. In: Ahrens TJ (ed) Rock physics and phase relations: a handbook of physical constants. American Geophysical Union, Reference shelf 3, pp 105–126
Côté J, Konrad J-M (2005) Thermal conductivity of base-course materials. Can Geotech J 42:61–78
Dakhnov VN (1972) Interpretation of geophysical investigations of borehole sections. Nedra, Moscow (in Russian)
Dakhnov VN, Dyakonov DI (1952) Thermal investigation of boreholes. Gostoptekhizdat, Leningrad (in Russian)
Dasgupta R, Hirschmann MM (2007) Effect of variable carbonate concentration on the solidus of mantle peridotite. Am Mineral 92:370–379

Del Gaudio P, Di Toro G, Han R, Hirose T, Nielsen S, Shimamoto T, Cavallo A (2009) Frictional melting of peridotite and seismic slip. J Geophys Res 114:B06306. doi:10.1029/2008JB005990
Dmitriev AP, Kuzyaev LS, Protasov YuI, Yamschikov VS (1969) Physical properties of rocks at high temperatures. Nedra, Moscow (in Russian)
Dortman NB (ed) (1976) Physical properties of rocks and minerals (petrophysics): handbook of geophysicist. Nedra, Moscow (in Russian)
Drake MJ (2000) Accretion and primary differentiation of the Earth: a personal journey. Geochim Cosmochim Acta 64:2363–2370
Drake MJ (2005) Origin of water in the terrestrial planets. Meteoritics Planet Sci 40:519–527
Driatskaya ZV, Mkhchiyan MA, Zhmikhova NM (eds) (1971) Oils of the USSR, handbook, vol I, oils of northern regions of the European part of the USSR and the Urals. Khimiya, Moscow (in Russian)
Driatskaya ZV, Mkhchiyan MA, Zhmikhova NM (eds) (1972) Oils of the USSR, handbook, vol II, oils of the middle and lover Volga region. Khimia, Moscow (in Russian)
Durham WB, Mirkovich VV, Heard HC (1987) Thermal diffusivity of igneous rocks at elevated pressure and temperature. J Geophys Res 92(B11):11615–11634. doi:10.1029/JB092iB11p11615
ETB (2011) The engineering toolbox. Solids: specific heat capacities
Eucken A (1911) Dependence of the thermal conductivity of certain gases on the temperature. Physihal Zeitsch 12:1101–1107
Falloon TJ, Green DH, Danyushevsky LV (2007) Crystallization temperatures of tholeiite parental liquids: implications for the existence of thermally driven mantle plumes. In: Foulger GR, Jurdy DM, (eds) Plates, plumes, and planetary processes. The Geological Society of America, special paper 430, Boulder, Colorado, pp 235–260
Faure G (2000) Origin of igneous rocks: the isotopic evidence. Springer, Berlin
Faure G, Mensing TM (2007) Introduction to planetary science: the geological perspective. Springer, Berlin
Genda H, Ikoma M (2008) Origin of the ocean on the Earth: early evolution of water D/H in a hydrogen-rich atmosphere. Icarus 194:42–52
Gillis K, Mével C, Allan J et al (1993) Proceedings of ODP, initial reports, 147: College Station, TX (Ocean Drilling Program). Leg 147
Golden DC, Ming DW, Lauer HV Jr, Morris RV (2004) Thermal decomposition of siderite pyrite assemblages: implications for sulfide mineralogy in martian meteorite ALH84001 carbonate globules. Lunar Planet Sci XXXV, No. 1396
Gretener PE (1981) Geothermics: using temperature in hydrocarbon exploration. AAPG, Short Course Notes, 17
Grove TL, Parman SW (2004) Thermal evolution of the Earth as recorded by komatiites. Earth Planet Sci Lett 219:173–187
Grove TL, Chatterjee N, Parman SW, Medard E (2006) The influence of H_2O on mantle wedge melting. Earth Plan Sci Lett 249:74–89
Hall H (1995) Igneous petrology. Longman Science and Technology, Singapore
Hanley EJ, Dewitt DP, Roy RF (1978) The thermal diffusivity of eight well-characterized rocks for the temperature range 300–1,000 K. Eng Geol 12:31–47
Hewins RH, Jones RH, Scott ERD (eds) (1996) Chondrules and the protoplanetary disk. Cambridge University Press, Cambridge
Hofmeister AM (2007) Pressure dependence of thermal transport properties. Proc Nat Acad Sci USA 104(22):9192–9197
Hofmeister AM, Perterman M (2008) Thermal diffusivity of clinopyroxenes at elevated temperature. Eur J Mineral 20:537–549
Holland HD (1984) The chemical evolution of atmosphere and oceans. Princeton University Press, Princeton, USA
Hurtig E, Brugger H (1970) Heat conductivity measurements under uniaxial pressure. Tectonophysics 10:67–77

Ihmels E, Clemmon EW, Gmehling J (2003) An equation of state and compressed liquid supercritical densities for sulfur dioxide. Fluid Phase Equilib 207:111–130
Kappelmeyer O, Hänel R (1974) Geothermics with special reference to application. Gebruder Borntrargen, Berlin, Stutgart
Kasting JF, Ackerman TP (1986) Climate consequences of very high carbon dioxide levels in the Earth's early atmosphere. Science 234:1383–1385
Kelemen PB, Kikawa E, Miller DJ et al. (2004) Proceedings of the ocean drilling program, initial reports, vol 209
Kerimov KM, Pilchin AN (1986a) Use of geothermics data for prognosis of abnormal stratum pressure and oil and gas perspectives at great depths. In: Kerimov KM (ed) Combined interpretation of geological-geophysical data with the goal to search oil and gas presence at great depths. Baku Book Publishers, Baku, pp 25–36 (in Russian)
Kerimov KM, Pilchin AN (1986b) Geothermal regime of the sedimentary cover of Azerbaijan and Caspian sea depression areas. Azerbaijan Oil Ind 1:9–13 (in Russian)
Kerimov KM, Pilchin AN, Ibragimov SM (1980) Influence of thermodynamical factor on the overhigh pressure in sedimentary strata. Azerbajan Oil Industry (Azerbaijanskoe Neftyanoe Khozyaistvo) 2:6–9 (in Russian)
Kim J, Lee Y, Koo M (2007) Thermal properties of granite from Korea. AGU Fall Meeting 2007, abstract #T11B-0576
Kukkonen IT, Jokinen J, Seipold U (1999) Temperature and pressure dependencies of thermal transport properties of rocks: implications for uncertainties in thermal lithosphere models and new laboratory measurements of high-grade rocks in the Central Fennoscandian Shield. Surv Geophys 20(1):33–59
Kushiro I, Syono Y, Akimoto S (1968) Melting of a peridotite nodule at high pressures and high water pressures. J Geophys Res 73(18):6023–6029
Kutas RI, Gordienko VV (1971) Heat flow of the Ukraine. Naukova Dumka, Kiev (in Russian)
Labrosse S, Hernlund JW, Coltice N (2007) A crystallizing dense magma ocean at the base of the Earth's mantle. Nature 450:866–869
Lee CTA, Luffi P, Plank T, Dalton H, Leeman WP (2009) Constraints on the depths and temperatures of basaltic magma generation on Earth and other terrestrial planets using new thermobarometers for mafic magmas. Earth Plan Sci Lett 279:20–33
Li J, Agee CB (1996) Geochemistry of mantle-core differentiation at high pressure. Nature 381:686–689
Lide DR (ed) (2005) CRC handbook of chemistry and physics, 86th edn
Litovsky E, Shapiro M (1992) Gas pressure and temperature dependencies of thermal conductivity of porous ceramic materials: part 1, refractories and ceramics with porospty below 30 %. J Am Ceramic Soc 75(12):3425–3439
Liu L (2004) The inception of the oceans and CO_2-atmosphere in the early history of the Earth. Earth Planet Sci Lett 227:179–184
Lubimova EA (1968a) Thermics of the Earth and Moon. Nauka, Moscow (in Russian)
Lubimova EA (1968a) Thermal history of the Earth. In: The Earth's crust and upper mantle. American Geophysical Union, geophysical monograph series, vol 13, pp 63–77
Lubimova EA, Smirnova EV (1974) Heat physical properties of rocks at high temperatures. In: Physical properties of rocks under high pressure and temperature. Trans. of IV All-Union Congress, Tbilisi, pp 171–172 (in Russian)
Lubimova EA, Lusova LN, Firsov FV (1964) Basics of heat flow from Earths depths determination and results of measurements. In: Geothermal researches. Nauka, Moscow, pp 5–103 (in Russian)
Lubimova EA, Maslennikov AI, Ganiyev YA (1978) Heat conductivity of sedimentary rocks under elevated pressure and temperatures and polymorphism. In: Physical properties of rocks under high thermodynamic parameters. Trans. of IV All-Union Congress, Baku, "Elm" Publication, pp 230–231 (in Russian)

Magara K (1978) Compaction and fluid migration: practical petroleum geology. Elsevier, NY
Magnitsky VA (1965) Internal structure and physics of the Earth. Nedra, Moscow (in Russian)
Matsui T, Abe Y (1986) Formation of a 'magma ocean' on the terrestrial planets due to the blanketing effect of an impact-induced atmosphere. Earth Moon Planet 34:223–230
McCall GJ (1973) Meteorites and their origins. Wiley, NY
McSween HY Jr (1993) Stardust to planets. St. Martin's Griffin, NY
Mekhtiev SF, Mirzajanzadeh AKh, Aliyev SA (1971) Geothermal investigation of oil and gas fields. Nedra, Moscow (in Russian)
Mekhtiev SF, Kashkay MA, Aliev SA (1972) Investigation of relationships of heat flow with construction and evolution tectonic structure and geophysical fields in different tectonic structures of USSR. (Pre-Kura oil and gas province, Apsheron oil and gas province). Scientific report for 1971–1972. Baku, Azerbaijan Geol. Fund
Mekhtiev SF, Geodekyan AA, Tsaturyants AB, Ter-Karapetyants ZN, Bayramov EM, Shabanov CF (1973) Geothermics of oil and gas fields of Azerbaijan and Turkmenistan. Nauka, Moscow (in Russian)
Mekhtiev SF, Kerimov KM, Pilchin AN (1982) Role of thermal factors on formation and preservation of AVPD in sedimentary cover of Kura depression. Azerbaijan Oil Industry (Azerbaijanskoye Neftyanoye Khozyaystvo) 3:1–5 (in Russian)
Mekhtiev SF, Kerimov KM, Pilchin AN, Agabekov AM (1985) Geothermal regime of depression zones of the Caucasus and SW part of Turanskaya plate and its influence on formation of abnormal pressures within their deposits. In: Ismail-Zade TA et al. (eds) Trans. of Scien-Techn. Meet. Geological-geophysical methods of searching oil and gas fields at great depths, Baku, pp 76–78 (in Russian)
Morse JW, Mackenzie FT (1998) Hadean ocean carbonate geochemistry. Aquat Geochem 4(3–4):301–319
Nikonova NS, Tikhomirova IN, Belyakov AV, Zakharov AI (2003) Wollastonite in silicate matrices. Glass Ceram 60(9–10):342–346
Nur A (1972) Dilatancy, pore fluids, and premonitory variations of T_S/T_P travel times. Bull Seismol Soc Am 62(5):1217–1222
Nur A (1975) A note on the constitutive law for dilatancy. Pure Appl Geophys 113(1):197–206
Pender MJ (1978) A model for the behaviour of overconsolidated soils. Geotechnique 28(1):1–25
Pertermann M, Hofmeister AM (2006) Thermal diffusivity of olivine-group minerals at high temperature. Am Mineral 91(11–12):1747–1760
Petrunin GI, Popov VG (1995) Temperature dependence of lattice thermal conductivity of Earth's mineral substance. Izv Russ Acad Sci, Phys Solid Earth 30(7–8)
Pilchin AN (1978a) Correction to hydrostatic pressure in the crust of the Middle Kura depression. In: Geophysical researches of the oil, gas and ore deposits in Azerbaijan, Baku, pp 78–80 (in Russian)
Pilchin A (1983) Geothermal regime of Earth's crust of the Kura depression and its influence on pressure distribution in it. Ph.D. thesis, Institute of Geophysics of the Georg. Academy of Science, Tbilisi (in Russian)
Pilchin AN (2011) Magnetite: the story of the mineral's formation and stability. In: Angrove DM (ed) Magnetite: structure, properties and applications. Nova Science Publishers, NY, pp 1–99 Chapter 1
Pilchin AN, Eppelbaum LV (2002) Some peculiarities of thermodynamic conditions of the Earth crust and upper mantle. Sci Isr 4(1–2):117–142
Pilchin AN, Eppelbaum LV (2004) On the stability of ferrous and ferric iron oxides and its role in rocks and rock-forming minerals stability. Sci Isr 6(3–4):119–135
Pilchin AN, Eppelbaum LV (2006) Iron and its unique role in earth evolution. Monograph 9, Mexican Geophys Soc

Pilchin AN, Eppelbaum LV (2009) The early Earth and formation of the lithosphere. In: Anderson JE, Coates RW (eds) The Lithosphere: Geochemistry, Geology and Geophysics. Nova Science Publishers, NY, pp 1–68 Chapter 1

Pilchin AN, Kerimov KM (1986) Some features of abnormality of pressure coefficient change in collectors with different character of saturation. In: Mikhailov IM, Rizhik VM, Shendrey LP (eds) Role of abnormal pressures in oil and gas field distribution. IGIRGI Publishers, Moscow, pp 140–143 (in Russian)

Poelchau HS, Baker DR, Hantschel Th, Horsfield B, Wygrala B (1997) Basin simulation and the design of the conceptual basin model. In: Welte DH, Horsfield B, Baker DR (eds) Petroleum and basin evaluation. Springer, Berlin, pp 36–41

Pollack HN (1997) Thermal characteristics of the Archaean. In: de Wit MJ, Ashwal MD (eds) Greenstone belts. Clarendon Press, Oxford, UK, pp 223–232

Popov YA, Pevzner LA, Romushkevich RA, Korostelev VM, Vorob'yev MG (1995) Thermophysical and geothermal sections obtained from Kolvinskaya well logging data. Izv Acad Sci Russ, Phys Solid Earth 30:778–789

Popov Y, Tertychnyi V, Romushkevich R, Korobkov D, Pohl J (2003) Interrelations between thermal conductivity and other physical properties of rocks: experimental data. Pure Appl Geophys 160:1137–1161

Prats M (1982) Thermal recovery, vol 7., Monograph SeriesSociety of Petroleum Engineers, Dallas

Pribnow D, Williams CF, Sass JH, Keating R (1996) Thermal conductivity of water-saturated rocks from the KTB pilot hole at temperatures of 25 to 300 °C. Geophys Res Lett 23(4):391–394

Proselkov YM (1975) Heat transfer in wells. Nedra, Moscow (in Russian)

Rau H, Kutty TRN, Guedes de Carvalho JRF (1973) High temperature saturated vapor pressure of sulphur and the estimation of its critical quantities. J Chem Thermodyn 5:291–302

Ray L, Roy S, Srinivasan R (2008) High radiogenic heat production in the Kerala Khondalite block, Southern Granulite province, India. Int J Earth Sci 97(2):257–267

Reid RC, Prausnitz JM, Poling BE (1987) The properties of gases and liquids, 4th edn. McGraw-Hill, NY

Reynolds O (1885) On the dilatancy of media composed of rigid particles in contact. Philos Mag 5(20):469–482

Righter K, Drake MJ (1997) Metal-silicate equilibrium in a homogeneously accreting earth: new results for Re. Earth Planet Sci Lett 146(3–4):541–553

Robertson EC (1979) Thermal conductivity of rocks. U.S. Geological Survey open file report 79–356

Roscoe KH, Burland JB (1968) On the generalized stress–strain behaviour of wet clay. In: Engineering plasticity, Cambridge, pp 535–609

Roscoe KH, Schofield AN, Thurairajah A (1963) Yielding of clays in state Wetter than critical. Geotechnique 13(3):211–240

Rowe PW (1962) The stress-dilatancy relation for static equilibrium of an assembly of particles in contact. Proc R Soc London, Ser A 269:500–527

Sass JH, Lachenbruch AH, Munroe RJ, Greene GW, Moses TH Jr (1971) Heat flow in the western United States. J Geophys Res 76:6376–6413

Schärli U, Rybach L (2001) Determination of specific heat capacity on rock fragments. Geothermics 30:93–110

Schofield AN, Wroth CP (1968) Critical state soil mechanics. McGraw-Hill, London

Scholz ChH, Sykes LR, Aggarwal YP (1973) Earthquake prediction: a physical basis. Science 181(4102):803–810

Schubert G, Turcotte DL, Olson P (2001) Mantle convection in the Earth and Planets two volume set. Cambridge University Press, Cambridge

Seipold U (2002) Investigation of the thermal transport properties of amphibolites: I. pressure dependence. High Temp High Pressures 34(3):299–306

Seipold U, Gutzeit W (1980) Measurements of the thermal properties of rocks under extreme conditions. Phys Earth Planet Inter 22(3–4):267–271
Seipold U, Huenges E (1998) Thermal properties of gneisses and amphibolites: high pressure and high temperature investigations of KTB-rock samples. Tectonophysics 291(1–4):173–178
Sharma PV (2002) Environmental and engineering geophysics. Cambridge University Press, Cambridge
Shim BO, Park JM, Kim HC, Lee Y (2010) Statistical analysis on the thermal conductivity of rocks in the Republic of Korea. In: Proceedings of the World Geothermal Congress 2010, Bali, Indonesia
Sibson RH (1981) Controls on low-stress hydro-fracture dilatancy in thrust, wrench and normal fault terrains. Nature 289:665–667
Simmons G (1961) Anisotropic thermal conductivity. J Geophys Res 66(7):2269–2270
Sleep NH, Zahnle K, Neuhoff PS (2001) Initiation of clement surface conditions on the earliest Earth. Proc Natl Acad Sci US 98(7):3666–3672
Solomatov VS (2000) Fluid dynamics of a terrestrial magma ocean. In: Canup R, Righter K (eds) Origin of the Earth and Moon. University of Arizona Press, Tucson, Arizona, pp 323–338
Somerton WH (1958) Some thermal characteristics of porous rocks. Trans AIME 213:375–378
Somerton WH (1992) Thermal properties and temperature related behavior of rock/fluid systems. Developments in Petroleum Science, 37. Elsevier, Amsterdam
Speight JG (2005) Lange's handbook of chemistry, 16th edn. McGaw-Hill, NY
Spohn T, Schubert G (1991) Thermal equilibration of the Earth following a giant impact. Geophys J Int 107:163–170
Starikova GN, Lubimova EA (1973) Heat properties of rocks from Kola peninsula. In: Heat flows from Earth crust and upper mantle. Nauka, Moscow, pp 112–124 (in Russian)
Stimpfl M, Lauretta DS, Drake MJ (2004) Adsorption as a mechanism to deliver water to the Earth (abstract). Meteorit Planet Sci 39:A99
Stoiber RE (1995) Volcanic gases from subaerial volcanoes on Earth. In: Global earth physics, a handbook of physical constants. AGU, Ref. Shelf 1, pp 308–319
Sukumaran PV (2001) Early planetary environments and the origin of life. Resonance 6(10):16–28
Tamura Y, Yuhara M, Ishii T, Irino N, Shukuno H (2003) Andesites and dacites from Daisen volcano, Japan: partial-to-total remelting of an andesite magma body. J Petrol 44(12):2243–2260
Téqui C, Robie RA, Hemingway BS, Neuville DR, Richet P (1991) Melting and thermodynamic properties of pyrope ($Mg_3Al_2Si_3O_{12}$). Geochim Cosmochim Acta 55(4):1005–1010
Textor C, Graf H-F, Timmreck C, Robock A (2004) Emissions from volcanoes. In: Granier C, Reeves C, Artaxo P (eds) Emissions of chemical compounds and aerosols in the atmosphere. Kluwer, Dordrecht, pp 269–303 Chapter 7
Thy P, Lesher CE, Mayfield JD (1999) Low-pressure melting studies of basalt and basaltic andesite from the southeast Greenland continental margin and the origin of dacites at site 917. In: Larsen HC, Duncan RA, Allan JF, Brooks K (eds) Proceedings of the ocean drilling program, scientific results, 163, Scient. Res. southeast Greenland Margin, Chapter 9, pp 95–112
Valley JW, Peck WH, King EM, Wilde SA (2002) A cool early Earth. Geology 30(4):351–354
Van Westrenen W, Wood BJ, Blundy JD (2001) A predictive thermodynamic model of garnet-melt trace element partitioning. Contrib Mineral Petrol 142:219–234
Volarovich MP (ed) (1978) Handbook on physical properties of minerals and rocks under high thermodynamic parameters. Nedra, Moscow (in Russian)
Vosteen H-D, Schellschmidt R (2003) Influence of temperature on thermal conductivity, thermal capacity and thermal diffusivity for different types of rock. Phys Chem Earth 28:499–509
Walker JCG (1985) Carbon dioxide on the early Earth. Orig Life Evol Biosp 16(2):117–127

Walter MJ, Trønnes RG (2004) Early Earth differentiation. Earth Planet Sci Lett 225(3–4):253–269
Wan RG, Guo PJ (2004) Stress dilatancy and fabric dependencies on sand behavior. J Eng Mech 130(6):635–645
Waples DW, Waples JS (2004) A review and evaluation of specific heat capacities of rocks, minerals, and subsurface fluids. Part 1: minerals and nonporous rocks. Nat Resour Res 13(2):97–122
Wenk H-R, Bulakh AG (2004) Minerals: their constitution and origin. Cambridge University Press, Cambridge
Whittington AG, Hofmeister AM, Nabelek PI (2009) Temperature-dependent thermal diffusivity of the Earth's crust and implications for magmatism. Nature 458:319–321
Yaws CL (2001) Matheson gas data book, 7th edn. Mcgraw-Hill, New York
Yaws CL (2008) Thermophysical properties of chemicals and hydrocarbons. William Andrew, Norwich
Yoder HS Jr (1976) Generation of basaltic magma. National Academy of Science, Washington, DC
Zahnle KJ, Kasting JF, Pollack JB (1988) Evolution of a steam atmosphere during Earth's accretion. Icarus 74:62–97
Zhang Y, Zindler A (1993) Distribution and evolution of carbon and nitrogen in Earth. Earth Planet Sci Lett 117:331–345
Zinger AS, Kotrovsky VV (1979) Hydro-geothermal conditions of water systems of western part of Pre-Caspian depression. Saratov University, Saratov (in Russian)
Zoth G, Hänel R (1988) Appendix. In: Hänel R, Rybach L, Stegena L (eds) Handbook of terrestrial heat flow density determination. Kluwer, Dordrecht, pp 449–466

Chapter 3
Methods of Thermal Field Measurements

3.1 Different Methods of Thermal Field Measurements

As described in Sect. 1.1.3, the first systematic temperature measurements were made in France, Germany and England in the second half of the 18th century and the beginning of the 19th century in mines, subsurface wells and hot springs. One of the first geothermal measurements in oil wells was carried out by Batzevich in 1880 in the Apsheron Peninsula, Azerbaijan (Eppelbaum and Khesin 2012).

In the early days of geothermics, temperature measurements were made mainly in soil, underground water, mines, tunnels, draw-wells, shafts and caves. Temperature was measured with various air, water and alcohol thermometers with inaccurate scales. The measurements were often inaccurate and not compatible. Relatively precise graduated mercury and alcohol thermometers with conventional scales have only been used since the middle of the 18th century. Today, geophysical temperature devices can register temperature values with an accuracy of 0.001 °C and higher.

A generalized scheme of thermal field observations in applied geophysics is presented in Fig. 3.1. The five main types of thermal observations ('Wells', 'Near-Surface', 'Underground', 'Wells in Water Basins' and 'Infrared Observations') and their subcategories are shown.

This chart is not exhaustive and does not include, for instance, thermal measurements in experimental laboratories on the marine floor and other rare types of observations.

3.2 The Use of Thermistors and Fiber Optic Temperature Sensors

3.2.1 Thermistors

A thermistor is a type of resistor whose resistance varies significantly with temperature, more so than in standard resistors. The word is a combination of two words: *thermal* and *resistor*. Thermistors are widely used in geophysics as temperature

L. Eppelbaum et al., *Applied Geothermics*, Lecture Notes in Earth System Sciences,
DOI: 10.1007/978-3-642-34023-9_3,

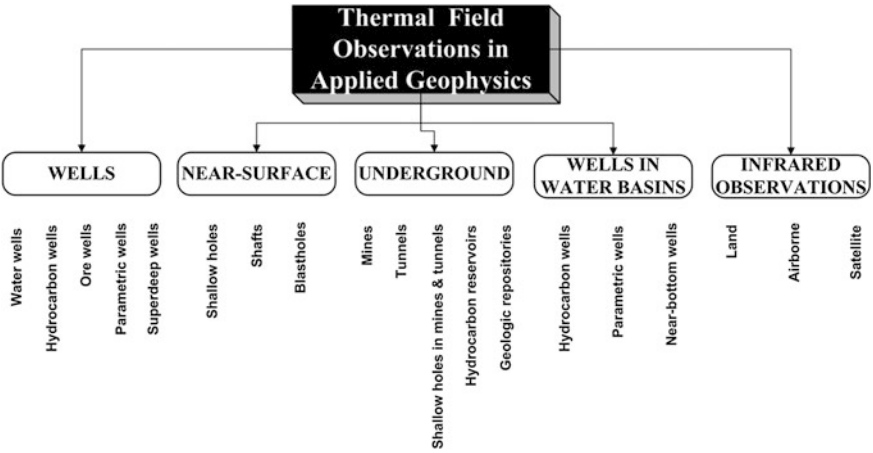

Fig. 3.1 A simplified scheme of the different modes of thermal field measurements in applied geophysics

sensors (e.g., Sass et al. 1971). Thermistors differ from resistance temperature detectors (RTD) in that the material used in a thermistor is generally a ceramic or polymer, while RTDs use pure metals. A generalized model of a thermistor is presented in Fig. 3.2. The temperature response is also different: RTDs are useful over larger temperature ranges, while thermistors typically achieve a higher precision within a limited temperature range, typically −90 to 130 °C. Based on this temperature range, thermistors can be applied without restriction in conditions of permafrost (even in the coolest regions of the Earth), and also to depths of approximately 3–5 km (depending on the geothermal gradient in the area under study).

3.2.2 Fiber Optic Temperature Sensors

Hurtig et al. (1992a, b) were the first to publish findings on applications of fiber optic temperature sensing in boreholes as well as long-term temperature monitoring for studying geotechnical and environmental problems (e.g., waste deposits). A typical optic sensing device is shown in Fig. 3.3.

These sensors work on optical time domain reflectometry. A laser pulse is coupled to an optical fiber and a small part of the light is backscattered as the pulse propagates through the fiber. The intensity and spectral composition of the backscattered light are determined by the molecules in the optical fiber. The Raman backscattering component is caused by thermally influenced molecular vibrations. Thus, its intensity depends on temperature. The velocity of light propagation in an optical fiber is known; therefore, the backscattering intensity can be related to distance using the travel time of the backscattered light. Thus, an optical fiber acts as a distributed temperature sensor which indicates the temperature and distance simultaneously for the entire length of the optical fiber.

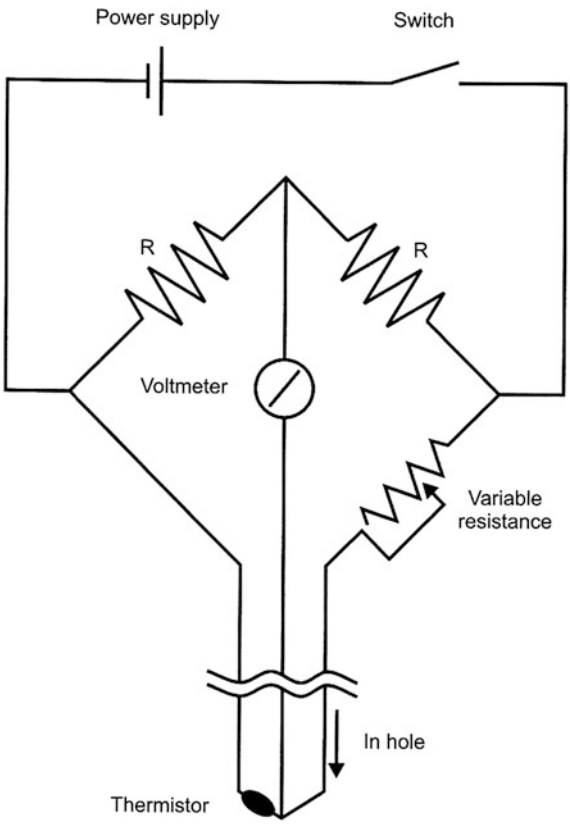

Fig. 3.2 Schematic diagram of a Wheatstone bridge circuit for measuring thermistor resistance (after Beardsmore and Cull 2001)

The system can also be installed in horizontal and inclined boreholes. Fiber optic temperature sensing is particularly valuable for long-term surveillance of the temperature field and its variations with time rather than for standard borehole logging. As the sensing cable can be laid in any configuration over an area, the ground temperature, even for larger areas, can be surveyed. This is of special importance for monitoring the ground temperature in hydrothermal and volcanic regions. As there are no active electronic circuits along the temperature sensing cable, the fiber optic sensing technique is well-suited for long-term temperature monitoring even in corrosive and hazardous environments (Hurtig et al. 1996).

3.3 Measurements in Wells

To measure temperature in wells, some temperature devices are lowered down the borehole when thermal observations will be carried out at some regular (or irregular) interval. These devices as a rule measure the temperature of wellbore fluid, which

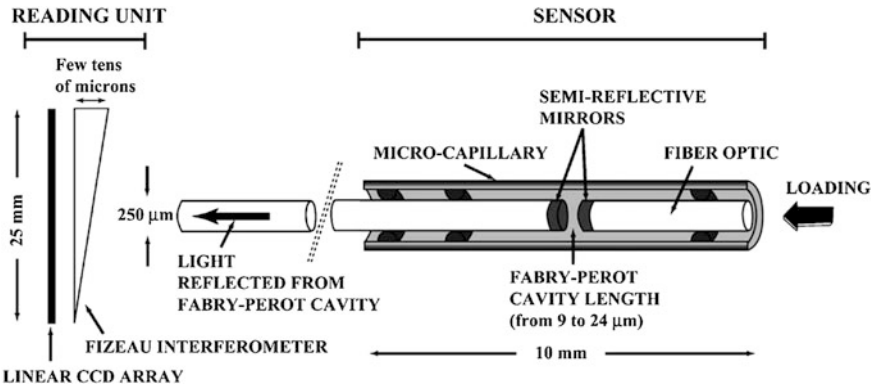

Fig. 3.3 Conceptual scheme of the Fabry-Perot fiber optic sensing device (after Cappa et al. 2006)

reflects the temperature of the surrounding rocks. Therefore, the bore fluid should be in thermal equilibrium with the surrounding geological formations. Physically, the temperature of the fluid in recently drilled boreholes will not be in thermal equilibrium. Therefore, undisturbed temperature measurements need to be delayed until sometime after the completion of the drilling process. This time delay depends on such physical-geological characteristics as the total drilling time, and the thermal conductivity of mud and surrounding rocks (see Sects. 8.1 and 8.2).

Land measurements in wells (shown in Fig. 3.1) are divided into hydrological, oil and gas, ore, parametric (reference) and superdeep. Methodologies of drilling and thermal measurements in different types of boreholes as a rule are different (their analysis is beyond the scope of this book).

In general, the shallowest are hydrological and ore wells (from several meters to a few tens of meters). The world databases of thermal measurements for different types of wells consist currently contain tens of millions of observations. Measurements in hydrocarbon wells are discussed in detail in Chap. 8, and hydrological wells in Chap. 9. The results of measurements of thermal fields in superdeep boreholes are briefly presented in Sects. 7.4 and 13.3.1.

3.4 Sea Measurements

Oceans cover about 71 % of the Earth's surface. There are roughly twice as many wells located on land than in the sea basins.

Subsurface sea thermal measurements in sediments are obtained in two ways. The first kind of measurements involves using two thermal elements mounted some distance apart in a hollow steel probe 2–8 m long and 20–50 mm in diameter (Bullard 1954; Lubimova et al. 1973). This probe is attached to a weight housing a

recorder and is lowered by winch to the sea floor. The temperature differences are recorded as a function of time just before the probe enters the sea floor, during its time subsurface and for a period after it is raised. Numerous experimental findings show that the temperature conditions in deep ocean (sea) basins are sufficiently stable to observe non-disturbing thermal gradients in the first few meters of sediments. The thermal conductivity λ of the sediments is usually a quasi-constant value (about 0.8–0.9 W/m °C), so in many cases it is sufficient to measure the thermal gradient alone. Given that the core does not contain the probe it can be inserted into the subsurface a few times. A photo of a Bullard penetrator (one of the first devices to study heat flow measurements at the sea bottom) is shown in Fig. 3.4.

A schematic diagram of the temperature gradient probe penetrating is shown in Fig. 3.5. The thermal conductivity thermistor (Tc in Fig. 3.5) and the matched water thermistor (Tw in Fig. 3.5) form two arms of a resistance ridge circuit. Their difference in resistance is recorded on the chart. Variations of water temperature are measured simultaneously by comparing Tw to a fixed resistor. The experimental reading error consisted of ±0.002 °C (Sclater et al. 1969) that is more than the required accuracy in the majority of researches.

The second type of subsurface sea thermal measurements is to use thermistors set at some distance apart on small outriggers strapped to the barrel of a gravity corer (Clarke et al. 1972).

Jones (1999) book contains a special chapter devoted to thermal measurements in marine areas.

3.5 Space Infrared Measurements

After the Second World War, the occasional use of near-infrared (NIR) sensitive emulsions suggested that invisible imaging had great potential. Space infrared measurements are now recognized as powerful tool for investigating the Earth's subsurface structure.

In general, passive remote sensing of the Earth's surface and subsurface done by using electromagnetic radiation in the visible (0.4–0.7 μm), near infrared (0.7–1.2 μm), short infrared (1.2–2.5 μm), and thermal infrared (3–14 μm) spectral regions. Whereas remote sensing in the diapason of 0.4–2.5 μm is based on reflected radiation from the Sun, the remote sensing in the diapason of 3–14 μm is based on the Earth's emitted radiation. Both reflected and emitted radiations contain important information about different subsurface targets (environmental, hydrogeological, archeological, military, etc.) because photon-matter interactions take place at specific wave lengths. The processing and interpretation of infrared measurements demand a separate detailed analysis. Readers can obtain useful information about applications of this method in Jacobs (2006) and Kaplan (2007).

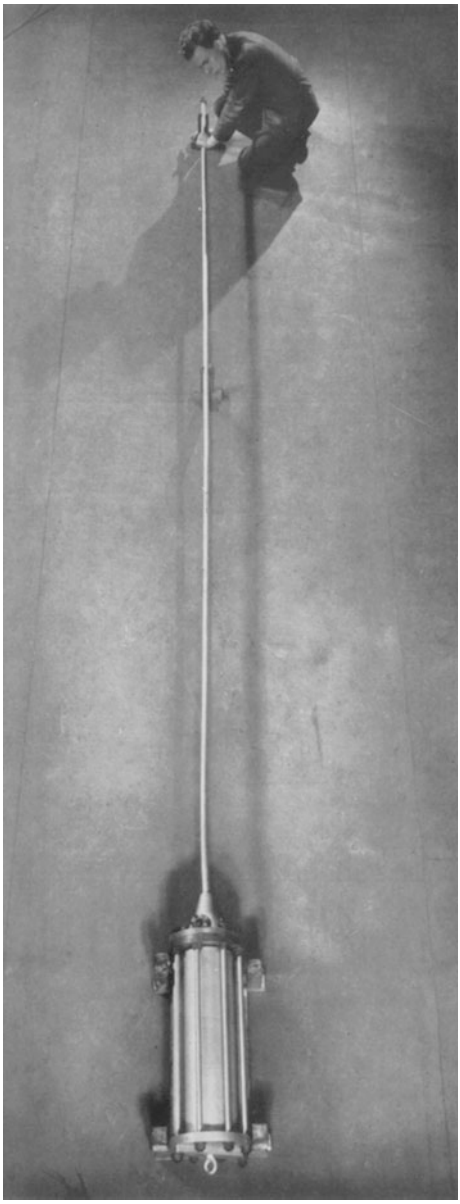

Fig. 3.4 Bullard's penetrator. The eye used for extracting the probe is visible on top of the cylinder housing the temperature recording equipment (after Bullard 1954)

3.6 Near-Surface Thermal Measurements

Near-surface (subsurface) thermal prospecting is based on temperature measurements in shallow (up to several meters deep) drill holes. These temperature measurements provide useful information about features of the areas under

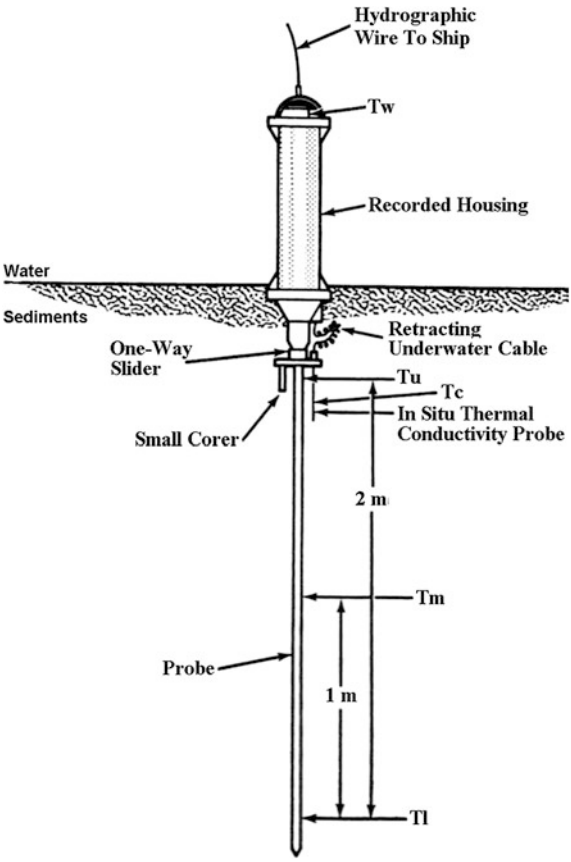

Fig. 3.5 The temperature gradient probe penetrating the sediments (after Sclater et al. 1969)

investigation since geological objects differ in terms of their thermal properties. One of the main advantages of near-surface thermal measurements is that they do not depend on the location of drilled deep wells and may be carried out in any suitable area. However, since the "neutral layer" usually occurs deeper than the observation points, at depths of 20–40 m, these measurements usually contain a significant noise component caused by seasonal temperature variations (Khesin and Eppelbaum 1994). This requires the use of specific methodology for the near-surface thermal measurements. The methodology of near-surface thermal measurements is described in detail in Chap. 10.

Near-surface thermal monitoring of areas of geological repositories (e.g., waste from the nuclear, chemical and hydrocarbon industries) can be carried out by thermal sensors located at different depths with automatic transfer of the observed data to a control organization.

3.7 Measurements in Mines and Tunnels

Measurements in mines and tunnels are based on measurements in blast-holes drilled in walls and the subsurface of underground openings (UO), as well as on observations made without blast-holes along the UO. UO can be ventilated or unventilated objects (which are preferred). In the case of ventilation, the artificial noise effects may reach several degrees that can result in very significant errors in thermal data analysis.

There are two principal differences between near-surface measurements and measurements in UO. On the positive side, in ventilated UO (especially in deep mines and in intervals located comparatively far from the entrance to mines) the amplitudes of the seasonal variations are incommensurably less than for near-surface thermal measurements. The negative side is that anomalous bodies may occur not only below the observation points (as in conventional near-surface thermal measurements), but above and surrounding them from the left and right which complicates the analysis of survey results.

As was shown in Ginzburg et al. (1981), temperature measurements can be successfully performed in small water reservoirs (for instance, glasses) located along the UO at interval of 2–5 m (after 2–3 days in a non-working mine water takes on the temperature of the surrounding medium and can be utilized for observations).

Thermal measurements in tunnels are usually for environmental or technical purposes (see Sect. 10.10.1).

References

Beardsmore GR, Gull JP (2001) Crustal heat flow: a guide to measurement and modelling. Cambridge University Press, Cambridge

Bullard EC (1954) The flow of heat through the floor of the Atlantic Ocean. Proc Royal Soc 222:408–429 London, A

Cappa F, Guglielmi Y, Gaffet S, Lancon H, Lamarque I (2006) Use of in situ fiber optic sensors to characterize highly heterogeneous elastic displacement fields in fractured rocks. Int J Rock Mech Min Sci 43:647–654

Clarke TF, Malcolm FJ, Korgen BJ (1972) An improved Ewing heat probe frame. Mar Geophys Res 1:451–455

Eppelbaum LV, Khesin BE (2012) Geophysical studies in the Caucasus. Springer, Berlin

Ginzburg S et al (1981) Underground geophysical investigations in ore deposits of Belokan-Zakatala ore field. Unpublished Report of TzNIGRI (Central Scient. Inst. of Non-Ferrous and Precious Metals), Moscow (in Russian)

Hurtig E, Čermák V, Hänel R, Zui VI et al (eds) (1992a) Geothermal Atlas of Europe. Hermann Haack Verlagsgesellschaft mbH, Geographisch-Kartographische Anstalt, Gotha. Set of 36 maps and Explanatory Note

Hurtig E, Schrötter J, Groβwig S, Kühn K, Harjes B, Wieferig W et al (1992b) Temperaturmessungen in Bohrlöchem mit Hilfe optischer Fasern. In: Forum für Zukunftsenergien e.V., Geothermische Vereinigung e.V., Geothermische Fachtagung 1992, Tagungsband, Bonn, pp 311–324

Hurtig E, Groβwig S, Kühn K (1996) Fibre optic temperature sensing: application for subsurface and ground temperature measurements. Tectonophysics 257:101–109

Jacobs PA (2006) Thermal infrared characterization of ground targets and backgrounds. SPIE Press, Washington

Jones EJW (1999) Marine geophysics. Willey, Toronto

Kaplan H (2007) Practical applications of infrared thermal sensing and imaging equipment, 3rd edn. SPIE Press, Washington

Khesin BE, Eppelbaum LV (1994) Near-surface thermal prospecting: Review of processing and interpretation. Geophysics 59(5):744–752

Lubimova EA, Alexandrov AL, Duchkov AD (1973) Methodology of studying thermal flows through the Ocean bottom. Nedra, Moscow

Sass JH, Lachenbruch AH, Munroe RJ, Greene GW, Moses TH Jr (1971) Heat flow in the western United States. J Geophys Res 76:6376–6413

Sclater JG, Corry CE, Vacquier V (1969) In situ measurement of the thermal conductivity of ocean-floor sediments. J Geophys Res 74(4):1070–1081

Chapter 4
Temperature Anomalies Associated with Some Natural Phenomena

Thermal waters (hot springs, geysers) and volcanoes were among the first manifestations of the Earth's internal heat that people encountered in ancient times. This helps explain the long history of scientific analysis of such events as volcano and geyser eruptions, hot spring regions, etc. The first tales of the Great Geysir (Iceland) date back to the year 1294 (Iceland on the Web 2013). One of the oldest publications on problems related to geysers is by Bunsen and Descloizeaux (1846) on the geysers of Iceland.

Depending on the amount of heat and energy released by an event, it may be source of heat (spa, a bathtub full of warm to hot water) or a natural hazard (volcanic eruption, volcanic gases, geyser eruption). Hot springs and geysers are typical features in volcanic regions or areas of other magmatic activity (continuing cooling of young intrusives), which are also seismically active. Some of the most thermally active regions in the world are Yellowstone National Park in the USA, one of the greatest volcanic zones on Earth, and areas with very strong volcanic and seismic activity in the Kamchatka Peninsula in Russia, Iceland which is located on the Mid-Atlantic Ridge, Japan, and New Zealand.

Let us take a look at some recent and ongoing events taking place around the world. In the region known as the Valley of Geysers in Kamchatka, two to three volcanoes erupt frequently and one to two earthquakes measuring at least 6.0 or more can be expected to take place regularly (Kiryukhin 2009). A disastrous volcano eruption in Iceland in 2010 forced the closure of the air spaces in Western Europe for some time, and catastrophic earthquakes took place in Japan and New Zealand in the beginning of 2011, and Chile in 2010. Such events can change the tectonic and geostructural composition of a region, as well as alter the regime of hot springs and geysers. For example, a massive landslide on June 3, 2007 in the Vodopadniy spring basin in the Valley of Geysers, Kamchatka resulted in significant changes in the behavior of some geysers in the region (Kiryukhin 2009). The Geysir geyser in Iceland was dormant for about two decades, whereas its neighboring geyser, Strokkur, which is less than 50 m away erupts about every 10 min, but a strong earthquake of 6.5 on the Richter scale on June 17, 2000 awoke Geysir once again (Iceland on the Web 2013). In another case, one of the most famous geysers on Earth, the Steamboat Geyser in Yellowstone National

L. Eppelbaum et al., *Applied Geothermics*, Lecture Notes in Earth System Sciences, 161
DOI: 10.1007/978-3-642-34023-9_4, © Springer-Verlag Berlin Heidelberg 2014

Park's Norris Geyser Basin, which is the world's highest currently active geyser with major eruptions of water reaching a height of up to 90 m, was dormant for a period of 60 years (Scott 1995).

One of the most graphic examples of the effect of some tectonic features on the regime of hot springs and geysers is the story of the formation and destruction of the Waimangu geyser in New Zealand (Jones 2006). The Waimangu geyser was created by a large volcanic eruption in 1888 and began erupting in 1900 with up to 490 m high jets of water; it erupted for 4 years before being destroyed by a landslide (Jones 2006). A rapid expansion of the geothermal field took place after the 2000 eruption of the Usu volcano in northeast Japan (Saba et al. 2007). Lardarello, the largest dry-steam field in Italy, which was active for over 100 years has only negligible subsidence; by contrast, in New Zealand both the Wairakei and Ohaaki fields have experienced significant subsidence over a relatively short period of time (DiPippo 2007). There are numerous similar cases all over the world. This means that data on volcanoes, geysers, and hot springs can change at any time and some published data may become outdated very quickly. For instance, the parameters of a number of geysers in Yellowstone National Park published in Allen and Day (1935) are quite different from those published in Jones (2006) and some other publications. The same can be said of data published in Barth (1950) on the hot springs and geysers of Iceland. Similarly, the first production well HV-1 drilled in 1974 in Husavik had hot water temperatures of 399 K in free flow (Georgsson et al. 2005), but later the temperature of the water dropped to 397 K (Hjartarson et al. 2003). In the Hatchobaru geothermal field of Japan, well H-4 was capable of generating 18 MW in 1973, but at the time it was connected to the Hatchobaru power plant in 1977 it was generating $\sim$13 MW. During the first three years of plant operations (between 1977 and 1980) the output declined dramatically to 1 MW; over the same time period, temperatures at the feed zone fell by about 50 K (DiPippo 2007). For these reason, we have attempted to use and reference the most recent information available on the Internet for key thermally active regions.

4.1 Thermal Waters, Hot Springs, Geysers and Fumaroles

The behavior of thermal waters, like any other ground waters, is described by hydrogeology and hydrology. For this reason, we will first take a look at some definitions and primary characteristics used in hydrogeology in Sect. 4.1.1. Thermal waters is a very broad term for all kinds of waters with high and elevated temperatures, which are usually divided into more specific kinds of waters such as hot springs, geysers and fumaroles in land areas, and different kinds of vents (including black and white smokers) in oceanic areas. The main difference between them is the temperature and state of the water, and its behavior upon discharge. Geysers differ from hot springs by the presence of a significant amount of steam along with water, and the way the water discharges. Fumaroles differ

from hot springs and geysers in that they have a vent that emits a mixture of steam and other volcanic gases. The difference between various vents is both in temperature and the fact that in some cases (mostly for black smokers) water may be in critical [have either temperature or pressure above their critical conditions; $T > 647$ K and $P > 21.8$ MPa (Hall 1995; Pilchin and Eppelbaum 2009; Pilchin 2011)], supercritical (both temperature and pressure above their critical conditions) or subcritical (the water temperature is above its boiling point but below the critical temperature) conditions. Thermal waters are extremely important features in geothermics, since they constitute one of the main causes of the distribution and redistribution of heat flow within the crust (mostly the upper crust) and one of the main mechanisms involved in the cooling of the upper part of the crust and the lithosphere as a whole.

4.1.1 Key Definitions of Hydrogeology and Related Characteristics

Any process involving water is a part of the water cycle, also known as the hydrologic cycle or H_2O cycle (Berner and Berner 1987), and plays an important role in the process of cooling of the Earth's lithosphere and Earth itself. From this point of view, processes involving ground waters (water infiltration and its underground flow; see Fig. 4.1) are related to the collection of heat energy by ground water and the delivery of this energy to the surface and surface water reservoirs. Infiltrating water (meteoric water; usually low-temperature rainwater or water from melting snow; etc.) in a recharge zone enters an aquifer and flows through it to the discharge zone (an artesian aquifer), where it exits the aquifer to the surface or surface water reservoir. However, while it is moving through the aquifer it is heated to higher temperatures than it initially had, and at the same time it reduces the temperature of the sedimentary layer by absorbing some of the heat from the layers confining the aquifer. In some cases infiltrating water moves through aquifers in regions of ongoing magmatic activity or past young magmatic activity. Under such circumstances, these ground waters may be heated to very high temperatures and can deliver significant amounts of heat to the surface or water reservoirs (i.e. ocean by vents) which assists in cooling the rock layers in contact with magma more quickly. In the case of magmatic activity in a region, significant amounts of magmatic waters (or juvenile waters), existing within and in equilibrium with the magma or water-rich volatile fluids related to the magma are released into the atmosphere during either a volcanic eruption or hydrothermal fluid release during the late stages of magmatic crystallization within the Earth's crust. It is clear that in all these cases some amount of heat energy is absorbed from rocks of different layers of the crust and delivered to the surface. Depending on the conditions governing each individual case, the location of the discharge of groundwater or thermal water is characterized by thermal anomalies of different

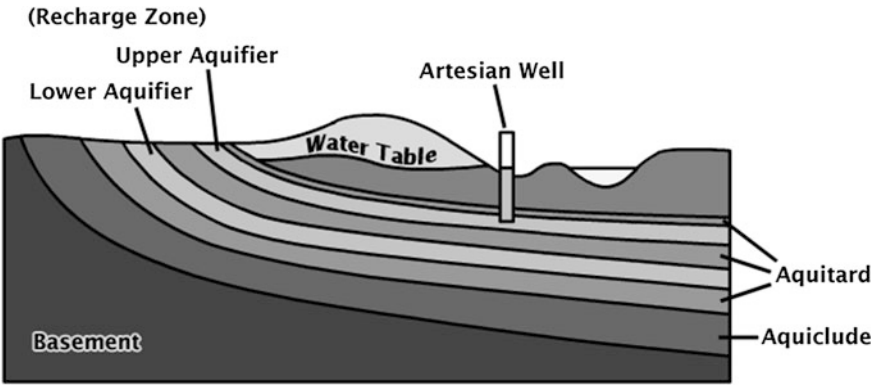

Fig. 4.1 Schematic structure of underground water systems

magnitudes, because heat transfer by circulating water is much more intensive than heat transferred by conduction. This thus leads to the cooling of crustal layers and the lithosphere.

It should be taken into account that ground waters mostly cool upper layers of the crust, which generate an increased gradient between the upper crustal layers and the lower crustal/lithosphere layers, hence increasing heat flow by heat conduction, which leads to quicker cooling of the lithosphere. In this section, we only discuss processes related to groundwater and thermal water activity.

Any manifestation of thermal waters (springs, geysers, fumaroles, etc.) on land or the sea bottom (vents, black and white smokers, etc.) is a hydrogeological process that follows the laws of hydrogeology and hydrology. Hydrogeology is the area of geology that deals with the distribution and movement of groundwater within the Earth's crust (mostly its sedimentary layer). Groundwater is water that fills pores and fractures in the ground. Let us first take a look at some key definitions in hydrogeology (e.g., Harter 2008).

An aquifer is an underground layer of water-bearing permeable rock or unconsolidated materials (e.g., sand and gravel or fractured rock) that transmits groundwater (i.e., lets water flow through it). An aquitard is a rock layer with very low permeability (silt, clay, etc.) within the Earth that restricts the flow of groundwater from one aquifer to another (a water barrier). An impermeable aquitard is usually called an aquiclude. Aquitards and/or aquicludes confine an aquifer (from its top and bottom) in a groundwater/hydrologic system. The bottommost aquiclude is known as the bedrock. If the impermeable or low-permeable layer overlies an aquifer, it is called a confined aquifer. If an aquifer is not capped by either an aquitard or an aquiclude (generally the topmost aquifer), it is known as an unconfined aquifer. Such an aquifer is in direct contact with the surface through porous space and, depending on the conditions, it may be unsaturated with water. The level to which water rises within an unconfined aquifer is the water table (the top of ground water). The water table is normally used to characterize the water

level on land, because in sea and ocean areas it is represented by the sea level. In most regions in California for instance, the water table is between 3 and 30 m below the land surface, though it is as deep as 90 m in some southern California desert basins (Harter 2008).

An unconfined aquifer usually has porous pressure below the hydrostatic pressure, which creates abnormally low stratum pressure and abnormally low porous pressure (ALSP/ALPP) in it. The entire layer above the first aquitard or aquiclude is characterized by low hydrostatic pressure, which can explain the presence of a low velocity zone near the surface known in continental areas from seismology. Only below the first aquitard or aquiclude can the pressure in the second aquifer be higher than or equal to the hydrostatic pressure (AHSP/AHPP), which may also indicate the beginning of an abnormally high stratum pressure or abnormally high porous pressure (AHSP/AHPP) zone. According to laws of physics, groundwater moves from higher elevations to lower elevations and from locations of higher pressures to those of lower ones.

The flow rate, Q, of underground water can be determined from the empirical relationship (Darcy's Law) that explains fluid flow in porous media (Hubbert 1969; Freeze and Cherry 1979):

$$Q = -KA\frac{h_2 - h_1}{L}, \tag{4.1.1}$$

where K is the permeability coefficient (describing the porosity of the underground formation), A is the cross-sectional area, h_1 is the initial height of the hydraulic head, h_2 is the final height of the hydraulic head, and L is the path length of the flow.

To characterize permeability, sometimes a parameter such as hydraulic conductivity (k) is used, which is related to permeability through the relationship below (Domenico and Schwartz 1998):

$$\kappa = K\sigma\frac{g}{\mu}, \tag{4.1.2}$$

where K is the permeability (in m^2), k is the hydraulic conductivity (in m/s), μ is the dynamic viscosity [in kg/(m · s)], σ is the density of the fluid (in kg/m^3) and g is the gravity acceleration (in m/s^2).

The key properties characterizing all of the different kinds of layers mentioned above are porosity and permeability (or hydraulic conductivity). To be an effective aquifer, a layer must be composed of rocks with high porosity and high permeability, but to be an effective aquitard or aquiclude, the layer must be composed of rocks with very low permeability or be impermeable. Relationships between porosity and permeability can be complicated, since such low permeable rocks like silt and clay have high porosity.

Bear (1972) classified rocks by their permeability into pervious ($K = 10^5$–10^8 mD), semi-pervious ($K = 1-10^4$ mD) and impervious ($K = 10^{-4}$–10^{-1} mD).

For example, the permeability of rocks in an oil reservoir (collectors) is in the range of 0.01–10.00 mD (Bear 1972; Middleton 2003). Neuman and Neretniecks (1990) also showed that rocks with very low permeability, such as shale, may have permeability as low as 10^{-9} Darcy.

4.1.2 Thermal Waters

Thermal water, another kind of groundwater, is usually related to the circulation of groundwater (*hydrothermal circulation*) in the vicinity of sources of heat within the Earth's crust. This generally occurs in zones of magmatic (volcanic, intrusive, etc.) activity, as well as in areas of solidification or continuous cooling of products of previous magmatic activity. Hydrothermal circulation on land usually presents itself in the form of hot springs, geysers and fumaroles, and in oceanic areas it is usually represented by vents, including black smokers and white smokers. The heat source for active vents in oceanic areas is newly formed basalt, and even the underlying magma chamber for vents with the highest temperatures. It can be seen from Table 1.31 and (Pilchin and Eppelbaum 2012) that the cooling of magma can take millions of years, and a significant amount of magma at depths close to the surface can provide heat to groundwater for a very long time. Hydrothermal circulating convection cells exist in every location where there are anomalous sources of heat, as though an intruding magma, volcanic channel or vent composed of volatiles of magmatic activity had come into contact with the groundwater system. Since the magma heats the surrounding rock wall, it is not necessary for the groundwater to come into direct contact with the magma. Rather it is sufficient to be in contact with rocks heated by it to absorb huge levels of heat and begin hydrothermal circulation. The heated water will have a lower density, causing it to flow toward the surface (through pores and cracks). These are not singular events, but an ongoing process that results in convection currents near the magma chamber, where instead of heated water simply being raised to the surface, new amounts of cool water perpetually come into contact with the hot rock, are heated, and start to rise towards the surface in a cycle. The water in a magma-driven hydrothermal system comes from one of two sources: the surface (meteoric water) or the magma (juvenile water) itself. Near the magmatic body or magma chamber, water may be under supercritical conditions (with $T > 647$ K and $P > 21.8$ MP; Hall 1995); however, magmatic water would most certainly be in a supercritical condition prior to its cooling during its rise to the surface and/or mixing with cold meteoric water. If a shallow active heat source is present, geysers and fumaroles can be formed.

A *geyser* is a hot spring containing significant amounts of steam and that erupts periodically (it needs recharging). Rinehart (1980) defined a geyser as a hot spring that periodically becomes hydrodynamically and thermodynamically unstable. There are two main kinds of geysers: cone geysers, which erupt from a mound of geyserites; and fountain geysers, which erupt from a pool. Geysers get their name

from the famous Icelandic geyser Geysir. A hot spring which does not need time for recharging and constantly ejects hot water into the air is not a geyser, but is known as a perpetual spouter.

Fumaroles (a fumarole rich in sulfur gases is also called a solfatara) are vents that expel gas (mostly pressurized steam, but they also expel other associated gases: SO_2, CO_2, HCl, H_2S, and etc.) through holes or fractures in a volcanic area. Depending on the conditions, the water may be subcritical; i.e., at a temperature above the boiling point and below the critical point of water. Fumaroles are the hottest of all hydrothermal features, since the major source of the steam emitted by them is groundwater heated by magma. Fumaroles form in areas with a shortage of water, because much of it easily converts to steam, or when overheated fluids find a way of escape from extremely hot layers adjacent to magmatic rocks.

In cases where mud and clay are present in a thermal area, the rising hot water can be mixed with these materials, and force its way upwards together with steam; this can cause fountains of mud to shoot into the air (i.e. a mud geyser). The water mixed with mud and clay can also form a mud pot (or mud pool). Mud pots are usually formed when the amount of hot water is limited and the pH is essentially acidic. When the amount of the mixture of mud, clay and water is significant, and ejects from the crater, the formation is called a mud volcano. The material ejected by a mud volcano is not necessarily hot.

4.1.3 Hot Springs, Geysers, Fumaroles

A hot spring is a natural discharge of groundwater with an elevated or high temperature. Most hot springs result from groundwater that has passed through or near recently formed igneous rocks. There are a number of definitions of hot springs: from groundwater with merely elevated temperatures, to water with a temperature of about 6.5 °C or more above the mean air temperature (Leet et al. 1982), to water above the core human body temperature (Pentecost et al. 2003). Hot springs represent the most usual kind and the most visible manifestation of hot water geothermal systems that transfer heat to the surface (White 1973). The temperature of a hot spring will not exceed that of the boiling point of water at the altitude of the spring (Wohletz and Heiken 1992). Hot springs range in size from small ones that produce barely enough hot water for a few individuals to bathe in, to giant thermal areas such as Yellowstone National Park, the North Island of New Zealand, Kamchatka, Iceland, etc., where hot water and steam can be used for heating buildings, greenhouses, and generating electricity (Wohletz and Heiken 1992). White and Williams (1975) divided the reservoir temperatures for hot-water systems into low temperature (<363 K), intermediate temperature (from 363 to 423 K), and high temperature (from 423 to 513 K). In the region of the Soufrière volcano, the hot springs are located around the base of the most recent dacite dome, which was recently modified by phreatic eruptions (Heiken et al. 1980). At Bouillante, the temperature of the spring is 371 K; the geothermal reservoir

located within Tertiary tuffs and andesitic lava flows, has temperatures in excess of 513 K at a depth of 500 m (Demians et al. 1972; Vatin-Perignon et al. 1984).

4.1.3.1 Yellowstone National Park, USA

Spanning the territories of Wyoming, Montana, and Idaho, Yellowstone National Park (about 9,000 km^2) is one of the true wonders of the world. It is located on the Yellowstone Plateau which is about 2,400 m above sea level. The plateau lies at the center of one of the Earth's largest volcanic fields. It is even called the *Yellowstone Supervolcano* (Watts 2007).

The *Yellowstone caldera*, nearly 80 km long and 50 km wide (Brantley 1994) is the youngest of three nested and overlapping calderas, and is filled with younger rhyolitic lavas (Keefer 1972; Christiansen 1992; Brantley 1994). The calderas were formed during three episodes of magmatic eruptions of catastrophic proportions culminating about 2 million years ago ($\sim$2,500 km^3 Huckleberry Ridge Tuff), 1.3 million years ago ($\sim$280 km^3 Mesa Falls Tuff), and 0.6 million years ago ($\sim$1,000 km^3 Lava Creek Tuff) (Christiansen 1992; Brantley 1994). Renewed magmatic activity in three major episodes approximately 150, 110, and 70 million years ago produced voluminous lavas in the Yellowstone caldera with an aggregate volume of about 1,000 km^3 (Christiansen 1992). Results of geophysical research have provided numerous indications that magma still underlies the Yellowstone caldera at a shallow depth. The Yellowstone caldera region hosts the world's largest known hydrothermal system with numerous manifestations of hydrothermal activity such as geysers, hot springs, fumaroles, etc. A schematic structure of a geyser is presented in Fig. 4.2.

The formation of hydrothermal features around the Yellowstone Lake area is related to convective meteoric hydrothermal fluid circulation above a cooling magma chamber. Hydrothermal explosions result from the accumulation and release of giant amounts of steam. For example, the estimated temperature prior to the explosion of the Mary Bay hydrothermal system was about 567 K (Morgan et al. 2009).

The Yellowstone National Park geothermal system contains such hydrothermal complexes as Mammoth Hot Springs, Clearwater Springs, Sheepeater Canyon Hot Spring, Hot River, and some others. The total fluid discharge from all thermal features of Yellowstone National Park averages an astounding $\sim$3,091 L/s (Breckenridge et al. 1978). The greatest hot water and gas discharges recorded are from the Mammoth Hot Springs system, which is composed of more than 100 springs with an estimated fluid flux of about 57 L/s. At the same time, the main outlet for the Mammoth system is the Hot River Spring, with a flow of nearly 631 L/s (Breckenridge et al. 1978). The Grand Prismatic Spring, America's largest hot spring, produces 33.3 L/s of water with a temperature of 344 K (http://www.mostinterestingfacts.com/nature/top-7-greatest-sources-hot-springs-in-the-world.html). The Green Dragon Spring is located in the One Hundred Springs Plain of the Norris Geyser Basin, and is a near boiling acid-sulfate-chloride spring with a

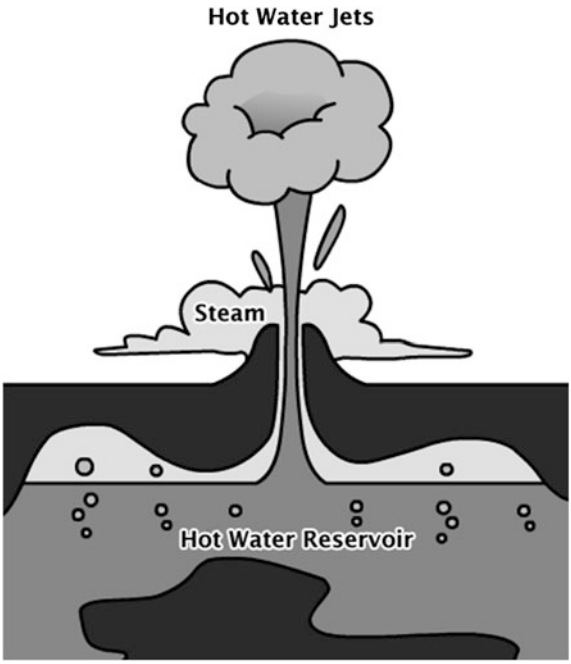

Fig. 4.2 Schematic structure of a geyser

pH of about 3 and water temperature ranging from 339 to 346 K (Boyd et al. 2007; D'Imperio et al. 2007).

Since thermodynamic and tectonic conditions in volcanically active regions are constantly changing, it is reasonable to expect changes in the regimes and behaviors of some geysers and hot springs. For example, the Steamboat Geyser in Yellowstone National Park's Norris Geyser Basin is the world's tallest active geyser with major eruptions shooting water more than 90 m into the air (Scott 1995; Jones 2006). However between 1911 and 1961, this geyser was dormant and minor eruptions of 3–5 m are now much more frequent (Scott 1995). Excelsior, another powerful geyser in Yellowstone's Midway Geyser Basin had eruptions reaching 91 m, but ceased erupting in 1985 and now behaves mostly like a hot spring. The Norris Geyser Basin straddles the intersection of three major faults, one of which (the Hebgen Lake fault) experienced an earthquake of about 7.4 on the Richter scale in 1959, leading to significant changes in the regime of some geysers in the area.

As was mentioned above, a geyser is a hot spring with a mixture of steam and water, which means that the temperature of its water is at about the boiling point of water for the thermodynamic conditions of the region. The boiling point of water at the discharge area is mostly dependent on the atmospheric pressure (elevation of an area above sea level), and it is about 366 K for Yellowstone National Park (Smith and Siegel 2000).

Yellowstone National Park has the largest number of geysers in the world (over 400, about half of all the geysers in the world), which are spread out over a number of geyser basins. The Norris Geyser Basin is the hottest of Yellowstone's thermal areas, in which the highest temperature on record (510 K) from all the geothermal areas of Yellowstone Park was measured at a depth of only 326 m, and there are very few thermal features in the Norris Geyser Basin that have a temperature below the boiling point.

The most spectacular mud pots in the Park are located in the Mud Volcano area on the west side of the Yellowstone River. In this area, such features as the Dragon's Mouth, the Black Dragon's Caldron, the Mud Geyser and the Mud Volcano are located. The water temperature in mud pots is only about 341 K, but the discharge of huge amounts of gas makes it appear to be boiling.

4.1.3.2 Kamchatka Peninsula, Russia

The Kamchatka Peninsula (Russia) is located in the Pacific Ring of Fire and is one of the most volcanically active regions on Earth. There are about 300 volcanoes on the peninsula, of which about 30 are still active (Vlodavetz and Piip 1959; Gushchenko 1979; Masurenkov 1980; Fedotov and Masurenkov 1991; Braitseva et al. 1995). Pirajno (2010) stated that the Kamchatka-Kuril Arc (~2,000 km) contains more than 100 active volcanoes in total. The best known volcanoes include Shiveluch, Krestovsky, Klyuchevskaya Sopka (Kluchevskoy, the highest active volcano in Eurasia at 4,750 m), Koryaksky, Kronotsky, Kamen, Karymsky, Bezymianny, Tolbachik, Avachinsky, and Mutnovskiy. A few calderas were also formed on Kamchatka Peninsula, the most famous of which are the Uzon, Akademia Nauk, Ksudach, Kurile Lake and Karymshina calderas (Belousov et al. 1984; Fedotov and Masurenkov 1991; Leonov et al. 1991; Braitseva et al. 1995; Izbekov et al. 2004; Ponomareva et al. 2004; Leonov and Rogozin 2010). The world famous Valley of Geysers is located within the Uzon caldera. Additionally, numerous hot springs and geysers are currently active along the fault in the vicinity of the Karymsky volcano and Akademia Nauk.

An estimated tephra volume of 140–170 km^3 makes the formation of the caldera the largest Holocene eruption in the Kuril–Kamchatka volcanic arc and one of Earth's largest Holocene explosive eruptions (Ponomareva et al. 2004). The Karymshina Caldera, discovered only in 2006 (Leonov and Rogozin 2010), was formed in about 1.2–1.5 Ma with some magmatic features (numerous emplacements of acid lavas forming domes, dikes, short lava flows) from <0.5 to 0.8 Ma, contains famous groups of thermal springs such as Bolshie-Bannie, Malie Bannie, Karymchina, Karymshina, and Verkhne-Paratunka. Since the Kamchatka Peninsula has numerous active volcanoes spread throughout, it is clear that the magma is located very near to the surface almost everywhere across the peninsula. This creates ideal conditions for the formation of hot springs, geysers and fumaroles.

The Mutnovsky Volcano, one of the largest and most active volcanoes of South Kamchatka, was in the fumarole stage throughout its long inactive period between

1961 and 2000, with its hydrothermal activity characterized by an extremely high energy output of about 1,800–1,900 MW (Bortnikova et al. 2008; Eichelberger et al. 2009).

Kamchatka was recognized for having great geothermal potential, and Paratunka, the world's first geothermal binary plant, was also built near Petropavlovsk Kamchatskiy (DiPippo 2007). The Upper-Mutnovsky power plant with a 12 MW capacity is located in the Mutnovsky Volcano area whose thermal-power peculiarities are presented in Table 4.1.

In some regions of the Kamchatka Peninsula the thermal waters are used for heating. For example, to heat the city of Vilyuchinsk, water is collected from wells characterized by a total flow rate of 371.1 L/s and an average temperature of 356.8 K (Nikolsky et al. 2010). A number of Kamchatka's hot springs are used for tourism as well as medicinal purposes.

The Valley of Geysers is located in the foothills of the Kikhpinych volcano in the Kronotsky Nature Reserve of Kamchatka Peninsula (Sugrobov et al. 2009; Slovtsov 2011) and contains about 20 major geysers (DiPippo 2007; Sugrobov et al. 2009) and a great number (about 200) of smaller ones. The Valley of Geysers probably has the highest density of geysers per area, since almost all its geysers are located within an area of about 5 km along the Geysernaya River. More than 60 geysers, including 19 of the 20 largest ones, and over 30 large boiling springs are found along the Geysernaya River within 2 km of the confluence point of the Geysernaya and Shumnaya Rivers. The largest pulsating springs and mud pots are also located there. The most powerful geysers in the Valley of Geysers are the Velican (Giant) and Grot Yubileinyi (Jubilee Grotto) which are known to spout water jets to a height of over 30 m (Jones 2006; Sugrobov et al. 2009). The temperature at a depth of 1 m in the Valley of Geysers is about 343 K. The water temperatures and pH of some of these geysers are presented in Table 4.2.

One of the most enigmatic features of the Geysernaya River area is the location at its upstream known as Death Valley (Sugrobov et al. 2009). It is found in the mouth of the Zheltiy (Yellow) Spring, which gets its name from presence of native sulfur creating a yellow streambed. Even though there are a number of streams with temperatures of about 327, 348 K, and steam-gas jets with temperatures of 366 K and higher in the vicinity of mount Zheltaya and the Kikhpinych volcano, the temperature of the water feeding into Zheltiy Spring is no higher than 292–293 K on gas discharge and for heated ground (Sugrobov et al. 2009). Moreover, the pH of the water is <2. This is very different from the conditions in such a highly active thermal area as the nearby Valley of Geysers and the kinds of water found there.

Death Valley is about 2 km in length and 10–500 m wide, with the deadliest area about 100×300 m. Research shows that during periods of no winds in Death Valley, gas containing mostly CO_2 and H_2S collects and creates a situation where there is almost no oxygen to a height of about 1 m and even higher (Sugrobov et al. 2009). Continuous monitoring of the area revealed that this is a seasonal feature and the period when animals die in most cases coincides with the period of snow melt, which lasts there from May until the middle of July. Strangely enough,

Table 4.1 Some geothermal features in the Mutnovsky Volcano area (after Vakin et al. 1986; Vereina, 2007)

Site, feature	Temperature on surface (in K)	Power (in mW)
Active vent	>973	700
Northeast crater	578	400
North Mutnovsky springs (east group)	371	19
North Mutnovsky springs (west group)	383	9
Dacha springs	371	73
Pereval springs	369	9
Upper Zhirovskie springs	369	18
Voinovskie springs	366	8
Vilucha springs	363	12

Table 4.2 Temperature of water on discharge and pH of some geysers in the Valley of Geysers, Kamchatka (after Slovtsov 2011)

Geyser	Temperature (in K)	pH
Pervenets	371–372.6	8.35
Troynoy	371	8.5
Sakharniy	371	8.74
Sosed	371	8.2
Konus	371	8.2
Maliy	371	8.74
Bol'shoy	371	8.74
Schel'	371	8.74
Velikan	371	8.74
Zhemchuzhniy	371	8.74
Fontan	371	8.74
Dvoynoy	371	8.74

most of these gases come from relatively cold springs and cold ground, though the Kikhpinych volcanic zones now in a state of fumarole-solfatara activity, with many highly thermal features (Slovtsov 2011).

Since the Kamchatka Peninsula has numerous areas that are very difficult to access, it is clear that numerous thermal features have yet to be discovered. In fact, the Valley of Geysers was only discovered in 1941, and Death Valley was only discovered in 1974 (Sugrobov et al. 2009), and the Karymshina Caldera just recently in 2006 (Leonov and Rogozin 2010).

4.1.3.3 Iceland

Iceland is located on the Mid Atlantic Ocean Ridge, and is entirely of volcanic origin. Iceland has about 130 volcanoes, 18 of which have erupted since the first settlement in 874 AD. Over the past 500 years, Iceland's volcanoes have erupted roughly a third of the total global lava output (Waugh 2002). As recently as 2010,

the eruption of the Eyjafjallajökull volcano was so powerful that the volcanic ash plume disrupted air travel in Northern and Western Europe for several weeks. Icelandic volcanoes have been the most powerful volcanoes in the world starting from at least the Holocene (Thordarson and Self 1993; Larsen et al. 2001; Thordarson and Larsen 2007; Larsen et al. 2008, etc.). For these reasons, Iceland obviously has many high temperature natural features (a great number of volcano eruptions, fumaroles, geysers, hot springs, etc.) and enormous resources of heat energy.

Outside the volcanic zones, the geothermal gradient in Iceland varies from about 50 K/km to about 150 K/km (Axelsson et al. 2010). Geothermal gradients as high as 400 K/km (Hofsstadir geothermal field) were recorded in volcanically active areas (Gaoxuan 2008). The first IDDP well drilled in the Krafla geothermal area in the first half of 2009 hit magma at a depth of about 2,100 m (Ármannsson 2010). The geothermal characteristics of some regions of Iceland sometimes look unusual for a region located so far North; for instance, the Krýsuvík geothermal field of the Reykjanes Peninsula (SW-Iceland) has temperatures measured in different hot grounds ranging from 333 to 368 K at depths of just 12–15 cm (Mawejje 2007). Some of the boiling springs of the field are so strong that they shoot water up to 0.3 m, and have a temperature of about 360 K at 20 cm that increases with depth to 383 K (Mawejje 2007). Temperatures measured in mud pots in the area were up to 368 K (Mawejje 2007). The Krýsuvík geothermal field is also characterized by a temperature reversal in most wells below 800 m (Arnórsson et al. 1975; Mawejje 2007), with maximum temperatures reported for depths 200–500 m. Analysis of hydrothermal alterations in the field reveals that they occurred at temperatures of <473 K at depth ∼140 m; 483–503 K at depths ≤380 m; >503 K at depths of ∼737 m, and ∼513–533 K at depths ≤1,220 m (Kamah 1996).

In the Reykjanes geothermal system of the Reykjanes Peninsula (SW-Iceland), the reservoir temperature below a depth of 1 km ranges from about 548 to 583 K, and some measurements indicate temperatures as high as 360 K for depths of 15 cm in the region (Fridriksson et al. 2010).

Hot springs are found throughout Iceland, but are rare in the eastern basalt area. There are about 250 low-temperature geothermal areas (regions with temperatures ≤423 K at depths ≤1,000 m), with a total of about 800 hot springs in Iceland. The average temperature of water in a hot spring is 348 K. Most of the high temperature areas of Iceland are located inside the volcanic zone; the heat in these areas is over 473 K within the top 1,000 m of the Earth's crust (Water and Fire 2011). Gudmundsson and Arnórsson (2002) reported that geothermal measurements at the Krafla and Námafjall high-temperature geothermal areas indicated maximum temperatures of 593 and 623 K, respectively, for wells in these areas. Giroud (2008) reported the maximum recorded temperature for wells of the Nesjavellir geothermal area to be >653 K, and 593 K for the Reykjanes area.

Today, about 85 % of Iceland's homes, as well as greenhouses, are heated by geothermal energy; the capital city of Reykjavik (Bay of Steam) pipes hot water to every house, and the Blue Lagoon, a lake south of Reykjavik is heated by a

Table 4.3 Some characteristics of geothermal systems from selected hot water production areas of Iceland (after Ragnarsson 2005; Axelsson 2008; Fridriksson et al. 2010; Pálsson et al. 2010)

Area/system	Number of production wells	Average production (in kg/s)	Reservoir temperature (in K)
Svartsengi (SW-Iceland)	10	380	513
Laugarnes (SW-Iceland)	10	160	400
Reykir (SW-Iceland)	34	850	343–370
Nesjavellir (SW-Iceland)	11	390	553–613
Hamar (N-Iceland)	2	30	337
Laugaland (N-Iceland)	3	40	368
Krafla (N-Iceland)	21	300	483–613
Urridavatn (E-Iceland)	3	25	348
Gata (S-Iceland)	2	17	373
Bjarnarflag (Namafjall field)	–	12.5	553
Reykjanes (SW-Iceland)	–	–	548–583
Theistareykir (NE-Iceland)	–	–	613–653
Húsavík (NE-Iceland)	–	–	393–403

geothermal power plant. Waters from hot springs and wells at Hveravellir geothermal field have a temperature in the range of 369–385 K and a pH of 9.32–9.44 (Georgsson et al. 2005). The first production well HV-1 was drilled there in 1974, hit water at a depth of 448–450 m, and produced 44 L/s of 399 K hot water in free flow for 25 years (Georgsson et al. 2005). Currently, 95 L/s of 397 K hot water is produced from wells at the Hveravellir geothermal field, while the hot springs discharge 35–40 L/s of 368–373 K of hot water (Georgsson et al. 2005).

Some characteristics of the geothermal systems in selected hot water production areas of Iceland are presented in Table 4.3.

Iceland also has a significant number of geysers (several dozen), but only the Geysir geyser is really powerful, with water jets of more than 30 m (its record height is about 60 m) (Barth 1950; Jones 2006). Most Icelandic geysers, including Geysir and the second most powerful geyser in Iceland Strokkur (producing water jets to the height of about 20 m), are located in the Haukadalur Geyser Basin. The Gamli Strokk geyser, with water jets of up to 45 m, is known to have been active in the 19th century, but is now extinct (Jones 2006).

4.1.3.4 New Zealand

Problems related to geothermal manifestations in New Zealand have been on minds of scientists for a long time (e.g., Houghton et al. 1989; Bain et al. 2006). Numerous volcanoes, hot springs, geysers, fumaroles, and other features are a constant reminder to scientists that New Zealand is one of the most active regions in the Pacific Ring of Fire.

All of the highly active geothermal fields in New Zealand, except Ngawha are located within the geologically young Taupo Volcanic Zone, which has shallow reservoirs/ aquifers (500–1,500 m depth) containing boiling or near-boiling water/ fluids (523–573 K) (Tamanyu and Wood 2003). Most of the hot springs, fumaroles and geysers of New Zealand are located in this area; and it is no coincidence that Whakarewarewa, New Zealand's most famous geothermal region, is located just south of the city of Rotorua and northeast of Wairakei, two of the most active geothermal fields in the Taupo Volcanic Zone. The most active geothermal fields of New Zealand, such as the Rotorua and the Wairakei, are known for changes in their thermal activity (Cody and Lumb 1992; Allis 2000; Cody 2007, etc.). The thermal characteristics of geothermal fields and the thermal and pH characteristics of waters in the Taupo Volcanic Zone are presented in Table 4.4 [compiled mainly using data from Cody (2007)].

There are a few dozen geysers in New Zealand, most of which are located in the Whakarewarewa Thermal Valley, Rotorua. Another of the most spectacular geysers in history, Geyser Minquini (up to 90 m), became extinct in 1961 along with dozens of other geysers and hot springs when the Orakei Korako Geyser Field was flooded after the building of a dam (Evening Times 1961; Jones 2006). Now there are only two powerful geysers remaining in New Zealand: the Pohutu geyser (up to 30 m) in the Whakarewarewa Thermal Valley, Rotorua; and the Lady Knox geyser (up to 20 m) in the Waiotapu area. Both of these areas are located within the Taupo Volcanic Zone. The Kereru and Prince of Wales' Feathers geysers are also found in the Whakarewarewa Thermal Valley. Additionally, there are a number of geysers such as Te Horu, Mahanga, Wairoa, Waikite, and Papakura which have been dormant for a several decades, but any earthquake or volcanic activity, typical events in the region, could trigger them back into activity.

Even the geological position of the highly active geothermal fields of New Zealand is not stable. For example, such geothermal fields as Wairakei and Ohaaki have experienced significant subsidence (Allis 2000; DiPippo 2007), which reflects permanent changes in tectonic structure and creates huge problems for drilling and exploiting wells.

4.1.3.5 Japan

The islands of Japan represent another segment of the Pacific Ring of Fire, and are also of volcanic origin. Japan is a very seismically and volcanically active region (e.g., a catastrophic earthquake of 9 on the Richter scale took place in March 2011). It also has the greatest number of hot springs on Earth (many thousands). For these reasons Japan has one of the highest potentials for geothermal energy in the world. Analysis of geothermal systems of the Kuju-Beppu Graben of Japan and a comparison with those of the Taupo Volcanic Zone of New Zealand showed (Tamanyu and Wood 2003) that (1) the main water reservoirs in the Kuju-Beppu Graben are at least 500 m deeper (at 1,000–2,000 m), and they have a water temperature of about 30–80 K lower (493 K) than those in the Taupo Volcanic

Table 4.4 Thermal characteristics of geothermal fields, thermal and pH characteristics of waters in the Taupo Volcanic Zone

Geothermal field	Maximum reservoir temperature (K)	Water temperature on discharge (K)	pH
Atiamuri	438–473	338–346	7
Broadlands (Ohaaki)	581	371	<3–8
Golden Springs	–	313–333	6.5–7
Crater Lake (Ruapehu)	–	308–371	<3
Horohoro	>433	352	8.5
Kawerau	>588	371	6.5–7
Mokai	597–599	371	<2–7.6
Orakeikorako	538	338–371	7–9.2
Orakeikorako	–	313–363	2–3.5
Mangakino (excl. Whakamaru or Ongaroto)	527	371	8.5
Moutohora	–	371.5	<4
Reporoa (excl. Golden Springs)	513	371	<3–8.7
Rotokawau (Rotokawa) (Rotorua)	428	320–323	6.5–6.7
Rotokawa (Taupo)	593	313–363	2.5–5.5
Rotorua	523	363–371	<2–9
Taheke	–	313–372	2–5
Tarawera	–	293–371.6	7–8.7
Tauhara (excl. Wairakei)	552	335–371	2–8
Te Kopia	514	318–378	<2–7.5
Tikitere (Hell's Gate, Ruahine Springs)	503	313–371	2–7.6
Tokaanu	523	371	3.5–8.7
Tongariro	523	343	<2.5
Waihi (see Tokaanu)	523	371	6.6–7.9
Waimangu (and Rotomahana)	543	328–371	<3–9
Waiotapu	568	371	1.8–8
Whakaari (White Island)	1,073	573–773 gas	
Ketetahi	–	327–411	2.0–6.5
Waikite Valley	–	371	8–8.7
Wairakei	544	371	<3
Whangairorohea	–	311	7.4
Okataina	–	312	7
Longview Road	–	306–365	3.7–6
Opaheke (Opateketeke)	–	318–371	3–8
De Bretts (Terraces)	–	323–353	7.8
Waiora Valley	–	371	3
Ngatamariki	563	–	–
Rotoma	493–523	–	–

Zone; (2) the active geothermal fields in the Kuju-Beppu Graben are restricted solely to areas on and behind the youngest volcanic front which is dated to <0.3 Ma, but is much younger in the Taupo Volcanic Zone, in which active geothermal fields are evenly spaced throughout the zone.

An exploration well WD-1A was drilled in the Kakkonda geothermal field to a depth of 3,729 m and hit a temperature of over 773 K (Saito et al. 1997; Kato et al. 1999). The Kakkonda Granite which intruded by 0.07–0.34 Ma is present at depths of about 1,140–2,840 m within the area. The well encountered two reservoirs (Kato et al. 1999): a shallow permeable reservoir with a temperature of 503–533 K and a deep, less permeable reservoir with a temperature of 623–633 K. In general, formation temperatures in this area (from exploration well WD-1A) reach 473 K at a depth of a few 100 m, 573 K at 1,500 m, and over 623 K at around 2,000 m (Saito et al. 1997).

Analysis of 3,686 hot springs in Japan showed that they belong to relatively low-temperature geothermal fields with a reservoir temperature >533 K (Muraoka et al. 2006). Fumarolic gases in the Owakudani geothermal area (in the vicinity of the Hakone Volcano) are composed mostly of H_2O (98.2 to 99.7 %) with temperatures of 368.4–370.8 K (the local boiling point is about 369 K) (Sawa et al. 2006), whereas steam with a temperature of 418.8 K at a depth of ~800 m is emitted from steam well No. 52. An examination of the steam from fumaroles and wells in the Takinoue geothermal area (Kiyosui and Yoshida 1988) shows that the fumarole steam discharge is formed from rising geothermal fluid through a single-step steam separation process at temperatures of about 423–513 K and that the temperature on discharge in 11 wells is 360–372 K. The geothermal characteristics of some geothermal fields in Japan are presented in Table 4.5.

One of the largest hot spring fields in Japan is the Beppu Geothermal area that contains numerous fumaroles, hot springs, mud pots, a geyser, etc. (Taguchi et al. 1996). The source of heat for all the high temperature manifestations in the area is related to the middle-to-late Pleistocene Yufu volcanic formations (<0.32 Ma) and lava domes younger than 100,000 years. The Beppu Geothermal Area has a total of 579 L/s of water estimated to be discharged from the hot springs, and its features include the Bozu jigoku (boiling gray viscous mud), the Umi Jigoku (Sea Hell), Chinoike Jigoku (Blood-Pond Hell) which is vermillion, the Tatsumaki Jigoku (Water-spout Hell) which is actually a geyser shooting water to a height of 20 m every 25 min, etc. (Taguchi et al. 1996). The temperature of the hot springs in Beppu ranges between 323 and 373 K, and so the spring water must be cooled to about 314–321 K to use for bathing. The estimated subsurface temperatures in a few locations of the area are over 473 K. The Chinoike Jigoku is a hydrothermal eruption crater, where nine recorded eruptions took place between 1875 and 1927 (Yoshida et al. 1978; Taguchi et al. 1996). The total output of hot water from the crater is 1.7 L/s with a maximum temperature of 409.8 K at a depth of 26 m. The chemical composition of the water in the hot springs in the Beppu Geothermal area also varies from near-neutral to very acidic. The thermal and pH characteristics of some hot springs in Japan are presented in Table 4.6.

The most powerful hot spring in Japan is the Obuki Spring in the Tamagawa springs area, which has a discharge of about 166 L/s of highly acidic water (pH just above 1) with an average temperature of 371 K (Yoshiike 2003). This spring has been active for over 300 years, and it feeds the highly acidic river Yukawa. The Obuki Spring is also known for significant fluctuations in sulfur content

Table. 4.5 Some geothermal characteristics of thermal water reservoirs and the pH of waters for selected geothermal fields in Japan

Geothermal field	Reservoir	Temperature in the production zone (in K)	pH	References
Sumikawa	–	573	7.6	Ariki et al. (2000)
Kakkonda	Upper	493–533	–	Muraoka et al. (1998)
Kakkonda	Lower	553–613	–	Muraoka et al. (1998)
Uenotai	–	573	9.5	Takeno (2000)
Okuaizu	–	523–573	6.6	Mizugaki (2000)
Hachijojima	–	573	6.2	Matsuyama et al. (2000)
Ogiri	–	505	8.7	Goko (2000)
Fushime	–	≥573	6.9	Okada et al. (2000)
Hijiori	Upper	523	Neutral	Koseki (2010)
Hijiori	Lower	543	Neutral	Koseki (2010)
Hatchobaru	–	523	–	Pritchett et al. (1985)
Kakkonda	Upper	503–533	–	Kato et al. (1999)
Takigami	–	433–523	–	Jalilinasrabady et al. (2010)

(Yoshiike 2003), that increased from ∼1 g/L in 1972 to ∼3 g/L in 1978, and gradually decreased back to ∼1 g/L by 1990.

Even though Japan probably has the highest number of hot springs in the world, there are very few geysers. Among these are such geysers as Shikabe Geyser (Hokkaido), Jigoku Geyser in Beppu and Suwa Geyser near Nagano. The reason for the absence of geysers in such a thermally active region is related to the greater depth in Japan of the main thermal sources (see also Tamanyu and Wood 2003) than in active geyser regions (for example in New Zealand), as well as the much lower temperatures at shallow depths than in such areas.

4.1.3.6 Chile and Other Regions

Chile represents another segment of the Pacific Ring of Fire, and is also famous for the presence of active volcanoes and catastrophic earthquakes in the recent past. Terrible earthquakes have taken place in Chile. In Valdivia on May 22, 1960 there was a 9.5 magnitude earthquake and one offshore of Bio-Bio on February 27, 2010 (with a magnitude of 8.8). The country has a great number of hot springs, geysers and fumaroles. It is among the five main locations on Earth in terms of the number of geysers. However, the most unique feature is the El Tatio Geyser Field, located at a height of about 4,200 m above sea level, which is home to most of the geysers of Chile. The boiling point of water in the Upper Geyser Basin of El Tatio Geyser Field is 359.45 K. The El Tatio Geyser Feld is found in a region of the Andean Altiplano. A detailed report on geysers of the El Tatio Geyser Feld was presented in Glennon and Pfaff (2003), which is actually a catalogue of the geysers there. Most of the geysers found there are dwarf geysers with water ejecting to a height of only about 10–30 cm, but there are also geysers ejecting hot water to heights of

Table 4.6 Thermal and pH characteristics of some hot springs in Japan (after Oki and Hirano 1974; Taguchi et al. 1996; Yoshiike 2003; Sawa et al. 2006; Koseki 2010)

Hot spring	Temperature on discharge (in K)	pH
Kannawa Ishimatsu	373	7.7
Kannawa Chinoike	333	2.4
Myoban Yamadaya	340.5	1.7
Kamegawa Shinoyu	329.6	8.2
Old-City Kimura	328.6	7.4
Hotta Hotta	348.5	6.2
Kankaiji Jizouyu	323	6.9
Nasu	318.2–346.1	1.5–1.7
Takao	307	5.6
Sandogoya	365	2.6
Nikko-yumoto	328.2–342	6.0–6.8
Yunohanazawa, Hakone	306–350.2	2.0–2.6
Ashi-no-yu	313–314	6.4
Kowakudani	334	8
Ubako	318	5
Kusatsu	330–338	1.5–1.6
Isobe	288.5	6.6
Ikao	317.2	6.2
Tanigawa	315.3	8.2
Tateyama	315	1.2
Arima	334–364.3	6.0–6.6
Hakone Springs:[a]		
Zone I	322.7	2.9
Zone II	330.5	8.1
Zone III	364.5	7.7
Zone IV[a]	338.5	8.4
Zone IVb	329	8
Ground water	286.1	7.2
Obuki[b](Tamagawa springs)	369–372	1.22–1.42
Owakudani	309.3–369	2.48–4.25
Azuma	320–373	Neutral
Zao	338	Neutral
Hijiori	357	Neutral
Akakura	347	Neutral
Akayu	336	Neutral

[a] Zonation of Hakone spring area after (Oki and Hirano 1974)
[b] Fluctuation of temperature (1962–2000) and pH (1959–2000) after (Yoshiike 2003)

1–3 m, and one geyser shoots water jets to a height of up to 8 m (Glennon and Pfaff 2003). Since the formation of geysers is only possible when hot magmatic rocks are very close to the surface, the most important fact about Chilean geysers is that they represent extremely hot cooling magmatic rocks that are located at very elevated sites in the region.

Manifestations of thermal and hydrothermal features can be found almost everywhere in the world, but in tectonically and magmatically active regions such features are present in much greater numbers and varieties. Unfortunately, it is not possible to adequately discuss in greater detail the thermal and hydrothermal conditions of some of the other most thermally active regions, such as those in other parts of the Pacific Ring of Fire (the Philippines, Indonesia, Peru, Ecuador, Panama, Western Mexico, Westernmost USA and Canada, South-Western Alaska, Aleutian Islands, and some others), as it would require a whole separate volume to focus on these issues. However, the geothermal characteristics of a number of the thermally active regions on Earth are discussed in different parts of this book.

4.1.3.7 Concluding Remarks on Thermal Waters on Land

The average rates of the discharge of some hot springs in different locations are listed in Table 4.7.

There is no doubt that all of these high temperature features are spectacular, and definitely represent the release of enormous amounts of heat from the upper crustal layers. However, it is worth examining how significant this heat discharge is compared to other hydrological features.

Table 4.8 shows rate of discharge of some of the largest non-thermal springs.

Comparing the data from Tables 4.7 and 4.8 with those in Table 4.5 shows that none of most powerful hot springs on the Earth, or any system of hot springs, and not even a single hot spring/geyser basin with strong hydrothermal manifestations even comes close to the average discharge rates of the most powerful non-thermal springs on the Earth. In terms of rate of discharge of water, only the total discharge of all the hydrothermal features in Yellowstone National Park as a whole (Table 4.7) approaches the average discharge of some of the weakest non-thermal springs of the first magnitude (rate greater than about 2,800 L/s). To take another example, let's examine the rate of discharge of water in the Geysernaya River, which collects water from all the hydrothermal features in the Valley of Geysers in Russia. This rate is also comparable to the weakest non-thermal water springs of the first magnitude, but the discharge rate of all thermal features from the Valley of Geysers only makes up about 9 % of the total discharge of the Geysernaya river (see Table 4.7). Similarly, even though every eruption of the most powerful geyser in the Valley of Geysers, Geyser Velikan, is very powerful and there were 1271 eruptions during the period from August 2007 to July 2008 (Kiryukhin 2009), its average discharge rate was just 2.4 L/s, since it takes time to recharge as well.

All 320 known springs in Florida have a combined average discharge of about 348,297 L/s of water (Spechler and Schiffer 1995), which includes the rates of all first magnitude springs, second magnitude springs (about 70 springs with a total average rate of 73,623 L/s) and third magnitude springs or less (more than 190 springs with an average discharge rate of 8,495 L/s). In fact, the total discharge rate of all the thermal features in Yellowstone National Park is about 110 times less than the total discharge rate of water in non-thermal springs across the state of

Table 4.7 Rate of discharge of some hot springs and hot spring systems

Spring or system of springs	Average rate of discharge (in L/s)	Magnitude of spring
Yellowstone National Park, USA:		
Total for all thermal features in the Park	3,091	–
Upper Geyser Basin	696	2
Lower Geyser Basin	662	2
Midway Geyser Basin	252	3
Mammoth Hot Springs	57	3
Shoshone Geyser Basin	66	3
Heart Lake Geyser Basin	104	3
West Thumb Geyser Basin	47	3
Kamchatka Peninsula, Russia:		
Paratunka geothermal field	221	3
Esso geothermal field	168	3
Anavgay geothermal field	34	3
Springs in vicinity of rivers Goryachaya and Zholtaya	80–110	3
Taloviye	6	5
Krayevedcheskie	7	4
Verkhne-Schapinskie	40	3
Valley of Geysers, Kamchatka Peninsula:		
Total for the basin	300–315	2
River Geysernaya	3,340	–
Podskalniy	5	5
Bolshoy	3	5
Geyser Velikan	2.4	5
Deildartunguhver, Iceland	180	3
Hveravellir, Iceland	35–40	3
Gata, Iceland	10–22	4
Thorleifskot, Iceland	70–80	3
Yamagata prefecture, Japan, total of 140 springs	916	–
Zao, Yamagata prefecture, Japan	92	3
Bepu Geothermal Area, Japan, Total	579	2
Obuki, Tamagawa springs, Japan	166	3

Florida. Curiously, this means that if the temperature of water in the springs of Florida from the moment of their recharge to the moment of their discharge were increased by only 1 K, the discharge of heat from the non-thermal springs in Florida would be much greater than the discharge of heat from all the thermal features of Yellowstone National Park. In actual fact of course, the water of non-thermal springs would be heated by more than only a single degree Kelvin. For instance, the heating of the spring waters of Florida by as little as 1, 2, 3, 4 or 5 K would generate a heat energy discharge with a rate of 1,458, 2,916, 4,374, 5,832, and 7,290 MW, respectively. The heat released by Mutnovsky Volcano, one of the most powerful active volcanoes in the Kamchatka Peninsula of Russia, along with all its thermal features averages to only about 1,800–1,900 MW (Polyak 1966;

Table 4.8 Rate of discharge of some of the largest non-thermal springs in the world (after Meinzer 1927; Burdon and Safadi 1963; Davis and DeWiest 1966; Smith 1989; Spechler and Schiffer 1995; Ponder 2002)

Spring or system of springs	Average rate of discharge (in L/s)	Magnitude of spring
Greek Springs, Wakulla, Florida USA	56634	1
Crystal River Springs, Citrus, Florida, USA	24862	1
Fontaine de Vaucluse, France	22,653	1
Ras el 'Ain, Syria	38,567	1
Stella Spring, Italy	36,585	1
Rio Maule River, Chile	28,317	1
Malade Springs, Idaho	28,317	1
Giant Springs, Montana	16,990	1
Great Australian Artesial Basin (in 1915)	23,148	–
Great Australian Artesial Basin (in 2000)	17,361	–
Witjira-Dalhousie Springs, Australia (in 1985)	612	2

Melekestsev et al. 1987; Bortnikova et al. 2008). Since the difference between the temperatures of discharging spring water could easily exceed the temperature of water precipitating in a recharge zone by about five degrees or more, it is clear that the heat discharge from Florida's non-thermal water springs alone would be comparable to that of five powerful active volcanoes. Thus similar heat discharges from non-thermal water springs of other regions around the world, even ones smaller than those in Florida, would greatly exceed the amount of heat released by active volcanoes and thermal features related to volcanism.

Comparing the rates of water discharge for different hot, warm and non-thermal springs shows that non-thermal springs require higher flow rates, and in turn require the presence of more permeable aquifers than those in warm or hot spring waters. At the same time, warm springs have higher discharge rates than hot springs, and they require intermediate permeability between non-thermal spring aquifers and hot spring aquifers. Hot spring aquifers are among the least-permeable aquifers of all springs. This is explains why there are such huge differences between the temperatures of different kinds of springs: because the flow rate is as important for discharge as the temperature of the media surrounding the aquifer, more lengthy contact of water flowing through the aquifer provides better heating conditions for the spring water, which causes the water to be heated to higher temperatures. In contrast, water with a high flowing rate does not get much heat from contact with even hotter media.

4.1.4 Oceanic Vents

Hot springs in oceanic areas are called vents. Hydrothermal systems are usually found in vents ranging from about 623 K (high-temperature vents) generally

located in the axial zone of ridge segments to 293 K (low-temperature vents) located on a ridge axis or flanks. Most low temperature vents in oceanic areas are fairly similar to those formed on land areas, such as the Champagne Hot Springs, which are composed of a shallow submarine hydrothermal system located along the submerged flank of the Plat Pays volcanic system on the southwest section of the island of Dominica, in the Lesser Antilles (McCarthy et al. 2005), with a temperature at the point of discharge in the range of 314–344.4 K and pH between 5.95 and 6.15. The nearby Sulfur Springs have a temperature of 366.5 K and pH of 4.03 (McCarthy et al. 2005).

Some unique extra-hot vents are divided into 'black smokers' and 'white smokers', depending on the temperature and content of the ejecting fluid jets. A black smoker is a vent emitting hydrothermal fluid with temperatures mostly within the range of about 573–673 K, though they can be even greater, and containing dissolved metals which mix at discharge with sulfur and form tiny black particles, giving the fluid jets a dark to black color. At discharge, on contact with cold oceanic water, minerals rich in metals and sulfur precipitate from the ejected fluid forming chimneys and/or mounds, which can be considered as the initial components of ore deposits (mostly sulfide). The chimneys can be tens of meters in height. White smokers eject fluid with temperatures usually in the range of 523–573 K, but in some cases their temperatures can go as high as the minimum temperature for black smokers. They have many fewer or almost no metals in the ejected fluids, making the color of the fluid jets lighter (white). White smoker fluids usually flow much slower than black smoker fluids, and they generally have much smaller chimneys as well. Both black and white smokers are formed when strongly overheated fluids rise up through the ocean floor. In numerous cases, black smokers and white smokers are found within the same small area (e.g., Graham et al. 1988; Fouquet et al. 1998; Van Dover et al. 2001). Estimates of black smoker water fluxes and those of low-temperature vents yielded values of $\sim 3.5 \times 10^{12}$ and $\sim 6.4 \times 10^{14}$ kg/year, respectively (Elderfield and Schultz 1996; Staudigel 2005). Similarly, estimates of the mid-ocean ridge axial heat flow and the total hydrothermal heat flow indicate values of about $(2–4) \times 10^{12}$ W and $(9 \pm 2) \times 10^{12}$ W, respectively (Elderfield and Schultz 1996).

Since the main component of these overheated fluids is water, their behavior is affected by the thermodynamic properties of water. These fluids are in a liquid state, because under the extreme pressures at the ocean bottom, the boiling point of water increases to very high temperatures. For instance, pure water has a boiling temperature of 623 K under pressure of 16.5 MPa (Grichuk 2000), whereas water with a salinity of 3.5 wt% at depths of ~2,500 m has a boiling temperature above 663 K. Bischoff and Rosenbauer (1985) reported a boiling temperature of ~648 K at a depth of 2,200 m. The presence of boiling fluids was reported by Michard et al. (1984) for a hydrothermal system at 13°N from the East Pacific Rise. However, in some cases related to the exceptionally great depths of the sea bottom, the water can be in supercritical condition right before it mixes with the regular cold oceanic water. The critical point of seawater has 29.8 MPa and 680 K (Von Damm et al. 2003; Koschinsky et al. 2008; Coumou 2009). Even though the

Table 4.9 Temperatures of discharged fluids for some black and white smokers

Vent type and location	Temperature of water (in K)	References
Black smokers:		
Mid-Atlantic Ridge:	613–663	Petersen et al. (2000)
TAG at 26°N	636	Fouquet et al. (1998)
TAG at 26°08′N	583–593	Pedersen et al. (2010)
Loki's Castle, 73°30′N and 8°E	573–673	McCaig et al. (2007)
low-angle detachment fault at 15°45 N	600–654	Herzig et al. (1998)
Black smoker complex (TAG-1) at 26°N	~638	German et al. (2010)
Rainbow hydrothermal field at 36°14′N 5°S	680–737	Haase et al. (2007)
East Pacific Rise:		
Galapagos Rift, 21°N	623	Köhler et al. (1994)
East Pacific Rise	603–678	Tivey (2007)
9–10°N	656	John et al. (2008)
Site #7 at 12° 49′N	653	Graham et al. (1988)
Site #10 at l0°58′N	620	Graham et al. (1988)
Central Indian Ridge:		
Kairei vent field at 25°19.239S, 70°02.429	579–638	Van Dover et al. (2001)
Edmond vent field at 23°52.689S, 69°35.809E	up to 655	Van Dover et al. (2001)
Juan de Fuca Ridge:		
Middle Valley in the area of active venting	up to 633	Turner et al. (1993)
'Sully' and 'Puffer' vents	628–633	Crone et al. (2006)
Izena Hole, Mid Okinawa Trough	593	Sakai and Nozaki (1995)
White smokers:		
Mid-Atlantic Ridge:		
TAG at 26°08′N, the Kremlin area	533–573	Herzig et al. (1998)
East Pacific Rise:		
Galapagos Rift, 21°N	543	Köhler et al. (1994)
9–10°N	480	John et al. (2008)
Site #9 at 11°14′N	~543	Graham et al. (1988)
Site #3 at 12°51′N	>483	Graham et al. (1988)
Juan de Fuca Ridge:		
Middle Valley in the area of active Venting	457–553	Turner et al. (1993)
Northern Okinawa Trough	551	Sakai and Nozaki (1995)

average depth of black smokers is about 2,100 m, there are some located at depths of ~3,650 m within the Trans-Atlantic Geotraverse (TAG) (Fouquet et al. 1998) and even at 5,000 m within the Cayman Trough in the Caribbean Sea (Showstack 2010), where the pressure is much greater than the critical pressure for oceanic water. Temperatures higher than critical for oceanic water were found in black smokers at 5°S on the Mid-Atlantic Ridge (Haase et al. 2007; Koschinsky et al. 2008) (see also Table 4.9), where they are located at a depth of about 3,000 m (Koschinsky et al. 2008), thus rendering their pressure critical, and the overall conditions of the water in these black smokers supercritical. Such conditions of the discharge of overheated water through the sea bottom make them different from

fumaroles discharging on land. At the same time, it is clear that in both of these cases the presence of magma (liquid or solidifying) is required.

The rate of discharge for black smokers can be extremely high. For example, the water discharge from the high-temperature submarine Rainbow hydrothermal field (at 36°14′N on the Mid-Atlantic Ridge) has a rate of ∼450 L/s of 638 K fluid (German et al. 2010) that is comparable to the discharge rates of hot springs and geysers from the most powerful geyser fields of Yellowstone National Park.

The first hydrothermal system containing ore deposits was discovered in the Atlantis II area of the Red Sea in 1963 (Degens and Ross 1969; Grichuk 2000). The Atlantis II Deep, in the Red Sea, is characterized by high temperature brines (up to 340 K) with a very high salinity (270 g/kg) (Winckler et al. 2000). The Atlantis II brine system was considered to be a special case of the hydrothermal field at a mid-ocean ridge, and even though the hot fluid was not sampled directly at the discharge site, a temperature discharge was estimated to be within the range 473–673 K but most authors suggest it is in excess of 603 K (Winckler et al. 2000). The first deep-sea hydrothermal vent in oceanic areas was discovered in 1977 along the Galapagos Rift (Weiss et al. 1977).

Since black and white smokers are usually found in mid-ocean ridges, the main search for them is concentrated along a global ridge system of about 67,000 km (Baker and German 2004). Baker and German (2004) reported that searches along the global ridge system (only about 20 % of the system has been explored so far) led to the discovery of about 280 high temperature vents, of which 145 were confirmed visually and about 130 were determined based on water column observations alone. Baker et al. (1987) reported a 700-m-thick, 20-km-diameter megaplume created by a brief but massive release of high-temperature hydrothermal fluids near 44°49′N, 130°14′W on the Juan de Fuca Ridge. Data on some black and white smokers are presented in Table 4.9.

Black and white smokers have attracted the attention of scientists because they constitute an ongoing process of the formation of ore deposits, and are considered potential locations for finding large amounts of valuable minerals and metals at the sea bottom.

4.2 Volcanic Eruptions

One of the most powerful and dramatically energetic features on Earth is volcanism. A schematic structure of a volcano is presented in Fig. 4.3.

Numerous active volcanoes releasing enormous amounts of heat energy to the surface and into the atmosphere contribute considerably to the cooling of the Earth. Volcanoes are also one of the biggest natural hazards on Earth, destroying animal and plant life, and even people through the release of enormous amounts of hot lava, volcanic material and ash, as well as great quantities of poisonous gases such as SO_2, CO, CO_2, HCl, HF, etc.

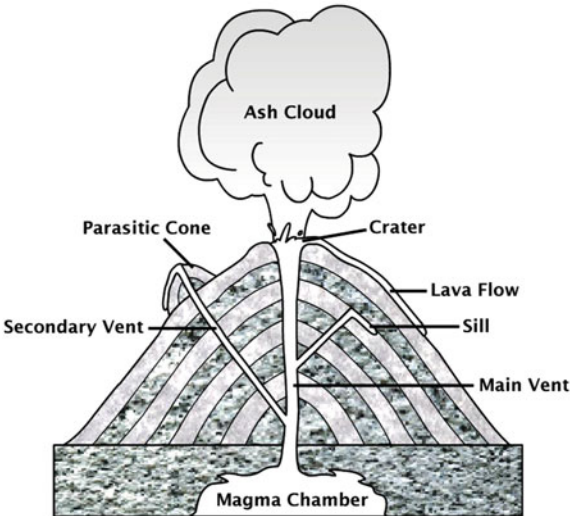

Fig. 4.3 Schematic structure of a volcano

There are four main types of volcanic landforms: (1) lava plateau (extremely flat-laying accumulations of lava sheets, usually plato-basalts or flood-basalts); (2) shield volcanoes (conical structures with generally ~5–10° sloped shield-shaped mountains); (3) composite volcanoes or strato-volcanoes (massive, steep sided mountains with slopes of about 30–35°); and (4) pyroclastic sheet deposits (extensive and relatively flat-laying accumulations of pyroclastic rocks) (Macdonald 1972; Simkin and Siebert 1994; Hall 1995; Fedotov 2006; Parfitt and Wilson 2008; Lockwood and Hazlett 2010).

The molten rock in a volcano (the magma) rises from the depths through the main vent and erupts onto the surface as liquid lava, forming bodies of magmatic rocks on the surface called lava flows. All volcanoes have a crater at the top of the vent, which is a small depression usually located in the center and measuring less than 1 km in diameter. Large depressions of over 1 km in diameter are usually called caldera. A caldera is generally formed by the collapse of the ground above the magma chamber. Some magma does not rise directly from its source to the site of eruption, but rather forms a magma chamber at an intermediate depth.

The products of volcanic eruptions are lavas, pyroclastic rocks and volcanic gases. The behavior of any volcano depends primarily on its content, temperature and the viscosity of the magma, water content, and the pressure generated within the magma chamber. Magmas with low viscosity and a low content of dissolved gases (basalts and other basic rocks, some intermediate and felsic rocks with temperatures much higher than their liquidus temperatures) erupt quietly as lava flows. This kind of eruption is called effusive. The viscosity of basic lavas is about 10–10^4 Pa s (for comparison, the viscosity of water is ~10^{-3} Pa s). In contrast, lavas with high viscosity (felsic lavas with viscosity of ~10^{11}–10^{12} Pa s to intermediate magmas with a viscosity of 10^3–10^6 Pa s, and basic magmas with temperatures just below their liquidus temperature) and/or a high concentration of

volcanic gases erupt explosively, creating huge amounts of pyroclastic products and relatively little lava. This kind of eruption is called explosive. Pyroclastic rocks are those associated with explosive volcanic activity and eruption of volcanic bombs (fragments with a grain size >32 mm in diameter) ejected as liquid or solid blocks, volcanic lapilli (grain size of about 32–4 mm in diameter), and volcanic ash (grain size of <4 mm in diameter).

The explosive behavior of highly viscous magmas is related to the fact that different gases, including water, which are mostly in supercritical conditions, can easily be trapped in different parts of the magma and are delivered along with it to the surface. At the surface, where the lithostatic pressure within the erupting magma drops down to atmospheric pressure, the gases squeezed within the magma by the lithostatic pressure force themselves out, leading to the explosion of erupting rocks. As was shown in Sect. 2.7, to be in equilibrium the pressure of volcanic gases trapped within highly viscous magma should be the same as the lithostatic pressure within the magma. This means that the effect of the explosion is stronger for magma raised from greater depths. Wallace and Anderson (2000) showed that rhyolite melted at a depth of ~4 km can dissolve ~4 wt% of water, but if the pressure drops to 0.1 MPa, no water is soluble in the melt and it would all have to exsolve with a very rapid 1,000-fold volume expansion, fragmenting the magma. At the same time, significant water content can considerably decrease the viscosity of granitic (Hall 1995) and other silica-rich magma. For instance, the viscosity of granitic magma at a temperature of 1,473 K with a $P_{H_2O} = 200$ MPa is as low as 0.5×10^3 Pa s (Hall 1995), which is within the range of the viscosity of basalts.

When highly viscous lava erupts to the surface, it has great yield strength that tends to pile up rather than flowing down the slope, forming a steep-sided hill directly over and around the vent called a volcanic dome or lava dome. These are mound-shaped structures mostly formed by silica-rich magmatic rocks (Newhall and Melson 1983; Fink and Anderson 2001) such as rhyolites and dacites. Dome structures usually form within calderas.

The examples of lava plateau type volcanism presented in (Yoder 1976; LIPC 2003) contain information about magmatism in the major Large Igneous Provinces (LIP) in continental and oceanic areas during the Phanerozoic. An excellent resource on about 2,000 volcanoes is available on the website Volcanoes of the World (Seach 2011).

Analysis of available data on the subject indicates that the most highly active volcanoes (over 450) and the most powerful volcanic eruptions (over 85 % of the strongest volcanic eruptions) are located unsurprisingly within the Pacific Ring of Fire. An astounding 83.3 % of all volcanic eruptions taking place in the world from 1976 to 1980 occurred in the Pacific Ring of Fire (Hall 1995). Similar results were found for the most powerful volcanic eruptions over the last 10,000 years, with ~85 % taking place in this same region.

Another fact related to volcanic activity is that the most powerful volcanic eruptions are related to the formation of calderas. This is in complete agreement with the fact that the most powerful manifestations of hot springs, geysers and

fumaroles are related to calderas, and particularly to nested calderas (e.g., Yellowstone National Park in the USA and Valley of Geysers in Russia; see Sect. 4.1). At first glance it seems strange that calderas, the lavas of which are almost entirely represented by rhyolites and dacites which have much lower melting points and much higher viscosity than basalts and other basic magmatic rocks, should be the most thermally active volcanic structures. Since their melting point is about 200–400 K higher than the melting points of rhyolite and dacite, basaltic magmas should be able to deliver much more heat energy to the surface than the same volume of rhyolitic and/or dacitic magma. This is true for cases involving the formation of LIP with enormous amounts of flood-basalts (plato-basalts). However, in many cases huge amounts of basaltic (basic) magmas do not reach the surface for different reasons (e.g., underplating, formation of magma chambers within the crust, etc.). Under these circumstances, the tremendous heat energy delivered to different crustal layers re-melts the crustal rocks, which are mostly of intermediate and felsic composition.

It was shown (Pilchin and Eppelbaum 2009; Pilchin 2011) that after solidification of the magma-ocean, the depths of the main sources of forming magma continually increase as the lithosphere gradually thickens, which can be proven by the significant increase of the iron content within magma over time. This means that the considerable amounts of rhyolites and/or dacites filling calderas and continuing to erupt within these calderas are products of the re-melting of crustal rocks, but the heat energy causing this re-melting was delivered by basic magmas from the asthenosphere. The most significant effect of such re-melting is the fact that the same amount of available heat is capable of forming much greater volumes of molten rocks of felsic (rhyolite and/or dacite) composition than those of basic or intermediate composition, since they have much lower melting points than those of basic and intermediate rocks. In other words, basic magmas underplating some layers of crust or forming magma chambers at shallow depths within the crust generate huge volumes of silica-rich felsic magmas having an extremely high viscosity that in most cases prevents their direct eruption to the surface. This means that silica-rich and highly viscous magmas can come very close to the surface, but in most cases stop short of erupting onto it.

All the above suggest that there is a way for huge amounts of silica-rich magmas to form that concentrate at shallow depths but do not erupt onto the surface. This corresponds to the fact that the absolute majority of intrusive rocks are of granitic (felsic or intermediate) composition. This also means that enormous amounts of hot felsic magmas concentrated at shallow depths are prevented from having direct contact with surface waters and the atmosphere, thus keeping these magmas hot for a long time (hundreds of thousands to millions of years as in Yellowstone National Park).

Let us analyze the conditions within the source area, magma chamber and main vent of a volcano using thermodynamics. The relationships between pressure, temperature and volume within each of these parts of a volcano is described by Eq. (2.7.4), from which it is clear that the pressure within the magma source area is highly dependent on the value of the lithostatic pressure (P_0) which in turn is relative

to the density of magma. For the magma within a vent to begin rising, the pressure P within the magma must be greater than the lithostatic pressure ($P > P_0$), which is determined by the density of magma for the volcano. Lower density magma imposes a lower lithostatic pressure on both the magma in the source area and the magma chamber. This means that lower pressures within these parts of the volcanic system are required for the magma to start rising. As can be seen from Eq. (2.7.4), the temperature of the magma is crucial for the formation of overpressure, as a higher temperature of magma increases the excess pressure [as in term $(\alpha/\beta)(T - T_0)$ in Eq. (2.7.4)]. A change in volume is also crucial [as in term $\frac{1}{\beta}\frac{\Delta V}{V_0}$ in Eq. (2.7.4)], since the increase in volume ($\Delta V > 0$) leads to a decrease in pressure and respectively to a decrease in excess pressure, whereas a decrease in volume ($\Delta V < 0$) leads to an increase in pressure and hence to an increase in excess pressure.

A complete volcanic process unfolds in the following steps: formation of magma, rising magma, and magmatic eruption onto the surface. Even though a volcanic process does not necessarily have to be complete and may cease at earlier steps, a manifestation of a volcanic eruption on the surface means it was complete. The absence of heat energy needed to form melt, the absence of excess temperature needed to form excess pressure, a quick drop in pressure, or many other causes can stop a volcano from forming at any step of its evolution. However, let us focus on a case where the volcanic process was completed. The formation of magma requires the raising of the rock temperature to its melting point (T_m), though to melt the rock completely, additional heat energy dictated by the *latent heat of fusion* is necessary to turn solid rock into liquid at the melting temperature of the rock. Obviously, temperatures of the forming melt may be above the melting point of the rock, but they cannot be less. This means that the minimal additional pressure formed by the excess temperature within the forming magma (P_T) is:

$$P_T = \frac{\alpha}{\beta}(T_m - T_0). \tag{4.2.1}$$

One of the main peculiarities of the process of magma formation is the fact that any molten rock has less density than it does as a solid, and thus requires more volume as a melt. However, there is no free space available at great depths, and the magma only occupies the volume that was previously occupied by the solid rock. Therefore, the forming magma cannot expand. This situation is similar to a case where magma previously occupying a volume was squeezed into a smaller one (Pilchin 1986; Pilchin and Eppelbaum 2009). This case should be treated as one involving a decrease in volume ($\Delta V < 0$) leading to an additional increase in pressure (compressional pressure P_c) rather than its decline:

$$P_c = -\frac{1}{\beta}\frac{\Delta V}{V_0}. \tag{4.2.2}$$

Using the relationship between the change in volume and change in density described in Eq. (2.7.7), Eq. (4.2.2) can be written as:

Table 4.10 Changes in densities of some typical magmatic rocks upon melting

Rock	Density of molten rock (in kg/m^3)	Density of solid rock (in kg/m^3)	Relative change of density on fusion ($\Delta\sigma/\sigma$)
Rhyolites[a]	2,170	2,280	−0.0482
Andesite[a]	2,410	2,590	−0.0695
Tholeiite basalt	2,600	2,760	−0.0580
Alkali olivine basalt	2,680	2,830	−0.0530
Diabase[a]	2,640	2,960	−0.1081
Basalt, gabbro	2,600	2,900	−0.1034
Rhyolite, granite	2,300–2,400	2,600	−(0.0769–0.1154)
Diabase[a]	2,603	2,890	−0.0993
Diabase[a]	2,640	2,880	−0.0833
Rhyolite[a]	2,310	2,450	−0.0571
Andesite[a]	2,580	2,830	−0.0883
MORB	2,650	2,950	−0.1017
Mars basalts	2,720	3,130	−0.1310
Komatiites	2,730	3,090	−0.1165
Basalt	2,600	2,800	−0.0714
Silicic melt	2,300	2,600	−0.1154

[a] Samples from different sources and/or having different rock densities

$$P_c = \frac{1}{\beta}\frac{\Delta\sigma}{\sigma}. \tag{4.2.3}$$

Examples of changes in densities of some typical magmatic rocks upon melting have been calculated from published data (Clark 1966; Hall 1995; Woods and Huppert 2003; Guillot and Sator 2007) and are presented in Table 4.10.

It is clear from Table 4.10 that the process of magma formation requires a change in volume of about 4.8–13.1 %. Best (2002) also stated that the density of magmatic rocks is 10–20 % greater than their corresponding melts. Calculations of the relative change in density ($\Delta\sigma/\sigma$) on fusion for minerals using published data (Courtial and Dingwell 1999) yielded −0.0845 for periclase, −0.2012 for both diopside and for enstatite, and −0.0462 for anorthite. Similar estimates for olivine indicated values for $\Delta\sigma/\sigma$ of −0.0779 for forsterite and −0.1138 for fayalite.

From Eqs. (2.7.4), (4.2.1), and (4.2.2), the total pressure within the source layer of the forming magma or magma chamber at any depth is:

$$P = P_0 + P_T + P_c. \tag{4.2.4}$$

Excess pressure can be determined from:

$$P - P_0 = P_T + P_c. \tag{4.2.5}$$

Thus the minimum requirements for magma to start rising are:

$$P - P_0 > 0. \tag{4.2.6}$$

However, some additional excess pressure is required to overcome the forces of friction in rising magma. It is evident from Eqs. (4.2.1–4.2.3) that to estimate the excess pressure (overpressure) generated within a source layer (either in magma chamber or a vent), we need the values of the thermal expansion coefficient (α) and compressibility coefficient (β) of the magma. The values of these coefficients for some typical kinds of magma are presented in Table 4.11.

It is clear from Table 4.11 that the presence of gases and water in magma will significantly increase the compressibility coefficient. Knittle (1995) reported a compressibility coefficient (β) of about 0.041 GPa^{-1} for liquid fayalite.

The melting point of a magmatic rock is usually similar to its solidus temperature, but is not enough to form magma, since it represents the temperature at which the melting process begins. This means that the formed magma would be at the liquidus temperature of the magmatic rock. Of course, it can have a temperature higher than its liquidus if the magma is overheated. Since most of the upper mantle is represented by peridotites which are the main source rocks for magmas, the temperature of magma formation should be above the solidus temperature of peridotite, and depends on the percentage of peridotite melted during its formation. At the same time, both the melting point and liquidus temperature of any dry magmatic rock increase considerably with increase of pressure. Additionally, the melting point and liquidus temperature are tightly dependent on the composition of magma, which in turn is a product of the composition of rocks in the magma source layer in the upper mantle of any particular region. Such properties of magma as the thermal expansion (α) and compressibility (β) coefficients therefore vary greatly depending on the magma composition, as well as its temperature and pressure.

It is well known that the melting of rocks begins at much lower temperatures in the presence of water and/or carbon dioxide than for dry rocks (Kawamoto and Holloway 1997; Ochs and Lange 1997; Hogan et al. 2001; Grove et al. 2006; Dasgupta and Hirschmann 2007; Pilchin and Eppelbaum 2009, etc.), and that the effect of water on reduction of the solidus temperature is much greater than the effect of carbon dioxide. At a depth of about 100 km, peridotite begins to melt at around 1,073 K in the presence of excess water, while its melting point in the absence of water is about 1,773 K (Grove et al. 2006). Similarly, dissolving only 0.4 wt% of water in a basalt melt at 1,473 K and 70 MPa has the same effect as increasing the temperature by 175 K or decreasing the pressure by 230 MPa (Ochs and Lange 1997). The solidus temperature of granitic melt drops from $\sim$1,233 K with no water to 953 K with a water content increase to $\sim$6.0 wt%, while the solidus temperature for relatively dry granites containing only 1–2 wt% of water is about 1,053–1,093 K (Hogan et al. 2001). Lee et al. (2009) also reported that the

Table 4.11 Thermal expansion coefficient (α) and compressibility coefficient (β) values for some typical magmatic melts

Molten rock	Thermal expansion coefficient (α), 10−51/K	Compressibility coefficient (β), 1/GPa	References
Average silicate melt	3	0.07	McBirney (2000)
Average silicate melt	3	0.07	Best (2002)
Kilauea gas poor magma	–	0.06–0.10	Rivalta and Segall (2008)
Rhyolite[a]	7.1	–	Guillot and Sator (2007)
Andesite[a]	9.8	–	Guillot and Sator (2007)
MORB[a]	11.1	–	Guillot and Sator (2007)
Mars basalts[a]	12.3	–	Guillot and Sator (2007)
Komatiites[a]	13.1	–	Guillot and Sator (2007)
Rhyolite	10.1	–	Nelson and Carmichael (1979)
Rhyolite	3.8	–	Lange and Carmichael (1987)
Rhyolite	5.3	–	Ghiorso (2004)
Andesite	8.1	–	Nelson and Carmichael (1979)
Andesite	5.5	–	Lange and Carmichael (1987)
Andesite	6.0	–	Ghiorso (2004)
MORB	10.6	–	Nelson and Carmichael (1979)
MORB	6.4	–	Lange and Carmichael (1987)
MORB	7.0	–	Ghiorso (2004)
Komatiites	4.7	–	Courtial et al. (1997)
Komatiites	9.7	–	Ghiorso (2004)
Komatiites	8.1	–	Lange and Carmichael (1987)
Peridotite	6.2	0.05587	Suzuki et al. (1998)
Peridotite	5.9	0.05649	Suzuki et al. (1998)
Basalt	–	0.1	Rivalta and Segall (2008)
Mount St. Helens Magma	–	0.28[b]	Mastin et al. (2008)
Magma, Soufrière Hills Volcano, Montserrat	–	0.758[c]	Voight et al. (2010)

[a] At a temperature of 1,800 K and low pressure
[b] Magma contains ~1.2 % bubbles
[c] Saturated magma plus exsolved gas

solidus of lherzolite containing 5 % water is 1,273 K at 0.5 GPa and ~1,653 K at ~4 GPa, while for 10 % content of water it is 1,273 K at 1.25 GPa and ~1,543 K at ~4 GPa.

The presence of gas or water as well as their level of concentration significantly influences the thermal expansion values and compressibility coefficients of magma. The solubility of water in a melt depends closely on the pressure. With an increase of pressure from 0 to 200 MPa, the solubility of H_2O in a granitic melt increases from 0 to ~6.0 wt% (Hogan et al. 2001).

The melting point/solidus temperature and liquidus temperature of most typical magmatic rocks at pressures of 0.1 MPa and 1 GPa were compiled for both dry

and wet conditions using published data (Bayly 1968; Stern and Wyllie 1973; Mysen and Boettcher 1975; Green 1982; Karsten et al. 1982; Takahashi and Kushiro 1983; Litvinovsky et al. 1990; Hall 1995; Faure 2000; Herzberg et al. 2000; Thompson and Gibson 2000; Hogan et al. 2001; Schubert et al. 2001; Attrill and Gibb 2003; Pertermann and Hirschmann 2003; Grove and Parman 2004; Liaw et al. 2006; Falloon et al. 2007; Faure and Mensing 2007) and are presented in Table 4.12.

The data presented in Table 4.12 shows that both the melting point and liquidus temperature of most typical magmatic rocks are strongly influenced by the water content, and that in most cases for water-rich magmas these parameters have a negative gradient of $\Delta T/\Delta P < 0$ within the pressure range of 0–1 GPa. The gradient is usually negative up to a pressure of about 2 GPa and stabilizes at higher values of pressure, eventually even starting to slightly increase. This can create a situation where the melting point and liquidus temperatures of a water-rich rising magma gradually continue to increase with added pressure. This can sometimes be an obstacle to the formation of a volcano. For more information on the melting points of rocks and minerals and the dependence of the melting point of peridotites on pressure, see Sect. 2.4.

These features thus paint a complicated and ambiguous picture of the process of magma formation and the rise of magma to the surface to form a volcano. The most typical rock in the upper mantle is peridotite, which is believed to be the source material for the generation of almost all basic and ultrabasic magmas (e.g., Hall 1995). Basalts, andesites and rhyolites are among the most typical rocks in volcanic eruptions (e.g., Hall 1995). The most common magmatic rock within calderas is rhyolite (see Sect. 4.1); which was clearly formed within the crust, since rocks so rich in silica cannot be formed in the upper mantle. This is also supported by the fact that in many cases, signs of basic magmatic rocks formed at great depths are also present in regions of active magmatic activity, including calderas. For example, a significant amount of iron-rich tholeiite is present among the magmatic rocks of the Mutnovsky Volcano, Kamchatka Peninsula, Russia. Iron-rich rocks with a FeO content of about 13.5 % were also found among the magmatic rocks of the Gorely Volcanic Center of Kamchatka Peninsula, which includes a huge caldera. Rocks with such rich iron content cannot be formed higher than at least the 'Forsterite layer', which is located at depths of about 100–120 km in continental areas (Pilchin and Eppelbaum 2009). It is clear that rhyolites from the caldera of the Gorely Volcanic Center could not have been generated at depths greater than 100–120 km, and were formed in a magma chamber within the crust by basic magmas rising from depths of over 100–120 km. This is also supported by the fact that a bimodal assemblage of basalt and rhyolite is known to have erupted in the Yellowstone caldera (Christiansen 1992). The generation of felsic (granitic) magmas by the intrusion of basalts is also known to exist in the continental crust (Huppert and Sparks 1988).

Let us estimate the possible excess pressure within a magma source layer with a lithostatic pressure P_0 of about 4 GPa at a depth of about 115–120 km, rising to a depth where it creates a magma chamber in which wet rhyolite melt forms. Since

Table 4.12 Melting point/solidus temperature (in K) and liquidus temperature (in K) of most typical magmatic rocks for dry and wet conditions at pressures of 0.1 MPa and 1 GPa

Rock	Melting point or solidus temperature of dry rock at 0.1 MPa/1 GPa	Melting point or solidus temperature of wet rock at 0.1 MPa/1 GPa	Melting point or solidus temperature of saturated rock at 0.1 MPa/ 1 GPa	Liquidus temperature of dry rock 0.1 MPa/1 GPa	Liquidus temperature of wet rock 0.1 MPa/ 1 GPa
Granites	1,233/–	1,233/953[a]		1,569/–	
Granite	1,223/1,333		1,223/893	1,293/–	1,293/983
Granite	1,153/1,333		1,153/893		1,293/993
Andesite	1,263/1,343		–/903	–/1,513	1,473/1,213
Tholeiite basalt	1,353/1,413	1,303/913		1,483/1,533	1,463/1,463
Basalt	1,353/1,413		1,343/913	–/1,523	–/1,333
Peridotite	1,403/1,493		1,403/1,153		
Peridotite	1,518/1,587				
Rhyolite	943–953/–	923/–	923–973/–		
Peridotite	1,363/1,613[b]	–/1,353			–/1,523
Peridotite	1,400/1,700[b]	1,340/1,270[b]			
Basalts	1,525[c]/–				
MORB	1,516–1,624[d]/–				
OIB	1,559–1,645[d]/–				
Picrite	–/1,798				
Komatiite	2,063/–				
Tonalite	1,173/–		1,153/903		1,293/993
Peridotite	1,405/1,535				
Quartz eclogite	–/1,588[b]			–/1,773–1,798[b]	

[a] At 200 MPa
[b] At ~3 GPa
[c] Eruption temperature of most basalts (Schubert et al. 2001)
[d] The parental liquids (Falloon et al. 2007)

most basic rocks are believed to have been formed by the partial melting of peridotite (e.g., Hall 1995), it is clear that for the formation of parent magma in the source layer of volcanic magma, the temperature must be above the solidus temperature of peridotite and its value should also be relative to the percentage of partial melting of the peridotite. As for the magma forming at depths of ~120 km, the initial magma composition would be dry. It is clear from Tables 2.14 and 4.12 that the temperature at a depth of ~90 km (~3 GPa) should be >1,613–1,713 K, and >1,743–1,843 K at a depth of ~115–120 km (~4 GPa), given that the gradient dT/dP of the solidus for a variety of peridotite compositions is 130–132 K/GPa (Herzberg et al. 2000). These values correspond to other published data showing that the solidus temperature of dry peridotite at a depth of ~100 km is around 1,700 K (Schubert et al. 2001). Research also shows that the temperature of parent magmas is usually very high. For example, the liquidus temperatures of

parent magmas for a number of known basaltic magmas at a pressure of 0.2 GPa are within the range of 1,516–1,645 K (Falloon et al. 2007). At the same time, the mantle potential temperatures in regions and depths of formation of mid-ocean ridge basalts (MORB) (1–2 GPa) and Ocean Island Basalts (OIB) (1–2.5 GPa) are estimated to be in the range of 1,591–1,661 K and 1,775–1,838 K, respectively (Falloon et al. 2007). Green et al. (2001) reported that 'Hot-Spot' and MOR primary basalts are derived from the mantle with a potential temperature of ~1,703 K. Thompson and Gibson (2000) reported a mantle potential temperature of ~1,898 K for Mauna Loa picrite. They also showed that the potential temperatures are ~150–250 K higher than those calculated for steady-state Phanerozoic plumes and ~400 K above ambient mantle temperatures.

The conditions in forming and rising magma calculated for pressures of 4 to 0 GPa and temperatures of 1,600, 1,700, 1,800 and 1,900 K are presented in Table 4.13. For values of the thermal expansion coefficient (α) and compressibility coefficient (β) for basic magmatic rocks, the average values from Table 4.11 for molten MORB (8.8×10^{-5} 1/K) and peridotite melt (0.056 1/GPa) were used. Similar calculations for magma of wet rhyolitic composition were conducted for pressures of 1 to 0 GPa and temperatures of 1,500, 1,200 and 1,000 K and are presented in Table 4.14. Again, the average values of molten rhyolites (6.6×10^{-5} 1/K) and average silicate melt (0.07 1/GPa) from Table 4.11 were accepted as values for the thermal expansion coefficient (α) and compressibility coefficient (β) for rhyolotic magmatic rocks, respectively. It was shown (Pilchin 1986; Pilchin and Eppelbaum 2009; see also Sect. 2.7) that conditions of equilibrium can be used to determine the corresponding pairs of values P_0, T_0, which vary for different types of matter and at different depths for the same matter, and which ultimately characterize the normal conditions of the matter. From Eq. (2.7.5) representing conditions of equilibrium, the ratio $\Delta P/\Delta T$ can be defined as:

$$\frac{\Delta P}{\Delta T} = \frac{\alpha}{\beta}. \tag{4.2.7}$$

Equation (4.2.7) can also be used to determine the increase in pressure under excess temperature (P_T). For example, using data from Table 4.11 for the average silicate melt ratio $\alpha/\beta = 0.43$ MPa/K, the increase of pressure will be 0.43 MPa with an increase in temperature of 1 K. Estimates of this ratio for melts by Lowenstern (1995) gave values of about 0.5–1.5 MPa/K, which is higher than the average value for silicate melt. The accepted values for the thermal expansion coefficient (α) and the compressibility coefficient (β) for basaltic and rhyolitic magmatic rocks have α/β ratios of 1.571 and 0.943 MPa/K, respectively, which are in line with the estimates by Lowenstern (1995). The value of P_C for Tables 4.13 and 4.14 was calculated using Eq. (4.2.3) and data from Table 4.13; however it should also be taken into consideration that at great depths where the expansion of volume is usually impossible, the melt occupies the same volume that was previously occupied by solid rock. Instead of leading to the expansion of molten basic $(\Delta\sigma/\sigma) = -(0.0530 - 0.1081)$ and rhyolitic $(\Delta\sigma/\sigma) = -(0.0482 - 0.1154)$

Table 4.13 Thermodynamic conditions within forming and rising magma of basaltic composition

Temperature of magma (K)	Lithostatic pressure (P_0) (GPa)	Normal temperature (T_0) (K)	P_T (GPa)	P_C (GPa)	Total P[a] (GPa)
1,600	4	2,818	−1.911	1.00–2.16	3.09–4.25
	3	2,182	−0.913	0.24–1.42	2.33–3.51
	2	1,546	0.085	−0.48–0.64	1.61–2.63
	1	909	1.084	−(1.24–0.12)	1.16–1.96
	0.5	591	1.583	−(1.62–0.88)	0.46–1.20
	0	273	2.082	−(2.00–1.26)	0.08–0.82
1,700	4	2,818	−1.754	1.00–2.16	3.25–4.31
	3	2,182	−0.752	0.24–1.42	2.49–3.67
	2	1,546	0.242	−0.48–0.64	1.76–2.88
	1	909	1.241	−(1.24–0.12)	1.00–2.12
	0.5	591	1.740	−(1.62–0.88)	0.62–1.36
	0	273	2.238	−(2.00–1.26)	0.24–0.98
1,800	4	2,818	−1.597	1.00–2.16	3.40–4.56
	3	2,182	−0.599	0.24–1.42	2.64–3.82
	2	1,546	0.399	−0.48–0.64	1.92–3.04
	1	909	1.398	−(1.24–0.12)	1.16–2.28
	0.5	591	1.897	−(1.62–0.88)	0.78–1.52
	0	273	2.396	−(2.00–1.26)	0.40–1.14
1,900	4	2,818	−1.440	1.00–2.16	3.56–4.72
	3	2,182	−0.442	0.24–1.42	2.80–3.98
	2	1,546	0.555	−0.48–0.64	2.08–3.20
	1	909	1.555	−(1.24–0.12)	1.32–2.44
	0.5	591	2.054	−(1.62–0.88)	0.93–1.67
	0	273	2.553	−(2.00–1.26)	0.55–1.29

[a] Total pressure P calculated using Eq. (4.2.4)

Table 4.14 Thermodynamic conditions within forming and rising magma of rhyolitic composition

Temperature of magma (K)	Lithostatic pressure (P_0) (GPa)	Normal temperature (T_0) (K)	P_T (GPa)	P_C (GPa)	Total P (GPa)
1,500	1	1,333	0.16	0.72–1.86	1.88–3.02
	0.7	1,012	0.46	0.53–1.67	1.69–2.73
	0.5	803	0.66	0.40–1.54	1.56–2.70
	0.3	591	0.86	0.27–1.41	1.43–2.57
	0	273	1.16	0.08–1.22	1.24–2.38
1,200	1	1,333	−0.13	0.72–1.86	1.59–2.73
	0.7	1,012	0.18	0.53–1.67	1.41–2.55
	0.5	803	0.37	0.40–1.54	1.27–2.41
	0.3	591	0.57	0.27–1.41	1.07–2.28
	0	273	0.87	0.08–1.22	0.95–2.09
1,000	1	1,333	−0.31	0.72–1.86	1.41–2.55
	0.7	1,012	−0.01	0.53–1.67	1.22–2.36
	0.5	803	0.19	0.40–1.54	1.09–2.21
	0.3	591	0.39	0.27–1.41	0.96–2.10
	0	273	0.69	0.08–1.22	0.77–1.91

rocks, this would result in the compressing of the basic and rhyolitic melt respectively by $(\Delta\sigma/\sigma) = (0.0560 - 0.1212)$ and $(\Delta\sigma/\sigma) = (0.0506 - 0.1305)$, to the volume of the original solid rocks. Changes of P_C within a magma conduit can be calculated by subtracting the value of pressure generated by the magma within it at the depth of calculation from the initial value of P_C within the magma source layer.

Let us analyze the results for the pressures listed in Tables 4.13 and 4.14. First, it should be noted that for both basaltic and rhyolitic rocks the calculated value of total P represents the maximum, since it does not take into account the unloading of pressure caused by the increase of magma volume as it rises through the conduit (the volume of the conduit—ΔV_C) and the erupted magma volume (ΔV_E). The levels of unloading of pressure with increases of volume can be significant, and can equal 0.179 and 0.143 GPa per 1 % of increased volume for basaltic and rhyolitic magmas, respectively. Estimates of the minimal volume increase caused by magma rising within a conduit (ΔV_C) for basalt rising from the depths with pressures of 4, 3, 2 and 1 GPa report volume increases of 0.0030, 0.0023, 0.0015 and 0.0008 km^3, respectively. Similar calculations for the volume change within rhyolitic magma rising from depths corresponding to lithostatic pressures of 1, 0.7, 0.5 and 0.3 GPa yielded values of volume change (ΔV_C) of 0.0008 km, 0.0005 km^3, 0.0004 km^3 and 0.0002 km^3, respectively. The volume change resulting from erupted magma (ΔV_E) is equal to the real volume of a magmatic eruption by a volcano. It is clear from Table 4.13 that at depths corresponding to lithostatic pressures of 4, 3 GPa and even lower (>2.0–2.5 GPa), the effect of compressibility overcomes that of thermal expansion, leading to a decrease in

pressure ($P_T < 0$) within the magma source layer (or magma chamber). It is clear that this effect only increases with depth, making it more difficult for magma to be formed at greater depths than at a pressure of 4 GPa. This also creates a huge problem for the formation of magma plumes at great depths within the mantle.

Furthermore, for magmas that have minimal differences in density between their solid and molten states ($\Delta\sigma/\sigma \sim 0.0560$) at temperatures within the range of 1,600–1,900 K, the pressure within the magma is not strong enough for it to start to rise. Only a magma temperature of 1,900 K at a depth corresponding to a lithostatic pressure of 2 GPa would cause the pressure within the magma to be $\sim$0.08 GPa greater than the lithostatic pressure, but such a small excess in pressure is not enough to overcome the friction of magma against the conduit walls or even the smallest increases in magma volume. However, in cases of rock with a maximum or quasi-maximum difference of density between its solid and molten states ($\Delta\sigma/\sigma \sim 0.1212$), the excess in pressure would indeed be high enough for the magma to begin rising from depths with a pressure of 4 GPa or lower, and it could even preserve such high pressures within the magma until it reached the surface and thus could cause significant tectonic destruction on its way by forming faults, dykes, etc. At the same time, the formation of such tectonic elements would lead to an increase in volume and additional unloading of pressure. In magmas with intermediate differences in density values between their solid and molten states ($\Delta\sigma/\sigma$ somewhere is between 0.0560 and 0.1212), the excess pressure would not be enough to reach the surface either, and the magma would stop at a certain depth and form a magma chamber. In fact, even for magmas with a high difference in density between the solid and molten states ($\Delta\sigma/\sigma$ close to 0.1212), the unloading of pressure by changes in volume can be great enough to stop its rising for a variety of reasons.

In a volcano, excess pressure is also required for the magma to reach the crater. For basaltic magmas within volcanoes as high as 2, 3, 4 and 5 km, the minimal additional pressure for the magma to reach their craters would be 0.051, 0.076, 0.101 and 0.127 GPa, respectively; in rhyolitic magmas within such volcanoes, the minimal additional pressure for them to reach the craters would be 0.043, 0.064, 0.085 and 0.107 GPa, respectively. Another important feature shown in Tables 4.13 and 4.14 is that for both basalts and rhyolites the value of P_T increases with decrease in depth. This effect has been analyzed (Pilchin 1986; Pilchin and Eppelbaum 2009) and is related to the fact that normal temperature (T_0) declines with decreases in depth. Therefore the change of pressure caused by thermal conditions is characterized by the value:

$$\Delta P_T = \frac{\alpha}{\beta}(T_{02} - T_{01}), \tag{4.2.8}$$

where T_{02} and T_{01} are the normal temperatures of magma at two different depths (T_{02} representing the deeper one).

Since the value of the normal temperature (T_0) of magma declines with decreases in depth (see Tables 4.13 and 4.14), the excess pressure caused by the thermal regime will always increase with decreases in depth. All of the above

highlights the importance of understanding and using the correct thermal expansion coefficient (α) and compressibility coefficient (β) values for magmatic rock. Unfortunately, in a number of studies related to calculations of the influence of conditions within magma, density of rocks at great depths, etc., either thermal expansion (e.g., Karlstrom et al. 2010) or compressibility (e.g., Percival and Pysklywec 2007) are often ignored.

It is clear from Table 4.14 that across a wide range of temperatures, the total pressure in absolutely all cases involving the formation of rhyolitic magmas is much greater than the lithostatic pressure. This means that in all these cases there are no obstacles preventing the rhyolite magma from reaching the surface. It is also evident that the excess pressure within rhyolitic magmas is much higher than within basaltic magmas, making rhyolitic magmas more powerful in terms of initiating various tectonic processes, and they can be much more destructive than basaltic magmas. This is consistent with the fact that caldera formations are usually related to rhyolitic magmatism. The data in Table 4.14 show that even though pressure within volatiles accounts for the explosive nature of the eruption in rhyolitic magmas, the main cause of the more powerful and explosive eruptions of rhyolitic magmas is really the greater excess pressure as compared to basaltic magmas. In fact, such significant excess pressures require much greater pressure unloading, which is mostly caused by increases in volume during eruption or various tectonic processes (formation of faults, dykes, etc.).

Another important feature that should be taken into account is the value of the initial volume of the magma source layer or magma chamber. The unloading of pressure, as was seen from Eq. (4.2.2) is dependent on the value of $\Delta V/V_0$, which can be the same for both huge and small volumes of the magma chamber (V_0). The only difference is that for a similar unloading of pressure, magma chambers with a large initial volume require a much a greater change in volume (ΔV) than magma chambers with a small initial volume (V_0) for the same value of $\Delta V/V_0$. The magma for all LIP had enormous volumes of magma in source layers without any intermediate magma chambers. However, it is quite a different story for most ordinary magmatic events and volcanoes. For instance, the 1980 eruption of the Mount St. Helens volcano had an estimated conduit length of $\sim$7,200 m, a channel diameter of $\sim$18 m, but a volume of the magma chamber as small as 0.56 km^3 (Swanson and Holcomb 1990; Mel'nik et al. 2006). In contrast, estimates indicate a huge volume magma chamber for the Santiaguito in Santa María volcano in Guatemala (Mel'nik et al. 2006), whose catastrophic eruption in 1902 brought about 10 km^3 of magma to the surface without even forming a caldera. However, the latter could have been caused by the relatively deep location of the magma chamber (a conduit length of $\sim$5,000 m with a diameter of $\sim$20 m) with an estimated magma chamber volume of $\sim$64 km^3 (Mel'nik et al. 2006). An interesting case of volume change can also be seen in the formation of a caldera, in which the collapse of layers above the magma chamber lead to a change in the initial volume of the magma chamber (V_0), as well as additional pressure from the collapsed layers upon the magma within the chamber. Such circumstances can

actually facilitate the continuous eruption of rhyolitic magmas and increase the amounts of magma brought forth.

Most research on this topic indicates that on average, magmatic volatiles are composed of mostly water, CO_2 as the second largest component, and then SO_2 (e.g., Bayly 1968; Stoiber 1995; Scaillet and Pichavant 2005; Shinohara 2008; Shinohara et al. 2008). This is in line with the estimated content of water, carbon and sulfur in the crust which adheres to a ratio of water:carbon:sulfur in proportions of 40:6:1 (Holland 1984). It also corresponds to data reported by Lowenstern (1995) showing that silicate-melt inclusions (MI) in rhyolites usually contain between 69 and 78 wt% Si, between 3 and 7 wt% water (generally >4 wt%), carbon dioxide up to 1,000 ppm, chlorine 600 to 2,700 ppm, fluorine 400 to 1,500 ppm, and sulfur <200 ppm. This variation in the content of the most common components of volcanic gases is easy to explain. Water has the highest abundance among volatiles within the crust, and it is also the most soluble volatile in any magma. Carbon is the second most abundant component of magmatic volatiles within the crust; CO_2 is usually produced within the crust by the decomposition of carbonates at high temperatures (Pilchin and Eppelbaum 2006) and no carbonates are stable on contact with basaltic magma or felsic magma. The SO_2 within the crust is a product of the oxidation of elemental sulfur released during the decomposition of sulfides at high temperatures (Pilchin and Eppelbaum 2009); sulfides have a high enough stability temperature to withstand contact with most felsic melts, but they decompose on contact with basaltic magma. This helps explain why most felsic magmas have a higher content of CO_2 than of SO_2.

Based on the nature of the formation (mostly in oceanic areas) and the temperature of formation ≥473 K (Pilchin and Eppelbaum 2006), the concentration of carbonate rocks is the greatest in the upper part of the crust, where they can be decomposed by magma on its way up to the surface or within a shallow magma chamber. This is in line with data (Bayly 1968) showing that the concentration of sulfur volatiles in acidic magmas is much lower than in basic magmas. If felsic magmas (rhyolitic, dacitic, etc.) contain significant amounts of sulfur-based volatiles, this may be an indication that these felsic magmas were either initially overheated or generated within a magma chamber formed during basaltic magma underplating. In either case, the presence of enormous volumes of basaltic magmas would necessarily deliver a significant amount of volatiles, including SO_2 and H_2S, picked up by the basaltic magma on its way up. In all instances the concentration of volcanic gases depends to a great extent on the rock composition of layers through which the magma rises, and the gas is a product of the types of rocks (carbonates, sulfides, etc.) or volatiles present.

The amount of volatiles released by erupting magmas is always much greater than the amount dissolved in it (Wallace 2001). This also supports the assumption that carbonates, sulfides, and certain other kinds of rocks are decomposed by the magma on its way up to the surface, because regardless of the limited solubility of any volatile component within the magma, saturated magma continues the decomposition of rocks and minerals as a function of their conditions of stability. The extra quantities of volatiles are then contained within the porous space formed

within the magma. Estimates show that during the decompression of magma with an initial dissolved gas content of 5–7 wt%, the bubbles could occupy up to 99 % of its volume, though magmatic matter with such porosity is unknown in nature (Mel'nik et al. 2006). On the other hand, even though the solubility of volatiles, which increases with rising pressure (P) and decreases with rising temperature (T) could be high, saturated magmas are likely to release volatiles at shallow depths as they rise due to the progressive drop of pressure within them. Research on the solubility of water and CO_2 in some magmas (Gramenitsky et al. 2000) showed that the solubility of water in some magmas can reach 9–12 wt%, the highest solubility of water is in granitic and syenite magmas, solubility of water increases with increases in pressure, and the solubility of CO_2 in magmas is less than that of water reaching values of 0.5–4.0 wt%. At the same time, it is obvious that neither water nor CO_2 can remain dissolved in such quantities within the rising magma since the pressure continually drops down to atmospheric 0.1 MPa. The release of volatiles from the magma is thus maximal near and at the surface, because the solubility of volatiles in magma at a pressure of $\sim$0.1 MPa is close to 0.

4.3 Mud Volcanoes

Mud volcanoes are widespread both on land and in marine basins, in collision and transtensional settings (e.g., Kholodov 2002; Limonov 2004). The main conditions for mud volcano formation are a thick sedimentary cover (several kilometers) and plastic clayey components with an anomalously high formation of pore pressure and the presence of thermal water (Pilchin 1985b; Limonov 2004). Currently, more than 900 terrestrial and 800 offshore mud volcanoes are known or presumed to exist (Dimitrov 2002). More than a quarter of all the known mud volcanoes are concentrated within the Caucasus (e.g., Kadirov et al. 2005) and most (more than 220) (Kholodov 2002) are located within the "Abich triangle" (Abich 1863) near Baku.

One of the most interesting problems in oil and gas geology is related to the genesis of mud volcanoes and their relationship to oil and gas fields and deposits. A mud volcano is a tectonic structure formed during the formation and eruption of significant amounts of water-rich sedimentary rocks (mostly clays and/or silts) in regions usually characterized by enormous amounts of sedimentary deposits collected over a short time. As it erupts, a mud volcano forms a mound up to a few 100 m high. They are known to form both onshore and offshore, and can in some cases create huge island structures (e.g., Bulla Island in the Caspian Sea). Researchers usually make a distinction between mud intrusions (called mud diapirs) and extrusions (called mud volcanos) (Dimitrov 2002), even though their origin can be similar. The term sedimentary volcanism is also used to refer to mud volcanoes (Kopf 2002). In many cases, the appearance of mud volcanoes is linked to regions of formation of oil and gas fields, volcanic and seismic activity, and orogenic belts (Kopf 2002). Some mud volcanoes have additional small craters somewhere off their main crater which are called gryphons. Most mud volcanoes

are located within the Alpine-Mediterranean belt with the highest concentration (over 600) found in Azerbaijan and adjacent parts of the Caspian Sea. For more details on locations and distribution of mud volcanoes around the world, see reviews on the issues of mud volcanoes in (Dimitrov 2002; Kopf 2002).

Combined thermal and gravity field studies on the mud volcanoes in central Azerbaijan are presented in Fig. 4.4. This figure reveals the clear inverse correlation between the observed heat flow (positive, Fig. 4.4a) and significant Bouguer gravity (negative, Fig. 4.4b) anomalies over mud volcanoes. On the other hand, the direct correlation between gravity anomalies (Fig. 4.4a) and topography (Fig. 4.4c) can be explained by an insufficient Bouguer reduction. Obviously, further integrated gravity-thermal field modeling will enable to solve this problem.

All geologists, without exception, have come to the conclusion that the presence of a thick clay-rich plastic sedimentary layer is necessary for the formation of mud volcanoes (Durmish'yan 1961; Kalinko 1968; Magara 1978; Pilchin 1985b; Dimitrov 2002; Kopf 2002). Because this waterproof cap layer has a very small heat conductivity coefficient, this can lead to the accumulation of huge amounts of heat energy below it. At the same time, it can prevent convective heat loss to fluids, mainly water, which has an extremely high heat capacity and is capable of absorbing vast amounts of heat. Since a thick clay cap layer is also necessary for the formation and preservation of oil and gas deposits, both the problem of their formation and the formation of mud volcanoes are interrelated. Some researchers believe that mud volcanoes are markers of the presence of oil and gas fields in the area (Jakubov et al. 1971; Rakhmanov 1987).

It is generally accepted that the presence of huge amounts of water at depths below the clay-rich sedimentary layer is also necessary for the formation of mud volcanoes (Pilchin 1985b; Rakhmanov 1987; Kopf 2002). This is obvious given the known pervasiveness of huge amounts of water and even water-rich mud volcanoes, as well as the presence of signs of hydrothermal activity and water-containing and water-altered rocks and minerals (Pilchin 1985b; Rakhmanov 1987).

Some researchers also believe that the formation of mud volcanoes requires the presence of huge volumes of gases (Kalinko 1964; Durmish'yan 1961; Jakubov et al. 1971; Salayev and Mamedov 1971; Brown 1990; Warn and Ichram 1997; Kopf 2002). However, as it was shown in (Durmish'yan and Khalilov 1972; Khalilov and Kerimov 1981), the presence of gas during the eruption of mud volcanoes is not necessary. Moreover, Khalilov and Kerimov (1981) suggested placing mud volcanoes that erupt without a significant quantity of gases into a different category. Kalinko (1968) also stated that mud volcano chambers usually do not contain any significant gas deposits. The absence of any relationship between large gas deposits and mud volcanoes also supports this fact (Kalinko 1968). Research shows (Pilchin 1985b; see also Sect. 2.7) that the coefficient of abnormal stratum pressure (K_{aP}) in fluid is minimal in pure gas fields, and that the value of K_{aP} in numerous cases is lower than the hydrostatic pressure. In addition, the compressibility coefficient of any gas is very high. However, the K_{aP} significantly increases with the presence of water in a gas field. This proves that water plays a more important role in the formation of overpressure than gas. All of the

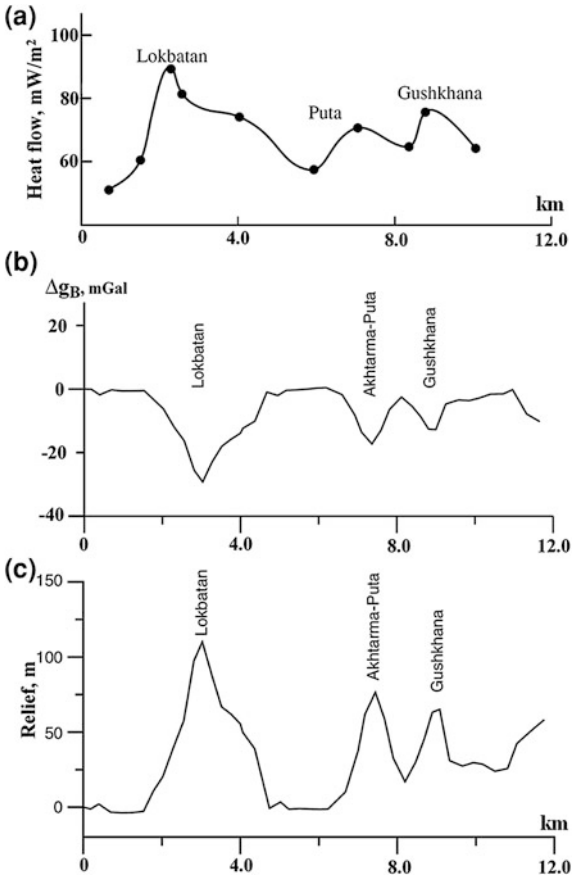

Fig. 4.4 Changes in heat flow (**a**), Bouguer gravity (**b**), and topography (**c**) along the profile crossing the Lokbatan–Akhtarma-Puta–Gushkhana mud volcanoes (compiled from Kadirov and Mukhtarov 2004; Kadirov et al. 2005, with modifications after Eppelbaum and Khesin 2012)

above suggests that the presence of significant gas deposits is not necessary for the generation and evolution of mud volcanoes. Furthermore, mud volcanoes actually play a destructive role in oil and gas fields, and can deliver hydrocarbons to the surface during eruption (Salayev and Mamedov 1971; Pilchin 1985b). The absence of any significant oil or gas deposits in the Shemakha-Gobustan zone of Azerbaijan, in which greatest number of mud volcanoes are found, also argues in favor of this conclusion.

Research points to the important role of deep faults under the clay-rich layer in the formation of mud volcanoes (Durmish'yan 1961; Jakubov et al. 1971; Pilchin 1985b; Rakhmanov 1987; Kopf 2002). However, some researchers (Kalinko 1964, 1968) believe that while faults could assist in their genesis, their presence is not necessary, and that some faults could have even been formed by mud volcano activity itself. Magara (1978) suggested that the only features that are important to the formation of mud volcanoes are fractures above the clay-rich layer.

Without question, one of the key roles in mud volcano formation is the emergence of abnormally high stratum pressure (AHSP) or abnormally high

porous pressure (AHPP), which can in some cases be greater than the lithostatic pressure (Hubbert and Rubey 1959; Kalinko 1964, 1968; Durmish'yan 1961; Miffin 1970; Hedberg 1974; Ozernii 1981; Mekhtiev et al. 1982; Williams et al. 1984; Pilchin 1985b; Reed et al. 1990; Maltman 1994; Dimitrov 2002; Pilchin and Eppelbaum 2002; Mazzini et al. 2007; see also Sect. 2.7). However, there are different points of view as regards the origins of this AHSP/AHPP. Some authors have argued that the formation of AHSP is caused by the compression of layers by an overburdening weight (Kalinko 1964, 1968; Magara 1978). Other scientists believe that the primary factor in the formation of AHSP is the effect of temperature (an aqua-thermal effect) (Magara 1978; Kerimov et al. 1980; Mekhtiev et al. 1982; Pilchin 1985b; Pilchin and Eppelbaum 2002). Still others claim that AHSP depends on the height of hydrocarbon deposits (Durmish'yan 1961; Durmish'yan and Khalilov 1972). In the first case, it is clear that the lithostatic pressure cannot generate an AHSP greater than itself (Pilchin 1985b). In fact, the AHSP generated by lithostatic pressure would be much lower than the lithostatic pressure due to unloading of pressure with change of volume (Mekhtiev et al. 1982; Pilchin and Eppelbaum 2002; see also Sect. 2.7). The increase in overpressure within the chamber of a mud volcano is the cause of its formation, not a consequence (Pilchin 1985b). The generation of AHSP/AHPP by the aqua-thermal effect is described in detail in Sect. 2.7, and occurs according to Eq. (2.7.4). Last, the height of hydrocarbon deposits would be unable to generate significant AHSP, because of their thermal expansion and compressibility (Pilchin 1985b). Moreover, the data in Table 2.16 show that gas, oil and gas and oil fields have the lowest measured values of K_{aP}.

Many researchers believe that one of the main forces causing the ascent of mud is the force of buoyancy (Kopf 2002), since the content of mud volcanoes is low in density and no additional driving forces beyond this density inversion are required to trigger its rise. Dimitrov (2002) showed that even though buoyancy forces provide the driving mechanism and mud diapirs are formed in a very similar way to salt diapirs in their diapiric stage, they are not powerful enough to cause a mud magma eruption, and an additional force is needed. This additional force is abnormal porous pressure.

With respect to the role of buoyancy in the formation of mud volcanoes, it is erroneous to refer to buoyancy forces for upper crustal layers that have a viscosity on the order of up to 10^{23}–10^{25} Pa s, since they are most certainly not composed of liquid. An excellent example of the absence of buoyancy within the upper crust is the huge eclogite massif in Norway that has large amounts of extremely dense rocks (density about 3,300–3,400 kg/m^3) that have been in place for over 400 Ma and are not in any hurry to sink (Pilchin 2005). Another piece of evidence for the incompatibility of Archimedes' Law for upper crustal layers is related to the presence of numerous diapir structures which have never reached the surface within regions of mud volcano activity (Lower Kura Depression, Gobustan, South Caspian Depression). Similar situations exist for numerous salt diapirs in the Precaspian Depression in Russia, which likewise have not reached the surface. Numerous cases of felsic magmas, some of which have densities as low as

2,200 kg/m^3, are also known to have never reached the surface. Moreover, using the isostatic theory of floating, Pilchin (1986) calculated the necessary dimensions for a mud volcano chamber. The calculations show that for clay material from a mud volcano chamber to reach the surface, the presence of pressure in the chamber must be greater than the lithostatic pressure exerted by the weight of the column of clay rocks from the chamber to the surface. Simple arithmetic shows that for the creation of such pressures at the expense of the insufficient density of clay, the thickness of the mud volcano chamber would have to be 4–5 times greater than its height. Given that the depth of the chambers for most mud volcanoes is about 5 km or more, for a mud volcano to form, the chamber thickness would have to be no less than 20–25 km, which is impossible.

Mud volcanoes are known to form in regions of significant tectonic and seismic activity (Brown 1990; Kopf 2002, 2008; Bonini 2007; Mazzini et al. 2007, 2009; Rukavičková and Hanžl 2008). This led Kopf (2002) to suggest that tectonic activity and earthquakes are also causes of mud volcanoes. In numerous cases, mud volcanoes are located in regions with compressional tectonics (Dimitrov 2002; Kopf 2002). Dimitrov (2002) came to the conclusion that the tectonic forces of compression represent an important additional factor in creating high fluid pressure.

In numerous cases (e.g., Mediterranean mud volcanoes), mud volcanoes have formed in regions with large layers of salt deposits. Such salt deposits were generated in the Mediterranean during the Messinian Salinity Crisis at the end of the Miocene (from about 5.96 to 5.33 Ma) (e.g., Camerlenghi et al. 1995; Eppelbaum et al. 2012). In this instance the mud layers are located below the layers of salt covering almost the entire Mediterranean region. In another case, large-scale mud diapirism took place in the Gulf of Mexico, where salt domes are very common features and can provide pathways for the plastic mud above the salt layer (Hovland and Judd 1988).

Many mud volcanoes were formed in regions of volcanic activity (White 1955; Freeman 1968; Sheppard et al. 1992; Chiodini et al. 1996; Kopf 2002; Mazzini et al. 2007; Rukavičková and Hanžl 2008). They exist in virtually all regions across the Pacific Ring of Fire (Kopf 2002), the most active volcanic regions on Earth. In the Copper River Basin of Alaska, mud volcanism has been reported to be associated with the occurrence of hot springs (Nichols and Yehle 1961). Interestingly, the mud volcanoes of the Klawasi group release large amounts of CO_2 (Nichols and Yehle 1961), making them possibly of volcanic-related origin. The hydrothermal Cu–Zn–Pb deposits of Mount Sullivan (southeastern British Columbia, Canada) are thought to have evolved from a mud volcano complex as well (Slack et al. 1998). Among other cases of relationships between thermal activity and mud volcanism are the hot springs of Lake City of northeastern California (White 1955) and Yellowstone National Park (Sheppard et al. 1992). The mud volcanoes in Yellowstone National Park emit mostly CO_2 and other gases of volcanic origin (Sheppard et al. 1992). Rukavičková and Hanžl (2008) used the term *hydrothermal mud volcanoes* to describe mud volcanoes occurring in regions of recent volcanic activity. They are also found in some cases in

association with regions of serpentinization and formation of serpentinite domes, for instance in the Mariana Islands (Mottl 1992) and the Diablo mountain range in the Franciscan Belt of California (Oakeshott 1968).

Mud volcanoes are also frequently found in association with regions of elevated and high temperatures within the crust (e.g., Pilchin 1985b; Kholodov 2002). In general, the mud and fluid temperatures within mud volcanoes are only slightly elevated with respect to the surrounding strata, but even in relation to active volcanoes they rarely show an increase over about 1–5 K (e.g., Robertson et al. 1996). However, in some cases the temperature difference can be significant. For instance, the difference in temperature between mud volcano Håkon Mosby's fluid and the water column at the Norwegian margin is about 10–12 K (Kopf 2002). Heat flow values exceeding 1,000 mW m^{-2} are present in this area (Eldholm et al. 1999).

Waters from mud volcanoes near Etna, Sicily have temperatures of up to 319 K (Chiodini et al. 1996), and the composition of the gas and liquid phases indicates the presence of a hydrothermal reservoir with a temperature of 373–423 K. Cumin (1954) reported temperatures of freshly erupted mud as high as 319–322 K. Analysis of the isotopic composition of fluid from ODP sites in the Eastern Mediterranean shows that the fluid is a product of clay mineral dehydration (mainly smectite-illite transformation), corresponding to a depth in the range of 3.5–7 km and an elevated temperature of about 393–438 K (Dählmann and de Lange 2003). The eruption of 373 K of mud and gas that began on May 29, 2006 flooded a large area within the Sidoarjo village in Northeast Java (Mazzini et al. 2007). The eruption of boiling water was accompanied by mud, aqueous vapor, as well as CO_2- and CH_4-rich gas.

Mud volcanoes are present in such regions of the Pacific Ring of Fire as the Aleutian/Alaskan Margin, British Columbia, Cascadia Margin/Oregon, Washington, California/Nevada, Mexico, Costa Rica, Colombia and Panama, Ecuador, Java and Sumatra (Indonesia), Ryukyu Trench, Nankai Trough, Japan Trench, Japan, New Zealand, and Sakhalin (Kopf 2002). Mud pools are also located in regions of hot spring and geyser activity in such areas of the Pacific Ring of Fire as the Kamchatka Peninsula (Russia), Japan, New Zealand, as well as in such active volcanic, geyser and hot spring regions as Yellowstone National Park (see Sect. 4.1). A number of hydrothermal mud pots are also found in Yellowstone (Pitt and Hutchinson 1982).

Experimental research on water-rock interaction (You et al. 1996) shows that with an increase in temperature from 298 to 623 K, the boron content increases in porous fluid. At the same time, the boron content in the mud of Caucasian mud volcanoes is eight times greater than in regular marine clays (Ishikawa and Nakamura 1993). Similar excursions of boron content were found in mud volcanoes of certain other regions as well (Kopf 2002). This also suggests that a high temperature regime is a cause of mud volcano formation.

Based on an analysis of all the available data on mud volcanoes, the most important general conditions of mud volcano formation are as follows: (1) the sedimentary rocks that form mud volcanoes are very similar all over the world and

are mostly represented by clays, which make up the matrix of any mud volcano; (2) mud volcanoes require the presence of a thick sedimentary clay-rich layer within the sedimentary cover; (3) mud volcanoes require the presence of huge compressive forces (compressive tectonic regime); (4) mud volcanoes require the presence of a deep seated fault or faults below the thick plastic clay-rich layer, which can act as a pathway for upward migration of overheated fluids; and (5) the formation of mud volcanoes requires the presence of excess temperature under the main plastic clay-rich layer. It should be pointed out that a combination of factors is necessary for the formation of mud volcanoes. For example, the Lower Kura Depression and South Caspian Depression are not overly active tectonic zones, but they host an enormous number of mud volcanoes.

Let us analyze the causes and conditions for mud volcano formation. Clays usually have a porosity (K_p is the porosity coefficient) of up to 55 %, but in some cases their initial porosity may be as high as 80 % (Kopf 2002). For instance, the sample with the highest clay content (71.6 wt% at the Digity mud volcano in Trinidad) had the highest plasticity (47.8 %), which is in line with the maximum values of 41 wt% clay and 42 % plasticity found at the Napoli mud volcano on the Mediterranean Ridge (Kopf 2002). Water content as high as 65 % (with mud viscosity of $\sim 10^6$ Pa s) was also reported for some mud volcanoes located along the Mediterranean Ridge (Kopf 2002). It was shown (Pilchin 1985b) that the porosity of clays on average is about 45 % or even higher. In clay sedimentary layers, this porous volume is filled with water. Furthermore, the main part of the water content within clays is bound to the clay minerals, thus preventing it from leaving the clay. Given that the thermal expansion coefficient of water is about two orders of magnitude higher than any ordinary solid rock or mineral, it is clear that the thermal expansion coefficient of any clay (α_c) will mostly depend on the thermal expansion coefficient of water (α_w). The value of the thermal expansion coefficient of clay can then be defined as (Pilchin 1985b):

$$a_c \approx K_p \cdot a_w. \tag{4.2.9}$$

This means that the thermal expansion of clay is about one to two orders greater than that of any other sedimentary rock, as well as any magmatic or metamorphic rock. On the other hand, such a high concentration of water considerably decreases the viscosity of wet clay, which can be as low as $\sim 10^6$ Pa s. In comparison, the viscosity of rocks of the upper crust can be as high as $\sim 10^{23}$–10^{25} Pa s, and salt diapirs have viscosities ranging from 10^{10} to 10^{17} Pa s (depending on mineralogy) (Odé 1968). The mud in a mud diapir or mud volcano thus behaves like a single-phase viscous fluid, and according Pascal's law it transfers the pressure applied to it in all directions. This makes clay one of the best rocks for the formation and transfer of pressure, not to mention one capable of significantly increasing its volume upon heating. These features are extremely important in the generation of tectonic activity, since greater volumes of clays in a layer have a greater effect. Interestingly, other rocks and matter capable of forming diapir structures are salts,

serpentinites, and in some cases molten magmatic rocks, all of which are capable of significant increases in volume as well.

It was shown by Gavshin and Volontay (1969) and discussed in (Pilchin 1985b) that the thermal expansion coefficient of salt is about one order of magnitude greater than that of any other rock or mineral and could be the cause of the formation salt diapir structures. Serpentinites are known for their potential to increase the original volume of a rock or mineral during serpentinization by up to 40 % (Pilchin 2005). It is also known (see Sect. 4.2) that upon melting, the main magmatic rocks can increase in volume by up to 10–20 %. Strikingly, as was mentioned above, mud volcanoes are known to form in association with all three features—salt deposits, serpentinites and magmatic rocks. In addition, the value of AHSP/AHPP formed by the aqua-thermal effect can be higher than the hydrostatic pressure by $\sim$6 fold for Azerbaijan and the PreCaucasian, and by $\sim$7 fold for Turkmenistan (Mekhtiev et al. 1982; Pilchin 1985b; see also Sect. 2.7); 2–3 times greater than the lithostatic pressure in sedimentary layers. As was shown in Sect. 2.7, these values of pressure are maximal and are unloaded from time to time rather than accumulating to reach their maximum value. The eruption of a mud volcano is one such instance of unloading of pressure according to Eq. (2.7.4).

The presence of higher AHSP/AHPP than the lithostatic pressure is not enough to form a mud volcano. For example, the highest AHSP in Azerbaijan is found in the Middle Kura Depression, which has no mud volcanoes at all. The same can be observed in the Eastern Turkmenistan, Western Uzbekistan and the Pre Caucasian, in which sedimentary layers have the highest AHSP, but there are no mud volcanoes in these regions. In contrast, the lowest values of AHSP are in the Lower Kura Depression, the western part of the South Caspian Depression, the Apsheron Peninsula of Azerbaijan and in Western Turkmenistan, all of which have a great number of mud volcanoes. This discrepancy can be explained by the presence of thick clay layers only found in regions where mud volcanoes are present. A key point is that clays have a very low heat conduction coefficient and a very high specific heat capacity (due to their huge concentration of water), which allows them to accumulate great amounts of heat energy without significantly increasing their temperature and without significant heat transfer. Under conditions such as those in the South Caspian Depression, in which the sedimentary cover is up to 25 km deep and was formed over an extremely short time, the heating of clay layers requires relatively more heat to increase the temperature by the same amount than any other sedimentary layer. This is the reason why temperatures within the western part of the South Caspian Depression are only about 373 K at depths of $\sim$6 km.

By the same token, the clay layers accumulate much greater amounts of heat energy than any other sedimentary layer, which have higher coefficients of heat conduction and open porosity for fluid migration and convection, allowing much more heat energy to pass through such a layer. At the same time, most of the heat energy is absorbed by the lower parts of the clay layer, thus greatly increasing its volume and AHSP in the bottom part of clay layer. This increase of volume and AHSP is transferred through the plastic clay to all parts of the layer, exerting great

pressure on the overburden. However, as was explained in Sect. 4.2, there is no room for such an increase in volume within the layer, whose position is restricted by the surrounding layers until the pressure within it becomes greater than the lithostatic pressure and the clay breaks through the overburden, starting the rise of a diapir and forming the mud volcano.

It is important to note that the upper part of a clay layer may be cold, since there is very low heat conduction and no water convection within clays. It was shown (Pilchin 1986; Pilchin and Eppelbaum 2002; see also Sect. 4.2) that in a case where a volume cannot expand, this leads to the additional increase of pressure within the volume according to Eq. (2.7.4), since the pressure cannot be unloaded. However, as was shown in Pilchin (1985b), the formation of a mud volcano and the start of its eruption cannot take place until the AHSP becomes higher than the lithostatic pressure, which is consistent with other studies (Kalinko 1964, 1968). On the other hand, the internal energy of the layer containing the mud volcano chamber and the energy of the overlying layers of sedimentary rocks is not enough to form and support such an AHSP, and additional energy from external sources is required.

The requirements for the formation of mud volcanoes discussed above are present in about 170 oil and gas basins around the world, there are mud volcanoes in only about 25 of them (Pilchin 1985b; Rakhmanov 1987). Thus there are other likely causes entering into their formation. It is clear from all of the above that there should be some source of energy capable of forming AHSP greater than the lithostatic pressure within the clay layer.

There are numerous indicators of the presence of high temperatures in mud volcano chambers, especially those associated with volcanic activity. In addition, there are numerous cases showing hydrothermal alteration of rocks within mud volcano breccia (e.g., Pilchin 1985b). This presence of products of hydrothermal processes and hydrothermal alteration of rocks can be used to estimate the lower temperature limit during hydrothermal activity. The lowest temperatures for the formation of chalcopyrite and pyrite, which are present among other products of the breccia of mud volcanoes, are about 483 and 573–579 K, respectively (Pilchin 1985b; Pilchin and Eppelbaum 2009). Given that pyrite is present in the breccia of all mud volcanoes in Azerbaijan (Pilchin 1985b; Rakhmanov 1987, etc.), whereas chalcopyrite is not always present, Pilchin (1985b) came to the conclusion that the temperature in a mud volcano chamber should be $\geq$573 K (within a range of 573–733 K). Such a high temperature at the base of a thick clay layer would definitely be capable of generating extremely high AHSP: 3–6 times greater than the hydrostatic pressure, and about 1.5–3.0 times greater than the lithostatic pressure (Pilchin 1983, 1985b). However, analysis of the regional distribution of temperatures in the Lower Kura Depression, South Caspian Depression, and the Apsheron Peninsula showed that such high temperatures within clay layers cannot be regionally distributed, and can only be caused by local thermal anomalies formed by excess heat delivered to the clay layers from below (Pilchin 1985b).

The fact that an AHSP greater than the lithostatic pressure prevents immersion of sedimentary layers under the weight of overburden, whereas mud volcanoes are

usually formed in quick-forming depressions with a significant rate of immersion, also points to the local character of thermal anomalies in the chambers of mud volcanoes (Pilchin 1985b). At the same time, a very powerful heat source is required for local heating within a mud volcano chamber by 100–200 K and higher. Such a source of heat energy could be generated by overheated water or a water-vapor mixture (possibly in critical or supercritical condition) arriving from great depths. It is also clear that the direct contact of rising water (water-vapor mixture) with plastic clays within a mud volcano chamber is required for fast heat exchange. This would also make the presence of a deep fault or system of fractures necessary. The presence of xenoliths of Mesozoic-age rocks in the breccia of mud volcanoes in Azerbaijan (Pilchin 1985b) indicates the presence of such faults. This is also in agreement with the fact that mud volcanoes tend to form immediately after powerful earthquakes. For instance, a number of new mud volcanoes and hot springs were formed right after the catastrophic Ashkhabad earthquake of 1948. The powerful mud volcano Lusi (Java, Indonesia) began erupting 373 K of mud (Mazzini et al. 2007) on May 29, 2006 after an earthquake on the 27th (Mazzini et al. 2009). There is no doubt that in both cases, the earthquakes resulted in the formation of new fractures (or re-opening of old fractures), which became new pathways for overheated fluids and could have sped up the process of the formation and activity of mud volcanoes. An earthquake alone cannot form a mud volcano, since there are a number of other conditions that must be met. However, it could certainly help to accelerate the formation of a mud volcano and trigger its eruption, as was the case for Lusi in Indonesia.

It is also clear that the accumulation of huge amounts of overheated water-vapor mixture is only possible under a thick layer of clays, which is also a good cap rock, because a thin clay layer could not prevent it from breaking through together with the clay material, and forming a kind of mud volcano with excess hot water. Such water-rich mud volcanoes are present in regions of Kerch-Taman and on Sakhalin Island (Pilchin 1985b; Rakhmanov 1987). Meanwhile, in regions where mud volcanoes form with extremely thick clay layers, the plastic clays can resist significant stresses, transfer pressure, and accumulate the significant amounts of energy necessary to form mud volcanoes.

This said, in some regions the main causes of mud volcano formation can differ. For example, in regions of compressional tectonics, a thick clay layer can be squeezed by a moving tectonic block and since the change in volume of the plastic clay layer is negative ($\Delta V < 0$), again according to Eq. (2.7.4) rather than unloading the pressure, the term $(-(1/\beta)\Delta V/V_0)$ would cause it to increase and potentially generate a much greater AHSP than the lithostatic pressure, and could trigger formation of a mud diapir or mud volcano. For instance, in the case of the Lusi mud volcano (Java, Indonesia), both the high temperature of the mud (Mazzini et al. 2007) and the compressive strike-slip movement of the Watukosek fault (Mazzini et al. 2009) were among the main causes of its formation.

It should be stressed that in regions where mud volcanoes are found in association with the serpentinization process, both the effect of temperature (the main interval of serpentinization temperature is in the range of 473–673 K; Pilchin and

Eppelbaum 2009) and the compressional effect come into play. In cases where a thick clay layer is present, the increase in volume of the serpentinizing rock/mineral (which can reach 40 %) could easily lead to the formation of a mud volcano. When mud volcanoes are related to volcanic activity, the high temperature of the magma and pressure of rising magma flow could lead to their formation. In cases where mud volcanoes are found in association with salt layers and/or salt diapirs, the very high thermal expansion of salt would cause it to expand greatly upon heating, and apply compressive pressure on the thick clay layer, such that AHSP greater than the lithostatic pressure could be generated similar to the effect of compressive tectonics.

In conclusion, it should be emphasized that mud volcanoes are geologically significant manifestations of vertical fluid flow, and mud eruptions in sedimentary basins worldwide cause the unloading of overpressure accumulated in overheated fluid trapped under thick layers of water-rich plastic clay layers.

4.4 Formation of Overpressures and Ultrahigh Pressures in the Earth's Strata

The presence of tectonic processes is a clear indication of the formation of overpressure and ultra-high pressure (UHP) within the lithosphere and asthenosphere. For instance, processes which are usually called anti-isostatic movements (e.g., Pilchin and Eppelbaum 2002) such as orogenic movements (uplift of huge amounts of rock), the formation of uplift and/or diapir structures, obduction, etc. defy the law of gravity. This means that at a certain depth, forces greater than that of gravity must be generated. With respect to pressure, this means that there are sources of overpressure or UHP that can overcome the lithostatic pressure (Pilchin and Eppelbaum 2009). Cases of formation of volcanoes, mud volcanoes, hot springs, and rock exhumation, among others, defy gravity as well, even though these processes could be generated by buoyancy or some other isostatic forces, because these forces work against the force of gravity. Any violation of the law of gravity must have a physical explanation behind it. It is also clear that for an uplifting process to begin, overpressure (P) is necessary and must be greater than the lithostatic pressure (P_{Lh}):

$$P > P_{Lh}. \tag{4.4.1}$$

In fact, the pressure P must overcome not only the lithostatic pressure (P_{Lh}) but also all the forces of friction along the way, which can be very high (Byerlee's law: the coefficient of friction of almost every type of crustal rock falls within the range of 0.6–0.85; Byerlee 1978). Conversely, any process of immersion of a sedimentary basin or lithospheric block represents the fact that the pressure generated beneath it falls short of the lithostatic pressure. This also means that they are out of isostatic equilibrium. The most graphic violation of the law of gravity is the

obduction process, where in numerous cases extremely dense peridotite and eclogite rocks are thrust on top of light upper crustal rocks (Pilchin 2005; Pilchin and Eppelbaum 2009). Such a process most certainly requires gigantic external forces moving the obducting plates. The causes of formation of overpressure and UHP may be different, but none of them should violate the laws of physics.

On the other hand, any process of geological change or development in a region related to specific changes in matter (rocks, minerals, fluids) is subjected to the laws of thermodynamics. It is well known from physics that any force creates pressure (P), which is one of the main parameters of thermodynamics. Furthermore, pressure cannot exist independently of such important thermodynamic parameters as temperature (T) and volume (V). Thus, it crucial to analyze the current thermodynamic conditions for any geological region, and define possible thermodynamic conditions for different periods during the region's evolution using results of certain processes in the past.

The presence of such contrasting tectonic processes as orogeny, obduction, subduction, uplift, immersion, and related ones means that in these cases the lithostatic pressure cannot be taken as the real pressure, since there is no isostatic equilibrium (Pilchin and Eppelbaum 2009). In other words, the lithostatic pressure generated by gravity cannot represent the real pressure in tectonically active regions, which are very common throughout the world.

Let us discuss some processes of overpressure and UHP formation. The causes of formation of overpressure, including overpressure greater than the lithostatic pressure, in porous fluid (see Sect. 2.7), volcanic magma (see Sect. 4.2) and mud volcanoes (see Sect. 4.3) were discussed in other sections. Wangen (2001) showed that mechanical compaction and cementation of porous space are the mechanisms generating high overpressure and the strongest expulsions. A number of models of the generation of overpressure and UHP have been developed to explain the enigmatic exhumation of high pressure—low temperature (HP-LT) and UHP-LT rocks (Burov et al. 2001). One of the models is based on deep subduction of the continental crust to depths of about 200–250 km (Chemenda et al. 1995), followed by decoupling and positive buoyancy-driven exhumation of the crustal material from about 100 km. However, this model does not take thermal evolution into account, which is crucial for reproducing P–T relationships, not to mention that rheology and buoyancy forces are highly dependent on temperature (Burov et al. 2001). There are also models of overpressure formation using subduction and large-scale compressive instabilities (Cloetingh et al. 1999; Burg and Podladchikov 1999).

Burov et al. (2001) divided models on exhumation of HP and UHP rocks into two groups: (1) extension and erosion causing the removal of the overburden and (2) lithospheric scale processes explaining the exhumation of UHP metamorphic rocks. They came to the conclusion that in most cases extension and erosion cannot be considered efficient mechanisms for the exhumation of UHP rocks from mantle depths. In reality, extensional forces can only weaken the upper layers of the crust (or lithosphere, depending on scale of the process) but they do not have any effect on rocks at great depth. Moreover, strong extensional forces cannot be

generated within the layer itself without an external force. In most cases, the extension of the upper layer is related to expansion of one of the layers below it. It should also be taken into account that UHP rocks (coesite- and diamond-containing rocks) formed at such great depths, unless in the presence of giant external horizontal forces, cannot come up to the surface by fast erosion of overburden.

A thermodynamic method for calculating overpressure and UHP was devised by Pilchin (1976, 1978a) and modified in (Pilchin 1983, 1986; Pilchin and Eppelbaum 2009). This method (see also Sect. 2.7) can be used to calculate overpressure and UHP formed by excess temperature and the presence of compressive stress, as well as unloading of pressure with change (increase) of volume.

Burov et al. (2001) showed that in cases with no significant tectonic overpressure, rocks must be driven along the subduction plane to depths of about 100–150 km in order to attain pressures on the order of those expected in the mantle. At the same time, most of the existing overpressure models account only poorly for actual data (Burov et al. 2001).

Mancktelow (1995) formulated a channel flow model, which assumes that the flow of the sedimentary/crustal material in a narrow channel between the subducting and overriding plates can produce pressure as high as 2 GPa at a depth of about 40 km. However, having such a channel, in addition to the problems of both subducting and the overriding plate by clinching them, also violates the laws of physics, since it would be impossible for the nearly doubled pressure formed within a channel in either the crust or lithosphere not to have an effect or interact with the surrounding rocks.

The overpressure model by Petrini and Podladchikov (2000) suggests that compressive tectonic forces as high as the lithostatic pressure are required to maintain stability in regions with ongoing horizontal shortening and crustal thickening, which would double the total pressure in the belts. According to this model, increases in pressure with respect to lithostatic conditions result from both the contribution of horizontal stresses and flexural vertical loads. The model predicts different types of increases in pressure with depth for different rheological behaviors. However, as the authors themselves note, their model conflicts with thermodynamics: “Indeed, at high differential stresses, it is legitimate to question the validity of classical thermodynamics” (Petrini and Podladchikov 2000, p 73). In point of fact, classical thermodynamics can easily explain the presence of pressures two or more times greater than the lithostatic pressure (Pilchin 1986, 2005; Pilchin and Eppelbaum 2009), especially in case of compression (see Sects. 2.7, 4.2 and 4.3). Petrini and Podladchikov (2000) also try to use cases with metamorphic ‘soles’ beneath ophiolites, and in particular the case of the Oman (Semail) ophiolite in an attempt to prove that classical thermodynamics does not apply to their formation, since the pressure involved in their formation was much higher than the lithostatic pressure. It should be stated that Petrini and Podladchikov (2000) misinterpreted these examples, because metamorphic ‘soles’ beneath ophiolites are usually formed during obduction processes which are characterized by giant horizontal pressures much greater than the lithostatic pressure. This is most notably the case for the Oman ophiolite which was formed

as a result of one of the most powerful obduction processes in the Earth's history. It is clear that in both cases of compressional shortening and obduction processes, giant horizontal pressures were involved that could easily generate pressures much higher than the lithostatic pressure at any level of their activity.

Burov et al. (2001) presented a 'nozzle' model for exhumation in continental collision zones, which looks like a modernized version of the channel flow model by Mancktelow (1995). This model considers two low or high buoyancy cases of the down-going crust. The model predicts UHP–HT exhumation from a lower chamber, forming at a depth of 100–120 km and separated from the upper one by a narrow channel. The width of this channel can vary during the shortening process. Burov et al. (2001) stated that the 'nozzle' appears to be too soft to produce any significant overpressures in excess of 20–40 MPa. Such values of overpressure are even too small for such processes as the formation of mud volcanoes, not to mention overcoming friction forces (Byerlee's law) between the exhuming and surrounding rocks.

It is well known that overpressure and UHP can be generated during certain tectonic processes (usually compressional processes such as continental collisions, obduction, etc.), but they cannot operate solely on their own and require additional processes that generating huge forces (pressures) which can initiate these compressive processes, because each force has its own physical cause.

Ishida et al. (2003) reported an unusual abundance of microdiamonds in dolomite marble from Kumdy-kol in the Kokchetav Massif. This case is another clear example of the formation of UHP that is much greater than the lithostatic pressure at lower depths. Since no carbonate can remain stable at high temperatures (see review in Pilchin and Eppelbaum 2006, 2009), these dolomite marbles must have been formed within the crust. Furthermore, it is possible that temperatures in the low crust were also too great for the stability of this rock.

Cases of rocks forming under pressures as high as up to 1.0–1.5 GPa above the lithostatic pressure within the lower crust have been documented in different regions of the Earth (Miyashiro 1961; Sobolev 1964; Dobretsov 1964; Sobolev 1972; Pilchin 1986, etc.).

The main parameters of thermodynamics are pressure (P), temperature (T) and volume (V) which are inter-related, and this relationship is usually presented in the most common form (i.e., Pilchin and Eppelbaum 2002) as:

$$V = V(P, T). \tag{4.4.2}$$

Since there is no reference to the state or kind of matter, Eq. (4.4.2) can be applied to any matter and any physical state. It is clear that any change in parameters can lead to a corresponding change in the other ones. For instance, a change in temperature (T) alone or both temperature (T) and pressure (P) results in a change in volume (V_0) that can be expressed as:

$$dV = (dV/dP)_T dP + (dV/dT)_P dT. \tag{4.4.3}$$

Again, Eq. (4.4.3) is still in the most common form with no restrictions for type of matter or its state.

Dividing both sides of Eq. (4.4.3) by the value of the initial volume (V_0) of a matter yields:

$$\frac{dV}{V_0} = \frac{1}{V_0}(dV/dP)_T dP + \frac{1}{V_0}(dV/dT)_P dT. \tag{4.4.4}$$

As was shown in Eqs. (2.7.2) and (2.7.3), the coefficients of heat expansion α and compressibility β are defined as:

$$\alpha = \frac{\left(\frac{\partial V}{\partial T}\right)_P}{V_0} \quad \text{and} \quad \beta = -\frac{\left(\frac{\partial V}{\partial P}\right)_T}{V_0}.$$

Substituting these coefficients into Eq. (4.4.4) gives us Eq. (2.7.19):

$$\frac{dV}{V_0} = -\beta dP + \alpha dT.$$

Solving Eq. (2.7.19) for pressure P and taking into account that $dP = P - P_0$ (here P_0 is the initial or *normal pressure*) and $dT = T - T_0$ (where T_0 is the *initial* or *normal temperature*) gives us Eq. (2.7.4):

$$P = P_0 + \frac{\alpha}{\beta}(T - T_0) - \frac{1}{\beta}\frac{\Delta V}{V_0}.$$

Since there are no assumptions or limitations about the matter or its state, all these equations are in general form and can be applied to any type of matter in any physical state (solid, liquid, or gas). However, there is one exception: depending on the matter itself and its physical state the main parameters of these equations (such as α, β, P_0, T_0) are different. The relationship between parameters P_0 and T_0 can be determined from the condition of equilibrium ($\Delta V = 0$) which is the condition of constant volume (or constant density) described by Eq. (2.7.5):

$$P = P_0 + \frac{\alpha}{\beta}(T - T_0).$$

It was shown (Pilchin and Eppelbaum 2002) that to analyze changes thermodynamic parameters with depth Eq. (2.7.19) can be written as:

$$\frac{dV}{Vo} = \left(\alpha\frac{\partial T}{\partial z} - \beta\frac{\partial P}{\partial z}\right)dz \tag{4.4.5}$$

which for the purposes of practical calculation can be transformed into:

$$\frac{\Delta V/Vo}{\Delta z} = \alpha \frac{\Delta T}{\Delta z} - \beta \frac{\Delta P}{\Delta z}. \tag{4.4.6}$$

Equation (4.4.6) indicates the relationship between relative change in volume with depth $\frac{\Delta V/V_0}{\Delta z}$, the vertical geothermal gradient $(\Delta T/\Delta z)$, and the gradient of pressure with depth $(\Delta P/\Delta z)$. This equation can be used to determine the type of tension in a region (Pilchin 1985a). There are only three possible choices:

(a) $\Delta V = 0$. This corresponds to equilibrium and an absence of tension

$$\frac{\Delta P}{\Delta z} = \frac{\alpha}{\beta} \frac{\Delta T}{\Delta z}. \tag{4.4.7}$$

(b) $\Delta V < 0$. This corresponds to compressional tension

$$\frac{\Delta P}{\Delta z} > \frac{\alpha}{\beta} \frac{\Delta T}{\Delta z}. \tag{4.4.8}$$

(c) $\Delta V > 0$. This corresponds to expansion

$$\frac{\Delta P}{\Delta z} < \frac{\alpha}{\beta} \frac{\Delta T}{\Delta z}. \tag{4.4.9}$$

Since the most advanced seismic methods have been developed in geophysics, including the determination of such physical properties of rocks and minerals as seismic velocity (v), change of seismic velocity with change in temperature (dv/dT) and pressure (dv/dP), in some cases it is preferable to use seismic data to analyze thermodynamic conditions at great depths (Pilchin and Eppelbaum 2002). The seismic wave velocity (v) depends to a great extent on the values of temperature (T) and pressure (P). The relationship between velocity (v), temperature (T) and pressure (P) can be described by the following equation (Pilchin and Eppelbaum 2002):

$$v = v(P, T). \tag{4.4.10}$$

Again, Eq. (4.4.10) describes the relationship between these parameters in the most general form as no assumptions are made about the kind of matter or any initial conditions. To express any changes in the value of velocity (v) under variable thermodynamic conditions, we can then use equation:

$$dv = \left(\frac{dv}{dT}\right)_P dT + \left(\frac{dv}{dP}\right)_T dP. \tag{4.4.11}$$

Clearly parameters $(dv/dT)_P$ and $(dv/dP)_T$ in Eq. (4.4.11) will vary for different kinds of rocks.

An important case that calls for Eq. (4.4.11) is the condition of equilibrium for velocity (v):

$$dv = 0. \tag{4.4.12}$$

which indicates a state in which the increase in velocity (v) with an increase of pressure (P) is counterbalanced by a decrease in the velocity (v) with an increase in temperature (T). For the condition ($dv = 0$) we must have:

$$\left(\frac{dv}{dT}\right)_P dT + \left(\frac{dv}{dP}\right)_T dP = 0. \tag{4.4.13}$$

Let us look at how conditions of constant velocity ($\Delta v = 0$), constant volume ($\Delta V = 0$) and constant density ($\Delta\sigma = 0$) are related. It is clear that conditions $\Delta V = 0$ and $\Delta\sigma = 0$ are similar. Birch's law has been used in many cases to determine the density of rocks within different slabs of the lithosphere (Birch 1960, 1961; Anderson 1967; Sobolev and Babeyko 1994; Pilchin and Eppelbaum 2009). This law describes the variation of the compressional velocity (v_p) of rocks and minerals at a constant average atomic weight with density σ as:

$$v_P = a\sigma + b. \tag{4.4.14}$$

Here a and b are constants usually calculated from the correlation between compressional wave velocity (v_P) and density (σ) obtained experimentally for different rocks and minerals.

Equation (4.4.14) shows that change in velocity v_P ($\Delta v_P = 0$) is related to change in density ($\Delta\sigma = 0$) as:

$$\Delta v_P = a \cdot \Delta\sigma. \tag{4.4.15}$$

It is clear from Eq. (4.4.15) that conditions ($\Delta\sigma = 0$) and ($\Delta v = 0$) take place simultaneously. If we take into account that for both Eqs. (2.7.4) and (4.4.13) the lithostatic pressure P_0 is the same, this supports the conclusion (Pilchin and Eppelbaum 2009) that conditions of equilibrium for constant volume, constant density and constant seismic velocity are similar.

It is evident that Eq. (4.4.13) can be used to determine the velocity equilibrium conditions for different rocks and minerals. For example, the velocity equilibrium conditions for bytownite gabbro, dunite, pink granite, grey granite and gabbro are presented in Fig. 4.5. Data from (Birch et al. 1942; Clark 1966; Dmitriev et al. 1969; Galdin 1970; Balashov and Volarovich 1971; Volarovich and Stiller 1977;

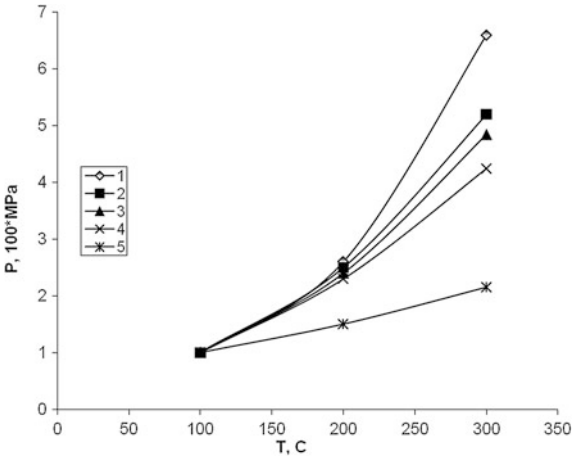

Fig. 4.5 Conditions of thermodynamic equilibrium for some rocks ($dv = 0$): *1* bytownite gabbro, *2* dunite, *3* pink granite, *4* grey granite, *5* gabbro (0 °C = 273.15 K)

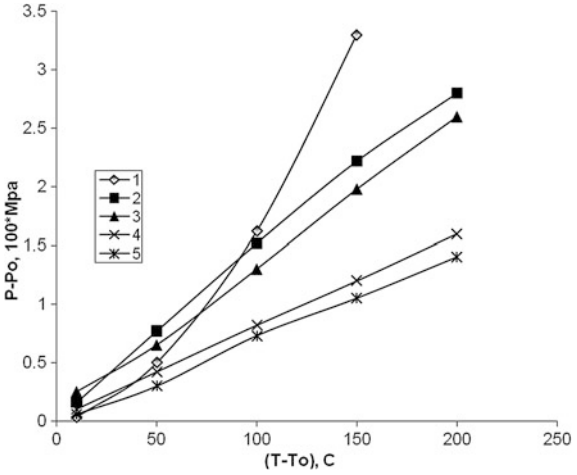

Fig. 4.6 Increase of excess pressure ($P - P_0$) with increase of excess temperature ($T - T_0$) for some rocks. *1* wet clay, *2* limestone, *3* granite, *4* sandstone, *5* basalt (0 °C = 273.15 K)

Stiller et al. 1979; Carmichael 1982) were used for compiling Fig. 4.5, as well as Figs. 4.6, 4.7, 4.8, 4.9.

It is clear from Fig. 4.5 that the equilibrium conditions are quite different even for rocks of the same kind (granite and gabbro). Thus whenever using seismic velocity to analyze the thermodynamic conditions at great depths, the conditions of velocity equilibrium and values of the parameters $(dv/dT)_P$ and $(dv/dP)_T$ should be selected very carefully.

Equation (4.4.13) may be used to calculate or estimate some very important thermodynamic parameters. Estimates were calculated for the temperatures under the southern slope of the Greater Caucasus (Pilchin and Kerimov 1987). Based on Eq. (4.4.13) the values of temperature and pressure can be estimated using equations:

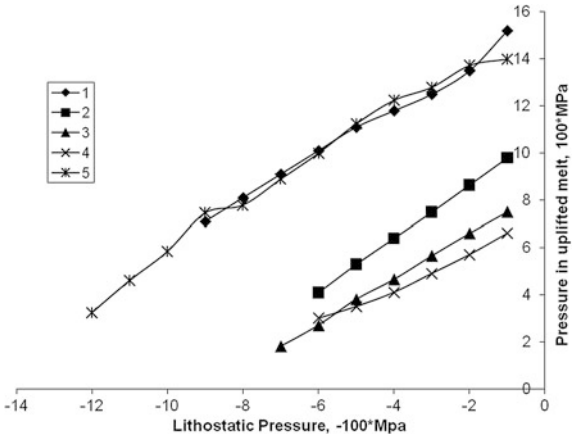

Fig. 4.7 Formation of overpressure by rising melt. *1* gabbro, *2* granite, *3* basalt, *4* diorite, *5* diabase (0 °C = 273.15 K)

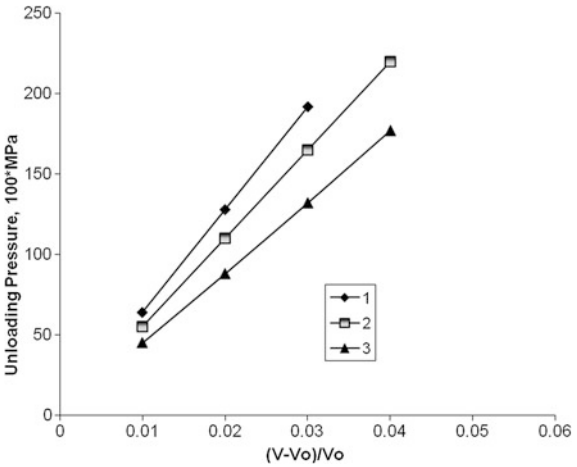

Fig. 4.8 Unloading of pressure in the case of expansion ($\Delta V > 0$) and loading of pressure in the case of compression ($\Delta V < 0$) for *1* limestone, *2* granite, and *3* basalt (0 °C = 273.15 K)

$$\Delta P = -\left[\left(\frac{dv}{dT}\right)\Big/\left(\frac{dv}{dP}\right)\right]\Delta T, \tag{4.4.16}$$

$$\Delta T = -\left[\left(\frac{dv}{dP}\right)\Big/\left(\frac{dv}{dT}\right)\right]\Delta P. \tag{4.4.17}$$

A thermodynamic analysis of different processes (Pilchin 1986; Eppelbaum et al. 1996; Pilchin and Eppelbaum 2009) shows that some processes can generate gigantic pressures and forces capable of moving continents, uplifting lithospheric blocks and building mountains. The analysis shows that the main causes of high and ultra-high pressure formation are: (1) decompression of rocks in the crust and upper mantle (including cases of significant increases in volume by physical,

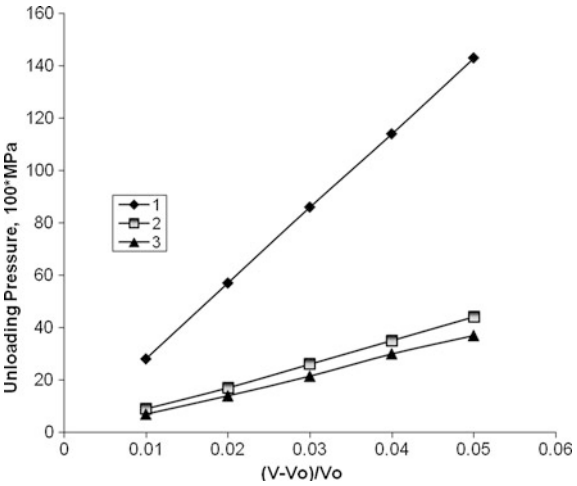

Fig. 4.9 Unloading of pressure in the case of expansion ($\Delta V > 0$) and loading of pressure in the case of compression ($\Delta V < 0$) for *1* sandstone, *2* basaltic melt, and *3* wet clay (0 °C = 273.15 K)

chemical and/or geologic processes); (2) melting of rocks at any depth; (3) uplifting of melt to the surface; (4) heating of great volumes of rock (including salt and clay layers); (5) heating of underground water; (6) compressive tectonic overpressure. Each of these causes may be responsible for a number of different kinds of tectonic activities and different geological processes. In all cases, the most obvious manifestations of high pressure activity are related to significant visible increases in volume (mountain building, obduction of giant plates on continental margins, formation of uplifts, etc.). In cases of heating significant amounts of rocks (including salt and clay layers) and porous water, the formation of high pressure depends mostly on the property of thermal expansion, which happens to be maximal for water, water-containing clays and salt (Pilchin 1985b; Pilchin and Eppelbaum 2002). In cases of heating wet clays, salt and/or porous water, the manifestations of the formation of high pressure are mud volcanoes, salt diapirs, AHSP/AHPP, geysers, fumaroles, volcanic gases, etc. An increase in pressure with an excess increase in temperature can be calculated using the second term on the right side of Eq. (2.7.4):

$$P_T = \frac{\alpha}{\beta}(T - T_0). \tag{4.4.18}$$

In cases of heating of solid rock blocks or layers, the increase in pressure is also caused by their thermal expansion properties, but unlike water and wet clay, or even salt, solid rocks have a much greater viscosity and do not behave either like a liquid (water) or like plastic rock (wet mud and salt). In addition because they are fixed in position by surrounding solid rocks, which may attempt to expand themselves, the block or layer of solid rock has no chance to expand, leading to an increase in pressure according to the third term on the left side of Eq. (2.7.4).

$$P_U = \frac{1}{\beta}\frac{\Delta V}{V_0}. \tag{4.4.19}$$

This case is discussed in detail in Sect. 6.9.

Examples of increases in pressure resulting from increases in temperature for some rocks using Eq. (4.4.18) are presented in Fig. 4.6. It is clear from Fig. 4.6 that temperatures in excess of 100 K generate greater pressure increases in wet clays than in other rocks and the excess pressure climbs very rapidly with increasing excess temperature. This supports the role of excess temperature in the formation of mud volcanoes.

The increase in pressure during the rise of magma caused by a decrease in the value of normal temperature with the decrease in depth with a near constant temperature of the rising magma is discussed in Sect. 4.2 [see Eq. (4.2.8)]. Some examples of calculated values of increased pressure during the rise of some magmas are presented in Fig. 4.7. It is clear from these data that out of the five kinds of melts, the additional increase in pressure caused by rising magma is the greatest in gabbro and diabase compositions and lowest in basalt and diorite melts.

Equation (4.4.19) can be used to calculate both the value of unloaded pressure in the case of expansion ($\Delta V > 0$) or added pressure in the case of compression ($\Delta V < 0$) by processes with increases of volume either through rock melting (up to 10–20 %) or certain physical, chemical or geological effects (such as serpentinization with increases in volume to up to 40 %). The amount of unloaded pressure can also be used to estimate the total pressure prior to its unloading (Pilchin 1986; Pilchin and Eppelbaum 2009). Examples of unloading of pressure with increases in volume ($\Delta V > 0$) for some rocks are presented in Figs. 4.8 and 4.9. It is clear that in the case of compression with a decrease in volume ($\Delta V < 0$), Figs. 4.8 and 4.9 would show a loading of pressure for the same rocks. These figures also show that the rate of pressure unloading with increases in volume is the highest for limestone, granite and basalt, and the lowest for wet clay and basaltic melt. This means that both wet clay in mud volcano eruptions and basaltic melt in volcano eruptions have a relatively slow pressure unloading, which would help them retain high excess pressure during eruption for a longer period. At the same time, under compressive tectonic pressures both wet clay and basaltic melt accrue pressure much slower than rocks with higher rates of pressure unloading/loading.

The formation of overpressure by compressive tectonic forces is not an independent process and any compressive tectonics (continental collision, obduction, etc.) process will also involve forces generated by the processes mentioned above. For instance, obduction processes are always related to processes of serpentinization in which the pressure increases as a result of a significant increase in volume during serpentinization. A key tool in determining the change in volume, which can be calculated using either Eqs. (2.7.4 or 2.7.19), is the dilatancy model.

Based on advances in the stress-dilatancy relationship for some sedimentary rocks (see Sect. 2.7), the dilatancy theory/model of earthquake prediction (sometimes called the dilatancy/fluid-diffusion hypothesis or model) was put

forward in the 1970s (Nur 1972; Anderson and Whitcomb 1973; Scholz et al. 1973; Whitcomb et al. 1973; Cherry et al. 1975; Nur 1975). Dilatancy is the process where the volume of rock increases under stress (during deformation) and is derived from the word dilation (volume expansion of brittle rock). In this case it represents an increase in volume caused by the opening of cracks, increased porosity, and/or micro-fracturing of rocks. Sibson (1981) defined hydro-fracture dilatancy as basically a low differential stress phenomenon. Initially the stress-dilatancy theory/model was introduced for sands (Rowe 1962) and later for soft clays (Roscoe et al. 1963), and was summarized by Roscoe and Burland (1968), Schofield and Wroth (1968), Chu et al. (2004), etc. The stress-dilatancy theory/model is based on an experimentally derived relationship between the principal effect of dilatancy and shear strength (Rowe 1962) linking the stress ratio to dilatancy rate.

Initially the dilatancy/fluid-diffusion model was formulated to explain the observed precursory effects of shallow crustal earthquakes (Nur 1972; Whitcomb et al. 1973; Scholz et al. 1973). The model was based on experimental data indicating that dilatancy in rocks is responsible for in situ premonitory changes of velocities and other rock properties prior to the main failure. Nur's (1972) model was based on field observations and experimental results showing that the dilatancy of rocks can cause the travel-time ratio of shear and compressional waves (t_s/t_p) to decrease before the failure (earthquake) and then subsequently increase with its termination with an earthquake.

Based on the Nur and Simmons (1969) findings that saturated crystalline rocks have much higher seismic velocities than unsaturated rocks, Nur assumed that the velocity anomalies prior to earthquakes could be explained by the opening of dry cracks during dilatancy followed by a reversion to previous conditions as water flowed into the newly formed cracks, resulting in an increase of pore pressure that weakens the rock, and to the observed ground failure (Nur 1972). Scholz et al. (1973) showed that precursory effects occur before many, perhaps all, shallow earthquakes and that these phenomena have a common physical basis. Analysis of a number of earthquakes revealed that prior to each of them, the ratio of seismic velocities v_P/v_s decreased to anomalously low values and the actual quakes occurred shortly after their return to normal values (Scholz et al. 1973). These observed v_p/v_s anomalies can be explained if we assume that dilatancy precedes the earthquake, and the low v_p/v_s ratio occurs because it causes the rock to become under-saturated hence strongly reducing v_p in the process, but having little effect on v_s (Scholz et al. 1973). Scholz et al. (1973) also analyzed laboratory data on the dependence of v_p and v_s on effective pressure (total pressure minus porous pressure) for saturated and dry rocks. Whitcomb et al. (1973) reported that a large precursory change in seismic body-wave velocities took place before the earthquake in San Fernando, California in 1971, and that this change was mainly in the *P*-wave velocity, which is clearly related to the effect of dilatancy on fluid-filled rocks. Anderson and Whitcomb (1973) used experimental data on the dilatancy of granites and other rocks (Brace and Martin 1968) to show that the dilatancy model can be applied to midcrustal conditions as well. Volume changes of a granite, a

marble, and an aplite were measured during deformation in a triaxial compression at confining pressures of as much as 800 MPa were also reported by Brace et al. (1966).

As demonstrated in laboratory experiments, the bulk of microcrack dilatancy occurs just prior to fracture. This led Nur (1975) to conclude that mechanisms contributing to the bulk dilatant strain may include microcrack dilatancy, band pile dilatancy and macroscopic fracture dilatancy. Another problem in the model was related to the fact that only limited dilatant volume expansion was observed in experiments (Nur 1975). Cherry et al. (1975) also summarized experimental results showing that the volume expansion of brittle rock takes place prior to the onset of unstable fracture propagation. The analysis showed (Cherry et al. 1975) that dilation increases as the induced stress state approaches the fracture strength of the material, and decreases as the confining pressure on the test sample is increased. Some authors have stressed the importance of effective pressure for saturated and dry rocks (i.e. Anderson and Whitcomb 1973; Scholz et al. 1973; Brace 1972) for analyzing rock dilatancy.

From the mid-1970s to early 1980s there were great hopes in seismology that the dilatancy theory/model could predict earthquakes. Unfortunately, although effect of increased dilatancy before the final rock failure was observed in laboratories and some data supported this effect in real situations for numerous earthquakes as well, the model did not yield any breakthroughs in earthquake prediction.

A number of explanations have been forward to account for the failure of the dilatancy model/theory to predict earthquakes : (1) the formation of cracks with increase of volume (dilation) is an effect of stress, but not the cause; (2) the effect depends to a great extent on the loading rate and strain rate (i.e., Brace and Martin 1968), which are different for each earthquake; (3) the results of any experiment depend on the shape and size of the sample, and there were considerable discrepancies in most cases between laboratory results and similar effects in nature; (4) a number of key parameters (porosity, permeability, porous pressure, size of cracks, saturation, etc.) which cannot be precisely defined for conditions found in real rock layers; (5) data analysis was restricted mostly to seismic measurements without analyzing the thermodynamic conditions of the region; (6) the lack a stronger effect of dilatancy in such rocks as eclogites (Rao and Raman 1974), serpentinized peridotites and pure serpentinites (Escartín et al. 2001), which are always present in regions of greater stress around the world; (7) ignoring physical properties as ultimate stress and its increase with increasing confined pressure (i.e., Clark 1966); (8) failure to differentiate between tensile and compressive stress and their stress limits (i.e., Clark 1966), etc. This failure of the dilatancy model/theory to live up to the hopes of the scientific community led to significant controversy among scientists. For example, Haase et al. (1995) called the dilatancy theory of earthquake prediction short-lived, but Hough (2010) nevertheless commented that "Still, the results remind us that the theory of dilatancy was never dead and buried." (Hough 2010, p. 223).

References

Abich GV (1863) New Islands on the Caspian Sea and the cognition of mud volcanoes of the Caspian Region. Mem Acad Sci Peterbourg Ser VIII(6):5

Allen ET, Day AL (1935) Hot springs of the Yellowstone National Park. Carnegie Institute of Washington, Washington, DC (Publication 466)

Allis RG (2000) Review of subsidence at Wairakei field, New Zealand. Geothermics 29(4/5):455–478

Anderson DL (1967) A seismic equation of state. Geophys J R Astron Soc 13:9–30

Anderson DL, Whitcomb JH (1973) The dilatancy-diffusion model of earthquake prediction. In: Kovach RL, Nur A (eds) Proceedings of the conference on tectonic problems of the San Andreas fault, geological sciences, vol 13. pp 417–426

Ariki K, Kato H, Ueda A, Bamba M (2000) Characteristics and management of the sumikawa geothermal reservoir, Northeastern Japan. Geothermics, 29:171–189

Ármannsson H (2010) IDDP. The chemistry of the Krafla geothermal system in relation to the IDDP well. In: Proceedings of the World geothermal congress 2010, Bali, Indonesia

Arnórsson S, Björnsson A, Gíslason G, Gudmundsson G (1975) Systematic exploration of the Krýsuvík high-temperature area, Reykjanes Peninsula, Iceland. In: Proceedings of the 2nd U.N. Symposium on the development and use of geothermal resources, vol 1. San Francisco, pp 853–864

Attrill PG, Gibb FGF (2003) Partial melting and recrystallization of granite and their application to deep disposal of radioactive waste: Part 1—Rationale and partial melting. Lithos 67(1–2):103–117

Axelsson G (2008) Production capacity of geothermal systems. Workshop for decision makers on direct heating use of geothermal resources in Asia (UNU-GTP, TBLRREM and TBGMED) Tianjin, China

Axelsson G, Jónasson T, Ólafsson M, Egilson T, Ragnarsson Á (2010) Successful Utilization of low-temperature geothermal resources in Iceland for district heating for 80 years. In: Proceedings of the World geothermal congress 2010, Bali, Indonesia

Bain C, Dunford G, MillerK, O'Brien S (2006) New Zealand (Lonely Planet Country Guide), 13th edn. Lonely Planet Publications, Melbourne

Baker ET, German CR (2004) On the global distribution 195 of hydrothermal vent fields. In: German CR et al (eds) Mid-ocean ridges: hydrothermal interactions between the lithosphere and oceans, American Geophysical Union, Washington, pp 245–266

Baker ET, Massoth GJ, Feely RA (1987) Cataclysmic hydrothermal venting on the Juan de Fuca Ridge. Nature 329(6135):149–151

Balashov DB, Volarovich MP (1971) Investigation on isothermic compression of magmatic rocks under pressure up tp 32000 bar. Izv AN SSSR Ser Phys Earth 2:24–32 (in Russian)

Barth TFW (1950) Volcanic geology: hot springs and Geysers of Iceland. Carnegie Institute of Washington, Washington, D.C (Publication 587)

Bayly B (1968) Introduction to petrology. Prentice-Hall Inc, Englewood Cliffs

Bear J (1972) Dynamics of fluids in porous media. American Elsevier Publication Co., NY

Belousov VI, Grib EN, Leonov VL (1984) The geological setting of the hydrothermal systems in the Geysers Valley and Uzon caldera. Volcanol Seismol 5:67–81

Berner EK, Berner RA (1987) Global water cycle, the geochemistry and environment. Prentice Hall, Englewood Cliffs

Best MG (2002) Igneous and metamorphic petrology, 2nd edn. Wiley-Blackwell, Oxford, p 752

Birch F (1960) The velocity of compressional waves in rocks to 10 kilobars. Part I. J Geophys Res 65:1083–1102

Birch F (1961) The velocity of compressional waves in rocks to 10 kilobars. Part 2. J Geophys Res 66:2199–2224

Birch F, Schairer JF, Spicer HC (eds) (1942) Handbook of physical constants. Geological Society of America. Special papers, No. 36

Bischoff JL, Rosenbauer RJ (1985) An empirical equation of state for hydrothermal seawater (3.2 percent NaCl). Am J Sci 285:725–763

Bonini M (2007) Interrelations of mud volcanism, fluid venting, and thrust-anticline folding: examples from the external northern Apennines (Emilia-Romagna, Italy). J Geophys Res 112:B08413

Bortnikova SB, Bessonova EP, Gavrilenko GM, Vernikovskaya IV, Bortnikova SP, Palchik NA (2008) Hydrogeochemistry of thermal sources, Mutnovskiy volcano, South Kamchatka (Russia). In: Proceedings of the 33rd workshop on geothermal reservoir engineering, Stanford University, Stanford, SGP-TR-185

Boyd ES, Jackson RA, Encarnacion G, Zahn JA, Beard T, Leavitt WD, Pi Y, Zhang CL, Pearson A, Geesey GG (2007) Isolation, characterization, and ecology of sulfur-respiring Crenarchaea inhabiting acid-sulfate-chloride-containing geothermal springs in Yellowstone National Park. Appl Env Microbiol 73(20):6669–6677

Brace WF (1972) Pore pressure in geophysics. In: Heard HC, Borg IY, Carter NL, Raleigh CB (eds) Flow and fracture of rocks: american geophysical union monograph 16, pp 265–273

Brace WF, Martin JR III (1968) A test of the law of effective stress for crystalline rocks of low porosity. Intl J Rock Mech Min Sci 5:415–426

Brace WF, Paulding BW Jr, Scholz C (1966) Dilatancy in the fracture of crystalline rocks. J Geophys Res 71(16):3939–3953

Braitseva OA, Melekestsev IV, Ponomareva VV, Sulerzhitsky LD (1995) Ages of calderas, large explosive craters and active volcanoes in the Kuril-Kamchatka region, Russia. Bull Volc 57:383–402 (in Russian)

Brantley SR (1994) Volcanoes of the United States. U.S. Department of the Interior, U.S. Geological Survey

Breckenridge RM, Hinckley BS, Terrell TT (1978) Thermal springs of Wyoming. The geological survey of Wyoming, Bulletin, vol 60

Brown KM (1990) Nature and hydrogeologic significance of mud diapirs and diatremes for accretionary systems. J Geophys Res 95:8969–8982

Bunsen RW, et Descloizeaux (1846) Note sur la temperature des Geysers d'Islande. Comptes Rendus, Paris XXIII:934–937 (in French)

Burdon DJ, Safadi C (1963) Ras-el-Ain, the great karst spring of Mesopotamia. J Hydrol 1:58–95

Burg JP, Podladchikov Y (1999) Lithospheric scale folding and rock exhumation: numerical modelling and application to the Himalayan syntaxes. In: Khan MA, Treloar PJ, Searle MP, Jan MQ (eds) Tectonics of the Nanga Parbat syntaxis and the Western Himalaya. Geol Soc London Spec Publ 170:219–236

Burov E, Jolivet L, le Pourhiet L, Poliakov A (2001) A thermomechanical model of exhumation of high pressure (HP) and ultra-high pressure (UHP) metamorphic rocks in Alpine-type collision belts. Tectonophysics 342:113–136

Byerlee JD (1978) Friction of rocks. Pure Appl Geophys 116:615–626

Camerlenghi A, Cita MB, Della Vedova B, Fusi N, Mirabile L, Pellis G (1995) Geophysical evidence of mud diapirism on the Mediterranean Ridge accretionary complex. Mar Geophys Res 17:115–141

Carmichael RS (ed) (1982) Handbook of physical properties of rocks, vol. II. CRC Press, Boca Raton

Chemenda AI, Mattauer M, Malavieille J, Bokun AN (1995) A mechanism for syn-collision rock exhumation and associated normal faulting: results from physical modelling. Earth Planet Sci Lett 132:225–232

Cherry JT, Schock RN, Sweet J (1975) A theoretical model of the dilatant behavior of a brittle rock. Pure Appl Geophys 113(1):183–196

Chiodini G, D'Alessandro W, Parello F (1996) Geochemistry of gases and waters discharged by the mud volcanoes at Paterno, Mt. Etna (Italy). Bull Volcanol 58:51–58

Christiansen RL (1992) Volcanoes of Wyoming. In: Wood CA, Kienle J (eds) Volcanoes of North America: The United States and Canada. Cambridge University Press, Cambridge, pp 263–267

Chu J, Kim SR, Oh YN, Balasubramaniam AS, Bergado DT (2004) An experimental and theoretical study on the dilatancy of sand and clays. In: Proceedings of the 9th Australia–New Zealand. Conference on geomechanics, vol 2. Auckland, New Zealand, pp 654–660
Clark SP Jr (ed) (1966) Handbook of physical constants. Revised Edition, Geological Society of America. Memoir 97, Washington, DC
Cloetingh S, Burov EB, Poliakov A (1999) Lithosphere folding: primary response to compression? (from central Asia to Paris Basin). Tectonics 18:1064–1083
Cody AD (2007) Geodiversity of geothermal fields in the Taupo Volcanic Zone. DOC Research & Development Series 281. Department of Conservation, Wellington, 70 p
Cody AD, Lumb JT (1992) Changes in thermal activity in the Rotorua geothermal field. Geothermics 21:215–230
Coumou D, Driesner T, Geiger S, Paluszny A, Heinrich CA (2009) High-resolution three-dimensional simulations of mid-ocean ridge hydrothermal systems. J Geophys Res 114:B07104. doi:10.1029/2008JB006121
Courtial P, Dingwell DB (1999) Densities of melts in the CaO-MgO-Al_2O_3-SiO_2 system. Am Mineral 84:465–476
Courtial P, Ohtani E, Dingwell DR (1997) High-temperature densities of some mantle melts. Geochim et Cosmochim Acta 61:3111–3119
Crone TJ, Wilcock WSD, Barclay AH, Parsons JD (2006) The sound generated by mid-ocean ridge black smoker hydrothermal vents. PLoS One 1(1):e133
Cumin G (1954) La salinelle di Paterno e la loro attuale attivita. Boll Natl Acad Gioenia Sci Catanias 4(2):9, 515–528
D'Imperio S, Lehr CR, Breary M, McDermott TR (2007) Autecology of an arsenite chemolithotroph: sulfide constraints on function and distribution in a geothermal spring. Appl Environ Microbiol 73:7067–7074
Dählmann A, de Lange GJ (2003) Fluid-sediment interactions at Eastern Mediterranean mud volcanoes: a stable isotope study from ODP Leg 160. Earth Plan Sci Lett 212:377–391
Dasgupta R, Hirschmann MM (2007) Effect of variable carbonate concentration on the solidus of mantle peridotite. Am Mineral 92:370–379
Davis SN, DeWiest RJM (1966) Hydrogeology. Wiley, NY
Degens ET, Ross DA (eds) (1969) Hot brines and recent heavy metal deposits in the Red Sea. Springer, NY
Demians J, Archimbaud J, Surcin J (1972) Récherches géothermiques en Guadeloupe. Rev Geograph Geol Dyn 14:211–228
Dimitrov LI (2002) Mud volcanoes—the most important pathway for degassing deeply buried sediments. Earth Sci Rev 59:49–76
DiPippo R (2007) Geothermal power plants: principles, applications, case studies and environmental impact, 2nd edn. Butterworth-Heinemann, Oxford
Dmitriev AP, Kuzyaev LS, Protasov YI, Yamschikov VS (1969) Physical properties of rocks at high temperatures. Nedra, Moscow (in Russian)
Dobretsov NL (1964) The jadeite rocks as indicators of high pressure. In: The Earth's crust. In: Proceedings of the 22nd internatational geology congress, India, vol 16. pp 177–196
Domenico PA, Schwartz FW (1998) Physical and chemical hydrogeology, 2nd edn. Wiley, NY
Durmish'yan AG (1961) On the genesis of mud volcanoes in light of new data. Izv Vuzov Oil Gas (Neft' i Gaz) 12:21–26 (in Russian)
Durmish'yan AG, Khalilov NY (1972) Abnormally high stratum pressures on areas of Baku Archipelago and causes of their formation. Geol Oil Gas 8:34–38 (in Russian)
Eichelberger J, Kiryukhin A, Simon A (2009) The magma-hydrothermal system at Mutnovskiy volcano, Kamchatka Peninsula, Russia. Sci Drill 7:54–59
Elderfield H, Schultz A (1996) Mid-oceanic ridge hydrothermal fluxes and the chemical composition of the ocean. Ann Rev Earth Plan Sci 24:191–224

Eldholm O, Sundvor E, Vogt PR, Hjelstuen BO, Crane K, Nilsen AK, Gladczenko TP (1999) SW Barents Sea continental margin heat ffow and Håkon Mosby mud volcano. Geo Mar Lett 19:29–37

Eppelbaum LV, Khesin BE (2012) Geophysical studies in the Caucasus. Springer, Berlin

Eppelbaum LV, Modelevsky MM, Pilchin AN (1996) Geothermal investigations in the Dead Sea Rift zone, Israel: implications for petroleum geology. J Pet Geol 19(4):425–444

Eppelbaum LV, Katz YI, Ben-Avraham Z (2012) Israel—petroleum geology and prospective provinces. AAPG Eur Newslett 4:4–9

Escartín J, Hirth G, Evans B (2001) Strength of slightly serpentinized peridotites: implications for the tectonics of oceanic lithosphere. Geology 29(11):1023–1026

Evening Times (Glasgow) (1961) The final blow for a geyser. February 17, p 17

Falloon TJ, Green DH, Danyushevsky LV (2007) Crystallization temperatures of tholeiite parental liquids: implications for the existence of thermally driven mantle plumes. In: Foulger GR, Jurdy DM (eds) Plates, plumes, and planetary processes, The Geological Society of America, Special paper 430, Boulder, Colorado, pp 235–260

Faure G (2000) Origin of igneous rocks: the isotopic evidence. Springer, Berlin

Faure G, Mensing TM (2007) Introduction to planetary science: the geological perspective. Springer, Berlin

Fedotov SA (2006) Magma feeding systems and mechanism of volcanoes eruption. Nauka, Moscow (in Russian)

Fedotov SA, Masurenkov YP (eds) (1991) Active volcanoes of Kamchatka, vols 1 and 2. Nauka, Moscow (in Russian)

Fink JH, Anderson SW (2001) Bernard lewis. In Sigursson H (ed) Encyclopedia of volcanoes. Academic, New York, pp 307–319

Fouquet Y, Henry K, Knott R, Cambon P (1998) Geochemical section of the TAG hydrothermal mound. In: Herzig PM, Humphris SE, Miller DJ, Zierenberg RA (eds) Proceedings of the Ocean drilling program, scientific results, vol 158, pp 363–387

Freeman PS (1968) Diapirism and diapers. AAPG Mem 8:137–144

Freeze RA, Cherry JA (1979) Groundwater. Prentice Hall Inc, Englewood Cliffs

Fridriksson T, Oladottir AA, Jonsson P, Eyjolfsdottir EI (2010) The response of the Reykjanes geothermal system to 100 MWe power production: fluid chemistry and surface activity. In: Proceedings of the World geothermal congress 2010, Bali, Indonesia

Galdin NE (1970) About relative changes of elastic characteristics of rocks and minerals with pressure. In: Problems of composition of Earth's crust and Upper Mantle. Upper Mantle, No. 7, pp 224–234 (in Russian)

Gaoxuan G (2008) Assessment of the hofsstadir geothermal field, W-Iceland, by lumped parameter modelling, Monte Carlo simulation and tracer test analysis. Geothermal training programme. Reports. Orkustofnun, Grensásvegur, vol 9, No. 18, IS-108 Reykjavík, Iceland, pp 247–279

Gavshin VM, Volontay GM (1969) Heat expansion of salt as possible tectonic factor. Geol Geophys No.11, 146–148 (in Russian)

Georgsson LS, Saemundsson K, Hjartarson H (2005) Exploration and development of the Hveravellir geothermal field, N-Iceland. In: Proceedings of the World geothermal congress, Antalya, Turkey, paper 0945

German CR, Thurnherrb AM, Knoery J, Charlou J-L, Jean-Baptiste P, Edmonds HN (2010) Heat, volume and chemical fluxes from submarine venting: A synthesis of results from the Rainbow hydrothermal field, 36°N MAR. Deep Sea Res Part I Oceanogr Res Papers 57(4):518–527

Ghiorso M (2004) An equation of state for silicate melts. Parts I, III, IV. Am J Sci 304:637–678, 752–810, 811–838

Giroud N (2008) A chemical study of arsenic, boron and gases in high-temperature geothermal fluids in Iceland. PhD Thesis, University of Iceland Faculty of Science

Glennon JA, Pfaff RM (2003) The extraordinary thermal activity of El Tatio Geyser field, Antofagasta Region, Chile. GOSA Trans 8:31–78
Goko K (2000) Structure and hydrology of the Ogiri field, West Kirishima geothermal area, Kyushu, Japan. Geothermics 29(2):127–149
Graham UM, Bluth GJ, Ohmoto H (1988) Sulfide-sulfate chimneys on the East Pacific rise, 11° and 13°N latitudes. Part II: mineralogy and paragenesis. Can Miner 26:487–504
Gramenitsky EN, Kotel'nikov AR, Batanova AM, Schekina TI, Plechov PY (2000) Experimental and technical petrology. Nauchniy Mir, Moscow (in Russian)
Green TH (1982) Anatexis of mafic crust and high pressure crystallization of andesite. In: Thorpe RS (ed) Andesites. Wiley, NY, pp 465–487
Green DH, Falloon TJ, Eggins SM, Yaxley GM (2001) Primary magmas and mantle temperatures. Eur J Mineral 13(3):437–452
Grichuk DV (2000) Thermodynamic models of submarine hydrothermal systems. Nauchnyi Mir, Moscow
Grove TL, Parman SW (2004) Thermal evolution of the Earth as recorded by komatiites. Earth Planet Sci Lett 219:173–187
Grove TL, Chatterjee N, Parman SW, Medard E (2006) The influence of H_2O on mantle wedge melting. Earth Plan Sci Lett 249:74–89
Gudmundsson BT, Arnórsson S (2002) Geochemical monitoring of the Krafla and Námafjall geothermal areas, N-Iceland. Geothermics 31(2):195–243
Guillot B, Sator N (2007) A computer simulation study of natural silicate melts. Part I: low pressure properties. Geochim et Cosmochim Acta 71:1249–1265
Gushchenko II (1979) Eruptions of Volcanoes of the World: a catalog. Nauka and Academy Science USSR, Moscow, Far Eastern Science Center (in Russian)
Haase JS, Shearer PM, Aster RC (1995) Constraints on temporal variations in velocity near Anza, California, from analysis of similar event pairs. Bull Seismol Soc Am 85(1):194–206
Haase KM, Petersen S, Koschinsky A et al (2007) Young volcanism and related hydrothermal activity at 5°S on the slow-spreading southern Mid-Atlantic Ridge. Geochem Geophys Geosyst 8:Q11002
Hall H (1995) Igneous petrology. Longman Science and Technology, Singapore
Harter T (2008) Watersheds, groundwater and drinking water: a practical guide, vol 3497. University of California, Division of Agriculture and Natural Resources. ANR Publications
Hedberg HD (1974) Relation of methane generation to undercompacted shales, sale diapirs, and mud volcanoes. AAPG Bull 58(4):661–673
Heiken G, Crowe B, McGetchin T, West F, Eichelberger J, Bartram D, Peterson R, Wohletz K (1980) Phreatic eruption clouds: the activity of La Soufrière de Guadeloupe, French West Indies, August–October 1976. Bull Volcanol 43:383–395
Herzberg C, Raterron P, Zhang J (2000) New experimental observations on the anhydrous solidus for peridotite KLB-1. Geochem Geophys Geosyst 1, Paper number 2000GC000089
Herzig PM, Humphris SE, Miller DJ, Zierenberg RA (eds) (1998) Proceedings of the Ocean drilling program, scientific results, vol 158, College Station, TX (Ocean Drilling Program)
Hjartarson H, Maack R, Johannesson S (2003) Husavik Energy—multiple use of geothermal energy. Thermie project no. GE 321/98/IS/DK. In: Proceedings of the internat. Geothermal conference IGC2003 "Multiple Integrated Use of Geothermal Resources", Reykjavik, pp 1–12
Hogan JP, Gilbert CM, Price JD (2001) Crystallisation of fine- and coarse-grained A-type granite sheets of the Southern Aulacogen, U.S.A. In: Barbarin B, Stephens WE, Bonin B, Bouchez J-L, Clarke DB, Cuney M, Martin H (eds) Transactions of the 4th Hutton symposium "*The Origin of Granites and Related Rocks*", The Royal Society of Edinburgh, Bristol, pp 139–150
Holland HD (1984) The chemical evolution of atmosphere and Oceans. Princeton University Press, Princeton

Hough SE (2010) Predicting the unpredictable: the tumultuous science of earthquake prediction. Prinston University Press, Prinston

Houghton BF, Lloyd EF, Keam RF, Johnston DM (1989) Inventory of New Zealand geothermal fields and features, 2nd edn. Ecological Society of New Zealand Miscellaneous Publication No. 44

Hovland M, Judd A (1988) Seabed pockmarks and seepages. Impact in geology, biology and the marine environment. Graham and Trotman, London

Hubbert MK (1969) The theory of groundwater motion and related papers. Hafner, NY

Hubbert M, Rubey W (1959) Role of fluid pressure in mechanisms of overthrust faulting, I, mechanics of fluid-filled porous solids and its application to overthrust faulting. Geol Soc Am Bull 70:115–160

Huppert HE, Sparks RSJ (1988) The generation of granitic magmas by intrusion of basalt into continental crust. J Petrol 29(3):599–624

Iceland on the Web (2013) http://iceland.vefur.is/iceland_nature/geology_of_iceland/%20geysir.htm. Accessed on 6 Apr 2013

Ishida H, Ogasawara Y, Ohsumi K, Saito A (2003) Two stage growth of microdiamond in UHP dolomite marble from Kokchetav Massif, Kazakhstan. J Metam Geol 21(6):515–522

Ishikawa T, Nakamura E (1993) Boron isotope systematics of marine sediments. Earth Plan Sci Lett 117:567–580

Izbekov PE, Eichelberger JC, Ivanov BV (2004) The 1996 eruption of Karymsky volcano, Kamchatka: historical record of basaltic replenishment of an andesite reservoir. J Petrol 45(11):2325–2345

Jakubov AA, Ali-Zade AA, Zeinalov MM (1971) Mud volcanoes of the Azerbaijan SSR. Academy of Science of the Azerbaijan SSR, Baku (in Russian)

Jalilinasrabady S, Itoi R, Gotoh H, Tanaka T (2010) The natural state numerical model of Takigami geothermal reservoir, Oita, Japan. In: Proceedings, of the 35th workshop on geothermal reservoir engineering, Stanford University, Stanford, SGP-TR-188

John SG, Rouxel OJ, Craddock PR, Engwall AM, Boyle EA (2008) Zinc stable isotopes in seafloor hydrothermal vent fluids and chimneys. Earth Plan Sci Lett 269:17–28

Jones GL (2006) Wyo Jones's Geyser Page. http://www.wyojones.com/tall.htm. Retrieved on 2 Apr 2013

Kadirov FA, Mukhtarov AS (2004) Geophysical fields, deep structure, and dynamics of the Lokbatan Mud volcano. Izv Phys Solid Earth 40:327–333

Kadirov FA, Lerche I, Guliyev IS, Kadyrov AG, Fezullayev AA, Mukhtarov AS (2005) Deep structure model and dynamics of mud volcanoes, southwest Absheron Peninsula (Azerbaijan). Energy Explor Exploit 23(5):307–332

Kalinko MK (1964) Mud volcanoes, reasons of their origin, development and fading. Trans VNIGRI 40:30–54 (in Russian)

Kalinko MK (1968) Non-organic origin of oil in light of Modern data. Nedra, Moscow (in Russian)

Kamah MY (1996) Borehole geology, hydrothermal alteration and temperature evolution of well KR-2, Krýsuvík, SW-Iceland. Report 5. In: Geothermal training in Iceland 1996, UNU-GTP, Iceland, pp 71–102

Karlstrom L, Dufek J, Manga M (2010) Magma chamber stability in arc and continental crust. J Volcan Geoth Res 190:249–270

Karsten JL, Holloway JR, Delaney JR (1982) Ion microprobe studies of water in silicate melts: temperature-dependent water diffusion in obsidian. Earth Plan Sci Lett 59(2):420–428

Kato O, Sakagawa Y, Doi N, Akaku K, Ohkubo Y (1999) Permeable fractures in the Kakkonda granite of wellL WD-1B, Japan. In: Proceedings, of 24th workshop on geothermal reservoir engineering, Stanford University, California, SGP-TR-162

Kawamoto T, Holloway JR (1997) Melting temperature and partial melt chemistry of H_2O-saturated mantle peridotite to 11 Gigapascals. Science 276:240–243

Keefer WR (1972) The geologic story of Yellowstone National Park. US Geol Surv Bull 1347:1–92

Kerimov KM, Pilchin AN, Ibragimov SM (1980) Influence of thermodynamical factor on the overhigh pressure in sedimentary strata. Azerbajan Oil Ind (Azerbaijanskoe Neftyanoe Khozyaistvo) 2:6–9 (in Russian)

Khalilov NY, Kerimov AA (1981) On genesis of mud volcanism and diapirism. Izv VUZov Geol Prospect 11:23–28 (in Russian)

Kholodov VN (2002) Mud volcanoes, their distribution regularities and genesis: communication 1. Mud volcanic provinces and morphology of mud volcanoes. Lithol Miner Res 37:197–209

Kiryukhin AB (2009) Investigation of heat-mass-transfer in high-temperature hydrothermal systems. In: Proceedings of the All-Russian Science Meeting. "100-years of Kamchatka expedition of Russian Geographic Society 1908–1910", Petropavlovsk-Kamchatskiy, pp 140–149

Kiyosui Y, Yoshida Y (1988) Origin of some gases from the Takinoue geothermal area in Japan. Geochem J 22:183–193

Knittle E (1995) Static compression measurements of equations of state. In: Ahrens TJ (ed) Mineral physics & crystallography: a handbook of physical constants. American Geophysical Union, pp 98–142

Köhler B, Singer A, Stoffers P (1994) Biogenic nontronite from marine white smoker chimneys. Clays Clay Miner 42(6):689–701

Kopf AJ (2002) Significance of mud volcanism. Rev Geophys 40(2):1–52

Koschinsky A, Garbe-Schönberg D, Sander S, Schmidt K, Gennerich H-H, Strauss H (2008) Hydrothermal venting at pressure-temperature conditions above the critical point of seawater, 5°S on the Mid-Atlantic Ridge. Geology 36(8):615–618

Koseki T (2010) Geothermal features of Yamagata prefecture, Northeast Japan. In: Proceedings of the World geothermal congress 2010, Bali, Indonesia

Lange RA, Carmichael ISE (1987) Densities of Na_2O–K_2O–CaO–MgO–FeO–Fe_2O_3–Al_2O_3–TiO_2–SiO_2 liquids: new measurements and derived partial molar properties. Geochim et Cosmochim Acta 51:2931–2946

Larsen G, Newton AJ, Dugmore AJ, Vilmundardóttir EG (2001) Geochemistry, dispersal, volumes and chronology of holocene silicic tephras from the Katla volcanic system, Iceland. J Quat Sci 16:119–132

Larsen G, Thordarson T, Oladottir BA (2008) Phreatomagmatism in the Eastern Volcanic Zone. IAVCEI 2008. In: Conference field excursions, excursion 7. University of Iceland and University Blaise Pascal, 23–25 Aug 2008

Lee C-TA, Luffi P, Plank T, Dalton H, Leeman WP (2009) Constraints on the depths and temperatures of basaltic magma generation on Earth and other terrestrial planets using new thermobarometers for mafic magmas. Earth Plan Sci Lett 279:20–33

Lett DL, Judson SH, Kauffman ME (1982) Physical geology, 6th edn. Prentice-Hall, Englewood Cliffs

Leonov VL, Rogozin AN (2010) Geologic development of the Karymshina Caldera, Kamchatka, Russia, with special reference to its hydrothermal systems. In: Proceedings of the World geothermal congress 2010, Bali, Indonesia

Leonov VL, Grib EN, Karpov GA, Sugrobov VM, Sugrobova NG, Zubin ZI (1991) Uzon caldera and valley of Geysers. In: Fedotov SA, Masurenkov YP (eds) Active volcanoes of Kamchatka, Nauka, Moscow, pp 92–141

Liaw C-W, Liu T-C, Iizuka Y, Yang H-Y (2006) Anhydrous melting and crystallization of granite from the transition zone of the Qilian orogenic belt, NW China: an experimental study at atmospheric pressure. TAO 17(1):233–251

Limonov AF (2004) Mud volcanoes. Soros' Educ J 8(1):63–69 (in Russian, abstract in English)

LIPC (2003) LIP record. Large Igneous Provinces Commission. International Association of Volcanology and Chemistry of the Earth's interior. http://www.largeigneousprovinces.org/record. Accessed on 30 Apr 2013
Litvinovsky BA, Podladchikov YY, Zanvilevich AN, Dunichev VM (1990) Melting of acid volcanites in contact with a shallow basite magma. Geochemistry (Geokhimiya) 6:807–814 (in Russian)
Lockwood JP, Hazlett RW (2010) Volcanoes: global perspectives. Wiley-Blackwell, Oxford
Lowenstern JB (1995) Applications of silicate melt inclusions to the study of magmatic volatiles. In: Thompson JFH (ed) Magmas, fluids and ore deposits. Mineralogical Association of Canada Short Course, vol. 23, pp 71–99
Macdonald G (1972) Volcanoes. Prentice-Hall, Englewood Cliffs
Magara K (1978) Compaction and fluid migration: practical petroleum geology. Elsevier, NY
Maltman A (ed) (1994) The geological deformation of sediments. Chapman and Hall, NY
Mancktelow N (1995) Nonlithostatic pressure during sediment subduction and the development and exhumation of high pressure metamorphic rocks. J Geophys Res 100:571–583
Mastin LG, Roeloffs E, Beeler NM, Quick JE (2008) Constraints on the size, overpressure, and volatile content of the Mount St. Helens Magma System from geodetic and dome-growth measurements during the 2004–2006+ Eruption. In: Sherrod DR, Scott WE, Stauffer PH (eds) A volcano Rekindled: the renewed eruption of Mount St. Helens, 2004–2006. U.S. Geological Survey, Chap. 22. Profess. Paper 1750, pp 461–488
Masurenkov YP (ed) (1980) Long existing center of endogenic activity in South Kamchatka. Nauka, Moscow (in Russian)
Matsuyama K, Narita N, Tomita K, Majima T (2000) Geothermal resources of Hachijojima. Geothermics 29:213–232
Mawejje P (2007) Geothermal exploration and geological mapping at Seltun in Krysuvik geothermal field, Reykjanes peninsula, SW-Iceland. Geothermal training programme. Reports of 2007. Orkustofnun, Grensásvegur 9, No. 12, Reykjavík, Iceland, pp 257–276
Mazzini A, Svensen H, Akhmanov GG, Aloisi G, Planke S, Malthe-Sorenssen A, Istadi B (2007) Triggering and dynamic evolution of the LUSI mud volcano, Indonesia. Earth Plan Sci Lett 261(3–4):375–388
Mazzini A, Nermoen A, Krotkiewski M, Podladchikov Y, Planke S, Svensen H (2009) Strike-slip faulting as a trigger mechanism for overpressure release through piercement structures. Implications for the LUSI mud volcano, Indonesia. Mar Petrol Geol 26(8):1751–1765
McBirney AR (2000) Igneous petrology, 2nd Edn. Jones & Bartlett Learning, Boston
McCaig AM, Cliff RA, Escartin J, Fallick AE, MacLeod CJ (2007) Oceanic detachment faults focus very large volumes of black smoker fluids. Geology 35(10):935–938
McCarthy KT, Pichler Th, Price RE (2005) Geochemistry of Champagne Hot Springs shallow hydrothermal vent field and associated sediments, Dominica, Lesser Antilles. Chem Geol 224:55–68
Meinzer OE (1927) Large springs in the United States. U.S. geological survey, water-supply Paper 557
Mekhtiev SF, Kerimov KM, Pilchin AN (1982) Role of thermal factors on formation and preservation of AVPD in sedimentary cover of Kura depression. Azerbaijan Oil Ind (Azerbaijanskoye Neftyanoye Khozyaystvo) 3:1–5 (in Russian)
Mel'nik OE, Barmin AA, Sparks S (2006) Unrestive life of lava domes. Russian fund of fundamental researches. Mechanics, pp 46–55 (in Russian)
Melekestsev IV, Braitseva OA, Ponomareva VV (1987) Activity dynamics of Mutnovsky and Gorely volcanos in Golocene and volcanic dangerous for surrounding regions. Volcanol Seismolog 3:3–18 (in Russian)
Michard G, Albarede F, Michard A, Minster JF, Charlou JL, Tan N (1984) Chemistry of solutions from the 13°N East Pacific Rise hydrothermal site. Earth Plan Sci Lett 67(3):297–307
Middleton GV (ed) (2003) Encyclopedia of sediments and sedimentary rocks. Kluwer Academic Publishers, Dordrecht

Miffin MD (1970) Mudlumps and suggested genesis in Pyramid Lake, Nevada. In: Hydrology of deltas: proceedings of the Bucharest symposium, May 1969, vol 1. UN Educational, Scientific, and Cultural Organization, pp 75–88

Miyashiro A (1961) Evolution of metamorphic belts. J Petrol 2:277–311

Mizugaki K (2000) Geologic structure and volcanic history of the Yanaizu-Nishiyama (Okuaizu) geothermal field, Northeast Japan. Geothermics 29:233–256

Morgan LA, Shanks WCP, Price KL (2009) Hydrothermal processes above the Yellowstone magma chamber: large hydrothermal systems and large hydrothermal explosions. Geological Society of America, 95 p (Paper 459)

Mottl MJ (1992) Pore waters from serpentinite seamounts in the Mariana and Izu-Bonin forearcs, Leg 125: evidence for volatiles from the subducting slab. In: Proceedings of scientific results, Leg 125, Ocean Drill. Program, College Station, Texas, pp 373–386

Muraoka H, Uchida T, Sasada M, Yagi M, Akaku K, Sasaki M, Yasukawa K, Miyazaki S, Doi N, Saito S, Sato K, Tanaka S (1998) Deep geothermal resources survey program: igneous, metamorphic and hydrothermal processes in a well encountering 500 °C at 3729 m depth, Kakkonda, Japan. Geothermics 27(5–6):507–534

Muraoka H, Sakaguchi K, Nakao S, Kimbara K (2006) Discharge temperature—discharge rate correlation of Japanese hot springs driven by buoyancy and its application to permeability mapping. Geophys Res Lett 33:L10405

Mysen BO, Boettcher AL (1975) Melting of a hydrous mantle: I. Phase relations of natural peridotite at high pressures and temperatures with controlled activities of water, carbon dioxide, and hydrogen. J Petrol 16(3):520–548

Nelson SA, Carmichael ISE (1979) Partial molar volumes of oxide components in silicate liquids. Contrib Mineral Petrol 71:117–124

Neuman SP, Neretniecks I (eds) (1990) Hydrogeology of low permeability environments. Verlag Heinz Heise, Hannover

Newhall CG, Melson WG (1983) Explosive activity associated with the growth of volcanic domes. J Volcan Geoth Res 17(1–4):111–131

Nichols DR, Yehle LA (1961) Mud volcanoes in the Copper River Basin, Alaska. In: Geology of the Arctic, vol II, University of Toronto Press, Toronto, pp 1063–1087

Nikolsky AI, Semenov VV, Tomarov GV, Shipkov AA (2010) Geothermal district heating of Vilyuchinsk city (Kamchatka). In: Proceedings of the World geothermal congress 2010, Bali, Indonesia

Nur A (1972) Dilatancy, pore fluids, and premonitory variations of T_S/T_P travel times. Bull Seismol Soc Am 62(5):1217–1222

Nur A (1975) A note on the constitutive law for dilatancy. Pure Appl Geophys 113(1):197–206

Nur A, Simmons G (1969) The effect of saturation on velocity in low porosity rocks. Earth Plan Sci Lett 7(2):183–193

Oakeshott GB (1968) Diapiric structures in diablo range, California. In: Braunstein G, O'Brien GD (eds) Diapirism and diapirs, AAPG Mem 8:228–243

Ochs FA, Lange RA (1997) The partial molar volume, thermal expansivity, and compressibility of H_2O in $NaAlSi_3O_8$ liquid: new measurements and an internally consistent model. Contrib Mineral Petrol 129:155–165

Odé H (1968) Review of mechanical properties of salt relating to salt-dome genesis. In: Braunstein G, O'Brien GD (eds) Diapirism and Diapirs, AAPG Mem 8:53–78

Okada H, Yasuda Y, Yagi M, Kai K (2000) Geology and fluid chemistry of the Fushime geothermal field, Kyushu, Japan. Geothermics 29:279–311

Oki Y, Hirano T (1974) Hydrothermal system and seismic activity of Hakone Volcano. In: Colp JL, Furumoto AS (eds) The utilization of volcano energy, Hillo, Hawaii, pp 13–40

Ozernii O (1981) Regularities of distribution of the overpressured layers in Southern Ukraine. Geol Oil Gas 6:50–56 (in Russian)

Pálsson B, Gunnarsson Á, Ingason K, Gudmundsson Á, Hjartarson H, Júlíusson BM (2010) Development of the 400 MW Northeast Iceland geothermal project. In: Proceedings of the World geothermal congress 2010, Bali, Indonesia

Parfitt EA, Wilson L (2008) Fundamentals of physical volcanology. Blackwell, Carlton
Pedersen RB, Rapp HT, Thorseth IH, Lilley MD, Barriga FJAS, Baumberger T, Flesland K, Fonseca R, Früh-Green GL, Jorgensen SL (2010) Discovery of a black smoker vent field and vent fauna at the Arctic Mid-Ocean Ridge. Nat Commun 1:126
Pentecost A, Jones B, Renaut RW (2003) What is a hot spring? Can J Earth Sci 40(11):1443–1446
Percival JA, Pysklywec RN (2007) Are Archean lithospheric keels inverted? Earth Plan Sci Lett 254(3–4):393–403
Pertermann M, Hirschmann MM (2003) Anhydrous partial melting experiments on MORB-like eclogite: Phase relations, phase compositions and mineral–melt partitioning of major elements at 2–3 GPa. J Petrol 44(12):2173–2201
Petersen S, Herzig PM, Hannington MD (2000) Third dimension of a presently forming VMS deposit: TAG hydrothermal mound, mid-atlantic ridge, 26°N. Miner Deposita 35(2–3):233–259
Petrini K, Podladchikov Y (2000) Lithospheric pressure-depth relationship in compressive regions of thickened crust. J Metamorph Geol 18:67–78
Pilchin AN (1976) On correction of hydrostatic pressure distribution with depth under control of temperature change. VINITI Press, No. 3307, 1–8 (in Russian)
Pilchin AN (1978a) Correction to hydrostatic pressure in the crust of the Middle Kura depression. In: Geophysical researches of the oil, gas and ore deposits in Azerbaijan, Baku, pp 78–80 (in Russian)
Pilchin A (1983) Geothermal regime of Earth's crust of the Kura depression and its influence on pressure distribution in it. Ph.D Thesis, Institute of Geophysics of the Georg. Academy of Science, Tbilisi (in Russian)
Pilchin AN (1985a) Method of the stresses in a mountain massif determination, USSR, Patent No. 1170143, Bulletin of Inventions, No. 28 (in Russian)
Pilchin AN (1985b) On the origin of mud volcanoes. Sov Geol (Sovetskaia Geologiya) 10:78–81 (in Russian)
Pilchin AN (1986) On the role of pressures in tectonic processes. VINITI Press, No. 3723–3786, 1–23 (in Russian)
Pilchin AN (2005) The role of serpentinization in exhumation of high- to ultra-high-pressure metamorphic rocks. Earth Plan Sci Lett 237(3–4):815–828
Pilchin AN (2011) Magnetite: the story of the mineral's formation and stability. In: Angrove DM (ed) Magnetite: structure, properties and applications, Chap. 1. Nova Science Publication, NY, pp 1–99
Pilchin AN, Eppelbaum LV (2002) Some peculiarities of thermodynamic conditions of the Earth crust and upper mantle. Sci Israel 4(1–2):117–142
Pilchin AN, Eppelbaum LV (2006) Iron and its unique role in Earth evolution. Monograph 9, Mexican Geophys. Soc
Pilchin AN, Eppelbaum LV (2009) The early Earth and formation of the lithosphere. In: Anderson JE, Coates RW (eds) The lithosphere: geochemistry, geology and geophysics, Chap. 1, Nova Science Publication, NY, pp 1–68
Pilchin A, Eppelbaum L (2012) The early Earth formation and evolution of the lithosphere in the Hadean—Middle Archean. In: Sato F, Nakamura S (eds) Encyclopedia of Earth science research, Chap. 1, vol 1, pp 1–93
Pilchin AN, Kerimov KM (1987) Prognosis of temperatures and pressures at in depth intervals not uncovered by drilling in oil and gas fields of Azerbaijan using seismic data. In: Kerimov KM (ed) Prognosis of oil and gas fields presence by methods of exploration geophysics. Baku, No 3, pp 55–61
Pirajno F (2010) Hydrothermal processes and mineral systems. Springer, Berlin
Pitt AM, Hutchinson RA (1982) Hydrothermal changes related to earthquake activity at Mud Volcano, Yellowstone National Park, Wyoming. J Geophys Res 87(B4):2762–2766
Polyak BG (1966) Geothermal features of present volcanism areas on example of Kamchatka. Nedra, Moscow (in Russian)

Ponder WF (2002) Desert springs of Great Australian Arterial Basin. In: Proceedings of the conference important scientific and cultural resources of the intermountain region, Spring-fed Wetlands

Ponomareva VV, Kyle PR, Melekestsev IV, Rinkleff PG, Dirksen OV, Sulerzhitsky LD, Zaretskaia NE, Rourke R (2004) The 7600 (14C) year BP Kurile Lake caldera-forming eruption, Kamchatka, Russia: stratigraphy and field relationships. J Volcan Geoth Res 136:199–222

Pritchett JW, Garg SK, Farrell WE, Ishido T, Yoshimura T, Murakami K, Nakanishi S (1985) The Hohi geothermal area, Kyushu, Japan. In: Proceedings of the 10th workshop on geothermal reservoir Engineering, Stanford University, CA, SGP-Tu-84, pp 79–87

Ragnarsson Á (2005) Geothermal development in Iceland 2000–2004. In: Proceedings of the World geothermal congress 2005, Antalya, Turkey, pp 1–12

Rakhmanov RR (1987) Mud volcanoes and their importance in forecasting of subsurface petroleum potential. Nedra, Moscow (in Russian)

Rao MVMS, Raman YV (1974) Dilatant behaviour of ultramafic rocks during fracture. Int J Rock Mech Min Sci Geomech 11(5):193–203

Reed DL, Silver EA, Tagudin JE, Shipley TH, Vrolijk P (1990) Relations between mud volcanoes, thrust deformation, slope sedimentation, and gas hydrate, offshore north Panama. Mar Petrol Geol 7:44–54

Rinehart JS (1980) Geysers and geothermal energy. Springer, NY

Rivalta E, Segall P (2008) Magma compressibility and the missing source for some dike intrusions. Geophys Res Lett 35:L04306

Robertson AHF, Party Scientific (1996) Mud volcanism on the Mediterranean Ridge: initial results of Ocean Drilling Program Leg 160. Geology 24:239–242

Roscoe KH, Burland JB (1968) On the generalized stress-strain behaviour of wet clay. In: Engineering plasticity, Cambridge, pp 535–609

Roscoe KH, Schofield AN, Thurairajah A (1963) Yielding of clays in state wetter than critical. Geotechnique 13(3):211–240

Rowe PW (1962) The stress-dilatancy relation for static equilibrium of an assembly of particles in contact. Proc R Soc London Ser A 269:500–527

Rukavičková L, Hanžl P (2008) Mud volcanoes in the Khar Argalantyn Nuruu, NW Gobi Altay, Mongolia as manifestation of recent seismic activity. J Geosci 53:181–191

Saba M, Nishida Y, Mogi T, Takakura S, Matsushima N (2007) Development of geothermal field following the 2000 eruption of Usu volcano as revealed by ground temperature, resistivity and self-potential variations. Ann Geophys 50(1):79–92

Saito S, Sakuma S, Uchida T (1997) Frontier geothermal drilling operations succeed at 500 C BHST. Transactions of the SPE/IADC drilling conference, Amsterdam, Paper 37625-MS, pp 445–458

Sakai H, Nozaki Y (eds) (1995) Biogeochemical processes and ocean flux in the Western Pacific. Terra Scien Publ Comp, Tokyo, pp 537–559

Salayev SG, Mamedov AM (1971) On role of mud volcanism in formation oil and gas deposits. Dokl Acad Sci Azerb SSR XXVII(10):68–71

Sawa T, Ohba T, Hirabayashi J-I (2006) The hydrothermal system beneath Owakudani on Hakone Volcano, Japan; Traced by Stable Isotopic Ratios of H_2O. J Nucl Sci Technol 43(4):468–473

Scaillet B, Pichavant M (2005) A model of sulphur solubility for hydrous mafic melts: application to the determination of magmatic fluid compositions of Italian volcanoes. Ann Geophys 48(4–5):671–698

Schofield AN, Wroth CP (1968) Critical state soil mechanics. McGraw-Hill, London

Scholz CH, Sykes LR, Aggarwal YP (1973) Earthquake prediction: a physical basis. Science 181(4102):803–810

Schubert G, Turcotte DL, Olson P (2001) Mantle convection in the Earth and Planets, two set. Cambridge University Press, Cambridge

Scott BT (1995) The Geysers of Yellowstone, 3rd edn. Colorado University Press, USA

Seach J (2011) Volcanoes of the World. http://www.volcanolive.com/world.html. Accessed last time on 1 May 2013
Sheppard DS, Truesdell AH, Janik CJ (1992) Geothermal gas compositions in Yellowstone National Park, USA. J Volcanol Geotherm Res 51:79–93
Shinohara H (2008) Excess degassing from volcanoes and its role on eruptive and intrusive activity. Rev Geophys 46:RG4005
Showstack R (2010) In brief: volcanic vents found in deep Caribbean waters. Eos Transactions AGU, 91, No. 16
Sibson RH (1981) Controls on low-stress hydro-fracture dilatancy in thrust, wrench and normal fault terrains. Nature 289:665–667
Simkin T, Siebert L (1994) Volcanoes of the World. Geoscience Press, Tucson
Slack JF, Turner RJW, Ware PLG (1998) Boron-rich mud volcanoes of the Black Sea region: modern analogues to ancient sea-ffoor tourmalinites associated with Sullivan-type Pb-Zn deposits? Geology 26:439–442
Slovtsov IB (2011) Geological map of Geysers Valley and Kikhpinych volcano. http://www.pdfio.com/k-226178.html. Accessed on 15 Apr 2013
Smith PC (1989) Hydrogeology. In: Zeidler W, Ponder WF (eds) Natural history of Dalhousie Springs South Australian Museum, Adelaide, pp 27–40
Smith RB, Siegel LJ (2000) Windows into the Earth: the geologic story of Yellowstone and Grand Teton National Parks. Oxford University Press, Oxford
Sobolev VS (1964) Physicochemical conditions of mineral formation in the Earth's crust and mantle. Geol Geophys (Geologiya i Geofizika) 2(11):7–22
Sobolev VS (ed) (1972) The facies of metamorphism. Nedra, Moscow (in Russian)
Sobolev SV, Babeyko AY (1994) Modeling of mineralogical composition, density and elastic wave velocities in anhydrous magmatic rocks. Surv Geophys 15(5):515–544
Spechler RM, Schiffer DM (1995) Springs of Florida. USGS, U.S. Geological Survey Fact Sheet FS-151-95
Staudigel H (2005) Hydrothermal alteration processes in the oceanic crust. In: Rudnick RL (ed) The crust: treatise on geochemistry, Chap. 3, vol 15. pp 511–536
Stern CR, Wyllie PJ (1973) Melting relations of basalt-andesite-rhyolite-H_2O and a pelagic red clay at 30 kb. Contrib Mineral Petrol 42(4):313–323
Stiller H, Volarovich MP, Lebedev TS, Vollstaedt H, Freund D (eds) (1979) Theoretical and experimental investigations of physical properties of rocks and minerals under extreme P, T-conditions. Akad Verlag, Berlin
Stoiber RE (1995) Volcanic gases from subaerial volcanoes on Earth. In: Global Earth physics, a handbook of physical constants. AGU, Reference Shelf, vol 1, pp 308–319
Sugrobov VM, Sugrobova NG, Droznin VA, Karpov GA, Leonov VL (2009) The pearl of Kamchatka: valley of geysers. Kamchatpress (in Russian)
Suzuki A, Ohtani E, Kato T (1998) Density and thermal expansion of a peridotite melt at high pressure. Phys Earth Planet Inter 107:53–61
Swanson DA, Holcomb RT (1990) Regularities in growth of the Mount St. Helens dacite dome in 1980–1986. In: Fink JH (ed) Lava flows and domes; emplacement mechanisms and hazard implications. Springer, Berlin, pp 3–24
Taguchi S, Itoi R, Yuki Y (1996) Beppu hot springs. GHC Bull 17:1–6
Takahashi E, Kushiro I (1983) Melting of a dry peridotite at high pressures and basalt magma genesis. Am Mineral 68:859–879
Takeno N (2000) Thermal and geochemical structure of the Uenotai geothermal system, Japan. Geothermics 29:257–277
Tamanyu S, Wood CP (2003) Characterization of geothermal systems in volcano-tectonic depressions: Japan and New Zealand. Bull Geol Surv Jpn 54(3/4):117–129
Thompson RN, Gibson SA (2000) Extremely magnesian olivines in Phanerozoic picrites signify transient high temperatures during mantle plume impact. Goldschmidt 2000. J Conf Abs 5(2):1001

Thordarson T, Larsen G (2007) Volcanism in Iceland in historical time, volcano types, eruptions styles and eruptive history. J Geodyn 43:118–152
Thordarson Th, Self S (1993) The Laki (Skaftar Fires) and Grimsvotn eruptions in 1783–1785. Bull Volcanol 55:233–263
Tivey MK (2007) Generation of seafloor hydrothermal vent fluids and associated mineral deposits. Oceanography 20(1):50–65
Turner RW, Ames DE, Franklin JM, Goodfellow WD, Leitch CHB, Höy T (1993) Character of active hydrothermal mounds and nearby altered hemipelagic sediments in the hydrothermal areas of Middle Valley, Northern Juan De Fuca Ridge: data on shallow cores. Can Mineral 31:973–995
Vakin EA, Pilipenko GF, Sugrobov VM (1986) General description of Mutnovskiy field and the resource assessment. In: Geothermal and geochemical studies of high-temperature hydrothermal systems. Nauka, Moscow, pp 6–40 (in Russian)
Van Dover CL, Humphris SE, Fornari D et al (2001) Biogeography and ecological setting of Indian Ocean hydrothermal vents. Science 294(5543):818–823
Vatin-Perignon N, Semet MP, Blanc F, Joron JL (1984) Petrochemistry of quaternary pumiceous pyroclastic products in southern Guadeloupe (F.W.I.). Bull Volcanol 47:749–767
Vereina OB (2007) Output of thermal energy from Mutnovskiy volcano (Kamchatka) and thermal feeding of Mutnovskiy hydrothermal system. In: Proceedings of the 32nd workshop on geothermal reservoir enginering, Stanford University, Stanford, SGP-TR-183
Vlodavetz VI, Piip BI (1959) Kamchatka and continental areas of Asia. Catalog of active volcanoes of the World and Solfatara fields. IAVCEI Rome 8:1–110
Voight B, Widiwijayanti C, Mattioli G, Elsworth D, Hidayat D, Strutt M (2010) Magma-sponge hypothesis and stratovolcanoes: case for a compressible reservoir and quasi-steady deep influx at Soufrière Hills Volcano, Montserrat. Geoph Res Lett 37:L00E05
Volarovich MP, Stiller KH (eds) (1977) Investigation of physical properties of mineral matter of Earth under high thermodynamic parameters. Naukova Dumka, Kiev (in Russian)
von Damm, K, Lilley M, Shanks W, Brockington M, Bray A, O'Grady K, Olson E, Graham A, Proskurowski G, The SouEPR Science Party (2003) Extraordinary phase separation and segregation in vent fluids from the southern East Pacific Rise. Earth Plan Sci Lett 206:365–378
Waugh D (2002) Geography: an integrated approach. Nelson Thornes, United Kingdom
Wallace PJ (2001) Volcanic SO_2 emissions and the abundance and distribution of exsolved gas in magma bodies. J Volcan Geoth Res 108:85–106
Wallace P, Anderson AT Jr (2000) Volatiles in magmas. In: Sigurdsson H et al (eds) Encyclopedia of volcanoes. Academic, San Diego, pp 149–170
Wangen M (2001) A quantitative comparison of some mechanisms generating overpressure in sedimentary basins. Tectonophysics 334(3–4):211–234
Warn P, Ichram LO (1997) Role of mud volcanoes in petroleum systems: examples from Timor, the South Caspian and the Caribbean. In: Proceedings of the international conference on petrological system of SE Asia and Australasia, pp 955–970
Water and Fire (2011) High and low temperature fields. http://waterfire.fas.is/GeothermalEnergy/%20Highandlowtemperatureareas.php. Accessed on 6 Apr 2013
Watts K (2007) Yellowstone and heise: supervolcanoes that lighten up. Geotimes 52(11):24
Weiss RF, Lonsdale P, Lupton JE, Bainbridge AE, Craig H (1977) Hydrothermal plumes in the Galapagos Rift. Nature 267:600–603
Whitcomb JH, Garmany JD, Anderson DL (1973) Earthquake prediction: variation of seismic velocities before the San Francisco earthquake. Science 180:632–635
White DE (1955) Violent mud volcano eruption of Lake City hot springs, northeast California. GSA Bull 66:1109–1130
White DE (1973) Characteristics of geothermal resources and problems of utilization. In: Kruger P, Otte C (eds) Geothermal energy—resources, production, stimulation. Stanford University Press, Stanford, pp 69–94

White DE, Williams DL (eds) (1975) Assessment of geothermal resources of the United States—1975. U.S. Geol Surv Circ 726:155

Williams P, Pigram C, Dow D (1984) Melange production and the importance of shale diapirism in accretionary terrains. Nature 309:145–146

Winckler G, Kipfer R, Aeschbach-Hertig W, Botz R, Schmidt M, Schuler S, Bayer R (2000) Sub sea floor boiling of Red Sea Brines: new indication from noble gas data. Geochim et Cosmochim Acta 64(9):1567–1575

Wohletz K, Heiken G (1992) Volcanology and geothermal energy. University of California Press, Berkeley

Woods AW, Huppert HE (2003) On magma chamber evolution during slow effusive eruptions. J Geoph Res 108(B8):2403

Yoder HS Jr (1976) Generation of basaltic magma. National Academy of Science, Washington, DC

Yoshida T, Yuhara K, Nakae Y, Noda T (1978) Hot-water and precipitates in the hot pool 'Chinoike-Jigoku' Beppu geothermal area, Kyushu, Japan. J Balneo Soc Jpn 29:10–18 (in Japanese with English abstract)

Yoshiike Y (2003) Variation in the chemical composition of Obuki Spring, Tamagawa hot springs (1951–2000). Geochem J 37:649–662

You C-F, Castillo PR, Gieskes JM, Chan LH, Spivack AJ (1996) Trace element behavior in hydrothermal experiments: implications for fluid processes at shallow depths in subduction zones. Earth Planet Sci Lett 140:41–52

Chapter 5
The Thermal Regime of Permafrost Regions

5.1 The Temperature of Frozen Rocks

Permanent ice is found on or beneath approximately 20 % of dry land: 75 % of Alaska, 63 % of Canada, and 47 % of the Russian Federation are covered by permafrost. Wherever permanent ice is found, a necessary condition is satisfied for the existence of permafrost. The permafrost base is defined as 0 °C isotherm, and thickness is defined as the depth from the surface to that isotherm. Hence, an accurate temperature-depth curve is needed to obtain the value of the permafrost thickness. At a given location the permafrost depth depends mainly on following factors: long-term annual mean surface temperature, thermal conductivity, ice (water) content of formations, salinity of unfrozen water, heat flow density (heat flow from the Earth's interior), and past climate. For these reasons the thickness of permafrost can vary within wide limits even for neighboring sites. Permafrost was formed and exists in definite thermal conditions, which were initially characterized by a field of negative temperatures (in °C) and phase transitions of water into ice. The temperature field in permafrost regions is formed under the influence of the heat exchange on the surface, the composition and structure of the formations, the heat flow density, local sources of heat, and phase transitions of water. In permafrost areas the rate of heat flow serves as the main criterion for the steadiness or non-steadiness of the thermal regime. In fact, this directly follows from Stefan's condition at the phase boundary,

$$q_f - q_t = \pm Q\frac{dl}{dt} \tag{5.1.1}$$

where q_t and q_f are the heat flow at the phase boundary in the thawed and frozen zone respectively, Q is the amount of heat released (absorbed) per unit of volume at freezing (thawing), l is the thickness of the frozen formations, and t is the time.

It is clear that the condition where $q_f = q_t$ corresponds to a steady regime, the condition where $q_f > q_t$ corresponds to a regime of freezing and the condition where $q_f < q_t$ corresponds to a thawing regime. An analysis of geothermal field and

L. Eppelbaum et al., *Applied Geothermics*, Lecture Notes in Earth System Sciences,
DOI: 10.1007/978-3-642-34023-9_5, © Springer-Verlag Berlin Heidelberg 2014

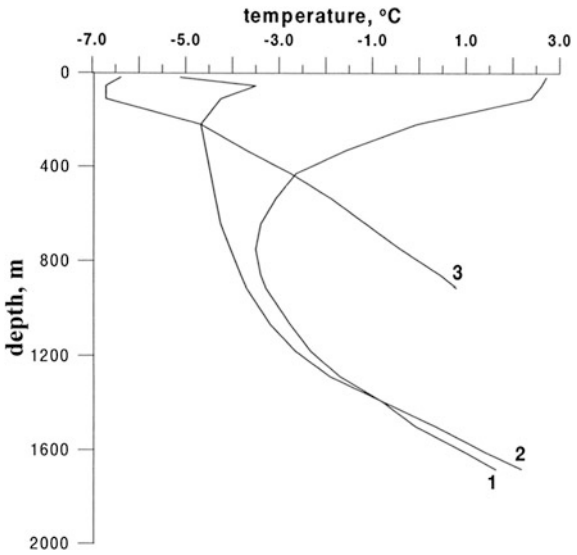

Fig. 5.1 Vertical profiles of the temperature field of rocks west of the East Siberian platform. (*1*) Markhinskaya well 1, (*2*) Markhinskaya well 2, (*3*) well of the "Udachnaya" pipe (Balobayev et al. 1973)

laboratory data; i.e., determination of formations thermal properties, estimates of the values of q_f and q_t showed that the temperature profiles in permafrost regions can be divided into three groups (Balobayev et al. 1973).

In the first group, which comprises the greater part of geothermal data, the temperature field of permafrost is steady and corresponds to contemporary conditions of heat exchange on the surface and geothermal heat flow ($q_f = q_t$).

Examples of the second group of the geothermal data are presented in Fig. 5.1.

The unusual temperature profiles are due to the fact that the heat flow increases constantly with depth, while in the area of well 1, it even changes sign because of the development of a local surface talik. The analysis of the field data (Fig. 5.1) shows that the absorption of the heat flow due to physicochemical processes may cause changes in the heat flow with depth. Subterranean waters in these areas are brines with a salt content of 250–350 g/l. A number of dissolved substances can be found in saturated conditions, and in these conditions processes of crystallization, exchange, and replacement with absorption of heat can take place. It should be noted that ice bounded formations can be found only in the upper (100–300 m) near-surface part.

The third group of geothermic data (Fig. 5.2) is characterized by a clearly transient temperature field accompanied by thawing at the permafrost base. This is indicative of a more severe climate in the past.

The rate of current-day thawing can be estimated from Eq. (5.1.2)

$$-\frac{dl}{dt} = \frac{q_t - q_f}{Q} \tag{5.1.2}$$

and its estimated value from field data is 1–2 cm/year (Melnikov et al. 1973).

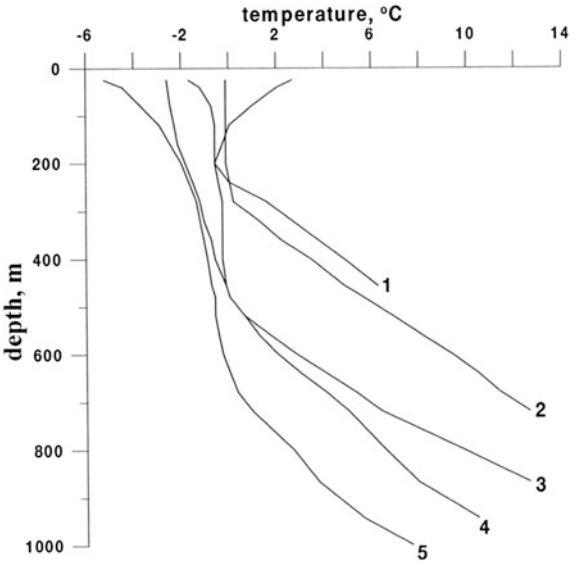

Fig. 5.2 Vertical profiles of a transient temperature field of rocks in different areas. (*1*) Lower Ob', (*2*) Kostrovskii, (*3*) Middle Vilyui, (*4*) Namtsy, (*5*) Bakhynai (Balobayev et al. 1973)

Balobayev et al. (1973) suggested an approximate formula which can be used to evaluate changes in the permafrost thickness when the surface temperature is a linear function of time. It is worth pointing out that at present there are no data showing a contemporary increase of the permafrost thickness with time. Thus the temperature profiles in the permafrost contain a record of the change in the surface temperature in the past. When interpreted in conjunction with heat conduction theory, this source can provide important information on patterns of contemporary climate change. Precision measurements in oil wells in the Alaskan Arctic indicate a widespread warming (2–4 °C) at the permafrost surface during the 20th century (Lachenbruch et al. 1988). It should be noted that the "permafrost surface" is the surface of permafrost which lies beneath an annually thawing (active) layer. Below we present the Berggren formula which can be used to calculate the depth of this layer.

5.2 Changes in the Mechanical and Thermal Properties of Formations at Thawing

Knowing the mechanical properties of frozen formations is the key to understanding the problem of surface and well stability. The mechanical properties of frozen formations depend to a great extent on moisture content and cryogeneous texture. Data on the ice and unfrozen water content of permafrost are essential to predicting permafrost behavior during well drilling and production. Ice content

Table 5.1 Instantaneous and ultimate long term cohesion (in kg/cm^2) of permafrost (Tsytovich 1975)

Type of soil	W_d (%)	$T = -0.3$ to -0.4 °C		$T = -4.0$ to -4.2 °C	
		C_{inst}	C_{lt}	C_{inst}	C_{lt}
Dense varied clay (mineral inter-layers)	30–40	5.7	1.8	16.0	4.2
Silty heavy loam	36	4.3	0.6	12.0	
Silty light loam	30	4.1	0.9	11.0	−2.0
Heavy silty sandy loam	28–34	4.0–4.5	0.9–1.0	8.0–15.0	2.8–3.2
Same, high moisture	43	6.0	1.8	11.0	2.0
Silty sand	23	11.0	2.1	20.0	3.7–4.5

varies widely and depends primarily on the formation type, and the thermal and depositional history of the formation profile (Smith and Clegg 1971).

Only part of a formation's pore water changes to ice at 0 °C. With further drops in temperature, the phase transition of the water continues, but at steadily decreasing rates. The amount of unfrozen water is practically independent of the total moisture content of a given soil (Tsytovich 1975). Frozen soils are bodies in which stresses and strains that arise under the influence of an external constant load are not constant, but vary with time, giving rise to the relaxation of stresses and creep (an increase in strains with the passage of time). These processes are called rheological. The emergence of rheological processes in frozen soils is due to a peculiarity of their internal bonds in which ice plays a role of major importance (Tsytovich 1975). Some values for instantaneous ($C_{\text{ins}}t$) and long term ($C_{\text{l}}t$) cohesion for frozen soils are presented in Table 5.1.

In this table W_d is the ratio (in %) of the total ice-water content to the dry unit weight of the soil. The impact of sea water on mechanical properties of submerged frozen soil is very important for the upper layer of frozen bottom sediments. The results of experimental studies designed to determine the effect of the concentration of pore solution on the strength of the frozen ground are presented in Table 5.2 (Tsytovich et al. 1973).

Research has shown that the long term compressive strength of frozen soils σ_{1t} is well described as a function of the negative temperature (in °C),

$$\delta_{lt} = a + b\sqrt{-T}, \tag{5.2.1}$$

where a and b are constants.

Figure 5.3 shows the relationship between compressive strength and temperature for various types of sand at salt concentrations of 0 and 3 %, and Fig. 5.4 presents a similar relationship for cohesive soils. The compressive strength of frozen soils is highly dependent on the amount of unfrozen water. The measured values of the unfrozen water content for the samples (Figs. 5.3 and 5.4) are presented in Fig. 5.5.

The curves depicting the relationship between the amount of unfrozen water and temperature show that the amount of unfrozen water is closely associated with

Table 5.2 Values of C_8 for soils having different granulometric compositions (Tsytovich et al. 1973). C_8 is the 8 h cohesion

Type of soil	Salt concentration (%)	C_8 (kg/cm^2)		T (°C)	
		−1	−2	−3	−4
Quartz sand with a silt-clay fraction content of 25 %	0.0	4.7	5.4	7.9	9.3
	0.26	1.5	3.1	5.7	7.1
	0.52	0.6	1.2	2.3	3.5
	1.04	–	0.6	1.2	2.3
The same with a silt-clay fraction content of 45 % hydromica clayey sand	0.26	2.6	3.7	6.5	7.4
	0.52	1.3	2.6	–	–
	2.6	–	–	0.6	0.7
	0.23–0.27	2.6	6.1	8.0	12.5
	0.64	2.5	3.7	7.0	11.3
	1.1–1.2	1.2	2.1	5.3	8.7
	2.1–2.5	–	0.4	0.9	1.5
	4.4–5.0	–	–	–	0.4
Quaternary clayey silt (hydromica with montmorillonite admixture)	1.35	–	0.64	1.56	2.35
	2.2	–	0.46	0.78	1.05
	3.2	–	–	0.54	0.87
	4.3	–	–	–	0.5

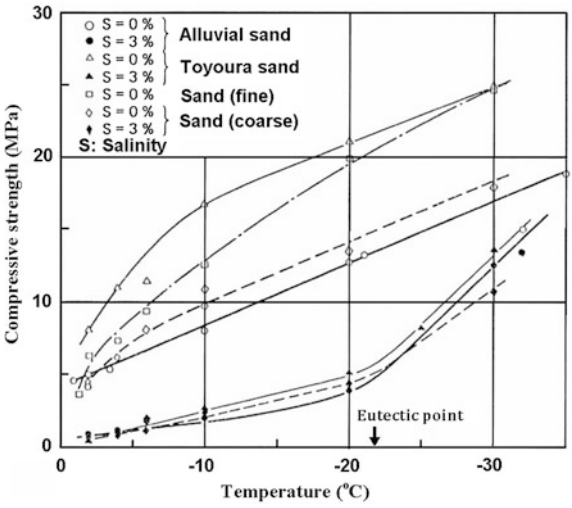

Fig. 5.3 Relation between compressive strength and temperature for sands (Ogata et al. 1982)

the specific surface area of each sample (Ogata et al. 1982). A simple power law (Romanovsky and Osterkamp 2000) is customarily used to relate temperature T (°C) and gravimetric unfrozen water content W_u (kg of H_2O per kg of dry soil):

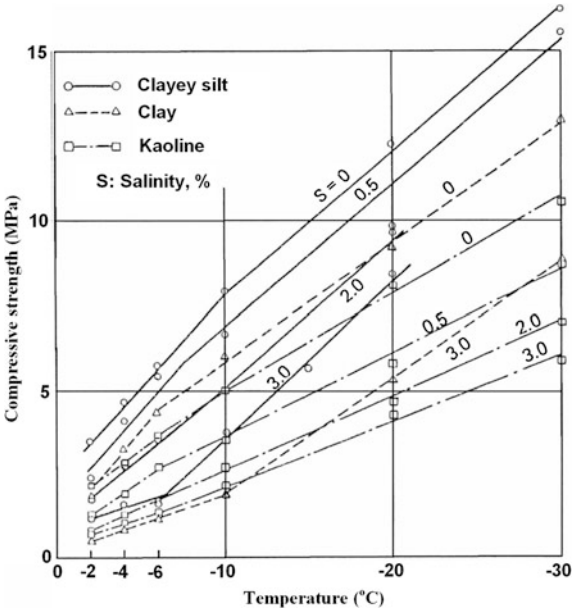

Fig. 5.4 Relation between compressive strength and temperature at various salinities (Ogata et al. 1982)

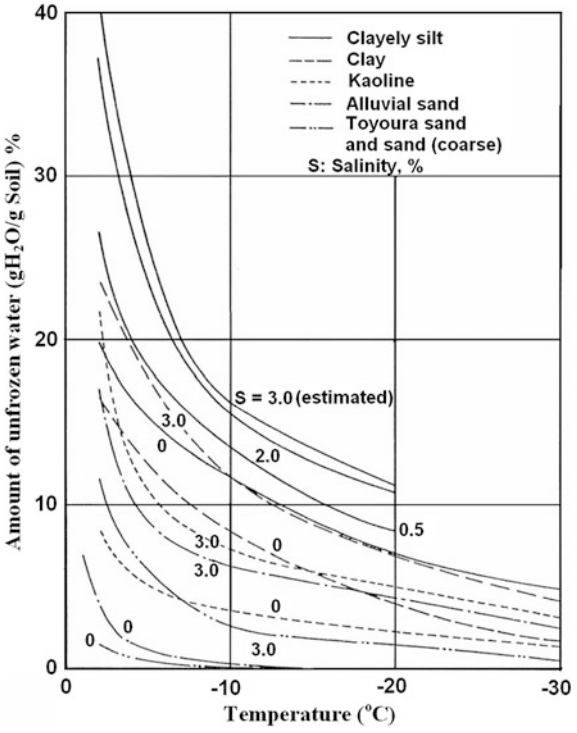

Fig. 5.5 Relation between unfrozen water content and temperature (Ogata et al. 1982)

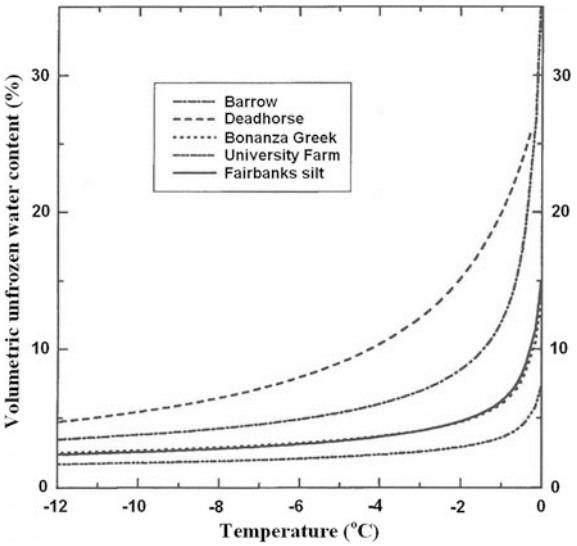

Fig. 5.6 Unfrozen water content curves (Romanovsky and Osterkamp 1999)

$$W_u = A|T|^B, \tag{5.2.2}$$

where A and B are the empirical constants.

However, it is the volumetric unfrozen water $\theta_u = W_u \frac{\rho_b}{\rho_u}$, where ρ_b is the bulk density of the frozen soil and ρ_u is the density of the unfrozen water that is usually measured in the field (Romanovsky and Osterkamp 2000). The unfrozen water content curves for silts at five Alaskan permafrost sites are presented in Fig. 5.6.

For example, the empirical relationship for the University Farm site is $\theta_u = 3.6(-T)^{-0.3}$.

Elastic deformations of frozen soils are governed by purely reversible changes in the crystal lattices of the mineral particles and ice, the elastic properties of the thin films of unfrozen water, and the elastic properties of enclosed air bubbles (Tsytovich 1975). Experiments have shown that the modulus of normal elasticity of frozen soils is tens to hundreds of times larger than that of unfrozen soils. The integrity and stability of pipelines, derricks, and foundations of structures are thus affected by the processes of frost heave and surface subsidence. Both frost heave and surface subsidence are associated with volume changes (about 9 %) at the ice–water–ice transition. In the annual cycle, water phase transitions occur in the active layer; i.e., the layer of seasonal thawing (freezing). Hence, the intensity of the frost heave and surface subsidence are related to the depth of the active layer (h_{al}). To estimate the value of h_{al} the Berggren formula can be used (Pavlov 1974; Lunardini 1988):

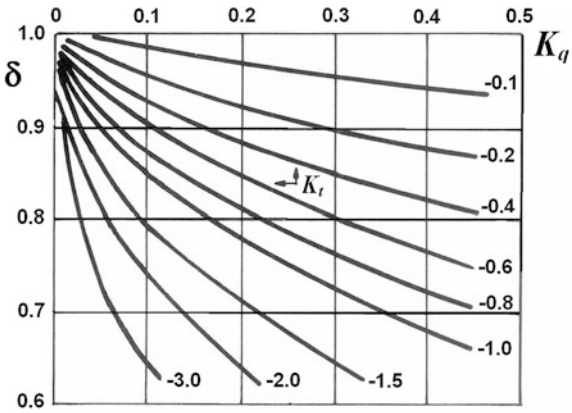

Fig. 5.7 The $\delta = \delta\ (K_t, K_q)$ coefficient (Pavlov 1974)

$$h_{al} = \delta\sqrt{\frac{2\lambda_t T_{et} t_t}{L(w - w_u)}}, \tag{5.2.3}$$

where λ_t is the thermal conductivity of thawed soil, T_{et} is the mean effective temperature of air in degrees above the freezing point (in °C), t_t is the time of thawing, L is the latent heat per unit of weight, w is the total moisture content per unit of soil volume, w_u is the content of unfrozen water per unit of soil volume, and δ a coefficient that can be obtained from Fig. 5.7.

The parameters K_t and K_q are:

$$K_t = \frac{T_0 - T_{fr}}{T_{et}}; \quad K_q = \frac{C_f + C_t}{2L(w - w_u)}, \tag{5.2.4}$$

where T_{fr} is the freezing temperature (in °C), T_0 is the temperature of the layer with zero amplitude of annual temperature change, and C_f, C_t are the volumetric heat capacity of frozen and thawed soil. For calculations, the curves $\delta = \delta(K_t, K_q)$ can be approximated by

$$\begin{aligned} &\delta = 1 - 1.6|K_t K_g|; \quad |K_t K_g| \le 0.06; \\ &\delta = 1 - 1.278|K_t K_g| + (K_t K_g)^2; \quad 0.06 < |K_t K_g| \le 0.45 \end{aligned} \tag{5.2.5}$$

Data on changes in the thermal properties of formations due to thawing are needed to estimate the effect of climate changes on the temperature regime of permafrost and when estimating the rate of thawing at the top and bottom of the permafrost zone.

The melting of ice is accompanied by changes in thermal conductivity (λ), density (ρ), specific heat capacity (c_p) and thermal diffusivity (α), (Tables 5.3 and 5.4, Fig. 5.8). In calculations, the volumetric heat capacity ($C_v = c_p\rho$) is often used.

Table 5.3 Coefficients of thermal conductivity (kcal/m °C h) for typical formations in thawed (at +4 °C) and frozen (at −10 °C) states (Vyalov 1974)

W_c	Sands		Clays		Silts		W_c	Sands		Clays		Silts	
	K_t	K_f	K_t	K_f	K_t	K_f		K_t	K_f	K_t	K_f	K_t	K_f
ρ_d = 1,200 kg/m^3							ρ_d = 1,300 kg/m^3						
0.05	0.51	0.56	0.40	0.46	0.30	0.38	0.05	0.61	0.67	0.50	0.56	0.39	0.49
0.10	0.78	0.92	0.64	0.78	0.46	0.63	0.10	0.90	1.06	0.77	0.89	0.55	0.72
0.15	0.99	1.23	0.83	1.03	0.62	0.84	0.15	1.13	1.37	0.99	1.16	0.73	0.95
0.20	1.15	1.48	1.00	1.26	0.75	1.02	0.20	1.32	1.63	1.18	1.43	0.89	1.16
0.25	1.29	1.70	1.13	1.45	0.89	1.19	0.25	1.48	1.81	1.31	1.64	1.03	1.32
0.30	1.43	1.87	1.22	1.62	1.00	1.33	0.30	1.62	2	1.42	1.81	1.15	1.47
0.35	1.55	1.99	1.28	1.75	1.10	1.47	0.35	1.76	2.17	1.50	1.96	1.26	1.64
0.40	1.65	2.08	1.31	1.86	1.20	1.60	0.40	1.86	2.29	1.57	2.11	1.36	1.76
0.45	1.75	–	1.38	–	1.28	1.70							
ρ_d = 1,400 kg/m^3							ρ_d = 1,500 kg/m^3						
0.05	0.73	0.80	0.62	0.70	0.49	0.63	0.05	0.85	0.94	0.73	0.82	0.60	0.75
0.10	1.03	1.23	0.90	1.05	0.70	0.85	0.10	1.19	1.40	1.03	1.20	0.80	0.99
0.15	1.28	1.56	1.15	1.35	0.85	1.07	0.15	1.45	1.77	1.30	1.53	1.00	1.22
0.20	1.50	1.85	1.35	1.61	1.01	1.27	0.20	1.68	2.11	1.51	1.81	1.16	1.41
0.25	1.68	2.11	1.50	1.84	1.16	1.48	0.25	1.88	2.44	1.69	2.07	1.32	1.59
0.30	1.85	2.30	1.63	2.04	1.29	1.64	0.30	2.05	2.64	1.83	2.27	1.45	1.75
0.35	1.97	–	1.72	–	1.41								
ρ_d = 1,600 kg/m^3							ρ_d = 1,700 kg/m^3						
0.05	0.96	1.06	0.84	0.97	0.70	0.88	0.05	1.09	1.20	0.96	1.07	0.82	1.00
0.10	1.34	1.57	1.18	1.34	0.92	1.12	0.10	1.50	1.71	1.33	1.50	1.06	1.25
0.15	1.63	1.98	1.46	1.71	1.14	1.34	0.15	1.85	1.21	1.66	1.91	1.28	1.50
0.20	1.89	2.33	1.70	2.03	1.32	1.54	0.20	2.15	2.52	1.96	2.23	1.47	1.71
0.25	2.10	2.64	1.88	2.31	1.47	1.71	0.25	2.39	–	2.11	–	1.62	–
ρ_d = 1,800 kg/m^3													
0.05	1.22	1.36	1.06	1.22	0.93	1.12	0.20	2.45	2.58	2.20	2.31	1.64	1.86
0.10	1.77	1.93	1.53	1.68	1.21	1.38	0	2					
0.15	2.13	2.23	1.83	2.08	1.42	1.63							

$W_c = W/\rho_d$; ρ_d is the dry unit weight; W is the total ice-water content of the formation; the unit weight is $\rho = \rho_d(1 + W_c)$

The thermal diffusivity value can be determined from the following relationship $\alpha = \frac{\lambda}{C_v}$. For consolidated formations

$$\lambda_f = (1.1 - 1.3)\lambda_t,$$

where λ_f and λ_t are thermal conductivities of frozen and thawed formations.

Let us assume that q_f and q_t are heat flow densities in the frozen zone and thawed zones at the permafrost base. The condition $q_t/q_f > 1.1$–1.3 indicates that degradation of the permafrost has occurred. For increases in the permafrost thickness to take place, the condition $q_f > q_t$ must be fulfilled.

Table 5.4 Volumetric thermal capacity (kcal/m^3 °C) of typical formations in thawed (at +4 °C) and frozen (at −10 °C) states (Vyalov 1974)

W_c	Sands		Clays		Silts		W_c	Sands		Clays		silts	
	V_t	V_f	V_t	V_f	V_t	V_f		V_t	V_f	V_t	V_f	V_t	V_f
ρ_d = 1,200 kg/m^3							ρ_d = 1,300 kg/m^3						
0.05	260	230	270	260	300	300	0.05	280	245	290	280	325	325
0.10	320	260	330	290	360	340	0.10	345	280	360	310	390	370
0.15	380	290	390	320	420	370	0.15	410	315	425	345	455	405
0.20	440	320	450	350	480	400	0.20	475	345	490	380	520	435
0.25	500	350	510	380	540	430	0.25	540	380	555	410	585	470
0.30	560	380	570	410	600	460	0.30	605	410	620	440	600	500
0.35	620	410	630	440	660	480	0.35	670	445	685	475	715	535
0.40	680	440	690	470	720	520	0.40	735	475	750	510	780	565
0.45	740	470	750	500	780	550							
ρ_d = 1,400 kg/m^3							ρ_d = 1,500 kg/m^3						
0.05	300	265	315	300	350	350	0.05	325	285	335	320	375	375
0.10	370	300	385	335	420	400	0.10	400	325	415	360	450	430
0.15	425	335	455	370	490	435	0.15	475	360	490	400	525	465
0.20	510	370	525	405	560	470	0.20	550	395	560	435	600	505
0.25	580	405	595	440	630	505	0.25	625	435	635	475	675	540
0.30	650	440	665	475	700	540	0.30	700	475	715	510	750	575
0.35	720	475	735	510	770	575							
ρ_d = 1,600 kg/m^3							ρ_d = 1,700 kg/m^3						
0.05	345	305	360	345	400	400	0.05	365	325	385	365	425	425
0.10	425	345	440	385	480	455	0.10	450	365	470	410	510	485
0.15	505	385	520	425	560	495	0.15	535	410	545	450	595	525
0.20	585	425	600	465	640	535	0.20	620	450	640	495	680	570
0.25	665	465	680	505	720	575	0.25	705	490	725	535	765	615
ρ_d = 1,800 kg/m^3													
0.05	390	345	405	385	450	450	0.20	665	475	675	520	720	605
0.10	475	390	495	430	540	515	0.25	750	520	765	565	810	650
0.15	570	430	585	475	630	560	0	7	5	7			

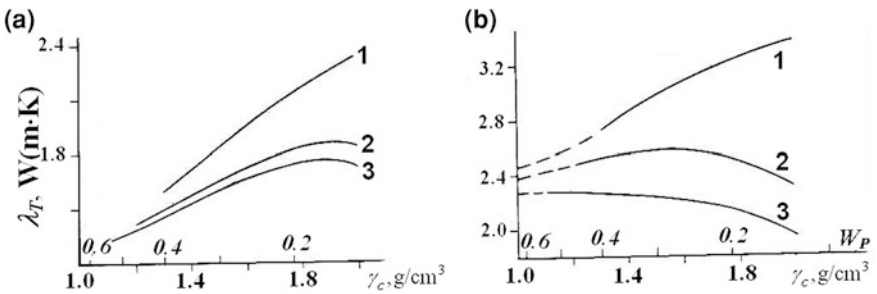

Fig. 5.8 Thermal conductivity dependence of thawed (**a**) and frozen (**b**) formations: γ_c is the dry unit weight, W_p is the water saturation. *1* sand, *2* loamy sand, *3* loamy soil (Balobaev 1991)

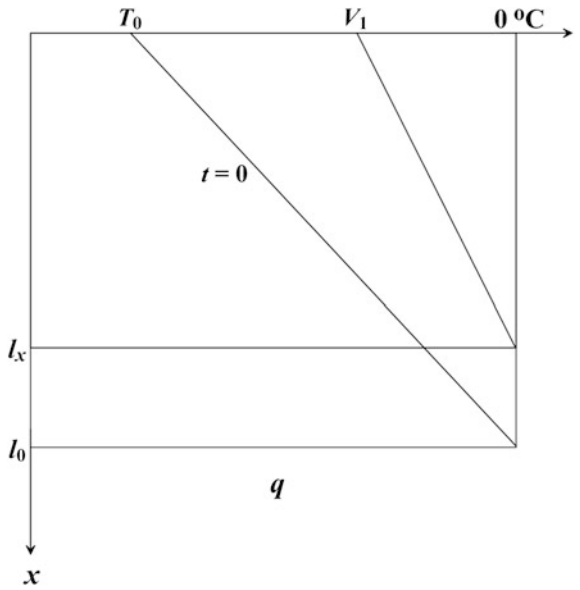

Fig. 5.9 Dynamics of permafrost thickness—a schematic model

5.3 Thickness and Dynamics of the Permafrost

In this section we present a simple model describing the permafrost response to climate change. The schematic model is presented in Fig. 5.9.

Let us assume that at some point in time the temperature of permafrost is given by the curve at $t = 0$; thereafter the top of the ice-bound permafrost is maintained at temperature V_1, and the melting temperature of ice is equal to 0 °C. When the salinity of frozen formations can be estimated, the melting temperature at the permafrost base should be specified (Osterkamp 1983). For small values of time t we can assume that the heat flow from the base of the permafrost into the frozen zone is equal to heat flow for the case when the base of permafrost remains fixed (Lachenbruch and Marshall 1977; Lachenbruch et al. 1982; Osterkamp 1983).

In this case, we need to approximate the transient behavior of the temperature in a slab (T_s) of a constant thickness, l_0, with an initial linear temperature distribution and with the upper and lower surfaces maintained at constant temperatures (V_1 and 0 °C) for $t > 0$. The corresponding diffusivity equation is:

$$\alpha_f \frac{\partial^2 T_s}{\partial x^2} = \frac{\partial T_s}{\partial t}; \quad t > 0, \quad 0 \le x \le l_0 \tag{5.3.1}$$

with the initial an boundary conditions

$$\begin{aligned} &T_s = T_0 + kx; \quad k = -\frac{T_0}{l_0} \quad at \;\; t = 0, \\ &T_s(0,t) = V_1; \quad T_s(l_0,t) = 0 \quad at \;\; t > 0, \end{aligned} \tag{5.3.2}$$

where l_0 is the initial depth of the permafrost, T_0 is the long-term mean annual temperature at $t = 0$, and V_1 is the long-term mean annual temperature of the top of ice-bounded permafrost at $t > 0$.

The solution of this equation is known (Carslaw and Jaeger 1959):

$$T_s = V_1 - V_1 \frac{x}{l_0} + \frac{2(T_0 - V_1)}{\pi} \sum_{n=1}^{\infty} \frac{1}{n} \sin \frac{\pi n x}{l_0} \exp\left(-F_0 n^2 \pi^2\right), \tag{5.3.3}$$

where the dimensionless time-Fourier number is

$$F_0 = \frac{\alpha_f t}{l_o^2}$$

and a_f is the thermal diffusivity of the ice-bound permafrost. The temperature gradient at the base of the permafrost ($x = l_0$) from Eq. (5.3.3) is:

$$\Gamma_b = \frac{dT_s}{dx} = -V_1 \frac{x}{l_0} + \frac{2(T_0 - V_1)}{\pi} \sum_{n=1}^{\infty} (-1)^n \exp\left(-F_0 n^2 \pi^2\right). \tag{5.3.4}$$

The temperatures of frozen formations near the permafrost base are close to 0 °C. Hence, the amount of heat which is consumed in warming the permafrost to the melting temperature is small and can be neglected. The value of l_x under these assumptions can be obtained from the thermal balance condition

$$-\lambda_f \int_0^t \Gamma_b \, dt + qt = L_v (l_0 - l_x), \tag{5.3.5}$$

where q is the heat flow density (geothermal flux), L_v is the latent heat of melting per unit of volume of the frozen formation, and l_x is current depth of the permafrost base.

From formulas (5.3.4) and (5.3.5) we obtain

$$l_x = l_0 + \frac{\lambda_f (T_0 - V_1)}{L_v l_0} \left(t_0 - \int_0^t \psi \, dt \right), \tag{5.3.6}$$

$$\psi = -\sum_{n=1}^{\infty} \left(-F_0 n^2 \pi^2\right)^n \exp\left(-F_0 n^2 \pi^2\right). \tag{5.3.7}$$

A simple computer program can be used to estimate the value of l_x. For approximate calculations Table 5.5 can be used.

Table 5.5 The function $\Psi = \Psi(F_0)$

Ψ	F_0
0.5	$0.04 \geq F_0 > 0$
$0.592\exp(-4.223F_0)$	$0.06 \geq F_0 \geq 0.04$
$\exp(-\pi^2 F_0) - \exp(-4\pi^2 F_0)$	$0.15F_0 \geq 0.06$
$\exp(-\pi^2 F_0)$	$F_0 \geq 0.15$

For large values of time, assuming a steady-state distribution of temperatures in the frozen zone, the Stefan equation is

$$-\lambda_f \frac{V_1}{l_x} - L_v \frac{dl_x}{dt} = q. \tag{5.3.8}$$

Now the temperature distribution is

$$T_s = V_1 - \frac{V_1}{l_x} x; \quad x \leq l_x. \tag{5.3.9}$$

The solution of Eq. (5.3.8) is

$$t = \frac{L_v}{q^2}\left[q(l_0 - l_x) + \lambda_f V_1 \ln\frac{\lambda_f V_1 + q l_x}{\lambda_f V_1 + q l_0}\right]_x. \tag{5.3.10}$$

From Eq. (5.3.8) the minimum value of l_x is when

$$\frac{dl_x}{dt} = 0 \quad at\ t \to \infty,$$

$$l_{x,\min} = -\frac{\lambda_f V_1}{q}. \tag{5.3.11}$$

For Prudhoe Bay (Alaska) this simple model characterizes the response of the permafrost to a sudden change in the mean annual surface temperature as shown in Fig. 5.10.

Note that here the thawing temperature at the permafrost base is assumed to be -1 °C. Melting at the base of the permafrost amounts to ≈ 3.5 m during the first 1,800 years and is ignored in this graph. A more realistic model of the dynamics of the temperature field and the permafrost thickness that accounts for the possible time variations in surface temperature can be represented by an expression of the form (Lachenbruch et al. 1982, 1988):

$$T_0(0, t) = Dt^{n/2}, \quad 0 < t < t_0, \tag{5.3.12}$$

where D is a constant, n can be any positive integer, and t is the time since the start of the warming; $t = t_0$ represents the present day.

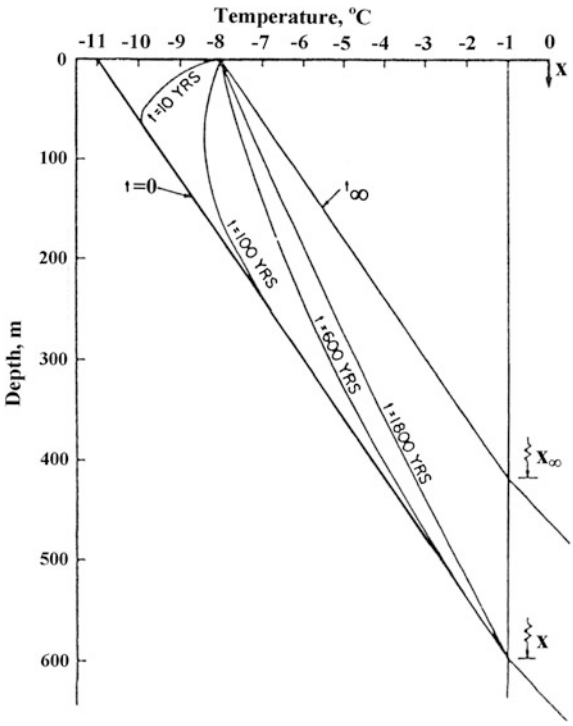

Fig. 5.10 Thermal warming model for the continuous permafrost zone (Osterkamp 1983)

Duchkov et al. (1997) used numerical modelling to predict the possible evolution of the temperature field of permafrost rocks until the year 2100. The authors assumed a stable increase in the permafrost surface temperature at a rate of 0.02–0.06 °C/year. It has been shown that the past climate may considerably accelerate the permafrost degradation in the West-Siberian region. This may cause serious problems for oil and gas exploration and production in the future.

5.4 Results of Long Term Temperature Surveys

Investigations of the temperature field of the permafrost zone and calculations of the permafrost thickness are based mainly on the results of temperature surveys in deep boreholes. Due to the thawing of the surroundings of these wellbore formations, representative data can be obtained only by repeated observations over a long period of time. In the last several decades long term temperature observations in deep boreholes have been conducted in Alaska, Canada, and Russia (Lachenbruch and Brewer 1959; Melnikov et al. 1973; Taylor et al. 1982; Kutasov and Eppelbaum 2012b). The temperature observations in deep wells have shown

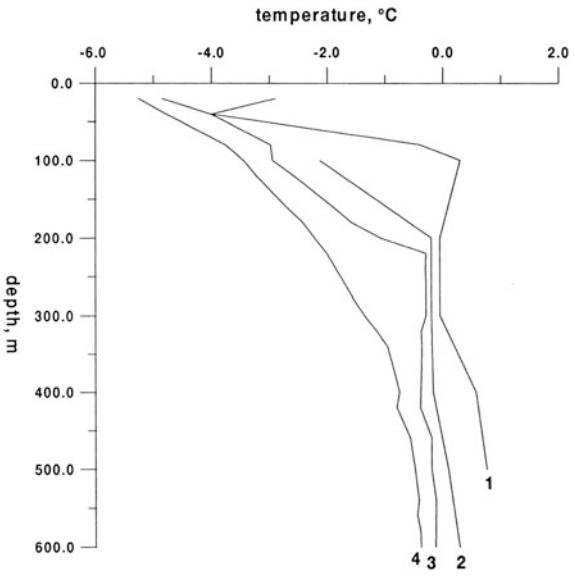

Fig. 5.11 Restoration of the temperature profile in the Bakhynay borehole 1-R (Melnikov et al. 1973). Temperature surveys (*1*), (*2*), (*3*), and (*4*) were conducted for shut-in times of 0.4, 1.5, 3.4 and 10.4 years respectively

that that the temperature of frozen formations can be only be estimated with sufficient accuracy after a lengthy shut-in period. Hence a single temperature log cannot be reliable. Let us examine the restoration of the natural temperature field by taking the example of the Bakhynay borehole 1-R (Melnikov et al. 1973). The borehole was drilled for 23 months (1956–1958) to a depth of 2,824 m. Sands and weakly cemented sandstones with clay and siltstone partings were revealed in the range from 19 to 1,500 m. Nine temperature logs were collected over a shut-in period of 10 years, but the difference between the temperature of the formations and the temperature in the borehole nevertheless exceeded measurement accuracy (0.03–0.05 °C). After a shut-in period of 1.5 years the thickness of the permafrost was estimated as 470 m instead of 650 m. The restoration of the temperature regime was accompanied by the formation of practically zero temperature gradient intervals (Fig. 5.11). Therefore, if the shut-in time is insufficient, zero temperature gradient intervals can be erroneously attributed to geological-geographical factors. Here, the factor was the warming effect of the Lena River (the drilling site is the bank of the river). Temperature observations in the Amga borehole (Central Yakutia, Russia; well depth 1,109 m, drilling time 13 months) for a period of 14 years (Fig. 5.12) showed that 8–9 years are needed to determine the position of the permafrost base.

Extensive temperature measurements in the Northern Canada were conducted by the Geothermal Service of Canada (Judge et al. 1981; Taylor et al. 1982). For example, Fig. 5.13 presents the results of temperature surveys in the Kamik D-48 well (Mackenzie delta, Canada). The well was drilled for 102 days, and drilling operations were stopped on April 4, 1976 at a total depth of 3,235 m. The field data also showed

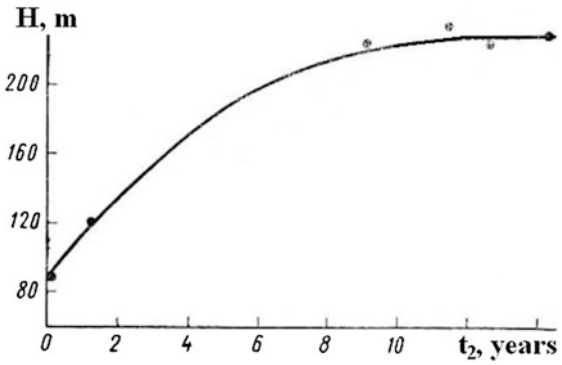

Fig. 5.12 The position of the 0 °C isotherm versus the shut-in time, the Amga borehole (Kutasov 1976)

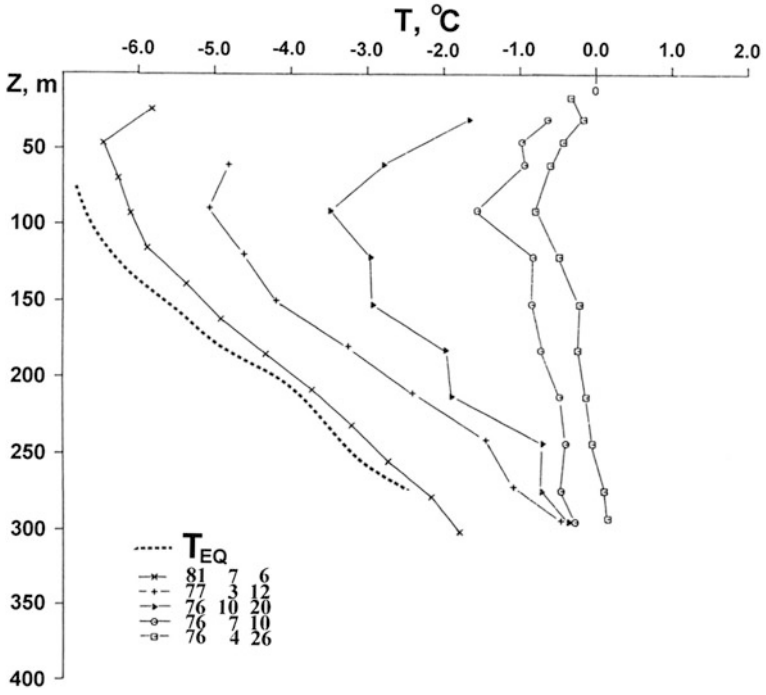

Fig. 5.13 Temperature profiles in the Kamik D-48 well, *TEQ*—the predicted temperature versus depth *curve* (Taylor et al. 1982)

that the duration of refreezing of the formation thawed out during drilling depends crucially on its natural (undisturbed) temperature. For low temperature permafrost, the refreezing period is relatively short (see Fig. 8.6 in Chap. 8).

5.5 Climate Change and the Temperature Regime of Permafrost

5.5.1 Forecasting Climate Change and the Permafrost Thickness for Central Yakutia

Geothermal measurements (temperature profiles, thermal conductivity of formations) in permafrost regions (Alaska, Northern Canada, Siberia, etc.) can provide a good source of information related to the widely discussed issue of global warming during the last century. In fact, the anomalies in the temperature profiles (the departure of temperature profiles from linearity at a constant thermal conductivity of the formations) in the permafrost contain a record of changes in the surface temperature in the past (Osterkamp 1983). In addition, changes in the heat flow density at the permafrost base (frozen–unfrozen interface) are also an indicator of climate change in the past (Melnikov et al. 1973). For example, precision measurements in oil wells in the Alaskan Arctic indicated a widespread warming (2–4 °C) at the permafrost surface during the 20th century (Lachenbruch et al. 1988). The issue of global warming has been debated for the last 20–25 years. Although most of the observed warming over the last 25 years is now considered a firmly established scientific fact, the causes of global warming remain unclear. The scientific community is divided into two "camps" supporting opposing views: one camp argues that global warming is a naturally occurring process triggered by an external energy source having a periodic origin and leading to a continual change of cold and warm eras on the globe. Hence the current period of warming is a transient phenomenon which must give way to a cooling within some time interval. The other camp is of the opinion that this most recent episode of warming coincides with industrialization, the rapid growth of the human population, and the large-scale use of fossil fuels. As a result substantially increased amounts of industrial gases (mainly carbon dioxide) are released into the atmosphere. These gases are lumped together as "greenhouse" gases, because they prevent heat from being lost by the surface via long-wavelength radiation into space. As a consequence, the observed increase in the amount of greenhouse gases in the Earth's atmosphere resulting from this anthropogenic effect leads to a rise in ground-level air temperatures. The controversy over global warming has become a challenge to permafrost researchers, who are concerned about the degradation of the permafrost and the subsequent destruction of the natural environment. Thus to be able to forecast changes in the temperature regime and phase state of permafrost, scientists have attempted to model the time variation of the permafrost surface for the near future. Below we present the results of long term investigations of the temperature regime in two permafrost regions (Balobaev et al. 2009a, b; Osterkamp 2005).

5.5.2 Characteristics of Global Warming in Central Yakutia

According to data from the Yakutsk meteorological station, the yearly mean air temperature for the last 40 years has increased by 2.5 °C (Fig. 5.14). This is an impressive figure, but it would not be warranted to call it global warming. For specific territories, temperature is, to a large extent, determined by the nature and intensity of the transport of air masses, and by their variability in the case of global warming.

In the Arctic regions of Yakutia, which have a different atmospheric circulation pattern, the current rise in temperature does not exceed 1 °C, and there has been no temperature increase in some places. The greatest concern has been directed toward the state of the permafrost occupying more than half of the territory of Russia, its possible thawing out, and the increase in its seasonal thawing from the surface. In 1998, the Permafrost Institute (Russia) in collaboration with the Geophysical Institute of the University of Alaska (USA) carried out a harmonic analysis of long series of air temperature observations from Yakutsk and Fairbanks. These observations indicated that the temperature variations at Yakutsk are reasonably well described by a constant component and four fundamental harmonics with periods of 300, 110, 75 and 14 years. Analysis of the constant component for the period 1950–2000 characterized by the greatest amount of climate change did not reveal any rise in temperature (Balobaev et al. 2009a). Nor was there any linear component of the curve, which would correspond to an increase in CO_2. This implies that no greenhouse effect on temperature was observed in the area of Yakutsk. A temperature maximum occurred due to the fact that the maxima of positive harmonic amplitudes coincided in phase. It was observed in 2008 and was followed by cooling. From the date of maximum warming onward, the temperature behavior after 2008 can be reasonably well described by the formula:

$$\left\{\begin{array}{l} T = A_1 \cos\left(2\pi \frac{t-2008}{P_1}\right) + A_2 \cos\left(2\pi \frac{t-2008}{P_2}\right) \\ \quad + A_3 \cos\left(2\pi \frac{t-2008}{P_3}\right) - A_4 \cos\left(2\pi \frac{t-2008}{P_4}\right) - 10.0 \\ A_1 = 0.63\ ^{o}\mathrm{C}, \quad A_2 = 0.67\ ^{o}\mathrm{C}, \quad A_3 = 0.67\ ^{o}\mathrm{C}, \quad A_4 = 0.25\ ^{o}\mathrm{C} \\ P_1 = 300 \text{ years}, \quad P_2 = 110 \text{ years}, \quad P_3 = 75 \text{ years}, \quad P_4 = 14 \text{ years} \end{array}\right\}, \tag{5.5.1.}$$

where P_1 –P_4 are the harmonic periods.

Figure 5.15 presents the air temperature behavior in the area of Yakutsk for the period into 2200 as plotted using the suggested formula or graphically by combining all harmonics for each year. The results of this analysis indicate the end of warming in the time interval from 2005 to 2017, when the temperature will reach −8.0 °C. After that, the period into 2054 will show an intense decrease in temperature to −11 °C, which will be followed by the next period of warming from 2088 to 2098, when the temperature will increase to −(8.5 ÷ 9.0) °C. The next

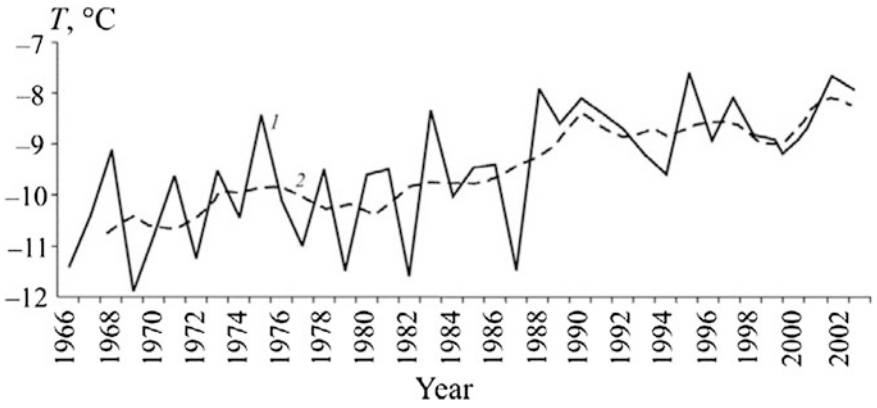

Fig. 5.14 Yearly mean temperature variability based on data from the Yakutsk meteorological station for the time interval from 1966 to 2002. Temperature: (*1*) yearly mean, (*2*) moving average for five years (Balobaev et al. 2009a)

century will be characterized by relatively consistent temperatures, but it will decrease to −11.5 °C by the end of the 22nd century. This will be the lowest temperature since 1900.

Thus climate changes as inferred from long-term meteorological observations are caused by a variety of energetic effects on the terrestrial system. Their periodicity suggests that they have an extraterrestrial origin. The terrestrial system is in energetic equilibrium, but when external effects begin to cause it to depart from equilibrium, processes arise on Earth which not only impede this but also enhance the energetic influences. Analysis of the terrestrial climate changes for the last 400 thousand years using ice cores from a deep Antarctic borehole at the "Vostok" station revealed enhanced warming when there is coincidence of the positive harmonic phases caused by changes in the orbital characteristics of the Earth (Balobaev et al. 2009a).

As regards the current global warming debate, the resonance effect manifests itself as follows. In a normal situation, heat from solar energy leads to a definite yearly mean temperature on the terrestrial surface which differs across different latitudes, natural zones, oceans, and continents. Under these conditions, a certain background temperature is reached (in the area of Yakutsk it is −10 °C).

Additional energy (whose source is not always easy to define) when applied to the terrestrial system, leads to an uneven increase in temperature of different elements on the planet's surface. The ocean is heated faster and more strongly because of its high energy capacity, and its high heat assimilation. As a consequence of the rise in temperature of the oceanic waters, part of the gases diluted in them (including greenhouse gases) is released into the atmosphere. In the case of carbon dioxide, there is some evidence that there is a factor of 60 more CO_2 in the ocean than in the entire atmosphere. To increase the CO_2 concentration in the atmosphere by a factor of two, the ocean would need only get rid of less than 2 %

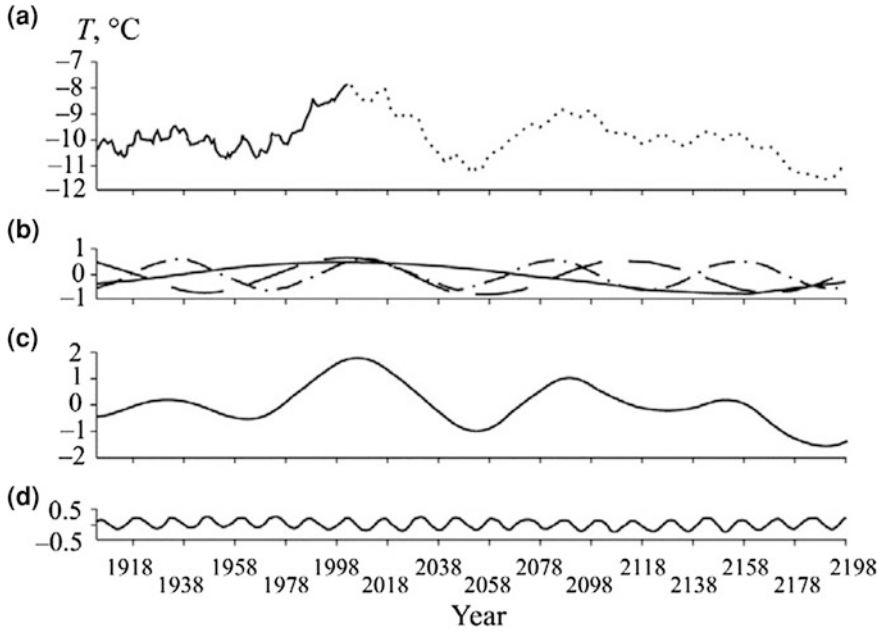

Fig. 5.15 *Predictive curve* of temperature variation for Yakutsk from 2000 to 2200 (**a**), and its component harmonics (**b**–**d**). (**a**) *solid* portion of the line—according to the field measurements, *dashes*—forecast; (**b**) harmonics forming part of *curve* (**a**); (**c**) *curve* combining the influence of three harmonics (**b**) and repeating the main temperature behavior plotted in (**a**); (**d**) low-period and low-amplitude oscillations (Balobaev et al. 2009a)

of the diluted gas. Hence warming of the oceanic waters is always accompanied by an increase in the concentration of greenhouse gases in the atmosphere without any input from industrial society, which does however lead to some rises in temperature in the terrestrial system through the greenhouse effect and impact the equilibrium state even more powerfully. This is what is known as the resonance effect.

In the terrestrial system, the resonance effect accelerates the development of processes aimed at a minimization and attenuation of the influence of external energy sources. One such energy-intensive process is the weak response of the ocean. Its warming leads to an increase in evaporation from the surface of the water. The water-saturated air weighs less than the dry air; therefore, it goes up to the upper layers in the troposphere. It is superseded by the drier air from the mainland. Between the ocean and the mainland a closed convective heat exchange chain is created. The water-saturated air moves toward the continent in the upper atmospheric layers, whereas the lower layer moves in the opposite direction from the drier air toward the ocean (Balobaev et al. 2009). Over the mainland condensation of moisture takes place with a release of thermal energy. However, only a very small part of this energy returns to the terrestrial surface. Most of the energy

is radiated into space. Thus the closed evaporation cycle of the water from the ocean and its condensation in the troposphere is largely aimed at cooling the terrestrial surface. This process leads to an intensification of the circulation processes in the atmosphere, and to an enhancement of cyclonic weather conditions. This is confirmed by hurricanes and rainstorms in countries near oceans as well as by abrupt changes in weather patterns. These are especially exacerbated in the spring and the summer, when a rapid alternation of warming and cooling of the ocean and land surface takes place. Even in very continental regions such as Yakutia, an enhancement of cyclonic processes has been observed. Analysis of the weather conditions for the last 10–15 years shows that the winter season has experienced warming because of the increasing number of cloudy days and there is scarcely any warming in the summer for the same reason. In the wintertime, clouds act to warm the terrestrial surface, thereby decreasing its long-wavelength radiation, whereas in the summer they cool it, thus impeding solar radiation from reaching the Earth.

To forecast changes in the thermal and phase state of the permafrost caused by current-day warming and the subsequent climate change requires a transition from air temperature to permafrost temperature. The difference between them is considerable and depends on many natural factors, including snow cover, the properties of the soil and vegetation. For that reason, Balobaev et al. (2009a) decided on one very simple approach; namely, to calculate whether the correlation between air temperatures and permafrost surface temperature were similar to the correlations observed in previous years. The authors compared air temperatures with permafrost temperatures at a depth of 3.2 m using the data from the Yakutsk meteorological station between 1963 and 2003 (Table 5.6). This correlation was used to infer the permafrost surface temperature and its variations in the next 200 years (see Fig. 5.15). Using the known permafrost surface temperature, it is possible to calculate the variation in permafrost thickness (Table 5.7), and the nature of the permafrost temperature field. To do so, the computational formulas below were used for the following initial and boundary-value conditions (Balobaev et al. 2009a).

On the permafrost surface, $z = 0$:

$$T_s = T_0 + bt. \tag{5.5.2.}$$

On the permafrost base the Stefan equation is specified

$$\lambda \frac{dT}{dz} - q = Q \frac{dH}{dt}, \tag{5.5.3}$$

where λ is the thermal conductivity of the frozen zone, q the heat flow flux to the base of the permafrost, Q is the heat of phase transitions, and H is the permafrost thickness.

Table 5.6 Air temperatures and permafrost temperatures (Balobaev et al. 2009a)

Years	1963–1966	1967–1972	1973–1979	1980–1984	1985–1990	1991–1996	1997–2003
T air	–11.5	–11.0	–10.5	–10.0	–9.5	–9.0	–8.5
T soil	–2.6	–2.3	–2.0	–1.6	–1.2	–0.9	–0.5
ΔT	–8.9	–8.7	–8.5	–8.4	–8.3	–8.1	–8.0

$$Q = \delta\sigma\frac{W}{1+W}, \tag{5.5.4}$$

where δ is the specific heat of melting ice, σ is the formation density, and W is rock moisture capacity: $W = W_c\rho_d$ (W_c is the total ice-water content of the formation, ρ_d is the dry unit weight).

In its final form, this problem cannot be solved because of its nonlinearity. It can only be approximately solved numerically by specifying the piecewise linear nature of surface temperature variation across time. With these conditions taken into consideration, formulas were derived for calculating the movement of the lower boundary of permafrost.

When $\Delta = (4\beta - 1) > 0$, we have

$$2\ln\frac{T_s}{T_0} = \ln\frac{x^2\left(x_0^2 + x_0 + \beta\right)}{x_0^2\left(x^2 + x + \beta\right)} + \frac{2}{\sqrt{\Delta}}ctg^{-1}\left[\frac{2(x - x_0)\sqrt{\Delta}}{\Delta + (2x+1)(2x_0+1)}\right]. \tag{5.5.5}$$

When $\Delta = (4\beta - 1) < 0$, we have

$$2\ln\frac{T_s}{T_0} = \ln\frac{x^2\left(x_0^2 + x_0 + \beta\right)}{x_0^2\left(x^2 + x + \beta\right)} + \frac{2}{\sqrt{-\Delta}}th^{-1}\left[\frac{2(x - x_0)\sqrt{-\Delta}}{-\Delta + (2x+1)(2x_0+1)}\right]. \tag{5.5.6}$$

When $T_s = \text{const}$ ($b = 0$), we have

$$\frac{tq}{Q} = (H_0 - H) + \frac{\lambda T_s}{q}\ln\frac{\lambda T_s + qH}{\lambda T_s + qH_0}. \tag{5.5.7}$$

In the formulas, we used the following notations

$$x = \frac{T_s\lambda}{qH}, \quad x_o = \frac{T_o\lambda}{qH_o}, \quad \beta = \frac{\lambda bQ}{q^2}.$$

The results derived from forecasting the changes in permafrost temperature and thickness for the period into 2200 are presented in Fig. 5.16. Notwithstanding the considerable surface temperature changes (by more than 2 °C) the permafrost thickness changes little. By and large the permafrost zone is an exceptionally inertial natural system. As a result, changes in the conditions on the terrestrial surface propagate slowly and to small depths and attenuate rapidly. When the

Table 5.7 Variation in permafrost thickness for the period from 1950 to 2200 (Balobaev et al. 2009a)

Index	Years										
	1950	1975	2000	2025	2050	2075	2100	2125	2150	2175	2200
Surface temperature (°C)	–2.0	–1.5	–0.5	–0.9	–2.3	–1.1	–0.9	–1.6	–1.6	–2.2	–2.4
Permafrost thickness (m)	326	324	321	321	321	317	316	316	315	314	313

climate changes, the only risk factor is the transition in the permafrost surface temperature to the region of positive values. If this is the case, the permafrost will start to thaw out from its surface or there will be a significant increase in summertime thawing. If so, the natural landscape envelope will be altered drastically, and the stability of the life-supporting and engineering infrastructure systems will reach a critical threshold, followed by the onset of their complete destruction. Thawing from the surface need only reach a depth of 4–5 m for destruction of all ground-based structures in the region of the permafrost zone. The predictive analysis of the development of a cryogenic situation shows that such a situation is not likely to occur in the near future. However, it must be taken into consideration that such forecasts over a very long period of time are largely inaccurate and the predictive value is low or null. To calculate the nature of the temperature field in the permafrost the surface temperature changes inferred here, the heat conduction equation can be applied. Balobaev et al. (2009a) specified the temperature on the surface in the form of a piecewise linear function. The calculations were made for the dates of transition in the direction of temperature reversal from cooling to warming and back.

For instance, using the initial temperature distribution inferred from measurements in a borehole in the area of Yakutsk in 1960, the geothermal curve was constructed. Unfortunately, it was not preserved, so we do not know to what extent the calculated and actual fields coincide. However, the other parameters for the same area indicate that from 1991 to 2003 the temperature to a depth of 70 m rose slightly (Table 5.8). The permafrost temperature and thickness for the period into 2200 is presented in Fig. 5.16.

5.5.3 Recent Warming of the Permafrost in Alaska

Global circulation models predict that air temperatures in the Arctic will rise 2 to 5 °C in the next half century (Osterkamp 2005). Since continuous permafrost is typically colder than −5 °C, no widespread thawing is expected although some areas may experience localized thawing, slope instability and ice wedge thawing. Discontinuous permafrost is much warmer so that the effects of climatic warming

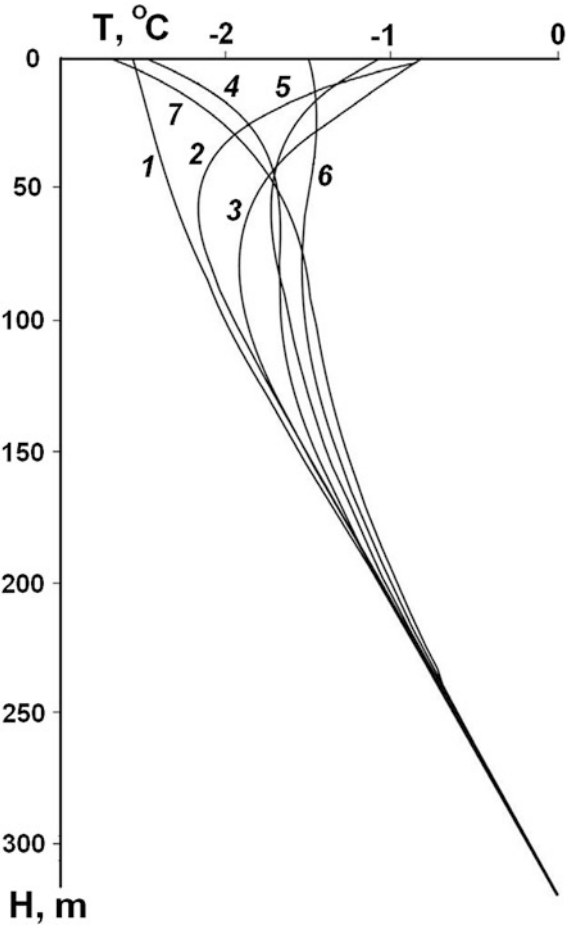

Fig. 5.16 Forecasted changes in the permafrost temperature field in the area of Yakutsk for the period 1960–2200. Years: (*1*) 1960, (*2*) 2000, (*3*) 2025, (*4*) 2050, (*5*) 2105, (*6*) 2150, (*7*) 2190 (Balobaev et al. 2009a)

Table 5.8 Permafrost temperature variation at different depths for the period 1991–2003

Index	Depth (m)							
	5	10	20	30	40	50	60	70
T–1991	–1.5	–2.0	–2.1	–2.2	–2.2	–2.2	–2.2	–2.1
T–2003	–1.9	–2.3	–2.0	–2.1	–2.1	–2.2	–2.1	–2.1
Δ*T*	–0.4	–0.3	0.1	0.1	0.1	0	0.1	0

will have a much greater impact (Osterkamp et al. 1997). Additional warming will cause more of it to thaw and a warming of several degrees would cause most of it to begin thawing. Thawing proceeds from the top downward and, eventually, from the bottom upward. Thawing rates are slow, initially on the order of 10 cm/year near the surface, and theoretically less than 2 cm/year at the base

(Lachenbruch et al. 1982; Osterkamp 1983) so that times on the order of decades to millennia are required to thaw discontinuous permafrost. Given the above conditions and the predictions of current climatic models, it is important to monitor the thermal regime of permafrost and to determine the effects of recent climatic variations on it. Osrerkamp (2005) described the results of temperature measurements recorded during the last quarter century in Alaska at permafrost observatories along a north–south transect that spans the continuous and discontinuous permafrost zones. In 1977, a project was initiated to measure the thermal regime of undisturbed permafrost in Alaska to determine the effects of climate and environmental conditions on permafrost. Permafrost observatories, where active layer and permafrost temperatures and other quantities are measured, were established along a north–south transect of Alaska in undisturbed terrain from Prudhoe Bay to Glennallen and in a few other areas of the state. Automated temperature loggers were installed at some sites in 1986. Since then, temperatures have been measured six times a day. Access holes, typically 60 m in depth (range 15–80 m), were drilled. More detailed information on the observatories and measurements can be found in Osterkamp (2003). Figure 5.17 shows selected annual temperature profiles at a site on the Arctic Coastal Plain in continuous permafrost (Deadhorse) and in southern mainland Alaska in discontinuous permafrost (Gulkana). The data from these two sites, near each end of the transect, illustrate the persistent warming that has occurred at most sites along the transect. Deadhorse continued to warm through 2003 while a slight cooling occurred in the 2000 and 2002 profiles for Gulkana.

Osrerkamp (2005) pointed out there are several methods to calculate approximate temperature changes at the permafrost surface from the borehole temperature measurements. Visual extrapolation of the curved temperature profiles to the surface yielded values ranging from about 1/2 to 5 °C considering all the holes. A more satisfactory method was to fit a curve (usually linear or exponential) to a profile at depth and extrapolate it to the surface. The third method was to calculate the changes in temperatures with depth, fit a curve to these changes (exponential or power law) and extrapolate that curve to the surface (Fig. 5.18).

Lachenbruch and Marshall (1986) used the second and third methods with linear and power law fits in their analyses of the century-long warming of permafrost in Northern Alaska. Except for a few sites along the transect, the exponential curves gave the best fits.

On the basis of these two methods employing exponential or linear functions, results (Fig. 5.19) for the magnitude of the total warming at the surface of the permafrost were shown to fall into three groups; 3–4 °C for the Arctic Coastal Plain, 1–2 °C for the northern foothills of the Brooks Range through the southern foothills, and 0.3–1 °C south of the Yukon River.

The timing of the recent warming (late 1980s) suggests that the thin discontinuous permafrost may be thawing from the bottom at some sites. Figure 5.20 shows the position of the bottom of the permafrost (0 °C) at the Gulkana site obtained by extrapolation of measured temperatures. The mean thawing rate was about 4 cm/year (1989–2002) with a value of 9 cm/year from 2000 to 2002.

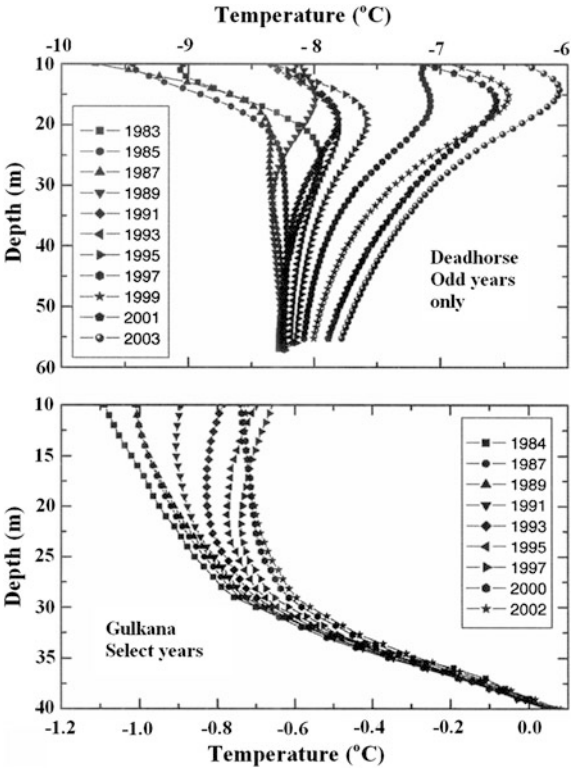

Fig. 5.17 Selected annual temperature profiles, 1983–2003, at sites near each end of the transect (Osrerkamp 2005)

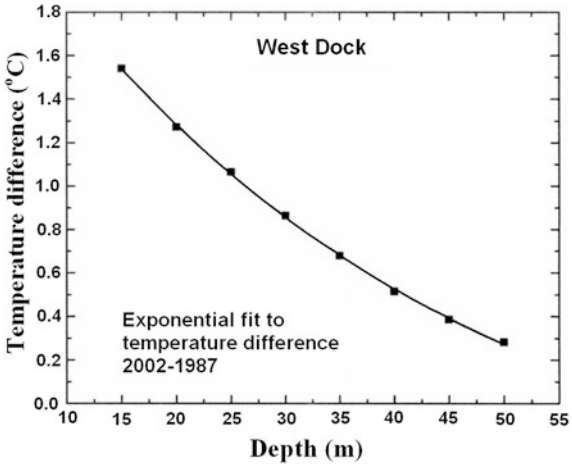

Fig. 5.18 An exponential fit to temperature differences between 1987 and 2002 for 5 m depth increments at the West Dock site (Osrerkamp 2005)

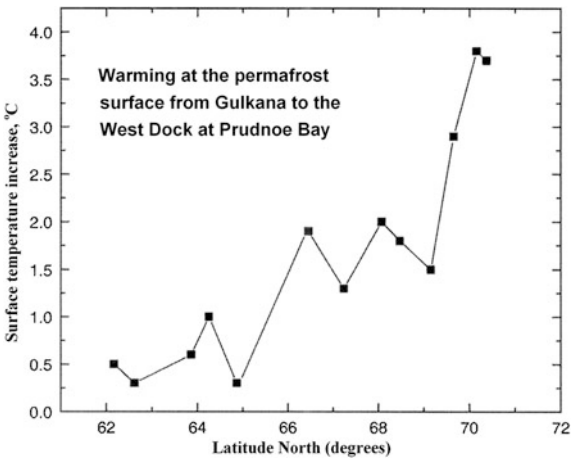

Fig. 5.19 Warming at the permafrost surface with latitude along the transect from Gulkana in south-central Alaska to Prudhoe Bay on the Beaufort Sea Coast (after Osrerkamp 2005)

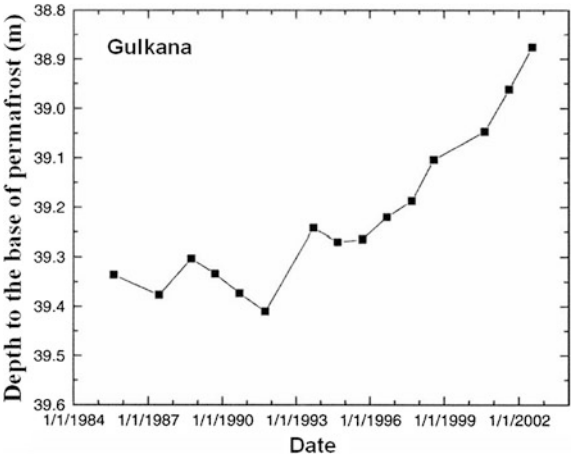

Fig. 5.20 Depth to the bottom of permafrost (0 °C) at the Gulkana site (1984–2002)

More than half a meter has thawed at the bottom of the permafrost since 1991 (Osrerkamp 2005).

Hence in the first case (Balobaev et al. 2009a) the analysis of air temperature changes for the last 200 years revealed no influence of "greenhouse" gases. Warming has reached its maximum to date and will soon be followed by cooling. In the permafrost zone, the thermal state of the permafrost was slightly affected by the current warming (Table 5.8).

The results of the second experimental study (Ostercamp 2005) show that from 1977 to 2003 a significant warming of permafrost zone occurred along the north–south transect of Alaska (Figs. 5.18, 5.19 and 5.20) which coincided with a statewide warming of air temperatures that began in 1977. This result is consistent with greenhouse-forced climate models that predict greater climate change at high latitudes.

References

Balobaev VT (1991) Geothermics of permafrost of Northern Asia lithosphere. Nauka, Novosibirsk (in Russian)

Balobayev VT, Devyatkin VN, Kutasov IM (1973) Contemporary geothermal conditions of the existence and development of permafrost. Proceedings of the 2nd International Conference on Permafrost, Yakutsk, Soviet Contribution, National Academy of Sciences, Washington, D.C., pp 619–624

Balobaev VT, Skachkov YuB, Shender NI (2009a) Forecasting climate changes and the permafrost thickness for Central Yakutia into the year 2200. Geogr Nat Res 30:141–145

Balobaev VT, Kutasov IM, Eppelbaum LV (2009b) The maximum effect of deep lakes on temperature profiles—determination of the geothermal gradient. Earth Sci Res J 13(1):54–63

Carslow HS, Jaeger JC (1959) Conduction of heat in solids, 2nd edn. Oxford University Press, Oxford

Duchkov AD, Sokolova LS, Balobaev VT, Devyatkin VN, Kononov, VI, Lysak, SV (1997) Heat flow and geothermal field in Siberia. Geol Geophys 38:1716–1729

Judge AS, Taylor AE, Burgess M, Allen VS (1981) Canadian geothermal data collection-northern wells 1978–80. Geothermal Series, vol 12. Earth Physics Branch, Energy, Mines and Resources, Ottawa

Kutasov IM (1976) Thermal parameters of wells drilled in permafrost regions. Nedra, Moscow

Kutasov IM, Eppelbaum LV (2012b) Geothermal investigations in permafrost regions—the duration of temperature monitoring after wellbores shut-in. Geomaterials No. 10, 2(4):82–93

Lachenbruch AH (1959) Periodic heat flow in a stratified medium with application to permafrost problems. Geol. Surv. Bull. 1083-A. USA Government Printing Office, Washington

Lachenbruch AH, Marshall BV (1977) Subsea temperatures and a simple tentative model for offshore permafrost at Prudhoe Bay, Alaska, pp 77–395

Lachenbruch AH, Sass JH, Marshall BV, Moses TH Jr (1982) Permafrost, heat flow, and the geothermal regime at Prudhoe Bay, Alaska. J Geophys Research 87:9301–9316

Lachenbruch AH, Marshall BV (1986) Changing climate: geothermal evidence from permafrost in the Alaskan Arctic. Science 234:689–696

Lachenbruch AH, Cladouhos TT, Saltus RW (1988) Permafrost temperature and the changing climate. Proceedings of the fifth international conference on permafrost, vol 3. Tapir Publishers, Trondheim, pp 9–17

Lunardini VJ (1988) Heat conduction with freezing or Thawing. CRREL monograph 88-1, Hanover, NH, pp 187–214

Melnikov PI, Balobayev VT, Kutasov IM, Devyatkin VN (1973) Geothermal studies in Central Yakutia. Int Geol Rev 16:565–568

Ogata N, Yasuda M, Kataoka T (1982) Salt concentration effects on strength of frozen soils. In: Proceedings of the 3rd international symposium on ground freezing, Hanover, New Hampshire, pp 3–17, 22–24 June 1982

Osterkamp TE (1983) Response of Alaska permafrost to climate. Proceedings of the 4th international permafrost conferences, Fairbanks, Alaska, National academy of Sciences, Washington, DC, pp 145–151, 17–22

Osterkamp TE (2003) Establishing long-term permafrost observato-ries for active layer and permafrost investigations in Alaska: 1977–2002. Permafrost Periglac Process 14(4):331–342

Osterkamp TE (2005) The recent warming of permafrost in Alaska. Global Planet Change 49:187–202

Osterkamp TE, Gosink JP (1984) A reconnaissance study of the hydrothermal characteristics of Pilgrim Springs, Alaska. J Energy Resour Tech 106:96–102

Osterkamp TE, Esch DC, Romanovsky VE (1997) Infrastructure: effects of climatic warming on planning, construction and maintenance. Proceedings of the Bering Sea impact assessment workshop. University of Alaska Climate Center, Fairbanks, AK

Pavlov AV (1974) Seasonal freezing and thawing rocks. In: Melnikov PI, Tolstikhin NI (eds) General geokriology. Nauka, Novosibirsk, pp 66–68

Romanovsky VE, Osterkamp TE (2000) Effects of unfrozen water on heat and mass transport processes in the active layer and permafrost. Permafrost Periglac Process 11:219–239

Smith RE, Clegg MW (1971) Analyses and design of production wells through thick permafrost. Proceedings of the 8th World petroleum congress, Moscow, June, pp 379–389

Taylor AE, Burgess M, Judge AS, Allen VS (1982) Canadian Geothermal Data Collection-Northern Wells 1981. Geothermal Series, vol 13, Earth Physics Branch, Energy, Mines and Resources, Ottawa

Tsytovich NA (1975) The mechanics of Frozen Ground. Scripta Book Company, Washington, DC, pp 8–250

Tsytovich NA, Kronik Ya A, Markin KF, Aksenov VI, Samuel'son MV (1973) Physical and mechanical properties of saline soils. In: Proceedings of the 2nd international conference on Permafroist, Yakutsk, National Academy of Sciences, Washington, DC, pp 238–247

Vyalov SS (1974) Physical-mechanical, thermal and electrical properties of frozen rocks. In: Melnikov PI, Tolstikni NI (Eds) General geogriology. Nauka, Novosibirsk, pp 161–191

Chapter 6
Investigating Deep Lithospheric Structures

As discussed in Chaps. 1 and 4, during the accretion process heat energy released by accretion and certain other contributory processes was sufficient to heat the entire Earth beyond the melting point of rocks. This led to a situation in which the entire planet or most of it was molten and a magma-ocean covered the entire Earth for some time. Other processes which may have taken place during the evolution of the early Earth (collision with a Mars-sized body, bombardment of the surface by huge cosmic objects, etc.) could also have led to the formation of a planet-wide magma-ocean or local magma-oceans, or prevented the existing one from solidifying. It is clear that neither the lithosphere nor the asthenosphere could have existed during the formation and evolution of the magma-ocean. No solid rock or water oceans could have existed on the surface at this period of time either. All water and other volatiles were part of the thick early terrestrial atmosphere (Pilchin and Eppelbaum 2006).

The formation of the lithosphere (comprised of the Earth's crust and the rigid outer part of the upper mantle) began with the beginning of the solidification of the magma-ocean, and continues to this day. The formation of the asthenosphere (which is believed to be either in a plastic condition or partially molten) is thought to have begun once some kind of early lithosphere was formed, and has not ceased since then. The evolution of both the lithosphere and the asthenosphere is closely related, because the lithosphere is perpetually growing at the expense of the asthenosphere. This led to the cooling of the Earth, as the solidified and cooled parts of the asthenosphere merged with the lithosphere.

At the time of the magma-ocean, the early terrestrial atmosphere was very hot and thick, creating pressures of at least about 35 MPa (Pilchin and Eppelbaum 2006; Pilchin 2011). This means that at some point during the cooling of both the Earth's surface and the atmosphere, a water-ocean was created and most volatiles were transferred from the atmosphere to the crust during their interaction with surface rocks. At this point the atmospheric pressure dropped to its present value of about 0.1 MPa. Numerous important and even unique processes took place during the period between the start of solidification of the magma-ocean and the present.

L. Eppelbaum et al., *Applied Geothermics*, Lecture Notes in Earth System Sciences,
DOI: 10.1007/978-3-642-34023-9_6, © Springer-Verlag Berlin Heidelberg 2014

In this section, the key problems and processes related to the formation of the water ocean, and the evolution of the magma-ocean, lithosphere, asthenosphere, and the early terrestrial atmosphere are discussed.

6.1 The Formation and Evolution of the Magma-Ocean

During the formation of the Earth and its evolution there were various sources producing energy, the most significant of which were planetary accretion and differentiation, bombardment of the planet by huge astronomic objects (planetesimals, asteroids, etc.), and the radioactive decay of short- and long-lived radioactive isotopes (Lubimova 1968a; Pollack 1997). Estimates of the combined energy released by these processes, as well as the Earth's possible collision with a Mars-sized body show that the value was sufficient to melt the entire planet during its accretion (Safronov 1978; Pollack 1997; Valley et al. 2002). A review of the literature on thermal conditions within the Solar nebula (Pilchin and Eppelbaum 2006) shows that the temperature at the distance of Earth from the Sun was within the range of 600–700 K, which implies that the energy released during planetary accretion was enough to melt the entire Earth. This means that by the end of accretion the Earth was covered with a magma-ocean (Pilchin and Eppelbaum 2009).

A possible collision of the Earth with a Mars-sized body (the Moon-forming event) at about 4.48 Ga (Halliday 2008) could have led to conditions with a mean temperature in excess of 4,000 K out to about 8 Earth radii and in excess of 2,000 K out to about 20 Earth radii (Cameron 1997). Stevenson (2008) also suggested that such an impact would have led to a mean rise in the Earth's temperature by 4,000 K, whereas other estimates indicate that such an event would have caused an average temperature increase on the order of 7,500 K (Melosh 1990; Pollack 1997). Sleep (2010) claims that after this collision the effective temperature of the top of the vapor atmosphere would have been about 2,300 K, and after cooling the surface temperature would have dropped to about 1,800–2,000 K. This means that if the initial magma-ocean had solidified prior to this collision, the Earth's surface layers would have been re-melted and the magma-ocean would have formed once again.

Safronov (1978) and Kaula (1979) highlighted the important role of the impact of large bodies in heating the upper layers of the Earth to the melting point to a depth of up to 1,200 km during the last stage of the Earth's formation (Safronov 1978). It is generally accepted that the planets of the inner Solar System experienced a heavy bombardment of debris from planetary formation, which lasted from $\sim$4.5 to 3.8 Ga (Lubimova 1968a; Kaula 1979; Chyba 1990; Tonks and Melosh 1993; Abe 1997; Righter and Drake 1997a, b; Bennett et al. 2004; Anderson 2007) and could have led to additional heating of Earth's crust and mantle, as well as the formation of local magma-oceans. Even though the post-accretional bombardment of the terrestrial planets and the moon continued

unabated from roughly 4.5 to 3.8 billion years ago, some evidence from lunar rocks points to intense "*late heavy bombardment*" at about 3.85–3.9 Ga (Koeberl 2006; Marty and Meibom 2007). This means that during the Hadean and beginning of the Archean, the surface temperature of the Earth was high and that there were total or local magma-oceans for a significant part of these time periods (Pilchin and Eppelbaum 2009). Vacquier (1998) showed that runaway accretion, the formation of the Moon and the impact that tilted the axis of rotation could have created a situation where the Earth melted and solidified three times.

Research has shown that the initial magma-ocean was between several hundred (Walter and Trønnes 2004) and about 1,000 km deep (Li and Agee 1996; Labrosse et al. 2007). Some scientists believe that this magma-ocean could only have existed for about 1–10 million years (Spohn and Schubert 1991), but others have argued that it could have lasted for 100–200 million years (Abe 1997; Pollack 1997) and perhaps even a few hundred million years in the case of a thick early atmosphere (Abe 1997; Solomatov 2000).

The estimated surface temperature of the magma-ocean (Abe 1997) is thought to have ranged from 1,500 to 4,700 K. Pollack (1997) showed that only the heat from short-lived radio-isotopes could have created a surface temperature in the range of 1,200–1,700 K. Abe (1997) showed that in the case of a blanketing effect of the atmosphere, the estimated surface temperature of the magma-ocean could have exceeded 2,100 K. Brown and Mussett (1993) also determined that the surface temperature of the magma-ocean could have reached a few thousand degrees Kelvin.

Given that virtually all of the Early Archean rocks are felsic or intermediate, it is obvious that the surface temperature of the magma-ocean right before the start of its solidification at some point in the Hadean must have been about 1,300–1,500 K to keep these rocks molten. But even though it is obvious that during the formation and evolution of magma-ocean its surface temperature could have been very high (much higher than the melting point of surface rocks) the formation of the solid lithosphere started when the surface temperature dropped to the upper limit of the melting point of dry felsic magmatic rocks, which is about 1,300 K. It is also clear that the content and composition of the early Earth's atmosphere above such a magma-ocean would have been determined by the stability conditions of chemical compounds existing in the solar nebula and the forming planetesimals, asteroids and other cosmic objects. Clearly during the time of the magma-ocean, neither water-oceans nor solid rocks and continents were present. The only forms of matter that were present at or near the surface at that point in time of the Earth's evolution were molten rocks of the magma-ocean and volatiles within the early Earth's atmosphere.

Research shows (Pilchin and Eppelbaum 2009) that during formation of the magma-ocean, melts formed magmatic layers in ascending order of their density and Fe-content. This differentiation of the Earth's layers began with the start of planetary accretion and continued until the solidification of the magma-ocean. It should be noted that deep magma-ocean is a perfect structure for differentiation and stratification of matter. Other studies (Anderson 1989, 2002a, 2006, 2007) also

point to the differentiation and stratification of rocks within the magma-ocean. Some research shows that even small differences in density were enough to gravitationally stratify the mantle (Anderson 2002a, 2002b; Davaille 1999; Tackley 1998, 2000) and that at internal chemical boundaries, the density jump was thought to be only about 30–100 kg/m^3 (Anderson 2002a). Anderson (2006) showed that mantle-wide convection could homogenize the mantle if the various components did not differ in intrinsic density by more than 2 or 3 %. According to Archimedes' Law, within the magma-ocean the uppermost layer/layers would have been represented by the lightest of the magmatic rock felsic magmas. Intermediate magmas were layered right below felsic magmatic layers. Mafic magmas were layered below the intermediate magmatic layers, and ultramafic magmas were layered below the mafic magmatic layers. The position of each magmatic layer coincided with the density of its magma. The fact that almost all of the Archean magmatic rocks are either felsic or intermediate is consistent with the position of such kinds of magmas within the magma-ocean. Among the mafic and ultramafic layers, lighter Mg-rich and Fe-poor magmas would have formed the upper part and Fe-rich magmas would have formed the lower portion of the corresponding magmatic layers within the magma-ocean.

The densities of some typical molten magmatic rocks are presented in Table 4.10. It is clear from the table that the differences between densities of felsic melts, intermediate melts, mafic melts and ultramafic melts were high enough for their separation by density. Research shows (Pilchin and Eppelbaum 2009) that the density of rocks and minerals, as well as their melts is dependent on the thermodynamic conditions, melting points, and conditions of stability, phase transformation and Fe-content of rocks. The iron content and density of the most common rock-forming minerals are presented in Table 6.1.

As an example of the dependence of the density of molten rocks and minerals on iron content, in Table 6.2 the density of liquid olivine (forsterite, fayalite at different temperatures and olivine Fo_{93}) one of the main components of peridotites composing most of the upper mantle is presented.

It is obvious from Tables 6.1 and 6.2 that the difference in density between iron-rich and iron-poor rocks and minerals is large enough to separate them by density in the liquid state. The data presented in Tables 4.10, 6.1 and 6.2 also show that differences in density between different kinds of melts and different iron content exceeds the 2–3 % required (Anderson 2006) for stratification of layers within the Earth, and it could definitely prevent different kinds of magma from significant mixing and exchange (Pilchin and Eppelbaum 2009). But the main reason why mixtures of different kinds of melt did not take place is the fact that different kinds of melt are composed of different minerals and their combinations, and the presence of different minerals in different rocks is affected by P–T conditions and conditions of their stability. These are the main factors keeping different kinds of molten rocks separate by density.

Further evidence for the differentiation of rocks within the Earth and their stratification by iron content can be drawn from changes in the iron content of magmatic rocks during the Earth's evolution. The distribution of iron-content within

Table 6.1 Iron content and density of the most common rock-forming minerals

Minerals	Density range, kg/cm^3	Comments
K-feldspars	2,520–2,560	On average albite is ~2.76 % denser than K-feldspars;
Plagioclases	2,610–2,760	anorthite is ~5.75 % denser than albite
Quartz	2,600–2,650	–
Micas	2,700–3,170	Fe-rich mica is ~10.4 % (for biotite) and ~13.2 % (for annite) denser than Mg-rich micas
Clynopyroxene	3,200–3,900	On average Fe-enriched clinopyroxenes are ~4.4–7.6 % denser than Mg-enriched
Orthopyroxenes	3,100–4,020	On average Fe-rich orthopyroxene is ~23.4 % denser than Mg-rich orthopyroxene
Amphiboles	2,900–3,500	On average Fe-enrich amphiboles are ~6.25 % denser than Mg-enriched
Olivine	3,200–4,390+	The density of fayalite is ~34.4 % higher than the density of forsterite
Garnets	3,420–4,310	The density of almandine is ~19.4 % higher than the density of pyrope and ~22.9 % higher than the density of grossular

Table 6.2 Density of molten forsterite, fayalite and olivine Fo_{93}

Mineral	Temperature, K	Density, kg/m^3	References
Forsterite	2,163	2,970	Coombs and Gardner (2004)
Fayalite	1,573	3,757	Shiraishi et al. (1978)
	1,673	3,725	Shiraishi et al. (1978)
	3,000	3,529	de Koker et al. (2008)[a]
	2,163	3,810	Lange (1997)
		3,893	Lange and Carmichael (1987)
	1,773	3,747	Knittle (1995)
	1,573	3,750	Chen et al. (2002)
	1,300	~3,875	Ghiorso (2004)
	1,500	~3,861	Ghiorso (2004)
	1,600	3,850	Ghiorso (2004)
	1,973	3,593	Courtial et al. (1997)
	2,023	3,586	Courtial et al. (1997)
	2,073	3,587	Courtial et al. (1997)
	2,123	3,560	Courtial et al. (1997)
Fo_{93}		2,865	Walker et al. (1988)

[a] Calculated using data reported in de Koker et al. (2008)

the mantle is one of the prime ways of characterizing stratification of the mantle because iron is the most abundant element on the Earth (Pilchin 2011). As shown in Tables 6.1 and 6.2 its content is the main factor in rock density and the increase in their melts. It is obvious that according to Archimedes' Law denser melts should sink within the magma-ocean and lighter melts should float. Hence iron-rich melts should sink within magma-ocean and the greater their iron-content (greater density)

the deeper they should sink. On the other hand it is obvious that denser magmas could not float within the magma-ocean. This means that intermediate magmas could only start to erupt to the surface when felsic magmas on the top of the magma-ocean had solidified. Similarly, for mafic and ultramafic magmas to begin erupting on the surface there must have been total solidification of felsic and intermediate magmas and felsic-intermediate-mafic magmas, respectively. Since the solidification of magma-ocean and the formation of the lithosphere took time and the formation of lithosphere is still taking place today, the source layers of formation of magmas should correspond to greater depths with the age of the Earth.

In fact, since the lithosphere is a rigid layer and its thickness is permanently increasing at the expense of the cooling asthenosphere, which is believed to be partially molten and to contain most of the source regions of magma formation. Thus most of the basic and ultrabasic magmas (especially huge amounts of magma such as LIP and flood basalts) should have formed under the lithosphere and the depth of the magma forming layers should increase permanently. This means that if there was stratification of magma within the magma-ocean, the deeper layers should be more iron-rich than the shallow layers. In turn this implies that the magmas formed at greater depths and that those that came from greater depths should be more iron-rich. Moreover, the increase in iron content with the increase of depth of magma formation should prove the existence of the magma-ocean in the past and the stratification of magmas within the magma-ocean by iron-content. To test these assumptions, the iron content of magmatic rocks was analyzed (Pilchin and Eppelbaum 2006).

The data on the iron content in magmatic rocks indicate that the iron content in magmas increases systematically with decrease in their age and is minimal for the Archean rocks and maximal for rocks from the Cenozoic to the present. It should be noted that iron-rich magmatic rocks comprise only a small fraction of magmatic rocks, virtually all of these rocks were formed after the Archean, and virtually all iron-rich rocks were formed within continental areas. Their quantity and iron-content is permanently increasing with decrease in the age of the magma. The term ferrobasalts is usually reserved for rocks with an iron content $\geq$12 wt.%. Cenozoic and later flood basalts and most of other continental basalts on average are almost all ferrobasalts. At the same time, the relatively low iron content of basalts in oceanic regions (about 8.3–9.1 wt.% for mid-ocean ridge basalts, 8.5–9.7 wt.% for island arc basalts, 10.2 wt.% for ocean floor basalts, and 10.6–12.6 wt.% for oceanic intraplate volcanism) (Pilchin and Eppelbaum 2009) suggests that these basalts were formed at lower depths, which is consistent with the shallower asthenosphere in oceanic regions compared to continental areas. All these data undoubtedly prove the existence of the magma-ocean in the past and show that the magma-ocean was stratified by iron content within melts. The very high iron content in basaltic meteorites (eucrites) of about 18.27 wt.% (BVSP 1981) shows that the stratification of the mantle by iron content could have taken place on other terrestrial planets as well. This is in line with the data suggesting the formation of magma-oceans on all other terrestrial planets and some moons.

Another important peculiarity of the magma-ocean is that no overpressure can be generated, because according to Pascal's law for liquids, any pressure applied to

a liquid in an open system is transmitted by the liquid in all directions. This means that the pressure within the layers of the magma-ocean could not have exceeded the value of the lithostatic pressure. According to a number of physical laws, the formation of overpressure within the magma-ocean would also not have been possible during the solidification and cooling of the magma-ocean (Pilchin and Eppelbaum 2009) and would have only been possible at a stage of re-heating of some layers of the solidified magma-ocean.

It is very important to note that forsterite is a relatively light mineral (with a density of 3,222 kg/m^3) and can float in some Fe-rich magmas. It was argued in (Pilchin and Eppelbaum 2009) that there were two possible scenarios right before the start of solidification of the magma-ocean: (1) the temperature within the magma-ocean was lower than the melting point of forsterite (2,163 K); (2) the temperature within the evolving magma-ocean was higher than the melting point of forsterite. In both cases Mg-rich rocks would have formed a layer separating the dense Fe-rich magmas at the bottom of the magma-ocean from the less dense Fe-poor magmas above. However, in the second scenario, forsterite-rich and other Mg-rich melts would have formed a layer (*forsterite layer*) which could have had a higher temperature than the denser Fe-rich melts beneath it. Analysis of xenoliths of peridotites from Archean cratons indicates that most were brought up from depths greater than 100 km (Pilchin and Eppelbaum 2009). This and the formation of komatiites at depths of about 200 km support the formation of such a Mg-rich layer. Thus the solidification of the magma-ocean most likely started with the formation of forsterite layer at a depth of about 100–120 km in areas of the current-day continental lithosphere (Pilchin and Eppelbaum 2008b).

Estimates of the density of mantle rocks at the present time using different geophysical methods show that their density ranges from $\sim$3,200 kg/m^3 in the uppermost mantle to $\sim$5,500–5,600 kg/m^3 near the mantle-core boundary. This difference in density is large enough for the formation of numerous layers (with a density difference >2–3 wt.%; Anderson 2002a) separated by density. This means that during the accretion and formation of the magma-ocean, the matter representing the current composition of the mantle could have been separated into dozens of separate layers with a minimum interaction between them. It is important to mention that separate convection would exist in each layer, since mantle-wide convection cannot exist if the various components differ in intrinsic density by more than 2 or 3 % (Anderson 2002a, b, 2006).

6.2 The Early Earth's Atmosphere and the Cooling of the Earth

During accretion, a magma-ocean with a surface temperature of at least about 1,300–1,500 K was formed along with the thick, dense early terrestrial atmosphere (minimum pressure of 35 MPa) composed of supercritical fluids (see Sect. 2.8) with

its main layers (sulfur-layer, carbon-layer, and water-layer) separated by density. It is known (Malyshev 2004) that SO_2 is the most stable sulfur oxide at high temperatures and at temperatures of ~1,073–1,373 K it would have been the main component of the sulfur-layer of the early Earth's atmosphere. At the same time, above 1,073 K, CO is the dominant carbon oxide (Holleman et al. 2001; Gupta 2003) and at temperatures above 1,253 K, carbon oxide mixtures would contain only 1 % CO_2 (Gupta 2003). This means that at the beginning of the magma-ocean, solidification took place at a temperature of ~1,273 K within the early Earth's atmosphere at a pressure of ~35 MPa (see Fig. 2.16). The sulfur-layer would have been composed almost entirely of SO_2 and would have had a density of ~292 kg/m^3, the carbon-layer would have been composed almost completely of CO and would have had a density of ~314.5 kg/m^3, and the water layer would have had a density of 60.35 kg/m^3. Taking into account partial pressures of the sulfur-layer, carbon-layer and water-layer (Pilchin and Eppelbaum 2012) the estimated thickness of these layers under thermodynamic conditions would have been ~1.3 km for the CO-layer (the first layer from the surface), ~2.4 km for SO_2-layer (the second layer from the surface) and ~43.8 km for H_2O-layer (the third layer from the surface). This means that the water layer was not in contact with the magma-ocean during the beginning of its solidification. This also means that oxygen, which would have been present in the upper layers of the early Earth's atmosphere (Pilchin 2011), would also have had no access to the surface.

We saw above that (Pilchin and Eppelbaum 2009; Pilchin 2011) solidification of the magma-ocean started with the formation of the forsterite layer. Fosterites have a melting point 2,163 K at 0.1 MPa (Hewins et al. 1996) and 2,307 K at 3 GPa (Davis and England 1964) which is the highest among silicates, and thus were the first to solidify and settle within the magma-ocean to a depth corresponding to its low density (3,222 kg/m^3 at ambient conditions).

Regardless of whether the temperature within the magma-ocean was above or below the melting point of forsterite, solid or crystallized forsterite and forsterite rich olivines (Fo_{94}–Fo_{100}) would have formed a solid forsterite layer which would separate the magma-ocean into two parts with the lower Fe-rich magmas below the forsterite layer and the upper Fe-poor magmas above the forsterite layer. The felsic magma layer with the lowest melting point and cooled by the early Earth's atmosphere started to solidify first within the upper part of the magma-ocean. Surviving Hadean zircons can indicate the minimum age of the solidification of the felsic layer of the magma-ocean. Zircon ($ZrSiO_4$) which is an extremely stable mineral with no crystallographic transformation until its dissociation at ~1,943 K (Tartaj et al. 1996), is highly resistant to alteration by weathering, dissolution, diffusive exchange, and very specific U-Pb systematics are widely recognized as one of the best geochronometers (Tartaj et al. 1996; Cherniak and Watson 2000, 2003).

The most important property of zircon for geochronology it its high closure temperature (>1,173 K) of the U-Pb system (Cherniak and Watson 2000, 2003; Möller et al. 2002). Since the lowest temperature of the magma-ocean was at its surface, it is evident that the oldest age defined by any zircon was the age when the

surface temperature of the magma-ocean dropped below the zircon closure temperature of ~1,173 K. This also leads to the conclusion if there is no age resetting in a zircon it was never heated above 1,173 K. Hence none of surviving Hadean and Early Archean zircons was ever heated to a temperature above 1,173 K. This places constraints on temperatures during the Hadean and Early Archean in regions in which these zircons were formed. Analysis of the density and thicknesses of the main layers of the early Earth's atmosphere at the time of surface cooling below 1,173 K under pressure of ~35 MPa shows that the density of SO_2-layer was ~322 kg/m^3 and its thickness was ~2.2 km (second layer), the density of CO-layer was ~341 kg/m^3 and its thickness was ~1.2 km (first layer), the density of water-layer was 75.3 kg/m^3 and its thickness was ~39.5 km (third layer). The water-layer still had no access to the surface.

Another important reaction for determining the evolution of atmosphere during that period of time is the Boudouard reaction (Akhmetov 1992b; Gupta 2003):

$$2CO = CO_2 + C \tag{6.2.1}$$

which can also use iron and ferrous iron oxide as catalysts (Geurts and Sacco 1992; Cheng et al. 1999).

Since the mixture of CO and CO_2 contains <1 % carbon, CO2 at temperatures above 1,253 K; Gupta 2003), is equimolar at 947 K and would contain <1 % of CO at a temperature of 673 K, it is obvious that the cooling of the early Earth's atmosphere would lead to the deposition of significant amounts of elemental carbon formed by the Boudouard reaction. The deposited elemental carbon could be a source for graphite formation and could also be involved in numerous chemical reactions as a reductant and as a catalyst. At the same time, during the cooling of the atmosphere and the formation of the surface through reaction Eq. (6.2.1), CO_2 would be less dense than SO_2 and denser than water and it would form another layer between the SO_2-layer and H_2O-layer thus separating those layers from each other.

The calculated density values for SO_2 and CO show that in the temperature range between 1,023 K and 873 K the densities of SO_2 and CO are very close and this could have led to a situation where the first layer of early Earth's atmosphere could have been made up of a mixture of these two compounds, but at temperatures below 873 K the sulfur-layer would be the first layer in the early Earth's atmosphere.

Akhmetov (1992b) reported results of experimental research on the transfer of SO_2 to SO_3 showing that the mixture of these sulfur oxides would contain ~10 % of SO_3 at 1,273 K, ~20 % of SO_3 at 1,073 K, ~55 % of SO_3 at 873 K, ~90 % of SO_3 at 773 K, and up to 100 % of SO_3 at 673 K. In other words, at ~873 K the sulfur-layer would contain about equal amounts of these sulfur oxides forming a SO_3–SO_2-layer, and for temperatures below ~773 K this layer would be referenced as a SO_3-layer. Because the density of carbon oxides CO and CO_2 and sulfur oxides SO_2 and SO_3 could have differed at different *P*–*T*-conditions, each could have formed an individual sub-layer, the position of which would be controlled by

each oxide's density under the corresponding *P–T*-conditions. Note that because the densities of SO_2 and CO were only calculated, the real relationships between them could be slightly different from those presented here.

When the surface temperature fell below 843 K and within the temperature range of 723–843 K (the upper limit of TFFI) the TFFI in the surface rocks began and would continue at the surface and within layers of the forming crust until the temperature dropped below ~473–523 K (the lower limit of TFFI). TFFI does not require the presence of oxygen (Pilchin and Eppelbaum 2006; Pilchin 2011). This is consistent with an experiment in which the growth of magnetite crystals on carbonate was observed when single crystals of chalybite (FeCO3) were sealed in a vacuum tubes and heated under their own CO_2 pressure to 823 K (Bernal et al. 1959).

The fact that magnetite can be formed under specific thermodynamic conditions in a vacuum means that oxygen is not necessarily required for the formation of BIFs. This means that appearance of the first Algoma-type BIFs points to the fact that the surface temperature in the region of these BIFs deposition had dropped to the temperature just below the upper limit of the TFFI (723–843 K; Pilchin and Eppelbaum 2009). This temperature range (~723–843 K) is too high for formation of oceans, and it is possible that the first Algoma-type BIFs were formed before the oceans. Thus, at the time of the first Algoma-type BIF deposition in 3.85–3.50 Ga, the surface temperature had dropped below 843 K in some regions of Earth and the ocean had possibly still not formed. The source of iron ores for the first Algoma-type BIFs were likely to be a decomposition of iron containing minerals caused by the TFFI (Pilchin and Eppelbaum 2006). But conditions favorable to the deposition of BIFs could be local and different for different regions. Since the content of free oxygen in the atmosphere started to rise only after about 2.3 Ga (Holland 1984; Kasting and Ackerman 1986), it is obvious that oxidation processes did not play a significant role in the deposition of BIFs during the Early Archean. The outcome of the TFFI could have been the decomposition of rocks and minerals with a separation of iron oxides, silica and some other oxides. These compounds could have become important components in the formation of BIF later when chemically active remnants of rock and mineral decomposition were dissolved in the water of the forming water-ocean and silica and iron oxides were the main leftover minerals (Pilchin 2011).

Analysis of density and thicknesses of the main layers of the early Earth's atmosphere at the time of surface cooling below 823 K under pressure of ~35 MPa shows that the density of SO_3–SO_2-layer was ~505 kg/m^3 and its thickness was ~1.4 km (first layer), the density of CO_2-layer was ~210 kg/m^3 and its thickness was ~1.0 km (second layer), the density of water-layer was 119.9 kg/m^3 and its thickness was ~22.1 km (third layer). The water layer still had no access to the surface.

The next important point to keep in mind as regards the evolution of the early Earth's atmosphere and the Earth's surface is that at a temperature of about 700 K the density of water-layer became greater than the density of the CO_2-layer and the water-layer became the second layer and came into contact with the first SO_3-layer

of the atmosphere. Analysis of density and thicknesses of main layers of the early Earth's atmosphere at the time of surface cooling below 673 K under pressure of ~35 MPa shows that the density of the SO_3-layer was ~676 kg/m^3 and its thickness was ~1.1 km (first layer), the density of the CO_2-layer was ~265 kg/m^3 and its thickness was ~0.6 km (third layer), the density of the water-layer was 470.1 kg/m^3 and its thickness was ~5.6 km (second layer). The water-layer still had no access to the surface.

This led to formation of different concentrations of sulfuric acid (H_2SO_4) that had a significant effect on the interaction between the early Earth's atmosphere and the Earth's surface. It initiated the main period of leaching of the Earth's surface rocks, which ended only with either the total re-distribution of the sulfur layer or cooling to temperatures below ~550 K when the density of the water-layer became greater than the density of the SO_3-layer and water became the first layer of the early Earth's atmosphere to come into contact with the surface and form the water-ocean. Analysis of the density and thicknesses of the main layers of the early Earth's atmosphere at the time of surface cooling below 573 K under pressure of ~35 MPa, right before water became denser than the SO_3-layer, shows that the density of SO_3-layer was ~835 kg/m^3 (a calculated value is used, because of the absence of experimental data under these *P*–*T*-conditions) and its thickness was ~0.9 km (first layer), the density of CO_2-layer was ~327.9 kg/m^3 and its thickness was ~0.8 km (third layer), the density of the water-layer was 758.1 kg/m^3 and its thickness was ~3.5 km (second layer). The water-layer still had no access to the surface.

It should also be taken into account that at the beginning of the formation of water-ocean the water was very hot and contained minimal or no salts, which made it a very aggressive leaching medium for surface rocks. Analysis of the density and thicknesses of the main layers of the early Earth's atmosphere at the time of surface cooling below 523 K under pressure of ~35 MPa, right after water became denser than the SO_3-layer, shows that the density of SO_3-layer was ~794.4 kg/m^3 (an experimental value) and its thickness was ~0.9 km (second layer), the density of the CO_2-layer was ~377.3 kg/m^3 and its thickness was ~0.5 km (third layer), the density of the water-layer was 829.7 kg/m^3 and its thickness was ~3.2 km (first layer). The water-layer had access to the surface.

Depending on the composition of the bottom layer of the early Earth's atmosphere, the surface rocks and minerals interacted differently with the atmosphere, which led to different degrees of rock alteration. To better understand the conditions affecting this alteration it is also important to take the resistance of certain elements, rocks and minerals to different weathering agents into account. A good grasp of the weathering environment and conditions during rock alteration is crucial to studying the provenance of the Earth on local, regional and global scales. On the other hand, as was shown above, at the time of magma-ocean the hot early Earth's atmosphere was $SO_2 + SO_3$, $CO_2 + CO$ and H_2O rich, but all these compounds are only minor components of the present-day cold atmosphere. This means that all these components were cooled down and re-distributed at some point in time and somewhere during the Earth's evolution. This makes it very

important to look for possible signs of this re-distribution in different time periods of the Earth's evolution. In addition, depending on the temperature of the surface and the early Earth's atmosphere, as well as the rates of re-distribution of different components of the early Earth's atmosphere, the surface could have been in contact with CO, SO_2, SO_3, CO_2 and H_2O singly or in combination, which would definitely create different weathering environments at different temperature conditions. There are numerous cases of extremely strong alteration of the Early Archean rocks in both the Pilbara Craton and Barberton GSB. It is also obvious that the extent of alteration also depends on the position of main layers of the early Earth's atmosphere, which are temperature dependent. For example, as soon as the SO_3-layer became denser than the CO_2-layer and CO_2-layer was denser than H_2O-layer, SO_3 would not have had direct contact with H_2O and the surface would be in direct contact with the supercritical SO_3-layer.

SO_3 is an extremely active weathering agent which reacts with such minerals as plagioclase and pyroxenes (Treiman and Schwenzer 2009) and can cause significant rock alteration. But as soon as H_2O became denser than CO_2, the H_2O-layer would be located right above the SO_3-layer and it would lead to the formation of H_2SO_4 which is denser than SO_3. This would result in direct contact of the surface with sulfuric acid (H_2SO_4) which is of course one of the strongest alteration agents in existence. Selvig et al. (2005) showed that the involvement of H_2SO_4 in the dissolution process resulted in $\sim$25 % overall increase in the dissolving of minerals. On the other hand, as was shown above, depending on temperature and density of the components, the thickness of the main layers of the early Earth's atmosphere differed and the elevation of the surface in different regions would govern the weathering environment and in particular which layer of the early Earth's atmosphere surface would interact with it.

It should also be taken into account that at some point the whole surface could have been covered by the nascent water-ocean, which, under conditions when the water became denser than sulfur oxide or the sulfur-layer was re-distributed, had a thickness of $\sim$3.2 km. This means that the entire early Earth's surface at that point in time was interacting with the hot water of the emerging water-ocean and it was subject to strong hydrothermal alteration. The crucial issue is which weathering environment the surface was in contact with, and interacted with before the formation of the water-ocean. Clearly, the interaction of the surface with the CO_2-layer would not lead to such massive alterations as the interaction of the surface with the SO_3-layer or the H_2SO_4-layer. It is obvious that all these events and processes have a chronology; determining this time line is one of the most important tasks for scientists investigating the Earth's evolution. Of course some or all of these features and processes could have taken place during the Hadean, but the geological record of the Hadean is so scanty that it is virtually impossible to trace any of these features or processes.

The only remnants of the Hadean that have been preserved are zircons from a very few places in the world and the rocks of the Acasta Gneiss Complex mentioned above. These remnants only show that there was solid surface in the Hadean and the existence of these zircons and rocks suggests that they were deposited at

elevated levels which were not covered by H_2SO_4 either in the Hadean, or later, because Zr, ZrO2, $ZrSiO_4$ and even ZrO_2-SiO_2 films are not resistant to sulfuric acid at a concentration of about ≥80 % (Jakubke and Jeschkeit 1993; Garverick 1994; Cramer and Covino 2005; Shin et al. 2006). This is the case for the early Earth's evolution, because the boiling point of sulfuric acid increases with its concentration (Lillo and Delezene-Briggs 2005) reaching a maximum at 610 K under 0.1 MPa pressure (Lide 2005). Lillo and Delezene-Briggs (2005) showed that with an increase of pressure, the boiling point of sulfuric acid also increases and can reach ∼684 K, at a pressure ∼3.5 MPa for a sulfuric acid concentration of 96–98 wt% H_2SO_4. It is obvious that it could be even higher for the minimal pressure of 35 MPa for the early Earth's atmosphere, but the water would only have been denser than CO_2 below ∼700 K. This means that the water-layer would become the second layer and next to the SO_3-layer only at a temperature below 700 K and that H_2SO_4 started to form only below 700 K. But at this temperature only concentrated sulfuric acid would be in a liquid state and would have been in contact with the surface. This means that any zircon which was in contact with concentrated sulfuric acid was destroyed and only those zircons that were deposited at elevated levels above the sulfur-layer could have survived. It was shown above that the maximal thickness of the sulfur layer, disregarding its previous re-distribution, was about 0.9 km. Hence, any zircon or rock located at ∼0.9 km or higher would have survived. Of course concentrated sulfuric acid is a weathering agent that could completely erase the geological record that actually took place for the most of the Hadean and the Early Archean. Thus knowing which elements, rocks and minerals are resistant to sulfuric acid and comparing them to the elements, rocks and minerals that survived alteration by silicification, as well as new rocks and minerals formed during silification, can indicate whether the rocks were altered by sulfuric acid.

Analysis of experimental data shows that the materials resistant to sulfuric acid includes Hf that resists concentrations up to 80 % (Cramer and Covino 2005), Zr that resists concentrations up to 70–75 % (Cramer and Covino 2005), Ni-based alloys that resist up to a concentration of 60 % (Davis 2000), Ti only resists dilute concentrations (Garverick 1994), carbon and graphite have excellent resistance to any concentration (Garverick 1994), Pb resists concentrations up to 90 % (Garverick 1994), and U resists concentrations up to 40 % (Gates-Anderson et al. 2004). Studies show that K_2SiO_3 (Louie 1961; Garverick 1994), some SiO_2-A_2O_3 based compounds (Garverick 1994; King et al. 2008; Carbajal de la Torre et al. 2009), Si-enriched oxide (Kim et al. 2002), and some alumina and calcium alumina cements (Sugiyama 2010) are strongly resistant to sulfuric acid. Iron has excellent resistance to sulfuric acid with a concentration >75 % (Akhmetov 1992a). Ni–Fe alloys are also resistant to sulfuric acid with a concentration >50 %, and Ni-Si alloys resist hot concentrated acid (Davis 2000). Silica (SiO_2) is insoluble in H_2SO_4 (Martienssen and Warlimont 2005).

Hydrothermal alteration of the surface rocks by the hot water of the emerging water-ocean could also have caused significant geochemical changes. Results of

experiments on the action of hot water on albite showed (Morey and Chen 1955) that the amounts of constituent oxides (Na_2O, Al_2O_3, SiO_2) dissolved increases significantly with increases in temperature and pressure from 6.4 ppm at 373 K and 0.276 MPa to 53 ppm at 473 K and 13.79 MPa, and 318 ppm at 623 K and 34.47 MPa. Another study (Hellmann 1994) also found a significant increase in the rate of albite component dissolution in water with an increase in temperature from 373 to 573 K. Experimental results on albite feldspar dissolution at 573 K and 17 MPa in acid, neutral, and basic pH conditions were reported by Hellmann et al. (1997). Results of research at lower temperatures (320, 353 and 393 K) also point (Tsuzuki and Ogasawara 1987) to an increase in solubility of Si and Na from albite and basalt glass with increases in temperature. Experimental results reported by Tsuzuki and Ogasawara (1987) showed that after the interaction of water with albite, the resulting solution is primarily enriched with Na and Si, and after the interaction of water with basaltic glass the resulting solution has increased Na, Si, K and Fe, and much less Mg and Ca. Another study on the action of 523 K water on olivine, orthopyroxene and plagioclase showed (Gislason and Arnórsson 1993) that with increases in Mg content the stability of olivine and orthopyroxene decreased, and the stability of plagioclase decreases with increasing anorthite content. The alteration processes of biotite to chlorite, plagioclase to sericite and plagioclase to albite that occur during the hydrothermal alteration of granites at temperatures of $\sim$603–613 K were also investigated by Eggleton and Banfield (1985).

Significant amounts of graphite in the Early Archean rocks ($\geq$3.6 Ga) have been found in South-West Greenland (Naraoka et al. 1996; Mojzsis 2009; Whitehouse et al. 2009; Papineau et al. 2010; Lepland et al. 2011), which can prove that the Boudouard reaction (Eq. 6.2.1) indeed took place in this region during the Early Archean. Naraoka et al. (1996) reported the presence in the Isua Supracrustal Belt of Greenland rocks containing up to $\sim$5.5 wt% reduced carbon as graphite. This should not come as a surprise, since a simple calculation shows that if a mixture of CO and CO_2 contains <1 % CO_2 at temperatures above 1,253 K Gupta (2003) it would have contained <1 % of CO at a temperature of 673 K (Gupta 2003); during the cooling of the atmosphere from 1,253 to 673 K roughly about half of the carbon content of the carbon-layer of the atmosphere would have been deposited as elemental carbon on the surface.

There is also extensive evidence that enormous amounts of sulfur were present during the formation of both the Pilbara Craton and Barberton GSB. Some data point to the existence of a $\sim$3.42 Ga acid-sulfate epithermal system and acidic sulfur-rich hydrothermal activity during the deposition of the Strelley Pool Formation/Chert of the Pilbara craton (Brown et al. 2004; Van Kranendonk and Pirajno 2004; Brown et al. 2006). Van Kranendonk et al. (2008) stated that during the forming of the Dresser Formation there was widespread acid-sulfate alteration and crystallization of hydrothermal chert-barite-pyrite in veins, and that a chert-barite unit took place within an active volcanic caldera. The deposition of the chert horizons of the Dresser Formation and the Apex chert from acid-sulphate, high-sulphidation epithermal systems was also reported by Pirajno (2010). At the same

time, the chert-barite unit is characterized by the presence of microscopic sulfides contained within barite crystals (Wacey et al. 2009). The chert-barite unit is comprised of thousands of centimeter to kilometer long silica and barite veins (Pinti et al. 2009). A ~3.4 Ga source area for clastic metasedimentary rocks was locally subjected to hydrothermal alteration under acidic (pH < 4) conditions (Sugitani et al. 2006b). Among the other numerous signs of sulfur involvement in the interaction and alteration of surface rocks the following should be noted: the base of an acid-sulfate epithermal system at the top of 3.459 Ga Panorama Formation unconformably overlain by a 3.42 Ga Strelley Pool Chert (Brown et al. 2006); hydrothermal circulation, syngenetic with bedded chert deposition, in the distal parts of the high-sulphidation epithermal systems in the Strelley Pool Chert, Pilbara Craton (Van Kranendonk and Pirajno 2004); the ~3.49 Ga Dresser Formation is known to contain ~0.13 Mt of barite deposits in the North Pole area (up to 40 m thick chert-barite unit) (Huston et al. 2006; Harris et al. 2009); hot acidic water at the time of deposition of felsic volcaniclastic/epiclastic sedimentary rocks of the 3.45 Ga Hooggenoeg Formation, Barberton GSB (Rouchon et al. 2009); hydrothermal alteration of the sediment source area under acidic conditions in rocks of ~3.4 Ga in Mt. Goldsworthy, Pilbara Craton (Sugitani et al. 2006b); association of cherts in the lower succession of the Strelley Pool Chert with swarms of underlying hydrothermal chert ± barite veins (Van Kranendonk et al. 2003); locally pseudomorphic evaporitic minerals in the Strelley Pool Chert (Sugitani et al. 2006a), 3.2 Ga Dixon Island Formation of the Pilbara Craton (Kiyokawa et al. 2006), 3.51–3.52 Ga Coucal Formation of the Pilbara Craton (Bjonnes and Lindsay 2005), ~4.16 Buck Reef Chert of the Barberton GSB (Lowe and Worrell 1999; Stiegler et al. 2010), the Hooggenoeg Formation of Barberton GSB (Lowe and Worrell 1999); deposition of the chert-barite units in the Dresser Formation of the Pilbara Craton (Huston and Logan 2004; Orberger et al. 2006; Huston et al. 2006; Harris et al. 2009; Pirajno 2010; Golding et al. 2011), Mt. Goldworthy area of the Pilbara Craton (Sugitani et al. 2006b), 3.23–3.26 Ga Mapepe Formation of Barberton GSB (Lowe and Byerly 1999); volcanic-hosted massive sulfide and barite deposits in the 3.47 Ga Duffer Formation of the Pilbara Craton and 3.23–3.26 Ga Fig Tree Group of Barberton GSB (Huston and Logan 2004); barite deposits in 3.45 Ga rocks from the Hooggenoeg Formation of Barberton GSB (Huston and Logan 2004), >3.5 Ga rocks at the base of the Onerwacht Group of the Barberton GSB (Huston and Logan 2004), Panorama Formation of the Pilbara Craton (Huston and Logan 2004), ~3.3 Ga Wyman Formation of the Pilbara Craton (Huston and Logan 2004), 3.24 Ga Golden Cockatoo Formation of the Pilbara Craton (Huston and Logan 2004), 3.24–3.26 Ga Sulphur Springs Group of the Pilbara Craton (Huston and Logan 2004), 3.24 Ga Kangaroo Caves Formation of the Pilbara Craton (Huston and Logan 2004), Gorge Creek Group of the Pilbara Craton (Huston and Logan 2004), 3.3 Ga Mt. Goldworthy of the Pilbara Craton (Sugitani et al. 2003), Witkop Formation of the Nondweni GSB (Huston and Logan 2004; Hofmann and Wilson 2007); elevated S content related to a hydrothermal event in the Coonterunah Group of the Pilbara Caron (Altinok and Ohmoto 2006); syndepositional sulphide

minerals in cherts of the McPhee and the Towers Formations of the Pilbara Craton (Kojima et al. 1998), etc.

Pirajno (2010) came to conclusion that the chert ± barite horizons of the Warrawoona Group are associated with an alteration in the mineral assemblage related either to venting of low-temperature fluids with high concentrations of H_2S, SO_4^{2-} and Si, or to the distal sulphate-rich facies of high temperature hydrothermal systems. All these data point to the definite involvement of huge amounts of sulfur in the rock alteration and formation of cherty sediment deposits in all these regions over a significant period of time covering almost the entire span of deposition of both the Swaziland and Pilbara Supergroups. It strongly supports the involvement of sulfur (including sulfuric acid) in rock alteration and the formation of sulfur-rich rocks during the deposition of both Swaziland and Pilbara Supergroups. The known fact that there was no formation of barite deposits after 3.2 Ga until at least 2.4 Ga (Huston and Logan 2004; Huston et al. 2006) shows that the sulfur-layer of the early Earth's atmosphere was completely re-distributed by ~3.2 Ga. This is also supported by the abrupt change in the MIF (mass-independent fractionation) of sulfur isotopes at about 3.2 Ga (Kasting and Howard 2006; Kasting and Ono 2006) which could hint at the total re-distribution of sulfur of early generations by this point in time. The presence of the MIF of sulfur isotopes prior to about 2.4 Ga was first reported by Farquhar et al. (2000), but later researchers (Goldman and Kasting 2005; Ohmoto et al. 2005, 2006; Kasting and Howard 2006; Kasting and Ono 2006) indicated numerous cases with the absence or a very low MIF of sulfur isotopes ($\Delta^{33}S$ within the range of ±0.5 ‰) between 3.2 and 2.8 Ga. Goldman and Kasting (2005) suggested that the MIF of sulfur isotopes vanished sometime between 3.4 and 2.7 Ga. These data are consistent with the signs of enormous amounts of sulfur and its compounds prior 3.2 Ga in both the Pilbara craton and Barberton GSB (see above) and the cessation of the formation of barites between 3.2 and 1.8 Ga (Huston and Logan 2004). The absence of the MIF of sulfur isotopes from about 3.4–3.2 Ga to about 2.8–2.7 Ga could be due to the total re-distribution of the sulfur-layer of the early Earth's atmosphere by 3.2 Ga. But it should be taken into account that some areas could be more elevated than others which would create a situation where the H_2SO_4-layer would not cover more elevated areas after 3.4 Ga and would lead to different conditions governing the interactions between the surface and the sulfur-layer. At the same time after the total redistribution of the sulfur-layer of the early Earth's atmosphere sulfur isotopes supporting the formation of the MIF of sulfur had disappeared from the atmosphere. This time period 2.8–2.7 Ga is also known to have had intense magmatic activity with a peak of komatiite magmatism at about 2.8 Ga and the peak of the second pulse of granulite formation at about 2.7 Ga (Pilchin and Eppelbaum 2009). Thus from 2.8 to 2.7 Ga very high temperature komatiitic and high temperature mafic magmas intruded into and erupted onto the surface of crust. Given the limited range of temperature stability of sulfides which are much lower than melting points of komatiites, picrites, and mafic magmas, it is obvious that all the sulfides that were in contact with these magmas decomposed

and formed a new generation of sulfur and its compounds that led to a new stage of formation of MIF of sulfur isotopes.

However, the formation of sulfuric acid is affected by the *P–T*-conditions of stability of H_2SO_4 and SO_3, as well as the boiling point of water. The formation of sulfuric acid would have stopped only when sulfur-layer had been completely redistributed. The complete redistribution of the sulfur-layer is also the precondition for water contact with the early Earth's surface if the temperature was in the range of ~500–550 K. This was indeed the case for the early Earth, because the boiling point of sulfuric acid increases with its concentration (Lillo and Delezene-Briggs 2005) reaching a maximum at 610 K under 0.1 MPa pressure (Lide 2005).

The presence of huge amounts of bedded barites in the Barberton greenstone belt of South Africa and the Pilbara Craton of Western Australia that formed over the course of a significant time interval proves the presence of significant amounts of sulfuric acid. The formation of both sulfides and barites establishes the redistribution of the SO_3–SO_2-layer of the atmosphere before the water-layer had access to the surface.

Obvious signs of strong leaching of rocks during the deposition of the Warrawoona Group of Western Australia and Onverwacht Group of South Africa (Lowe and Worrell 1999; Van Kranendonk and Pirajno 2004, Kiyokawa et al. 2006; Sugitani et al. 2006a; Van Kranendonk et al. 2008; Stiegler et al. 2010) are also proof of the presence of sulfuric acid layer for some time and its contact with these deposits. The almost complete disappearance of crust sometime between 3.55 and 3.8 Ga (e.g., Nutman 2006; Kamber 2007) could also point to the interaction of the Earth's surface with the sulfuric acid layer sometime within that age range.

It is obvious that to cool the upper layers of the Earth and form the lithosphere the presence of a water-ocean is crucial, because only liquid water can penetrate to deep levels and speed up the cooling. However the formation of water-ocean is subject to certain constraints which govern the thermodynamic conditions needed for its formation. The main obstacle to the formation of the water-ocean is that water must be in its liquid state under a given surface temperature and atmospheric pressure. It is also obvious that the formation of a water-ocean is possible only on a solid and relatively cold surface, and it requires direct contact of water with the surface.

The formation of a liquid water-ocean is constrained by both the boiling point of water under the given atmospheric pressure, and its critical point (Pilchin and Eppelbaum 2006). Under a pressure of 0.1 MPa, water has a boiling point of 373.16 °K, and any increase in pressure would increase the boiling point of water (Lide 2005; Speight 2005; Pilchin and Eppelbaum 2006). The experimental data on changes in the boiling point of water with increases in pressure up to 6.895 MPa was presented in Speight (2005). These data were used to compile Fig. 6.1.

Unfortunately, the experimental data presented in Speight (2005) has an upper limit of pressure of 6.895 MPa; for the analysis of the boiling point of water at

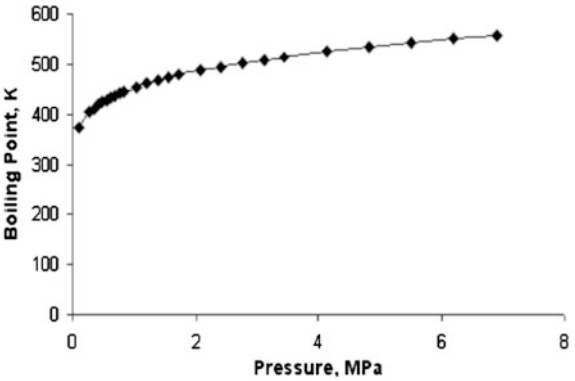

Fig. 6.1 Changes in the boiling point of water with increases in pressure in the range 0.101–6.895 MPa [compiled using data from (Speight 2005)]

higher pressures, extrapolation was needed. It is clear from Fig. 6.1 that the changes in the boiling point of water with increases in pressure can best be modeled using a square root functional relationship. Several extrapolation models have been developed, and the results of one of these models are presented in Fig. 6.2 (curve 4).

In Fig. 6.2 the values of the *P*–*T*-conditions for densities of water of 958.36 kg/m^3 (at a boiling point of 373.16 K and a pressure of 0.1 MPa; Speight 2005) and 1,000 kg/m^3 (NDW at a temperature of 277 K and a pressure of 0.1 MPa) are also presented. An interpolation-extrapolation model of the change in the boiling point of water using as initial and boundary conditions a boiling point of 373.16 K at 0.1 MPa and the supercritical point of water T = 647.36 K at P = 22.12 MPa is also presented (Line 2) in Fig. 6.2. In both models, the relationship between the boiling point of water and pressure was approximated using the following equation:

$$T_B - T_{B0} = A\sqrt{(P - P_0)}\,. \tag{6.2.2}$$

Here T_B and T_{BO} are the boiling points of water at pressure P and the initial boiling point of water at pressure P_0; A is the constant defined by initial and boundary conditions.

The evolution of the subsequent atmosphere, as well as the formation of the water-ocean depended to a great extension the rate of solidification and cooling of the magma-ocean. Another important characteristic affecting the evolution of both the early atmosphere and ocean was the temperature of water condensation under the high pressure of the early atmosphere. Analysis of the temperature necessary for maintaining the water density at 1,000 kg/m^3 (NDW at 277 K and 0.1 MPa) and 958.36 kg/m^3 (the density of water at its boiling point of 373.16 K at 0.1 MPa) for an atmospheric pressure of 35 MPa shows (Fig. 6.2) that the values of these temperatures need to be 329 and 395 K, respectively. The boiling temperature at an atmospheric pressure 35 MPa for two other models is shown in Fig. 6.2 would be 615.5 and 717.9 K, respectively. This means that for the

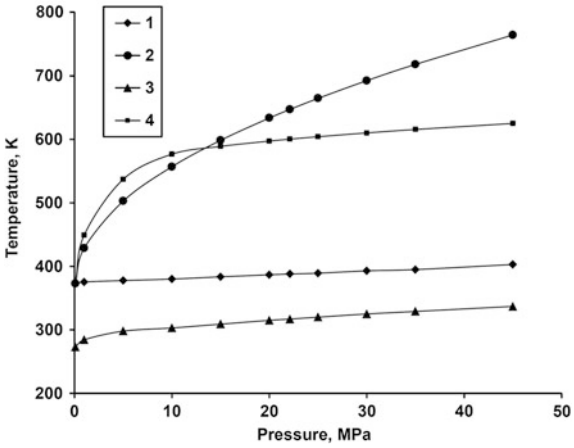

Fig. 6.2 Water at different *P–T* conditions: (*1*) *P–T* conditions for a constant density of water at 958.36 kg/m^3; (*2*) interpolation-extrapolation model of the variable boiling point of water with increases in pressure using as initial and boundary conditions the boiling point of water at 373.16 K at 0.1 MPa and the critical boiling point of water $T = 647.36$ K at $P = 22.12$ MPa; (*3*) *P–T* conditions of constant density of water at 1,000 kg/m^3; (*4*) extrapolation model of the variable boiling point of water with increases in pressure using data from (Speight 2005)

formation of liquid water from vapor under an atmospheric pressure of ~35 MPa the temperature of the Earth's surface and the atmosphere had to be below 615.5–717.9 K. At the same time, to maintain a state between the normal density of water and its density at the boiling point at pressure 0.1 MPa, the temperature needed to be in the range of 329–395 K.

It was also shown (ThermExce 2003) that at temperatures of 373, 473, 523 and 573 K the vaporization pressure and density of water is 0.1 MPa and 985.05 kg/m^3, 1.55 MPa and 864.58 kg/m^3, 3.98 MPa and 799.05 kg/m^3, and 8.59 MPa and 712.04 kg/m^3, respectively. Using these data for purposes of extrapolation yielded the following values of 601.4, 667.3, 692.7 and 722.9 K, respectively for a boiling point of water at pressures 10, 25, 35 and 50 MPa. These values are in line with the estimates of the boiling point of water shown above.

On the other hand, the presence and evolution of the water-ocean was doubtless affected by the presence of specific rocks usually formed within ocean and sea environments. The main rocks formed within the oceanic environment, and which can be used as markers of the existence of the water-ocean are the thick deposits of sediments, but first of all carbonates and evaporites. The formation of ophiolites also marks the presence of an oceanic lithosphere.

Early Archean sedimentary rocks are rare (Condie 1981, 1997). The only sedimentary rocks deposited before the deposits found in the Fig Tree and Moodies Groups in South Africa and the Gorge Creek Group of Western Australia are mostly chert- containing thin layers in the Barberton GSB and the Pilbara Craton. Some researchers consider BIF rocks as the oldest known sediments, for example

the BIF of Akilia (Myers and Crowley 2000). However, as was discussed above (Pilchin and Eppelbaum 2007) BIFs cannot precipitate directly from the oceanic water. But the Fig Tree and Moodies Groups of South Africa and Gorge Creek Group of Western Australia deposits contain significant amounts of sediments which suggests the possible formation of a water-ocean right before or before and during the deposition of these groups.

The most specific rocks in both the Barberton GSB and Pilbara Craton formed during the Early Archean are silica- rich sedimentary rocks including cherts and some related rock formations (BIFs, barites, etc.). Even though these rock formations obviously reflect considerable alteration and silicification, their origin remains unclear. Nevertheless, these silica-rich horizons (with a SiO_2 content of up to 98 wt.%) are the most widely used for stratigraphic and geological correlations between cross-sections of the Early Archean formations in both regions. At the same time, cherts, fine-grained silica-rich rocks, are remnants of the most heavily altered rocks in the horizon/area, which makes features related to their formation extremely important for determining the causes of their formation and the interaction of the surface with the early Earth's atmosphere/ocean.

The Barberton GSB and the Pilbara Craton thin silica-rich sedimentary layers separate all significant magma flows regardless of the kind and composition. The most important silica-rich layers were even given names, as is traditional for rock formations and were classified into different groups, formations and members within the Swaziland Supergroup of the Barberton GSB and the Pilbara Supergroup of the Pilbara Craton. These layers include the Buck Reef Chert, Footbridge Chert, Msauli Chert, Middle Marker of the Barberton GSB and Strelley Pool Chert, Marble Bar Chert, Coonterunah Chert, Kittys Gap Chert, McPhee Chert, Apex Chert of Pilbara Craton. Some silica-rich layers can be traced over significant areas and distances. For example the Strelley Pool Chert layer is present in all greenstone belts of the Pilbara terrane (Van Kranendonk et al. 2004) and extends for a distance of about 220 km (Van Kranendonk et al. 2002). Similarly, in the Barberton GSB such layers as the Middle Marker and Buck Reef Chert are also regionally extended (Lowe and Byerly 1999).

Geological records on the Early Archean carbonates show that sedimentary carbonates are rare in Archean greenstone belts (Condie 1981). Brasier et al. (2006) also stated that carbonates are rare in sediments prior to about 2.9 Ga. Myers (2004) analyzed carbonates from 3.71 to 3.85 Ga deposits of the Isua Supracrustal Belt of Greenland and came to conclusion that the carbonates are metasomatic in origin and not sediments (see also Shervais 2006).

Nakamura and Kato (2002) showed that in the Warrawoona Group, Pilbara Craton, sedimentary carbonate rocks such as limestone and dolostone are very rare, and only a small amount of sedimentary carbonate minerals are sometimes contained in the hydrothermal bedded chert, implying that a sink of CO_2 was minor in the Early Archean sediments. 3.22–3.25 Ga old carbonate-derived clay minerals in the Fig Tree Group of Barberton GSB (possibly the oldest clay minerals on Earth) were reported by Toulkeridis et al. (1994). A 20- to 50-m-thick unit of carbonaceous shale was also reported in the Ulundi Formation of the Fig Tree

Group (Lowe and Byerly 1999). Lowe (1994) based on an analysis of data from the Pilbara Craton suggesting that the paucity of Archean stromatolites older than 3.2 Ga probably reflects the paucity of known and possibly extant carbonate deposits of this age.

The above data show that even though there are signs of carbonate presence in the Early Archean, these carbonates were not present in significant amounts. Moreover, these carbon containing rocks are not those usually formed in the oceanic environment. At the same time, there are signs that the amount of carbonates in sediments started increasing at the end of the Early Archean. This may hint that the water-ocean did not exist in the early part of the Early Archean and only started to form at the very end of the Early Archean. Alternatively, however, the scarcity of carbonates at the end of the Early Archean could be explained by the low solubility of CO_2 in the hot/very hot water of the forming water-ocean, because one of general properties of gases is the significant drop in their solubility in water with increases in temperature and virtually zero solubility in water near its boiling point.

Another important fact that should be taken in consideration is the difference between the temperature conditions for carbonate stability and carbonate formation (Pilchin and Eppelbaum 2006). Analysis of experimental data on carbonate stability shows (Pilchin and Eppelbaum 2009) that calcite and dolomite, the most common carbonates, decompose within a range of 773–1,193 K. However temperature conditions for the formation of carbonates are $\leq$673 K, but most likely $\leq$473 K (Pilchin and Eppelbaum 2012). Thus in the Early Archean, the temperature of the ocean was either above 473–673 K, or all existing carbonates were totally destroyed. On another hand if carbonates were formed, some would have survived the thermal condition because of their relatively high stability temperature. But they could have been destroyed by powerful alteration media such as H_2SO_4.

No ophiolites from the Archean age have been found (Pilchin 2005). In the case of the Early Archean there are no any significant amounts of sediments until the very end of the Early Archean, no any significant amounts of carbonate sediments until the very end of the Early Archean, no any known evaporite deposits (except barite deposits) and only traces of evaporites marked by pseudomorphs of silicified evaporites in the 3.3–3.5 Ga Panorama Formation and Duffer Formation (DiMarco and Lowe 1989), 3.42 Ga the Strelley Pool Chert (Sugitani et al. 2006a), 3.3 Ga deposits of Mt. Goldsworthy (Sugitani et al. 2003, 2006a), 3.2 Ga the Dixon Island Formation (Kiyokawa et al. 2006) of Pilbara Craton; Kromberg Formation (Lowe and Worrell 1999) and the Fig Tree Group Formation (Condie 2001) of the Barberton GSB.

Analysis of the relative amounts of sediments compared to the amounts of magmatic rocks during the Early Archean (Fig. 6.3) and the thickness of sediments during the Early Archean (Fig. 6.4) using data on both the Pilbara Craton and the Barberton GSB shows that significant local amounts of sediment started to form at about 3.26 Ga with slight attempt at about 3.42 Ga.

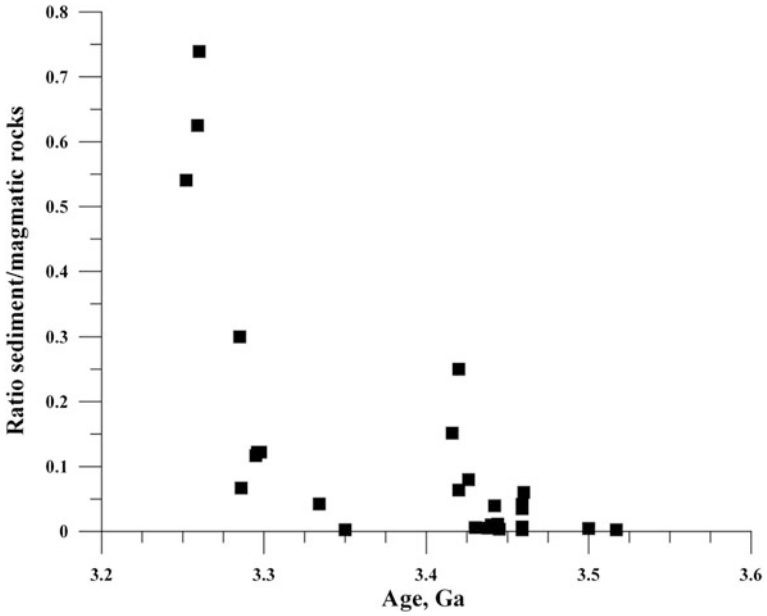

Fig. 6.3 Ratio of sedimentary to magmatic rocks in different formations of Early Archean rocks in the Pilbara Craton and Barberton greenstone belt (after Pilchin and Eppelbaum 2012)

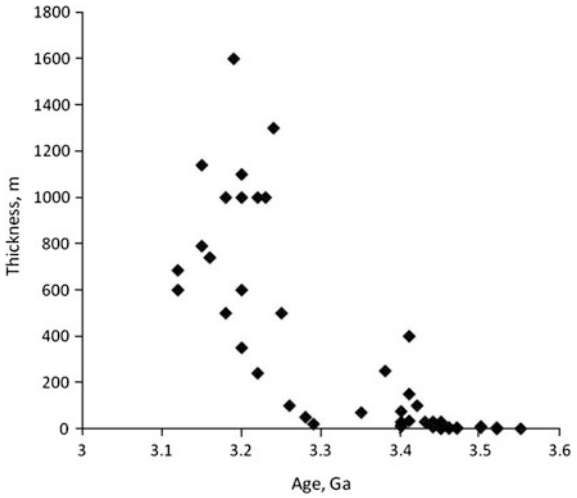

Fig. 6.4 Thickness of sediments in different formations of Early Archean rocks of the Pilbara Craton and Barberton greenstone belt (after Pilchin and Eppelbaum 2012)

Let us look at possible signs of the presence of liquid water in the Early Archean. The Early Archean rocks of the Barberton GSB were mostly komatiitic and contained Mg-rich olivine. This means that when contact with water took place at temperatures within the range of the serpentinization process 473–723 K

(Pilchin and Eppelbaum 2007) serpentinization with formation of serpentines began. Analysis of data on the alteration of Early Archean rocks shows that serpentinization has only been found for ~3.4 Ga komatiitic lapillistone of the K2 member of the Kromberg Formation (Lowe and Byerly 1999), <3.334 Ga komatiites of the M1 member of Mendon Formation (Lowe and Byerly 1999), ~3.286 Ga komatiites (very strong serpentinization) of the Weltevreden Formation (Stiegler et al. 2010) and ~3.25 Ga komatiites of the Belvue Road Formation of the Fig Tree Group (Lowe and Byerly 1999).

Analysis of data on fluid inclusions shows that in barites of ~3.46 Ga deposits in North Pole area of the Pilbara Craton, carbonate-free assemblages and carbonate-bearing assemblages equilibrated with H_2O-rich and CO_2-rich fluid inclusions (Kitajima et al. 2001), ~3.47 Ga deposits in the North Pole area of the Pilbara Craton CO_2-rich inclusions (Harris et al. 2009) and in quartz grains of the ~3.42–3.45 Ga Buck Riff Chert of the Barberton GSB (de Vries and Touret 2007) aqueous, H_2O–CO_2 mixed and unmixed and CO_2-rich fluids are present. Unusually high CO_2 content in fluid inclusions in barite and quartz-barite units of the ~3.49 Ga Dresser Formation were reported by Harris et al. (2009). These data show that at about 3.45–3.47 Ga, the density of the carbon-layer and the water-layers of the atmosphere became very close and they started to combine. These data, along with the signs of the presence of carbon-containing rocks mentioned above show that at this point in time of the early Earth's evolution, the carbonate layer was still the second layer of early Earth atmosphere separating the sulfur-layer (the first layer of the early Earth's atmosphere) from the water-layer (the third layer of the early Earth's atmosphere) but some amount of water could have already come into contact with the SO_3-layer, thus initiating the formation of H_2SO_4. Signs of the presence of water indicate that the appearance of water in both Barberton GSB and Pilbara Craton started from about 3.49 to 3.42 Ga.

All of the above indicates that during the period from ~3.85 to ~3.26 Ga there were no significant amounts of sediment and an almost complete absence of carbonates and evaporites. Clearly, it is difficult to assume that a water-ocean was present. At the same time the above data suggest that at about 3.42–3.52 Ga, the water-layer became the second layer of the early Earth's atmosphere and was placed next to the sulfur-layer; some water may have had access to the surface in some elevated areas. This is consistent with the appearance of Early Archean barite deposits at about 3.46–3.55 Ga (Huston and Logan 2004) which most likely means that the water-layer came in contact with the sulfur-layer that caused the formation of H_2SO_4, the compound necessary for the formation of significant amounts of barites. At about 3.26 Ga, water had access to most of the surface, and at about 3.20 Ga when last barite deposits of the Early Archean were formed (Huston and Logan 2004), which most likely marks the total redistribution of the sulfur-layer of early Earth's atmosphere, water had access to the whole surface and most likely completely covered all the relief structures of the Early Archean surface of the Earth. This means that the main phase of formation of the water-ocean took place somewhere between 3.46 and 3.26 Ga (most likely between ~3.42 and ~3.26 Ga). But it is obvious from available data that at the time of the

deposition of the Fig Tree and Moodies Groups of the Barberton GSB and the Gorge Creek Group of the Pilbara Craton, the water-ocean was present, and the presence of carbonate rocks in these group deposits shows that at that time the temperature of water was below ~473 K.

6.3 The Thermal Regime During Early Lithosphere Formation

The formation of the lithosphere started with the solidification of the stratified magma-ocean. Some scientists believe that the magma ocean solidified from the bottom, but that a thin chill layer may have formed at the surface (Abe 1997; Walter and Trønnes 2004; Anderson 2007). This assumption is based on results of petrological experiments under high *P–T* conditions showing that denser minerals solidify first and sink to the bottom (see review in Pilchin and Eppelbaum 2009). However it is highly unlikely that there was solidification of the magma-ocean from the bottom because the magma-ocean was stratified by iron content which increased with depth, and an increase in iron always leads to a decrease in the melting point of rocks and minerals (Pilchin and Eppelbaum 2006). So in the case of the magma-ocean, denser rock layers containing more iron and located deeper in the magmatic layers would have lower melting points which would prevent solidification of the magma-ocean from the bottom.

By contrast, the cooling of the magma-ocean would be slow because numerous layers would only allow for separate convection within each layer and a significant temperature gradient at a depth enabling the formation of heat flow would only be found at the borders between layers because the adiabatic thermal gradient within the molten layer would be too low for the generation of a significant heat flow. At the same time, the cooling of the surface was related to radiation of heat energy from the surface, and the coolant effect of the thick early Earth's atmosphere would make surface and near surface magmatic layers among the first to have solidified in the magma-ocean. Solidification and cooling of the surface and near surface magma layers would have increased the geothermal gradient, which in turn would have increased the surface heat flow and hence the rate of cooling of the surface and near surface magmatic layers. Anderson (2007) also reported data showing that a chemically stratified mantle cools more slowly than a homogenous Earth.

Experiments show that in the upper mantle, olivine with 95–97 % forsterite content and a density of ~3,300 kg/m^3 can float in liquid peridotite (Agee 1998; Hirschmann 2006). Anderson (2007) also showed that magnesium-rich minerals, Mg_2SiO_4 and $MgSiO_3$, have high melting points and if the accreting material was completely melted during the formation of the Earth, these silicates would have been the first to freeze and they would still separate from the remaining melt. These data are consistent with the conclusion in (Pilchin and Eppelbaum 2008a, b;

Pilchin 2011) that solidification of the magma-ocean started with the formation of the forsterite layer. Since forsterite has the highest melting point among the silicates 2,163 K at 0.1 MPa (Hewins et al. 1996) and ~2,307 K at 3 GPa (Davis and England 1964), it was probably the first to solidify and settle within the magma-ocean to a depth corresponding to its low density (3,222 kg/m^3 at ambient conditions). At the same time, enstatite has a melting point ~1,830 K (Best 2002) which is significantly lower than that of forsterite (2,163 K) and it would have solidified later during cooling of the magma-ocean. This means that the dropping temperature within the magma-ocean most likely crossed the point of solidification of forsterite prior to that of any other silicate rock or mineral; it is very important to note that forsterite is a relatively light mineral and would float in a Fe-rich magma (Pilchin and Eppelbaum 2009). Hence a forsterite (or forsterite-rich peridotite) layer could have started forming first at some depth within the magma-ocean.

The presence of olivines with so high a content of forsterite (Fo#) in different regions undoubtedly proves the existence of the forsterite layer. Nevertheless, it should be stated that numerous meteorites contain such extremely Mg-rich olivine. This fact is important since a magma-ocean was formed on all terrestrial planets and some moons (including the moons of Jupiter) and olivines with such extreme Mg content could actually present a similar forsterite layer on some other planets, moons or objects of the Solar System. For example a planet probably existed between Mars and Jupiter. It is believed to have been destroyed and now forms the asteroid belt which could have had a forsterite layer. The existence of such forsterite-rich olivines in meteorites also proves the presence of olivine with extremely high Mg content within the solar nebula. It is possible that the formation of the forsterite layer took place within melt with olivine of this Mg content of forsterite. The formation of the forsterite layer would have separated the magma-ocean into two sets of molten rocks, one above and another below the forsterite layer. The upper part would have been extremely poor in iron and could contain only olivine with an extremely high and high Mg content whose density in the liquid state was less than the density of solid forsterite. It was shown in (Pilchin and Eppelbaum 2008b) that even in the case where the temperature within magma-ocean was below the melting point of forsterite, the forsterite layer could have been formed by solid forsterite. It is obvious that xenoliths or phenocrysts from the forsterite layer could be delivered to the surface only by magmas from below that layer, and it actually requires complete or almost complete solidification of the upper part of the magma-ocean above the layer.

Since peridotite is believed to be the main rock of the upper mantle and olivine is the main component of any peridotite, one of the main problems related to formation of lithosphere and asthenosphere is the problem of olivine and peridotite. Analysis of peridotite xenoliths shows (Pilchin and Eppelbaum 2009) that most of the olivine/peridotite xenoliths and phenocrysts were delivered to the surface from a depth of more than 100 km. This concurs with other data such as the fact that the peridotite component is less than 1 % for Archean greenstone belts (Nalivkina 1978); in Archean magmatic rocks of the Superior Province of Canada,

the content of olivine is less than 0.4–0.9 % (Goodwin 1977); and among Archean rocks, olivine is either absent or extremely rare, and it is not one of the main mafic minerals (Pilchin 2005) and point to a lack of olivine/peridotite in the uppermost mantle. This is also in agreement with data presented in Fig. 6.6 in (Pearson et al. 2003) showing that for most Archean cratons, garnet peridotite xenoliths were delivered from depths usually greater than $\sim$70 km and that the quantity of xenoliths significantly increases with depth, with most xenoliths originating at 100 km or deeper. Since the delivery of xenoliths to the surface is much easier from shallower depths, it also points to a lack of peridotites in the uppermost mantle. Investigations of the *P–T* conditions of the equilibration of peridotite xenoliths show that peridotites were equilibrated under pressures of 2–6, 2.5–5.0, and 3–7 GPa (Lee et al. 2003), which correspond to minimum depths of about 70, 85 and 100 km, respectively. This means that olivine could not be present in significant amounts at shallow depths in the mantle under the forming Archean cratons, and especially at depths less than 100 km.

The presence of a forsterite layer is also consistent with seismic data; Pavlenkova (1995) reported a regional seismic boundary in the uppermost mantle, which she termed the *N* boundary that exists at a depth of about 100 km with a *P* wave velocity of 8.4–8.5 km/s. Further research indicates that this boundary represents a thin layer which is globally observed at a depth of 80–100 km (Pavlenkova 1996; Pavlenkova and Pavlenkova 2003). This layer is located in the thermal lithosphere beneath old platforms, at the bottom of the lithosphere under active tectonic areas and within the asthenosphere below mid-oceanic ridges (Pavlenkova 1996). Relatively high velocities (8.4–8.5 km/s) are typical of this boundary both in the old platforms and in high heat flow oceanic areas (Pavlenkova 1996; Pavlenkova and Pavlenkova 2003). Results of seismic studies (Pavlenkova et al. 2002) show that at a depth of about 100 km beneath the western Siberian craton, there is a velocity inversion with a strong reflecting interface at its base; however, for the entire Siberian Platform the boundary *N* at depths of 70–120 km is the most persistent and often underlies low-velocity zones (Pavlenkova 2006). Recent studies show (Pavlenkova 2009) that layer *N* can be characterized by two boundaries: a N_1 boundary with 8.35 km/s at a depth interval 70–120 km; and a N_2 boundary with 8.4 km/s at a depth of 100–130 km.

This is also congruent with geothermal data showing that the total thermal conductivity of the lithosphere passes through a minimum at depths of 50–100 km (Lubimova and Mayeva 1982), as well as the fact that a low conductivity zone (LCZ) was formed within the top thermal boundary slab in mantle convection (van den Berg and Yuen 2002). The potential of this LCZ would have caused secular cooling of the mantle for a longer period of time (van den Berg and Yuen 2002).

All the xenolith, geothermal, and seismic data presented above strongly support the formation of a forsterite/peridotite layer at depths of about 100 km in the Archean cratons. This is also in agreement with the abovementioned fact that forsterite has high values of *P* waves, and that the contrasts of its seismic velocity with the velocities of rocks above and below the forsterite layer could create Low Velocity Zones (LVZs) above and/or below it. The formation of the forsterite

(forsterite-rich peridotite) layer could be considered as the first step or one of first steps in the formation of the lithosphere.

On the other hand, forsterite has the highest melting point among silicates of the upper mantle. This means that the forming forsterite (or forsterite-rich peridotite) layer could take a shallow position within the upper mantle, but that the temperature of the layer would be much greater than denser iron-rich underlying layers. This would create a situation where a portion of the heat of the cooling forsterite layer would be transferred to the colder underlying layers, which would accrue additional heat rather than cooling. At the same time, solid forsterite has a low heat conduction coefficient and would block the transfer of heat from the upper mantle below the forsterite layer to the surface. These processes could significantly slow down the cooling of the upper mantle below the forsterite layer, causing the bottom part of the present continental lithosphere to form at a later time with a significant delay. It is obvious that for the cooling of Earth's surface and its upper layers, a significant amount of heat energy had to be lost.

There are three main kinds of heat transfer: heat conduction, heat convection, and heat radiation. However, in the case of the Earth's upper slabs, we are dealing with rocks which have very small heat conduction coefficient values, such that significant heat transfer could only be provided by heat radiation and convection (in the atmosphere, ocean, circulating underground waters). On the other hand, a planet is isolated from the matter of the universe by space, which does not contain any substance to facilitate either the transfer or the convection of heat outside Earth. Hence the only ways in which the Earth can give off heat energy into space are either heat radiation or the escape of some matter, for example hydrogen. Since hydrogen can absorb a significant amount of heat (its specific heat capacity is $\sim$14,300 J/(kg K)), it can be a very important means of heat loss after such causes as the decomposition of water by UV rays (Kasting and Donahue 1981; Zahnle et al. 1988).

Previous research has shown (Pilchin 2005; Pilchin and Eppelbaum 2009) that among metamorphic rocks, greenschist rocks were first to appear followed by granulites and amphibolites, but the oldest eclogites appear only in the Early Proterozoic and blueschists only in the middle-late Proterozoic. The thermodynamic conditions of some metamorphic processes are presented in Table 6.3.

In Table 6.3 the average depths corresponding to the average pressure of different metamorphic facies rocks, as well as geothermal gradients for contemporary surface temperature conditions and the temperature of $\sim$573 K that existed at some point during the Hadean or Early Archean are presented.

Since granulites are metamorphic rocks that formed under the highest temperature conditions among all metamorphic rocks, and since that most of the low crustal xenoliths are granulites, a more detailed analysis of granulites is presented in Table 6.4.

The data Table 6.4 can be used to characterize the temperature conditions in lower crust of the forming lithosphere during the Archean, Early Proterozoic and Grenvillian ages.

Table 6.3 Thermodynamic conditions of some metamorphic processes (adapted from Pilchin and Eppelbaum 2009)

Type of metamorphism	Average temperature, K	Average pressure, MPa	Average depth of lithostatic pressure, km	Average geothermal gradient (K/km) for present surface conditions	Average geothermal gradient (K/km) for surface temperature ~573 K
Blueschists ($n = 265$)	677	1,000	~35	11.5	2.97
Eclogites ($n = 556$)	856	1,900	~64	9.1	4.42
Amphibolites ($n = 353$)	925	770	~26–27	24.1	17.41
Granulites[a] ($n = 601$)	1,075	820	~28	28.6	17.93
Greenschist ($n = 188$)	681	420	14–15	27	8.28

[a] Granulites of the Archean and Early Proterozoic

Table 6.4 Thermodynamic conditions of metamorphic processes of granulites of different origin (adapted from Pilchin and Eppelbaum 2009)

Rock (n)	Average T, K	Average P, MPa	Average P/T, MPa/°C	Average depth of lithostatic pressure, km	Average geothermal gradient, K/km
Granulites average[a] ($n = 601$)	1,075	822	1.02	~28	28.6
Granulites of:					
Early and Middle Archean	1,059	880	1.14	30.3	25.3
Late Archean	1,127	871	0.87	30.0	27.8
Early Palaeo-Proterozoic	1,040	667	0.86	23.0	32.6
End of Palaeo-Proterozoic	1,087	825	1.01	28.4	28.0
Granulites of Grenvillian ($n = 96$)	1,050	968	1.25	34.0	22.4
Granulites average, including Grenvillian granulites ($n = 697$)	1,071	842	1.05	29.5	26.4

[a] Only granulites of the Archean and Early Proterozoic age

6.4 Markers of Thermal Conditions Within the Lithosphere During Its Evolution

There are a number of events and processes that can take place at some very specific thermodynamic conditions which can serve as markers of these specific conditions. Some examples of such events and processes are the formation of BIFs, red beds and/or paleosols, the state of decomposition of carbonates, iron sulfides and other rocks and minerals, the process of serpentinization, the

formation of oxic or anoxic environments, and many others. At the same time there are situations where the expected process or event did not take place and this could be used as a marker of specific conditions which prevented some events and processes from occurring, and some rocks and minerals from forming. For example, the absence of significant amounts of sediments in the Early Archean (before ~3.26 Ga), as well as the absence of carbonate rocks and evaporites in the Early Archean point to the absence of water-oceans. There are numerous cases with *P–T* conditions when both eclogites and blueschists were formed, but there are a number of cases when even though *P–T* conditions (overlapping conditions) were favorable for the formation both eclogites and blueschists only one of them was formed and not the other. In another case, ultrahigh-pressure (UHP) conditions are defined by the presence of coesite, or diamond (Carswell and Zhang 1999). Thus, the absence of either coesite or diamond indicates the absence of UHP conditions. By contrast, there are cases of the formation of some rocks or formations only during specific time periods which were not formed at any other time or for a long period of time. For example, the formation of BIFs took place mostly during the period of time from ~3.85 to ~1.80 Ga and was never formed again except during a very short time interval in Late Proterozoic (Klein 2005; Pilchin and Eppelbaum 2006). Similarly, barites formed during the period from 3.5 to 3.2 Ga and then did not form until 1.8 Ga (Huston and Logan 2004).

Iron is known to be the most abundant element on Earth; oxygen is the second most abundant and the most abundant in the Earth's crust (Anderson 1989; Clark 1982; Pilchin and Eppelbaum 2006). This makes these two elements, that make up nearly two- thirds of the Earth's mass, key players in different processes and features in the evolution and in particular the early evolution of the Earth. Even though the oxygen content on Earth is so great, most scientists believe that the early Earth (before about 2.2–2.3 Ga) was essentially anoxic (e.g., Holland 1984; Kasting and Donahue 1980). This conclusion is based on the fact that some processes that took place during the early Earth's evolution could only have occurred in a strictly anoxic environment. Among these processes are the deposition of banded iron formations (BIFs), and the formation of pyrite and uraninite deposits. On the other hand, there are known processes which could only have taken place in oxygen-rich environments. These processes include the oxidation of iron from its ferrous to ferric condition, the formation of paleosols, and the formation of red beds. This makes it possible to use the time spans and/or occurrence of these processes to determine the point in time in the Earth's evolution when its atmosphere transformed from anoxic to oxic conditions (Holland 1984; Kasting and Donahue 1980). This means that such processes as the deposition of BIFs, and the formation of pyrite and uraninite deposits could be employed as markers of anoxic atmospheric environments, and that such processes as the start of the formation of red beds and paleosols could be regarded as markers of the start of the atmospheric transition from the anoxic to the oxic state.

The role of thermodynamic conditions on the stability of iron oxides has been known for decades in physics, chemistry, geophysics and metallurgy (Pilchin and Khesin 1981; Pilchin and Eppelbaum 1997, 2004; Tokumitsu and Nasu 2000).

This is caused by the fact that ferrous iron is stable under high-temperature and high-pressure conditions, and ferric iron is stable at low-temperature and low-pressure conditions. Therefore the TFFI could take place during the cooling of iron compounds from high temperatures to low temperatures, and the transformation of ferric iron to ferrous iron, with an increase of temperatures from low to high values.

Under thermodynamic conditions with a pressure of 0.1 MPa, TFFI takes place at temperatures below or equal to 843 K (see review in Pilchin and Eppelbaum 1997, 2006) and follows Eq. (1.1.10). This reaction has been proven experimentally (Grønvold et al. 1993; Redl et al. 2004). It is clear from the Eq. (1.1.10) that it does not require the presence of oxygen or any other oxidizing agent. At the same time, Eq. (1.1.10) is not really an oxidation reaction, because along with the oxidation of two iron atoms there is the reduction of one iron atom to native iron.

It was shown earlier that Eq. (1.1.10) of TFFI can be used for the characterization of the stability of rocks and minerals, the thermodynamic conditions of the transformation, the oxidation conditions, and the magnetic properties of rocks and minerals (Pilchin and Eppelbaum 1997, 2006; Eppelbaum and Pilchin 2004, 2006). However, the presence of a temperature of 843 K does not necessarily guarantee the transformation from ferrous to ferric iron, since the upper temperature limit of TFFI is highly dependent on the pressure applied. Even a small increase in pressure of up to 10 MPa can decrease the upper temperature limit of TFFI to 723 K (Pilchin and Khesin 1981; Pilchin and Eppelbaum 1997).

Other researchers have shown that ferrous iron oxide is stable in a vacuum below 673 K (Tokumitsu, and Nasu 2000) and below a temperature of 723 K (Redl et al. 2004). These experiments clearly show that the presence of oxygen or any other oxidizing agent is not required for TFFI, and that oxygen would generally play a more significant role only at temperatures below 673–723 K. This could also explain the very specific role of low temperature oxidation in rock magnetism.

Experiments with heating magnetite show (Mazo-Zuluaga et al. 2003) that samples treated at 793 K consist only of well-crystallized hematite, but magnetite treated at 623 K consists of mixtures of hematite, maghemite and magnetite. At the same time, there is virtually no decomposition of ferrous iron oxide below approximately 523 K (Myers and Eugster 1983). This is in agreement with other studies showing that magnetization usually increases at temperatures above 530 K, which indicates that FeO decomposes into α-Fe + Fe_3O_4 (Redl et al. 2004). These temperature values coincide with the main temperature range of the serpentinization process from $\sim$473 to $\sim$673–723 K (Hess 1955; Pilchin and Eppelbaum 1997), which is also known for the presence of TFFI.

All of the above argues in favor of a temperature interval with a lower temperature limit of about 473–523 K and an upper temperature limit of about 723–843 K as the temperature range of TFFI.

BIFs are among the oldest rock formations on the Earth preserved from the Early Archean ($\sim$3.85 Ga in Western Greenland). BIFs were deposited mostly in greenstone belts during a significant time span starting as early as 3.85 Ga in

Greenland (Klein 2005) and 3.5 Ga in Australia (Klein 2005) and ending around 1.80–1.85 Ga (Huston and Logan 2004; Klein 2005). BIFs are usually classified as either the Algoma- or Superior-type (Huston and Logan 2004; James 1983; Klein 2005). However only the Late Archean and early Paleoproterozoic BIFs are characterized by a maximum of both their number and the amount of iron ore deposits in them (Huston and Logan 2004; James 1983). It is believed that 90 % of the iron ores in all BIFs were deposited during the Early Proterozoic (James 1983). The maximum amount of Superior-type BIFs and the maximum amount of iron ores were deposited during the period of 2.5–2.4 Ga. The next greatest amount of Superior-type BIFs deposits, along with the next greatest amount of deposited iron ores took place during the period of 1.9–1.8 Ga. Interestingly, the maximum amount of Algoma-type BIFs was deposited during 2.8–2.7 Ga, a period that coincides with the start of worldwide magmatic activity. Some studies point to a decline in BIF deposition between 2.47 and 2.40 Ga (Barley et al. 2005), and an absence of BIF deposition during the time period from 2.4 Ga to around 2.0 Ga (Isley and Abbott 1999).

For additional information about the distribution of BIFs through time, the number of BIFs per 100 Ma was calculated for different periods of the Early Precambrian (Fig. 6.5).

It was shown (Pilchin and Eppelbaum 2009) that at the time of magma-ocean neither magnetite nor hematite had chances of survival and the formation of these minerals could have started only after the solidification of the magma-ocean and when the surface temperature dropped below the upper limit of transformation of ferrous to ferric iron (TFFI) (723–843 K). During the solidification of the magma-ocean and during the cooling of its surface and the early atmosphere, different volatiles, depending on their properties, would have started to condense. Water condensation would have started at temperatures below its critical point 647.2 K (Speight 2005). A comparison of these temperature values with the upper limit of TFFI (723–843 K) shows that the formation of magnetite would have first started as stated in Eq. (1.1.10) of TFFI. This means that the formation of magnetite through Eq. (1.1.10) could have started before the formation of the water-ocean. In other words at least the first BIFs could not have been deposited in the oceanic environment. When the subsequent cooling of Earth's surface and the atmosphere lowered the temperature to below 647.2 K, the water-ocean could have started to form.

For analysis of the oxidation conditions and stability of ferrous iron oxide, a special coefficient (υ) of the transformation of FeO to Fe_2O_3 was introduced (Pilchin and Khesin 1981):

$$\upsilon = \frac{\mathrm{FeO}}{\mathrm{FeO} + \mathrm{Fe_2O_3}}. \tag{6.4.1}$$

Here FeO and Fe_2O_3 are the weight content of iron(II) and iron(III) oxides, respectively.

It is obvious from Eq. (6.4.1) that for hematite relative ferrous iron oxide content should be $\upsilon = 0$ and for magnetite it should be $\upsilon = 0.31$.

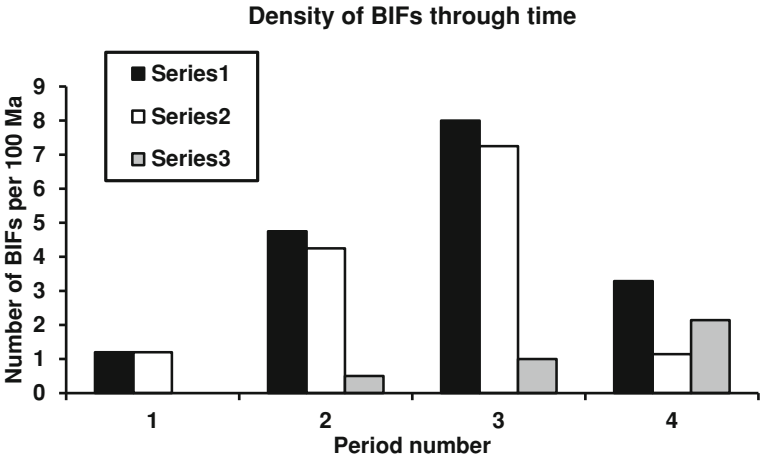

Fig. 6.5 Number of banded iron formations (Total—series 1, Algoma-type—series 2, and Superior-type—series 3) deposited during 100 Ma in different periods of the Early Precambrian (*1* Early Archean, *2* Middle Archean, *3* Late Archean, and *4* Early Proterozoic)

This coefficient can be used for characterizing both ferrous iron stability and the oxidation conditions during the formation of rocks (Pilchin and Khesin 1981; Pilchin and Eppelbaum 1997).

The relative ferrous iron oxide content in some BIFs of the Archean and the Early Proterozoic is presented in Table 6.5.

The iron-quartzite rocks of Pervomayskiy area in Table 6.5 were progressively metamorphosed under conditions of amphibolite sub-facies of granulite facies (Galetsky et al. 1985).

Analysis of relative ferrous iron oxide content in BIFs of the Archean and the Early Proterozoic presented in Table 6.5 shows that neither hematite nor magnetite is the main compound of BIFs and they definitely contain an excess of ferrous iron oxide compared to their content in magnetite. This feature is puzzling especially for BIFs. Analysis of the relative content of iron(II) in numerous magmatic rocks (Pilchin and Eppelbaum 2007; Pilchin 2011) shows that is also unexpectedly high, because during the cooling of magmatic rocks through the range of TFFI iron(II) was assumed to transform into iron(III) but this did not occur. It is also clear from Table 6.5 that the coefficient of stability of iron(II) oxide ($v = \mathrm{FeO}/(\mathrm{FeO} \pm \mathrm{Fe_2O_3})$) for the Archean BIFs is in the range of 0.44–0.55, and for the Early Proterozoic BIFs it is in the range of 0.51–0.66. This means that the conditions for ferrous–ferric iron transformation were better in the Archean than in the Early Proterozoic. This could be explained by the reduction in temperatures to the zone of iron(II) stability or the rapid cooling of forming deposits. It is also obvious that processes of metamorphism preserve iron(II) from its transformation to iron(III).

Let us analyze the possible causes and conditions that could have stopped iron(II) in magmatic rocks from transforming into iron(III). How was it actually

Table 6.5 Relative content of ferrous iron calculated for the average of bulk analyses of Precambrian banded iron formations presented in (Gole and Klein 1981; Holland 1984; Galetsky et al. 1985)

Rocks	Fe_2O_3	FeO	$FeO/(Fe_2O_3+FeO)$
Archean:			
Yilgarn Block	18.98	23.65	0.55
Montana	26.91	17.51	0.44
Proterozoic:			
Hammersley Basin			
Marra Mamba	12.93	25.49	0.66
Dalles Gorge Member	18.40	23.88	0.56
Joffre Member	20.16	22.53	0.53
Labrador Trough			
Unmet.	19.96	21.69	0.52
Met.	16.87	23.68	0.58
Biwabik	20.28	21.43	0.51
Ukrainian Shield[a]:			
Pervomayskiy area:			
Quartzite pyroxene-magnetite	24.32	29.55	0.55
Quartz-pyroxene schists	1.91	50.9	0.96
Quartz-pyroxene schists	2.93	40.45	0.93
Quartz-garnet-pyroxene schist	1.16	16.3	0.94
Quartz-garnet-pyroxene schist	1.84	28.64	0.94
Biotite-cilimanite schist	1.16	4.93	0.81
Petrovskiy area:			
Quartz-biotite-amphibol schists	1.12	37.67	0.97
Quartz-biotite-amphibol schists	3.83	27.1	0.88
Garnet-biotite-quartz schists	2.02	11.62	0.85
Garnet-biotite-quartz schists	3.33	14.31	0.81

[a] $FeO/(Fe_2O_3 + FeO)$ values calculated using data in (Galetsky et al. 1985) for the Froonzovskikh magnetic anomalies, the Belozerskaya-Odesskaya metallogenic zone of the Ukrainian Shield

possible that iron(II) in magmatic rocks, which erupted onto the surface or intruded into the crust at temperatures definitely above the upper limit of TFFI and cooled to present ambient temperatures, could have survived cooling in the temperature range of TFFI (723–843 K upper limit and 473–523 K lower limit)? According to the reaction (see Eq. (1.1.10)) of TFFI iron(II) oxide should transfer totally to iron(III) oxide or at least to a mixture of hematite (Fe_2O_3) and magnetite ($FeO \times Fe_2O_3$), but in fact all rocks of magmatic or metamorphic origin still have an excess of iron(II) oxide, and sometimes very extreme excesses, even in intrusive magmatic rocks which require longer to cool and hence had more time for the transformation from iron(II) oxide to iron(III) oxide. It was shown (Pilchin and Eppelbaum 2006) that magnetite in most cases is a more stable iron compound than hematite even within the temperature range of TFFI. On the other hand it was also shown (Akhmetov 1992b; Lide 2005; Pilchin and Eppelbaum 2007) that hematite can be formed and is stable only in the presence of both water and

oxygen. The main components of rust are $Fe(OH)_3$ and $Fe_2O_3 \times nH_2O$ which are usually formed as the result of the following reactions (Akhmetov 1992b; Benali et al. 2001):

$$4Fe(OH)_2 + O_2 + 2H_2O = 4Fe(OH)_3 \tag{6.4.2}$$

and

$$4Fe + 3O_2 + 2nH_2O = 2FeO_3 \times nH_2O. \tag{6.4.3}$$

It is clear that for reactions Eqs. (6.4.2) and (6.4.3) the presence of both water and oxygen is required.

The fact that clay minerals from deep-sea sediments containing iron(II) readily oxidize into iron(III) upon contact with atmospheric oxygen (König et al. 1999) also supports the need for both oxygen and water for oxidation to take place, because without such contact with the air it would remain iron(II). On the other hand, the natural dehydration of goethite (or its laboratory heating to 573–673 K) produces hematite, which is an important process in the formation of red sediments (Butler 1998). All this suggests that the formation of significant amounts of hematite during the Early Archean and the earliest Early Proterozoic before the oxidation event at about 2.3 Ga was impossible. But the formation of magnetite through the reaction indicated in Eq. (1.1.10) does not require the presence of oxygen and in any case not all iron(II) oxides were transformed into magnetite.

Important processes related to the preservation of iron(II) oxide in rocks could relate to the following features. Since the CO-layer and the SO_2-layer were in direct contact with each other (see Sect. 6.2) the key processes in their interaction deserve attention. One of the reactions between these two compounds is the reduction of SO_2 to elemental sulfur through:

$$2CO + SO_2 \rightarrow CO_2 + S^0 \tag{6.4.4}$$

which can be speeded up by some catalysts (Palmqvist et al. 1997). This reaction together with the Boudouard reaction (see Eq. (6.2.1) controlled the transformations between carbon and sulfur compounds within the early Earth's atmosphere and the formation of such important reducing agents as elemental carbon and sulfur. Another important reaction involving elemental carbon as a reductant was the reduction of SO_2 to elemental sulfur through the following equation (Bejarano et al. 2001):

$$SO_2 + C \rightarrow CO_2 + S^0 \tag{6.4.5}$$

which is most efficient at temperatures of 873–973 K.

Even though the most efficient temperatures for reaction Eq. (6.4.5) are a little bit high for some periods of the Earth's atmosphere and surface evolution, they could easily be reached upon contact with erupting magma. Both reactions

Eqs. (6.4.4) and (6.4.5) lead to the formation of elemental sulfur, which is the best chemical to react with elemental iron formed by reaction Eq. (1.1.10) with the formation of iron sulfides. Iron sulfides are widely known within Early Archean formations and they are always among the essential components of BIFs. There are a number of important reactions involving the reduction of iron(III) oxide to magnetite, among which the most crucial for the conditions of the early Earth's atmosphere are (1) the reduction of hematite to magnetite at temperatures of 723–873 K (Wana et al. 2006):

$$3Fe_2O_3 + C \rightarrow 2Fe_3O_4 + CO \tag{6.4.6}$$

and (2) the reduction of hematite to magnetite by carbon monoxide, which proceeds through the following reaction (Rao 1974):

$$3Fe_2O_3 + CO \rightarrow 2Fe_3O_4 + CO_2. \tag{6.4.7}$$

Both reactions in Eqs. (6.4.6) and (6.4.7) could have played a significant role in protecting ferrous iron oxide (FeO) from its conversion to ferric iron oxide (Fe_2O_3) and preventing BIFs from turning into rust during cooling at the temperature range of the TFFI (Pilchin and Eppelbaum 2006).

Another important reduction reaction for iron(III) oxide to magnetite is the reduction of hematite by SO_2 (McMullen and Thomas 2002):

$$6Fe_2O_3 + 2SO_2 \rightarrow 4Fe_3O_4 + 2SO_3. \tag{6.4.8}$$

Reaction Eq. (6.4.8) could have played an important role in the formation of SO_3 and sulfuric acid within the early Earth's atmosphere. It is obvious that magnetite itself could be similarly reduced by some carbonate and sulfur compounds to iron(II) oxide and/or elemental iron. Given that the early Earth's atmosphere was CO, CO_2, S, SO_2 and SO_3 rich (see Sect. 6.1) it is obvious that these compounds played a crucial role in the preservation of ferrous iron oxide in Archean and Early Proterozoic rocks, including BIFs, from its transformation to iron(III) oxide. It was shown (Pilchin and Eppelbaum 2007) that fast cooling during later periods of the Earth's evolution was capable of preservation of ferrous iron oxide from its transformation into iron(III) oxide.

All of the above shows that the formation of BIFs took place under conditions with temperatures within the range of TFFI (between 723–843 K and 473–523 K) especially before the formation of water-ocean. In particular, the first BIFs of the Algoma type were formed when the Earth's temperature dropped to or below the upper limit of the temperature range of TFFI (723–843 K). In later cases of BIFs, the surface temperature must also have been within the temperature range of TFFI, but it had to either cool down to the temperature within the range of TFFI or be heated to these temperatures. This does not mean that the Earth's surface temperature was within the temperature range of TFFI throughout the entire time span of BIF deposition, from 3.85 Ga until 1.85–1.80 Ga; such conditions could in

many cases have only been regional or local. At the same time it is obvious that the preservation of ferrous iron oxide in the absolute majority of rocks and minerals supports the assumption of a sulfur- and carbon-rich early Earth atmosphere.

The two other widely distributed processes involving iron in the early Earth's evolution were the formation of paleosols and red beds (Pilchin and Eppelbaum 2006).

The chemical profiles of paleosols have been used by numerous authors (e.g., Holland 1984; Rye and Holland 1998; Utsunomiya et al. 2003, etc.) to reconstruct the atmospheric oxygen level, as well as markers of the start of the transformation of the Earth's atmosphere from an anoxic to an oxic environment. It has been argued that the most important feature of the weathering of paleosols is the mobility of iron (Rye and Holland 1998) caused in theory by the fact that iron(II)-compounds are soluble in water, whereas iron(III)-compounds are not. This means that if there was enough oxygen in the atmosphere, ferrous iron(II) would have oxidized to ferric iron(III) during weathering, and the iron within the paleosol would not be soluble or mobile. Analysis of identified paleosols shows (Rye and Holland 1998) that there are paleosols dating to the Late Archean, Early Proterozoic, Grenvillian and Paleozoic ages. Other studies also report paleosols dating to the Archean (Grandstaff et al. 1986), Early Proterozoic (Utsunomiya et al. 2003), and Grenvillian (Zbinden et al. 1988). Research also indicates (Rye and Holland 1998) that out of 50 investigated paleosols 48 were older than 1.7 Ga; and that pre-2.44 Ga paleosols suffered significant iron loss during weathering, whereas the iron loss was negligible during the formation of the 2.2–2.0 Ga and all later paleosols examined (Rye and Holland 1998).

Red beds are detrital sedimentary rocks rich in reddish-brown ferric oxide; this is why some researchers believe that the appearance of red beds is an indicator of oxygen build-up in the atmosphere. Different studies point to the absence of red beds before about 2 Ga (Kasting 1993), 2.2 Ga (Nisbet and Sleep 2001). Research has found that red beds were formed in the Early Proterozoic (Eriksson et al. 1997; Utsunomiya et al. 2003), Middle Proterozoic (Eriksson et al. 1997), and Late Proterozoic (Knoll et al. 1995).

Since both the formation of paleosols and red beds are involving in the formation of iron(III) oxide, it is obvious that during their formation both water and oxygen were present. But, as was shown in Pilchin (2011), the early Earth's atmosphere was stratified by the density of supercritical volatiles, with the main layers of the atmosphere composed of SO_2–SO_3, CO_2–CO, and H_2O. It was also shown (see Sects. 2.7 and 6.1) that the water layer did not have access to the surface until the SO_2–SO_3-layer was re-distributed or the temperature of early Earth's atmosphere dropped below $\sim$500–550 K. At the same time, because oxygen has a relatively low density, it did not have access to the surface either and could only be present in the upper layers of the atmosphere (Pilchin and Eppelbaum 2006). It is evident that the absence of direct contact of oxygen with the surface would make the atmosphere appear anoxic, even though some amount of oxygen was present in the atmosphere. It is obvious that even after the re-distribution of sulfur-layer of the early Earth's atmosphere and the formation of

water-ocean, the early Earth's atmosphere was still CO_2-rich, which also could prevent oxygen from accessing the surface. But in some elevated areas of the Earth, oxygen could have access to the surface and this could explain why studies differ as to the start of oxidation of the Earth's atmosphere and range from ~2.4 to ~2.2 Ga. In fact, with the re-distribution of CO_2-layer of the early Earth's atmosphere oxygen would have had access to the surface in less and less elevated areas. But as soon as oxygen had access to the surface, conditions would have been created with the presence of both water and oxygen and the formation of paleosols and red beds would have been possible.

Analysis of data shows that such a wide dispersion of iron-containing deposits over time, and the obvious overlapping of the processes of BIF deposition with processes of paleosols and red bed formation impede an unambiguous definition of any specific time point that could be accepted as the dividing line between anoxic and oxic atmospheric environments (Pilchin and Eppelbaum 2006).

Certain geological and tectonic processes require the presence of specific and sometimes unique conditions. It is well known that the origin of different geological and tectonic processes depends to a great extent on the thermodynamic conditions in a region. Hence the development of methods for the determination of the temperature and pressure distribution in different layers of the lithosphere makes research in experimental petrology on the *P–T*-conditions of stability different rocks and main rock-forming minerals extremely important. But direct measurements of temperature and pressure in most cases are impossible during a geological or tectonic process itself. Moreover, simple data on the temperature and pressure distribution in the crust and upper mantle are not enough for modelling the petrological composition of different lithosphere layers. In many cases other features need to be known such as the relative stability of different rocks and minerals, their density and seismic velocity in order to correlate these data with estimates of *P–T*-conditions and data obtained by gravity and seismology. On the other hand, to estimate the *P–T*-conditions in metamorphic belts, kimberlites, lamproites, and regions of other specific rock and mineral formations, data obtained by experimental petrology for these rocks and minerals are widely used. These methods, known as geothermometers and geobarometers, are based on the experimental determination of the *P–T*-conditions for transfer of one mineral or rock to another one.

It was shown that lithostatic pressure and gravity forces cannot explain a number of geological and tectonic processes, such as orogenic processes, obduction, block uplift, formation of thrust nappes, continental collisions, etc. (Pilchin 2005). These processes are usually called anti-isostatic processes, which require the presence of force greater than the gravity and directed in the opposite direction to the force of gravity or in a horizontal direction. It is obvious that such a force or combination of forces have nothing to do with lithostatic pressure but rather will create pressure directed against the lithostatic pressure. However, knowing the origin of this force (net force) can help better understand different geological and tectonic processes. Any unit of volume is subjected to the laws of thermodynamics, and the main thermodynamic parameters are pressure (*P*), temperature (*T*),

and volume (V). Since all matter obeys the laws of thermodynamics, which control the state and even appearance of matter, it is very important to analyze present thermodynamic conditions in geological regions or layers. It was shown (Pilchin and Eppelbaum 2012) that the presence of such contrasting tectonic processes as orogeny, obduction, subduction, uplift, immersion etc. indicates that in those cases the lithostatic pressure cannot be used as the real pressure, because of the absence of isostatic equilibrium.

The value of the lithostatic pressure P_l for depth z may be calculated or estimated using equation

$$P_l = \sigma g z. \tag{6.4.9}$$

Here σ is average density of overlaying rocks, and the g is the acceleration of gravity.

For the layered model the value of lithostatic pressure can be calculated using equation

$$P_l = \sum_i \sigma_i g_i z_i. \tag{6.4.10}$$

Here σ_i and z_i are the density and thickness of some layer i.

However the real pressure can be calculated using Eq. (2.7.4), and the conditions of equilibrium for any form of matter can be calculated using Eq. (2.7.5). It was shown in Sects. 2.7 and 4.4 (and emphasized in Pilchin and Eppelbaum 2009) that the real pressure P can be very different from its lithostatic value P_l. It also means that any pressure value determined by any method should not be simply accepted as being its lithostatic value. For example, pressure values obtained using mineral geobarometers cannot be used as the lithostatic pressure for estimating the real depth of the mineral or rock, because they could indicate the pressure formed by net forces that could include forces forming overpressure and/or horizontal forces.

To calculate and/or estimate temperature values at different depths in geologically stable regions, a one- dimensional heat conduction equation can be used (Pilchin 1983; Eppelbaum et al. 1996):

$$\frac{dQ}{dz} + A = 0. \tag{6.4.11}$$

Here Q is the heat flow, z is depth, and A is the heat production.

$$Q = \lambda \frac{dT}{dz}. \tag{6.4.12}$$

Here λ is heat conductivity, and dT/dz is the geothermal gradient.

Simple integration of Eq. (6.4.11) in the depth interval (z_0, z_l) gives the following equation for Q change with depth

$$Q_i = Q_0 - A(z_1 - z_0). \tag{6.4.13}$$

Equation (6.4.13) shows that the value of the heat flow reduces with depth. This equation using the definition for the heat flow Eq. (6.4.12) can be rewritten as

$$\left(\frac{dT}{dz}\right)_l = \left(\frac{dT}{dz}\right)_0 - \frac{A}{\lambda}(z_l - z_0). \tag{6.4.14}$$

Equation (6.4.14) shows that the value of the geothermal gradient also reduces with depth. This result was proven by geothermal research in the Caucasus, the Caspian Sea, the Middle Asian Republics of the former Soviet Union and Eastern Mediterranean (Pilchin 1978a, b; Eppelbaum et al. 1996; Pilchin and Eppelbaum 2005; Eppelbaum and Pilchin 2004, 2006).

It is well known in petrology (Pilchin and Eppelbaum 2005), that one of the most important parameters for rock and mineral stability is the slope dP/dT (or $\Delta P/\Delta T$). From this point of view, it is very important to analyze relationships between the values of the P/T ratio and the dP/dT slope for different rocks and minerals.

From Eq. (6.4.9) the pressure change with change of temperature can be calculated by the following equation

$$\frac{P}{T} = \sigma g \frac{z}{T}. \tag{6.4.15}$$

An equation for the corresponding slope is

$$\frac{dP}{dT} = \sigma g \frac{dz}{dT}. \tag{6.4.16}$$

Taking into account that geothermal gradient G is

$$G = \frac{dT}{dz}, \tag{6.4.17}$$

Equation (6.4.16) can be rewritten as

$$\frac{dP}{dT} = \frac{\sigma g}{G}. \tag{6.4.18}$$

In Eq. (6.4.17) the value z/T is the inverted value of the average geothermal gradient. Equation (6.4.18) can be used to estimate the slope of the lithostatic pressure by temperature at an arbitrary depth.

Most geologists believe that high-grade metamorphic processes are related to the subduction of rock blocks and their subsequent exhumation. The subduction

process is related to the sinking of the lithosphere block/plate into the upper mantle. The main condition for block/plate sinking is the presence of a down-directed net force (Pilchin and Eppelbaum 2005), which creates pressure higher than the value of the lithostatic pressure under the block. This type of force can be created by gravitational attraction (weight of the block) or by gravitational attraction along with an external force (forces) with a component of the force applied downwards. In the case of subduction there are two possibilities: (1) the force that makes the subducting plate sink into the upper mantle is gravity, (2) part of the force is an external force that forces the subducting block to sink.

The first case is not applicable here (Pilchin and Eppelbaum 2002, 2005), because there is no likelihood that a light (less dense) continental block will sink into a denser upper mantle by the force generated by its weight alone. On the other hand, a sinking block should have a very low geothermal gradient, because the block had similar or neighboring temperature distribution values at the same depths within the block. So it should create giant slopes, which no crustal rock can withstand. The second case signifies that in addition to the force of gravity, there is some extra force which pushes the block down within the upper mantle. But such force can only be external. In such a case we have:

$$dP = \sigma g \cdot dz + dP_e. \tag{6.4.19}$$

Here P_e is pressure created by the external (tectonic) force.

The value for the slope will be

$$\frac{dP}{dT} = \frac{\sigma g}{G} + \frac{dP_e}{dT}. \tag{6.4.20}$$

In this case the slope should be greater than the slope specified by the force of gravity alone. However at the same time value of the ratio *P/T* should also be greater than the ratio without external force. The extensional force can reduce the pressure and hence reduce the slope (*dP/dT*) and the ratio *P/T*.

The values of the *P/T* ratio and the slope (*dP/dT*) can also be calculated for the case where there is an absence of external force from Eq. ((2.7.5), and for pressure with the effect of an external force from Eq. (2.7.4). For example, the slope (*dP/dT*) will be

$$\frac{dP}{dT} = \frac{\sigma g}{G} + \frac{\alpha}{\beta} \tag{6.4.21}$$

in the case without external force and pressure unloading, and

$$\frac{dP}{dT} = \frac{\sigma g}{G} + \frac{\alpha}{\beta} - \frac{d}{dT}\left(\frac{1}{\beta}\frac{\Delta V}{V}\right) \tag{6.4.22}$$

in the case with external force and pressure unloading.

Equations (6.4.21) and (6.4.22) show that value of the slope (dP/dT) is quite different from its value for lithostatic pressure alone, and depends on ratio of the volume thermal expansion (α) and compressibility (β). Since the pressure defined by Eq. (2.7.5) is the maximal potential pressure with no pressure unloading (see above), it is clear that the value of the slope estimated using Eq. (6.4.21) is the maximal potential slope in the absence of external force. The value of the slope estimated using Eq. (6.4.22) gives its real value. Equation (6.4.22) shows that in the case of pressure unloading ($\Delta V > 0$) the real slope should be lower than that determined by Eq. (6.4.21). And in the case of the presence of an external force ($\Delta V < 0$) the value of the slope estimated using Eq. (6.4.22) could be even greater than that determined by Eq. (6.4.21). Thus any case where the value of slope is greater than that determined by Eq. (6.4.21) an external force was applied to rocks or minerals. This shows that the α/β ratio is extremely important for the analysis of P–T-conditions of different rock and mineral stability.

It is clear from Eqs. (6.4.15) and (6.4.16) that

$$\frac{dP/dT}{P/T} = \frac{T/z}{dT/dz}. \tag{6.4.23}$$

Equation (6.4.23) shows that the slope (dP/dT) and the ratio P/T depend on the average geothermal gradient (T/z) and the instant geothermal gradient (dT/dz). But as was shown above (see Eq. 6.4.14) the value of the geothermal gradient reduces with depth. Hence the value of the geothermal gradient at a depth should be lower than that of the average geothermal gradient in the area ($dT/dz < T/z$). This proves that under normal circumstances the value of the slope (dP/dT) should be higher than that for the ratio P/T.

A great number of excellent studies on problems of rock and mineral stability have been conducted in the last few decades. The findings are usually implemented for the development of mineral barometers and thermometers to estimate P–T conditions in different metamorphic regions based on the specific mineral content of the metamorphic rocks. In many cases when we do not have clear cut information on P–T conditions during the different periods of geological evolution of a region, this is the only way to estimate these conditions. Analysis of published data on the thermodynamic conditions for the formation of such metamorphic rocks as eclogites, blueschists, granulites and amphibolites collected from hundreds of publications along with calculated values of the ratio P/T are presented in Table 6.3.

The results of Table 6.3 show that P/T ratio can be used along with the P and T values as a parameter to characterize some specific thermodynamic conditions for high-grade metamorphic rocks.

It is obvious that to analyze the conditions of stability of rocks and minerals the values of such parameters as volume thermal expansion (α) and compressibility (β) should be measured and such parameters as the ratio P/T and the slope (dP/dT) should be calculated. Data on these measured and calculated parameters are presented in Tables 6.6, 6.7, 6.8, 6.9, 6.10, 6.11, 6.12 and 6.13.

Table 6.6 *P–T* conditions of garnet stability

Mineral	Temperature, K	Pressure, GPa	*P/T*, MPa/K	Δ*P*/Δ*T*, MPa/K	References
Pyrope					
To majorite	2,273	19.0	9.5	–	Heinemann et al. (1997)
To ilmenite	1,273	20.0–26.0	20.0–26.0	–	Akaogi et al. (2002)
Almandine					
+sillimanite	1,153–1,293	0.52–0.88	0.60–0.85	2.45	Bohlen et al. (1986)
+Rutile	1,023–1,373	1.15–1.59	1.445–1.53	1.257	Bohlen et al. (1983)
+oxygen	923–1,173	2.15–2.85	3.167–3.308	2.80	Harlov and Newton (1992)
Grossular					
+Rutile	1,073–1,373	1.06–1.44	13.00–13.44	1.20	Bohlen and Liotta (1986)

Table 6.7 *P–T* conditions of coesite stability

Temperature, K	Pressure, GPa	*P/T*, MPa/K	Δ*P*/Δ*T*, MPa/K	References
623–1,273	2.46–2.97	2.970–7.029	0.686–0.815	Bohlen and Boettcher (1982)
773–1,473	2.74–3.24	2.70–5.48	0.714	Bose and Ganguly (1995)
1,073–1,373	3.05–3.50	3.18–3.94	1.17	Huang and Wylley (1975)
1,673	3.75	2.679	–	Johannes et al. (1971)
973–1,023	2.75–2.95	3.47–3.929	1.333	Smith (1984)
873–1,173	2.65–2.95	3.278–4.417	1.00	Smith and Lappin (1989)

Table 6.8 *P–T* conditions of some eclogite stability

Additional mineral(s)	*T*, K	*P*, GPa	*P/T*, MPa/K	Δ*P*/Δ*T*, MPa/K	References
+coesite	933 ± 40	3.0	4.545	–	Banno et al. 2000
+coesite	1,025–1,245	3.6–4.2	3.879–4.321	13.636	Gilotti and Ravna 2001
+coesite	1,033–1,243	4.0–6.5	5.263–6.701	11.905	Zhang et al. 2000
+kyanite	1,099	2.5	3.027	–	Gilotti and Ravna 2001
+kyanite	1,023	1.6	2.13	–	Manning and Bohlen 1991
+kyanite	1,073	3.4	4.25	–	Nakamura and Banno 1997
+kyanite +coesite	1,093	3.0–3.9	4.024–4.451	–	Terry et al. 2000
+kyanite +coesite	1,143	2.9	3.333	–	Schmädicke and Müller 2000

Table 6.9 *P–T* conditions of kyanite stability at their reverse to sillimanite and corundum

Mineral	*T*, K	*P*, GPa	*P/T*, MPa/K	$\Delta P/\Delta T$, MPa/K	References
To sillimanite	873–1,273	0.60–1.46	1.041–1.445	2.05	Bohlen et al. (1991)
To corundum	1,073–1,123	0.60–1.15	0.810–1.03	2.00	Harlov and Newton (1993)
To corundum	1,273–2,273	1.40–1.75	14.00–8.75	3.50	Schmidt et al. (1997)

Table 6.10 *P–T*conditions of albite stability

Mineral	*T*, K	*P*, GPa	*P/T*, MPa/K	$\Delta P/\Delta T$, MPa/K	References
+nepheline	1,073	1.4	1.75	–	Gasparik (1985)
	873–1,473	1.6–3.3	2.583–2.75	2.625	Holland (1980)
	1,073–1,373	2.08–3.10	2.75–2.82	3.00	Huang and Wylley (1975)
	873	1.63	2.717	–	Johannes et al., (1971)
	873–1,173	1.67–2.48	2.70–2.808	2.58	Liu and Bohlen (1995)
	873–1,073	1.71–2.18	2.613–3.000	1.90	Newton and Kennedy (1968)
	700–1,073	1.33–1.61	1.90–2.03	2.90	Newton and Kennedy (1968)
+nepheline	1,373–1,498	2.10–2.35	1.836–1.982	1.304	Windom and Unger (1988)
+ forsterite	1,148–1,473	1.60–2.10	1.75–1.803	1.60	Windom and Unger (1988)

Table 6.11 The volume thermal expansion α for some minerals

Mineral	Temperature interval, K	The volume thermal expansion, 10^{-5} 1/K	References
High Albite	297–1,378	2.68	Prewitt et al. (1976)
Plagioclase	293–1,273	0.89–1.54	Skinner (1966)
Plagioclase	673–1,073	1.2–3.3	Skinner (1966)
Almandine	294–1,044	1.58	Skinner (1966)
Grossularite	292–9,80	1.64	Skinner (1966)
Grossular	–	2.78	Pavese et al. (2001)
Pyrope	283–1,031	1.99	Skinner (1966)
Natural garnet	298–1,000	2.36	Suzuki and Anderson (1983)
Wüstite	293–873	3.39	Skinner (1966)
Magnetite	293–843	2.06	Skinner (1966)
Clinopyroxenes	673–1,073	3.5–3.8	Skinner (1966)
Omphacite	–	2.2	Nishihara et al. (2003)

The thermodynamic method described above can be used for the analysis of *P–T* conditions and some of their applications to the problem of rock and mineral stability. For example, the average value for the density σ of the continental crust is 2,850 kg/m^3 and the average value for the geothermal gradient *G* in the upper

Table 6.12 The volume thermal expansion α for plagioclase for different temperatures, after Clark (1966)

Composition	The volume thermal expansion, 10^{-5} 1/K, for temperature		
	293 K	673 K	1073 K
$Ab_{99}An_1$	18	27	33
$Ab_{77}An_{23}$	12	19	24
$Ab_{56}An_{44}$	13	17	20
Ab_5An_{95}	12	12	20

Here Ab and An are albite and anorthite, respectively

Table 6.13 The compressibility β of some minerals

Mineral	Compressibility, 10^{-5} 1/MPa	References
Omphacite	0.79	Nishihara et al. (2003)
Grossular	0.59	Pavese et al. (2001)
Low Albite	1.85	Downs et al. (1999)
Magnetite	0.62	Hearmon (1984)
Wüstite	0.65	Jackson and Khanna (1990)
Pyrope	0.58	O'Neill et al. (1991)
Grossular	0.59	Bass (1989)
Alm_{74} $Py_{20}Gr_3Sp_3$	0.56	Soga (1967)
Clinopyroxenes	0.88–1.05	Alexandrov et al. (1964)
Albite	1.76	Hearmon (1979)
Anorthite	1.19	Hearmon (1984)

Here Alm, Py, Gr and Sp are almandine, pyrope, grossular and spessartine respectively

crust is $\sim$30 K/km. Using these values, the estimated slope for the upper crust is 28.5 MPa/30 K = 0.95 MPa/K. If we accept $G = 10$ K/km for the lower crust geothermal gradient, the average slope will be $\sim$2.85 MPa/K. In contrast, Eq. (6.4.15) shows the relationships between the *P/T* ratio and the average geothermal gradient *T/z*. Using the average values of the *P/T* ratio for high-grade metamorphic rocks from Table 6.3, we obtain 9.1, 11.5, 28.6, and 24.1 K/km respectively for the necessary average geothermal gradient crust conditions for formation of eclogites, blueschists, granulites, and amphibolites. Average values for the geothermal gradient such as 9.1 and 11.5 K/km are unknown for the crust. Nevertheless, such average geothermal gradients as 28.6 and 24.1 K/km are possible mainly in the upper crust.

Equation (6.4.18) can also be used to estimate the geothermal gradient at a depth with a known slope of lithostatic pressure by temperature. For example, for lower crust areas with a slope of 4.0 MPa/K, the geothermal gradient would be $\sim$7 K/km, and for a slope of about 5.0 MPa/K the *G* would be $\sim$5.5 K/km.

Estimates of the critical geothermal gradient for the crust and upper mantle conditions (Christensen 1979) yielded values between 10 and 14 K/km at pressures of 0.5–0.8 GPa, and at higher pressures (1.0–3.0 GPa) the estimated critical geothermal gradient was 6.3 K/km for dunite and eclogite.

Unfortunately almost all definitions of the volume thermal expansion α and the compressibility β have been obtained for different mineral samples. Data from Table 6.12 clearly shows the influence of temperature on the value of α. But the values of α and β from Tables 6.11 and 6.13 can be used for rough estimates of the ratio α/β for some minerals. For example the values of ratio α/β calculated using the (Clark 1966) data for plagioclases with different contents of albite (Ab) and anorthite (An) are presented in Table 6.14.

Rough estimates of ratio α/β values for some minerals using data from Tables 6.11 and 6.13 are presented in Table 6.15.

Analysis of values for α and β as well as estimates of the ratio α/β have been calculated for water (Kerimov et al. 1980; Pilchin 1983) and some rocks (Pilchin 1983; Pilchin and Eppelbaum 2002, 2005). The calculated ratio α/β for such rocks as granite, diabase and gabbro are respectively 1.333, 1.35 and 1.295 MPa/K. Similar ratios for limestone and sandstone yielded values of 1.393–1.61 and 0.621–1.25 MPa/K, respectively.

The above analysis of such parameters as the volume thermal expansion α and compressibility β and calculation the α/β ratio shows that for specific thermodynamic conditions (depth, pressure, and temperature) this ratio characterizes the normal conditions for a rock or mineral. This condition should correspond to Eq. (6.4.21). Thus any deviation in value of the slope (dP/dT) from its value for normal thermodynamic conditions is indicative of the presence of some external force (extensional or compressive). This deviation could be the result of both deviations of temperature and pressure from their normal values. The deviation of the slope (dP/dT) from its value for normal thermodynamic conditions can thus be used to calculate the kind of force (extensional or compressive) at work (Pilchin 1985a; Pilchin and Eppelbaum 2005). On the other hand, it shows that both extreme deviations of temperature and pressure can create the conditions where a rock or mineral becomes unstable.

An obviously high grade mineral such as almandine is unstable under P–T conditions in the range of 0.52–0.88 GPa and 1,153–1,293 K (Bohlen et al. 1986) with a P/T ratio of only 0.60–0.85 MPa/K and the slope $dP/dT = 2.45$ MPa/K (see Table 6.6). The data in Table 6.6 show that both almandine and grossular become unstable under high temperature with moderate pressure. Similar results for garnets under high temperature conditions were also found by Bohlen et al. (1983) for the transition between garnets and anorthite (P/T ratio in the range of 0.62–0.667 MPa/K and a slope of $dP/dT = 0.767$ MPa/K), and Perkins (1983) for garnet stability in different reactions (P/T ratio in the range of 1.16–1.722 MPa/K and a slope dP/dT in the range from 0.20 to 1.333 MPa/K) in temperatures in the range of 1,273–1,573 K. A simple analysis of the data presented in Tables 6.6, 6.8 and 6.9 shows that the values needed for the P/T ratio are in obvious conflict, because it is much higher for eclogites than for garnets and kyanite. Comparison of the data from Tables 6.3, 6.6, and 6.15 shows that values of the P/T ratio for eclogites (see Table 6.3) are much higher than those defined by Eq. (2.7.5) using the data from Table 6.15. This points to the obvious involvement of external (tectonic) force during eclogite formation. In contrast, the P–T-conditions of coesite stability

Table 6.14 Values of the α/β ratio calculated using data from Clark (1966)

Composition	Ratio α/β, MPa/K	
	673 K	1,073 K
$Ab_{99}An_1$	2.214	2.707
$Ab_{77}An_{23}$	1.557	1.967
$Ab_{56}An_{44}$	1.393	1.639
Ab_5An_{95}	0.984	1.639

Table 6.15 Values of the α/β ratio estimated for some minerals

Mineral	Ratio α/β, MPa/K
Omphacite	2.785
Grossular	2.780 and 4.712
Almandine	2.821
Pyrope	3.431
Wüstite	5.215
Magnetite	3.323
Clinopyroxenes	3.333–4.318
Albite	1.523

(see Table 6.7) show that this UHP mineral requires extremely high values for *P/T* (2.679–7.029 MPa/K) and very low values for the slope *dP/dT* (0.686–1.333 MPa/K). Other studies have also attributed a very low value of 1.0 MPa/K to the slope *dP/dT* for coesite (Hemingway et al. 1998). Nevertheless, even the finding that under normal circumstances the value of the slope (*dP/dT*) should be higher than that for the *P/T* ratio (see above), conflicts with the data for coesite (see Table 6.7). These data show that the conditions of coesite stability have extremely high values for the *P/T* ratio and very low values for the slope (*dP/dT*). In case of coesite, the value of $(dP/dT)/(P/T)$ is about 0.12–0.38, but the value of $(T/z)/(dT/dz)$ should be greater than 1. This shows that lithostatic pressure alone cannot form coesite, and that an extremely strong external tectonic force is necessary to form coesite.

However, the presence of such enormous values for the slope (dP/dT) as 11.905 MPa/K and 13.636 MPa/K (see Table 6.8) requires corresponding values for the geothermal gradient in the layer: about 2.4–2.8 K/km and 2.1–2.4 K/km. Extremely high values for *P/T* (4.098–5.303 MPa/K) and the slope dP/dT (20.0 MPa/K) were estimated for UHP marble and eclogite in the Su–Lu UHP terrane of Eastern China (Kato et al. 1997). The corresponding value to this slope's geothermal gradient should be about 1.4–1.7 K/km. Very high values of *P/T* (7.86–15.00 MPa/K) were estimated for the synthesis of lawsonite (Okamoto and Maruyama 1999), which requires geothermal gradients of about 2.0–4.2 K/km. Such low geothermal gradient values cannot be accurate even for lower crust and upper mantle conditions. These facts clearly point to the presence of a giant external force during metamorphism. By contrast, there is evidence for the presence of negative values for the slope *dP/dT* (−1.0 MPa/K) with extremely high

values for the P/T ratio (3.393–4.545 MPa/K) for conditions of paragonite = jadeite + kyanite + water transfer (Holland 1979). This situation also could not have occurred without the presence of a strong external force. Analysis of the available data shows that those sources of external compressive force were of tectonic origin alone.

The minimum pressure–temperature pairs for the creation of ultra-high pressure (UHP) metamorphic conditions were discussed in Carswell et al. (1999) and Carswell and Zhang (1999). These pairs are 2.63 GPa at 873 K ($P/T = 4.383$ MPa/K), and 2.73 GPa at 973 K ($P/T = 3.9$ MPa/K) with a very low slope $dP/dT = 1.0$ MPa/K (Carswell et al. 1999). But these values are significantly higher than those for coesite stability (see Table 6.7). The significant difference between the P/T ratio and the slope dP/dT shows that formation of such UHP metamorphic rocks requires the presence of a very strong external force.

The analysis of albite stability (see Table 6.10) shows that values of the P/T ratio and the slope dP/dT vary considerably (1.75–3.00 MPa/K and 1.304–3.00 MPa/K, respectively). The minimal values for P/T were found for cases when nepheline was present in the reaction of the albite breakdown. However, all studies show that the zone of albite stability requires significantly higher pressure for a similar temperature compared to that of anorthite (Holland 1980). Such a wide range of P/T and dP/dT values for stability can be explained by differences in the conditions required for the stability of albite under high-temperature compared to high-pressure conditions. Numerous studies have indicated that the P/T for high temperature conditions varies within an interval of 1.36–2.40 MPa/K (Green and Ringwood 1967; Pugin and Khitarov 1978; Ito and Kennedy 1971; Green and Ringwood 1972; Green 1967). On the other hand the stability of albite under high pressure conditions is characterized by P/T values in the range of 2.613–3.000 MPa/K (Johannes et al. 1971; Liu and Bohlen 1995; Newton and Kennedy 1968). This means that there is some limit to the deviation from the equilibrium condition for both temperature and pressure. Since the equation for equilibrium Eq. (2.7.5) represents the potential maximum for pressure (without any unloading of pressure), any deviation in high pressure from the equilibrium condition is likely to be caused by an external (tectonic) force, which creates conditions for the mineral's breakdown.

From all of the above it is clear that acceptance of pressure alone as the lithostatic pressure can lead to significant errors in the calculated value of the depth of rock or mineral formation.

Unfortunately, most authors ignore the role of tangential forces as sources of ultrahigh pressure. However, previous studies (Pilchin 1986; Pilchin and Eppelbaum 2005) show that the value of horizontal pressure can be significant when analyzing the P–T conditions and metamorphic grades at different depths in different regions. For example, the horizontal force applied to a tectonic block/plate will create pressure which should be fully or partially added to the lithostatic pressure formed by the force of gravity. Hence in all cases overpressure will be created and added to 0 for the surface layers and 1.0–1.2 GPa for the Moho of continental crust. Thus in the case of underthrusting of the ocean layer under the

continental crust, the resulting pressure will be the combination of lithostatic pressure below the continental Moho and the pressure created by the force applied to the continental block below the Moho discontinuity. In this case greater pressures could be created at lower depths than for lithostatic pressure alone, because they are just partly composed of lithostatic pressure. Crucially, although any overpressure in a vertical direction immediately creates isostatic or antiisostatic movements, this will not necessarily occur in the case of horizontal pressure, which in some cases can be greater than the lithostatic pressure.

As was mentioned above, one of main markers of the presence of a water-ocean is the formation of carbonate sediments. But no significant amounts of sediments and particularly carbonate sediments were formed during the period from $\sim$3.9 to 3.26 Ga (see Sect. 6.2). This would have been possible in only a few cases such as: (1) the absence of a water-ocean during this period of time; (2) absence of Ca, Mg, Fe and/or CO_2 in the water-ocean and CO_2 in the atmosphere; (3) decomposition of carbonates after their formation. The second possibility is clearly not the case because it is known that the early Earth's atmosphere was CO_2-rich (see Sects. 2.7 and 6.2) and the re-distribution of the CO_2-layer of the atmosphere was a key issue during the early Earth's evolution. It was shown in Sect. 6.2 that during this period the water-ocean probably did not exist and started to form only at the end of the Early Archean; nevertheless, let us analyze the possibility that water-ocean did exist, and that carbonate sediments were formed, but they were decomposed by temperature or other processes. The results of experiments on the stability of carbonates are presented in Table 6.16.

Pilchin and Eppelbaum (2009) showed that the carbonate decomposition temperatures presented in various studies should be viewed as the maximal values of the decomposition temperature, since all of these works considered a fast and quickly visible decomposition of carbonates. For example in a study by Koziol (2001) only the decomposition of siderite, magnesite, and siderite-magnesite carbonates within 5–15 min periods at a temperature of 743 K was considered.

It is clear from Table 6.16 that none of the carbonates would survive in the conditions within the magma-ocean and any carbonate rock must have formed after solidification of the magma-ocean.

By contrast, the temperature of carbonate rock formation is significantly lower than temperature of their decomposition. Kent et al. (2001) demonstrated that carbonates on Mars were formed at no higher than 673 K and most probably less than 473 K. Experimental results reported in Stoessell et al. (1987) show that between 373 and 473 K, the mode of calcite formation changed from direct precipitation into void space produced by the dissolving of dolomite into a pseudomorphic replacement of dolomite, and that dedolomitization textures formed in these experiments are similar to those found in the rock record. Bech et al. (2001) estimated the temperature of the formation of carbonates is 375 K. Perry et al. (1985) reported that with increases in the hydrogenation temperature, the temperature of carbonate formation could increase to 653–713 K. It is obvious that carbonate formation temperatures are much lower than the temperatures of their decomposition. Hence if carbonates were formed during the early periods of the

Table 6.16 Temperature conditions for the stability of carbonates

Carbonate	Temperature of decomposition, K	References
Limestone	973	Ninomiya et al. (2004)
Limestone	1,098–1,145	Mattisson and Lyngfelt (1999)
Limestone	1,053	Trikkel and Kuusik (2003)
Calcite	923–1173	Misra et al. (1993)
Calcite	1,073–1,193	Kubota et al. (2000)
Calcite	993–1,093	Sharp et al. (2003)
Calcite	1,158	Birch et al. (1942)
Calcite	by 773	Scott et al. (2004)
Dolomite	873–973	Sharp et al. (2003)
Dolomite	773–873	Sharma and Clayton (1965)
Dolomite	773	Birch et al. (1942)
Magnesite	646	Birch et al. (1942)
Siderite	653–923	Koziol (2004)
Siderite	723–773	Sharp et al. (2003)
K_2CO_3	1,173	Misra et al. (1993)
Na_2CO_3	1,124	Bird et al. (1999)

Table 6.17 Temperature conditions for the decomposition and formation of pyrite

Process	Temperature, K	References
Decomposition of pyrite	523–1,016	Lambert et al. (1998)
Decomposition of pyrite	673–863	Hong and Fegley (1997)
Decomposition of pyrite	930	Conard et al. (1980)
Decomposition of pyrite	~740	Seiff et al. (1986)
Formation of pyrite	601 and > 743	Marschik and Fontboté (2001)
Formation of pyrite	up to 1,015 K	Brostigen and Kjekshus (1969)
Formation of pyrite	653–773	Grapes and Challis (1999)
Formation of pyrite	875	Speight (2005)
Pyrite formation in gold deposits	~623	Gaboury et al. (2000)
Pyrite formation in gold deposits	563–653	Yao et al. (1999)
Pyrite formation in gold deposits	623	Hannington et al. (1991)
Pyrite formation in gold deposits	~723	Passier et al. (2001)
Pyrite formation in gold deposits	~773	Lindblom et al. (1996)

Earth's evolution, they could have survived if they had much higher stability and decomposition temperatures. The absence of carbonates shows that they were not formed, and the water-ocean most likely was not formed until the end of the Early Archean.

One of the compounds considered to be a marker of anoxic atmosphere environments in the Early and Middle Precambrian is pyrite. In Table 6.17 the results of experiments on temperature conditions of decomposition and formation of pyrite are presented.

A number of studies have also reported that the formation of pyrite in gold deposits took place at temperatures in the range of 548 K to 623 K (Fripp 1976; Groves et al. 1987; Phillips et al. 1984). Experiments show that pyrite decomposes at temperatures of 743 K in a CO_2 atmosphere (Golden et al. 2004). However, pyrite could not be produced experimentally at temperatures in the range of 298 and 373 K (Luther 1991). Studies on the temperature conditions for the decomposition and formation of pyrite clearly show that pyrite could not have existed at the time of the magma-ocean and was formed later during the cooling of rock layers after the solidification of the magma-ocean.

6.5 Dynamic Interactions of the Asthenosphere and the Lithosphere

The asthenosphere is the next layer of the Earth below the lithosphere and shares the same lithosphere–asthenosphere boundary (LAB). Both the lithosphere and the asthenosphere are characterized by different rheology and physical, particularly mechanical, properties. The asthenosphere is thought to be either in a plastic condition or partially molten. The LAB is the most extensive and active plate boundary on the planet. The LAB is extremely important for plate tectonics because it separates the non-convecting subcontinental lithospheric mantle (SCLM) from the convecting asthenosphere (O'Reilly and Griffin 2010). The position and primary physical characteristics of both the lithosphere and the asthenosphere call for investigative methods pertaining to seismic, thermal and gravitational modes of inquiry, as well as analysis of the mineral composition of xenoliths and the conditions of their stability. In the case of the asthenosphere, magnetotelluric methods can also be used for imaging an "electrical asthenosphere" layer. The seismic LAB beneath cratons is typically regarded as the base of a high-velocity mantle lid.

Based on the analysis of global seismic data, Rychert and Shearer (2009) came to the conclusion that the LAB ranges from 95 ± 4 km beneath the Precambrian shields and platforms to 81 ± 2 km beneath tectonically altered regions and 70 ± 4 km at oceanic island stations. These data are in agreement with data reported by Kumar et al. (2005) showing that the thickness of lithosphere (depth of the LAB) is: 70–120 km under Greenland, 40–60 km below Jan Mayen and 50–110 km below Iceland. They also stated that the thickness of the lithosphere is close to zero at mid-ocean ridges, about 200 km beneath stable cratons, with a global average about 80–100 km. Thybo and Perchuc (1997) estimated that a global zone of reduced velocity underlies continental regions at about 100 km in depth. O'Reilly and Griffin (2010) also estimated a depth of the LAB in young continental regions of about 80–100 km and suggested a value for a number of cratons the range of ~ 175 to >210 km.

Seismic methods are among the most powerful and precise methods of determining the thickness of the lithosphere, because they can pinpoint the position of the LVZ which is usually associated with the asthenosphere (Gutenberg 1959; Lehrnann 1961; Anderson 1989, 2007); Schubert et al. 2001. The joint evolution of the asthenosphere and the lithosphere started with the solidification of the magma-ocean. The solidified part of the magma-ocean became the lithosphere and solidified, and part of the still molten magma-ocean became the early asthenosphere. The lithosphere continues to grow at the expense of the asthenosphere, because the cooling of Earth always leads to increases in the thickness of the lithosphere and a decrease in the thickness of the asthenosphere. Continuous cooling of the Earth has led to a reduction in temperature in its outer layers and the conversion of molten and partially molten parts of the asthenosphere which first become solid and then rigid. This process will continue until the whole asthenosphere solidifies and then becomes rigid and at that point in time only the lithosphere will cover the entire Earth.

Pilchin and Eppelbaum (2009) showed that in some continental regions, mostly in cratonic areas, the thickness of the lithosphere reaches depths of about 350–400 km and in many cases there are no signs of the presence of the asthenosphere. Lerner-Lam and Jordan (1983) suggested that the tectonically stable part of northern Eurasia, including the Siberian platform, has a thick seismic lithosphere extending to a depth of about 400 km. Artemieva and Mooney (2001) found the thermal lithosphere beneath the Siberian platform to be about 350 km thick. A high velocity layer traced down to about 300–400 km and identified as seismic lithosphere was found beneath the East-European platform (Shumlyanska et al. 2006). For different parts of the Ukrainian Shield the lithosphere thickness is 350–400 km beneath the easternmost Pre-Azovian block, about 350 km beneath the Ros-Tikich block and about 400 km beneath the Volyn-Podolie block (Shumlyanska et al. 2006). Other examinations based on seismic data also show regions of anomalously high velocity in the mantle underlying the Archean cratons at depths of 300–400 km (Rudnick 1997; Gung et al. 2003). Geophysical studies of Northern Eurasia have failed to reveal a well-defined and continuous asthenosphere (Pavlenkova 1995), in many cases the asthenosphere cannot be traced from the seismic data (Pavlenkova and Pavlenkova 2003), and the asthenosphere-lithosphere boundary in numerous cases has not been differentiated from velocity cross-sections (Pavlenkova 2006).

Let us discuss some features which could cause the formation of the LVZ in the upper mantle. Schubert et al. (2001) stated that there are two reasonable explanations for the LVZ: (1) steep thermal gradient and (2) small concentrations of partial melt, distributed through the crystalline matrix in the form of intergranular films and small droplets. Anderson (1995) pointed out that minor components (hydrous phases, vapor, melt) can reduce seismic velocities appreciably. Anderson (2007) argued that partial melting is still required to explain the regions of very low velocity, and that the LVZ is undoubtedly a region of high thermal gradient. Eggler (1976) claimed that in a CO_2-bearing oceanic mantle, the LVZ can be explained by the sharp decrease in the peridotite solidus temperature at a depth of

about 90 km causing melting, and that such conditions could be found in continental areas at depths greater than 120 km. Mao et al. (2010) reported results of research showing that hydrous forsterite has velocity crossovers at ~3–4 GPa resulting in higher hydrous forsterite velocities at pressures corresponding to depths below ~120 km than in anhydrous forsterite. Song et al. (1996) reported results of research showing that v_p in olivine for conditions with a continental and an oceanic geothermal gradient reaches a maximum at pressures 3.8 and 3.6 GPa respectively. Their data also show that v_p reaches a maximum in clino- and ortho-pyroxenes at a pressure of 4.0 GPa for the continental geothermal gradient and at a pressure of 4.0 and 3.8 GPa in clino- and ortho-pyroxenes respectively for the oceanic geothermal gradient.

It was shown in Sects. 4.2 that at depths of about 4 GPa, the effect of compressibility is greater than the effect of thermal expansion. Such a situation could impede the formation of the LVZ at depths of about 110 km and greater.

Pilchin and Eppelbaum (2009) noted that for the formation the LVZ, the change in velocity should satisfy the following condition:

$$dv < 0. \tag{6.5.1}$$

Applying this condition, Eq. (4.4.11) becomes:

$$\left(\frac{dv}{dT}\right)_P dT + \left(\frac{dv}{dp}\right)_T dp < 0. \tag{6.5.2}$$

Inequality Eq. (6.5.2) shows that velocity in different rocks and minerals can decrease under specific *P–T* conditions. This means that the presence of melt in the asthenosphere is not necessary for the formation of a LVZ.

It is known that an increase in the iron content of rocks also reduces their melting point (Pilchin and Eppelbaum 2006). Thus with increasing depth within the upper mantle, the melting point of rocks should decrease, because the iron content in rocks increases with depth as a result of stratification of the magma-ocean. This leads to the possibility that the formation of partial melt should increase with depth below the forsterite layer. In other words, with increased lithospheric thickness, the iron content of erupting magmas should increase. At the same time it is obvious that the thickness of the lithosphere increases in general with increases in age of the lithosphere and those younger magmatic rocks should be richer in iron than older rocks, because they erupted from greater depths. To confirm these assumptions an analysis of the iron content in magmas of the Large Igneous Provinces (LIP) was carried out. The results are presented in Table 6.18.

It is clear from Table 6.18 that its data completely support the above statements that the iron content in younger magmas is higher than in old ones. Table 6.19 also shows that the rate of magmatism increased from the Archean to the Mesozoic and then declined in the Cenozoic. But although magmas in LIP, which most likely formed in the asthenosphere, generally could reach the surface without forming an intermediate chamber, because of their giant volumes, magmas erupted outside of

Table 6.18 Iron content in continental mafic igneous rocks of different ages

Age	Iron content of regular magmas as FeO total	Iron content of Fe-rich magmas as FeO total	Rate of magmatism in LIP, km^2/100 M.y.
Archean	<10.00–11.00[a] (7.57–12.72)	13.33–17.73	136,514[b] (34,129)
Proterozoic	11.00–12.00[a] (8.06–14.60)	13.58–21.10	961,578
Paleozoic	11.00–12.00[a] (8.42–16.13)	13.41–23.30	3,014,130
Mesozoic	>12.00[a] (9.17–15.98)	16.03–25.92	12,530,055
Cenozoic	12.25–14.00[a] (9.25–15.90)	16.00–23.70	8,098,462

[a] Estimated average iron content
[b] Since certain LIP in the Archean are believed to have started forming from about 3.0 Ga the rate of magmatism is presented for the period from 3.0 Ga to 2.5 Ga and in brackets the rate is presented for the whole Archean eon

Table 6.19 Estimated melting point of olivine as a function of forsterite content

Fo#	Melting point (in K) at 4 GPa
Fo_{100}	2,339
Fo_{90}	2,271
Fo_{80}	2,204
Fo_{70}	2,136
Fo_{60}	2,069
Fo_{50}	2,002
Fo_{40}	1,934
Fo_{30}	1,867
Fo_{20}	1,800
Fo_{10}	1,733
Fo_{0}	1,666

LIP do not contain such huge volumes of magma and in most cases need the formation of intermediate magma chambers within either the lithospheric part of the upper mantle or within the crust. In some cases magma could not reach the surface and would form intrusive structures in which the magmas were always either contaminated with re-melted crustal rocks, or mostly remelted crustal rocks. Depending on the temperature and volume of magmatic rocks rising from the asthenosphere, their interaction would be different and would cause the formation of mostly basaltic (higher portion of rising magma) or either intermediate or felsic magmas (higher portion of re-melted crustal rocks).

It is obvious that all magmatic rocks, whether they reached the surface or not, played a crucial role in formation and evolution of the lithosphere, including its local and regional thermal regime. Condie (2005) stated that main the Precambrian mantle-plume events at 2.7 and 1.9 Ga correlate with maxima in the worldwide production rate of juvenile crust.

Modelling shows two possible scenarios for mantle evolution after the final differentiation of the magma-ocean (Pilchin and Eppelbaum 2008a): (1) a relatively slow solidification of the magma-ocean with the eruption of magmatic rocks

from lower magma layers after adjacent layers above had completed their solidification; (2) a relatively fast solidification of magma-ocean with subsequent reheating, and re-melting and eruption of rocks from different layers. However, the presence of significant amounts of such unique rocks as komatiites which have possibly the highest melting point among magmatic rocks and are characterized by their extremely high content of Mg tends to support the first possibility. In fact, estimates of the melting point of komatiites and the temperature of their formation show that they could have been formed at temperatures as high as about 1,973–2,123 K (Svetov and Smolkin 2003) and about 1,923–2,073 K (Takahashi 1990) during the Archean and at temperatures of about 1,846 K in the Early Proterozoic (Svetov and Smolkin 2003). However, Takahashi (1990) argued that peridotitic komatiites (with a MgO content $\geq$33 wt.%) which are restricted to the oldest cratons were formed only in the Early Archean ($\geq$3.3 Ga) at temperatures $\geq$2,073 K. Given that the maximal referenced temperatures for komatiite formation are very close to the melting point of forsterite (olivine—Fo_{100}), which is 2,163 K at 0.1 MPa and $\sim$2,339 K at 4 GPa, virtually all komatiites were formed and erupted during the Archean (Arndt and Nisbet 1982; Barley et al. 2000; Svetov and Smolkin 2003), and the temperature of komatiite formation and their Mg content were in constant decline during the Archean (Takahashi 1990; Svetov and Smolkin 2003), it is evident that these magmatic rocks developed during the initial cooling of the Earth and were not rocks that had solidified earlier and then re-melted. It is also obvious that such Mg-rich rocks had a very low density to be formed at great depths and they were formed just below the forsterite layer. Their relatively low iron content also points at their formation just below the forsterite layer. It is also evident that the appearance of komatiites on the surface means that the layers above had already solidified and that the early Earth's lithosphere was already in place and its thickness was more likely represented by the upper layer of the Earth from the surface to the forsterite layer at the bottom.

For comparison, the melting points of olivines with varying forsterite content at a pressure of 4 GPa are presented in Table 6.19.

It is clear from Table 6.19 that for nodules of olivine containing forsterite such as Fo_{100}, Fo_{50} or Fo_0 (Fa_{100}) the melt temperature at a pressure of 4 GPa must have been below 2,339, 2,002 or 1,666 K respectively. Since the melting point of dry peridotite at a depth of $\sim$100 km is 1,613 K (Faure and Mensing 2007) and the vapor-saturated peridotite liquidus temperature at a pressure of 3 GPa is 1,573 K (Mysen and Boettcher 1975) it is reasonable to assume that for peridotite composition of the upper mantle, even nodules of olivine of Fo_0 have a chance to survive, but that the likelihood of survival was greater for olivines containing more forsterite. It is also obvious that xenoliths and nodules could most likely have been delivered to the surface when magma reached the surface without forming an intermediate magma chamber, because otherwise these xenoliths and nodules would have been left within the magma chamber.

From all of the above it is clear that most magmas, especially those enriched in iron, were formed within the asthenosphere and they found a way to reach the surface or to some depths within the lithosphere (e.g. in cases of underplating).

These magmatic rocks, along with xenoliths, nodules and phenocrysts delivered by them to the surface and into the lithosphere played a crucial role in the formation and evolution of the lithosphere and particularly the crust.

6.6 Reflecting the Earth's Crust Structure in the Thermal Field

The Earth's crust is the topmost brittle layer of the lithosphere. Its thickness varies in the range of 5–15 km for oceanic crust (in oceanic plateaus the crust can have thicknesses greater than 30 km), 15–30 km for the transitional crust and generally 30–50 km for the continental crust (thicknesses up to 80 km are also reported) (Anderson 1989). Calculated values of the temperature on the Moho discontinuity reported for different regions range from 560 K at a depth of ~40 km for Labrador, Canada (Jaupart and Mareschal 2007) to about 1,473 K at depths of up to 40 km in the Baikal rift zone (Zorin 1981). The calculated values of temperatures on the Moho discontinuity are highly dependent on age, tectonic activity, thermal regime and the thickness of the crust. These values are about: 673–773 K at a depth of ~40 km in Proterozoic crust of Central Australia (Müller and Hillis 2003); 598–701 K at a depth of ~40 km in Archean crust of the Superior and Slave Cratons of Canada (Jaupart and Mareschal 2007); 560–908 K at depths of ~40 km in Proterozoic crust of Canada (Jaupart and Mareschal 2007); 699 K at depths of ~40 km in Paleozoic Appalachians (Jaupart and Mareschal 2007); 773–1,273 K at different depths in Tibet (Klemperer 2006); ~873 K for sedimentary basins (Hatton 2009); 823–1,173 K for different areas of the Indian Shield (Singh and Negi 1982); 1,173 K at depths of ~22.5–30 km in thermally very active Pannonian Basin, Hungary (Bodri 1981); 1,073–1,273 km at depths of 60–75 km beneath the Altiplano, Andes (ANCORP 2003), etc.

The thermal processes taking place in the Earth's crust can be divided into either heat sources or heat sinks. These processes within the crust and its thermal regime depend on crust heat content (heat and temperature distribution), heat radiated from the surface, heat entering the crust from the upper mantle through the Moho discontinuity, heat production by long-lived radioactive isotopes within the crust, heat delivered to the crust by plutonic and volcanic processes, endergonic and exergonic chemical reactions, interaction of the surface with the atmosphere and ocean, heat of the Sun, etc.

The crust is the last layer of the Earth involving the transfer of heat from the inner layers of the Earth and particularly from the mantle to the surface. There are three main kinds of heat transfer: radiation, convection and conduction. Heat radiation is the most effective from an open surface. It is one of the fastest ways of surface cooling and it is the only kind of radiation of heat through space without matter (through a vacuum). Convection is a very effective method of heat transfer by a fluid medium. This kind of heat transfer is a relatively fast way of cooling

based on circulation of cold fluid down and hot fluid up. The most effective media for heat convection are hydrogen, helium, water and any water-rich fluid, since fluids have the highest specific heat capacity that helps them carry more heat. The specific heat capacity of hydrogen, helium and water is 14.30, 5.19 and 4.18 J g^{-1} K^{-1}, respectively. Heat conduction is the slowest kind of heat transfer. It is based on heat conductivity of rocks and requires direct contact between medias transferring heat. But even though heat conduction is the slowest kind of heat transfer it is the main method for transferring heat within the lithosphere, especially in the lithospheric part of the upper mantle, the lower crust, middle crust, and most of upper crust. This relates to the fact that more effective kinds of heat transfer, such as heat radiation and heat convection, have limiting conditions on their operation: heat radiation requires an open surface, and heat convection requires an open system conditions for the free movement of fluids (atmosphere, oceans, open systems of faults and/or fractures, open pore space within sedimentary rocks, etc.). These limitations make heat radiation dominate the Earth's surface, whereas heat convection is seen primarily both on the Earth's surface and mostly within the sedimentary layer of the crust.

It should be noted that mass transfer can transport heat, and in such cases as volcanic and plutonic magmatic activities, it can play significant role in local transport of heat energy. Among the mass transfer processes capable of transferring significant amounts of heat, the most important are subduction related to plunging a cold slab into the hot deep layers of mantle, obduction which is related to the transfer of a hot slab onto the surface, block uplift, block immersion, magma rise for the formation of both plutonic and volcanic magmatic rocks, thermal springs, rock exhumation, etc.

For example, ground waters (see Sect. 4.1) can be involved in both heat convection, when an aquifer is trapped by cap rocks and surrounding rocks and it can circulate within the closed volume, and heat transport by mass-transfer, when an aquifer is open for water flow on both sides as is the case in recharge zones and discharge zones. Convection of thermal waters within a trapped aquifer transfers heat mostly from bottom of the layer of these waters to its top. By contrast, in the case of mass transfer, ground waters can remove heat from a layer (by cooling it) in any direction. For example, cold meteoric water entering an aquifer in its recharge zone definitely has a much lower temperature than the temperature of the rock layer through which the water of the aquifer is flowing. This creates conditions where the exchange of heat between the layer and water moving through it will lead to the heating of cold water and the cooling of the rocks of the layer. This process leads to a situation where the cold water that enters the aquifer in the recharge zone is heated during its flow through the aquifer and exits it in the discharge zone with a higher temperature because it has removed a significant amount of heat energy from the layer. It is clear that the temperature of water on discharge and the heat it transports depends on the discharge rate of the water. In fact, if the discharge rate is high, the temperature of water cannot be as high, but the mass (or volume) of the water moving through the aquifer is high. In contrast, in the case of a low discharge rate, the temperature of the discharging water is

higher (slow flow through the aquifer lets water absorb more heat) but the mass (volume) of the transferred water is smaller. Such heat transport is extremely important in regions of young magmatism where heat exchanges between flow--through aquifer water heats to such high temperatures that it forms hot springs, geysers and fumaroles (see Sect. 4.1).

The Earth's crust is the only layer that deals fully with all the main kinds of heat and mass transfer. Only the crust has an open surface for heat radiation and heat convection within the atmosphere and ocean. Only the crust has sedimentary layer for heat convection by fluids within sediments. Only the crust has direct contact with such cooling agents as the atmosphere and ocean. The crust also has the highest geothermal gradient, which declines with depth; this makes heat conduction a very important kind of heat transfer. Only the crust has open faults and fracture systems for fluid and heat convection. The crust and its surface are the final destinations for both intrusive and effusive magmatic rocks. The crust, along with oceans and the atmosphere, is the final destination of heat transferred from great depths before its radiation into cosmic space. But the uppermost crustal layers along with oceans and the atmosphere are the only media that receive the Sun's radiation. This makes the crust, the ocean and the atmosphere the media of active heat exchange with the cosmos.

Different kinds of heat transfer played different roles during different periods of the Earth's evolution. During the Hadean and Early Archean the most effective kinds of heat transfer were heat radiation from the surface of magma-ocean in the Hadean and from its solidified hot surface in the Hadean–Early Archean, convection of heat within the thick early Earth's atmosphere, radiation of heat by hot thick atmosphere, and convection within layers of the magma-ocean. Nevertheless, heat conduction did not play a significant role at that time because within the magma-ocean the geothermal gradient was close to its adiabatic value (about 0.3 K km^{-1}; Clauser 2009) and during the solidification of the magma-ocean the geothermal gradient still so low that could not support significant values of heat flow density (HFD).

During the Earth's evolution the impact of different kinds of heat transfer and mass transfer changed significantly. For example, the subduction process was impossible until a strong lithosphere had formed; heat convection in deep Earth layers had limited impact only within the asthenosphere because of the very high viscosity of rocks; heat radiation by the atmosphere is no longer significant because today's atmosphere is so cold and has a very low density and quantity of matter; the role of mass transfer by magmatic activity, especially in LIP and regions of flood basalt eruptions, rose significantly compared to the Archean and Proterozoic, but reached its maximum in the Mesozoic (see Table 6.18); the constant increase in iron content in magmas with increases in the amounts of erupting magmatic rocks (see Table 6.18) increases the average density of lithospheric blocks that creates more favorable conditions for the subduction process; there were no sedimentary layers before $\sim$3.26 Ga and the convection of fluids within sedimentary layers was impossible at that time but today the thickness of sedimentary layers is maximal and as is the importance of heat convection by

fluids within sedimentary layers; the cooling of the surface and upper layers of crust led to an increase of the geothermal gradient that has increased the role of heat conduction in heat transfer, etc.

The constantly increasing role of heat conduction makes heat transfer within the crust dependent on such thermo-physical properties of rocks as heat conductivity (see Sect. 2.1) and heat production (see Sect. 1.7.4). However, heat conductivity and heat production in turn are affected by the kind of rocks. This makes heat transfer by heat conduction extremely lithology- dependent when heat transfer depends not only on the kind of rocks in the region but also on the thickness of different kinds of rock within the crust. It is clear from rock heat conductivity (see Sect. 2.1) that its value is highest for basic magmatic rocks, a little bit lower for acidic (felsic) magmatic rocks and the lowest for sedimentary rocks. This parameter controls heat transfer within the layers of the crust. Nevertheless, the different amounts of heat generated by heat production are the highest for granitoids (felsic rocks), significantly less for sedimentary rocks, much lower for basic (mafic) rocks and the lowest for ultrabasic rocks. Heat production in granitic rocks, sedimentary rocks and basaltic rocks is 2.39–2.57, 1.39–1.70 and 0.30–0.54 μWm^{-3}, respectively (see Sect. 1.7.4).

It is clear that the temperature on the Moho discontinuity depends on the kind of crust (oceanic, transitional or continental), its thickness, the thickness of its layers, the age of the crust formation, present thermal conditions of the crust, etc., and that different sources of heat, heat sinks, and heat transfer features play a crucial role in the thermal regime of different areas and regions. For example, the HFD from the mantle plays a crucial role in regions with an oceanic crust, which is extremely thin compared to the continental crust, lacks a granitic layer (the most powerful source of heat production), has little sediment (second most powerful source of heat production) but is characterized by the highest average HFD from the surface (see Table 1.10). Similarly, regions of the Archean cratons, which have the thickest granitic and granitoid layers (with the highest heat production) are characterized by the lowest HFD values from the surface that relate to low HFD from the mantle (see Sect. 1.7). At the same time, young sedimentary basins with thickness of sedimentary layers up to 25 km in case of the South Caspian Depression contain very thick layers of clays (the most heat productive sedimentary rocks; Pilchin 1983) are also characterized by a low HFD which can be explained by the enormous amounts of water contained in pores of sediments that can absorb huge amounts of heat without a significant increase of temperature, because water has one of the highest specific heat capacities ($c = 4.18$ J g^{-1} K^{-1}).

One kind of process that almost entirely takes place within the crust (mostly continental crust) and is strongly dependent on thermodynamic conditions is metamorphism. Rocks of different metamorphic facies contain different mineral assemblages according to these minerals' stability under different thermodynamic conditions and range from low temperatures (LT) to high temperatures (HT) and from low pressure (LP) to high pressure (HP). Some rocks of metamorphic facies are formed under medium temperature (MT) and medium pressure (MP). Metamorphic facies can be categorized as Zeolite facies (LP and LT), Prehnite-pumpellyite-facies

(LP and LT), Greenschist facies (MP and MT), Amphibolite-facies (MP and MT-HT), Granulite facies (MP-HP and HT), Blueschist facies (MP-HP and LT), Eclogite facies (HP and MT-HT, the only metamorphic facies which can take place at UHP - ultrahigh pressure), Albite-epidote-hornfels facies (LP and LT-MT), Hornblende-hornfels facies (LP and MT), Pyroxene-hornfels facies (LP and MT-HT), Sanidinite facies (LP and HT) (e.g., Sobolev 1972; Philpotts 1990). The most important and widespread metamorphic facies are amphibolite facies, granulite facies, greenschist facies, eclogite facies and blueschist facies. The main characteristics of these metamorphic rocks are presented in Table 6.3. Pilchin and Eppelbaum (2006, 2009) noted that among the most important metamorphic facies on Earth, the greenschist facies rocks were the earliest to appear. The granulite facies rocks were second to appear followed by amphibolite facies rocks. Rocks of eclogite facies were unknown before the Early Proterozoic and blueschist facies rocks were unknown before Middle Proterozoic. It is clear from Table 6.3 that except for eclogites, all other major metamorphic processes only take place within the crust. Eclogites are essential rocks in kimberlites, which were definitely formed within subcontinental lithospheric mantle. The importance of the presence of rocks of different metamorphic facies in an area or region is related to fact that thermodynamic conditions reveal the temperature conditions and depth of metamorphic rock formation; the age of these rocks helps define the time period in the Earth's evolution when such thermal conditions took place at the specific depth in the region in which these metamorphic rocks are located. Such data can be used for the analysis of thermal evolution of any region; this feature is extremely important for research on thermal evolution of a given region or the Earth as a whole.

The appearance of the main kinds of metamorphic facies rocks in a sequence beginning with greenschist facies followed by granulite facies in second place and amphibolite facies third is understandable from the point of view of the early Earth's evolution. In fact, the solidification of the magma-ocean started from the formation of the forsterite layer (Pilchin and Eppelbaum 2009), when the upper felsic and intermediate layers of the magma-ocean had the lowest melting points among magmatic rocks, and the cooling effect of the thick early Earth's atmosphere. However, only greenschists, granulites and amphibolites could be formed under lithostatic pressure (see Table 6.3) but metamorphic rocks such as eclogites and blueschists require the presence of overpressure.

Within magma-ocean and during the first stages of its solidification only lithostatic pressure was present (Pilchin 2005; Pilchin and Eppelbaum 2012). The formation of metamorphic rocks requiring the presence of overpressure was not possible during the early Earth's evolution for a number of reasons. (1) metamorphic processes can take place only within solid rock layers and they require partial or total solidification of the magma-ocean first; (2) overpressure is not possible in liquid magma (according to Pascal's law); (3) overpressure cannot be formed during a cooling process (unless it is tectonic overpressure which is also impossible within a magma-ocean); (4) overpressure during the solidification of the magma-ocean could only have been reached by increased temperature

(heating) within a solid rock layer; (5) raising the temperature within the solidified part of the magma-ocean was possible only by injections of rising magma, which could rise only through solid rock layers; (6) solid rock layers had to be cold enough not to be re-melted by rising magmas with temperatures higher (basic magmas) or much higher (komatiites and picrites) than the melting point of rocks in the solidified upper layers of the magma-ocean; (7) denser magma cannot rise within less dense magma layers.

Since the formation of overpressure requires conditions which meet the above limitations, it is understandable why eclogite and blueschist metamorphic facies rocks appeared much later than greenschist, granulite and amphibolite facies rocks. For example, it is clear from Table 6.3 that for eclogite metamorphism, the solidified upper layer of the magma-ocean must have been >64 km thick, but for the formation of greenschists, granulites and amphibolites it only needed to be >14–15 km, >28 km and >26–27 km thick, respectively (Pilchin and Eppelbaum 2012). Taking into account that the majority of eclogites were formed under moderate and even low temperature conditions (see Table 6.20), it is obvious that for the formation of eclogite facies rocks, the magma-ocean should have been not only solidified to depths >64 km but also significantly cool down to temperatures conducive to the formation of eclogites. Excluding kimberlites, which are relatively rare geological structures that require much greater solidified magma-ocean layer thicknesses, eclogites are known exclusively in regions characterized by great horizontal displacements and great horizontal pressures (regions of obduction of oceanic lithospheric blocks on continental margins; regions of intensive thrusting, etc.). Our research also shows that the formation of eclogites requires the presence of both the continental and oceanic lithosphere and could have been formed in regions of modern day or ancient transitional zones from continents to oceans (mostly continental margins). It was shown that the presence of significant horizontal pressure (overpressure) could have created conditions favorable to such metamorphic facies as eclogitic and blueschist at much lower depths (Pilchin 2005). Analysis of data on the formation of blueschist facies rocks shows that in almost all cases their formation was associated with areas of formation of ophiolites and serpentinization that generally took place at relatively shallow depths. The issues related to the formation of ophiolites and serpentinization are discussed in more detail in Sect. 6.7.

Since the formation of greenschist facies rocks requires a thinner solidified upper layer of the magma-ocean (>14–15 km; see Table 6.3) it is evident why greenschists were the first to appear (Pilchin and Eppelbaum 2012). The appearance of granulites before amphibolites can be explained by several reasons: (1) both granulites and amphibolites require about the same depth (>28 km for granulites and >26–27 km for amphibolites; see Table 6.3) of solidified upper layer of the magma-ocean; (2) granulites require higher temperatures for their formation than amphibolites, which would be reached first during the cooling of solidified layer of the magma-ocean; (3) amphibolites require the presence of basic rocks for their formation which could only be delivered by basic (mafic) magmas

Table 6.20 Thermodynamic conditions for the formation of eclogites with different origins (after Pilchin 2011)

Eclogites formed at temperatures K, (n)	Average T, K	Average P, GPa	Average P/T [a], MPa/C	Average depth of lithostatic pressure, km	Average geothermal gradient, K/km
$T < 843$, ($n = 279$)	762	1.51	3.10	50	9.8
$843 < T < 993$ ($n = 216$)	910	2.13	3.34	70	9.1
$T > 993$ ($n = 61$)	1075.3	2.77	3.46	90	8.7

[a] Average value P/T was calculated as the average of the P/T ratios

that were not present in uppermost layers of magma-ocean, but granulites could have been formed as felsic granulites, as well as mafic granulites; (4) amphibolites require the presence of water which was in the early Earth's atmosphere but the water-ocean was only formed at the very end of Early Archean (see Sect. 6.2), however the formation of water-ocean is not enough. For the formation of amphibolites water would have needed to penetrate through extremely hot rock layers of the young forming Archean crust to a depth of ~26–27 km; (5) numerous obvious cases of magma underplating causing the formation of granulites from the Early Archean to the Early Proterozoic (see Table 6.4) would have maintained the temperature at depths of ~23–30 km which was too high for the formation of amphibolites.

Thermodynamic conditions for the formation of eclogites with different origins are presented in Table 6.20.

In Table 6.20, the eclogites were divided into three groups: eclogites of low-moderate temperatures ($T < 843$), eclogites of moderate temperatures ($843 < T < 993$) and eclogites of high temperatures ($T > 993$) (Pilchin 2011). The low-moderate temperature eclogites were classified separately because they require the transformation of ferrous iron oxide to ferric iron oxide (TFFI) below a temperature of 843 K. This division is based on the fact that eclogites contain almandine (iron-garnet) which contains iron(II) oxide and aegirine (an essential component of omphfacite) that contains both iron(II) and iron(III) oxides. From the point of view of iron stability iron(II) oxide is unstable at temperatures below 843 K. This was used (Pilchin 2011) to define the category of low-moderate temperature eclogites. The temperature of 993 K was selected (Pilchin 2011) as the temperature dividing moderate eclogites from high temperature eclogites.

Bar graphs depicting the formation of metamorphic rocks of greenschist, granulite and amphibolite facies are presented in Figs. 6.6 and 6.7.

Figure 6.6 shows the distribution (in percent) of greenschist, granulite and amphibolite metamorphic facies in terms of the number of formations during the Precambrian, and Fig. 6.7 displays the distribution (in percent) of the formation of greenschist, granulite and amphibolite metamorphic facies by rate during the Precambrian.

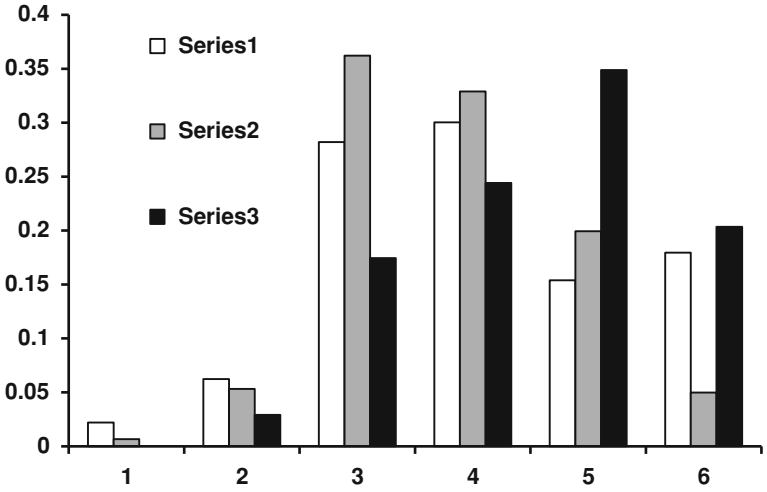

Fig. 6.6 Distribution (in percent of greenschist (Series 1), granulite (Series 2) and amphibolite (Series 3) metamorphic facies by number of formations during the Precambrian: (*1*) Early Archean (*2*) Middle Archean (*3*) Late Archean (*4*) Early Proterozoic (*5*) Middle Proterozoic (*6*) Late Proterozoic

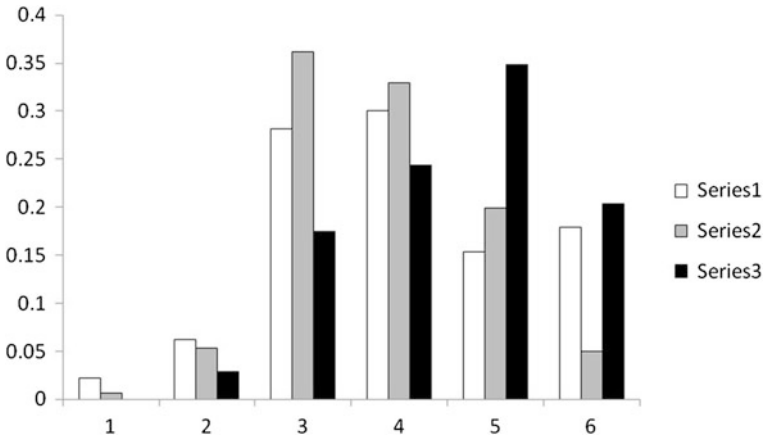

Fig. 6.7 Distribution (in percent) of the formation of greenschist (Series 1), granulite (Series 2) and amphibolite (Series 3) metamorphic facies by rate during the Precambrian: (*1*) Early Archean (*2*) Middle Archean (*3*) Late Archean (*4*) Early Proterozoic (*5*) Middle Proterozoic (*6*) Late Proterozoic

Analysis of Figs. 6.6 and 6.7 shows that the number of greenschist facies rock formations had two maxima during the Precambrian in the Early Proterozoic (absolute maximum by number of formations during the Precambrian) and the Late Proterozoic, but the highest rates of greenschist formations were during the Late

Archean and the Late Proterozoic; for granulite formations, both the maximum number and rate were during the Late Archean but subsequently both the number of formations and the rate of formation gradually declined by the end of Proterozoic; for amphibolites, the maximum number of formations was reached during the Middle Proterozoic, but there were two peaks in terms of rate of amphibolite formation in the Late Archean and the Late Proterozoic (mainly during the Precambrian). It is obvious that greenschist metamorphic facies requiring low to moderate temperatures and low pressures always had favorable conditions within the crust, but the likelihood of the formation of granulite facies rocks declined constantly with the cooling of the upper layers of the Earth, because conditions with temperatures of around 1,073 K at depths of about 28 km became increasingly less realistic. In contrast, conditions with medium temperatures required for formation of amphibolites are still favorable within the crust.

6.7 Computing the Curie Discontinuity Depth

The anomalous magnetic field of the Earth is caused by the presence of highly magnetized minerals (ferro- and ferri-magnetic) and compounds of iron oxides, but primarily iron(III) oxide which is an essential component of a number of strong ferrimagnetic minerals. Both kinds of strong magnetic (ferro- and ferri-magnetic) compounds are characterized by the Curie point (T_C) which differs for each magnetic compound, above which they lose their strong magnetic properties and become paramagnetic ones.

The Curie point of rocks and minerals, as well as the Curie point depth (CPD), is the depth at which temperature reaches the value of the Curie point of magnetite ($\sim$851 K) as defined in physics. In most cases in geophysics, the accepted values are within the range of 848–853 K (Pilchin and Khesin 1981; Pilchin and Eppelbaum 2006; Eppelbaum and Pilchin 2006; Pilchin 2011). It plays an important role in the interpretation of magnetic data and geophysical modeling of lithospheric composition based on the stability of iron-containing rocks and minerals. The CPD is the "bottom edge" of the magneto-active layer which plays a crucial role in the formation of the abnormal magnetic field of the Earth.

The CPD or Curie surface is a good way to use geothermic methods for the analysis of a thermal regime within the medium-lower crust to upper mantle by compiling a Curie map (see for example Sect. 1.8). The main idea behind calculating the CPD and compiling CPD maps is to determine the thickness of a magneto-active layer in a given region, because above the CPD surface virtually all magnetic rocks and minerals are in their magnetic state, but below the surface they are in a paramagnetic state. Similarly, above the CPD surface iron(II) oxide containing rocks are unstable and iron(III) oxide containing rocks are stable, but below the surface iron(II) oxide containing rocks are stable and iron(III) oxide containing rocks are not stable because of the TFFI.

Thus to define the CPD, the Curie point should be selected based on its values for more typical rocks and the distribution of these rocks. The most widespread magnetic minerals on Earth are iron, magnetite and titanomagnetites (the latter is a family of minerals; Nagatha 1961; Pilchin and Eppelbaum 2007) which tend to have the strongest magnetic properties. The Curie points of these minerals are 1,043 K for pure iron, 851 K for magnetite and ~373–813 K for titanomagnetites depending on their TiO_2 content (Nagatha 1961; Pechersky et al. 1975; Nishitani and Kono 1983; Calvo et al. 2002). But pure iron, which is present in huge quantities within the Earth's core where the temperature is evidently much higher than its Curie point, is extremely rare within the crust. By contrast, magnetite is an accessory mineral of almost all common sedimentary, metamorphic and magmatic rocks (Pilchin and Eppelbaum 2007; Pilchin 2011). Titan-rich magmatic rocks are unusual for the Archean and Early Proterozoic and their content is much higher in younger magmatic rocks in both continental and oceanic regions. There is a lack of titanomagnetites within the lower crust and the uppermost lithospheric mantle in continental areas. But some relatively young regions are also poor in Ti-content as is the case for the Kura Depression (Pilchin and Khesin 1981). This makes magnetite the dominant strongly magnetic component within the lower crust and the uppermost lithospheric mantle on continents. These features, along with the fact that the Curie point of magnetite is higher than the Curie points for titanomagnetites is why the Curie point of magnetite 851 K was accepted as the Curie point for calculating CPD and compiling CPD maps (Pilchin and Khesin 1981; Eppelbaum and Pilchin 2006; Pilchin and Eppelbaum 2006). It is clear that these are the maximal Curie points for rocks and minerals and the CPD compiled using these values will show the maximal depths above which rocks and minerals can be in magnetic state, but not below the surface. Some examples of CPD calculations using geothermal data are presented in Table 6.21.

Calculating the CPD in such thermally active regions as Armenia (with near-surface geothermal gradients of about 30–100 K/km; Kerimov et al. 1989) yielding CPD values between 6 and 12 km (Badalyan 2000) are extremely complicated to interpret because of the unstable geothermal regime of Armenia which has obvious visible signs of Quaternary volcanic activity. However, the presence of temperatures below the Curie point of magnetite cannot guarantee strong magnetic properties in rocks because within the main range of the TFFI (between 473–523 and 723–843 K) iron(III) oxide would not necessarily be the main iron oxide, as was shown by analysis of the iron(II) oxide and iron(III) oxide content in most typical rocks and minerals (e.g., Pilchin and Eppelbaum 2007). It is also possible that within the temperature range of TFFI, a transformation of iron(III) oxide to iron(II) oxide could take place especially near the upper limit of the TFFI. On the other hand, magnetite is not necessarily present in the lower crust of all regions. All these features highlight the ambiguity surrounding the magnetic properties of rocks and minerals, because they can lose their magnetic properties not only above their Curie point but also at any temperature within the range of 473–851 K. The presence of titanomagnetites only increases the confusion because the Curie point of titanomagnetites lies within a wide range of temperatures (373–813 K) and depending on their

Table 6.21 Calculation of Curie point depths for some regions using geothermal data (modified after Eppelbaum and Pilchin 2006)

Region	Heat flow, mWm^{-2}	Geothermal gradient, K/km	Curie point depth, km	References
Basin and range Province, W. USA[a]	35–105	25–45	22	Blackwell (1971)
Eastern USA[a]	35–63	15–25	37	Blackwell (1971)
Middle Kura depression, Azerbaijan (western part)	45–104	30–43	18–32	Pilchin and Khesin (1981)
Middle Kura depression, Azerbaijan (eastern part)	33–50	20–30	32–42	Pilchin and Khesin, (1981)
Lower Kura depression, Azerbaijan	17–42	10–25	42–46	Pilchin and Khesin (1981)
South Caspian depression, Azerbaijan	17–42	10–20	44–50	Eppelbaum and Pilchin (2006)
Jordan	16–123	11–94	10–35	Al-Zoubi (1992)
Armenia	38–157	30–100	6–12	Badalyan (2000)
Israel	35–40	16–22	38–46	Eppelbaum and Pilchin (2006)

[a] The values of the heat flow and geothermal gradients for these regions are taken from (Nathenson and Guffanti 1988)

titanomagnetite composition as well as iron and titan content they can also lose their strong magnetic properties within the range of the Curie points of titanomagnetite.

All this means that calculations based on magnetic data for the depth of the bottom edges of magnetized bodies (BEMB) do not necessarily coincide with the depth of the Curie point of magnetite, because there is no guarantee that magnetite is stable or is present at great depths within an area or region (Pilchin and Khesin 1981; Pilchin and Eppelbaum 1997, 2007; Eppelbaum and Pilchin 2006). To verify these claims studies in regions of the Middle Kura Depression of Azerbaijan (Pilchin and Khesin 1981) and Israel (Pilchin and Eppelbaum 1997) were carried out. In both studies along with the CPD depths of isotherms, 473 and 673 K were also calculated, as well as depths of BEMB for some areas of the Middle Kura Depression and Israel. The results of these parameters for both regions are presented in Tables 6.22 and 6.23.

It is clear from Tables 6.22 and 6.23 that for both regions, in absolutely all cases the CPD is much greater than the values of BEMB depths. In virtually all cases the depth of the BEMB is within the temperature range of 473–673 K which is the main temperature range of the TFFI that reflects its dependence on pressure; in a few cases when the values of BEMB are close to the values of CPD, the areas are located near or enclosing deep faults in which oxidation conditions can be preserved to great depths (Pilchin and Khesin 1981; Pilchin and Eppelbaum 1997; Eppelbaum and Pilchin 2006). These data support the fact that the CPD is the maximal depth for strong magnetic properties of rocks and minerals and that the BEMB in virtually all cases is much lower than the CPD for same areas.

Table 6.22 CPD (H_C), depths of isotherms (473 and 673 K) and lower edges of magnetized bodies (H_m) in the Middle Kura Depression, Azerbaijan (after Pilchin and Khesin 1981)

Name of magnetic anomaly	Depth of 473 K isotherm, km	Depth of 673 K isotherm, km	H_C, km	H_m, km
Ismailly	5.5–6.5	14–16	25–30	14
Shamkhor	5.0–6.0	12–13	18–22	20
Sarkyar	5.5	13–14	22–24	18
Borsunly	5.5–6.5	14–15	24–28	16
Lyaky	5.5–6.5	15–17	30–32	22
Karajaly	5.5–6.5	15–17	30–32	14
Sor-Sor	6.0–7.9	16–17	30–34	13
Ragimly	6.0–7.0	16–17	32–34	12
Imishly	7.5	20–22	44–46	11
Comushly	7.5	19–21	42–44	14
Saatly	7.5	18–19	40–42	9
Levonarch	5.5–6.6	14–15	24–26	16
Bashkarvand	5.5–6.5	15–16	26–28	10
Gindarch	5.5–6.5	15–16	25–30	15
Beilagan	6.5–7.0	15–16	25–30	26
Pervomai	6.5–7.5	19–20	42–44	7

Table 6.23 CPD (H_C), depth of isotherms of 473 and 673 K, and BEMB (H_m) depth for some areas of Israel (modified after Pilchin and Eppelbaum 1997)

Area	Depth of 473 K isotherm, km	Depth of 673 K isotherm, km	H_C, km	H_m, km
Ramat HaGolan	13	31	44	23–28
Atlit, Carmel (Mediterranean coast)	12	30	46	22–25
Belvoir1 well (Galilee)	10.5	25.5	44	23–27
Rosh Pina, Hazon	10	24.5	46	22–26
between the Pleshet1 & Ein Gedi wells	11.5	28	38	25–28
Boker1 (central Negev)	11.5	29	38	31–35
Dead Sea S-W coast	10.5	25.5	39	–
northern Arava Valley	11.5	30	39	29–34
Hod Ahsdod1 (Ashdod)	10.5	26	39	23–27
Ashkelon	11	28	38	25–29
Be'er-Sheva	13	30	38	29–33

Unfortunately for quite some time there have been attempts to calculate CPD by simply placing an equal sign between the depth of the BEMB obtained by exclusively using magnetic data and CPD, which, as is clear from all of the above, is erroneous. Calculations of the CPD by magnetic data for some regions are presented in Table 6.24.

Moreover, the temperature accepted for BEMB in these cases is the Curie point of magnetite -851 K, which is absolutely incorrect (Eppelbaum and Pilchin 2006).

Table 6.24 The Curie point depth calculated for some regions using magnetic methods

Region	Curie point depth, km	References
NW Ontario, Canada	9–16	Bhattacharyya and Morley (1965)
Yellowstone national park, USA	4–22	Bhattacharyya and Leu (1975)
Yellowstone national park, USA	7–17	Shuey et al. (1977)
Arizona, USA	2–30	Byerly and Stolt (1977)
Quseir, Egypt	10	Salem et al. (2000)
Kyushu, Japan	6.5–15	Okubo et al. (1985)
Nevada, USA	5–30	Blakely (1988)
Cascade range, USA	9–15	Connard et al. (1983)
S and S-E Asia	9–46	Tanaka et al. (1999)
Volcanic area	4–22	Tanaka et al. (1999)
Island arc	13–25	Tanaka et al. (1999)
Back-arc rift	14–26	Tanaka et al. (1999)
Marginal sea	12–30	Tanaka et al. (1999)
Continent	9–45	Tanaka et al. (1999)
Trench	30–45	Tanaka et al. (1999)
Central Anatolia	13.7	Maden (2009b)
Macedonia and Thrace, Greece	11.2–17.3	Stampolidis and Tsokas (2002)
SW Turkey	9–20	Dolmaz et al. (2005)
North Evian Gulf area, Greece	7–8	Karastathis et al. (2010)
East Anatolia, Turkey	14.1–22.6	Büyüksaraç and Bektaş (2007)
Nupe Basin, Central Nigeria	12–30	Nwankwo et al. (2009)
Sulu UHP belt, China	18.5–27	Qingqing et al. (2008)
Barramiya–Red Sea coast, Egypt	22.5–40	El Nabi (2012)
Mexico	10–32	Manea and Manea (2011)
S Sinai Peninsula, Egypt	15–18	Aboud et al. (2011)
NW Sinai Peninsula, Egypt	20–25	Aboud et al. (2011)
Greece	1–20	Tselentis (1991)
Germany	22–45	Gabriel et al., (2012)
Coast Ranges, California, USA	20–30	Ross et al. (2006)
Great Valley, California, USA	30–45	Ross et al. (2006)
Eastern Turkey	20–29	Aydın et al. (2005)
the Aegean region	6–10	Aydın et al. (2005)
Central Pontides, Turkey	14.8–21.8	Maden (2009a)
Central Anatolia, Turkey	7.9–22.6	Ateş et al. (2005)
Eastern Anatolia, Turkey	12.9–22.6	Bektaş et al. (2007)
Bulgaria	17–35	Trifonova et al. (2007)

Even worse, there are attempts to use magnetic data to calculate heat flow density, geothermal gradients and other parameters (e.g., Sharma et al. 2005; Büyüksaraç and Bektaş 2007; Maden 2009a), all of which are mistaken.

The idea of using magnetic methods to calculate the Curie isotherm depth is based on a theory proposed by Bhattacharyya (1966) and elaborated further in (Spector and Grant 1970) and (Bhattacharyya and Leu 1975). This method applies a spectrum analysis of magnetic data (Bhattacharyya and Leu 1975; Spector and

Grant 1970). The rationale for the use of magnetic methods to calculate the CPD is based on the idea that since magnetic minerals lose their magnetic properties below the CPD, the depth of BEMB in an area should represent its CPD. The term "magnetic crust" is interpreted as the position of the Curie point isotherm (Byerly and Stolt 1977). This makes it possible to use magnetic data which is more common and relatively easily measured for estimates of the CPD (Bhattacharyya and Leu 1975; Byerly and Stolt 1977; Okubo and Matsunaga 1994; Tanaka et al. 1999). It has been argued that the most common magnetic materials of the Earth's crust are titanomagnetites (Nagatha 1961; Pechersky et al. 1975), whose Curie temperatures are lower than that of magnetite. This enabled Pechersky et al. (1975) to account for the shallow depths of the lower edges of magnetized bodies in the majority of regions by the presence of titanomagnetites.

However, the use of magnetic methods also raises a certain number of problems, because it is unclear which value should be accepted as the Curie point. Should it be the Curie point of magnetite, or that of titanomagnetite? If it is the Curie point of titanomagnetite, which value between 373 and 823 K is the best match for the region under study if we know nothing about the concentration of Ti-oxides at different depths? On the other hand, magnetic methods are the only methods to calculate the BEMB depth and currently there is no way to convert these parameters into real temperature values within the crust and upper mantle. It is obvious that in different regions, the mineral concentration can also differ. Thus the CP for different regions will relate to different Curie points whose values cannot be compared. For example, in one study, Chiozzi et al. (2005) examined three different Curie points (823, 833 and 853 K) for different regions. Moreover, in some regions, the Ti-oxide concentration may be very low, as is the case for the Kura Depression of Azerbaijan (Pilchin and Khesin 1981). Such low Ti-oxide concentrations cannot represent their regional values, and can only be local. On the other hand, the BEMB values in regions of ancient platforms usually do not exceed 10–15 km (Bulina 1970; Pechersky et al. 1975; Pilchin and Khesin 1981; Pilchin and Eppelbaum 1997), even though the Curie temperature depth of magnetite in such regions (calculated using geothermal data) is located at depths of 40–50 km and more (Kutas 1978; Pilchin 1983; Pilchin and Eppelbaum 1997). In many cases, the shallow depths of the BEMB can be explained by ferric iron(III) instability under high *P*–*T* conditions with its transformation to ferrous iron(II) (Nagatha 1961; Sherman 1989; Pilchin and Eppelbaum 1997). Such a transition usually takes place at a temperature of about 843 K, but this temperature can be significantly less with increased pressure (Kurepin 1975; Pilchin and Eppelbaum 1997) since pressure increases with depth. These data clearly show (Eppelbaum and Pilchin 2006) that it is unacceptable to use the depth of the BEMB instead of CPD.

6.8 Role of the Thermal Regime in Fold Formation in Sedimentary Strata

Sediments are formed at the surface of Earth as a result of weathering and erosion of pre-existing rocks. Loose sediments are transported to a place of their deposition in the sea or another sedimentary environment where they are converted to sedimentary rocks after compaction and sedimentation (e.g., Prothero and Schwab 1996; Nichols 1999). Formation sediments require the presence of a source region (elevated areas) and basins for their deposition and collection. The types and extent of weathering reflect the climate of the source region, and are also known as the sedimentary provenance. The primary types of sedimentary rocks are clastics, carbonates, evaporites, and chemical (in many cases last three groups are combined into one). Clastic sedimentary rocks are further classified by the size of their clasts which range from nearly boulder (>256 mm) and cobble (64–256 mm) size in the coarsest conglomerates and breccias to gravel (2–64 mm), sand (62.5 μm–2 mm) and the very fine grain size of silt (3.9–62.5 μm) and clay (<3.9 μm).

Sediments are usually transported by running water (the most effective form of transport), wind, and glacial ice to their place of deposition. Gravity plays a significant role in the sedimentation process because it acts on the particles themselves and controls the direction of water flow. Almost all sediments are deposited in intracontinental seas and oceanic environments. Sediments are usually deposited in horizontal layers. Deposited sediments are the source of sedimentary rocks. The final stage in the formation of sedimentary rocks is the transformation of unconsolidated sediments into solid rock through their compaction and cementation. Compaction takes place when overlying accumulating sediments compress the buried sediments. Cementation (sometimes also called lithification) takes place when dissolved ions, carried by water within pores, react to form specific cementing minerals, which are precipitated within pores. Some common cementing minerals are calcite, quartz, iron oxides, etc. Layers of sedimentary rocks are grouped into formations, and formations are grouped into sequences.

Sedimentary rocks represent one of key types of rocks of the crust. Since sedimentary rocks are the weakest of all the crustal rocks, formed and forming sedimentary layers, formations and sequences are subject to deformations caused by different tectonic forces. Different deformations cause the formation of sedimentary structures that are investigated by a branch of geology known as structural geology that deals with the arrangement, internal rock structures and external forms resulting from the deformation of the Earth's crust. The formation of sedimentary structures depends to a great extent on the mechanical properties, lithological composition and rheology of sedimentary rocks, as well as on the kinds of stress and type of deformation processes taking place. For example brittle sedimentary rocks can be fractured easily, but plastic sedimentary rocks can form soft-*sediment* deformation structures. The main kind of soft-*sediment* deformation structures is known as a fold. Folds are classified into a number of main types such as anticline, syncline,

antiform, synform, dome, monocline, chevron, etc. (e.g., Khain 1973; Davis and Reynolds 1996; Pollard and Fletcher 2005). The most typical types of folds are the anticline, syncline and dome. An anticline is a fold that is convex upward and has its oldest layers at its core, and a syncline is a concave fold where younger layers dip downward closer to the center of the structure. A dome is a fold with round or elliptical upwarp of strata resembling a short anticline. Folds in rocks vary in size from microscopic wrinkles to mountain-sized folds. A set of folds distributed on a regional scale constitutes a fold belt (also called an orogenic zone/belt or anticlinorium). A large syncline with superimposed smaller folds is called synclinorium.

Folds appear on all scales, in all rock types (sedimentary, magmatic and metamorphic), at all levels in the crust and arise from a variety of causes. Folds are formed under varied conditions of stress: lithostatic pressure, pore pressure, temperature gradient, tectonic pressure, etc. Sedimentary folds are characterized by a crest (the highest point), a hinge, a trough (the lowest point) and limbs (the flanks).

From mechanical point of view, the folding of rocks must balance the deformation of layers in terms of the conservation of rock mass and in some cases volume as well. The main cause of fold formation is horizontal compression. Folds are commonly formed when a sequence of layered rocks is shortened parallel to its layering. For plastic rocks folding typically occurs by simple buckling of a planar surface and its confining volume.

Since folding can only take place in a compressional regime and not in an extensional one, it can only occur during the heating of rocks or in the presence of an external force. During the early Earth's evolution, with dominating cooling regime conditions folds were either absent or limited. Since the formation of greenschists can take place under natural lithostatic pressure conditions, the earliest formation of greenschists could have taken place during the cooling of the upper layers of the magma-ocean after their solidification. But pulses of granulite formation at least starting from the second pulse in the Late Archean were related to processes of heating and magma underplating. On the other hand, the formation of folds of sedimentary rocks could only have taken place after beginning of the sedimentary layer formation, which started with the formation of the water ocean at the very end of Early Archean ($\sim$3.26 Ga; see Sect. 6.2) and started amassing significant amounts of sediment in the Barberton GSB (Fig Tree Group) and the Pilbara Craton (Gorge Creek Group) between the Early and Middle Archean.

It is obvious that the scale of processes of fold formation is dependent on the volume of sediments involved (thickness of sedimentary basin), mechanical conditions within the basin and rock rheology. The presence of weak (e.g., salt) or plastic (e.g., clay or silt) rocks or their content within sedimentary formations eases the process of fold formation and increases the amplitude of the folds. By contrast, amassing brittle rocks in formations would limit their capabilities for fold formation but would increase the likelihood of faults and fractures. The formation of fractures and faults within rocks and rock formations is governed by the type of deformation applied. There are three main types of deformations: compressive, tensile and shear. Different rocks have different strength limits (the maximal stress

that a material can withstand before failure) for each type of deformation which is usually termed the ultimate compressive strength, ultimate tensile strength and ultimate shear strength. Values of ultimate tensile and shear strengths are very low compared to the values of ultimate compressive strength (Clark 1966) which makes different rocks withstand much higher stress under compression than in the case of extension and shearing before failure.

It is widely accepted that the formation of folds requires the presence of giant horizontal pressures (horizontal movement of plate or plates). The sedimentary layer (formation, series) is the weakest layer and can be easily compressed (or squeezed) by any strong tectonic movement in a horizontal direction (obduction, thrusting, continent–continent collision, etc.). Such processes can generate so huge a horizontal pressure (forces) that it easily causes significant shortening of the sedimentary layer (or even basin) resulting in the formation of folds. But any horizontal movement of a plate has its own origin and cannot take place without its own cause. Hence prior to any horizontal movement of a plate there is source of overpressure formation. On the other hand in most cases sedimentary basins are formed on the top of immersing blocks containing a crystalline basement which should protect overlying sediments from pressure by horizontal forces. Thus to start compressing sedimentary rocks lying on the top of any lithospheric block, its crystalline basement either needs to have been destroyed or a pushing block has overthrust it.

Another kind of force that can form folds is the force of gravity, which is more visible in cases of orogenic processes when sedimentary rocks are uplifted by certain processes at great heights over a short period of time. However the force of gravity is only applied in a vertical direction. Lithostatic forces only work in cases when the consolidated part of the lithosphere of a block/plate is separated into a number of sub-blocks which can be independently involved in their independent uplift or immersion. It is obvious that more plastic rocks slide more easily from uplifted mountain structures. For example, the Greater Caucasus is mostly composed of sedimentary rocks (Milanovsky 1968; V Ye Khain 1984) and experienced significant uplift in the Quaternary period. Estimates by Milanovsky (1968) show that the uplift in the regions of the Central and Eastern Caucasus during the Anthropogenic Period (between about 600,000–1,000,000 and 2,500,000–3,500,000 years) reached 0.8–1 km per 0.5 M.y. or 2 mm per year on average. Estimates by Tsagarelli (1964) assigned even greater values of about 2,500 m during the Anthropogenic Period with a maximum in the Lower Pleistocene. More precise estimates were obtained for the Tsiv-Gomborskiy range of the Greater Caucasus where Pliocene deposits were uplifted to a height of about 2,000 m (Tsagarelli 1964).

The third way folds can be formed is related to the thermal regime of a sedimentary basin (e.g., Pilchin 1986). It was mentioned above that in many cases only compressing the sedimentary rocks of a sedimentary basin by external tectonic forces is impossible, because the crystalline basement of the basin would be the first to be affected by the tectonic forces. Thus before compressing the sedimentary

layers of the basin its crystalline basement needs to be destroyed or overridden by an active plate first. Actually, in some cases the formation of folds has nothing to do with shortening, which is prevented by the stable consolidated basement of the basin. For example, folding not possible in cases of weak tectonic forces/pressures, because the stress limit for rocks is maximal for compression and is minimal for extension and shearing of rocks (Clark 1966). In other words, shortening of the basin is only possible after destruction of its crystalline basement by formation decollements and consequently thrusting or underthrusting of parts of the basement, which leaves parts of sedimentary basin unprotected. If there are no obvious signs of formation of decollement and/or thrust or underthrust of crystalline basement blocks within the basin, it did not experience shortening stage in its evolution and all the sedimentary structures formed within the basin took place by means other than tectonic compression by outside external forces.

There are extremely thick sedimentary layers in deep sedimentary basins in which signs of obduction or any other significant thrusting are absent (e.g., South Caspian Depression, Precaspian Depression, Black Sea Basin, etc.). Deep sedimentary basins correspond to specific kind of structure formed in many regions of the Earth. They usually develop in regions of relatively fast subsidence of the surface and can amass different thickness of sedimentary rocks. The deepest sedimentary basins on Earth include the South Caspian Basin (15–28 km thick; Kaz'min and Verzhbitskii 2011), the Precaspian Basin in Russia and Kazakhstan (up to 20 km thick; Volozh et al. 2003), the Barents—North Kam Megabasin in Arctic ocean (20–22 km thick; Gramberg et al. 1999), the Yenisei-Khatanga Megabasin in Russia (14–16 km; Gramberg et al. 1999), the Bengal Basin in India (up to 15 km; Mukhopadhyay and Krishna 1991), the Yinggehai Basin in Southeast Asia (15–20 km; Wheeler and White 2002) the Northern Gulf of Mexico Continental Margin (17–19 km; Lowrie and Fillon 2011) southeast of the Dniepr–Donets Basin (15–19 km; Stovba et al. 2003) the Belt-Purcell Basin in British Columbia (up to 19 km; Hartlaub et al. 2009) the Vrancea Zone in Romania (up to 18 km; Landes et al. 2002), the Black Sea Basin (14–18 km; Kutas et al. 1998) the Gregory Subbasin in Western Australia (18 km; Driscoll et al. 2009), etc. Most of the thickest sedimentary basins were formed in intracontinental seas because they: (1) are surrounded by source regions that make them the best areas for collecting huge amounts of sediments; (2) contain water in sedimentary pores which facilitates the bending of rocks in folds and in some cases prevents them from fracturing. In the South Caspian Depression, the Caspian Sea itself is below sea level and the depression is surrounded by such orogenic belts as the Greater Caucasus (N–W), the Talysh and the Lesser Caucasus (S–W), Alborz (S), the Kopetdag (E), as well as the Kura Depression (W) and West Turkmenian Depression (E). Thus the South Caspian Depression is a source region with unlimited amounts of rocks ready for relatively easy weathering and sedimentation. Even though in these regions the consolidated part of crust is much thinner than in the surrounding regions, it is not usually significantly destroyed and thus should protect sediments on its top against horizontal pressure from neighboring blocks/plates. Moreover, there are signs of some strong tectonic activity within

sedimentary formations of these basins involving sedimentary rocks themselves. For example, in the South Caspian Depression and north of Black Sea Basin mud volcanoes, and in the Precaspian Depression and the Dniepr–Donets Basin strong salt tectonics have been identified. Hence there are causes internal to the sedimentary basin which can generate tectonic processes including folding within it even without the involvement of external horizontal forces.

It is obvious that the effect of the thermal regime on the formation of sedimentary structures is affected by the shape of the basin, as well as by the lithology and thickness of the sedimentary layers in it. The thickness of a basin is governed by its initial depth, rate of immersion and source region. In numerous cases the thickness of sedimentary rocks is greater in the middle of a basin (e.g., the South Caspian Depression), but in other cases the thickness can vary from a few kilometers on one side of the basin to a significant thickness on its opposite side. For example, in the Dniepr–Donets Basin the maximal thickness of the sediments ranges from 2–6 km in the northwest to 15–19 km in the southeast (Stovba et al. 2003). But in most cases sediments are never the thickest at the edge of the basin. This creates a situation where the thickest inner part of a sedimentary basin is characterized by the highest rate of immersion (subsidence) and the highest rate of sediment deposition. This also means that the part of the basin with the greatest sediment thickness is characterized by the fastest rate of heating (temperature increase) and hence the fastest increase in pressure (overpressure) within these parts of the sedimentary layer (according to Eqs. 2.7.4 and 2.7.5). Thus at some point when the overpressure exceeds the value of the lithostatic pressure, the surface in that inner part of the basin will start buckling, forming an anticline type of structure. The fact that in the inner part of basin the temperature will increase faster than in marginal areas of the basin is supported not only by the fact that temperature increases with depth, but also by the fact that sedimentary rocks have minimal values of heat conductivity among crustal rocks. Upon contact with the sediments surrounding them, and consolidated rocks at the margins of the basin, the horizontal heat flow between sedimentary rocks and non-sedimentary rocks is greater than within the basin, which would lead to additional cooling of the margins.

When the layer of sedimentary rocks was deposited ~ 1 million years ago, it was at a depth of 1 km, with a temperature of ~ 307 K in a region with an average annual surface temperature of ~ 287 K. Hence for 1 million years the temperature of rocks within the layer was heated by 20 K. The same time layer, which 1 million years ago was at a depth 1 km in the same area and had a temperature of ~ 307 K, is now at a depth of 2 km and has a temperature of about 327 K. Clearly this layer was also heated by 20 K during last 1 million years. Such heating would create conditions for heat expansion and increased pressure in rocks of the layer (see Eq. 2.7.4). This example is real, since in the South Caspian Basin, the thickness of the Pliocene–Quaternary sediments is about 10 km (Kaz'min and Verzhbitskii 2011) which makes the rate of sedimentation almost 2 km per 1 million years. Given that the temperature in deep boreholes within the South Caspian Depression is about 368–383 K at depths of ~ 6 km and the average annual temperature at the surface in

the region is about 287 K (Pilchin 1983), the rate of heating in the region was about 27–32 K per million years. Similar estimates for areas of the Kura Depression yielded rates of heating of about 4–12 K per million years.

The values of thermal expansion for the main sedimentary rocks (except clays) are within the range of (2.4–3.3) $\times 10^{-5}$ 1/K (Clark 1966) and their value is almost one order greater for wet clays (of about (1–2) $\times 10^{-4}$ 1/C). Thus for rocks heated by $\sim$100 K as is the case at a depth of $\sim$6 km in the South Caspian Depression, the volume expansion will be about 0.24–0.33 % for brittle rocks and $\sim$1–2 % for plastic rocks, which makes the total surface uplift about 2.4–3.3 m for brittle sedimentary rocks and 10–20 m for plastic sedimentary rocks for each 1 km of thickness of sedimentary rocks. For the upper 12 km of the sedimentary layer, an average temperature increase of 100 K would yield a total surface uplift of 24–34 to 120–240 m, which would be much more significant on the local scale, because the main uplifts would take place in anticline folds. Note as well that the formation of fractures and faults within layers of brittle sedimentary rocks would significantly increase the lower limit of the volume of expanding rocks. This effect for the South Caspian Depression, which has a thickness of up to 28 km (Kaz'min and Verzhbitskii 2011) could be huge. It is obvious that such a significant increase of volume in different local structures is easily capable of significant folding especially in thick sedimentary basins. The geothermal gradient in the South Caspian Depression is low (>20 K/km), and a similar effect of volume increase in basins with higher geothermal gradients could be much higher. For example in areas of the Middle Kura Depression, the temperature of 373 K is reached at depths of 2.3–3.5 km, and in areas of Northern Caucasus, 373 K is reached at depths of about 2.2–3.0 km (Pilchin 1983; Kerimov et al. 1989).

The formation of anticline structures is related to higher temperatures, and all other conditions being equal, the pressure generated by the excess temperature (see Eqs. 2.7.4 and 2.7.5) will be greater in the core of the anticline structure and this pressure will be applied in vertical direction (up) as well as in all other directions. In the case of a cap-rock layer, which is the usual case for anticlines, the pressure created under the cap-rock layer can exceed the lithostatic pressure. It was shown in Sect. 2.7 that AHSP/AHPP can reach values a number of times greater than the lithostatic pressure and in the case of the formation of such pressure under a cap-rock layer the unloading of this pressure would be limited. Moreover, cap-rock layers, which are usually represented by plastic clays or weak salts, are themselves a perfect medium for the formation of overpressure (see Sect. 4.3), as well as for transfer pressure applied to it in any direction. Nevertheless, volume increase only takes place in the upward direction, and the formation of overpressure greater than the lithostatic pressure would start movement of the surface upwards. The greater movement of the surface would correspond to areas of greater overpressure values, which are within and above the core of the anticline fold. From this point of view, the formation of anticlines is the primary folding process and the formation of synclines is the secondary folding process, because synclines are usually formed between anticlines, most likely as a passive secondary product of formation anticlines.

It is no accident that anticline structures are always characterized by higher temperatures than neighboring syncline structures and for some processes are in fact more favorable (e.g., formation, collection and preservation of oil and gas fields).

Although the vertical component of pressure can easily be relaxed in a vertical direction to the surface in a relatively short time, the horizontal components of pressure cannot be relaxed easily because all volumes are fixed in their position in the horizontal direction by other volumes of the layer surrounding the volume (Fig. 6.8). It is obvious from Fig. 6.8 that the only direction for expansion of any volume is up. Thus the only way to relax pressure is either to move (tectonically) other volumes by pressure (force) generated by expanding the volume or expansion in the up direction. At the same time tectonic movements can cause faults, fractures, uplifts, formation of folds, etc.

It is obvious from Fig. 6.8 that any expansion in the down direction is prevented by the absence of empty space below the active volume and similar attempts to expand by the layers below the active volume. The only "easy" way for expansion is in the up direction, because the active volume has a free surface at the top. Thus most of the changes of volume within a sedimentary layer end up with changes in the position of the surface with relatively small changes in the horizontal direction. It is also obvious that any volume exchange within any active sedimentary volume will not have a significant effect on the underlying consolidated basement. By contrast, any overpressure generated within the consolidated basement or transferred to it from below can be easily transferred to the sedimentary layer which would lead to additional tectonic changes at all levels within the sedimentary layer.

It is known that *stress* is generated within a volume under pressure to confront and withstand it. But in some cases internal pressure can be generated within the volume that attempts to increase this volume. In this case it would generate different amounts of stress within volumes surrounding the active volume to oppose the pressure.

The formation of pressure (overpressure) within any volume of a layer surrounded by other volumes actually creates a situation where attempts by the volume to expand are impeded by similar attempts of its surrounding volumes to expand themselves. This creates a situation similar to compression of the active volume by pressure equal to its internal stress. In such a situation the volume will be in condition of equilibrium until its stress overcomes the external pressure on the volume in any direction. At that point, the equilibrium will be broken and the volume will start expanding until new equilibrium conditions are reached. But any state of equilibrium can be disrupted at any time and in any place of the layer.

It is known that the volume thermal expansion (α_V) is about 3 times greater than the linear thermal expansion (α_L). In other words, since any volume of sedimentary rocks within a sedimentary basin is controlled by its surrounding volumes of sedimentary rocks and is limited from the bottom by the consolidated rocks of a lithospheric block, it has only the upward direction in which to expand. Thus even though its expansion can take place in only direction, this expansion includes the

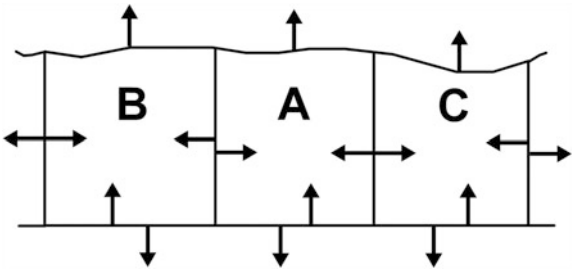

Fig. 6.8 Schematic diagram of pressures (forces) interacting between the active volume (*A*), volumes (*B* and *C*) surrounding it in same sedimentary underlying layer (possibly basement) and the atmosphere on the surface. Arrows representing the direction of forces (or pressure) applied to different parts of a structure

total volume expansion, which equals 3 times of their regular expansion in a single dimension. It is obvious that this has an impact on both the amplitude of forming folds and the change in the length of the curved surface, which will not be proportional to the probable/visible shortening of the basin.

Even though active volume generates pressure in all directions, the pressure is more effective in the vertical (up) direction that forms an uplift, because in horizontal or inclined directions the distance through layers is so much greater than in the up direction that it can be easily relaxed through the length of the layers. But it could play a significant role in the formation of folds. By contrast, in the vertical direction, applied pressure forces the volume to buckle up, whereas in a horizontal direction the pressure is distributed along the layers by different values and the effect of layer displacement is constrained by the low pressure gradient and high friction forces between layers.

The compaction of sediments is limited by the porous fluid content in sedimentary rocks and the AHSP/AHPP value in these rocks. In the case of open porous spaces and an absence of a cap-rock layer, porous fluid can be forced out of the pores, but in the case of clays, the absence of open porous spaces and the presence of a cap-rock layer, this is impossible or very difficult, and the AHSP/AHPP will not allow any outer pressure to compress sedimentary rocks. In numerous cases (see Sect. 2.2) AHSP/AHPP can reach values greater than the lithostatic pressure and in such a case they themselves can cause or contribute to significant tectonic effects including the formation of faults, fractures, mud volcanoes, folding, etc.

6.9 The Thermodynamic Regime and Its Influence on Tectonic Processes

In numerous regions it is difficult to gather geothermal data (e.g. inability to drill even shallow boreholes, etc.). In such cases the thermodynamic conditions of different processes (e.g. serpentinization, different facies of metamorphism, rock

and mineral stability, etc.) are the only way to estimate the temperature at various depths at different time periods in these regions. Orogenic belts are one of the regions where it is difficult to obtain reliable geothermal data. However, a number of different processes are involved in the formation of orogenic belts and the thermal/thermodynamic conditions during the formation of these belts can be exploited to estimate the temperature at different levels within the orogenic belts.

One of the main problems in geology is to determine the origin of different geological and tectonic processes governing geological structures and the evolution of tectonic units in a region. Without information on the origin of these processes and the causes of change in a geological environment any geological theory or idea will simply be a hypothesis.

It is clear that such global scale processes as continental collision, orogeny, subduction, obduction, regional metamorphism, regional uplift, regional immersion and others require the presence of specific and sometimes unique conditions. All lithospheric blocks, at all layers of the Earth, and all units of volume on the Earth lie in the Earth's gravity field and are subjected to the forces of gravity created by the field. Thus all geological processes and components of the geological structure in a region must obey the laws of gravity. All the forces of gravity are directed toward the center of the Earth's mass with a correction for the abnormal gravity effect of masses distributed within the surface relief of an area. But unlike gravity forces directed downward there are obvious tectonic processes such as the uplift of slabs and vertical elements of orogenic processes which require a force (or forces) directed upward against the laws of gravity. To explain such vertical movements, the theory of isostasy was introduced (see review in Pilchin and Eppelbaum 2009). The main idea behind isostasy is that in general all slabs forming the upper brittle layers of the Earth float on top of more viscous layers and their movements are controlled by Archimedes' Law which states that denser and heavier slabs will sink, whereas less dense and lighter slabs will float and uplift. However neither the laws of gravity nor Archimedes' Law can explain such obvious tectonic processes as continental collision, subduction (especially low angle subduction), obduction, continental drift, sea bottom spreading, thrusting and nappe formation, etc., because both gravity and isostatic forces are strictly vertical and they cannot create forces in the horizontal direction. This means that forces with other origins must be present to move such giant volumes of rocks, rock complexes, slabs and even continents in the horizontal direction. Such forces must generate giant overpressures and to achieve this effect they must be generated within the moving layer or next to the layer to be able to create and apply these huge forces in a horizontal direction.

Nevertheless, any movement of giant volume in the form of a continent, slab, thrust nappe, etc. will encounter great friction, which according to Byerlee's law (e.g., Davis et al. 1983; Bunds 2001; Abers 2009) for brittle rocks could reach values with a friction coefficient μ as high as 0.85. This law is based on the results of experimental research (Byerlee 1978) showing that the friction coefficient between brittle rocks is $\mu = 0.85$ for normal stresses up to 200 MPa and $\mu = 0.6$ for normal stresses between 200 and 2,000 MPa. Byerlee (1978) also stated that if

the sliding surfaces are separated by a gouge composed of montmorillonite or vermiculite (clay minerals), friction can be very low. Recent experimental studies indicate $\mu = 0.2–0.3$ (Abers 2009; Ikari et al. 2009) for clay-rich fault gouges, and $\mu = 0.21–0.3$ (Kopf et al. 2003; Abers 2009) for talc-rich serpentinites. The most recent findings are consistent with the fact that in numerous cases serpentinites are in the base, under thrusts and nappes forming in orogenic belts.

Hence such processes as obduction and thrust formation require external forces which can overcome the force of gravity during the lifting of a slab (or layer) to some height and the friction forces between allochthonous and autochthon (or earlier allochthon and forming allochthon) layers.

It was shown (Pilchin and Eppelbaum 2002) that the subduction process also requires a giant external force (or forces) generating overpressure at least during the first phase of its evolution to overcome the forces of buoyancy and friction between the subducting slab and the surrounding brittle and/or plastic rocks. Since the only known rock denser than mantle peridotites and other mantle rocks is eclogite, which can be formed at depth of $\sim$64 km (see Table 6.3) it is clear that the lithospheric slab (including its crust) needs to be pushed to a depth greater than 64 km, so that it transforms into eclogite first, because the average density of a lithospheric slab including its crust is much lower than the average density of the upper mantle. Thus for the start of the subduction process and its maintenance until most of the slab rocks are transformed into eclogite, a huge initial external force (or forces) is required.

However, to have the density of eclogites in the range of 3,400–3,500 kg/m^3 all rocks must be iron-rich (Pilchin 2011), because Mg-rich eclogites have densities in the range of 3,300–3,350 kg/m^3 which is not enough to continue the subduction process. It was shown that the iron content in magmatic rocks increases as the rocks are younger. This means that the more recently formed crust/lithosphere should be richer in iron and is the best material for the formation iron-rich eclogites. On the other hand to be iron-rich, eclogites must contain as much iron-rich garnet (almandine) and iron-rich pyroxene (aegerine/acmite) as possible. But aegirine (an essential component of omphacite) contains both ferric and ferrous iron oxides which impedes this mineral's stability at great depths, because ferric iron oxide is not stable at temperatures above 843 K and transforms into ferrous iron oxide as part of TFFI. This means that the formation of extremely dense eclogites can only take place in very specific thermodynamic conditions. The depth of subduction of a lithospheric slab hence depends to a great extent on thermodynamic conditions and the physical state of the rocks in the asthenosphere, because in the partially molten state they would behave like a viscous liquid and further subduction of the slab would only be possible through Archimedes' Law and only in the vertical direction. No external force can be applied to a slab within a partially molten asthenosphere, because according to Pascal's law of transmission of fluid pressure, pressure exerted anywhere in a confined incompressible fluid is transmitted equally in all directions throughout the fluid, which would lead to fast unloading of any overpressure. In the case of subduction, external forces must overcome friction and need additional force to overcome buoyancy (if any) and

extra force to support the downward movement of the subducting slab through rocks of the upper mantle.

It is clear that regardless of the kind of process requiring horizontal movement of huge volumes of rocks, an external force must be present. But all forces have an origin and a source. Different processes capable of generating overpressure are discussed in Sect. 4.4.

Given that any rock, rock volume, slab or layer is under thermodynamic conditions characterized by such general parameters as temperature (T), pressure (P) and volume (V), Pilchin (1978a, b) put forward a theory of the formation of overpressure in the Earth's layers, which was extended in (Pilchin 1986; Pilchin and Eppelbaum 2002, 2009). This theory is fully described in Sects. 2.7 and 4.4. According to this theory, an increase or decrease in the temperature of a volume leads to increase or decrease of pressure, respectively; and a change in the initial value of the volume is governed by temperature, pressure, as well as such properties as thermal expansion and the compressibility of rock (rocks) of the volume. In the presence of external forces, which can control changes in volume (e.g., prevent it from expanding) stress within the volume increases to extremely high values. The relationship between temperature, pressure and volume are fully described by Eq. (2.7.4). Problems of overpressure are discussed in Pilchin (1983, 2005), Pilchin and Eppelbaum (2002, 2009), see also Sects. 2.7 and 4.4). It was shown that both the processes of formation of overpressure and its unloading can be modeled using Eq. (2.7.4) for overpressure and Eq. (2.7.5) for equilibrium conditions. It is clear from Eq. (2.7.4) that both loading and unloading of pressure are strongly dependent on thermal conditions (T) active volume (V_0) and its change (ΔV). It was also shown that among the most important applications of the theory there are cases where changes in volume are controlled by external forces and some processes leading to the volume change. Such cases are dealt with by the third term on the right-hand side of Eq. (2.7.4) which also described by Eq. (4.4.19):

$$P_U = -\frac{1}{\beta}\frac{\Delta V}{V_0}.$$

This component of Eq. (2.7.4) usually describes pressure unloading (see Sect. 2.7) but in a number of cases when the volume changes as a result of some process (e.g. a process of transformation of one mineral into another) the values of pressure and temperature can also change accordingly. For example, if the volume being investigated is under compressive force created by the activity of moving slab, the value of the volume change (ΔV) would be negative and it would lead according to Eqs. (2.7.4) and (4.4.19) to an increase in pressure (Pilchin 1986; Pilchin and Eppelbaum 2009). Alternatively, if the volume has changed as a result of some chemical process (e.g. serpentinization of Mg-rich minerals) the obvious increase of volume would lead to a decrease in pressure only in the case where the actual increase of volume was equal or greater than the change in volume caused by the process, but in all other cases it would lead to an increase in pressure (Pilchin 1983; Pilchin and Eppelbaum 2002). Since the value of the compressibility coefficient for solid rocks is

$\sim 10^{-5}$ 1/MPa, a simple estimate shows that an increase in volume of only 1 % can cause composite unloading of pressure of about 1,000 MPa. More precise estimates of pressure unloading for increases in volume by only 1 % for garnet and olivine yielded values of about 1,724 MPa and 1,299 MPa, respectively (Pilchin 2005). Clearly the pressure will be unloaded gradually, but over period of time, during which the volume will expand 1 %, the composite unloading of pressure can take on this value. This means that if there were not any change in volume, the pressure would increase by about 1,000 MPa (Pilchin 2005; Pilchin and Eppelbaum 2002).

Analyses of cases of overpressure formation controlled by a thermal regime and thermodynamic conditions show that there are a few processes that lead to the formation of significant overpressure capable of causing tectonic processes (Pilchin 1986; Pilchin and Eppelbaum 2009): (1) heating of underground water; (2) heating of great volumes of rocks (including salt and clay layers); (3) melting of rocks at any depth; (4) rising of melt to the Earth's surface; (5) decompaction (decondensation, deconsolidation, decompression, increase in volume by any means) of rocks in the crust and the upper mantle. The formation of overpressure as AHSP/AHPP by the heating of underground water which can exceed the lithostatic pressure is discussed in Sect. 2.7. It was shown (Pilchin 2005) that at a depth of $\sim$32 km, the lithostatic pressure is about 912 MPa and an excess temperature for eclogites and granulites would generate pressure of about 322.5 MPa and 1032.7 MPa, respectively. Generation of overpressure by heating of huge volumes of rocks is discussed in Sects. 4.3, 4.4 and 6.8. Estimates and formation of overpressure during the melting of rocks at any depth and the rising of melt to the Earth's surface show (Pilchin 1987b, 2005) that depending on the physical properties of rocks, their increases in volume by 15 % during melting and conditions can prevent volume expansion at great depths and can generate pressure of up to 300–3,000 MPa. In the case of rising basic melt from a depth of 20 to 4 km, the pressure could rise by 300 MPa, and in the case of the rising of granitic melt from a depth 12 to 4 km, the pressure could rise by 75 MPa (Pilchin 1986). These kinds of pressure increases are discussed in Sect. 4.2.

This section concentrates on the formation of pressure by processes causing an increase in the volume of a solid rock. Previous studies (Hess 1955, 1962; Pilchin 2005; Pilchin and Eppelbaum 2009) have shown that the maximal increase in the volume of solid rocks could be caused by a process of serpentinization of Mg-rich minerals (e.g., olivine and orthopyroxene) and rocks (e.g., peridotites), during which the increase in volume could reach 40 % (Hess 1955). This makes the serpentinization of Mg-rich rocks and minerals extremely important as a process which can cause considerable variations in volume and hence wide variations in pressure which are crucial for tectonic processes. Thus serpentinization is one of the best possible examples of significant increases in volume.

The closer the active volume is to the surface, the less overpressure it requires to start tectonic processes (it needs to overcome much lower lithospheric pressure) but it becomes more difficult to retain the overpressure from its unloading. The peridotite layers are well known in the oceanic lithosphere, and it is possible that they are present in the upper mantle of continental regions. It is highly unlikely

that there is a huge amount of water in the mantle under the continental crust, and it is also unrealistic to expect the occurrence of 473–773 K temperatures in the continental mantle, where the temperatures are much higher. It was shown that the presence of peridotites in the Archean craton lithosphere at depths of less than ~70 km is rare (Pilchin and Eppelbaum 2012). This makes the process of serpentinization under these cratons impossible at present because it is impossible to have temperatures at or below 773 K at such great depths even in such thermally-low active regions as the Archean cratons. Since the thermal regime is higher for post-Archean continental lithosphere regions, it is not possible to have such low temperatures in the upper mantle of these regions either. Hence serpentinization can only take place in continental areas that have peridotite layers within the continental crust, which is possible only as a result of previous obduction of this layer from the oceanic lithosphere onto or within the continental crust. At the same time, low Moho depths in oceanic regions make it possible to have temperatures within the range of 473–773 K in the upper mantle which is mostly composed of peridotites.

This is the reason why serpentinization of the peridotite layer of the oceanic lithosphere causes the obduction process, but the activity of ophiolites and serpentinites within the continental crust is possible only when they are present in the middle or upper crust layers.

To calculate the value and size of pressures applied in regions of peridotite, ophiolite or serpentinite activity, it is important to bear in mind that the only important factors for pressure formation are the volume of the peridotite (actually olivine and orthopyroxene) component and the degree of serpentinization, because a change in the volume of peridotite, ophiolite or serpentinite depends on it. Serpentinite change of volume depends on a change in the degree of serpentinization. In the case of ophiolite, only the peridotite/serpentinite part is important for calculating volume changes (increases). In 1972, one definition of ophiolite was put forward (Anonymous 1972), but later researchers came to conclusion that there are different types of ophiolites and a classification by type was suggested in 1998 (e.g., Dilek 2003). This led to the additional issue of classifying peridotites/ophiolites older than ~1,000 Ma (e.g., Moores 2002; Dilek 2003). For example, Yakubchuk et al. (1994) argued that ophiolitic complexes older than 1,000 Ma are not ophiolites, because they do not adequately correspond to the definition. This debate on the composition of ophiolite association and the presence or absence of some of its typical components in different regions of the world will not be discussed further since this section only examines issues related to the formation of overpressure and the causes of tectonic processes related to formation and activity of peridotite, ophiolite and serpentinite layers.

Ophiolites are a compound assemblage of different rocks (e.g., Anonymous 1972; Pilchin 2005; Pilchin and Eppelbaum 2009) and they usually contain an ultramafic complex (more or less serpentinized peridotites), a gabbroic complex, a mafic sheeted dike complex, a mafic volcanic complex (usually pillow-lavas), and some associated rocks. However the composition of ophiolites is not stable, and

the only rock present in all ophiolites is a peridotite/serpentinized peridotite. There is also a significant difference in the melting points of peridotites and all magmatic rocks belonging to the ophiolite association. Hence not all ophiolite associations were formed at the same time or during a given time period (Pilchin 2005). This also places a number of special constraints on the formation of ophiolite association, because the peridotite layer, which has the highest melting point among the components of ophiolite association, was likely to have been formed first, and other magmatic components were added later to the association. Furthermore, there is a huge difference between the melting point of any magmatic ophiolite association and the temperature of serpentinization. This implies that such processes as melting and serpentinization cannot take place simultaneously. Hence the behavior of ophiolites under low or moderate temperature should be under control of serpentinization. In fact, the serpentinization of a peridotite component that belongs to the ophiolite sequence may create a buoyancy effect, but this effect is weaker than serpentinization of a pure peridotite layer. Research has shown that serpentinization plays a crucial role during all phases of obduction of the oceanic crust. Moreover, it is clear that serpentinization also plays an important role in the formation of thrusts and serpentinite mélanges (Pilchin 2005; Pilchin and Eppelbaum 2002).

Serpentinites are the key component of ophiolite association (Pilchin 2005) and all peridotite plates obducted onto the surface are serpentinized to different extents. The presence of ophiolites, serpentinites, and peridotites is considered to be a marker of oceanic lithosphere activity (Coleman 1977; V Ye Khain 1984; Desmons 1985; Pilchin 2005). Peridotites and ophiolites are the main components of any obducted block of oceanic crust (Coleman 1977; V Ye Khain 1984; Michard et al. 1993; Coleman and Wang 1995; Pilchin 2005). Serpentinites and ophiolites are always present in the most active tectonic structures including in any orogeny process since the Mid Proterozoic, in main thrusts and nappes, ocean ridges, island arcs, main transform faults, etc. (Coleman 1977; V Ye Khain 1984; Pilchin 1986; 2005; Berhe 1990; Hsü 1994; Yakubchuk et al. 1994; Varlakov 1996; O'Hanley 1996). The protrusive nature of serpentinization in many cases and traces of plastic deformations of serpentinized rocks in different regions point to the presence of great pressure (Hess 1955; Boland 1977; Post 1977; Wright et al. 1982; Savelieva and Denisova 1983; Benn and Allard 1989; Fügenschuh et al. 2000; Nicolas et al. 2000). Thus overall, ophiolites, serpentinites, and peridotites are indicators of the most powerful tectonic processes, and it is likely that the serpentinization process is one of the main causes of the formation of these pressures. The serpentinization of the ocean's peridotite layer may easily explain such phenomena as the spreading of ocean bottom (Hess 1962). Hess (1962) believed that $\sim$70 % of the oceanic crust is made up of serpentinites. The relationship between these two processes is well known (Nicolas et al. 1999, 2000). It is clear that an increase in the volume of the peridotite layer will cause an increase in its dimensions in both the horizontal and vertical directions. But the oceanic peridotite layer is thousand times greater horizontally than in terms of thickness. Hence the process of oceanic

peridotite layer serpentinization will mostly cause a horizontal expansion. Simple calculations show that increases of 15–25 % in the volume of the peridotite layer of oceanic lithosphere during its serpentinization can cause the horizontal expansion of the layer in any direction of at least 5–8 % or 50–80 km for every 1,000 km of oceanic lithosphere on the horizontal plane. By contrast, the vertical expansion of the ocean's peridotite layer can affect the sea level.

Starting from the early Proterozoic, it is known that oceanic lithosphere activity played a significant and sometimes key role in orogenic processes. Here and later under oceanic lithosphere activity we discuss the primary (direct) activity of oceanic lithosphere (its pressure on the continental margin, obduction of the oceanic lithosphere on the continental margin, obduction of the oceanic lithosphere on the oceanic lithosphere, tectonic activities during island arc formation, underplating, subduction of oceanic lithosphere slabs beneath the continental margin, etc.) as well as secondary tectonic activities of the oceanic lithosphere slab. Ophiolite and/or serpentinite activity refers to activity of remnants of previously obducted slabs of oceanic lithosphere. The secondary activities of oceanic lithosphere slabs or their remnants include such tectonic processes as immersion of obducted oceanic lithospheric slabs (remnants of Cretaceous oceanic lithospheric slabs in Oman originally $\sim$20 km thick are now only a few hundred meters to $\sim$2 km above sea level), repeated (second, third, etc.) steps of obduction (3 or 4 in the Baltic Shield from the Early Proterozoic, 5 or 6 in the Mozambique belt since the Proterozoic (Berhe 1990), at least three periods of ophiolite activity during the Proterozoic in the Arabian Shield (Pallister et al. 1988), at least two in Oman in the Cretaceous, etc.), formation of ophiolites during initial obduction or secondary obduction/thrusting of remnants of initial slabs of oceanic lithosphere, serpentinization of the peridotite part of remnants of a slab of oceanic lithosphere, etc. It is obvious that after either subduction of the oceanic lithosphere slab (OLS) beneath a continental margin or its obduction and then immersion of the oceanic lithosphere, the slab or its remnants/fragments can be present at any depth within the continental crust and their subsequent activity will take place within the continental crust. Such processes as the formation of peridotite blocks are obviously related to fragments of oceanic lithosphere slabs, because the peridotite layer is a key part of the oceanic lithosphere but not part of the continental crust. For example, in the Alpine-Himalayan orogenic belt, the Appalachians, Tien Shans, the Norwegian Caledonides, and the Urals, thrusts, ophiolites and serpentinites are omnipresent and in most cases they were formed during different periods in continental environments. Serpentinization is a key process in the formation of ophiolites, and both the processes of serpentinization of peridotites and the formation of ophiolites are involved in the formation of thrusts within orogenic belts. From this point of view both of these processes (formation of ophiolites and serpentinization of peridotites) should be viewed as either ophiolite or serpentinite activity. In all cases these processes cause thrust formation (Pilchin 1986, 2005; Pilchin and Eppelbaum 2002).

The key point of the serpentinization process is the serpentinization temperature. There are three main serpentine minerals: lizardite, chrysotile and antigorite,

which are formed and are stable at different temperatures. Serpentine minerals have several distinctive characteristics: they contain up to 13 wt% in water, they have a low density of about 2600 kg/m^3, and a low viscosity of about 4×10^{19} Pas (Guillot et al. 2009).

Based on analysis of data on O^{18}/O^{16} fractionation between coexisting serpentine and magnetite, Wenner and Taylor (1971) suggested that the equilibrium temperatures are 358–388 K for continental lizardite and chrysotile, 403 and 458 K for oceanic lizardite and chrysotile, respectively, 508 K for oceanic antigorite and 493–733 K for continental antigorites. There is a tight relationship between TFFI and the serpentinization temperature and the upper limit of the TFFI temperature range drops to ~723 K with even a small increase in pressure (Pilchin 2005, 2011; Pilchin and Eppelbaum 1997, 2007, 2009). This makes it legitimate to use the serpentine-magnetite geothermometer to calculate the serpentinization temperature. Agrinier and Cannat (1997) also used oxygen-isotope constraints on serpentinization processes to calculate serpentinization temperatures for extensively serpentinized peridotites drilled in the Mid-Atlantic Ridge south of the Kane Fracture Zone, in a range between 703 and 863 K, and they came to conclusion that even though errors of temperature calculation using this method could be as high as about ±120 K, the temperature of serpentinization was above 623 K. Experimental data suggest (Evans 2004) that antigorite is the highest temperature form of serpentine and is usually formed at temperatures from ~523 K to more than 773 K, whereas lizardite and chrysotile can be stable probably to temperatures as high as 673 K. At the same time antigorite is more stable than chrysotile at temperatures >573 K and chrysotile is transformed into antigorite + brucite at temperatures ≥573 K (Evans et al. 1976; Evans 2004). Berman et al. (1986) showed that the transformation of chrysotile into antigorite takes place at temperatures ≥533 K, and antigorite is stable to temperatures of about 823 K. The stability of antigorite above 773 K was also noted by Wang et al. (2009). Other experimental data show that serpentinization of forsterite takes place at temperatures below 703–773 K (Bowen and Tuttle 1949), or below 623–703 K (Johannes 1968). Hess (1955, 1962) thought that the peridotite was serpentinized as it rose through the 500 °C (773 K) isotherm.

Because magnetite is the essential mineral in serpentinites it is obvious that the formation of significant amounts of serpentinites should take place at temperatures above the lower limit of TFFI (473–523 K), or magnetite would not be formed. Thus even though serpentine (especially chrysotile and lizardite) can be formed at temperatures below 473–523 K (Wenner and Taylor 1971) they cannot form serpentinite and especially giant masses of serpentinites at such low temperatures and their presence would not have any significant effect on tectonic processes. Hence the main serpentine mineral in serpentinite massifs must be antigorite. This coincides with data (Coleman 1971) showing that in areas of high-grade metamorphism, antigorite is the predominant serpentine mineral.

The above data are consistent with values within the range of ~473 K to ~673–773 K (e.g. Hess 1955, 1962; Coleman 1977; Pilchin 2005; Pilchin and Eppelbaum 2002) which are usually accepted as the serpentinization temperature.

A comparison of the above data with the fact that ophiolites always contain a peridotite layer serpentinized to different extents shows that ophiolite association must have been formed first (at least its main components) after which its peridotite layer was serpentinized when the temperature of association dropped below the upper limit of the temperature range of serpentinization. It is important to note that during the evolution of any peridotite layer or ophiolite association, peridotite can be serpentinized any time when temperature is within the temperature range of the serpentinization temperature regardless of kind of thermal process (cooling or heating to the serpentinization temperature) taking place. This means that when the ophiolite association first cooled to temperatures within the temperature range of serpentinization, its serpentinization started, but when its temperature dropped below the temperature range of serpentinization (thrusting onto surface, cooling, etc.) the serpentinization process stopped. The process will also stop if temperature within serpentinizing peridotite layer rises above the upper limit of temperature range of serpentinization (rise in temperature, immersion of the layer to greater hotter depths, etc.). But if the temperature within the layer drops or rises at some point to the serpentinization temperature, the serpentinization process will start again. This makes serpentinization a unique process which can operate during both heating and cooling (Pilchin 2005) and in each case it leads to different tectonic processes depending on the rate and extent of serpentinization.

The best example of ocean lithosphere activity involving serpentinization is obduction. A model together with the subsequent activity of remnants of the obducted slab of oceanic lithosphere is discussed in detail in Pilchin and Eppelbaum (2002). The model describes the key steps in the formation and evolution of the obduction process and post-obduction evolution of the continental margin with remnants of an obducted oceanic lithosphere slab (OLS). These steps cover: (1) the start of the activity of OLS caused by the serpentinization process in its peridotite layer to attainment of the ultimate strength limit by rocks of the continental margin under pressure pushing the OLS; (2) the start of destruction of the continental margin by pushing the OLS to the formation of a detachment wedge and the beginning of thrusting of the OLS onto the continental margin; (3) thrusting (obduction) of the OLS onto the continental margin; (4) immersion of a complex slab containing both a detached continental margin wedge and overlying it, part of an OLS to form an isostatic equilibrium to the depth that corresponds to the temperature within the range of serpentinization; (5) start of serpentinization of remnants of the OLS and a new stage of ophiolite/serpentinite activity with the formation of thrusts and other tectonic structures; (6) cessation of the tectonic activity of remnants of OLS each time they are cooled below the lower limit or heated above the upper limit of the serpentinization temperature and re-activation of their activity when their temperature once again is within the range of serpentinization temperature.

It is obvious that the start of serpentinization of the peridotite layer of an OLS will cause either an increase in its volume or an increase of pressure in it when the increase in volume is not possible (Pilchin and Eppelbaum 2002). At the same time, if in the vertical direction (usually up) the increase in volume is not impeded,

its increase in horizontal direction is constrained by surrounding slabs and first of all by the continental margin. This means that attempts to expand in the horizontal direction are blocked by the continental margin, which needs to be removed or destroyed before starting to increase the volume of the OLS in the horizontal direction. It also means that continuing serpentinization will cause a continuing increase of either the volume or the pressure. But pressure cannot grow indefinitely and when its value reaches the ultimate strength of the rocks forming the continental margin, destruction of the continental margin will begin. There are various forms of destruction for instance in the form of detachment of a continental margin wedge, which depending on the detachment fault would be forced by obducting the OLS either below the continent (forcible subduction) or above the continent (obduction) (Pilchin and Eppelbaum 2002). It is clear that depending on extent and rate of serpentinization, the pressure of the OLS on the continental margin can differ and its growth will proceed at a different rate, but in each case the maximum possible pressure occurs immediately before the start of the destruction of the continental margin and/or during the formation of the detachment fault.

Metamorphic rocks with the highest pressure would have been formed at the time of maximal pressure of the OLS onto the continental margin. This is consistent with the fact that in zones of obduction, metamorphic rocks such as eclogites and blueschists are always present (Coleman 1977; Pilchin 2005; Pilchin and Eppelbaum 2002). It was shown (Pilchin and Eppelbaum 2002) that serpentinization of the peridotite layer only by 1 % can generate pressure on order of 1,000 MPa. Hence serpentinization of a peridotite layer by a few percent can generate overpressure capable of the formation of eclogites and blueschists. The *P–T* conditions of metamorphic rocks formed during peak metamorphic conditions in some regions of obduction, ophiolite and serpentinite activity are presented in Table 6.25.

Analysis of the temperatures for the metamorphic conditions with the highest maximal pressures presented in Table 6.25 shows that their corresponding temperatures are too low for depths with such high lithostatic pressure. This means that these rocks could not have been formed at such great depths, but rather that they were formed at much shallower depths in the presence of giant overpressure which could be formed only by horizontal forces. These pressures could be formed not only during the push of the OLS against continental margin, but also during thrusting of the OLS onto the continental margin as a metamorphic sole under the peridotite or ophiolite layer, or during secondary activation of fragments of previously obducted OLS. However, in the case of Oman, the *P–T* conditions with $P = 2.35$ GPa and $T = 653–753$ K (see Table 6.25) definitely took place during the obduction of the Oman ophiolite and such low temperatures could not have been present at depths of ~ 75 km.

The data in Table 6.3 show that there is a discrepancy between the conditions for the maximum temperature (for granulites) and the maximum pressure (for eclogites). In fact, this is consistent with Eq. (2.7.4). The implication is that an external tectonic force was applied on both the eclogite and blueschist facies. The existence of different time periods for maximal pressure and maximal temperature

Table 6.25 Temperatures during peak metamorphic conditions for HP and UHP metamorphic rocks from different regions

Region	*P*, pressure (100 MPa)	*T*, K	References
Saih Hatat, Oman			
Upper plate	6–10	453–708	Gregory et al. (1998)
Lower plate	11–15	773–853	Gregory et al. (1998)
Oman Ophiolite	23.5	653–753	Gregory et al. (1998)
WGR, southeast	15–17.5	~813	Carswell et al. (1999)
Western Tian Shan	14–21	753–853	Gao and Klemd (2003)
South Carpathians	16.1	833	Medaris et al. (2003)
Beigua serpentinite, Ligurian Alps	17.5 ± 0.5	773	Brouwer et al. (2002a)
Gran Paradiso massif, The Alps	12–14	798	Brouwer et al. (2002b)
Western Alps	13–20	603–773	Beyssac et al. (2002)
Ötztal Crystalline Basement, The Alps	27	823-873	Miller and Thöni (1995)
Monte Rosa, Gran Paradiso and Dora-Maira massifs, Westem Alps	15–20	773–823	Chopin (2000)
Lower Austroalpine Nappe	~10	~623	Koller and Höck (1999)
Calcareous Alps	6–10	633–673	Massone and Schreyer (1987)
Acadian metamorphism, Quebec	Peak conditions	< 623	Whitehead et al. (1996)
Yukon-Tanana terrane, Canada	11	~ 783	Perchuk et al. (1999)
Mazatzal-related deformation and metamorphism, The USA	Deformation and metamorphism	≥ 573–623	Romano et al. (2000)
Maksyutovo Complex, Southern Urals	18–21	793–813	Schulte and Sindern (2002)
Palmaro-Caffarella	10–15	723–773	Malatesta et al. (2011)
Voltri Massif	22–28	733–773	Malatesta et al. (2011)
Ambin dome, Western Alps	14–16	773	Ganne et al. (2003)
Ambin–South Vanoise, Western Alps	12–15	<673	Ganne et al. (2003)
Schistes Lustrés,W. Alps	18–20	723–773	Agard et al. (2001)
West Sudetes, Bohemian Massif	≥18–19	733–793	Žačková et al. (2010)
Kaczawa Mts, Poland	8.5	543	Kryza et al. (2011)

(continued)

Table 6.25 (continued)

Region	*P*, pressure (100 MPa)	*T*, K	References
Jędrzychowice, Poland	10–11	603	Achramowicz and Wajsprych (2004)
Schistes Lustrés,W. Alps	18–20	773	Agard et al. (2009)
Monviso, Alps	24	903	Agard et al. (2009)
Zermatt-Saas, Alps	27	823–873	Agard et al. (2009)
Voltri massif, Alps	13–20	773–823	Agard et al. (2009)
Seward Peninsula	12	733	Patrick and Evans (1989)
Meliata, Westerm Carpathians	12	733	Faryad (1999)
South Fork Mountain, California	7	543–583	Brown and Ghent (1983)
Western Tianshans	14–21	753–873	Klemd et al. (2005)
Tavşanlı Zone, Turkey	~24	703–773	Okay and Whitney (2010)
Halilbağı region, Turkey	22–24	793	Okay and Whitney (2010)
Qinghai-Tibet plateau, China	15.6–23.5	<773	Li et al. (2009)
Sesia Zone, Alps (blueschists)	10–15	773–823	Babist et al. (2006)
Sesia Zone, Alps (eclogites)	15–20	773–873	Babist et al. (2006)

is well established for UHP-LT rocks (Carswell and Zhang 1999; Thöni 2002; Pilchin 2005).

As can be seen from Table 6.3, the average temperature and average depth of lithostatic pressure for rocks of the main metamorphic facies are 681 K and 14–15 km for greenschists; 925 K and ~26–27 km for amphibolites, 1,075 K and ~28 km for granulites, 677 K and ~35 km for blueschists, and 856 K and ~64 km for eclogites. These data clearly indicate that in general no two main metamorphic facies took place at the same time at the same depth, because at the same depth the lithostatic pressure is the same, and the temperature values are the same or similar. Even granulites and amphibolites, which can have the same pressures and temperatures, pose a problem since granulites require essentially dry conditions but amphibolites require wet conditions.

The transition from one metamorphic facia to another is also complex because such processes as cooling at great depths cannot be fast and the unloading or loading of lithostatic pressure cannot take place without exhumation or immersion, respectively. Nevertheless, the formation of rocks of different metamorphic facies has been identified in soles below ophiolite thrusts. This is only possible in instances where there was a non-homogeneous distribution of pressure and temperature, such as during an obduction or thrusting process. The best example is the obduction and formation of the Oman ophiolite when up to 20 km thick OLS was obducted onto the Arabian Peninsula in the Cretaceous. Interestingly, during the obduction all five metamorphic facies (greenschists, amphibolites, granulites, eclogites and blueschists) rocks were formed (Lippard 1983; Hacker 1990; Searle and Cox 1999; Bosch et al. 2004). Metamorphic rocks from all five main facies of metamorphism (greenschists, amphibolites, granulites, eclogites and blueschists) have also been found in the Franciscan complex in California (Wakabayashi et al. 2005), the Central Alps (Braga et al. 2003; Liati et al. 2009; Engi 2011) and the Sanbagava Cretaceous metamorphic belt in Japan (Wallis et al. 2000), and rocks of four metamorphic facies (greenschists, amphibolites, eclogites and blueschists) were found in Northern Tien Shan (Mikolaichuk et al. 2008; Togonbaeva et al. 2009). Clearly, favorable *P–T* conditions for the simultaneous formation of all five kinds of metamorphic facies rocks is impossible at any depth within the crust or upper mantle and must take place at or near the surface under non-homogeneous horizontal pressure. A simultaneous non-homogeneous distribution of temperatures could then be generated by friction of an obducting giant plate onto the continental crust, which can be seen in the inversion of metamorphic conditions in all ophiolitic soles and the thickness of these metamorphic soles which depend on the thickness of the obducting plate and the rate of obduction.

The thickness of metamorphic soles under ophiolitic thrusts can vary widely from ~8 m for the Jurassic Donqiao ophiolite of northern Tibet (Zhou et al. 1997) to >870 m in the northern part of the Oman Mountains in the Bani Hamid area of the United Arab Emirates (Searle and Cox 1999). Although the ~8 m thick metamorphic sole under the Donqiao ophiolite ranges from high-grade amphibolites at contact with the overlying harzburgites to greenschist facies metasedimentary rocks lower down (Zhou et al. 1997), the metamorphic sole under the

Oman ophiolite contains up to ~870 m of granulites (Searle and Cox 1999). Based on a review of studies of the metamorphic soles of numerous ophiolite complexes Cox (2000) came to some general conclusions, the most important of which are as follows: metamorphic isotherms inverted through the sole with amphibolite to granulite facies conditions prevailing at the contact with overlaying peridotite and metamorphic conditions are graded structurally down through epidote amphibolite and greenschist facies at the bottom part of the sole over a thickness that rarely exceeds ~500 m; metamorphic isobars are also inverted with the pressure contrasts between the top and the base of the sole; peak pressures computed in metamorphic sole metabasites commonly exceed 1 GPa (~2 GPa in Saih Hatat) despite the fact that overlaying ophiolite complexes never generate lithostatic pressure >0.6 GPa.

It was shown (Pilchin 2005) that from the moment the oceanic lithosphere starts to push against the continental lithosphere, the processes that follow depend on the magnitude of the pushing force, the angle at which the force is applied, the mechanical properties of the contacting rocks and the direction of the formed detachment fault after the applied force overcomes the strength limit of the rock. At this point the presence of a layer, which can be a detachment layer, is very important. The most suitable rocks for a detachment layer are evaporites, carbonates and serpentinites. The hardness of calcite, gypsum and talc is 3, 2 and 1 respectively (Birkeland and Larson 1989), and makes them perfect for detachment formation. Research shows (Allison et al. 1974) that an increase in both temperature and pressure leads to plasticity of limestone. This makes limestone an ideal rock for detachment formation as well. Since the hardness and strength limits of rocks in the upper continental crust are much lower than those of lower continental crust and upper mantle, it is obvious that in most cases the detachment fault is likely to develop within the upper continental crust (obduction). But this does not exclude the possibility of a detachment fault formation in the lower continental crust or its upper mantle (underthrusting).

Some examples of the second stage of OLS activity with a formation decollement fault and thrusting of the continental margin onto continent include the total Grenville belt of Canada (Pilchin 1996a) and the Svecofennian orogeny on the Baltic Shield (Pilchin 1996b). In the case of the Grenville Province, the margin of the Archean-Early Proterozoic craton was detached and thrust onto the craton (Canadian Shield), but the obducting peridotite plate most likely outcropped in the region of the current day Appalachians, because neither the peridotite plate nor serpentinites are present in the Grenvillian province, but they are widely spread throughout the Appalachians. Analysis of geological and geophysical data shows (Rivers et al. 1989) that the Grenville Front fault is the only deep fault within the Grenville Province reaching the crust-mantle boundary and that it continues beneath the Appalachians (see Plate 1 in Rivers et al. 1989). Moreover, the Grenville Front fault zone is composed of a mixture of Archean, Early Proterozoic and Middle Proterozoic rocks with no signs of serpentinites. In the case of the Svecofennian orogeny, Early Proterozoic slabs thrust onto the Archean Baltic

Shield and the only known peridotite/ophiolite layer present are the Jormua suite in northern Finland (Kontinen 1987; Peltonen et al. 1996).

The obvious presence of primary or secondary obduction can be found in regions of the Central and Southern Alps (Bernoulli et al. 1990), the Appalachians (Spencer et al. 1989; Hughes and Luetgert 1991), the Urals (Thouvenot et al. 1995), Oman (Gregory et al. 1998), Northeast Africa (Berhe 1990), the Rocky Mountains (van der Velden and Cook 1996) and many others. In many cases obduction began on the margin of the Archean—Early Proterozoic cratons in regions of the Canadian Shield, the Baltic Shield, the Siberian cratons, Tien Shan, Central and Eastern Europe, etc. In all cases, secondary activations caused either Caledonian or Hercynian orogeny processes with the formation of ophiolitic nappes. It is also well established that the metamorphic sole under the ophiolite thrust or obducted plate was formed during emplacement of the thrust or obducted plate (Gregory et al. 1998; Abd El-Naby et al. 2000; Önen and Hall 2000; Pilchin and Eppelbaum 2002).

It is obvious that in cases of obduction of an OLS on the oceanic lithosphere within mid-ocean ridges (MOR) (e.g., Atlantic MOR) or island arcs regions, the unloading of energy and HP and/or UHP will take place at a distance from continents and it could cease or significantly decrease activity near its contact with a continental margin. For example, obduction of an OLS onto the oceanic lithosphere some time in Mesozoic in the Atlantic MOR (Pilchin 1986) stopped any significant oceanic lithosphere activity on the margins of the Atlantic Ocean to the extent that significant orogenic processes did not take place after the Caledonian orogeny. But the Mid-Atlantic Ridge itself is an orogenic belt. By contrast, the absence of such kind of obduction in the Pacific Ocean, where so huge a MOR as in the Atlantic Ocean was not formed, is the cause of the main activity of Pacific lithosphere on and near its margins by the formation of the Pacific Ring of Fire and young numerous obductions everywhere around the Pacific Ocean.

There are numerous indications of immersion of peridotite plates to different levels within the crust in many regions. Peridotites are present in the middle and lower continental crust of the Bay of Iland Ophiolite, Canada (Bédard and Hébert 1996), under the Lizard Complex, SW England in the Devonian (Cook et al. 2000), and under the Italian Alps in the Late Permian (Mukasa and Shervais 1999). An ophiolitic basement is present in the Coast Range/Great Valley Ophiolite, California (Godfrey and Klemperer 1998), a subhorizontal reflector at 20-km depth beneath the Yarlung Zangbo suture in southern Tibet (Makovsky et al. 1999), etc. The seismology data show that in the middle of the alpine orogeny crust (about 15–30 km depth in Central Alps) and in its upper crust (about 6–10 km) there are two layers with an inversion of seismic velocity and density (Giese et al. 1973; Rybach et al. 1977; Bernoulli et al. 1990). The values of density and seismic velocity in these layers are similar to those of serpentinites. Probably they are fragments of the immersed oceanic plate (or two plates), which was obducted in the Precambrian period. It is obvious that the lower plate has immersed by at least 15 km since the time of obduction. The initial thickness of the Oman Ophiolite

obducted in the Cretaceous was about 10–15 km (Nicolas et al. 2000), and clearly its main part has immersed by now.

Upon the re-activation of remnants of previously obducted OLS, such features as repeated ophiolite/serpentinite activity in the same area, main uplifting processes during cooling of tectonically active units up to a temperature of about 473–723 K, and LT-HP metamorphism at extremely high pressures and low temperatures, etc. take place. For example, in the Greater Caucasus and adjacent areas, ophiolites of Precambrian (Nikishin et al. 2011), Early Paleozoic (Ordovician; Zakariadze et al. 2007), Silurian (V Ye Khain 1984; VE Khain 1984), Carboniferous (V Ye Khain 1984; VE Khain 1984) and eclogites of the Permian age (Philippot et al. 2001) are present. In the Tien Shan region, ophiolites of the Mid-Proterozoic (Makarichev 1978), Early Paleozoic (Lomize et al. 1997; Mikolaichuk et al. 2008), Devonian-Carboniferous (Makarichev 1978; Mikolaichuk et al. 2008), Permian (Mikolaichuk et al. 2008), as well as eclogites of the Ordovician (Togonbaeva et al. 2009) and Devonian (Gao et al. 2000) are present. In the orogenic belt of California, ophiolites dated to the Early-Middle Paleozoic (Wright and Wyld 2006) and Mesozoic (Harper et al. 1994) have been identified in the Klamath Mountains; and Early-Middle Paleozoic (Wright and Wyld 2006), Late Paleozoic (Saleeby 1982) and Mesozoic (Saleeby 1982) age have been found in the Sierra Nevada ophiolite belt. Serpentinites and ophiolites of the Early Paleozoic (e.g., Melcher et al. 2002), Late Paleozoic (e.g., Masson et al. 2008), Mesozoic and Cenozoic (e.g., Dal Piaz et al. 2001; Dal Piaz 2010) age have been found in the Alps. In Japan, ophiolites of the Early Paleozoic, Late Paleozoic, Mesozoic and Cenozoic age are present (Ishiwatari 1994; Ishiwatari et al. 2003; Ishiwatari and Tsujimori 2003). In the Primorye region, in the Russian Far East Early Paleozoic and Late Paleozoic ophiolites and Mesozoic blueschists have been reported (Ishiwatari et al. 2003). In the Koryak Mountains region of Russia, ophiolites from the Early Paleozoic, Late Paleozoic and Mesozoic are known (Ishiwatari et al. 2003). Neoproterozoic, Early Paleozoic, Late Paleozoic and Mesozoic–Cenozoic ophiolites have been found in China (Zhang et al. 2008). One of the clearest proofs of the repeating activity of ophiolites and serpentinites within single orogenic belts is the fact that in many circum-Pacific orogenic belts, the tectonic superposition of ophiolite nappes and mélanges of widely varying ages is present, and these are generally younger in structurally lower nappes (Ishiwatari 1994). For example, in Japan the Ordovician Oeyama ophiolite is thrust over the early Permian Yakuno ophiolite, which in turn is thrust over the Permian Ultra-Tamba accretionary complex, which is underlain by the Jurassic Tamba (Mino) accretionary complex, which is further underlain by the Cretaceous Shimanto and then by the Tertiary Mineoka-Setogawa accretionary complexes (Ishiwatari 1994). This proves that each ophiolite sequence was later re-activated and thrust onto younger ophiolite sequences.

Orogenic belts are among the most important processes related to re-activation of remnants of previously obducted and then immersed peridotite plates. The role of thrusts in orogenic processes is especially visible in the formation of some certain orogenic belts. For example, thrusts are everywhere in the Alps, and they are so strong in Cyprus that some authors (e.g. Kaz'min 1991) claimed that the

autochthon is not visible there. In the case of serpentinization of a peridotite plate which was previously obducted and then immersed to the depth of the serpentinization temperature, the volume increase depends on extent of serpentinization (increase in volume of up to 40 % for 100 % serpentinization; Hess 1955), the thickness of the peridotite layer and its position. The position of the peridotite layer is important because its orientation can affect the increase of volume in the favored upward direction. In some cases exhumed peridotites have been found to be up to 95–100 % serpentinized (Skelton and Valley 2000). This is consistent with the fact that in many cases thrusts are not the main components of orogenic belt formation (as in the Greater Caucasus and Tien Shan) or they are the main visible formations along with other powerful processes in the background (as in the Alps). The Greater Caucasus is mostly composed of rocks of sedimentary origin that have no magmatic activity and only a few manifestations of serpentinites. But the appearance of a thick plate at a depth of $\sim$15 km below the Greater Caucasus as was preliminary calculated by Kerimov et al. (1988) and quantitatively estimated in Eppelbaum and Khesin (2012), and the rapid uplift of the orogenic belt during the Quaternary period (Milanovsky 1968; V Ye Khain 1984) point at a serpentinization process in the middle crust of the belt. In Tien Shan, the presence of serpentinites in the orogenic belt is more common than in the Greater Caucasus, with obvious signs of thrusting of rocks of the Northern Tien Shan onto the continental margin of Archean-Early Proterozoic (Djenchuraeva et al. 2008), and the Southern Tien Shan onto the Northern Tien Shan (Makarichev 1978), but the main cause of rapid uplift of the belt during the Late Cenozoic (Miocene) (Cunningham et al. 2003) most likely younger than 7–10 Ma (Wen et al. 2011) was serpentinization of the peridotite plate in the middle crust. Interestingly, in the Alps region, where both serpentinites and thrusts are present everywhere, seismic data have revealed the presence of thick, low velocity zones at depths of $\sim$15–30 and 6–10 km (Giese et al. 1973; Rybach et al. 1977; Bernoulli et al. 1990) characterized by seismic velocities and densities equal to those of serpentinites, and a rapid uplift of the belt took place in the Lower and Middle Miocene (Champagnac et al. 2009).

The tight links between exhumation and serpentinization and uplift and serpentinization are well known (Pilchin 2005). It is also known that during periods of mountain building, in the Alps the temperature was within the main interval of serpentinization temperature (Pilchin 2005). Research shows (Hurford et al. 1991) a differential cooling of the Penninic Gran Paradiso massif, the Dent Blanche nappe, the Sesia–Lanzo Zone, and the Ivrea Zone blocks (the Alps) to $\sim$498 K by 33 Ma with a few periods of cooling between 33 Ma and the present. Episodic cooling and uplift took place in the Sesia–Lanzo Zone at about 25 and $\sim$12 Ma. In the Lepontine region rapid cooling and uplift took place between 23 and 19 Ma with slower cooling and uplift later (Schmid et al. 1989). In the Alps serpentinization at depth caused unroofing and exhumation of metamorphic and tectonic units including complete massifs and nappes. Interestingly, in all these orogenic belts, the ages of the exposed ophiolites and serpentinites and thrusts are much older than the main stage of these belts' uplift. These orogenic belts are very

different from the Lesser Caucasus orogenic belt, which contains enormous amounts of serpentinites and magmatic rocks. The formation of orogenic belt by melting and eruption of magmatic rocks alone is very problematic, because the increase in the volume of the rocks upon melting would be compensated for by a decrease in volume on crystallization of the erupted lava. Such a rollback is impossible if there is an increase in volume during serpentinization. It is obvious that no orogenic belt formed by magmatic rocks alone would last tens to hundred millions of years. But an orogenic belt formed by both the eruption of magmatic rocks and the formation of serpentinites could last for a long time. The best example of this kind of orogenic belt is the Lesser Caucasus which is composed of enormous amounts of both magmatic rocks and ophiolites/serpentinites. Notably, the Tien Shan main orogenic stage developed after the end of main thrust formations, even though there are numerous signs of serpentinites present (Pilchin 1986).

Main uplifting processes during the cooling of tectonically active units to a temperature within the range 473–723 K took place in such regions as the Alps (Selverstone 1988; Mainprice et al. 1990; Hurford et al. 1991; Ring 1992a), Median Europe (O'Brien 1991; Thury et al. 1994), the Carpathians (Dallmeyer et al. 1998), Oman (Gnos and Nicolas 1996), and the Aegean Zone (Theye and Seidel 1993). The estimated temperature under the footwall of the Ötztal Ophiolite nappe of the Eastern Alps was about 563–623 K during the nappe formation (Froitzheim et al. 1997). It is obvious that metamorphism under temperature conditions of about 473–773 K in regions of obvious serpentinite presence and ophiolite activity is most likely caused by the serpentinization process. This kind of metamorphism is well known in regions of the Alps (Blanckenburg et al. 1989; Von Quadt 1992; Zimmermann et al. 1994), Urals (Leech and Stockli 2000), Oman (Lippard 1983; Gregory et al. 1998), etc. There is also clear evidence of high pressure metamorphism during ophiolite nappe formation (Polino et al. 1990; Ring 1992a). The tight relationships between serpentinites/serpentinized peridotites and HP-LT/UHP-LT rocks have been identified in other regions as well (Pilchin 2005). It is known that the most favorable temperature conditions for both serpentinization and blueschist metamorphism are related to the temperature interval 473–723 K, and blueschists, in almost all cases, have been discovered in regions with serpentinite and/or ophiolite (Pilchin 2005). Both eclogites and blueschists coexist with thrusts and nappes containing peridotites, serpentinites and/or ophiolites in numerous metamorphic belts. Hermann et al. (2000) stated that all eclogites that derive from remnants of the oceanic crust in the Alps are within the stability conditions of serpentine. It is also known (Pilchin 2005) that serpentinites are perfect carriers for exhuming HP-LT and UHP-LT metamorphic rocks. The age of LT deformation and metamorphism for some regions of the Alps and different regions of the world are presented in Tables 6.26 and 6.27, respectively.

All of the above shows that significant tectonic activity of serpentinites and ophiolites was impossible during the Archean (Pilchin 2005; Pilchin and Eppelbaum 2009), because: (1) the peridotite component was less than 1 % of the

Table 6.26 Age of LT deformation and metamorphism in some regions of the Alps

Region	Age, Ma	*p*, pressure 100 MPa	*T*, K	References
Gran Paradiso, Dent Blanche, Sessia - Lanso, and Ivrea Zone Some areas South Pennine nappe North Pennine nappe Suretta nappe Avers Bündnerschiefer Northern Tambo nappe Northern Adula nappe Avers Bündnerschiefer, Suretta nappe, and Northern Tambo nappe	~60		573–623	Hurford et al. (1991)
	~33		498	Hurford et al. (1991)
	D1[a]	12	583–653	Ring (1992b)
	D1	12	693–833	Ring (1992b)
	D2–D3	5	723–773	Ring (1992b)
	D1	8–10	653–693	Ring (1992b)
	Post D1		623–673	Ring (1992a)
	D1	8–10	643–753	Ring (1992a)
	D1		723–823	Ring (1992a)
	D2		673	Ring (1992a)
Same tectonic units	D3		553–563	Ring (1992a)
Adula nappe	D3		573	Ring (1992a)
Northeastern Simano nappe	D3		673	Ring (1992a)
W Tauern Window	Pre-Hercynian	8–12	568–803	Blanckenburg et al. (1989)
SE Tauern Window	240–330		723–773	Von Quadt (1992)
Tauern Window, Lower Schieferhülle	42–39		803	Selverstone (1985)
Same unit	20–17		623	Selverstone (1985)
Same unit	14.5–13		573	Selverstone (1985)
South Vanoise, W. Alps	Pre-D1	12	573	Ganne et al. (2003)
South Vanoise, W. Alps	D1	11	< 673	Ganne et al. (2003)
Ambin, Western Alps	D1	14–16	773	Ganne et al. (2003)

(continued)

Table 6.26 (continued)

Region	Age, Ma	*p*, pressure 100 MPa	*T*, K	References
Ambin, Western Alps	D2	7	673	Ganne et al. (2003)
Engadine window, Alps	Tertiary	12–13	623–673	Bousquet et al. (2002)
Grisons area, Alps Petit St.	Tertiary	12–13	623–673	Bousquet et al. (2002)
Bernard, Alps	Tertiary	15–16	773	Bousquet et al. (2002)
Versoyen unit, Alps	Tertiary	15–16	773	Bousquet et al. (2002)
Schists Lustrés,W. Alps	Mesozoic	8–12	623	Agard et al. (2001)
Sesia Zone, Alps	D1	10–15	773–823	Babist et al. (2006)
Schistes Lustrés,W. Alps	Mesozoic	12–13	623	Agard et al. (2009)

[a] D1, D2 and D3 are deformations in the Pennine zone of the eastern Central Alps (after Ring 1992b)

Table 6.27 Age of LT deformation and metamorphism events in some regions of the world

Region	Age, Ma	*p*, pressure 100 MPa	*T*, K	References
Kvarkush, N. Urals	536	7–8	623–673	Beckholmen and Glodny (2004)
Sanbagawa belt, Japan		5–6	523–573	Banno and Sakai (1989)
Evvia island, Greece	Paleoz-Mesoz	8–9	< 663	Reinecke (1986)
West Sudetes, Bohemia	0.328–330	10.5–13.5	733–793	Žácková et al. (2010)
Kaczawa Mts, Poland	Paleozoic	6	583	Kryza et al. (2011)
Franciscan Complex,USA	Mesozoic	10–12	673	Agard et al. (2009)
Meliata, W. Carpathians	Jurassic	9–10	673	Faryad (1999)
Meliata, W. Carpathians	Jurassic	7–9	623–653	Faryad (1999)
Sanbagawa belt, Japan	Mesozoic	10	823	Wintsch et al. (1999)
Sanbagawa belt, Japan	Mesozoic	4	< 573	Wintsch et al. (1999)
Diego de Almagro Island, Chili	Cretaceous	15	723–773	Hyppolito and Juliani (2011)
Diego de Almagro Island, Chili	Cretaceous	20.4–21.2	803–888	Hyppolito and Juliani (2011)
Western Tien Shan	302–323	9–14	753–843	Klemd et al. (2005)
Çamlıca unit, Anatolia	65–69	11	783	Sengün et al. (2011)
Tavşanlı Zone, Turkey	Cretaceous	9–11	648–673	Okay and Whitney (2010)
Scottish SW Highlands	590	8–10	683–803	Sandiford and Dymoke (1991)
Qinghai-Tibet plateau	215–223	6.7–7.5	683–733	Li et al. (2009)
South Achill, Ireland	460	10.5	733	Chew et al. (2003)
South Achill Beg, Ireland	460	10	598–673	Chew et al. (2003)
Clew Bay Complex, Ireland	460	10	598–673	Chew et al. (2003)
Ile de Groix, France	Variscan	10–12	673–773	Schulz et al. (2001)
Sugözü Nappe, Turkey	Cretaceous	13.5	783	Okay (1989)
Mahmutlar Nappe, Turkey	Permian	6.5	742	Okay (1989)

Archean greenstone belts (GSB) (Nalivkina 1978), and did not exceed 8 % in the Early Proterozoic GSB (Nalivkina 1979); (2) in the Archean magmatic rocks of the Superior Province of Canada the content of olivine is less than 0.4–0.9 % (Goodwin 1977); (3) among the Archean rocks olivine is absent, or extremely rare, and is not even one of the main mafic minerals (Pilchin and Pilchin 1996); (4) ophiolites and serpentinites older than the Early Proterozoic (Desmons 1985; Helmstaedt and Scott 1992; Yakubchuk et al. 1994; Carswell et al. 1999; Pilchin and Eppelbaum 2002) are not known; (5) regions of the Greenstone Belts are not related to the ocean crust (Bickle et al. 1994).

In the Early Precambrian, the temperature within the mantle was a few hundred degrees higher than now (Pilchin and Eppelbaum 2009). This means that the conditions were not present for serpentinization of the peridotite layer of the oceanic lithosphere. This also means that serpentinization did not take place during the Early Precambrian until the first obduction processes in the Early Proterozoic. Only in the early Proterozoic did the temperature of the oceanic lithosphere below oceanic crust cool below the upper limit of serpentinization at about 673–773 K.

References

Abd El-Naby H, Frisch W, Hegner E (2000) Evolution of the Pan-African Haimur metamorphic sole, eastern Desert. Egypt J Metamorph Geol 18(6):639–652

Abe Y (1997) Thermal and chemical evolution of the terrestrial magma ocean. Phys Earth Plan Inter 100(1–4):27–39

Abers GA (2009) Slip on shallow-dipping normal faults. Geology 37(8):767–768

Aboud E, Salem A, Mekkawi M (2011) Curie depth map for Sinai Peninsula, Egypt deduced from the analysis of magnetic data. Tectonophysics 506:1–4, 46–54

Achramowicz S, Wajsprych B (2004) First Sudetic occurrence of jadeite in metabasalts. Mineral Soc Pol Spec Pap 24:53–56

Agard P, Vidal O, Goffé B (2001) Interlayer and Si content of phengite in HP–LT carpholite-bearing metapelites. J Metamorph Geol 19(5):479–495

Agard P, Yamato P, Jolivet L, Burov E (2009) Exhumation of oceanic blueschists and eclogites in subduction zones: timing and mechanisms. Earth Sci Rev 92:53–79

Agee CB (1998) Crystal-liquid density inversions in terrestrial and lunar magmas. Phys Earth Planet Int 107:63–74

Agrinier P, Cannat M (1997) Oxygen-isotope constraints on serpentinization process in ultramafic rocks from the Mid-Atlantic Ridge (23°N). In: Karson JA, Cannat M, Miller DJ, Elthon D (eds) Proceedings of the ocean drilling program, scientific results, vol 153, pp 381–388 (Chapter 20)

Akaogi M, Tanaka A, Ito E (2002) Garnet-ilmenite-perovskite transitions in the system $Mg_4Si_4O_{12}$-$Mg_3Al_2Si_3O_{12}$ at high pressures and high temperatures: phase equilibria, calorimetry and implications for mantle structure. Phys Earth Planet Inter 132(4):303–324

Akhmetov NS (1992a) Inorganic chemistry, vol 1, 3rd edn. "Prosvescheniye" Publisher. Moscow

Akhmetov NS (1992b) Inorganic chemistry, vol 2, 3rd edn. "Prosvescheniye" Publishers, Moscow

Alexandrov KS, Ryzhova TV, Belikov BP (1964) The elastic properties of pyroxenes. Sov Phys Crystallogr 8:589–591

Allison IS, Black RF, Dennison JM, Fahnestock RK, White SM (1974) Geology: the science of a changing Earth, 6th edn. McGraw-Hill Book Co., USA
Altinok E, Ohmoto H (2006) Soil formation beneath the Earth's oldest known (3.46 Ga) unconformity? Geol Soc Am Ann Meet 38(7):533 (abstracts with programs)
Al-Zoubi A (1992) *Deep geologic composition of Jordan by geophysical data*. Ph.D. Thesis, Mining Institute, Sankt-Petersburg (in Russian)
ANCORP (2003) Seismic imaging of a convergent continental margin and plateau in the central Andes (Andean Continental Research Project 1996 (ANCORP'96)), ANCORP working group. J Geophys Res 108(B7, 2328):1–25
Anderson DL (1989) Theory of the Earth. Blackwell Science, Hoboken
Anderson DL (1995) Lithosphere, asthenosphere, and perisphere. Rev Geophys 33(1):125–149
Anderson DL (2002a) The case for irreversible chemical stratification of the mantle. Int Geol Rev 44(2):97–116
Anderson DL (2002b) The inner inner core of Earth. Proc Nat Acad Sci USA 99(22):13966–13968
Anderson DL (2006) Speculations on the nature and cause of mantle heterogeneity. Tectonophysics 416(1–4):7–22
Anderson DL (2007) New theory of the Earth. Cambridge University Press, Cambridge
Anonymous (1972) Penrose Field Conference on ophiolites. Geotimes, 17:24–25
Arndt NT, Nisbet EG (eds) (1982) Komatiites. George Allen & Unwin, London
Artemieva IM, Mooney WD (2001) Thermal thickness and evolution of Precambrian lithosphere: a global study. J Geophys Res 106(B8):16387–16414
Ateş A, Bılım F, Buyuksarac A (2005) Curie point depth investigation of Central Anatolian Turkey. Pure Appl Geophys 162:357–371
Aydın İH, Karat İ, Koçak A (2005) Curie-point depth map of Turkey. Geophys J Int 162(2):633–640
Babist J, Handy MR, Konrad-Schmolke M, Hammerschmidt K (2006) Precollisional, multistage exhumation of subducted continental crust: the Sesia Zone, western Alps. Tectonics 25(TC6008):1–25
Badalyan M (2000) Geothermal features of armenia: a country update. In: Transactions of the world geothermal congress, Kyushu-Tohoku, Japan, pp 71–76
Banno S, Enami M, Hirajima T, Ishiwatari A, Wang QC (2000) Decompression P–T path of coesite eclogite to granulite from Weihai, Eastern China. Lithos 52:97–108
Banno S, Sakai C (1989) Geology and metamorphic evolution of the Sanbagawa metamorphic belt, Japan. In: Daly JS, Cliff RH, Yardley BWD (eds) Evolution of metamorphic belts, vol 43. Geol Soc Spec Publ, pp 519-532
Barley ME, Bekker A, Krapež B (2005) Late Archean to Early Paleoproterozoic global tectonics, environmental change and the rise of atmospheric oxygen. Earth Plan Sci Lett 238:156–171
Barley ME, Kerrich R, Reudavy I, Xie Q (2000) Late Archaean Ti-rich, Al-depleted komatiites and komatiitic volcaniclastic rocks from the Murchison Terrane in western Australia. Aust J Earth Sci 47(5):873–883
Bass JD (1989) Elasticity of grossular and spessartite garnets by Brillouin spectroscopy. J Geophys Res 84:7621–7628
Bech L, Onsgaard J, Hoffmann SV, Godowski PJ (2001) CO dissociation on K-modified Cu(112) and Cu(117). Surf Sci 482–485:243–249
Beckholmen M, Glodny J (2004) Timanian blueschist-facies metamorphism in the Kvarkush metamorphic basement, Northern Urals, Russia. Geol Soc Lond Mem 30:125–134
Bédard JH, Hébert R (1996) The lower crust of the Bay of Islands ophiolite, Canada: Petrology, mineralogy, and the importance of syntexis in magmatic differentiation in ophiolites and at ocean ridges. J Geophys Res Solid Earth 101(B11):25105–25124
Bejarano CA, Jia CQ, Chung KH (2001) A study on carbothermal reduction of sulfur dioxide to elemental sulfur using oilsands fluid coke. Environ Sci Technol 35(4):800–804

Bektaş O, Ravat D, Buyuksarac A, Bılım F, Ateş A (2007) Regional geothermal characterization of East Anatolia from aeromagnetic, heat flow and gravity data. Pure Appl Geophys 164:975–998

Benali O, Abdelmoula M, Refait Ph, Génin J-MR (2001) Effect of orthophosphate on the oxidation products of Fe(II)-Fe(III) hydroxycarbonate: the transformation of green rust to ferrihydrite. Geochim et Cosmochim Acta 65:1715–1726

Benn K, Allard B (1989) Preffered mineral orientations related to magmatic flow in ophiolite layered gabbros. J Petrol 30:925–946

Bennett J, Donahue M, Schneider N, Voit M (2004) The cosmic perspective, 3rd edn. San Francisco Pearson Education Inc. Publishers, Addison Wesley

Berhe SM (1990) Ophiolites in Northeast Africa: implications for Proterozoic crustal growth. J Geol Soc Lond 147:41–57

Berman RG, Engi M, Greenwoood HJ, Brown TH (1986) Derivation of internally-consistent thermodynamic data by the technique of mathematical programming: a review with application to the system MgO-SiO_2-H_2O. J Petrol 21:1331–1364

Bernal JO, Dasgupta DR, Mackay AL (1959) The oxides and hydroxides of iron and their structural inter-relationships. Clay Min Bull 4:15–30

Bernoulli D, Heitzmann P, Zinng A (1990) Central and Southern Alps in southern Switzerland. Tectonic evolution and first results of reflection seismic. In: Roure F, Heitzmann P, Polino R (eds) Deep structure of the Alps. Mém Soc Géol France, 156; Mém Soc Géol Suisse, 1; Mem Soc Geol. Italiana, vol Spec 1, pp 289–303

Best MG (2002) Igneous and metamorphic petrology, 2nd edn. Wiley-Blackwell, Hoboken, 752p

Beyssac O, Rouzaud J-N, Goffé B, Brunet F, Chopin Ch (2002) Graphitization in a high-pressure, low-temperature metamorphic gradient: a Raman microspectroscopy and HRTEM study. Contrib Mineral Petrol 143:19–31

Bhattacharyya BK (1966) Continuous spectrum of the total magnetic field anomaly due to a rectangular prismatic body. Geophysics 31:97–121

Bhattacharyya BK, Leu LK (1975) Analysis of magnetic anomalies over Yellowstone National Park. Mapping the Curie-point isotherm surface for geothermal reconnaissance. J Geophys Res 80:461–465

Bhattacharyya BK, Morley LW (1965) The delineation of deep crustal magnetic bodies from total field aeromagnetic anomalies. J Geomagn Geoelectr 17:237–252

Bickle MJ, Nisbet EG, Martin A (1994) Archean greenstone belts are not oceanic crust? J Geol 102:121–138

Birch F, Schairer JF, Spicer HC (eds) (1942) Handbook of physical constants. Geol Soc Am. Special papers, No. 36

Bird MI, Ayliffe LK, Fifield LK, Turney CSM, Cresswell RG, Barrows TT, David B (1999) Radiocarbon dating of "old" charcoal using a wet oxidation, stepped-combustion procedure. Radiocarbon 41(2):127–140

Birkeland PW, Larson EE (1989) Putnam's geology, 5th edn. Oxford University Press, Oxford

Blackwell DD (1971) The thermal structure of the continental crust. In: Heacock JD (ed) The structure and physical properties of the Earth's crust. AGU, Geophys Monogr Ser, vol 14, pp 169–184

Blakely RJ (1988) Curie temperature isotherm analysis and tectonic implications of aeromagnetic data from Nevada. J Geophys Res 93:817–832

Blanckenburg FV, Villa IM, Baur H, Morteani G, Steiger RH (1989) Time calibration of a PT-path from the western Tauern Window, eastern Alps: the problem of closure temperatures. Contrib Mineral Petrol 101:1–11

Bodri L (1981) Geothermal model of the earth's crust in the Pannonian basin. Tectonophysics 72:61–73

Bohlen SR, Boettcher AL (1982) The quartz $\rightleftharpoons$ coesite transformation: a presize determination and the effects of other components. J Geophys Res 87(B8):7073–7078

Bohlen SR, Dollase WA, Wall VJ (1986) Calibration and applications of spinel equilibria in the system FeO-Al_2O_3-SiO_2. J Petrol 27(Part 5):1143–1156

Bohlen SR, Liotta JJ (1986) A barometer for garnet amphibolites and garnet granulites. J Petrol 27(Part 5):1025–1034
Bohlen SR, Montana A, Kerrick DM (1991) Precise determination of the equilibria kyanite ⇆ sillimanite and kyanite ⇆ andalusite and a revised triple point for Al_2SiO_5 polymorphs. Am Mineral 76:677–680
Bohlen SR, Wall VJ, Boettcher AL (1983) Experimental investigation and application of garnet granulite equilibria. Contrib Mineral Petrol 83:52–61
Bohlen SR, Wall VJ, Boettcher AL (1983a) Experimental investigation and application of garnet granulite equilibria. Contrib Mineral Petrol 83:52–61
Bohlen SR, Wall VJ, Boettcher AL (1983b) Experimental investigations and geological applications of equilibria in the system $FeO\text{-}TiO_2\text{-}Al_2O_3\text{-}SiO_2\text{-}H_2O$. Am Mineral 68:1049–1058
Boland JN (1977) Deformation mechanisms in Alpine-type ultramafic rocks from New Zealand. Tectonophysics 39(1–3):215–230
Bosch D, Jamais M, Boudier F, Nicholas A, Dautria J-M, Agrinier P (2004) Deep and High-temperature Hydrothermal Circulation in the Oman Ophiolite—Petrological and Isotopic Evidence. J Petrol 45(6):1181–1208
Bose K, Ganguly J (1995) Quartz-coesite transition revisited: reversed experimental determination at 500–1200 °C and retrieved thermochemical properties. Am Mineral 80:231–238
Bousquet R, Goffé B, Vidal O, Oberhänsli R, Patriat M (2002) The tectono-metamorphic history of the Valaisan domain from the western to the central Alps: new constraints on the evolution of the Alps. Bull Geol Soc Am 114(2):207–225
Bowen NL, Tuttle OF (1949) The system $MgO\text{-}SiO_2\text{-}H_2O$. Bull Geol Soc Am 60:439–460
Braga R, Callegari A, Messiga B, Ottolini L, Renna MR, Tribuzio R (2003) Origin of prismatine from the Sondalo granulites (Central Alps, northern Italy). Eur J Mineral 15(2):393–400
Brasier M, McLoughlin N, Green O, Wacey D (2006) A fresh look at the fossil evidence for early Archaean cellular life. Phil Trans R. Soc B 361(1470):887–902
Brostigen G, Kjekshus A (1969) Redetermined crystal structure of FeS_2 (pyrite). Acta Chem Scand 23:2186–2188
Brouwer FM, Vissers RLM, Lamb WM (2002a) Metamorphic history of eclogitic metagabbro blocks from a tectonic mélange in the Voltri Massif, Ligurian Alps, Italy. Ofioliti 27:1–16
Brouwer FM, Vissers RLM, Lamb WM (2002b) Structure and metamorphism of the Gran Paradiso massif, western Alps, Italy. Contrib Mineral Petrol 143:450–470
Brown A, Walter M, Cudahy Th (2004) Short-wave infrared reflectance investigation of sites of paleobiological interest: applications for mars exploration. Astrobiology 4(3):359–376
Brown AJ, Cudahy ThJ, Walter MR (2006) Hydrothermal alteration at the Panorama Formation, North Pole Dome, Pilbara Craton, Western Australia. Precambrian Res 151:211–223
Brown EH, Ghent ED (1983) Mineralogy and phase relations in the blueschist facies of the Black Butte and Ball Rock areas, northern California Coast Ranges. Am Mineral 68:365–372
Brown GC, Mussett AE (1993) The Inaccessible Earth. Chapman & Hall, London
Bulina LV (1970) Peculiarities of space distribution of the magnetized formations lower edges for consolidated Earth crust. Izv AN USSR Ser Geol 5:70–75 (in Russian)
Bunds MP (2001) Fault strength and transpressional tectonics along the Castle Mountain strike-slip fault, southern Alaska. GSA Bull 113(7):908–919
Butler RF (1998) Paleomagnetism: magnetic domains to geologic terranes, Electronic edn. Department of Geosciences, University of Arizona Tucson, Arizona
Büyüksaraç A, Bektaş Ö (2007) Curie point depth of inner East Anatolia (Turkey). Geophys Res Abstr, vol 9, 00384, SRef-ID: 1607-7962/gra/EGU2007-A-00384
Basaltic Volcanism on the Terrestrial Planets (BVSP) (1981) By members of the basaltic volcanism study project. Pergamon Press, New York
Byerlee JD (1978) Friction of rocks. Pure Appl Geophys 116:615–626
Byerly PE, Stolt RH (1977) An attempt to define the Curie point isotherm in northern and central Arizona. Geophysics 42:1394–1400

Calvo M, Prévot M, Perrin M, Riisager J (2002) Investigating the reasons for the failure of palaeointensity experiments: a study on historical lava flows from Mt. Etna (Italy). Geophys J Int 149:44–63
Cameron AGW (1997) The origin of the Moon and the single impact hypothesis V. Icarus 126(1):126–137
Carbajal de la Torre G, Espinosa-Medina MA, Martinez-Villafañe A, Gonzalez-Rodriguez JG, Castaño VM (2009) Study of ceramic and hybrid coatings produced by the sol-gel method for corrosion protection. Open Corros J 2:197–203
Carswell DA, Cuthbert SJ, Krogh-Ravna EJ (1999) Ultrahigh-pressure metamorphism in the Western Gneiss Region of the Norwegian Caledonides. Int Geol Rev 41:955–966
Carswell DA, Zhang RY (1999) Petrographic characteristics and metamorphic evolution of ultrahigh-pressure eclogites in plate-collision belts. Int Geol Rev 41:781–798
Champagnac J-D, Schunegger F, Norton K, von Blanckenburg F, Abbühl LM, Schwab M (2009) Erosion-driven uplift of the modern Central Alps. Tectonophysics 474(1–2):236–249
Chen GQ, Ahrens TJ, Stolper EM (2002) Shock-wave equation of state of molten and solid fayalite. Phys Earth Plan Inter 134(1–2):35–52
Cheng H, Reiser DB, Dean S Jr (1999) On the mechanism and energetics of Boudouard reaction at FeO(1 0 0) surface: $2CO \rightarrow C + CO_2$. Catal Today 50(3–4):579–588
Cherniak DJ, Watson EB (2000) Pb diffusion in zircon. Chem Geol 172:5–24
Cherniak DJ, Watson EB (2003) Diffusion in zircon. Rev Mineral Geochem 53:113–143
Chew DM, Daly JS, Page LM, Kennedy MJ (2003) Grampian orogenesis and the development of blueschist-facies metamorphism in western Ireland. J Geol Soc Lond 160:911–924
Chiozzi P, Matsushima J, Okubo Y, Pasquale V, Verdoya M (2005) Curie-point depth from spectral analysis of magnetic data in central–southern Europe. Phys Earth Plan Int 152(4):267–276
Chopin Ch (2000) The internal massifs of the Westem Alps: Monte Rosa, Gran Paradiso and Dora-Maira. In: Proceedings of annual meeting, Swiss Society of Mineralogy and Petrology, Winterthur
Christensen NI (1979) Compressional wave velocities in rocks at high temperatures and pressures, critical thermal gradients, and crustal low-velocity zones. J Geophys Res 84(B12):6849–6859
Chyba ChF (1990) Impact delivery and erosion of planetary oceans in the early inner solar system. Nature 343:129–133
Clark KF (1982) Mineral composition of rocks. In: Carmichael RS (ed) Handbook of physical properties of Rocks, vol I. CRC Press, Florida
Clark SP Jr. (ed) (1966) Handbook of physical constants, revised edn. Geol Soc Am. Memoir 97, Washington, D.C.
Clauser Ch (2009) Heat transport processes in the Earth's crust. Surv Geophys 30:163–191
Coleman RG (1971) Petrologic and geophysical nature of serpentinites. GSA Bull 82(4):897–918
Coleman RG (1977) Ophiolites (Ancient oceanic lithosphere?). Springer, Berlin
Coleman RG, Wang X (1995) Overview of the geology and tectonics of UHPM. In: Coleman RG, Wang X (eds) Ultrahigh pressure metamorphism, Cambridge University Press, Cambridge, pp 1–32
Conard BR, Sridhar R, Warner JS (1980) High-temperature thermodynamic properties of chalcopyrite. J Chem Thermodyn 12:817–833
Condie KC (1981) Archean greenstone belts. Elsevier, Amsterdam
Condie KC (1997) Plate tectonics and crustal evolution, 4th edn. Butterworth Heinemann, Oxford
Condie KC (2001) Mantle plumes and their record in earth history. Cambridge University Press, Cambridge
Condie KC (2005) Earth as an evolving planetary system. Elsevier, Amsterdam
Connard G, Couch R, Gemperle M (1983) Analysis of aeromagnetic measurements from the Cascade range in central Oregon. Geophysics 48:376–390

Cook CA, Holdsworth RE, Styles MT, Pearce JA (2000) Pre-emplacement structural history recorded by mantle peridotites: an example from the Lizard Complex, SW England. J Geol Soc Lond 157:1049–1064

Coombs ML, Gardner JE (2004) Reaction rim growth on olivine in silicic melts –implications for magma mixing. Am Mineral 89(5–6):748–759

Courtial Ph, Ohtani E, Dingwell DR (1997) High-temperature densities of some mantle melts. Geochim et Cosmochim Acta 61:3111–3119

Cox J (2000) Subduction-obduction related petrogenetic and metamorphic evolution of the Semail ophiolite sole in Oman and the United Arab Emirates. PhD thesis, University of Oxford

Cramer SD, Covino BS Jr (eds) (2005) ASM handbook volume 13B, corrosion, 10th edn. Materials ASM International

Cunningham D, Owen LA, Snee LW, Jilliang L (2003) Structural framework of a major intracontinental orogenic termination zone: the easternmost Tien Shan, China. J Geol Soc Lond 160:575–590

Bjonnes E, Lindsay JF (2005) The depositional setting of earth's earliest sedimentary rocks. Lunar and Plan Sci XXXVI:1821

Dal Piaz G (2010) The Italian Alps: a journey across two centuries of Alpine geology. In: Beltrando M, Peccerillo A, Mattei M, Conticelli S, Doglioni C (eds) The geology of Italy: tectonics and life along plate margins, electronic edn, vol 36, paper 8. J Virtual Explorer. doi: 10.3809/jvirtex.2010.00234

Dal Piaz GV, Cortiana G, Del Moro A, Martin S, Pennacchioni G, Tartarotti P (2001) Tertiary age and paleostructural inferences of the eclogitic imprint in the Austroalpine outliers and Zermatt-Saas ophiolite, Western Alps. Int J Earth Sci 90:668–684

Dallmeyer RD, Neubauer F, Fritz H, Mocanu V (1998) Variscan vs. Alpine tectonothermal evolution of the southern Carpathian orogen: constraints from $^{40}Ar/^{39}Ar$ ages. Tectonophysics 290:111–135

Davaille A (1999) Simultaneous generation of hotspots and superswells by convection in a heterogeneous planetary mantle. Nature 402:756–760

Davis BTC, England JL (1964) The melting of forsterite up to 50 kilobars. J Geophys Res 69:1113–1116

Davis D, Suppe J, Dahlen FA (1983) Mechanics of fold-and-thrust belts and accretionary wedges. J Geophys Res 88(B2):1153–1172

Davis GH, Reynolds SJ (1996) Structural geology of rocks and regions. Wiley, NY

Davis JR (ed) (2000) Nickel, cobalt, and their alloys. ASM International Handbook Comm

de Koker NP, Stixrude L, Karki BB (2008) Thermodynamics, structure, dynamics, and freezing of Mg_2SiO_4 liquid at high pressure. Geochim et Cosmochim Acta 72:1427–1441

de Vries ST, Touret JLR (2007) Early Archaean hydrothermal fluids; a study of inclusions from the ~3.4 Ga Buck Ridge Chert, Barberton Greenstone Belt, South Africa. Chem Geol 237:289–302

Desmons J (1985) Ophiolites through time: an introductions. Ofioliti 10(2/3):103–108

Dilek Y (2003) Ophiolite concept and its evolution. In: Dilek Y, Newcomb S (eds) Ophiolite concept and the evolution of geological thought: Boulder, Colorado. Geol Soc Am Spec Pap 373, pp 1–16

DiMarco MJ, Lowe DR (1989) Petrography and provenance of silicified early Archaean volcaniclastic sandstones, eastern Pilbara Block, western Australia. Sedimentology 36(5):821–836

Djenchuraeva RD, Borisov FI, Pak NT, Malyukova NN (2008) Metallogeny and geodynamics of the Aktiuz-Boordu Mining District, Northern Tien Shan, Kyrgyzstan. J Asian Earth Sci 32(2–4):280–299

Dolmaz MN, Ustäomer T, Hisarli ZM, Orbay N (2005) Curie Point Depth variations to infer thermal structure of the crust at the African-Eurasian convergence zone, SW Turkey. Earth Plan Space 57:373–383

Downs RT, Yang H, Hazen RM, Finger LW, Prewitt CT (1999) Compressibility mechanisms of alkali feldspars: New data from reedmergnerite. Am Mineral 84:333–340

Driscoll JP, Mortimer L, Waining B, Cordon E, Beardsmore GR (2009) Geothermal energy potential in selected Aareas of Western Australia (Canning Basin). A report prepared for the Department of Mines and Petroleum, Western Australia. Report DOIR0681008

Eggler DH (1976) Does CO_2 cause partial melting in the low-velocity layer of the mantle? Geology 4(2):69–72

Eggleton RA, Banfield JF (1985) The alteration of granitic biotite to chlorite. Am Mineral 70:902–910

El Nabi SHA (2012) Curie point depth beneath the barramiya–Red Sea coast area estimated from aeromagnetic spectral analysis. Arab J Geosci 5(6):1209–1221

Engi M (2011) Metamorphic structure and evolution of the central Alps. Géochronique 117:1–11

Eppelbaum LV, Khesin BE (2012) Geophysical studies in the Caucasus. Springer, Berlin

Eppelbaum LV, Modelevsky MM, Pilchin AN (1996) Geothermal investigations in the Dead Sea Rift zone, Israel: implications for petroleum geology. J Pet Geol 19(4):425–444

Eppelbaum LV, Pilchin AN (2004) Newly developed maps of Moho and Curie discontinuities for Levant as a basis for innovative models of the Earth's crust on Cyprus and in southern Israel. Transactions of special session of the 2004 CGU/AGU/SEG joint assembly. Montreal, Canada, GP21A-01

Eppelbaum LV, Pilchin AN (2006) Methodology of Curie discontinuity map development for regions with low thermal characteristics: an example from Israel. Earth Plan Sci Lett 243(3–4):536–551

Eriksson PG, Reczko BFF, Callaghan CC (1997) The economic mineral potential of the mid-Proterozoic Waterberg Group, northwestern Kaapvaal craton, South Africa. Miner Deposita 32:401–409

Evans B (2004) The serpentinite multisystem revisited: Chrysotile is metastable. Int Geol Rev 46(6):479–506

Evans BW, Johannes W, Oterdoom H, Trommsdorff V (1976) Stability of chrysotile and antigorite in the serpentinite multisystem. Schweiz Mineral Petrogr Mitt 56:79–93

Farquhar J, Bao H, Thiemans M (2000) Atmospheric influence of Earth's earliest sulfur cycle. Science 289:756–758

Faryad SW (1999) Exhumation of the Meliata high-pressure rocks (Westerm Carpathians): petrological and structural records in blueschists. Acta Monstanistica Slovaca Ročnik 4(2):137–144

Faure G, Mensing TM (2007) Introduction to planetary science: the geological perspective. Springer, Berlin

Fripp REP (1976) Stratabound gold deposits in Archean banded iron-formation, Rhodesia. Economic Geol 71:58–75

Froitzheim N, Conti P, van Daalen M (1997) Late Cretaceous, synorogenic, low-angle normal faulting along the Schlinig fault (Switzerland, Italy, Austria) and its significance for the tectonics of the Eastern Alps. Tectonophysics 280:267–293

Fügenschuh B, Mancktelow NS, Seward D (2000) The Cretaceous to Neogene cooling and exhumation history of the Oetztal-Stubai basement complex, eastern Alps: a structural and fission-track study. Tectonics 19:905–918

Gaboury D, Daigneault D, Beaudoin G (2000) Volcanogenic-related origin of sulfide-rich quartz veins: evidence from O and S isotopes at the Géant Dormant gold mine, Abitibi belt, Canada. Mineral Deposita 35:21–36

Gabriel G, Dressel I, Vogel D (2012) Depths to the bottom of magnetic sources and geothermal prospectivity in southern Germany. First Break 30(4):39–47

Galetsky LS, Derenyuk NE, Bogach DI, Yaroschuk MA, Lebedev YuS, Vaylo AB (1985) Iron-silica rocks of Froonzovskikh magnetic anomalies of the Ukrainean shield. Geophys J 45(5):1–12 (in Russian)

Ganne J, Bussy F, Vidal O (2003) Multi-stage Garnet in the Internal Briançonnais Basement (Ambin Massif, Savoy): New Petrological Constraints on the Blueschist-facies Metamorphism in the Western Alps and Tectonic Implications. J Petrol 44(7):1281–1308

Gao J, Klemd R (2003) Formation of HP–LT rocks and their tectonic implications in the western Tianshan Orogen, NW China: geochemical and age constraints. Lithos 66:1–22

Gao J, Zhang L, Liu Sh (2000) The $^{40}Ar/^{39}Ar$ age record of formation and uplift of the blueschists and eclogites in the western Tianshan Mountains. Chinese Sci Bull 45(11):1047–1051

Garverick L (1994) Corrosion in the petrochemical Industry. ASM International

Gasparik T (1985) Experimentally determined compositions of diopside-jadeite pyroxene in equilibrium with albite and quartz at 1200–1350°C and 15–34 kbar. Geochim et Cosmochim Acta 49:865–870

Gates-Anderson DD, Laue CA, Fitch TE (2004) Dissolution treatment of depleted uranium waste. The US Department of Energy by University of California, Lawrence Livermore National Laboratory, Livermore, UCRL-TR-202275

Geurts FWAH, Sacco A Jr (1992) The relative rates of the boudouard reaction and hydrogenation of CO over Fe and Co foils. Carbon 30(3):415–418

Ghiorso M (2004) An equation of state for silicate melts. Parts I, III, IV. Am J Sci 304:637–678, 752–810, 811–838

Giese P, Morelli C, Steinmetz L (1973) Main features of crustal structure in Western and Southern Europe based on data of explosion seismology. Tectonophysics 20:367–379

Gilotti JA, Ravna EJK (2001) Ultrahigh-pressure metamorphism in the Greenland Caledonides–Microstructural and thermobarometric evidence. GSA annual meeting, Nov 5–8, Paper No. 157-094

Gislason SR, Arnórsson S (1993) Dissolution of primary basaltic minerals in natural waters: saturation state and kinetics. Chem Geol 105(1–3):117–135

Gnos E, Nicolas A (1996) Structural evolution of the northern end of the Oman Ophiolite and enclosed granulites. Tectonophysics 254:111–137

Godfrey NJ, Klemperer SL (1998) Ophiolitic basement to a forearc basin and implications for continental growth: the Coast Range/Great Valley Ophiolite, California. Tectonics 17(4):558–570

Golden DC, Ming DW, Lauer HV Jr, Morris RV (2004) Thermal decomposition of sideritepyrite assemblages: implications for sulfide mineralogy in martian meteorite ALH84001 carbonate globules. Lunar Plan Sci XXXV:1396

Golding SD, Duck LJ, Young E, Baublys KA, Glikson M, Kamber BS (2011) Earliest seafloor hydrothermal systems on Earth: comparison with modern analogues. In: Golding SD, Glikson M (eds) Earliest life on Earth: habitats, environments and methods of detection. Springer B.V., Dordrecht, pp 15–50

Goldman SD, Kasting JF (2005) What does the absence of mass-independent fractionation of sulfur isotopes at 2.8–3.2 Ga say about the early atmosphere? In: EOS, Transactions of AGU, vol 86, No 52, fall meeting supplementry, abstract V21F-06

Gole MJ, Klein C (1981) Banded iron-formations through much of Precambrian time. J Geol 89:169–183

Goodwin AM (1977) Archean volcanism in Superior Proince, Canada Shield. Geol Assoc Can 16:205–241 (special paper)

Gramberg IS, Verba VV, Verba ML, Kos'ko MK (1999) Sedimentary cover thickness map sedimentary basins in the Arctic. Polarforschung 69:243–249

Grandstaff DE, Edelman MJ, Foster RW, Zbinden E, Kimberley MM (1986) Chemistry and mineralogy of Precambrian paleosols at the base of the Dominion and Pongola Groups (Transvaal, South Africa). Precambr Res 32:97–131

Grapes RH, Challis GA (1999) Gersdorffite with pentlandite, violarite, pyrrhotite, and pyrite, northwest Nelson, New Zealand. NZ J Geol Geophys 42:189–204

Green DH, Ringwood AE (1967) An experimental investigation of of the gabbro to eclogite transformation and its petrological applications. Geochim et Cosmochim Acta 31:767–833

Green DH, Ringwood AE (1972) A comparison of recent experimental data on the gabbro—garnet granulite—eclogite transition. J Geol 80(3):277–288

Green TH (1967) An experimental investigation of sub-solidus assemblages formed at high pressure in high-alumina basalt, kyanite eclogite and grosspydite compositions. Contrib Mineral Petrol 16:84–114

Gregory RT, Gray DR, Miller JMcL (1998) Tectonics of the Arabian margin associated with the formation and exhumation of high-pressure rocks, Sultanate of Oman. Tectonics 17(5):657–670

Grønvold F, Stølen S, Tolmach P, Westrum EF Jr (1993) Heat capacities of the wüstite $Fe_{0.9379O}$ and $Fe_{0.9254}O$) at temperatures T from 5 K to 350 K. Thermodynamics of the reaction:$xFe(s) + (1/4)Fe_3O_4(s) = Fe_{0.7500} + xO(s) = Fe_{1-y}O(s)$ at $\approx$850 K, and properties of $Fe_{1-y}O(s)$ to T = 1000 K. Thermodynamics of formation of wüstite. J Chem Thermodyn 25:1089–1117

Groves DI, Phillips GN, Falconer LJ, Houstoun SM, Ho SE, Browning P, Dahl N, Mcnaughton MJ (1987) Evidence for an epigenetic origin for BIF-hosted gold deposits in the greenstone belts of the Yilgarn Block, Western Australia. In: Ho SE, Groves DI (eds) Recent advances in understanding precambrian gold deposits. University of Western Australia, Perth, Publ. 2, pp 167–179

Guillot S, Hattori K, Agard Ph, Schwartz S, Vidal O (2009) In: Lallemand S, Funiciello F (eds) Subduction zone geodynamics. Springer, Berlin, pp 175–205

Gung Y, Panning M, Romanowicz B (2003) Global anisotropy and the thickness of continents. Nature 422:707–711

Gupta CK (2003) Chemical metallurgy: principles and practice. Wiley, Hoboken

Gutenberg B (1959) Physics of the Earth's interior. Academic Press, NY

Hacker BR (1990) Simulation of the metamorphic and deformational history of the metamorphic sole of the Oman Ophiolite. J Geophys Res 95(84):4895–4907

Halliday AN (2008) A young Moon-forming giant impact at 70–110 million years accompanied by late-stage mixing, core formation and degassing of the Earth. Philosoph Trans Ser A, Math Phys Eng Sci 366:4163–4181

Hannington MD, Herzig PM, Scott SD (1991) Auriferous hydrothermal precipitates on the modern seafloor. In: Foster RP (eds) Gold metallogeny and exploration. Blackie & Son Ltd., London, pp 249–282

Harlov DE, Newton RC (1992) Experimental determination of the reaction 2magnetite + 2Kyanite + 4quartz = 2almandine + O_2 at high pressure on the magnetite-hematite buffer. Am Mineral 77:558–564

Harlov DE, Newton RC (1993) Reversal of metastable kyanite + corundum + quartz and andalusite + corundum + quartz equilibria and the enthalpy of formation of kyanite and andalusite. Am Mineral 78:594–600

Harper G, Saleeby J, Heizler M (1994) Formation and emplacement of the Josephine ophiolite and the Nevadan orogeny in the Klamath Mountains, California-Oregon: U/Pb zircon and 40Ar/39Ar geochronology. J Geophys Res 99(B3):4293–4321

Harris AC, White NC, McPhie J, Bull SW, Line MA, Skrzeczynski R, Mernagh TP, Tosdal RM (2009) Early Archean hot springs above epithermal veins, North Pole, Western Australia: new insights from fluid inclusion microanalysis. Econ Geol 104:793–814

Hartlaub R, Dunn C, Davis B (2009) Sediment hosted Cu mineralization of the mesoproterozoic belt-purcell basin, southeast British Columbia. Eos Trans AGU, 90, No 22, Jt. Assem. Suppl, Abstract GA71A-12

Hatton C (2009) Geotherms, lithosphere and sedimentary basins. In: Transactions of the 11th SAGA Biennial technical meeting and exhibition, Swaziland, pp 217–220

Hearmon RFS (1979) The elastic constants of crystals and other anisotropic materials. In: Hellwege KH, Hellwege AM (eds) Landolt-Biirnstein tables, III/11. Springer, Berlin, p l-244

Hearmon RFS (1984) The elastic constants of crystals and other anisotropic materials. In: Hellwege KH, Hellwege AM (eds) Landolt-Biirnstein tables, III/18, Springer, Berlin, pp 1–153

Heinemann S, Sharp TG, Seifert F, Rubie DC (1997) The cubic-tetragonal phase transition in the system majorite ($Mg_4Si_4O_{12}$)—pyrope ($Mg_3Al_2Si_3O_{12}$), and garnet symmetry in the Earth's transition zone. Phys Chem Miner 24(3):206–221

Hellmann R (1994) The albite-water system: part I. The kinetics of dissolution as a function of pH at 100, 200 and 300°C. Geochim et Cosmochim Acta 58(2):595–611

Hellmann R, Dran J-C, Della Mea G (1997) The albite-water system: Part III. Characterization of leached and hydrogen-enriched layers formed at 300°C using MeV ion beam techniques. Geochim et Cosmochim Acta 61(8):1575–1594

Helmstaedt H, Scott DJ (1992) The Proterozoic ophiolite problem. In: Condie KC (ed) Proterozoic crustal evolution: developments in precambrian geology, vol 10. Elsevier, Amsterdam, pp 55–95

Hemingway BS, Bohlen SR, Hankins WB, Westrum EJ, Kuskov OL (1998) Heat capasity and thermodynamic properties for coesite and jadeite: Reexamination of the quartz-coesite equilibrium boundary. Am Mineral 83:409–418

Hermann J, Müntener O, Scambelluri M (2000) The importance of serpentinite mylonites for subduction and exhumation of oceanic crust. Tectonophysics 327:225–238

Hess HH (1955) Serpentinites, orogeny and epeirogeny. Geol Soc Am Spec Pap 62:391–407

Hess HH (1962) History of ocean basins. In: Engel AEJ, James HL, Leonard BF (eds) Petrologic studies: a volume in honor of A.F. Buddington. Geol Soc Am NY, pp 599–620

Hewins RH, Jones RH, Scott ERD (eds) (1996) Chondrules and the protoplanetary disk. Cambridge University Press, Cambridge

Hirschmann MM (2006) Water, melting, and the deep Earth H_2O cycle. Annu Rev Earth Planet Sci 34:629–653

Hofmann A, Wilson AH (2007) Silicified basalts, bedded cherts and other sea floor alteration phenomena of the 3.4 Ga Nondweni Greenstone Belt, South Africa. In: Van Kranendonk MJ, Smithies RH, Bennett VC (eds) Earth's oldest rocks, developments in precambrian geology, vol 15, Condie KC, (series ed), Elsevier, Amsterdam, 571–605 (Chapter 5.5)

Holland HD (1984) The chemical evolution of atmosphere and oceans. Princeton University Press, Princeton

Holland TJB (1979) Experimental determination of the reaction paragonite = jadeite + kyanite + H2O, and internally consistent thermodynamic data for part of the system Na_2O–Al_2O_3–SiO_2–H_2O, with applications to eclogites and blueschists. Contrib Miner Petrol 68:293–301

Holland TJB (1980) The reaction albite = jadeite + quartz determined experimentally in the range 600–1200 °C. Am Mineral 65:129–134

Holleman AF, Wiberg E, Wiberg N (2001) Inorganic chemistry. Academic Press, San Diego

Hong Y, Fegley B Jr (1997) Kinetics and mechanism of pyrite thermal decomposition. Ber Bunsenges Phys Chem 101:1870–1881

Hsü KJ (1994) The geology of switzerland (an introduction to tectonic facies). Princeton University Press, Princeton

Huang W-L, Wylley PJ (1975) Melting reactions in the system $NaAlSi_3O_8$−$KalSi_3O_8$−SiO_2 to 35 kilobars, dry and with excess water. J Geol 83:737–748

Hughes S, Luetgert J (1991) Crustal structure of the western New England appalachians and the adirondack mountains. J Geophys Res 96(B10):16471–16494

Hurford A, Hunziker J, Stöckhert B (1991) Constraints on the late thermotectonic evolution of the western Alps: evidence for episodic rapid uplift. Tectonics 10(4):758–769

Huston DL, Logan GA (2004) Barite, BIFs and bugs: evidence for the evolution of the Earth's early hydrosphere. Earth Plan Sci Lett 220:41–55

Huston DL, Stevens B, Southgate PN, Muhling P, Wyborn L (2006) Australian Zn-Pb-Ag Ore-forming systems: a review and analysis. Econ Geol 101:1117–1157

Hyppolito T, Juliani C (2011) Atoll garnet textures in eclogitic rocks of the Diego de Almagro Island, Chilean Patagonia: Genesis and tectono-metamorphic implications. Geoph Res Abstr, vol 13, EGU2011-786-3

Ikari MJ, Saffer DM, Marone C (2009) Frictional and hydrologic properties of clay-rich fault gouge. J Geophys Res 114:B05409

Ishiwatari A (1994) Circum-Pacific Phanerozoic multiple ophiolite belts. In: Ishiwatari A et al. (eds) Circum-Pacific ophiolites: proceedings of the 29th IGC ophiolite symposium, VSP Publ. Netherlands, pp 7–28

Ishiwatari A, Sokolov SD, Vysotskiy SV (2003) Petrological diversity and origin of ophiolites in Japan and Far East Russia with emphasis on depleted harzburgite. In: Dilek Y, Robinson PT (eds) Ophiolites in Earth history. Geol Soc LondSpec Publ 218, pp 597–617

Ishiwatari A, Tsujimori T (2003) Paleozoic ophiolites and blueschists in Japan and Russian Primorye in the tectonic framework of east Asia: a synthesis. Island Arc 12:190–206

Isley AE, Abbott DH (1999) Plume-related mafic volcanism and the deposition of banded iron formation. J Geophys Res 104:15461–15477

Ito K, Kennedy GC (1971) An experimental stady of basalt—garnet granulite—eclogite transition. In: The structure and physical properties of the Earth's crust, vol 14. Am Geophys Union Geophys Monogr, pp 303–314

Jackson I, Khanna SK (1990) Elasticity, shear-mode softening and high pressure polymorphism of Wiistite (Fe1-xO). J Geophys Res 95:21671–21685

Jakubke H-D, Jeschkeit H (1993) Concise encyclopedia chemistry, revised edn. ABC Chemie, Walter De Gruyter & CO., Berlin

James HL (1983) Distribution of banded iron-formation in space and time. In: Trendall AFR, Morris C (eds) Iron-formation facts and problems. Elsevier, Amsterdam, pp 471–490

Jaupart C, Mareschal JC (2007) Heat flow and thermal structure of the lithosphere. In: Schubert G (ed) Treatise of geophysics vol 6. Elsevier, Oxford, pp 217–252

Johannes W (1968) Experimental investigation of the reaction forsterite + H_2O $\rightleftharpoons$ serpentine + brucite. Contrib Mineral Petrol 19(4):309–315

Johannes W, Chipman DW, Hays JF, Bell PM, Mao HK, Newton RC, Boetcher AL, Seifert F (1971) An Interlaboratory comparison of piston-cylinder pressure calibration using the albite-breakdown reaction. Contrib Miner Petrol 32:24–38

Kamber BS (2007) The enigma of the terrestrial protocrust: Evidence for its former existence and the importance of its complete disappearance. In: van Kranendonk MJ, Smithies HRH, Bennett V (eds) Earth's oldest rocks. Elsevier, Amsterdam, pp 75–90

Karastathis VK, Papoulia J, Di Fiore B, Makris J, Tsambas A, Stampolidis A, Papadopoulos GA (2010) Exploration of the deep structure of the central Greece geothermal field by passive seismic and Curie depth analysis. in: Transactions of the 72nd EAGE conference and exhibition incorporating SPE EUROPEC 2010, Barcelona, Spain

Kasting JF (1993) Earth's early atmosphere. Special section: evolution of atmospheres. Science 259:920–926

Kasting JF, Ackerman TP (1986) Climate consequences of very high carbon dioxide levels in the Earth's early atmosphere. Science 234:1383–1385

Kasting JF, Donahue TM (1980) The evolution of atmospheric oxygen. J Geophys Res 85:3255–3263

Kasting JF, Donahue TM (1981) Evolution of oxygen and ozone in the earth's atmosphere. In: Billingham J (ed) Life in the universe. MIT Press, Cambridge pp 149–162

Kasting JF, Howard MT (2006) Atmospheric composition and climate on the early Earth. Phil Trans R Soc B 361:1733–1742

Kasting JF, Ono S (2006) Palaeoclimates: the first two billion years. Phil Trans R Soc B 361:917–929

Kato T, Enami M, Zhai M (1997) Ultra-high pressure (UHP) marble and eclogite in the Su-Lu UHP terrane, eastern China. J Metamorphic Geol 15:169–182

Kaula WM (1979) Thermal evolution of the Earth and Moon growing by planetesimal impacts. J Geophys Res 84:999–1008

Kaz'min VG (1991) On tectonic conditions of formation of Troodos and Mamonia complexes (Cyprus island). Geotectonics (Geotektonika) 6:104–116 (in Russian)

Kaz'min VG, Verzhbitskii EV (2011) Age and origin of the south Caspian Basin. Oceanology 51(1):131–140

Kent AJR, Hutcheon ID, Ryerson FJ, Phinney DL (2001) The temperature of formation of carbonate in martian meteorite ALH84001: constraints from cation diffusion. Geochim et Cosmochim Acta 65(2):311–321

Kerimov KM, Andreev LI, Pilchin AN et al (1988) Development of the combined geological and geophysical model of the Earth crust of the Caucasus. Scientific report 002-1, Baku, YuzhVNIIGeofizika (in Russian)

Kerimov KM, Pilchin AN, Gadzhiev TG, Buachidze GY (1989). Geothermal map of the Caucasus, scale 1:1,000,000, Baku, cartographic plant No. 11 (in Russian)

Kerimov KM, Pilchin AN, Ibragimov SM (1980) Influence of thermodynamical factor on the overhigh pressure in sedimentary strata. Azerbajan Oil Industry (Azerbaijanskoe Neftyanoe Khozyaistvo) 2:6–9 (in Russian)

Khain V Ye (1973) General geothectonics, 2nd edn. Nedra, Moscow (in Russian)

Khain V Ye (1984) Regional geotectonics. The alpine mediterranean belt. Nauka, Moscow (in Russian)

Khain VE (1984) The alpine-mediterranean fold belt of the USSR. Episodes 7(3):20–29

King DM, Liang X, Burton BB, Akhtar MK, Weimer AW (2008) Passivation of pigment-grade TiO_2 particles by nanothick atomic layer deposited SiO_2 films. Nanotechnology 19(25):255604

Kim RH, Yum BW, Chang HW (2002) Hydrogeochemical and isotopic characteristics for salinization of a shallow groundwater in a coastal area, Youngkwang, Korea Translation in: Proceedings of the 17th salt water intrusion meet., Delft, The Netherlands, 227–237

Kitajima K, Maruyama S, Utsunomiya S, Liou JG (2001) Seafloor hydrothermal alteration at an Archaean mid-ocean ridge. J Metamorphic Geol 19:583–599

Kiyokawa S, Ito T, Ikehara M, Kitajima F (2006) Middle Archean volcano-hydrothermal sequence: bacterial microfossil-bearing 3.2 Ga Dixon Island Formation, coastal Pilbara terrane, Australia. GSA Bull 118(1–2):3–22

Klein C (2005) Some Precambrian banded ironformations (BIFs) from around the world: their age, geologic setting, mineralogy, metamorphism, geochemistry, and origin. Am Miner 90:1473–1499

Klemd R, Bröcker M, Hacker BR, Gao J, Gans P, Wemmer K (2005) New age constraints on the metamorphic evolution of the high-pressure/low-temperature belt in the Western Tianshan Mountains, NW China. J Geol 113:157–168

Klemperer SL (2006) Crustal flow in Tibet: geophysical evidence for the physical state of Tibetan lithosphere, and inferred patterns of active flow. In: Law RD, Searle MP, Godin L (eds) Channel flow, ductile extrusion and exhumation in continental collision zones. Geol Soc Spec Publ 268, pp 39–70

Knittle E (1995) Static compression measurements of equations of state. In: Ahrens TJ (ed) Mineral physics and crystallography: a handbook of physical constants. American Geophysical Union, Washington, DC, pp 98–142

Knoll AH, Grotzinger JP, Kaufman AJ, Kolosov P (1995) Integrated approaches to terminal Proterozoic stratigraphy: an example from the Olenek Uplift, northeastern Siberia. Precambr Res 73:251–270

Koeberl Ch (2006) Impact processes on the early Earth. Elements 2(4):211–216

Kojima S, Hanamuro T, Hayashi K, Haruna M, Ohmoto H (1998) Sulphide minerals in early Archean chemical sedimentary rocks of the eastern Pilbara district, Western Australia. J Miner Petrol 64(1–4):219–235

Koller F, Höck V (1999) Comparison of LT/HP Metamorphism in Mesozoic units of the eastern Alps, Tübinger Geowissenschaftliche Arbeiten. Abstracts of the 4th workshop on alpine geological studies, Tübingen, series A, vol 52, pp 37–38

König I, Haeckel M, Drodt M, Suess E, Trautwein AX (1999) Reactive Fe(II) layers in deep-sea sediments. Geochim et Cosmochim Acta 63:1517–1526

Kontinen A (1987) An early Proterozoic ophiolite—the Jormua mafic—ultramafic Complex, northeastern Finland. Precambr Res 35:313–341

Kopf A, Behrmann JH, Deyhle A, Roller S, Erlenkeuser H (2003) Isotopic evidence (B, C, O) of deep fluid processes in fault rocks from the active Woodlark Basin detachment zone. Earth Plan Sci Lett 208:51–68

Koziol AM (2001) A siderite-magnesite decarbonation study. In: Proceedings of the geological society of america national meeting, vol 33, Abstract No. 25840

Koziol AM (2004) Experimental determination of siderite stability and application to Martian Meteorite ALH84001. Am Mineral 89(2–3):294–300

Kryza R, Willner AP, Massonne H-J, Muszyński A, Schertl H-P (2011) Blueschist-facies metamorphism in the Kaczawa Mountains (Sudetes, SW Poland) of the Central-European Variscides: P–T constraints from a jadeite-bearing metatrachyte. Mineral Mag 75(1):241–263

Kubota M, Kyaw K, Watanabe F, Matsuda H, Hasatani M (2000) Study of decarbonation of $CaCO_3$ for high temperature thermal energy storage. JCEJAB J Chem Eng Jpn 33(5):797–800

Kumar P, Kind R, Hanka W, Wylegalla K, Reigber Ch, Yuan X, Woelbern I, Schwintzer P, Fleming K, Dahl-Jensen T, Larsen TB, Schweitzer J, Priestley K, Gudmundsson O, Wolf D (2005) The lithosphere–asthenosphere boundary in the North-West Atlantic region. Earth Plan Sci Lett 236:249–257

Kurepin VA (1975) Activity of components, thermodynamic characteristics of reactions and phase equilibrium in system Fe–O by high temperature and pressure. Geochemistry (Geokhimiya) 10:1475–1483 (in Russian)

Kutas RI (1978) Field of heat flows and thermal model of earth crust. Naukova Dumka, Kiev (in Russian)

Kutas RI, Kobolev VP, Tsvyashchenko VA (1998) Heat flow and geothermal model of the Black Sea depression. Tectonophysics 291:91–100

Labrosse S, Hernlund JW, Coltice N (2007) A crystallizing dense magma ocean at the base of the Earth's mantle. Nature 450:866–869

Lambert DD, Foster JG, Frick LR, Ripley EM, Zientek ML (1998) Geodynamics of magmatic Cu-Ni-PGE deposits: new insights from the Re-Os isotope system. Econ Geol 93:121–136

Landes M, Hauser F, Popa M (2002) 3-D crustal velocity structure across the Vrancea Zone in Romania, derived from seismic data. In: Transactions of the AGU fall meeting, abstract #S62D-07

Lange RA (1997) A revised model for the density and thermal expansivity of K_2O–Na_2O–CaO–MgO–Al_2O_3–SiO_2 liquids from 700 to 1900 K: extension to crustal magmatic temperatures. Contrib Miner Petrol 130:1–11

Lange RA, Carmichael ISE (1987) Densities of Na_2O–K_2O–CaO–MgO–FeO–Fe_2O_3–Al_2O_3–TiO_2–SiO_2 liquids: new measurements and derived partial molar properties. Geochim et Cosmochim Acta 51:2931–2946

Lee CA, Brandon AD, Norman M (2003) Vanadium in peridotites as a proxy for paleo-fO_2 during partial melting: Prospects, limitations, and implications. Geochim et Cosmochim Acta 67(16):3045–3064

Leech ML, Stockli DF (2000) The late exhumation history of the ultrahighpressure Maksyutov Complex, south Ural Mountains, from new apatite fission track data. Tectonics 19:153–167

Lehrnann I (1961) S and the structure of the upper mantle. Geophys J Roy Astron Soc 4:124–138

Lepland A, Van Zuilen MA, Phillippot P (2011) Fluid-deposited graphite and its geobiological implications in early Archean gneiss from Akilia, Greenland. Geobiology 9(1):2–9

Lerner-Lam A, Jordan T (1983) Earth structure from fundamental and higher-mode waveform analysis. Geophys J R Astron Soc 56:759–797

Li C, Zhai Q, Dong Y, Liu Sh, Xie Ch, Wu Y (2009) High-pressure eclogite-blueschist metamorphic belt and closure of Paleo-Tethis ocean in Central Qingtang, Qinghai-Tibet plateau. J Earth Sci 20(2):209–218

Li J, Agee CB (1996) Geochemistry of mantle-core differentiation at high pressure. Nature 381:686–689

Liati A, Gebauer D, Fanning CM (2009) Geochronological evolution of HP metamorphic rocks of the Adula nappe, Central Alps, in pre-Alpine and Alpine subduction cycles. J Geol Soc 166(4):797–810

Lide DR (ed) (2005) Handbook of chemistry and physics, 86th edn, CRC Press, Taylor & Francis, US

Lillo TM, Delezene-Briggs KM (2005) Commercial alloys for sulfuric acid vaporization in thermochemical hydrogen cycles. In: Transactions of the AiChE 2005 annual meeting, pp 1–11

Lindblom S, Broman S, Martinsson O (1996) Magmatic-hydrothermal fluids in the Pahtohavare Cu-Au deposit in greenstone at Kiruna, Sweden. Miner Deposita 31(4):307–318

Lippard SJ (1983) Cretaceous high pressure metamorphism in NE Oman and its relationship to subduction and ophiolite nappe emplacement. J Geol Soc 140:97–104

Liu J, Bohlen SR (1995) Mixing properties and stability of jadeite-acmite pyroxene in the presence of albite and quartz. Contrib Miner Petrol 119(4):433–440

Lomize MG, Demina MI, Zarschikova AA (1997) Kirgizian-Terseyskiy paleo-ocean basin (Tien Shan). Geotectonics (Geotektonika) 6:35–55 (in Russian)

Louie DK (1961) Handbook of sulfuric acid manufacturing. DKL Engineering Inc., Richmond Hill

Lowe DR (1994) Accretionary history of the Archean Barberton Greenstone Belt (3.55–3.22 Ga), southern Africa. Geology 22(12):1099–1102

Lowe DR, Byerly GR (1999) Stratigraphy of the west-central part of the barberton greenstone belt, South Africa. In: Lowe DR, Byerly GR (eds) Geological evolution of the barberton greenstone belt. Geol Soc Am Spec Pap 329, pp 1–36

Lowe DR, Worrell G (1999) Sedimentology, mineralogy, and implications of silicified evaporites in the Kromberg Formation, Barberton Greenstone Belt, South Africa. In: Lowe DR, Byerly GR (eds) Geologic evolution of the barberton greenstone belt, south Africa. Geol Soc Am Spec Pap 329, pp 167–188

Lowrie A, Fillon RH (2011) Northern Gulf of Mexico continental margin deformation proposed to be by simple shear with regional basal horizon terminating under Yucatan. In: Transactions of the AAPG annual conference and exhibition. Houston, Texas

Lubimova EA (1968a) Thermal history of the earth. In: The earth's crust and upper mantle. Am Geophys Union Geophys Monogr Ser 13:63–77

Lubimova EA, Mayeva SV (1982) Models of the thermal evolution of the Earth. Izv Acad Sci USSR Ser Geophys 6:8–93

Luther GW III (1991) Pyrite synthesis via polysulfide compounds. Geochim et Cosmochim Acta 55:2839–2849

Maden N (2009a) Curie-point depth from spectral analysis of magnetic data in Erciyes Stratovolcano (central Turkey). Pure Appl Geophys 167(3):349–358

Maden N (2009b) Crustal thermal properties of the Central Pontides (Northern Turkey) deduced from spectral analysis of magnetic data, Turkish. J Earth Sci 18:383–392

Mainprice D, Casey M, Schmid S (1990) The seismic properties of Alpine calcite and quartz mylonites determined from the orientation distribution function. In: Rouse F, Heitzmann P, Polino R (eds) Deep structure of the Alps. Mémoires Société Géologique de France, Paris, 156; Mémoires Société Géologique de la Suisse; Zürich, vol. spec. Memorie della Società Geoligica Italiana, Roma, pp 85–96

Makarichev GI (1978) Geosyncline process and formation of the continental crust of the Tien Shan. Priroda, Moscow (in Russian)

Makovsky Y, Klemperer SL, Ratschbacher L, Alsdorf D (1999) Midcrustal reflector on INDEPTH wide angle profiles: an ophiolitic slab beneath the India-Asia suture in southern Tibet? Tectonics 18:793–808

Malatesta C, Gerya T, Scambelluri M, Federico L, Crispini L, Capponi G (2011) Serpentinite channel and the role of serpentinite buoyancy for exhumation of HP rocks (Voltri Massif, Western Alps). Goldschmidt conference abstracts, 1393

Malyshev AI (2004) Sulfur in magmatic ore formation. In: The urals branch of the Russian academy of sciences, Ekaterinburg (in Russian)
Manea M, Manea VC (2011) Curie Point depth estimates and correlation with flat-slab subduction in Mexico. Geophys Res Abst EGU Gen Ass, vol 13, EGU2011-6995
Manning CE, Bohlen SR (1991) The reaction titanite + kyanite = anorthite + rutile and titanite-rutile barometry in eclogites. Contrib Miner Petrol 109:1–9
Mao Z, Jacobsen SD, Jiang F, Smyth JR, Holl CM, Frost DJ, Duffy TS (2010) Velocity crossover between hydrous and anhydrous forsterite at high pressures. Earth Plan Sci Lett 293:250–258
Marschik R, Fontboté L (2001) The Candelaria-Punta del Cobre iron oxide (Cu-Au-Zn-Ag) deposits, Chile. Econ Geol 96:1799–1826
Martienssen W, Warlimont H (eds) (2005) Handbook of condensed matter and materials data, vol 1. Springer, Berlin
Marty B, Meibom A (2007) Noble gas signature of the Late Heavy Bombardment in the Earth's atmosphere. eEarth 2:43–49
Masson H, Bussy F, Eichenberger M, Giroud N, Meilhac C, Presniakov S (2008) Early Carboniferous age of the Versoyen ophiolites and consequences: non-existence of a "Valais ocean" (Lower Penninic, western Alps), vol 179(4). Bull de la Soc Geologique de France, pp 337–355
Massone HJ, Schreyer W (1987) Phengite geobarometry based on the limiting assemblage with K-feldspar, phlogopite and quartz. Contrib Mineral Petrol 96:212–224
Mattisson T, Lyngfelt A (1999) The reaction between limestone and SO_2 under periodically changing oxidizing and reducing conditions - Effect of temperature and limestone type. Thermochim Acta 325(1):59–67
Mazo-Zuluaga J, Barrero CA, Díaz-Terán J, Jerez A (2003) Thermally induced magnetite–haematite transformation. Hyperfine Interact 148–149:153–160
McMullen J, Thomas KG (2002) Gold roasting, autoclaving or bio-oxidation process selection dased on bench-scale and plant test work and costs. In: Mular AL, Halbe DN, Barratt DJ (eds) Mineral processing plant design, practice, and control proceedings, vol. 1, pp 211–250
Medaris G Jr, Ducea M, Ghent E, Iancu V (2003) Conditions and timing of high-pressure Variscan metamorphism in the South Carpathians, Romania. Lithos 70:141–161
Melcher F, Meisel T, Puhl J, Koller F (2002) Petrogenesis and geotectonic setting of ultramafic rocks in the Eastern Alps: constraints from geochemistry. Lithos 65(1–2):69–112
Melosh HJ (1990) Giant impacts and the thermal state of the early Earth. In: Jones J (ed) Origin of the Earth. Oxford University Press, Oxford, pp 69–83
Michard A, Chopin C, Henry C (1993) Compression versus extension in the exhumation of the Dora-Maira coesite-bearing unit, Western Alps, Italy. Tectonophysics 221:173–193
Mikolaichuk AV, Apayarov FKh, Buchroithner MF Chernavskaja ZI, Skrinnik LI, Ghes MD, Neyevin AV, Charimov TA (2008) Geological map of Khan Tengri Massif explanatory note. ISTC Project No. #KR-920, Bishkek
Milanovsky YeYe (1968) Newest geotectonics of the Caucasus. Nauka, Moscow (in Russian)
Miller Ch, Thöni M (1995) Origin of eclogites from the Austroalpine Ötztal basement (Tirol, Austria): geochemistry and Sm-Nd versus Rb-Sr isotope systematics. Chem Geology 122:199–225
Misra MK, Ragland KW, Baker AJ (1993) Wood ash composition as a function of furnace temperature. Biomass Bioenergy 4(2):103–116
Mojzsis S (2009) Geology of 3830 Ma ferruginous quartz-pyroxene (supracrustal) rocks from the Akilia association, southern West Greenland. In: 2009 portland GSA annual meeting. Geological society of America abstracts with programs,vol 41(7), p 394
Möller A, O'Brien PJ, Kennedy A, Kröner A (2002) Polyphase zircon in ultrahigh-temperature granulites (Rogaland, SW Norway): constraints for Pb diffusion in zircon. J Metamorp Geol 20(8):727–740
Moores EM (2002) Pre-1 Ga (pre-Rodinian) ophiolites: their tectonic and environmental implications. Geol Soc Am Bull 114:80–95

Morey GW, Chen WT (1955) The action of hot water on some feldspars. Am Mineral 40:996–1000
Mukasa SB, Shervais JW (1999) Growth of subcontinental lithosphere: evidence from repeated dike injections in the Balmuccia lherzolite massif, Italian Alps. Lithos 48:287–316
Mukhopadhyay M, Krishna MR (1991) Gravity field and deep structure of the Bengal Fan and its surrounding continental margins, northeast Indian Ocean. Tectonophysics 186:365–386
Müller RD, Hillis RR (eds) (2003) Evolution and dynamics of the Australian plate (special papers 372). Geol Soc Am
Myers J, Eugster HP (1983) The system Fe-Si-O: Oxygen buffer calibrations to 1,500 K. Contrib Miner Petrol 82:75–90
Myers JS (2004) Isua enigmas: illusive tectonics, sedimentary, volcanic and organic features of the >3.7 Ga Isua greenstone belt, Southwest Greenland. In: Eriksson PG, Altermann W, Nelson DR, Mueller WU, Catuneanu O (eds) The precambrian Earth: tempos and events. Developments in precambrian geology, vol 12, Condie KC (series ed), Elsevier, Amsterdam, pp 66–74
Myers JS, Crowley JL (2000) Vestiges of life in the oldest Greenland rocks? A review of early Archean geology in the Godthåbsfjord region, and reappraisal of field evidence for >3,850 Ma life on Akilia. Precambr Res 103(3–4):101–124
Mysen BO, Boettcher AL (1975) Melting of a hydrous mantle: I. Phase relations of natural peridotite at high pressures and temperatures with controlled activities of water, carbon dioxide, and hydrogen. J Petrol 16(3):520–548
Nagatha T (1961) Rock magnetism. Maruzen Co., Tokyo
Nakamura D, Banno S (1997) Thermodynamic modelling of sodic pyroxene solid-solution and its application in a garnet-omphacite-kyanite-coesite geothermobarometer for UHP metamorphic rocks. Contrib Miner Petrol 130:93–102
Nakamura K, Kato Y (2002) Carbonate minerals in the Warrawoona Group, Pilbara Craton: Implications for continental crust, life, and global carbon cycle in the Early Archean. Resour Geol 52(2):91–100
Nalivkina AB (1978) Archean ophiolite association: on example of Ukraine. Soviet Geol 3:93–102 (in Russian)
Nalivkina AB (1979) Early proterozoic ophiolite association: on example of Ukraine). Sov Geol 2:112–120 (in Russian)
Naraoka H, Ohtake M, Maruyama S, Ohmoto H (1996) Non-biogenic graphite in 3.8-Ga metamorphic rocks from the Isua district, Greenland. Chem Geol 133(1–4):251–260
Nathenson M, Guffanti M (1988) Geothermal gradients in the conterminous United States. J Geophys Res 93(B6):6437–6450
Newton MS, Kennedy GC (1968) Jadeite, analcite, nepheline, and albite at high temperatures and pressures. Am J Sci 266:728–735
Nichols G (1999) Sedimentology and stratigraphy. Wiley-Blackwell, Malden
Nicolas A, Boudier F, Ildefonse B, Ball E (2000) Accretion of Oman and United Arab Emirates Ophiolite – Discussion of a new structural map. Mar Geophys Resear 21:147–179
Nicolas A, Boudier F, Meshi A (1999) Slow spreading accretion and mantle denudation in the Mirdita optiolite (Albania). J Geophys Res 104(B7):15155–15167
Nikishin AM, Ziegler PA, Bolotov SN, Fokin PA (2011) Late Palaeozoic to Cenozoic evolution of the Black Sea-Southern Eastern Europe region: a view from the Russian platform, Turkish. J Earth Sci 20:1–64
Ninomiya Y, Zhang L, Nagashima T, Koketsu J, Sato A (2004) Combustion and De–SO_x behavior of high-sulfur coals added with calcium acetate produced from biomass pyroligneous acid. Fuel 83(16):2123–2131
Nisbet EG, Sleep NH (2001) The habitat and nature of early life. Nature 409:1083–1091
Nishihara Y, Takahashi E, Matsukage K, Kikegawa T (2003) Thermal equation of state of omphacite. Am Mineral 88:80–86
Nishitani T, Kono M (1983) Curie temperature and lattice constant of oxidized titanomagnetite. Geophys J R Astron Soc 74:585–600

Nutman AP (2006) Antiquity of the oceans and continents. Elements 2(4):223–227
Nwankwo LI, Olasehinde PI, Akoshile CO (2009) An attempt to estimate the Curie-point isotherm depths in the Nupe Basin, West Central Nigeria. Glob J Pure Appl Sci 15(3–4):427–234
O'Brien PJ (1991) Fe rich olivine development during breakdown of eclogite, gt clinopyroxenite and gt websterite from the Variscan basement of NE Bavaria, Germany. In: International eclogite conference and 2nd eclogite field symposium, Granada, Malaga, Spain, Terra Abstracts suppl. 6 to Terra Nova, 3, pp 8–9
O'Hanley DS (1996) Serpentinites. Records of tectonic and petrological history. Oxford University Press, Oxford
O'Neill B, Bass JD, Rossman GR, Geiger CA, Langer K (1991) Elastic properties of pyrope. Phys Chem Miner 17:617–621
O'Reilly SY, Griffin WL (2010) The continental lithosphere–asthenosphere boundary: can we sample it? Lithos 120:1–13
Ohmoto H, Watanabe Y, Ikemi H (2005) The absence of mass independent fractionation of sulfur isotopes in Archean sedimentary rocks; an insignificant phenomenon? Geochim et Cosmochim Acta 69(10):A450
Ohmoto H, Watanabe Y, Ikemi H, Poulson SR, Taylor BE (2006) Sulphur isotope evidence for an oxic Archaean atmosphere. Nature 442:908–911
Okamoto K, Maruyama S (1999) The high-pressure synthesis of lawsonite in the MORB + H_2O system. Am Mineral 84:362–373
Okay AI (1989) An exotic eclogite/blueschist slice in a barrovian style metamorphic terrain, Alanya Nappes, Southern Turkey. J Petrol 30(1):107–132
Okay AI, Whitney DL (2010) Blueschists, eclogites, ophiolites and suture zones in Northwest Turkey: a review and a field excursion guide. Ofioliti 35(2):131–172
Okubo Y, Graf RJ, Hansent RO, Ogawa K, Tsu H (1985) Curie point depths of the island of Kyushu and surrounding areas Japan. Geophysics 53:481–494
Okubo Y, Matsunaga T (1994) Curie-point depth in northeast Japan and its correlation with regional thermal structure and seismicity. J Geophys Res Solid Earth 99(B11):22363–23371
Önen AP, Hall R (2000) Sub-ophiolite metamorphic rocks from NW Anatolia, Turkey. J Metamor Geol 18:483–495
Orberger B, Rouchon V, Westall F, de Vries ST, Pinti DL, Wagner Ch, Wirth R, Hashizume K (2006) Microfacies and origin of some Archean cherts (Pilbara, Australia). In: Reimond WU, Gibson RL (eds) Processes on the early Earth. Geol Soc Am Spec Pap 405, pp 133–156
Pallister JS, Stacey JS, Fischer LB, Premo WR (1988) Precambrian ophiolites of Arabia: geologic setting, U—Pb geochronology, Pb—isotope characteristics, and implications for continental accretion. Precambr Res 38:1–54
Palmqvist AEC, Zwinkels MFM, Zang Y, Järås SG, Muhammed M (1997) Reduction of sulfur dioxide by carbon monoxide over doped nanophase cerium oxides. Nanostruct Naterials 8(7):801–813
Papineau D, DeGregorio BT, Cody GD, Fries MD, Mojzsis SJ, Steele A, Stroud RM, Fogel ML (2010) Ancient graphite in the Eoarchean quartz-pyroxene rock from Akilia in southwest Greenland I: petrographic and spectroscopic characterization. Geochim et Cosmochim Acta 74:5862–5883
Passier HF, de Lange GJ, Dekkers MJ (2001) Magnetic properties and geochemistry of the active oxidation front and the youngest sapropel in the eastern Mediterranean Sea. Geophys J Int 145(3):604–614
Patrick BE, Evans BW (1989) Metamorphic evolution of the Seward Peninsula Blueschist terrane. J Petrol 30(3):531–555
Pavese A, Diella V, Pischedda V, Merli M, Bocchio R, Mezouar M (2001) Pressure-volume-temperature equation of state of andradite and grossular, by high-pressure and -temperature powder diffraction. Phys Chem Miner 28(4):242–248

Pavlenkova GA, Pavlenkova NI (2003) 3-D velocity model of the upper mantle in the northern Eurasia. In: Proceedings of the European geophysical society, geophysical research abstract, vol 5, No. 02666

Pavlenkova GA, Priestley K, Cipar J (2002) 2D model of the crust and uppermost mantle along rift profile, Siberian craton. Tectonophysics 355(1–4):171–186

Pavlenkova NI (1995) On a regional seismic boundary in the uppermost mantle. Izv Russ Acad Sci Phys Solid Earth 31(12):58–71

Pavlenkova NI (1996) General features of the uppermost mantle stratification from long-range seismic profiles. Tectonophysics 264(1–4):261–278

Pavlenkova NI (2006) Long-range profile data on the upper-mantle structure in the Siberian Platform. Russ Geol Geophys 47(5):626–641

Pavlenkova NI (2009). Continental and oceanic lithosphere structure from the long-range seismic profiling. In: Anderson JE, Coates RW (eds) The lithosphere: geochemistry, geology and geophysics. Nova Science Publishers, New York, pp 69–122

Pearson DG, Canil D, Shirey SB (2003) Mantle samples included in volcanic rocks: xenoliths and diamonds. In: Carlson RW (ed) Treatise on geochemistry, vol 2, the Mantle. Elsevier, New York, pp 171–277

Pechersky DM, Bagin VI, Brodskaya SYu, Sharonov ZV (1975) Magnetism and conditions of generation for igneous mountainous rocks. Nauka, Moscow (in Russian)

Peltonen P, Kontinen A, Huhma H (1996) Petrology and geochemistry of metabasalts from the 1.95 Ga Jormua ophiolite, northeastern Finland. J Petrol 376:1359–1383

Perchuk A, Philippot P, Erdmer Ph, Fialin M (1999) Rates of thermal equilibration at the onset of subduction deduced from diffusion modeling of eclogitic garnets, Yukon-Tanana terrane, Canada. Geology 27:531–534

Perkins D III (1983) The stability of Mg-rich garnet in the system CaO-MgO-Al_2O_3-SiO_2 at 1000–1300 °C and high pressure. Am Mineral 68:355–364

Perry GJ, Gray A, Mackay GH (1985) Carbonate formation during hydrogenation of Victorian brown coal. Fuel Process Technol 10(3):285–297

Philippot P, Blichert-Toft J, Perchuk A, Costa S, Gerasimov V (2001) Lu–Hf and Ar–Ar chronometry supports extreme rate of subduction zone metamorphism deduced from geospeedometry. Tectonophysics 342(1–2):23–38

Phillips GN, Groves DI, Martyn JE (1984) An epigenetic origin for Archaean banded iron-formation-hosted gold deposits. Econ Geol 79:162–171

Philpotts AR (1990) Principles of igneous and metamorphic petrology. Prentice Hall, Upper Saddle River

Pilchin A (1983) Geothermal regime of Earth's crust of the Kura depression and its influence on pressure distribution in it. PhD thesis, Institute of Geophysics of the Georgia Academy of Sciences, Tbilisi (in Russian)

Pilchin A, Eppelbaum L (2012) The early Earth formation and evolution of the lithosphere in the Hadean–Middle Archean. In: Sato F, Nakamura Sh (eds) Encyclopedia of Earth science research, vol 1. pp 1–93 (Chapter 1)

Pilchin AN (1978a) Correction to hydrostatic pressure in the crust of the Middle Kura depression. In: Geophysical researches of the oil, gas and ore deposits in Azerbaijan, Baku, pp 78–80 (in Russian)

Pilchin AN (1978b) Estimation of thermodynamic condition of intervals of terrigenous transsection by speead of change of geothermal gradient with depth. Explor Geophys (Razvedochnaya Geofizika) 83:112–116

Pilchin AN (1985a) Method of the stresses in a mountain massif determination, USSR, Patent No. 1,170,143, Bulletin of inventions, No. 28 (in Russian)

Pilchin AN (1986) On the role of pressures in tectonic processes. VINITI Press, No. 3723-86, pp 1–23 (in Russian)

Pilchin AN (1987b) The origin of ultra high pressures generation in the oceans earth crust and upper mantle. In: Transaction of the 1st All-Union meeting on marine geophysics, Baku, p 31 (in Russian)

Pilchin AN (1996a) Tectonic and petrologic peculiarities of the Grenville province formation. In: Transactions of geological association of Canada and mineral association of Canada annual meeting, vol 21, p A-75

Pilchin AN (1996b) Tectonic and petrologic peculiarities of the Precambrian evolution of the Baltic shield. Extended abstracts book, 58th EAGE conference and technical exhibition, Amsterdam, p P-513

Pilchin AN (2005) The role of serpentinization in exhumation of high- to ultra-high-pressure metamorphic rocks. Earth Plan Sci Lett 237(3–4):815–828

Pilchin AN (2011) Magnetite: the story of the mineral′s formation and stability. In: Angrove DM (ed) Magnetite: structure, properties and applications. Nova Science Publishers, New York, pp 1–99 (Chapter 1)

Pilchin AN, Eppelbaum LV (1997) Determination of the lower edges of magnetized bodies by using geothermal data. Geophys J Int 128:167–174

Pilchin AN, Eppelbaum LV (2002) Some peculiarities of thermodynamic conditions of the Earth crust and upper mantle. Sci Isr 4(1–2):117–142

Pilchin AN, Eppelbaum LV (2004) On the stability of ferrous and ferric iron oxides and its role in rocks and rock-forming minerals stability. Sci Isr 6(3–4):119–135

Pilchin AN, Eppelbaum LV (2005) On the role of thermodynamic conditions in rocks and minerals stability. Sci Isr 7(1–2):88–105

Pilchin AN, Eppelbaum LV (2006) Iron and its unique role in earth evolution, vol 9. Mexican Geophysics Society, pp 1–67

Pilchin AN, Eppelbaum LV (2007) Stability of iron oxides in the Earth and their role in the formation of rock magnetism. Acta Geofisica 55(2):133–153

Pilchin AN, Eppelbaum LV (2008a) Iron content of magmatic rocks as a marker of mantle heterogeneity. Transactions of the 33rd international geological conference, Oslo, Norway, EID05421P

Pilchin AN, Eppelbaum LV (2008b) Some causes of initial mantle heterogeneity. In: Transactions of the 33rd international geological conference, Oslo, Norway, EID05422P

Pilchin AN, Eppelbaum LV (2009) The early Earth and formation of the lithosphere. In: Anderson JE, Coates RW (eds) The lithosphere: geochemistry, geology and geophysics. Nova Science Publishers, New York, pp 1–68 (Chapter 1)

Pilchin AN, Khesin BE (1981) On possible nature of the magnitoactive bodies of bottom edges. Explor Geophys (Razvedochnaya Geofizika) 92:123–127 (in Russian)

Pilchin MM, Pilchin AN (1996) Petrology and some peculiarities of mineral composition of the early Precambrian rocks of Canadian shield. In: Transaction of geological associationof Canada and mineral. Association of Canada annual meeting, vol 21, p A-75

Pinti DL, Mineau R, Clement V (2009) Hydrothermal alteration and microfossil artefacts of the 3,465-million-year-old Apex chert. Nat Geosci 2:640–643

Pirajno F (2010) Hydrothermal processes and mineral systems. Springer, Berlin

Polino R, Dal Piaz GV, Gosso G (1990) Tectonic evolution at the Adria margin and accretionaly processes for the Cretaceous orogeny in the Alps. In: Roure F, Heitzmann P, Polino R (eds) Deep Structure of the Alps. Mémoires Société Géologique de France, Paris, 156; Mémoires Société Géologique de la Suisse; Zürich, Memorie della Società Geoligica Italiana, Roma, pp 345–367

Pollack HN (1997) Thermal characteristics of the Archaean. In: de Wit MJ, Ashwal MD (eds) Greenstone belts. Clarendon Press, Oxford, pp 223–232

Pollard DD, Fletcher RC (2005) Fundamentals of structural geology. Cambridge University Press, Cambridge

Post RL (1977) High-temperature creep of Mt. Barnet Dunite. Tectonophysics 42(2):75–110

Prewitt CT, Sueno S, Papike JJ (1976) The crystal structures of high albite and monalbite at high temperatures. Am Mineral 61:1213–1225

Prothero DR, Schwab F (1996) Sedimentary geology: an introduction to sedimentary rocks and stratigraphy. Freeman, W. H

Pugin VA, Khitarov NI (1978) Eclogites as source of quartz-normative magmas. Geochemistry (Geokhimia) 10:1506–1512
Qingqing Q, Qingsheng L, Ning Q, Yuanyuan F, Sutao Z, Yao Q, Tao Y, Zhenmin J (2008) Investigation of curie point depth in sulu ultrahigh-pressure metamorphic belt, eastern China. J China Univ Geosci 19(3):282–291
Rao YK (1974) A physical-chemical model for reactions between particulate solids occurring through gaseous intermediates—1. Reduction of hematite by carbon. Chem Eng Sci 29:1435–1445
Redl FX, Black CT, Papaefthymiou GC, Sandstrom RL, Yin M, Zeng H, Murray ChB, O'Brien SP (2004) Magnetic, electronic, and structural characterization of nonstoichiometric iron oxides at the nanoscale. J Am Chem Soc 126:14583–14599
Reinecke T (1986) Crystal chemistry and reaction relations of piemontites and thulites from highly oxidized low grade metamorphic rocks at Vitali, Andros Island, Greece. Contrib Mineral Petrol 93:56–76
Righter K, Drake MJ (1997a) A magma ocean on Vesta: Core formation and petrogenesis of eucrites and diogenites. Met Planet Sci 32:929–944
Righter K, Drake MJ (1997b) Metal-silicate equilibrium in a homogeneously accreting earth: new results for Re. Earth Plan Sci Lett 146(3–4):541–553
Ring U (1992a) The Alpine geodynamic evolution of Penninic nappes in the eastern Central Alps: geothermobarometric and kinematic data. J Metamorphic Geol 10:33–53
Ring U (1992b) The kinematic history of the Penninic napes east of the Lepontine dome: implications for the tectonic evolution of the central Alps. Tectonics 11(6):1139–1158
Rivers T, Martignole J, Gower C, Davidson A (1989) New tectonic divisions of the Grenville province, southeast Canadian shield. Tectonics 8(1):63–84
Romano D, Holm DK, Foland KA (2000) Determining the extent and nature of Mazatzal-related overprinting of the Penokean orogenic belt in the southern Lake Superior region, north-central USA. Precambr Res 104:25–46
Ross HE, Blakely RJ, Zoback MD (2006) Testing the use of aeromagnetic data for the determination of Curie depth in California. Geophysics 71(5):L51–L59
Rouchon V, Orberger B, Hofmann A, Pinti DL (2009) Diagenetic Fe-carbonates in Paleoarchean felsic sedimentary rocks (Hooggenoeg Formation, Barberton greenstone belt, South Africa): Implications for CO_2 sequestration and the chemical budget of seawater. Precambr Res 172:255–278
Rudnick RL (1997) Thermal structure of Archean cratons: a new look at conductive geotherms and xenolith P–T arrays. In: Proceedings of the 7th annual V.M. Goldschmidt conference, No. 2281
Rybach L, Werner D, Mueller S, Berset G (1977) Heat flow, heat production and crustal dynamics in the Central Alps, Switzerland. Tectonophysics 41:113–126
Rychert CA, Shearer PM (2009) A global view of the lithosphere-asthenosphere boundary. Science 324(5926):495–498
Rye R, Holland HD (1998) Paleosols and the evolution of atmospheric oxygen: a critical review. Am J Sci 298:621–672
Safronov VS (1978) The heating of the earth during its formation. Icarus 33(1):3–12
Saleeby J (1982) Polygenetic ophiolite belt of the California Sierra Nevada: Geochronological and tectonostratigraphic development. J Geophys Res 87(B3):1803–1824
Salem A, Ushijima K, Elsirafi A, Mizunaga H (2000) Spectral analysis of aeromagnetic data for geothermal reconnaissance of Quseir area, Northern Red Sea, Egypt. In: Proceedings of the world geothermal congress, Kyushu-Tohoku, Japan, pp 1669–1674
Sandiford M, Dymoke P (1991) Some remarks on the stability of blueschists and related high P-low T assemblages in continental orogens. EarthPlan Sci Lett 102:14–23
Savelieva GN, Denisova EA (1983) Structure and petrology of ultrabasit Nuraly massif of the Soutern Urals. Geotectonics (Geotektonika) 2:42–57 (in Russian)

Schmädicke E, Müller WF (2000) Unusual exsolution phenomena in omphacite and partial replacement of phengite by phlogopite + kyanite in an eclogite from the Erzgebirge. Contrib Miner Petrol 139(6):629–642

Schmid SM, Aebli HR, Heller F, Zingg A (1989) The role of the Periadriatic Line in the tectonic evolution of the Alps. Geol Soc Spec Publ Lond 45:153–171

Schmidt MW, Poli S, Comodi P, Zanazzi PF (1997) High-pressure behavior of kyanite: decomposition of kyanite into stishovite and corundum. Am Mineral 82:460–466

Schubert G, Turcotte DL, Olson P (2001) Mantle convection in the earth and planets, 2 volume set. Cambridge University Press, Cambridge

Schulte B, Sindern S (2002) K-rich fluid metasomatism at high-pressure metamorphic conditions: Lawsonite decomposition in rodingitized ultramafite of the Maksyutovo Complex, Southern Urals (Russia). J Metamorp Geol 20:529–542

Schulz B, Triboulet C, Audren C, Pfeifer H-R, Gilg A (2001) Two-stage prograde and retrograde Variscan metamorphism of glaucophane-eclogites, blueschists and greenschists from Ile de Groix (Brittany, France). Int J Earth Sci 90(4):871–889

Scott HP, Hemley RJ, Mao H, Herschbach DR, Fried LE, Howard WM, Bastea S (2004) Generation of methane in the Earth's mantle: in situ high pressure–temperature measurements of carbonate reduction. In: Proceedings of the national acadamic science, USA, vol 101(39), pp 14023–14026

Searle M, Cox J (1999) Tectonic setting, origin, and obduction of the Oman ophiolite. GSA Bull 111(1):104–122

Seiff A, Shofield JT, Kliore AJ, Taylor FW, Limaye SS, Revercomb HE, Sromovsky LA, Kerzhanovich VI, Moroz VI, Marov MY (1986) Models of the structure of the atmosphere of Venus from the surface to 100 km altitude. In: Kliore AJ, Moroz VI, Keating GM (eds) The venus international reference atmosphere. Pergamon, Oxford, pp 3–58

Selverstone J (1985) Petrologic constants on imbrication, metamorphism, and uplift in the SW Tauern Window, Eastern Alps. Tectonics 4:687–704

Selverstone J (1988) Evidence for east-west crustal extension in the eastern Alps: implications for the unroofing history of the Tauern window. Tectonics 7(1):87–105

Selvig LK, Inn KGW, Outola IMJ, Kurosaki H, Lee KA (2005) Dissolution of resistate minerals containing uranium and thorium: Environmental implications. J Radioanal Nucl Chem 263(2):341–348

Şengün F, Yığıtbaş E, Tunç İO (2011) Geology and tectonic emplacement of eclogite and blueschists, Biga Peninsula, Northwest Turkey, Turkish. J Earth Sci 20:273–285

Sharma SR, Rao VK, Mall DM, Gowd TN (2005) Geothermal structure in a seismoactive region of central India. Pure Appl Geophys 162(1):129–144

Sharma T, Clayton RN (1965) Measurement of 0-18/0-16 ratios of total oxygen of carbonates. Geochim et Cosmochim Acta 29:1347–1353

Sharp ZD, Papike JJ, Durakiewicz T (2003) The effect of thermal decarbonation on stable isotope compositions of carbonates. Am Mineral 88(1):87–92

Sherman DM (1989) The nature of the pressure induced metallization of FeO and its implications to the core–mantle boundary. Geophys Res Lett 16(6):515–518

Shervais JW (2006) Significance of subduction-related accretionary complexes in early Earth processes. In: Reimold U, Gibson R (eds) Early earth processes, Geol Soc Am Spec Pap 405, pp 173–192

Shin DY, Kim KN, Nam I-T, Han SM (2006) Improvement of corrosion resistance of stainless steel by ZrO_2–SiO_2 Sol-gel coatings. In: Kim HS, Li YB, Lee SW (eds) Eco-materials processing & design VII, materials science forum, vol 510–511, pp 442–445

Shiraishi Y, Ikeda K, Tamura A, Saito T (1978) On the viscosity and density of the molten FeO-SiO_2 system. Trans Jpn Inst Metal 19:264–274

Shuey RT, Schellinger DK, Tripp AC, Alley LB (1977) Curie depth determination from aeromagnetic spectra. Geophys. J Roy Astron Soc 50:75–101

Shumlyanska L, Tsvetkova T, Bugaenko I, Zayets L (2006) 3-D velocity model of the upper mantle of the south-western part of the east-European platform. Geophys Res Abstr 8:00762
Singh RN, Negi JG (1982) High Moho temperature in the Indian shield. Tectonophysics 82(3–4):299–306
Skelton ADL, Valley JW (2000) The relative timing of serpentinisation and mantle exhumation at the ocean-continent transition, Iberia: constraints from oxygen isotopes. Earth Plan Sci Lett 178:327–338
Skinner BJ (1966) Thermal expansion. In: Clark SP Jr. (ed) Handbook of physical constants, Geol Sot Am Mem, pp 75–95
Sleep NH (2010) The Hadean-Archaean environment. Cold Spring Harb Perspect Biol 2(6):a002527
Smith DC (1984) Coesite in clinopyroxene in the Caledonides and its implications for geodynamics. Nature 310:641–644
Smith DC, Lappin MA (1989) Coesite in the Straumen kyanite-eclogite pod, Norway. Terra Nova 1:47–56
Sobolev VS (ed) (1972) The facies of metamorphism. Nedra, Moscow (in Russian)
Soga N (1967) Elastic constants of garnet under pressure and temperature. J Geophys Res 72:4227–4234
Solomatov VS (2000) Fluid dynamics of a terrestrial magma ocean. In: Canup R, Righter K (eds) Origin of the Earth and Moon. University of Arizona Press, Tucson, pp 323–338
Song M, Xie H, Zheng H, Xu Y, Guo J, Xu Z (1996) P-wave velocities of main upper mantle minerals at high temperature and high pressure and its geological implications. Sci China Ser D 39(1):93–100
Spector A, Grant FS (1970) Statistical models for interpreting aeromagnetic data. Geophys 35:293–302
Speight JG (2005) Lange's handbook of chemistry, 16th edn. McGaw-Hill, New York
Spencer C, Green A, Morel-à-l'Huissier P, Milkereit B, Luetgert J, Stewart D, Unger J, Phillips J (1989) The extension of Grenville basement beneath the northern Appalachians: Results from the Quebec-Maine reflection and refraction surveys. Tectonics 8(4):677–696
Spohn T, Schubert G (1991) Thermal equilibration of the Earth following a giant impact. Geophys J Int 107:163–170
Stampolidis A, Tsokas GN (2002) Curie point depths of Macedonia and Thrace, N Greece. Pure Appl Geophys 159:2659–2671
Stevenson DJ (2008) A planetary perspective on the deep Earth. Nature 451:261–265
Stiegler MT, Lowe DR, Byerly GR (2010) The Petrogenesis of Volcaniclastic Komatiites in the Barberton Greenstone Belt, South Africa: a textural and geochemical study. J Petrol 51(4):947–972
Stoessell RK, Klimentidis RE, Prezbindowski DR (1987) Dedolomitization in Na–Ca–Cl brines from 100° to 200°C at 300 bars. Geochim et Cosmochim Acta 51(4):847–855
Stovba SM, Maystrenko YuP, Stephenson RA, Kusznir NJ (2003) The formation of the south-eastern part of the Dniepr-Donets Basin: 2-D forward and reverse modelling taking into account post-rift redeposition of syn-rift salt. Sediment Geol 156:11–33
Sugitani K, Mimura K, Suzuki K, Nagamine K, Sugisaki R (2003) Stratigraphy and sedimentary petrology of an Archean volcanic-sedimentary succession at Mt. Goldsworthy in the Pilbara Block, Western Australia: implications of evaporite (nahcolite) and barite deposition. Precambrian Res 120:55–79
Sugitani K, Yamashita F, Nagaoka T, Minami M, Yamamoto K (2006b) Geochemistry of heavily altered Archean volcanic and volcaniclastic rocks of the Warrawoona Group, at Mt. Goldsworthy in the Pilbara Craton, Western Australia: implications for alteration and origin. Geochem J 40:523–535
Sugitani K, Yamashita F, Nagaoka T, Yamamoto K, Minami M, Mimura K, Suzuki K (2006a) Geochemistry and sedimentary petrology of Archean clastic sedimentary rocks at Mt. Goldsworthy, Pilbara Craton, Western Australia: evidence for the early evolution of continental crust and hydrothermal alteration. Precambrian Res 147:124–147

Sugiyama T (2010) Material design of sulfuric acid resistance material. In: Proceedings of Tokyo Tech—EPFL joint workshop, No. 09D06020

Suzuki I, Anderson OL (1983) Elasticity and thermal expansion of a natural garnet up to 1,080 K. J Phys Earth 31:125–138

Svetov SA, Smolkin VF (2003) Model P–T conditions of high-magnesia magma generation in the Precambrian of the fennoscandian shield. Geochem Int 41(8):799–811

Tackley PJ (1998) Three dimensional simulations of mantle convection with a thermo-chemical basal boundary layer. In: Gurnis M, Wysession ME, Knittle E, Buffett BA (eds) The core-mantle boundary region. Geophysics union, geodynamics series, vol 28. Washington, DC., pp 231–253

Tackley PJ (2000) Mantle convection and plate tectonics: toward an integrated physical and chemical theory. Science 288:2002–2007

Takahashi E (1990) Speculations on the Archean mantle: missing link between komatiite and depleted garnet peridotite. J Geophys Res 95(B10):15941–15954

Tanaka A, Okubo Y, Matsubayashi O (1999) Curie point depth based on spectrum analysis of the magnetic anomaly data in East and Southeast Asia. Tectonophysics 306:461–470

Tartaj P, Serna CJ, Moya JS, Requena J, Ocaña M, De Aza S, Guitian F (1996) The formation of zircon from amorphous $ZrO_2{\cdot}SiO_2$ powders. J Mater Sci 31(22):6089–6094

Terry MP, Robinson P, Krough Ravna EJ (2000) Kyanite eclogite thermobarometry and evidence for thrusting of UHP over HP metamorphic rocks, Nordøyane, Western Gneiss Region. Norway Am Mineral 85:1637–1650

ThermExce (2003) http://www.thermexcel.com/english/tables/eau_boui.htm. Retrieved on 12 Nov 2013

Theye T, Seidel E (1993) Uplift-related retrogression history of aragonite marbles in Western Crete (Greece). Contrib Mineral Petrol 114:349–356

Thöni M (2002) Sm-Nd isotope systematics in garnet from different lithologies (Eastern Alps): age results, and an evaluation of potential problems for garnet Sm-Nd chronometry. Chem Geol 185:255–281

Thouvenot F, Kashubin SN, Poupinet G, Makovskiy VV, Kashubina TV, Matte Ph, Jenatton L (1995) The root of the Urals: evidence from wide-angle reflection seismics. Tectonophysics 250(1–3):1–13

Thury M, Gautschi A, Mazurek M, Müller WH, Naef H, Pearson FJ, Vomvoris S, Wilson W (1994) Geology and Hydrogeology of the crystalline basement of Northern Switzerland. Geologische Berichte—Rapports geplogiques, No. 18, Bern

Thybo H, Perchuc E (1997) The seismic 8 discontinuity and partial melting in the continental mantle. Science 275:1626–1629

Togonbaeva A, Takasu A, Bakirov AA, Sakurai T, Tagiri M, Bakirov AB, Sakiev K (2009) CHIME monazite ages of garnet-chloritoid-talc schists in the Makbal Complex, Northern Kyrgyz Tien-Shan: first report of the age of the UHP metamorphism. J Mineral Petrol Sci 104(2):77–81

Tokumitsu K, Nasu T (2000) Synthesis of nano-structured Fe/Fe_3O_4 complex particle by thermal decomposition of wustite. J Metastable Nanocryst Mater 8:562–567

Tonks WB, Melosh HJ (1993) Magma ocean formation due to giant impacts. J Geophys Res 98:5319–5333

Toulkeridis T, Goldstein SL, Clauer N, Kröner A, Lowe DR (1994) Sm-Nd dating of Fig Tree clay minerals of the Barberton greenstone belt, South Africa. Geology 22:199–202

Treiman AH, Schwenzer SP (2009) Basalt–atmosphere interaction on Venus: Preliminary results on weathering of minerals and bulk rock. In: Transactions of workshop: venus geochemistry: progress, prospects, and new missions, No. 2011

Trifonova P, Zhelev Zh, Petrova T (2007) Locations of Curie point depths and Moho of the Bulgarian territory. Geophys Res Abstr 9, 00771, SRef-ID: 1607-7962/gra/EGU2007-A-00771

Trikkel A, Kuusik R (2003) Modeling of decomposition and sulphation of oil shale carbonates on the basis of natural limestone. Est Acad Publ Oil Shale 20(4):491–500

Tsagarelli AL (1964) Geomorphology of georgia, quaternary system. In: Gamkrelidze P (ed) Geology of the USSR, vol X, Georgian SSR. Moscow-Leningrad, pp 332–352, 559–569 (in Russian)
Tselentis G-A (1991) An attempt to define Curie point depths in Greece from aeromagnetic and heat flow data. Pure Appl Geoph 136(1):87–101
Tsuzuki Y, Ogasawara K (1987) Dissolution experiments on albite and basalt glasses at various temperatures and their application to hydrothermal alteration in geothermal fields. Geochem J 21:262–281
Utsunomiya S, Murakami T, Nakada M, Kasama T (2003) Iron oxidation state of a 2.45-Byr-old paleosol developed on mafic volcanics. Geochim et Cosmochim Acta 67:213–221
Vacquier V (1998) A theory of the origin of the Earth's internal heat. Tectonophysics 291(1–4):1–7
Valley JW, Peck WH, King EM, Wilde SA (2002) A cool early Earth. Geology 30(4):351–354
van den Berg AP, Yuen DA (2002) Delayed cooling of the Earth's mantle due to variable thermal conductivity and the formation of a low conductivity zone. Earth Plan Sci Lett 199(3–4):403–413
van der Velden A, Cook F (1996) Structure and tectonic development of the southern Rocky Mountain trench. Tectonics 15(3):517–544
Van Kranendonk MJ, Collins WJ, Hickman A, Pawley MJ (2004) Critical tests of vertical vs. horizontal tectonic models for the Archaean East Pilbara Granite-Greenstone Terrane, Pilbara Craton, Western Australia. Precambr Res 131(3–4):173–211
Van Kranendonk MJ, Hickman AR, Smithies H, Nelson DR (2002) Geology and tectonic evolution of the Archean North Pilbara Terrain, Pilbara Craton, western Australia. Econ Geol 97(4):695–732
Van Kranendonk MJ, Philippot P, Lepot K, Bodorkos S, Pirajno F (2008) Geological setting of Earth's oldest fossils in the ca. 3.5 Ga Dresser Formation, Pilbara Craton, western Australia. Precambr Res 167(1–2):93–124
Van Kranendonk MJ, Pirajno F (2004) Geochemistry of metabasalts and hydrothermal alteration zones associated with c. 3.45 Ga chert and barite deposits: implications for the geological setting of the Warrawoona Group, Pilbara Craton, Australia. Geochem Explor Environ Anal 4(3):253–278
Van Kranendonk MJ, Webb GE, Kamber BS (2003) Geological and trace element evidence for a marine sedimentary environment of deposition and biogenicity of 3.45 Ga stromatolitic carbonates in the Pilbara Craton, and support for a reducing Archaean Ocean. Geobiology 1:91–108
Varlakov AS (1996) Riftogenic ophiolites in geological evolution of the Earth. Bull Moscow Soc Nat Invest Geol Branch 71(3):19–30 (in Russian)
Volozh YuA, Antipov MP, Brunet M-F, Garagash IA, Lobkovskii LI, Cadet J-P (2003) Pre-Mesozoic geodynamics of the Precaspian Basin (Kazakhstan). Sedim Geol 156(1–4):35–58
Von Quadt A (1992) U-Pb zircon and Sm–Nd geochronology of mafic and ultramafic rocks from the central part of the Tauern Window (eastern Alps). Contrib Mineral Petrol 110:57–67
Wacey D, McLoughlin N, Brasier M (2009) Looking through windows onto the earliest history of life on Earth and Mars. In: Seckbach J, Walsh M (eds) From fossils to astrobiology. Springer, Berlin, pp 39–68
Wakabayashi J, Guha T, Detterman M (2005) Brewschist and Breweries (Brewschist II): A tour of fine rocks and the west coast brewing art field trip. Field trip guide, 2005
Walker D, Agee CB, Zhang Y (1988) Fusion curve slope and crystal/liquid buoyancy. J Geophys Res 93(B1):313–323
Wallis S, Takasu A, Enami M, Tsujimori T (2000) Eclogite and Related Metamorphism in the Sanbagawa belt, Southwest Japan. Bull Res Inst Nat Sci Okayama Univ Sci 26:3–18
Walter MJ, Trønnes RG (2004) Early Earth differentiation. Earth Plan Sci Lett 225(3–4):253–269
Wana JHM, Couceiro PRC, Pereira MC, Fabris JD, Fernandes FEI, Schaefer CEGR, Rechenberg HR, Abrahao WAP, Mantovani EC (2006) Occurrence of magnetite in the sand fraction of an

Oxisol in the Brazilian savanna ecosystem, developed from a magnetite-free lithology. Aust J Soil Res 44(1):71–83
Wang X, Zeng Z, Chen J (2009) Serpentinization of peridotites from the southern Mariana forearc. Progr Nat Sci 19:1287–1295
Wen C, Jinbo S, Hongwei J, Jie L, Jiyuan Y, Jungfeng G, Xinyu L (2011) (U-Th)/He geochronological evidence for rapid uplift of Tianshan orogenic belt since Miocene. Goldschmidt conference abstracts, p 657
Wenner DB, Taylor HP Jr (1971) Temperatures of serpentinization of ultramafic rocks based on O^{18}/O^{16} fractionation between coexisting serpentine and magnetite. Contrib Mineral Petrol 32:165–185
Wheeler P, White N (2002) Measuring dynamic topography: an analysis of Southeast Asia. Tectonics 21(5):1040. doi:10.1029/2001TC900023
Whitehead J, Reynolds PH, Spray JG (1996) $^{40}Ar/^{39}Ar$ age constraints on Taconian and Acadian events in the Quebec Appalachians, Appalachians. Geology 24:359–362
Whitehouse MJ, Myers JS, Fedo CM (2009) The Akilia controversy: field, structural and geochronological evidence questions interpretations of >3.8 Ga life in SW Greenland. J Geol Soc 166(2):335–348
Windom KE, Unger CP (1988) Stability of the assemblage albite plus forsterite at high temperatures and pressures with petrologic implications. Contrib Mineral Petrol 98:390–400
Wintsch RP, Byrne T, Toriumi M (1999) Exhumation of the Sanbagawa blueschist belt, SW Japan, by lateral flow and extrusion: evidence from structural kinematics and retrograde P–T–t paths, vol 154. Geological Society of London, London, pp 129–155
Wright JE, Wyld SJ (2006) Gondwanan, Iapetan, Cordilleran interactions: A geodynamic model for the Paleozoic tectonic evolution of the North American Cordillera. In: Haggart JW, Enkin RJ, Monger JWH (eds) Paleogeography of the north American Cordillera: evidence for and against large-scale displacements. Geol Assoc Can Spec Pap 46, pp 377–408
Wright RL, Nagel J, McTaggart KC (1982) Alpine ultramafic rocks of southwestern British Columbia. Can J Earth Sci 19(6):1156–1173
Yakubchuk AS, Nikishin AM, Ishiwatari A (1994) A Late Proterozoic ophiolite pulse. In: Ishiwatari A, Malpas J, Ishizuka H (eds) Circum-Pacific ophiolites. Proc 29th Int Geol Congr, Part D, Kyoto 92, Utrecht, The Netherlands, pp 273–286
Yao Y, Morteani G, Trumbull RB (1999) Fluid inclusion microthermometry and the P–T evolution of gold-bearing hydrothermal fluids in the Niuxinshan gold deposit, eastern Hebei province, NE China. Mineral Deposita 34:348–365
Žáčková E, Konopásek J, Jeřábek P, Finger F, Košler J (2010) Early Carboniferous blueschist facies metamorphism in metapelites of the West Sudetes (Northern Saxothuringian Domain, Bohemian Massif). J Metamorp Geol 28(4):361–379
Zahnle KJ, Kasting JF, Pollack JB (1988) Evolution of a steam atmosphere during Earth's accretion. Icarus 74:62–97
Zakariadze GS, Karamata S, Bayanova TB, Karpenko SF, Korikovsky SP, Mitrofanov FP, Sergeyev SA (2007) Composition and problems of origin of Paleozoic oceanic lithosphere framing European platform from south, exemplified by Eastern Mediterranean area. In: Geochemical, petrological and geophysical segmentation of the mid-oceanic ridges and its relationships with geodynamic parameters of the oceanic lithosphere accretion, Russian ridge workshop, Moscow, pp 23–24
Zbinden EA, Holland HD, Feakes CR, Dobos SK (1988) The sturgeon falls paleosol and the composition of the atmosphere 1.1 Ga BP. Precambr Res 42:141–163
Zhang Q, Wang ChY, Liu D, Jian P, Qian Q, Zhou G, Robinson PT (2008) A brief review of ophiolites in China. J Asian Earth Sci 32(5–6):308–324
Zhang RY, Liou JG, Yang JS, Yui T-F (2000) Petrochemical constraints for dual origin of garnet peridotites from the Dabie-Sulu UHP terrane, eastern-central China. J Metamorphic Geol 18:149–166
Zhou M-F, Malpas J, Robinson PT, Reynolds PH (1997) The dynamothermal aureole of the Donqiao ophiolite (northern Tibet). Can J Earth Sci 34(1):59–65

Zimmermann R, Hammerschmidt K, Franz G (1994) Eocene high pressure metamorphism in the Penninic units of the Tauern Window (Eastern Alps): evidence from ^{40}Ar-^{39}Ar dating and petrological investigations. Contrib Mineral Petrol 117:175–186

Zorin YuA (1981) The Baikal rift: an example of the intrusion of asthenospheric material into the lithosphere as the cause of disruption of lithospheric plates. Tectonophysics 73(1–3):91–104

Chapter 7
Interpretation of Thermal Measurements

To analyze the thermal regime of any area/region, a certain number of key measurements of thermal parameters are needed. The thermal regime in geothermics applies such parameters as temperature (T), the geothermal gradient (G or Γ), heat flow (Q or q), heat generation (A or H), heat conductivity (λ or κ), heat capacity (c) and heat diffusivity (a). Some of these parameters are primary parameters and some are derived. All the primary parameters (T, A, λ, c) must be measured, but the derived parameters (G, Q, a) can be calculated using the primary parameter values.

The geothermal gradient is either vertical ($G_z = \Delta T/\Delta z$) or horizontal ($G_x = \Delta T/\Delta x$; $G_y = \Delta T/\Delta y$) and is calculated as the rate of temperature change in either direction. The temperature values for two points in the chosen direction are obtained, the temperature change in that direction ($\Delta T = T_2 - T_1$) is calculated, and the result is divided by the distance between the temperature measurement points. Heat flow Q is calculated by multiplying the geothermal gradient by heat conductivity ($Q = \lambda G$). Thermal diffusivity is calculated as $a = \lambda/(\sigma c)$, where σ is the density of the rock.

To analyze the distribution of temperature within a body/layer the heat conduction equation is usually employed. Depending on the specific question in geothermics, two kinds of heat conduction equation can be used: the transient or non steady-state heat conduction equation (variation with time or time dependence) or the steady-state heat conduction equation (no change with time). The heat conduction equation may also be termed stationary (no change with time), nonstationary (variation with time or time dependence), homogeneous (parameters a, λ, σ, c and A are constant within a body/layer), nonhomogeneous (parameters a, λ, σ, c and A changes within a body/layer). Steady state conduction is the form of conduction when the distribution of temperatures within an object/layer does not change over time. Geothermal measurements in a borehole in a thermally stable region are made after an equilibration time for the borehole.

The non steady-state heat conduction equation is the most common and takes the following form:

L. Eppelbaum et al., *Applied Geothermics*, Lecture Notes in Earth System Sciences,
DOI: 10.1007/978-3-642-34023-9_7,

$$c\sigma\frac{\partial T}{\partial t}=\frac{\partial}{\partial z}\left(\lambda\frac{\partial T}{\partial z}\right)+\frac{\partial}{\partial x}\left(\lambda\frac{\partial T}{\partial x}\right)+\frac{\partial}{\partial y}\left(\lambda\frac{\partial T}{\partial y}\right)+A. \tag{7.0.1}$$

Here $T = T(x, y, z, t)$ is a function of the temperature distribution.

Equation (7.0.1) is quite complicated to solve in its most common form, and depending on the problem at hand, some initial conditions and boundary conditions are required to solve it. By contrast, in a stable geological region with no strong hydrothermal activity and no volcanic activity for a long time, the distribution of temperature within a geological layer is usually assumed not to change with time. For geothermal problems of this kind, the steady-state heat conduction equation

$$\frac{\partial}{\partial z}\left(\lambda\frac{\partial T}{\partial z}\right)+\frac{\partial}{\partial x}\left(\lambda\frac{\partial T}{\partial x}\right)+\frac{\partial}{\partial y}\left(\lambda\frac{\partial T}{\partial y}\right)=-A. \tag{7.0.2}$$

is usually employed.

But solving Eq. (7.0.2) in its typical form is also quite complicated and depending on the problem, some pre-conditions and limitations usually enter into its solution. However in many cases the steady-state heat conduction equation can be further simplified. For example, for huge regions with steady-state conduction within such stable structures as the Archean and Early Proterozoic cratons, ancient platforms, and huge depression zones, a one-dimensional steady-state heat conduction equation is sufficient:

$$\frac{\partial}{\partial z}\left(\lambda\frac{\partial T}{\partial z}\right)=-A. \tag{7.0.3}$$

The one-dimensional non steady-state heat conduction equation is also used to calculate the temperature distribution with depth in regions in which heat conduction is time dependent but there are no significant changes in the horizontal direction.

Another way of solving geothermal problems is to split them into easier sub problems which are then summed (Carslaw and Jaeger 1959). This method is based on the fact that the distribution of heat flow and temperature adheres to the superposition principle, and solutions of parts of the problem can be added to get the complete solution. This method has significant advantages, because mathematical solutions to both the non steady-state and steady-state heat conduction equation for numerous problems with different body shapes, initial and boundary conditions have been published (Carslaw and Jaeger 1959) and can be applied easily to solve heat conduction problems or their parts. Let us analyze following example of a geothermal problem.

In a layer near the Earth's surface $0 \le z \le L$ initial distribution of temperature is described by equation:

$$T(z,0) = T(0,0) + bz. \tag{7.0.4}$$

Heat released within the layer is defined by heat generation A. Heat flow entering the layer on the surface $z = L$ is constant and equals Q_1.

By analogy with (Carslaw and Jaeger 1959) this problem can be replaced by three other problems (Pilchin 1983):

The top and bottom surfaces of a layer $0 \le z \le L$ are kept at temperatures T_0 and T_L, respectively. There are no sources of heat generation within the layer and the initial temperature distribution is represented by Eq. (7.0.4).

The top and bottom surfaces of a layer $0 \le z \le L$ are kept at zero temperature (0 °C = 273 K), the initial temperature within the layer is zero (0 °C = 273 K), and heat generation within the layer is A.

Layer $0 \le z \le L$ has zero initial temperature and its top surface is kept at zero temperature. Heat flow entering the layer on surface $z = L$ is constant and equals Q_1.

It is obvious that solution to problem 1 is:

$$T_1 = T_0 + bz. \tag{7.0.5}$$

The solution to problem 2 in the case where L is very large is given in Carslaw and Jaeger (1959):

$$T_2 = \frac{aAt}{\lambda}\left\{1 - 2i^2\Phi^*\left(\frac{L-z}{2\sqrt{at}}\right) + 2i^2\Phi^*\left(\frac{L+z}{2\sqrt{at}}\right) - 4i^2\Phi^*\left(\frac{z}{2\sqrt{at}}\right)\right\}. \tag{7.0.6}$$

Here $a = \lambda/(\sigma c)$, and Φ^* is complementary error function ($\Phi^* = 1 - \Phi$) of the Gaussian error function Φ:

$$\Phi = erf(x) = \frac{2}{\sqrt{\pi}}\int_0^x e^{-t^2}dt. \tag{7.0.7}$$

$$\Phi^* = erfc(x) = 1 - erf(x) = \frac{2}{\sqrt{\pi}}\int_x^\infty e^{-t^2}dt. \tag{7.0.8}$$

The solution to problem 3 is (Carslaw and Jaeger 1959):

$$T_3 = \frac{Q_1\sqrt{at}}{\lambda}\sum_{n=0}^{\infty}(-1)^n\left\{i\Phi^*\left(\frac{(2n+1)L - z}{2\sqrt{at}}\right) + i\Phi^*\left(\frac{(2n+1)L + z}{2\sqrt{at}}\right)\right\}. \tag{7.0.9}$$

Tables of values for Φ, Φ^*, $i\Phi^*$ and $i^2\Phi^*$ are presented in (Carslaw and Jaeger 1959).

The final solution of the main (combined) problem according the superposition principle is:

$$T_{\text{total}} = T_1 + T_2 + T_3. \tag{7.0.10}$$

7.1 Development of a Geothermal Model

It is obvious that the distribution of thermal parameters with depth (T, a, λ, σ, c, A) for any given moment is fixed and their variation with time or time dependence does not mean that their values will change every day. Actually in most cases these parameters are stationary or quasi-stationary for long periods of time (thousands, millions of years) depending on processes taking place in an area/region. Of course, in cases of material transfer (active volcanism, hot springs, geysers, etc.) and problems investigating variations of processes with time changes involving parameters used in heat conduction, the equation will not be stationary, but these areas and regions are rare and clearly visible and should be separated from areas and regions with stationary or quasi-stationary geothermal regimes. Thus for most areas and regions, for the present and near future the steady-state heat conduction equation can be used, because analysis of current day thermal conditions in such areas and regions will not be affected by a time factor in the short term. This makes it possible to use the steady-state heat conduction equation for such issues as calculating the current day distribution temperatures, geothermal gradients and heat flow in areas/regions where active mass transfer is absent.

It is known that there are daily and annual fluctuations of temperature which take place over a thin layer at the surface with a thickness of about 0.9–1.2 m for daily fluctuations, and about 18–21 m for annual fluctuations (surface of mean invariable surface-temperature; see for example, Lubimova 1968a). This means that measurements of geothermal parameters can be counted as stationary (steady) at depths greater than about 0.9–1.2 m for time greater than 1 day and at depths greater than about 18–21 m for time greater than 1 year.

Another problem related to the selection of the kind of heat conduction equations has to do with the petrological composition of the layer and its thickness. For practical purposes certain facts and features should be taken into account: (1) a naturally stratified layer cannot be represented by a single layer model; (2) a thick layer cannot be considered to be totally homogeneous for geothermal parameters; (3) in most cases there are no reliable measurements of temperature and calculated heat flow entering a thick layer through its bottom surface; (4) for petrologically homogeneous thick layers the dependence of the heat conduction coefficient on temperature and the change of heat generation with depth need to be taken into consideration; (5) in depression zones whose sedimentary layers are rich with thermal waters it is impossible to get a good estimate of heat generation (discussed in Sect. 7.4); (6) in some layers the value of the geothermal gradient increases with

depth, which contradicts the theory of the decline of the geothermal gradient with depth (Pilchin 1979; Eppelbaum and Pilchin 2006), and also runs counter the theory that heat generation is caused exclusively by radioactive sources, etc.

In non-orogenic regions, rocks are usually formed of layers composed of similar rocks. This is the outcome of amassing sediments, regional metamorphism and other processes. Seismic studies have shown that within the crust there are numerous reflective horizons which prove that the crust is stratified. Seismic methods can be used to identify the position of some main surfaces of regional significance within the crust. It forms the basis for different layering models of crust composition in geothermics. Layering models are frequently employed to solve general geothermal problems of regional significance.

Clearly if there is natural stratification of a layer (sedimentary deposits of different lithology and different compaction, rocks of different rheology, etc.) the whole layer must not be considered as homogeneous, because different rocks have different values for geothermal parameters such as a, λ, σ, c, A.

One of the key publications, in which one of the first and most complete theoretical analysis of the thermal regime of the Earth's crust for both stationary and nonstationary heat flows was developed, was published by Tikhonov (1937). In this work, an extensive analysis of heat conduction equations was presented. Tikhonov (1937) analyzed the solutions to stationary nonhomogeneous heat conduction equations for one and two layered models with a concentration of radioactive elements in one or two layers near the Earth's surface. He also discussed problems relating to estimating the nonstationary component of temperature in nonhomogeneous nonstationary heat conduction equations.

Lachenbruch (1959) showed that the heat conduction equation for a stratified medium should not be treated as homogeneous. This was the main motivation for using layering models to solve the heat conduction equation for a horizontally stratified medium (e.g. Tikhonov 1937; Lachenbruch 1959; Negi and Singh 1967; Lubimova 1968a; Kutas and Gordienko 1971; Cheremensky 1977; Pilchin 1978, 1983; Nielsen and Balling 1985, etc.). As a function of the problem and the specifics of geological composition (stratification) of an area or region, different researchers use different layer models for solving geothermal problems: Tikhonov (1937) used a single layer and 2-layer models for the crust, Lachenbruch (1959) used 2- and 3-layered models, Pilchin (1983) used 3-, 4- and 5-layered models for the Kura Depression, Krupsky et al. (2006) used an 11-layer model for the Precaspian Depression, Cacace and Scheck-Wenderoth (2010) treated the sedimentary layer of the north east German Basin as 13-layer system, Lévy et al. (2010) used a 2-layer model for the crust, etc. McGahan and Cole (1992) and Grosse and Wynands (1989) used multilayer models for solving the heat conduction equation for certain physical problems. Thus layered models are often employed for solving heat conduction equations. Clauser (2006) stated that the parallel and series model for thermal resistance of layered media are easy to understand, but have the disadvantage of being rather special cases, applicable mostly to bedded sediments. However, most geothermal studies so far have been conducted in sedimentary basins, and the crust and mantle are composed of layers. Moreover, any thick rock

layer that has significant horizontal dimensions can be represented as an n-layer structure (Pilchin 1978).

Nevertheless, even a petrologically homogeneous layer (e.g. "granite" layer or "basalt" layer of crust), especially a thick layer, cannot necessarily be treated as homogeneous in geothermics, because of the dependence of parameters a, λ, c on temperature and pressure and A on depth, which increase with depth. In this case the thick layer could be represented by an n-layer model provided that in each layer parameters a, λ, c, A are constant (Pilchin 1983).

All of the above shows that an n-layer model can be used for solving heat conduction equations for numerous geological problems in regions of different types. Let us discuss a general solution to the heat conduction equation for an arbitrary geological medium with a stable or quasi-stable heat flow. Any layer of the crust and upper mantle ($0 \leq z \leq L$), from the point of view of its thermal energetics, should be viewed in terms of the following factors: the presence of heat flow through the bottom surface of the layer Q_L, release of heat within the layer caused by sources of heat A; heat flow through the upper surface of the layer Q_0, layer boundary conditions of $T(0) = T_0;\ T(L) = T_L$, and the fact that rocks of the layer are characterized by geothermal parameters a, λ, c, A which generally differ for different kinds of rocks and are also dependent on pressure and temperature. T_0 usually has the value of the mean invariable surface-temperature of an area or region. It was shown (Tikhonov 1937; Lubimova 1968b; Pilchin 1983; Eppelbaum and Pilchin 2006) that for area (or region) with significant horizontal dimensions, the stationary (or quasi-stationary) heat flow and vertical geothermal gradients are two orders of magnitude greater than the horizontal gradients, and a one dimensional heat conduction equation can be used. Estimates of the error when calculating temperatures at great depths using the heat conduction equation indicate values at or above 15 % (Kutas 1978). This means that ignoring the dependence of the main geothermal parameters (a, λ, c, A) on lithological composition, compaction, change with temperature and pressure, etc. leads to additional errors.

Non-layered models use the average values of the main geothermal parameters. Thus the error is the greatest for estimates of the distribution of temperature, geothermal gradient and heat flow in such models. The implication is that the layering model is preferable for solving heat conduction equations in all cases where it is applicable. For initial calculations, the natural stratification of the main layers of the crust may be used. The position of natural layers is easy to determine by methods of seismic stratigraphy, as well as data from borehole drilling. However to construct a layered model of a medium to solve heat conduction equations, stratification is not necessary, even though it is very important for practical applications of the model. For both cases with either a stratified medium or non-stratified huge slab, the regional geological layer (even petrologically homogeneous layer) can be subdivided into a number of sub-layers (n; here n represents the number of sub-layers from 1 to n: $1, 2, 3, \ldots, i-1, i, i+1, \ldots, n$; i is an arbitrary sub-layer within the main layer $0 \leq z \leq L$) for which conditions for any arbitrary sub-layer i whose geothermal parameters (a_i, λ_i, c_i, A_i) are constant can be accepted.

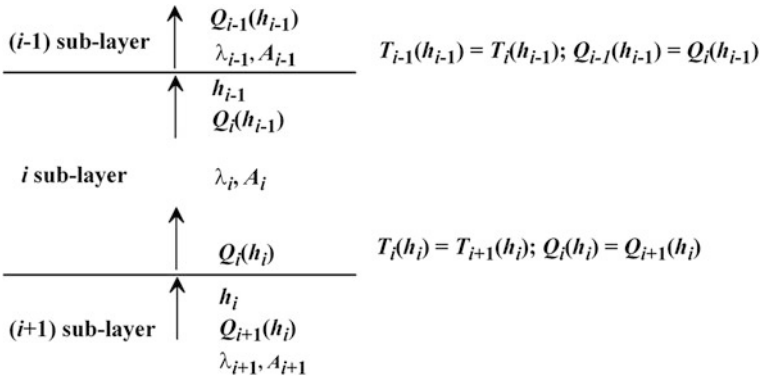

Fig. 7.1 Model of three consecutive sub-layers ($i - 1$, i and $i + 1$) with their geothermal parameters and boundary conditions

An example of the position and geothermal characteristics of three consecutive sub-layers $i - 1$, i and $i + 1$ are presented in Fig. 7.1.

An arbitrary sub-layer i ($h_{i-1} \le z \le h_i$) is defined as a function of the temperature distribution with depth within the sub-layer $T_i(z)$ with top and bottom boundaries at depths h_{i-1} and h_i, respectively; the distribution of the heat flow with depth is described by function $Q_i(z)$. It is obvious that the surface at depth h_{i-1} is the boundary between sub-layers $i - 1$ and i, and the surface at depths h_i is the boundary between sub-layers i and $i + 1$. Since the temperature at the same boundary between two sub-layers is the same for both sub-layers, and the heat flow exiting one sub-layer must be equal to the heat flow entering another sub-layer separated by the same boundary, the border conditions for surfaces at depths h_{i-1} and h_i, will be:

$$T_{i-1}(h_{i-1}) = T_i(h_{i-1}); \quad Q_{i-1}(h_{i-1}) = Q_i(h_{i-1}). \tag{7.1.1}$$

$$T_i(h_i) = T_{i+1}(h_{i+1}); \quad Q_i(h_i) = Q_{i+1}(h_i). \tag{7.1.2}$$

$$T_i(h_i) = T_i; \quad T_i(h_{i-1}) = T_{i-1}. \tag{7.1.3}$$

$$Q_{i-1}(h_{i-1}) = Q_i(h_{i-1}) = \lambda_{i-1}\left(\frac{dT_{i-1}(z)}{dz}\right)_{h_{i-1}} = \lambda_i\left(\frac{dT_i(z)}{dz}\right)_{h_{i-1}}. \tag{7.1.4}$$

For such an arbitrary sub-layer i the heat conduction equation (7.1.4) will be:

$$\frac{\partial}{\partial z}\left(\lambda_i \frac{\partial T_i(z)}{\partial z}\right) + A_i = 0 \tag{7.1.5}$$

Since geothermal parameters within each sub-layer are constant, Eq. (7.1.5) may be written as:

$$\frac{d^2T_i(z)}{dz^2} = -\frac{A_i}{\lambda_i}. \tag{7.1.6}$$

To solve the heat conduction equation, it is assumed that the positive change of depth is downwards (from 0 to L) and the positive direction of the heat flow is in the upward direction.

Equation (7.1.6) may be used for establishing the following relationship:

$$\frac{\lambda_{i-1}}{A_{i-1}}\left(\frac{d^2T_{i-1}(z)}{dz^2}\right)_{h_{i-1}} = \frac{\lambda_i}{A_i}\left(\frac{d^2T_i(z)}{dz^2}\right)_{h_{i-1}}. \tag{7.1.7}$$

Dividing both sides of Eq. (7.1.7) by $\lambda_i\left(\frac{dT_i}{dz}\right)_{h_{i-1}}$ and taking into account Eq. (7.1.4) we get following equation which is convenient for practical use:

$$\frac{A_{i-1}\left(\frac{dT_{i-1}(z)}{dz}\right)_{h_{i-1}}}{\left(\frac{d^2T_{i-1}(z)}{dz^2}\right)_{h_{i-1}}} = \frac{A_i\left(\frac{dT_i(z)}{dz}\right)_{h_{i-1}}}{\left(\frac{d^2T_i(z)}{dz^2}\right)_{h_{i-1}}}. \tag{7.1.8}$$

Equations (7.1.4)–(7.1.8) can be used to calculate the thermal parameters (λ_i and A_i) in the lower consecutive sub-layer if we know the values of these parameters and the first and second derivatives of temperature with depth in the upper consecutive sub-layer and the first and second derivatives of temperature with depth in the lower consecutive sub-layer.

Integration of Eq. (7.1.6) with z for depth interval $h_{i-1} \le z \le h_i$ yields:

$$\left(\frac{dT_i}{dz}\right)_{h_i} = \left(\frac{dT_i}{dz}\right)_{h_{i-1}} - \frac{A_i}{\lambda_i}(h_i - h_{i-1}). \tag{7.1.9}$$

It is clear from Eq. (7.1.9) that the value of $(-A_i/\lambda_i)$ represents the change of the geothermal gradient with depth.

Equation (7.1.9) can be transformed to

$$-A_i(h_i - h_{i-1}) = \lambda_i\left(\frac{dT_i}{dz}\right)_{h_i} - \lambda_i\left(\frac{dT_i}{dz}\right)_{h_{i-1}}. \tag{7.1.10}$$

Taking into account that

$$\lambda_i\left(\frac{dT_i}{dz}\right)_{h_i} = Q_i \tag{7.1.11}$$

Table 7.1 Value of A (average cross-section) in the upper part of sedimentary strata for some oil and gas fields of the Apsheron peninsula and the Apsheron archipelago calculated using Eq. (7.1.9)

Area	Depth interval (m)	Average value of A ($\mu W/m^3$)
Neftyanie Kamni	0–5,000	1.34
Lokbatan, Puta, Binagady	0–5,000	0.89
Bibi-Eybat	0–5,000	0.89
Balakhany, Sabunchy, Ramany	0–5,000	0.59
Surakhany	0–5,000	1.04
Zykh, Kara-Chukhur	0–5,000	0.89
Peschaniy island	0–5,000	0.59
Buzovny, Mashtagy Kala, Zirya	0–5,000	0.59
Pirallahi,	0–5,000	1.04
Gousany	0–5,000	0.45

and

$$\lambda_i \left(\frac{dT_i}{dz}\right)_{h_{i-1}} = Q_{i0} \tag{7.1.12}$$

Equation (7.1.10) can be transformed to

$$A_i = \frac{Q_{i0} - Q_i}{h_i - h_{i-1}}. \tag{7.1.13}$$

Here Q_i and Q_{i0} are the heat flow densities entering sub-layer i from the bottom surface and exiting it from the top surface respectively.

Equation (7.1.13) shows that A_i represents the change in heat flow density with depth within sub-layer i. It is obvious that A_i represents the sum of all sources of generation and drops in heat within sub-layer i.

Double integration of Eq. (7.1.6) with z for depth interval $h_{i-1} \le z \le h_i$ gives:

$$T_i(h_i) = T_i(h_{i-1}) + \left(\frac{dT_i}{dz}\right)_{h_{i-1}} (h_i - h_{i-1}) - \frac{A_i}{2\lambda_i}(h_i - h_{i-1})^2. \tag{7.1.14}$$

Equations (7.1.9) and (7.1.14) with boundary conditions can be used to calculate the geothermal gradient and temperature at different depths. They can also be used to find the values of A_i if we know the values of the heat conduction coefficient and the first derivative of temperature with depth, or the values of the second derivative of temperature with depth. For example, in Table 7.1 the average cross-section values of A in the upper part of sedimentary strata for some oil and gas fields of the Apsheron peninsula and Apsheron archipelago (Azerbaijan) calculated using Eq. (7.1.9) are presented.

It is obvious from Eqs. (7.1.9) and (7.1.14) that to calculate the distribution of the geothermal gradient with depth and temperature with depth it is enough to know the values of the ratio A_i/λ_i and not the values of heat production and heat conductivity coefficient themselves.

The values of A for rocks of acidic composition are $A = 1.8$ μW/m^3 and similarly, the values for rocks of intermediate and basic compositions are 0.8 and 0.67 μW/m^3, respectively.

The almost total absence of granites in rock samples in Azerbaijan, as well as the results of drilling the Saatly superdeep borehole and geophysical studies all show that granites cannot be the main representative rock of the "granite" layer of the crust in the Kura Depression, and the main rocks of this layer are intermediate rocks (Pilchin 1983).

Let us analyze the change in heat generation with depth within the "granite layer" and the "basaltic layer" of the Kura Depression. We assume that A within the "granite layer" drops from 0.8 μW/m^3 near its upper surface to 0.67 μW/m^3 near its lower surface (this is the maximal possible change of A within this layer). It was shown that A changes with depth according to exponential law (Lubimova 1968b; Cheremensky 1977):

$$A = A_0 \exp(-b\Delta h). \tag{7.1.15}$$

Here A and A_0 are heat production near the bottom and top surfaces of a layer with thickness Δh, respectively, and b is a constant for the layer. Since the thickness of the "granite layer" within the Kura Depression ranges from 3 to 5 km at N–W to 10–15 km at S–E of the Kura Depression and is only greater than 10 km within the Novogolovskaya anticline, and accepting $A_0 = 0.8$ μW/m^3 and $A = 0.67$ μW/m^3 the calculated value for b is on average 1×10^{-5} 1/m. This means that for the "granite layer" with a thickness of about 10 km the product $b{\cdot}\Delta h$ is very small. Using the Taylor series for Eq. (7.1.15) the heat production can be expressed as follows:

$$A = A_0(1 - b\Delta h). \tag{7.1.16}$$

Estimates of the value of b for the "basalt layer" are significantly smaller than for the "granite layer" and can be explained by the significantly greater thickness of the "basalt layer" (on average $\sim$30 km). Hence Eqs. (7.1.15) and (7.1.16) can be used for the "basalt layer" as well.

Research has shown that for temperatures above 373–573 K the value of the heat conductivity coefficient is almost linear with increases in temperature for most rocks and can be written as:

$$\lambda = \lambda_0(1 - a\Delta T). \tag{7.1.17}$$

Here λ and λ_0 are the heat conduction coefficients near the upper and lower values of the temperature interval ΔT, respectively, and a is the constant for each rock.

Replacing ΔT with the geothermal gradient G $(\Delta T = G \cdot \Delta h)$ [Eq. (7.1.17)] transforms the equation to:

$$\lambda = \lambda_0(1 - aG\Delta h). \tag{7.1.18}$$

Changes in heat conduction for such rocks as granite, gabbro, diabase and other magmatic rocks within the temperature interval of 473–723 K do not exceed 8 %. This gives us the estimated value to use in Eq. (7.1.17) of $\sim 0.3 \times 10^{-4}$ 1/K. Since the value of the geothermal gradient near the surface of the "granite layer" within the Kura Depression does not exceed 30 K/km, the estimated value of the product aG will be about 1×10^{-6} 1/m.

Using Eqs. (7.1.16) and (7.1.18) the ratio A/λ can be written as:

$$\frac{A}{\lambda} = \frac{A_0}{\lambda_0} \cdot \frac{1 - b \cdot \Delta h}{1 - aG \cdot \Delta h}. \tag{7.1.19}$$

Since the estimated value of b is about one order greater than the estimated value of aG for ratio A/λ it is true to say that (Pilchin 1983):

$$\frac{A}{\lambda} \cong \frac{A_0}{\lambda_0}. \tag{7.1.20}$$

Estimates of calculation errors for the values of the ratio A/λ for the "granite layer" of the Kura Depression (Azerbaijan) show that for a thickness of the "granite layer" of ~ 10 km these errors do not exceed 9 %. Errors in calculating temperatures within the "granite layer" are thus likely to be less than 0.5 %. Similar estimates of errors for the "basalt layer" of the Kura Depression indicate a maximum value of ~ 2 % for the thickness of the "basaltic layer": ~ 30 km. The estimated values of the ratio A/λ for the "granite layer", the "basalt layer" and the bottom part of the sedimentary layer within the Kura Depression yielded values of $(0.33-0.45) \times 10^{-6}$ K/m^2 $(0.26-0.27) \times 10^{-6}$ K/m^2, and 1.06×10^{-6} K/m^2, respectively.

The geothermal model described above has been used for the investigation of the thermal regime of the crust in the Kura Depression (Pilchin et al. 1978; Pilchin and Kerimov 1980; Kerimov and Pilchin 1986a; Pilchin 1983; Kerimov et al. 1989) and Israel (Eppelbaum et al. 1996; Pilchin and Eppelbaum 1997; Eppelbaum and Pilchin 2006), analysis of the distribution of horizontal and vertical geothermal gradients in regions of the Caucasus (Kerimov et al. 1989) and Israel (Eppelbaum et al. 1996), compilation of geothermal maps with temperature distribution at depths of 2,000, 4,000 and 6,000 m for regions of the Caucasus (Kerimov et al. 1989) and Azerbaijan, the South Caspian Depression and Western Turkmenistan (Kerimov and Pilchin 1986a), analysis of the geothermal regime in the Salton Trough in the USA (Pilchin and Eppelbaum 1994a), the Los Angeles

Basin (Pilchin and Eppelbaum 1994b) and regions of South and Central Alberta, Canada (Pilchin 1995b), etc. It can also be used for analysis of the thermal conditions in other regions.

7.2 Methods of Geothermal Regime Analysis

The key problem facing geothermal measurements and their interpretation is accuracy. It is clear that temperature measurements made in a borehole before its equilibration will be not accurate. Similarly, it is evident that the use of inaccurate data for interpretation (e.g., calculation of geothermal gradients, heat flows, temperatures at great depths, etc.) will lead to even more erroneous results. In cases where the geothermal measurements (e.g. temperature measurements) were taken in non-equilibrated boreholes or in layers which cannot represent the whole sequence of deposits, the use of these measurements is risky. For example calculating the heat flow from the ocean bottom in shallow boreholes may give values that are distorted by the cooling effect of oceanic water and in many cases the accuracy will be poor. In the case of a recharge zone for ground waters, cold precipitating waters collect some heat and transfer it through the aquifer to the discharge zone, collecting additional heat from rocks of the aquifer layer on the way and containing it in the aquitard layers. This leads to significant reduction in temperatures and heat flow in the recharge zone and some increase in temperatures and heat flow in the discharge zone. This could distort the picture of thermal conditions at a depth, and of course the use of such data for the calculation of the temperature distribution at great depths would lead to significant errors. Estimates of errors in the calculation of temperature at great depths using heat conduction equations show that their values are equal to or higher than 15 % (Kutas 1978). But this is the best way to estimate temperatures at great depths.

For geothermal regime analysis, depending on the problem requirements, geothermal parameters such as temperature (T), horizontal (G_x and G_y) and vertical (G_z) geothermal gradients, heat flow (Q or q), rate of geothermal gradient change with depth ($\Delta G/\Delta z$) or any of the horizontal directions ($\Delta G/\Delta x$ and $\Delta G/\Delta y$), temperature excess ($T - T_0$) and relative temperature excess ($T - T_0)/T_0$ (here T_0 is the normal temperature of water at different depths are used; for more details see Sect. 2.7), coefficient of temperature abnormality ($K_T = T/T_0$) can be used.

During 1960s and1970s most geothermal regime analysis methods dealt with the calculation and analysis of the distribution of heat flow in different regions of the Earth, and obtaining the average heat flows for different local areas, regions (geological provinces, countries, continents, oceans), types of crust/lithosphere (oceanic, continental), etc. Unfortunately, as was shown in Chap. 1, the range of heat flows even within small areas is so significant that in most cases the average values of heat flows have little meaning and cannot represent a real geothermal field in many cases. In addition, the presence of outliers (extremely high or extremely low values of heat flow), which are usually ignored for the calculation

of average values of heat flow, make these average values meaningless. Moreover, in most cases, the values obtained for heat flow are biased because they were usually calculated for prospective oil and gas regions, high temperature regions (e.g., anticlines, rifts), prospective heat energy regions, or regions rich in thermal waters, etc. and were not calculated for low temperature regions (e.g., synclines) or regions where temperature measurements are impossible or complicated, etc.

Temperature is one of the key parameters for many geological and geophysical methods and affects the conditions for many processes (metamorphism, volcanism, borehole drilling, etc.), the analysis of physical properties of rocks and minerals under different *P-T* conditions, the petrological and petrophysical modelling of conditions and the composition of different layers of the crust, lithosphere, asthenosphere, lower mantle and core, etc.

Geothermal gradients are usually employed to calculate heat flow and analysis of the rate of temperature change in a specific direction (directions). It was shown (Pilchin 1983; Kerimov and Pilchin 1986a; Eppelbaum and Pilchin 2006) that on average, the value of the geothermal gradient declines with depth for different regions and areas, and the sharpest drop in the geothermal gradient takes place in the uppermost layers of sedimentary cover, usually at depths of less than 2.0 km. For example, the geothermal gradient at depths of up to 2.0 km in areas of the Middle Kura Depression, Lower Kura Depression, Apsheron Peninsula, and Apsheron archipelago varies by $-(2.2–3.0) \times 10^{-6}$ K/m^2, $-(4.5–5.8) \times 10^{-6}$ K/m^2, $-(8.0–13.0) \times 10^{-6}$ K/m^2, and $-(6.0–16.5) \times 10^{-6}$ K/m^2 respectively (Pilchin 1983; Kerimov and Pilchin 1986a). The minus means that the geothermal gradient declines with depth. The values of the geothermal gradient decline with depth for some areas of depression zones of Azerbaijan are presented in Tables 7.2 and 7.3.

The significant decline in the geothermal gradients with depth for areas of the Apsheron Peninsula and the Apsheron archipelago (see Table 7.3) points to their significant heterogeneity with depth (at depths up to 1,000 m in some areas the values of the geothermal gradient decline with depth is about $-(10–30)$ K/km^2) (Pilchin 1983; Kerimov and Pilchin 1986a). The high geothermal gradient decline values with depth at levels up to 2,000 m are possibly caused by water content and its circulation in the upper layers of the sedimentary cover. This is consistent with the fact that at depths of about 3,000–5,000 m for areas of the Middle Kura and Lower Kura Depressions, the Apsheron Peninsula, and the Apsheron archipelago the geothermal gradient decline values vary with depth by $-(1.0–2.2) \times 10^{-6}$ K/m^2, $-(0.4–0.6) \times 10^{-6}$ K/m^2, $-(0.4–0.7) \times 10^{-6}$ K/m^2, and $-(0.4–0.9) \times 10^{-6}$ K/m^2, respectively (see Tables 7.2, 7.3). This means that in the upper part of the sedimentary layer (up to 5,000 m), which mostly represents the part uncovered by drilling, measurements of geothermal gradients and densities of heat flow with depth show that the most stable as regards changes in thermal characteristics is the Middle Kura Depression. But it also means that in regions of the Lower Kura Depression, the Apsheron Peninsula, and the Apsheron archipelago, the values of the geothermal gradient are almost stabilized at depths of 3,000–5,000 m.

Table 7.2 Average value of geothermal gradient decline with depth for oil and gas fields of the Kura Depression (Azerbaijan) (in 10^{-6} K/m^2)

Region, area	Investigated depth interval (m)			
	500–1,500	1,500–2,500	2,500–3,500	3,500–4,500
Shamkhor	−2.8	−2.4	−2	−1.0
Ganja	−3.2	−2.1	−1.9	−2.2
Sheki-Zakataly	−3.0	−2.5	−2.2	−1.8
Evlakh	−2.8	−2.4	−2.2	−1.9
Barda-Shirvanly	−3.0	−2.5	−2.2	−2.0
Gyullyudja	−3.7	−2.0	−1.9	−1.6
Agdzhabedi-Beilagan	−3.9	−1.6	−1.5	−1.3
Agdash	−2.5	−2.2	−2.0	−1.7
Ismailly	−2.4	−2.2	−1.9	−1.6
Akhsu	−2.2	−2	−1.9	−1.6
Kurdamir	−3.9	−1.6	−1.5	−1.3
Sabirabad	−2.7	−2.3	−1.3	−0.6
Kazi-Magomed	−5.8	−1.1	−0.6	−0.4
Imishly	−2.3	−1.3	−1.2	−1.1
Saliany-Garabagly	−4.8	−1.2	−0.2	−0.5

The changes in the vertical geothermal gradient with depth for some regions are presented in Table 7.4.

It was shown above (see Sect. 2.7) that there is a strong functional relationship between excess pressure $(P - P_0)$ and excess/change of temperature $(T - T_0)$ [see Eqs. (2.7.4) and (2.7.5)] and a strong correlational relationship between relative change/excess pressure $(P - P_0)/P_0$ and temperature $(T - T_0)/T_0$. Thus it is important to analyze changes in excess temperature $(T - T_0)$ and relative excesses of temperature $(T - T_0)/T_0$ with depth in different regions. Examples of changes in excess temperature with depth for some oil and gas regions of the Kura Depression and adjacent regions of the Caspian Sea are presented in Fig. 7.2.

The values of temperature excess $(T - T_0)$ and relative excess temperature $(T - T_0)/T_0$ at different depths for some areas of the Kura Depression are presented in Tables 7.5 and 7.6, respectively.

It is clear from Tables 7.5 and 7.6 that for all the areas, the $(T - T_0)$ and $(T - T_0)/T_0$ values increase with depth. This means that in these regions the temperature T increases with depth faster than the normal temperature T_0.

Section 2.7 showed that to analyze the thermodynamic conditions of porous fluids, parameters such as the coefficient of abnormality of pressure $K_{aP} = P_{AHSP}/P_0$, the coefficient of abnormality of temperature $K_{aT} = T/T_0$, excess pressure $(P - P_0)$, and excess temperature $(T - T_0)$ are usually employed. Here P_0 and T_0 are the hydrostatic pressure and normal temperature of water, respectively. The hydrostatic pressure at any depth is calculated using Eq. (2.7.1), and similarly, the value of the normal temperature is determined using the condition of equilibrium

Table 7.3 Average value of geothermal gradient decline with depth for oil and gas fields of the Apsheron Peninsula and the Apsheron archipelago (in 10^{-6} K/m^2)

Area	Investigated depth interval (m)						
	250–750	750–1,250	1,250–1,750	1,750–2,250	2,250–2,750	2,750–3,500	3,500–4,500
Neftyanie Kamni	−12.2	−6.0	−7.0	−8.6	−6.8	−3	−0.9
Lokbatan, Puta, Binagady	−27.6	−7.6	−3.4	−2.2	−2	−1.5	−0.6
Bibi-Eybat	−19.4	−9.4	−7.0	−3.6	−2	−1.5	−0.6
Balakhany, Sabunchi, Ramany	−9.0	−10.8	−6.2	−4.0	−5.6	−0.7	−0.4
Surukhany	−11.6	−8	−12.2	−4.0	−3.2	−1.8	−0.7
Zykh, Gara-Chyukhur	−30	−9.2	−6.8	−8.0	−5.4	−1.1	−0.6
Peschaniy island	−45.2	−12.6	−5.8	−3.0	−2.6	−1.2	−0.4
Buzovny, Mashtagy, Kala, Zirya,	−16.8	−2.8	−4.6	−2.6	−1.8	−1.2	−0.4
Pirallahi (Artem Island), Gousany	−11.0	−5.6	−3.4	−3.2	−1.8	−1.8	−0.7
	−16.8	−8.6	−3.4	−1.8	−5	−1.5	−0.3

Table 7.4 Changes in the vertical geothermal gradient with depth for some regions (after Eppelbaum and Pilchin 2006)

Region	Depth interval (m)	Average geothermal gradient (K/km)	Percentage of geothermal gradient near the surface
Krasnodar region, Russia	0–2,000	30–40	70
	2,000–4,000	30–35	65
	4,000–6,000	25–32	57
Stavropol region, Russia	0–2,000	35–50	71
	2,000–4,000	35–45	67
	4,000–6,000	30–35	54
Middle-Kura Depression, Azerbaijan	0–2,000	25–43	76
	2,000–4,000	20–35	61
	4,000–6,000	20–30	42
Northern Israel	2,300	18–20	46–54
Dead Sea region, Israel	2,350–2,750	16–22	20–61
Utah, USA	440–619	48	83
Salton Sea, USA	762–884	178.9	73
Central Ventura Basin, USA	1,900–3,600	23–27	70–86
Williston Basin, Canada	2,000–3,000	20-Oct	30–80
Michigan Basin, USA	Phanerozoic	17.5	41

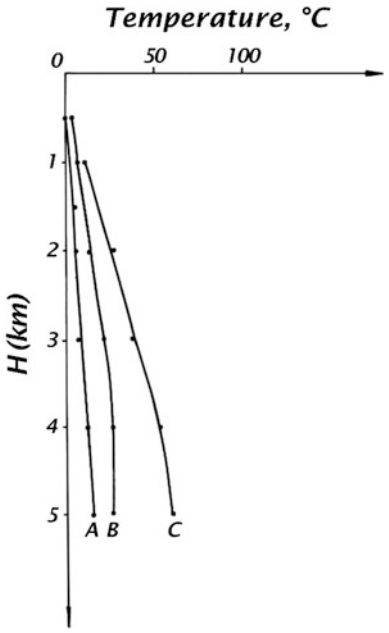

Fig. 7.2 Changes in excess temperature ($T - T_0$) with depth for some oil and gas regions of the Kura Depression and the Caspian Sea: (*A*)—the region of Sangachaly Sea—Duvanniy Sea—Bulla Island (Caspian Sea; average for 22 deep wells); (*B*) Kyurovdag (Lower Kura Depression; average for 117 deep wells); (*C*) Muradkhanly (Middle Kura Depression; average for 16 deep wells)

Table 7.5 Changes in excess temperature ($T - T_0$) with depth (in K) for some oil and gas areas of the Kura Depression

Area	Excess temperature ($T - T_0$) in K at depth (m)				
	1,000	2,000	3,000	4,000	5,000
Padar	5	8	20	27	31
Kyursangya	5	18	22	27	31
Kalmas	10	19	23	27	32
Mishowdag	5	12	13	22	28
Garabagly	2	8	13	20	28
Neftechala	5	8	19	35	42
Kyurovdag	5	8	16.5	22	28
Borsunly	–	–	46	64	86
Zardob	–	–	25	41	48
Muradkhanly	–	21	38	45	73
Dzharly—Sor-Sor	–	–	2.5	38	43
Beilagan	–	–	40.5	66	80
Mir-Bashir	–	–	37	53	75
Garaddzhally	–	–	36	55	75
Gazanbulag	–	–	28	35	42

Table 7.6 Changes in relative excess temperature $(T - T_0)/T_0$ with depth for some oil and gas areas of the Caspian Sea and the Kura Depression

Area	Value of $(T - T_0)/T_0$ at depth		
	3,000 (m)	4,000 (m)	5,000 (m)
Alyaty-sea	0.35	0.53	0.7
Garadag	0.5	0.63	0.75
Garasu	0.15	0.25	0.36
Oblivnoy island	0.19	0.3	0.39
Golovacheva	0.25	0.32	0.43
Bahar	0.35	0.55	0.79
Padar	0.38	0.45	0.46
Kyursangya	0.42	0.45	0.46
Kalmas	0.44	0.45	0.48
Mishovdag	0.25	0.37	0.42
Garabagly	0.25	0.33	0.42
Neftechala	0.37	0.58	0.63
Kyurovdag	0.31	0.37	0.42
Borsunly	0.88	1.07	1.28
Zardob	0.48	0.68	0.72
Muradkhanly	0.73	0.75	1.09
Dzharly—Sor-Sor	0.35	0.48	0.66
Beilagan	0.78	1.1	1.19
Mir-Bashir	0.71	0.88	1.12
Garadzhally	0.69	0.92	1.12
Gazanbulag	0.54	0.58	0.63

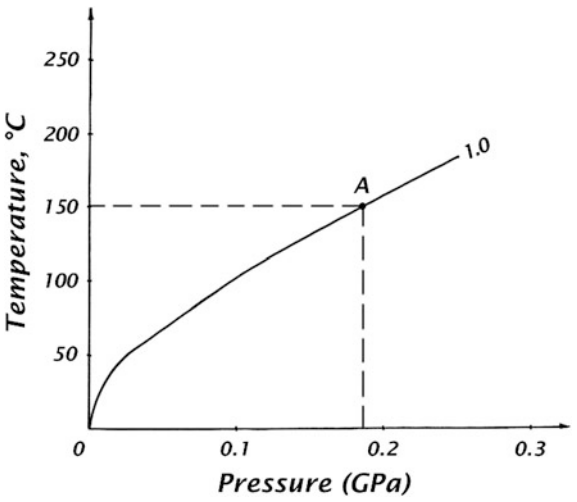

Fig. 7.3 Condition of equilibrium of water (either $\Delta V = 0$ or $\Delta\sigma = 0$) in a wide range of temperatures and pressure

of water (either $\Delta V = 0$ or $\Delta\sigma = 0$; see Fig. 7.3.). The normal temperature (T_0) is a temperature which in combination with hydrostatic (or lithostatic) pressure (P_0) keeps the volume and density of a liquid (or solid rock) unchanged from its value near the surface.

It is obvious from Fig. 7.3 that each hydrostatic pressure (P_0) value has only one corresponding value of normal temperature (T_0) for condition of equilibrium of water. For example, point A on the equilibrium line (see Fig. 7.3) is represented by a single pair of values (P_A, T_A) at a depth of point A for which water will be in thermodynamic equilibrium. If calculated using the equilibrium of water, any pair of values P_0 and T_0 has same base for both pressure and temperature. It is obvious that the values of both P_0 and T_0 change with depth, but if a pair of P_0 and T_0 is calculated for any particular depth, the values of this pair are related to each other and can be used for the analysis of thermal, baric and the thermo-baric conditions of a layer with correlated basic/normal values of temperature and pressure. This makes it possible to use the pressure abnormality coefficient pressure (K_{aP}) and the temperature abnormality coefficient of abnormality (K_{aT}) for separate or simultaneous analysis of baric and thermal conditions of porous fluids using compatible initial data.

Based on the analysis of temperature data the in oil and gas fields of the oil and gas provinces of the USSR (over 12,000 temperature readings) Pilchin (in Kerimov et al. 1986, 1988) presented a method to detect the possible presence of oil and gas field at depth using values of the temperature abnormality coefficient (K_{aT}) for shallow depths. The analysis showed that in oil and gas fields, in most cases values of K_{aT} were low ($K_{aT} \leq 1$), normal ($K_{aT} \approx 1$) and moderate ($1 \leq K_{aT} \leq 2$), and the most significant oil and gas fields (in terms of reserves) are present in regions with moderate temperature abnormality coefficient values ($1 \leq K_{aT} \leq 2$), and with increases in the K_{aT} value there are likely to be fewer

reserves of hydrocarbons. The rationale behind the method is based on the fact that even though specific thermal (and thermodynamic) conditions are necessary for formation of oil and gas fields (e.g., Tissot and Welte 1984; Galushkin 1990; Hunt 1996; Hyne 2001; Tucker 2001; Deffeyes 2005; Peters et al. 2005; Wei et al. 2007; etc.), after their formation the most important conditions are those that allow for preservation of the deposits.

The occurrence of oil and gas fields points to the presence of thermal (thermodynamic) conditions favorable for their preservation. On the other hand, as is clear from Table 7.6, the value of K_{aT} increases with depth in oil and gas areas of the Caspian Sea and the Kura Depression. It also increases with depth for other oil and gas provinces of the former USSR (Kerimov et al. 1986, 1988). These facts make it possible to predict the thermal (thermodynamic) conditions favorable to the preservation of oil and gas fields at great depths without actual drilling deep boreholes. If the value of K_{aT} increases with depth, it is sufficient to calculate this value at a relatively shallow depth (a few hundred meters) to be sure that it is within the range of K_{aT} favorable for the preservation of oil and gas fields. Of course, the presence of $1 \leq K_{aT} \leq 2$ at a depth in any sedimentary basin cannot guarantee that oil and gas fields are present at a depth in the basin, but it can show that if oil and gas fields were formed in the basin they would be preserved there. Results of analysis of the thermal conditions in the oil and gas rich provinces of the former USSR were conducted for such regions as the Urals-Povolzhie, Siberia, the Caucasus, Middle Asia, South Caspian Depression, etc. (Kerimov and Pilchin 1987a, b; Pilchin 1987a).

Analysis of temperatures in sedimentary strata in the South Caspian Depression showed that it is characterized by heat absorption (it is in the heating stage; see more details in Sect. 6.4). The temperature regime in the uppermost part of sedimentary layer of the depression is significantly low and is characterized by a temperature abnormality coefficient (K_{aT}) of 1.36–1.75 at a depth up to 5 km. The lowest values of K_{aT} were found in Garasu, Oblivnoy Island and Golovachev bank (1.36, 1.39, and 1.43 respectively) (Kerimov and Pilchin 1987b). Thus most areas of the South Caspian Depression are highly favorable to the formation and preservation of oil and gas fields at great depths (Kerimov and Pilchin 1987b). A similar analysis showed (Kerimov et al. 1988; Kerimov and Pilchin 1987a) that all areas of the Lower Kura Depression and the Western Turkmenian Depression are also probable sites for the preservation oil and gas fields.

In the Caucasus, the highest temperatures are present in the epi-Hercinian platform and the values of K_{aT} are greatest in the Krasnodar (up to 3.07 in Eastern-Kuban' Depression) and Stavropol' (up to 2.91 in Stavropol' arch) provinces (Kerimov and Pilchin 1987a). But both the Eastern-Kuban' Depression and Stavropol' arch are characterized by very low values of K_{aP}, which were caused by pressure unloading during previous geological periods that could mean destruction of the fields. The sedimentary strata of the Middle Kura and Lower-Kura Depressions are characterized by heat absorption and have values of K_{aT} at depths of 3–5 km in the range of 1.25–2.29 and 1.25–1.63, respectively (Kerimov and Pilchin 1987a). In a depth range of 3–5 km in areas of the Baku archipelago, the

values of K_{aT} are 1.15–1.75 (Kerimov and Pilchin 1987a). In the oil and gas fields of Middle Asia, excluding the Western Turkmenian Depression that has a $K_{aT} = 1.18–1.75$ at depths of 3–4 km, the values of K_{aT} are high and reach 2.83 in Eastern Turkmenistan, 2.53 in Central Turkmenistan (at depths as low as 1.0–1.5 km), 2.45 in Western Uzbekistan, 1.68–1.85 at depths of 2–3 km in the Fergana Depression, 1.81–1.85 at depths of less than 1 km in Tajikistan (Kerimov and Pilchin 1987a). It should be noted that there are no significant oil and gas fields in the Eastern Turkmenistan and Western Uzbekistan. Moreover, areas of these regions are characterized by the presence of brines with very high salt content ("rapa" in Russian; with density of up to 1,500 kg/m^3 and higher) having extremely high overpressure at shallow depths, which causes huge problems for drilling.

Analysis of temperature data shows that for the preservation of oil and gas fields in the regions of the Caucasus and Middle Asia, the most favorable conditions are those with low ($K_{aT} < 1$), normal ($K_{aT} \approx 1$) and moderate ($1 \leq K_{aT} \leq 2$) temperature conditions in sedimentary layers. At the same time, the oil and gas reserves in fields decrease with increases in K_{aT}. This led to the conclusion that in the depression regions of the Caucasus and Middle Asia the presence of significant reserves of oil and gas at great depths is most probable in regions with a moderate thermal regime ($1 \leq K_T \leq 2$), because oil and gas fields with low and normal K_{aT} are present here only at depths of less or about 0.5–1.0 km (Kerimov and Pilchin 1987a).

The values of K_{aT} in depression regions of the Urals-Povolzhie and Siberia (Russia) are usually very low (Pilchin 1987a). Analysis shows that sedimentary layers containing oil and gas fields in regions of the Urals-Povolzhie are the coldest in the USSR with the lowest temperatures in the gas and gas-condensate fields. The lowest geothermal regime was found in areas of Bashkirian, Permian and Orenburg provinces (with K_{aT} reaching values as low as 0.17, 0.53, and 0.29, respectively) in which mostly $K_{aT} < 1$ (Pilchin 1987a). In gas and gas-condensate fields of Kuibyshev province, mostly $K_{aT} < 1$, but in the oil-gas-condensate and oil fields $K_{aT} > 1$. The hottest sedimentary layers are in Saratov province (K_{aT} up to 2.03). Low values of K_{aT} (from 0.47 to 1.54) are present in the oil and gas fields of the Timan-Pechora province (Russia). In Siberia, low K_{aT} are present in the northern part of Tumen' province, where occur the largest oil and gas fields. The highest temperatures within sedimentary layers of Siberia are found in the oil and gas fields of Tomsk province (K_{aT} up to 2.11 at depths of less than 3 km) and the Berezovskiy region of Tumen' province (K_{aT} up to 1.97 at depths of less than 3 km). At depths of 3–4 km the lowest K_{aT} for Siberia are present in Yakutia ($K_{aT} = 1.25–1.57$) and the northern Tumen' province (K_{aT} up to 1.44–1.64). The lowest K_{aT} are present in the Verkhnevilu-chanskiy (from 0.15 to 0.42) and Srednebotuobinskiy (from 0.14 to 0.24) regions of Yakutia, but for most fields of Yakutia $K_{aT} > 1$. Analysis of the thermo-baric regime of oil and gas fields of the Northern Tumen' province shows that fields with the

greatest reserves of hydrocarbons are characterized by temperatures close to normal or slightly elevated temperatures (the only exception is the field in the Lower Cretaceous layer of the Urengoy area (Russia); $K_{aT} = 1.38–1.73$ at a depth of 2.99–3.09 km) and close to normal or slightly lower pressures. There is a tendency toward reduction of gas reserves with temperature increases. In fields in Senomanian in the Urengoy area $K_{aT} = 0.97$; Yamburgskaya area $K_{aT} = 0.97$; Zapolyarnoe area $K_{aT} = 1.12$; Kruzenshternovskiy area $K_{aT} = 0.95$. In the largest fields of Yakutia $K_{aT} \leq 1.09$ and $K_{aP} \leq 1.01$, but in smaller fields K_{aT} is up to 1.57 and K_{aP} is up to 1.44. Analysis of temperature data shows that for the preservation of oil and gas fields in regions of the Urals-Povolzhie and Siberia the most favorable conditions are those with low ($K_{aT} < 1$), normal ($K_{aT} \approx 1$) and moderate ($1 \leq K_{aT} \leq 2$) temperature conditions in sedimentary layers. Thus, in depression zones of the Urals-Povolzhie and Siberia the presence of oil and gas fields with significant hydrocarbon resources is possible in Bashkiria ($K_{aT} = 1.24$ at depths of 3–4 km), Orenburg province ($K_{aT} = 0.89$ at depths up to 3 km), the Permian province (K_{aT} up to 1.65 at depths up to 4 km), the Timan-Pechora oil and gas province ($K_{aT} = 1.22–1.31$ at depths 3–4 km), Volgograd province ($K_{aT} = 1.72–1.82$ at depths up to 4 km), some areas of the Precaspian Depression ($K_{aT} = 1.64$ at depths of 2–3 km), Yakutia ($K_{aT} = 1.25–1.57$), the northern part of Tumen' province ($K_{aT} = 1.44–1.64$), etc. (Pilchin 1987a). Analysis of geothermal data points to the presence of heat absorption layers in all these regions of the Urals-Povolzhie excluding Orenburg province.

It is obvious that such an analysis of temperature conditions within sedimentary layers of depression zones should be conducted in conjunction with analysis of thermal conditions of generation and maturity of oil and gas fields of these zones, because oil and gas fields must first be formed and only then are preserved from destruction. The most important factor controlling the generation of oil and gas is the hydrogen content of the organic matter. The quantity of petroleum generated and expelled increases as the ratio of hydrogen to carbon (H/C) increases (Hunt 1996).

There are a few methods which are usually employed to calculate or estimate paleotemperatures during the generation and maturity of oil and gas. Among these are methods based on analysis of kerogen color (Staplin 1969; Schwab 1977; Tissot and Welte 1984), vitrinite reflectance (Tissot and Welte 1984; Allen and Allen 1990; Peters et al. 2005), and Rock Eval pyrolysis (Tissot and Welte 1984; Tissot et al. 1987; Hunt 1996; Price 1999; Price et al. 1999; Helgeson et al. 2009).

Kerogen color and vitrinite reflectance are used as paleothermometers to determine paleotemperatures reached by source rocks. These optical properties of organic matter are affected by both time and temperature, and they reflect the stage of thermal maturity reached by the sediments (Tissot and Welte 1984; Peters 1986; Tissot et al. 1987). The color of kerogen changes progressively from colorless to dark brown and black with increasing temperature and can be used as an indicator of the degree of thermal alteration and is usually characterized by the thermal alteration index (TAI) (Staplin 1969). The initial scale from 1 to 5 for the TAI of kerogen used to estimate paleotemperature (Staplin 1969) was modified to scale from 1 to 8 for a TAI of kerogen by Schwab (1977).

Estimates of paleotemperature based on the analysis of vitrinite reflectance relies on the property of vitrinite to undergo increasing reflectance with increasing temperature (Tissot and Welte 1984; Tissot et al. 1987; Allen and Allen 1990). The method is based on the fact that the amount of light reflected by vitrinite particles (R_0) is affected by time and temperature of burial and irreversibly changes with increases in temperature. It was shown (Tissot and Welte 1984) that a vitrinite reflectance of less than 0.5–0.7 % indicates that the source rocks are immature, whereas reflectance between 0.5–0.7 and 1.3 % indicates that the source rocks have reached the principal zone of oil generation.

Based on analysis of the empirical relationship between vitrinite reflectance and petroleum formation Lopatin (1971) put forward a simple method that uses both time and temperature to calculate the thermal maturity of the organic matter in sediments. The method is based on the determination of the Time-Temperature index (*TTI*) of maturity, which is a theoretical measure of organic matter maturity and oil generation. It was modified by Waples (1980). This method is widely used for determination of the oil window in sedimentary basins. Within the oil window increasingly more oil is generated with increases in temperature until maximal production is reached, at which point the quantity of oil decreases and increasingly more gas is formed (Tucker 2001). Deffeyes (2005) came to conclusion that the organic rich source rock must be buried to at least 2,100 m, but never deeper than 5,400 m and the temperature must reach values of 352.6 K and greater, but not 422 K. Tucker (2001) also came to conclusion that most oil generation occurs in the "oil window" at temperatures of around 348–392 K at depths of 2.0–3.5 km. Helgeson et al. (2009) showed that the petroleum generated in the process progresses from heavy naphthenic crude oils at low temperatures to mature petroleum at $\sim$423 K. They argued that oil generation takes place in the oil window and further increases in temperature lead to thermal destruction of oil in the reservoir and the generation of natural gas.

The temperature limits of the oil window are within the range of about 323–423 K (Tissot and Welte 1984) and they depend on the age of source rocks with significant decreases in temperature with increases in age. For deposits of $\sim$300 Ma, the formation of oil starts at temperatures of $<$323 K and continues to temperatures of $\geq$373 K and gas is formed above this temperature to temperatures of $\sim$488 K, but above that limit, the temperature both oil and gas are destroyed. In contrast, for rocks dated to $\sim$10 Ma, the generation of oil starts at temperatures of $\sim$356 K and continues to about 443 K, above which gas is usually formed to temperatures of $>$573 K. Paleozoic basins generate significant oil at 323 K whereas the younger Mio-Pliocene basins require temperatures closer to 388 K at roughly the same burial depth (Tissot and Welte 1984). The predicted temperatures for oil generation in Jurassic sediments of the Paris Basin are in the range of $\sim$323–463 K (Helgeson et al. 2009). Sajgó (2000) came to conclusion that at the onset of oil generation in the Neogene hydrocarbon source rocks of Eastern Hungary, temperatures higher than 403 K were required and would reach temperatures exceeding 488 K. For the Neogene to Late Neogene source rocks of basins of California, temperatures during main stage of oil generation were in the

range of 363–493 K in the Los Angeles Basin, 408–487 K in the Southern San Joaquin Valley Basin and above 413 K in the Ventura Basin (Price 1999; Price et al. 1999).

At the same time, with the increasing age of the deposits, the temperature at which oil and gas is destroyed drops (Tissot and Welte 1984). For example, for deposits of about 300 Ma the temperature required for destruction is above about 488 K but it is about 573 K for deposits of ~30 Ma. This proves that both oil generation and its destruction are controlled by both the temperature and the time elapsed since burial.

Another frequently used technique for identifying the type and maturity of organic matter is Rock-Eval pyrolysis, which involves the progressive heating of a sample in a pyrolysis oven (e.g., Tissot et al. 1987; Hunt 1996; Price 1999; Price et al. 1999). The method is based on determination and analysis of a number of parameters such as the total organic carbon (TOC), S_1, S_2, S_3, T_{max} range, hydrogen index (*HI*), oxygen index (*OI*), production index (*PI*), pyrolyzable carbon (*PC*). The four basic parameters obtained by pyrolysis (S_1, S_2, S_3, T_{max}) are defined (Tissot and Welte 1984; Tissot et al. 1987) as follows: S_1 is the amount of free hydrocarbons in the sample (in milligrams of hydrocarbon per gram of rock) volatilized at a temperature of 573 K; S_2 is the amount of hydrocarbons generated through thermal cracking of nonvolatile organic matter by heating in temperature intervals from 573 to 823 K (~923 K at the start and upwards to 1,073 K (Oba et al. 2002) and 1,123 K (Behar et al. 2001); S_3 is the amount of CO_2 (in milligrams CO_2 per gram of rock) produced during pyrolysis of kerogen within the 573–673 K range; T_{max} is the temperature at which the maximum release of hydrocarbons from cracking of kerogen occurs during pyrolysis (top of S_2 peak). S_1 normally increases with depth. S_2 normally decreases with burial depths >1 km. T_{max} = 673–703 K represents immature organic matter; T_{max} = 708–723 K indicates a mature or oil zone; $T_{max} > 723$ K represents an over-mature zone. T_{max} ranges can be also used to classify kerogen types: 713–721 K for type I kerogen, 703–728 K for type II kerogen, and 703–743 K for type III kerogen (Peters 1986). Other important parameters are defined as follows: the total organic carbon (TOC) is expressed as a weight percentage and is the percentage of carbon in CO_2 formed during pyrolysis below 673 K, and in CO formed below 773 K, and in the hydrocarbon peaks, S_1 and S_2; the hydrogen index $HI = (100 \times S_2)/\text{TOC}$; oxygen index $OI = (100 \times S_3)/\text{TOC}$; production index $PI = S_1/(S_1 + S_2)$; pyrolyzable carbon $PC = 0.083 \times (S_1 + S_2)$.

Research using rock-eval pyrolysis shows (Price et al. 1999) that in the Los Angeles Basin, the main stage of hydrocarbon generation commenced in the type III/IV organic matter at present-day burial temperatures of 358–383 K and was largely completed by 493 K; in the southern San Joaquin Valley Basin the main stage of hydrocarbon generation commenced in type III/IV organic matter at 423 K and was also largely complete by 493 K, and in the Ventura basin the main stage of hydrocarbon generation commenced above 413 K in type III/IV organic matter.

Oil generation curves indicate that peak oil yields occur between 613 and 633 K, followed by intense oil cracking (at >643 K) in different samples (Wei et al. 2007). Wei et al. (2007) showed that the concentrations of diamondoids increase with thermal stress, and their abundance is highly sensitive to thermal exposure above temperatures of 633–643 K (equivalent $R_0 = 1.3$–1.5 %). This suggests that they can be used as a molecular proxy for thermal maturity of source rocks and crude oils.

Wang et al. (2006) found that in laboratory heating rates, oil cracking started at 663–673 K and the laboratory cracking was complete at around 923 K, but at geological heating rates, the onset temperature is about 421–435 K for the start of cracking and was complete at 518–549 K.

The sole use of geothermal methods for calculating the temperature at great depths may lead to error, because the estimated values usually cannot be double-checked by an independent method and the geothermal regime at great depths could be quite different from the accepted model. This is the reason why it is so important to estimate temperature at great depths using independent of geothermics data to confirm geothermal results. Nevertheless, geothermal methods cannot be used for calculating the temperature at great depths in regions where measurements of basic geothermal parameters are impossible (mountain areas, mountain slopes, zones of active faults, inaccessible areas, etc.) or can be done only in very shallow boreholes. To solve these problems an attempt to estimate temperature values at great depth for some areas of the southern slope of the Greater Caucasus using seismic data along with thermodynamic data on seismic velocity was carried out (Pilchin and Kerimov 1987). This method was used to calculate temperatures at great depths in regions of the Kura Depression where geothermal data were also used to calculate temperatures at great depths to compare results. The state equation seismic velocity is shown in Eq. (4.4.11):

$$\Delta v = \left(\frac{\partial v}{\partial P}\right)_T \Delta P + \left(\frac{\partial v}{\partial T}\right)_P \Delta T.$$

Here $\Delta v = v_1 - v_0$ is change in seismic velocity v_1 (at pressure P_1 and temperature T_1) compared to its value v_0 under normal conditions (with P_0, T_0) for the investigated layer; $(\partial v/\partial P)_T$ and $(\partial v/\partial T)_P$ are changes in seismic velocity with changes in pressure and temperature in the investigated layer, respectively.

For overpressure $(\Delta P = P_1 - P_0)$ caused by excess temperature $(\Delta T = T_1 - T_0)$ without including volume change, it was shown (Pilchin 1983) that changes in pressure and temperature are related through the equilibrium equation (2.7.5):

$$\Delta P = \frac{\alpha}{\beta}\Delta T.$$

Here α and β are coefficients of thermal expansion and compressibility of rock of the investigated layer, respectively.

Table 7.7 Comparison of values of temperature calculated using Eq. (7.2.3) for different types of rocks and geothermal data obtained for surfaces of consolidated crusts for some regions of Azerbaijan (after Pilchin and Kerimov 1987)

Region, area	Type of rock	v_0 (km/s)	v_1 (km/s)	T, (K) using data	
				Equation (7.2.3)	Geothermics
Evlakh-Agdjabedy	Medium composition	6.2	6.4	403–443	653–773
	Acidic composition, gneisses	5.9	6.4	593–683	653–773
Saatly	Medium composition	6.2	6.7	553–583	623
	Acidic composition, gneisses	6.0	6.7	673–733	623
Muradkhanly	Medium composition	6.2	6.4	403–443	613
	Acidic composition, gneisses	6	6.4	513–573	613

Substituting Eq. (2.7.5) into Eq. (4.4.11) gives:

$$\Delta v = J \cdot \Delta T. \tag{7.2.1}$$

Here

$$J = \left(\frac{\partial v}{\partial T}\right)_P + \frac{\alpha}{\beta}\left(\frac{\partial v}{\partial P}\right)_T. \tag{7.2.2}$$

Equation (7.2.1) may be transformed to:

$$T = T_0 + \frac{\Delta v}{J}. \tag{7.2.3}$$

It is clear from Eq. (4.4.11) and Eqs. (7.2.1)–(7.2.3) that to estimate temperature at depths which have not been determined by drilling using seismic data, the value of v_1 should be calculated, and the petrological composition of layer should be hypothesized to determine the value J using experimental data. The method was used to compile two maps of temperature distribution at depths of 5 and 10 km, as well as to estimate the temperature at depths of 15 and 20 km for joint regions of the southern slope of the Greater Caucasus and Kura Depression (Pilchin and Kerimov 1987).

Table 7.7 compares temperature values calculated using Eq. (7.2.3) for different types of rocks, and geothermal data obtained for the surface of consolidated crusts for some regions of Azerbaijan are presented.

In Table 7.7 the values of seismic velocity in normal conditions v_0 were taken from (Clark 1966), the measured values of seismic velocities v_1 were obtained from seismic data along the deep seismic profile 3-GSZ in the Kura Depression; temperature values were calculated using the method in (Pilchin 1983) and

Eq. (6.2.3). The margin of error for temperature values using this method show that the errors did not exceed 9–14 % (Pilchin 1983) which is in line with errors (10–15 %) for similar estimates by other authors (Kutas 1978). For comparison of data in Table 7.7 two different petrological compositions (acidic and intermediate) were taken into account to calculate the right petrological composition of the layer. It is clear from Table 7.7 that this method can be used for modeling the petrological composition of deep layers of crust.

It was shown (Pilchin 1981) that in data on seismic velocities, velocity jumps at boundaries between seismic layers and thermodynamic characteristics of seismic velocities $(\partial v/\partial P)_T$ and $(\partial v/\partial T)_P$ may be used for the analysis of petrological compositions of seismic layers above and below such boundaries.

7.3 Calculation of Horizontal and Vertical Gradients

The geothermal gradient (G or Γ) is a key parameter that captures the dynamics of temperature change in different directions. The geothermal gradient is also a key component in calculating the heat flow density $Q(Q = \lambda G)$.

Mathematically, a gradient is a vector, which is defined as the partial derivative of a scalar function pointing in the direction of the most rapid increase of the function. In Cartesian coordinates the gradient of temperature can be presented as:

$$grad(T(x,y,z)) = \left(\frac{\partial T(x,y,z)}{\partial x}\mathbf{i} + \frac{\partial T(x,y,z)}{\partial y}\mathbf{j} + \frac{\partial T(x,y,z)}{\partial z}\mathbf{k}\right). \tag{7.3.1}$$

Here **i**, **j** and **k** are the unit vectors.

For single-variable functions, instead of the term gradient, the terms slope or rate of change are often used. However, in geothermics instead of the total gradient of temperature, the vertical ($G_z = dT/dz$) and horizontal ($G_x = dT/dx$ and $G_y = dT/dy$) gradients are typically used for analyses of the temperature distribution and calculations of the heat flow. Each presents the rate of change in either direction (x, y or z).

It is clear from the above that the components of the temperature gradient (see Eq. (7.3.1)) and geothermal gradients are derivatives. According to the definition of a derivative, the vertical geothermal gradient can be written as

$$G_z = \lim_{\Delta h \to 0} \frac{T(x,y,z+\Delta h) - T(x,y,z)}{\Delta h}. \tag{7.3.2}$$

But in practice it is impossible to obtain two accurate measurements of the temperature at a zero distance ($\Delta h \to 0$) (e.g., Pilchin 1978). Thus instead, finite difference methods are used to calculate geothermal gradients. Finite difference methods are well known in mathematics and widely used in other sciences (Forsythe and Wasow 1960). The difference between the values of a function at

two discrete points is used to approximate the derivative of the function. Only three forms of finite difference are usually considered:forward difference:

$$\Delta_h(T(z)) = T(z + \Delta h) - T(z). \tag{7.3.3}$$

backward difference:

$$\Delta_h(T(z)) = T(z) - T(z - \Delta h). \tag{7.3.4}$$

and central difference:

$$\Delta_h(T(z)) = T(z + \Delta h) - T(z - \Delta h). \tag{7.3.5}$$

Using the central difference form, the value of the vertical geothermal gradient at an arbitrary depth h_i in a borehole can be written as (Pilchin 1978):

$$\left(\frac{dT(z)}{dz}\right)_{h_i} = \frac{T(h_i + \Delta h) - T(h_i - \Delta h)}{2 \cdot \Delta h}. \tag{7.3.6}$$

Similarly, the horizontal geothermal gradient can be expressed as:

$$\left(\frac{dT(x)}{dz}\right)_{l_i} = \frac{T(l_i + \Delta l) - T(l_i - \Delta l)}{2 \cdot \Delta l} \tag{7.3.7}$$

Equations (7.3.6) and (7.3.7) are an approximation of the vertical and horizontal geothermal gradients. Horizontal geothermal gradients can be approximated in a similar fashion. It is clear that to calculate the vertical geothermal gradient using Eq. (7.3.6), as an average vertical geothermal gradient in a borehole, temperature values at two different depths ($h_i + \Delta h$ and $h_i - \Delta h$) need to be measured.

Finite difference methods can also be used to find the second derivative of a function. For example, the second derivative of the temperature with depth at an arbitrary depth h_i in a borehole can be written as:

$$\left(\frac{d^2T(z)}{dz^2}\right)_{h_i} = \frac{T(h_i + \Delta h) - 2T(h_i) + T(h_i - \Delta h)}{(\Delta h)^2}. \tag{7.3.8}$$

To use Eq. (7.3.8) temperature measurements at three different depths ($h_i + \Delta h, h_i$ and $h_i - \Delta h$)are required.

Thus to obtain accurate vertical geothermal gradient values using Eq. (7.3.6) we also need an accurate reading of the depth difference (Δh) with correction for possible borehole inclination. Similarly, to calculate the horizontal geothermal gradient using Eq. (7.3.7) the temperatures must be measured at the same depth in two different boreholes. In the case where the temperature readings in two different boreholes were taken at different depths, the temperature values in either of boreholes need to be adjusted using the vertical geothermal gradient to calculate

the temperature at the same depth as in the other borehole. It is obvious that for more accurate calculation of geothermal gradients, temperature measurements should be made within a homogeneous layer (sub-layer). This condition is much more easily met when calculating horizontal geothermal gradients because of the natural stratification of sedimentary layers. But for rough estimates of geothermal gradients and analysis of the temperature regime less accurate temperature measurements could also be used because there is no alternative method to do so.

This approach was used for calculation and analysis of both vertical and horizontal geothermal gradients for regions of Azerbaijan and the Caspian Sea (Kerimov and Pilchin 1986a, b; Pilchin 1983), the Caucasus (Kerimov et al. 1989), Israel (Eppelbaum et al. 1996), the Los Angeles Basin (using data from Sawyer et al. 1987), the Williston Basin (using data from Majorowicz et al. 1986), etc. The main aim of analysis of both the vertical and horizontal gradients was to determine which conditions would make it possible to apply a one-dimensional heat conduction equation for these different regions. The findings indicated (Kerimov and Pilchin 1986a, b; Pilchin 1983) that the one-dimensional thermal conduction equation can be used if: (1) the thermal regime shows little variation, and (2) the vertical gradient is more than one order of magnitude greater than the horizontal gradient. For example the value of the vertical geothermal gradient in the Middle-Kura Depression (30–42 K/km) is almost two orders greater than the values of the horizontal geothermal gradient (Kerimov and Pilchin 1981; Pilchin 1983). For an analysis of vertical geothermal gradients in regions of Azerbaijan and the Caspian Sea, see Sect. 7.2.

Vertical geothermal gradients and their changes with depth for boreholes of some areas of Northern Israel and around the Dead Sea are presented in Tables 7.8 and 7.9.

Tables 7.8 and 7.9 clearly show that in regions of Israel, the vertical geothermal gradient is relatively high near the surface but declines rapidly with depth. It is similar to the distribution of the vertical geothermal gradient in the Kura Depression (see Sect. 7.2) and many other regions. This profile is normal for the distribution of vertical geothermal gradients as seen in Eq. (7.1.9). At the same time it is clear from Table 7.9 that the second derivative of the temperature with depth, which represents the rate of change of the vertical geothermal gradient, increases with depth in many intervals of all boreholes. Such intervals are anomalous and they will be discussed in Sect. 7.4.

Values of horizontal geothermal gradients calculated for some regions around the Dead Sea are presented in Table 7.10.

Table 7.10 shows that horizontal geothermal gradients are generally low in the area and their values do not usually exceed 1 K/km except in the Dead Sea fault zone. In the southern Dead Sea Basin, the highest temperatures at depths of 1,500–2,000 m were encountered in the Lot-1 well, and horizontal geothermal gradients increase towards this well. From the north, the geothermal gradient increases from 0.21 to 1.29 K/km; from the south, 0.62–1.3 K/km; and from the SE by an average of 1.6 K/km (Table 7.11).

Table 7.8 Vertical geothermal gradients in boreholes of some areas of northern Israel and the Dead Sea region (after Eppelbaum et al. 1996)

Boreholes	Depth (m)	Vertical geothermal gradient (K/km)
Northern Israel		
Asher-3	0–302	51.8
	302–1,000	27.8
Belvoir-1	0–562	33.9
	562–2,280	18.0
Canusa-10	0–460	45.6
	460–2,000	20.8
Areas of the Dead Sea region		
Massada-1	0–353	52.4
	353–2,750	22.0
Lot-1	0–1,050	37.6
Heimar-1	0–600	37.3
	600–2,370	19.7
Ammiaz-1	2,020–4,600	21.9
Arava-1	0–417	62.8
	417–2,653	12.4
Ein-Gedi-2	0–1,670	29.0
	1,670–2,550	17.7
Sodom-1	0–300	56.5
	300–2,308	18.5
Zohar Deep-8	1,120–3,560	26.7

These relatively high horizontal geothermal gradients are caused by the numerous minor faults associated with the Dead Sea Transform Zone. Horizontal geothermal gradients around the Hakanaim-3, Lot-1 and Massada-1 boreholes vary from 0.69 to 1.2 K/km. In the northern Arava Valley their values are within a range of 0.23–0.46 K/km, and low values 0.33–0.78 K/km were also observed at some distance from the Dead Sea Transform Zone. Analysis of the data distribution shows that on the western flank of the Dead Sea fault zone the values of the horizontal geothermal gradient decrease with depth. Overall, the values of the horizontal geothermal gradients are less than 10 % of the values of the vertical geothermal gradients in corresponding areas and the ratio of $(G_x, G_y)/G_z$ is less than 4 % within stable blocks of the crust in the region (Eppelbaum et al. 1996). This means that the one-dimensional heat conduction equation can be used to calculate the temperature at great depths for this region.

In Table 7.11, the pressure gradient within porous fluids is also presented. The value of this gradient was calculated using equation (Eppelbaum et al. 1996):

$$\frac{dP}{dx} = \frac{\alpha}{\beta}\frac{dT}{dx}. \tag{7.3.9}$$

Table 7.9 The depth distribution of average geothermal gradients and the second derivative of temperature with depth in some boreholes of the Dead Sea region (after Eppelbaum et al. 1996)

Borehole	Depth (m)	Gradient (K/km)	Second derivative (K/km^2)
Lot-1	0–1,050	37.6	
			−28.5
	1,050–1,785	12.2	
			22.4
	1,785–2,180	23.1	
Heimar-1	0–600	38.9	
			−8.6
	600–1,000	32.2	
			0
	1,000–1,180	32.2	
			−58.7
	1,180–1,490	6.1	
			33.0
	1,490–2,370	25.7	
Hakanaim-1	0–250	40.0	
		–	−64.0
	250–500	8.0	
			26.5
	500–650	13.3	
			44.7
	650–800	20.0	
			0
	800–1,000	20.0	
			29.3
	1,000–1,083	24.1	
Massada-1	0–353	52.4	
			−5.8
	353–527	5.8	
			45.6
	527–670	13.0	
			20.6
	670–1,001	18.9	
			13.4
	1,001–1,356	23.5	
			−40.9
	1,356–1,516	15.0	
			56.8
	1,516–1,708	25.0	
			−18.4
	1,708–1,940	21.1	
			−28
	1,940–2,200	14.2	
			96.9
	2,200–2,580	45.3	
			−106.9
	2,580–2,750	15.9	

Table 7.10 Horizontal geothermal gradients in areas around the Dead Sea (after Eppelbaum et al. 1996)

Points of measurement[a]	Depth (m)	Horizontal geothermal gradient (K/km)
Massada-1 ⇒ Lot-1	1,100	0.47
	2,180	0.29
Heimar-1 ⇒ Lot-1	1,100	1.3
	1,500	1.2
	2,180	0.62
Hakanaim-1-3 ⇒ Massada-1	1,700	0.96
	2,150	0.69
Zohar Deep-8 ⇒ Hakanaim-3	1,100	0.78
	1,850	0.78
	2,380	0.55
	3,000	0.03
Zohar Deep-8 ⇒ Lot-1	1,100	1.42
	1,785	1.06
	2,180	0.89
Hakanaim-3 ⇒ Lot-1	1,500	1.27
	2,180	0.9
Ammiaz-1 ⇒ Sedom-1	2,300	0.01
Arava-1 ⇒ Sedom-1	2,300	0.23
Arava-1 ⇒ Ammiaz-1	2,650	0.35
Ammiaz-1 ⇒ Heimar-1	2,370	0.29
Heimar-1 ⇒ Arava-1	2,370	0.46
Sedom-1 ⇒ Heimar-1	2,370	0.46
Massada-1 ⇒ Ein Gedi-2	1,670	0.6
	2,370	0.21
Hakanaim-3 ⇒ Ein Gedi-2	1,670	0.87
	2,370	0.24
	2,550	0.1
El Lisan-1 ⇒ Lot-1	2,180	0.92
Ammiaz-1 ⇒ El Lisan-1	3,580	0.01

[a] Arrow shows the direction of the increase in horizontal geothermal gradient

Equation (7.3.9) can be used to estimate the potential horizontal pressure within porous fluids caused by a heterogeneous distribution of horizontal geothermal gradients.

Kerimov et al. (1989) presented two maps comparing the vertical geothermal gradients and horizontal geothermal gradients at depths of 4,000 and 6,000 m for regions of the Caucasus. The average values of these gradients for some regions of the Caucasus are presented in Table 7.12.

Analysis of geothermal data for Azerbaijan, Georgia, the Caucasus regions of Russia and Israel shows that the heterogeneity of a geothermal regime is mostly related to the presence of fractures and hydrothermal water activity. It was shown in

Table 7.11 Horizontal geothermal and pressure gradients for the southern Dead Sea Basin (after Eppelbaum et al. 1996)

Points of measurement[a]	Depth (m)	Horizontal geothermal gradient (K/km)	Pressure gradient (MPa/km)
Massada-1 ⇒ Lot-1	1,100	0.47	0.395
	1,750	0.21	0.258
	2,180	0.29	0.394
Heimar-1 ⇒ Lot-1	1,100	1.3	1.092
	1,500	1.2	1.32
	2,180	0.62	0.843
Zohar Deep-8 ⇒ Lot-1	1,100	1.42	1.193
	1,785	1.06	1.325
	2,180	0.89	1.21
Ammiaz-1 ⇒ Lot-1	2,020	1.6	2.176
Hakanaim-3 ⇒ Lot-1	1,100	1.09	0.916
	1,500	1.27	1.397
	2,180	0.9	1.224

Table 7.12 Average values of vertical and horizontal geothermal gradients for some regions of the Caucasus

Region	At a depth of 4,000 m		At a depth of 6,000 m	
	Vertical geothermal gradient	Horizontal geothermal gradient	Vertical geothermal gradient	Horizontal geothermal gradient
Low Kura Depression	15–20	0.2–0.6	15–20	0.4–0.8
Middle Kura Depression	20–30	0.4–1.0	20–30	0.8–1.6
Kolkhida Depression	25–30	0.4–1.4	20–30	0.8–2.0
Dagestan	25–30	0.4–0.8	25	0.6–0.8
Stavropol province	35–40	0.4–0.8	25–30	0.2–1.0
Krasnodar province	30–35	0.2–0.8	30	0.2–1.0
Chechnya	30–35	0.4–0.8	25–30	0.4–0.8
South Caspian Depression	15	0.2–0.4	15	0.4–0.6

(Kerimov and Pilchin 1981, 1986a, b; Pilchin 1983; Eppelbaum et al. 1996) that this feature is most apparent in the distribution of horizontal geothermal gradients. In the most stable parts of the Evlakh-Agdzhabedi Depression and the Kurdamir—Sor-Sor—Djarly—Saatly zone the value of the horizontal geothermal gradient does not exceed 0.4 K/km, but it is significantly higher in areas in which huge fractures and fracture zones are present. In the vicinity of the Western Caspian fracture and areas along the southern slope of the Greater Caucasus, the value of the horizontal geothermal gradient rises to 1.0–1.2 K/km, and in the PreLesser-Caucasian fault zone it reaches 0.7–1.0 K/km. Values of the horizontal geothermal gradients between areas of the Middle Kura Depression such as Sor-Sor—Djarly—Saatly and

Zardob—Muradkhanly—Mil'skaya are within the range of 0.03–0.50 K/km, and between in areas located near the Pre-Lesser Caucasus deep fault area Sovetlyar and the values for Barda, Borsunly, Zardob and Muradkhanly are 0.67, 0.11, 0.25–0.30 and 0.1–0.25 K/km, respectively. The horizontal geothermal gradient values are even lower in the Lower Kura Depression and the South Caspian Depression. This means that in all these areas of Azerbaijan and the South Caspian Depression, the values of the vertical geothermal gradients are almost two orders of magnitude greater than the corresponding horizontal geothermal gradient values. It also means that the one-dimensional heat conduction equation can be used to calculate temperatures at great depths for all depression zones of Azerbaijan and the South Caspian Depression.

A similar analysis of the geothermal gradient distribution in the Los Angeles Basin using data in (Sawyer et al. 1987) yielded average vertical geothermal gradient values of 18–25 K/km at depths of 2–4 km; 21.5–24 K/km at depths of 4–6 km; 17.5–23.5 K/km at depths of 6–8 km; with an average for depths of 2–8 km of 20.2–23.3 K/km. For horizontal geothermal gradients, the average values were 0.0–0.6 K/km at a depth of 2 km; 0.0–1.5 K/km at a depth of 4 km; 0.0–2.0 K/km at a depth of 6 km, 0.2–1.5 K/km at a depth of 8 km (Pilchin and Eppelbaum 1994b). These values show that in the Los Angeles Basin, the vertical geothermal gradient values are more than an order of magnitude greater than the values of the corresponding horizontal geothermal gradients.

Geothermal data presented by Majorowicz et al. (1986) was used to calculate vertical and horizontal geothermal gradients in sedimentary layers of the Canadian part of the Williston Basin (Pilchin 1995b). The results showed that the values of the vertical geothermal gradients were in the range of 25–30 K/km in the West and Center, and 30–45 K/km to the East of the Canadian part of Williston Basin of Saskatchewan and S–E Manitoba for the upper intervals of Mesozoic-Cenozoic formations, and in range of 10–25 in the West and Center, and 10–25 to the East of the Canadian part of Williston Basin of Saskatchewan and S–E Manitoba for the upper intervals below the Paleozoic erosional surface (Paleozoic formations). The horizontal geothermal gradients (G_H) were very low at a depth of $\sim$1 km in Southern Saskatchewan and S–E Manitoba, close to 0.0 K/km in the S–W part of Saskatchewan, not higher than 0.6 K/km but changed in the range of 0.05-0.60 K/km in the central part of Southern Saskatchewan, 0.05–0.45 K/km in the S–E part of Southern Saskatchewan, 0.0–0.65 K/km at a depth of 2 km in the Western part of Southern Saskatchewan; and reached its highest values of 0.45–0.65 K/km only in the northern part of Southern Saskatchewan, 0.06–0.65 K/km in central part of Southern Saskatchewan;. 0.1–1.2 K/km in the Eastern part of Southern Saskatchewan, reaching values 0.65–1.20 K/km only within a small area of the S–E part of Southern Saskatchewan and 0.6–0.7 K/km within a small area S–E of Southern Saskatchewan and the south-westernmost part of Manitoba. On the Precambrian surface, values of G_H ranged from 0.22 to 1.60 K/km but were very seldom greater than 0.6 K/km. Values of G_H greater than 1.0 K/km were usually caused by different depths of Precambrian surface. These data clearly show that in the Canadian part of the Williston Basin, the vertical geothermal gradient is more

than an order of magnitude (in most cases almost two orders of magnitude) greater than the corresponding horizontal geothermal gradients.

Extremely high horizontal geothermal gradient values have been found near salt domes. For example the horizontal geothermal gradients near a typical salt dome in the North Louisiana Salt Basin calculated using data from (Petersen and Lerche 1995a, b) at depths of 2,000–2,500 m were up to 12 K/km near the salt dome, ~7 K/km at 500 m from the salt dome, and ~2.3 K/km at 1,000–1,500 m from the dome, whereas the vertical geothermal gradient at these depths was about 25 K/km. Interestingly, within the salt dome, minimal vertical geothermal gradients hit values as low as ~8.5 K/km at a depth of ~1,500 m. Such a significant increase in horizontal geothermal gradient values near salt domes and low vertical geothermal gradients within the salt dome can be explained by the very high thermal conductivity of salt (Petersen and Lerche 1995a, b).

All of the above clearly shows that in most depression zones, the values of the vertical geothermal gradient are almost two orders of magnitude greater than the corresponding values of the horizontal geothermal gradient, and the ratio of these gradients is only greater than one order of magnitude in close proximity to active deep faults. The horizontal geothermal gradient values are only on the same order of magnitude near salt domes, which are extremely rare structures.

This analysis did not include volcanic and other magmatic activity, given the significant disturbance of both the vertical and horizontal temperature distributions in these instances.

7.4 Heat Absorption in the Earth's Strata

The upper layers of the Earth (at least its upper 800–1,000 km) are known to be cooling (e.g., Lubimova 1956, 1968b).

Equations (6.1.5), (6.1.6), (6.1.9) and (6.1.13) show that within a homogeneous layer (sub-layer) the vertical geothermal gradient (G_z) and heat flow density (Q) values normally decrease with depth. Moreover, since the compaction and density of rocks increase with depth, the heat conductivity (λ) value of rocks should also increase with depth. Thus according Eq. (7.1.4) the vertical geothermal gradient value should decrease with depth even for non-homogeneous layers. This is well established (Lubimova 1956, 1968b; Pilchin 1978, 1979, 1983; Eppelbaum and Pilchin 2006) and coincides with the fact that layers of crust and the whole lithosphere are cooling. However, in practice in numerous cases this was not observed (Pilchin 1983; Pilchin and Kerimov 1980), and even though the crust is cooling it contains numerous layers (sub-layer) absorbing heat. For example, all vertical geothermal gradient distribution models incorporating depth put forward by different authors for the Los Angeles Basin integrate an increase of the gradient with depth (see Table 2 in Price et al. 1999). Since the upper layers of the Earth are cooling, the presence of any layer (sub-layer) absorbing heat should be viewed as an abnormality, and such a layer should be treated as anomalous. We next discuss

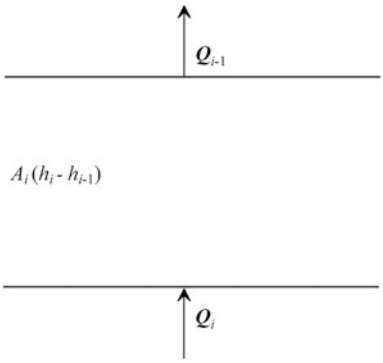

Fig. 7.4 Geothermal characteristics of an arbitrary sub-layer i

how to calculate these anomalous layers. The model in Fig. 7.1, as well as its simplified form for any arbitrary sub-layer, is illustrated in Fig. 7.4.

It is obvious from Fig. 7.4 that the condition for heat absorption is

$$Q_i(h_i) > Q_i(h_{i-1}). \tag{7.4.1}$$

Here $Q_i(h_i)$ and $Q_i(h_{i-1})$ are the heat flow density on surfaces of h_i and h_{i-1}, respectively.

These values can be used to calculate heat absorption when ignoring the heat production within sub-layer i. For example, Westbrook et al. (1994) reported an increase of heat flow density from about 73 mW m^{-2} near the seafloor that increased through Unit I to reach a value of 84 mW m^{-2} through Units II and III of the Cascadia continental margin (the authors interpreted these facts as a probable consequence of the absorption of heat).

The amount of absorbed heat for conditions with $A_i = 0$ is

$$\Delta Q = Q_i(h_i) - Q_i(h_{i-1}). \tag{7.4.2}$$

But in the case of heat generation, A_i does not equal zero, and during a unit of time in sub-layer i, the following amount of heat will be released:

$$\Delta Q = A_i(h_i - h_{i-1}). \tag{7.4.3}$$

This leads to the condition for heat absorption:

$$Q_i(h_{i-1}) < Q_i(h_i) + A_i(h_i - h_{i-1}). \tag{7.4.4}$$

At the same time it is obvious that even in the case where

$$Q_i(h_i) < Q_i(h_{i-1}) \tag{7.4.5}$$

there will be some heat absorption but the amount of absorbed heat will be less than the amount of heat released within sub-layer i. This is consistent with the conditions in Eq. (7.4.4) which can be written as

$$\Delta Q = Q_i(h_{i-1}) - Q_i(h_i) < A_i(h_i - h_{i-1}). \tag{7.4.6}$$

It is also clear that condition:

$$Q_i(h_i) = Q_i(h_{i-1}). \tag{7.4.7}$$

means that sub-layer i is in thermal equilibrium, because it absorbs an amount of heat exactly equal to the amount of heat released within the sub-layer.

Such conditions with unchanging values of heat flow were found in a depth range of 310–2,763 m in well 1 of the Octemberyan area, Armenia ($Q = 49.7$ mW m^{-2}) and a depth range of 378–2,870 m in well 4 of the Lukashin area, Armenia ($Q = 53.1$ mW m^{-2}) (Avetis'yantz 1979).

Equation (7.1.9) can be rewritten as:

$$-\frac{A_i}{\lambda_i} = \frac{\left(\frac{dT_i}{dz}\right)_{h_i} - \left(\frac{dT_i}{dz}\right)_{h_{i-1}}}{h_i - h_{i-1}}. \tag{7.4.8}$$

Equation (7.4.8) presents the relationship between vertical geothermal gradients at the lower and upper surfaces of sub-layer i and the values of heat generation (A_i) and heat conductivity (λ_i) within the sub-layer. It is clear from Eq. (7.4.8) that the value ($-A_i/\lambda_i$) represents the rate of change (or slope) of the vertical geothermal gradient with depth. Equation (7.4.8) also shows that the value of ($-A_i/\lambda_i$) represents the second derivative of temperature by depth [see Eq. (7.1.6)].

Since the value of λ_i is always positive ($\lambda_i > 0$), it is clear from Eq. (7.4.8) that A_i is positive ($A_i > 0$) if the sub-layer is releasing heat, and A_i is negative ($A_i < 0$) if the sub-layer is absorbing heat. Note that negative rates of change of geothermal gradient with depth correspond to heat release in sub-layers and positive rates of geothermal gradient change with depth correspond to heat absorption in the sub-layer.

Equations (7.1.6), (7.1.9), (7.1.13) and (7.4.8) can be used to calculate heat generation (A_i), but the heat generation values obtained using these equations represent the total heat generation, which includes all sources and all sinks of heat within arbitrary sub-layer i. The value of A (the average for the cross-section) in the upper part of the sedimentary strata for some oil and gas fields of the Apsheron peninsula and Apsheron archipelago are presented in Table 7.1. The average values of heat generation for areas presented in Table 7.1 range from 0.45 to 1.34 μW/m^3 which is significantly lower than the radiogenic heat generation values reported for different stratigraphic layers of the eastern Azerbaijan and the adjacent part of the Caspian Sea 1.84–4.41 μW/m^3 (Kerimov and Pilchin 1986a).

Table 7.13 Values of heat flow density in the Saatly super-deep SG-1borehole (after Pilchin 1983)

Depth interval (m)	Stratigraphy	Lithology	Heat flow density (mWm^{-2})
800–2,150	Apsheron	Siltstones, aleurites, clays	18.0
2,150–2,320	Akchagyl	Clays	17.2
2,320–2,600	Productive layers	Sands, sandstones, clays, conglomerates	19.7
2,600–2,765	Productive layers	Same	11.3/23.0
2,765–2,896	Sarmatian	Sandstones, clays, tuffs	30.6
2,896–3,500	Upper Cretaceous	Limestone, sandstones, tuffs	35.6
3,500–4,400	Volcanogenic layers	Basalts, porphyrites	51.1
4,400–5,000	Volcanogenic layers	Basalts, porphyrites	96.7
5,000–5,650	Volcanogenic layers	Basalts, porphyrites	36.4

Such a huge difference in heat generation values means that part of generated heat is being absorbed in these areas.

Significant increases in heat flow density with depth (heat absorption) were observed within the Saatly superdeep SG-1 borehole (see Table 7.13) at depth intervals of 800–5,000 m.

There are numerous examples of heat flow density increases with depth. Some of these obtained for boreholes from different regions of the former USSR are presented in Table 7.14.

Heat flow density increases with depth in boreholes of some areas from different regions of the USA are presented in Table 7.15.

Some calculated values of heat generation (A) using geothermal data for some areas of the Kura Depression are presented in Fig. 7.5.

It is clear from Fig. 7.5 that the total heat generation (A) for all areas declines with depth and for Salyany-Karabagly area it reaches zero ($A = 0$) at a depth of $\sim$4.5 km. This means that at this depth, the value of heat released within a sub-layer equals the value of heat absorbed by heat sinks within the sub-layer and the sub-layer is in thermodynamic equilibrium.

Analysis of changes with depth of the vertical geothermal gradient ($-A/\lambda$) in the Muradkhanly, Garabagly, Djarly and Kurovdag shows (Pilchin 1979) that in all four areas at different depths the rate of change of the vertical geothermal gradient with depth ($-A/\lambda$) equals zero ($-A/\lambda = 0$) which means that at those depths the value of the total heat generation is zero ($A = 0$). Interestingly, such sub-layers which evidence an equilibrium ($-A/\lambda = 0$) of their thermodynamic regime were present at 4 different depths at a depth interval of 1.0–5.0 km in the Muradkhanly area, 3 different depths at a depth interval of 2.0–4.5 km in the Garabagly area, and 1 at a depth interval of 3.5–4.0 km in both the Djarly and Kurovdag areas. In all

Table 7.14 Heat flow density at different depths in boreholes of some areas of the former USSR (after Pilchin (1983), with modifications)

Region, area	Borehole (boreholes)	Depth interval (m)	Heat flow density (mW m^{-2})
Muradkhanly, Azerbaijan	1, 2, 3, 5, 6, 8, 11	2,186–2,508	25.5
		3,888–5,000	45.11
Karadjaly, Azerbaijan	1, 3	3,280–3,286	10.98
		3,528–3,655	27.95
Djarly, Azerbaijan	1, 3, 4, 5, 10	2,879–3,763	23.46
		>4,000	38.5
Zardob, Azerbaijan	1	4,072–4,077	11.69
		4,418–4,420	21.19
Dnieper-Donets, the Ukraine	Koshelevka-204	1,350–1,900	34.3
		2,000–2,600	37.2
Krivoi Rog, the Ukraine	8,500	675–925	9.2–14.6
		925–1,425	27.3
Gorokhov, the Ukraine	1	450–670	25.8
		1,080–2,300	37.6–50.2
Olesko, the Ukraine	1	Upper Devonian	35.5
		Lower Devonian	42.4
Melovaya, Crimea, the Ukraine	6	1,292–1,342	67.0
		1,342–1,737	78.3
Oktyabr'skaya, Crimea, the Ukraine	20	1,740	61.6
		1,938	76.2
Taratashski, the Urals	1	300–540	27.5
		1,000–1,380	38.9
Taratashski, the Urals	3	220–480	23.8
		800–1,040	35.1
Yakovlevskoye, Belgorod province	384	425–445	40.1
		540–590	81.8
Staraya Matsesta, Russia	3T	315–328	15.9
		375–950	36.2
Khosta, Russia	2T	675–950	43.5
		1,225–1,350	49.3
Cheladidy, Georgia	4	2,700–2,720	27.2
		2,900–2,920	32.6
Chatirkul, Kirgizstan	591	112	49.3
		623	61.0
Alma-Ata, Kazakhstan	10Г	350–400	46
		1,800–1,850	60.6
		2,650–2,700	48.1
Central Fergana, Uzbekistan	1	800–950	27.9
		1,050–1,400	51.8
Khadzhiabad, Uzbekistan	570	400–450	31.8
		1,962–2,011	79

(continued)

Table 7.14 (continued)

Region, area	Borehole (boreholes)	Depth interval (m)	Heat flow density (mW m^{-2})
Izbaskent, Uzbekistan	108	971–1,046	39
		1,466–1,541	68.9
Ravat, Uzbekistan	4	210–2,325	58.1
		2,625–2,869	76.1
Razdan, Armenia	4	342–935	58.9
		1,233–1,558	65.2
Nidjerlu, Armenia	12	203–306	29.7
		306–1,655	32.2
Karabohlar, Armenia	1	50–117	46.8
		855–2,300	53.9

cases the sub-layers at equilibrium ($-A/\lambda = 0$) separated the sub-layers releasing heat from the sub-layers absorbing heat.

The distribution of A/λ values with depth is presented for different areas of the Kura Depression (Figs. 7.6, 7.7, 7.8) and Stavropol' province (Fig. 7.9).

It is obvious from Figs. 7.6, 7.7 and 7.9 that in the cross-section of boreholes there are a number of interlayered sub-layers releasing and absorbing heat. This highlights the complex thermal regime of these regions in which some sub-layers heat (absorb heat) and other sub-layers cool (release heat). It is also clear from Fig. 7.8 that sub-layers can also release and absorb heat energy at a very high rate. Extremely high rates of heat release and heat absorption were found in the VC-1 borehole of Valles Caldera, where a minimal heat flow of <100 mW m^{-2} at a depth of ~280 m was followed by a maximum of heat flow density of ~540 mW m^{-2} at a depth of about 300 m (Sass and Morgan 1988).

The distribution of heat flow density in the super-deep borehole SG-1 (Saatly) shows (see Table 7.13) that there are layers absorbing heat and layers releasing heat with very high release of heat between layers in depth intervals of 5,000–5,650 and 4,400–5,000 m, but on average the whole interval 800–5,650 m absorbs heat.

The distribution of heat flow with depth in the super-deep borehole SG-3 (Kola Peninsula) is presented in Table 7.16.

Slightly different values of heat flow densities for different depths of the superdeep borehole SG-3 (Kola) have been reported in other studies. Mottaghy et al. (2005) found an increase with depth in heat flow from 34–36 to 55–58 mW m^{-2} in the top 2 km, and an average value of 38 mW m^{-2} (ranging from 31 to 45 mW m^{-2}) in the upper ~900 m depths in boreholes around the super-deep borehole SG-3 (Kola). Popov et al. (1999) reported average heat flow density values of 63 mW m^{-2} in the 5.2–7.5 km interval with a gradual decrease from 62 to 51 mW m^{-2} at depths of 7.6–8.2 km. These values in general are in line with the values in Table 7.16 and the slight differences could be caused by difference in the measurements or the samples, or different averaging intervals. Nevertheless, in

Table 7.15 Heat flow density at different depths in boreholes of some areas from different regions of the USA

Region, area	Borehole (boreholes)	Depth interval (m)	Heat flow density (mW m^{-2})	Reference
Yucca Mountain, Nevada	USWGl	91–427 1,524–1,697	26 54	Sass and Lachenbruch (1982)
Woodside, Colorado	WSR-1	45–105 455–515	60 72	Kutasov (1999)
Fifth Water Site, Utah	DH101	0–240 440–586	103 150	Powell and Chapman (1990)
Fifth Water Site, Utah	DH103	0–240 440–619	106 171	Powell and Chapman (1990)
Salton Sea, California	State 2–14	305–457 457–610	399 518	Sass et al. (1988)
Pearsburg, VA	CL1	113.4–171.4 188.2–195.4	114.7 131.6	Costain et al. (1986)
Palmetto, GA	PM1	89.5–148.5 161.4–205.0	37.5 41.9	Costain et al. (1986)
State farm, VA	SF1	50.0–92.5 185.0–192.5 197.5–207.5	37 44.4 38.8	Costain et al. (1986)
Southport, NC	C14A	200.8–206.4 361.6–371.3 478.2–545.4	53.6 54.9 53.7	Costain et al. (1986)
Kinston, NC	C16A	81.0–87.1 174.7–180.8	26.3 71.2	Costain et al. (1986)
Eatontown, NJ	C40	230.2–237.8 292.2–303.4	33.1 51.5	Costain et al. (1986)
Princess Anne, MD	C52	212.2–223.4 300.1–310.2	51.1 59.6	Costain et al. (1986)
Snow Hill, MD	C53	234.4–242.6 297.0–306.7	45.0 53.7	Costain et al. (1986)
Eastville, VA	C56	118.1–124.7 121.1–125.7	55.5 62	Costain et al. (1986)
Valles Caldera, New Mexico	VC-1	128–229 335–530 628–737	247 525 482	Sass and Morgan (1988)
Salton Trough, California	ERQU	38–59 56–59	43 77	Lachenbruch et al. (1985)
Salton Trough, California	GSLN	46–145 152–239	84 89	Lachenbruch et al. (1985)

(continued)

Table 7.15 (continued)

Region, area	Borehole (boreholes)	Depth interval (m)	Heat flow density (mW m^{-2})	Reference
Salton Trough, California	ORCA	30–69 70–122	109 112	Lachenbruch et al. (1985)
Salton Trough, California	DSRT	46–85 85–162	57 61	Lachenbruch et al. (1985)
Salton Trough, California	PALN	61–122 128–177	106 112	Lachenbruch et al. (1985)
Salton Trough, California	RIVM	46–114 122–175	74 81	Lachenbruch et al. (1985)

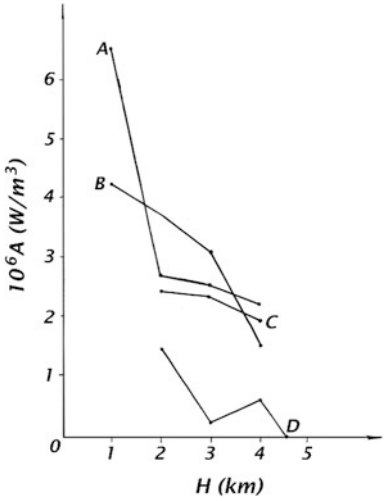

Fig. 7.5 Changes in heat generation values (A) for some areas of the Kura Depression (Azerbaijan): (*A*) Agdzhabedy-Beilagan (Zardob); (*B*) Kirovabad (Ganja); (*C*) Kurdamir; (*D*) Sal'yani-Karabagly (after Pilchin 1979)

both cases it is clear that on average, the value of heat flow density is increasing in the superdeep borehole SG-3. It is obvious from Table 7.16 that in many cases heat flow density is transferred from heat releasing layers to heat absorbing layers. More detailed compilations of the heat flow density distribution with depth in super-deep borehole SG-3 (Kola) show numerous interlayered sub-layers releasing and absorbing heat (Popov et al. 1999), but in general the heat flow density on average is increasing with depth within the whole cross-section of the borehole (0–9,000 m), even though it reaches a maximum of $\sim$68 mW m^{-2} at depths of about 4,900 m (Borevsky et al. 1995; Popov et al. 1999).

Similar results from areas in the US (see Table 7.15) help confirm this heat flow density distribution in boreholes including SF1 (State farm, VA, USA), C14A (Southport, NC, USA), VC-1 (Valles Caldera, New Mexico, USA).

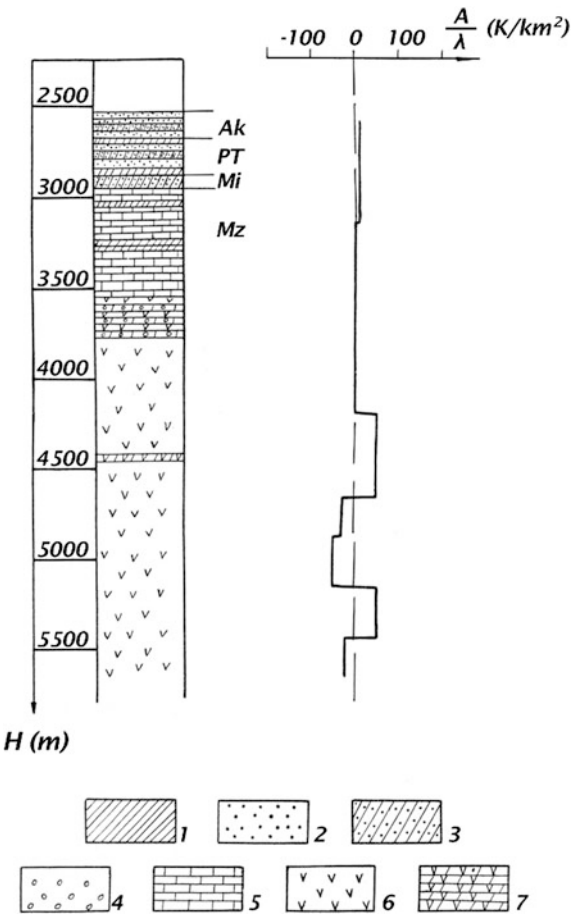

Fig. 7.6 Distribution of rate of change of the geothermal gradient (A/λ) with depth in the OP-1 borehole (Saatly, Azerbaijan) satellite of the super-deep SG-1borehole (Saatly). Lithology: (*1*) clays, (*2*) sands, (*3*) clayish sands (sandy clays), (*4*) gravelites, (*5*) mergels and limestones, (*6*) magmatic rocks, (*7*) interlayering of magmatic and sedimentary rocks. Stratigraphy: *Ak* akchagyl (Pliocene); *PT* productive series (Pliocene); *Mi* Maykop suite (Oligocene-Miocene); *Mz* mesozoic

In the Central graben and Anglo-Dutch Basin, in the western North Sea, the heat flow in the upper 1–2 km is around 50 mW m^{-2} and increases downward to about 100 mW m^{-2} (Andrews-Speed and Oxbu 1984).

The presence of sub-layers absorbing heat is also found within stratigraphically homogeneous layers. Analysis of a detailed distribution of heat flow density within boreholes of the North Western Desert, Egypt (discussed in Maky and Ramadan 2010) shows that within any stratigraphic unit there are a number of sub-layers absorbing and releasing heat (see Table 7.17).

Table 7.17 clearly shows that sub-layers absorbing and releasing heat are interlayered and how heat is transferred to the surface.

Heat absorbing intervals were observed in Grosmont and Beaverhile intervals of the Swan Hills area, Alberta (Canada), and in the northern part of the Williston Basin (Canada) (Pilchin 1995a, b). In the USA, heat absorbing intervals were found (Pilchin 1995a) in sedimentary cover of areas including the Fifth Water Site

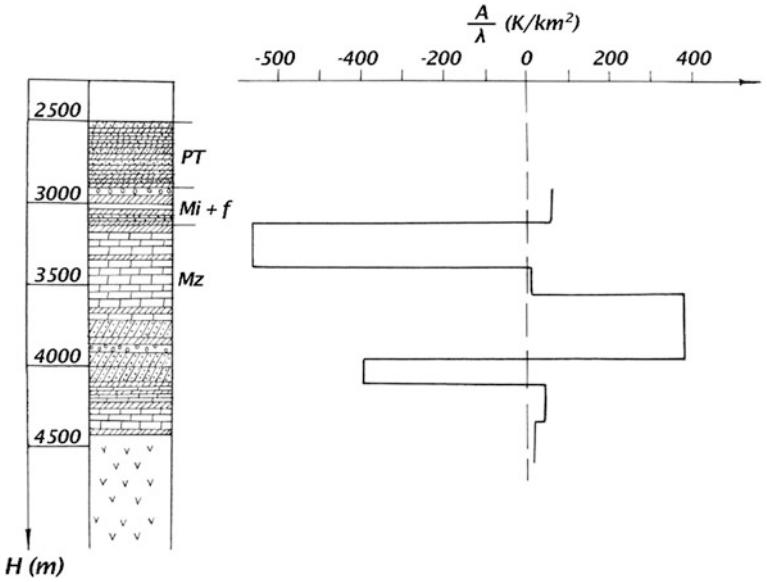

Fig. 7.7 Distribution of rate of change of the geothermal gradient (A/λ) with depth in the Djarly-1 borehole. Lithology is the same as in Fig. 7.6. Stratigraphy: *PT* productive series (Pliocene); *Mi* Maykop suite (Oligocene-Miocene); *f* foraminiferal interval (Eocene); *Mz* (Mesozoic)

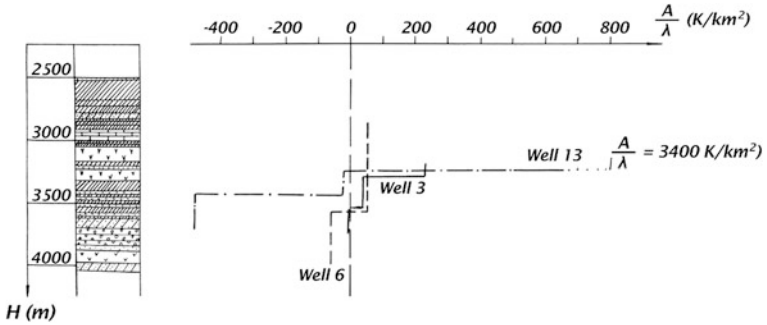

Fig. 7.8 Distribution of rate of change of the geothermal gradient (A/λ) with depth in the Muradkhanly-6 borehole. Lithology is the same as in Fig. 7.6

(Utah), Valles Caldera (New Mexico) and also in the Michigan Basin, the Central Ventura Basin and the Salton Sea. The average heat generation is -0.04 mW m^{-3} in the Cretaceous-Paleocene of the Fifth Water Site area, -0.11 mW m^{-3} in the VC-1 Well (Valles Caldera, 20–760 m), -0.06 mW m^{-3} in the State 2–14 Well (Salton Sea, 300–900 m). In the Michigan Basin heat absorption was discovered in the upper Michigan formation, Sunbury Shale and Clinton Shale. In the Central Ventura Basin the average heat generation is -0.007 and -0.018 mW m^{-3}

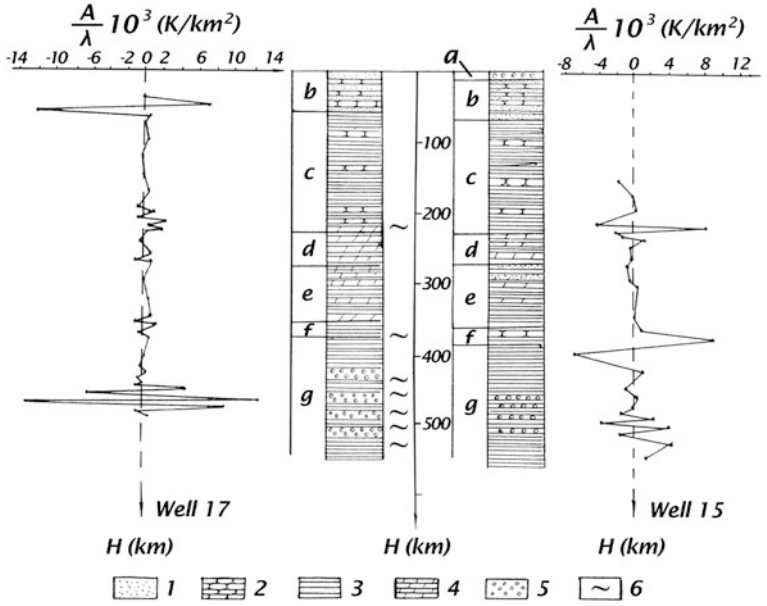

Fig. 7.9 Distribution of rate of change of the geothermal gradient (A/λ) with depth in boreholes No. 1 and No. 2 of the Petrovsko-Blagodarnenskaya area of Stavropol province, Russia. Lithology: (*1*) sand, (*2*) sandstone, (*3*) clay, (*4*) marl, (*5*) siltstone, (*6*) water-bearing horizons, Stratigraphy: (*a*) quaternary, (*b*) upper Sarmatian (Miocene), (*c*) middle Sarmatian (Miocene), (*d*) lower Sarmatian and Konkskiy horizon (Miocene), (*e*) Karaganskiy horizon (Miocene), (*f*) Chokracskiy horizon (Miocene) and (*g*) Maykop suite (Oligocene-Miocene)

Table 7.16 Summary of geothermal data for the Kola super-deep borehole SG-3 (Kola Peninsula, Russia) (after Borevsky et al. 1995)

Depth interval (m)	Average heat flow density (mWm^{-2})
0–1,200	29.7
1,200–1,600	36.9
1,600–2,000	31.2
2,000–2,805	39.6–40.8
2,805–4,500	49.5
4,500–4,900	66.6–68.4
4,900–5,642	52.5–54.6
5,642–5,717	52.5–61.2
5,717–6,400	52.5–54.6
6,400–6,800	58.7
6,800–7,200	44.4
7,200–9,456	45.6

respectively, calculated in the Pfeiler-10 and the Diedrich-l Wells (Oxnard Field) and 0 for the Lloyd-26 and Lloyd-161 Wells (Ventura Avenue Field).

Analysis of geothermal data in (Speece et al. 1985) for the Michigan Basin shows that the layer of Phanerozoic rocks tends to absorb heat (see Table 7.18)

Table 7.17 Changes in heat flow with depth and number of sub-layers absorbing heat in some Upper Cretaceous rock units, North Western Desert, Egypt

Well	Horizon	Depth interval (m)	Change of heat ($Q_{i0} - Q_i$) (mWm^{-2})	Number of intervals	Number of heat absorbing intervals
Raml-1	Abu Roash M[a]	1,080–1,211	5.95	15	9
Raml-1	Abu Roash "D" M[a]	935–991	0.84	13	7
Raml-1	Abu Roash "E" M[a]	991–1,031	−27.62	9	4
Raml-3	Bahariya Formation	1,205–1,402	−41.48	30	15
Raml-3	Abu Roash "G" M[a]	1,083–1,204	−11.22	19	9
Raml-3	Abu Roash "D" M[a]	940–994	4.88	14	6
Raml-3	Abu Roash "E" M[a]	995–1,036	−30.74	9	5
El-Faras-1	Bahariya Formation	765–973	10.15	21	10
El-Faras-1	Abu Roash "G" M[a]	649–765	−21.11	12	7
El-Faras-3	Bahariya Formation	795–985	−21.41	19	10
El-Faras-3	Abu Roash "G" M[a]	677–795	−23.82	10	5

Calculated using data in Maky and Ramadan 2010
[a] *M* member

with an average heat generation of about 13.5 μW m^{-3} [calculated using data in Speece et al. (1985)] that point to heat release.

Nevertheless, the average heat generation of layer including rocks of the Ordovician to Jurassic eras has an average heat generation of about (−0.183 mW m^{-3}) that suggests strong heat absorption. Similarly, the layer only containing rocks from the Cambrian to the Pennsylvanian age has an average heat generation (−0.0174 mW m^{-3}) that indicates heat absorption. These features show that finding the average heat absorbing intervals and heat releasing intervals within a cross-section of any depression basin depends on the choice of the layers (or sub-layers). Table 7.19 presents the average heat generation (A) values calculated for different layers/sub-layer combinations in the State 2–14 well, in the Salton Sea, California using data in (Sass et al. 1988).

Table 7.19 clearly shows that depending on the choice of layer/sub-layer of sedimentary rocks, not only do the average heat generation values change significantly but also their sign, which indicates either heat release or heat absorption.

It is clear from Table 7.18 that the average values of heat generation, either positive or negative, are significantly greater than the typical values of radiogenic heat generation. This implies that radioactive heat sources did not play a main role in heat generation in the Michigan Basin. The results also show that deposits of Mississippian, Devonian and Ordovician age are absorbing heat. It is also obvious from the analysis that Cambrian deposits, which are roughly a few meters thick in the Michigan Basin, are characterized by enormous heat release. Table 7.18 also proves that interlayering of heat absorbing and heat generating layers/sub-layers exists within every sedimentary basin.

Examples of the range of second derivative values for temperature with depth are presented in Table 7.9 for boreholes in some areas of Israel. It is clear from

Table 7.18 Characteristics of average heat absorption in Phanerozoic layers of the Michigan Basin

Period	Average (or range) of heat flow (mW m^{-2})	Average heat generation (A) (mW m^{-3})	Number of intervals	Number of heat absorbing intervals
Jurassic	6.4–37.5	0.63	2	0
Pennsylvanian	2.16	0.23	1	0
Mississippian	0–158.1	−0.39	6	2
Devonian	25.6–159.0	−0.35	5	4
Silurian	0–149.5	0.28	6	3
Ordovician	21–260.6	−1.95	5	3
Cambrian	22.59	22.59	2	0
Phanerozoic (whole)	0–260.6	0.0135	27	12

Calculated using data in (Speece et al. 1985)

Table 7.19 Average heat generation (A) calculated for different layer/sub-layer combinations in the State 2–14 well, Salton Sea, California

Depth interval (m)	Average heat generation (A) (mW m^{-3})
91–457	0.242
91–610	−0.137
91–762	−0.028
91–884	0.070
305–610	−0.783
305–884	−0.032
457–884	0.362
610–884	0.474

these values that in all boreholes, heat absorbing sub-layers are present and they are interlayered with sub-layers releasing heat. The distribution of average heat generation values with depth in the VC-1 borehole of Valles Caldera in the Jemez Mountains of New Mexico calculated using data (Sass and Morgan 1988) are presented in Table 7.20.

Table 7.20 clearly shows that the average heat generation (A) within the VC-1 borehole of Valles Caldera attains extremely high values that could be caused by extremely high geothermal activity of the cross-section of the borehole in which heat flow densities reach values of 500–550 mW m^{-2}. In this borehole, the interlayering of heat absorbing and heat releasing sub-layers is also obvious.

The average rates of change of the geothermal gradient with depth in boreholes of some areas of the former USSR are presented in Table 7.21.

It should be noted that heat absorption takes place not only within certain random boreholes, but also for huge regions (Pilchin 1983). The heat flow density calculated as the average for different depths up to 5,000 m in the Middle and Lower Kura Depressions is known to be increasingly monotonously with depth (Aliev and Rustamov 1977): in the Middle Kura Depression the value of Q is

Table 7.20 Average heat generation at different depths in the VC-1 borehole of Valles Caldera, Jemez Mountains, New Mexico, USA

Depth interval (m)	Average heat generation (A) (mW m^{-3})
20–70	−1.200
70–100	−6.667
100–150	3.800
150–200	−1.400
200–250	1.700
250–280	5.167
280–300	−25.000
300–350	0.800
350–400	0
400–450	−1.000
450–500	1.000
500–540	4.250
540–600	−2.500
600–650	0
650–700	0
20–700	−0.500

increasing from 33.5 mW m^{-2} at 10–1,000 m to 75.4 mW m^{-2} at 4,001–5,000 m, and in the Lower Kura Depression it is increasing from 16.7 mW m^{-2} at depths of 100–1,000 m to 29.3 mW m^{-2} at 4,001–5,000 m. The heat flow density is increasing from 15.0–31.0 mW m^{-2} at 25–50 m to 33–46 mW m^{-2} at over 1,000 m for the Dnieper-Donets Depression (the Ukraine) (Kutas et al. 1979). Research shows that sedimentary strata of the Western Turkmenian and South Caspian Depressions are absorbing heat (Kerimov and Pilchin 1987b). However, research shows that in depressions of the Krasnodar and Stavropol' provinces, as well as depressions of Western Uzbekistan, Eastern Turkmenistan and Central Turkmenistan sedimentary layer on average are releasing heat.

Heat absorption is not only found in sedimentary layers. For example, almost the whole crystalline shield of the Ukraine is characterized by heat flow densities that are about 10–15 % lower at depths of 100–150 m and in some areas up to 20–30 % lower at depths up to 300–350 m than at deeper layers (Kutas et al. 1979).

Bulashevich (1980) reported the HFD in some parts of the Urals, Russia, with values in Borehole 1 of the Taratashskiy Massif increasing with depth from 27.5 mW m^{-2} at depths 300–540 m to 38.9 mW m^{-2} at depths 1,000–1,380 m. Similarly, the HFD increased with depth in Borehole 3 of the same region from 23.8 mW m^{-2} at depths of 220–480 m to 35.1 mW m^{-2} at depths of 800–1,040 m; a lesser increase of HFD values with depth was found in Borehole 1 of the Tagil-Magnitogorsk Zone, in the Urals, Russia from 19.7 mW m^{-2} at depths of 640–920 m to 20.9 mW m^{-2} at depths of 920–1,010 m.

It should be noted that the fact of either absorbing or releasing heat by any sub-layer does not mean that the sub-layer will be in such a regime indefinitely. Any sub-layer absorbing heat will be able to continue absorbing up to some limit, after

Table 7.21 Average rates of change of the geothermal gradient with depth in boreholes of some areas of the former USSR

Area	Well number	Depth interval (m)	Average rate of change of geothermal gradient with depth $(-A_i/\lambda_i) \times 10^5$ K/m^2
Gazanbulag, Azerbaijan	16	230–530	10.60
	41	140–990	5.34
	55	260–820	4.80
	115	115–485	0.63
	200	90–625	0.37
Cheleken, Turkmenistan	151	75–1,900	−5.80
	335	75–1,875	−4.10
	355	75–2,225	−1.00
Rasshevatsk	11	60–1,130	3.40
	14	60–1,120	4.80
	16	60–1,130	3.50
Petrovsko-Blagodarnensk	15	140–540	−5.25
	16	75–500	5.70
	17	25-490	8.30
Chkalovsko-Prikumsk	8	90–2,518	0.50
Aralsor superdeep borehole	SG-2	2,790–5,250	0.75

which it will either be in equilibrium or start releasing heat. Similarly, any sublayer releasing heat will release it until reaching some limit after which it will either be in equilibrium or start absorbing heat.

Analysis of geothermal data within boreholes 16, 41, 55, 115, 200 of the Gazanbulag area (Middle-Kura Depression, Azerbaijan), 151, 335, 355 of the Cheleken area (Western Turkmenian Depression), 11, 14, 16 of the Rasshevatskaya area (Stavropol' province, Russia), 15, 16, 17 of the Petrovsko-Blagodarnenskaya area (Stavropol' province, Russia), 8 in the Chkalov-Prikumskaya area (Stavropol' province, Russia) shows (Pilchin 1978) that in all these boreholes, layers indicative of oil and gas presence and containing thermal water have a positive rate of change of the geothermal gradient with depth $(-A_i/\lambda_i)$ (absorbing heat). For example, analysis of geothermal data in boreholes 15 and 17 of the Petrovsko-Blagodarnensk area (Stavropol' province, Russia) (see Fig. 7.9) shows (Pilchin 1978) that in borehole 17 the rate of change of the geothermal gradient with depth is positive for the whole transection ($-A_i/\lambda_i = 8.3 \times 10^{-5}$ K/m^2; heat absorption) and for borehole 15 the rate of change of the geothermal gradient with depth is negative for the whole transection ($-A_i/\lambda_i = -5.25 \times 10^{-5}$ K/m^2; heat release). But the rate of change of the geothermal gradient with depth within the Maykop suite of borehole 15 is positive ($-A_i/\lambda_i = 15.1 \times 10^{-5}$ K/m^2; heat absorption). It was shown (Pilchin 1983; Kerimov and Pilchin 1986a) that oil and gas layers in other areas of the Kura Depression and the South Caspian Depression are also characterized by heat absorption. This means that heat absorbing intervals

within a sedimentary basin are usually a sign of hydrocarbons (oil and gas) and/or water.

Kerimov and Pilchin (1987b) showed that one of main causes of low temperatures in sedimentary layers of the South Caspian Depression is the high clay content: clay deposits there are characterized by the lowest geothermal gradients and they contain huge amounts of bound water, which is capable of absorbing vast amounts of heat, because of their high heat capacity. In contrast, the clay deposits in the fields of the North Caucasus, in regions of heat release (cooling), are characterized by the highest values of the geothermal gradient (for example, in clays of the Maykop series of the Krasnodar and Stavropol' provinces).

Other events may be signs of heat absorption (Pilchin 1983). These include abnormally low heat flow density near the surface, abnormally high geothermal gradients at some depths within boreholes, etc. In fact, such low values of heat flow density as 1.3 and 8.36 mW m^{-2} in areas of the Saratov province, Russia, 8.36 mW m^{-2} in the Astrakhan' province, Russia, 8.36 mW m^{-2} in areas of the North Caucasus, Russia, etc. definitely point to heat absorption in the crust layers in such areas (Pilchin 1983). Thus low values of heat flow density may also indicate the presence of a groundwater recharge area.

For example, a vertical geothermal gradient value of 901 K/km was reported in Armenia (Avetis'yantz 1979), and a 906 K/km gradient (range of 25.3–906 K/km) was reported for the Coso Geothermal Field, Inyo County, California (Combs 1980). In the geothermally active Kutaro area (Japan) in borehole GK-2 at a depth interval of 216–1,100 m the vertical geothermal gradient is negative and in a depth range of 0–200 m the value of gradient is 500 K/km (Tongiorgi 1975). In the geothermal area of Onikobe (Japan), the vertical geothermal gradient reaches values of 1,000 K/km in well GO-1 and 1,360 K/km in well GO-8 (Tongiorgi 1975). Since the heat flow density Q is defined as the product of the geothermic gradient multiplied by the heat conductivity($Q = G\lambda$), it is obvious that such high geothermal gradients would produce a maximum of heat flow density that suggests heat absorption in sub-layers above the sub-layer with maximal Q.

7.4.1 Formal Theory of Heat Absorption in Layers of Crust

A formal theory of heat absorption in layers of crust was presented in (Pilchin 1979, 1983). From all of the above in Sect. 7.4 it is obvious that within any borehole at different depth intervals, layers absorbing heat ($A_i < 0$) and layers releasing heat ($A_i > 0$) are present. This means that between these layers there must be a layer (or surface) in which $A_i = 0$. Therefore, as was shown previously (Pilchin 1979, 1983) in such a layer the total value of heat generation and heat sinks is zero, and the layer is in thermal equilibrium. Let us call such a layer a stationary layer. Such a layer can be very thin and in this case it would be called a stationary surface. There can be a few stationary surfaces in any borehole. The first stationary surface is the surface of constant annual average temperatures. A

number of stationary surfaces/layers are presented in Figs. 7.6, 7.7 and 7.9. Below this surface, the heat flow density is positive ($A_i > 0$) because energy released by heat generation overcomes heat sinks (except for abnormal layers). It causes the release of heat within the layer between the first and second stationary surfaces. The second stationary surface is characterized by the condition $A_i = 0$. The presence of such stationary surfaces is consistent with geothermal measurements in boreholes. For example, for the Salyany-Karabagly region of the Kura Depression $A_i = 0$ is true at a depth of 4.5 km (see Fig. 7.5). It is possible that for other areas and regions $A_i = 0$ is present at greater depths that have yet to be revealed by drilling, because the value of A_i decreases fast with depth (see Fig. 7.5). Therefore, it can be assumed that the lower layers of sedimentary strata of the Kura Depression are heating (absorbing heat), which is extremely important for research on processes of oil and gas field formation and metamorphic processes in sedimentary strata. Even though layers between the stationary surfaces are in a heating or cooling regime, the stationary surfaces themselves can be relatively stable during one or a few periods of the Earth's evolution (Pilchin 1983). This means that finding the positions of such stationary surfaces and estimating their geothermal parameters is extremely important in investigations of the thermal conditions and evolution of different layers of the Earth, as well as in defining the boundary conditions for the heat conduction equation. Knowledge of such boundary conditions is crucial for solving the heat conduction equation for deep layers within the crust and upper mantle.

The one-dimensional non steady-state (transient) heat conduction equation for an arbitrary sub-layer i is:

$$\frac{\partial}{\partial z}\left(\lambda_i \frac{\partial T_i}{\partial z}\right) + A_i = c_i \sigma_i \frac{\partial T_i}{\partial t}. \tag{7.4.9}$$

Taking the derivative of both sides of Eq. (7.4.9) by z gives:

$$\frac{\partial^2}{\partial z^2} Q_i(z,t) = \frac{1}{\alpha_i} \frac{\partial Q_i(z,t)}{\partial t}. \tag{7.4.10}$$

Equation (7.4.10) is a homogeneous non-stationary heat conduction equation. Methods of solving this kind of equation are presented in Tikhonov and Samarsky (1963). Let us use the method of separation variables. For this purpose let us represent the function of heat flow density as:

$$Q_i(z,t) = Q_{1i}(z) Q_{2i}(t). \tag{7.4.11}$$

Heat flow density within a sub-layer (layer) is caused by heat flow entering it through its bottom surface, heat released by heat generation within it and heat absorbed in it by heat sinks. The distribution of heat flow entering the sub-layer through its bottom surface within the sub-layer can be formally represented as the

usual absorption law (Pilchin 1983) by analogy with absorption laws in physics (absorption of light, absorption of radiation, etc.) as:

$$Q_i(z,t) = Q_i(h_i,t)\exp[-\gamma_i(h_i - z)]. \tag{7.4.12}$$

Here γ_i is the formal coefficient of heat absorption in a layer. It is obvious that Eq. (7.4.12) represents a function with separation of variables, because $Q_i(h_i, t)$ depends on time alone. Finding the distribution of heat flow density caused by the generation of heat within a layer is more complicated, because part of this heat energy is absorbed within the layer itself. For the purpose of calculating the functional representation of heat generated within the layer let us separate the whole layer into n equal sub-layers. In each such sub-layer there will be a generated heat of $A_i z/n$ (here z is the thickness of the investigated layer). Heat generated in the uppermost sub-layer will be totally released through the upper surface of the layer. Heat generated in the second sub-layer from the top will be partially absorbed by the first sub-layer and only its part equal to $A_i(z/n)\exp[-\gamma_i(z/n)]$ will be released through the upper surface of the layer. Heat generated in the third sub-layer will be partially absorbed by the above two sub-layers and from the investigated layer only its part equal to $A_i(z/n)\exp[-2\gamma_i(z/n)]$. Similarly, heat generated within the bottommost sub-layer will be partially absorbed by the $(n-1)$ layers above it and the heat released from the layer will be $A_i(z/n)\exp[-(n-1)\gamma_i(z/n)]$. It is clear that the parts of heat generated within the sub-layers and released from the layer form a geometric sequence. This geometric sequence can be written as:

$$Q_{A_i} = A_i \frac{z}{n}\frac{\exp(-\gamma_i z) - 1}{\exp(-\gamma_i z/n) - 1}. \tag{7.4.13}$$

Taking into account that $\gamma_i z = \frac{Q_i - Q_{i-1}}{Q_i} < 1$ and that Eq. (7.4.13) is more precise as n becomes larger, it is possible to state that $\gamma_i z/n \ll 1$. Using the Taylor series it is possible to represent the exponential function as:

$$\exp(-\gamma_i z/n) = 1 - \gamma_i \frac{z}{n}. \tag{7.4.14}$$

Elements of the sequence from the third and up are too small and they can be dropped. Using this condition in Eq. (7.4.13) gives:

$$Q_i = -\frac{A_i}{\gamma_i}[\exp(-\gamma_i z) - 1]. \tag{7.4.15}$$

Since A_i is a function of time, it is possible to state that Eqs. (7.4.13) and (7.4.15) represent equations with separated variables. The absorbed part of the heat generated within the layer can also be expressed by Eq. (7.4.12). From the principle of superposition it is clear that for both components the heat flow entering the

layer through its bottom surface and the heat generated within the layer, the heat conduction equation in Eq. (7.1.5) can be applied. Therefore, at arbitrary time point $\tau = t_0$, for an arbitrary component of heat flow density Q_j (here j is some kind of heat source) using Eq. (7.1.5) the non-homogeneous stationary heat conduction equation will be:

$$\frac{dQ_j}{dz} + A_j = 0. \tag{7.4.16}$$

Given that any component of heat flow density absorbed by the layer can be described by Eq. (7.4.12), and substituting it into Eq. (7.4.16) we get:

$$\gamma_i Q_j + A_j = 0. \tag{7.4.17}$$

Equation (7.4.17) leads to a very important conclusion: for a homogeneous sublayer, the ratio of the value of heat production (sink) of any kind (A_j) to the heat flow of this kind (Q_j) absorbed by the layer is a constant value and equals the value of the formal heat absorption coefficient γ_i. It was shown in (Pilchin 1979) that the ratio of total heat generation (sink) ΣA_j to total heat flow density ΣQ_j also equals the heat absorption coefficient, which is consistent with the superposition principle. This can be formulated as:

$$\frac{A_j}{Q_j} = \frac{\sum_j A_j}{\sum_j Q_j} = -\gamma_i. \tag{7.4.18}$$

The function of heat flow density can be expressed as the product of functions of single arguments in the form of Eq. (7.4.11). Using Eq. (7.4.11) in Eq. (7.4.10) and dividing both sides of the equation by $Q_{1i}(z)Q_{2i}(t))$, by analogy with Tikhonov and Samarsky (1963) we get:

$$\frac{1}{Q_{1i}z}\frac{\partial^2}{\partial z^2}Q_{1i}(z) = \frac{1}{\alpha_i}\frac{1}{Q_{2i}(t)}\frac{\partial Q_{2i}(t)}{\partial t} = \gamma_i^2. \tag{7.4.19}$$

The solution to these equations yields Eq. (7.4.12) and

$$Q_{2i}(t) = Q_{2i}(t_0)\exp\left[\gamma_i^2\alpha_i(t - t_0)\right]. \tag{7.4.20}$$

Here t_0 is the starting time point.

Substituting Eqs. (7.4.12) and (7.4.20) into Eq. (7.4.11) gives:

$$Q_i(z,t) = Q_i(h_{i-1},t)\exp\left[\gamma_i^2\alpha_i(t - t_0) - \gamma_i(h_i - z)\right]. \tag{7.4.21}$$

Equation (7.4.21) shows that to be in thermal equilibrium $Q_i(h_i, t_0) = Q_i(h_{i-1}, t_0)$, without either absorbing or releasing heat energy (heat energy generated is compensated by heat sinks) the following condition must hold:

$$\gamma_i \alpha_i (t - t_0) - (h_i - h_{i-1}) = 0. \tag{7.4.22}$$

Equation (7.4.22) can be used to calculate the thickness of a layer in thermal equilibrium.

The value of heat flow density exiting a sub-layer i through its surface at depth h_{i-1}, will be:

$$Q_i(h_i, t) = Q_i(h_i, t_0) \exp\left[\gamma_i^2 a_i (t - t_0) - \gamma_i \Delta h\right] - \frac{A_i}{\gamma_i} [\exp(-\gamma_i \Delta h) - 1]. \tag{7.4.23}$$

Here $\Delta h = h_i - h_{i-1}$.

To estimate the order of the heat absorption coefficient γ, Eq. (7.4.18) can be used. Since for the Kura Depression A is $\sim 10^{-7}$ W/m^3 and Q is $\sim 10^{-2}$ W/m^2, the estimated value of γ should be $\sim 10^{-5}$ 1/m. Using these data in the part of the solution dependent on time and taking into account that for sedimentary rocks of the Kura Depression α is $\sim 10^{-7}$–10^{-6} m^2/s, the estimated time needed for a change in heat flow density of 3 % will be $\sim 10^6$–10^7 years if we the neglect time dependence of heat flow density for geologically short time intervals. Taking this into consideration in Eq. (7.4.23) and applying Eq. (7.4.12) for the sedimentary layer of the Kura Depression we get:

$$Q_i(h_i) = \left\{ Q_{i(h_i)} + \frac{A}{\gamma_i} [\exp(-\gamma_i \Delta h) - 1] \right\} \exp(\gamma_i \Delta h). \tag{7.4.24}$$

If we know the value of the heat flow density near the surface, the value of heat production A and the heat absorption coefficient γ within the layer Eq. (7.4.24) can be used to calculate the value of heat flow density entering the layer through its bottom surface. Unfortunately, there are no experimental data for the heat absorption coefficient. But it is possible to estimate these values with acceptable precision. For this purpose let us use the method of estimation of heat flow density near the base of sedimentary strata when we know the heat flow density near the layer's upper surface and the rate of sediment collection (Ashirov et al. 1976). Such estimates were made for 9 areas of the Middle Kura Depression (Table 7.22). For these areas (Table 7.22) the rate of sediment collection changes in the range of (3.6–5.8) $\times$ 10^{-3} cm/year, and the average heat flow near the surface of Earth is Q_0 = 33.6–46.0 W m^{-2} (after Mekhtiev et al. 1972). The calculated values of thermal diffusivity for selected areas are in the range of (0.48–0.65) $\times$ 10^{-6} m^2/s. The estimated values of heat flow density Q_1 near the base of sedimentary layer for selected areas are presented in Table 7.22.

The part of the total heat flow density absorbed within the sedimentary layer can be written as:

Table 7.22 Thermal parameters of some areas of the Kura Depression

Area	Average rate of sediment collection, in 10^{-5} (m/year)	Heat flow density (W m^{-2})			Heat absorption coefficient γ, in 10^{-5} 1/m
		Near the Earth's surface, $10^2 \times Q_0$	Near the bottom of the sedimentary layer, $10^2 \times Q_1$	Absorbed within the sedimentary layer, $10^2 \times Q_2$	
Djarly	4.4	3.77	4.40	1.97	6.00
Sor-Sor	4.4	5.02	5.94	2.26	5.10
Muradhanly	5.8	3.35	4.23	2.64	5.80
Gazanbulag	4.4	3.77	4.40	1.97	6.00
Naftalan	4.7	4.60	5.40	2.22	5.30
Sovetlyar	3.8	3.77	4.35	1.76	6.10
Agdzhabedy	3.6	4.60	5.40	1.72	5.00
Beilagan	3.8	4.60	5.23	1.80	5.00
Mirbashir	3.8	3.35	4.10	2.51	5.70

$$Q_2 = Q_1 - Q_0 + \chi_i(h_i - h_{i-1}). \tag{7.4.25}$$

The values of Q_2 for selected areas are presented in Table 7.22.

It is clear from Table 7.22 that the value of heat flow density entering the sedimentary layer is greater than the value of heat flow density exiting it for all areas. This means that the sedimentary layer for all these areas is absorbing heat (heating up). This result is very important for analysis of the thermal regimes of sedimentary layers.

7.5 Quantitative Interpretation of Temperature Anomalies

7.5.1 Typical Features of Gravitational, Magnetic and Temperature Anomalies

Simmons (1967) suggested a method for interpreting heat flow anomalies analogous to methods in gravity. The similarity between gravimetric and temperature anomalies was also noted by Poley and Steveninck (1970) and Kappelmeyer and Hänel (1974). However, in these studies, no examples of quantitative application are provided. Zorin and Lysak (1972) made an attempt to use the proportionality of analytical expressions for gravitational and temperature fields of a point source and to apply techniques developed in gravitational prospecting to interpret anomalies in thermal prospecting. The regional anomaly from a deep-seated source in a rift area of Lake Baikal (Russia) was interpreted as an example. The quantitative interpretation was carried out, employing the Smith inequalities developed in gravitational prospecting (Parasnis 1997); however, the use of these inequalities under difficult conditions (e.g., rugged topography, complex geological media, inclined polarization, and unknown level of the normal field) was ineffective.

Carslaw and Jaeger (1959) noted that the problem of the disturbance of the steady linear flow of heat in a uniform medium by an object of different conductivity is precisely the same mathematically as that of the induced magnetization in a body of the same shape placed in a uniform external field. This suggests that it is advantageous to adapt techniques from magnetic prospecting to thermal prospecting.

Conduction is the main process of heat transfer in the upper layers of the Earth's crust (Lakhtionov and Tarkhov 1967; Cheremensky 1977). In fractures, where the fluids do not circulate, heat is also transferred through conduction. The differential equation for heat field transfer via conduction in a space containing no heat sources takes the following form (Tikhonov and Samarsky 1963) [see also Eq. (7.4.9)]:

$$\frac{\partial T}{\partial t} = \frac{\nabla^2 T\lambda}{C\rho}, \tag{7.5.1}$$

where T is temperature, t is the time, λ and C are the thermal conductivity and temperature capacitance coefficients respectively, ρ is the density, and $\nabla^2 T$ is the Laplacian operator.

The temperature variation rate in nonstationary thermal processes is evaluated in terms of the $\frac{\lambda}{C\rho}$ ratio from Eq. (7.5.1). Once the seasonal temperature variations, which affect the stationary temperature field, are eliminated, $\partial T/\partial t \to 0$. Then Eq. (7.5.1) takes the standard form of the Laplace equation $\nabla^2 T = 0$, i.e., the nondisturbed temperature field is a potential field.

Under stationary thermal conditions, heat propagation via conduction in solid bodies follows Fourier's law [see Eq. (1.6.1)]:

$$\mathbf{q} = -\lambda \text{ grad T}.$$

The magnetic field is also potential one (Tikhonov et al. 1983) when the value of the magnetization is below 0.1 SI unit, i.e.,

$$\mathbf{U_a} = -\text{ grad } V. \tag{7.5.2}$$

where $\mathbf{U_a}$ is the anomalous magnetic field, and V is the magnetic potential. Expression (7.5.2) satisfies Poisson's equation.

It is obvious that expressions (1.6.1) and (7.5.2) are proportional. It follows that there is a theoretical basis for extending the well-developed techniques of magnetic anomaly interpretation to the interpretation of thermal observations.

An advanced method for quantitative magnetic anomaly interpretation (enhanced modifications of the tangent and characteristic point methods) for complex geological conditions including oblique magnetization, rugged terrain relief and unknown levels of the total magnetic field were put forward in (Khesin et al. 1996). Unlike some conventional procedures (Naudy 1970; Nabighian 1972; Rao and Babu 1984), these methods are applicable to conditions of rugged terrain relief and arbitrary magnetization of objects where the normal field level is an unknown (Khesin et al. 1996). Somewhat later, the viability of these methods was established for treating other geophysical fields.

Table 7.23 Comparison of some analytical expressions for models employed in magnetic and temperature fields

Magnetic field		Temperature field	
Point mass		*Sphere*	
$Z = \frac{mz}{(x^2+z^2)^{3/2}}$	(7.5.3)	$T = \frac{q}{\lambda_{an}} \frac{1-\mu}{2+\mu} \frac{R^3}{(x^2+z^2)^{3/2}}$	(7.5.4)
Thin bed		*Horizontal circular cylinder (HCC)*	
$Z = 2J2b \frac{z}{(x^2+z^2)}$	(7.5.5)	$T = \frac{q}{\lambda_{an}} \frac{1-\mu}{1+\mu} \frac{R_C^3}{(x^2+z^2)}$	(7.5.6)

A disturbing object model in the form of a sphere or horizontal circular cylinder (*HCC*) is fairly frequently used in thermal prospecting (Carslaw and Jaeger 1959; Cheremensky 1977; Lakhtionov and Tarkhov 1967; Kappelmeyer and Hänel 1974). The anomalous effect of a homogeneous sphere does not depend upon its volume; therefore, when volume and thermal conductivity are not of fundamental importance, a material point may be substituted for a model of the sphere. The model of the HCC is a convenience for the approximation of elongated objects having a circular cross-section area.

The analytical expressions for the vertical component of magnetic field of a point mass and thin bed, respectively, can be found (Parasnis 1997; Telford et al. 1990) (Eqs. (7.5.3) and (7.5.5) in Table 7.23).

The analytical expressions for the geothermal field of a sphere and *HCC*, respectively, can be written as shown below (Carslaw and Jaeger, 1959; Cheremensky, 1977; Lakhtionov and Tarkhov, 1967) (Eqs. (7.5.4) and (7.5.6) in Table 7.23).

Here m is the magnetic mass, J is the magnetization, and b is the half-width of the thin bed's upper edge, μ is the body-medium thermal conductivity ratio, R is the radius of sphere, R_c is the radius of HCC, z is depth of sphere (HCC) center, and x is the running coordinate.

The proportionality of the expressions (7.5.3) and (7.5.4), (7.5.5) and (7.5.6), respectively, is evident.

It follows that: (1) the compared fields are physically different but have mathematical expressions in common with potential fields; (2) the fields of the compared models are proportional. Hence rapid interpretation methods, such as modifications of the characteristic points and tangent methods, can be applied to quantitative interpretation of geothermal anomalies (Eppelbaum 1989). This conclusion allows us to test and employ the methods of interpretation described below.

7.5.2 *Brief Description of the Methods Employed for Quantitative Interpretation of Magnetic Anomalies in Complex Conditions*

Improved methodologies of characteristic point, tangent and areal methods have been developed to interpret magnetic anomalies in conditions of oblique

magnetization, rugged relief and unknown levels of the normal magnetic field (Khesin et al. 1996). A brief explanation of the characteristic point, tangent and areal methods is presented below.

7.5.2.1 Characteristic Point Method

The following characteristic points are used in the interpretation (after Khesin et al. (1996), with modifications): abscissas and ordinates (x and y coordinates) of the anomaly maximum ($x_{\max}$, $z_{\max}$) and minimum ($x_{\min}$, $z_{\min}$), x-coordinates of the right and left points of the anomaly half-maximum $(x_{0.5T_A})_r$ and $(x_{0.5T_A})_l$, respectively; x-coordinates of the right and left inflection points of the anomaly plot x_r and x_l, respectively (Fig. 7.10).

The formulas used for quantitative interpretation are given in Table 7.24.

7.5.2.2 Tangent Method

The tangent method employs the first horizontal derivative in inflection points (where the first derivative has its extrema). These values can be obtained from the anomaly plot as tangents of the inclination angles of the tangents to the curves at the inflection points (see Fig. 7.10).

This technique serves to calculate the generalized angle θ and to locate the origin (i.e. position of the body's epicenter) not beforehand, but in the course of analysis (Khesin et al. 1996). Four tangents are used: two inclined ones, passing through the inflection points with the largest in absolute value for the horizontal gradients of the field, and two horizontal ones, passing through the maximum and the largest in absolute value for the minimum of the anomaly. The inflection points at the inclined tangents are those closest to the largest in absolute values extrema of the anomaly (see Fig. 7.10).

When interpreting anomaly ΔT due to a thin bed (TB) or a horizontal circular cylinder (HCC), the segments d_3 and d_4 are used, taken from the anomaly plot (see Fig. 7.10). The following expressions are obtained (Khesin et al. 1996):for an anomaly due to TB:

$$\left.\begin{aligned} h_3 &= d_3 \sin^3(60^\circ + \theta/3) \\ h_4 &= d_4 \sin^3(60^\circ - \theta/3) \end{aligned}\right\}, \tag{7.5.7}$$

for an anomaly due to HCC:

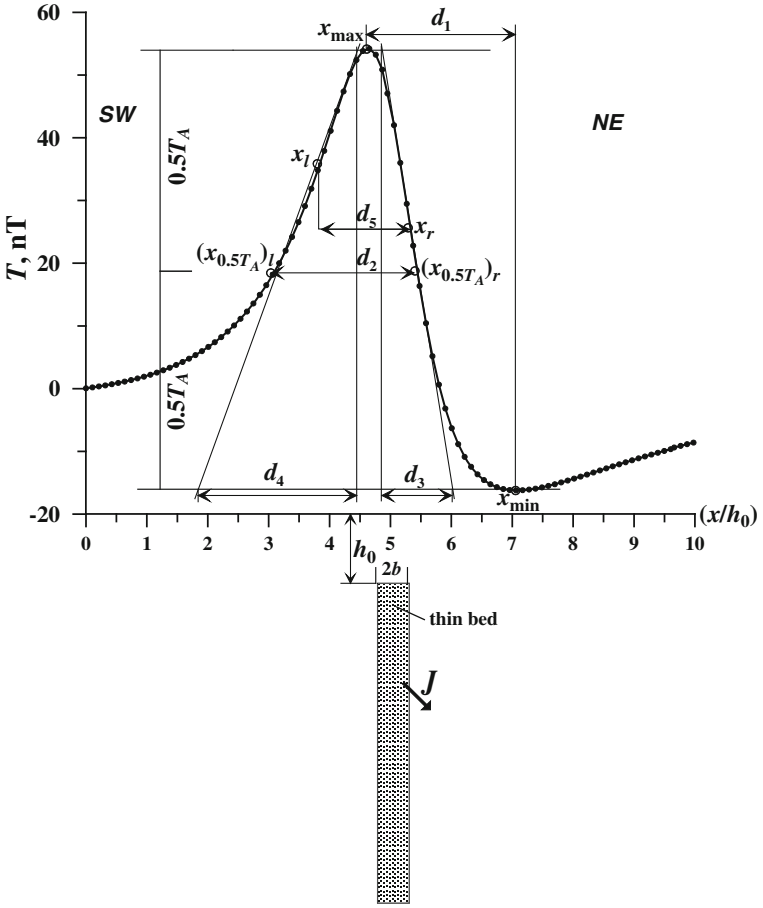

Fig. 7.10 Distribution of characteristic points and tangents on an anomaly plot for an obliquely magnetized thin bed (J is the magnetization vector) situated in a non-magnetic medium. *Open circles* are points of extrema and semiamplitude; *closed circles* are inflection points of the anomaly plot

$$\left.\begin{aligned} h_3 &= d_3 \frac{8\cos^4[(90-\theta)/4]}{3\sqrt{3}\cos[(90-\theta)/3]} \\ h_4 &= d_4 \frac{8\cos^4[(90+\theta)/4]}{3\sqrt{3}\cos[(90-\theta)/3]} \end{aligned}\right\}. \tag{7.5.8}$$

In both cases the ratio $k_\theta = d_3/d_4$ is a function of the angle θ only and is used to determine this angle either by the formulasfor an anomaly due to TB:

Table 7.24 Formulas for interpreting anomalies over a thin bed and a horizontal circular cylinder by the characteristic point method

Parameters to be calculated	Parameters used for anomalies resulting from models		Formulae to calculate parameters by the anomalies resulting from models	
	Thin bed	HCC	Thin bed	HCC
Generalized angle θ	$d, \Delta h$ d_1, d_2 d_{1r}, d_{1l} d_1, d_5 d_{1r}, d_5 $d = x_{\max} - x_{\max}(\Delta h)$ $d_1 = x_{\min} - x_{\max}$ $d_2 = (x_{0.5T_A})_r - (x_{0.5T_A})_l$ $d_5 = x_r - x_l$ $T_A = T_{\max} - T_{\min}$		$\tan(\theta/2) = d/\Delta h$ $\tan(\theta) = d_2/d_1$ $\sin(\theta/3) = d_5/\sqrt{3}d_1$	$\tan(\theta/3) = d/\Delta h$ $\cot(\theta/3) = \sqrt{3}\frac{(d_{1l}+d_{1r})}{(d_{1l}-d_{1r})}$ $k'_\theta = \frac{\sqrt{2}\cos(\theta/2)-1}{\sqrt{3}\cos(60^0+\theta/3)} = \frac{d_5}{d_{1r}}$
Depth h_0, h_c	d_1, d_2, θ d_{1r}, θ d_{1r}, $d_{1r}(\Delta h)$ d_5, θ		$h_0 = \sqrt{d_1 d_2}\big/k_{1,2}$, $h_c = d_{1r}/k_{1r}$, where k_{1r} where $k_{1,2}$ $= 2\sqrt{3}\frac{\cos(60^\circ+\theta/3)}{\cos\theta}$ $= \frac{2}{\sqrt{\sin\theta\cos\theta}}$ $h_c = \frac{d_{1r}}{d_{1r}-d_{1r}(\Delta h)}\Delta h$ $h = d_5/k_5$, where $k_5 = 2\sqrt{3}\frac{\sin(\theta/3)}{\sin\theta}$ $k_5 = 2\sqrt{2}\frac{\cos(\theta/2)-1}{\cos\theta}$	
Effective magnetic moment M_e	T_A, h_0, h_c		$M_e = 0.5T_A h$ $M_e = T_A h_c^2/k_m$, where $k_m = (3\sqrt{3}/2)\cos(30^\circ - \theta/3)$	

(continued)

Table 7.24 (continued)

Parameters to be calculated	Parameters used for anomalies resulting from models		Formulae to calculate parameters by the anomalies resulting from models	
	Thin bed	HCC	Thin bed	HCC
Horizontal displacement x_0, x_c	$h, \theta, x_{\max}, x_{\min,r}$ $(x_{0.5T_A})_r$, x_r, x_l $(x_{0.5T_A})_l$		$x_0 = 0.5(x_{\max} + x_{\min,r}) - h_0 \cot\theta$ $x_0 = 0.5\left[(x_{0.5T_A})_r - (x_{0.5T_A})_l\right] + h_0 \tan\theta$	$x_c = 0.5\left(x_{\max} + x_{\min,r}\right) - h_c \frac{\sin(60^\circ + \theta/3)}{\cos\theta} + h_c \tan\theta$ $x_c = 0.5(x_r + x_l) + h_c \tan\theta - \sqrt{2} h_c \frac{\sin(\theta/2)}{\cos\theta}$
Normal background ΔT_{backgr}	$T_{\min}$, T_A, θ		$\Delta T_{backr} = T_{\min} + T_A \frac{k_0}{1+k_0}$, where $k_0 = \frac{1-\cos\theta}{1+\cos\theta}$	$k_0 = \frac{\cos^3(60^\circ+\theta/3)}{\cos^3(\theta/3)}$

After Khesin et al. (1996), revised and modified

Indices "o" and "c" designate the models for the thin seam and horizontal circular cylinder (*HCC*), respectively. Values h_0 and h_c are the depths to the upper edge of the thin bed and center of the *HCC*, respectively

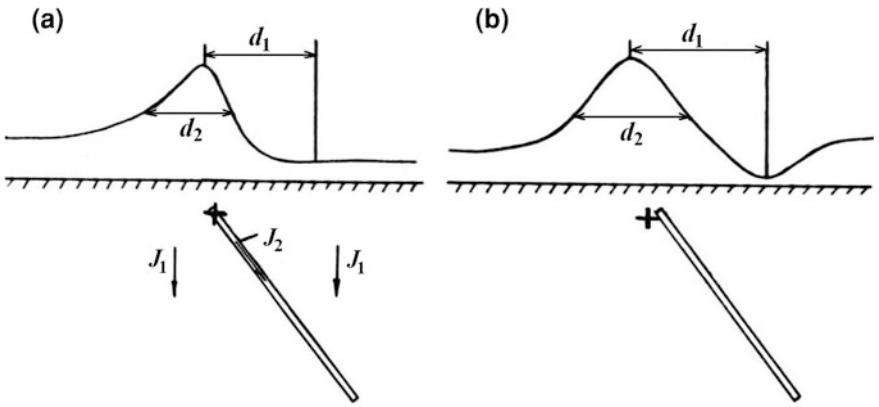

Fig. 7.11 Comparison of magnetic (**a**) and temperature (**b**) anomalies over a model of an inclined thin body. The *arrows* show the direction of the magnetization vectors *J*. The "+"symbol marks the position of the upper edge of the thin body as obtained from analysis of the anomalous graphs (Eppelbaum 2009)

$$\tan(\theta/3) = \sqrt[3]{\frac{\left(1 - \sqrt[3]{k_\theta}\right)}{1 + \sqrt[3]{k_\theta}}}, \tag{7.5.9a}$$

for an anomaly due to HCC:

$$\cot(\theta/2) = 1 + 2\frac{\sqrt[4]{4k_\theta}}{1 - \sqrt{k_\theta}}. \tag{7.5.9b}$$

The average depth h is obtained by the formula

$$h_{aver} = \frac{h_3 + h_4}{2}, \tag{7.5.10}$$

for both the TB and HCC models.

Other parameters of thin bed and cylinder (magnetic moment M_e, and the epicenter location) can be calculated from the values of θ and h as in the characteristic point method by the formulas in Table 7.24.

Figure 7.11 compares magnetic (a) and temperature (b) anomalies from an inclined thin bed (rod) and the results of their quantitative interpretation. The ΔZ anomaly was computed by one of the authors (Eppelbaum 1989), and the temperature anomaly was obtained by physical modeling (Ismail-Zade et al. 1980). A rod with a raised thermal conductivity, like a magnetic rod with a distant bottom edge, can be approximated by a point source located at the upper end of the rod. As can be seen from Fig. 7.11, the similarity between the ΔZ (nT) and T (°C) anomalies is consistent with this comparison. The results of quantitative

Table 7.25 Formulas for quantitative interpretation of magnetic anomalies over anomalous bodies approximated by a thin bed and horizontal circular cylinder using the improved characteristic areal method (Khesin et al. 1996; Eppelbaum and Khesin 2012)

Anomalous bodies	Analytical expressions for calculation of characteristic areas	Formulae for calculating M_e and h
Thin bed	$Q_1 = \int_{-h\tan(\theta/2)}^{h\cot(\theta/2)} (T - T_{\min})dx$	$M_e = Q_1/q_m, \quad h = 2Q_1/(T_A q_M)$,
	$= 2M_e\left[\frac{1}{2}\pi\cos\theta + \sin\theta\ln\left(\tan\frac{\theta}{2}\right) + \tan\frac{\theta}{2}\right]$,	where q_M
	$Q_2 = \int_{-h\cot(60^\circ-\theta/3)}^{h\cot(60^\circ+\theta/3)} (T - T_{\min})dx$	$= 2\left[\frac{1}{2}\pi\cos\theta - \sin\theta\ln(\tan\theta/2) + \tan(\theta/2)\right]$
	$= 2M_e\left[\frac{1}{3}\pi\cos\theta - \sin\theta\ln\left(\frac{\sin(60^\circ+\theta/3)}{\sin(60^\circ-\theta/3)}\right) + 4\sqrt{3}\tan\frac{\theta}{2}\sin\frac{\theta}{3}\right]$	
HCC	$Q_1 = \int_{-h\tan(\theta/3)}^{h\tan(60^\circ-\theta/3)} (T - T_{\min})dx = 3\sqrt{3}\frac{M_e}{h}\sec\frac{\theta}{3}$,	$M_e = Q_1 h \Big/ q_M = \frac{Q_1^2}{T_A}\frac{q_h}{q_M}$,
	$Q_2 = \int_{-h\tan[(90^\circ-\theta)/4]}^{h\tan[(90^\circ-\theta)/4]} (T - T_{\min})dx$	$h = q_h\frac{Q_1}{T_A}$,
	$= \frac{M_e}{h}\left[1 + \frac{3\cos(60^\circ - \theta/3)}{2\cos\frac{\theta}{2} + 1}\right]$	where $q_M = \frac{3\sqrt{3}}{4}\sec(\theta/3)$, $q_h = 2\cos(\theta/3)\cos(30^\circ - \theta/3)$

interpretation of these anomalies obtained by using the techniques described in the previous section, are also similar.

These temperature anomaly interpretation methods can be applied to a range of geological problems, including investigation of ore bodies in mountainous regions, faults in structures containing oil and gas accumulations, and solutions to problems in engineering geophysics.

7.5.2.3 Areal Method

In the areal method are used the squares (Q_1 and Q_2) occupying by thermal anomalies (Table 7.25). Parameters of the magnetic (temperature) moment, anomaly epicenter location and normal background level could be determined from the values of Q and h as in the characteristic point method by the formulae presented in Table 7.24.

7.5.2.4 Observations on Inclined Profile

If anomalies are observed on an inclined profile, the obtained parameters characterize a certain fictitious body. The transition from fictitious body parameters to those of the real body is done using the following expressions (the subscript "r" stands for a parameter of the real body) (Eppelbaum and Khesin 2012):

$$h_r = h + x \tan \omega_0, \tag{7.5.11}$$

$$x_r = -h \tan \omega_0 + x_0, \tag{7.5.12}$$

where h is the depth of the upper edge occurrence, x_0 is the location of the source's projection to the plane relative to the extremum having the greatest magnitude, and ω_0 is the angle of the terrain relief inclination ($\omega_0 > 0$ when the inclination is toward the positive direction of the x-axis).

7.5.2.5 Calculation of a Temperature Moment

To estimate the intensity of a thermal anomaly, a value equivalent to the magnetic moment M_e can be used (Eppelbaum et al. 1996; Eppelbaum 2009). This value depends on contrasts in physical parameters between the anomalous body and the host rock, and also on the form and depth of the body. Thus, the value may be used in the interpretation of geothermal data during initial data interpretation. Using the equation for the magnetic moment (see Tables 7.24, 7.25), the value of an analogous "temperature moment", TM, can be found (Eppelbaum et al. 2006):

$$\left.\begin{array}{rc} \text{for a model of thin bed:} & \mathrm{TM} = 0.5\,T_A h,\ (\mathrm{m}\,^{\circ}\mathrm{C}) \\ \text{for a model of horizontal circular cylinder:} & \mathrm{TM} = T_A h_c^2/k_m,\ (\mathrm{m}^2\,^{\circ}\mathrm{C}) \end{array}\right\}. \tag{7.5.13}$$

where k_m is some coefficient (see Table 7.24).

This kind of dataset is useful for classification of buried targets by their geometric and thermophysical properties.

7.5.2.6 Some Specifics Concerning the Application of These Methods

When interpreting plots of the temperature field recorded on an inclined relief, the observation and measurement point heights have an inverse correlation. This causes the reflection of the temperature anomaly plot about the vertical axis as compared to the magnetic ΔT-anomaly presented in Fig. 7.10. The angle of terrain relief is equivalent to that of the polarization vector on the magnetic field but with the sign inverted for the thermal field (Eppelbaum 2009). Therefore parameters d_3 and d_4 on the temperature anomaly plot change places, and the parameter d_1 is measured from the opposite side.

7.6 Investigation of Strongly Nonlinear Thermal Sources

7.6.1 Nonlinear Effects in Geophysics and Thermal Processes in the Earth

There is growing recognition of the importance of nonlinear phenomena in many branches of geophysics, and first of all in thermal data analysis. It has recently been shown that phenomena such as earthquakes, volcanoes, plate tectonics, core motions and their reflection in geophysical fields, as well as the propagation of geophysical fields in nonuniform geological media are nonlinear processes (e.g., Bercovici and Kelly 1997; Hofmeister 1999; Newman et al. 1994; Beck and Schlögl 1995; Rowlands 1995; Keilis-Borok 1990; Starin et al. 2000; Vasilyev et al. 1997; Eppelbaum and Kardashov 1998, Einav et al. 2006; Kardashov and Eppelbaum 2008). Nevertheless, it is still common practice to solve complex geophysical problems by removing the visible nonlinear effects and reducing the problem to a linear one. Such a linearization can however eliminate useful effects and even dramatically change the notion of targets. Therefore, many important geophysical problems should be solved using special nonlinear procedures.

It is widely recognized that the study of the thermal behavior of the Earth is one of the most speculative branches of geophysics. This is caused, mainly, by the absence of reliable information about heat sources and mechanisms of heat transfer

and mixing. Nevertheless, thermal field detection is widely used to search for useful minerals (first of all oil and gas), to investigate near-surface and deep geological structures, and to predict seismological events (Newman et al. 1994; Eppelbaum et al. 1996; Main 1996; Rybach and Muffer 1981; Sharma 2002).

The problem of influence of *strongly* nonlinear source on transitional dynamics has rarely been investigated in geophysics. However this problem can have important implications as regards the detection of viscous heating and nonlinear heat diffusion. Below, we discuss the key specifics of the problem in thermal field investigations.

7.6.2 Problem Definition and Discussion

A process of thermal wave propagation can be described by the following evolution equation:

$$\frac{\partial u}{\partial t} = \Delta u + f(u), \tag{7.6.1}$$

where $\Delta = \partial^2/\partial x^2 + \partial^2/\partial y^2 + \partial^2/\partial y^2$ is the Laplace operator, $f(u)$ is a nonlinear function of a thermal source.

Let us assume the following form of the thermal source:

$$f(u) = \alpha u + \varepsilon g(u), \tag{7.6.2}$$

where α and ε are some parameters, and $g(u)$ is the nonlinear function which describes disturbances of the studied thermal field. Function $g(u)$ can be presented both as a conventional deterministic function and a random distribution function. If $\varepsilon = 0$, we obtain a linear equation corresponding to the conventional problem with a linear source term:

$$\frac{\partial u}{\partial t} = \Delta u + \alpha u. \tag{7.6.3}$$

The case of $\varepsilon \neq 0$ corresponds to the situation where the normal thermal field is disturbed by anomalous sources.

A nonlinear disturbance under specific conditions can cause the appearance of a shock wave even for extremely small values of parameter ε. This effect can be used to identify the desired target. On the other hand, Eq. (7.6.1) under special conditions admits the appearance of transient solutions in the form of localized or switched (kink) waves.

Note that the properties of both localized and shock waves are determined by characteristics of the source function $f(u)$. Consequently, this allows us to estimate some parameters of the medium.

It was noted that nonlinear processes can often be approximated by cubic nonlinearity (Wold 1974; Kosevich and Kovalev 1989; Friedman 1991; Grimshaw et al. 1997). Here we limit our considerations to nonlinearities of the type (Kardashov et al. 2000):

$$g(u) = u^3, \tag{7.6.4}$$

since it allows us to obtain analytical solutions.

Other types of nonlinearity can be considered as well. The temperature source term of the form $f(u) = \alpha u + \varepsilon u^3$ enables solutions to the traveling wave type:

$$u(t, x, y, z) = \psi(k_x x + k_y y + k_z z + vt), \tag{7.6.5}$$

where v is the wave propagation speed and $\vec{k} = (k_x, k_y, k_z)$ is the unit vector in the direction of wave propagation. Similar solutions were considered in detail in (Barenblatt 1996).

Substitution of Eq. (7.6.5) to Eq. (7.6.1) yields:

$$v\psi'(s) = \psi''(s) + \alpha\psi(s) + \varepsilon\psi^3(s), \tag{7.6.6}$$

where $s = k_x x + k_y y + k_z z + vt$ and we used this fact that $k_x^2 + k_y^2 + k_z^2 = 1$.

7.6.3 Transition Waves and Their Definitions

The next step introduces non-conventional definitions for transition waves. In these definitions values s_1 and s_2 can be either finite or infinite $(-\infty, +\infty)$ as in the traditional definitions (Eppelbaum and Kardashov 1998).

A differentiable solution $\vec{\psi}(s)$ of Eq. (7.6.6) is defined as switch (kink) wave if the solution satisfies the following conditions:

(a) $\lim_{s\to s_1} \bar{\psi}(s) = \psi_1$ and $\lim_{s\to s_2} \bar{\psi}(s) = \psi_2$, where $\psi_1, \psi_2 = \text{const}$;
(b) $\lim_{s\to s_1} \bar{\psi}'(s) = \lim_{s\to s_2} \bar{\psi}'(s) = 0$.

Note that Ψ_1 and Ψ_2 are constant stationary solutions of Eq. (7.6.1).

These solutions are the nontrivial roots of the algebraic equation $\alpha u + \varepsilon u^3 = 0$ given by

$$\psi_1 = -\sqrt{-\frac{\alpha}{\varepsilon}}, \quad \psi_2 = \sqrt{-\frac{\alpha}{\varepsilon}}. \tag{7.6.7}$$

Differentiable solutions $\psi_0^i(s)$ $(i = 1, 2)$ of Eq. (7.6.6) are defined as localized waves if these solutions satisfy the following conditions:

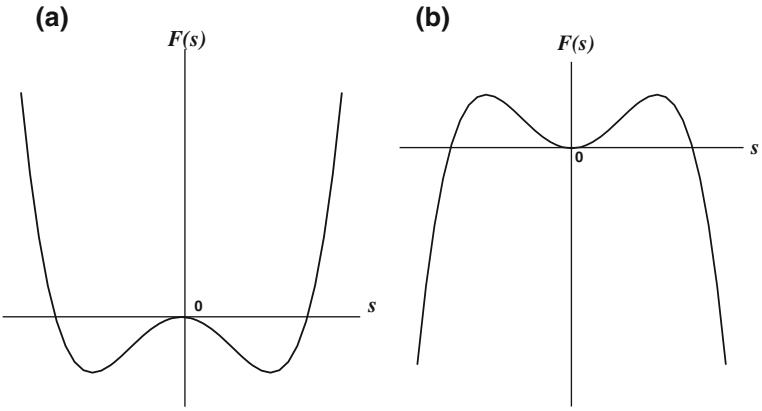

Fig. 7.12 Potential function $F(u)$ from source $f(u) = \alpha u + \varepsilon u^3$: (**a**) $\alpha < 0, \varepsilon > 0$, (**b**) $\alpha > 0, \varepsilon < 0$

(a) $\lim_{s\to s_1} \psi_0^i(s) = \lim_{s\to s_2} \psi_0^i(s) = 0$;
(b) $\lim_{s\to s_1} \frac{d}{ds}\psi_0^i(s) = \lim_{s\to s_2} \frac{d}{ds}\psi_0^i(s) = 0$.
(c) $\psi_0^i(0) = \psi_0^i \quad (i = 1, 2)$.

The values ψ_0^i $(i = 1, 2)$, determining the amplitude of the localized waves, are the roots of the potential function $F(u) = \frac{1}{2}\alpha u^2 + \frac{1}{4}\varepsilon u^4$, i.e.

$$\psi_0^1 = \sqrt{-\frac{2\alpha}{\varepsilon}}, \quad \psi_0^2 = -\sqrt{-\frac{2\alpha}{\varepsilon}}. \tag{7.6.8}$$

The solution $\psi_0^1(s)$ is defined as a localized wave of positive polarity and $\psi_0^2(s)$ as the localized wave of negative polarity. Without loss of generality let us consider the localized wave of positive polarity. We assume that the potential function $F(u)$ satisfies the condition $\alpha\varepsilon < 0$. The functions presented in Fig. 7.12a $(\varepsilon > 0,\ \alpha < 0)$ and Fig. 7.12b $(\varepsilon < 0,\ \alpha > 0)$ correspond to localized and switch waves, respectively.

The principal structures of the localized and switch waves are shown respectively in Fig. 7.13a, b.

It was shown in Kardashov (1999) that transition waves (both switch and localized waves) corresponding to the source function of type Eq. (7.6.2) are the steady-state solutions ($v = 0$) of Eq. (7.6.6). Thus, the transitional solutions satisfy the following ordinary differential equation:

$$\psi'' + \alpha\psi + \varepsilon\psi^3 = 0. \tag{7.6.9}$$

This is a Duffing equation and its localized waves (Jacobi elliptical functions) can be written using exact expressions. The solutions for both the switch and localized waves are respectively given by

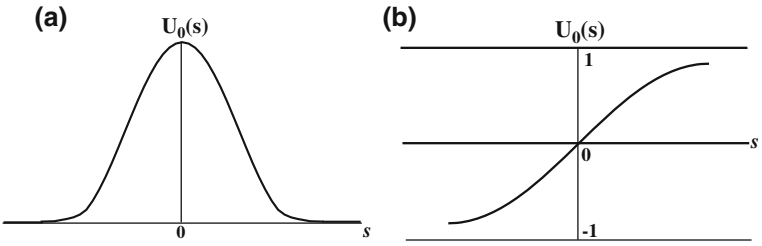

Fig. 7.13 Localized and switch waves corresponding to potential functions presented in Fig. 7.12

$$\bar{\psi}(s) = \sqrt{-\frac{\alpha}{\varepsilon}}\tanh\left(\sqrt{\frac{\alpha}{2}}s\right), \tag{7.6.10}$$

$$\psi_0^i(s) = \pm\sqrt{-\frac{2\alpha}{\varepsilon}}\mathrm{sh}\left(\sqrt{-\alpha}s\right), \quad i = 1, 2, \tag{7.6.11}$$

where $\tanh x = \frac{e^x - e^{-x}}{e^x + e^{-x}}$ and $\mathrm{sh}\, x = \frac{2}{e^x + e^{-x}}$. For details of the derivation refer to Nayfeh (1973) and Kosevich and Kovalev (1989).

Note that the main parameters (amplitude and width) of both switch and localized waves can be identically determined by the structural parameters of the source term. In addition the amplitudes of the transitive solutions increase as ε decreases, which means that the corresponding solutions of Eq. (7.6.1) are shock waves when $\varepsilon \to 0$. Visualization of these effects can be used for nonlinear source recognition.

Equation (7.6.1) can be generalized to include the effect of nonlinear diffusion. Such models are widely used for descriptions of thermal propagation processes in media with nonlinear coefficients of thermal conductivity (Beck and Schlögl 1995; Hofmeister 1999; Natale and Salusti 1996; Starin et al. 2000; Wheatcraft and Gushman 1991).

We will consider the following physically justified generalization of Eq. (7.6.1) with different types of thermal conductivity k_i (Kardashov et al. 2000):

$$\frac{\partial u}{\partial t} = \sum_{i=1}^{3}\frac{\partial}{\partial x_i}\left[k_i\left(\frac{\partial u}{\partial x_i}\right)\frac{\partial u}{\partial x_i}\right] + f(u), \tag{7.6.12}$$

$$\frac{\partial u}{\partial t} = \sum_{i=1}^{3}\frac{\partial}{\partial x_i}\left[\bar{k}_i(u)\frac{\partial u}{\partial x_i}\right] + f(u). \tag{7.6.13}$$

Equation (7.6.12) was used to describe strongly nonlinear heat catalytic processes in absorbing-reacting media (Diaz 1985), whereas equations of type (7.6.13) can be used to describe heat wave propagation in porous media (Kamin and Vazquez 1991).

Equation (7.6.13) is a strongly nonlinear thermal evolution equation of a gradient type and can be rewritten as

$$\frac{\partial u}{\partial t} = \sum_{i=1}^{3} \frac{\partial}{\partial x_i} G_i\left(\frac{\partial u}{\partial x_i}\right) + f(u). \tag{7.6.14}$$

This equation can be investigated by variational methods (e.g., Diaz 1985; Kardashov 1999). On the other hand, the transformation

$$\frac{\partial}{\partial x_i}\left(\bar{k}_i'(u)\frac{\partial u}{\partial x_i}\right) = \bar{k}_i'\left(\frac{\partial u}{\partial x_i}\right)^2 + \bar{k}_i(u)\frac{\partial^2 u}{\partial x_i^2} \tag{7.6.15}$$

implies that Eq. (7.6.13) includes nonlinear terms discussed in some publications (e.g., Hofmeister 1999; Starin et al. 2000). It should be noted that Barenblatt (1996) used the intermediate asymptotics for entering similar nonlinearities.

It was shown in Kardashov (1999) that if

$$\left.\begin{aligned} k_i(u) &= O(|u|^{\alpha_i}) \\ \bar{k}_i(u) &= O(|u|^{\beta_i}) \\ f(u) &= O(|u|^{\gamma}) \end{aligned}\right\} u \to 0 \tag{7.6.16}$$

and $\gamma \geq 1,\ \alpha_i > \gamma - 1,\ \beta_i > \gamma - 1,$ then the transients have finite-localized structure.

In particular, for sources of the form $f(u) = \alpha u + \varepsilon u^3,\ (\alpha \neq 0)$, transients have a finite-localized or periodic structure if the following conditions are satisfied

$$f(u) = \alpha u + \varepsilon u^3, \quad (\alpha \neq 0).$$

In this case oscillating fronts may appear and localized waves of the compacton type (Rosenau and Hyman 1993) may arise. In other words, localized waves have a compact support and switch waves are either periodic or have finite support as well. Examples of compacton, periodic switch waves, and switch waves with compact support are given in Figs. 7.14 and 7.15a, b respectively.

Note that the main difference between Figs. 7.13a and 7.14 and Figs. 7.13b and 7.15b is the compact support of compactons and finite switch waves. The compactons and localized/periodic switch waves present more visible images and allow us to estimate not only the parameters of the source but also the intensity of the nonlinear diffusion:

$$\bar{k}_i = Bu^{\beta_i} \quad (\beta_i > 0). \tag{7.6.17}$$

Conditions (7.6.17) or (7.6.18) guarantee that the values s_1 and s_2 are finite numbers.

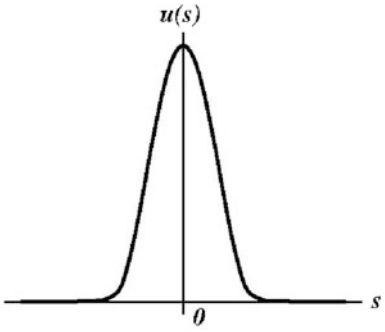

Fig. 7.14 Finite-localized solution—compacton

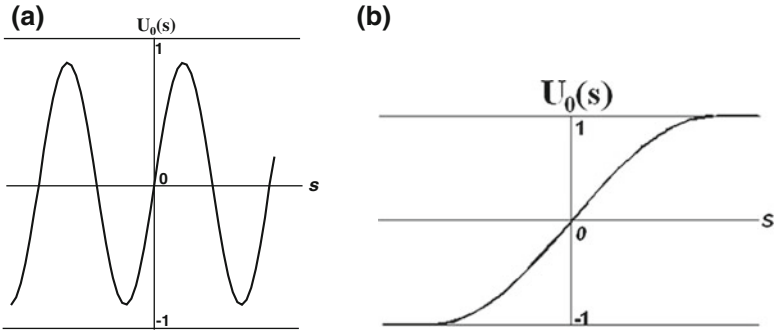

Fig. 7.15 Periodic (**a**) and finite-width (**b**) switch waves

The width λ of a transient wave can be easily calculated from the values of s_1 and s_2, i.e., $\lambda = s_2 - s_1$. The value of λ is determined by other parameters of the problem and can be viewed as some function

$$\lambda = \lambda\left(\alpha_i, \beta_i, A, B, \sqrt{\frac{-\alpha}{\varepsilon}}\right). \tag{7.6.18}$$

Values $\alpha_i, \beta_i, A, B, \sqrt{\frac{-\alpha}{\varepsilon}}$ can be considered as structural parameters, which can be determined from measurements. These parameters describe structural properties of the strongly nonlinear sources and nonlinear diffusion.

7.6.4 Some Applications of this Approach

The property of finite localization of the transients highlights the possibility of wave front propagation in finite time. It presents physically important phenomena

that can serve to recognize and control the temporal and spatial bounds of the patterns.

Another possible application of this approach can be illustrated on a simple example. The thermal method of geophysical prospecting is used, for instance, for detection and recognition of anomalies from buried oil pools. The generation and migration of oil are complex nonlinear processes (Hunt 1990). If the pool occurs at a comparatively small depth, the heat front potential generated by such a source can be approximated by a function of type

$$f(u) = \alpha u + \varepsilon u^3 \quad (\alpha > 0,\ \varepsilon < 0)$$

at least in the interval limited by two maximal points—see Fig. 7.12b. Taking into account that in this case a strong thermal gradient can be observed, Eq. (7.6.14) describing the heat wave propagation, can be used. Assuming that $\alpha_i > 0$, we can construct an exact periodic switch wave solution (Kardashov et al. 1999). Visualization of such parameters as wave amplitude and wavelength allow us to re-establish the desired structural parameters of the investigated source using the abovementioned method.

It should be noted that Bouzat and Wio (1998) obtained an exact expression for the nonequilibrium potential of a Lyapunov functional type for a three-component reaction-diffusion system. Unlike the approach in Bouzat and Wio (1998) we consider the problem of the direct estimation of the deterministic parameters of a thermal source.

This approach to the recognition and visualization of nonequilibrium potential sources indicates that transition waves deterministically characterize the structural parameters of the nonlinear sources (Eppelbaum and Kardashov 1998; Kardashov et al. 2000). The obtained results show that:

1. Parameters of transition waves characterize the structure and main characteristics of the geophysical (thermal) source function. The set of the observed data of transient time values or other parameters of the transients can be used to estimate and even to re-establish the target characteristics.
2. Models with nonlinear diffusion and sources can be effectively applied to solve various geothermal problems). The transition waves obtained using these models can enable investigators to calculate and estimate not only the parameters of the sources in question but also the nonlinear diffusion.

7.7 Thermal Anomalies as Precursors of Dangerous Geodynamic Events

It is no coincidence that out of the six regions with high thermal and hydrothermal characteristics and manifestations of some unique hydrothermal features, four are segments of the Pacific Ring of Fire (Kamchatka, Japan, New Zealand and Chile).

The Pacific Ring of Fire is the sequence of the most active volcanic regions on Earth (more than 75 % of the Earth's volcanoes are located there), which are also characterized by most of the Earth's earthquakes (over 90 % of all earthquakes and over 80 % of all powerful earthquakes). It constitutes a chain of regions with the most active tectonics of the modern era; this is evidenced by the fact that out of the 12 most catastrophic earthquakes since 1900, 11 (including the 9 most disastrous ones) took place in regions of the Pacific Ring of Fire. Another geodynamically dangerous region is the Alpine-Himalayan seismotectonic belt with known volcanic activity (the main components of the belt are the Caucasus, Kopetdag, Mt. Crimea, Alps, the Apennines, the northern part of the Eastern Mediterranean, Zagros and Himalayas). Here about 6–7 % of all the Earth's earthquakes take place. In these regions utilization of thermal anomalies possible precursors of dangerous geodynamic events at a depth (earthquakes) is especially important.

7.7.1 *Mathematical Models of Strongly Nonlinear Geophysical Phenomena*

It is well-known that many geological and environmental processes express nonlinear features as seen in fluid turbulence, heat transfer, kimberlite pipe propagation through the Earth's crust, plume effects, plate tectonics, etc. (e.g., Keilis-Borok 1990; Beck and Schlögl 1995; Turcotte 1995; Bercovici and Kelly 1997; Eppelbaum and Kardashov 2001; Valentine et al. 2002; Eppelbaum 2013b). Among these nonlinear processes, critical values cause dangerous geodynamic events at a depth.

This section presents analytical methods for the construction and monitoring of the compact transients using natural signals recorded by geophysical devices. This provides external feedback control of the structural functions and parameters describing the intensity of nonlinear diffusion and nonlinear reaction (sources).

This approach can be seen as the diffusion-limited method using the shape of recorded signals for feedback control of the interaction between the system's reaction-diffusion and external parameters. The role of nonlinear reaction-diffusion interactions in the formation of the localized transients is analyzed in (Kardashov et al. 2000).

The processes which may be described by the following strongly nonlinear non-stationary equation:

$$\frac{\partial u}{\partial t} = A_i(u) \quad (i = 1, 2) \tag{7.7.1}$$

are analyzed and modeled below.

Here $A_i(u)$ is the nonlinear operator either of two types (Einav et al. 2006):

$$A_1(u) = \Delta\Phi(u, C, d) + f(u, A, b), \tag{7.7.2}$$

$$A_2(u) = \sum_{i=1}^{m} \frac{\partial}{\partial x_i} G_i\left(\frac{\partial u}{\partial x_i}, C, d\right) + h(u, A, b). \tag{7.7.3}$$

where $\Delta = \sum_{i=1}^{m} \frac{\partial^2}{\partial x_i^2}$ is the Laplace operator, $\Phi(s, C, d)$, $G_i(\omega, C, d)$, $f(s, A, b)$ and $h(s, A, b)$ are the real-value structural functions that determine nonlinear diffusion and nonlinear source intensity; A and C are the real-value parameters describing some internal properties of the sources and nonlinear diffusion (structural parameters); b and d are the averaged external control parameters.

The first goal is to select the classes of the structural functions and formulate the parametric relationships for the transients having the compact localized or shockwave structure that may be controlled in the finite temporal-spatial domain. It was shown (Natale and Salusti 1996; Kardashov et al. 2000) that by fulfilling the following conditions:

$$\Phi(u, C, d) = O\left(u^k\right), \quad f(u, a, b) = O\left(u^l\right) \quad \text{on } u \to 0 \text{ and } k > l \tag{7.7.4a}$$

or

$$G_i(\omega, C, d) = O\left(\omega^k\right), \quad h(u, a, b) = O\left(u^l\right) \quad \text{on } u, \omega \to 0 \text{ and } k > l \tag{7.7.4b}$$

the transients have a finitely localized or periodic structure unlike semi-linear models. It only admits existing transients with an asymptotic structure.

The second component in this approach is the analysis of the reaction-diffusion structural parameters A and C by adaptive virtual external subjection that is determined by the average control parameters b and d. The solution of the traveling-wave type is considered ($m = 1$):

$$u(t, x) = \varphi\left(\sum_{i=1}^{m} h_i x_i + vt\right). \tag{7.7.5}$$

Here v is the so-called group wave velocity of the traveling wave, $h = (h_1,\ldots,h_m)$ is the normal unit vector to the wave propagation plane, e.g. $\sum_{i=1}^{m} h_i^2 h$. Equations (7.7.1), (7.7.2) and (7.7.3) are reduced to an ordinary differential equation (Einav et al. 2006):

$$v\varphi' = \frac{d}{ds} \sum_{i=1}^{m} G_i\left(h_i \frac{d\varphi}{ds}, C, d\right) + h(\varphi, A, b). \tag{7.7.6}$$

Let us assume that the transient implies a transition of the system from the condition (steady-state solution) $\varphi_1 = \varphi(s_1)$ to condition $\varphi_2 = \varphi(s_2)$. It captures the transition of the heart beat from systolic to diastolic values, and the *ECG* signal-transition from peak to minimal value. Then by integrating the equality

through interval $[s_1, s_2]$, we can obtain an important expression for calculating the phase transition velocity and phase transition time $S = s_2 - s_1$:

$$v(A,B,c,d) = \left\{ \frac{\sum_{i=1}^{m} \left[G_i\left(h_i \frac{d\varphi}{ds}\Big|_{s=s_1}, C, d\right) - G_i\left(h_i \frac{d\varphi}{ds}\Big|_{s=s_2}, C, d\right) \right]}{\varphi_2 - \varphi_1} + \frac{\int_{s_1}^{s_2} h[\varphi(s), A, b]ds}{\varphi_2 - \varphi_1} \right\}. \tag{7.7.7}$$

Here function $\varphi = \varphi(s)$ is the natural signal recorded by corresponding devices.

Equation (7.7.7) may be used for coupled reaction-diffusion interaction and feedback external control of the transient velocity (phase transition intensity). Specifically, by selecting the parametric complex (A, B, c, d) in such a way that the following equality is satisfied:

$$v(A,B,c,d) = 0,$$

we can obtain the steady-state transient. Furthermore, by subsequent multiplication of this equation by $\varphi^k(s)$ $(k = 1, 4)$ and integrating through interval $[s_1, s_2]$, we obtain a set of nonlinear algebraic equations to calculate the parametric complexes (A, B, c, d). Such a system can be applied for feedback interactive control of transient dynamics. It is important to note that the abovementioned formulas can be used to estimate the transition time of a nonlinear process.

We propose that application of the techniques presented in Sects. 7.6 and 7.7.1 to thermal data observed in seismically active areas can improve the forecasting of dangerous geodynamic events at a depth.

7.7.2 Thermal Precursors of Earthquakes

The relationship between the anomalous variations in temperature observed in boreholes and dangerous geodynamic activity is known (e.g., Mogi et al. 1989; Singh and Dey 2003; Ouyang et al. 2009).

Temperature measurements over quite a long period at an artesian spring at Usami Hot Springs located on the NE coast of the Izu Peninsula (Japan), which has recently been characterized by considerable seismic activity, reveal that the variations in temperature of this hot spring are closely linked to the occurrence of earthquakes (Fig. 7.16).

Temperature monitoring was carried out in the Biladzhik well (Sheki region of Azerbaijan, southern part of the Greater Caucasus) to correlate temperature variations with the earthquakes recorded in the region (Lubimova et al. 1982). Monitoring was conducted at a depth of 110 and 335 m (Fig. 7.17). This figure shows that in general the temperature graphs are synchronous at both depths, but in the two most striking cases the distribution of the anomalous curves went in opposite directions. Before the Kutkashen event, the temperature anomaly

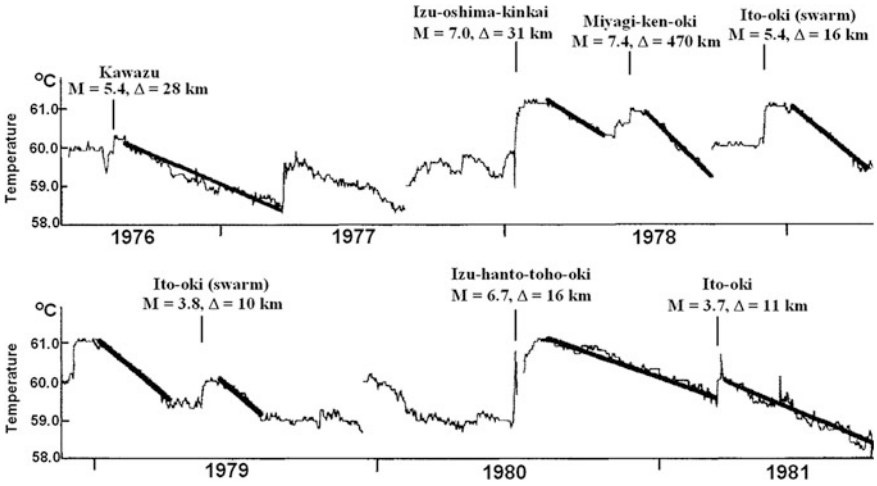

Fig. 7.16 Temporal variations in temperature at Usami No. 24 hot spring (Izu Peninsula, Japan) between 1976 and 1981. *Heavy solid lines* show the linear decline in temperature in normal times. Abnormal changes before large earthquakes are designated as precursory phenomena; the thermal measurements were carried out at a depth of 42 m (after Mogi et al. 1989, with slight modifications)

observed at a depth of 335 m exceeded the temperature anomaly at 110 m (which seems logical). However, before the Checheno-Ingushetiya event the temperature anomaly observed at 110 m exceeded the 335 m anomaly tenfold. This phenomenon is difficult to explain from a physical-tectonical point of view.

For purposes of earthquake prediction, subsurface thermal monitoring may be used. However, as follows from the analysis of data presented in Resapour et al. (2008), it is necessary to introduce special corrections for seasonal temperature variations that propagate at a certain delay from the Earth's surface (e.g., Khesin and Eppelbaum 1994).

Another approach consists of investigating the thermal balance of the boundary layer in the ionosphere (e.g., Tramutoli et al. 2001; Ouzounov and Freund 2004; Pulinets et al. 2006). In these investigations it was assumed that in seismically active areas the increased radon emanation from active faults and cracks before an earthquake may be a primary source of air ionization. Such effects can be monitored by remote sensing satellites and ground based measurements (Pulinets et al. 2006).

Sibson (1984) and Chen and Molnar (1983) noted an inverse relationship between the terrestrial heat flow and the thickness of the seismogenic crust. Bonner and Blackwell (1998) found a tight inverse correlation between heat flow and cutout depth of earthquakes. Nevertheless, these relationships do not appear in all regions of the world.

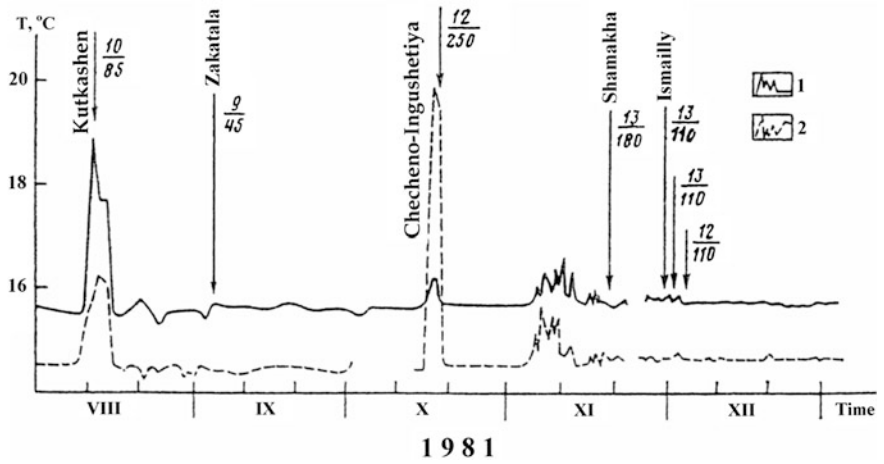

Fig. 7.17 Temperature variations in the Biladzhik well (Azerbaijan) and their comparison with the geodynamic events in the Caucasus. (*1*) and (*2*) are the temperatures observed at a depth of 335 and 110 m, respectively. The *arrows* indicate the time of the earthquake. The *numbers* in the *numerator* and *denominator* show the energy class of the earthquake and the epicentral distance in km between the earthquake and the well, respectively (Lubimova et al. 1982)

Salman and Tronin (1990) reported, in particular, about appearing vast infrared anomalies in the areas of Gazly (Uzbekistan) 1976 and 1984 earthquakes a few days before these geodynamic events.

Tronin et al. (2004) suggested monitoring thermal behavior as a possible indicator of geodynamic activity by the use of the mean night thermal gradient (dT/dt) calculated as the linear regression of the thermal data of each pixel (T is the temperature and t is the time).

According to Noda et al. (2009) ruptures on faults weaken in response to flash heating of microscopic asperity contacts (within a rate-and-state framework) and cause the thermal pressurization of pore fluid. These are arguably the primary weakening mechanisms on mature faults at coseismic slip rates, at least prior to large slip accumulation.

Thus, the application of the mathematical techniques presented in Sects. 7.6 and 7.7.1 to thermal data observed in seismically active areas can improve the forecasting of dangerous geodynamic events at a depth.

References

Aliev SA, Rustamov RI (1977) Geothermal characteristics of the Azerbaijan's part of the Kura Depression. Oil Gas Geol Geophys (Neftegazovaya Geologiya i Geofizika) 4:17–19 (in Russian)

Allen PA, Allen JR (1990) Basin analysis: principles and applications. Blackwell Scientific Publications, Oxford

Andrews-Speed CP, Oxbu ER (1984) Temperatures and depth-dependent heat flow in Western North Sea. AAPG Bull 68(11):1764–1781

Ashirov T, Dubrovskiy VG, Odekov OA, Smirnov YB (1976) Geothermal conditions in Probalkhan depression. In: Geothermal researches in the USSR, vol 1. Nauka, Moscow, pp 59–64 (in Russian)

Avetis'yantz AA (1979) Geothermic conditions of entrails of Armenia. Nauka, Moscow, 76 p (in Russian)

Barenblatt GI (1996) Scaling, self-similarity, and intermediate asymptotics. Cambridge University Press, Cambridge

Beck C, Schlögl F (1995) Thermodynamics of chaotic systems: an introduction. Cambridge nonlinear science series. Cambridge University Press, Cambridge

Behar F, Beaumont V, De Penteado HLB (2001) Rock-Eval 6 technology: performances and developments technologie Rock-Eval 6: performances et développements. Oil Gas Sci Technol: Rev IFP 56(2):111–134

Bercovici D, Kelly A (1997) Nonlinear initiation of diapirs and plume heads. Phys Earth Planet Inter 101:119–130

Bonner JK, Blackwell, DD (1998) Temperatures and earthquakes in California. In: Proceedings of the international conference "The Earth's Thermal Field and Related Research Methods", Moscow, Russia, pp 41–46

Borevsky L, Milanovsky S, Yakovlev L (1995) Fluid-thermal regime in the crust-superdeep drilling data. In: Proceedings of the World geothermal congress, Florence, 1995, pp 975–981

Bouzat S, Wio HS (1998) Nonequilibrium potential and pattern formation in a three-component reaction-diffusion system. Phys Lett A 247:297–302

Bulashevich YP (1980) One dimentional heat flow counting convection. Transaction of the conference "Present condition of methodics and devices for geothermal researches", Sverdlovsk, IVC PGO "UralGeology", pp 4–6 (in Russian)

Cacace M, Scheck-Wenderoth M (2010) Modeling the thermal field and the impact of salt structures in the north east German Basin. Proceedings of the World geothermal congress 2010, Bali, Indonesia, pp 1–8

Carslaw HS, Jaeger JC (1959) Conduction of heat in solids, 2nd edn. Oxford University Press, Oxford

Chen W, Molnar P (1983) Focal depths of intracontinental earthquakes and intraplate earthquakes and their correlation with heat flow and tectonic age. J Geophys Res 88:4183–4214

Cheremensky GA (1977) Applied geothermics. Nedra, Leningrad (in Russian)

Clark SP Jr, (ed) (1966) Handbook of physical constants (revised edition). Geological Society of America, Memoir 97, Washington DC

Clauser C (2006) Geothermal energy. In: Heinloth K (ed), Landolt-Börnstein, Group VIII: advanced materials and technologies, vol 3. Energy technologies, subvol. C: renewable energies. Springer, Heidelberg-Berlin, pp 493–604

Combs J (1980) Heat flow in the Coso geothermal area, Inyo County, California. J Geophys Res 85(B5):2411–2424

Costain JK, Speer JA, Glover L III, Perry L, Dashevsky S, McKinney M (1986) Heat flow in the Piedmont and Atlantic Coastal Plain of the southeastern United States. J Geophys Res 91(B2):2123–2136

Deffeyes KS (2005) Beyond oil: the view from Hubbert's Peak. Hill and Wang, New York

Diaz JI (1985) Nonlinear partial differential equations and free boundaries, I: elliptic equations. Res notes in Mathematics, vol 106. Pitman, New York

Einav S, Eppelbaum L, Kardashov V (2006) Structural control of transient waves in strongly nonlinear reaction-diffusion systems. Transaction of the international congress of mathematics, Madrid, Spain, pp 151–152

Eppelbaum LV (1989) The development of methods for processing and interpretation of natural geophysical fields in prospecting for pyrite ores under mountainous conditions. Ph.D Thesis, institute of geophysics (Georgian Acadamey of Sciences), Tbilisi (in Russian)

Eppelbaum LV (2009) Near-surface temperature survey: an independent tool for buried archaeological targets delineation. J Cult Heritage 12(1):e93–e103
Eppelbaum LV (2013b) Non-stochastic long-term prediction model for US tornado level. Nat Hazards 1–10. doi:10.1007/s11069-013-0787-7
Eppelbaum LV, Kardashov VR (1998) Nonlinear geothermal processes in the Earth crust and transition waves. In: Proceedings of the international conference "The Earth's Thermal Field and Related Research Methods", Moscow, pp 82–85
Eppelbaum LV, Kardashov VR (2001) Analysis of strongly nonlinear processes in geophysics. In: Moresi L, Müller D (eds) Proceedings of the Chapman conference on exploration geodynamics. Dunsborough, Western Australia, pp 43–44
Eppelbaum LV, Khesin BE (2012) Geophysical studies in the Caucasus. Springer, Berlin
Eppelbaum LV, Pilchin AN (2006) Methodology of Curie discontinuity map development for regions with low thermal characteristics: an example from Israel. Earth Planet Sci Lett 243(3–4):536–551
Eppelbaum LV, Modelevsky MM, Pilchin AN (1996) Geothermal investigations in the Dead Sea Rift zone, Israel: implications for petroleum geology. J Petrol Geol 19(4):425–444
Eppelbaum LV, Kutasov IM, Barak G (2006) Ground surface temperature histories inferred from 15 boreholes temperature profiles: Comparison of two approaches. Earth Sci Res J 10(1):25–34
Forsythe GE, Wasow WR (1960) Finite difference methods for partial differential equations. Wiley, New York
Friedman JH (1991) Multivariate adaptive regression splines. Ann Statist 19:1–144
Galushkin YI (1990) Thermal regime and location of zones for hydrocarbon generation during basin evolution: description of the methods and computer program. In: Ushakov SA (ed) Earth life, evolution of Earth and planets. Moscow University Press, Moscow, pp 102–108 (in Russian)
Grimshaw R, Pelinovsky E, Tanpova T (1997) The modified Korteweg-de Vries equation in the theory of large-amplitude internal waves. Nonlinear Process Geophys 4(4):237–250
Grosse P, Wynands R (1989) Simulation of photoacoustic IR spectra of multilayer structures. Appl Phys B 48:59–65
Helgeson HC, Richard L, McKenzie WF, Norton DL, Schmitt A (2009) A chemical and thermodynamic model of oil generation in hydrocarbon source rocks. Geochim et Cosmochim Acta 73:594–695
Hofmeister AM (1999) Mantle values of thermal conductivity and the geotherm from phonon lifetimes. Science 283:1699–1706
Hunt JM (1990) Generation and migration of petroleum from abnormally pressured fluid compartments. Am Assoc Petrol Geol 74:1–12
Hunt JM (1996) Petroleum geochemistry and geology, 2nd edn. W.H. Freeman, San Francisco
Hyne NJ (2001) Nontechnical guide to petroleum geology, exploration, drilling, and production. PennWell Corporation, Oklahoma
Ismail-Zade TA, Askerov RB, Aliyev SA (1980) A method for determining crust fractures. Soviet Inventor Certificate no. 792198 MKI GOIV9/00 (in Russian)
Kamin S, Vazquez JL (1991) Asymptotic behavior of solution of the porous medium equation with changing sign. SIAM J Math Anal 22(1):34–45
Kappelmeyer O, Hänel R (1974) Geothermics with special reference to application. Gebruder Borntrargen, Berlin—Stutgart
Kardashov V (1999) Finite control of unsteady-state singular processes. Nonlinear Anal 38(3):361–374
Kardashov VR, Eppelbaum LV (2008) Mathematical models of strongly nonlinear geophysical phenomena. Transaction of the 5th European conference of mathematicians, Amsterdam, The Netherlands, 2 pp
Kardashov V, Einav S, Eppelbaum L, Ismail-Zadeh A (1999) A novel approach to investigation and control of nonlinear nonstationary processes: application to environments and biomedical engineering. Sci Israel 3:24–33

Kardashov VR, Eppelbaum LV, Vasilyev OV (2000) The role of nonlinear source terms in geophysics. Geophys Res Lett 27(14):2069–2073

Keilis-Borok VI (1990) The lithosphere of the earth as a nonlinear system with implications for earthquake prediction. Rev Geophys 28:19–34

Kerimov KM, Pilchin AN (1981) Some peculiarities of geothermal characteristic of deep seated faults of Aserbaijan. Azerbaijan Oil Ind 10:18–22 (in Russian)

Kerimov KM, Pilchin AN (1986a) Geothermal regime of the sedimentary cover of Azerbaijan and Caspian Sea depression areas. Azerbaijan Oil Ind 1:9–13 (in Russian)

Kerimov KM, Pilchin AN (1986b) Use of geothermics data for prognosis of abnormal stratum pressure and oil and gas perspectives at great depths. In: Kerimov KM (ed) Combined interpretation of geological-geophysical data with the goal to search oil and gas presence at great depths. Baku Book Publ., Baku, pp 25–36 (in Russian)

Kerimov KM, Pilchin AN (1987a) Analysis of thermo-baric conditions in oil and gas fields in depression regions of the Caucasus and Middle Asia. In: Ismail-Zade TA et al (eds) Transaction of the 2nd scien-techn meeting "Problems of Oil and Gas Production at Great Depths and Ways to Increase an Effectiveness of Investigation". Baku Book Publ., pp 115–117 (in Russian)

Kerimov KM, Pilchin AN (1987b) Thermo-baric regime of sedimentary layer of the South-Caspian Mega-depression and its relation with oil and gas prospecting. In: Neprochnov YP et al (eds) Problems of geophysics of Ocean's bottom, transaction of 1st All-Union meeting on marine geophysics, Moscow, vol 2, p 93

Kerimov KM, Pilchin AN, Ibragimov SM et al (1986) Improvement of prognosis methods and overhigh stratum pressure zones study in foothills and interhills depressions of the South USSR in connection with search and prospecting of oil and gas at the great depths. Scientific report 363-85, Baku, YuzhVNIIGeofizika, 289 p (in Russian)

Kerimov KM, Andreev LI, Pilchin AN et al (1988) Development of the combined geological and geophysical model of the Earth crust of the Caucasus. Scientific report 002-1, Baku, YuzhVNIIGeofizika, 400 p (in Russian)

Kerimov KM, Pilchin AN, Gadzhiev TG, Buachidze GY (1989) Geothermal map of the Caucasus, Scale 1:1,000,000, Baku, Cartographic Plant no. 11 (in Russian)

Khesin BE, Eppelbaum LV (1994) Near-surface thermal prospecting: Review of processing and interpretation. Geophysics 59(5):744–752

Khesin BE, Alexeyev VV, Eppelbaum LV (1996) Interpretation of geophysical fields in complicated environments. Series: modern approaches in geophysics. Kluwer Academic Publishers (Springer), Boston, Dordrecht, London

Kosevich AM, Kovalev AS (1989) Introduction to nonlinear physical mechanics. Naukova Dumka, Kiev

Krupsky D, Ismail-Zadeh A, Wilhelm H, Volozh Y (2006) Geothermal evolution of the Astrakhan Crest region of the Pricaspian Basin, Russia. In: Recent geodynamics, Georisk and sustainable development in the Black Sea to Caspian Sea region. AIP conference proceeding, vol 825(1), pp 120–131

Kutas RI (1978) Field of heat flows and thermal model of Earth Crust. Naukova Dumka, Kiev (in Russian)

Kutas RI, Gordienko VV (1971) Heat flow of the Ukraine. Naukova Dumka, Kiev (in Russian)

Kutas RI, Bevzyuk MI, Vigovsky VF, Mikhaylyuk SF (1979) Investigation of geologic origin of heat field heterogeneities. Report on problem no. 39-76-102/3. Institute of Geophysics, Ukrainian Academy of Science, Kiev (in Russian)

Kutasov IM (1999) Applied geothermics for petroleum engineers. Elsevier, Amsterdam

Lachenbruch AH (1959) Periodic heat flow in a stratified medium with application to permafrost problems. Geol Surv Bull 1083-A (USA Government Printing Office, Washington)

Lachenbruch AH, Sass JH, Galanis SP Jr (1985) Heat flow in southernmost California and the origin of the Salton Trough. J Geophys Res 90:6709–6736

Lakhtionov MO, Tarkhov AG (1967) Experience in thermal prospecting at pyrite deposits of the Urals. Izv VUZOV, Ser: Geol Prospect 5:87–94 (in Russian)

Lévy F, Jaupart C, Mareschal J-C, Bienfait G, Limare A (2010) Low heat flux and large variations of lithospheric thickness in the Canadian Shield. J Geophys Res 115:B06404
Lopatin NV (1971) Temperature and geologic time as a factor in coalification. Izv Acad Sci USSR, Ser: Geol 3:95–106
Lubimova EA (1956) Influence of radioactive sources redistribution on heat history of Earth. Izv Acad Sci USSR, Ser: Geophys 10:1145–1160 (in Russian)
Lubimova EA, Mukhtarov ASh, Ismail-Zadeh, TA (1982) Temperature variations in the "Biladzhik" drill hole (Azerbaijan) during regional seismic activity. Izvestiya, Phys of the Earth 21(4):319–322
Lubimova EA (1968a) Thermal history of the Earth. In: The Earth's crust and upper mantle, vol 13. Geophysical Monograph Series. American Geophysical Union, pp 63–77
Lubimova EA (1968b) Thermics of the Earth and Moon. Nauka, Moscow (in Russian)
Main I (1996) Statistical physics, seismogenesis and seismic hazard. Rev Geophys 34:433–462
Majorowicz JA, Jones FW, Jessop AM (1986) Geothermics of the Williston basin in Canada in relation to hydrodynamics and hydrocarbon occurrences. Geophysics 51:767–779
Maky AF, Ramadan MAM (2010) Thermal conductivity, radiogenic heat production and heat flow of some upper cretaceous rock units, North Western Desert, Egypt. J Appl Sci Res 6(5):483–510
McGahan WA, Cole KD (1992) Solutions of the heat conduction equation in multilayers for photothermal deflection experiments. Mechanical Engineering Faculty of Public. University of Nebraska, Lincoln
Mekhtiev SF, Kashkay MA, Aliev SA (1972) Investigation of relationships of heat flow with construction and evolution tectonic structure and geophysical fields in different tectonic structures of USSR. (Pre-Kura Oil and Gas Province, Apsheron Oil and Gas Province). Scientific report for 1971–1972. Azerbaijan Geological Fund, Baku
Mogi K, Mochizuki H, Kurokawa Y (1989) Temperature changes in an artesian spring at Usami in the Izu peninsula (Japan) and their relation to earthquakes. Tectonophysics 159:95–108
Mottaghy D, Schellschmidt R, Popov YA, Clauser C, Kukkonen IT, Nover G, Milanovsky S, Romushkevich RA (2005) New heat flow data from the immediate vicinity of the Kola super-deep borehole: vertical variation in heat flow confirmed and attributed to advection. Tectonophysics 401:119–142
Nabighian MN (1972) The analytic signal of two-dimensional magnetic bodies with polygonal cross-section: its properties and use for automated anomaly interpretation. Geophysics 37(3):507–517
Natale G, Salusti E (1996) Transient solutions for temperature and pressure waves in fluid-saturated porous rocks. Geophys J Int 124:649–656
Naudy H (1970) Une methode d'analyse fine des profiles aeromagnetiques. Geophys Prospect 18:56–63
Nayfeh AN (1973) Perturbation methods. Wiley, Toronto
Negi JG, Singh RN (1967) On heat transfer in layered ocean sediments. Earth planet Sci Lett 2:335–336
Newman WI, Gabrielov A, Turcotte DL (eds) (1994) Nonlinear dynamics and predictability of geophysical phenomena, vol 83. AGU Press (Geoph Monogr)
Nielsen SB, Balling N (1985) Transient heat flow in a stratified medium. Tectonophysics 121(1):1–10
Noda H, Dunham EM, Rice JR (2009) Earthquake ruptures with thermal weakening and the operation of major faults at low overall stress levels. J Geophys Res 114:B07302, 1–27. doi:10.1029/2008JB006143
Oba M, Mita H, Shimoyama A (2002) Determination of activation energy and pre-exponential factor for individual compounds on release from kerogen by a laboratory heating experiment. Geochem J 36:51–60
Ouyang Z, Zhang H, Fu Z, Gou B, Jiang W (2009) Abnormal phenomena recorded by several earthquake precursor observation instruments before the M_s 8.0 Wenchuan, Sichuan earthquake. Acta Geol Sinica 83(4):834–844

Ouzounov D, Freund F (2004) Mid-infrared emission prior to strong earthquakes analyzed by remote sensing data. Adv Space Res 33:268–273
Parasnis DS (1997) Principles of applied geophysics (revised and supplumented), 5th edn. Chapman & Hall, London
Peters KE (1986) Guidelines for evaluating petroleum source rock using programmed pyrolysis. AAPG Bull 70(3):318–329
Peters KE, Walters CC, Moldowan JM (2005) The biomarker guide: biomarkers and isotopes in the environment and human history, 2nd edn, vol 1. Cambridge University Press, Cambridge
Petersen K, Lerche I (1995a) Quantification of thermal anomalies in sediments around salt structures. Geothermics 24(2):253–268
Petersen K, Lerche I (1995b) Quantitative modelling of salt and sediment interactions: evolution of a North Louisiana salt diapir. J Petrol Geol 18(4):365–396
Pilchin AN (1978) Estimation of thermodynamic condition of intervals of terrigenous transsection by speed of change of geothermal gradient with depth. Explor Geophys (Razvedochnaya Geofizika) 83:112–116
Pilchin AN (1979) On heat absorption in the earth strata (on example of the Middle Kura Depression), VINITI Press No. 183-79, p 21 (in Russian)
Pilchin AN (1981) Influence of additional pressure on seismic velocity and density of rocks in Middle-Kura depression. Explor Geophys (Razvedochnaya Geofizika) 91:122–127 (in Russian)
Pilchin A (1983) Geothermal regime of Earth's crust of the Kura depression and its influence on pressure distribution in it. Ph.D. thesis, Institute of Geophysics of the Georg. Academy of Science, Tbilisi (in Russian)
Pilchin AN (1987a) Analysis of thermo-baric conditions in oil and gas fields of the Urals-Povolzhie and Siberia. In: Ismail-Zade TA et al (eds) Transaction of II scien-techn meeting problems of oil and gas production at great depths and ways of increase of effectiveness of prospecting, pp 108–110
Pilchin AN (1995a) Heat absorption in sedimentary cover in some areas of the USA and Canada. AAPG search and discovery article #90957, AAPG Mid-Continent section meeting, Tulsa, Oklahoma
Pilchin AN (1995b) The geothermal state of sedimentary cover of South and Central Alberta, vol 20. Transaction of Geological Association of Canada and Mineral. Association of Canada Annual Meeting, p 84
Pilchin AN, Eppelbaum LV (1994a) Comparison of thermodynamic conditions between Salton Trough region (USA) and the region of the Dead Sea Rift. Transaction of VII European geoscience conference, Strasbourg, France, C1, p 174
Pilchin AN, Eppelbaum LV (1994b) Los Angeles Basin and South part of the Dead Sea Basin: comparative analysis and possible character of origin. Transaction of the 90th annual meeting of Cordilleran Section of the Geological Society of America, p 81
Pilchin AN, Eppelbaum LV (1997) Determination of the lower edges of magnetized bodies by using geothermal data. Geophys J Int 128:167–174
Pilchin AN, Kerimov KM (1980) Some peculiarities of thermal regime of central part of Kura depression. Oil Gas Geol Geophys (Neftegazovaya Geologiya i Geofizika) 4:23–25 (in Russian)
Pilchin AN, Kerimov KM (1987) Prognosis of temperatures and pressures at in depth intervals not uncovered by drilling in oil and gas fields of Azerbaijan using seismic data. In: Kerimov KM (ed) Prognosis of oil and gas fields presence by methods of exploration geophysics, Baku, vol 3, pp 55–61
Pilchin AN, Khesin BE, Kerimov KM (1978) Geothermal regime of sedimentary cover of Kura Depression. Geol Oil Gas (Geologiya Nefti i Gaza) 8:46–49 (in Russian)
Poley JP, Steveninck JV (1970) Delineation of shallow salt domes and surface faults by temperature measurements at a depth of approximately 2 m. Geophys Prospect 18:666–700
Popov YA, Pevzner SL, Pimenov VP, Romushkevich RA (1999) New geothermal data from the Kola superdeep well SG-3. Tectonophysics 306(3–4):345–366

Powell WG, Chapman DS (1990) A detailed study of heat flow at the Fifth Water Site, Utah, in the Basin and Range-Colorado Plateaus transition. Tectonophysics 176(3–4):291–314
Price LC (1999) Organic metamorphism in the California petroleum basins: chapter B—Insights from extractable bitumen and saturated hydrocarbons. US Geol Surv Bull 2174-B
Price LC, Daws T, Pawlewicz M (1999) Organic metamorphism in the California Petroleum Basins: chapter A—Rock-Eval and vitrinite reflectance. US Geol Surv Bull 2174-A
Pulinets SA, Ouzounov D, Karelin AV, Boyarchuk KA, Pokhmelnykh LA (2006) The physical nature of thermal anomalies observed before strong earthquakes. Phys Chem Earth 31:143–153
Rao DA, Babu HV (1984) On the half-slope and straight-slope methods of basement depth determination. Geophysics 49:1365–1368
Resapour N, Bidokhti AA, Fattahi M (2008) Thermal properties of the ground as an earthquake precursor. Transaction of the 2nd IASME /WSEAS international conference on geology and seismology, Cambridge, 23–25 Feb 2008, pp 63–65
Rosenau P, Hyman JM (1993) Compactons: solitons with finite wavelength. Phys Rev Lett 70(5):564–567
Rowlands G (1995) Non-linear phenomena in science and engineering. Ellis Horwood, West Sussex
Rybach L, Muffer LJP (1981) Geothermal systems: principles and histories. Wiley, Chichester
Sajgó C (2000) Assessment of generation temperatures of crude oils. Organ Geochem 31:1301–1323
Salman AG, Tronon AA (1990) Variations of Earth infrared outgoing flow in seismically active regions of the Middle Asia. Izv Russ Acad Sci, Phys Earth 7:67–69
Sass JH, Lachenbruch AH (1982) Preliminary interpretation of thermal data from the Nevada test site. Open-file report 82-973, US Geological Survey, Menlo Park
Sass JH, Morgan P (1988) Conductive heat flux in VC-1 and the thermal regime of Valles Caldera, Jemez Mountains, New Mexico. J Geophys Res 93(B6):6027–6039
Sass JH, Priest SS, Duda LE, Carson CC, Hendricks JD, Robison LC (1988) Thermal regime of the State 2–14 well, Salton Sea Scientific Drilling Project. J Geophys Res 93(B11):12995–13004
Sawyer DS, Hsui AT, Toksoz MN (1987) Extension, subsidence and thermal evolution of the Los Angeles Basin—a two-dimensional model. Tectonophysics 133(1–2):15–32
Schwab KW (1977) Source rock evaluation (visual kerogen). Geo-Strat Inc., Comm, Brochure, Houston
Sharma PV (2002) Environmental and engineering geophysics. Cambridge University Press, Cambridge
Sibson R (1984) Roughness at the base of the seismogenic zone: contributing factors. J Geophys Res 89:5791–5799
Simmons G (1967) Interpretation of heat flow anomalies. Rev Geophys 5(2):42–52
Singh RP, Dey S (2003) Surface latent heat flux as an earthquake precursor. Nat Hazards Earth Syst Sci 3:749–755
Speece MA, Bowen TD, Folcik JL, Pollack HN (1985) Analysis of temperatures in sedimentary basins: the Michigan Basin. Geophysics 50(8):1318–1334
Staplin FL (1969) Sedimentary organic matter, organic metamorphism, and oil and gas occurrence. Canad Petrol Geol Bull 17(1):47–66
Starin L, Yuen DA, Bergeron Y (2000) Thermal evolution of sedimentary basin formation with variable thermal conductivity. Geophys Res Lett 27(2):265–268
Telford WM, Geldart LP, Sheriff RE (1990) Applied geophysics. Cambridge University Press, Cambridge
Tikhonov AN (1937) On influence of radioactive decay on the earth crust temperature. Izv Acad Sci USSR, Ser Geogr Geophys 3:431–458
Tikhonov AN, Samarsky AA (1963) Equations of mathematical physics. Pergamon Press. Oxford
Tikhonov AN, Dmitriev VI, Glasko VV (1983) Mathematical methods in prospecting for useful minerals. Znanie (in Russian)

Tissot BP, Welte DH (1984) Petroleum formation and occurrence. Springer, Berlin
Tissot BP, Pelet R, Ungerer P (1987) Thermal history of sedimentary basins, maturation indices, and kinetics of oil and gas generation. AAPG Bull 71:1445–1466
Tongiorgi E (ed) (1975) Study and use of geothermal resources. Mir, Moscow (in Russian)
Tramutoli V, DiBello G, Pergola N, Piscitelli S (2001) Robust satellite techniques for remote sensing of seismically active areas. Ann Geophys 44:295–312
Tronin AA, Biagi PF, Molchanov OA, Khatkevich YM, Gordeev EI (2004) Temperature variations related to earthquakes from observation at the ground stations and by satellites in Kamchatka area. Phys Chem Earth 29:501–506
Tucker ME (2001) Sedimentary petrology, 3rd edn. Blackwells, Oxford
Turcotte DL (1995) Chaos, fractals, nonlinear phenomena in Earth sciences. Rev Geophys 341–343
Valentine GA, Zhang D, Robinson BA (2002) Modeling complex, nonlinear geological processes. Ann Rev Earth Planet Sci 30:35–64
Vasilyev OV, Yuen DA, Poladchikov YuYu (1997) Applicability of wavelet algorithm for geophysical viscoelastic flow. Geophys Res Lett 24(23):3097–3100
Wang Y, Zhang S, Wang F, Wang Z, Zhao C, Wang H, Liu J, Lu J, Geng A, Liu D (2006) Thermal cracking history by laboratory kinetic simulation of Paleozoic oil in eastern Tarim Basin, NW China, implications for the occurrence of residual oil reservoirs. Org Geochem 37:1803–1815
Waples DW (1980) Time and temperature in petroleum formation: application of Lopatim's method to petroleum exploration. AAPG Bull 64:916–926
Wei Z, Moldowan JM, Zhang S, Hill R, Jarvie DM, Wang H, Song F, Fago F (2007) Diamondoid hydrocarbons as a molecular proxy for thermal maturity and oil cracking: geochemical models from hydrous pyrolysis. Organ Geochem 38:227–249
Westbrook GK, Carson B, Shipboard Scientific Party (1994) Summary of Cascadia drilling results. In: Westbrook GK, Carson B, Musgrave RJ et al. (eds) Proceedings of the Ocean Drilling Program. Initial reports, vol 146 (Part 1), Chap. 9, pp 389–396
Wheatcraft SW, Gushman JH (1991) Hierarchical approaches to transport in heterogeneous porous media. Rev Geophys 3:263–269
Wold S (1974) Spline functions in data analysis. Technometrics 16:1–11
Zorin YA, Lysak SV (1972) Quantitative interpretation of geothermal anomalies. Izv Acad Nauk SSSR, Ser Fizika Zemli 9:68–73 (in Russian)

Chapter 8
Temperature Investigations in the Petroleum Industry

8.1 Wellbore and Formation Temperatures During Drilling

8.1.1 Heat Exchange in the Wellbore-Formation System

The wellbore temperature during drilling is a complex function of wellbore geometry, wellbore depth, penetration rate, flow rate, duration of the shut-in intervals, pump and rotary inputs, fluid and formation properties, and geothermal gradients (Dyakonov 1958; Mekhtiev et al. 1960; Edwardson et al. 1962). Edwardson et al. (1962) made the first attempt to evaluate the effect of shut-in periods during drilling on the temperature distribution in wells and surrounding formations. The authors numerically solved the differential heat conduction equations to predict formation temperature distributions during mud circulation and shut-in periods. The results were presented in a graphical form, making it possible to determine the formation temperature disturbance around the wellbore. As pointed out by Sump and Williams (1973), since Edwardson et al. (1962) used assumed formation temperature profiles at the end of circulation, the wellbore temperature cannot be calculated directly. Edwardson et al. (1962) took into account that the circulating drilling mud temperature, T_m, at any depth is not constant but rather changes as the well is drilled deeper, and the maximum temperature occurs not at the end of the drill string but somewhere in the annulus. It was suggested that the following formula can be used to approximate the downhole circulating mud temperature

$$T_m = a_0 + a_1 z + a_2 z^2, \tag{8.1.1}$$

where a_0 is the outlet temperature of the mud, a_1 and a_2 are constants. The undisturbed formation temperature T_f is expressed by the relationship

L. Eppelbaum et al., *Applied Geothermics*, Lecture Notes in Earth System Sciences,
DOI: 10.1007/978-3-642-34023-9_8,

$$T_f = b + \Gamma z, \tag{8.1.2}$$

where b is the local surface formation temperature.

Edwardson et al. (1962) assumed that $z = z_x$ is the depth with the maximum mud temperature, when T_m and T_f are the same. It was also assumed that the bottom-hole circulating temperature (BHCT) (at $z = H$) is known

$$T_{bh} = a_0 + a_1 H + a_2 H^2. \tag{8.1.3}$$

In this case the values of a_1 and a_2 can be expressed through the parameter z_x. Finally, the value of z_x can be determined from a quadratic equation.

Two approaches are used in studies of heat interactions of the circulating fluid with formation. In the first case, heat interactions of circulating fluid and formation are treated under the condition of constant-bore face temperature or heat flux (e.g. Edwardson et al. 1962; Ramey 1962; Lachenbruch and Brewer 1959; Shen and Beck 1986; Kutasov 1987, 1999). In the second approach the thermal interaction of the circulating fluid with formation is approximated by the Newton relationship on the bore-face (Tragesser et al. 1967; Raymond 1969; Holmes and Swift 1970; Keller et al. 1973; Sump and Williams 1973; Wooley 1980; Thompson and Burgess 1985; Hasan and Kabir 1994; Fomin et al. 2003; Espinosa-Paredes et al. 2009). As shown by Fomin et al. (2003) the first approach can be used in the case of highly intensive heat transfer between the circulating fluid and surrounding rocks, which takes place for fully developed turbulent flows in the well. However, in all our studies we used the term effective temperature (at a given depth) of the drilling fluid (Kutasov 1987, 1999; Kutasov and Eppelbaum 2005a, b). This unknown parameter is introduced solely to evaluate the amount of heat obtained (or lost) during the entire drilling period. In their classical work Lachenbruch and Brewer (1959) showed that the wellbore shut-in temperature mainly depends on the amount of thermal energy transferred to (or from) formations during drilling. Our reservations as regards the application of the Newtonian relationship are presented below. Raymond (1969) developed generalized techniques to predict downhole fluid temperatures in a circulating fluid system during both transient and pseudo-steady state conditions. The fluid circulation in over 70 wells was simulated to generate charts of $\Delta T = T_{bh} - T_{ou}$ (bottom-hole and outlet mud temperature) versus the flow rate for oil and water base muds (Raymond 1969). These charts were obtained for a geothermal gradient of 0.017 °F/ft (0.031 °C/m), 4.5 in. drill pipe, and a hole size of 8.625 in. Raymond conducted a sensitivity study and found that the drill pipe and hole sizes have little effect on circulating temperatures. In Raymond's (1969) model the circulation time was constant for all sections of the well. The well depth was also constant and the initial formation temperatures (prior to circulation) were equal to the geothermal (undisturbed) temperature.

Several main characteristics of the drilling process were not taken into consideration in this model:

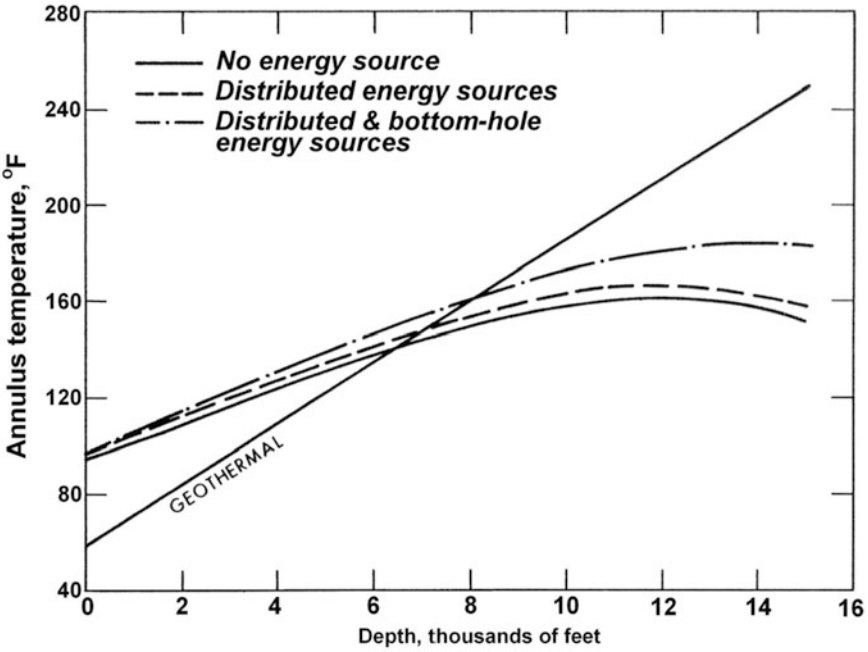

Fig. 8.1 The effect of energy sources on the annulus temperatures in a drilling well (Keller et al. 1973)

1. The amount of time that a formation is exposed to drilling fluid circulation depends on the depth (maximum periods of exposure correspond to the shallowest depths).
2. The temperature of the drilling fluid at a given depth depends on the current total depth.
3. The discontinuity of the mud circulation process during drilling.
4. The presence of the casing strings cemented at various depths.
5. The impact of the energy sources caused by drilling. The influence of energy sources on the temperature distribution in circulating mud columns was considered by Keller et al. (1973). Usually only the thermal energy of the inlet drilling mud is taken into account. However, during drilling, heat is also generated by fluid friction in the drill pipe and annulus, by the rotary input needed to rotate the drill string, and by the bit work. It is commonly assumed that during drilling more than 99 % of mechanical energy (rotary and pump inputs) is transformed into thermal energy. For one Gulf Coast well the effect of including heat sources in the calculations is shown in Fig. 8.1.

It was assumed that the casing was initially (prior to the last circulation period) at the same temperature as the geothermal temperature (Keller et al. 1973). For this reason, this example has only an illustrative interest. The lower curve in Fig. 8.1

gives the temperature distribution after 24 h of mud circulation for no energy sources. The center curve was calculated with a uniform energy source of 8.17 W/m inside the drill string and a uniform source of 15.90 W/m in the annulus. The upper curve was calculated using the same energy sources as for the center curve plus a source of 1.68×10^5 W at the bottom of the hole. The pump energy sources used were calculated from pressure drop readings from charts. The total pump input was 1.86×10^5 W and the rotary input was 125 hp (9.32×10^4 W). Thus these calculations (Keller et al. 1973) indicate that the energy source terms have a marked effect on the computed downhole temperature (Fig. 8.1). A comprehensive two dimensional, axisymmetric, transient computer model of wellbore temperatures (WELLTEMP) was created and used to calculate temperatures of wellbore fluids, cement, steel, and surrounding formations as functions of depth and time (Wooley 1980; Mitchell 1981; Wooley et al. 1984). WELLTEMP is linked to another program that computes temperature and pressure dependent fluid properties, fluid pressures, and fluid velocities. Thus this wellbore thermal simulator can account for several main features of the drilling process: well depth change with time, discontinuity of mud circulation, variation of mud properties with depth and time, and the complexity of the completion design. Beirute (1991) developed a computer simulator that can predict downhole temperatures during fluid circulation and shut-in periods. The simulator can be used for any well configuration and handles several fluids in the wellbore at one time.

8.1.1.1 Newtonian Relationship

The discontinuity of the mud circulation process during drilling poses a serious problem in using the Newtonian relationship for determining the heat flow from the mud in the drill pipe to the wall of the drill pipe as well as the heat flow through the formation-annulus interface (q_f). According to the Newtonian relationship

$$q_f = \alpha_{fa}\left(T_m - T_{fa}\right), \tag{8.1.4}$$

where α_{fa} is the film heat transfer coefficient from mud in the annulus to the formation, T_m is the average mud temperature (in annulus section), and T_{fa} is the temperature at the formation-annulus interface.

For a developed turbulent flow, the Dittus-Boelter formula is usually employed to estimate the value of the film heat transfer coefficient, and for applications in which the temperature influence on fluid properties is significant, the Sieder-Tate correlation is recommended (Bejan 1993). For theoretical reasons, the Newtonian equation is applicable only to steady-state conditions. This means that in our case both temperatures (T_{fa}, T_m) cannot be time dependent functions. In practice, however, the Newtonian relationship is successful in many areas when the temperature of the fluids and the temperatures at the fluid–solid wall interfaces are slowly changing with time. Hence there is a need to determine under which

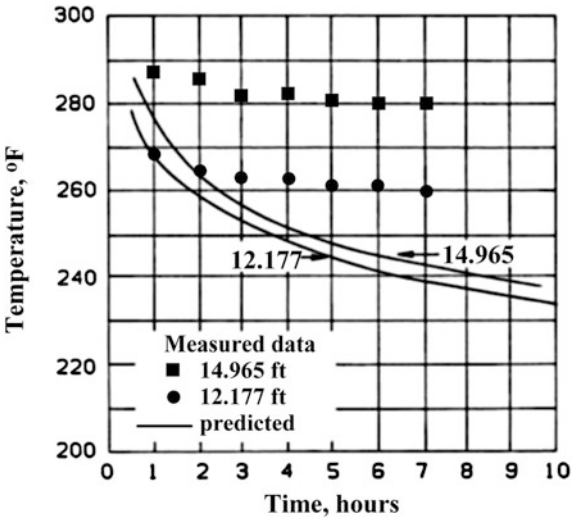

Fig. 8.2 Comparison of measured and predicted mud temperatures from Well 1 (Sump and Williams 1973)

conditions Eq. (8.1.4) can be used to predict the wellbore temperatures during drilling. In fact, the wellbore temperature during mud circulation is a complex function of time, wellbore geometry, well bore depth, penetration rate, circulation mud rate, fluid and formation properties and geothermal gradients. Drilling records show that mud circulates only a certain part of the time required to drill a well. For example, in the Montana well (9,222 ft), the circulation history at a depth of 8,812 ft was presented by Edwardson et al. (1962). Nine drilling mud circulation periods were required to drill the 8,812–9,222 ft section of the well. The cumulative circulation time at a depth 8,812 ft was 80.1 h or 44.3 % of the drilling time. Some results of field investigations in the USA and Russia have shown that using conventional values of the film heat transfer coefficients in predicting wellbore temperatures during drilling are very questionable (Deykin et al. 1973; Sump and Williams 1973). Predictions using Raymond's (1969) method for 7 wells, for example, differed from the measured values by 12 % on average (Fig. 8.2) and in one case missed the measured temperature by 65 °F (36 °C) (Sump and Williams 1973).

When water based drilling fluids are used, mud cake is formed. Mud cake is a plastic-like coating of the borehole formed by the solids in the drilling fluid adhering and building up on the wall of the hole. As a consequence of drilling and completion operations most wells have reduced permeability near the borehole (skin zone). The skin factor is a composite parameter and takes into account the permeability of different layers by introducing the effective (equivalent) permeability k_s. Quantitatively the skin is defined as a parameter (skin factor) which depends on the thickness and the effective permeability of the skin zone (Hawkins 1956):

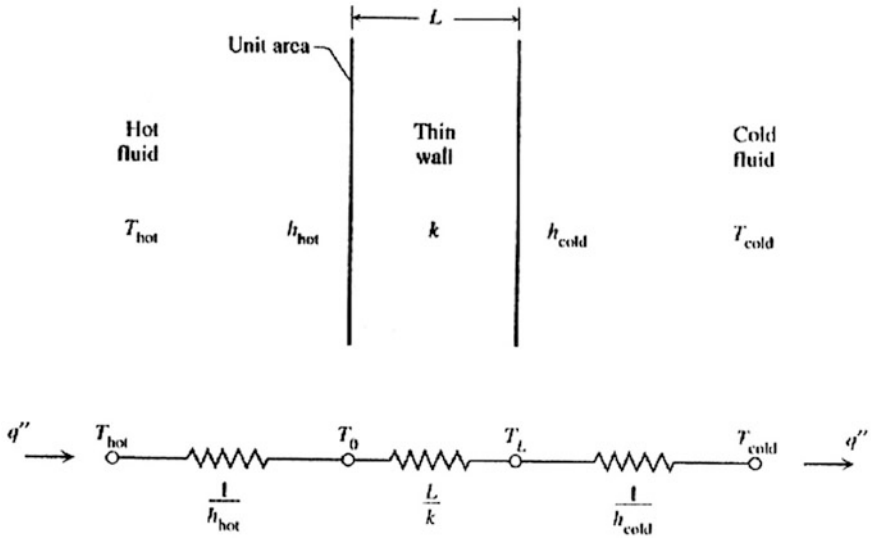

Fig. 8.3 Thin wall sandwiched between two flows: The definition of overall heat transfer coefficient (Bejan 1993)

$$s = \left(\frac{k}{k_s} - 1\right) \ln \frac{r_s}{r_w}, \tag{8.1.5}$$

where k is the permeability of an undamaged formation.

This may result in a corresponding change of thermal conductivity of formations near the borehole. Thus in practice the contact fluid-formation can be replaced by the fluid-mud cake or fluid-mud cake-skin zone contacts. Note that the maximum deviation between experimental values of heat transfer coefficients and those predicted from the Dittus-Boelter formula can be on the order of 40 % (Bejan 1993).

8.1.1.2 Overall Heat Transfer Coefficient

During mud circulation the thin steel wall of the drill pipe creates two separate streams of fluid. To determine the radial heat flow from (or into) the drill pipe to (or from) the annulus, the value of the overall heat transfer coefficient (U) should be calculated. The calculation procedure to obtain the value of U is clear from Fig. 8.3.

In our case the wall thickness and drill pipe radius ratio is very small, and we can assume that the radial heat flow (q'') is constant inside the wall. From the Newtonian relationship and the Fourier law it follows that

$$T_{\text{hot}} - T_0 = \frac{q''}{h_{\text{hot}}}, \tag{8.1.6}$$

$$T_L - T_{\text{cold}} = \frac{q''}{h_{\text{cold}}}, \tag{8.1.7}$$

$$T_0 - T_L = \frac{Lq''}{k}. \tag{8.1.8}$$

From Eqs. (8.1.6)–(8.1.8) we obtain

$$Q'' = U(T_{\text{hot}} - T_{\text{cold}}), \tag{8.1.9}$$

$$\frac{1}{U} = \frac{1}{h_{\text{hot}}} + \frac{L}{k} + \frac{1}{h_{\text{cold}}}, \tag{8.1.10}$$

where k is the thermal conductivity of steel, T_{hot} is the bulk mud temperature in the annulus, and T_{cold} is bulk mud temperature in the drill pipe.

8.1.1.3 Effect of Hydraulic and Rotary Inputs

To evaluate the influence of drilling technology on the temperature of the circulating fluid, we will assume that 100 % of the hydraulic and rotary inputs are used for heating the drilling mud. Due to frictional losses the mud pump must provide the circulating fluid with a continuous supply of mechanical energy. This amount of energy per unit of time—the hydraulic power output of the pump (H_h) in oilfield units—can be expressed by the following formula (Craft et al. 1962):

$$H_h = \frac{q\Delta p}{1714}(\text{hp}), \tag{8.1.11}$$

where H_h is usually expressed in units of horsepower, q is the flow rate in gallons per minute (gpm), and Δp is the discharge pressure (differential pressure) developed by the pump in psig.

To determine the rotary horsepower (R_h)—the amount of energy needed to rotate the drill pipe and penetrate the formations—the surface torque (T_s) and speed of rotation (S_r) should be recorded while drilling. The rotary horsepower in oilfield units can be expressed by the relationship (API Bulletin 1982):

$$R_h = \frac{T_s S_r}{5250} \ (\text{hp}), \tag{8.1.12}$$

where the surface torque (bending moment) is in ft · lbf and the speed of rotation is in revolutions per minute, rpm.

Below we present a field example. The following (average) parameters were recorded while drilling a 6,200–7,800 ft section of an oil well:

$$q = 470\,\text{gpm},\ \Delta p = 3,000\,\text{psig}, T_s = 5,000\,\text{ft}\cdot\text{lbf},\ \text{and}\ S_r = 80\,\text{rpm}.$$

From Eqs. (8.1.11) and (8.1.12) we obtain

$$H_h = (470 \times 3,000)/1,714 = 822.6\,(\text{hp}); R_h = (5,000 \times 80)/5,250 = 76.2\,(\text{hp}).$$

The total input of mechanical energy was 822.6 + 76.2 = 898.8 (hp). In our case the density of the drilling mud was 9.3 ppg and specific heat capacity was 0.854 Btu/lb °F. Taking into account that 1 hp = 2,545 Btu/h, we obtain that the equivalent average temperature increase (ΔT) of the drilling fluid is

$$\Delta T - \frac{898.8 \times 2,545}{9.3 \times 470 \times 0.854 \times 60} = 10.2\,(^\circ\text{F}) = 5.7\,(^\circ\text{C}).$$

8.1.1.4 Radial Heat Flow Rate

The results of field and analytical investigations have shown that in many cases the temperature of the circulating fluid (mud) at a given depth $T_m(z)$ can be assumed to be constant during drilling or production (Lachenbruch and Brewer 1959; Ramey 1962; Edwardson et al. 1962; Jaeger 1961; Kutasov et al. 1966; Raymond 1969). However for super deep wells (5000–7000 m) the temperature of the circulating fluid is a function of the vertical depth (z) and time (t). Thus the estimate of heat losses from the wellbore is an important factor which shows to what extent the drilling process disturbs the temperature field of formations surrounding the wellbore. If the temperature distribution $T(r, z, t)$ or the heat flow rate $q(r = r_w, z, t)$ (r_w is the well radius) are known for the case of a well with a constant bore-face temperature, the functions $T(r, z, t)$ and $q(r = r_w, z, t)$ for the case of a time dependent bore-face temperature can be found through the Duhamel's integral. In this section we present an approximate formula for calculating the rate of heat losses for wells with a constant bore-face temperature (T_w) at a given depth. The heat flow rate from the wellbore per unit of length is given by:

$$q = 2\pi\lambda(T_w - T_i)q_D(t_D), \tag{8.1.13}$$

where T_f is the undisturbed formation temperature, λ is the thermal conductivity of the formation, q_D is the dimensionless heat flow rate. Here we introduce the dimensionless mud circulation time t_D:

$$t_D = \frac{\alpha t}{r_w^2}, \tag{8.1.14}$$

Table 8.1 Comparison of values of dimensionless heat flow rate for a well with constant bore-face temperature; q_D*—Sengul (1983); q_D—Eq. (8.1.15)

t_D	q_D*	q_D	$\Delta q/q_D$* (%)
2	0.80058	0.80877	1.02
3	0.7162	0.72402	1.09
5	0.62818	0.63555	1.17
10	0.53392	0.54068	1.27
20	0.46114	0.4673	1.34
50	0.38818	0.39351	1.37
100	0.34556	0.35025	1.36
200	0.3108	0.31484	1.30
500	0.27381	0.27706	1.19
1,000	0.25096	0.25366	1.08

where α is the thermal diffusivity of the formation.

The dimensionless heat flow rate was calculated by Jacob and Lohman (1952). Sengul (1983) computed values of $q_D(t_D)$ for a wider range of t_D and with more table entries. We found (Kutasov 1987) that the dimensionless heat flow rate can be approximated by:

$$q_D = \frac{1}{\ln\left(1 + D\sqrt{t_D}\right)}, \tag{8.1.15}$$

$$D = d + \frac{1}{\sqrt{t_D} + b}, \quad d = \frac{\pi}{2}, \tag{8.1.16}$$

$$b = \frac{2}{2\sqrt{\pi} - \pi}, \quad b = 4.9589.$$

In Table 8.1 values of q_D calculated after Eq. (8.1.15) and the results of a numerical solution are compared. The agreement between values of q_D calculated by these two methods is good. The suggested Eq. (8.1.15) is valid for any value of fluid circulation time. Equations (8.1.13) and (8.1.15) were used to develop a new technique for the determination of the formation thermal conductivity and contact thermal resistance (expressed through the skin factor). It is assumed that the volumetric heat capacity of formations is known and the instantaneous heat flow rate and time data are available for a linear probe with a constant temperature placed in a wellbore. A simulated example is presented in Kutasov and Kagan (2003). A further evaluation this methodology—cylindrical probe with a variable heat flow rate—is shown in Eppelbaum and Kutasov (2013).

8.1.1.5 Adjusted Circulation Time Concept

In his classical paper Ramey (1962) drew the attention of petroleum engineers to the fact that three solutions; namely a cylinder losing heat at constant temperature, a constant heat flow line source, and a cylinder losing heat under the convection

boundary all practically converge after some time. The simple solution for a constant fluid flow (or heat flow) line source is expressed through the exponential integral, and is widely used in reservoir engineering. To use this solution for any value of circulation time, below we introduce the adjusted circulation time. Let us assume that at a given depth the fluid circulation started at a moment in time $t = 0$ and stopped at $t = t_c$. The corresponding values of the dimensionless heat flow rates (Eq. 8.1.15) are

$$q_D(t = 0) = \infty, \quad q_D(t = t_c) = q_D$$

and the values of the dimensionless cumulative heat flow are $Q_D(0) = 0$ and $Q_D(t_c) = Q_D$.

Assuming that during the circulation period $0 < t \leq t_c$ the value of $q_D(t) = q_D = \text{constant}$, the dimensionless adjusted circulation time is

$$t_D^* = \frac{Q_D}{q_D}, \quad or \quad Q_D = q_D \cdot t_D^*. \tag{8.1.17}$$

The actual adjusted circulation time is

$$t_c^* = \frac{t_D^* r_w^2}{a}. \tag{8.1.18}$$

The values of Q_D are presented in the literature van Everdingen and Hurst (1949), Jacob and Lohman (1952) and Edwardson et al. (1962). Using these data we obtained:

$$t_D^* = G t_D, \tag{8.1.19}$$

$$\left\{ \begin{array}{c} G = 1 + \frac{1}{1+AF}, \quad t_D \leq 10, \\ F = [\ln(1 + t_D)]^n, \quad n = \frac{2}{3}, \quad A = \frac{7}{8}. \end{array} \right\}, \tag{8.1.20}$$

$$G = \frac{\ln t_D - \exp(-0.236\sqrt{t_D})}{\ln t_{cD} - 1}, \qquad t_D > 10. \tag{8.1.21}$$

The correlation coefficient $G(t_D)$ varies with the narrow limits of $G(0) = 2$ and $G(\infty) = 1$ (Fig. 8.4). Thus by using the adjusted circulation time concept (Kutasov 1987, 1989) a well with a constant borehole wall temperature can be replaced by a cylindrical source with a constant heat flow rate.

The dimensionless cumulative heat flow is calculated from Eqs. (8.1.15)–(8.1.19). The values of Q_D are presented in Table 8.2 and compared with the results of a numerical solution.

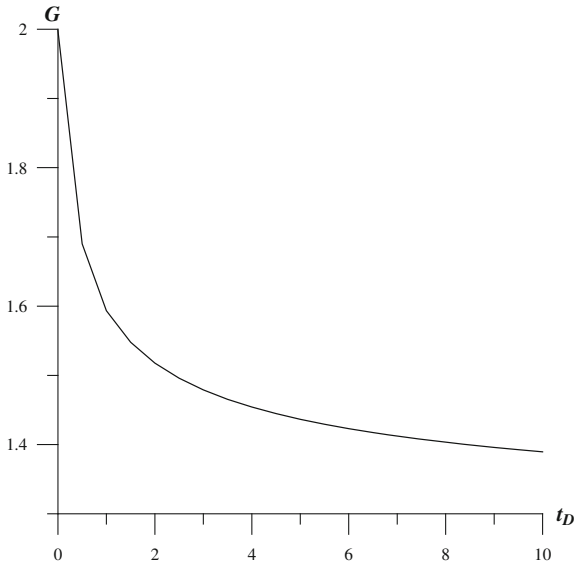

Fig. 8.4 Correlation coefficient versus dimensionless time

Table 8.2 Comparison of values of dimensionless cumulative heat flow for a well with constant bore-face temperature. Q_D* according to van Everdingen and Hurst (1949); Q_D according to Eq. (8.1.17)

t_D	Q_D*	Q_D	$\Delta Q_D/Q_D$* × 100 (%)
2	0.2447E+01	0.2445E+01	0.32
3	0.3202E+01	0.3212E+01	0.32
5	0.4539E+01	0.456E+01	0.57
10	0.7411E+01	0.7512E+01	1.37
20	0.1232E+02	0.1240E+02	0.65
50	0.2486E+02	0.2516E+02	1.22
100	0.4313E+02	0.4382E+02	1.61
200	0.7579E+02	0.7710E+02	1.73
500	0.1627E+03	0.1650E+03	1.39
1,000	0.2935E+03	0.2966E+02	1.04
2,000	0.5341E+03	0.5382E+03	0.77
5,000	0.1192E+04	0.1198E+04	0.52
10,000	0.2204E+04	0.2213E+04	0.42

8.1.1.6 Radial Temperature Distribution

To determine the temperature distribution $T(r, t)$ in formations near a wellbore with a constant bore-face temperature it is necessary to obtain the solution to the diffusivity equation for the following boundary and initial conditions:

$$\left\{ \begin{array}{ll} T(r,0) = T_f, & r_w \le r \le \infty, \quad t > 0, \\ T(r_w,t) = T_w, & T(\infty,t) = T_f. \end{array} \right\}.$$

It is well-known that in this case the diffusivity equation has a solution in a complex integral form (Jaeger 1956; Carslaw and Jaeger 1959). Jaeger (1956) presented results of a numerical solution for the dimensionless temperature $T_D(r_D, t_D)$ with values of r_D ranging from 1.1 to 100 and t_D ranging from 0.001 to 1,000. We found that the exponential integral (a tabulated function) can be used to describe the temperature field of formations around a well with a constant bore-face temperature (Kutasov 1999):

$$T_D(r_D,t_D) = \frac{T(r,t) - T_f}{T_w - T_f} = \frac{Ei\left(\frac{-r_D^2}{4t_D^*}\right)}{Ei\left(\frac{-1}{4t_D^*}\right)}, \qquad r_D = \frac{r}{r_w}. \tag{8.1.22}$$

8.1.1.7 Radius of Thermal Influence

Interpretation of electric logs, evaluation of the thermal stresses arising from the difference between the wellbore temperature and undisturbed formation temperature, and estimates of static formation temperatures from well logs require knowledge of the temperature disturbance of formations produced by the circulating drilling mud. The drilling process greatly alters the temperature field of formations surrounding the wellbore. The temperature change is affected by the duration of fluid circulation (depth penetration, hole cleaning, cementing), the duration of shut-in periods (tripping of drill pipe, running of casing, logging), the temperature difference between the formation and drilling mud, the well radius, the thermal properties of formations, and the drilling technology used. The results of field and analytical investigations have shown that in many cases the effective temperature (T_w) of the circulating fluid (mud) at a given depth can be assumed constant during drilling or production (Lachenbruch and Brewer 1959; Ramey 1962; Edwardson et al. 1962; Jaeger 1961; Kutasov et al. 1966; Raymond 1969). Note that even for a continuous mud circulation process the wellbore temperature is dependent on the current well depth and other factors. The term effective fluid "temperature" is used to describe the temperature disturbance of formations while drilling. Lachenbruch and Brewer (1959) showed that the wellbore shut-in temperature mainly depends on the amount of thermal energy transferred to (or from) formations. Thus for every depth, a value of T_w can be estimated from shut-in temperature logs. In theory the drilling process affects the temperature field of formations at very long radial distances. There is, however, a practical limit to the distance; namely, the radius of thermal influence (r_{in}), where for a given

circulation period ($t = t_c$) the temperature $T(r_{in}, t_c)$ is practically equal to the geothermal temperature T_f. To avoid uncertainty, however, it is essential that the parameter r_{in} must not be dependent on the temperature difference $T(r_{in}, t_c) - T_f$. For this reason we used the thermal balance method to calculate the radius of thermal influence. The results of modelling, experimental work, and field observations showed that the temperature distribution around the wellbore during drilling can be approximated by the following relation (Kutasov 1968, 1976):

8.1.1.8 Borehole as a Cylindrical Source with a Constant Temperature

$$\frac{T(r,t) - T_f}{T_w - T_f} = 1 - \frac{\ln \frac{r}{r_w}}{\ln \frac{r_{in}}{r_w}}, \quad r_w \le r \le r_{in}. \tag{8.1.23}$$

Introducing the dimensionless values of circulation time, radial distance, radius of thermal influence, and temperature

$$t_D = \frac{at_c}{r_w^2}, \quad r_D = \frac{r}{r_w}, \quad R_{in} = \frac{r_{in}}{r_w}, \quad T_D(r_D, t_D) = \frac{T(r,t) - T_f}{T_w - T_f},$$

we obtain

$$T_D(r_D, t_D) = 1 - \frac{\ln r_D}{\ln R_{in}}, \quad 1 \le r_D \le R_{in}. \tag{8.1.24}$$

It is known that the cumulative heat flow from the wellbore per unit of length is given by:

$$Q = 2\pi\rho c_p r_w^2 \left(T_w - T_f\right) Q_D(t_D), \tag{8.1.25}$$

where ρ is the density of formations, c_p is the specific heat of formations, r_w is the well radius, and Q_D *i*s the dimensionless cumulative heat flow. The time dependent function Q_D can be expressed as

$$Q_D = \int_1^{R_{in}} T_D \, r_D \, dr_D. \tag{8.1.26}$$

From Eqs. (8.1.24) and (8.1.26) we obtain

$$Q_D = \frac{R_{in}^2 - 1}{4 \ln R_{in}} - \frac{1}{2}. \tag{8.1.27}$$

Table 8.3 Dimensionless temperature $T_D(r_D, t_D) \times 1000$ for a well with constant bore-face temperature, first line—Eq. (8.1.24); second line—Eq. (8.1.22); third line—numerical solution (Jaeger 1956)

t_D	Dimensionless distance, r_D							
	1.1	1.2	1.5	2	3	5	7	10
5	946	897	771	609	380	92	0	0
	934	875	726	543	310	97	26	2
	940	886	746	568	332	101	24	2
10	954	912	804	665	469	222	59	0
	945	896	771	614	404	180	77	18
	949	903	784	631	422	188	77	16
20	960	923	829	708	538	323	181	31
	953	912	804	668	481	266	148	59
	956	916	813	681	497	277	153	57
50	966	935	855	752	608	425	305	178
	961	926	837	723	564	370	253	144
	963	929	843	731	574	381	260	146
100	970	942	870	778	649	486	378	264
	966	935	856	755	613	437	326	216
	967	937	860	760	621	446	334	222
200	972	947	883	800	683	535	438	335
	969	942	871	780	653	493	390	285
	970	943	874	784	658	500	397	291

The results of a numerical solution (Jaeger 1956) for a cylindrical source with a constant wall temperature were used to obtain the values of $Q_D(t_D)$. From the last equation we found that the dimensionless radius of thermal influence can be approximated by:

$$R_{in} = 1 + D_o\sqrt{t_D}\,, \tag{8.1.28}$$

$$\left\{\begin{array}{l} D_0 = 2.184, \quad 5 \le t_D < 10^4 \\ D_0 = 2.143, \quad 5 \le t_D < 10^6 \end{array}\right\}.$$

Table 8.3 shows that the suggested Eqs. (8.1.24) and (8.1.22) can be used to determine the formation temperatures with sufficient accuracy.

From Eqs. (8.1.22) and (8.1.26) we obtain

$$Q_D = -\frac{1}{2} - \frac{2Gt_D \exp\left(-\frac{1}{4Gt_D}\right)}{Ei\left(-\frac{1}{4Gt_D}\right)}\,. \tag{8.1.29}$$

Combining Eqs. (8.1.29) and (8.1.27) we obtain the equation for the dimensionless radius of thermal influence

$$-\frac{1}{2}-\frac{2Gt_D\exp\left(-\frac{1}{4Gt_D}\right)}{Ei\left(-\frac{1}{4Gt_D}\right)}=\frac{1}{4}\frac{R_{in}^2-2\ln(R_{in})-1}{\ln(R_{in})}. \tag{8.1.30}$$

8.1.1.9 The Borehole as a Cylindrical Source with a Constant Heat Flow Rate

For a borehole as a cylindrical source of heat, the wall temperature is (Kutasov 2003)

$$T_w=T(t,r_w)=T_i+\frac{q}{2\pi\lambda}\ln\left[1+\left(c-\frac{1}{a+\sqrt{t_D}}\right)\sqrt{t_D}\right], \tag{8.1.31}$$

$$t_D=\frac{at}{r_w^2}=\frac{\lambda t}{c_p\rho r_w^2},\qquad a=2.70105,\quad c=1.4986, \tag{8.1.32}$$

where λ is the thermal conductivity of formations, ρ is the density of formations, c_p is the specific heat, and q is the heat flow rate per unit of length.

The cumulative heat flow per unit of length is given by

$$Q=qt=2\pi\rho c r_w^2(T_w-T_i)Q_D. \tag{8.1.33}$$

Combining Eqs. (8.1.31)–(8.1.33) and (8.1.27) we obtain an equation to determine the value of R_{in}:

$$t_D=\frac{1}{4}\frac{R_{in}^2-2\ln(R_{in})-1}{\ln(R_{in})}\ln\left[1+\left(c-\frac{1}{a+\sqrt{t_D}}\right)\sqrt{t_D}\right]. \tag{8.1.34}$$

Equations (8.1.30) and (8.1.34) can be used when the radius of thermal influence (radius of investigation) is specified and is needed to estimate the maximal value of t_D. The results of calculations of the dimensionless radius of thermal influence are presented in Fig. 8.5.

8.1.2 Downhole Circulating Mud Temperature

8.1.2.1 Analytical Methods and Computer Programs

A prediction of the downhole mud temperatures during well drilling and completion is needed for drilling fluid and cement slurry design, for drilling bit design and in evaluations of the thermal stresses in tubing and casings. One of best attempts at

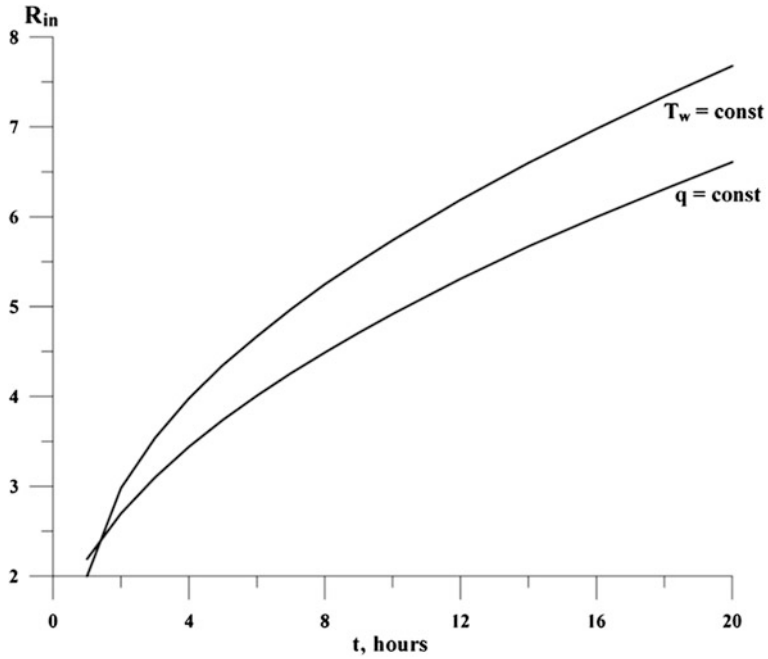

Fig. 8.5 Dimensionless radius of thermal influence versus time: T_w = const (Eq. 8.1.30), q = const (Eq. 8.1.34), $\alpha = 0.0040\ m^2 \cdot h^{-1}$, $r_w = 0.1$ m

predicting the fluid temperature during mud circulation was made by Raymond (1969). For the first time a comprehensive technique to predict transient formations profiles and downhole fluid temperatures in a circulating fluid system was developed. The calculating procedure suggested by Raymond can be modified to account for the presence of the casing strings cemented at various depths. However, the main features of the drilling process were not considered in Raymond's (1969) model, which include the change of the well's depth with time, the disturbance of the formation temperature field by previous circulation cycles, the discontinuity of the mud circulation while drilling, and the effect of the energy sources caused by drilling. Nevertheless, Raymond's model can be used to evaluate the effect of circulation time and depth on downhole temperatures, and to estimate the effect of mud type weight on the difference between bottom-hole fluid and outlet temperatures. Crucially, this model can also be used to find the duration of the circulation period, since the downhole temperatures calculated from the pseudo-state equations are practically identical to those computed from unsteady state equations. The system of differential equations which describes the heat conduction in the drill pipe-annulus-formation system was solved numerically to obtain the transient circulating fluid temperature profiles for a simulated well (Raymond 1969). The input parameters were: vertical well depth = 20,000 ft, diameter of drill pipe = 4 1/2 in., well diameter = 8 5/8 in., mud density = 18 ppg (oil-base mud), inlet mud

temperature = 135 °F, surface formation temperature = 80 °F, and geothermal gradient = 0.016 °F/ft. The flow rate was held constant at 200 gpm during the entire 16 h of circulation. The main results of these calculations were as follows:

The outlet temperature rose rapidly 147 °F and in the last 9 h of circulation the outlet temperature changed 1 °F.

A practically constant temperature difference between the bottom-hole fluid and the rock emerged after 2–3 h of the circulation process. It changed continually with time and a steady-state condition was never attained.

The overall effect of circulation was to heat the upper section of the simulated well and cool the lower section of the well. This means that at some depth $z = z_1$, the annular temperature of the drilling mud (for a given circulation time) was equal to the geothermal temperature. For example, for 2 h of mud circulation, the value of z_1 was 12,000 ft. The parameter z_1 reduced with circulation time.

After a short circulation period (for a constant inlet mud temperature) the unsteady-state terms in differential equations can be neglected and a pseudo-state solution can be used. This indicates that the rate of heat flow from formation (or into formation) to annulus becomes a dominant factor.

In an actual drilling process, many time-dependent variables influence down-hole temperatures. The composition of annular materials (steel, cement, fluids), the drilling history (vertical depth versus time), the duration of short shut-in periods, fluid flow history, radial and vertical heat conduction in formations, the change of geothermal gradient with depth, and other factors should be accounted for and their effects on the wellbore temperatures while drilling should be determined. It is clear that only transient computer models can be used to calculate temperatures in the wellbore and surrounding formations as functions of depth and time (Wooley 1980; Mitchell 1981; Wooley et al. 1984; Beirute 1991). Usually computer simulations are tested against analytical solutions and in some cases field tests data have been used to verify the results of modelling.

An example of circulating temperatures predictions by the WELLTEMP computer code is presented in Fig. 8.6.

As can be seen from Fig. 8.6, the computed circulating temperatures coincide with the field data. Due to incompleteness of the input data (fluid and formations properties, geothermal gradients) some assumptions were made before the simulation was conducted. A drilling simulation was conducted on the geothermal Republic 56–30 well (Imperial Valley, California). Table 8.4 summarizes the drilling history of this well. As can be seen from Table 8.4 a thermal simulation of this well requires four different wellbore fluids, four different flow rates, and varying depths (Mitchell 1981). Mitchell (1981) computed wellbore temperatures for selected time periods (circulation and shut-in), estimated the temperatures at the drill bit over the drilling history of the well, and calculated the time- dependent casing temperature for two depths.

A new method evaluated efficiency of wellbore stimulation was demonstrated in Kutasov and Eppelbaum (2012).

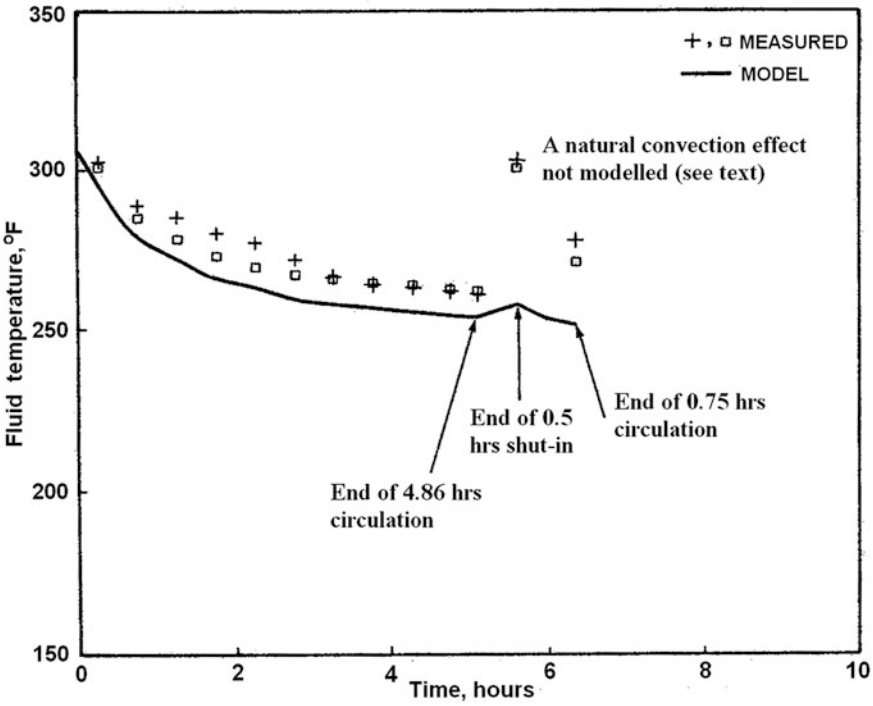

Fig. 8.6 Circulating mud temperature at 16,079 ft, Mississippi Well (Wooley et al. 1984)

8.1.2.2 Empirical Equation, Utilization of Field Data

Temperature surveys in many deep wells have shown that both the outlet drilling fluid temperature and the bottom-hole temperature vary monotonically with the vertical depth (Fig. 8.7). It was suggested (Kuliev et al. 1968) that the stabilized circulating fluid temperature in the annulus (T_m) at any point can be expressed as

$$T_m = A_0 + A_1 h + A_2 h, \quad h < H, \tag{8.1.35}$$

where the values A_0, A_1 and A_2 are constants for a given area, h is the current vertical depth and H is the total vertical depth of the well (the position of the bottom of the drill pipe at fluid circulation).

The values of A_0, A_1 and A_2 are dependent on drilling technology (flow rate, well design, fluid properties, penetration rate, etc.), the geothermal gradient and the thermal properties of the formation. It is assumed that for a given area, the above-mentioned parameters vary within narrow limits. In order to obtain the values of A_0, A_1, and A_2 the records of the outlet fluid (mud) temperature (at $h = 0$) and results of downhole temperature surveys are needed. In Eq. (8.1.35) the value of T_m is the stabilized downhole circulating temperature. The time of the downhole temperature stabilization (t_s) can be estimated from the routinely

Table 8.4 Republic 56–30 well: drilling history, fluid properties, and well completion data (Mitchell 1981)

Drilling history

Time, days	Depth, ft	Circ. rate, gal/min	Circ. time, per day	Fluid
0	0	480	17.0	1
1	1,513	480	5.0	1
2	1,513	500	20.0	2
10	5,330	360	2.0	3
17	5,330	360	17.0	4
24	7,520	400	2.0	4

Drilling fluid properties

Fluid	Density, lb/gal	Plastic visc., centipoise	Yield point, lb/100 ft^2
1	8.8	4.0	4.0
2	9.0	7.0	4.0
3	8.9	22.0	17.0
4	8.9	9.0	5.0

Well completion

Casing, Pipe	Size, in.	Weight, lbf/ft	Setting depth, ft
Conductor	20	94.0	90.
Surface	13–3/8	54.5	1503.
Production	8–5/8	32.0	5320.
Protective	6–5/8	28.0	7520.
Drill pipe	3–1/2	9.5	N.A

recorded outlet mud temperature logs. Let us assume that the pump started to operate at time $t = 0$. In this case, to get the stabilized values of the outlet mud temperature, one must take readings at $t > t_s$.

The value of t_s can be obtained from an empirical formula (Kuliev et al. 1968):

$$t_s = b_0 + b_1 H, \tag{8.1.36}$$

where the values b_0 and b_1 are constants and time t_s is in hours.

Recording the values of the outlet mud temperature (T_{mo}) at times during mud circulation without penetration we can determine the moment in time after which the value of T_{mo} is practically constant.

Hence for some depth $H = H_1$:

$$t_{s1} = b_0 + b_1 H_1. \tag{8.1.37}$$

Similarly, for the vertical depth of the well $H = H_2$:

$$t_{s2} = b_0 + b_1 H_2. \tag{8.1.38}$$

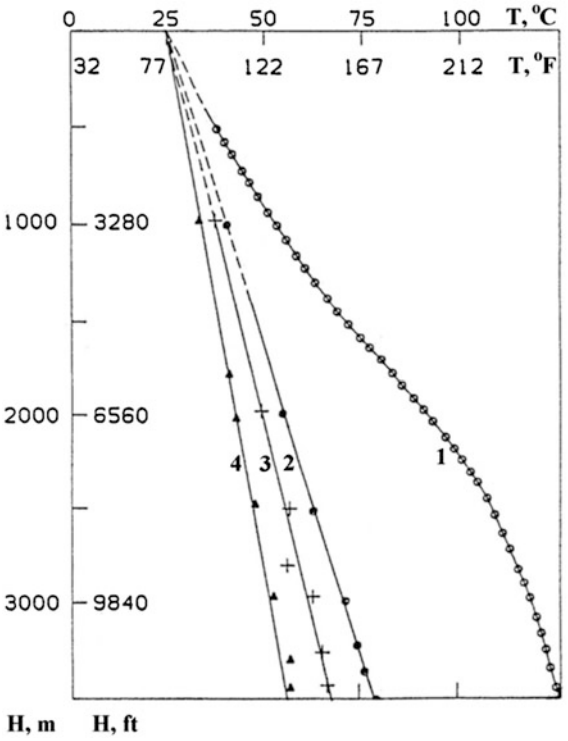

Fig. 8.7 Temperature curves versus current well depth. Well 12-PXC, Stavropol district, Russia (Proselkov 1975). *1* Geothermal curve *2* circulating bottom-hole temperature *3* outlet drilling mud temperature, *4* Inlet drilling mud temperature

From Eqs. (8.1.37) and (8.1.38) we obtain

$$b_1 = \frac{t_{s2} - t_{s1}}{H_2 - H_1}, \quad b_0 = t_{s1} - b_1 H_1. \tag{8.1.39}$$

Equation (8.1.35) was verified (Kutasov et al. 1988a, b) on more than 10 deep wells, including two offshore wells, and the results were satisfactory. Here we present two examples of applying Eq. (8.1.35) to predict downhole circulating temperatures. It will be shown that only a minimum of field data are needed to use this empirical method.

Mississippi Well

The results of field temperature surveys and additional data (Table 8.5) were taken from the article by Wooley et al. (1984).

The stabilized values of the BHCT were measured at $H = 4{,}900$ m, $H = 6{,}534$ m, and $H = 7{,}214$ m. The outlet mud temperature (at $h = 0$) was also recorded. For a depth of 7,214 m (23,669 ft) the actual outlet (flowline) and bottom-hole temperatures recorded during logging are presented in Figs. 8.8 and 8.9.

From plots of the outlet mud temperature versus time, the values of stabilization time were obtained,

Table 8.5 Measured (T_m*) and predicted (T_m) values of wellbore circulating temperature

h (m)	H (m)	T_m* (°C)	T_m (°C)	T_m* − T_m (°C)
Mississippi Well				
4,900	4,900	129.4	130.7	−1.3
6,534	6,534	162.8	163.4	−0.6
7,214	7,214	178.3	177.0	1.36
0	4,900	50.0	48.1	1.9
0	6,534	51.7	53.2	−1.5
0	7,214	55.6	55.4	0.2
Webb County, Texas				
2,805	2,805	70.6	71.6	−1.0
3,048	3,048	78.3	77.3	1.0
3,449	3,449	86.7	86.7	0.0
0	2,805	53.3	53.8	−0.5
0	3,048	60.0	57.9	2.1
0	3,261	60.0	61.6	−1.6

$$t_{s1} = 3.1\,\text{h at } H = H_1 = 4,900\,\text{m},$$
$$t_{s2} = 4.2\,\text{h at } H = H_1 = 7,214\,\text{m}.$$

From Eq. (8.1.39) we obtain

$$b_0 = 0.77\,\text{h}, \quad b_1 = 0.000475\,\text{h/m}.$$

Therefore, the stabilization time for this Mississippi well for any total vertical depth (the position of the end of the drill pipe) can be estimated from Eq. (8.1.36):

$$t_s = 0.77 + 0.0004754\,H.$$

Three measurements of stabilized BHCT and three values of stabilized outlet mud temperatures were run in a computerized multiple regression analysis and the coefficients of the empirical Eq. (8.1.35) were obtained

$$A_0 = 32.68\,^\circ\text{C}, \quad A_1 = 0.01685\,^\circ\text{C/m} \quad A_2 = 0.003148\,^\circ\text{C/m}.$$

Thus, the equation for the downhole circulating temperature is

$$T_m = 32.68 + 0.01685\,h + 0.003148\,H. \tag{8.1.40}$$

Webb County, Texas

The temperature measurements (Table 8.5) in this location were obtained from an article by Venditto and George (1984). It is not known whether these measurements were taken in a single well or in wells in the same area. But since this empirical method can be applied to an entire area as well as to a single well, the

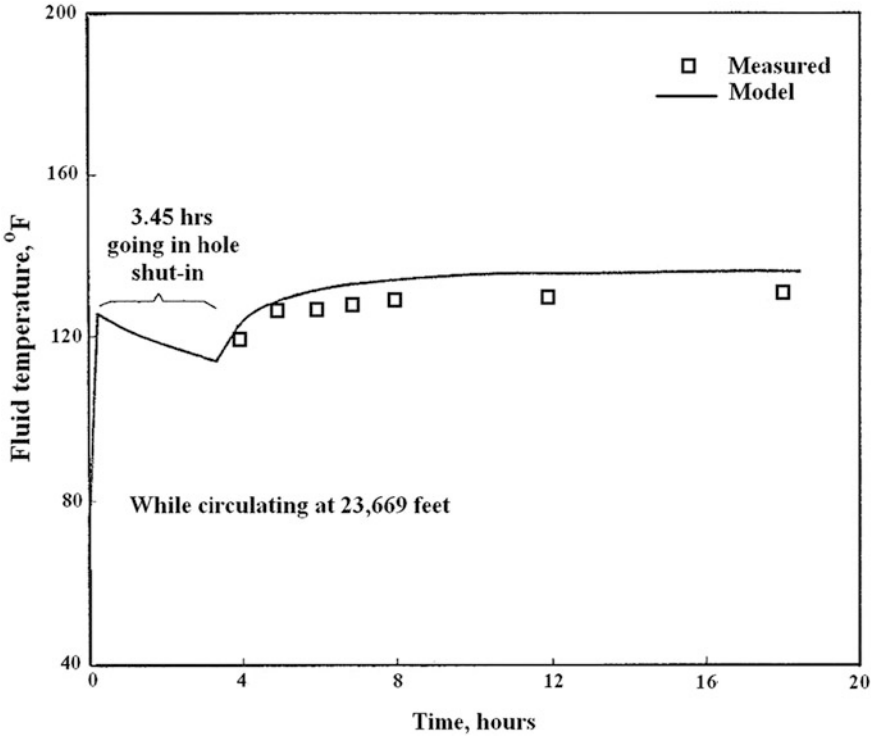

Fig. 8.8 Outlet mud temperature while circulating at 23,669 ft (7,214 m)—Mississippi Well (Wooley et al. 1984)

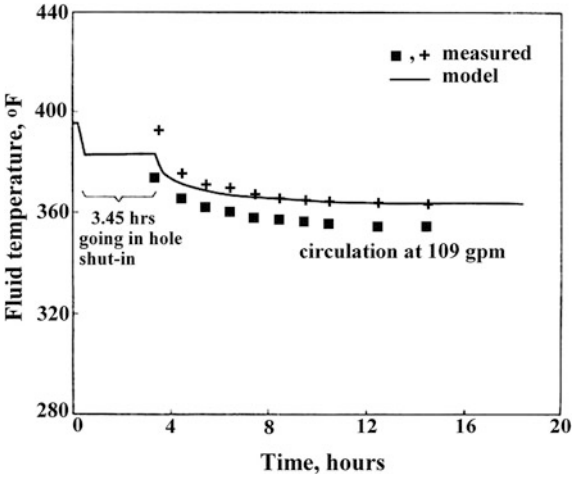

Fig. 8.9 Circulating mud temperature at 23,669 ft (7,214 m)—Mississippi Well (Wooley et al. 1984)

data points were used simultaneously to calculate the coefficients in Eq. (8.1.35). The multiple regression analysis computer program yielded

$$A_0 = 5.69\,^{\circ}\text{C}, \quad A_1 = 0.00636\,^{\circ}\text{C/m} \quad A_2 = 0.01714\,^{\circ}\text{C/m}.$$

In Table 8.5 the measured and predicted values of bottom-hole and outlet circulating temperatures are compared and the agreement was good in both cases. The significant difference in values of A_0, A_1, and A_2 for the Mississippi and the Texas wells indicates that these coefficients are valid only within a given area (Kutasov and Eppelbaum 2011).

8.1.2.3 Bottom-Hole Circulating Temperatures: Field Data and Empirical Formula

Accurate prediction of bottom-hole circulating temperatures (BHCT) and bottom-hole static temperatures (BHST) is important during the drilling and completion of a well. The downhole temperature is an important factor affecting the thickening time of cement, rheological properties, compressive strength development, and set time. In 1941, Farris developed bottom-hole temperature charts based on measurements of mud circulating temperatures in five Gulf Coast wells. These charts were then used by the American Petroleum Institute (API) to develop a pumping test procedure to predict bottomhole temperatures during mud circulation (T_{mb}). In 1977 the API task group presented new casing cementing and well-simulation test schedules (New Cement Test Schedules 1977). Forty-one measurements of BHCT in water muds were available to estimate the correlation between the values of T_{mb}, geothermal gradient Γ, and vertical depth. Curves were fitted through the measured points for each of the geothermal gradient ranges, thus developing a family of curves. From the curves, schedules were developed to provide laboratory test procedures for simulating cementing of casing (New Cement Test 1977; API Specifications 1982). Although some studies (Venditto and George 1984; Jones 1986) showed an overall agreement with the API schedules, some operators felt that these schedules overestimated the BHCT in deep wells and modified them (Bradford 1985). More recently (1995) API has developed new temperature correlations for estimating circulating temperatures for cementing (Table 8.6). To use the current API bottom-hole temperature circulation correlations for designing the thickening time of cement slurries, the average static temperature gradient is required. The surface formation temperature (T_0) for the current API test schedules is assumed to be 80 °F.

It should also be mentioned that for high geothermal gradients and deep wells, the API circulating temperatures are estimated by extrapolation. Here the current API correlations used to determine the BHCT permit prediction in wells with geothermal gradients up to only 1.9 °F/100 ft. In an analysis of available field measurements of bottom-hole circulating temperatures (Kutasov and Targhi 1987) it was found that the BHCT (T_{mb}) can be approximated with sufficient accuracy as

Table 8.6 The new API temperature correlations (Covan and Sabins 1995)

Depth, ft	Temperature gradient (°F/100 ft)					
	0.9	1.1	1.3	1.5	1.7	1.9
8,000	118	129	140	151	162	173
10,000	132	147	161	175	189	204
12,000	148	165	183	201	219	236
14,000	164	185	207	228	250	271
16,000	182	207	233	258	284	309
18,000	201	231	261	291	321	350
20,000	222	256	291	326	360	395

a function of two independent variables: the geothermal gradient, Γ and the bottom-hole static (undisturbed) temperature T_{fb} .

$$T_{\text{bot}} = d_1 + d_2\Gamma + (d_3 - d_4\Gamma)T_{fb}. \tag{8.1.41}$$

For 79 field measurements (Kutasov and Targhi 1987), a computerized multiple regression analysis was used to obtain the coefficients of the formula

$$d_1 = -50.64\,^{\circ}\text{C}\ (-102.1\,^{\circ}\text{F}), \quad d_2 = 804.9\,\text{m}\ (3,354\,\text{ft}),$$
$$d_3 = 1.342, \quad d_4 = 12.22\ \text{m/}^{\circ}\text{C}(22.28\ \ \text{ft/}^{\circ}\text{F}).$$

These coefficients were obtained for

$$74.4\,^{\circ}\text{C}(166\,^{\circ}\text{F}) \le T_{fb} \le 212.2\,^{\circ}\text{C}(414\,^{\circ}\text{F}),$$
$$1.51\,^{\circ}\text{C}/100\,\text{m}\ (0.83\,^{\circ}\text{F}/100\ \text{ft}) \le \Gamma \le 4.45\,^{\circ}\text{C}/100\,\text{m}\ (2.44\,^{\circ}\text{F}/100\,\text{ft}).$$

Therefore, Eq. (8.1.41) should be used with caution for extrapolated values of T_{fb} and Γ. The accuracy of the results (Eq. 8.1.41) is 4.6 °C, and was estimated from the sum of squared residuals. The values of T_{fb} can also be expressed as a function of average surface temperature T_0 and total vertical depth (H). For on-land wells the value of T_0 is the temperature of formations at a depth of about 20 m.

$$T_{fb} = T_0 + \Gamma(H - 20). \tag{8.1.42}$$

For offshore wells the value T_0 is the temperature of bottom sea sediments. It can be assumed that $T_0 \approx 4.4$ °C (40 °F) and if the thickness of the water layer is H_w then

$$T_{fb} = T_0 + \Gamma(H - H_w). \tag{8.1.43}$$

In Eqs. (8.1.42) and (8.1.43) Γ is the average geothermal gradient. In Table 8.7 the measured and calculated values of BHCT for wells with $T_{fb} > 138$ °C are

Table 8.7 Measured T^*_{mb} and predicted T_{mb} bottom-hole circulating temperatures (BHCT). T_{fb} is the bottom-hole static temperature, $\Delta T = T^*_{mb} - T_{mb}$

No.	Well	H (m)	Γ (°C/100 m)	T_{fb} (°C)	T^*_{mb} (°C)	T_{mb} (°C)	ΔT (°C)
1	8	6,050	3.01	205	177	173	4
2	9	6,926	2.08	167	146	147	−1
3	10	4,237	4.45	212	145	154	−9
4	12	4,876	3.14	176	146	143	3
5	16	3,747	3.70	162	121	123	−2
6	16	3,461	3.44	143	112	109	3
7	16	4,887	3.30	185	140	149	−9
8	4	3,962	3.37	160	130	125	5
9	5	4,454	3.24	171	134	137	−3
10	16	5,333	2.46	158	128	133	−5
11	22	4,206	2.90	148	118	119	−1
12	27	3,352	3.54	145	106	109	−3
13	27	3,535	3.52	151	113	115	−2
14	35	3,627	3.68	160	131	121	10
15	36	5,427	2.48	161	131	136	−5
16	38	5,056	2.64	160	138	133	5
17	38	5,529	2.57	168	148	143	5
18	38	5,898	2.68	184	165	158	7
19	40	3,266	3.44	139	110	105	5
20	46	4,389	3.17	165	141	132	9
21	47	4,079	3.63	175	137	135	2
22	47	4,518	3.43	181	142	144	−2
23	51	3,806	3.30	152	121	118	3
24	4	3,718	3.28	145	112	112	0
25	MS	4,900	2.72	153	129	126	3
26	MS	6,534	2.55	187	163	162	1
27	MS	7,214	2.57	206	178	182	−4
28	1	4,578	2.86	157	137	128	9
29	2	4,971	2.95	169	142	139	3
30	3	4,571	2.92	156	123	127	−4
31	8	5,486	3.46	211	179	171	8
32	9	6,926	2.11	167	146	148	−2

compared. Measurements 1–7 (West Texas, Gulf Coast of Texas and Louisiana), 8–23 (Texas, Louisiana), 24, 25–27 (Mississippi) and 28–32 (Table 8.5) were taken from Shell and Tragesser (1972), Venditto and George (1984), Jones (1986), Wooley et al. (1984) and Sump and Williams (1973) respectively.

8.1.2.4 Comparison with API Schedules

In Table 8.8 the current API schedules (Covan and Sabins 1995) and values of T_{mb} calculated by Eq. (8.1.41) are compared. It can be concluded that for deep wells

Table 8.8 Bottom-hole circulating temperatures (BHCT). The values on the first line are predicted values by empirical Eq. (8.1.41); the second line is from current API schedules (Covan and Sabins 1995)

Depth	Geothermal gradient (°F/100 ft)								
(ft)	0.9	1.1	1.3	1.5	1.7	1.9	2.1	2.3	2.5
4,000	–	–	–	–	–	100	107	113	119
	99	100	101	103	104	–	–	–	–
6,000	–	–	102	114	125	135	143	151	158
	99	100	101	102	103	104	–	–	–
8,000	–	113	129	144	158	170	180	189	197
	118	129	140	151	162	173	–	–	–
10,000	116	137	157	174	190	205	217	227	236
	132	147	161	175	189	204	–	–	–
12,000	136	161	184	205	223	239	254	226	276
	148	165	183	201	219	236	–	–	–
14,000	157	185	211	235	256	274	290	304	315
	164	185	207	228	250	270	–	–	–
16,000	178	210	239	265	289	309	327	342	354
	182	207	233	258	284	309	–	–	–
18,000	198	234	266	295	321	344	364	380	393
	201	231	261	291	321	350	–	–	–
20,000	219	258	293	326	354	379	400	418	433
	222	256	291	321	360	395	–	–	–

and high temperature gradients the API BHCT are too high. We recommend the use of Eq. (8.1.41) for estimating the BHCT for high geothermal gradients. It is possible that the coefficients in Eq. (8.1.41) should be corrected to account for very high geothermal gradients which are common in geothermal wells.

8.1.2.5 The Equivalent "API Wellbore" Method

As mentioned earlier, the American Petroleum Institute (API), Sub-committee 10 (Well Cements) has developed new temperature correlations for estimating circulating temperatures for cementing (Covan and Sabins 1995; API Specifications, 1982). To use the current API BHCT correlations (schedules) for designing the thickening time of cement slurries (for a given depth) the average static temperature gradient needs to be known. The surface formation temperature (SFT) for the current API test schedules is assumed to be 80 °F. Thus to calculate the static temperature gradient, the static (undisturbed) temperature profile of formations should be determined with reasonable accuracy. A value of SFT (the undisturbed formation temperature at a depth of approximately of 50 ft, where the temperature is practically constant) of about 80 °F is typical only for wells in the southern U.S. and some other regions. For this reason the API test schedules cannot be used to calculate values of BHCT for cementing in wells drilled in deep waters, in areas

remote from the tropics, or in Arctic regions. For example, the equivalent parameter of SFT for offshore wells is the temperature of sea bottom sediments (mud line) close to 40 °F. In Arctic areas the value of SFT is well below the freezing point of water. Many drilling operators came to the conclusion that computer temperature simulation models (instead of the API schedules) should be used to estimate the cementing temperatures (Honore et al. 1993; Guillot et al. 1993; Calvert and Griffin 1998). This section presents a novel concept—the Equivalent "API Wellbore Method" (Kutasov 2002)—and shows that the current API bottom-hole temperature circulation (BHCT) correlations can be used for any deep well and for any values of surface formation temperature. We call this technique the "API-EW Method". An empirical formula and the results of computer simulations were utilized to verify the applicability of the technique.

Empirical equation

It was shown that the BHCT can be approximated with sufficient accuracy by an empirical Kutasov-Targhi (KT) formula (Eq. 8.1.41) as a function of two independent variables: the static temperature gradient (Γ) and the bottom-hole static (undisturbed) temperature (T_{fb}). The values of T_{fb} can also be expressed as a function of surface formation temperature T_0 and total vertical depth (H). As was mentioned above, for on-land wells the value of T_0 is the temperature of formations at a depth of about 50 ft.

$$T_{f0} = T_0 + \Gamma(H - 50).$$

In practice, for deep wells is usually assumed that

$$T_{f0} = T_0 + \Gamma H. \tag{8.1.44}$$

For offshore wells the value T_0 is the temperature of bottom sea sediments. It can be assumed that $T_0 \approx 40$ °F and if the thickness of the water layer is H_w, then

$$T_{f0} = T_0 + \Gamma(H - H_w). \tag{8.1.45}$$

8.1.2.6 The "API-EW Method"

Note that the API BHCT correlations are based on field measurements in many deep wells. To process field data, the staff of the API Sub-Committee 10 used two variables—the average static temperature gradient and the vertical depth. The problem is in assuming a constant value of the surface formation temperature. In fact, to use the API schedules, the drilling engineer has to estimate the static temperature gradient from the following formula

Table 8.9 Range of errors obtained with the simulation and the new API method (Guillot et al. 1993)

	Standard deviation (°F)	Maximum overestimation (°F)	Maximum underestimation (°F)
New API	18.3	36	−29
Simulator	10.9	17	−19

$$\Gamma = \frac{T_{fb} - 80}{H}. \tag{8.1.46}$$

The reader can see the difference between relationships (8.1.44) and (8.1.45) and the last formula. This is why significant deviations between measured and predicted values of BHCT were observed (Table 8.9). It is logical to assume that for wells with $T_0 = 80$ °F good agreement between measured and estimated from API correlations values of BHCT should be expected. Therefore we suggest "transforming" a real wellbore into an "Equivalent API Wellbore". For purposes of illustration, let us consider a well with following parameters: $H = 20{,}000$ ft, $\Gamma = 0.020$ °F/ft and $T_0 = 60$ °F. The depth of the 80 °F isotherm is: $(80 - 60)/0.020 = 1{,}000$ (ft).

Thus the vertical depth of the "Equivalent API Wellbore" is

$$H^* = 20,000 - 1,000 = 19,000\,(\text{ft}).$$

Similarly, for a well with $T_0 = 100$ °F

$$H^* = 20,000 + 1,000 = 21,000\,(\text{ft}).$$

Below we present simple equations to estimate the equivalent vertical depth (H^*). For an on-land well

$$T_{fb} = T_0 + \Gamma H = 80 + \Gamma H^*. \tag{8.1.47}$$

$$H^* = H + \frac{T_0 - 80}{\Gamma}. \tag{8.1.48}$$

For an offshore well

$$H^* = (H - H_w) + \frac{T_0 - 80}{\Gamma}, \tag{8.1.49}$$

where T_0 is the temperature of bottom sediments (mud line) and Γ is the average temperature gradient in the $H - H_w$ section of the wellbore.

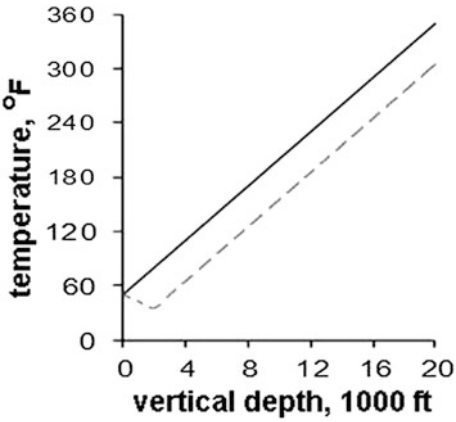

Fig. 8.10 Temperature profiles: A—on land well, B—offshore well

$$\Gamma = \frac{T_{fb} - T_0}{H - H_w}. \tag{8.1.50}$$

Examples

Below we present six examples of ways to calculate the BHCT by the API-EW Method.

Example 1—on-land well A (Fig. 8.10). The surface temperature $T_0 = 50$ °F, vertical depth $H = 20{,}000$ ft, and the static temperature gradient $\Gamma = 0.015$ °F/ft, and the bottom-hole static temperature is 350 °F.

From Eq. (8.1.48) we obtain

$$H^* = 20,000 + (50 - 80)/0.015 = 18,000 \text{ (ft)}.$$

Using the new API BHCT correlations (Covan and Sabins 1995) for $H^* = 18{,}000$ ft and $\Gamma = 0.015$ °F/ft we estimate that BHCT = 291 °F and this is in fairly good agreement with the value of 301 °F determined from Eq. (8.1.41) (note that the average accuracy of Eq. (8.1.41) is 8.2 °F).

Example 2—offshore well B (Fig. 8.10). The water surface temperature is 50 °F, the temperature of bottom sediments a $T_0 = 35$ °F, $H = 20{,}000$ ft, $\Gamma = 0.015$ °F/ft, water depth $H_w = 2{,}000$ ft, and the bottom-hole static temperature is 305 °F.

From Eq. (8.1.50) we obtain

$$H^* = (20,000 - 2,000) + (35 - 80)/0.015 = 15,000\,(\text{ft})\ .$$

Based on the new API correlations (Covan and Sabins 1995) for $H^* = 15{,}000$ ft and $\Gamma = 0.015$ °F/ft we found that BHCT = 244 °F which is consistent with the value of 256 °F calculated from Eq. (8.1.41).

Example 3—offshore well (Calvert and Griffin 1998). The sea-surface temperature is 76 °F, the temperature of bottom sediments (mud-line temperature)

Table 8.10 Results of simulations and calculations of bottom-hole circulating temperatures (BHCT) (Calvert and Griffin 1998, modified)

Model	BHCT, °F
Simulator A	99
Simulator B	108
API (Spec 10, 1990)	144
API (RP 10B, 1997)	140
API–EW	116

Table 8.11 Results of simulations and calculations of the BHCT

Parameters	Well 2	Well 6	Well 8
TVD, ft	15,000	15,000	11,000
Water Depth, ft	0	1,000	1,000
Equivalent TVD, ft	15,000	12,000	8,000
Surface Temp., °F	80	80	80
Seabed Temp., °F	–	50	50
Static Gradient, °F/ft	0.015	0.015	0.015
BHST, °F	305	260	200
BHCT: API-EW, °F	244	201	140
BHCT: Stimulator, °F	248	189	157
BHCT: KT-Formula, °F	255	210	150

$T_0 = 38$ °F, $H = 10{,}125$ ft, water depth $H_w = 3{,}828$ ft, and the bottom-hole static temperature is 180 °F. In this case

$$\Gamma = (180-38)/(10,125 - 3,828) = 0.02255\,(^\circ\text{F/ft}).$$

From Eq. (8.1.50) we obtain

$$H^* = (10,125 - 3,828) + (38 - 80)/0.02255 = 4,434 \ \text{(ft)}.$$

Using the new API correlations (Covan and Sabins 1995) for $H^* = 4{,}434$ ft and $\Gamma = 0.02255$ °F/ft we determined (extrapolation was used) that BHCT = 116 °F which is in line with the results of computer simulations (Table 8.10). The depth of $H^* = 4{,}434$ ft is beyond the range of applicability of Eq. (8.1.41) and for this reason we did not use this formula.

Examples 4, 5, 6—the parameters for three wells (cases) were taken from an article by Goodman et al. (1988). The results of calculations and computer simulations are presented in Table 8.11. It shows that the API-EW Method predicts the BHCT with satisfactory accuracy. The average deviation from the computer stimulation results (for three cases) was 11 °F.

Table 8.12 Coefficients in Eq. (8.1.51)

Fluid No.	Mud, Brine	ρ_0, ppg	α, 10^{-6} 1/psig	β, 10^{-4} (°F)$^{-1}$	γ, 10^{-7} (°F)$^{-2}$	$\Delta\rho/\rho$ 100, %
1	Water base	10.770	3.3815	−2.3489	−4.2366	0.22
2	Water base	13.684	3.2976	−1.7702	−5.2126	0.15
3	Water-base	18.079	3.0296	−1.3547	−4.1444	0.16
4	Oil-base	11.02	6.5146	−4.3414	1.4144	0.32
5	Oil-base	14.257	6.0527	−3.0027	−0.5156	0.34
6	Oil-base	18.049	5.1951	−2.9637	0.7460	0.21
7	Sodium chloride	8.591	3.9414	−1.6008	−4.5254	0.34
8	Sodium chloride	9.886	3.0519	−2.1967	−1.4840	0.21
9	Calcium bromide	15.227	1.3506	−2.4383	−0.3618	0.20

8.1.3 Drilling Fluid Densities at High Temperatures and Pressures

8.1.3.1 Experimental Data

In deep and hot wells, the densities of water/oil muds and brines can be significantly different from those measured at surface conditions. Calculations have shown that bottom-hole pressures predicted with constant surface densities can be off by hundreds of psi (Hoberock et al. 1982). Determining the accurate density of drilling mud under downhole conditions is therefore needed for calculating the actual hydrostatic pressure in a well, and is very important for estimating the effect of pressure and temperature on the density of the formation fluid. This will permit a more accurate prediction of differential pressure at the bottom-hole and will help to reduce the fluid losses resulting from miscalculated pressure differentials. In areas with high geothermal gradients, the thermal expansion of drilling muds can lead to unintentional underbalance, and a kick may occur. In the following section we present an empirical equation of state (pressure-density-temperature dependence) for drilling muds and brines. Below we present information about the database which was used to estimate the accuracy of the formulas. McMordie et al. (1982) presented laboratory data on the changes in density of three types of water base muds (Table 8.12, fluid numbers 1, 2, and 3) and three types of diesel oil muds (fluid numbers 4, 5, and 6) in temperature and pressure ranges of 70–400 °F (21–204 °C) and 0–14,000 psig (0–965 bar). The densities of thirteen sodium chloride solutions in the temperature and pressure ranges of 70–482 °F (21–250 °C) and 0–29,000 psig (0–2,000 bar) at various weight concentrations were obtained from tables presented by Potter et al. (1977). Two sodium chloride solutions will be referred to below as fluids No. 7 and 8. Reliable established laboratory densities of water (Burnham et al. 1969) were used to compare the densities of NaCl brines and water under downhole conditions. For 7.0 molal

calcium bromide brine (fluid No. 9) the density-pressure-temperature data were taken from a plot (Hubbard 1984).

8.1.3.2 Empirical Formula

At present, a material balance compositional model is used to predict the density of drilling muds and brines at downhole conditions (Hoberock et al. 1982; Sorelle et al. 1982). To use this method, only laboratory density measurements for oils and brines at elevated temperatures and pressures are needed because conventionally the compressibility and thermal expansion of the solid components are assumed to be very small and therefore can be neglected. But if a significant amount of chemicals is present in the mud, some chemical interaction can cause changes in the solid-fluid system. It is known, for example, that water base muds start to degenerate at elevated temperatures. In these cases the compositional model cannot be used and laboratory density measurements of water/oil base muds and brines at elevated temperatures and pressures are needed. Here we present an empirical equation of state for drilling muds and brines (Kutasov 1988b). This simple formula can be used to predict the density of water/oil base muds and brines at downhole conditions. A minimum of input data is required to calculate the coefficients in this formula. Application of the formula may reduce the time and cost of laboratory density tests. In physics, pressures encountered in deep wells (up to 30,000 psia) are considered only moderate. Within this range of pressures, the coefficient of isothermal compressibility is a weak function of pressure and can be assumed to be a constant for many fluids. Our analysis of laboratory density test data (Hubbard 1984; McMordie et al. 1982; Potter et al. 1977) for water and oil base muds and brines showed that their coefficient of thermal (volumetric) expansion can be expressed as a linear function of temperature and the coefficient of isothermal compressibility is practically a constant.

We found (Kutasov 1988b) that the following empirical formula can be used as an equation of state for either water or oil-base drilling muds, or for brines:

$$\rho = \rho_0 \exp\left[\alpha p + \beta(T - T_s) + \gamma(T - T_s)^2\right], \tag{8.1.51}$$

where T is the temperature, °F; p is the pressure, psig; $T_s = 59$ °F $= 15$ °C (International standard temperature); ρ is the fluid density, ppg; ρ_0 is the fluid density (ppg) at standard conditions ($p = 0$ psig, $T = 59$ °F); α (isothermal compressibility), β, and γ are constants.

Babu (1996) demonstrated that this equation represents the data more accurately that other models for the majority of drilling muds. A regression analysis was used to process density-pressure-temperature data to provide the coefficients of Eq. (8.1.51) (Table 8.12). The accuracy of the results was estimated from the sum of squared residuals and is presented in Table 8.12 (last column). The measured (ρ*) and calculated (ρ) values of fluid density are compared. The results

Table 8.13 Measured (McMordie et al. 1982) ρ^* and predicted ρ densities for two water-based muds

p, psig	T, °F	Fluid No. 1			Fluid No. 3		
		ρ^*, ppg	P, ppg	$\Delta\rho$, ppg	ρ^*, ppg	ρ, ppg	$\Delta\rho$, ppg
2,000	100	10.75	10.73	−0.02	18.11	18.08	−0.03
2,000	200	10.44	10.40	−0.04	17.73	17.7	−0.03
2,000	300	9.98	10.00	0.02	17.19	17.19	0.00
4,000	100	10.82	10.80	−0.02	18.23	18.19	−0.04
4,000	200	10.50	10.47	−0.03	17.81	17.81	0.00
4,000	300	10.05	10.07	0.02	17.29	17.29	0.00
4,000	400	9.59	9.59	0.00	16.64	16.65	0.01
6,000	100	10.87	10.88	0.01	18.32	18.3	−0.02
6,000	200	10.55	10.54	−0.01	17.89	17.91	0.02
6,000	300	10.11	10.13	0.02	17.38	17.4	0.02
6,000	400	9.67	9.66	−0.01	16.76	16.75	−0.01
8,000	300	10.17	10.2	0.03	17.47	17.5	0.03
8,000	400	9.74	9.72	−0.02	16.87	16.85	−0.02
10,000	300	10.23	10.27	0.04	17.56	17.61	0.05
10,000	400	9.81	9.79	−0.02	16.98	16.96	−0.02
12,000	400	9.88	9.86	−0.02	17.08	17.06	−0.02
14,000	400	9.95	9.92	−0.03	17.17	17.16	−0.01

show good agreement between the measured and predicted densities (Eq. 8.1.51) (Tables 8.13, 8.14, 8.15, 8.16, 8.17).

8.1.3.3 Processing of Laboratory Data: An Example

The following example shows that with a minimum laboratory density data, the coefficients in Eq. (8.1.51) can be calculated and can predict the mud density under downhole conditions with sufficient accuracy. Assuming that, for fluid No. 5 (Table 8.12) only 6 laboratory density tests (instead of 39) were conducted (Table 8.18).

By using a multiple linear progression program the coefficients of Eq. (8.1.51) were found to be: $\rho_0 = 13.627$ ppg, $\alpha = 3.597 \times 10^{-6}$ 1/psig, $\beta = -1.3063 \times 10^{-4}$ 1/°F, $\gamma = -6.6128 \times 10^{-7}$ 1/(°F)^2. In Table 8.18 the measured ρ^* and calculated ρ values of fluid density are compared. By assuming that the bottom-hole pressure and temperature are: $p = 6{,}000$ psig; $T = 400$ °F, from Eq. (8.1.51), the mud density was calculated to be:

$$\rho = 13.637 \cdot \exp\left[\begin{array}{l}\left(3.5967 \times 10^{-6} \times 6000\right) - 1.3063 \times 10^{-4} \times (400 - 59) \\ - 6.6128 \times 10^{-7} \times (400 - 59)^2\end{array}\right]$$
$$= 12.33 \text{ (ppg)}.$$

Table 8.14 Measured (McMordie et al. 1982) ρ^* and predicted ρ densities for two oil-based muds

p, psig	T, °F	Fluid No. 4			Fluid No. 6		
		ρ^*, ppg	ρ, ppg	$\Delta\rho$, ppg	ρ^*, ppg	ρ, ppg	$\Delta\rho$, ppg
2,000	100	11.04	10.97	−0.07	18.08	18.02	0.01
2,000	200	10.56	10.53	−0.03	17.56	17.52	−0.04
2,000	300	10.12	10.14	0.02	17.05	17.05	0.00
4,000	100	11.14	11.11	−0.03	18.22	18.21	−0.01
4,000	200	10.70	10.67	−0.03	17.73	17.70	−0.03
4,000	300	10.29	10.27	−0.02	17.26	17.23	−0.03
4,000	400	9.92	9.92	0.00	16.78	16.80	0.02
6,000	100	11.24	11.26	0.02	18.35	18.40	0.05
6,000	200	10.81	10.81	0.00	17.88	17.89	0.01
6,000	300	10.43	10.41	−0.02	17.43	17.41	−0.02
6,000	400	10.08	10.05	−0.03	16.99	16.98	−0.01
8,000	300	10.55	10.54	−0.01	17.60	17.59	−0.01
8,000	400	10.22	10.18	−0.04	17.18	17.15	−0.03
10,000	300	10.67	10.68	0.01	17.74	17.78	0.04
10,000	400	10.35	10.31	−0.04	17.35	17.33	−0.02
12,000	400	10.46	10.45	−0.01	17.54	17.52	−0.02
14,000	400	10.57	10.58	0.01	17.69	17.70	0.01

This value is in satisfactory agreement with the measured mud density of 12.36 ppg (McMordie et al. 1982).

8.1.4 Hydrostatic Mud Pressure

8.1.4.1 Equivalent Static Density

For a static well, the pressure at any well depth is equal to the hydrostatic pressure exerted by the column of the drilling mud. During drilling mud circulation, an additional pressure drop is required to overcome friction forces opposing the flow of fluid in the annulus. The total pressure during circulation is expressed through the equivalent circulating density. For successful drilling, the mud weight should comply with two conditions: the static mud weight must be able to control the formation pressures and to provide sufficient support to prevent hole collapse, and the equivalent circulating density during circulation should not exceed the fracture gradient (French and McLean 1993).

The mud density increases with pressure and reduces with increases in temperature. Many drilling operators consider this compensating effect as a basis for the using the surface mud density for calculations of the hydrostatic pressure. In oilfield units (ppg, psig, ft) the following relationship is usually applied

Table 8.15 Measured (Potter and Brown 1977) ρ^* and predicted ρ densities for two sodium chloride solutions

p, psig	T, °F	Fluid No. 7			Fluid No. 8		
		ρ^*, ppg	ρ, ppg	$\Delta\rho$, ppg	ρ^*, ppg	ρ, ppg	$\Delta\rho$, ppg
8,688	167	8.696	8.692	−0.004	9.889	9.897	0.008
11,588	167	8.763	8.792	0.029	9.964	9.985	0.021
8,688	212	8.604	8.584	−0.021	9.789	9.783	−0.007
11,588	212	8.679	8.682	0.003	9.873	9.869	−0.003
14,489	212	8.738	8.782	0.044	9.931	9.957	0.026
11,588	257	8.579	8.559	−0.021	9.772	9.750	−0.023
14,489	257	8.637	8.657	0.019	9.831	9.836	0.005
18,115	257	8.704	8.782	0.077	9.898	9.946	0.048
14,489	302	8.521	8.518	−0.003	9.714	9.711	−0.003
18,115	302	8.596	8.641	0.045	9.798	9.819	0.021
21,741	302	8.688	8.765	0.077	9.881	9.928	0.047
14,489	347	8.379	8.366	−0.013	9.597	9.581	−0.016
18,115	347	8.462	8.486	0.024	9.681	9.688	0.007
21,741	347	8.562	8.608	0.046	9.772	9.796	0.023
18,115	392	8.312	8.320	0.007	9.564	9.553	−0.011
21,741	392	8.454	8.439	−0.015	9.656	9.659	0.004
25,367	392	8.537	8.561	0.023	9.739	9.767	0.028
18,115	437	8.153	8.141	−0.012	9.430	9.414	−0.016
21,741	437	8.270	8.258	−0.012	9.530	9.519	−0.012
25,367	437	8.404	8.377	−0.027	9.631	9.625	−0.006
21,741	482	8.103	8.066	−0.037	9.405	9.375	−0.030
25,367	482	8.237	8.182	−0.054	9.505	9.479	−0.026
28,993	482	8.362	8.300	−0.062	9.606	9.585	−0.021

Table 8.16 Coefficients in Eq. (8.1.51) for NaCl brines (Kutasov 1991)

W, %	ρ_0, ppg	α, 1/psig × 10^{-6}	$-\beta$, 1/°F × 10^{-4}	$-\gamma$, 1/(°F)^2 × 10^{-7}	$\Delta\rho/\rho \times 100$ %
1	8.3562	4.3447	1.807	4.90363	0.41
3	8.4742	4.1310	1.7128	4.67334	0.37
5	8.5908	3.9414	1.6008	4.52541	0.34
7	8.7128	3.7431	1.5436	4.2834	0.34
9	8.835	3.5928	1.5105	4.05636	0.34
11	8.9624	3.4504	1.5421	3.7104	0.35
13	9.087	3.3187	1.5505	3.43119	0.35
15	9.2152	3.2549	1.5682	3.21697	0.34
17	9.3472	3.1678	1.6837	2.84163	0.33
19	9.4779	3.1076	1.7719	2.52752	0.30
21	9.6242	3.0667	1.8977	2.18582	0.27
23	9.7504	3.0466	2.0438	1.82556	0.24
25	9.8865	3.0519	2.1967	1.48402	0.21

Table 8.17 Coefficients in Eq. (8.1.51) for water (Kutasov 1999)

Temperature interval, °C (°F)	Pressure interval, bar (psig)	No. of points	ρ_o, ppg	α, 1/ psig·10^{-6}	β, 1/ °F × 10^{-4}	$\Gamma(1/^{\circ}\mathrm{F})^2$ × 10^{-7}	$\Delta\rho/\rho$ × 100 %
20–100 (68–212)	100–1,100 (1,436–15,939)	36	8.3555	2.7384	−1.5353	−7.4690	0.039
100–200 (212–392)	300–1,800 (4,336–26,092)	76	8.4172	3.1403	−2.8348	−3.7549	0.175
20–200 (68–392)	100–1,800 (1,436–26,092)	103	8.3619	3.0997	−2.2139	−5.0123	0.172

Table 8.18 Comparison of measured (McMordie et al. 1982) ρ^* and predicted ρ densities

p, psig	T, °F	ρ^*, ppg	ρ, ppg	$\Delta\rho$, ppg
0	70	13.6	13.61	0.01
0	200	13.22	13.20	−0.02
0	300	12.70	12.71	0.01
4,000	200	13.40	13.39	−0.01
8,000	300	13.06	13.08	0.02
14,000	400	12.70	12.69	−0.01

$$p^* = B_c \rho_0 h, \qquad B_c = 0.052 \frac{\text{psi}}{\text{ppg} \cdot \text{ft}}, \tag{8.1.52}$$

where h is the vertical depth, p^* is the pressure at constant density ρ_o, g is the gravity acceleration constant, and B_c is the conversion factor.

In practice, pressure and pressure gradients are conveniently expressed in density units. Therefore, it is helpful to introduce an equivalent static density (ESD) variable which incorporates the equation of state (pressure-density-temperature dependence) of the drilling mud, well depth and downhole temperatures. This makes it possible to evaluate the effect of the vertical depth and downhole temperature on hydrostatic pressure. The difference between the surface mud density and the depth dependent values of ESD shows to what extent the downhole conditions may affect the drilling mud program design for high pressure high temperature (HPHT) wells. In oilfield units the equivalent static density is defined by

$$\text{ESD} = \frac{p}{B_c D}, \tag{8.1.53}$$

where D is the vertical depth (ft).

Below we present a formula for calculating the downhole hydrostatic mud pressure. It will be shown that in many cases the effect of the temperature and pressure on drilling mud density should be taken into account at downhole mud pressure predictions.

8.1.4.2 Hydrostatic Pressure for Water Based Muds and Brines

From physics is known that

$$dp = \rho g \, dh, \tag{8.1.54}$$

where dp is the increment given to pressure, $\rho(T, p)$ is the mud density, g is acceleration constant due to gravity, and dh is the increment given to the vertical depth. As was shown earlier, the following empirical formula can be used as an equation of state for either water or oil-base drilling muds, or for brines:

$$\rho = \rho_o \exp\left[\alpha p + \beta(T - T_s) + \gamma(T - T_s)^2\right]. \tag{8.1.55}$$

Field and analytical investigations (see Eq. 8.1.35) have shown that the downhole circulating temperatures can be approximated by a linear function of depth

$$T = a_0 + a_1 h. \tag{8.1.56}$$

From this formula it follows that the stabilized outlet (at $h = 0$) fluid temperature is $T_{out} = a_0$ and the stabilized bottom-hole mud temperature is

$$T_{bot} = T_{out} + a_1 H, \qquad a_1 = \frac{T_{bot} - T_{out}}{H}. \tag{8.1.57}$$

Therefore, to calculate the coefficients, a_0 and a_1 the values of the outlet (flowline) and the bottom-hole circulating mud temperature need to be known. The outlet mud temperature is routinely recorded at mud density logging. The BHCT can be approximated with sufficient accuracy by an empirical equation as a function of two independent variables: the geothermal gradient and the bottom-hole static (undisturbed) temperature (see Eq. 8.1.41). For water-based muds and brines the coefficient γ in Eq. (8.1.51) is always a negative quantity and the integration of the Eq. (8.1.54) presents no special problems (Babu 1996; Kårstad and Aadnøy 1998). Taking into account Eqs. (8.1.56) and (8.1.57) the integration of Eq. (8.1.54) yields (Babu 1996; Kårstad and Aadnøy 1998):

$$p = \frac{1}{\alpha} \ln \frac{1}{1 - F(h)}, \tag{8.1.58}$$

$$\left\{ \begin{array}{l} F(h) = B_c \alpha \rho_0 \sqrt{\pi b} \exp\left(b a^2 + b_1\right) \cdot \\ \left[\Phi\left(a\sqrt{b} + \dfrac{h}{2\sqrt{b}}\right) - \Phi\left(a\sqrt{b}\right)\right], \quad B_c = 0.052 \dfrac{\text{psi}}{\text{ppg} \cdot \text{ft}} \end{array} \right\}, \tag{8.1.59}$$

$$a = -b_2, \quad b = -\frac{1}{4b_3}, \tag{8.1.60}$$

$$b_1 = \beta(a_0 - T_s) + \gamma(a_0 - T_s)^2, \tag{8.1.61}$$

$$b_2 = \beta a_1 + 2a_1\gamma(a_0 - T_s), \tag{8.1.62}$$

$$b_3 = \gamma a_1^2, \tag{8.1.63}$$

where Φ is the error function.

8.1.4.3 General Equation for Oil and Water Based Muds

For oil-based muds the coefficient γ mainly has a positive sign. The values of αp and γx^2 are very small and we can assume that

$$\exp[\gamma(T - T_s)] \approx 1 + \gamma(T - T_s)^2, \quad \exp(-\alpha p) \approx 1 - \alpha p + \frac{(\alpha p)^2}{2}. \tag{8.1.64}$$

Taking into account Eqs. (8.1.55), (8.1.56), and (8.1.64), the integration of Eq. (8.1.54), yields (Kutasov 1999)

$$p = \frac{1}{\alpha} - \sqrt{\frac{1}{\alpha^2} - \frac{2F}{\alpha}}, \tag{8.1.65}$$

where

$$F = B_0(B_1B_2 - A_0), \tag{8.1.66}$$

$$A_0 = 1 + \gamma\left[(a_0 - T_s)^2 - \frac{2}{\beta}(a_0 - T_s) + \frac{2}{\beta^2}\right], \tag{8.1.67}$$

$$B_0 = \frac{\rho_o g}{a_1\beta}\exp[\beta(a_0 - T_s)], \tag{8.1.68}$$

$$B_1 = \exp(\beta_1 h), \tag{8.1.69}$$

$$B_2 = 1 + \gamma\left[(a_0 + a_1h - T_s)^2 - \frac{2}{\beta}(a_0 + a_1h - T_s) + \frac{2}{\beta^2}\right]. \tag{8.1.70}$$

8.1.4.4 Differential Pressure

The hydrostatic mud pressure required to prevent the influx of reservoir fluid into the well is equal to the formation pressure plus a safe overbalance. Let us consider a simple case where the formation pore pressure is equal to the hydrostatic pressure of the formation fluid. In this case the pore pressure can be calculated from Eq. (8.1.65). The differential pressure—downhole mud pressure minus the pore pressure—can be calculated, and a safe overbalance can be selected. When, according to the drilling mud program, the density (or the type) of the inlet fluid is changed, new values of coefficients α, β, and γ are introduced and the Eq. (8.1.65) is applied again. However, for high temperature, high pressure (HTHP) wells, the pore pressures depend on many factors and may increase drastically with depth. For example, for HTHP wells drilled in the Central Graben (North Sea) a sharp increase in pore pressure over a short vertical interval, sometimes less than 100 ft (30 m), was observed (MacAndrew et al. 1993). In this case Eq. (8.1.65) can be used only to evaluate the pressure change due to mud and formation density variation with depth.

8.1.4.5 Examples of Calculations

To speed up calculations after Eq. (8.1.65) we devised a computer program dubbed "Hypres" (Kutasov 1999). In this program the formation fluid is water or sodium chloride brine with a density of 9 ppg (1.1 g/cm^3) in normal conditions. However, by introducing new values of coefficients ρ_0, α, β, and γ in the "Data" statement, the program can be used for any formation fluid. In the program the downhole mud hydrostatic pressures computed from Eq. (8.1.65) are compared with those calculated by the conventional constant-surface-mud-density method (Eq. 8.1.52). Note that in the "Hypres" program a more accurate value of the conversion factor B_c (0.051947 instead of 0.052) is used. Below we present several examples which show that in deep, hot wells the actual mud column pressure (p) can be hundreds of psi less than those calculated by the conventional (constant mud density) method (p^*).

Example
A major oil company took extensive circulating temperature data while drilling and completing a deep Mississippi well (Wooley et al. 1984). For a depth of 23,669 ft the measured values of the stabilized outlet (flowline) and bottom-hole mud temperatures were: $T_{out} = 132$ °F and $T_{bot} = 351$ °F.

For comparison we made calculations assuming that both water-base and oil-base muds (McMordie et al. 1982) were considered in the design of the drilling mud program (Table 8.19). The results after applying Eq. (8.1.65) are presented in Tables 8.20 and 8.21 and Fig. 8.11. We also compared the values of hydrostatic pressure with those (p^*) calculated by the conventional constant-surface-

Table 8.19 Coefficients in Eq. (8.1.51) (Kutasov 1988b)

Fluid no.	Mud type	ρ_o, ppg	α, 1/psig $\times 10^{-6}$	β, 1/°F $\times 10^{-4}$	γ, 1/°F^2 $\times 10^{-7}$
3	Water base	18.079	3.0296	−1.3547	−4.1444
6	Oil base	18.049	5.1951	−2.9637	0.7460

Table 8.20 Calculated hydrostatic pressure, density, temperature, and equivalent static density profiles. Mississippi well, diesel oil-based mud (Table 8.12, Fluid No. 6)

D (ft)	p, psig	$p - p^*$, psig	ρ, ppg	$\rho - \rho_0$, ppg	ESD, ppg	T, °F
2,000	1840.4	−36.7	17.746	−0.303	17.696	150.5
4,000	3689.0	−65.2	17.824	−0.225	17.736	169.0
6,000	5546.2	−85.1	17.904	−0.145	17.776	187.5
8,000	7412.4	−96.0	17.987	−0.062	17.818	206.0
10,000	9288.0	−97.5	18.071	0.022	17.862	224.5
12,000	11173.4	−89.2	18.158	0.109	17.906	243.0
14,000	13069.2	−70.5	18.247	0.198	17.952	261.5
16,000	14975.7	−41.1	18.339	0.290	18.000	280.0
18,000	16893.5	−0.4	18.433	0.384	18.049	298.5
20,000	18823.1	52.1	18.530	0.481	18.099	317.1
22,000	20765.0	116.9	18.629	0.580	18.151	335.6
23,669	22395.4	180.9	18.714	0.665	18.196	351.0

Table 8.21 Calculated hydrostatic pressure, density, temperature, and equivalent static density (ESD) profiles. Mississippi well, water-based mud (Fluid No. 3)

D, ft	P, psig	$p - p^*$, psig	ρ, ppg	$\rho - \rho_o$, ppg	ESD, ppg	T, °F
2,000	1858.2	−22.1	17.895	−0.184	17.867	150.5
4,000	3719.6	−40.9	17.923	−0.156	17.883	169.0
6,000	5583.8	−56.9	17.947	−0.132	17.897	187.5
8,000	7450.3	−70.5	17.965	−0.114	17.909	206.0
10,000	9318.8	−82.3	17.979	−0.100	17.921	224.5
12,000	11188.6	−92.7	17.988	−0.091	17.930	243.0
14,000	13059.4	−102.1	17.991	−0.088	17.939	261.5
16,000	14930.6	−111.1	17.990	−0.089	17.945	280.0
18000	16801.8	−120.2	17.983	−0.096	17.951	298.5
20,000	18672.4	−129.8	17.971	−0.108	17.954	317.1
22,000	20541.9	−140.5	17.954	−0.125	17.956	335.6
23,669	22100.8	−150.6	17.936	−0.143	17.957	351.0

mud-density method. As follows from Tables 8.20 and 8.21 the effect of the temperature and pressure on drilling mud density should be taken into account at downhole mud pressure predictions.

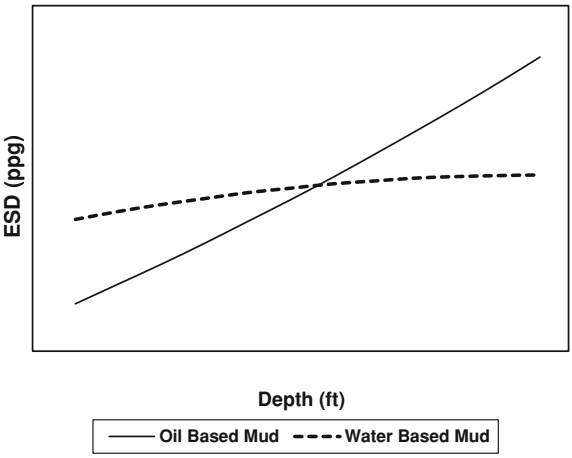

Fig. 8.11 Equivalent static density temperature profile (CDTP). Mississippi Well

8.1.4.6 Prediction of Hydrostatic Pressure While Drilling

In this section we assume that the well is drilled in a new area and the geothermal profile is not known. Given economic considerations, is also clear that all input data should be obtained from temperature logs while drilling. Let now assume that the static temperature gradient cannot be determined with sufficient accuracy. In this case, only empirical methods can be used to estimate the downhole circulating temperatures. The temperature surveys in many deep wells have shown that both the outlet drilling fluid temperature and the bottom-hole temperature vary monotonically with the vertical depth. It was suggested that the stabilized circulating fluid temperature in the annulus (T_m) at any point can be expressed by Eq. (8.1.35):

$$T_m = A_0 + A_1 h + A_2 H, \; h \le H, \tag{8.1.71}$$

where A_0, A_1, and A_2 are empirical coefficients; h is the current depth, and H is the total vertical depth.

For offshore wells the Eq. (8.1.35) should be modified

$$T_m = A_0 + A_1(h - D_R) + A_2(H - D_R), \quad D_R \le h \le H, \tag{8.1.72}$$

where D_R is the length of the riser.

Calculating coefficients A_0, A_1, and A_2 for deep-water wells is more complicated. In this case computer models can be used to determine the "outlet mud temperature" ($at\ h = D_R$) from the recorded values of T_{out} (at $h = 0$). In order to obtain values for A_0, A_1, and A_2, the records of outlet mud temperature (at $h = 0$) and results of downhole surveys are needed. In Eq. (8.1.71) the value of T_m is the stabilized downhole circulating temperature. The time of the downhole temperature stabilization can be estimated from the routinely recorded outlet mud temperature (T_{out}) logs. By recording the values of the outlet mud temperature during

mud circulation without penetration we can determine the moment after which the value of T_{out} is practically constant (Kutasov 1988a).

Example
One major oil company took extensive circulating temperature data while drilling and completing a deep Mississippi well. The stabilized values of bottomhole circulating temperature were measured while drilling at $H = 16{,}079$ ft, $H = 21{,}439$ ft, and $H = 23{,}669$ ft. The outlet mud temperature (at $h = 0$) was also recorded. The actual outlet (flowline) and bottomhole temperatures recorded during logging are presented in Table 8.5. From plots of outlet mud temperature versus time the values of stabilization time (t_s) were obtained (see Sect. 8.1.2.2). Three measurements of stabilized bottomhole circulating temperatures and three values of stabilized outlet mud temperatures were run in a multiple regression analysis and the coefficients of the empirical Eq. (8.1.35) were obtained:

$$A_0 = 90.82\,^{\circ}\mathrm{F}; \quad A_1 = 0.00924\,^{\circ}\mathrm{F/ft}; \quad A_2 = 0.001728\,^{\circ}\mathrm{F/ft}.$$

Thus, the equation for the downhole circulating temperature is (see Eq. 8.1.35)

$$T_m = 90.82 + 0.00924h + 0.001728H,\ h \le H. \tag{8.1.73}$$

We compared the measured and calculated (Eq. 8.1.73) values of the bottomhole and outlet circulating temperature (Table 8.5). It can be seen that the measured and predicted values are in satisfactory agreement. From the latter formula follows that

$$T_{bot} = 90.82 + (0.00924 + 0.001728)H = 90.82 + 0.010968H, \tag{8.1.74}$$

$$T_{out} = 90.82 + 0.001728H, \tag{8.1.75}$$

The gradient of the mud circulating temperature is

$$a_1 = (T_{bot} - T_{out})/H = 0.00924\,^{\circ}\mathrm{F/ft}. \tag{8.1.76}$$

Let us assume that a water base mud was used with the following parameters (fluid 6, Table 8.12, Eq. 8.1.41):

$$\rho_0 = 18.079 \text{ ppg}, \quad \alpha = 3.0296 \times 10^{-6}\ 1/\text{psig},$$
$$\beta = -1.3547 \times 10^{-4}\ 1/^{\circ}\mathrm{F}, \quad \gamma = -4.1444 \times 10^{-7}\,1/^{\circ}\mathrm{F}^2.$$

The results of calculations after formulas (8.1.65)–(8.1.70) are presented in Table 8.22. We also compared values of hydrostatic pressure with those (p^*) calculated by the conventional constant-surface-mud-density method (Eq. 8.1.52). As follows from Table 8.22, the effect of the temperature and pressure on drilling mud density should be taken into account in downhole mud pressure predictions. Thus the determination of the coefficients of Eq. (8.1.71) makes it possible to

Table 8.22 Calculated hydrostatic pressure

h, ft	Total vertical depth, ft					
	23,669		21,439		16,079	
	p, psig	$p - p^*$, psig	p, psig	$p - p^*$, psig	p, psig	$p - p^*$, psig
2,000	1,859	−20	1,857	−22	1,864	−14
4,000	3,722	−34	3,718	−38	3,728	−28
6,000	5,582	−53	5,588	−47	5,600	−35
8,000	7,447	−66	7,454	−60	7,470	−43
10,000	9,317	−75	9,324	−67	9,343	−48
12,000	11,186	−84	11,194	−76	11,221	−49
14,000	13,057	−91	13,066	−82	13,098	−50
16,079	14,999	−102	15,015	−86	15,049	−51
21,439	20,012	−123	20,031	−104		
23,669	22,097	−132				

predict the downhole circulating mud temperatures and to calculate hydrostatic pressures while drilling.

Some similarities and differences for temperature and pressure drawdown well testing were analyzed in Eppelbaum and Kutasov (2006a).

8.1.5 Drilling Through Hydrates

Gas hydrates are considered a future source of energy which may replace natural gas. Deposits of gas hydrates are located in permafrost and offshore areas. To date, there are no economical methods of mining gas hydrate deposits. When developing gas and oil reservoirs, the main problem is to prevent the formation of gas hydrates in reservoirs, wellbores and in transportation lines. During drilling the dissociation of gas hydrates can lead to gasification of drilling fluids and as a result a kick may occur.

Gas hydrates are ice-like crystalline materials that contain water and gases with small molecules, and can occur at temperatures above the freezing point of water. The gas molecules are trapped in the cage-like structure of the surrounding water molecules, which gives them their tight structure. One volume of hydrate can release 150–180 volumes of natural gas at standard conditions. This high concentration of natural gas puts the energy content of hydrate-bearing formations on a par with bitumen and heavy-oil reservoirs. The formation of gas hydrates requires the presence of hydrate-forming gases and water under appropriate pressures and temperatures. Figure 8.12 shows the three-phase hydrate-equilibrium line and identifies the area above the curve as the hydrate-stability zone. As depicted in Fig. 8.13, low temperatures and/or high pressure are required for the stability of the hydrate structure. In natural environments, these conditions can

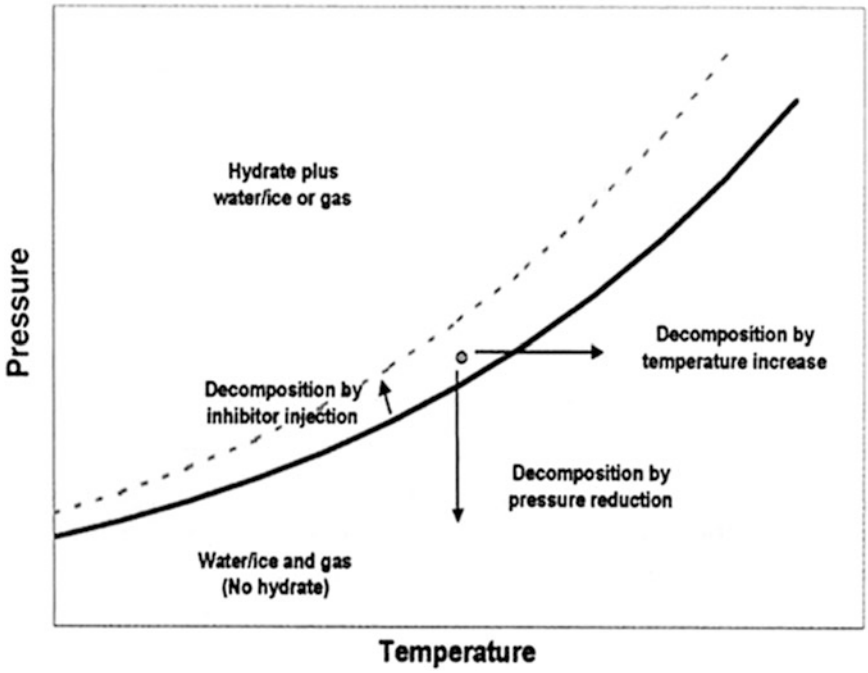

Fig. 8.12 Schematic representation of the three-phase equilibrium curve and methods of hydrate decomposition (Pooladi-Darvish 2004)

occur offshore in shallow depths below the ocean floor and onshore beneath the permafrost. The geothermal gradient of the Earth increases the pressure requirement for the stability of the hydrate at a much greater rate than that provided by the available increased pressure from the hydrostatic gradient. Therefore, there is a depth interval where hydrates may be stable.

Figure 8.13 illustrates hydrate stability with depth in permafrost and marine environments. In permafrost regions, in which surface temperatures are well below freezing, gas hydrates can be present at depths of 150–2000 m. Under offshore conditions, gas hydrate-hydrate stability conditions usually extend to depths of 100–500 m below the ocean floor, although hydrates have been recovered from the ocean floor in some cases. In addition to the required pressure and temperature conditions, hydrate-forming gases also must be available to form gas hydrates. These may be a product of the breakdown of organic matter by bacteria under the seafloor, or the gases may have a thermogenic source from hydrocarbons generated much deeper that have flowed upward through fractures and faults.

The formation of gas hydrates occurs according to the following scheme

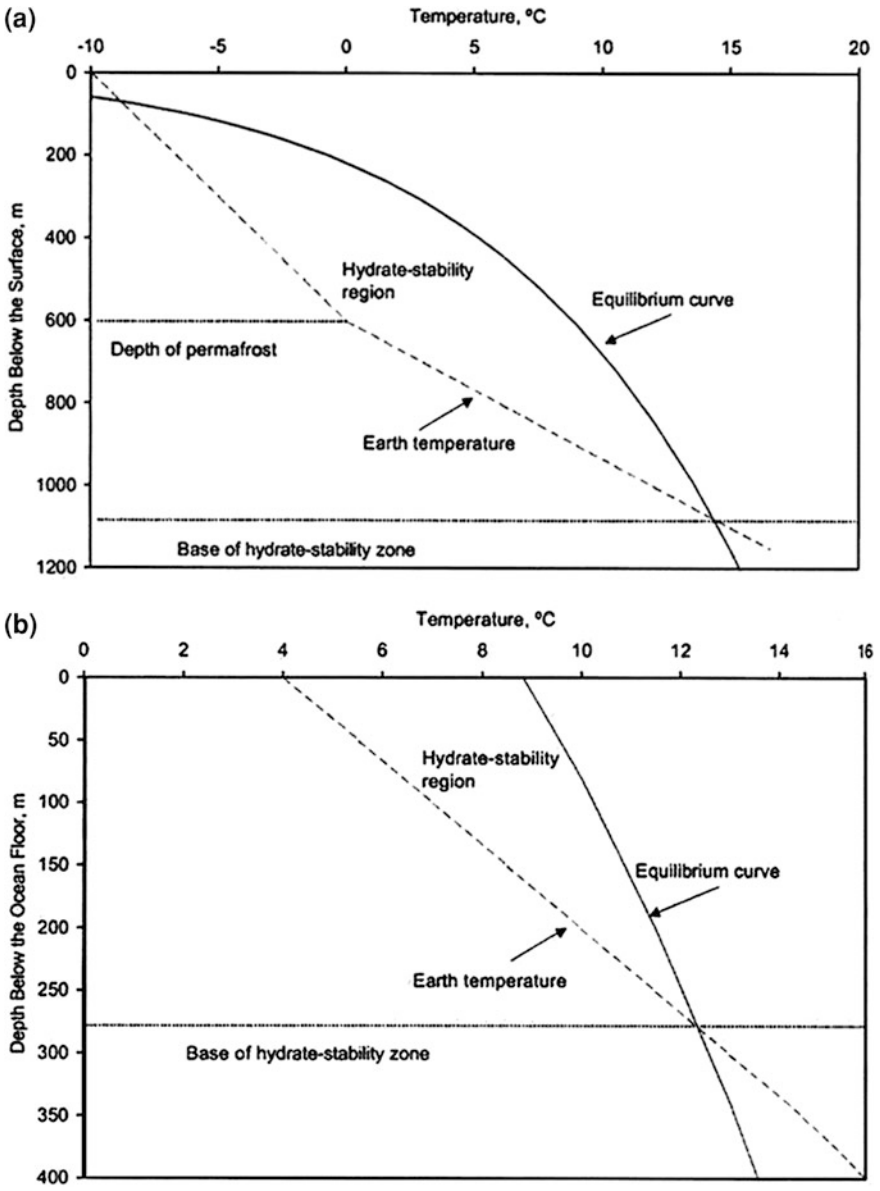

Fig. 8.13 An example of hydrate-stability zones in the Earth for (**a**) permafrost and (**b**) marine environments (geothermal gradient = 0.03 °C/m, pore-pressure gradient 10 KPa/m, depth of ocean and permafrost = 600 m, ocean-floor temperature = 4 °C, temperature of permafrost surface = −10 °C (Pooladi-Darvish 2004)

Table 8.23 The values of empirical coefficients in Eq. (8.1.78) (Bondarev et al. 1976)

Gas	T, K (Kelvin)	A	B	C
Methane, CH_4	273.1–300	−526.4	−19258.2	187.719
Ethane, C_2H_6	273.1–287.5	18.32221	4678.7140	0
Propane, C_3H_8	273.1–277.0	26.4081	7149.1062	0
Isobutene, i-C_4H_{10}	273.1–275,0	27.6860	6762.4	0
Hydrogen sulphide, H_2S	273.1–302.6	13.9648	3826.3495	0
Carbon dioxide, CO_2	273.1–283.1	16.685	4323.5675	0

$$\mathrm{M} + n \cdot \mathrm{H_2O} \rightarrow \mathrm{M} \cdot n \cdot \mathrm{H_2O} + \Delta H,$$

where ΔH is the enthalpy of gas hydrate formation, and M is the gas molecule.

The values of ΔH for gas hydrates with a structure of $\mathrm{M} \cdot 6 \cdot \mathrm{H_2O}$ are in the 14–17 kcal/mol. range, and for structures of $\mathrm{M} \cdot 8 \cdot \mathrm{H_2O}$ and $\mathrm{M} \cdot 17 \cdot \mathrm{H_2O}$ in the ranges of 19–20 and 29–32 kcal/mol., respectively (Bondarev et al. 1976). The heat of the hydrate formation (ΔH) is a function of the temperature

$$\Delta H = (\Delta H)_0 + \frac{d(\Delta H)}{dT} T,$$

where $(\Delta H)_0$ is the heat of the hydrate formation at 0 °C

$$\frac{d(\Delta H)}{dT} = c_{p,\mathrm{gas}} + n \cdot c_{p,\mathrm{water}} - c_{p,\mathrm{hydrate}}, \qquad T > 0\,^{\circ}\mathrm{C}, \tag{8.1.77}$$

where $c_{p,\mathrm{gas}}$, $c_{p,\mathrm{water}}$ and $c_{p,\mathrm{hydrate}}$ are the specific heats of the gas, water and hydrate respectively.

The pressure-temperature dependence of dissociation (formation) of gas hydrates can be expressed by the following empirical equation (Bondarev et al. 1976)

$$\log p_{dis} = A - \frac{B}{T} + C \log T, \tag{8.1.78}$$

where pressure p is in atm, T is the temperature in K and A, B, C are the empirical coefficients (Tables 8.23, 8.24).

Methane hydrate, which makes up most of the naturally occurring hydrates, is composed of roughly six molecules of water for each molecule of methane. Therefore, the decomposition reaction can be represented by

$$(\mathrm{CH_4} \cdot 6\mathrm{H_2O})_{\mathrm{solid}} \rightarrow (\mathrm{CH_4})_{\mathrm{gas}} + 6(\mathrm{H_2O})_{\mathrm{liquid}} + \Delta H.$$

Holder et al. (1982) showed that the energy value of the gas produced is approximately 10 times the energy required to dissociate hydrates in typical reservoirs. This additional energy is the potential prize that all recovery techniques

Table 8.24 Pressure of dissociation of methane hydrate (Eq. 8.1.78)

T, °C	p_{dis}	
	atm	psia
4.0	42.7	628
6.0	52.3	770
8.0	64.6	949
10.0	80.2	1,179
13.0	112.3	1,651
16.0	159.3	2,342
19.0	229.0	3,366
22.0	333.2	4,898
25.0	490.5	7,211
27.0	638.7	9,389

are after. Injecting inhibitors causes decomposition of a gas hydrate by shifting the thermodynamic-equilibrium curve (Fig. 8.13).

Drilling through hydrate bearing formations can pose problems and downhole mud density and temperature control is required. Due to the drastic increase in the gas volume at hydrate decomposition, the hydrate zones may cause the drilling mud to become highly gasified, resulting in an intense gas kick. Billy and Dick (1974) described the first experience of drilling through gas hydrate zones. In two exploratory wells (Imperial Oil Ltd., Mackenzie delta area, Canada) significant gas shows were observed in the drilling mud while penetrating what was considered to be gas-bearing reservoirs. The results of logging and formations tests showed that the gas was in hydrate form. Water-based drilling fluids contain many sites for crystal nucleation and this creates favorable conditions for the formation of hydrates. Hydrate formation in water-based fluids was first observed while drilling offshore wells (California, Gulf of Mexico) and a number of water-based mud formulations have been suggested as inhibitors (Sloan 1991). The composition of natural gases is the major factor determining the ranges of pressure and temperature required for the formation or decomposition of hydrates (Fig. 8.14).

The temperature-pressure stability diagram makes it clear that if hydrates are contained in a confined space and the temperature is raised, high pressures can be generated. For example, when methane hydrate forms at 0 °C, and then decomposes as a result of heating to a temperature of 100 °C (in a confined space) the pressure increases from 2.6 to 2500 MPa (Gritsenko and Makogon 1984). The depth of hydrate stability in the Earth can be obtained by plotting the geothermal gradient and the hydrate temperature-depth (pressure) stability envelope (Fig. 8.13). The mean temperature on the Earth's surface and the geothermal gradient are needed to predict the hydrate-prone zone (Fig. 8.15).

Goodman and Franklin (1982) suggested controlling the hydrate gas influx by increasing the decomposition temperature by using high density drilling muds. Figure 8.16 presents the drilling mud density curves needed to ensure hydrostatic pressures that will exceed the decomposition of hydrates of the natural gas

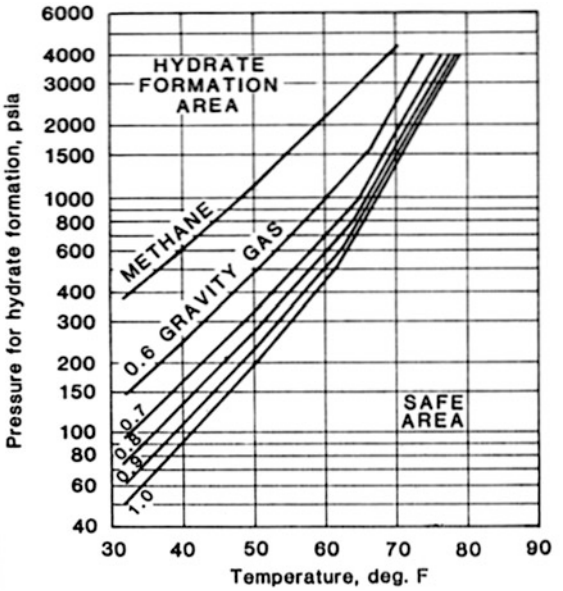

Fig. 8.14 Temperature-pressure chart of natural gas hydrate formation (Katz 1945)

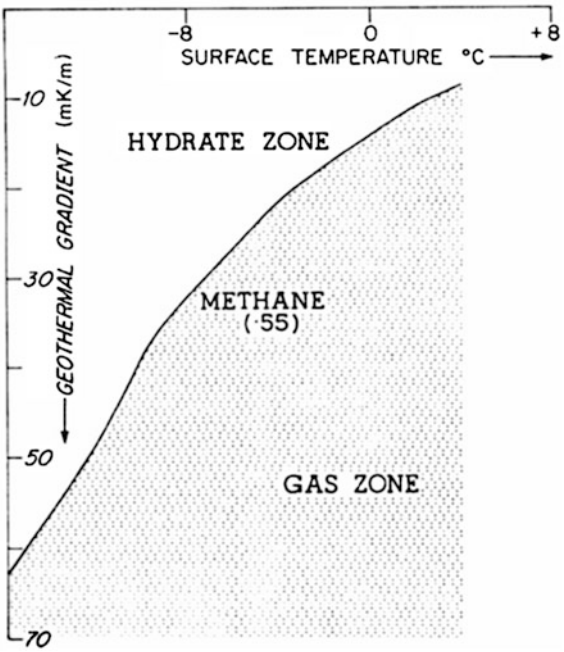

Fig. 8.15 Relationship between mean surface temperature and temperature gradient for the occurrence of methane gas hydrate (Judge 1982)

(specific gravity 0.6) depending on the depth and on the mud temperature (Gritsenko and Makogon 1984). Barker and Gomez (1989) described well-control problems in deep-water operations in which gas hydrates plugged subsea risers,

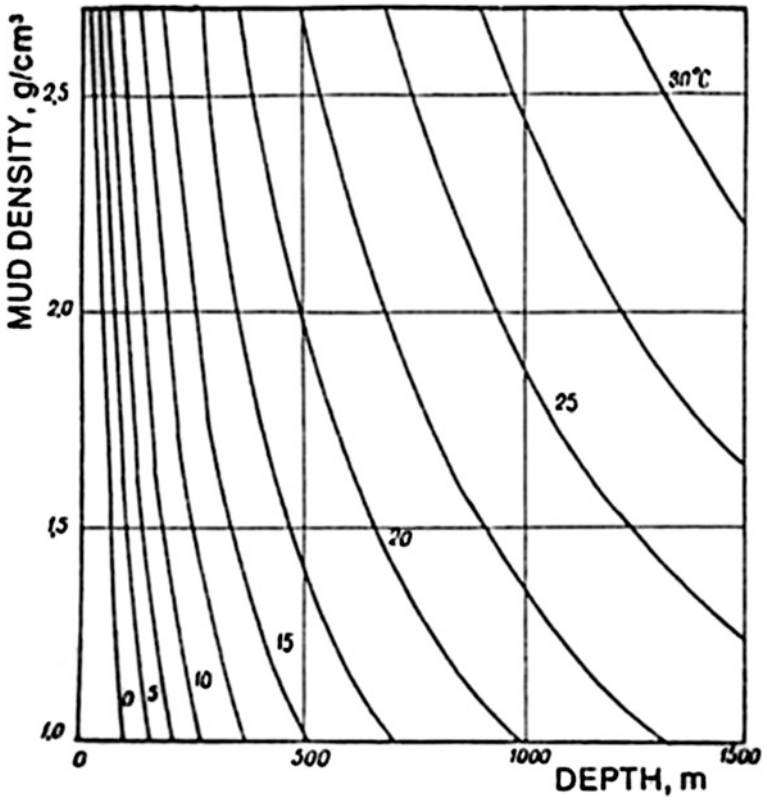

Fig. 8.16 Minimum mud density to prevent decomposition of natural gas (Gritsenko and Makogon 1984)

blowout preventers, as well as choke and kill lines. Seabed temperatures were above 40 °F. Although few such incidents have been reported, the potential hazards are great.

Although hydrates form readily in water-based muds, the content of a typical oil-based mud is sufficient to cause their formation, but the reaction is considerably slower. Extensive research has been conducted on the formulation of water-based muds suitable for use in deep water environments. The current industry standard for water-based fluids is a PHPA—polymer mud containing up to 22 % NaCl. Other salts are also effective, but they are less compatible with standard mud products. Dispersants (lignosulfonate, lignite) do not inhibit hydrate formation; rather, they tend to increase the hydrate formation rate. Methanol and ethylene glycol, two inhibiting compounds frequently added to water in other applications, have limited use in drilling fluids for environmental and safety reasons.

8.2 Wellbore and Formation Temperatures During Shut-In

8.2.1 Calculating the Downhole Shut-In Temperatures

8.2.1.1 Introduction

The first attempt to determine theoretically the required shut-in time of a well for a given accuracy of formation temperature was made by Sir Edward Bullard (1947), who approximated the thermal effect of drilling by a constant linear heat source. This energy source is assumed to be in operation for some time t_c and represents the time elapsed since the drill bit first reached the given depth. For a continuous drilling period the value of t_c is identical to the duration of mud circulation at a given depth. Bullard (1947) used the principle of superposition and obtained the following equation for shut-in temperature $T_s(t,\ r = r_w)$

$$T_{cD} = \frac{T_s(r_w, t_s) - T_f}{T_m - T_f} = \frac{Ei\left(-\frac{r_w^2}{4a(t_c+t_s)}\right) - Ei\left(-\frac{r_w^2}{4at_c}\right)}{Ei\left(-\frac{r_w^2}{4at_c}\right)}. \tag{8.2.1}$$

The logarithmic approximation of the *Ei*-function (with good accuracy) is valid for small arguments

$$Ei(-x) = \ln x + 0.5772, \quad x < 0.01, \tag{8.2.2}$$

where 0.5772 is Euler's constant. Thus

$$\frac{T_s(r_w, t_s) - T_f}{T_m - T_f} = \frac{\ln(1 + t_c/t_s)}{\ln\left(4at_c/r_w^2\right) - 0.5772}. \tag{8.2.3}$$

Bullard concluded from this formula that for accurate geothermal measurements the shut-in time of a well is very long. For example, at a given depth the shut-in time (t_s) must be longer than the circulation time of the drilling fluid by a factor of 10–20, if the required relative accuracy of measurement is 0.01.

In their classic work, Lachenbruch and Brewer (1959) investigated the effect of variation with time of the heat source strength on the shut-in temperatures (Table 8.25). In this table $t = t_c + t_s$ is the total time, q^- represents the mean value of the radial (at $r = r_w$) flow rate $q(t)$ at $0 < t < t_c$, and Q is identified with the product qt_c. The term t_c/t shows the relative error that would result for large a value of time ($t \gg t_c$). It should be noted that the total amount of heat is the same in all six assumed distributions of heat source strength with time.

The first case (Table 8.25) gives the axial temperature due to an instantaneous linear source of strength, Q units of heat per unit depth released at time $t = t_0$ (λ is thermal conductivity of the formation). The fourth case corresponds to the assumption made by Bullard (1947). From the drilling data the authors concluded

Table 8.25 Comparison of cooling formulas based on six different distributions of source strength with time (Lachenbruch and Brewer 1959)

Case	Description	Axial temperature $t > t_0$ or $t > t_c$	Error from treating by case IV, $t \gg t_c$
I	Instantaneous $t_0 = 0$	$\frac{Q}{4\pi\lambda t}$	$1 - \frac{t_c}{2t} + 0\left(\frac{t_c}{t}\right)^2$
II	Instantaneous $t_0 = t_c$	$\frac{Q}{4\pi\lambda(t-t_c)}$	$1 + \frac{t_c}{2t} + 0\left(\frac{t_c}{t}\right)^2$
III	Instantaneous $t_0 = \frac{t_c}{2}$	$\frac{Q}{4\pi\lambda(t-t_c/2)}$	$1 + 0\left(\frac{t_c}{t}\right)^2$
IV	Continuous $q = q-$, $0 > t > t_c$	$\frac{q^-}{4\pi\lambda} \ln \frac{t}{t-t_c}$	1
V	Continuous $q = 2q-(1 - t/t_c)$, $0 < t < t_c$	$\frac{q^-}{4\pi\lambda}\left[\left(\frac{1-t}{t_c}\right) \ln \frac{t}{t-t_c} + 1\right]$	$1 - \frac{t_c}{6t} + 0\left(\frac{t_c}{t}\right)^2$
VI	Continuous	$q = q^- \sqrt{t_c/t}$, $0 > t > t_c$	
		$\frac{q^-}{8\pi\lambda}\sqrt{t_c/t}\left[\begin{array}{r}\ln \frac{t}{t-t_c} \\ +2 \ln\left(1 + \sqrt{t_c/t}\right)\end{array}\right]$	$1 - \frac{t_c}{6t} + 0\left(\frac{t_c}{t}\right)$

that the effective temperature of the walls of the hole at a given depth could be considered constant during drilling. The results of temperature surveys in deep wells have shown that this assumption is valid (Jaeger 1961; Kutasov et al. 1966; Kutasov 1968). Lachenbruch and Brewer (1959) suggested that a limiting case of the heat source distribution might be given by the heat flux through the surface of a region bounded internally by a circular cylinder, where this surface is maintained at a constant temperature (for $0 < t < t_c$). Hence cases V and VI (Table 8.25) are more realistic and represent instances where the source strength decreases with time. Comparing cases IV, V, and VI suggests that treating the effect of variation of heat source strength by case IV will not introduce a relative error greater than $-t_c/6t$ for $t \gg t_c$. From Eq. (8.2.3) we obtain

$$\left\{\begin{array}{l} T_s(t_s, r = r_w) = T_f - B \ln(1 + t_c/t_s), \\ B = \dfrac{T_f - T_m}{\ln(4t_D) - 0.5772}, t_D = \dfrac{at_c}{r_w^2} \end{array}\right\}, \tag{8.2.4}$$

where B is an unknown parameter.

The latter relationship (temperature Horner plot) is used for predictions of formation temperature from bottomhole temperature (BHT) surveys (Timko and Fertl 1972; Dowdle and Cobb 1975). However, in many cases, the dimensionless circulation time is small and the logarithmic approximation of the *Ei*-function cannot be used. The evaluation and limitations of the Horner technique are discussed in the literature Dowdle and Cobb (1975), Drury (1984) and Beck and Balling (1988). Middleton (1979) and Leblanc et al. (1981) assumed that near the bottom of the well the circulation time is small and the temperature disturbance of formations can be neglected. They suggested models to simulate short-term temperature dissipation in mud columns near the bottomhole. It was assumed that

the thermal properties of the drilling mud and formation are identical. In practice, however, due to sedimentation of cuttings, it is very difficult for the temperature probes to reach the bottomhole (Kutasov et al. 1966). An interesting method known as the formation temperature estimation (FTE) model was suggested by Cao et al. (1988). In this model, to determine the value of formation temperature, nonlinear inverse techniques are used. The mud circulation time does not need to be known. To use the FTE model more than two BHT measurements are required. The FTE model is implemented numerically and the following five parameters can be determined: formation temperature, mud temperature at the time the mud circulation stops, radius of thermal influence, the formation thermal conductivity, and the fractional factor for heating the mud (in a purely conductive case this factor is equal to 1). Field and synthetic data were used to verify the FTE method (Cao et al. 1988). The authors concluded that is possible to accurately determine the formation temperature and roughly estimate the other four parameters, providing that the input BHT data are high quality.

8.2.1.2 The Basic Formula

To determine the temperature in a well ($r = 0$) after the circulation of fluid has ceased, we used the solution of the diffusivity equation that describes cooling along the axis of a cylindrical body with a known initial temperature distribution $\left(T'_D\right)$, placed in an infinite medium of constant temperature (Carslaw and Jaeger 1959; p. 260).

$$T_{sD} = \frac{1}{2at_s}\int_0^{\infty} \exp\left(-\frac{\tau^2}{4at_s}\right) T'_D(\tau,\, t_D)\, \tau d\tau, \tag{8.2.5}$$

$$T_{sD} = \frac{T_s(0,t_s) - T_f}{T_m - T_f}, \tag{8.2.6}$$

$$T'_D(\tau,\, t_D) = T_D(\tau,\, t_D)\,, \quad r \geq r_w \qquad \text{see Eq.(8.1.24)} \quad \tau = r_D, \quad t = t_c,$$
$$T'_D(\tau,\, t_D) = 1, \quad r < r_w.$$

where τ is the variable of integration. From Eq. (8.2.4), we obtained the following expression for T_{sD} (Kutasov 1988b).

$$T_{sD} = 1 - \frac{Ei\left[-\beta\left(1 + t^*_D/t_{sD}\right)\right]}{Ei(-\beta)}, \qquad t_{sD} = \frac{at_s}{r_w^2} \tag{8.2.7}$$

$$\beta = \frac{1}{4t^*_D}, \quad t^*_D = Gt_D. \tag{8.2.8}$$

Table 8.26 Values of the dimensionless shut-in temperature T_{sD}

t_D	$t_s/t_c = 0.1$		$t_s/t_c = 1.0$	
	Jaeger (1956)	Equation (8.2.7)	Jaeger (1956)	Equation (8.2.7)
1	0.988	0.9858	0.543	0.5155
10	0.722	0.7315	0.252	0.2446
100	0.477	0.4570	0.143	0.1432
1,000	0.324	0.3104	0.098	0.0983

The function $G(t_D)$ was presented earlier (Eq. 8.1.19). At derivation of Eq. (8.2.6) it is assumed that the thermal diffusivity is the same both within the well and in the surrounding formations. The values T_{sD} for $t_D = 1$, 10, 100, and 1,000 are presented in Table 8.26. The good agreement between Jaeger's numerical solution and the calculated values of T_{sD} shows that Eq. (8.2.7) can be used for temperature predictions during the shut-in period.

Using the logarithmic approximation of the *Ei*-function for small arguments

$$\beta\left(1+\frac{t_D^*}{t_{sD}}\right)<0.01\,. \tag{8.2.9}$$

Then

$$Ei(-\beta)=\ln t_D^*+\ln 4\ -\ 0.5772, \tag{8.2.10}$$

$$Ei\left[-\beta\left(1+\frac{t_D^*}{t_{sD}}\right)\right]=\ln t_D^*-\ln\left(1+\frac{t_c^*}{t_s}\right)+\ln 4\ -\ 0.5772,$$

where $t_c^* = t_c G(t_D)$ and from Eqs. (8.2.6)–(8.2.9) we obtain

$$T_s = T_f - M\ \ln\left(1+\frac{t_c^*}{t_s}\right), \tag{8.2.11}$$

$$M=\frac{(T_f-T_m)}{Ei(-\beta)}. \tag{8.2.12}$$

At large circulation times $\frac{t_D^*}{t_D}=\frac{t_c^*}{t_c}\rightarrow 1$ and from Eq. (8.2.10) we obtain

$$T_s = T_f - M\ \ln\left(\frac{1+t_c}{t_s}\right). \tag{8.2.13}$$

This relationship is identical to Eq. (8.2.3). However, in many cases the dimensionless circulation time is small and the logarithmic approximation of the *Ei*-function cannot be used. In this case Eq. (8.2.6) should be used for predicting

the undisturbed temperature of formations. Let us assume that two temperature measurements (T_{s1}, T_{s2}) are available for a given depth with $t_s = t_{s1}$ and $t_s = t_{s2}$.

From formula (8.2.6) we obtain

$$\frac{T_{s1} - T_f}{T_{s2} - T_f} = \gamma, \qquad T_f = \frac{T_{s1} - T_{s2}}{1 - \gamma}, \tag{8.2.14}$$

$$\gamma = \frac{Ei(-\beta) - Ei\left[-\beta\left(1 + \frac{t_c^*}{t_{s1}}\right)\right]}{Ei(-\beta) - Ei\left[-\beta\left(1 + \frac{t_c^*}{t_{s2}}\right)\right]}. \tag{8.2.15}$$

In the bottomhole, a temperature stabilization model was suggested by Leblanc et al. (1981) in which the temperature disturbance of formations is neglected and the shut-in temperature is given by

$$T_s = T_f - (T_f - T_m)\left[1 - \exp\left(-\frac{r_w^2}{4at_s}\right)\right].$$

Here it also assumed that the thermal diffusivity of mud in the well is equal to the thermal diffusivity of formations. The temperature of the circulating (T_m) is not known and therefore two measurements of the shut-in temperature are needed to predict the value of T_f.

8.2.1.3 Effect of the Formation Thermal Diffusivity

Many investigators believe that the thermal properties of formations measured in the laboratory differ substantially from those in natural (in situ) conditions. As a consequence, some transient temperature anomalies may be associated with the variation of thermal diffusivity of formations. Equation (8.2.7) can be used to estimate the effect of formation diffusivity on the shut-in temperatures.

8.2.2 Prediction of Formation Temperatures

8.2.2.1 "Two Temperature Logs" Method

The mathematical "two temperature logs" method is based on the assumption that in deep wells the effective temperature of drilling mud (T_w) at a given depth is assumed to be constant during the drilling process. As was shown above, for moderate and large values of the dimensionless circulation time ($t_D > 5$) the temperature distribution function T_{cD} (r_D, t_D) in the vicinity of the well can be

described by a simple Eq. (8.1.23). Thus the dimensionless temperature in the wellbore and in the formation at the end of the mud circulation (at a given depth) can be expressed as:

$$\left\{ T_{cD}(r_D, t_D) = \begin{array}{ll} 1 & 0 \le r_D \le 1 \\ 1 - \frac{\ln r_D}{R_D} & 1 \le r_D \le R_{in} \\ 0 & r_D > R_{in} \end{array} \right\}, \tag{8.2.16}$$

where

$$T_{cD} = \frac{T(r_D, t_D) - T_f}{T_w - T_f}.$$

To determine the temperature in the well ($r = 0$) after the circulation of fluid has ceased, we used the radial temperature profile (Eq. 8.2.16) and integrated the integral (8.2.9). We obtained the following expression for T_{sD}

$$T_{sD} = \frac{T(0, t_s) - T_f}{T_w - T_f} = 1 - \frac{Ei\left(-pR_{in}^2\right) - Ei(-p)}{2\ \ln R_{in}}, \quad t_D > 5, \tag{8.2.17}$$

where

$$p = \frac{1}{4nt_D}, \quad n = \frac{t_s}{t_c}. \tag{8.2.18}$$

It was assumed that for deep wells the radius of thermal influence is much larger than the well radius; hence the difference in thermal properties of drilling muds and formations can be neglected. As mentioned above, in the analytical derivation of Eq. (8.2.17) two main simplifications of the drilling process were made: it was assumed that drilling is a continuous process and the effective mud temperature (at a given depth) is constant. For this reason field data were used to verify the Eq. (8.2.17). Long term temperature observations in deep wells of Russia, Belarus, and Canada were used for this purpose (Kutasov 1968; Djamalova 1969; Bogomolov et al. 1972; Kritikos and Kutasov 1988). The shut-in times for these wells covered a wide range (12 h to 10 years) and the drilling time varied from 3 to 20 months. The observations showed that Eq. (8.2.17) gives a sufficiently accurate description of the process by which temperature equilibrium comes about in the borehole. Figure 8.17 presents the temperature versus shut-in time curve at a depth in the Namskoe deep well (Yakutia republic, Russia; depth is 3,003 m, total drilling time is 578 days).

The T_f and T_w values were determined from observed temperatures at $t_s = 200$ and 3,210 days. At this depth calculating the formation (undisturbed) temperature with an accuracy of 0.1 °C requires a shut-in time of about eight years. In practice, for deep wells (large t_D and small p) we can assume that $R_{in} \approx \mathrm{D_o}\sqrt{t_D}$ and

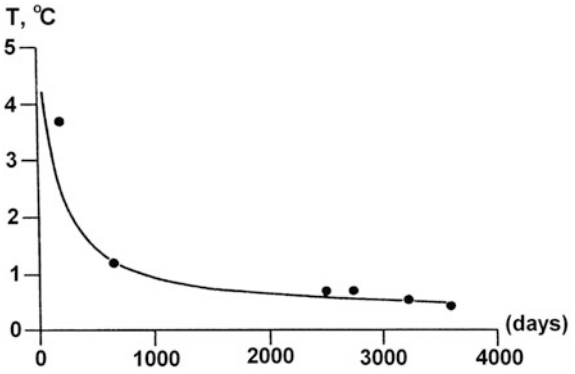

Fig. 8.17 Rate of the temperature recovery at 500 m in depth in the Namskoe Well (sand $a = 0.0020\ \mathrm{m^2\ h^{-1}}$). *Solid curve* Eq. (8.2.17); *points* physical measurements (Kutasov 1968)

$$\frac{T(0,t_s)-T_f}{T_w-T_f}=\frac{Ei\left(-\frac{D}{n}\right)+\ln\ n-D_1}{2\ \ln t_D+2\ \ln D_0}\ , \tag{8.2.19}$$

$$Ei(-p)\approx-\ln t_D-\ln\ n-\ln\ 4\ +0.5772\,. \tag{8.2.20}$$

Inserting Eqs. (8.2.18) and (8.2.19) into Eq. (8.2.16) yields:

$$\frac{T(0,t_s)-T_f}{T_w-T_f}=\frac{Ei\left(-\frac{D}{n}\right)+\ln\ n-D_1}{2\ \ln t_D+2\ \ln D_0}, \tag{8.2.21}$$

where

$$D=D_0^2/4=1.1925,\qquad D_1=0.5772+\ln D=0.7532.$$

If two measured shut-in temperatures (T_{s1}, T_{s2}) are available for the given depth with $t_2 = t_{s1}$ and $t_s = t_{s2}$ we obtain:

$$\frac{T_{s1}-T_f}{T_{s2}-T_f}=\frac{Ei\left(-\frac{D}{n_1}\right)+\ln\ n_1-D_1}{Ei\left(-\frac{D}{n_2}\right)+\ln\ n_1-\ D_1} \tag{8.2.22}$$

Therefore:

$$T_f=T_{s2}-\gamma(T_{s1}-T_{s2}), \tag{8.2.23}$$

where

$$\gamma=\frac{Ei\left(-\frac{D}{n_2}\right)+\ln\ n_2-D_1}{Ei\left(-\frac{D}{n_2}\right)-Ei\left(-\frac{D}{n_1}\right)+\ln\ \frac{n_2}{n_1}} \tag{8.2.24}$$

Table 8.27 Calculated formation temperatures, Rechitskaya 17-P well (Kutasov et al. 1971)

H, m	T_{s1}	T_{s2}	$-\gamma$	$\gamma(T_{s1} - T_{s2})$	T_f
500	24.9	24.21	0.215	−0.15	24.06
700	25.5	27.45	0.206	0.40	27.85
900	27.5	29.99	0.194	0.48	30.47
1,100	29.35	32.84	0.183	0.64	33.48
1,400	31.7	36.49	0.166	0.80	37.29
1,600	33.8	39.09	0.154	0.81	39.90
1,800	35.65	41.70	0.140	0.85	42.55
2,000	37.4	44.32	0.128	0.88	45.20
2,300	42.05	52.82	0.105	1.13	53.93
2,600	46.0	57.49	0.082	0.95	58.44

$$n_1 = \frac{t_{s1}}{t_c}, \quad n_2 = \frac{t_{s2}}{t_c} \tag{8.2.25}$$

Thus the well radius and thermal diffusivity of the formation have no influence on value of T_f, because the unknown parameters T_w and t_D have been eliminated. The quantities r_w and a, however, affect the value of T_f through T_{s1} and T_{s2}. The correlation coefficient γ monotonically changes with depth. For purposes of illustration Table 8.27 presents data for the Rechitskaya 17-P well (Rechitskaya oil field, Belarus: duration of drilling 340 days, vertical depth 3,375 m), $t_{s1} = 1$ day and $t_{s2} = 209$ days.

Figure 8.18 presents the values T_f for well 1,225 (Kola Peninsula, Russia). The measured temperatures observed at $t_{s1} = 4.5$ days and $t_{s2} = 20$ days were used (a total of seven temperature logs were made with $0.5 \leq t_s \leq 63$ days).

The total drilling time of this well was 94 days.

The field data and the calculated T_f values show that for a depth range of 200–500 m, a shut-in time of two months is adequate at a calculation accuracy of T_f is 0.03 °C.

Temperature data analysis from the measurements in deep boreholes are of greatest interest. The drilling process greatly alters the temperature field of formations surrounding the wellbore. The temperature change is affected by many factors and the exact determination of formation temperature at any depth requires a certain length of shut-in time. In theory this shut-in time is infinitely long. There is, however, a practical limit to the time required for the difference in the temperature between the well wall and surrounding reservoir to become a negligible quantity. Eppelbaum and Kutasov (2006b) conducted a comparison of three methods of predicting the undisturbed formation temperatures from shut-in temperature logs in deep wells: Horner method, three-point method, two logs method. It was found that the best agreement is observed with values calculated by the 'three-point method' and measured during shut-in period transient temperatures.

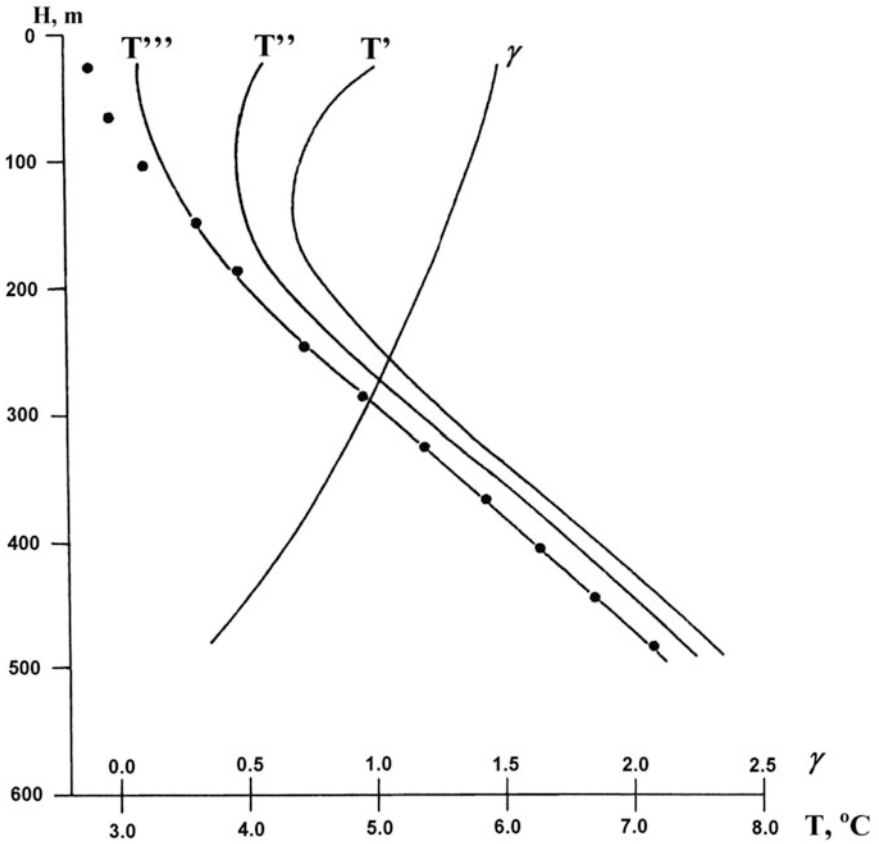

Fig. 8.18 Rate of the temperature recovery in well 1225. Termograms T'', T''' and T' were observed at $t_s = 0.5$; 4.5; and 63 days respectively. *Dots* calculated values of T_f, γ correlation coefficient (Kutasov 1968)

8.2.2.2 Geothermal Gradient

The temperature gradient is a differential quantity; hence the process by which the geothermal (undisturbed) gradient (Γ) is restored is distinct from the temperature recovery process. This leads to the following question: how accurately is the value of Γ determined from temperature measurements taken a short time after cessation of drilling? On the basis of Eq. (8.2.17) below we derive a relationship linking the geothermal gradient to the transient vertical temperature gradients. Two cases will be considered.

1. The average temperature of the circulating fluid while penetrating some section of the well (ΔH) is not known. Let us assume that two temperature logs $T_{s1} = T(0, t_{s1})$ and $T_{s2} = T(0, t_{s2})$ are available and the parameters for two points (depths) are:

$$H + \Delta H, \quad t_c, \quad r_w, \quad T_w, \quad a, \quad t_D = \frac{at_c}{r_w^2},$$

$$H, \quad t'_c, \quad r'_w, \quad T'_{ww}, \quad a, \quad t'_D = \frac{at'_c}{\left(r'_w\right)^2}.$$

Substituting these parameters into Eq. (8.2.17) we obtain a system of equations

$$\frac{T_{s1} - T_f}{T_{s2} - T_f} = \frac{T_{sD}\left(t_{D,} t_{s1}/t_c\right)}{T_{sD}\left(t_{D,} t_{s2}/t_c\right)} = \gamma_1. \tag{8.2.26}$$

$$\frac{T'_{s1} - T'_f}{T'_{s2} - T'_f} = \frac{T_{sD}\left(t'_D, t_{s1}/t'_c\right)}{T_{sD}\left(t'_D, t_{s2}/t'_c\right)} = \gamma'_1. \tag{8.2.27}$$

$$\Gamma = \frac{A_1 - \gamma'_1 A_2}{1 - \gamma'_1} + \frac{\left(T_{s1} - T_{s2}\right)\left(\gamma_1 - \gamma'_1\right)}{\Delta H\left(1 - \gamma'_1\right)\left(1 - \gamma_1\right)}. \tag{8.2.28}$$

$$\Gamma = \frac{T_f - T'_f}{\Delta H}, \tag{8.2.29}$$

$$A_1 = \frac{T_{s1} - T'_{s1}}{\Delta H}, \quad A_2 = \frac{T_{s2} - T'_{s2}}{\Delta H}. \tag{8.2.30}$$

2. The average temperature of the circulating fluid is known. In this case, only one temperature log is needed to determine the value of Γ.

   From the following system of equations

$$\frac{T_{s1} - T_f}{T_w - T_f} = T_{sD}(t_{D,} t_{s1}/t_c) = T_{sD}, \tag{8.2.31}$$

$$\frac{T'_{s1} - T_f}{T'_w - T_f} = T_{sD}(t'_D, t_{s1}/t^1_c) = T'_{sD}. \tag{8.2.32}$$

$$\Gamma = A_1 \frac{1}{1 - T'_{sD}} + \frac{T_{s1}\left(T_{sD} - T'_{sD}\right) + T_{sD}T'_{sD}\left(T_w - T'_w\right) + \left(T'_{sD}T'_w - T_{sD}T_w\right)}{\Delta H(1 - T'_{sD})(1 - T_{sD})}. \tag{8.2.33}$$

   For small values of ΔH we can assume that $T_w = T'_w$. Then

$$\Gamma = A_1 \frac{1}{1 - T'_{sD}} + \frac{\left(T_{s1} - T_w\right)\left(T_{sD} - T'_{sD}\right)}{\Delta H(1 - T'_{sD})(1 - T_{sD})}. \tag{8.2.34}$$

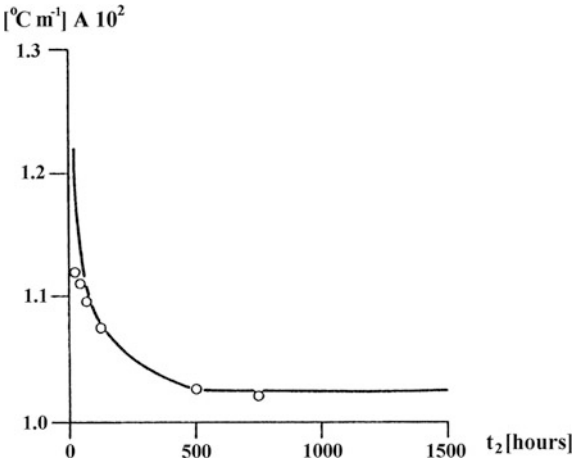

Fig. 8.19 Temperature gradient recovery in the 407–467 m section of the well 1225 (diorites, $a = 0.0027$ m^2 h^{-1}). *Solid curve* calculated values, and *open circles* from field data (Kutasov 1968)

Calculations of the geothermal gradient in the 407–467 m depth interval in well 1225 (Fig. 8.19) showed that the geothermal gradient can be found with an accuracy of 10 % only two days after drilling has ceased, and with an accuracy of 3 % after 20 days.

In the depth range of 500–700 m in the Namskoe well, the geothermal gradient can be estimated with an accuracy of 6 % after only 50 days (Kutasov 1999). The rate of temperature gradient recovery depends on many parameters (a, r_w, T_w, t_c) that can vary over wide ranges. This must be taken into account when interpreting field data, so that the temperature anomalies associated with the thermal recovery process are not attributed to features or anomalies of the geological structure. For example, in the upper section of well 1,225, the temperature gradient for small values of t_s was near zero. This might be misinterpreted as a water encroachment or as an ore body.

An improved methodology for estimation of the geothermal gradients from singular temperature log-field cases was shown in Kutasov and Eppelbaum (2009).

8.2.3 Temperature Distribution in Formations

The temperature distribution around the wellbore as a function of the circulation time, shut-in time, and the radial distance are needed to estimate the electrical resistance of the formation water. This facilitates the quantitative interpretation of the electric logs. The temperature distribution around a shut-in well is an important factor affecting the thickening time of cement, rheological properties, compressive strength development, and set time. For the fluid circulating period, an approximate analytical solution was obtained (Eq. 8.1.22) which describes with high accuracy the temperature field of formations around a well with a constant boreface temperature. Using the principle of superposition for the shut-in period we present an approximate analytical solution which describes the temperature distribution in formations surrounding the wellbore during the shut-in period

Table 8.28 Dimensionless shut-in temperature $T_{sD} \times 1000$. First line—Eq. (8.2.35), second line—numerical solution (Taylor 1978)

t_D	r_D	Dimensionless shut-in time							
		5	10	20	30	40	50	70	100
10	1	374	248	151	109	86	71	52	38
		369	247	150	108	85	70	52	–
	2	344	236	147	107	84	70	52	37
		342	235	146	106	84	69	51	–
	3	301	217	140	103	82	68	51	37
		300	216	139	103	81	67	50	–
	5	199	167	120	93	75	63	48	35
		199	166	9	92	75	63	48	–
100	1	569	458	349	290	251	222	181	144
		–	459	352	292	251	223	182	144
	2	545	446	344	287	248	220	180	143
		–	447	346	289	250	221	181	143
	3	509	427	335	281	244	217	178	142
		–	429	337	283	246	218	179	142
	5	418	374	308	263	231	207	172	138
		–	377	310	265	233	208	173	138

$$T_{sD} = \frac{T_s(r, t_s) - T_f}{T_w - T_f} = \frac{Ei\left(-\frac{r_D^2}{4\left(t_D^* + t_{sD}\right)}\right) - Ei\left(-\frac{r_D^2}{4t_{sD}}\right)}{Ei\left(-\frac{r_D^2}{4t_D^*}\right)}, \tag{8.2.35}$$

$$t_D = \frac{at}{r_w^2}, \quad t_D = \frac{at_s}{r_w^2}, \quad r_D = \frac{r}{r_w}, \quad t_D^* = Gt_D,$$

where t_D* is the adjusted dimensionless circulation time and G is a function of t_D (Eq. 8.1.19). The values of dimensionless radial temperature of formations calculated on the basis of Eq. (8.2.35) are in good agreement with the results of a numerical solution (Table 8.28).

The "Shutemp" (Kutasov 1999) computer program was used to calculate the function $T_{sD} = T_{sD}(r_D, t_D, t_{sD})$ and tables were constructed that make it possible to determine the radial temperature at several dimensionless radial distances during the shut-in period (Kutasov 1993).

Example

A well was drilled to a depth of 12,490 ft in Webb County, Texas (Venditto and George 1984). The values of the static temperature of formations and circulating temperature at the bottomhole were: $T_f = 306$ °F and $T_m = T_w = 251$ °F. Let us assume that after 50 h of mud circulation the well was shut-in for 100 h after which time an electrical log was run (near the bottomhole); the radius of

investigation, bit diameter, and the thermal diffusivity of formations were: $r_{inv} = 22$ in., $2_{rw} = 8.75$ in., $a = 0.04$ ft/h.

The following steps are needed to calculate the radial temperature.

Step 1. Compute the dimensionless circulation time, dimensionless shut-in time, and dimensionless radial distance (dimensionless radius of investigation)

$$t_D = \frac{(50 \cdot 0.04) \cdot (2 \cdot 12)^2}{8.75^2} \cong 15,\ t_{sD} = \frac{(100 \cdot 0.04) \cdot (2 \cdot 12)^2}{8.75^2} \cong 30,$$
$$r_D = \frac{22.0 \cdot 2}{8.75} \cong 5.$$

Step 2. From Eq. (8.2.35) determine the value of function T_{sD} for $t_D = 15$, $t_{sD} = 30$, and $r_D = 5$. The value of T_{sD} is 0.115 and $T_s(r_{inv}, t_s) = 0.115 \cdot (251 - 306) + 30\ 6 = 300$ (°F).

Step 3. From Eq. (8.2.35) estimate the function T_{sD} at $r = r_w$.

The value of T_{sD} is 0.134 and $T_s(r_w, t_s) = 0.134 \cdot (251 - 306) + 306 = 299$ (°F).

Thus, in this example the radial temperature of the formations changes from 299 °F at the wellbore face to 300 °F at $r_{\text{inv}} = 22$ in. The temperatures are close to the static temperature of 306 °F (152 °C) rather than the value of the circulating temperature 251 °F (122 °C). This should be taken into account when interpreting the electric logs.

8.2.4 Calculating the Formation Temperature from BHT Logs

We proposed a new method for the prediction of formation temperatures in permafrost regions from temperature transient temperature measurements in deep wells (Kutasov and Eppelbaum 2003). The main features of this method were: (1) in the permafrost section of the well, the starting point in the well thermal recovery is shifted from the end of well completion to the moment when the refreezing of formations was completed. It is taken into account that the refreezing of thawed formations occurs in some temperature interval; (2) below the permafrost base the starting point in the well thermal recovery is shifted from the end of well completion to the moment when the first shut-in temperature log was taken. The application of this method of predicting the undisturbed formation temperature does not depend on the well drilling history (vertical depth versus time, stops in mud circulation). The specification of two parameters—thermal diffusivity of formations and well radius—are not needed to compute the value of the undisturbed formation temperature (Kutasov and Eppelbaum 2003). In the conducting

bottom-hole temperature (BHT) logs, the thermal disturbance of formations (near the well's bottom) is caused mainly by one short continuous drilling fluid circulation period (prior to logging). The duration of this period is usually 3–24 h. As will be shown below this method (Kutasov and Eppelbaum 2003) can be extended to calculate the formation temperature from bottom-hole temperature (BHT) surveys. Three field cases and one synthetic example will be used to show the validity of this approach. The results will be compared to those obtained with the generalized Horner method (GHM), where the values of the well radius and formation diffusivity need tube specified.

8.2.4.1 The New (NM) Method

In theory the drilling process affects the temperature field of formations at very long radial distances. There is, however, a practical limit to the distance—the radius of thermal influence (r_{in}), where for a given circulation period ($t = t_c$) the temperature $T(r_{in}, t_c)$ is "practically" equal to the geothermal temperature T_f. To avoid uncertainty, however, parameter r_{in} must not be dependent on the temperature difference $T(r_{in}, t_c) - T_f$. For this reason we used the thermal balance method to calculate the radius of thermal influence. The results of modelling, experimental work and field observations showed that the temperature distribution around the wellbore during drilling could be approximated by the following relation (Kutasov 1968, 1999). Let us assume that three shut-in temperatures T_{s1}, T_{s2}, and T_{s3} are measured at a given depth. We can consider that the period of time $t_c^* = t_c + t_{s1}$ is the new "thermal disturbance" period. Thus the "shut-in times" are

$$t_{s1}^* = t_{s2} - t_{s1}, \quad t_{s2}^* = t_{s3} - t_{s1}. \tag{8.2.36}$$

Now, the dimensionless temperature distribution at $t = t_{s1}$ (Fig. 8.20)

$$\left\{ \begin{array}{ll} T_{cD}^*(r_D, t_{xD}) = 1, & 0 \le r_D \le 1, \\ T_{cD}^*(r_D, t_{xD}) = 1 - \ln r_D / \ln R_x, & 1 \le r_D \le R_x \\ T_{cD}^*(r_D, t_{xD}) = 0, & r_D > R_x. \end{array} \right\}, \tag{8.2.37}$$

$$R_x = 1 + 2.184\sqrt{t_{xD}}, \qquad t_{xD} = \frac{at_c^*}{r_{wx}^2}, \qquad R_x = \frac{r_{ix}}{r_{wx}}, \tag{8.2.38}$$

$$T_{cD}^*(r_D, t_{xD}) = \frac{T_c(r,t) - T_f}{T_{s1} - T_f}, \quad r_D = \frac{r}{r_{wx}}, \tag{8.2.39}$$

where r_{wx} is the radius of a cylindrical source with a constant wall temperature (T_{s1}) during the thermal disturbance period (t_c^*), a is the thermal diffusivity of formations, t_c is the duration of the circulation period (at the bottom-hole), T_f is the undisturbed temperature of formations, and r_{ix} is the radius of thermal influence.

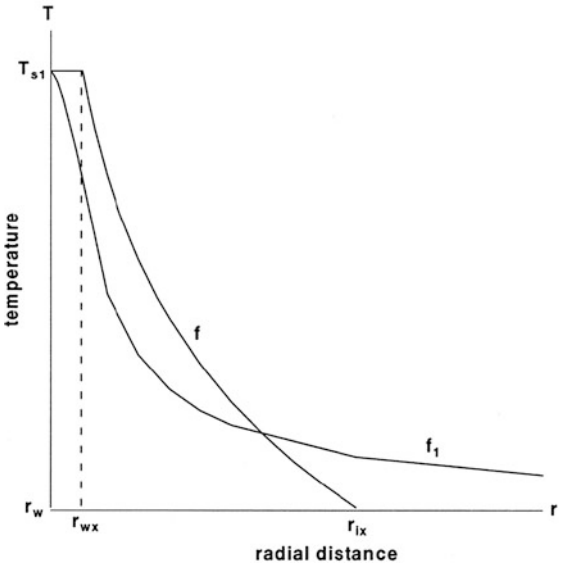

Fig. 8.20 Actual (*curve* f_1) and assumed (*curve f*) radial temperature distributions at $t = t_{s1}$ schematic curves

For the initial radial temperature distributions (Eq. 8.2.37) the dimensionless shut-in wellbore temperature (at $t_s > t_{s1}$) was presented (Kritikos and Kutasov 1988; Kutasov 1999):

$$T^*_{sD} = \frac{T\left(0, t^*_s\right) - T_f}{T_{s1} - T_f} = 1 - \frac{Ei\left(-p^* R^2_x\right) - Ei(-p^*)}{2 \ln R_x}, \tag{8.2.40}$$

where

$$p^* = \frac{1}{4n^* t_{xD}} \qquad n^* = \frac{t^*_s}{t^*_c}. \tag{8.2.41}$$

By using measurements T_{s2}, T_{s3} and Eq. (8.2.40) we can eliminate the formation temperature T_f. After simple transformations we obtain (Kutasov and Eppelbaum 2003)

$$\gamma = \frac{T_{s2} - T_{s1}}{T_{s3} - T_{s1}} = \frac{Ei\left(-p^*_1 R^2_x\right) - Ei\left(-p^*_1\right)}{Ei\left(-p^*_2 R^2_x\right) - Ei\left(-p^*_2\right)}, \tag{8.2.42}$$

where

$$p^*_1 = \frac{1}{4n^*_1 t_{xD}}, \qquad n^*_1 = \frac{t^*_{s1}}{t^*_c}, \quad p^*_2 = \frac{1}{4n^*_2 t_{xD}}, \qquad n^*_2 = \frac{t^*_{s2}}{t^*_c}. \tag{8.2.43}$$

Substituting the value of R_x in Eq. (8.2.38) into Eq. (8.2.42) we can obtain a formula for calculating the dimensionless disturbance time, t_{xD}. After this step, the values of T_f, R_x, and $A = a_f \Big/ (r_{wx})^2$can be obtained.

Although Eq. (8.2.42) is based on an analytical solution, there are several limitations when applying this method. First, the temperature ratio γ (Eq. 8.2.42) should be determined with high accuracy. This means that temperature measurements (T_{s1}, T_{s2}, T_{s3}) must be extremely accurate. The temperature differences $T_{s2} - T_{s1}$ and $T_{s3} - T_{s1}$ should be significantly larger than the absolute accuracy of temperature measurements.

8.2.4.2 Generalized Horner Method (GHM)

Field investigations have shown that the bottomhole circulating (without penetration) fluid temperature can be considered constant (Figs. 8.21 and 8.22) after some stabilization time. The solid curves in Fig. 8.21 present the circulating mud temperatures (at a constant heat transfer coefficient) calculated using the Raymond (1969) model.

It was shown that by using the adjusted circulation time concept (Kutasov 1987, 1989) a well with a constant borehole wall temperature can be replaced by a cylindrical source with a constant heat flow rate. Let us assume that at a given depth the fluid circulation started at time $t = 0$ and stopped at $t = t_c$. The corresponding values of the flow rates are

$$q(t = 0) = \infty, \qquad q(t = t_c) = q.$$

Using the adjusted circulation time concept and the principle of superposition for a well as a cylindrical source with a constant heat flow rate $q = q(t_c)$ which operates during time $t = G \cdot t_c$ and shut-in thereafter, we obtained a working formula for processing field data (Kutasov and Eppelbaum 2005a, b)

$$T(r_w, t_s) = T_i + m \ \ln X; \quad m = \frac{q}{2\pi\lambda}, \tag{8.2.44}$$

$$X = \frac{1 + \left(c - \frac{1}{a + \sqrt{Gt_{cD} + t_{sD}}}\right)\sqrt{Gt_{cD} + t_{sD}}}{1 + \left(c - \frac{1}{a + \sqrt{t_{sD}}}\right)\sqrt{t_{sD}}}, \tag{8.2.45}$$

$$a = 2.7010505; \qquad c = 1.4986055,$$

The correlation coefficient $G(t_{cD})$ varies in narrow limits: $G(0) = 2$ and $G(\infty) = 1$ (Eq. 8.1.20 and 8.1.21). As can be seen from Eq. (8.2.44) the processing of field data (semilog linear log) is similar to that of the Horner method. For this reason we dubbed this procedure for determining the static temperature of formations the "Generalized Horner Method" (GHM). To calculate the ratio, X the

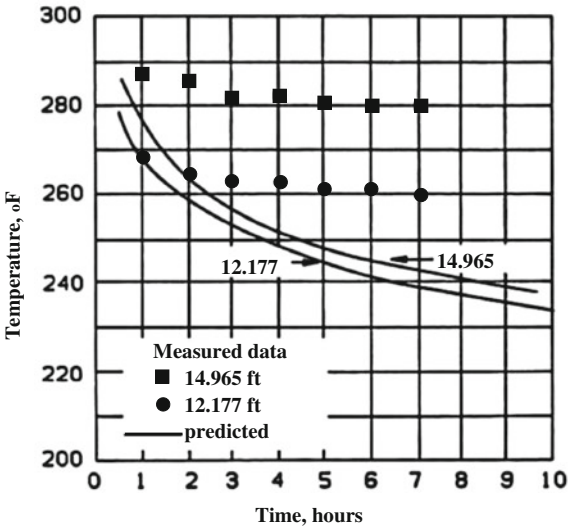

Fig. 8.21 Comparison of measured and predicted circulating mud temperatures, Well 1 (after Sump and Williams 1973)

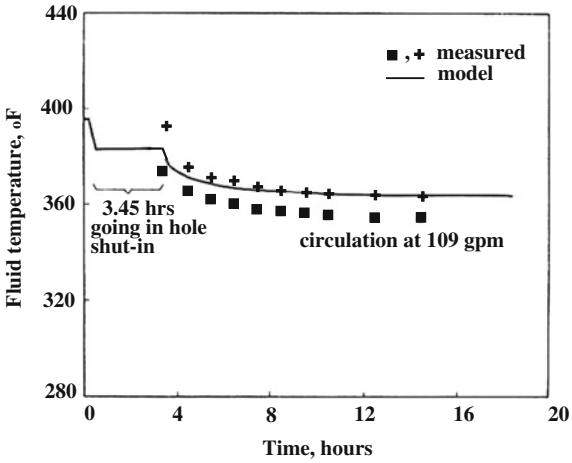

Fig. 8.22 Circulating mud temperature at 23,669 ft (7214 m)—Mississippi Well (Wooley et al. 1984). Courtesy of the Society of Petroleum Engineers

thermal diffusivity of formations (a) should be determined with reasonable accuracy. An example showing the effect of variation of this parameter on the accuracy of determining the undisturbed formation temperature was presented in Kutasov and Eppelbaum (2005a). It is easy to see that for large values of t_{cD} ($G \to 1$) and t_{sD} we obtain the well-known Horner equation (8.2.46).

$$T_s(r_w, t_s) = T_i + M \ln\left(\frac{t_s + t_c}{t_s}\right), \qquad M = \frac{m}{2} = \frac{q}{4\pi\lambda}. \tag{8.2.46}$$

Table 8.29 Input data—field cases

No.	t_{s1}, h (hour)	t_{s2}, h (hour)	t_{s3}, h (hour)	T_{s1}, °C	T_{s2}, °C	T_{s3}, °C
	Andaverde et al. (2005), Hl31, $t_c = 2.5$ h					
1	6	12	18	186.3	206.9	219.0
2	6	12	24	186.3	206.9	231.9
3	6	12	30	186.3	206.9	239.8
4	6	12	36	186.3	206.9	247.7
5	12	18	24	206.9	219.0	231.9
6	12	18	30	206.9	219.0	239.8
7	12	18	36	206.9	219.0	247.7
8	18	24	30	219.0	231.9	239.8
9	18	24	36	219.0	231.9	247.7
10	24	30	36	231.9	239.8	247.7
	Andaverde et al. (2005), Hl30, $t_c = 2.5$ h					
11	6	12	18	178.6	198.9	211.4
12	6	12	24	178.6	198.9	225.8
13	6	12	30	178.6	198.9	235.1
14	6	12	36	178.6	198.9	240.4
15	6	12	42	178.6	198.9	247.1
16	12	18	24	198.9	211.4	225.8
17	12	18	30	198.9	211.4	235.1
18	12	18	36	198.9	211.4	240.4
19	12	18	42	198.9	211.4	247.1
20	18	24	30	211.4	225.8	235.1
21	18	24	36	211.4	225.8	240.4
22	18	24	42	211.4	225.8	247.1
23	24	30	36	225.8	235.1	240.4
24	24	30	42	225.8	235.1	247.1
	Roux et al. (1980), $t_c = 12.0$ h					
25	14.3	22.3	29.3	83.9	90	94.4

8.2.4.3 Field Examples and Synthetic Example

Wells HL31 at a depth of 1,780 m, and HL30 at a depth of 1,394 m were described in (Andaverde et al. 2005). The third example is from the Kelley Hot Springs geothermal reservoir, Moduc County, California, with a depth of 1,035 m (Roux et al. 1980).

Synthetic Example

This example was taken from Cao et al. (1988). We used 8 points (out of 15) in our calculations and the assumed formation temperature was 120 °C. The input data for 3 field cases and one synthetic example are presented in Tables 8.29 and 8.30.

Table 8.30 Input data—synthetic example

No	t_{s1}, h (hour) Cao et al. (1988), $t_c = 5.0$ h	t_{s2}, h (hour)	t_{s3}, h (hour)	T_{s1} (°C)	T_{s2} (°C)	T_{s3} (°C)
26	2	6	10	91.7	102.4	107.9
27	2	6	14	91.7	102.4	111.3
28	2	6	18	91.7	102.4	113.6
29	2	6	22	91.7	102.4	115.2
30	2	6	30	91.7	102.4	117.1
31	2	6	50	91.7	102.4	119.1
32	6	10	14	102.4	107.9	111.3
33	6	10	18	102.4	107.9	113.6
34	6	10	22	102.4	107.9	115.2
35	6	10	30	102.4	107.9	117.1
36	6	10	50	102.4	107.9	119.1
37	10	14	18	107.9	111.3	113.6
38	10	14	22	107.9	111.3	115.2
39	10	14	30	107.9	111.3	117.1
40	10	14	50	107.9	111.3	119.1
41	14	18	22	111.3	113.6	115.2
42	14	18	30	111.3	113.6	117.1
43	14	18	50	111.3	113.6	119.1
44	18	22	30	113.6	115.2	117.1
45	18	22	50	113.6	115.2	119.1
46	22	30	50	115.2	117.1	119.1

8.2.4.4 Results

The values for the formation temperatures and certain parameters using the new method (Eq. 8.2.42) are presented in Table 8.31. For comparison we also used Eq. (8.2.44) (Generalized Horner Method) to calculate the values. The results are presented in Table 8.32. Comparing the computed values of T_f (Table 8.33) shows that the new method finds static formation temperatures with sufficient accuracy.

Thus the new method for prediction of formation temperatures in permafrost regions from temperature logs in deep wells (Kutasov and Eppelbaum 2003) can be applied to BHT surveys.

8.3 Permafrost Regions

8.3.1 Low and High Temperature Permafrost

The development of oil and gas reserves in permafrost areas has necessitated new drilling and well completion technology to deal with the issue of frozen soils. Drilling through permafrost creates some unique difficulties including intensive

Table 8.31 Results using Eqs. (8.2.38), (8.2.40) and (8.2.42)

t_{xD}	A, 1/h	R_x	T_f, °C	t_{xD}	A, 1/h	R_x	T_f, °C
Andaverde et al. (2005), Hl31, $t_c = 2.5$ h				Roux et al. (1980), $t_c = 12.0$ h			
1.07	0.125	3.26	245.3	1.80	0.068	3.93	111.0
0.73	0.086	2.86	261.9	Cao et al. (1988), $t_c = 5.0$ h			
0.68	0.079	2.79	266.5	1.71	0.245	3.86	120.0
0.61	0.072	2.71	273.2	1.57	0.225	3.74	121.1
0.90	0.062	3.07	276.1	1.50	0.214	3.67	121.9
0.92	0.064	3.10	274.0	1.46	0.209	3.64	122.3
0.85	0.059	3.02	279.7	1.44	0.206	3.62	122.5
2.81	0.137	4.66	263.3	1.45	0.207	3.63	122.4
2.05	0.100	4.13	273.2	2.18	0.198	4.22	120.7
1.82	0.069	3.94	280.4	2.01	0.183	4.10	121.5
Andaverde et al. (2005), Hl30, $t_c = 2.5$ h				1.94	0.176	4.04	122.0
1.00	0.117	3.18	239.1	1.90	0.173	4.01	122.2
0.66	0.077	2.77	259.3	1.91	0.173	4.02	122.2
0.60	0.071	2.69	265.8	2.65	0.177	4.56	121.0
0.59	0.070	2.68	266.7	2.48	0.166	4.44	121.6
0.56	0.065	2.63	271.9	2.41	0.161	4.39	121.8
0.82	0.056	2.97	277.4	2.40	0.160	4.38	121.9
0.83	0.057	2.99	275.8	3.25	0.171	4.93	120.9
0.87	0.060	3.04	272.4	3.03	0.160	4.80	121.4
0.82	0.057	2.98	277.0	2.93	0.154	4.74	121.6
2.58	0.126	4.51	263.4	3.74	0.162	5.22	120.9
2.67	0.130	4.57	262.4	3.40	0.148	5.03	121.4
2.17	0.106	4.22	269.5	3.02	0.112	4.79	121.4
4.16	0.157	5.45	257.4				
2.53	0.095	4.47	269.1				

washouts, caving of frozen soils, fill on the bottom, stuck pipes, and poor primary cement jobs. When the well is shut-in, it can be subjected to the potential hazards of external freezeback pressures, internal freezeback pressures, and thaw consolidation. As permafrost is not homogeneous but varies in thickness, lithology, mechanical and thermal properties, drilling methods that are successful in one area often cannot be used in another (Goodman 1978; Kutasov and Bates 1980; Kutasov 1999). As mentioned above, the mechanical properties of frozen formations vary significantly with temperature. This variation in mechanical properties with temperature is particularly evident in fine-grained, high clay content soils where all of the water does not freeze at 0 °C. The initial temperature profile in the permafrost interval also influences the extent of thawing during drilling and the speed with which the formations refreeze after completion of drilling operations.

A typical example of low temperature (cold) permafrost can be seen in the temperature profile of the Prudhoe Bay area (Fig. 8.23). High temperature (warm) permafrost is characterized by the profiles of the Medvezh'e area (Fig. 8.24) and

Table 8.32 Formation temperature values based on Eq. (8.2.44). R is the squared average temperature deviation

t_s h (hour)	T_s (°C)	T_s* (°C)	ΔT (°C)	t_s h (hour)	T_s (°C)	T_s* (°C)	ΔT (°C)
Andaverde et al. (2005), Hl31, $T_f = 262.9$ °C, $t_c = 2.5$ h, $r_w = 0.106$ m, $a = 0.0036$ m^2/h, $R = 4.3$ °C				Roux et al. (1980), $T_f = 111.3$ °C, $t_c = 12.0$ h, $r_w = 0.100$ m, $a = 0.0027$ m^2/h, $R = 0.4$ °C			
6	183.6	179.8	3.8	14.3	83.9	83.7	0.2
12	206.9	211.3	−4.4	22.3	90	90.5	−0.5
18	219	225.1	−6.1	29.3	94.4	94.1	0.3
24	231.9	233.0	−1.1				
30	239.8	238.1	1.7				
36	247.7	241.7	6.0				
Andaverde et al. (2005), Hl30, $T_f = 259.6$ °C, $t_c = 2.5$ h, $r_w = 0.106$ m, $a = 0.0036$ m^2/h, $R = 4.3$ °C				Cao et al. (1988), $T_f = 122.5$ °C, $t_c = 5.0$ h, $r_w = 0.108$ m, $a = 0.0054$ m^2/h, $R = 0.7$ °C			
6	178.6	172.5	6.1	2	91.7	90.7	1.0
2	198.9	205.5	−6.6	6	102.4	103.7	−1.3
8	211.4	220	−8.6	10	107.9	108.8	−0.9
4	225.8	228.2	−2.4	14	111.3	111.7	−0.4
30	235.1	233.6	1.5	18	113.6	113.5	0.1
36	240.4	237.3	3.1	22	115.2	114.8	0.4
42	247.1	240.1	7.0	30	117.1	116.5	0.6
				50	119.1	118.6	0.5

Table 8.33 Comparison of results obtained by the two methods. R is the squared average temperature deviation

Case, Reference	Points	t_c h (hour)	t_s h (hour)	$T_f \pm R$ (°C)	
				NM	GHM
HL31	6	2.5	6–36	269.4 ± 10.1	262.9 ± 4.3
HL30	7	2.5	6–42	266.2 ± 9.7	259.6 ± 4.3
Roux et al. (1980)	3	12.0	14.3–29.3	111.0	111.3 ± 0.3
Cao et al. (1988)	8	5.0	2–50	121.6 ± 0.6	122.5 ± 0.4

the Beaufort Sea (Fig. 8.24). The temperature of the permafrost section in each of the warm permafrost profiles is very near 0 °C. At negative temperatures close to 0 °C a significant part of the water is in an unfrozen state and as a result the strength of formations is low. There are three primary problems which occur during the drilling of cold permafrost wells; namely, freezeback, washouts, and cementing. The phenomenon of freezeback occurs when a formation which has been heated by circulation of warm drilling fluid begins to cool after the cessation of circulation. Since the fluid will expand upon freezing, the pipes left in the hole become exposed to large compressive loading which can lead to buckling. This was observed in wells in which drilling was temporarily suspended. Collapsed casing was not observed at depths greater than 150 m nor at temperatures warmer

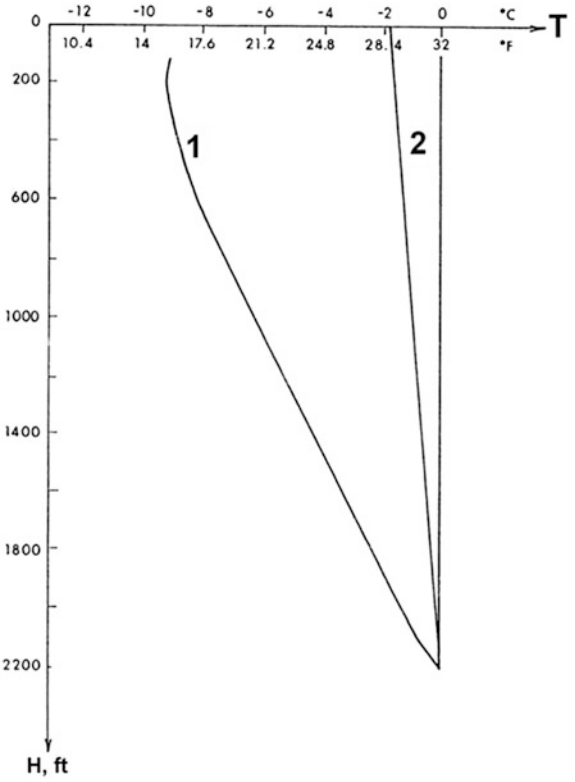

Fig. 8.23 Vertical temperature profile: *1* Prudhoe Bay, Alaska (Gold and Lachenbruch 1973); *2* Beaufort Sea (estimate)

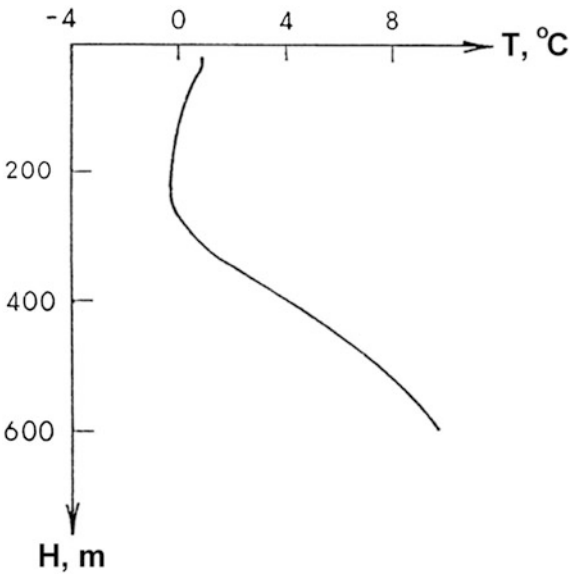

Fig. 8.24 Vertical temperature profile; Medvezh'e, Well 314, Tyumen district, Russia (Rusakov and Kononov 1976)

than −2 °C (Gryaznov 1978). Surprisingly, washouts can present a severe problem in cold permafrost regions. This is possible even in cases where the predicted radius of thawing is quite small in areas where the formations are unconsolidated (Perkins et al. 1974; Gryaznov 1978). Consolidated formations are not susceptible to washout problems. The third major problem observed in cold permafrost regions occurs during cementing. Because of the quick recovery of temperature in cold permafrost, a layer of frozen mud soon develops, particularly in washouts. This prevents good bonding to the formation in these zones. The cement set up is also hampered by the low temperature, and special low temperature cements should be used (Goodman 1978).

Several problems occur repeatedly in warm permafrost environments such as washouts, surface caving, and cementing. Washouts and surface caving are significantly greater problems in warm permafrost areas than in cold permafrost areas. Typical wells in the Medvezh'e natural gas deposit (Tyumen region, Russia) completely fill the reserve pit (150 m^3) with cuttings in a matter of days. Computations indicate that the volume of material removed is several times greater than would be indicated by the radius of thawing. This can only be explained by the additional volume of material added to the hole by caving of frozen soils due to reduction in their strength with the increase in temperature during drilling. It is interesting to note that in many cases the drilling operators in the Medvezh'e field observed ice crystals in the cuttings. The hole enlargement caused caving of the soil around the well head during drilling through permafrost. In some long term drilling wells, the derricks were repositioned (Kutasov and Bates 1980). The second major problem observed in high temperature permafrost is cementing. In many wells in the Medvezh'e deposit, gas migration to the surface was observed shortly after completion (Kutasov and Bates 1980).

8.3.2 *Temperature Distribution and the Radius of Thermal Influence*

To describe the temperature distributions in thawed and frozen zones, simple approximate formulas can be used (Kutasov 1976, 1999). For the thawed zone (the ice melting temperature is 0 °C) the radial temperature profile can be approximated by the following formula,

$$T_t(r,t) = T_m \frac{\ln h/r}{\ln h/r_w}, \qquad r \le h, \tag{8.3.1}$$

and the radius of thermal influence (r_{in}) is introduced for the frozen zone,

Table 8.34 Temperature distribution T_t (r, t) in the thawed zone. First line—numerical solution (Taylor 1978); second line—Eq. (8.3.1)

t_D	h/r_w	r_{in}/h	Dimensionless distance, r/r_w						
			1.2	1.5	2.0	2.5	3.0	4.0	5.0
7.29	2.856	3.06	8.10	5.79	2.96	1.11			
			8.26	6.14	3.38	1.27			
14.57	3.332	3.50	8.47	6.59	4.17	2.30	0.84		
			8.49	6.63	4.24	2.39	0.87		
36.43	4.326	3.96	8.74	7.21	5.22	3.69	2.43	0.52	
			8.76	7.23	5.27	3.74	2.50	0.53	
72.86	5.179	4.60	8.94	7.63	5.96	4.65	3.59	1.91	0.26
			8.89	7.53	5.79	4.43	3.32	1.57	0.21
145.71	7.200	4.66	9.07	7.93	6.47	5.33	4.41	2.95	1.83
			9.08	7.95	6.49	5.36	4.43	2.98	1.85
364.28	9.391	5.44	9.19	8.19	6.90	5.91	5.09	3.81	2.81
			9.19	8.19	6.91	5.91	5.09	3.81	2.81

$$r_{in} = h + 2.184\sqrt{a_f t}, \tag{8.3.2}$$

where a_f is the thermal diffusivity of frozen formations.

The temperature in the frozen zone can be approximated by the equation:

$$T_t(r,t) = T_f \frac{\ln r/h}{\ln r_{in}/h}, \quad r > h. \tag{8.3.3}$$

In Tables 8.34 and 8.35 temperatures calculated using Eqs. (8.3.1) and (8.3.3) and the results of a numerical solution (Taylor 1978) are compared for the case when $T_m = 10.00$ °C, $T_f = -5$ °C, and $I_f = 1.062$. The agreement between the temperatures calculated by these two methods is good.

The effect of radius of thermal influence is investigated in detail in Eppelbaum and Kutasov (2011).

8.3.3 *Radius of Thawing Around a Production or Injection Well*

In oil fields in permafrost regions the number of water injection wells can be close or even exceed the number of oil production wells. Water injection serves to maintain reservoir pressure (or reduce the rate of reservoir pressure decline) and to keep high oil flow rates. When wells are drilled through permafrost, the natural temperature field of the formations (in the vicinity of the borehole) is disturbed, and the frozen rocks thaw out for some distance from the borehole axis. For frozen

Table 8.35 Temperature distribution—$T_f(r, t)$ in the frozen zone. First line—numerical solution (Taylor 1978); second line—Eq. (8.3.3)

t_D	Dimensionless distance, r/r_w								
	4.0	5.0	7.0	10.0	12.0	15.0	20.0	25.0	30.0
7.29	2.01	2.99	4.16	4.81					
	1.50	2.50	4.01	5.00					
14.57	0.87	1.87	3.25	4.33	4.69				
	0.73	1.62	2.96	4.39	5.00				
36.43		0.61	1.97	3.26	3.84	4.38	4.81		
		0.51	1.75	3.04	3.70	4.51	5.00		
72.86			0.94	2.28	2.94	3.65	4.37	4.71	
			0.99	2.15	2.76	3.49	4.43	5.00	
145.71				1.28	1.98	2.78	3.67	4.20	4.53
				1.07	1.67	2.38	3.32	4.04	4.64
364.28				0.41	0.85	1.59	2.53	3.20	3.69
				0.17	0.73	1.39	2.23	2.89	3.43

soils, ice serves as a cementing material, and therefore the strength of frozen soils is significantly reduced at the ice-water transition. If the thawing soil cannot withstand the load of overlying layers, consolidation will take place, and the corresponding settlement can cause significant surface shifts. The settlement in the vertical direction has greater significance when the shear stress acts downward on the casing, causing compressive stresses which can deform the casing. Approximate estimates show that the magnitude of the settlement (the center displacement of the thawing soil ring) and the axial compressive stress are proportional to the squared values of the radius of thawing (Palmer 1978). Thus, for long term drilling, oil/gas production and water injection, the radius of thawing should be estimated to predict platform stability and the integrity of the well. To calculate the radius of thawing we will assume that a constant fluid temperature is maintained at the well wall. This case occurs when the flow rate is very large and the heat transfer coefficient from the fluid to the wall of the well approaches infinity. If a well is shut-in during drilling, the water base fluids in casing-casing, drill pipe-casing or tubing-casing annuli will refreeze and generate radial loads in the borehole. This process, termed internal freezeback, is distinguished from external freezeback of thawed permafrost and water base fluids outside of the casing (Goodman 1978). The internal freezeback starts only when the external freezeback is complete. Below we present a method to estimate the duration of the external freezeback for water injection wells. Freezeback can be a problem if it becomes necessary to temporarily abandon water injection operations. The reservoir engineer needs to be able to determine the amount of time he can suspend water injection circulation without the water (in the production strings) freezing. If the shut-in period is more than the "safety period" (without freezing of water in the well), the water in the upper permafrost section of the well has to be removed. We present an example which shows that the duration of the "safety period" depends

to a great extent on the temperature of frozen formations and radius of formation thawing zone.

8.3.3.1 Introduction

Kutasov et al. (1977) presented a novel approach to the problem of phase change (Stefan problem) around a cylindrical source of heat. It was shown that a known solution for a planar system can be utilized to obtain an approximate solution to the Stefan problem for a cylindrical source of heat with a constant temperature. Later Kutasov (1998) used the adjusted heating time concept (Kutasov 1987, 1989) to determine the position of the thawing temperature isotherm in cases without ice-water transition. The results of numerical solutions presented by Taylor (1978) were used to verify the calculations. Taking into account that our publications (Kutasov et al. 1977; Kutasov 1998) are not easily accessible to petroleum engineers, we present here a summary of the results of our investigation (Kutasov et al. 1977; Kutasov 1998, 1999).

It is beyond of the scope of this volume to present a review of the literature related to the problem of heat exchange in the wellbore-frozen formation system, or to discuss in what ways our results can assist in verifying modern numerical solutions.

8.3.3.2 Stefan Problem

The problem of phase change around a cylindrical source occurs in many engineering designs: oil/gas production/injection wells in permafrost areas, underground pipelines, steam production boreholes, melting of metals, and the storage of nuclear waste. In cylindrical coordinates an exact solution to the Stefan problem in the infinite domain exists for only two cases: subcooled liquid which freezes while the solidified region remains at the fusion temperature, and a line source which extracts energy at some constant rate per unit length (Carslaw and Jaeger 1959). Heat balance integral solutions were applied to the problem of finite superheat, when the initial temperature of the medium is lower than the fusion temperature (Tien and Churchill 1965; Sparrow et al. 1978; Lunardini 1988). Different numerical methods were used to solve the heat valence integral equations, but the results were essentially the same (Lunardini 1988). A coordinate transformation method reduces the problem with a variable phase change, such as cylinder, to one with a constant phase change area (Lin 1971). An interesting effective thermal diffusivity concept was introduced (Churchill and Gupta 1977). It was assumed that the actual thermal diffusivity can be replaced by the effective thermal diffusivity which includes the latent heat. The accuracy of these two methods is limited to certain ranges of dimensionless parameters (Lunardini 1988). Elsewhere we showed (Kutasov et al. 1977; Kutasov 1998) that for a cylindrical system the position of the phase interface in the Stefan problem can be

approximated through two functions: one function (r_m) determines the position of the melting-temperature isotherm in the problem without phase transitions, and the second function Ψ does not depend on time.

$$h_0 = r_w + \Psi(r_m - r_w), \qquad H_0 = 1 + \Psi(R_m - 1), \tag{8.3.4}$$

$$H_0 = \frac{h_0}{r_w}, \qquad R_m = \frac{r_m}{r_w},$$

where r_w is the radius of the well, h_0 is the radius of thawing for an uncased well.

The function Ψ shows to what extent the melting process affects the position of the melting-temperature isotherm. Based on physical considerations it follows that $0 < \Psi < 1$. The function r_m is known but is expressed through a complex integral. By introducing an adjusted dimensionless heating time (t_D*) we found (Kutasov 1987, 1989) that the exponential integral (a tabulated function) can be used to approximate the function $T_D = T(r_D, t_D)$:

$$T_D = \frac{T_m - T_f}{T_w - T_f} = \frac{Ei\left(-r_D^2/4t_D^*\right)}{Ei(-1/4t_D^*)}, \tag{8.3.5}$$

$$t_D^* = Gt_D, \qquad t_D = \frac{a_1 t}{r_w^2}, \qquad r_D = \frac{r}{r_w}.$$

The correlation coefficient $G(t_D)$ varies in the narrow limits of: $G(0) = 2$ and $G(\infty) = 1$ (Eqs. 8.1.19–8.1.21). Here r is the cylindrical coordinate, t is time, r_D is the dimensionless radial distance, $Ei(x)$ is the exponential integral, T_w is the temperature at the wall of the borehole, T_m is the temperature of melting, T_f is the initial temperature, $T(r, t)$ is the radial temperature, $T(_{rD}, t_D)$ is the dimensionless radial temperature, t_D is dimensionless time and a_1 is the thermal diffusivity of the frozen formation. Thus from Eq. (8.3.5) (assuming that $T = T_m$) we can determine the position of the melting-temperature isotherm. In our case the melting temperature (for pure ice) is 0 °C and the following equation can be used to determine r_m

$$\frac{\theta_0}{1 + \theta_0} = \frac{Ei\left(-r_{Dm}^2/4t_D^*\right)}{Ei\left(-1/4t_D^*\right)}, \qquad \theta_0 = -\frac{T_f}{T_w}, \qquad r_{Dm} = \frac{r_m}{r_w}. \tag{8.3.6}$$

8.3.3.3 Uncased Well

From physical considerations it follows that at very short durations the solutions for cylindrical systems approach those for plane systems. For this reason we assumed that the function ψ can be determined from the known solution for the

plane Stefan problem (Carslaw and Jaeger 1959). In a plane system the position of the solid/melted interface is:

$$X = 2\lambda\sqrt{a_2 t}\ , \tag{8.3.7}$$

$$\frac{\exp\left(-\lambda^2\right)}{\Phi(\lambda)} - \frac{k_1\sqrt{a_2}\left(T_m - T_f\right)\exp\left(-\lambda^2 a_2/a_1\right)}{k_2\sqrt{a_1}(T_s - T_m)\Phi^*\left(\lambda\sqrt{a_2/a_1}\right)} = \frac{\sqrt{\pi}\lambda L w}{c_2\,\rho(T_s - T_m)}. \tag{8.3.8}$$

Subscripts 1, 2 correspond to frozen and thawed zones and k is the thermal conductivity, c is specific heat, T_s is the surface temperature, ρ is the density, L is the latent heat per unit of mass, w is the ice mass content per unit of volume, Φ is the probability integral and $\Phi^* = 1 - \Phi$. Introducing the dimensionless parameters we obtain

$$\frac{\exp\left(-\lambda^2\right)}{\Phi(\lambda)} - \frac{I_{ka}\theta\exp\left(-\lambda^2 I_a\right)}{\Phi^*\left(\lambda\sqrt{I_a}\right)} = \sqrt{\pi} I_f \lambda, \tag{8.3.9}$$

$$I_{ka} = \frac{k_1\sqrt{a_2}}{k_2\sqrt{a_1}}, \qquad I_a = \frac{a_2}{a_1}, \qquad \theta = \frac{T_m - T_i}{T_s - T_m}, \quad I_f = \frac{Lw}{c_2\,\rho(T_s - T_m)}.$$

As we can see (Eq. 8.3.8) the depth of thawing X is the product of two functions and the function λ does not depend on time. The changes in thermal properties are due to thawing and therefore based on our assumption we obtain from Eq. (8.3.8) that

$$\Psi = \frac{\lambda(w)}{\lambda(k_1 = k_2,\ k_1 = k_2, w = 0)}. \tag{8.3.10}$$

Now the radius of thawing can be estimated from Eq. (8.3.4). In Table 8.36 the calculated values of the thawing radius (replacing parameter T_s by T_w) and the results of a numerical solution (Taylor 1978) are compared. Taking into account that this is a comparison of two approximate solutions, the results are in satisfactory agreement.

8.3.3.4 An Injection/Production Well

We can consider the annulus $r_w - r_1$ (r_1 is the inner radius of the producing string) as a ring of thermal insulation. In this case a constant temperature is maintained in the inner radius of the insulation and the outer radius of insulation is equal to the radius of the well. Let us assume that the amount of heat expended on thawing and heating the thawed zone is large in comparison to the amount of heat expended on heating the frozen zone (assuming that $\theta = 0$). Using the conventional assumption

Table 8.36 Dimensionless radius of melting for a cylindrical source with a constant temperature ($I_a = 0.7285$, $I_{ka} = 0.9780$). H^*—numerical solution (Taylor 1978; interpolation was used), H—suggested method, Eq. (8.3.4)

t_D	Θ	I_f	Ψ	H	H^*
1.0	0.5000	1.062	0.7125	1.65	1.70
2.0	0.5000	1.062	0.7125	1.90	1.88
4.0	0.5000	1.062	0.7125	2.22	2.20
5.0	0.5000	1.062	0.7125	2.33	2.27
3.0	1.000	1.062	0.852	1.80	1.70
6.0	1.000	1.062	0.852	2.05	2.10
7.0	1.000	1.062	0.852	2.11	2.20
40.0	1.000	1.062	0.852	3.02	2.90
500.0	1.000	1.062	0.852	5.34	5.00
1.0	0.1667	0.354	0.7522	2.19	2.20
4.0	0.1667	0.354	0.7522	3.29	2.90
10.0	0.1667	0.354	0.7522	4.44	4.00
20.0	0.1667	0.354	0.7522	5.61	5.00
50.0	0.1667	0.354	0.7522	7.81	7.00
200.0	0.1667	0.354	0.7522	13.18	11.90
2.0	0.3333	0.354	0.8511	2.35	2.27
30.0	0.3333	0.354	0.8511	5.22	4.90
90.0	0.3333	0.354	0.8511	7.49	6.90
900.0	0.3333	0.354	0.8511	16.52	15.00

of the semi-steady state radial temperature distribution in the thawed zone, we obtained the well-known equation for the dimensionless radius of thawing,

$$\frac{t_D}{I_f} = \frac{H_i^2}{2}\ln H_i - \frac{1}{4}\left(H_i^2 - 1\right) + \frac{1}{2}J\left(H_i^2 - 1\right), \tag{8.3.11}$$

$$H_i = \frac{h_i}{r_w}; \quad t_D = \frac{a_2\, t}{r_w^2}; \quad J = \frac{k_2}{k_i}\ln\frac{r_w}{r_i}, \tag{8.3.12}$$

$$k_i = \frac{\ln(r_w/r_1)}{\frac{1}{k_1}\ln\left(\frac{r_{12}}{r_1}\right) + \frac{1}{k_2}\ln\left(\frac{r_{23}}{r_{12}}\right) + \cdots \frac{1}{k_n}\ln\left(\frac{r_w}{r_{(n-1)n}}\right)}, \tag{8.3.13}$$

where h_i is the radius of thawing, k_i is the effective thermal conductivity of the insulation, J is the dimensionless thermal conductivity of the insulation and I_f is the dimensionless heat of thawing, r_{12}, r_{23} … $r_{(n\text{-}1)n}$ are the radii of the layer interfaces, and k_1, k_2, …, k_n are thermal conductivities of the layers.

The maximum value of the dimensionless radius of melting $u = H_{i,max}$ is when $J = 0$. Then from Eq. (8.3.11) we obtain

Table 8.37 Dimensionless radius of melting for an insulated cylindrical source with a constant temperature ($I_a = I_{ka} = 1$). H*—numerical solution (Kutasov et al. 1977), H—suggested method, Eq. (8.3.16)

t_D	θ	I_f	J	Ψ	Γ	H	H*
6.33	0.0526	0.526	4.611	0.5466	0.3699	2.14	2.00
17.96	0.0526	0.526	4.611	0.5466	0.4517	3.24	3.00
58.95	0.0526	0.526	4.611	0.5466	0.5261	5.46	5.00
125.30	0.0526	0.526	4.611	0.5466	0.5639	7.71	7.00
20.63	0.0526	0.526	12.047	0.5466	0.2686	2.42	2.00
35.72	0.0526	0.526	12.047	0.5466	0.3017	3.04	2.50
54.54	0.0526	0.526	12.047	0.5466	0.3255	3.66	3.00
168.60	0.0526	0.526	12.047	0.5466	0.3807	6.18	5.00
69.55	0.429	4.290	2.61	0.412	0.5275	2.25	2.00
215.50	0.429	4.290	2.61	0.412	0.6059	3.18	3.00
845.00	0.429	4.290	2.61	0.412	0.6743	4.97	5.00
1690.00	0.429	4.290	2.61	0.412	0.7008	6.27	6.50
100.60	0.429	4.290	3.165	0.412	0.5106	2.39	2.00
307.10	0.429	4.290	3.165	0.412	0.584	3.39	3.00
1195.00	0.429	4.290	3.165	0.412	0.6496	5.32	5.00
2903.00	0.429	4.290	3.165	0.412	0.6821	7.21	7.00

$$\frac{t_D}{I_f} = \frac{u^2}{2}\ln u - \frac{1}{4}\left(u^2 - 1\right). \tag{8.3.14}$$

Now we can introduce a thermal insulation efficiency coefficient

$$\gamma = \frac{H_i - 1}{u - 1}. \tag{8.3.15}$$

Assuming that $u = h_0$, the radius of thawing for an uncased well (Eq. 8.3.11), we can finally calculate the radius of melting (h)

$$\gamma = \frac{h - r_w}{h_0 - r_w}, \qquad H = 1 + \gamma(H_0 - 1), \qquad H = \frac{h}{r_w}. \tag{8.3.16}$$

To verify the above formula a computer program was used to obtain a numerical solution to a set of differential equations for heat conductivity (insulation, melted, and solid zones) and the Stefan equation. Some results of the numerical calculations are presented in Table 8.37. Comparison of the results shows that Eq. (8.3.16) can be used to estimate the radius of thawing around an injection well with a constant water temperature.

8.3.4 Time of Complete Freezback

8.3.4.1 Results of Modeling and Numerical Calculations

After the cessation of the drilling process the radius of thawing and the radius of thermal influence will increase for a defined period of time Δt_0 at the expense of the heat accumulated in the thawed zone. The parameter Δt_0 is a function of many variables and its value can be estimated from an approximate formula (Kutasov 1999). For long injection/production times the thawing radius increase after cessation of water injection can be neglected. To calculate the duration of the freezeback period we assumed that the heat flow from the thawed zone to the thawed zone—frozen zone interface can be neglected. The results of hydrodynamic modeling showed (Kutasov 1999) that this is a valid assumption. In this case the Stefan equation-energy conservation condition at phase change interface ($r = h$) is

$$k_1 \frac{dT_f(r,t)}{dr} = Lw \frac{dh}{dt} \quad \text{at } r = h. \tag{8.3.17}$$

Assuming the semi-steady temperature distribution in frozen zone (a conventional assumption) we obtain

$$T_f(r,t) = T_f \frac{\ln\left(\frac{r}{h}\right)}{\ln r_{if}}, \tag{8.3.18}$$

where r_{if} is the radius of thermal influence during the freezback period.

The ratio $D_f = r_{if}/h$ was obtained from a numerical solution. A computer program was used to find a numerical solution to a set of differential equations of heat conductivity for frozen and thawed zones and the Stefan equation (Kutasov et al. 1977). It was found that

$$D_f = \frac{r_{if}}{h} = 2.00 + 0.25 \ln\left(I_{fb} + 1\right), \qquad I_{fb} = -\frac{Lwa_1}{T_f k_1}. \tag{8.3.19}$$

$$1.5 < I_{fb} \leq 400, \qquad 1.25 < H < 23.4.$$

From Eqs. (8.3.17)–(8.3.19) and the condition $H(t = t_{cf}) = 1$ we obtain (Kutasov 1999):

$$t_{cfD} = \frac{a_f t_{cf}}{r_w^2} = \frac{D_f I_{fb}}{2}\left(H^2 - 1\right), \qquad t_{cf} = \frac{t_{cfD}\, r_w^2}{a_f}. \tag{8.3.20}$$

Table 8.38 Casing design for the example well

Section, m	Casing O.D., in.	Casing I.D., in.	Bit size, in.
0–600	13.375	12.415	17.500
600–2800	9.625	8.835	12.250
2800–3845	5.500	4.892	7.875

Table 8.39 The dimensionless radius of thawing and the duration of complete freezeback for the example injection well. $I_a = 0.7285$, $I_{ka} = 0.9780$, $t = 100$ days, $J = 4.45$, $\gamma = 0.6103$, $r_w = 0.222$ m, $L = 334{,}960$ J kg^{-1}, $w = 90$ kg m^{-3}, $a_1 = 1.865 \times 10^{-6}$ m^2 s^{-1}, $T_w = 20.0$ °C, $k_1 = 4.40$ W m^{-1} K^{-1}, $I_f = 0.531$

z, m	T_f, °C	Ψ	H,	t_{fb}, days
25	−19.82	0.9632	3.7	2.6
50	−16.46	0.9317	4.1	4.1
75	−15.77	0.9243	4.2	4.5
100	−15.3	0.9191	4.3	4.9
125	−14.64	0.9115	4.5	5.4
150	−13.29	0.8948	4.7	6.8
175	−11.99	0.8771	5.0	8.7
200	−10.60	0.8559	5.4	12
225	−9.36	0.8347	5.8	15
250	−8.36	0.8158	6.2	19
275	−7.29	0.7932	6.6	26
300	−6.12	0.7651	7.2	37
325	−5.25	0.7413	7.7	51
350	−4.42	0.7155	8.3	70
375	−3.53	0.6836	9.0	106
400	−2.76	0.6509	9.7	162
425	−1.92	0.607	10.7	292
450	−1.33	0.5676	11.6	511
475	−0.90	0.5308	12.4	893

8.3.4.2 An Example

Let us assume that an injection well has a natural temperature profile similar to that of the Canadian well Panarctic Gemini E-10 (Judge et al. 1981; Well No. 175), that this well was shut-in for a long time, and that for practical purposes the thermal disturbance caused by drilling operations can be neglected. The thickness of the permafrost layer is about 500 m. The assumed sizes of the surface, intermediate and production casings are presented in Table 8.38. Thus the insulation ring consisted of three steel and three cement layers. The thermal conductivities were 0.8655, 46.0 and 3.84 W m^{-1} K^{-1} for the cement, steel and thawed formation respectively. Using these data and Table 8.39 we obtained from Eq. (8.3.13) that $k_i = 1.10$ W m^{-1} K^{-1} and from Eq. (8.3.12) the value of $J = 4.45$. The results

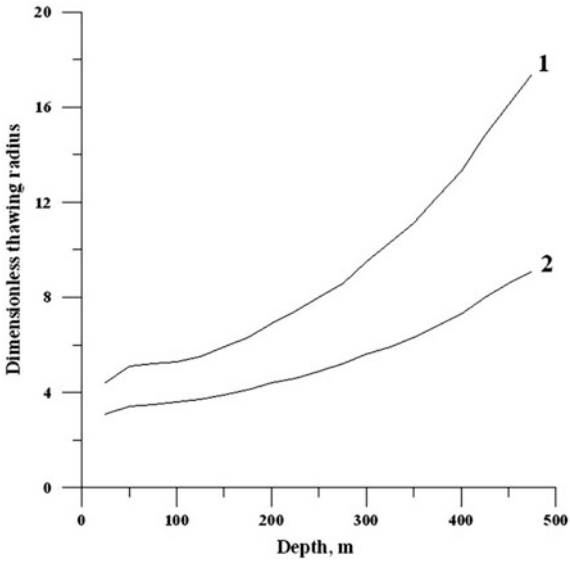

Fig. 8.25 Dimensionless thawing radius versus depth. *1* injection time 200 days, *2* injection time 50 days

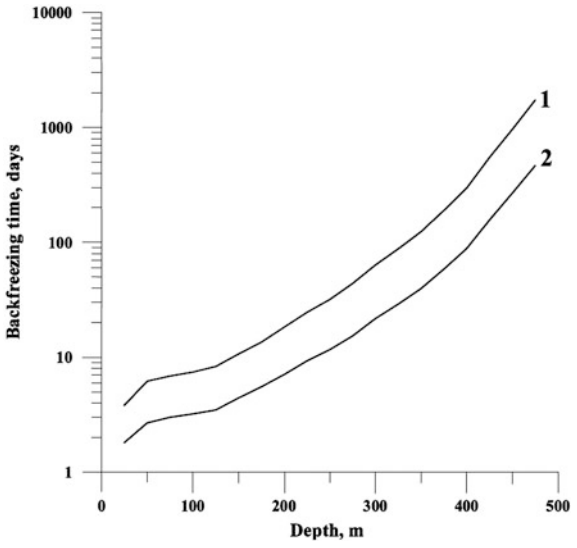

Fig. 8.26 The duration of the freezback period versus depth; *1* injection time 200 days, *2* injection time 50 days

after applying Eqs. (8.3.6) and (8.3.20) are presented in Table 8.39 and Figs. 8.25 and 8.26. Now let us assume that after 100 days of water injection the well needs to be shut-in for 3 weeks. Table 8.39 shows that the water in the producing (injection) string should be removed from the 0–275 m well section.

8.3.5 Prediction of Formation Temperatures: Field Cases

8.3.5.1 Introduction

In permafrost regions, due to thawing of the surrounding wellbore formations during drilling, data representative of the undisturbed geothermal temperature can be obtained only by repeated observations over a long period of time. The drilling process greatly alters the temperature field of formations surrounding the wellbore. The temperature change is affected by the duration of fluid circulation (depth penetration, hole cleaning, cementing), the duration of shut-in periods (tripping of drill pipe, running of casing, logging, etc.), the temperature difference between the formation and drilling mud, the well radius, the thermal properties of formations, and the drilling technology used.

The results of field and analytical investigations have shown that in many cases the effective temperature (T_w) of the circulating fluid (mud) at a given depth can be assumed constant during drilling or production (Lachenbruch and Brewer 1959; Ramey 1962; Edwardson et al. 1962; Jaeger 1961; Kutasov et al. 1966; Raymond 1969). Here we note that even for a continuous mud circulation process the wellbore temperature is dependent on the current well depth and other factors. The term "effective fluid temperature" is used to describe the temperature disturbance of formations while drilling. In their classic paper Lachenbruch and Brewer (1959) showed that the wellbore shut-in temperature mainly depends on the amount of thermal energy transferred to (or from) formations. The thermal effect of drilling operations on the temperature field of formations can be also approximated by a constant cylindrical source with a contact thermal resistance (Wilhelm et al. 1995). The mud circulation time and the total well drilling time ratio decrease with the increase of the well depth. For this reason, for deep wells neither model (constant temperature, constant cylindrical/linear source) can be used to describe the thermal disturbance of formations and the temperature recovery during the shut-in period. In addition, in an actual drilling process many time-dependent variables influence downhole temperatures. The composition of annular materials (steel, cement, fluids), the drilling history (vertical depth versus time), the duration of short shut-in periods, fluid flow history, radial and vertical heat conduction in formations, the change of geothermal gradient with depth, and other factors should be accounted for as well as their effects on the wellbore temperatures when drilling. It is clear that only transient computer models can be used to calculate temperatures in the wellbore and surrounding formations as functions of depth and time. However, in many cases it is difficult to compare the results of a computer simulation with actual temperatures measured in wells during circulation and/or shut-in periods. In fact, the data accompanying field-collected temperature measurements are often incomplete. For example, it is quite common not to have the mud composition or even the mud type. Also, in some cases, very little is known about the type of formations penetrated by the well.

The objective of this section is to suggest a new approach to the utilization of temperature logs in deep wells and present working formulas for determining the undisturbed formation temperature. A review and critical analysis of published methods for estimating the undisturbed formation temperature can be found elsewhere (Kutasov 1999). Below we introduce a new approach for predicting the undisturbed formations temperatures (and geothermal gradients) from shut-in temperature logs in deep wells.

The main features of the method are as follows:

In the permafrost section of the well under investigation, the starting point in the well thermal recovery is shifted from the end of well completion to the moment of time when the refreezing of formations was completed. It is taken into account that the refreezing of thawed formations occurs in some temperature interval. Below the permafrost base the starting point in the well thermal recovery is shifted from the end of well completion to the moment of time when the first shut-in temperature log was taken. Thus the application of the method of predicting the undisturbed formation temperature does not depend on:

(a) the well drilling history (vertical depth versus time, stops in mud circulation), drilling technology used (properties of drilling fluids, penetration rate, bit size, casings, cementing techniques);
(b) the duration of the complete refreezing formations thawed during drilling.

The limitations to the applicability of this method are discussed below. Temperature logs in five wells are used to verify the method.

Kutasov and Eppelbaum (2010) presented a new method for determination of formation temperature from bottom-hole temperature logs.

8.3.5.2 Shut-in Temperatures: Permafrost Zone

Let us assume that at the moment in time when $t = t_{ep}$ the phase transitions (water-ice) in formations at a selected depth $z < z_{pf}$ are complete; i.e., the thermally disturbed formation has frozen. In this case at $t > t_{ep}$ the cooling process is similar to that of temperature recovery in sections of the well below the permafrost base. It is well known (Tsytovich 1975) that the freezing of the water occurs at some temperature interval below 0 °C (Fig. 8.27).

In practice, however, the moment of time $t = t_{ep}$ cannot be determined. This can be done only by conducting long-term repetitive temperature observations in deep wells.

Let us assume that three shut-in temperature T_{s1}, T_{s2}, and T_{s3} are measured at a given depth (Fig. 8.27). We can consider the period of time $t_c^* = t_c + t_{s1}$ as a new "thermal disturbance" period. Hence the "shut-in times" are

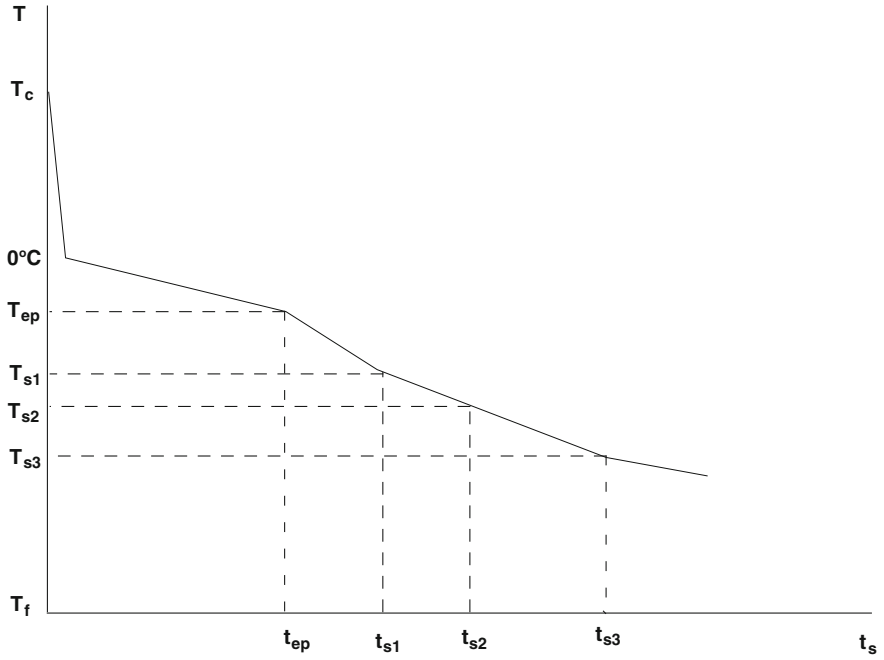

Fig. 8.27 Shut-in temperatures at a given depth (above the permafrost base)—schematic curve

$$t_{s1}^{*} = t_{s2} - t_{s1}, \quad t_{s2}^{*} = t_{s3} - t_{s1}. \tag{8.3.21}$$

Now, the dimensionless temperature distribution at $t = t_{s1}$

$$\left\{ \begin{array}{ll} T_{cD}^{*}(r_D, t_{xD}) = 1, & 0 \le r_D \le 1, \\ T_{cD}^{*}(r_D, t_{xD}) = 1 - \ln r_D / \ln R_x, & 1 \le r_D \le R_x, \\ T_{cD}^{*}(r_D, t_{xD}) = 0, & r_D > R_x. \end{array} \right\}, \tag{8.3.22}$$

$$R_x = 1 + 2.184\sqrt{t_{xD}}, \qquad t_{xD} = \frac{a_f t_c^{*}}{r_{wx}^2}, \qquad R_x = \frac{r_{ix}}{r_{wx}}, \tag{8.3.23}$$

$$T_{cD}^{*}(r_D, t_{xD}) = \frac{T_c(r,t) - T_f}{T_{s1} - T_f}, r_D = \frac{r}{r_{wx}}, \tag{8.3.24}$$

where r_{wx} is the radius of a cylindrical source with a constant wall temperature (T_{s1}) during the thermal disturbance period $\left(t_c^{*}\right)$, a_f is the thermal diffusivity of frozen formations, t_c is the time of "thermal disturbance" (at a given depth) during drilling, T_f is the undisturbed temperature of formations, and r_{ix} is the radius of thermal influence.

It is a reasonable assumption that the value of t_c (the "disturbance" period) is a linear function of the depth (z) (Kutasov and Eppelbaum 2003):

$$t_c = t_{tot}\left(1 - \frac{z}{H_t}\right), \tag{8.3.25}$$

where z is the depth, t_{tot} is the total drilling time, and H_t is the total well depth.

For the initial radial temperature distributions (Eq. 8.3.22) the dimensionless shut-in wellbore temperature (at $t_s > t_{s1}$) was presented earlier (Eq. 8.2.40).

By using measurements T_{s2}, T_{s3} and Eq. (8.2.40) we can eliminate the formation temperature T_f After simple transformations we obtain Eq. (8.2.42).

Substituting the value of R_x (Eq. 8.3.23) into Eq. (8.2.42) we can obtain a formula for calculating the dimensionless disturbance time, t_{xD}. After this, it is possible to calculate the values of T_f, R_x, and $A = a_f \Big/ (r_{wx})^2$.

As mentioned above, although Eq. (8.2.42) is based on an analytical solution, several limitations should be taken into account. First, the temperature ratio γ (Eq. 8.2.42) should be determined with high accuracy. This means that high accuracy of temperature measurements (T_{s1}, T_{s2}, T_{s3}) is needed. As mentioned in Sect. 8.2.4, the temperature differences $T_{s2} - T_{s1}$ and $T_{s3} - T_{s1}$ should be significantly larger than the absolute accuracy of the temperature measurements. For these reasons this method cannot be used for depths where the undisturbed formation temperature is close to 0 °C. Second, the lithological profile of the permafrost section of the well should be known. This will serve to find the temperature interval of the thawed formation refreezing, and to select the "initial" temperature log (T_{s1}, Fig. 8.26). To determine the depth of the 0 °C isotherm (the position of the permafrost base) we recommend using the "two point" method (Kutasov 1988a) based on determining the geothermal gradient in a uniform layer below the permafrost zone. Therefore, a lithological profile for this section of the well must be available. Only two shut-in temperature measurements for two depths are needed to determine the geothermal gradient. The position of the permafrost base is predicted by the extrapolation of the undisturbed formation temperature-depth curve to 0 °C. To speed up calculations we devised a computer program dubbed "Permtemp" (Kutasov 1999). This program was utilized to process field data for all five wells.

8.3.5.3 Unfrozen Well Section: The Initial Temperature Distribution

In theory the drilling process affects the temperature field of formations at very long radial distances. There is, however, a practical limit to the distance; namely, the radius of thermal influence (r_{in}), where for a given circulation period ($t = t_c$) the temperature $T(r_{in}, t_c)$ is "practically" equal to the geothermal temperature T_f. To avoid uncertainty, however, it is essential that the parameter r_{in} not to be dependent on the temperature difference $T(r_{in}, t_c) - T_f$. For this reason we used the thermal balance method to calculate the radius of thermal influence. The

results of modeling, experimental work and field observations showed that the temperature distribution around the wellbore during drilling can be approximated by the following relation (Kutasov 1968, 1999):

$$\frac{T(r,t)-T_f}{T_w-T_f}=1-\frac{\ln\, r/r_w}{\ln\, r_{in}/r_w},\qquad r_w\le r\le r_{in}, \tag{8.3.26}$$

where T_w is the effective temperature of the drilling fluid (at a given depth). Introducing the dimensionless values of circulation time, radial distance, radius of thermal influence, and temperature

$$t_D=\frac{a_f t_c}{r_w^2},\quad r_D=\frac{r}{r_w},\quad R_{in}=\frac{r_{in}}{r_w},\quad T_D(r_D,t_D)=\frac{T(r,t)\ -T_f}{T_w-T_f}, \tag{8.3.27}$$

we obtain

$$T_D(r_D,t_D)=1-\frac{\ln\, r_D}{\ln\, R_{in}},\qquad 1\le r_D\le R_{in}, \tag{8.3.28}$$

$$R_{in}=\frac{r_{in}}{r_w}=1+D_0\sqrt{t_D},\qquad D_0=2.184,\qquad t_D\le 10^4. \tag{8.3.29}$$

where a_f is the thermal diffusivity of the formation (Kutasov 1968, 1999).

The radius of thermal influence r_{in} in Eq. (8.3.29) was determined from the thermal balance condition (Fig. 8.20).

Again, the value of t_c (the "disturbance" period) can be estimated from Eq. (8.3.20). Let us also now assume that the three shut-in temperatures T_{s1}, T_{s2}, and T_{s3} are measured at a given depth. Similarly, as in the previous section, we can consider that the period of time $t_c^*=t_c+t_{s1}$ is a new "thermal disturbance" period and r_{wx} is an "effective" well radius:

$$\int_{r_w}^{\infty} rf_1(t_{s1},r)\,dr=\int_{r_{wx}}^{r_{ix}} rf(t_{s1},r)dr. \tag{8.3.30}$$

The dimensionless radial temperature distribution at $t_s=t_{s1}$ is also expressed by Eq. (8.3.22). Hence, for deep depths (below the permafrost base) Eq. (8.2.40) can be used for calculations of the undisturbed formations temperatures and geothermal gradients.

8.3.5.4 Field Cases

Extensive temperature measurements in Northern Canada and Alaska were conducted by the Geothermal Service of Canada (Taylor 1978; Judge et al. 1979,

1981; Taylor et al. 1982) and the U.S. Geological Survey (Lachenbruch and Brewer 1959; U.S. Geological Survey "Site" File—Alaska, Internet). We selected long term temperature surveys in five wells to verify Eq. (8.2.42).

Well 3, Alaska, South Barrow (Lachenbruch and Brewer 1959)
Temperature measurements to a depth of 595 ft were made during a period of six years after drilling. The well was drilled for 63 days to a total depth of 2,900 ft. Lachenbruch and Brewer (1959) predicted the equilibrium formation temperatures to be: −8.835 °C, −7.830 °C, and −6.735 °C for depths 355, 475, 595 ft respectively. Our results differed from these values [Table 8.40 by an average of 0.2 °C (for 31 runs)].

Our model did not take into account the effect of the geothermal gradient on the restoration of the natural temperature field of formations. This may have contributed to the difference of 0.2 °C. Note that when calculating T_f (Table 8.40) we used temperature measurements with short shut-in times. For a depth of 595 ft (Fig. 8.28) the average value of T_f was 6.568 °C (9 runs).

Freezing ceased at a temperature of about −0.6 °C and the duration of the complete freezeback was approximately 20 days (Fig. 8.28). Lachenbruch and Brewer (1959) used the following empirical formula to process the field temperature data:

$$T_w = C \ln\left(1 + \frac{t_c}{t_s}\right) + B, \tag{8.3.31}$$

where C and B are empirical coefficients from the field measurements.

Well No. 175 (Judge et al. 1981). The location and input data of this well are presented in Table 8.41. Figure 8.29 depicts a graph of 4 of the 7 temperature surveys in this well. The field data showed that the duration of refreezing of the formation thawed out during drilling depended significantly on its natural (undisturbed) temperature (or depth). For low temperature permafrost the refreezing period was relatively short (Fig. 8.27). The restoration of the temperature regime was accompanied by a nearly isothermal interval (Fig. 8.27). Therefore, if the shut-in time is insufficient, the zero temperature gradient intervals can be attributed to geological-geographical factors. Long-term temperature surveys showed that only after 28 ($z = 100$ m) and 17 years ($z = 650$ m) of shut-in periods could the undisturbed formations temperatures be measured with an accuracy of 0.1 °C (Judge et al. 1981). Comparison of the predicted undisturbed formation temperatures (Table 8.41) and those (T_{EQ}) determined from 7 long-term temperature logs (Judge et al. 1981, p. 131) were in fairly good agreement. Interpolation of temperature data was used to determine the values of T_{s2}, T_{s3}, and T_{EQ} (Table 8.42).

The authors used the empirical Lachenbruch-Brewer formula (Horner method) to estimate the undisturbed formation temperature (T_{EQ}). Note that it is difficult to determine the accuracy of the Horner method in predicting undisturbed formation temperature. The accuracy of the T_{EQ} prediction, as was shown in one example, depends on the duration of the shut-in period. At the same time the temperature

Table 8.40 Observed shut-in temperatures T_{s1}, T_{s2} and T_{s3} (Lachenbruch and Brewer 1959) and calculated formation temperature T_f. Alaska, South Barrow Well 3 (Kutasov and Eppelbaum 2003)

No	T_{s1} (°C)	T_{s2} (°C)	T_{s3} (°C)	t_{s1}* (day)	t_{s2}* (day)	t_{s3}* (day)	t_{xD}	A (1/day)	R_x	T_f (°C)
Depth 595 ft, t_c = 50 days										
1	−2.163	−3.345	−4.829	80	87	117	13.8	0.1721	9.10	−6.541
2	−2.163	−3.345	−5.155	80	87	133	13.7	0.1712	9.08	−6.552
3	−2.163	−3.345	−5.542	80	87	167	13.8	0.1726	9.12	−6.536
4	−2.163	−3.345	−5.764	80	87	197	13.6	0.1701	9.06	−6.567
5	−2.163	−3.345	−6.191	80	87	338	13.3	0.1667	8.98	−6.609
6	−3.345	−4.829	−5.155	87	117	133	6.59	0.0758	6.61	−6.574
7	−3.345	−4.829	−5.542	87	117	167	6.89	0.0792	6.73	−6.533
8	−3.345	−4.829	−5.764	87	117	197	6.55	0.0752	6.59	−6.58
9	−3.345	−4.829	−6.191	87	117	338	6.27	0.0721	6.47	−6.621
Depth 475 ft, t_c = 51 days										
10	−2.741	−3.78	−4.452	74	81	88	8.66	0.1164	7.43	−7.648
11	−2.741	−3.78	−5.751	74	81	118	8.65	0.1161	7.42	−7.654
12	−2.741	−3.78	−6.079	74	81	134	8.69	0.1167	7.44	−7.638
13	−2.741	−3.78	−6.517	74	81	168	8.61	0.1156	7.41	−7.669
14	−2.741	−3.78	−6.752	74	81	199	8.59	0.1153	7.40	−7.677
15	−2.741	−3.78	−7.219	74	81	339	8.49	0.1140	7.36	−7.712
16	−3.78	−4.452	−5.751	81	88	118	8.05	0.0993	7.20	−7.376
17	−3.78	−4.452	−6.079	81	88	134	7.87	0.0970	7.13	−7.437
18	−3.78	−4.452	−6.517	81	88	168	7.57	0.0933	7.01	−7.542
19	−3.78	−4.452	−6.752	81	88	199	7.46	0.0920	6.97	−7.582
20	−3.78	−4.452	−7.219	81	88	339	7.25	0.0894	6.88	−7.666
Depth 355 ft, t_c = 56 days										
21	−4.55	−5.565	−6.122	79	86	93	9.92	0.1257	7.88	−8.845
22	−4.55	−5.565	−7.141	79	86	123	10.5	0.1335	8.09	−8.702
23	−4.55	−5.565	−7.38	79	86	139	10.8	0.1361	8.16	−8.658
24	−4.55	−5.565	−7.706	79	86	173	10.9	0.1378	8.2	−8.632
25	−4.55	−5.565	−7.89	79	86	204	10.9	0.1375	8.2	−8.636
26	−4.55	−5.565	−8.289	79	86	344	10.6	0.1341	8.11	−8.692
27	−5.565	−6.122	−7.141	86	93	123	9.06	0.1050	7.57	−8.435
28	−5.565	−6.122	−7.38	86	93	139	8.93	0.1036	7.53	−8.463
29	−5.565	−6.122	−7.706	86	93	173	8.73	0.1012	7.45	−8.509
30	−5.565	−6.122	−7.89	86	93	204	8.58	0.0995	7.4	−8.544
31	−5.565	−6.122	−8.289	86	93	344	8.18	0.0948	7.24	−8.649

deviations from the Horner plot were small (Kutasov 1999; p. 259). Our model does not take into account the effect of the geothermal gradient on the restoration of the natural temperature field of formations. This may have some effect on the predicted values of T_f in regions with high geothermal gradients. In Fig. 8.30 the predicted and measured shut-in temperatures at two depths are compared.

It can be seen that Eq. (8.2.42) gives a sufficiently accurate description of the process by which temperature equilibrium comes about in the borehole (Table 8.43, Fig. 8.30).

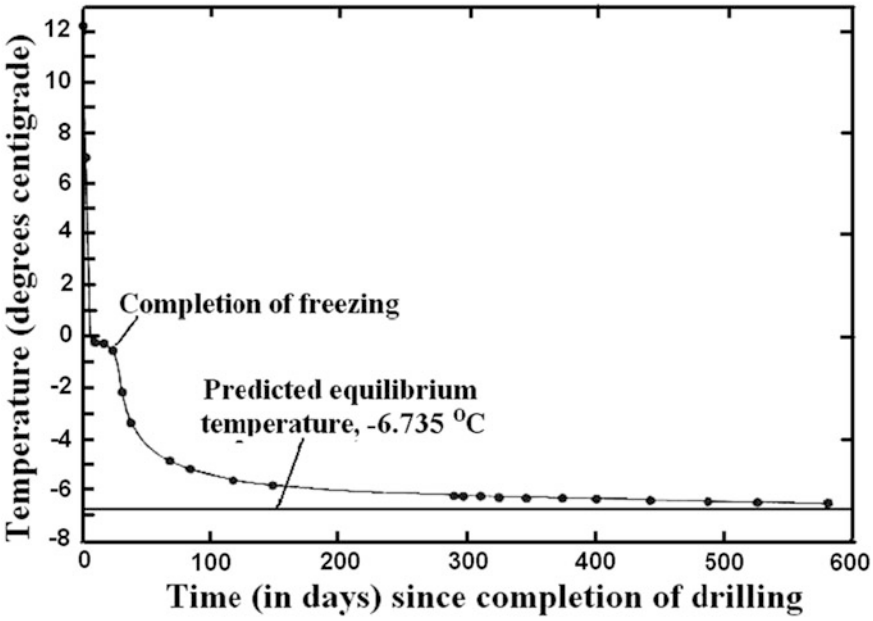

Fig. 8.28 Cooling of South Barrow (Alaska) well 3, 595-foot depth-temperature curve (Lachenbruch and Brewer 1959)

The temperature gradient is a differential quantity; hence the process by which the geothermal (undisturbed) gradient (Γ) is restored is distinct from the temperature recovery process. Equation (8.2.40) can be used to evaluate the accuracy of the value of Γ when calculated from temperature measurements taken a short time after cessation of drilling.

From Fig. 8.31 it follows that in the 589.5–650.1 m interval a shut-in of 800 days is required to determine the value of Γ with an accuracy of 5 %.

West Fish Creek well No. 1 (U.S. Geological Survey "Site" File—Alaska, Internet). The information about this well and the results of temperature surveys are presented in Tables 8.44 and 8.45.

The "Permtemp" (Kutasov 1999) program was used to calculate the values of undisturbed formation temperatures for frozen/unfrozen formations sections of the well (Table 8.46). Let us estimate the values of r_{wx} and r_{ix} for a depth of 112.78 m. From Table 8.45 we find that $A = a_f(r_{wx})^2 = 0.002250$ 1/day. Let us assume that the thermal diffusivity of the frozen formation is $a_f = 8.333 \times 10^{-7}$ m^2/s = 0.0030 m^2/h, then

$$r_{wx} = \sqrt{24 \cdot 0.0030/0.002250} = 5.657 \text{ (m)},$$
$$r_{ix} = 5.657 + 2.184 \cdot 5.657 \cdot \sqrt{0.650} = 15.62 \text{ (m)}.$$

Table 8.41 Input data and location of the well No. 175 (Judge et al. 1981)

Site name	Gemini E-10
Latitude	79°59′24″ N
Longitude	84°04′12″ W
Hole depth, m	3,845
Well spudded	14-10-72
Drilling time, days	145

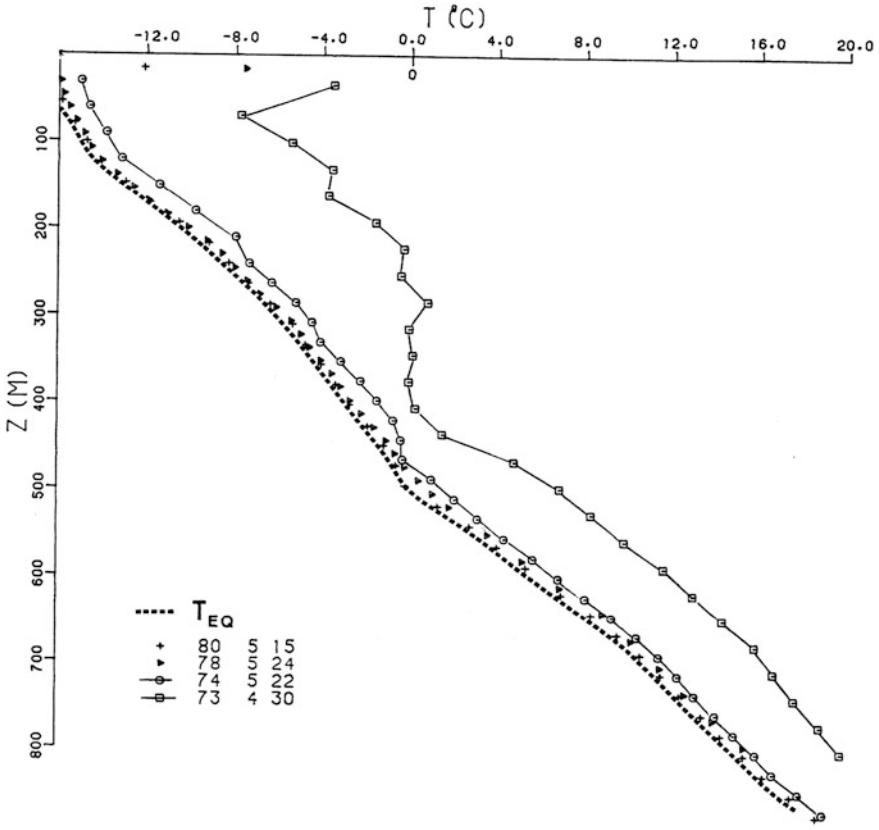

Fig. 8.29 Temperature profiles in well No. 175, T_{EQ}—the predicted temperature versus depth curve (Judge et al. 1981)

Similarly, for a depth of 704.09 m (here a_f is the thermal diffusivity of the formation) we obtain:

$$r_{wx} = \sqrt{24 \cdot 0.0030/0.002898} = 4.984 \text{ (m)}$$

Table 8.42 Observed shut-in temperatures T_{s1}, T_{s2}, and T_{s3} (Judge et al. 1981) and calculated formation temperature T_f and T_{EQ}, Well No. 175, $t_{s1} = 53$, $t_{s1} = 440$, and $t_{s1} = 795$ days

z (m)	t_{xD}	A, 1/day	R_x	T_{s1} (°C)	T_{s2} (°C)	T_{s3} (°C)	T_f (°C)	T_{EQ} (°C)
101.5	15.47	0.07968	9.59	−5.44	−13.57	−14.13	−14.86	−15.26
132.3	20.32	0.10525	10.84	−3.58	−12.44	−13.00	−13.72	−14.25
162.8	5.17	0.02695	5.97	−3.74	−10.74	−11.44	−12.38	−12.62
559.0	16.68	0.09431	9.92	9.79	4.47	4.14	3.72	3.32
589.5	58.25	0.33142	17.67	11.59	6.20	5.96	5.66	5.05
620.3	32.94	0.18864	13.53	12.96	7.84	7.58	7.25	6.78
650.1	9.95	0.05735	7.89	14.30	9.43	9.08	8.63	8.44

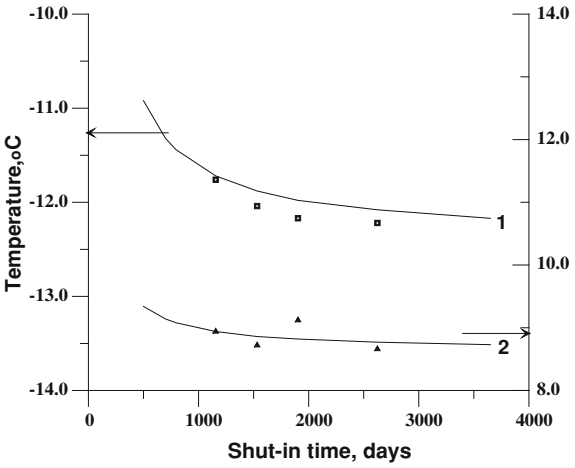

Fig. 8.30 Shut-in temperatures at two depths, well No. 175 (*1*) 162.8 m; (*2*) 650.1 m, $t_{s1} = 53$, $t_{s2} = 440$, and $t_{s3} = 795$ days. *Solid curves* show calculated values and points—observed temperatures (interpolated)

and

$$r_{ix} = 4.984 + 2.184 \cdot 4.984 \cdot \sqrt{0.667} = 13.87 \text{ (m)}.$$

Table 8.46 shows the accuracy of the shut-in temperature predictions. Let us determine the average squared temperature deviation:

$$\Delta T = \sqrt{\frac{\sum_{n=1}^{N} \left(T_n^* - T_n\right)^2}{N}},$$

where T^* is the observed temperature, T is calculated temperature, and N the number of readings. In our case $N = 23$ (Table 8.47) and $\Delta T = 0.099$ °C.

The Put River N-1 well. In Fig. 8.32 we present some results of temperature surveys in this well.

Table 8.43 Input data and location of three wells, Alaska (U.S. Geological Survey "Site" File—Alaska, Internet)

Site code	FCK	PBF	DRP
Site name	West Fish Creek No. 1	Put River N-1	Drew Point No. 1
Latitude	70°19′35.99″ N	70°19′07″ N	70°52′47.14″ N
Longitude	152°03′38.03″ W	148°54′35″ W	153°53′59.93″ W
Surface elevation, m	27	8	5
Casing diameter, cm	34	51	34
Hole depth, m	735	763	640
Date of drill start	14-02-77	02-09-70	13-01-78
Drilling time, days	73	44	60

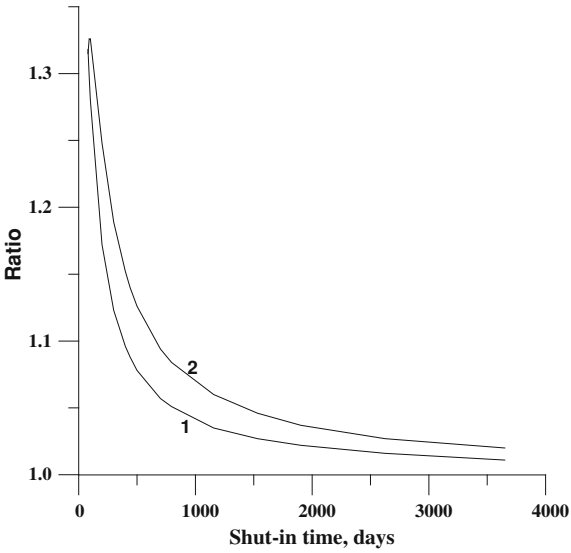

Fig. 8.31 The transient temperature gradient (G) and the geothermal gradient Γ ratio (B) for two sections, well No. 175: 101.5–162.8 m, $G(t_s = \infty) = \Gamma =$ 0.04049 m/K, 2–589.5-650.1 m, $G(t_s = \infty) = \Gamma = 0.04901$ m/K

In fact, the calculated values of ΔT (the average squared temperature deviation) are 0.070, 0.032, and 0.068 °C for depths 45.72, 60.96, and 91.44 m, respectively.

The Drew Point No. 1 well. In Tables 8.48 and 8.49 the results of temperature surveys and the predicted values of undisturbed formation temperatures are presented.

Figure 8.33 shows that the observed and calculated values of transient shut-in temperatures are in fairly good agreement. For depths of 120.40 and 170.69 m the calculated values of ΔT are 0.078 and 0.119 °C, respectively.

Table 8.44 Results of temperature surveys (°C) in West Fish Creek well No. 1, Alaska. U.S. Geological Survey "Site" File—Alaska (Internet)

z, m	Shut-in time, days					
	227	506	867	1232	1576	2657
30.48	−7.018	−7.815	−8.259	−8.411	−8.534	−8.831
60.96	−5.721	−7.134	−7.676	−7.849	−7.978	−8.094
91.44	−5.055	−6.285	−6.901	−7.065	−7.212	−7.409
112.78	−4.818	−5.584	−6.155	−6.285	−6.406	−6.625
146.3	−3.624	−4.196	−4.719	−4.795	−4.946	−5.103
179.83	−1.617	−2.391	−2.977	−3.053	−3.241	−3.423
210.31	−0.104	−0.924	−1.511	−1.587	–	−1.961
240.79	0.955	0.248	−0.235	−0.291	–	−0.666
271.27	2.161	1.437	0.984	0.892	0.718	0.539
301.75	3.22	2.523	2.071	2.015	1.829	1.662
332.23	4.315	3.643	3.221	3.147	2.989	2.800
368.81	5.861	4.972	4.563	4.543	4.348	4.182
399.29	6.818	6.165	5.743	5.702	5.503	5.335
432.82	7.978	7.346	6.954	6.955	6.731	6.563
478.54	9.656	9.020	8.587	8.597	8.333	8.157
512.07	10.647	10.033	9.650	10.000	9.456	9.284
542.55	12.014	11.439	11.067	11.099	10.864	10.658
573.03	13.023	12.433	12.111	12.136	11.926	11.739
606.55	14.191	13.618	13.308	13.362	13.13	12.934
640.08	15.225	14.838	14.552	14.606	14.329	14.176
670.56	16.357	15.843	15.572	15.578	15.362	15.238
704.09	17.935	17.431	17.137	17.188	16.931	16.705

8.4 Cementing of Casing: Cement Heat Generation

8.4.1 Strength and Thickening Time of Cement

In this section we consider methods of downhole temperature prediction while cementing the casing. It will be shown that for deep and hot wells the heat generation during cement hydration may cause a substantial temperature increase in the annulus. This factor must be taken into account in cement slurry design. Shut-in temperature and pressure are two basic influences on the downhole performance of cement slurries. They affect how long the slurry will pump and how it develops the strength necessary to support the pipe. Temperature has a more pronounced influence (Swayze 1954). The downhole temperature controls the pace of chemical reactions during cement hydration resulting in cement setting and strength development. As the formation temperature increases, the cement slurry hydrates and sets faster, and develops strength more rapidly. Cement slurries must be designed with sufficient pumping time to provide safe placement in the well. At the same time the cement slurry cannot be overly retarded as this will prevent the

Table 8.45 Predicted formation temperatures, West Fish Creek well No. 1, Alaska; $t_{s1} = 227$, $t_{s2} = 506$, and $t_{s3} = 867$ days

z, m	t_{xD}	A, 1/day	R_x	T_f, °C
30.48	1.011	0.003405	3.196	−8.898
60.96	1.826	0.006212	3.951	−8.374
91.44	1.155	0.003970	3.347	−7.754
112.78	0.650	0.002250	2.761	−7.063
146.3	0.497	0.001740	2.539	−5.623
179.83	0.618	0.002191	2.717	−3.910
368.81	1.144	0.004342	3.335	4.022
399.29	0.685	0.002632	2.808	5.120
432.82	0.712	0.002771	2.843	6.385
478.54	0.614	0.002431	2.711	7.939
512.07	0.678	0.002720	2.798	9.097
542.55	0.635	0.002579	2.740	10.524
573.03	0.790	0.003248	2.941	11.668
606.55	0.784	0.003271	2.934	12.884
640.08	0.507	0.002144	2.555	14.116
670.56	0.784	0.003359	2.934	15.206
704.09	0.667	0.002898	2.783	16.728

Table 8.46 Observed (T^*) and calculated (T) temperatures (°C) at three shut-in times, West Fish Creek No. 1 well, Alaska

z, m	Shut-in time, days					
	1,232		1,576		2,657	
	T	T^*	T	T^*	T	T^*
30.48	−8.449	−8.411	−8.547	−8.534	−8.691	−8.831
60.96	−7.891	−7.849	−8.000	−7.978	−8.156	−8.094
91.44	−7.158	−7.065	−7.290	−7.212	−7.481	−7.409
112.78	−6.415	−6.285	−6.554	−6.406	−6.759	−6.625
399.29	5.559	5.702	5.464	5.503	5.324	5.335
512.07	9.486	–	9.400	9.456	9.276	9.284
606.55	13.180	13.362	13.114	13.130	13.019	12.934
704.09	17.014	17.188	16.950	16.931	16.859	16.705

Table 8.47 Observed (T^*) and calculated (T) shut-in temperatures (°C) at three depths of the Put River N-1 well, Alaska; $t_{s1} = 34$, $t_{s2} = 48$, and $t_{s3} = 66$ days

t_s, days	45.72 m		60.96 m		91.44 m	
	T	T^*	T	T^*	T	T^*
91	−7.546	−7.511	−7.525	−7.497	−7.258	−7.227
117	−7.921	−7.900	−7.867	−7.860	−7.651	−7.620
163	−8.294	−8.428	−8.207	−8.263	−8.04	−7.965
1071	−9.098	−9.052	−8.946	−8.957	−8.875	−8.771

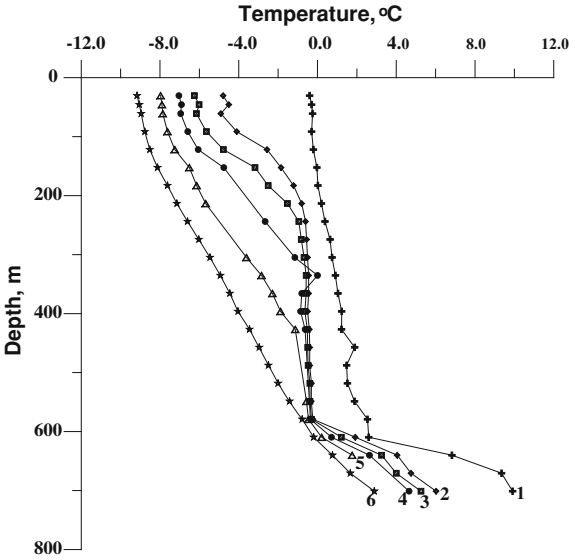

Fig. 8.32 Temperature profiles in the Put River N-1 well. The shut-in times for curves *1*, *2*, *3*, *4*, *5*, and *6* are 5, 34, 48, 66, 117, and 1,071 days respectively. U.S. Geological Survey "Site" File—Alaska (Internet). It can be seem from Table 8.45 that Eq. (8.2.40) approximates the transient shut-in temperatures with good accuracy

Table 8.48 Results of temperature surveys (°C) in the Drew Point No. 1 well, Alaska. U.S. Geological Survey "Site" File—Alaska (Internet)

z, m	Shut-in time, days					
	186	547	907	1,259	2,000	2,339
50.29	−7.373	−8.519	−8.726	−8.736	−8.937	−8.953
70.10	−6.925	−8.142	−8.355	−8.292	−8.552	−8.574
100.58	−5.892	−7.283	−7.470	−7.607	−7.709	−7.774
120.40	−5.309	−6.638	−6.852	−6.953	−7.094	−7.140
150.88	−4.466	−5.690	−5.856	−5.961	−6.096	−6.148
170.69	−3.951	−5.076	−5.233	−5.335	−5.481	−5.518
199.64	−3.247	−4.199	−4.342	−4.441	−4.571	−4.619
219.46	−2.698	−3.639	−3.760	−3.860	−3.977	−4.032

Table 8.49 Predicted formation temperatures, Drew Point well No. 1, Alaska. $t_{s1} = 186$, $t_{s2} = 547$, and $t_{s3} = 907$ days

z, m	t_{xD}	A, 1/day	R_x	T_f, °C
50.29	2.727	0.011302	4.607	−9.009
70.10	2.874	0.012002	4.702	−8.644
100.58	5.132	0.021692	5.947	−7.715
120.40	3.315	0.014124	4.976	−7.138
150.88	4.813	0.020758	5.791	−6.073
170.69	4.418	0.019210	5.591	−5.439
199.64	3.636	0.015997	5.164	−4.531
219.46	5.165	0.022913	5.964	−3.916

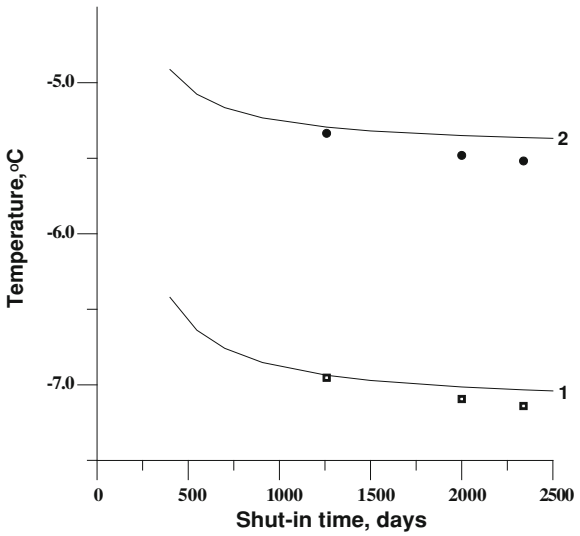

Fig. 8.33 Shut-in temperatures at two depths, well Drew Point No. 1, Alaska *1*—120.40 m; *2*—170.69 m, $t_{s1} = 186$, $t_{s2} = 547$, and $t_{s3} = 907$ days. *Solid curves* calculated values, *points* observed temperatures

development of satisfactory compressive strength. The thickening time of cement is the time that the slurry remains pumpable under set conditions. The specifications of circulation temperature in the design of thickening times for oil well cement are very important.

Two examples illustrate this point (Shell and Tragesser 1972). Neat cement was tested at simulated bottom-hole temperatures of 51.7 °C (125 °F) and 62.2 °C (144 °F). At 51.7 °C it had a thickening time of 4 h, 54 min. At 62.2 °C, the thickening time was only 2 h, 57 min. Increasing the temperature by 10.5 °C decreased the thickening time by nearly 2 h. Cement designed for greater depths was tested at schedules which went to 96.7 °C (206 °F) and 129 °C (248 °F). At the lower temperature, it pumped for 3 h, 2 min. The 23.3 °C increase to 120 °C reduced the pumping time by 88 min to 1 h, 34 min. While retarders can extend thickening times, the thickening time for a given concentration of retarder is still very sensitive to changes in temperature. Slurries designed for erroneously high circulating temperatures can have unacceptably long setting times at lower temperatures. Another example, taken from the files of the API Committee on Standardization of Oil Well Cements, shows the importance of temperature on compressive strength development (Shell and Tragesser 1972). One neat cement has an 8-hour compressive strength of 1,575 psi at 230 °F (110 °C), but it did not set in that time at 200 °F (93 °C).

The effect of temperature on compressive strength development and thickening time for Portland cements is shown in Figs. 8.34 and 8.35. A compressive strength of 500 psi (in 24 h) is usually considered acceptable for casing support (Romero and Loizzo 2000). From Fig. 8.36 it follows that a temperature difference of only 6 °F (3.3 °C) significantly affects the compressive strength development of the cement. To reduce the wait on cement we recommend increasing the outlet mud

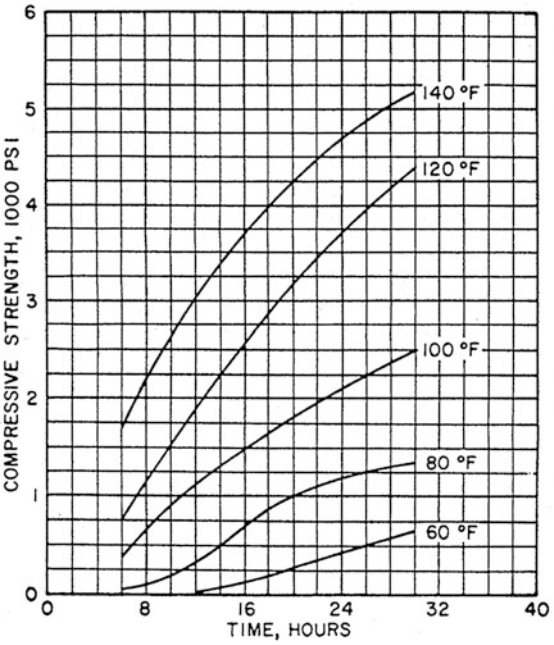

Fig. 8.34 Compressive strength of neat Class A cement (Davis and Faulk 1952)

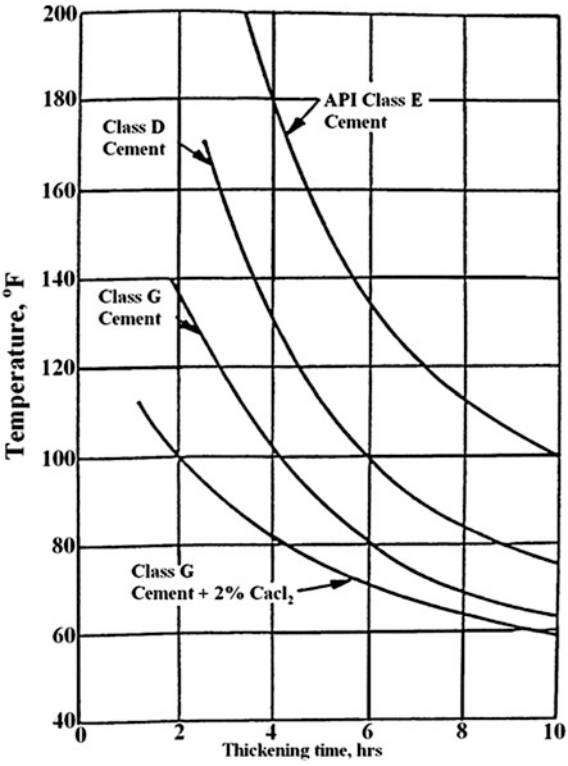

Fig. 8.35 The influence of temperature on thickening time of typical Portland cements at atmospheric pressure (Bearden 1959)

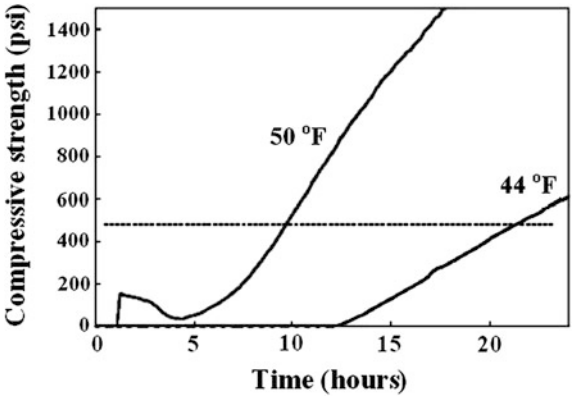

Fig. 8.36 Compressive strength development for a deep-water system at two temperatures (Romero and Loizzo 2000)

Table 8.50 Heat of hydration of pure cement compounds (Smith 1974)

Component	cal/g	Btu/lb
$3CaO \cdot Al_2O_3$ (C_3A)	207	373
$3CaO \cdot SiO_2$ (C_3S)	120	216
$4CaO \cdot Al_2O_3 \cdot Fe_2O_3$ (C_4AF)	100	180
$2CaO \cdot SiO_2$ (C_2S)	62	112

temperature. Earlier we suggested this technique to reduce the wait on cement at surface casing for wells in permafrost regions (Kutasov 1999). This may reduce the cost associated with cementing the conductor and surface casing.

8.4.2 Rate of Heat Generation Versus Time

When cement is mixed with water, an exothermic reaction occurs and a significant amount of heat is produced. This amount of heat depends mainly on the fineness and chemical composition of the cement, additives, and ambient temperature. The results of laboratory investigations of heat of hydration of pure cement compounds are presented in Table 8.50.

Tricalcium silicate $3CaO \cdot Al_2O_3(C_3A)$ hydrates rapidly and is the main contributor to the strength of the cement. In Portland cement the average tricalcium silicate content is 45 to 65 % with a maximum of 67 % for high early-strength cement (Craft et al. 1962). Table 8.50 shows that tricalcium silicate is the main contributor to the heat of hydration. As in any exothermic reaction, the rate of heat generation during cement hydration increases with the increase of the ambient temperature. For a Class "G" Neat System the hydration tests were performed at two different temperatures, 77 and 122 °F; the density of the slurry was 15.8 ppg (Romero and Loizzo 2000). Figure 8.37 lists the heat production rate per unit of weight as a function of time. We will call the two curves Ro77 and Ro122.

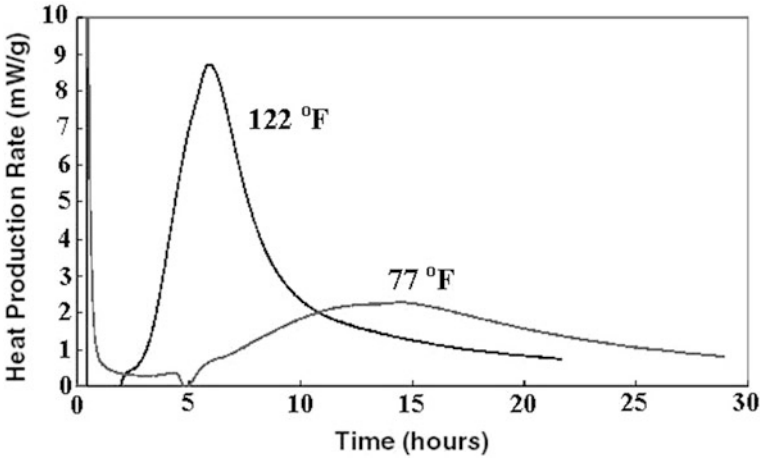

Fig. 8.37 Heat production rate per unit of mass as a function of time for class "G" neat cement at two temperatures (Romero and Loizzo 2000)

Thus to determine the amount of heat released by different cement systems during hydration, calometric measurements should be made. The measurements consist of recording the heat flux released by the system while held at constant temperature.

Previous studies of cement hydration tended only to measure the total heat evolution over a long time periods. However, cement hydration reactions are complicated and the rate of heat generation is not constant.

Assessment of temperature evolution during hydration is necessary to determine how fast the cement will reach an acceptable compressive strength before the casing can be released (Romero and Loizzo 2000). Therefore, for deep wells, heat generation during cement hydration has to be taken into account in cement slurry design. Experimental data show that the maximum value of heat generation occurs during the first 5 to 24 h. During this period the maximum temperature increase (ΔT_{max}) can be observed in the annulus. In order to evaluate the temperature increase during cement hydration the heat production versus time curve needs to be approximated by some analytical function $q = f(t)$. The condition $q = f(t = 0) = 0$ complicates the selection of this function.

Laboratory and field data show that a quadratic equation can be used for a short interval of time to approximate the rate of heat generation (q) per unit of length as a function of time

$$q = \pi\left(r_w^2 - r_c^2\right)\rho_c q_r q_D, \tag{8.4.1}$$

$$q_D = a_0 + a_1 t + a_2 t^2, \tag{8.4.2}$$

where t^* is the time since cement slurry placement, t_0 time period due to cement retardation, r_c is the outer radius of casing, ρ_c is the density of cement, q_r is the reference rate of heat generation per unit of mass, q_D is the dimensionless rate of heat generation, and a_0, a_1, a_2 are the coefficients.

The reference rate of heat generation per unit of mass is an arbitrary parameter and, for simplicity, we can assume that for the two curves in Fig. 8.37 $q_r = 1$ mW/g.

Equation (8.4.1) can be presented in the following form,

$$q = A_0 q_D, \qquad A_0 = \pi(r_w^2 - r_c^2)\rho_c q_r \tag{8.4.3}$$

where A_0 is the reference rate of heat generation per unit of length. We also assumed that cement slurry starts to generate heat only when the pumping of cement is finished at time $t = 0$. In practice, however, the cement slurry starts to generate heat during the final stages of pumping.

It was found that the following relationship (Eq. 8.4.4) can be used for a short interval of time (which includes time $t = t_x$, see below) to approximate the rate of heat generation (q) per unit of length as a function of time (Targhi 1987; Kutasov 1999).

Let now assume that at the moment of time $t = t_x$ the maximum value of $q = q_m$ is estimated from experimental data (Fig. 8.36). Usually the results of experiments are given per unit of annulus area and per unit of density. Then

$$a_1^* t_x + a_2^* t_x^2 = q_{mD}, \qquad \frac{dq_D}{dt} = 0, \qquad a_1^* + 2a_2^* t_x = 0, \tag{8.4.4}$$

$$a_1^* = \frac{2q_{mD}}{t_x}, \qquad a_2^* = -\frac{q_{mD}}{t_x^2}, \qquad q_{mD} = \frac{q_m}{q_r}. \tag{8.4.5}$$

Below we present the values for coefficients a_1^* and a_2^* for four field cases (Table 8.53). It should be recalled that the shape of $q = q(t)$ curves depends mainly on the ambient (formation) temperature and chemical composition of the cement slurry. For comprehensive design and evaluation of cementing operations, a major oilfield service company developed a temperature simulator (Romero and Loizzo 2000). The model incorporates a flow and thermal model, and accommodates complex wellbore geometries. During cement hydration, the thermal diffusivity equation is solved across the casing, cement and formation, and the radial temperature profile in a well configuration is determined. For the study of temperature development in cemented annuli, the degree of hydration is considered as a fundamental parameter. It is defined as the cement fraction that has reacted, and can be calculated as the fraction of the heat of hydration that has been released:

$$\xi(t) = \frac{Q(t)}{Q_{total}} = \frac{1}{Q_{total}} \int_0^t q(u)du,$$

where q is the heat production rate, Q_{total} the total heat of hydration. For cement slurry, the total heat Q_{total} can be calculated based on the slurry composition. A new hydration model was developed, and yields the heat production rate q which is related to the actual degree of hydration and actual temperature.

8.4.3 Hydration Test Data and Field Data

API Class "G" cement can be used for a wide range of depths and temperatures. Figure 8.37 presents results of neat cement Class "G" hydration tests at two temperatures. In order to test the mechanical properties of cement under well conditions more accurately, the cement must typically be cured or hydrated for the appropriate amount of time under temperature and pressure conditions as close as possible to downhole conditions in the well (Dillenbeck et al. 2002). The authors selected four wells. Since the wells had differing annular configurations and also because they used different cementing systems with different slurry densities, the authors determined that some type of correlation was needed between the wells and cement slurry used. The authors developed a value called Cement Density Factor or CDF. To determine the CDF for each well, the annular volume for one foot of the well was calculated based on casing outside diameter (O.D.) and drill bit size. The one-foot volume was then multiplied by the cement slurry density to obtain CDF (Dillenbeck et al. 2002). This CDF parameter is incorporated in Eq. (8.4.1).

Wells #2 and #3 were in Alaska. The true vertical depth of both wells was 7,400 ft. Both wells utilized 15.7 ppg class "G" based cement slurries. A 3 1/2-in. casing was run in in 8 1/2-in. hole in both wells. The results of tests for both wells are presented in Fig. 8.38. We will call these wells as Al80 an Al112.

Well #4, with a vertical wellbore, was in Venezuela and represented a more "conventional casing/hole" configuration. The total depth was 12,900 ft., the bottom hole static temperature *to* 12,600 ft. was 244 °F. The casing size of this well 5 1/2-in. The hole size was 8 1/2-in. 14.0 ppg composite blend cement slurry was used. The calculations used the heat evolution curve at 150 °F which is referred to as Ve150 (Fig. 8.39).

An isothermal cement calorimeter was used for the cement heat of hydration testing. The calorimeter used in the testing was based on the operational principle of the Seebeck Envelope Calorimeter (SEC). It is designed in such way that all heat generated must pass through the walls of the calorimeter. The envelope is maintained at a constant temperature by passing temperature-controlled water through the outer jacket of the calorimeter. Electrical Resonating Diaphragms (ERD) were used to detect all the downhole temperatures. Reliability is of utmost importance because the instrumentation is not retrievable. It was proven that the ERD device can reliably operate continuously at temperatures of up to 480 °F (Dillenbeck et al. 2002).

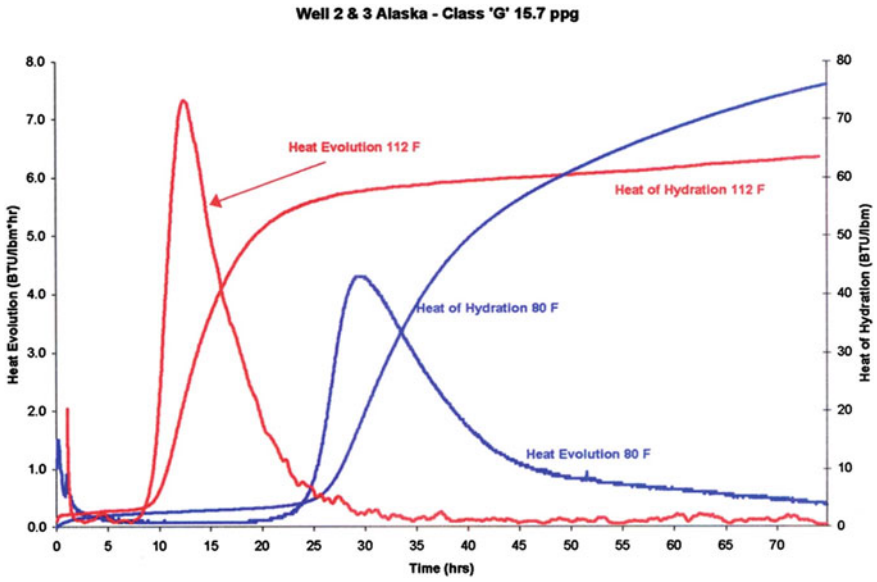

Fig. 8.38 Heat of hydration and heat of evolution per unit of mass as a function of time for two wells (Dillenbeck et al. 2002)

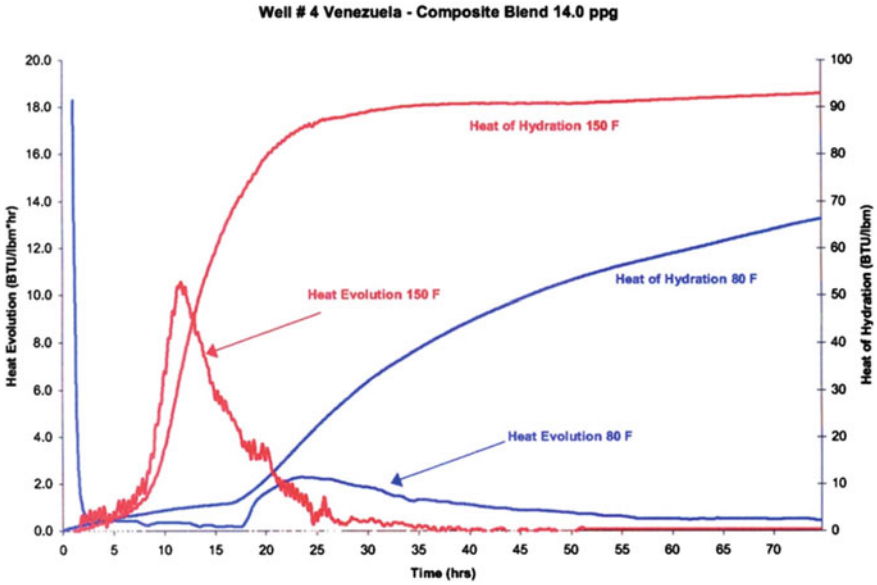

Fig. 8.39 Heat of hydration and heat of evolution per unit of mass as a function of time, Well #4, Venezuela (Dillenbeck et al. 2002)

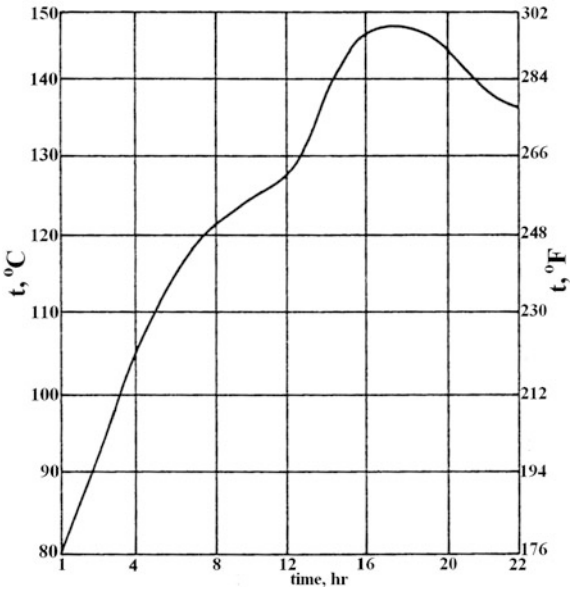

Fig. 8.40 Temperature during WOC (wait of cementing), well 38, depth 2,500 m; Stavropol district, Russia (Proselkov 1975)

8.4.4 Temperature Increase at Cement Hydration

Temperature surveys following the cementing operation are used for locating the top of the cement column behind the casing. Field experience shows that in some cases the temperature anomalies caused by the heat of cement hydration can be very substantial (Fig. 8.40).

However, even in such cases it is very important to predict the temperature increase during the cement setting. This serves to determine the optimal time lapse between cementing and temperature survey. Below we present a semi-analytical formula to estimate the temperature increase versus setting time (Kutasov 2007). This formula describes the transient temperature at the cylinder wall (T_v), while at the surface of the cylinder the radial heat flow rate (into formations) is a quadratic function of time.

$$\left\{\begin{array}{l} T_v(t) = T_i + \dfrac{A_0}{2\pi\lambda}\left[a_0 G_0(t) + a_1 G_1(t) + a_2 G_2(t)\right],\ \Delta T = T_V(t) - T_i, \\ G_0(t) = \ln\dfrac{\left(b + 2d\sqrt{t}\right)^2}{b\left(b + d\sqrt{t}\right)}, \\ G_1(t) = -\ln(b)\left(t + \dfrac{B}{2}\right) - \dfrac{1}{2}t + \ln\left(b + 2d\sqrt{t}\right)\left(2t - \dfrac{B}{2}\right) + \ln\left(b + d\sqrt{t}\right)(B - t), \\ G_2(t) = -\ln(b)\left(t^2 - \dfrac{7}{8}B^2 + Bt\right) - \dfrac{1}{4}\left(3t^2 + Bt\right) + \dfrac{3}{4}B\sqrt{Bt} \\ \qquad + \ln\left(b + 2d\sqrt{t}\right)\left(2t^2 + \dfrac{1}{8}B^2 - Bt\right) - \ln\left(b + d\sqrt{t}\right)(t - B)^2, \\ b = 2.6691, \qquad d = \dfrac{\sqrt{a}}{r_w}, \qquad B = \dfrac{b^2}{d^2} \end{array}\right\}, \tag{8.4.6}$$

where a is the thermal diffusivity of formations.

The time when the temperature increase reaches its maximum value can be determined from the following equation

$$y = \frac{dT_v}{dt} = a_0\frac{dG_o}{dt} + a_1\frac{dG_1}{dt} + a_2\frac{dG_2}{dt} = 0 \tag{8.4.7}$$

Maple 7 software was utilized to compute derivatives in the last equation. The formula is too cumbersome and is not presented here.

To conduct calculations after Eq. (8.4.6) the sections of the $q = q(t)$ curves need to be approximated by a quadratic equation. For this reason tables of q versus t are required. However, only plots of $q = q(t)$ were available (see Figs. 8.37, 8.38, 8.39 and 8.40). We selected values of $q_r = 1$ mW/g = 860.4 cal/(h kg) for the curve Ro77 (Fig. 8.37) and $q_r = 1$ BTU/(lbm h) = 553.1 cal/(h kg) for plots Al80, Al112 and Ve150 (Figs. 8.39 and 8.40). In this case the values of heat flow rates per unit of mass are numerically equal to their dimensionless values. To digitize plots and obtain numerical values of q_D and time we used *Grapher* software.

We used a quadratic regression program to determine the coefficients a_0, a_1 and a_2 (Table 8.53). The values of t_0 were obtained by extrapolation of q_D versus time plots ($q_D\ (t = t_0) \approx 0$). Some input data and results of calculations are presented in Tables 8.51, 8.52, 8.53 and Fig. 8.41.

In Table 8.53 R is the relative accuracy of approximation q_D by a quadratic equation, the time t_m when ΔT reaches its maximum value of $\Delta T_{\max}$ is estimated from Eq. (8.4.7). The maximum value of $\Delta T_{\max}$ is determined from Eq. (8.4.6) at $t = t_m$, and q_{Dm} is the corresponding value q_D.

Example

A temperature survey was conducted to locate the top of the cement column behind the casing. The rate of heat generation is presented in Fig. 8.36 (Curve at

Table 8.51 Input data: bit diameter $D = 8.5$ in., D_{oc} = outside diameter of casing

Reference	Class of cement	D_{oc}, in.	ρ_{cem}, ppg	q_r	A_0, kcal/m·hr
Ro77	G	3.5	15.8	1 mW/g	49.73
Al80	G	3.5	15.7	1 BTU/(lbm·hr)	31.60
Al112	G	3.5	15.7	1 BTU/(lbm·hr)	31.60
Ve150	Composite blend	5.5	14.0	1 BTU/(lbm·hr)	19.78

Table 8.52 Results of calculations of $\Delta T_x = T_v - T_f$ (Eq. 8.4.6), at $t = t_x$, $a_0 = 0$, $a_1^* = a_1$ and $a_2^* = a_2$). Formation: oil-bearing sandstone. Thermal conductivity: 1.46 kcal/(m h °C), thermal diffusivity: 0.0041 m^2/h)

Curve	t^*, h (hour)	$t_x = t^* - t_0$, h (hour)	q_{Dmax}	a_1^*, 1/h (hour)	a_2^*, $(1/h)^2$	t_o, h (hour)s	ΔT_x, °C
Ro77	14.590	9.59	2.291	0.4778	−0.0249	5.0	12.8
Al80	29.737	5.74	4.318	1.6696	−0.1613	24.4	13.2
Al112	12.307	3.61	7.355	4.0782	−0.5653	8.7	18.6
Ve150	11.492	3.79	10.529	5.5533	−0.7322	7.7	17.0

Table 8.53 Values of coefficients a_0, a_1 and a_2, results of calculations (Eq. 8.4.6). Formation: oil-bearing sandstone. Thermal conductivity: 1.46 kcal/(m h °C), thermal diffusivity: 0.0041 m^2/h

Well	a_0	a_1, h^{-1}	a_2, h^{-2}	t, h	R, %	t_m, hs	q_{Dm}	ΔT_{max}, °C
o77	0.205	0.448	−0.0249	4–14.9	2.4	12.1	1.98	13.7
Al80	1.7713	0.8810	−0.0757	4.0–9.8	1.6	8.40	3.83	15.6
Al112	−3.8733	5.8571	−0.7606	2.4–5.3	2.4	5.0	6.40	19.7
Ve150	−1.6355	5.8675	−0.7014	3.4–6.4	2.5	5.7	9.02	19.5

77 °F). The surrounding wellbore formation is sandstone with a thermal conductivity of 1.9 kcal/(m h °C), and a thermal diffusivity of 0.0034 m^2/h.

What are the values of temperature increase ΔT during cement hydration? The input parameters are presented in Tables 8.42 and 8.44, and the Eqs. (8.4.2) and (8.4.6) were used to calculate the values of ΔT and q_D (Fig. 8.41).

It is interesting to note that the maximum values of the temperature increase and the dimensionless heat flow rate do not coincide in time.

8.4.5 Size of the Annulus

From physical considerations it is clear that the maximum temperature anomaly (caused by cement hydration) depends on the actual well radius. For a gauge well the well diameter is equal to the bit size and the amount of cement slurry behind the casing can be estimated. In this case the transient temperatures during cement hydration can be determined from Eq. (8.4.6), provided that all input parameters

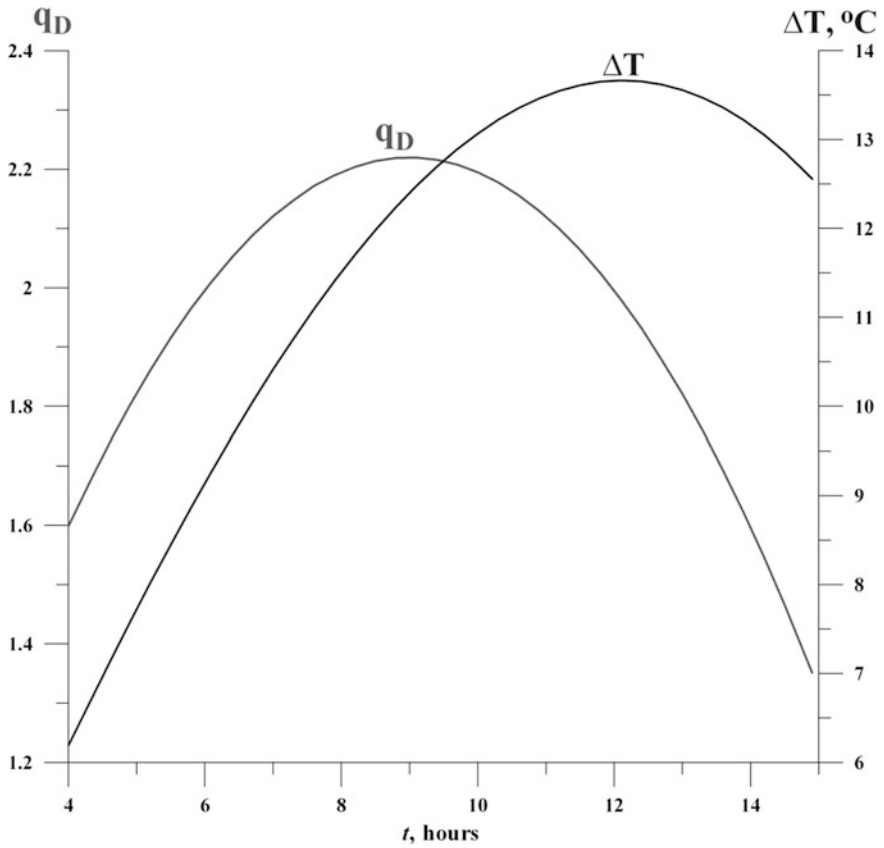

Fig. 8.41 The temperature increase during cement hydration: Curve Ro77, Fig. 8.36

are known. However, when some well sections are washed out, the interpretation of temperature anomalies becomes difficult and a calliper log should be conducted prior to the cementing operations. To demonstrate the impact of the annulus size on the maximum temperature increase we made calculations after Eq. (8.4.6) for the Venezuela well #4 (Fig. 8.39). The well was drilled with a bit size of 8 1/2-in. and the outside diameter of casing is 5 1/2-in. It was assumed that due to washouts the well diameter could be increased by up to 4 in. The value of reference heat flow rate per unit of length A_0 was increased from 19.78 to 59.32 kcal/m h.

The rate of heat generation is presented in Fig. 8.38, the density of cement slurry is $\rho_c = 14.0$ ppg, and the surrounding wellbore formation is sandstone with the following thermal properties $a_f = 0.0034$ m^2/h, $\lambda_f = 1.90$ kcal/h · m · °C. The results of the calculations are presented in Fig. 8.42.

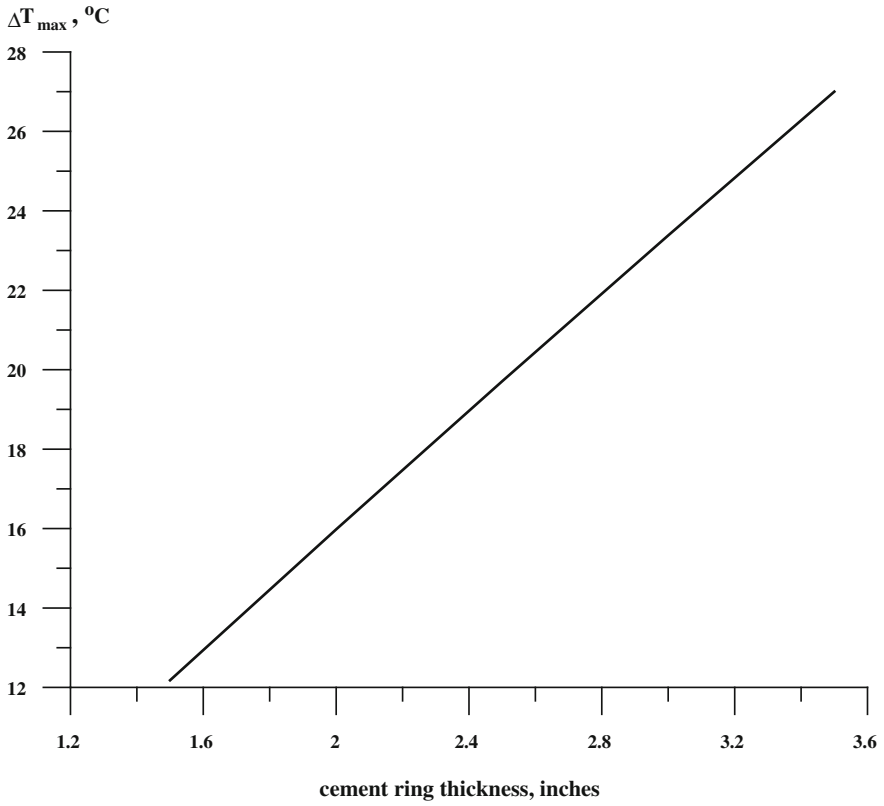

Fig. 8.42 Maximum temperature increase versus cement ring thickness, Venezuela well #4

As can be seen from Fig. 8.42 the hole enlargement significantly affects the maximum value of ΔT. An interesting experimental study of temperature anomalies associated with cement setting behind the casing was conducted by Gretener (1968). In the experimental setting the thickness of the inner annulus could be varied from 1/2 to 3 in., the outer radius was 12 in., and the height was 24 in. In the outer annulus either sand and water (high thermal conductivity) or polyfoam and water (low thermal conductivity) simulated the formations. Maximum temperature anomalies ranging from less than 5 °C to as high as 35 °C were observed during setting of Lone Star class "A" cement and Atlas Portland class "A" cement. The experiments showed that the maximum value of ΔT rises almost linearly with the increase of the cement ring thickness (Gretener 1968).

Table 8.54 The influence of formation thermal properties on the temperature increase during hydration of Class "G" cement. Well Ve150 T = 150 °F (65.6 °C), $r_w = 0.108$ m

Time, $t - t_0$, h (hours)	Sandstone $a = 0.0034$ m^2/h $\lambda = 1.9$ kcal/(h m °C)	Clay $a = 0.0015$ m^2/h $\lambda = 1.3$ kcal/(h m °C)	Clay shale $a = 0.0022$ m^2/h $\lambda = 1.4$ kcal/(h m °C)
	ΔT, °C	ΔT, °C	ΔT, °C
3.5	14.76	15.86	17.07
4.0	15.02	16.22	17.42
4.5	15.16	16.45	17.62
5.0	15.20	16.58	17.72
5.5	15.15	16.60	17.70
6.0	15.02	16.54	17.60
6.5	14.83	16.39	17.41
7.0	14.57	16.17	17.15
7.5	14.25	15.89	16.82
8.0	13.88	15.54	16.41
8.5	13.45	15.13	15.95
9.0	12.98	14.67	15.43
9.5	12.46	14.15	14.85
10.0	11.90	13.59	14.22

8.4.6 Thermal Properties and Temperature of Formations

From Eq. (8.4.6) it follows that the value of ΔT depends on thermal diffusivity and thermal conductivity of formations. We made a set of numerical calculations to estimate the effect of thermal parameters of formations on the transient temperatures during cement hydration. In all cases we used the Ve150 curve (Fig. 8.39). An unexpected outcome of these calculations was that for typical reservoir formations, variations of thermal properties had a small effect on the values of ΔT (Table 8.54). Targhi (1987) approximated the thermal effect of cement hydration by a linear source whose strength is a quadratic function of time. Targhi calculated ΔT (for Portland cements) for practically all possible combinations of bit and casing sizes. It was also shown that the impact of variation of thermal properties on temperature increase is not substantial (Targhi 1987). To determine the effect of formation (ambient) temperatures and pressures on the values of ΔT the rate heat flow $q = q(t)$ should be measured in the laboratory at temperatures and pressures which are close to those in downhole conditions.

8.4.7 Radius of Thermal Influence at Cementing

In Sect. 8.1.1 we used the thermal balance method to calculate the radius of thermal influence (r_{in}) as a function of time during drilling. Similarly, we will use the thermal balance method to evaluate the value of r_{in} for the cement hydration

period. This parameter serves to estimate the degree of thermal disturbance created by the heat of the cement hydration. Section 8.1.1 showed that the dimensionless temperature distribution around the wellbore during drilling fluid circulation can be approximated by the following equation

$$T_D(r_D, t_D) = \frac{T(r,t) - T_f}{T_w - T_f} = 1 - \frac{\ln r_D}{\ln R_{in}}, \quad R_{in} = \frac{r_{in}}{r_w}, \quad r_D = \frac{r}{r_w}, \quad 1 \le r_D < R_{in}, \tag{8.4.8}$$

$$t_D = \frac{\chi t}{r_w^2} = \frac{\lambda t}{c_p \rho r_w^2}. \tag{8.4.9}$$

and the dimensionless cumulative heat flow rate from the wellbore per unit of length (Q_D) was evaluated

$$Q_D = \frac{1}{4} \frac{R_{in}^2 - 2\ln(R_{in}) - 1}{\ln(R_{in})}. \tag{8.4.10}$$

As mentioned above, we obtained semi-analytical Eq. (8.4.6) which describes the borehole wall temperature when the borehole is a cylindrical source with a quadratic function of the heat flow rate per unit of length.

$$q(t) = A_0(a_o + a_1 t + a_2 t^2), \tag{8.4.11}$$

where A_0 is the reference heat flow rate per unit of length.

The cumulative heat flow per unit of length is

$$Q(t) = \int_0^t q(t)\, dt = q_0 t\left(a_0 + \frac{a_1 t}{2} + \frac{a_2 t^2}{3}\right). \tag{8.4.12}$$

The cumulative heat flow per unit of length can also be expressed by as

$$Q = 2\pi \rho c_p r_w^2 (T_v - T_f) Q_D. \tag{8.4.13}$$

Combining Eqs. (8.4.6), (8.4.9), (8.4.10), (8.4.12) and (8.4.13), we obtain an equation to determine the value of R_{in}

$$\frac{R_{in}^2 - 2\ln(R_{in}) - 1}{4\ln(R_{in})} \cdot \frac{a_0 G_0 + a_1 G_1 + a_2 G_2}{a_0 + \frac{a_1}{2} t + \frac{a_2}{3} t^2} = t_D. \tag{8.4.14}$$

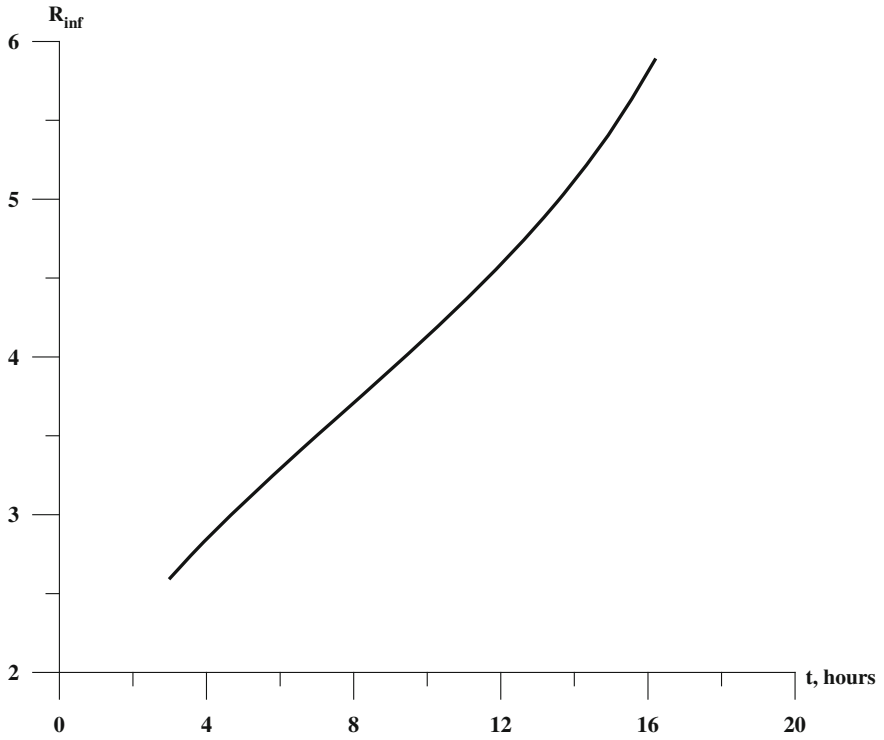

Fig. 8.43 The dimensionless radius of thermal influence versus time, wells Ro77, $r_w = 0.108$ m, $a = 0.0041\ \mathrm{m}^2 \cdot \mathrm{h}^{-1}$

We used the above formula and coefficients a_0, a_1, and a_2 (Table 8.53) to compute the dimensionless radius of thermal influence for well Ro77 (Fig. 8.43).

References

Andaverde J, Verma SP, Santoyo E (2005) Uncertainty estimates of static formation temperatures in boreholes and evaluation of regression models. Geophys J Int 160:1112–1122

API (1982) API specifications for materials and testing for well cements. Dallas, USA

Babu DR (1996) Effect of P-p-T behavior of muds on static pressure during deep well drilling. SPE paper 27419. SPEDC 6:91–97

Barker JW, Gomez RK (1989) Formation of hydrates during deepwater drilling operations. J Pet Technol 3:297–301

Bearden WG (1959) Effect of temperature and pressure on the physical properties of cement. In: Oil-well cementing practices in U.S., API, NY, pp 49–59

Beck AE, Balling N (1988) Determination of virgin rock temperatures. In: Hänel R, Rybach L, Stegena L (eds) Handbook of terrestrial heat-flow density determination. Kluwer Academic Publisher, Dordrect, pp 59–85

Beirute RM (1991) A circulating and shut-in well-temperature—profile simulator. J Pet Technol 9:1140–1146
Bejan A (1993) Heat transfer. Wiley, USA
Billy C, Dick JWL (1974) Naturally occurring gas hydrates in the Mackenzie Delta, N.W.T. Bull Can Pet Geol 22:340–353
Bogomolov GV, Tcibulya LA, Atroshenko PP (1972) Geothermal zones of the Belarus. Science and Technics, Minsk (in Russian)
Bondarev EA, Babe GD, Groysman AG, Kanibolotskiy MA (1976) Mechanics of hydrate formation in gas flows. Nauka, Novosibirsk (in Russian)
Bradford BB (1985) Attention to primary cementing practices leads to better jobs. Oil Gas J 21(Oct):59–63
Bullard EC (1947) The time necessary for a borehole to attain temperature equilibrium. Mon Not R Astron Soc, Geophys Suppl 5:127–130
Burnham CW, Hollaway JH, Davis NF (1969) Thermodynamic properties of water to 1,000 °C and 10,000 Bars. Geol Soc Am Spec Pap 132
Calvert DG, Griffin TJ Jr (1998) Determination of temperatures for cementing in wells drilled in deep water. In: SPE paper 39315 presented at the 1998 IADC/SPE Drilling Conference, Dallas, 3–6 Mar 1998
Cao S, Lerche I, Hermanrud C (1988) Formation temperature estimation by inversion of borehole measurements. Geophysics 53:979–988
Carslow HS, Jaeger JC (1959) Conduction of heat in solids, 2nd edn. Oxford University Press, Oxford
Churchill SW, Gupta JP (1977) Approximations for conduction with freezing or melting. Int J Heat Mass Transf 20:1251–1253
Covan M, Sabins F (1995) New correlations improve temperature predictions for cementing and squeezing. Oil Gas J, 53–58 (Aug 21)
Craft BC, Holden WR, Graves ED Jr (eds) (1962) Well design: drilling and production. Prentice-Hall, New Jersey
Davis SH, Faulk JH (1952) Have waiting—on cement practices kept pace with technology? Drilling and Production Practices, API, 180
Deykin VV, Kogan EV, Proselkov YM (1973) Film heat transfer coefficient in wells during drilling. In: Mud circulation and wells completion technology, Nedra, Moscow, 3–7
Dillenbeck RL, Heinold T, Rogers MJ, Mombouurquette IG (2002) The effect of cement heat hydration on the maximum annular temperature of oil and gas wells. In: SPE paper 77756 presented at the SPE annual technical conference and exhibition
Djamalova AS (1969) Heat flow of dagestan. Nauka, Moscow (in Russian)
Dowdle WL, Cobb WM (1975) Static formation temperatures from well logs—an empirical method. J Pet Technol 27(11):1326–1330
Drury ML (1984) On a possible source of error in extracting equilibrium formation temperatures from boreholes BHT Data. Geothermics 13:175–180
Dyakonov DI (1958) Geothermics in oil geology. Gostoptekhizdat, Moscow
Edwardson ML, Girner HM, Parkinson HR, Williams CD, Matthews CS (1962) Calculation of formation temperature disturbances caused by mud circulation. J Pet Technol 14:416–426
Eppelbaum LV, Kutasov IM (2006a) Temperature and pressure drawdown well testing: similarities and differences. J Geophys Eng 3(1):12–20
Eppelbaum LV, Kutasov IM (2006b) Determination of formation temperatures from temperature logs in deep boreholes: comparison of three methods. J Geophys Eng 3(4):348–355
Eppelbaum LV, Kutasov IM (2011) Determination of the formation temperature from shut-in logs: radius of thermal influence. J Appl Geophys 73:278–282
Eppelbaum LV, Kutasov IM (2013) Cylindrical probe with a variable heat flow rate: a new method for determination of the formation thermal conductivity. Cent Eur J Geosci 5(4):570–575

Espinosa-Paredes G, Morales-Diaz A, Olea-Gonzales U, Ambriz-Garcia JJ (2009) Application of proportional-integral control for the estimation of static formations temperatures in oil wells. Mar Pet Geol 26:259–268

Fomin S, Chugunov V, Hashida T (2003) Analytical modelling of the formation temperature stabilization during the borehole shut-in period. Geophys J Int 155:469–478

French FR, McLean MR (1993) Development drilling problems in high-pressure reservoirs. J Pet Technol 45(8):772–777

Gold LW, Lachenbruch AH (1973) Thermal conditions in permafrost: A review of North American literature. In: Permafrost (North American Contribution), 2nd international conference, 13–28 July, Yakutsk, USSR, Nat Acad Sci, Washington DC, p 10

Goodman MA (1978) World oil's handbook of Arctic well completions. Gulf Publication Co, Houston

Goodman MA, Franklin LJ (1982) Thermal model of a new concept for hydrate control during drilling. In: Proceedings of the 4th Canadian permafrost conference, Calgary, Alberta, pp 349–355, 2–6 March 1982

Goodman MA, Mitchell RF, Wedelich H, Galate JW, Presson DM (1988) Improved circulating temperature correlations for cementing. In: SPE paper 18029 presented at the 63rd SPE annual technical conference and exhibition, Houston, Texas, 2–5 Oct 1988

Gretener PE (1968) Temperature anomalies in wells due to cementing of casing. J Pet Technol 2:147–151

Gritsenko AI, Makogon YF (1984) Drilling and operation of gas wells in the presence of natural gas hydrates. In: Transactions of the 4th International permafrost conference, 17–22 July, 1983, Fairbanks, Alaska. Nat Acad Sci, Washington DC, pp 167–172

Gryaznov GS (1978) Designs of gas wells in permafrost Areas. Nedra, Moscow, 136 p (in Russian)

Guillot F, Boisnault JM, Hujeux JC (1993) A cementing temperature simulator to improve field practice. In: SPE paper 25696 presented at the 1993 SPE/ IADC drilling conference, Amsterdam, 23–25 Feb 1993

Hasan AR, Kabir CS (1994) Static reservoir temperature determination from transient data after mud circulation. SPE Drill Completion 3:17–24

Hawkins MF Jr (1956) A note on the skin effect. Trans AIME 207:356–357

Hoberock LL, Thomas DC, Nickens HV (1982) Here's how compressibility and temperature affect bottom-hole mud pressure. Oil Gas J 80(3):159–164

Holder GD, Angert PF, John VT, Yen S (1982) A thermodynamic evaluation of thermal recovery of gas from hydrates in the Earth. J Pet Technol 34:1127–1132

Holmes CS, Swift SC (1970) Calculation of circulating mud temperatures. J Pet Technol (6):670–674

Honore RS Jr., Tarr BA, Howard JA, Lang NK (1993) Cementing temperature predictions based on both downhole measurements and computer predictions: a case history. In: SPE paper 25436 presented at the production operations symposium, Oklahoma City, OK, USA, 21–23 Mar 1993

Hubbard JT (1984) How temperature and pressure affect clear brines. Pet Eng Int 4:58–64

Jacob CE, Lohman SW (1952) Non-steady flow to a well of constant drawdown in an extensive aquifer. Trans Am Geophys Un, 559–564

Jaeger JC (1956) Numerical values for the temperature in radial heat flow. J Math Phys 34:316–321

Jaeger JC (1961) The effect of the drilling fluid on temperature measured in boreholes. J Geophys Res 66:563–569

Jones RR (1986) A novel economical approach for accurate real time measurement of wellbore temperature. In: SPE Paper 15577, Richardson, Texas, USA

Judge A (1982) Natural gas hydrates in Canada. In: Proceedings of the 4th Canadian permafrost conference, Calgary, Alberta, pp 320–328, 2–6 March 1982

Judge AS, Taylor AE, Burgess M (1979) Canadian geothermal data collection—Northern wells 1977–78. Geothermal series, 11, Earth Physics Branch, Energy, Mines and Resources, Ottawa

Judge AS, Taylor AE, Burgess M, Allen VS (1981) Canadian geothermal data collection—Northern wells 1978–80. Geothermal Series, 12, Earth Physics Branch, Energy, Mines and Resources, Ottawa

Kårstad E, Aadnøy BS (1998) Density behavior of drilling fluids during high pressure high temperature drilling operations. In: SPE Paper 47806 presented at the 1998 IADC/SPE Asia Pacific drilling conference, Jakarta, Indonesia, 7–9 Sept 1998

Katz DL (1945) Predictions of conditions for hydrate formation in natural gases. Trans AIME 160:141

Keller HH, Couch EJ, Berry PM (1973) Temperature distribution in circulating mud columns. Soc Pet Eng J (2):23–30

Kritikos WP, Kutasov IM (1988) Two-point method for determination of undisturbed reservoir temperature. Formation Eval 3(1):222–226

Kuliev SM, Esman BI, Gabuzov GG (1968) Temperature regime of the drilling wells. Nedra, Moscow

Kutasov IM (1968) Determination of time required for the attainment of temperature equilibrium and geothermal gradient in deep boreholes. Freiberger Forshungshefte C238:55–61

Kutasov IM (1976) Thermal parameters of wells drilled in Permafrost regions. Nedra, Moscow

Kutasov IM (1987) Dimensionless temperature, cumulative heat flow and heat flow rate for a well with a constant bore-face temperature. Geothermics 16(2):467–472

Kutasov IM (1988a) Prediction of permafrost thickness by the "Two Point" method. In: Proceedings of the 5th International Confernce on Permafrost, 2, Tapir Publication, Trondheim, Norway, pp 965–970

Kutasov IM (1988b) Empirical correlation determines downhole mud density. Oil Gas J, 61–63 (12 Dec)

Kutasov IM (1989) Application of the Horner method for a well produced at a constant bottomhole pressure. Formation Eval 3, 90–92

Kutasov IM (1991) Correlation simplifies obtaining brine density. Oil Gas J, 48–49 (5 Aug)

Kutasov IM (1993) Tables simplify determining temperature around a shut-in well. Oil Gas J, 85–87 (26 July)

Kutasov IM (1998) Melting around a cylindrical source with a constant wall temperature. In: Proceedings Institute of Mathematics International Conference 'Mathematics of Heat Transfer' (University of Bradford, UK, 29 June–1 July 1998)

Kutasov IM (1999) Applied geothermics for petroleum engineers. Elsevier, Amsterdam

Kutasov IM (2002) Method corrects API bottom-hole circulating-temperature correlation. Oil Gas J (15 July)

Kutasov IM (2003) Dimensionless temperature at the wall of an infinite long cylindrical source with a constant heat flow rate. Geothermics 32:63–68

Kutasov IM (2007) Dimensionless temperatures at the wall of an infinitely long, variable-rate, cylindrical heat source. Geothermics 36:223–229

Kutasov IM, Bates TR (1980) Arctic drilling technology in the Soviet Union. In: Paper 80-Pet-73, presented at the 1980 ASME energy technical conference and exhibition, New Orleans, 3–7 Feb 1980

Kutasov IM, Eppelbaum LV (2003) Prediction of formation temperatures in permafrost regions from temperature logs in deep wells—field cases. Permafrost Periglac Process 14(3):247–258

Kutasov IM, Eppelbaum LV (2005a) Determination of formation temperature from bottom-hole temperature logs—a generalized Horner method. J Geophys Eng 2:90–96

Kutasov IM, Eppelbaum LV (2005b) Drawdown test for a stimulated well produced at a constant bottomhole pressure. First Break 23(2):25–28

Kutasov IM, Eppelbaum LV (2009) Estimation of the geothermal gradients from singular temperature log-field cases. J Geophys Eng 6(2):131–135

Kutasov IM, Eppelbaum LV (2010) A new method for determination of formation temperature from bottom-hole temperature logs. J Pet Gas Eng 1(1):1–8

Kutasov IM, Eppelbaum LV (2011) Recovery of the thermal equilibrium in deep and superdeep wells: utilization of measurements while drilling data. In: Proceedings of the 2011 Stanford Geothermal Workshop, Stanford, USA, SGP-TR-191, 1–7

Kutasov IM, Eppelbaum LV (2012) New method evaluated efficiency of wellbore stimulation. Oil Gas J 110(8):22–24

Kutasov IM, Kagan M (2003) Cylindrical probe with a constant temperature—determination of the formation thermal conductivity and contact thermal resistance. Geothermics 32:187–193

Kutasov IM, Targhi AK (1987) Better deep-hole BHCT estimations possible. Oil Gas J, 71–73 (May 25)

Kutasov IM, Lubimova EA, Firsov FV (1966) Rate of recovery of the temperature field in wells on Kola Peninsula. In: Problems of the heat flux at depth, Nauka, Moscow, 74–87 (in Russian)

Kutasov IM, Atroshenko PP, Tcibulya LA (1971) The use of temperature logs for predicting the static formation temperature. Dokl Acad Sci Belorussia 15(3):266–269 (in Russian)

Kutasov IM, Balobayev VT, Demchenko RY (1977) Method of "joining" of solutions in the determination of a plane and a cylindrical phase interface in the Stefan problem. Eng-Phys J (Inzhenerno-Fizicheskii Zhurnal) 33:148–152

Lachenbruch AH, Brewer MC (1959) Dissipation of the temperature effect of drilling a well in Arctic Alaska. US Geol Surv Bull 1083-C:74–109

Leblanc Y, Pascoe LJ, Jones FW (1981) The formation stabilization of the borehole. Geophysics 46:1301–1303

Lin S (1971) One-dimensional freezing or melting process in a body with variable cross-sectional area. Int J Heat Mass Transf 14:153–156

Lunardini VJ (1988) Heat conduction with freezing or thawing. CRREL Monograph 88-1, Hanover, USA, pp 187–214

MacAndrew R, Parry N, Prieur J-M, Wiggelman J, Diggins E, Guicheney P, Stewart A (1993) Drilling and testing hot, high-pressure wells. Oilfield Rev 4–5:15–23

McMordie WC Jr, Bland RG, Hauser JM (1982) Effect of temperature and pressure on the density of drilling fluids. In: SPE Paper 11114 presented at the 57th Annual Fall Technical Conference and Exhibition, New Orleans, LA, 26–29 Sept 1982

Mekhtiev SHF, Mirzajanzadeh AKH, Aliyev SA, Bagbanly EA, Motyakov VI (1960) Geothermal regime of oil and gas deposits. Azerneftneshr, Baku (in Russian)

Middleton MF (1979) A model for bottom-hole temperature stabilization. Geophysics 44:1458–1462

Mitchell RF (1981) Downhole temperature prediction for drilling geothermal wells. In: Proceedings of the international conference on geothermal drilling and completion technique, Albuquerque, New Mexico, 21–23 January 1981

New Cement Test Schedules Issued (1977) Oil Gas J, July 25, 179–182

Palmer A (1978) Thawing and the differential settlement of the ground around oil wells in permafrost. In: The USSR contributed to the 2nd international conference, 13–28 July, Nat Acad Sci, Washington DC, pp 619–624

Perkins TK, Rochon JA, Knowles CR (1974) Studies of pressure generated upon refreezing of thawed permafrost around a well bore. J Pet Technol 26(10):1159–1166

Pooladi-Darvish M (2004) Gas production from hydrates reservoirs and gas modelling. J Pet Technol 6:65–71

Potter RW II, Brown DL (1977) The volumetric properties of aqueous sodium chloride solutions from 0° to 500 °C at pressures up to 2000 bars based on a regression of available data in literature. In: Pleminary tables for NaCl solutions, Geol Surv Bull 1421-C, U.S. Gov't Printing Office, Washington, DC

Proselkov YM (1975) Heat transfer in wells. Nedra, Moscow (in Russian)

Ramey HJ Jr (1962) Wellbore heat transmission. J Pet Technol 14(4):427–435

Raymond LR (1969) Temperature distribution in a circulating drilling fluid. J Pet Technol, 333–341

Romero J, Loizzo M (2000) The importance of hydration heat on cement strength development for deep water wells. In: SPE paper 62894 presented at the 2000 SPE annual technical conference and exhibition, Dallas, Texas, 1–4 Oct 2000

Roux B, Sanyal SK, Brown SL (1980) An improved approach to estimating true reservoir temperature from transient temperature data. In: SPE paper 8888 presented at the 1980 SPE California Reg Meet, Los Angeles, 9–11 April 1980

Rusakov VG, Kononov Yu I (1976) The first results of field thermophysical investigations in a drilling well at natural gas deposit "Medvezhe". In: Problems of geocryology in works of young scientists and specialists, Yakutsk (in Russian)

Sengul MM (1983) Analysis of step-pressure tests. In: SPE paper 12175 presented at the 58th annual technical conference and exhibition, San Francisco, California, 5–8 Oct 1983

Shell F, Tragesser AF (1972) API is seeking more accurate bottom hole temperatures. Oil Gas J, 72–79 (July)

Shen PY, Beck AE (1986) Stabilization of bottom hole temperature with finite circulation time and fluid flow. Geophys J R Astron Soc 86:63–90

Sloan ED (1991) Natural gas hydrates. J Pet Technol 43(12):1414–1417

Smith DK (1974) Cementing. Monograph series 4, SPE, Dallas, USA

Sorelle RR, Jardiolin RA, Buckley P (1982) Mathematical field model predicts downhole density changes in static drilling fluids. In: SPE paper 11118 presented at the 57th Annual Fall Technical Conference and Exhibition of the SPE, New Orleans, LA, 26–29 Sept 1982

Sparrow SW, Ramadhyani S, Patankar SV (1978) Effect of subcooling on cylindrical melting. J Heat Transf 100:395–402

Sump GD, Williams BB (1973) Prediction of wellbore temperatures during mud circulation and cementing operations. J Eng Ind, 1083–1092

Swayze MA (1954) Effect of high temperature and pressure on cements. Oil Gas J (02 Aug)

Targhi AK (1987) Temperatures regime of deep wells during cementing (prediction of static, circulating, and shut-in temperatures; Evaluation of the thermal effects of cement hydration). PhD Thesis, Louisiana Tech University

Taylor AE (1978) Temperatures and heat flow in a system of cylindrical symmetry including a phase boundary. Geothermal Series, 7, Ottawa, Canada

Taylor AE, Burgess M, Judge AS, Allen VS (1982) Canadian geothermal data collection—Northern wells 1981. Geothermal series, 13, Earth Physics Branch, Energy, Mines and Resources, Ottawa

Thompson M, Burgess TM (1985) The prediction of interpretation of downhole mud temperature while drilling. SPE Paper 14180, Richardson, Texas, USA

Tien LC, Churchill SW (1965) Freezing front motion and heat transfer outside an infinite isothermal cylinder. AICE J 11(5):790–793

Timko DJ, Fertl WH (1972) How downhole temperatures and pressures affect drilling. World Oil 175:73–78

Tragesser AF, Crawford PB, Crawford HR (1967) A method for calculating circulating temperatures. Jour. Pet Tech, 1507–1512

Tsytovich NA (1975) The mechanics of frozen ground. Scripta Book Company, Washington DC, pp 8–250

Van Everdingen AF, Hurst W (1949) The application of the Laplace transformation to flow problems in reservoirs. Trans AIME 186:305–324

Venditto JJ, George CR (1984) Better wellbore temperature data equals better cement jobs. World Oil 2:47–50

Wooley GR, Giussani AP, Galate JW, Wederlich HF, III (1984) Cementing temperatures for deep-well production liners. In: SPE paper 13046 presented at the 59th Annual Technical Conference and Exhibition, Houston, Texas, 16–19 Sept 1984

Wilhelm H, Baumann C, Zoth G (1995) Some results of temperature measurements in KTB main borehole, Germany. Geothermics 24(1):101–113

Wooley GR (1980) Computing downhole temperatures in circulation, injection, and production wells. J Pet Technol, 1509–1522

Chapter 9
Temperature Analyses in Hydrology

Groundwater is one of the most valuable and widely available natural resources, because it is present practically everywhere. Groundwater is also an essential component of the water cycle and underground hydrological systems. Groundwater plays an extremely important role in the supply of drinking water, water for agriculture, water for industry, etc. Given the importance of this natural resource it is not surprising that problems of hydrology and hydrogeology have attracted significant attention on the part of scientists. Processes related to formation of typical hydrological systems, their evolution, methods of analysis, identification of their major characteristics, etc. have been discussed in numerous studies (Hubbert 1969; Bear 1972; Cheremensky 1977; Freeze and Cherry 1979; Eriksson 1985; Simmers 1988; Lerner et al. 1990; Domenico and Schwartz 1998).

Thermal field analysis in hydrogeology may be applied to solving the following problems:

1. Separation of geological sections, to reveal water-bearing horizons and aquicludes and determining their location.
2. Determination of filtration velocity of underground water at various depths and qualitative estimates of filtration properties in the zone of water exchange.
3. Determination of the direction of flow of underground water.
4. Searching and prospecting for thermal water.
5. Identification of water-bearing horizons, fault zones, karst terranes and estimates of the karst influence on the surrounding rocks.
6. Investigation of local and regional hydrogeological specificities of artesian basins and finding areas of water drainage and unloading water-bearing complexes.
7. Analysis of conditions of generation and dynamics of underground water.
8. Discovering hydrodynamic zones.

L. Eppelbaum et al., *Applied Geothermics*, Lecture Notes in Earth System Sciences,
DOI: 10.1007/978-3-642-34023-9_9, © Springer-Verlag Berlin Heidelberg 2014

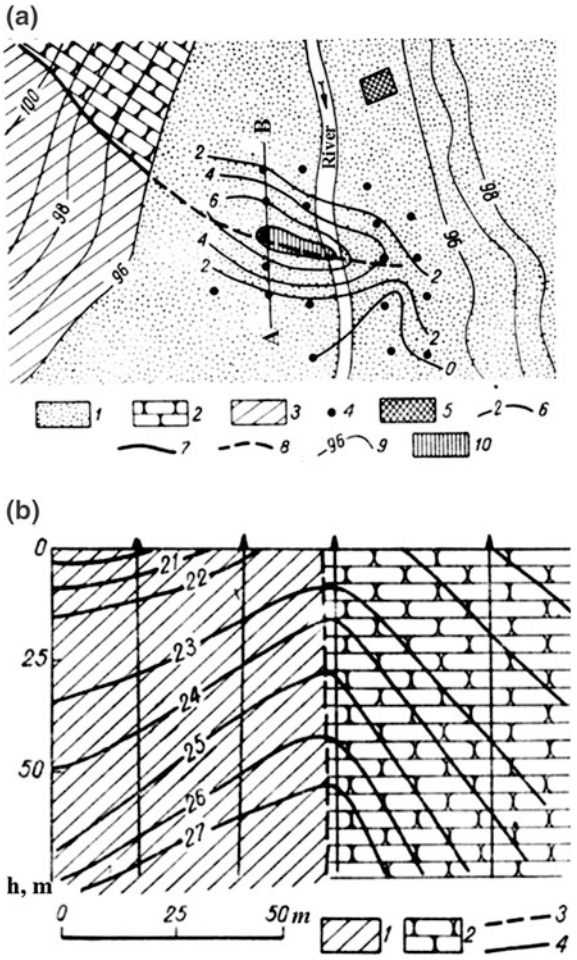

Fig. 9.1 **a** Characteristics of the unloading bed of water pressure on the map of thermoisoclines (after Semenova et al. 1964). (*1*) Alluvial sands (*2*) sandstones (*3*) clays (*4*) boreholes (*5*) thermometric station (*6*) thermoisoclines, fault *line*: (*7*) by geological data (*8*) by thermal survey (*9*) relief isolines (m) (*10*) unloading bed of underground water. **b** Characteristics of the unloading bed of water pressure on the map of thermoisoclines (after Semenova et al. 1964). (*1*) Clays (*2*) sandstones (*3*) proposed fault *line* (*4*) isotherms °C

Let's consider an example of temperature data analysis to detect the focus of unloading of water pressure and fault locations (Fig. 9.1a, b).

Figure 9.1a shows a map of equal deviations of temperature from the normal values of the thermal field of the region (map of thermoisoclines) at a selected depth which can be used to detect the location of faults and the focus of unloading of underground water. Reference data from a basis borehole was also used in this investigation. The temperature difference between the reference thermal field and thermal field in the water boreholes at different corresponding depths was utilized to plot the map of thermoisoclines. The maximum temperature in this map is linked to the focus of unloading which is associated with a tectonic fault (Fig. 9.1a, b). The location of fault zones and unloading beds may be detected by geothermal profiles (Cheremensky 1977).

9.1 The Horner Method and Its Modifications (Permeability and Skin Factor)

9.1.1 *Effect of Vertical and Horizontal Water Movements on Temperature Profiles*

Known analytical solutions (Bredehoeft and Papadopulos 1965; Lubimova et al. 1965; Osterkamp and Gosink 1984; Hänel et al. 1988) describing the vertical and horizontal steady-state flow of water and heat through an isotropic, homogeneous, porous and saturated horizontal layer can be used to estimate the effect of water flow on the temperature regime of formations. Consider a layer with the thickness of h and let z be the vertical coordinate axis taken as positive downward. Let us assume that the top ($z = 0$) and the bottom ($z = h$) of this layer are maintained at constant temperatures: $T(0) = T_1$ and $T(h) = T_h$. For the case of a constant vertical flow of fluid the one-dimensional, steady-state, heat transfer equation is (Bear 1972)

$$\frac{\partial^2 T}{\partial z^2} - \alpha v \frac{\partial T}{\partial z} = 0, \tag{9.1.1}$$

where v is the constant vertical velocity of water flow and α is a parameter that depends on the thermal properties and the porosity of the medium.

The solution of Eq. (9.1.1) for the given boundary conditions: $T(0) = T_1$ and $T(h) = T_h$ (Bredehoeft and Papadopulos 1965) is

$$T(z, v) = T_1 + \Delta T \left[\frac{\exp(avz) - 1}{\exp(avh) - 1}\right], \quad \Delta T = T_h - T_1. \tag{9.1.2}$$

For $v = 0$

$$T(z, v = 0) = T_1 + \Delta T \frac{z}{h} \tag{9.1.3}$$

and the temperature disturbance $\Delta T(z)$ due to vertical water flow from Eqs. (9.1.2) and (9.1.3) is

$$\delta T(z) = T(z, v) - T(z, v = 0) = \Delta T \left[\frac{\exp(avz) - 1}{\exp(avh) - 1} - \frac{z}{h}\right]. \tag{9.1.4}$$

The total heat flow density q_t which is the sum of conductivity of the heat-flow density q_d and the convective heat flow density q_v (Hänel et al. 1988) is

$$q_t = q_d + q_v = -\lambda_r \frac{T_h - T(z)}{h} - \phi \rho_w c_w v[T(z) - T_h], \tag{9.1.5}$$

where ϕ is the porosity, ρ_w is the water density, c_w is the specific heat of water, and λ_r is the thermal conductivity of water-saturated rock.

The maximum value of q_t occurs at $z = 0$ for an upward water flow

$$q_{t\max} = \left| \lambda_r \frac{T_h - T_z}{h} \right| + \rho_w c_w v[T_h - T_1]. \tag{9.1.6}$$

For the case of constant horizontal flow in a horizontal slab, the two-dimensional steady-state heat transfer equation for a saturated, homogeneous and isotropic porous medium is

$$\frac{\partial^2 T}{\partial z^2} - \alpha u \frac{\partial T}{\partial z} = 0, \tag{9.1.7}$$

where u is the constant horizontal velocity of water flow. When $\partial T/\partial x$ is constant and the boundary conditions are

$$T(z = h) = T_1, \quad T(z = -h) = T_2 \tag{9.1.8}$$

then (Osterkamp and Gosink 1984)

$$T(z) = \frac{\alpha u}{2} \frac{\partial T}{\partial x} \left(z^2 - h^2\right) + \frac{T_1 - T_2}{2} hz + \frac{T_1 + T_2}{2}. \tag{9.1.9}$$

Application of Eq. (9.1.9) requires knowledge of ∂T/∂x. Therefore, temperature measurements in two wells are needed to determine the horizontal temperature gradient.

9.1.2 Application of the Horner Method

The determination of physical properties of reservoir fluids, the calculation of hydrocarbon volumes (estimates of oil and gas formation volume factors, gas solubility), predictions of likely gas hydrate zones, well log interpretation, determination of heat flow density, and the evaluation of geothermal energy resources require data on the undisturbed formation temperature. In most cases bottom-hole temperature surveys are used to determine the temperature of the Earth's interior.

The objective of this section is to suggest a new approach to utilizing bottom-hole temperature logs in deep wells and to present a working formula for determining the undisturbed formation temperature. We restrict the discussion to the Horner method, which is often used in processing field data. The condition of material balance was used previously to describe the pressure build-up for wells produced at constant bottomhole pressure (Kutasov 1989). The build-up pressure equation was derived on the basis of an initial condition approximating the

pressure profile in the wellbore and in the reservoir at the time of shut-in. It was shown that a modified Horner method could be used to estimate the initial reservoir pressure and formation permeability. This methodology was elaborated in Kutasov and Eppelbaum (2005).

In many cases, the shut-in time (the time since the end of mud circulation, Δt) or the duration of the mud circulation period (t_c) cannot be estimated with sufficient accuracy from well reports. In these cases methods of correcting the bottomhole temperature data for the uncertainty in determining values of Δt and t_c can be utilized (Majorowicz et al. 1990; Waples and Ramly 2001; Waples et al. 2004).

For reservoirs with low formation permeability the duration of the test may require a long period of time and it can be difficult to maintain a constant flow rate. The developed working equations (Kutasov et al. 2008) enable us to process field data when the flow rate at the 'active' well is a quadratic function of time. At present the type-curve matching technique is used to estimate the porosity–total compressibility product and formation permeability from interference well tests. The disadvantage of this method is that only 2–3 values of pressure drops can be used. A more effective method for processing results of well interference tests is suggested (Kutasov et al. 2008) where all pressure drop points are used to obtain averaged values of formation hydraulic diffusivity and permeability.

9.1.2.1 Determination of the Formation Temperature

The thermal properties of formations (Kappelmeyer and Hänel 1974; Somerton 1992; Vosteen and Schellschmidt 2003) and initial formation temperature need to be known to evaluate the energy capacity of geothermal reservoirs. Due to the similarity of Darcy's and Fourier's laws, the same differential diffusivity equation describes the transient flow of incompressible fluid in a porous medium and heat conduction in solids. As a result, there is a correspondence between the following parameters: volumetric flow rate, pressure gradient, mobility (the permeability and hydrodynamic viscosity ratio), the hydraulic diffusivity coefficient and heat flow rate, the temperature gradient, thermal conductivity and thermal diffusivity. Thus, it is reasonable to assume that the techniques and data processing procedures used in pressure well tests can also be applied to temperature well tests (Muskat 1946; Carslaw and Jaeger 1959). Generally the mathematical model of pressure well tests is based on a presentation of the borehole as an infinitely long linear source with a constant fluid flow rate in an infinite-acting homogeneous reservoir. For this case the well-known solution of the differential diffusivity equation is expressed through the exponential integral (Carslaw and Jaeger 1959). However, when performing temperature well testing, the borehole cannot be considered as an infinitely long linear source of heat. This is due to low values of thermal diffusivity of formations (in comparison with the hydraulic diffusivity) and corresponding low values of drilling fluid circulation and shut-in dimensionless times (t_{cD} and t_{sD}):

$$t_{cD} = \frac{at_c}{r_w^2}, \quad t_{sD} = \frac{at_s}{r_w^2}. \tag{9.1.10}$$

As was shown (Kutasov 2003) the convergence of solutions of the diffusivity equation for cylindrical and linear sources occurs at a dimensionless time of about 500.

In some cases, the values of t_{cD} and t_{sD} are large and the logarithmic approximation (with some accuracy) of the *Ei*-function can be used (Eq. 8.2.46). Then

$$T_s(r_w, t_s) = T_f + M \ln\left(\frac{t_s + t_c}{t_s}\right), \quad M = \frac{q}{4\pi\lambda}. \tag{9.1.11}$$

Theoretically only two measurements of shut-in temperature are needed to determine the value of the formation temperature T_f. However, usually a semilog plot is used to obtain the value of T_f. In practice the latter relationship (Horner plot) is often used as an extrapolation formula (e.g., Lachenbruch and Brewer 1959). In most cases, the dimensionless circulation and shut-in times are small and the generalized Horner method should be used (Eq. 8.2.44).

9.1.2.2 Determination of Formation Permeability and Skin Factor

The forecasting of fluid flow rate of water production and water injection geothermal wells requires estimates of mobility (formation permeability and fluid viscosity ratio), porosity, total formation compressibility, skin factor, and initial reservoir pressure (Earlougher 1977; Elder 1981). In petroleum and geothermal reservoir engineering, pressure and flow well tests are routinely conducted to determine these parameters (Earlougher 1977; Lee 1982; Prats 1982; Edwards et al. 1982; Horne 1995). As mentioned above, the mathematical model used for pressure and flow well tests is based on the presentation of the borehole as an infinitely long linear source with a constant fluid flow rate in an infinite-acting homogeneous reservoir. For this case the well-known solution of the differential diffusivity equation is expressed through the exponential integral (Carslaw and Jaeger 1959).

The basic equation that describes the pressure distribution around an infinitely long linear source with a constant fluid flow rate is

$$p(r, t) = p_i + \frac{q\mu}{4\pi kh} Ei\left(-\frac{\phi\mu c r^2}{4kt}\right). \tag{9.1.12}$$

Using the principle of superposition we obtain a basic equation for the shut-in borehole pressure

$$p_{sw}(r_w, t_s) = p_i + \frac{q\mu}{4\pi kh} Ei\left(-\frac{\gamma\phi\mu c_t r_w^2}{4k(t_c + t_s)}\right) - \frac{q}{4\pi\lambda} Ei\left(-\frac{\gamma\phi\mu c_t r_w^2}{4t_s}\right). \quad (9.1.13)$$

The dimensionless values of the drilling mud circulation and shut-in times are usually very large:

$$t_{cD} = \frac{kt_c}{\gamma\phi\mu c_t r_w^2}, \qquad t_{sD} = \frac{kt_s}{\gamma\phi\mu c_t r_w^2}. \quad (9.1.14)$$

and the logarithmic approximation of the *Ei*-function can be used. Then Eq. (9.1.14) can be rewritten:

$$p_{sw}(r_w, t_s) = p_i - m \ln\left(\frac{t_c + t_s}{t_s}\right), \qquad m = \frac{q\mu}{4\pi kh}. \quad (9.1.15)$$

The above equation describes a straight line with an intercept p_i and slope $-m$.

Currently oilfield (practical) units are typically used to measure and process field data. The dimensions of the parameters are: $[q]$ = standard barrel per day (STB/D), $[B]$ = RB/STB, $[k]$ = md (millidarcy), $[p]$ = psi (pound-force per square inch), $[t]$ = h, $[h]$ = ft, $[\mu]$ = cp, $[c_t]$ = 1/psi, $[r_w]$ = ft, $[\phi]$ = fraction, and $[\eta]$ = ft^2/h. STB is one barrel at standard conditions (p = 14.7 psi, T = 60 °F) and RB is one barrel at reservoir pressure and temperature. Equation (9.1.5) in oilfield units is transformed to:

$$p_{sw}(r_w, t_s) = p_i - m \log\left(\frac{t_c + t_s}{t_s}\right), \qquad m = \frac{162.6\ qB\mu}{kh}. \quad (9.1.16)$$

and the formation permeability is

$$k = \frac{162.6\ qB\mu}{mh}. \quad (9.1.17)$$

The equation for estimating the skin factor (s) is (Earlougher 1977)

$$s = 1.1513\left[\frac{p_{1\text{ h}} - p_{wf}(t_s = 0)}{m} + \log\left(\frac{t_c + 1}{t_c}\right) - \log\left(\frac{k}{\phi\mu c_t r_w^2}\right) + 3.2275\right]. \quad (9.1.18)$$

In Eq. (9.1.18) $p_{wf}(t_s = 0)$ is the observed flowing bottom-hole pressure immediately before shut-in. The value $p_{1\text{ h}}$ must be taken from the Horner straight line at 1 h. Frequently, pressure data do not fall on the straight line at 1 h. In this case, the semilog line must be extrapolated to 1 h and the pressure read. To estimate the formation permeability (Eq. 9.1.17) at high temperatures the values of

Table 9.1 Physical properties of water (http://www.engineeringtoolbox.com/water-thermal-properties-d_162.html)

T, °C	μ, cp	ρ, kg/m^3	β, 10^{-3} 1/K	C_p, kJ/kg K	Pr	λ, W/m K
10	1.307	1000	0.088	4.193	9.47	0.5774
20	1.00	998	0.207	4.182	7.01	0.5978
30	0.798	996	0.303	4.179	5.43	0.6140
40	0.653	991	0.385	4.179	4.34	0.6279
50	0.547	988	0.457	4.182	3.56	0.6418
60	0.467	980	0.523	4.185	2.99	0.6502
70	0.404	978	0.585	4.190	2.56	0.6611
80	0.355	971	0.643	4.197	2.23	0.6670
90	0.315	962	0.698	4.205	1.96	0.6728
100	0.282	962	0.752	4.216	1.75	0.6837

the water formation volume factor (B_w) and water viscosity (μ) should be estimated.

To estimate the formation permeability (Eq. 9.1.17) the values of dynamic viscosity (μ) can be taken from Table 9.1.

For water production/injection boreholes, the mathematical models for calculating static formation temperatures from well logs and the temperature distributions in formations during drilling and shut-in periods are mathematically the same and are presented in detail in Chap. 8.

9.2 Temperature Profiles in Water Injection and Production Wells

Many variables influence transient temperature profiles in injection and production wells. It is very difficult to apply analytical techniques when predicting downhole temperatures. In fact, it is practically impossible to take into account the well configuration, time dependent flow rate, depth dependent formations thermal properties and temperatures, vertical heat transfer or the dependence of properties of producing fluids (gases) on temperature and pressure. At the same time the accuracy of downhole temperature predictions by computer models depends to a large extent on the availability and quality of the input data (Wooley 1980). However, in many cases simplified analytical solutions with sufficient accuracy can approximate the transient temperature profiles in production and injection wells.

Below we adapt the basic equation obtained by Ramey (1962) and modified by Prats (1982). The main assumptions are as follows: steady-state heat transfer within the borehole, constant formation and fluid (gas) properties, constant geothermal gradient, incompressible liquids or ideal gases, and only radial heat losses to the formation.

On the basis of these assumptions the temperature in an injection well is given by

$$T(z,t) = T_f(z) - \Gamma w_i c R_h + \left[T_{inj} - T_0 + \Gamma w_i c R_h\right] \exp\left(-\frac{z}{w_i c R_h}\right), \qquad (9.2.1)$$

where w_i is the mass rate, T_{inj} is the injection temperature of the fluid (gas), and c is the specific heat capacity of the fluid.

The undisturbed formation temperature is a linear function of depth

$$T_f(z) = T_0 + \Gamma z. \qquad (9.2.2)$$

For a production well, the mass rate w_p is used instead of w_i and the temperature is given by

$$T(z,t) = T_f(z) + \Gamma w_p c R_h + \left[T_p(t) - T_f(z_R) - \Gamma w_p c R_h\right] \exp\left(-\frac{(z_R - z)}{w_p c R_h}\right), \qquad (9.2.3)$$

where z_R is the reservoir depth and $T_p(t)$ is the temperature of the producing fluid at z_R.

We also introducing a parameter that serves to estimate the rate of heat loss to formations.

$$\Delta T(t) = Tp(t) - T(z = 0, t). \qquad (9.2.4)$$

9.2.1 Overall Coefficient of Heat Loss

Knowledge of the casing temperatures and wellbore heat losses are critical parameters in designing geothermal, steam injection, and production deep hot wells.

The interpretation of temperature logs from production and injection wells depends to a great extent on the heat transmission in the flowing fluid-well completion-formation system (Fig. 9.2).

Given that the specific (thermal resistance per unit of length) thermal resistance is time dependent, Prats (1982) introduced the overall specific thermal resistance coefficient (R_h),

$$R_h = \frac{1}{2\pi}\left[\frac{1}{h_f r_{ti}} + \frac{\ln\frac{r_{t0}}{r_{ti}}}{\lambda_{tub}} + \frac{\ln\frac{r_{ci}}{r_{t0}}}{\lambda_{an}} + \frac{\ln\frac{r_{c0}}{r_{ci}}}{\lambda_{cas}} + \frac{\ln\frac{r_w}{r_{ti}}}{\lambda_{cem}} + \frac{f(t_D)}{\lambda_f}\right], \qquad (9.2.5)$$

where $r_{ti,}$ $r_{t0,}$ $r_{ci,}$ r_{t0} are inside and outside radii of the tubing and casing, r_w is the well radius, λ_f is the thermal conductivity of the formation; h_f is the film transfer

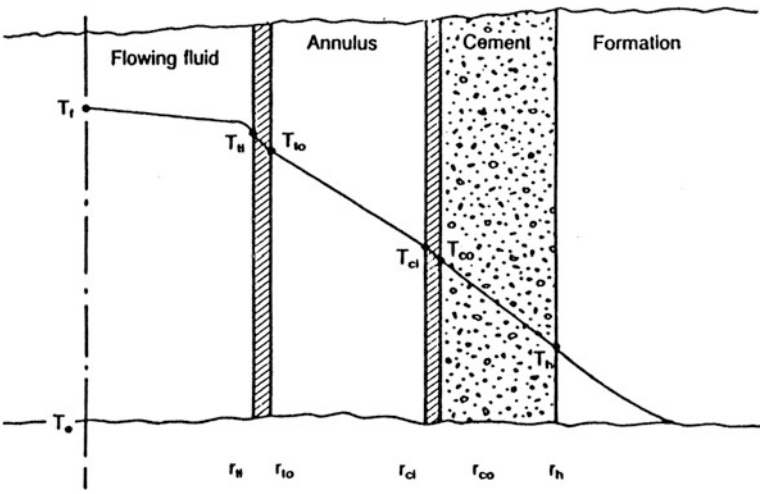

Fig. 9.2 Flowing fluid-well completion-formation system (White and Moss 1983)

coefficient of heat transfer between the fluid inside the tubing and the tubing wall, λ_{tub}, λ_{an}, λ_{cas}, and λ_{cem} are the thermal conductivities of the tubing, annular material, the casing, and the cement, respectively.

In his classic paper Ramey (1962) introduced the dimensionless "time function, $f(t_D)$" which accounts for the transient heat conduction in the formation.

In many cases the time function is equal to the reciprocal of the dimensionless heat flow rate from a constant temperature cylindrical source (Kutasov 1999):

$$\left\{ \begin{array}{l} f(t_D) = \ln(1 + D\sqrt{t_D}), \\ D = 1.5708 + \dfrac{1}{\sqrt{t_D} + 4.9589}, \quad t_D = \dfrac{a_f t}{r_w^2} \end{array} \right\},$$

where a_f is the thermal diffusivity of formation, and t is the time.

The value of h_f is calculated from the following equation (Kay 1963; Bejan 1993):

$$\mathrm{Nu} = \frac{h_f L}{k_f} = 0.023 \mathrm{Re}^{0.8} \mathrm{Pr}^{0.4}, \tag{9.2.6}$$

where Nu, Re, and Pr are Nusselt, Reynolds, and Prandtl numbers, respectively.

$$\mathrm{Nu} = h_f \frac{L}{k_f}, \quad \mathrm{Re} = u \frac{L}{v}, \quad \mathrm{Pr} = \frac{v}{a},$$

where h_f is the convective heat transfer coefficient, L is the characteristic length (in our case the inside radius of tubing), k_f is thermal conductivity of the fluid, u is the

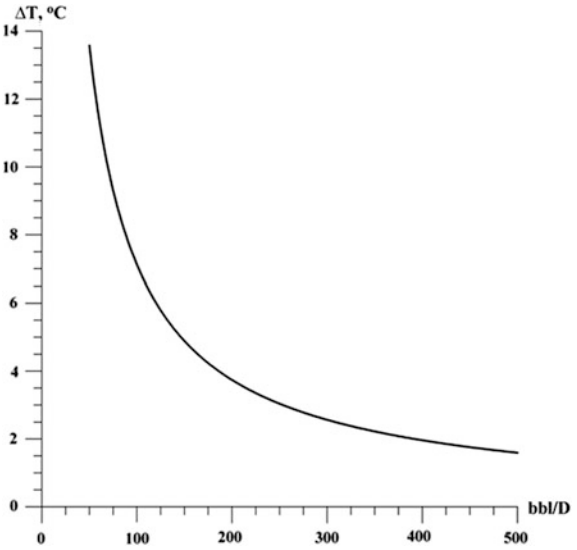

Fig. 9.3 The function ΔT ($z = 0$, $t = 200$ days) versus flow rate

velocity based on the actual cross section area of the pipe, v is the kinematic viscosity and a is the thermal diffusivity of fluid.

9.2.2 Example of a Calculation

In this example, the following data will be assumed: production rate $q = 500$ bbl/D $= 6.90 \times 10^{-4}$ m^3/s, the production time 200 days, geothermal temperature, $T_f(z) = 20$ °C + 0.03 °C/m z. The reservoir temperature at 2,000 m is 80 °C, tubing size is 4.5 in. (ID = 4.09 in.), casing size is 7 in. (ID = 6.538 in.), borehole diameter is 8 in.

The insulating material has an effective thermal conductivity, $\lambda_{an} = 0.1731$ W/(m K).

The thermal conductivities of the tubing/casing and cement are: $\lambda_{tub} = \lambda_{cas} = 43.3$, $\lambda_{cem} = 0.872$ W/(m K). The properties of water at 80 °C are: $k_f = 0.670$ W/(m K), $v = 3.562 \times 10^{-7}$ m^2/s, $a = 1.695 \times 10^{-7}$ m^2/s, density $\rho = 971.2$ kg m^{-3}, specific heat $C_p = 4.070 \times 10^3$ J/(kg K) (Internet, Microelectronics Heat Transfer Laboratory).

The velocity of flow u and the production mass rate w_p are:

$$u = \frac{q}{\pi r_{ti}^2}, \quad w_p = q\rho.$$

The findings are presented in Figs. 9.3 and 9.4.

The rate of heat loss Q to surrounding formations at 200 days is:

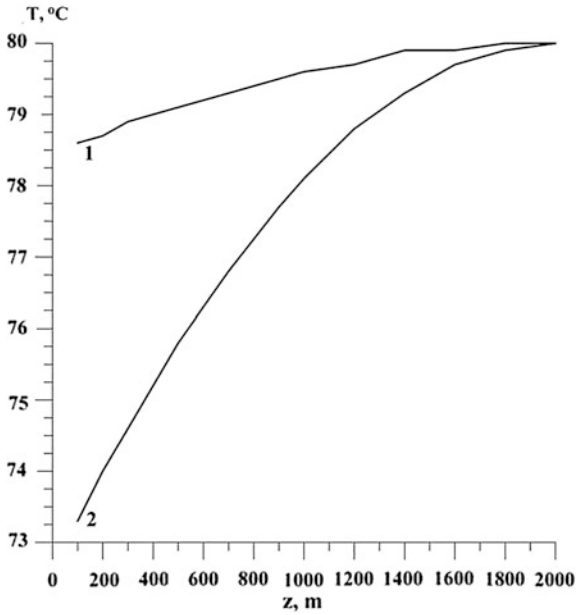

Fig. 9.4 The temperature profiles at $t = 200$ days for two flow rates (*1*) 500 bbl/D (*2*) 100 bbl/D

For $q = 500$ bbl/D,

$$Q = q \cdot \rho \cdot C_p \cdot \Delta T = 6.9 \times 10^{-4}\,\mathrm{m^3/s} \cdot 9{,}712\,\mathrm{kg/m^3}$$
$$4.070 \times 10^3\,\mathrm{J/(kg\,K)} \cdot 157\,^{\circ}\mathrm{C} = 2{,}726\,\mathrm{J/s},$$

and for $q = 50$ bbl/D

$$Q = 6.9 \times 10^{-4}\,\mathrm{m^3/s} \cdot 971.2\,\mathrm{kg/m^3}$$
$$4.070 \times 10^3\,\mathrm{J/(kg\,K)} \cdot 13.32\,^{\circ}\mathrm{C} = 23{,}130\,\mathrm{J/s}.$$

9.3 Monitoring Water Reserves

A typical hydrological system on land is composed of a vadose (or unsaturated) zone (region of aeration between the surface and the water table), an unconfined aquifer (between the water table and the first confining bed or aquitard), and confining aquifers separated by aquitards. An aquifer (saturated zone) is an underground layer of water-bearing permeable rock.

Some basics of hydrogeology, as well as the main characteristics of sedimentary rocks, are discussed in Sect. 4.1 in relation to thermal waters, including the key features of confined aquifers. In this section some specific characteristics of

recharge and *discharge* zones and *water flow* through aquifers will be discussed in more detail.

The importance of groundwater for geothermal research is related to the fact that water has an extremely high heat capacity compared to rocks and minerals that makes water rich layers powerful sinks of heat. In addition, the constant movement of groundwater makes heat transfer relatively fast. Both these features can lead to a significant disturbance of the heat field, especially in the uppermost layers of the Earth.

Most processes related to groundwater flow involve three major processes: groundwater recharge, groundwater flow through permeable aquifers, and groundwater discharge. In all these processes sedimentary rocks with high values of open porosity (effective porosity) and permeability are crucial, which explains why the presence of sedimentary rocks such as limestone, dolomite, shale, siltstone, sandstone, gravel, sand and conglomerate are key players in groundwater hydrology. All movements of groundwater are controlled by gravity. Water in underground storage is usually divided into two parts: the part that drains under the influence of gravity (specific yield), and the part that is retained as a film on rock surfaces and in very small pores (specific retention). Specific yield shows how much water is actually available, and specific retention shows how much water remains in the rock after it is drained by gravity.

Since groundwater flow follows the laws of fluid mechanics, let us first discuss some of its important parameters.

Bernoulli's principle states that for an ideal fluid flow, an increase in the speed of a fluid occurs simultaneously with a decrease in pressure or a decrease in the fluid's potential energy (Batchelor 1967). This principle may be described by the Bernoulli equation, which in its general form for any arbitrary point of a streamline is written as:

$$\frac{\sigma v^2}{2} + \sigma g z + P = const. \tag{9.3.1}$$

Here v is the fluid flow velocity at a point, g is the acceleration due to gravity, z is the elevation of the point above a reference plane (z is positive in the up direction), P is the *static pressure* at the point, and σ is the density of the fluid.

In Eq. (9.3.1)

$$\frac{\sigma v^2}{2} = P_D \tag{9.3.2}$$

P_D is the dynamic pressure, and $\sigma g z$ is the pressure formed by the elevation of the point above a reference plane.

The piezometric head (or hydraulic head) (h) is defined as (e.g., Chanson 2004; Mulley 2004):

$$h = z + \frac{P}{\sigma g}. \tag{9.3.3}$$

Here $\frac{P}{\sigma g}$ is called the pressure head (Chanson 2004; Mulley 2004).

The total pressure (P_T) is defined as (e.g., Oertel 2004):

$$P_T = P + P_D. \tag{9.3.4}$$

The total dynamic head (h_T) can be described as (e.g., Bear 1972):

$$h_T = h + v^2/2\mathrm{g}. \tag{9.3.5}$$

The term $\frac{v^2}{2g}$ is called the velocity head. Because ground water moves relatively slowly, the velocity head in most cases can be ignored. Groundwater moves in the direction in which the total head decreases.

Hydraulic head measurements may be used to calculate another important hydrological parameter known as the hydraulic gradient (I), which can be defined as (e.g., Bear 1972):

$$I = \frac{dh}{dl} = \frac{\Delta h}{\Delta l}. \tag{9.3.6}$$

Here $\Delta h = h_2 - h_1$ is the difference between hydraulic heads measured at two different points, and Δl is the distance between the points at which hydraulic heads were measured.

Another important law used to calculate the flow rate of underground water is Darcy's Law, which was discussed in Sect. 4.1 [see Eq. (4.1.1)].

A number of methods can be used to identify confining layers, and delineate recharge and discharge areas for basin-fill aquifers (Anderson et al. 1994; Snyder and Lowe 1998). To define recharge and discharge areas the principal aquifer and local overlying shallow unconfined aquifers need to be evaluated. The principal aquifer usually begins at a mountain front along the valley margins where coarse-grained alluvial-fan sediments predominate and groundwater is generally unconfined. Away from bedrock exposures, fine grained silt and clay may form confining layers above and below the principal aquifer. Water-well logs can be used to delineate primary and secondary recharge areas and discharge areas, based on the presence or absence of confining layers and relative water levels in the principal and shallow unconfined aquifers. Areas of secondary recharge can be determined by the hydraulic gradient when it is downward-directed.

Groundwater recharge is one of the most important parameters when assessing groundwater resources. Groundwater recharge is a hydrologic process where water infiltrates (moves downward) from the surface into underground horizons to replenish aquifers with water. This process usually occurs in the vadose zone and it controls the position of the water table. Recharge of the saturated zone occurs by

percolation of water from the land surface through the unsaturated zone. Recharge occurs both naturally (by natural precipitation) and artificially (by human activities). Infiltration of water from streams, rivers and lakes can also play a role in groundwater recharge, even though their formation and existence are usually related to discharge of groundwater.

Since groundwater movement is controlled by gravity, it is clear that groundwater recharge zones are present in topographically elevated areas. In terms of topology, groundwater recharge areas are at local heights and discharge areas are at local depressions. Most recharge occurs in mountain ranges and permeable rocks in areas bordering mountain ranges, as well as along the channels of major streams and rivers where they are underlain by thick and permeable sedimentary deposits.

The rate of replenishment of the water in aquifers (mainly by precipitation) is the groundwater recharge rate.

There are two main groups of sources of water in the recharge process which are related to natural recharge and artificial recharge. Natural recharge of an area comes from direct precipitation, influent seepage from rivers, and irrigation waters (Simmers 1988) whereas artificial recharge includes borehole injection, artificial ponds and other human-made water systems. The modes and mechanisms of recharge were classified by Simmers (1988) into downward flows of water through the unsaturated zone, lateral and/or vertical inter-aquifer flows, induced recharge from nearby surface water bodies, and artificial recharge. It is clear that the amount (or rate) of groundwater recharge that occurs in any particular area depends on the climate, topography, superficial geology, as well as the time and kind of aquifer of the area.

Mathematically the total groundwater recharge can be expressed as:

$$R_T = \sum_i R_i. \tag{9.3.7}$$

where i represents the type of recharge.

The main component of any groundwater recharge process is precipitation which can be determined using meteorological data. A statistical-topographic model can be also used to estimate regional precipitation (Daly et al. 1994).

One of the key characteristics of recharge is related to its timing. Since recharge depends heavily on precipitation, its main activity occurs during and immediately after precipitation and thus is intermittent. Recharge is also seasonally-dependent on annual cycles. In contrast, the discharge of groundwater is a continual or ongoing process.

There are a number of methods of estimating the groundwater recharge rate: the lysimeter method, soil water budget models, the water table fluctuation method, numerical modeling of the unsaturated zone, the zero flux plane method, the Darcy method, the tritium profiling method, the chloride profiling method, etc. (Allison and Hughes 1978; Adar et al. 1988; Simmers 1988; Lerner et al. 1990;

Sophocleous 1991; Zhang and Dawes 1998; Kumar and Seethapathi 2002; de Silva 2004; Crosbie et al. 2009; Huang and Pang 2011, etc.).

Some methods to estimate the groundwater recharge are area- and condition-dependent and cannot be universal. For example, the water table fluctuation method for groundwater recharge estimates is used only for unconfined aquifers, but even though it involves similar steps in all areas and regions it has many specifics. Thus the method needs to be adapted to different areas simply because each area is characterized by different a topographic relief, different amounts of rainfall, different kinds of human activity, etc. This has led to the development of different methods or empirical equations for recharge calculations. For example, based on the water level fluctuations and amount of rainfall in Ganges-Yamuna Doab in India, in 1936 Chaturvedi presented an empirical relationship for recharge as a function of annual precipitation (Kumar and Seethapathi 2002):

$$R = 2.0(\mathrm{Pr} - 15)^{0.4}, \tag{9.3.8}$$

where R is net recharge due to precipitation during the year (inch); and Pr is annual precipitation (inch).

Nevertheless, just as different empirical equations need to be used for different areas, different equations may also be required for the same area in different years or different periods, because recharge varies from year to year, depending on the amount of precipitation, its seasonal distribution, air temperature, etc. The best proof of this is the fact that for the same area of India, two different empirical equations were put forward much more recently (Kumar and Seethapathi 2002).

One of widely used methods of estimating recharge rate is the unsaturated zone chloride profiling method (Allison and Hughes 1978; de Silva 2004) which is based on the fact that chloride is deposited on land by atmospheric deposition processes (rainfall + dry fallout). If chloride is present in an unsaturated zone as a result of atmospheric deposition, and in the absence of other sources or sinks of chloride ions in the unsaturated zone, the recharge rate (R) leaving the root zone is expressed as:

$$R = \frac{C_{ic}}{C_Z}\mathrm{Pr}, \tag{9.3.9}$$

where C_Z is the mean chloride ion concentration in soil water (in mg/l), Pr is precipitation (in mm/year) and C_{ic} is the chloride ion concentration in rainfall (in mg/l).

Groundwater recharge methods can be combined. For example, Sophocleous (1991) described a "hybrid water-fluctuation method" based on combining the recharge estimates from the soil water balance analysis with the subsequent rises in the water table.

After entering aquifers during the recharge process, groundwater moves by gravity to the discharge areas. The process of groundwater flow through aquifers is one of the most important processes in hydrology and this movement is affected by

the permeability of rocks composing the aquifers. In hydrology instead of permeability such practical parameters as hydraulic conductivity (k), which is directly related to permeability [see Eq. (4.1.2)], and hydraulic gradient (I) [see Eq. (9.3.6)] are usually employed.

One of the most fundamental parameters of an aquifer is transmissivity (e.g., Freeze and Cherry 1979). Transmissivity is the rate at which water is transmitted through a unit width of an aquifer under a unit hydraulic gradient. The transmissivity (Tr) of an aquifer is equal to the hydraulic conductivity (κ) of the aquifer multiplied by the saturated thickness (b) of the aquifer (e.g., Heath 1989):

$$Tr = \kappa b. \tag{9.3.10}$$

The transmissivity of aquifer can be also calculated as (e.g., Heath 1989):

$$Tr = \frac{Q}{W}\left(\frac{dl}{dh}\right). \tag{9.3.11}$$

Here Q is the quantity of water moving through the width (W) of the aquifer.

Processes of recharge and transmissivity of an aquifer are heavily dependent on the kind of aquifer and its position. An aquifer system may contain a shallow aquifer (unconfined aquifer less than 60 m deep), an intermediate aquifer (confined aquifer 60–300 m deep), a deep aquifer (confined aquifer 300–800 m deep) or a super-deep aquifer (confined aquifer deeper than 800 m) (Li et al. 2005; Njamnsi and Mbue 2009).

After entering an aquifer, water moves slowly toward lower- lying places and eventually is discharged from the aquifer. The length of time water stays in aquifers is days in unconfined aquifer, years to decades in shallow confined aquifers and centuries to millennia in deep aquifers (Heath 1989).

Groundwater discharge also depends on the kind of aquifer and the geomorphological features of an area. For example in unconfined aquifers, evapotranspiration plays a significant role in groundwater discharge. There are two main forms of the discharge process which are related to natural discharge and artificial discharge. Natural discharge of an area includes groundwater outflow, seepage to rivers and other water bodies, evapotranspiration, etc. whereas artificial discharge is mostly related to groundwater extraction by wells. Hence the total groundwater discharge can be expressed as:

$$q_T = \sum_i q_i, \tag{9.3.12}$$

where i represents the type of discharge.

Groundwater discharge areas are always at lower elevations than recharge areas. In discharge areas (sometimes called discharge points) the water in confined aquifers discharges to existing surface waters (such as rivers, lakes, brooks, etc.) or

to a shallow unconfined aquifer. The rate of discharge of some of the most powerful non-thermal springs in the world is presented in Table 4.8.

One of the most significant differences between recharge areas and discharge areas is that discharge areas are much smaller than recharge areas. Discharge is a continuous process. It starts in areas where groundwater heads are above the level at which discharge occurs and it continues as long as this condition is satisfied.

Groundwater discharge (q) is the flow rate of groundwater through an aquifer, which can be expressed as (e.g., Freeze and Cherry 1979):

$$q = \kappa A \frac{dh}{dl}. \tag{9.3.13}$$

Here κ is the hydraulic conductivity of the aquifer and A is the area the groundwater is flowing through. The relationships between hydraulic conductivity and permeability are presented in Eq. (4.1.2).

A flow net analysis is a graphic method for estimating groundwater discharge from Darcy's Law (e.g., Freeze and Cherry 1979). This method is based on the assumption that an isotropic medium and the water table contours or potentiometric surfaces are separated graphically into equally spaced flow tubes. The equipotential contours show an evenly distributed change in head between adjacent flow tubes. The discharge flowing through the flow tube can be determined by rearranging Darcy's Law:

$$q = \frac{\kappa n \Delta h}{f}. \tag{9.3.14}$$

Here n is the number of flow paths bounded by adjacent pairs of stream lines, Δh is the total head loss over the length of the streamlines, and f is the number of squares bounded by any two adjacent streamlines and covering the entire length of flow (Freeze and Cherry 1979).

Groundwater discharge plays an extremely important role in processes of evapotranspiration from unconfined aquifers especially in cases where the water table is above the surface of constant annual average temperatures. In some areas (mostly in deserts) evapotranspiration may be the only form of groundwater discharge. For example in the Ash Meadows area of the Nevada Test Site (former atomic testing zone) the mean annual groundwater discharge was computed directly from estimates of evapotranspiration (Laczniak et al. 1999). This makes methods of estimation of groundwater discharge by evapotranspiration an extremely important technique. There are a number of evapotranspiration methods (e.g., Thornthwaite and Mather 1957; Walker and Eakin 1963; Nichols 2000). For example, Nichols (2000) found that groundwater discharge by evapotranspiration can be estimated as a function of plant cover, which can be determined from Landsat data using easily calculated vegetation indices. For these purposes remote sensing techniques developed by Nichols (2000) can be used. For example, satellite data have been used in Nevada to estimate groundwater discharge by

evapotranspiration based on the relations between vegetation indices derived from Landsat data and the measured plant cover (Nichols 2000; Berger et al. 2004).

Research shows that over a sufficiently long period of time under natural conditions, before the start of water withdrawals (groundwater systems in undeveloped basins), the discharge from every groundwater system equals the recharge into it (e.g., Theis 1940; Heath 1989):

$$q = R. \tag{9.3.15}$$

This suggests that the natural groundwater discharge from Dry Valley (in Antarctica) for instance can be equated to groundwater recharge from precipitation and that long term changes in groundwater storage are negligible (Watson et al. 1975; Berger et al. 2004).

At the same time Eq. (9.4.15) is not necessarily true for cases of artificial discharge, because over-pumping of groundwater from an aquifer can lead to loss of water from the aquifer. For example, after extensive groundwater irrigation, the water levels in the High Plains aquifer (a total area of about 450,660 km^2) in parts of Texas, Oklahoma, and southwestern Kansas declined more than 30 m by 1980 (Mcguire 2007). The multi-annual average loss of water in aquifers of the Zhongmu County Alluvial Plain Aquifer, Henan Province, China amounts 1.53×10^7 m^3/a (Njamnsi and Mbue 2009).

But in such cases, changes in the amount of water stored in an aquifer can be estimated using hydrodynamics. The amount of water entering a control volume during a defined time period (inflow, I), minus the amount leaving the volume during the time period (discharge, q), equals the change in the amount of water stored (ΔS) in the volume during that time period (Njamnsi and Mbue 2009). Thus in terms of an aquifer, the amount of water stored or taken from it may be written as:

$$\Delta S = \sum_i R_i - \sum_i q_i. \tag{9.3.16}$$

Water reserves can be calculated as the total porous space within aquifers and aquitards within a hydrologic system. But not all water can be used because significant amounts of water are within highly porous aquitards (e.g., clay layers) and retained in rock surfaces and in very small pores (specific retention). Only the part of aquifer porous water that will drain under the influence of gravity (specific yield) can be used theoretically. This means that the usable volume capacity can be evaluated as (e.g., George et al. 2011):

$$V_U = K_{\mathrm{OP}} V_0. \tag{9.3.17}$$

Here V_U is the usable volume capacity, V_0 is the total volume of aquifer and K_{OP} is the open (or effective) porosity of rock comprising the aquifer.

For an unconfined aquifer an open porosity value of 23 % can be used (e.g., George et al. 2011).

However, in addition to aquifers, underground water can also be contained in reservoirs confined in fields at much greater depths. Such reservoirs can be filled with water, water with oil, water with oil and gas, etc. Even though this water does not move and does not have discharge zone it can absorb significant amounts of heat given the very high heat capacity of water. This makes it important to determine the quantity of water in such reservoirs to calculate the extra heat energy absorbed by this water. For these purposes Eq. (2.7.4) can be used. If the initial volume of water in a reservoir filled only with water is V_0, and initial pressure and temperature within the reservoir are P_1 and T_1, respectively, Eq. (2.7.4) for the reservoir will be:

$$P_1 = P_0 + \frac{\alpha_W}{\beta_W}(T_1 - T_0) - \frac{1}{\beta_W}\frac{\Delta V}{V_0}. \tag{9.3.18}$$

Here α_W and β_W are coefficients of the thermal expansion volume and compressibility of water, respectively, P_0 and T_0 are the normal pressure and temperature of water in the reservoir and ΔV is change in the initial volume V_0.

If some water V_1 is pumped out of the reservoir at the pressure and temperature within the reservoir, the rest of water will take the initial volume of water within the reservoir V_0 and the pressure within the reservoir will drop to P_2. Since the volume change is $\Delta V = V_1$ and the change of temperature will be negligible Eq. (9.3.18) can be written as

$$P_2 - P_1 = -\frac{1}{\beta_W}\frac{V_1}{V_0}. \tag{9.3.19}$$

Solving Eq. (9.3.19) for initial volume V_0 gives:

$$V_0 = -\frac{1}{\beta_W}\frac{V_1}{(P_2 - P_1)} \tag{9.3.20}$$

Equation (9.3.20) may be used to calculate the initial volume V_0 of water within the reservoir.

In the case where a reservoir filled with water and oil has an initial pressure and temperature P_1 and T_1, respectively, it is possible to determine the volumes of both the water and oil if the reservoir is isolated. In such a case the total initial volume V_0 of the fluid can be represented as the sum of initial volumes of water (V_{W0}) and oil (V_{N0}):

$$V_0 = V_{W0} + V_{N0}. \tag{9.3.21}$$

If some water V_1 (or a mixture of water and oil) at the pressure and temperature within the reservoir is pumped out of the reservoir, the rest of water and oil will take the initial volume of the fluid within the reservoir V_0 and the pressure and temperature within the reservoir will drop to P_2 and T_2, respectively. The total change in the initial volume V_1 is represented by the volume change of both water (ΔV_{W1}) and oil (ΔV_{N1}):

$$V_1 = \Delta V_{W1} + \Delta V_{N1}. \tag{9.3.22}$$

The change ΔV_{N1} in the initial volume of oil V_{N0} can be represented using Eq. (9.3.22) as:

$$\Delta V_{N1} = V_1 - \Delta V_{W1}. \tag{9.3.23}$$

Using Eqs. (9.3.23) and (2.7.4) each of the fluid components in the reservoir can be represented as:

$$P_2 = P_1 + \frac{\alpha_W}{\beta_W}(T_2 - T_1) - \frac{1}{\beta_W}\frac{\Delta V_{W1}}{V_{W0}}. \tag{9.3.24}$$

$$P_2 = P_1 + \frac{\alpha_N}{\beta_N}(T_2 - T_1) - \frac{1}{\beta_N}\frac{V_1 - \Delta V_{W1}}{V_{N0}}. \tag{9.3.25}$$

Here α_W, β_W and α_N, β_N are the coefficients of the thermal expansion volume and compressibility for water and oil, respectively.

Pumping out additional water (or a mixture of water and oil) at the pressure and temperature within the reservoir together with V_1 equals V_2, the rest of the water and oil will take the initial volume of fluid within the reservoir V_0 and pressure and temperature within the reservoir will drop to P_3 and T_3, respectively. The change ΔV_{N2} in the initial volume of oil V_{N0} can be expressed similarly to Eq. (9.3.23) as:

$$\Delta V_{N2} = V_2 - \Delta V_{W2}. \tag{9.3.26}$$

Here ΔV_{W2} is the volume change in initial volume of water V_{W0}.

Similar to Eqs. (9.3.24) and (9.3.25) new equations for water and oil in this case can be written as:

$$P_3 = P_1 + \frac{\alpha_W}{\beta_W}(T_3 - T_1) - \frac{1}{\beta_W}\frac{\Delta V_{W2}}{V_{W0}}. \tag{9.3.27}$$

$$P_3 = P_1 + \frac{\alpha_N}{\beta_N}(T_3 - T_1) - \frac{1}{\beta_N}\frac{V_2 - \Delta V_{W2}}{V_{N0}}. \tag{9.3.28}$$

Equations (9.3.24) (9.3.25) (9.3.27) and (9.3.28) may be respectively written as:

$$-\frac{\Delta V_{W1}}{V_{W0}} = \beta_W(P_2 - P_1) - \alpha_W(T_2 - T_1). \tag{9.3.29}$$

$$-\frac{V_1 - \Delta V_{W1}}{V_{N0}} = \beta_N(P_2 - P_1) - \alpha_N(T_2 - T_1). \tag{9.3.30}$$

$$-\frac{\Delta V_{W2}}{V_{W0}} = \beta_W(P_3 - P_1) - \alpha_W(T_3 - T_1). \tag{9.3.31}$$

$$-\frac{V_2 - \Delta V_{W2}}{V_{N0}} = \beta_N(P_3 - P_1) - \alpha_N(T_3 - T_1). \tag{9.3.32}$$

Division of Eq. (9.3.29) by Eq. (9.3.31) gives:

$$\frac{\Delta V_{W1}}{\Delta V_{W2}} = \frac{\beta_W(P_2 - P_1) - \alpha_W(T_2 - T_1)}{\beta_W(P_3 - P_1) - \alpha_W(T_3 - T_1)} = a. \tag{9.3.33}$$

Here parameter a is used for simplification of the solution.

A similar division of Eq. (9.3.31) by Eq. (9.3.32) gives:

$$\frac{V_1 - \Delta V_{W1}}{V_2 - \Delta V_{W2}} = \frac{\beta_N(P_2 - P_1) - \alpha_N(T_2 - T_1)}{\beta_N(P_3 - P_1) - \alpha_N(T_3 - T_1)} = b. \tag{9.3.34}$$

Here parameter b is used for simplification of the solution.

Equations (9.3.33) and (9.3.34) represent a system of equations with two unknown variables ΔV_{W1} and ΔV_{W2}. Using Eq. (9.3.33) a value of ΔV_{W1} may be represented in terms of ΔV_{W2} as:

$$\Delta V_{W1} = a \cdot \Delta V_{W2}. \tag{9.3.35}$$

Substituting ΔV_{W1} using Eq. (9.3.35) in Eq. (9.3.34) and solving it for ΔV_{W2} gives:

$$\Delta V_{W2} = \frac{V_1 - bV_2}{a - b}. \tag{9.3.36}$$

Substituting Eq. (9.3.36) in Eq. (9.3.31) and solving it for the initial volume of water gives:

$$V_{W0} = \frac{bV_2 - V_1}{(a - b)[\beta_W(P_3 - P_1) - \alpha_W(T_3 - T_1)]}. \tag{9.3.37}$$

Substituting Eq. (9.3.36) in Eq. (9.3.26) gives:

$$\Delta V_{N2} = \frac{aV_2 - V_1}{a - b}. \tag{9.3.38}$$

Substituting Eq. (9.3.38) in Eq. (9.3.32) and solving it for the initial volume of oil gives:

$$V_{N0} = \frac{V_1 - aV_2}{(a-b)[\beta_N(P_3 - P_1) - \alpha_N(T_3 - T_1)]}. \tag{9.3.39}$$

Equations (9.3.37) and (9.3.39) may be used to estimate water resources in the reservoir.

It is obvious that fluids in reservoirs containing 3 or more components may be calculated using a similar approach by pumping out 3 or more volumes of fluid from the reservoir and solving the system with three or more equations for the corresponding number of unknown variables.

References

Adar EM, Neuman SP, Woolhiser DA (1988) Estimation of spatial recharge distribution using environmental isotopes and hydrochemical data, 1. Mathematical model and application to synthetic data. J Hydrol 97:251–277

Allison GB, Hughes MW (1978) The use of environmental chloride and tritium to estimate total recharge to an unconfined aquifer. Aust J Soil Res 16:181–195

Anderson PB, Susong DD, Wold SR, Heilweil VM, Baskin RL (1994) Hydrogeology of recharge areas and water quality of the principal aquifers along the Wasatch Front and adjacent areas, Utah. U.S. Geological Survey water-resources investigations report 93-4221, Scale 1:100,000

Batchelor GK (1967) An introduction to fluid dynamics. Cambridge University Press, Cambridge

Bear J (1972) Dynamics of fluids in porous media. American Elsevier Publishing Company, New York

Bejan A (1993) Heat transfer. Wiley, New Jersy

Berger DL, Maurer DK, Lopes TJ, Halford KJ (2004) Estimates of natural ground-water discharge and characterization of water quality in Dry Valley, Washoe County, West-Central Nevada, 2002–2003. U.S. Geological Survey, science investigation report 2004-5155. Carson City, Nevada

Bredehoeft JD, Papadopulos IS (1965) Rates of vertical groundwater movement from the earth's thermal profile. Water Resour Res 1(2):325–328

Carslow HS, Jaeger JC (1959) Conduction of heat in solids, 2nd edn. Oxford University Press, Oxford

Chanson H (2004) Hydraulics of open channel flow: an introduction. Butterworth-Heinemann, Oxford

Cheremensky GA (1977) Applied geothermics. Nedra, Leningrad ((in Russian))

Crosbie RS, McCallum JL, Harrington1 GA (2009) Estimation of groundwater recharge and discharge across northern Australia. In: Proceedings of transaction of the 18th world IMACS / MODSIM congress, Cairns, Australia, pp 3053–3059

Daly Ch, Neilson RP, Phillips DL (1994) A statistical topographic model for mapping climatological precipitation over mountainous terrain. J Appl Meteorol 33:140–158

de Silva RP (2004) Spatial variability of groundwater recharge—I. Is it really variable? J Spatial Hydrol 4(1):1–18

Domenico PA, Schwartz FW (1998) Physical and chemical hydrogeology, 2nd edn. Wiley, New York

Earlougher RC Jr (1977) Advances in well test analysis. SPE, New York

Edwards LM, Chilingar GV, Rieke HH, Fertl WH (1982) Handbook of geothermal energy. Gulf Publishing Company, Houston

Elder JW (1981) Geothermal systems. Academic Press, London

Eriksson E (1985) Principles and applications of hydrochemistry. Chapman & Hall, New York

Freeze RA, Cherry JA (1979) Groundwater. Prentice Hall Inc., Englewood Cliffs
George NJ, Obianwu VI, Obot IB (2011) Estimation of groundwater reserve in unconfined frequently exploited depth of aquifer using a combined surficial geophysical and laboratory techniques in The Niger Delta, South–South, Nigeria. Adv Appl Sci Res 2(1):163–177
Hänel R, Rybach L, Stegena L (1988) Fundamentals of geothermics. In: Rybach L, Stegena L, Hänel R (eds) Handbook of terrestrial heat-flow density determination. Kluwer Acad. Publ, Dordrecht/Boston/London, pp 9–57
Heath RC (1989) Basic ground-water hydrology. U.S. Geological Survey water-supply paper 2220
Horne RN (1995) Modern well test analysis, a Computer aided approach, 2nd ed. Petroway Inc., Palo Alto, CA
Huang Y, Pang Z (2011) Estimating groundwater recharge following land-use change using chloride mass balance of soil profiles: a case study at Guyuan and Xifeng in the Loess Plateau of China. Hydrogeol J 19(1):177–186
Hubbert MK (1969) The theory of groundwater motion and related papers. Hafner Publishing Company, New York
Kappelmeyer O, Hänel R (1974) Geothermics with special reference to application. Gebruder Borntrargen, Berlin, Stutgart
Kay JM (1963) Fluid mechanics and heat transfer. Cambridge University Press, Cambridge
Kumar CP, Seethapathi PV (2002) Assessment of natural groundwater recharge in Upper Ganga Canal Command area. J Appl Hydrol 15(4):13–20
Kutasov IM (1989) Application of the Horner method for a well produced at a constant bottomhole pressure. Formation Eval 3:90–92
Kutasov IM (1999) Applied geothermics for petroleum engineers. Elsevier
Kutasov IM (2003) Dimensionless temperature at the wall of an infinite long cylindrical source with a constant heat flow rate. Geothermics 32:63–68
Kutasov IM, Eppelbaum LV (2005) Drawdown test for a stimulated well produced at a constant bottomhole pressure. First Break 23(2):25–28
Kutasov IM, Eppelbaum LV, Kogan M (2008) Interference well testing—variable fluid flow rate. J Geophys Eng 5(1):86–91
Lachenbruch AH, Brewer MC (1959) Dissipation of the temperature effect of drilling a well in Arctic Alaska. U.S. Geol Surv Bull 1083-C:74-109
Laczniak RJ, DeMeo GA, Reiner SR, LaRue Smith J, Nylund WE (1999) Estimates of groundwater discharge as determined from measurements of evapotranspiration, ash Meadows area, Nye County, Nevada. Water-resources investigation report 99-4079. U.S. Geological Survey, Carson City, Nevada
Lee J (1982) Well Testing. SPE Monograph Series, Dallas, USA
Lerner DN, Issar AS, Simmers I (1990) Groundwater recharge: a guide to understanding and estimating natural recharge, vol 8. Heinz Heise, Hannover (Intern. Contrib. to Hydrogeol.)
Li GR, Wang XG, Guo YQ (2005) Concentrated groundwater development status of middle aquifer in Zhengzhou Municipal area. Yellow River 27(5):44–46 (in Chinese, abstract in English)
Lubimova EA, Von Herzen RR, Udintsev GB (1965) On heat transfer through the ocean floor. In: Lee WHK (ed) Terrestrial heat flow, vol 8. American Geophysical Union, Baltimore, Port City Press, Maryland, pp 78–86 (Geoph. Monog. Series)
Majorowicz JA, Jones FW, Judge AS (1990) Deep subpermafrost thermal regime in the Mackenzie Delta Basin, northern Canada—Analysis from petroleum bottom-hole temperature data. Geophysics 55:362–371
Mcguire VL (2007) Ground water depletion in the high plains aquifer water levels in some areas have declined over 150 Feet. USGS fact sheet 2007-3029
Mulley R (2004) Flow of industrial fluids: theory and equations. CRC Press, Boca Raton
Muskat M (1946) Flow of homogeneous fluids through porous media. J.W. Edwards Inc., Ann Arbor

Nichols WD (2000) Regional ground-water evapotranspiration and ground-water budgets, Great Basin, Nevada. U.S. Geological Survey professional paper 1628
Njamnsi YN, Mbue IN (2009) Estimation for groundwater balance based on recharge and discharge: a tool for sustainable groundwater management, Zhongmu County Alluvial Plain Aquifer, Henan Province, China. J Am Sci 5(2):83–90
Oertel H (ed) (2004) Prandtl's essentials of fluid mechanics, vol 158, 2nd edn., Applied mathematical sciences. Springer, Berlin
Osterkamp TE, Gosink JP (1984) A reconnaissance study of the hydrothermal characteristics of Pilgrim Springs. Alaska J Energy Resour Tech 106:96–102
Prats M (1982) Thermal recovery. Monograph series, vol 7. Society of Petroleum Engineers, Dallas, USA
Ramey HJ Jr (1962) Wellbore heat transmission. J Petrol Tech 14(4):427–435
Semenova SM, Gavich IK, Luchsheva AA (1964) Collection of tasks on hydrogeology. Vyshaya Shkola, Moscow
Simmers I (ed) (1988) Estimation of natural ground water recharge. Reidel, Dordrecht
Snyder NP, Lowe M (1998) Map of recharge and discharge areas for the principal valley-fill aquifer, Sanpete Valley, Sanpete County, Utah. Utah Geological Survey map 174, scale 1:125,000
Somerton WH (1992) Thermal properties and temperature related behavior of rock/fluid systems. Developments in Petroleum Science, vol 37. Elsevier, Amsterdam
Sophocleous MA (1991) Combining the soilwater balance and water-level fluctuation methods to estimate natural groundwater recharge: practical aspects. J Hydrol 124:229–241
Theis CV (1940) The sources of water derived from well. Civ Eng 10(5):277–280
Thornthwaite CW, Mather JR (1957) Instructions and tables for computing potential evapotranspiration and the water balance. Drexel Institute of Technology, Laboratory of Climatology. Publications in Climatology, 10, No. 3
Vosteen H-D, Schellschmidt R (2003) Influence of temperature on thermal conductivity, thermal capacity and thermal diffusivity for different types of rock. Phys Chem Earth 28:499–509
Walker GE, Eakin TE (1963) Geology and ground water of Amargosa Desert, Nevada-California. Nevada, USA. Reconnaissance report 14, Department of Conservation and National Research, Groundwater Research
Waples DW, Ramly M (2001) A statistical method for correcting log-derived temperatures. Petrol Geosci 7(3):231–240
Waples DW, Pachco J, Vera A (2004) A method for correcting log-derived temperatures deep wells calibrated in the Gulf of Mexico. Petrol Geosci 10:239–245
Watson Ph, Sinclair P, Waggoner R (1975) Quantitative evaluation of a method for estimating recharge to the desert basins of Nevada. J Hydrol 31:335–357
White PD, Moss JT (1983) Thermal recovery methods. Pennwell Publ. Co., Tulsa, pp 92–98
Wooley GR (1980) Computing downhole temperatures in circulation, injection, and production wells. J Petrol Techn 32:1509–1522
Zhang L, Dawes W (1998) WAVES—an integrated energy and water balance model. Technical report No. 31/98, CSIRO Land and Water

Chapter 10
Near-Surface Temperature Measurements

10.1 General Introduction

Near-surface thermal prospecting is based on temperature measurements in shallow (up to several meters in depth) drill holes. Since geological objects differ in terms of their thermal properties, these temperature measurements provide valuable information about features of the geological structures in the areas under investigation. Studying the thermal parameters associated with oil and gas exploration often plays a more important role than gravity, magnetic and sometimes even seismic investigations. However, the noise caused by seasonal temperature variations and terrain relief may significantly distort the temperature field observed in the near-surface layer.

This method is used to explore oil and gas pools, pyrite, and urano-organic/uraninite ores to locate faults or other discontinuities and to resolve other geological and geophysical problems. Unlike measurements in middle and deep wells where temperature observations depend on the drilling process, near-surface measurements constitute an independent investigation that can be conducted rapidly in any area.

In the mid-1930s, Rodionov and Sofronov (1935) were the first to introduce near-surface thermal prospecting in the USSR. It was used successfully in the Degtyarsk copper-pyrite deposit situated in the Middle Urals. At the same time, the method was used for the first time to study a faulted structure near Vintersweek in the Netherlands (van den Bouwhuysen 1934) and a salt stock near Hannover (Paul 1935). These investigations can be seen as the first steps in the application of near-surface thermal prospecting in petroleum geology. Many investigations have been made of thermal fields associated with hydrocarbon prospecting (Selig and Wallick 1966; Hutchins and Kading 1969; Poley and Steveninck 1970; Leschak and Lewis 1983, etc.). Khesin and Eppelbaum (1994) suggested a successive system of near-surface thermal data interpretation for complicated environments.

From 1950 to 1970 thermal prospecting was developed mainly for mineral exploration and was based on the fact that deep heat flow is redistributed by objects with enhanced thermal conductivity. More recently shallow thermal

L. Eppelbaum et al., *Applied Geothermics*, Lecture Notes in Earth System Sciences,
DOI: 10.1007/978-3-642-34023-9_10,

prospecting has been widely used to solve problems in petroleum geology and has emerged as a cost-effective and rapid means of singling out and tracing fractures. Kappelmeyer (1957) underlined that thermal logging in subsurface can be used to quantify the characteristics of anomalous bodies. Investigations conducted by Mongelli and Morelli (1961) showed that in many cases thermal observations in shallow wells (1.5 m) are similar to those at greater depths.

Suryaninov et al. (1983) derived certain functional dependencies between the thermal parameters of a geological body and the pattern of thermal anomalies due to this body, occurring in uniform host strata. A horizontal circular cylinder, which has the radius R, approximates the anomalous object with the center located at the depth h_0 below the earth's surface. In the mentioned article was shown that temperature prospecting is the most effective for delineation of anomalous bodies with parameters satisfying the following conditions:

$$0.1 \leq \frac{\lambda_2}{\lambda_1} \leq 10; \quad \frac{h_0}{R} < 5,$$

where λ_2 and λ_1 are the thermal conductivity values for the host medium and the anomalous object, respectively.

In most cases, however, the application of geothermal data was limited to simple qualitative interpretation; i.e., to the recording and tracing of temperature anomalies. Such simple analyses can contain considerable errors if time variations of the temperature field or the effect of rugged topography are neglected. To determine the parameters of disturbing bodies, noise must be eliminated from the observed temperature field before applying quantitative interpretation methods to the corrected field. A general scheme depicting the effects of noise on near-surface temperature data analysis is presented in Fig. 10.1.

Artificial noise (2). The *Instrumental* component (2.1 in the scheme in Fig. 10.1.) is associated with the technical properties of thermometers and their spatial location. The *Industrial* component (2.2) covers the technogenic impact of different industrial effects on the medium where temperature measurements are made. It should be noted that commonplace noise such as electric power lines do not affect NSTP observations (unlike magnetic and electromagnetic investigations), and the presence of underground metallic pipes does not affect *NSTP* to such an extent as in the aforementioned methods.

Natural disturbances (1). *Nonstationary* noise (1.1) comprises time variations in the temperature field propagating with different delays from the Earth's surface to the measurement point (this is the most basic kind of the *NSTP* noise). *Stationary* noise (1.3) reflects physical–*geological environments* (1.4). The first component of this noise is the *difficulty associated with drilling the hole* (1.4.1) associated with some types of geological rocks occurring in the upper part of the section and impeding borehole excavation. The second component is *dense vegetation* (1.4.2), which hampers temperature measurements and influences temperature field amplitude.

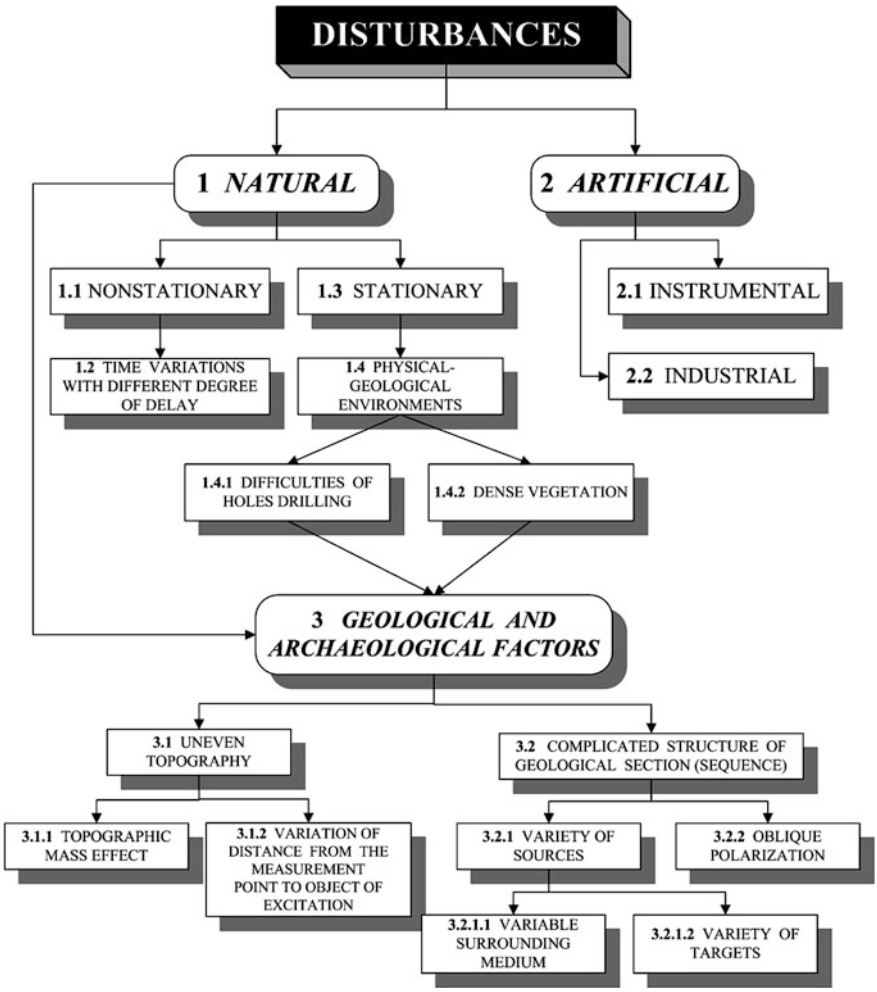

Fig. 10.1 Near-surface temperature measurements: classification of noise components (after Eppelbaum (2009), revised and supplemented)

Uneven terrain relief (3.1) is generally two-fold and involves the effect of the form and physical properties of the topographic bodies forming the relief and (3.1.1), the effect of variations in the distance from the measurement point to a hidden target (3.1.2) (Khesin et al. 1996).

The *complex structure of the geological section* (3.2) is a significant geological-geophysical disturbance. The *variety of anomalous sources* (3.2.1) is composed of two factors: *variable surrounding medium* (3.2.1.1) and *variety of desired targets* (3.2.1.2). Both these factors are crucial and contribute to complexifying the *NSTP* analysis.

Oblique polarization (3.2.2) disturbs the temperature field by shifting the extremum from the projection of the upper edge of the object on the plane, which can cause an additional extremum to appear (Eppelbaum and Khesin 2012).

10.2 Calculation of Temporary Variations

Various methods of geothermal surveying and data processing have been developed to eliminate temporary variations in temperature. The procedure suggested by Parasnis (1971) speeds up field work but does not eliminate seasonal variations. Another method consists of conducting a long-term geothermal investigation of the area under study and selecting the period when seasonal variations are minimal for the field survey (Dobrynina et al. 1985). However, this method suffers from such drawbacks as long duration, and hence the non-applicability of the results, since the fieldwork duration is frequently limited by organizational factors, etc.

Two other methods are worth mentioning: (1) synchronous measurements of the temperature variations within the field survey (Khutorsky et al. 1983) similar to the well-known method of eliminating magnetic field variations in magnetic prospecting; (2) measurement of the temperature simultaneously at all points of the profile (Chekalyuk et al. 1974). However, in the first method it is not always possible to avoid the influence of temperature waves delayed in diffusing from the surface. The second method (it should be noted that there is no real proof that such a procedure enables the removal of all temporary variations) demands simultaneous use of many temperature-measuring devices, which can impede the survey.

Eppelbaum and Mishne (1987, 1988) suggested a new method for eliminating temporary variations using repeated observations with subsequent linear filtering of the results. It is known that a regional thermal field is stable in time (Lubimova 1968) and temperature-wave propagation in the medium is linear (Tikhonov and Samarsky 1963). Taking these factors into consideration, a model of the total temperature field, recorded in the layer with annual temperature oscillations, can be represented in the following form:

$$Q_i = T_i + \sum_{j=t-t'}^{t} \tau(j) f(t-j), \tag{10.2.1}$$

where $Q_i(t)$ is the observation at the ith point (borehole); T_i is the temperature conditioned by redistributing the deep heat flow caused by the object with contrasting conductivity; $\tau(j)$ is the average temperature at a certain depth Δh at time j along the region including the district under investigation (data from meteorological stations are employed); $f(t-j)$ is the weight step function reflecting the temperature effect at the depth Δh, at time $t-j$ on the temperature measured in the borehole, at depth h at time j; and t' is the delay time of temperature waves diffusing down the surface.

Noises are assumed to be autocorrelative, and the autocorrelation matrix for noises $\mathbf{R}(t-j)$ can be written in the form:

$$\mathbf{R}(t-j) = \begin{matrix} \frac{1}{1+(t-j)^2} & |t-j| \le \psi \\ 0 & |t-j| \le \psi \end{matrix} \Bigg\} \tag{10.2.2}$$

where Ψ is some defined parameter.

Measurements at observation points made at different times t make it possible to obtain a solvable set of algebraic equations such that the desired signal T_i can be extracted with the required accuracy (Eppelbaum 1999). Research (for instance, Kumar and Kaleita 2003; Smerdon et al. 2004) confirms the applicability of this physical–mathematical model.

10.3 Calculation of Terrain Relief Influence

The problem of eliminating topographic effects was described in Khesin (1978). The main forms of relief can be represented by a combination of inclined slope(s). The idea behind this technique is to calculate the correlation between the field values (U) and the heights of observation points (H) in the middle part of the slope, and then calculate the regression coefficient(s) α and β. This yields an approximate linear relationship

$$U_{\text{appr}} = \alpha + \beta H. \tag{10.3.1}$$

The value U_{appr} is subtracted from the field value U observed at every point with known height H. Thus, we obtain the corrected field value U_{corr} which reflects the geological inhomogeneity of the section. The nature of the correlation is informative as to the presence and type of inhomogeneity.

The applicability of the above technique to thermal prospecting is substantiated by the following findings. The inverse dependence of the surface temperature on the height of observations was pointed out by Bullard (1940), and was noted subsequently by many investigators. Lachenbruch (1968) made a calculation of the change in heat flow that governs the temperature variation observed on an inclined slope. A comparison between the plots of the vertical magnetic field component (at vertical magnetization J) and the relative amount of the heat flow q/q_o is presented in Fig. 10.2.

The inverse correlation between the relief height and amplitudes of temperature values clearly confirm the data presented in Fig. 10.3.

Figure 10.4 illustrates the application of the correlation technique to eliminate the topographic effect in the Kyzylbulakh gold-pyrite deposit district (Lesser Caucasus, Azerbaijan). The equation for the terrain relief correction takes the form $= 15.6 - 0.07H$, where the correlation coefficient between the temperature T and the height H is -0.8. Once the inclined relief effect has been eliminated, the

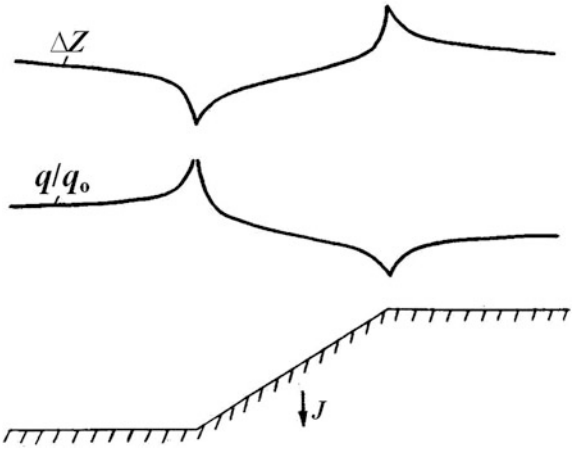

Fig. 10.2 Comparison of plots of **a** the magnetic field vertical component Z, and **b** relative heat flow q/q_o over, **c** a slope in terrain. Curves **a** and **b** are after Eppelbaum (1989) and Lachenbruch (1968), respectively

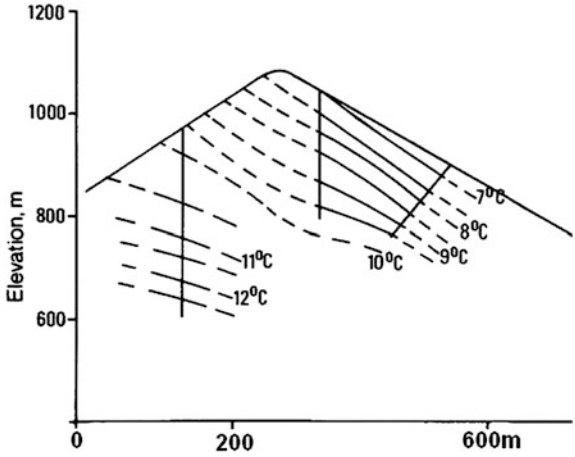

Fig. 10.3 Temperature cross-section for a hill near Wilbur (Washington, USA) as inferred from measured temperatures in three drill holes shown in the section (after Blackwell et al. 1980, with modifications)

anomalies from disturbing objects (massive ore in the southwestern part of the profile, and a vast zone of disseminated ore in the northeastern part) are more pronounced. Thermal, density and magnetic properties of ores and some host media rocks are presented in Table 10.1.

10.4 Quantitative Interpretation

The methodology for quantitative interpretation of temperature anomalies using advanced methods developed in magnetic prospecting is presented in detail in Sect. 7.5.

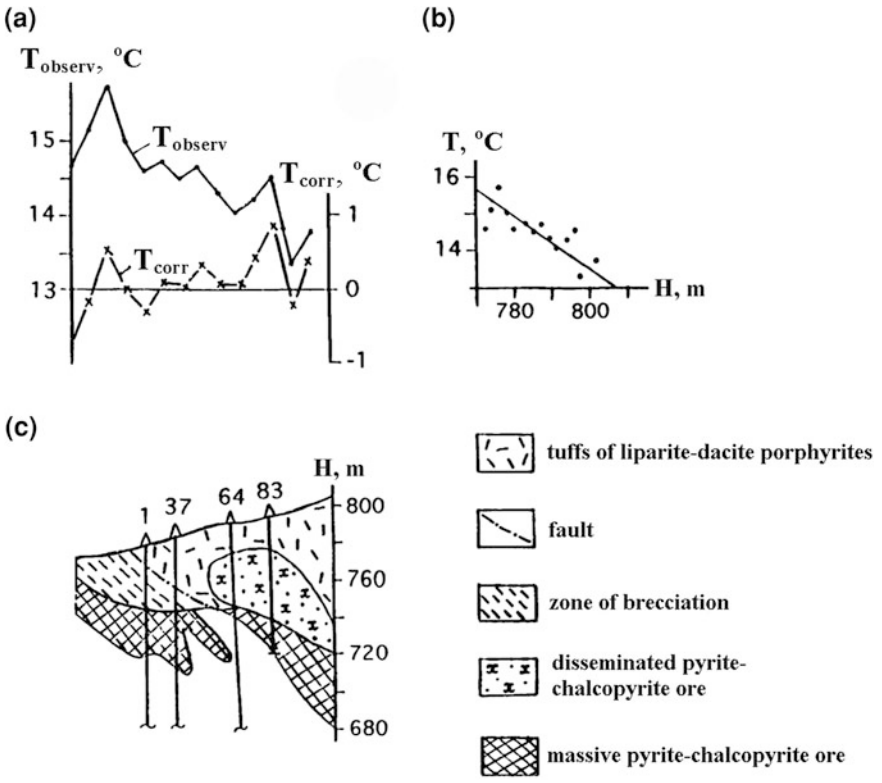

Fig. 10.4 Correlation technique of reducing the terrain relief effect in near-surface thermal prospecting in a district of the Kyzylbulakh gold-pyrite deposit (Nagorny Karabakh, Azerbaijan): **a** plots of observed and corrected temperature values, **b** correlation, **c** geological section (after Eppelbaum 1989)

10.5 Prospecting of Hard Economic Minerals

10.5.1 Surface Measurements

The investigation of physical properties in geothermics (as in other geophysical methods) is of great importance. Such measurements are necessary for the development of physical–geological models of the medium and contribute to the interpretation process. Table 10.2 (after Horai and Simmons 1969; Eppelbaum 1989; Khesin and Eppelbaum 1994; Eppelbaum and Khesin 2012) lists the thermal conductivity of some typical ore-forming minerals, ores, useful minerals and host rocks.

Figure 10.5 illustrates the temperature anomaly observed by a geophysical crew from TSNIGRI (Moscow) along the profile across the Kvaisa pyrite-polymetallic deposit (the Greater Caucasus). The anomaly amplitude exceeds 2 °C, which is traceable to the additional effect of the fracture located at the edge of the ore body.

Table 10.1 Physical properties of some rocks and ores in the Kyzyl-Bulakh gold-pyrite gold-pyrite deposit (simplified after Eppelbaum and Khesin 2012)

Lithology	σ, g/cm^3		κ, 10^{-5} SI		ρ, Ohm m		λ, W/(m °C)	
	Average	Range	Average	Range	Average	Range	Average	Range
Andesite-dacitic porphyrite	2.47	2.27–2.59	1,400	115–4,800	–	–	2.80	2.44–3.0
Intensely silicified andesitic porhyrite	2.45	2.36–2.56	210	30–660	–	–	2.87	2.72–3.0
Liparite-dacitic porphyrite	2.48	2.38–2.55	590	210–1,750	450	400–500	2.84	2.73–2.94
Dike of andesite-basalt composition	2.72	2.64–2.90	1,050	450–2,130	–	–	3.20	3.03–3.50
Disseminated pyrite-chalcopyrite ore	3.13	2.80–3.54	14	2–31	8	1–20	3.97	3.50–4.19
Dense-impregnated chalcopyrite ore	3.20	2.90–3.74	19	6–29	–	–	4.5	4.30–4.84
Massive pyrite-chalcopyrite ore	3.50	3.10–4.0	15	13–19	1	0.1–5	5.7	5.14–7.30

Table 10.2 Thermal conductivity of some ore-forming minerals, ores, useful minerals and host rocks

Ore-forming minerals	Thermal conductivity, W/(m °C)	Ores and some economic deposits	Thermal conductivity, W/(m °C)
Pyrite (monocrystal)	39–41.5	Massive pyrite-polymetallic ore	7–10
Sphalerite	26.7	Disseminated pyrite-chalcopyrite ore	3.2–5.0
Chalcopyrite	10.7	Magnetite ore	5.2
Pyrrotite	3.5	Coal	0.13–2.2
Galena	2.0	Rock salt	5.3–7.2
Haematite	26	Graphite	1.15–17
Ilmenite	5.2	Host rocks and environments	Thermal conductivity, W/(m °C)
Rutile	12.2	Marble	1.7–1.9
Magnetite	12.1	Granite	2.2–3.5
Baryte	3.2	Granodiorite	2.5–3.0
Anhydrite	11.3	Brick	0.6–1.2
Magnesite	13.9	Conglomerate	2.4–2.9
Olivine	7.6–12.3	Dry soil	0.3
Pyrope	7.6	Sand	0.3–2.95
Pyroxenes	8.5–16	Limestone	2.0–3.0
Mica	4.5–6.0	Sandstone	2.5–3.2
Quartz	18.3	Clay	0.25–1.08
		Dolomite	2.0–4.2
		Basalt	2.2–3.5
		Gabbro	2.0–2.3
		Water	0.59 (25 °C)

The temperature was measured in 1.0 m deep blast holes. The ore was pyrite-sphalerite in composition, and had a subvertical orientation in the volcanoclastic host rock. The thermal conductivity coefficients for the sandy-argillaceous host rock and thick pyrite-polymetallic ore were 2.0 ± 0.5 and 5.0 ± 1.0 W/(m °C), respectively, a difference of a factor of 2.5.

The quantitative interpretation was carried out by the use the characteristic point method. This served to locate the upper edge of the ore deposit, which occurred within unconsolidated volcanoclastic deposits from the Middle Jurassic. The results were confirmed by mining.

In Fig. 10.6, anomaly temperature interpretation results are presented for a district with a severely inclined relief in the Katekh deposit (the Greater Caucasus, Azerbaijan). The temperature was measured in 1.0 m deep blast holes. The T° plot shows two anomalies, one of which is from the sub-horizontal ore deposit and is not pronounced. The thermal conductivities for the host rock and thick pyrite-polymetallic ore were 1.45 ± 0.35 and 3.87 ± 0.57 W/m °C, respectively; i.e., when the coefficient ratio exceeded 2.5. The upper part of mineralization was completely oxidized and did not differ in thermal conductivity from the host

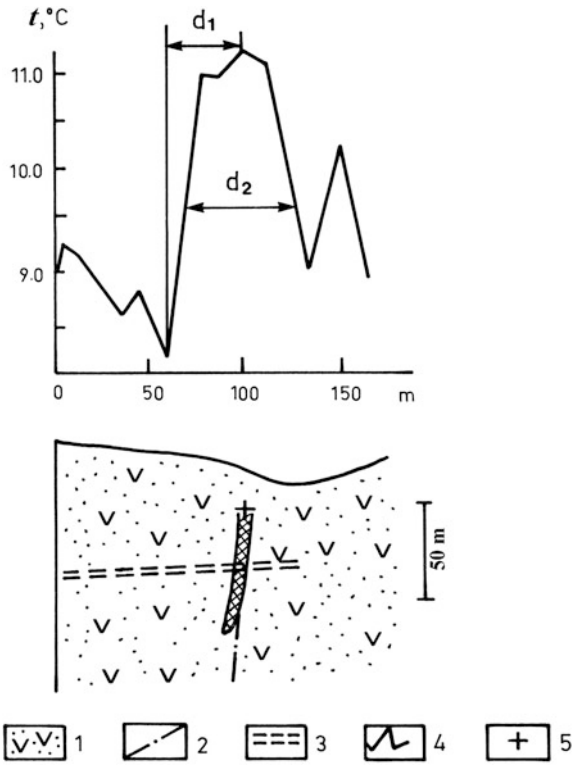

Fig. 10.5 Quantitative interpretation of temperature anomalies in the area of the Kvaisa pyrite-polymetallic deposit (southern slope of the Greater Caucasus, Georgia) (observed data and geological section after Ginzburg et al. 1974). (*1*) Volcanoclastic medium, (*2*) fault, (*3*) position of mine, (*4*) temperature graph, (*5*) determined position of the middle of upper edge of orebody. The massive sulfide ore body is *shaded*

medium. The analysis showed that the upper edge of the subvertical ore body was located within acceptable error margins.

An interesting example of a near-surface temperature survey over a quartz body is presented in Fig. 10.7. The thermal conductivity λ for quartz body is about 4.0 W/(m °C), λ for diorites and granites is about 2–2.5 W/(m °C), and λ of the weathering layer can consist of 1–1.5 W/(m °C). The temperature anomaly reached more than 6 °C (apparently due to the location of the quartz body very close to the surface).

A quantitative interpretation of temperature anomaly observed over an asphalt deposit is presented in Fig. 10.8. This led to successful identification of the position of the upper edge of the asphalt body.

10.5.2 Prospecting of Hard Economic Minerals in Mines

A temperature survey in adits was carried out with the following simple methodology. First of all, for this survey, non-working adits without any industrial activity (primarily, without air supply) were selected. On the basis of numerous

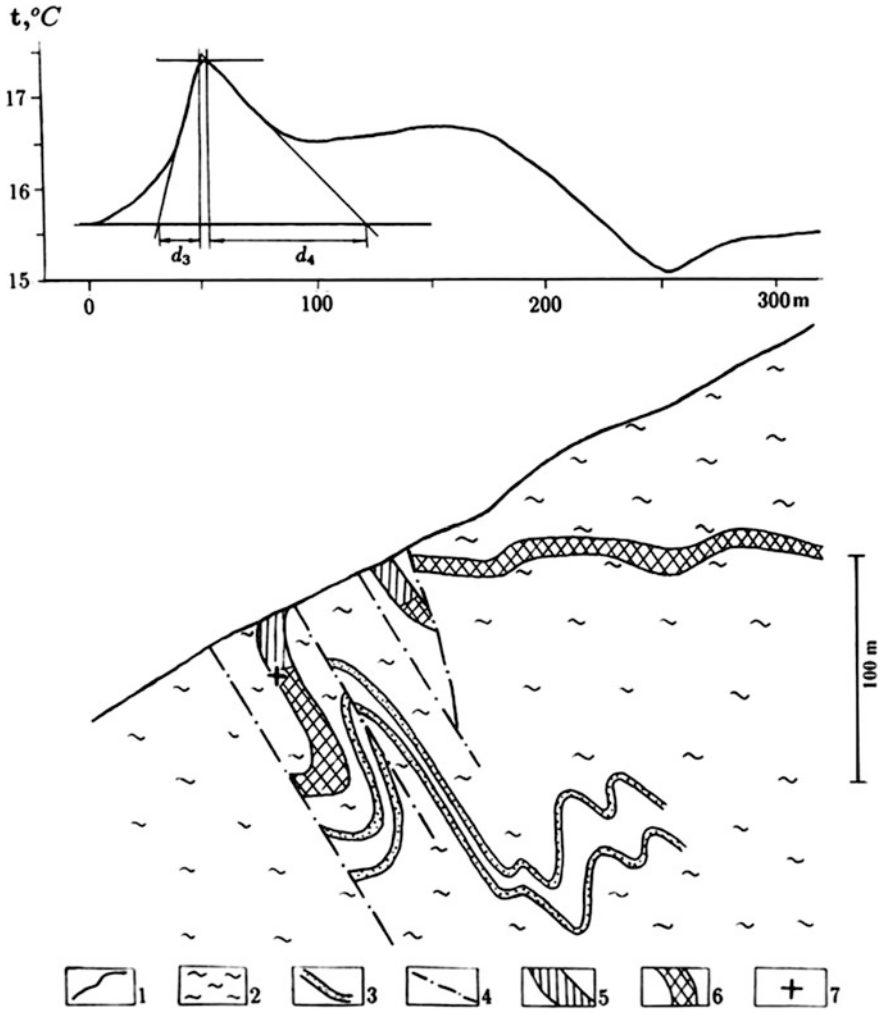

Fig. 10.6 Quantitative interpretation of the temperature anomaly in the Katekh pyrite-polymetallic deposit (southern slope of the Greater Caucasus, Azerbaijan). (*1*) Terrain relief, (*2*) sandy-argillaceous sediments, (*3*) band of sandstones, (*4*) fault, (*5*) oxidized pyrite-polymetallic ore, (*6*) massive pyrite-polymetallic ore, (*7*) determined position of the middle of upper edge of orebody (after Eppelbaum 1989). The observed temperature and geological sections are taken from Zverev et al. (1982) and an unpublished report of the "Azerbaijangeologiya"

field investigations, physical and mathematical modeling the following peculiarities were determined (Lakhtionov and Tarkhov 1967; Eppelbaum 1989; Ginzburg and Maslennikov 1989):

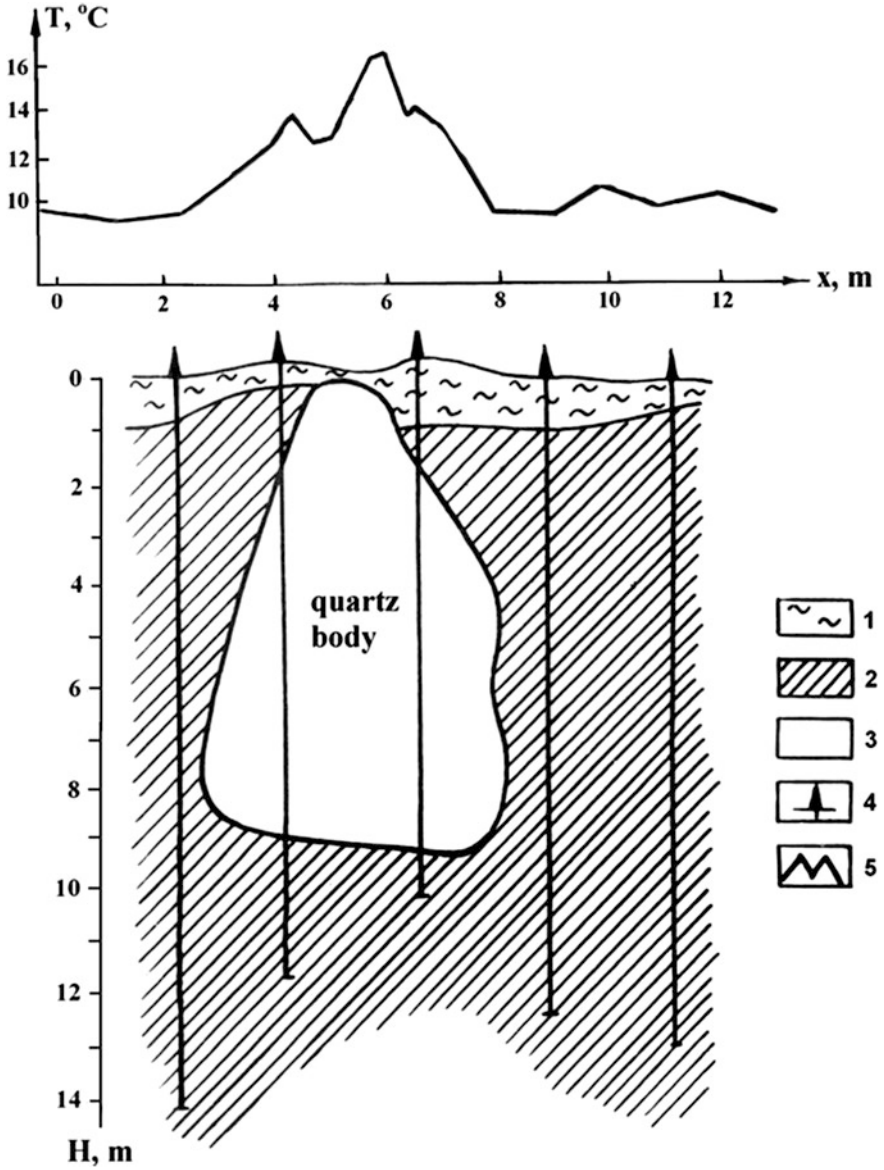

Fig. 10.7 Results of temperature survey over a quartz body (former USSR) (reconstructed after Bareyev et al. 1985). (*1*) Weathering layer, (*2*) host rocks (diorites and granites), (*3*) quartz body, (*4*) boreholes, (*5*) temperature curve

(1) Equipotential temperature surface over ore bodies have positive values and negative values below the bodies. Within the ore bodies the equipotential surfaces are practically parallel.

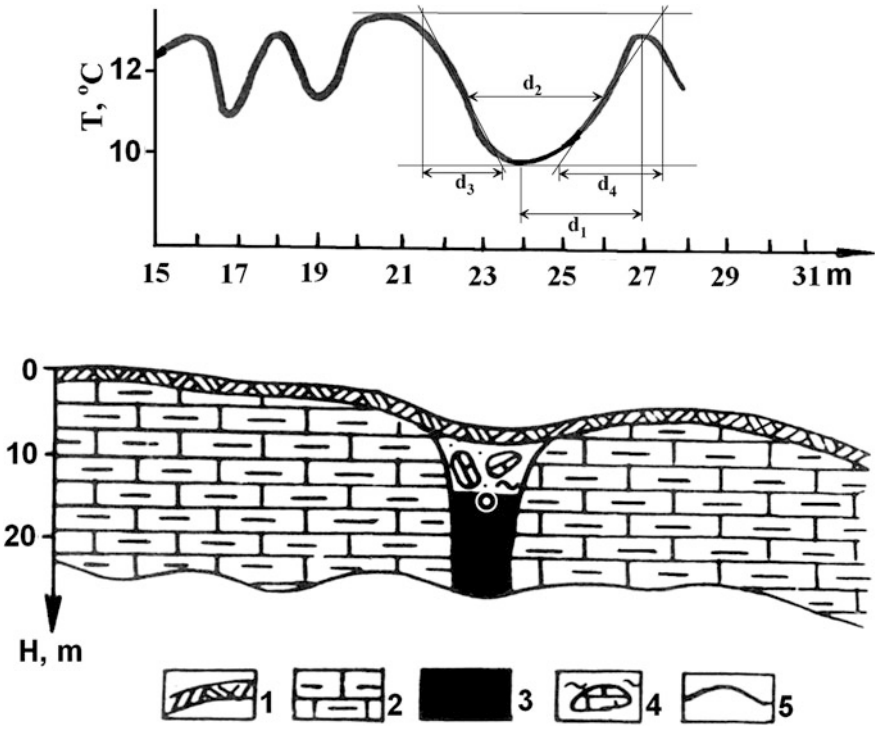

Fig. 10.8 Results of temperature survey at one of the asphalt deposits of the former Soviet Union. (*1*) Soil, (*2*) interbedding of carbonate and terrigeneous rocks, (*3*) asphaltite, (*4*) break zone, (*5*) temperature curve (observed temperature curve and geological section after Bareyev et al. 1985). Symbol *circle with dot* shows the determined position of the upper edge of asphaltic body

(2) Geothermal gradients both above and below the ore bodies have heightened values, but inside the ore bodies have lower values.
(3) In deep bodies, isothermic surfaces are inclined in such a way that within the same horizon the temperature in the roof is higher than at the bottom.
(4) Temperature anomalies reach values of 1 °C and more and maximal depths from the ore bodies where the anomalies can be reliably ascertained (with an accuracy of ±0.02 °C) can be many tens of meters.

The width of the anomalous temperature interval provides information about the size of an anomalous object, whereas the temperature gradient is indicative of the distance to the observation line. The distribution of the temperature graph can in many cases be used to draw conclusions about the location of the anomalous target.

In the Katsdag pyrite-polymetallic deposit (Azerbaijan), an areal temperature survey was performed (L. Eppelbaum, as a student in the Geophysical Dept. of the Azerbaijan Univ. of Oil and Chemistry, took part in these field works) in the

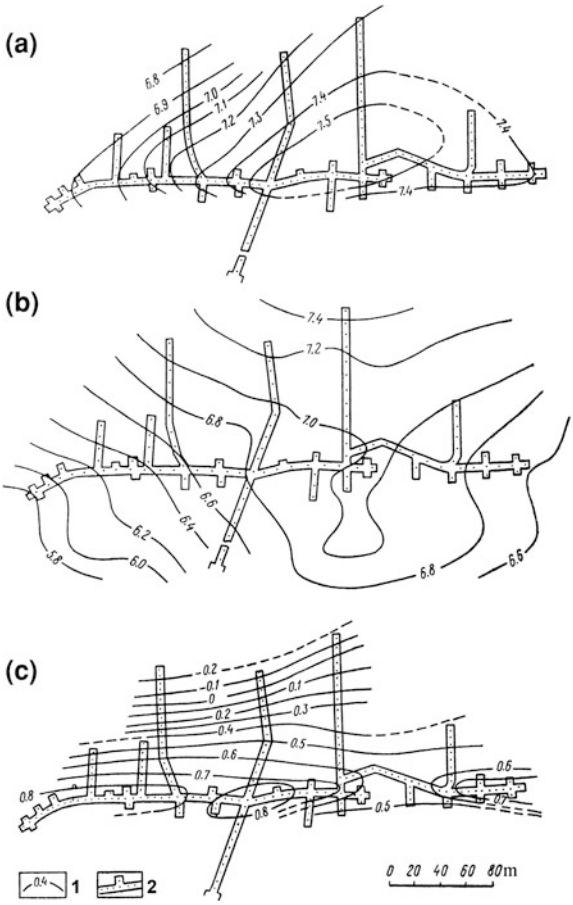

Fig. 10.9 Results of mine thermal prospecting in the Katsdag pyrite-polymetallic deposit (Azerbaijan, southern slope of the Greater Caucasus) (after Ginzburg and Maslennikov 1989, with minor modifications). Temperature maps: **a** observed values, **b** normal field, **c** anomalous values. (*1*) Temperature isolines, (*2*) underground shifts

underground drifts (Fig. 10.9a). The temperature map for the normal field (which incorporates the influence of the surface rugged relief, the depth of attenuation of annual temperature variations propagating from the Earth's surface and other factors) is shown in Fig. 10.9b. A residual anomalous temperature map is depicted in Fig. 10.9c. Clearly, the final anomalous map (Fig. 10.9c) differs considerably from the initial observations (Fig. 10.9a).

Temperature measurements in adit 10 of the Katsdag deposit were made in glasses filled with water at an observation step of 10 m (Fig. 10.10). Analysis of the temperature field indicated that the temperature anomaly observed in the right portion of this geological section in general corresponded to the anomalous body. At the same time, the temperature anomaly observed in the left portion of this section testified to the presence of some additional ore bodies not detected by geological means.

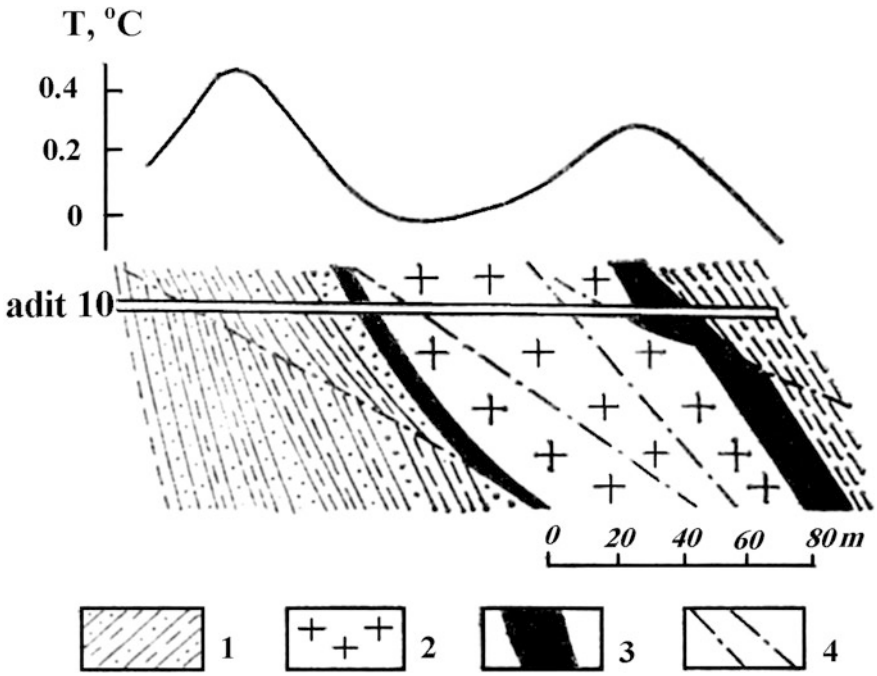

Fig. 10.10 Graph of anomalous temperature distribution along the main opening of adit 10 in the Katsdag polymetallic deposit, southern slope of the Greater Caucasus (Azerbaijan). (*1*) sandstone, (*2*) liparite dacites, (*3*) massive copper-pyrite ore, (*4*) faults

It is worth noting that when exploring pyrite deposits, there can be low-temperature ore oxidization that can lead to fire. Thermal prospecting is the most effective method for the early detection of such sites.

The next example shows the results of temperature measurements in a mine in one of the gold-sulfide deposits of Yakutia (Fig. 10.11) (after Brodovoi et al. 1988). Here the thermal conductivity of the anomalous bodies exceeded the thermal conductivity of the surrounding medium by 2–4 fold. Two closely disposed sulfide bodies produced one elongated temperature anomaly with amplitude of about 0.3 °C.

An example of the influence of rugged terrain relief on adit temperature measurements is presented in Fig. 10.12. It is known that the surface relief influences the temperature field at a distance of 4–5 amplitudes of the relief's maximal amplitude (e.g., Cheremensky 1977). A temperature survey was performed in blast holes of 1.5 m in the adit walls. The search targets in this case; namely, massive pyrite-polymetallic ore bodies, occurred in the sandy-argillaceous medium that provided a high thermophysical contrast. The observed temperature curve (Fig. 10.12b) was considerably distorted by the rugged relief influence. After application of a correlation approach (coefficients of linear regression were

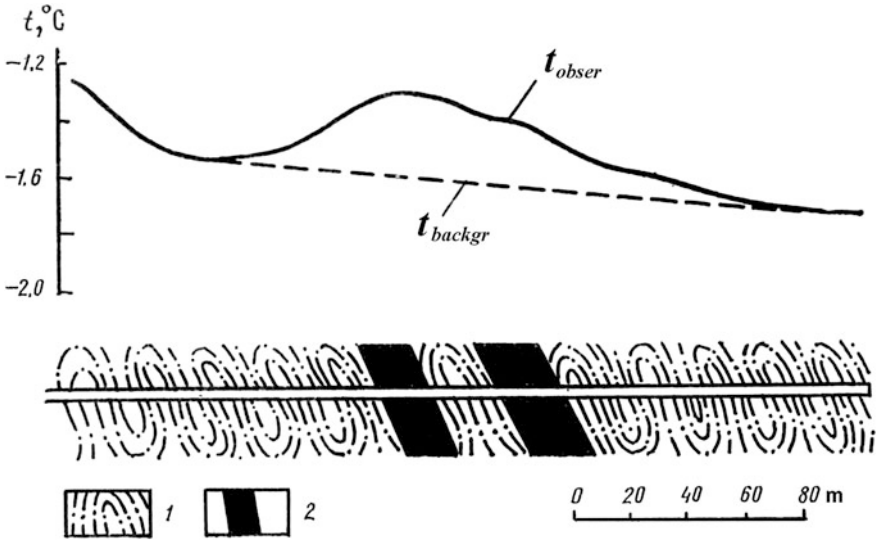

Fig. 10.11 Example of application of underground thermal prospecting in a gold-sulphide deposit in Yakutiya (Russia). (*1*) phyllites with siltstone, (*2*) gold-sulphide ore (Brodovoi et al. 1988)

obtained by the least-square method), the corrected temperature graph was constructed (Fig. 10.12a). Quantitative analysis of the graph led to calculation of the position of the center of the anomalous target.

10.6 Prospecting for Oil and Gas Deposits

An interesting thermal anomaly in the northern Dead Sea Basin was observed by Ben-Avraham and Ballard (1984). The amplitude of the anomaly exceeded 0.2 °C (the accuracy of these observations was about 0.01 °C). Its form suggested that the anomalous body (or its upper surface) had enhanced thermal conductivity, and could be approximated by a horizontal circular cylinder (HCC). Application of quantitative methods determined the position of the cylinder's center (Fig. 10.13); it was predicted to be at a depth of about 60 m. Here both the characteristic point method (parameters d_1 and d_2) and the tangent method (parameters d_3 and d_4) (Khesin and Eppelbaum 1994) were used (see Sect. 7.5). Parameter d_3 is the difference in the abscissa of the points of intersection of an inclined tangent with horizontal tangents on one branch; parameter d_4 is the same on the other branch; (d_3) is selected from the plot branch with conjugated extrema).

We suggested that the anomaly was caused by the upper surface of a small salt dome (there are numerous salt domes in this area). The temperature moment was found to be approximately 9 °C m.

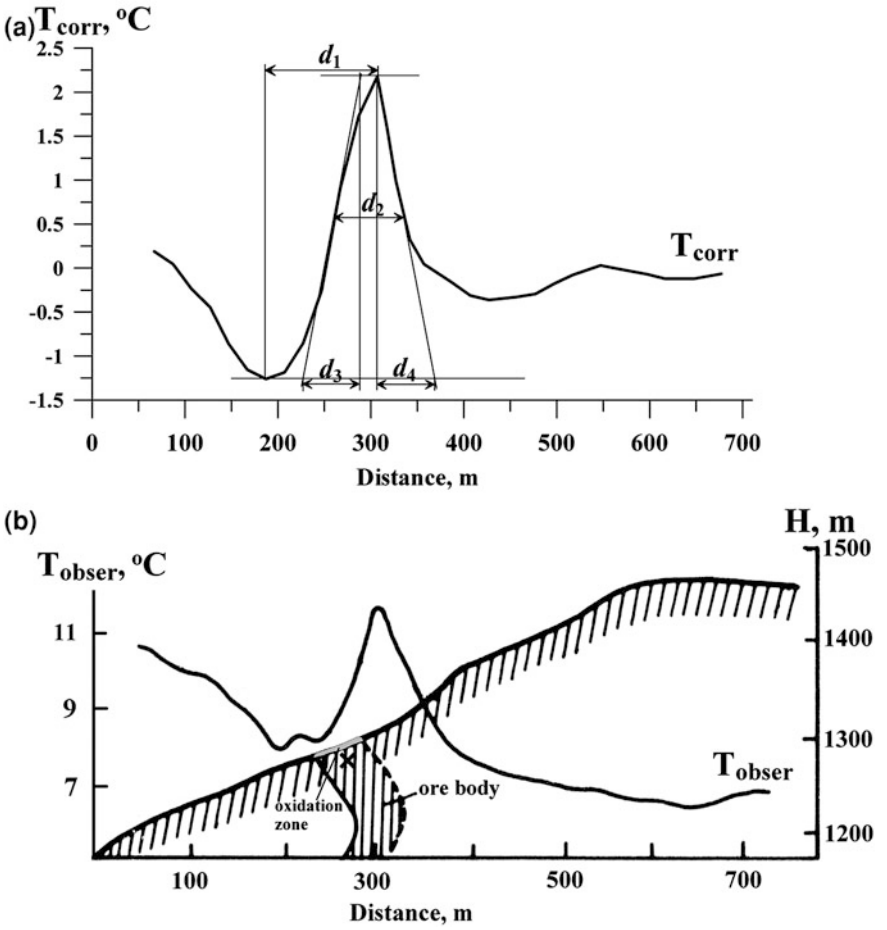

Fig. 10.12 Quantitative analysis of near-surface thermal investigations carried out in an adit of the Filizchay pyrite-polymetallic deposit (southern slope of the Greater Caucasus). Observed temperature field and geological section are adapted from (Borisovich et al. 1988). **a** Quantitative analysis of corrected temperature graph, **b** observed temperature field and geological section. The *plus* symbol designates the position of the middle of the upper edge of the anomalous body

The next example illustrates the application of these methods in the Muradkhanly oil deposit in Central Azerbaijan (Fig. 10.14), where the temperature was measured in 3 m deep wells and the data thus obtained were smoothed by the use of a sliding interval average of three points. A fault was revealed here by a field crew from "YuzhVNIIGeofizika" (Baku) using gravitational and magnetic methods of prospecting, which were tied in with drilling data.

Thermal observations were conducted by Sudzhadinov and Kosmodemyansky (1986). The position of the upper edge of the fault was calculated using the tangents and characteristic point methods; its projection in plane coincided exactly

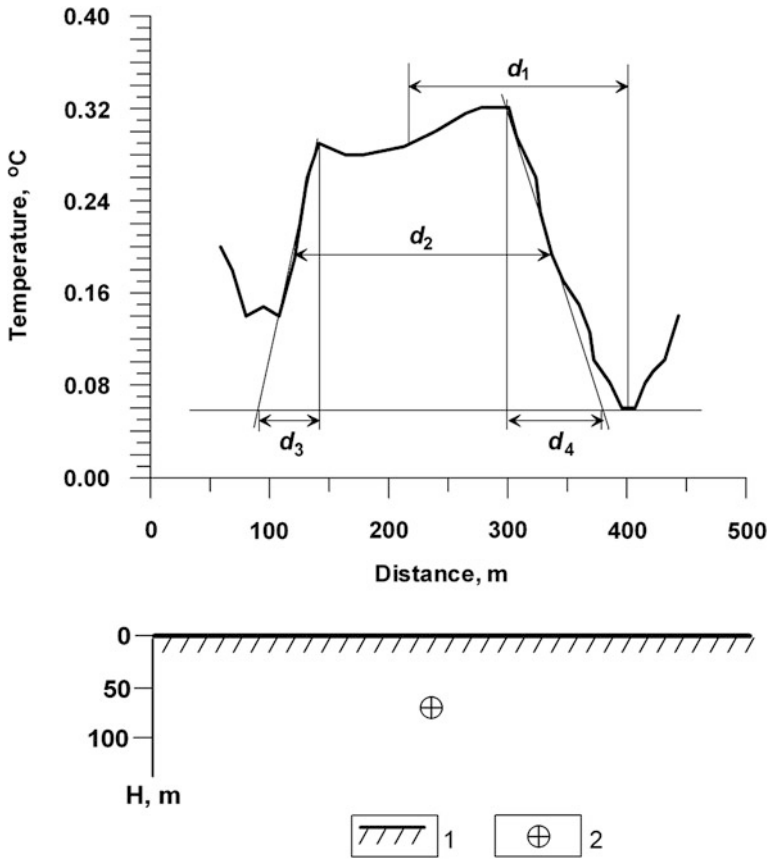

Fig. 10.13 Quantitative interpretation of temperature anomalies in the northern Dead Sea Basin (observed temperature curve after Ben-Avraham and Ballard 1984; interpretation after Eppelbaum et al. 1996). (*1*) Sea bottom; (*2*) position of center of a horizontal circular cylinder

with the fault position obtained from the independent geophysical and geological data. The value of the temperature moment here was sufficiently high: −230 °C m.

Another example of the inverse method application is presented in Fig. 10.15.

The calculated position of the fault upper edge coincided with the available geological data. Interestingly, the registered temperature curve was very similar to a magnetic anomaly from the same inclined thin bed magnetized along its dipping. The *TM* value was found to be $\approx$80 °C m.

The following example shows the feasibility of quantitative estimates of the position of an anticline structure containing oil and gas deposit (Fig. 10.16). The accuracy of near-bottom single temperature measurement was no less than 0.01 °C (Artemenko and Malovitsky 1977). The quantitative analysis (a model of a horizontal circular cylinder was used) the revealed the center of an anticline structure.

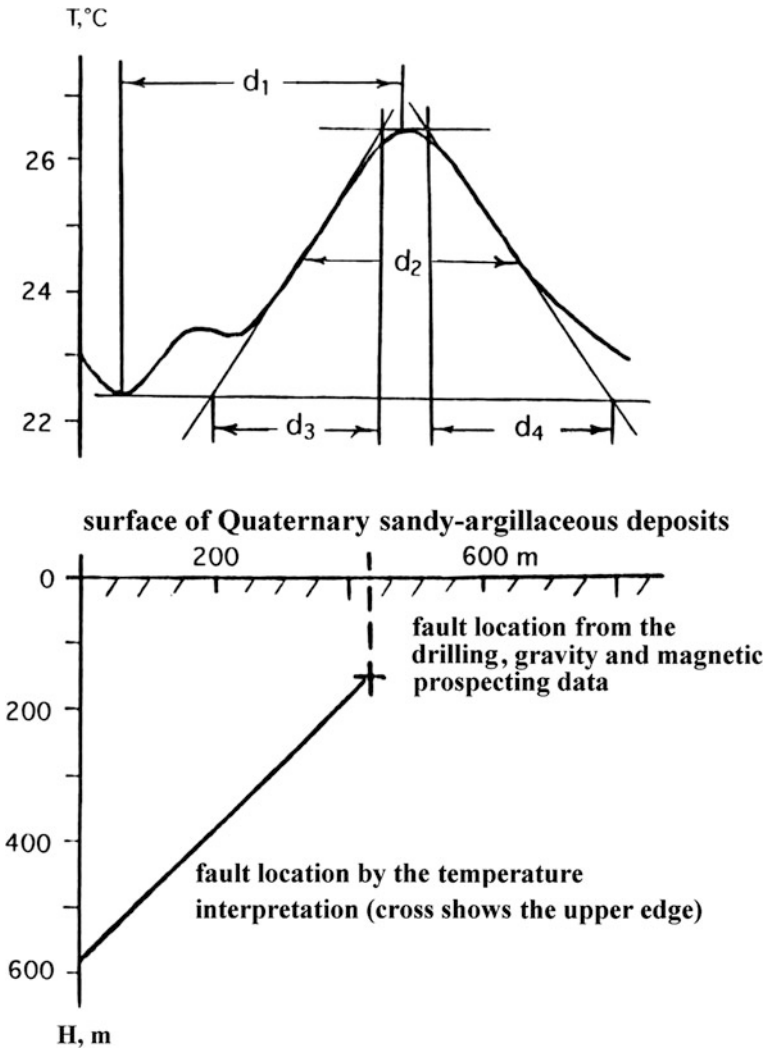

Fig. 10.14 Interpretation of the temperature anomaly in the district of the Muradkhanly oil field in the Middle Kura Depression (after Eppelbaum 1999)

It is thus likely that small negative temperature anomalies in the central part of the profile were caused by the influence of an oil and gas deposit.

A significant subsurface temperature anomaly was observed over the Black Lake hydrocarbon deposit (USA) (Fig. 10.17). Lasky (1967) suggested that this anomaly could be related to hydrocarbon occurrences, both structurally and stratigraphically.

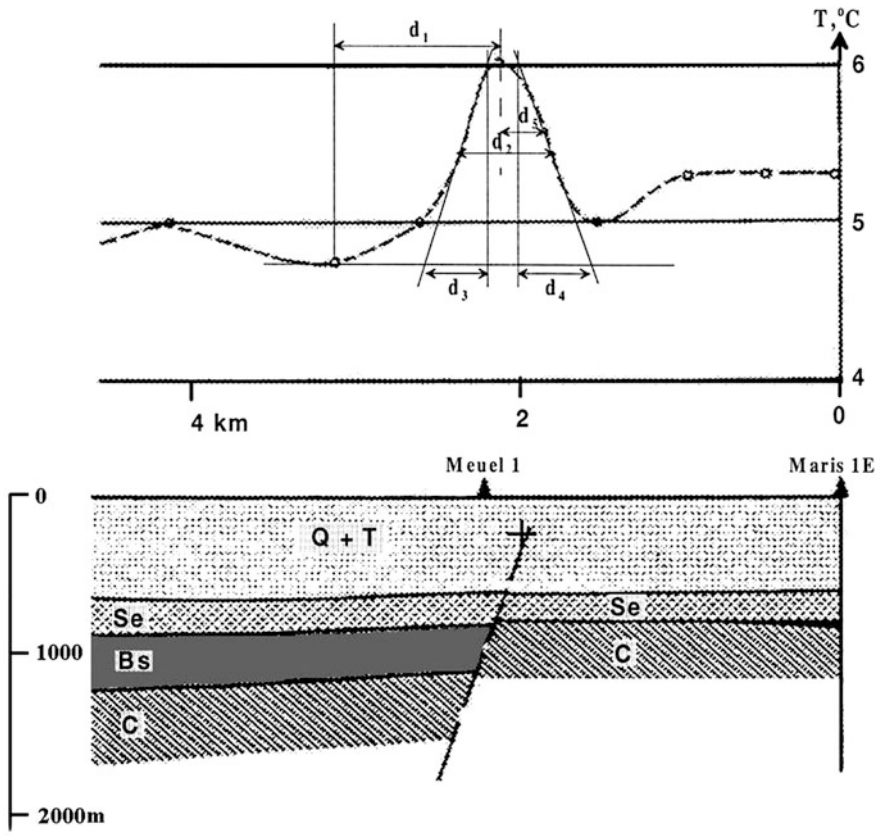

Fig. 10.15 Quantitative interpretation of a temperature anomaly over a fault in the "Peel" district, southern part of The Netherlands (observed curve and geological section after Poley and Steveninck 1970). The *plus* symbol marks the position of the upper edge of the fault

10.7 Delineation of Archaeological Features

10.7.1 Some Precursors of NSTM

Temperature measurements can often help locate ancient remains since the thermal properties of archeological targets can differ from their surrounding medium (Table 10.3). It should be underlined that studying the thermal parameters in archeological prospection can sometimes be as or more important than conventional geophysical methods (e.g., GPR, magnetic survey, electromagnetic tomography and microgravity) (Eppelbaum 2000).

Tabbagh's (1973) publication is considered to be the first to suggest applying *NSTP* in archeology. Périsset and Tabbagh (1981) presented the distribution of the heat of flux (derived from the *NSTP*) over the Neolithic camps in the

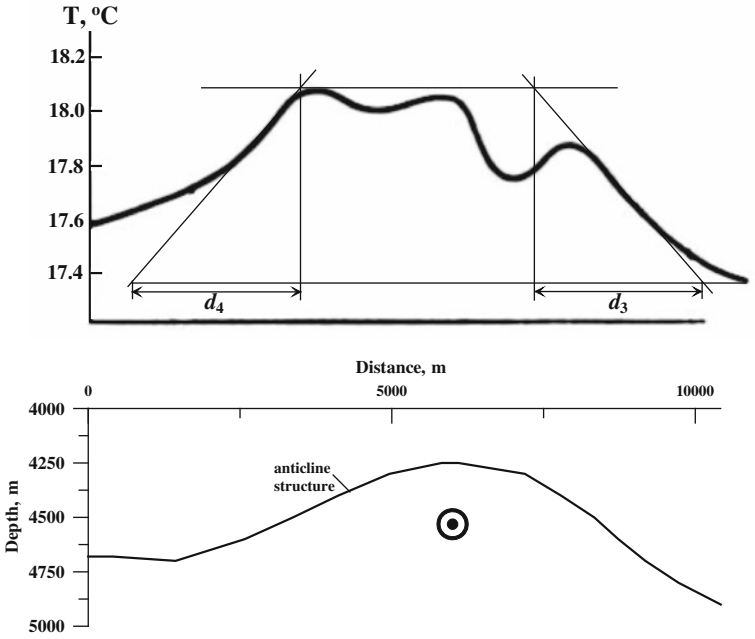

Fig. 10.16 Graph of the temperature anomaly observed in near-bottom sediments over the Bakhar oil and gas deposit, in the western part of the Caspian Sea (Azerbaijan) (initial data after Artemenko and Malovitsky 1977). The *circle with dot* symbol marks the position of the center of the anticline structure

Seine et Marne region (France). The differential heat analysis method was used to detect areas of discontinuity and heat transfer to differentiate archeological features (Benner and Brodkey 1984). An interesting and comprehensive set of the *NSTP* observations over various archeological objects in Poland was reported by Moscicki (1987). Noel and Bellerby (1990) provided a detailed analysis of thermal equipment needed for *NSTP* in archeology. A temperature survey was successfully applied in several archeological sites in Verulamium and at Fountains Abbey (England) (Bellerby et al. 1990).

NSTP was successfully applied to locate Crusader fortress remains in the city of Netanya (Israel) (Eppelbaum 2010). An effective integration of the *NSTP* with multiscale remote sensing was used at the Ponte del Passo archeological site (northern Italy) (Brivio et al. 2000). A modified sequential analysis *NSTP* data analysis method for archeological sites was developed recently (Eppelbaum 2009).

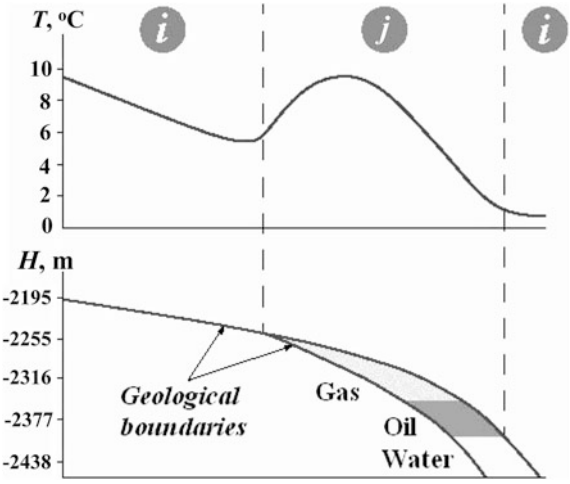

Fig. 10.17 Graph of the temperature field observed over the Black Lake deposit (Louisiana, USA) (after Lasky 1967). According to the author, intervals *i* and *j* designate background and anomalous parts of the temperature graph, respectively

10.7.2 Examples of Quantitative Analysis of Temperature Anomalies Observed Over Archeological Features

10.7.2.1 Temperature Anomaly Over a Set of Buried Walls in Verulamium, Hertfordshire, Great Britain

A temperature survey was carried out over the remains of walls (limestone walls occurring in dry soil) at a depth of 20 cm and corrected for diurnal effects using the combined base station least-square technique (Bellerby et al. 1990). Anomalies I and II (Fig. 10.18) were analyzed by the tangent and characteristic point methods. To interpret Anomaly I a model of a thin bed was employed, and for anomaly II a model of a horizontal circular cylinder. The obtained depth of the upper edge of the model of the thin bed was 80 cm and was in good agreement with the available archeological data (Bellerby et al. 1990). The calculated depth to the center of the horizontal circular cylinder was about 2.3 m. The rough calculation indicated that wall height consisted of no less than 3 m, which was in line with archeological data. The temperature moment (TM) for anomalies I and II were 0.04 and 0.86 m^2 °C, respectively.

10.7.2.2 Temperature Anomalies in an Archeological Site Near Ponte del Passo, Northern Italy

This archeological site is located in the upper Como region (northern Italy). The temperature anomaly was observed over abundant anthropogenic features occurring in lacustrine clay (Fig. 10.19). The temperature anomaly analysis was based

Table 10.3 Thermal conductivities of some rocks[a] environment features[a] and archaeological remains (supplemented after Eppelbaum 2009)

Geological rocks and objects	Thermal conductivity, W/(m °C)	Environmental features	Thermal conductivity, W/(m °C)
Clay	0.25–1.08	Air	0.026 (25 °C)
Sand	0.3–2.95	Water	0.59 (25 °C)
Limestone	2.0–3.0	Bitumen	0.2
Sandstone	2.5–3.2	Snow (fresh)	0.1-0.2
Dolomite	2.0–4.2	Snow (old)	0.5-1.8
Basalt	2.2–3.5	Ice	2
Gabbro	2.0–2.3	Archaeological remains	Thermal conductivity, W/(m °C)
Marble	1.7–1.9	Wood	0.09–0.14
Granite	2.2–3.5	Isolated cavity	0.05
Granodiorite	2.5–3.0	Ceramics	1.8–2.1
Brick	0.6–1.2	Glass	1.1–1.2
Conglomerate	2.4–2.9	Paper	0.4–0.6
Dry soil	0.3	Slag	0.5–1.0
Woodland soil	0.8	Iron	29.6 (25 °C)
Rock salt	5.3–7.2	Gold	317
Massive pyrite-polymetallic ore	7–10	Lead	35

[a] Many kinds of archeological remains are composed of geological rocks and contain environmental features

on the tangent and characteristic point methods (a model of a thin bed was employed). The depth of upper edge (about 3 m) was consistent with the archeological data. The TM value was 2.45 m °C. This value testifies to the comparatively large size of the archeological feature and the significant thermophysical contrast between the disturbing target and the surrounding medium.

10.7.3 Temperature Field Modeling by Mathematical Analogy to the Magnetic Field

The following example (Fig. 10.20) confirms the direct mathematical analogy between the magnetic and temperature anomalies suggested in (Carslow and Jaeger 1959) Temperature data were observed at a depth of 20 cm over an ancient crypt (the old family tomb of the proprietors of Ksiaz Castle), Lower Silesia, Poland (Moscicki 1987). This monumental crypt is located in a gravel-sand medium; several small vertical windows allow free air penetration (Moscicki 1987).

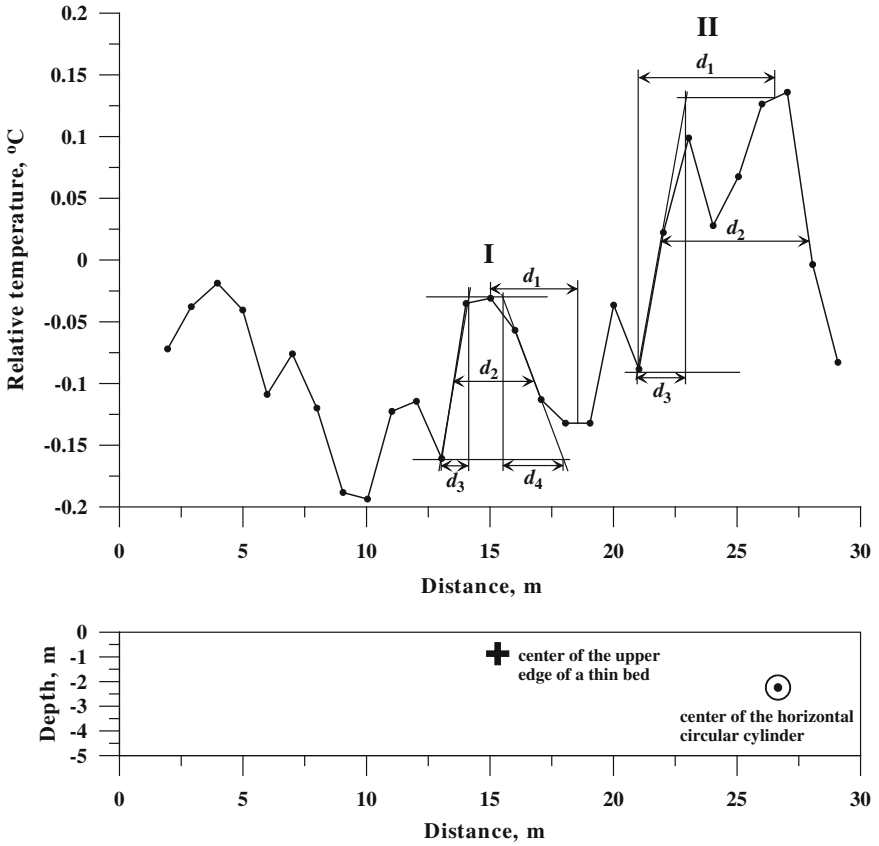

Fig. 10.18 Quantitative interpretation of temperature anomalies observed over a set of buried walls in Verulamium (Hertfordshire, Great Britain). The observed temperature profile is reconstructed from Bellerby et al. (1990). The *plus* and *circle with dot* symbols marks the position of the upper edge of the thin body and the center of horizontal circular cylinder, respectively, as obtained from analysis of Anomalies I and II (after Eppelbaum 2009)

The geometric shape of this crypt is between the thick bed and horizontal plate models [a quantitative analysis was applied based on a thick bed model (Khesin et al. 1996; Eppelbaum 2013)]. From the same model, the temperature and magnetic (ΔZ by vertical magnetization of the medium and archaeological features) fields were computed. As shown in Fig. 10.20, the difference between the observed and computed temperature fields was significantly larger than the difference between the observed temperature and the computed magnetic fields. This clearly demonstrates the applicability of corresponding magnetic field modelling in analyzing temperature anomalies (Eppelbaum 2009).

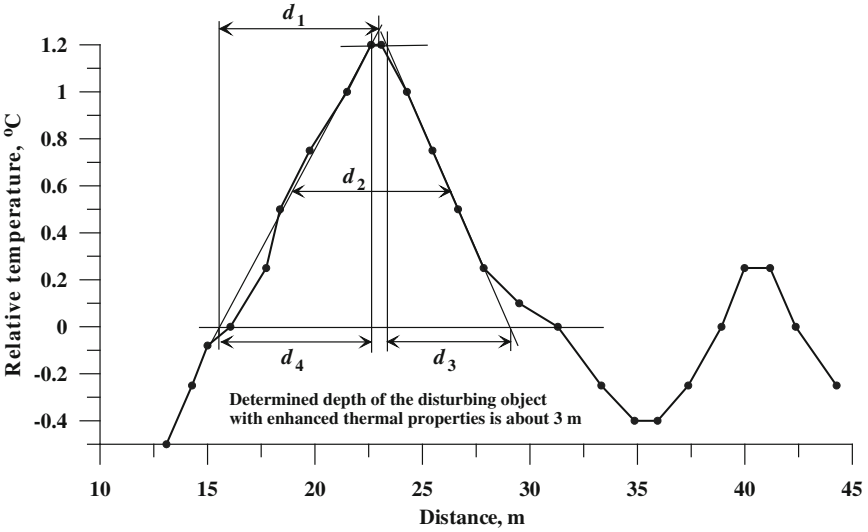

Fig. 10.19 Quantitative examination of temperature profile observed at an archeological site near Ponte del Passo, northern Italy (observed data after Brivio et al. 2000; interpretation after Eppelbaum 2009)

10.8 Mapping Underground Caves

Near-surface temperature surveys can also be used to locate underground caves. For example, the results of near-surface thermal prospecting over an underground cavity in Cracow, Poland, were interpreted by using the methods described above (Fig. 10.21). Measurements were made at a depth of 40 cm and the profile spacing was 1 m (Moscicki 1987). The square underground cavity was approximated by a horizontal circular cylinder (HCC). The methods described above successfully pinpointed the center of the HCC with acceptable accuracy. The calculated value of TM was very small: ≈ 0.3 °C m.

10.9 Mapping Karst Terranes

Figure 10.22 shows the results of subsurface temperature measurements in southern Germany (Neckar valley near Kiebingen) over deeply occurring karst terranes with comparatively hot water (see also Sect. 4.1.3). The objective was to locate the small areas (spots) at which warm water rises from a depth of about 100–150 m. Kappelmeyer and Hänel (1974) suggested using the following expression to calculate the quantity of heat flow from a depth:

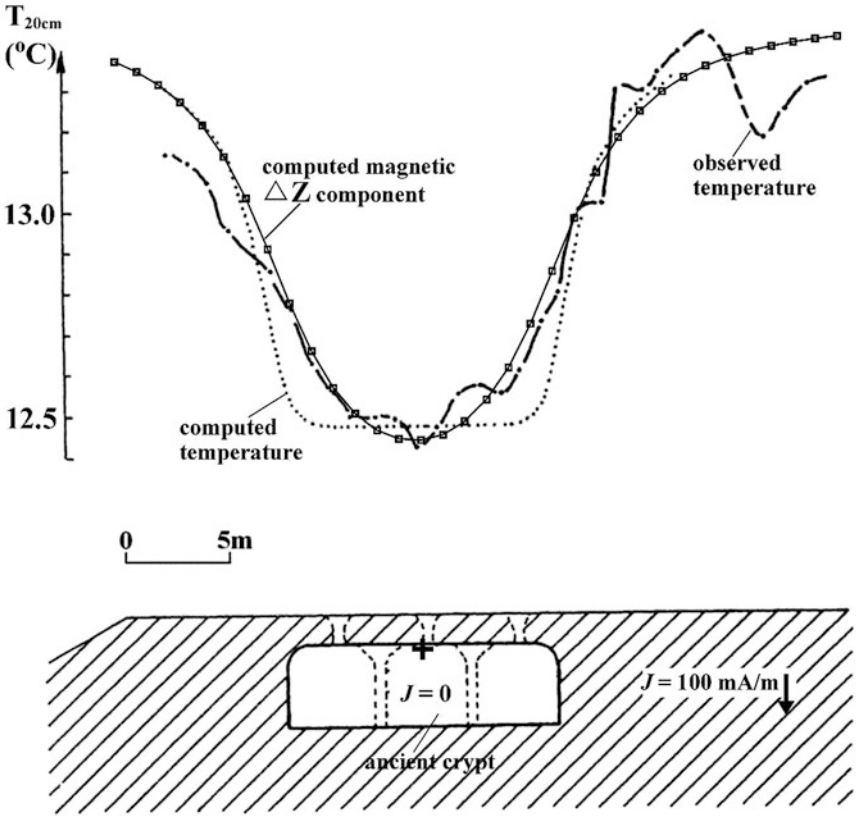

Fig. 10.20 Comparison of temperature data observed over an ancient buried crypt (Ksiaz Castle, Lower Silesia, Poland) with the 3D computed magnetic data from the same model. The *plus* symbol marks the position of the upper edge of the thick body as obtained from analysis of the observed temperature graph (archeological model, observed and computed temperature after Moscicki 1987)

$$Q = qF = \int_F \frac{\theta_m - \theta_b}{\lambda/\alpha + z} \lambda df, \tag{10.9.1}$$

where Q is the heat flow through anomalous area F, θ_m is the measured temperature at depth z inside the anomaly [°C], θ_b is the background temperature at depth z outside the anomaly [°C], z is the measured depth [m], λ is the thermal conductivity of the host rocks [W/m °C], and α is the thermal diffusivity [10^{-7} m^2/s].

The term λ/α is small for cases where $z > 1$–2 m and may be omitted. Then parameter Q can be easy estimated as 5.6×10^4 W (after Kappelmeyer and Hänel 1974, with modifications).

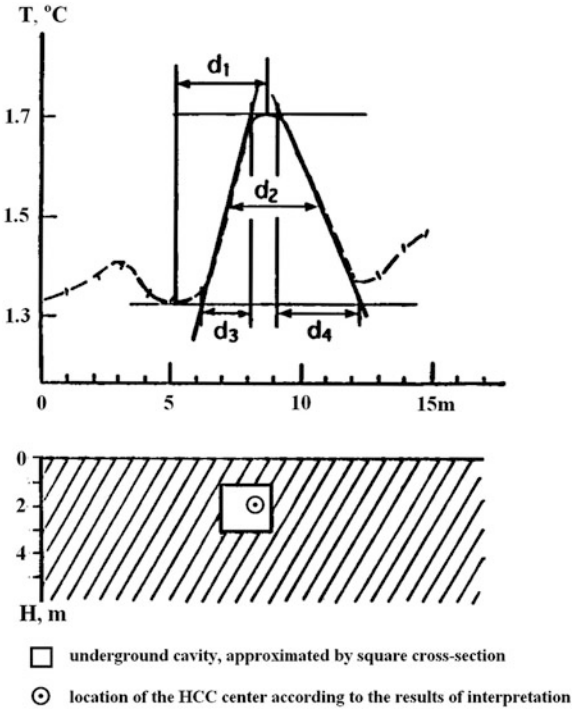

Fig. 10.21 Quantitative interpretation of the temperature anomaly over an underground cavity (Cracow's Planty Park). Observed temperature and geological section from Moscicki (1987), interpretation after Khesin and Eppelbaum (1994)

Near-surface thermal surveys are necessary component of the integrated subterranean karst localization (Eppelbaum 2007).

More deeply occurring karst terranes (caverns) can be analyzed by the joint use of subsurface and deep temperature observations in karst spring areas (Fig. 10.23).

10.10 Other Applications

10.10.1 Environmental and Engineering Investigations in Deep Tunnels

Thermal measurements in deep, long tunnels have special environmental and engineering interest due to the numerous changes in geothermal gradient in these areas (for example, Fig. 10.24). Obviously, engineering calculations preceding the tunnel construction must take the possible temperature behavior in these tunnels into account. For instance, as illustrated in Fig. 10.24, in some areas along the Simplon railway tunnel in the Swiss Alps, the temperature is close to 50 °C and even exceeds this value. The greatest disparity between the measured and calculated temperature data in this figure is located in the 15.4 km of the tunnel where a

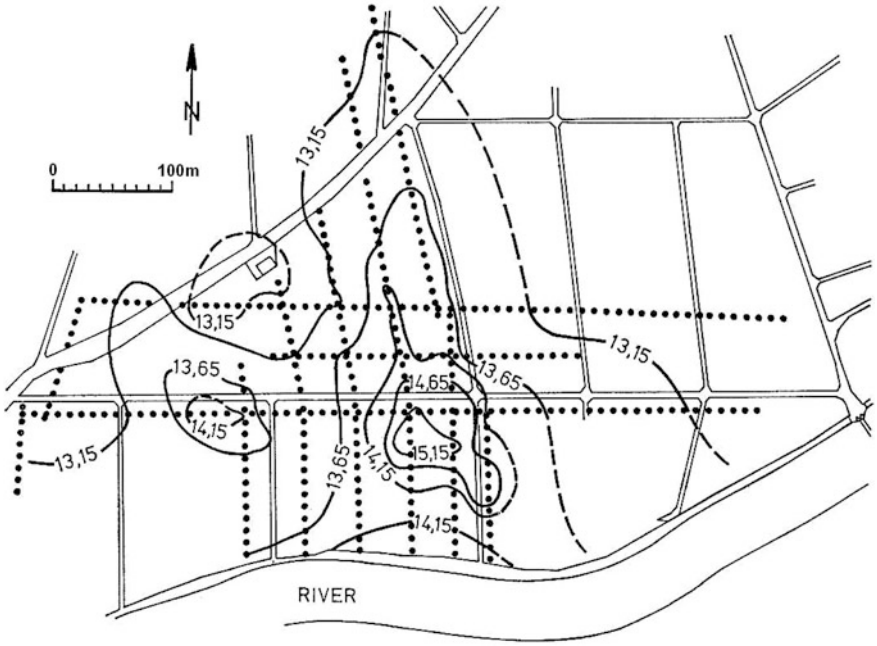

Fig. 10.22 Temperature anomalies observed at 1.5 m in depth in Kiebingen, Germany. These anomalies are caused by karst water emerging from a depth of 100–150 m in the groundwater at about 4–6 m in depth (after Kappelmeyer and Hänel 1974)

significant inflow of cold waters was revealed. Thus, such a comparison of observed and computed temperature data may be used for searching cold (and warm) waters, and some other geological peculiarities. Besides cool waters, deep tunnels usually contain a considerable inflow of warm waters. Such warm waters may be used for space heating in engineering constructions or utilized for certain agricultural purposes.

10.10.2 Delineation of a Flowing Landslide

Near-surface temperature and SP investigations were carried out in 1972 on a small flowing landslide near the town of Adler (coastal plain of Black Sea, Russia) (Fig. 10.25) (Bogoslovsky and Ogilvy 1977). The temperature anomaly pattern very clearly reflected the contour of a buried landslide. Two positive temperature anomalies in the center of landslide obviously indicated some uplifted forms of the landslide body.

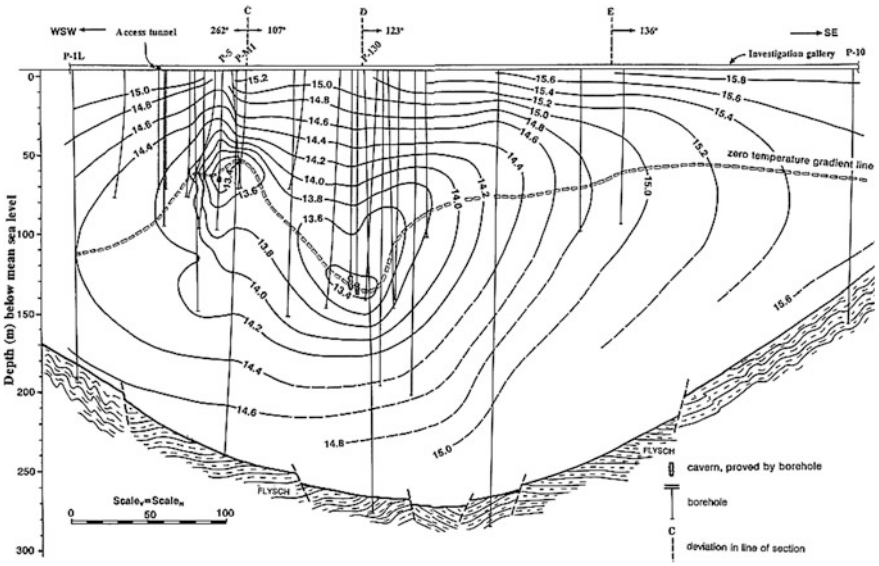

Fig. 10.23 Joint subsurface and deeper temperature observations in the Ombla karst spring near Dubrovnik, Croatia (after Ravnik and Rajver 1998)

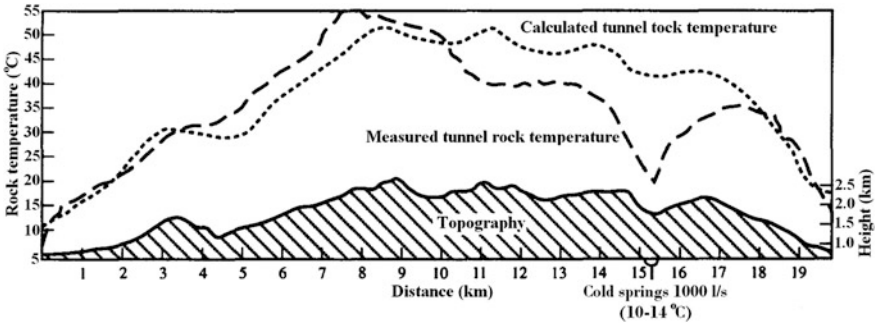

Fig. 10.24 Measured and computed (from the model of homogenous host rocks) temperature behavior in the Simplon railway tunnel (Swiss Alps). The lower temperatures around 15.4 km were observed where a strong cold inflow was discovered (after Niethammer 1910 and Rybach 1995)

10.10.3 Submarine Spring Mapping

Submarine spring temperature mapping was carried out on the Black Sea coast of Georgia to better understand the nature of the interaction of sea waters with the groundwater flow (Fig. 10.26). The thermometric and electrometric observations conducted on a stretch of the sea coast were aimed at mapping submarine springs

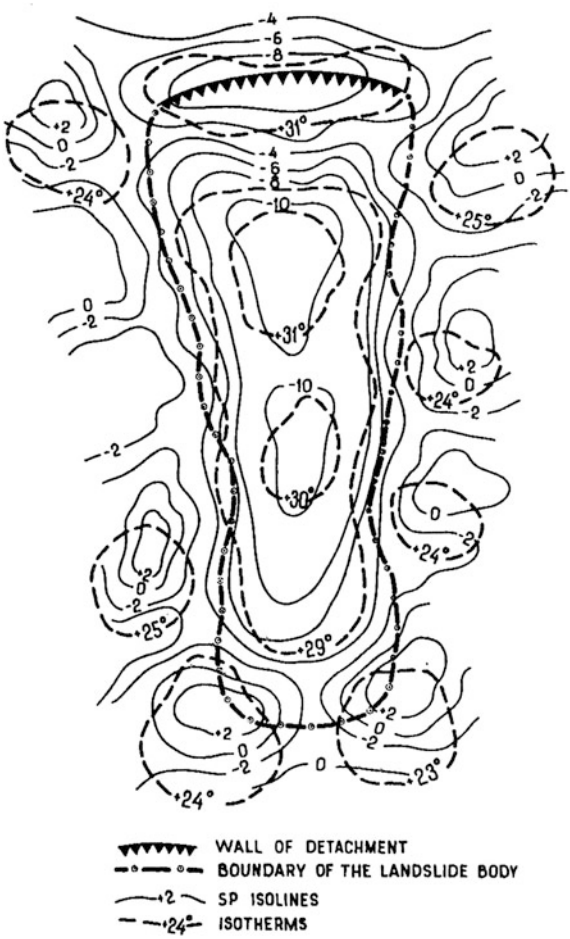

Fig. 10.25 The results of temperature and self-potential (SP) measurements on a flowing landslide near the town of Adler (coastal plain of the Black Sea, Russia). Temperature contours are labeled in °C; SP contours are marked in millivolts (Bogoslovsky and Ogilvy 1977)

of fresh water discharging near the coastline. These observations included self-potential (SP) measurements by a gradient array with a length of 2 m and resistivity observations. The location of spring No. I is indicated along profiles 0 + I at a distance of 30 m from the shore by a negative temperature anomaly with an absolute value of 1.2 °C. Spring No. 2 is indicated along profile 3 at a distance of 50 m from the edge of the water by a temperature anomaly reaching −1.0 °C. This example demonstrates that thermometric observations can provide a rather effective mapping of submarine springs (Bogolslovsky and Ogilvy 1974).

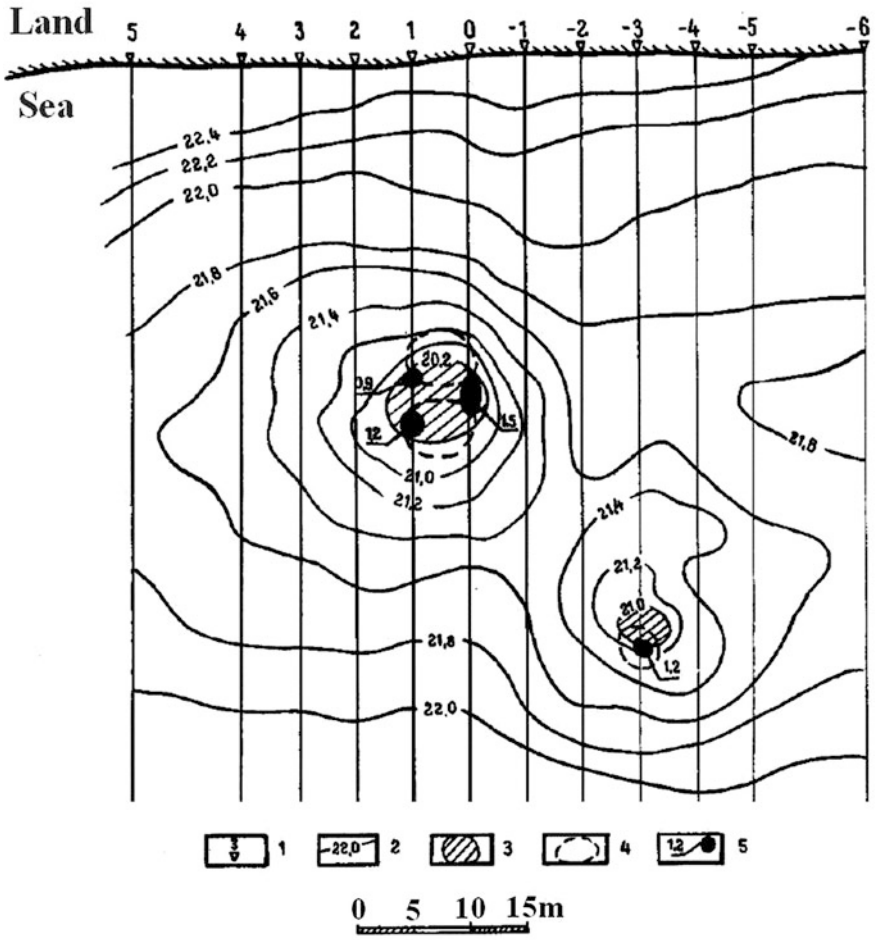

Fig. 10.26 The results of temperature mapping of submarine springs (fresh water) on the Black Sea coast (Bogoslovsky and Ogilvy 1974). (*1*) Observational profiles, (*2*) isotherms, (*3*) temperature anomalies, (*4*) ΔU_{sp} (self-potential) anomalies, (*5*) ρ_a (resistivity) anomalies

10.10.4 Monitoring Metallurgical Slag

The slag-dumps from metallurgical plants have chemical properties that make them liable to spontaneous combustion. Since drilling wells in this type of sources of heat (where temperatures can reach 300–400 °C) is impossible, temperature monitoring is a necessary component when monitoring such areas. Surface temperatures (combined with infrared measurements) were observed in the slopes of the dump of one metallurgical plant in Germany by needle probes. The length of the probes was 5 cm (Fig. 10.27). Constant monitoring this area helps avoid

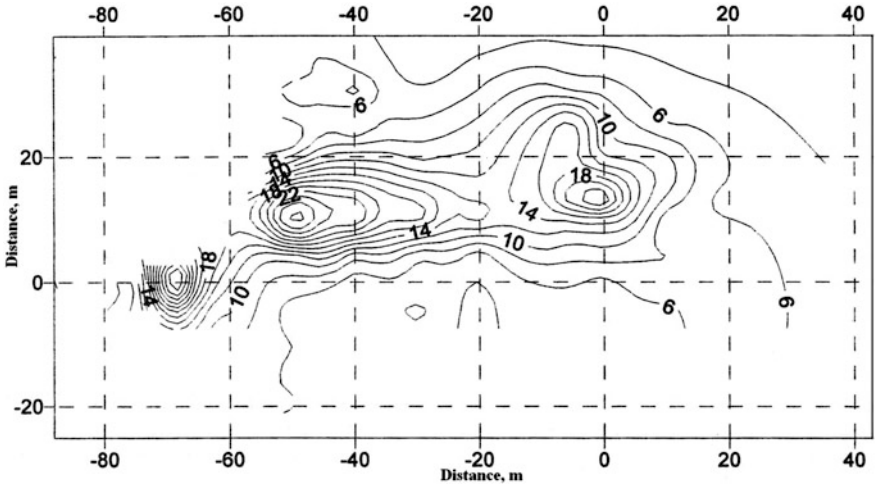

Fig. 10.27 Map of near-surface temperatures observed in slag-dumps of a metallurgical plant (Germany). The temperatures were measured at a depth of 5 cm (Oelsner 1998)

dangerous events. For the case presented in Fig. 10.27, the preliminary estimate of the anomaly source in the coordinates (0, 12) m indicated a depth of target occurrence of 8 m (Oelsner 1998).

10.11 Future Trends in Near-Surface Thermics

To reveal a stable geothermal anomaly that can be interpreted quantitatively, effects caused by time variations of temperature and influence of terrain relief must be eliminated from the observed temperature field. Techniques developed for this purpose include repeated geothermal observations at instants of time chosen to eliminate temperature variations. The correlation between the observed fields and observation point heights is a technique used for reducing the effect of terrain relief.

The applicability of methods of magnetic anomaly methods that have been developed for complicated models including rugged relief, inclined polarization and unknown levels of the normal field can be applied to models in thermal prospecting. The use of rapid methods of quantitative interpretation of temperature anomalies, such as the characteristic point, tangent and areal methods makes it possible to easily determine the parameters of disturbing thermally conductive bodies. This makes it possible to effectively apply near-surface thermal prospecting to explore for salt bodies, to examine faults in oil and gas fields, and to solve other problems (for instance, environmental and hydrogeological mapping, and archeological target delineation).

Given the contrast in thermal conductivity between oil and surrounding rocks these quantitative methods may be also applied for direct prospecting of shallow oil deposits. Future work on thermal observations in the near-surface layer can be associated with the development of reliable and flexible 3-D software for thermal field modelling, the application of different filtering methods for removing noise, and identifying and locating targets, integration with other geophysical as well as geochemical methods, and the development of an international near-surface thermal database.

References

Artemenko VI, Malovitsky YP (1977) Results of near-bottom temperature survey at oil and gas deposit Bakhar. Geol Oil Gas 4:50–54 (in Russian)

Bareyev IA, Wasserman VA, Vishnevsky PV, Verbitsky VA, Elizarov LI, Pomortzev GP, Prihodko AA (1985) The modern level and perspectives of geothermal survey application for nonmetallic deposits. In: Transactions of the 30th international geophysics symposium, Moscow, pp 60–69

Bellerby TJ, Noel M, Branigan K (1990) A thermal method for archaeological prospection: preliminary investigations. Archaeometry 32:191–203

Ben-Avraham Z, Ballard D (1984) Near bottom temperature anomalies in the Dead Sea. Earth Planet Sci Lett 71:356–360

Benner SM, Brodkey RS (1984) Underground detection using differential heat analysis. Archaeometry 26(1):21–36

Blackwell DD, Steele JL, Brott CA (1980) The terrain effect on terrestrial heat flow. J Geophys Res 85(B9):4757–4772

Bogoslovsky VA, Ogilvy AA (1974) Detailed electrometric and thermometric observations in offshore areas. Geophys Prospect 22:381–392

Bogoslovsky VA, Ogilvy AA (1977) Geophysical methods for the investigation of landslides. Geophysics 42(3):562–571

Borisovich VT, Eppelbaum VM, Ginzburg SN (1988) Optimization of geophysical investigations in mountainous regions on the basis of integration of geophysical and mining-drilling works. In: Borisovich VT, Eppelbaum VM (eds) Optimization of ore exploration in mountainous regions. Nedra, Moscow, pp 123–133 (in Russian)

Brivio PA, Pepe M, Tomasoni R (2000) Multispectral and multiscale remote sensing data for archaeological prospecting in an alpine alluvial plain. J Cultural Heritage 1:155–164

Brodovoi VV, Ginzburg SN, Leont'ev YV, Shafarenko VA (1988) In: Brodovoi VV (ed) Borehole and mining geophysics, vol 2, Chapter XVI: Regional Investigations and Geomapping, Nedra, Moscow, pp 343–352 (in Russian)

Bullard EC (1940) The disturbance of the temperature gradient in the Earth's crust by inequalities of height. Month Not Roy Astr Soc Geophys 4:300–362

Carslow HS, Jaeger JC (1959) Conduction of heat in solids, 2nd edn. Oxford University Press, Oxford

Chekalyuk EB, Fedortzev IM, Osadchy VG (1974) Geothermal field survey. Naukova Dumka, Kiev (in Russian)

Cheremensky GA (1977) Applied geothermics. Nedra, Leningrad (in Russian)

Dobrynina ZK, Dmitrieva TA, Pletnev AA, Semenov VG, Skornyakov SM (1985) Shaping of seasonal thermal anomalies over ore bodies. Izvestiya VUZOV Ser Geol Prospect 8:98–101 (in Russian)

Eppelbaum LV (1989) The development of methods for processing and interpretation of natural geophysical fields in prospecting for pyrite ores under mountainous conditions. Ph.D Thesis, Institute of Geophysics (Georgian Acad. of Sciences), Tbilisi, 1989 (in Russian)
Eppelbaum LV (1999) Near-surface thermal prospecting in petroleum geology. In: Kutasov MI (ed) Applied geothermics for petroleum engineers. Elsevier, London, pp 274–301
Eppelbaum LV (2000) Applicability of geophysical methods for localization of archaeological targets: an introduction. Geoinformatics 11(1):19–28
Eppelbaum LV (2007) Revealing of subterranean karst using modern analysis of potential and quasi-potential fields. In: Proceedings of the 2007 SAGEEP conference, vol 20, Denver, USA, pp 797–810
Eppelbaum LV (2009) Near-surface temperature survey: an independent tool for buried archaeological targets delineation. J Cultural Heritage 12(Suppl 1):e93–e103
Eppelbaum LV (2010) Archaeological geophysics in Israel: past, present and future. Adv Geosci 24:45–68
Eppelbaum LV (2013) Interpretation of magnetic anomalies due to archaeological and environmental targets classified as "quasi thick bed bodies" in complex physical-geological environments. In: Proceedings of the 2013 SAGEEP conference, vol 26(1), Denver, Colorado, USA, pp 415–424
Eppelbaum LV, Khesin BE (2012) Geophysical studies in the Caucasus. Springer, Berlin
Eppelbaum LV, Mishne LR (1987) Quantitative calculation of seasonal temperature variations in near-surface thermal prospecting. In: Transactions of the all-union conference on means for improving the effectiveness of geophysical methods, Moscow, USSR, p 54 (in Russian)
Eppelbaum LV, Mishne LR (1988) Some theoretical aspects of optimal filtration of geophysical signals with dependent noises. Deposited by VINITI, USSR Academy of Science, No. 6034-B88, pp 1–10 (in Russian)
Eppelbaum LV, Modelevsky MM, Pilchin AN (1996) Geothermal investigations in the Dead Sea Rift zone, Israel: implications for petroleum geology. J Petrol Geol 19(4):425–444
Ginzburg S, et al (1974) Integrated geophysical investigations in ore deposits of in Georgia (southern slope of the Greater Caucasus). Unpublished Report of TzNIGRI (Central Scientific Institution of Non-Ferrous and Precious Metals), Moscow (in Russian)
Ginzburg SN, Maslennikov AL (1989) Gravity prospecting. In: Brodovoi VV (ed) Borehole and mining geophysics, vol 2. Nedra, Moscow, pp 258–263 (in Russian)
Horai K, Simmons G (1969) Thermal conductivity of rock-forming minerals. Earth Planetary Sci Lett 6:359–368
Hutchins JS, Kading H (1969) How to interpret temperature surveys. Oil Gas J 1:96–103, 2:137–141
Kappelmeyer O (1957) The use of near-surface temperature measurements for discovering anomalies due to causes at depths. Geophys Prospect 5:239–258
Kappelmeyer O, Hänel R (1974) Geothermics with special reference to application. Gebruder Borntrargen, Berlin
Khesin BE (1978) Calculation of terrain relief influence in magnetic prospecting. Appl Geophys 83:102–111 (in Russian)
Khesin BE, Eppelbaum LV (1994) Near-surface thermal prospecting: review of processing and interpretation. Geophysics 59(5):744–752
Khesin BE, Alexeyev VV, Eppelbaum LV (1996) Interpretation of geophysical fields in complicated environments., Modern approaches in geophysics.Kluwer Academic Publishers (Springer), Boston
Khutorsky MD, Salnikov VE, Fotogdinov RA (1983) Geothermal prospecting of ore deposits. In: Kropotkin BM, Smirnov YB (eds) Methodical and experimental principles of geothermometry. Nauka, Moscow, pp 212–229 (in Russian)
Kumar P, Kaleita AL (2003) Assimilation of near-surface temperature using extended Kalman filter. Adv Water Resour 26:79–93
Lachenbruch AN (1968) Rapid estimation of the topographic disturbance to superficial thermal gradients. Rev Geophys 6(3):365–400

Lakhtionov MO, Tarkhov AG (1967) Experience in thermal prospecting at pyrite deposits of the Urals. Izvestiya VUZOV, Ser Geol Prospect 5:87–94 (in Russian)
Lasky BH (1967) Earth heat flow criteria may indicate porosity traps. World Oil 164(5):92–99
Leschak HA, Lewis JE (1983) Geothermal prospecting with shallow-temperature surveys. Geophysics 48(7):975–996
Lubimova EA (1968) Thermics of the earth and moon. Nauka, Moscow (in Russian)
Mongelli F, Morelli C (1961) Contributi alla prospezione geotermica. Boll Geofis Teor Applic 3:294–306
Moscicki WJ (1987) Temperature anomalies over underground cavities. Geophys Prospect 35:393–423
Niethammer G (1910) Die Warmeverteilung in Simplon. Eclogae Geol Helv 73:96–120
Noel M, Bellerby TJ (1990) Thermal archaeological surveying: a recording soil temperature probe. Archaoemetry 32(1):83–90
Oelsner C (1998) Integrated interpretation of direct and indirect (geoelectrical) temperature data. In: Proceedings of the international conference on the earth's thermal field and related research methods, Moscow, Russia, pp 187–191
Parasnis DS (1971) Temperature extrapolation to infinite time in geothermal measurements. Geophys Prospect 19:612–614
Paul M (1935) Uber Messingew der erdbodentemperatur and salzodomen. Z Geophys 11(7/8):388–392
Périsset MC, Tabbagh A (1981) Interpretation of thermal prospection on bare soils. Archaeometry 23(2):169–187
Poley JP, Steveninck JV (1970) Delineation of shallow salt domes and surface faults by temperature measurements at a depth of approximately 2 meters. Geophys Prospect 18:666–700
Ravnik D, Rajver D (1998) The use of inverse geotherms for determining underground water flow at the Ombla karst spring near Dubrovnik, Croatia. J Appl Geophys 39:177–190
Rodionov PF, Sofronov NI (1935) On the possibility of an application of thermal prospecting to search for sulphide deposits. Probl Sov Geol 8:257–268 (in Russian)
Rybach L (1995) Thermal waters in deep Alpine tunnels. Geothermics 24:631–637
Selig F, Wallick GC (1966) Temperature distribution in salt domes and surrounding sediments. Geophysics 31:346–361
Smerdon JE, Pollack HN, Cermak V, Enz JW, Kresl M, Safanda J, Wehmiller JF (2004) Air-ground temperature coupling and subsurface propagation of annual temperature signals. J Geophys Res 109:1–10. doi:10.1029/2004JD005056
Sudzhadinov RA, Kosmodemyansky VV (1986) Mapping for oil and gas structures at large depth. In: Ismail-Zade TA (ed) Combined interpretation of geological–geophysical materials for investigating the structure and prospecting for oil and gas at large depth. YuzhVNIIGeofizika, Baku, pp 94–103 (in Russian)
Suryaninov EYu, Vishnevsky PV, Vasserman VA (1983) Investigation of geothermal anomaly behavior over geological objects with contrasting thermal conductivity. Izvestiya Acad Sci USSR Ser Phys Earth 12:96–102
Tabbagh A (1973) Essai sur les conditions d'application des measures thermiques á la prospection archeologique. Ann Geophys 29(2):179–188
Tikhonov AN, Samarsky AA (1963) Equations of mathematical physics. Pergamon Press, Oxford
van den Bouwhuysen JNA (1934) The thermocouple proves useful on a geophysical survey. Eng Min J 135:342–344
Zverev VP, Dolnikov VA, Khutorsky MD, Fotogdinov RA (1982) Thermal effect and sulphide oxidation rate in the Katekh deposit (as applied to the southern slope of the Greater Caucasus). Doklady USSR Acad Sci 265(4):960–962

Chapter 11
Paleoclimate and Present Climate Warming Trends

Climate can be defined by the long-term statistics that describe the behavior and structure of the Earth's atmosphere, hydrosphere, cryosphere, and according to Vernadsky (1945) the noosphere ("mind-sphere" or the Earth's mental sheathe). Generally speaking, all life on the Earth depends on the hospitality of its climate. Any change in the Earth's climate will have an immediate impact on humankind, biodiversity, and on the health and services delivered by ecosystems around the globe, and it will alter the ability of the Earth's system to support socioeconomic development. Historical evidence shows that after massive volcanic eruptions the climate on the Earth altered dramatically and the failure of crops caused the death of many tens of thousands of people [for local estimates, see Ort et al. (2008)]. To adapt to and perhaps mitigate climate change, it is essential to understand the natural variability of climate, why and how climate changes, and how changes in climate impact the Earth's ecosystems. Recent historical and geophysical data indicate that the Earth's climate is changing, and such changes tend to take place with a distinctive spatial pattern(s) that may be characterized by one or several modes (repeating patterns of time space variability) of the climate system (Wang and Schimel 2003).

Analysis of a long core of ice drilled at Camp Century (Greenland) shows the proportions of different oxygen isotopes and provides a fairly straightforward record of temperature (Weart 2003) (Fig. 11.1). The ratio of oxygen-18 to oxygen-16 in the annual snow (ice) layers was utilized as natural thermometer. A sharp rise temperature started about 14,000 years ago at the end of the last ice age and varied by 1–2 °C. At the same time, the average global and regional paleotemperatures calculated for the last 250,000 years indicate that the temperature distribution (Fig. 11.2) is much more complex. Specifically, these data show an interaction between the modern day warming process and a global cooling tendency.

It is obvious that studies of past climatic changes and their environmental effects provide ways to understand the geological, geophysical and astronomic effects involved in this very complex process. Paleoclimate studies help pinpoint the main specificities of present (and future) climate changes. This chapter presents the methods used to derive useful information from thermal data observed at some depths below the Earth's surface.

L. Eppelbaum et al., *Applied Geothermics*, Lecture Notes in Earth System Sciences,
DOI: 10.1007/978-3-642-34023-9_11,

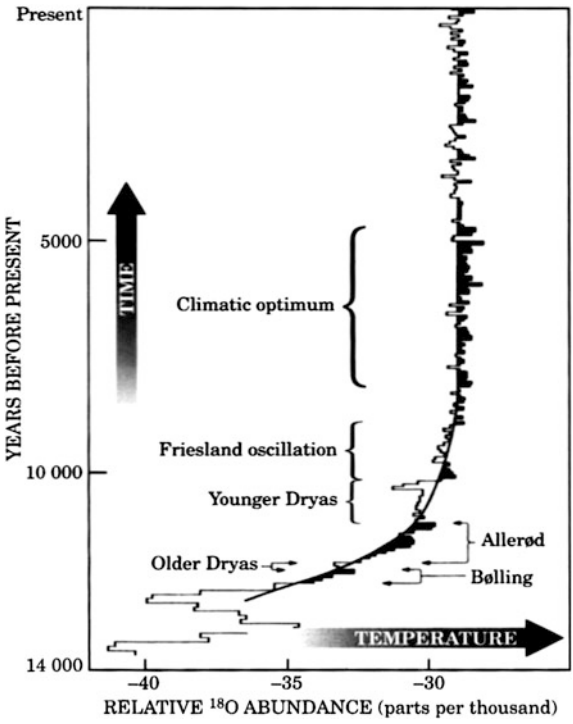

Fig. 11.1 Cores drilled from the ice at camp century, Greenland (after Weart 2003)

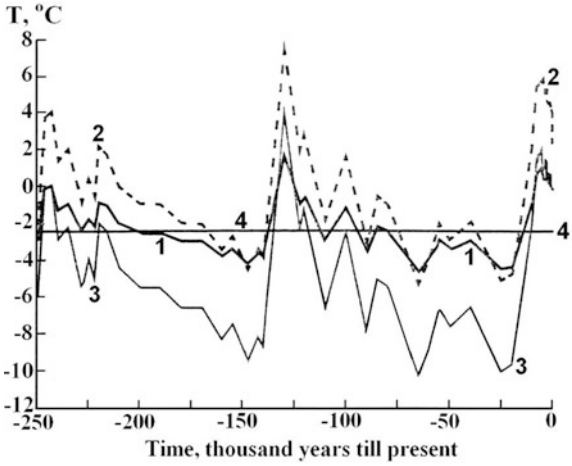

Fig. 11.2 Average global and regional paleotemperature for the last 250 T. y. (*1*) average global temperature for the northern semisphere (*2*) paleotemperature for the area of Vorotilov deep borehole (central part of the Russian platform, Russia) (*3*) paleotemperature for the area of Kola superdeep borehole (Kola Peninsula, Russia) (*4*) linearly averaged global temperature for the last 250 T. y. (after Pimenov et al. 1996, with small modifications)

11.1 Glaciations as a Strongly Nonlinear Phenomenon

The reasons for ice ages in the Earth's history—the so called Milankovitch cycles (Milankovitch 1941) are beyond the scope of this book. However, the mathematical model of glaciation is summarized briefly. It is widely accepted that such phenomena as the Earth's glaciations and other climatic phenomena are non-linear (Birchfield 1977; Moritz 1979; Sergin 1979; Kostizyn 1984; Schmidt 1997; Wang and Schimel 2003; Eppelbaum 2013b; Oh et al. 2014, etc.).

The first model of this strongly nonlinear effect in geophysics was formulated in Eppelbaum and Kardashov (2001). Generally speaking, periods of glaciation on Earth can be seen as strongly nonlinear oscillators. The most probable mechanism of glaciation oscillation was proposed by Kostizyn (1984) and operates like a "spring pendulum". We will consider this mechanism using a simplified geological model.

Let's consider a continental lump submersed in the Earth's mantle. This lump experiences vertical movement due to some mounting-building processes. At the top of the lump an ice sheet will form with a thickness y (Fig. 11.3). Symbol l designates the height below which ice generation is impossible and above which melting is impossible (we consider not seasonal, but average annual characteristics). Thus the amount of ice generation when $z > l$ is proportional to $z - l$. Analogously, melting when $z < l$ is proportional to $l - z$, i.e. the strength of the process can be calculated in terms of the distance on the vertical line to the horizontal line l.

Vertical movement of the continental lump due to increasing and decreasing ice sheet thickness can be described by series of ordinary differential equations. However, this effect is not only nonlinear (Birchfield 1977; Moritz 1979; Sergin 1979; Kostizyn 1984), but is likely to be extremely nonlinear (Eppelbaum and Kardashov 2003); hence analysis requires nonlinear equations with a power >1.

Detailed analyses show that glaciation periods (at times a glaciation regime with peaking) are associated with a number of factors (seismic and volcanic activity, atmospheric disturbances, changes in powerful streamflow directions, etc.). Small changes of known factors are sufficient to trigger global climate effects.

Let's now consider a non-linear multi-dimensional eigenvalue problem (Eppelbaum and Kardashov 2003):

$$-\sum_{i=1}^{m}\frac{\partial}{\partial x_i}\left[\left|\frac{\partial u}{\partial x_i}\right|^{p-1}\frac{\partial u}{\partial x_i}\right] = \lambda q(X)|u|^{q-1}u, \tag{11.1.1}$$

$$u|_{\Gamma} = 0. \tag{11.1.2}$$

Equation (11.1.1) should comply with the inner parallelepiped $\Phi = (X \in R^m : a_i \le x_i \le b_i, \quad i = \overline{1,m})$, Γ is the boundary of this parallelepiped, λ is the real value number and $p > 1$, $q > 1$. It is easy to see that when $p = 1$ and $q = 1$ we have the classic Sturm-Liouville problem.

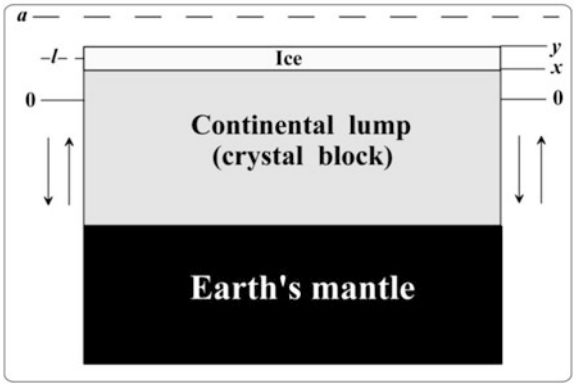

Fig. 11.3 A simplified physical-geological model of the Earth's glaciations [modified after Kostizyn (1984)]

We suggest that $q(X)$ is the separable function of the following type $q(X) = \prod_{i=1}^{m} q_i(x_i)$, where $q_i(x_i)$ are continuous functions on sets $[a_i \le x_i \le b_i]$. Assuming these conditions, the problem (11.1.1)–(11.1.2) admits a solution of the type:

$$u(X) = \prod_{i=1}^{m} u_i(x_i),$$

where $u_i(x_i)$ presents a solution to one-dimensional non-linear problem of Sturm-Liouville type:

$$-\frac{d_i}{dx_i}\left(\left|\frac{du}{dx_i}\right|^{p-1}\frac{du}{dx_i} = \mu_i q_i(x_i)|u|^{q-1}u_i\right), \tag{11.1.3}$$

$$u(a_i) = u(b_i) = 0, \quad \left(i = \overline{1,m}\right). \tag{11.1.4}$$

Kardashov (1993) showed that problems (11.1.3)–(11.1.4) admits a countable number of eigenfunctions normalized by condition:

$$\int_{a_i}^{b_i} |u(x_i)|^q dx_i = 1. \tag{11.1.5}$$

It should be noted that if potential $q_i(x_i)$ is not a function of limited variations, the eigenfunctions are not uniformly bounded. This makes it feasible to apply Eqs. (11.1.1)–(11.1.2) to various problems with aggravations and singularity. Eppelbaum and Kardashov (2003) proved that this mathematical formulation coincides with the physical-mathematical analysis of glaciation epochs as a highly nonlinear phenomenon.

11.2 Studying Recent Paleoclimatic Changes

11.2.1 Ground Surface Temperature Histories

Currently numerous efforts are underway to determine the trends in the ground surface temperature history (GSTH) from geothermal surveys (e.g., Cermak 1971; Lachenbruch and Marshall 1986; Beltrami et al. 1992; Shen and Beck 1992; Mareschal and Beltrami 1992; Wang 1992; Shen et al. 1992, 1995; Baker and Ruschy 1993; Kukkonen et al. 1994; Bodri and Cermak 2005, 1997; Harris and Chapman 1995; Huang et al. 1996; Pimenov et al. 1996; Guillou-Frottier et al. 1998; Huang and Pollack 1998; Kutasov et al. 2000; Pollack and Huang 2000; Pollack et al. 2000; Majorowicz and Safanda 2005; Eppelbaum et al. 2006; Hamza et al. 2007; Hopcroft et al. 2007; Rath and Mottaghy 2007; González-Rouco et al. 2008; Kooi 2008; Mukhtarov et al. 2010; Muto et al. 2011; Roy and Chapman 2012; Kutasov and Eppelbaum 2013).

Accurate subsurface temperature measurements are needed to solve this inverse problem; i.e., estimating the unknown time-dependent ground surface temperature (GST). Variations in the GST during long-term climate changes have led to disturbances (anomalies) in the temperature field of formations. Thus, the GST can be evaluated by analyzing current-day temperature-depth profiles. The effect of surface temperature variations in the past on the temperature field of formations is widely discussed in the literature.

Three approaches are used to derive climate information from borehole temperature profiles. In the first, the GSTH is reconstructed as an arbitrary function of time (e.g., Lachenbruch and Marshall 1986; Shen and Beck 1992; Baker and Ruschy 1993; Clauser and Mareschal 1995; Jain and Pulwarty 2006; Huang et al. 2000; Majorowicz et al. 2012; Roy and Chapman 2012). Huang et al. (1996) called this approach an arbitrary function reconstruction (AFR). The second approach for inversion of temperature profiles is termed the "few parameter estimation" (FPE) technique and was suggested by Huang et al. (1996). The FPE technique enables comparison of inversion results, both spatially and temporally. The third approach is the generalized inverse method dubbed the Functional Space Inversion (FSI) technique (Shen and Beck 1992; Shen et al. 1995). The FSI method allows for uncertainties in the temperature-depth data, the thermal properties of formations and heat flow density to be incorporated into the model. In this section we compare the results of our GSTH calculations with those obtained by the FPE technique.

The main reasons for using the FPE technique are as follows (Huang et al. 1996):

a. The resolving power of a temperature profile for GSTH reconstruction. Due to the amplitude attenuation of thermal diffusion and presence of observational and representational noise in borehole data, rigorous estimates can often only be made for a few parameters such as the trend, duration and the overall amplitude of the ground surface temperature change in the past.

Table 11.1 Input data for 15 boreholes and results of temperature inversions (Huang and Pollack 1998; www.geo.lsa.umich.edu/∼climate)

Well #	Well code	Longitude	Latitude	H_a–H_b (m)	H_t–H_c (m)	T_0 (°C)	R, rate after 1,900 K/100a
		North America					
1	Ca-9901	−101.50	54.72	49.81–119.58	189.47–596.47	2.7	2.487
2	Ca-9906	−101.84	54.77	49.97–149.78	199.38–599.14	2.1	1.219
3	Ca-9907	−100.56	54.93	48.00–113.78	196.03–523.34	1.1	1.384
4	Ca-9804	−100.76	55.16	48.30–106.25	154.41–307.76	2.1	0.378
5	Ca-9806	−101.57	54.79	42.49–84.52	167.22–498.78	2.8	0.803
6	Ca-9807	−101.57	54.79	47.06–100.80	175.81–446.92	2.5	0.419
		Europe					
7	CZ-127127	14.87	50.73	80.80–140.00	200.00–440.00	6.3	0.855
8	CZ-hu-7	12.81	50.11	50.00–120.00	180.00–350.00	5.6	1.533
9	CZ-hu-9	12.81	50.11	50.00–100.00	200.00–460.00	8.1	3.751
10	CZ-mj-5	14.86	50.57	60.00–180.00	230.00–290.00	5.5	0.212
11	CZ-mj-8	14.58	50.36	50.00–120.00	180.00–310.00	–	1.787
		Asia					
12	CN-FJ-ql17	116.94	26.33	60.000–100.00	140.000–430.00	18.5	2.532
13	CN-GD-c3901	113.18	25.42	50.000–120.00	160.000–260.00	18.4	1.870
14	CN-JXck46-25	116.33	27.97	60.00–140.00	200.000–300.00	19.9	1.181
15	CN-JXzk59-38	116.33	27.97	50.000–110.0	200.000–380.00	13.7	0.300

b. The need to simplify and standardize the procedures for reconstruction of GSTH. The problem of inverting borehole temperatures to yield a ground surface temperature (GST) is an ill-posed problem, and some constraints are required for a stable solution. To allow for a more consistent comparison of temperature inversion results, standardization of surface temperature reconstruction is needed. This standardization is a difficult task in an AFR due to the high numbers of degrees of freedom in representing a GSTH.
c. Convenience in comparing results. AFR techniques attempt to reconstruct a GSTH at various time scales and degrees of detail. However, in regional or continent-wide study only general features need to be compared rather than the details of GSTHs obtained from different areas.

The forward calculation approach (AFR) was used to analyze and interpret borehole temperatures in terms of GSTH. Fifteen borehole temperature profiles from Europe, Asia and North America were selected (Huang and Pollack 1998; www.geo.lsa.umich.edu/∼climate). Three groups based on geographical proximity were formed (Table 11.1). Four mathematical models to describe the GSTH (sudden change, linear increase, square root of time, exponential increase) were used to approximate the temperature-depth profiles of the boreholes. The objective was to calculate the warming rates (R) in the twentieth century by the AFR method and to compare them with those obtained by the Few Parameter Estimation (FPE) technique. For closely spaced boreholes it was assumed that the values of R should vary in narrow limits.

The results of inversions (FCA) showed that for boreholes in North America the current warming rates varied in the 0.41–2.45 K/100a range. The wide range for the warming rate of 0.33–2.48 K/100a was also determined for boreholes in Europe. Interesting results were obtained (Eppelbaum et al. 2006) for four boreholes in Asia (China). In this case the warming rate varied in relatively narrow limits (1.16–1.59 K/100a). The warming rate estimated by the FPE technique (Huang and Pollack 1998) differed widely: 0.38–2.49 K/100a (North America); 0.21–3.75 K/100a (Europe), and 0.30–2.53 K/100a (Asia). Thus, for boreholes in North America and Europe both approaches provide practically the same ranges of warming rates. For Asian boreholes the FCA approach gives a more consistent (narrow) range of warming rates (1.16–1.59 K/100a).

11.2.2 Introduction to the Problem

These results of temperature inversion by both techniques indicate that non-climatic effects such as vertical and horizontal water flows, steep topography, lakes, vertical variation in heat flow, lateral thermal conductivity contrasts, thermal conductivity anisotropy, deforestation, forest fires, mining, wetland drainage, agricultural development, urbanization, etc. may have perturbed the borehole temperature profiles. The influence of these factors has been examined extensively (e.g., Carslaw and Jaeger 1959; Lachenbruch 1965; Kappelmeyer and Hänel 1974; Blackwell et al. 1980; Lewis and Wang 1992, 1998; Majorowicz and Skinner 1997; Powell et al. 1988; Guillou-Frottier et al. 1998; Kohl 1999; Safanda 1999; Pollack and Huang 2000; Gosselin and Mareschal 2003; Gruber et al. 2004; Bodri and Cermak 2005; Mottaghy et al. 2005; Nitoiu and Beltrami 2005; Allen et al. 2006; Taniguchi 2006; Chouinard and Mareschal 2007; Safanda et al. 2007). However, the exact calculation of all these factors is a complex physical-mathematical problem, which may be completely solved in the future by the method of successive approximations.

11.2.3 Climate Reconstruction Methods: Some Typical Disturbances and Restrictions

All climate reconstruction methods are based on a one-dimensional heat conduction equation. It is assumed that a uniform boundary condition is applied on a plane surface, the formation is a laterally homogeneous medium, and the thermal properties can only depend on a given depth. For these reasons any subsurface temperature variations arising from conditions that depart from that theoretical model may be incorrectly interpreted as a climate change signature (Pollack and Huang 2000). As mentioned by Nitoiu and Beltrami (2005) out of over 10,000

borehole temperature logs worldwide (The International Heat Flow Commission global geothermal dataset), only about 10 % of these logs are currently used for climate studies because a number of known non-climatic energy perturbations are superimposed on the climatic signal. Therefore, extreme caution should be exercised in the selection of temperature-depth profiles when inferring the ground surface temperature histories. To illustrate well selection procedures, we briefly present two examples. In the study conducted by Guillou-Frottier et al. (1998), only 10 out of 57 temperature profiles were selected for inversion of past ground surface temperatures.

The following criteria were considered in rejecting boreholes from the study: steep topography, proximity of lakes, water circulation, instrumental problems, other identifiable terrain effects (such as heat refraction, permafrost effects), and recent changes in surface conditions (clearing of trees). For most of the boreholes that were discarded, the shallowest part of the temperature profile was perturbed. These perturbations were often similar to the perturbations due to changes in surface temperature. If the terrain conditions had not been considered, warming would have been inferred for 25 boreholes. Ten boreholes showed apparent cooling, and only one showed no difference. To screen out borehole temperature data from Eastern Brazil with indications of possible perturbations arising from non-climatic effects, the following quality assurance conditions were imposed (Hamza et al. 2007):

1. The borehole is sufficiently deep that the lower section of the temperature-depth profile allows for a reliable determination of the geothermal gradient, presumably free of the effects of recent climate changes. Order of magnitude calculations indicate that surface temperature changes of the last centuries would penetrate to depths of nearly 150 m,
2. The time elapsed between cessation of drilling and the temperature log is at least an order of magnitude larger than the duration of drilling,
3. The temperature-depth profile is free from the presence of any significant non-linear features in the bottom parts of the borehole, usually indicative of advection heat transfer by fluid movements, either in the surrounding formation or in the borehole itself.
4. The elevation changes at the site and in the vicinity of the borehole are relatively small so that the topographic perturbation of the subsurface temperature field at shallow depths is not significant.
5. The lithological sequences encountered in the borehole have relatively uniform thermal properties, and are sufficiently thick that the gradient changes related to variations in thermal properties do not lead to systematic errors in the procedure employed for extracting the climate related signal.

Out of a total of 129 temperature logs only 17 were found to satisfy the above set of quality assurance conditions (Hamza et al. 2007). Corrections can be applied, for example, to correct borehole temperature profiles for the effect of topography (Lachenbruch 1965; Blackwell et al. 1980; Safanda 1994, 1999). However, this is rarely done because the amplitude of the climatic signals is often

smaller than the uncertainty of these corrections (Chouinard and Mareschal 2007). Safanda et al. (2007) presented results of repeated temperature logs from Czech, Slovenian and Portuguese borehole climate observatories within a time span of 8–20 years. The repeated logs revealed subsurface warming in all the boreholes amounting to 0.2–0.6 °C below 20 m depth. The warming rate of 0.05 °C/year at the Czech observatory (located in a park within the campus of the Geophysical Institute in Prague) was estimated. This warming rate was twice the simulated value (using the surface air temperature as a forcing function). It was assumed that subsurface temperature at the station was influenced by a new structure on the campus of the Geophysical Institute within the last 10–20 years and/or by other components of infrastructure built 40–50 years ago. The authors (Safanda et al. 2007) conducted a quantitative analysis of these effects by solving the heat conduction equation numerically in a three dimensional geothermal model of the borehole site. It was found that the anthropogenic structures influenced the temperature in the borehole considerably.

Nitoiu and Beltrami (2005) attempted to correct borehole temperature data for the effects of deforestation. The authors simulated the ground surface temperature changes following deforestation by using a combined power exponential function describing the organic matter decay and recovery of the forest floor after a clear-cut (Covington 1981). The examples demonstrated that application of this correction could enable the incorporation of considerable borehole data into the borehole climatology database (Nitoiu and Beltrami 2005).

11.2.4 Mathematical Models and Assumptions

Let us assume that t_x years ago the ground surface temperature started to increase (warming) or decrease (cooling). Prior to this moment the subsurface temperature was (Fig. 11.4):

$$T_0(z, t = 0) = T_{0a} + \Gamma z, \tag{11.2.1}$$

where T_{0a} is the mean ground surface temperature at the moment in time $t = 0$ years; z is the vertical depth and Γ is the geothermal gradient. It is also assumed that the formation is a homogeneous medium with constant thermal properties. The current ($t = t_x$) subsurface temperature is (in the case of warming):

$$T_c(z, t = t_x) = T_{0c} + f(z), \tag{11.2.2}$$

where T_{0c} is the current (date of temperature logging) mean ground surface temperature; $f(z)$ is a function of depth and can be obtained from the field data.

In some cases the value of T_{0c} can be obtained by extrapolation of the function T_c to $z = 0$. However, in most cases, the value T_{0c} is estimated by trial and error:

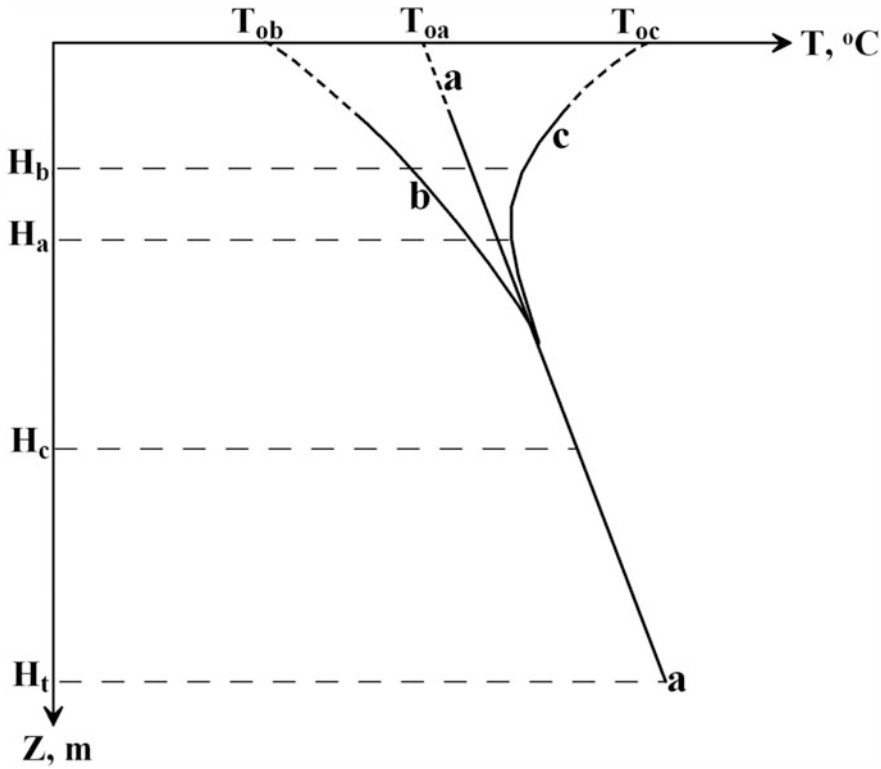

Fig. 11.4 Temperature profiles: a main scheme. ***ab***—cooling, ***ac***—warming

assuming an interval of values for T_{0c}, calculate for each T_{0c} the value of the temperature profiles T_c (by a computer program) for various models of different ground surface temperature (*GST*) with time and, finally, find the best match between the calculated and the field values for the T_c profiles. We found that a quadratic regression program for the section H_a–H_b (Fig. 11.4) can be utilized to estimate the value of $T_{0c} = a_0$ (Table 11.2).

$$T_c(z, t = t_x) = a_0 + a_1 z + a_2 z^2, \tag{11.2.3}$$

where a_0, a_1, and a_2 are the coefficients.

The temperature-depth values for all wells were taken from a database (Huang and Pollack 1998; www.geo.lsa.umich.edu/∼climate). Four models of changing *GST* values with time were considered. The corresponding mathematical solutions have been presented in the literature (e.g., Carslaw and Jaeger 1959; Cermak 1971; Lachenbruch and Marshall 1986; Lachenbruch et al. 1988; Powell et al. 1988).

Table 11.2 Reduced temperatures and results of temperature inversions for borehole Ca-9901

H (m)	T_{RC} (°C)	T_{RL} (°C)	T_{RS} (°C)	T_{RE} (°C)	T_{R0} (°C)
29.89	2.10	2.02	2.04	1.72	2.15
39.85	1.73	1.68	1.69	1.55	1.71
49.81	1.39	1.39	1.39	1.39	1.39
59.77	1.10	1.15	1.13	1.25	1.13
69.72	0.85	0.94	0.91	1.12	0.92
79.66	0.64	0.76	0.73	1.01	0.75
89.62	0.48	0.61	0.58	0.90	0.60
99.61	0.34	0.49	0.45	0.80	0.48
109.60	0.24	0.39	0.34	0.71	0.37
119.58	0.17	0.31	0.26	0.63	0.29

$t_{xC} = 52.9$ years, $t_{xL} = 137.5$ years, $t_{xS} = 94.0$ years, $t_{xE} = 282.8$ years,
$\Delta T_{RC} = 0.092°\text{C}, \Delta T_{RL} = 0.043°\text{C}, \Delta T_{RS} = 0.039°\text{C}, \Delta T_{RE} = 0.275°\text{C}$,
$\alpha_L = 0.0245°\text{C/year}, \alpha_L = 0.3474°\text{C/year}^{1/2}, \alpha_E = 0.002971°\text{C/year}$

In the first model (Model C) we assumed that t_{xC} years ago the *GST* value suddenly changed from T_0 to T_{0c}. The current temperature anomaly (the reduced temperature) is

$$T_R(z) = T_{0c} + f(z) - T_0 - \Gamma z \tag{11.2.4}$$

and the solution is

$$T_{RC} = T_R = \Delta T_0 \Phi^* \left(\frac{z}{2\sqrt{at}} \right), \quad t = t_{xC}, \tag{11.2.5}$$

$$\Delta T_0 = T_{0c} - T_0 \tag{11.2.6}$$

where a is the thermal diffusivity of formations and $\Phi^*(x)$ is the complementary error function.

In the second model (Model L) we assumed that t_{xL} years ago the *GST* value started to change gradually from T_0 to T_{0c}. We assumed that *GST* is a linear function of time and

$$T_{0c} = T_0 + \alpha_L t_{xL}, \tag{11.2.7}$$

where α_L is a some coefficient.

The solution is

$$T_{RL} = T_R = \alpha_L t \left\{ \left(1 + \frac{z^2}{2at} \right) \Phi^* \left(\frac{z}{2\sqrt{at}} \right) - \frac{z}{\sqrt{\pi at}} \exp\left(-\frac{z^2}{4at} \right) \right\}, \quad t = t_{xL}, \tag{11.2.8}$$

In the third model (Model *S*) we also assumed that t_{xS} years ago the *GST* value started to change gradually from T_0 to T_{0c}. We assumed that *GST* is a square root function of time and

$$T_{0c} = T_0 + \alpha_S \sqrt{t_{xS}}, \tag{11.2.9}$$

where α_s is a coefficient.

The solution is

$$T_{RS} = T_R = \alpha_S \sqrt{t} \left\{ \exp\left(-\frac{z^2}{4at} \right) - \frac{z\sqrt{\pi}}{2\sqrt{at}} \Phi^* \left(\frac{z}{2\sqrt{at}} \right) \right\}, \quad t = t_{xS}. \tag{11.2.10}$$

Finally, in the fourth model (Model *E*) we assumed that the *GST* value increases exponentially with time and

$$T_{0c} = T_0 \exp(\alpha_E t_{xE}), \tag{11.2.11}$$

where α_L is a coefficient.

The solution is ($T_{RE} = T_R$)

$$T_{RE} = \frac{1}{2} \exp(\alpha_E t) \left[\begin{array}{l} \exp\left(-z\sqrt{\frac{\alpha_E}{a}} \right) \Phi^* \left(\frac{z}{2\sqrt{at}} - \sqrt{\alpha_E t} \right) \\ + \exp\left(z\sqrt{\frac{\alpha_E}{a}} \right) \Phi^* \left(\frac{z}{2\sqrt{at}} + \sqrt{\alpha_E t} \right) \end{array} \right], \quad t = t_{xE} \tag{11.2.12}$$

Computer programs were used for processing field data and calculating the values of t_x, T_{0c}, T_0, Γ, $f(z)$, α_L, α_S, and α_E. To illustrate the calculation technique we present a field example below.

11.2.5 Example of Calculations

For the interval from 49.81 to 119.58 m of borehole Ca-9901 (Table 11.1 and Fig. 11.5) the temperature profile can be approximated by a quadratic equation (a standard regression program was applied)

$$T_c(z, t = t_x) = 5.92 - 0.03626z + 0.0001927z^2. \tag{11.2.13}$$

Therefore, the current mean GST is 5.92 °C [see parameter *Toa* (the mean ground surface temperature at the moment of time $t = 0$ years) in Fig. 11.4].

From the observed *T*–*z* data it follows that in the 189.47–596.47 m section of the well the temperature gradient was practically constant. It was assumed that the

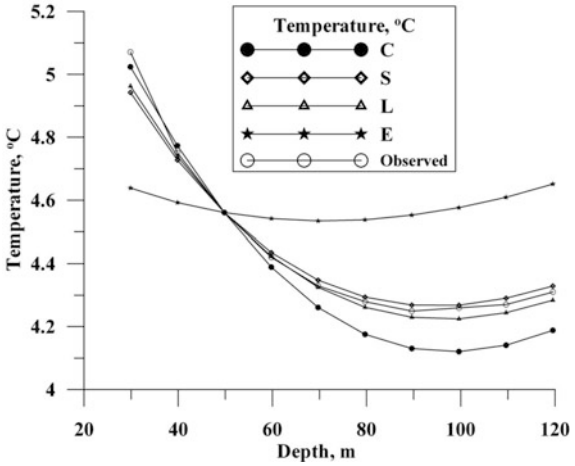

Fig. 11.5 Observed and calculated temperature profiles, borehole Ca-9901, North America (see Table 11.1)

temperature gradient in this section did not change. For this interval (here a standard regression program was applied)

$$T_c(z, t = 0) = 2.56 + 0.01224z. \tag{11.2.14}$$

Therefore, in the past (t_x years ago) the mean ground surface temperature $T_0 = 2.56$ °C and warming occurred. In our case the observed reduced temperatures (for $z < 119.6$ m) were:

$$T_{R0}(z) = T_{obs} - 2.56 - 0.01224z, \tag{11.2.15}$$

where the T_{obs} values were the measured temperatures (Fig. 11.5).

For the calculations below we used the depth $z = H_1 = 49.81$ m, where $T_R = 1.39$ °C.

The temperature change (anomaly) of the *GST* is 5.92 °C − 2.56 °C = 3.36 °C.

A computer program calculated the reduced temperatures versus depth for the four models of *GST* changes and compared them to the observed anomalies.

For the first model (Model *C*) the reduced temperature was T_{RC} (Eq. 11.2.5). In our case the *GST* changed from 2.56 to 5.92 °C.

In the second model (Model *L*) the reduced temperature was T_{RL} (Eq. 11.2.8) and the ground surface temperature changed linearly from 2.56 to 5.92 °C. We also have the following equation

$$5.92 = 2.56 + \alpha_L t_{xL}.$$

In the third model (Model *S*) the *GST* is a square root function of time. The reduced temperature was T_{RS} (Eq. 11.2.10) and

$$5.92 = 2.56 + \alpha_S \sqrt{t_{xS}}.$$

Table 11.3 Coefficients in Eq. (11.2.1) ($b_0 = T_{0a}$, $b_2 = \Gamma$) and Eq. (11.2.3). $T_{1,R}$ is the reduced temperature at $z = H_1$

Well no.	Well code	H_1 (m)	$T_{1,R}$ (°C)	Well section H_a–H_b (m)			Well section H_f–H_c (m)	
				a_0 (°C)	$a_1 \times 10^2$ (°C/m)	$a_2 \times 10^3$ (°C/m^2)	b_0 (°C)	$b_1 \times 10^2$ (°C/m)
				North America				
1	Ca-9901	49.81	1.39	5.92	−3.626	0.1927	2.56	1.224
2	Ca-9906	49.97	1.08	4.06	−0.954	0.0588	2.09	1.125
3	Ca-9907	48.00	0.76	2.51	−0.133	0.0317	1.19	1.211
4	Ca-9804	48.30	0.20	2.76	−0.241	0.0464	2.17	0.756
5	Ca-9806	42.49	0.48	3.97	−1.289	0.1354	2.69	1.134
6	Ca-9807	47.06	0.52	3.70	−0.210	0.0515	2.65	1.092
				Europe				
7	CZ-127127	70.00	0.91	8.68	−0.003	0.0328	6.85	1.562
8	CZ-hu-7	50.00	1.49	9.73	−1.825	0.2084	6.24	3.134
9	CZ-hu-9	50.00	0.80	10.38	−0.781	0.1606	8.07	3.056
10	CZ-mj-5	60.00	1.31	9.23	0.854	0.0503	6.65	3.211
11	CZ-mj-8	50.00	2.39	10.46	−1.042	0.1673	5.86	4.199
				Asia				
12	CN-FJ-ql17	60.00	0.44	19.77	−0.959	0.1132	18.18	1.723
13	CN-GD-c3901	50.00	1.08	21.32	−1.140	0.1023	19.02	1.846
14	CN-JXck46-25	40.00	1.54	24.07	−1.327	0.1027	20.77	2.154
15	CN-JXzk59-38	50.00	2.22	18.64	−1.161	0.1250	14.77	2.813

In the fourth model (Model *SE*) the *GST* is an exponential function of time. The reduced temperature was T_{RE} (Eq. 11.2.12) and

$$5.92 = 2.56 \exp(\alpha_E t_{xE}).$$

For all models the values of t_x and α were estimated by the computer program. The value of thermal diffusivity $a = 0.0040$ m^2/h was used for the temperature inversions. The results are presented in Tables 11.2 and 11.3, Figs. 11.5 and 11.6.

Analyzing the data from Table 11.2 and Fig. 11.5 suggests that the best match (minimum values of average square deviations $\Delta T_{RL} = 0.043$ °C and $\Delta T_{RS} = 0.039$) is when Models *L* or *S* are applied.

11.2.6 Inversion Results

In most cases Model *L* (linear increase) and Model *S* (square root time increase) provide the best match with the field data (Table 11.4 and Fig. 11.7).

In several cases Model *C* (sudden change) approximates the measured temperature-depth data with good accuracy (Figs. 11.8, 11.9). For boreholes No. 1–6

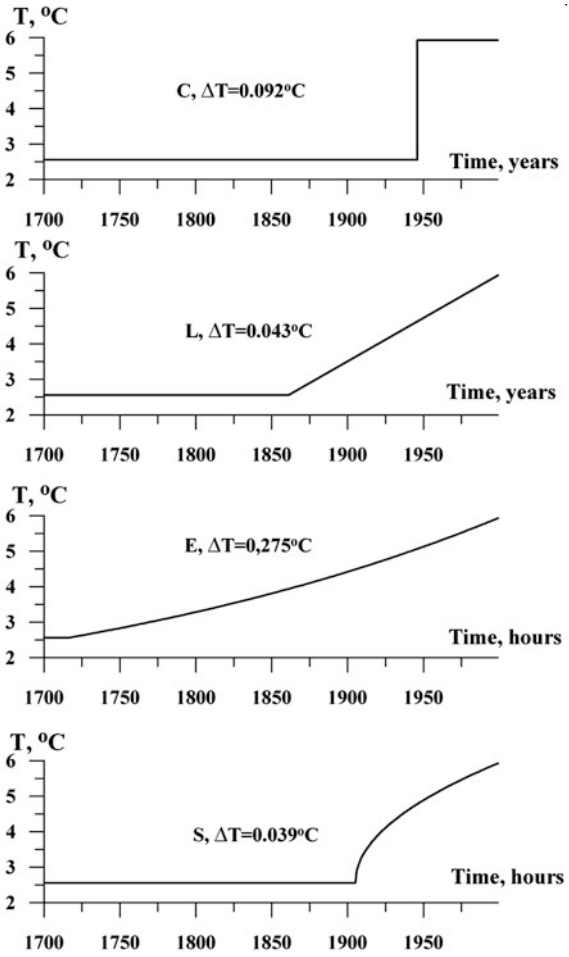

Fig. 11.6 Possible ground surface temperature history scenarios, borehole Ca-9901, North America (see Table 11.1)

(North America, Table 11.4, Model *L*) the current warming rates varied in the 0.411–2.450 K/100a range. A wide range for a warming rate of 0.328–2.482 K/100a was also found for five boreholes in Europe (Table 11.4, Model *L*). Interesting results were obtained for four boreholes in China (Table 11.4). In this case the warming rate (R_L) varied in relatively narrow limits (1.165–1.590 K/100a).

The duration of warming periods (Table 11.4, Model *L*) are as follows: 82–279 years for wells No. 1–6; 99–415 years for wells No. 7–11; and 100–332 years for wells No. 12–15. Similar results (R_S and t_{xS}, Table 11.4) were obtained for Model *S*.

Table 11.4 Results of temperature inversions for two models

Well #	Model L			Model S			R_L (K/100a)	R_S at $t = t_{xS}$ (K/100a)
	t_{xL} (year)	ΔT_L (K)	α_L (K/year)	t_{xS} (years)	ΔT_S (K)	α_S (K/year$^{0.5}$)		
	North America							
1	137.5	0.043	0.02450	94.0	0.039	0.3474	2.450	1.792
2	278.6	0.055	0.00786	185.4	0.032	0.1450	0.786	0.532
3	319.1	0.079	0.00411	210.8	0.068	0.0904	0.411	0.311
4	92.7	0.011	0.00636	64.3	0.012	0.0734	0.636	0.458
5	81.9	0.027	0.01558	56.5	0.033	0.1697	1.558	1.129
6	192.1	0.034	0.00545	128.9	0.040	0.0922	0.545	0.406
	Europe							
7	415.2	0.078	0.00441	279.0	0.064	0.10971	0.441	0.328
8	148.8	0.092	0.02341	101.4	0.118	0.34591	2.341	1.718
9	98.6	0.097	0.02343	68.5	0.079	0.27927	2.343	1.690
10	328.1	0.174	0.00785	219.8	0.144	0.17361	0.785	2.482
11	241.9	0.082	0.01901	161.7	0.037	0.36149	1.901	1.421
	Asia							
12	100.3	0.084	0.01590	70.9	0.078	0.18942	1.590	1.125
13	183.5	0.082	0.01251	124.0	0.062	0.20623	1.252	0.926
14	260.7	0.060	0.01268	176.2	0.061	0.24911	1.268	0.939
15	331.7	0.060	0.01165	219.5	0.041	0.26089	1.165	0.907

ΔT_L and ΔT_S are the average square temperature deviations, R_L and R_S are the warming rates. Well codes are presented in Tables 11.1 and 11.3

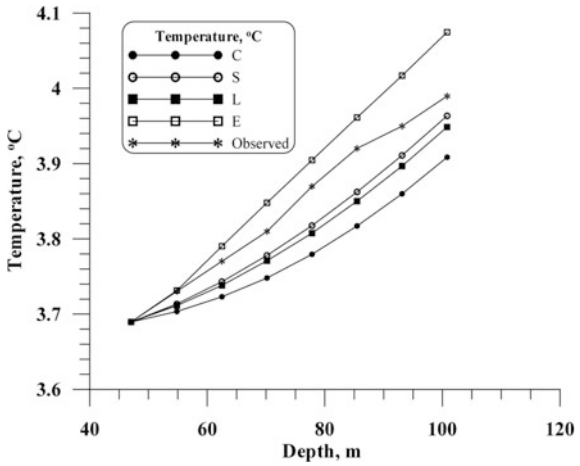

Fig. 11.7 Observed and calculated temperature profiles, borehole Ca-9807, North America (see Table 11.1)

11.2.7 Calculation of Warming Rates

As was mentioned above, the main objective was to calculate the warming rates (R) in the twentieth century by the AFR method and to compare these findings with those obtained by the Few Parameter Estimation (FPE) technique

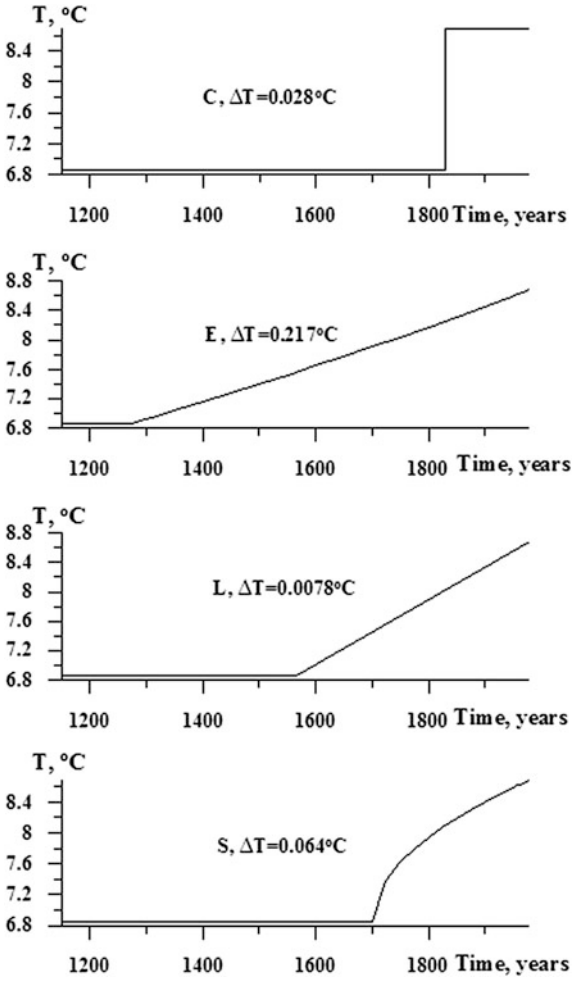

Fig. 11.8 The possible scenarios for ground surface temperature history, borehole CZ-127127, Europe (see Table 11.1)

(Table 11.1). The warming rate estimated by the FPE technique varied considerably: 0.378–2.487 K/100a (North America), 0.212–3.751 K/100a (Europe), and 0.300–2.532 K/100a (Asia). The FPE method successfully determined temperature trends (warming or cooling rates) over past five centuries (Huang et al. 2000). For the inversion, the a priori null hypothesis for the GSTH was stipulated; i.e. the initial estimate was that there had been no climate change. Tables 11.1 and 11.4 show that for the boreholes No. 1–11 (North America and Europe) both approaches (AFR and FPE) provide practically the same ranges of warming rates. For Asian boreholes (No. 12–15) the AFP technique gives a more consistent (narrow) range of warming rates (1.165–1.590 K/100a). Let us compare the GSTH of two closely spaced boreholes (Figs. 11.10, 11.11). Analysis of Fig. 11.10 indicates that the duration of the warming period was five centuries and the warming rate was minimal in the last century.

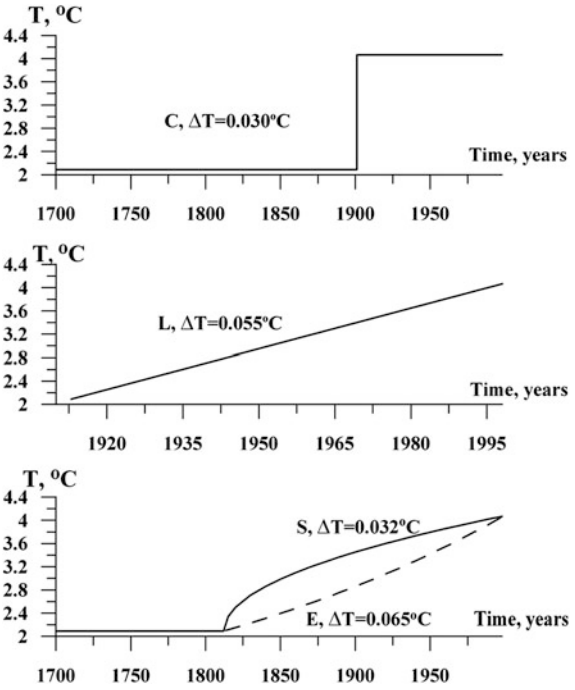

Fig. 11.9 Possible ground surface temperature history scenarios, borehole Ca-9806, North America (see Table 11.1)

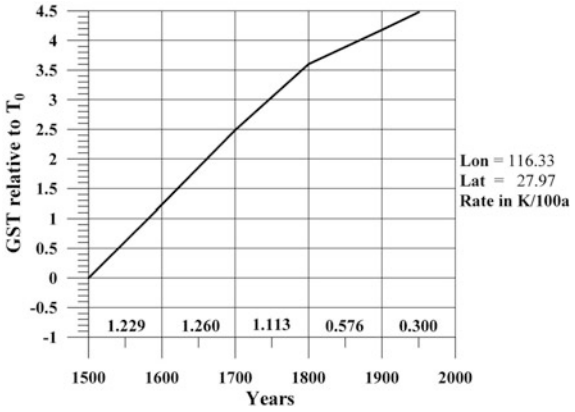

Fig. 11.10 The ground surface temperature history, borehole CN-JXzk59-38, Asia (see Table 11.1). Year of borehole logging: 1991; Mean ground surface temperature $T_0 = 13.7$ °C

However, it is widely accepted that the most warming occurred in the last century. However the GSTH reconstructed from borehole No. 12 temperature-depth data (Fig. 11.11) indicated that cooling period lasted for three centuries and a very high warming rate for the twentieth century was calculated by the FPE technique. The results of temperature inversion by both techniques show that probably some non-climatic effects (well shut-in periods, vertical and horizontal water flows, sedimentation, uplift, erosion, steep topography, lakes, vertical

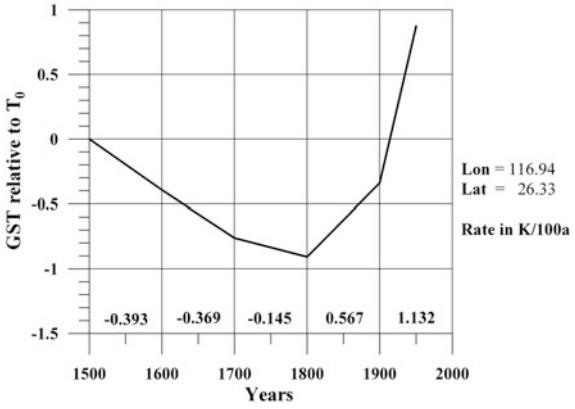

Fig. 11.11 The ground surface temperature history, borehole CN-FJ-q117, Asia (see Table 11.1). Year of borehole logging: 1987; Mean ground surface temperature $T_0 = 18.5$ °C

variation in heat flow, lateral thermal conductivity contrasts, thermal conductivity anisotropy, forest fires, farming, etc.) may have perturbed the borehole temperature profiles (e.g., Carslaw and Jaeger 1959; Lachenbruch 1965; Kappelmeyer and Hänel 1974; Powell et al. 1988; Majorowicz and Skinner 1997; Guillou-Frottier et al. 1998; Kutasov and Eppelbaum 2003, 2013; Gruber et al. 2004; Bodri and Cermak 2005; Majorowicz and Safanda 2005; Mottaghy et al. 2005; Eppelbaum et al. 2006).

These results show that extreme caution should be used in the selection of temperature-depth profiles when attempting to infer ground surface temperature histories. A good example in this regard is the study by Guillou-Frottier et al. (1998), where only 10 out of 57 temperature profiles were selected for inversion of past ground surface temperatures.

Hence only the calculated warming rates for Asian wells (1.2–1.6 K/100a for Model *L* or 0.9–1.1 K/100a for Model *S*, Table 11.4) can be used for forecasting short term warming trends.

Knowledge of the past climate in archaeology is necessary not only for tracing some ancient events and more deep understanding some historical facts, but also for estimation of past harvests, analysis of some physical conditions of different constructions built in the past, and for many other fields (Eppelbaum and Kutasov 2014).

11.3 Sea Level Changes and Paleoclimate

Section 11.2 dealt with recent paleoclimate changes on land. Since marine areas occupy the greater part of the Earth's surface (>70 %) the relationships between sea (lake) level changes and paleoclimate changes are presented separately in this section.

11.3.1 "Heat Island Effect" and Its Influence on Subsurface Temperature

In his study, Taniguchi (2006) attributed the rise in ground surface temperature in Bangkok to both global climate change and urbanization. He argued that the "heat island effect" on subsurface temperature due to urbanization is a key global environmental issue, and reported that the magnitude of surface warming, evaluated from the subsurface temperature in Bangkok, was 1.7 °C, which was consistent with the meteorological data for the previous 50 years. The findings showed that the urbanization in Bangkok extended up to 80 km from the city center (Taniguchi 2006).

Thus when analyzing regional temperature profiles it is important to note that changes in GST can be caused by many non-climatic effects. These effects need to be documented since they produce distortions of borehole temperature profiles similar to those produced by climate change (Chouinard and Mareschal 2007). In this section we estimate the maximum effect of deep lakes and "heat islands" on borehole temperature profiles. We consider areas of deforestation, urbanization, farming, mining and wetland drainage as "heat islands". In all cases we assume that surface temperature anomalies (due to lakes) and the above- mentioned non-climatological factors have existed for a very long time. Therefore, the Laplace differential equation can be utilized to evaluate the maximum impact of deep lakes and "thermal islands" on borehole temperature profiles (Balobaev et al. 2008).

The ultimate objective is to facilitate the selection of drilling sites for borehole climate observatories where the effect of lakes and non-climatological factors will be minimal. A simulated example that demonstrates the effect of a deep lake on temperature profiles of wellbores located within 300 m (400 m from the center of the lake) is presented.

11.3.2 Working Equations

Let us assume that the well site is located within or outside a deep lake. In our case the term "deep lake" means that the long term mean annual temperature of bottom sediments can be considered a constant value. We will assume that $z = 0$ is the vertical coordinate of the lake bottom.

The temperature regime of formations in this area (within and outside of the lake) is subjected to its thermal influence. The extent of this influence depends mainly on the lake's dimensions, the current depth, the distance from the lake, and the difference between the long term mean annual temperature of bottom sediments and the long term mean annual temperature of surrounding lake formations (at $z = 0$). We will assume that the island has existed for an infinitely long period of time.

The following designations will be used below:

ρ, φ, z are the cylindrical coordinates (ρ is the distance from the z axis, φ describes the angle from the positive xz-plane to the point, and z is depth), T_{is} is the long term mean annual temperature of the bottom sediments, and T_{ot} is the long term mean annual temperature of the surrounding lake formations at $z = 0$. First, let consider a lake with an arbitrary contour (Fig. 11.12).

The Laplace equation for the semi-infinite solid area is

$$\frac{\partial^2 T}{\partial \rho^2} + \frac{1}{r}\frac{\partial T}{\partial \rho} + \frac{1}{\rho^2}\frac{\partial^2 T}{\partial \varphi^2} + \frac{\partial^2 T}{\partial z^2} = 0 \tag{11.3.1}$$

The boundary conditions are:

$$\begin{aligned} T(\rho, \varphi, z = 0) &= T_{is} \quad \text{within the lake area} \\ T(\rho,\ \varphi,\ z = 0) &= T_{ot} \quad \text{outside the lake area} \\ T(\rho = \infty,\ \varphi,\ z) &= T_{ot} + \Gamma z \end{aligned}$$

where Γ is the regional (outside the lake area) geothermal gradient.

The solution to the Laplace equation is possible by division of the arbitrary contour lake into sectors. However, the solution is expressed through a complex Poisson integral and fairly elaborate and time-consuming computations are needed (Balobayev and Shastkevich 1974).

Let $\rho_{\max}$ be the maximum value of the set ρ_1, ρ_2 … ρ_n (Fig. 11.12). By introducing a safety factor (the maximum thermal effect of the lake on temperature profiles) we can assume that the lake has a circular shape with a radius $R_i = \rho_{\max}$. In some cases the radius of the lake can be approximated by

$$R_i = \sqrt{\frac{S}{\pi}},$$

where S is the surface area of the lake.

Now the Laplace equation and boundary conditions are

$$\frac{\partial^2 T}{\partial \rho^2} + \frac{1}{r}\frac{\partial T}{\partial \rho} + \frac{\partial^2 T}{\partial z^2} = 0, \tag{11.3.2}$$

$$\begin{aligned} T(\rho,\ z = 0) &= T_{is}, \quad \rho \le R_i, \\ T(\rho,\ \varphi,\ z = 0) &= T_{ot}, \quad \rho > R_i, \\ T(\rho = \infty,\ z) &= T_{ot} + \Gamma z. \end{aligned}$$

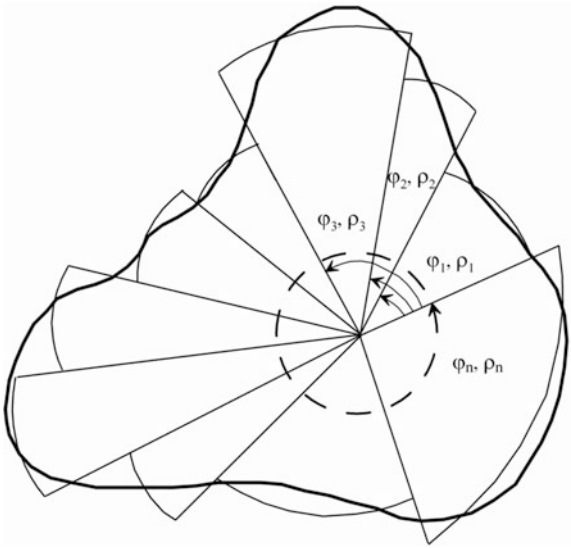

Fig. 11.12 Division of the arbitrary contour lake into sectors (after Balobayev and Shastkevich 1974)

The solution to Eq. (11.3.2) follows (Balobaev et al. 2008):

$$T(\rho, z) = T_{0t} + \Gamma z + M(T_{is} - T_{0t}) \tag{11.3.3}$$

$$M(\rho, z) = 1 - A_1 \left[A_2 \Pi(\alpha_1^2, k) + A_3 \Pi(\alpha_2^2, k) \right] \tag{11.3.4}$$

$$A_1 = \frac{z}{\pi \sqrt{z^2 + (R_i + \rho)^2}}; \quad A_2 = \frac{\sqrt{z^2 + \rho^2} - R_i}{\sqrt{z^2 + \rho^2} + \rho} \tag{11.3.5}$$

$$A_3 = \frac{\sqrt{z^2 + \rho^2} + R_i}{\sqrt{z^2 + \rho^2} - \rho}; \quad \alpha_1^2 = \frac{2\rho}{r + \rho}; \quad \alpha_2^2 = -\frac{2\rho}{r - \rho} \tag{11.3.6}$$

$$r^2 = \rho^2 + z^2; \quad k^2 = \frac{4\rho R_i}{z^2 + (R_i + \rho)^2} \tag{11.3.7}$$

where $\Pi(\alpha_1^2, k)$ and $\Pi(\alpha_2^2, k)$ are the complete elliptical integrals of the third order (Abramowitz and Stegun 1965).

In all climate reconstruction methods, the reduced temperatures, $T_R(\rho, z)$, are utilized.

From Eq. (11.3.3) we obtain

$$T_R(\rho, z) = T(\rho, z) - T_{ot} - \Gamma z = M(T_{is} - T_{ot}) \tag{11.3.8}$$

It is easy to see that the Eqs. (11.3.3)–(11.3.8) can also be used to describe the effect of "heat islands" on borehole temperature profiles. In this case R_i is the

Table 11.5 Function $M(\rho, z)$ for five boreholes

z (m)	Distance from the center of the lake (m)				
	100	150	200	300	400
20	0.3828	0.0525	0.0168	0.0042	0.0017
50	0.2815	0.0950	0.0370	0.0100	0.0041
70	0.2332	0.1023	0.0456	0.0134	0.0056
100	0.1787	0.0985	0.0518	0.0174	0.0076
120	0.1510	0.0919	0.0528	0.0193	0.0087
150	0.1189	0.0805	0.0512	0.0212	0.0101
200	0.0827	0.0628	0.0450	0.0222	0.0116
250	0.0598	0.0488	0.0379	0.0215	0.0122
300	0.0449	0.0384	0.0315	0.0198	0.0122
400	0.0275	0.0249	0.0219	0.0159	0.0111
500	0.0184	0.0172	0.0157	0.0125	0.0095

radius of the "heat island" (for example, an area of deforestation), T_{is} is its surface temperature, and T_{ot} is the land (outside of the "heat island") surface temperature. Both values (T_{is} and T_{ot}) are temperatures at depth with practically zero oscillation in the annual temperature (Balobaev et al. 2008).

11.3.3 Example of Calculations

Consider a 30 m deep lake with a radius of $R_i = 100$ m and $T_{is} = 10$ °C. The regional geothermal gradient is $\Gamma = 0.0300$ °C/m and $T_{ot} = 20$ °C. The drilling sites of 5 wellbores (500 m deep each) are located at distances ranging from 100 to 400 m from the center of the lake (Table 11.5).

What are the magnitudes of the formation temperature perturbations (expressed through the reduced temperatures) caused by the lake? The results of calculations after Eqs. (11.3.4) and (11.3.8) are presented in Table 11.5 and Figs. 11.13 and 11.14. Note that the bottom of the lake has a coordinate $z = 0$ and because of this, the actual depth is $z^* = z + 30$ m. In our case $T_{is} - T_{ot} = -10$ °C and the lake has a cooling effect on the temperature profiles. The values of $T_R(\rho, z)$ decrease with depth and can practically be neglected for radial distances of 550–600 m from the center of the lake (Figs. 11.13, 11.14). Software Maple 7 (Waterloo Maple 2001) was utilized to compute the function $M(\rho, z)$.

This method estimates the maximum effect of deep lakes and "heat islands" (areas of deforestation, urbanization, farming, mining and wetland drainage) on the borehole temperature profiles. An example of calculations is presented which shows to what extent the proximity of a deep lake affects the borehole temperature profiles.

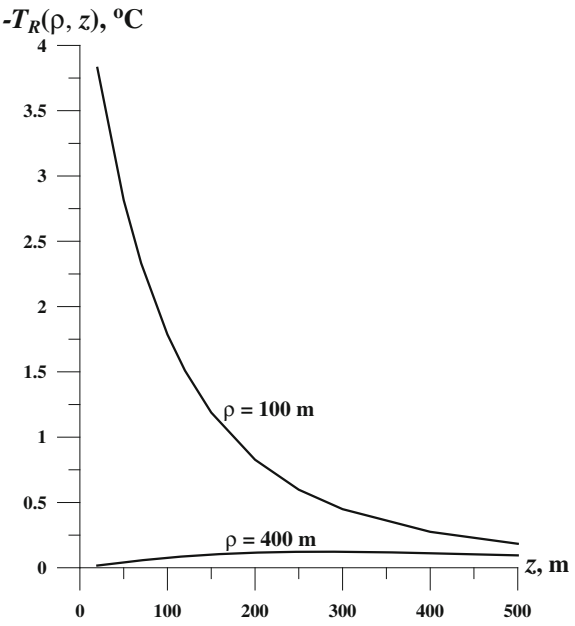

Fig. 11.13 The reduced temperatures for two wellbores

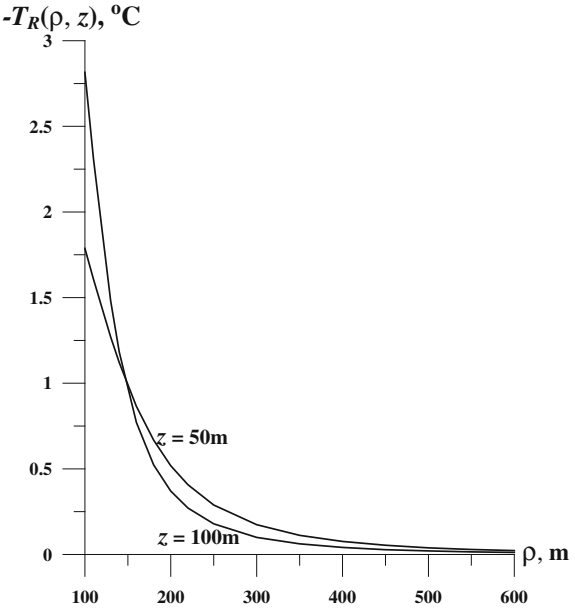

Fig. 11.14 The reduced temperatures versus radial distance for two depths

11.4 Long and Short Term Monitoring of Subsurface Temperatures in Observational Wells

11.4.1 Basic Issues

The variations of the GST during long-term climate changes result in disturbances (anomalies) of the temperature field of formations. For this reason the GSTH can be evaluated by analyzing precise current-day temperature-depth profiles (e.g., Balobaev et al. 2008).

Let us assume that t_x years ago the ground surface temperature started to increase (warming) or reduce (cooling). Prior to this moment the subsurface temperature exhibited behavior shown in Fig. 11.4 [see also Eq. (11.2.1)]. We also assume that the formation is a homogeneous medium with some constant thermal properties [see Eq. (11.2.2)].

11.4.2 A Simple Method of Temperature and Gradient Evaluation

Mathematical solutions to models of changing GST values with time have been presented in the literature (e.g., Carslaw and Jaeger 1959; Cermak 1971; Lachenbruch and Marshall 1986; Lachenbruch et al. 1988; Powell et al. 1988; Pollack et al. 2000; Balobaev et al. 2009b; Muto et al. 2011; Roy and Chapman 2012).

Below we present a simple method of evaluation of the perturbations to the temperatures ΔT_c and geothermal gradients $\Delta\Gamma$ due to past surface temperature changes (Powell et al. 1988). The values of ΔT_c and $\Delta\Gamma$ due to an instantaneous change of surface temperature ΔT_0 at time t before now are:

$$\Delta T_c(z,t) = \Delta T_0 \, erfc\left(\frac{z}{2\sqrt{at}}\right), \quad erfc(x) = 1 - erf(x), \tag{11.4.1}$$

$$\Delta\Gamma(z,t) = -\frac{\Delta T_0}{\sqrt{\pi a t}} \exp\left(-\frac{z^2}{4at}\right), \tag{11.4.2}$$

where $erf(x)$ is the error integral and a is the thermal diffusivity of homogenous formations.

The results of temperature inversion show that probably some non-climatic effects (vertical and horizontal water flows, sedimentation, uplift, erosion, steep topography, lakes, vertical variation in heat flow, lateral thermal conductivity contrasts, thermal conductivity anisotropy, forest fires, farming, etc.) may have perturbed the borehole temperature profiles (e.g., Carslaw and Jaeger 1959; Lachenbruch 1965; Kappelmeyer and Hänel 1974; Majorowicz and Skinner 1997;

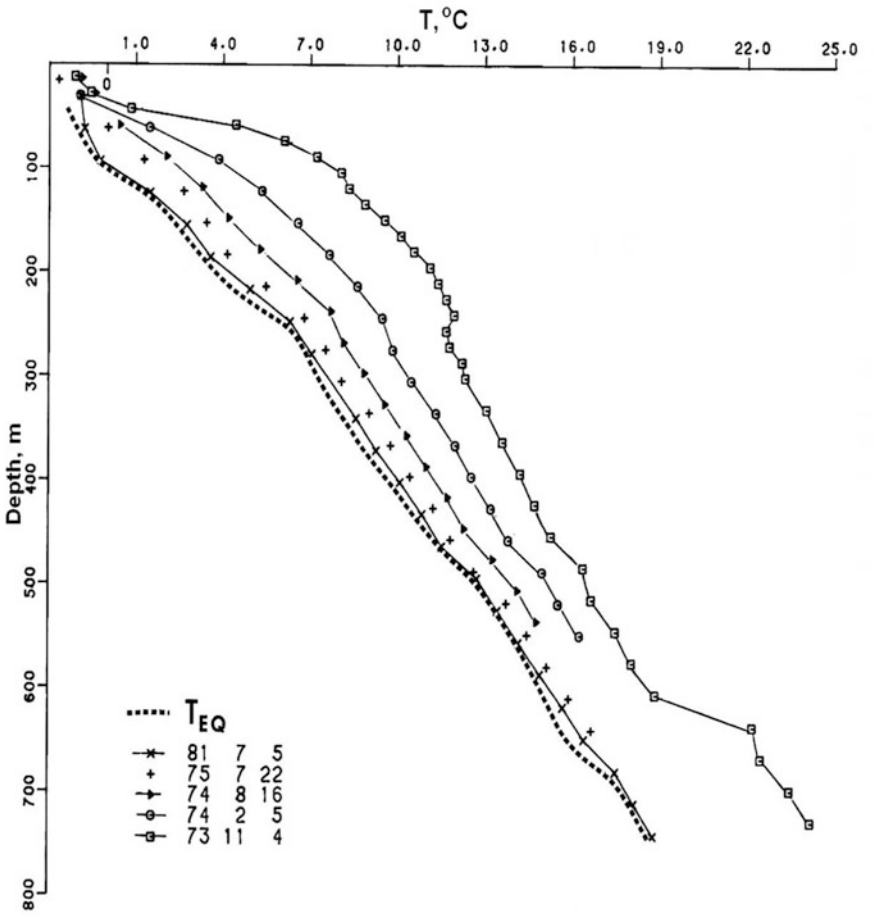

Fig. 11.15 Temperature profiles in the Kugpik O-13 well (Taylor et al. 1982). T_{EQ}—the predicted temperature versus depth curve; the data presented below T_{EQ} show the year, month and day when the temperature surveys were conducted

Powell et al. 1988; Guillou-Frottier et al. 1998; Gruber et al. 2004; Bodri and Cermak 2005; Mottaghy et al. 2005). Thus, extreme caution should be used in the selection of temperature-depth profiles when inferring ground surface temperature histories.

The method of temperature inversion to determine trends in the GSTH requires that the thermal recovery of a well be practically complete. We also assume a uniform lithology over hundreds of meters. The results of temperature surveys show that for large sections of the boreholes the geothermal gradient is practically constant (e.g., Judge et al. 1981; Taylor et al. 1982; Kutasov 1999, see also Fig. 11.15, the TEQ curve). This means that the thermal conductivity can be considered as constant within these sections of the boreholes.

In the ideal case, the shut-in temperature (T_s) should practically be equal to the formation temperature (T_f). In practice, however, we need to evaluate the following two parameters

$$\Delta T_c = T_f^* - T_f, \quad \Delta T_c = T_f - T_c,$$

where T_f^* is the temperature of formation after the change in the ground surface temperature.

The values of ΔT_c obtained from present-day precise temperature-depth profiles are used to determine the trends in ground surface temperature history. Thus to monitor the temperature change at a given depth (in an observational well) the following condition should be satisfied

$$\Delta T_c \gg \Delta T,$$

where ΔT_c is the temperature anomaly due to climate change and ΔT is the temperature difference between the formation and shut-in temperatures. The next section suggests a technique for the selection of ideal or more reliable observational temperature wells.

11.4.3 Application of the γ-Function

Shallow wells (20–30 m) can be used for short term monitoring of subsurface temperatures within the zone of annual temperature variations. Usually, a short period of drilling mud circulation is required to drill a shallow well. Although a short shut-in time period is sufficient to determine (with good accuracy) the formation temperature, we suggest an evaluation of the γ-function (Kutasov 1987, 1999):

$$\gamma = \frac{T(0,t_s) - T_f}{T_w - T_f} = 1 - \frac{Ei\left[-\beta\left(1 + \frac{t_D^*}{t_{sD}}\right)\right]}{Ei(-\beta)}, \quad t_{sD} = \frac{at_s}{r_w^2}, \tag{11.4.3}$$

$$t_D^* = Gt_D, \quad t_D = \frac{at_c}{r_w^2}, \quad \beta = \frac{1}{4t_D^*},$$

$$\left\{\begin{array}{ll} G = 1 + \frac{1}{1+AF} & t_D \le 10 \\ F = [\ln(1+1_D)]^n & n = 2/3\ A = 7/8 \end{array}\right\},$$

$$G = \frac{\ln t_D - \exp(-0.236\sqrt{t_D})}{\ln t_{cD} - 1}, \quad t_D > 10,$$

where t_s is the shut-in time (time since the end of drilling and well completion operations), t_c is the drilling fluid circulation time at a given depth, a is the thermal diffusivity of the formation and r_w is the well radius, T_w is the average mud

circulation temperature at given depth, t_{sD} is the dimensionless shut-in time, t_D is the dimensionless mud circulation shut-in time, T_f is formation temperature, $t_D{}^*$ is the drilling fluid adjusted dimensionless circulation time, G is the correlation coefficient, and $Ei(x)$ is an exponential integral.

As can be seen, the γ-function evaluates the relative accuracy in determining the formation temperature. When deriving Eq. (11.4.3) an adjusted circulation time concept (Kutasov 1987, 1989) was used which allows for the substitution of the well by a constant borehole wall temperature and a cylindrical source with a constant heat flow rate. It was also assumed that the thermal diffusivity is the same both within the well and in the surrounding formations. The constants in Eq. (11.4.3) are due to approximation of the results of numerical solutions of the diffusivity equations by an analytical relationship. The condition of energy heat balance was utilized (Kutasov 1999).

A number of investigators have conducted long term field studies of free thermal convection in deep boreholes. It was found that in deep wells the effect of convection is within 0.01–0.03 °C (Eppelbaum and Kutasov 2011). This effect of free thermal convection in shallow wells may be essential (Kutasov and Devyatkin 1977; Eppelbaum and Kutasov 2011). For shallow observational wells the effect of thermal convection on the temperature profiles should be minimized or even eliminated. For this reason the radii of these wells should be small and fluids or gases (as well fillers) that have low convective parameter values should be utilized.

The convective parameter is defined as

$$k_p = \frac{g\beta}{va},$$

where β is the coefficient of thermal volumetric expansion, g is the gravity of acceleration, v is the kinematic viscosity, and a is the thermal diffusivity of the fluid (gas). The best way to eliminate the effect of thermal convection is to use some types of soil (for example, sands) after setting the temperature sensors as natural well fillers (Kutasov and Devyatkin 1977).

For deep wells (>100–300 m) the drilling process, due to the lengthy period of drilling fluid circulation, greatly alters the temperature of the formation immediately surrounding the well. As a result, the determination of formation temperature at any depth requires a lengthy period of shut-in time.

The subsurface formation temperature is not only affected by the GSTH, but also by the well thermal recovery process. To estimate the effect of well thermal recovery process on subsurface formation temperatures we used Slider's method to calculate the in situ formation thermal conductivity, the skin factor, and contact thermal resistance for boreholes where the temperature recovery process after drilling operations was not complete (Kutasov and Eppelbaum 2007). It was assumed that the volumetric heat capacity of the formations is known and that the instantaneous wall heat temperature and time data are available for a cylindrical probe with a constant heat flow rate placed in a borehole. In this case Slider's

method is used to correct the shut-in temperature—time data for a short (10–20 h) field test. It was also shown that data on the undisturbed formation temperature is not necessary to conduct this test (Kutasov and Eppelbaum 2007).

11.4.4 Slider's Method

Slider suggested a technique for analyzing transient pressure (p) tests when conditions are not constant before testing (Earlougher 1977, pp. 27–29). Figure 11.16 schematically illustrates a situation with shut-in pressure declining (solid line) before a drawdown test starts at time t_1.

The dashed line, an extrapolation of pressure behavior into the future, represents the expected pressure behavior for continued shut-in. The constant flow rate starts at time t_1, and pressure behaves as shown by the solid line beyond t_1. Three steps are required to correctly analyze such drawdown behavior:

1. Determine the correct shut-in pressure extrapolation,
2. Estimate the difference between observed flowing pressure and the extrapolated pressure ($\Delta p_{\Delta t}$ in Fig. 11.16),
3. Plot $\Delta p_{\Delta t}$ versus log Δt.

Given the similarity between Darcy's and Fourier's laws, the same differential diffusivity equation describes the transient flow of an incompressible fluid in a porous medium and heat conduction in solids. As a result, there is a correspondence between the following parameters: volumetric flow rate, pressure gradient, mobility (formation permeability and the viscosity ratio), hydraulic diffusivity coefficient and heat flow rate, temperature gradient, thermal conductivity and thermal diffusivity. Thus, recovery of the well temperature regime after drilling can be considered to be a temperature drawdown test. For a temperature drawdown test analysis it is necessary to estimate the rate (b) of temperature decline (or increase at $t = t_1$) and to determine the values of the temperature decline ("correct extrapolation" as in Fig. 11.16). The last step is to introduce corrections (due to insufficient shut-in time) to the observed transient well temperatures.

11.4.5 Results of Computations

We selected long-term temperature surveys in three wells and a simulated example to demonstrate the application of Slider's method and the γ-function for analyzing results of temperature tests in deep wells (Table 11.6 and Fig. 11.15). For depths of 182.9 m (the Kugpik O-13 well, Beaufort-Mackenzie area, Alaska), 70.1 m (Drew Point No. 1, Beaufort Sea coast, Alaska) and 61.0 m (East Simpson well #1 located in Umiat Meridian, near the west shore of Smith Bay, Alaska) we assumed

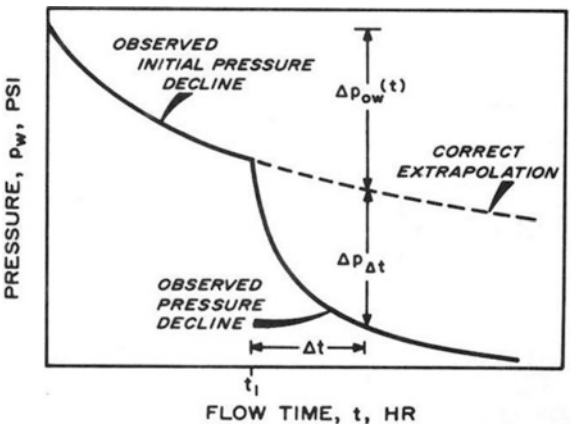

Fig. 11.16 Drawdown testing in a developed reservoir (Earlougher 1977). t_1 is the time period of the projected pressure decline, Δt is the time since t_1, Δp_{ow} is the projected pressure drop, and $\Delta p_{\Delta t}$ is the observed pressure drop

Table 11.6 Well data and references

Site name	Kugpik O-13 (Beaufort-Mackenzie area, Alaska)	Drew Point no. 1 (Beaufort Sea coast, Alaska)	East Simpson no. 1 (Umiat Meridian, Alaska)
Hole depth (m)	3,689	640	600
Drilling time (days)	188	60	51
Number of logs	6	6	5
Shut-in time (days)	35–2,835	186–2,339	155–1,947
Reference	Taylor et al. (1982)	Boreholes (1998)	

that the shut-in temperature recovery for long shut-in times can be approximated by the Horner plot (Timko and Fertl 1972; Dowdle and Cobb 1975).

The Horner equation represents the cooling of a well in which the drilling process is approximated by a constant (per unit of length) linear heat source. A logarithmic approximation of the *Ei*-function (the analytical solution, Earlougher 1977) is only possible for large values of dimensionless circulation and shut-in times (t_D, t_{sD}). However, the gamma function can be used for all values of t_D, and t_{sD}. Here we show how the two methods can be applied for temperature corrections

$$T_s = T_f + B \ln \frac{t_s + t_c}{t_s}, \quad B = \frac{q}{2\pi\lambda}, \tag{11.4.4}$$

where T_f is the formation temperature, λ is the thermal conductivity of the formation, T_s is the shut-in temperature, t_s is the shut-in time, q is a constant (per unit of length) linear heat source, and t_c is the thermal "disturbance" period for a given depth.

Equation (11.4.4) shows that the value of t_s is dependent on drilling technology (flow rate, well design, fluid properties, penetration rate, etc.), geothermal temperatures and mechanical properties of the formation.

It is a reasonable assumption that the value of t_c is a linear function of the depth (z):

$$t_c = t_{tot}\left(1 - \frac{z}{H_t}\right), \tag{11.4.5}$$

where z is the depth, t_{tot} is the total drilling time, and H_t is the total well depth. The values of $T^* = T_f$ were computed by using values of shut-in temperatures at $t_s = t_{s1}$ and $t_s = t_{s2}$ (Table 11.7).

From Eq. (11.4.4) the rate of the temperature decline is

$$b = \frac{dT_s}{dt_s} = B\left(\frac{1}{t_s + t_c} - \frac{1}{t_s}\right). \tag{11.4.6}$$

The same relationship was used to estimate of the rate of the temperature decline b for depths of 61.0 and 70.1 m which are located within the permafrost zone.

Let us now assume that at the moment in time $t = t_{ep}$ (Fig. 11.17) the phase transition (water-ice) in formations at these depths is complete; i.e., the thermally disturbed formation has frozen. In this case at $t > t_{ep}$ the cooling process is similar to that of temperature recovery in sections of the well below the permafrost base. It is well known (Tsytovich 1975) that the freezing of water occurs in some temperature interval below 0 °C (Fig. 11.17).

In practice, however, the moment of time $t = t_{ep}$ cannot be determined. This can only be done by conducting long-term repetitive temperature observations in deep wells. For the permafrost interval we assumed that at $t_s \gg t_{ep}$ and for long shut-in times the shut-in temperatures can be approximated by an empirical equation (Lachenbruch and Brewer 1959).

$$T_s = A + B\ln\frac{t_s + t_c}{t_s}. \tag{11.4.7}$$

The latter equation was successfully used to estimate the formation temperatures for an Alaskan well when $t_s \gg t_{ep}$. Equations (11.4.4) and (11.4.7) are identical and Eq. (11.4.6) was used to calculate the rate of the temperature decline at depths of 61.0 and 70.1 m (Table 11.7).

A simulated example is also presented below where Eq. (11.4.5) is used to estimate the difference between the formations and shut-in temperatures for various values of shut-in time (Fig. 11.18). For a depth of 182.9 m (Kugpik O-13 well) we assumed that the temperature recovery for long shut-in times can be approximated by the Horner plot (Eq. 11.4.4) (Kutasov and Eppelbaum 2013).

The rate of temperature decline (B) is given by Eq. (11.4.6).

Let us now assume that at the moment of time $t = t_{ep}$ (Fig. 11.18) the phase transition (water-ice) in formations at a depth of 30.5 is complete; i.e., the thermally disturbed formation has frozen. In this case at $t > t_{ep}$ the cooling process is

Table 11.7 The rate of temperature decline and the values of $T_f - T_s$

t_s (days)	East Simpson no. 1 $t_{s1} = 155$ days, $t_{s2} = 520$ days $T_{s1} = -7.145$ °C, $T_{s2} = -8.486$ °C $h = 61.0$ m, $T_f = -9.13$ °C			Drew point no. 1 $t_{s1} = 186$ days, $t_{s2} = 547$ days $T_{s1} = -6.925$ °C, $T_{s2} = -8.142$ °C $h = 70.1$ m, $T_f = -8.85$ °C			Kugpik O-13 $t_{s1} = 320$ days, $t_{s2} = 660$ days $T_{s1} = 5.51$ °C, $T_{s2} = 4.16$ °C $h = 182.9$ m, $T_f = 2.57$ °C		
	T_s (°C)	$T_f - T_s$ (°C)	$-b$, 10^{-3} (°C/day)	T_s(°C)	$T_f - T_s$ (°C)	$-b$, 10^{-3} (°C/day)	T_s (°C)	$T_f - T_s$ (°C)	$-b$,10^{-3} (°C/day)
200	−7.55	−1.58	7.2	−7.05	−1.81	8.0	6.80	−4.23	15.6
400	−8.30	−0.83	2.0	−7.90	−0.96	2.2	5.02	−2.45	5.1
600	−8.57	−0.57	0.9	−8.20	−0.65	1.0	4.30	−1.73	2.5
800	−8.71	−0.43	0.5	−8.36	−0.49	0.6	3.91	−1.34	1.5
1,000	−8.79	−0.34	0.3	−8.46	−0.40	0.4	3.66	−1.09	1.0
1,200	−8.85	−0.29	0.2	−8.52	−0.33	0.3	3.49	−0.92	0.7
1,500	−8.90	−0.23	0.2	−8.59	−0.27	0.2	3.32	−0.75	0.5
2,000	−8.96	−0.17	0.1	−8.65	−0.20	0.1	3.14	−0.57	0.3

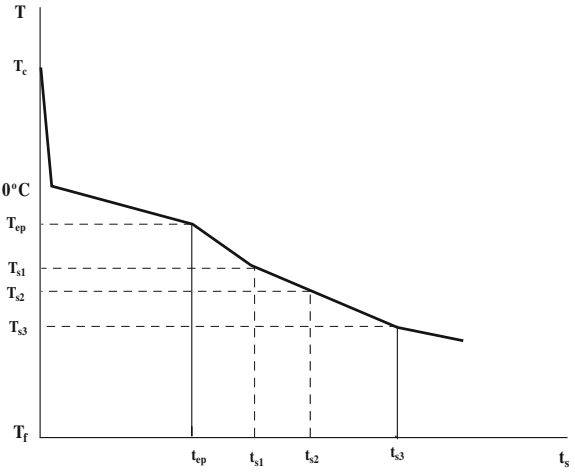

Fig. 11.17 Shut-in temperatures at a given depth (above the permafrost base)—schematic curve. T_f is the formation temperature, T_c is the fluid circulation temperature while drilling, T_{s1}, T_{s2}, and T_{s3} are shut-in temperatures, t_{s1}, t_{s2}, and t_{s3} are the shut-in times, T_{ep} is the refreezing temperature, and t_{ep} is the refreezing time

similar to that of the temperature recovery in sections of the well below the permafrost base.

Equation (11.4.6) was used to calculate the rate of temperature decline at depths of 61.0 and 70.1 m (Table 11.7).

The above mentioned methodology can help optimize the selection of observational wells in wellbore climatology.

Let us assume that 30 h were spent to drill a 200 m well. To clean up the well the drilling mud was circulated for 2 h. Thus the time of drilling fluid circulation (t_c) at a given depth (h) is

$$t_c = 30\left(1 - \frac{h}{200}\right) + 2. \tag{11.4.8}$$

Let also assume that the well radius (r_w) is 0.1 m, the thermal diffusivity of formation (a) is 0.0040 $m^2\ h^{-1}$, the geothermal gradient is 0.03 °C/m, the temperature of the drilling fluid (T_c) is 28 °C and the surface temperature is 20 °C. Thus the formation temperature is

$$T_f = 20 + 0.03\ h. \tag{11.4.9}$$

In the simulated example Eq. (11.4.5) was used to estimate the difference between the formation and shut-in temperatures for depths of 30, 50, 100 and 200 m at various values of shut-in time (Fig. 11.19) (Kutasov and Eppelbaum 2013).

Figure 11.19 depicts the results of calculations after Eq. (11.4.1) for a single temperature step $\Delta T_0 = 1$ °C. It can be seen that for short times, only shallow depths are affected by temperature changes.

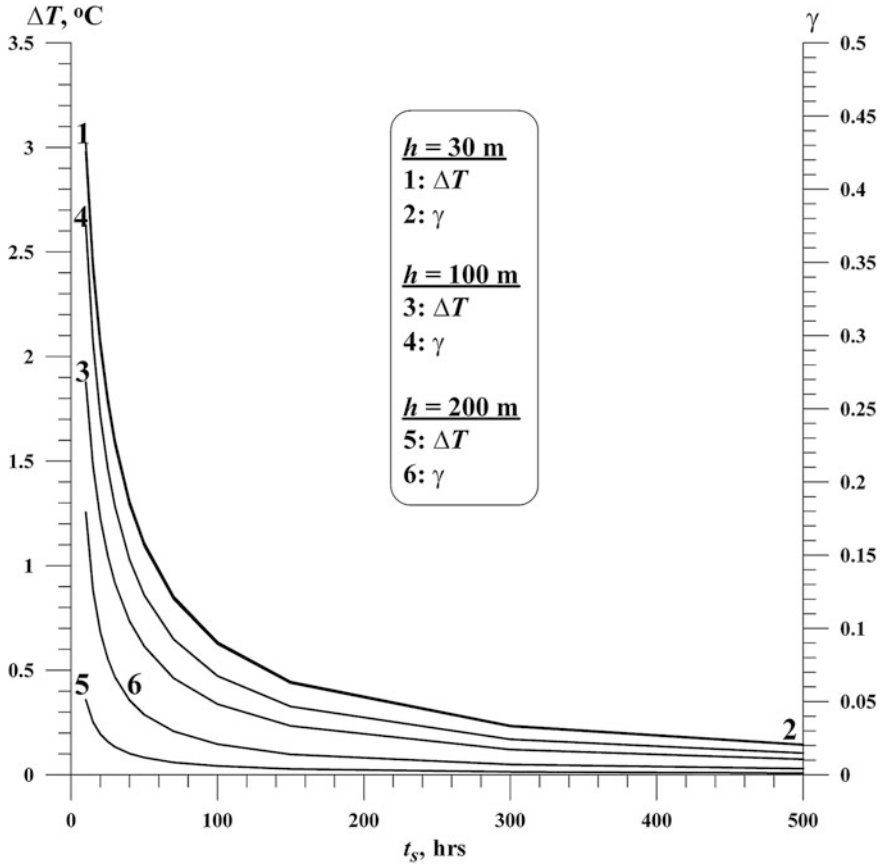

Fig. 11.18 Function γ and the values $\Delta T = T_f - T_s$

When, for example, $\Delta T_0 = 2°C$, the values of ΔT in Fig. 11.19 should be doubled. For several steps the superposition principle can be used to calculate the values of ΔT. From physical considerations the following conditions should be satisfied

$$\Delta T_c \gg \Delta T.$$

Equation (11.4.3) was used to calculate the function γ and estimate the difference between the shut-in and formation temperatures (Fig. 11.18).

Let us assume that 20, 50, 100, 200, 500 or 1,000 years ago due to climate change the GST was instantaneously increased by $\Delta T_0 = 1$ °C. The values of ΔT_c for several depths were estimated from Eq. (11.4.1) and are presented in Fig. 11.19. Let us also assume that from reliable values of $\Delta T_c = T_f^* - T_f$ we can obtain at $\Delta T \leq 0.2$ °C. For depths of 30, 100 and 200 m (the simulated example)

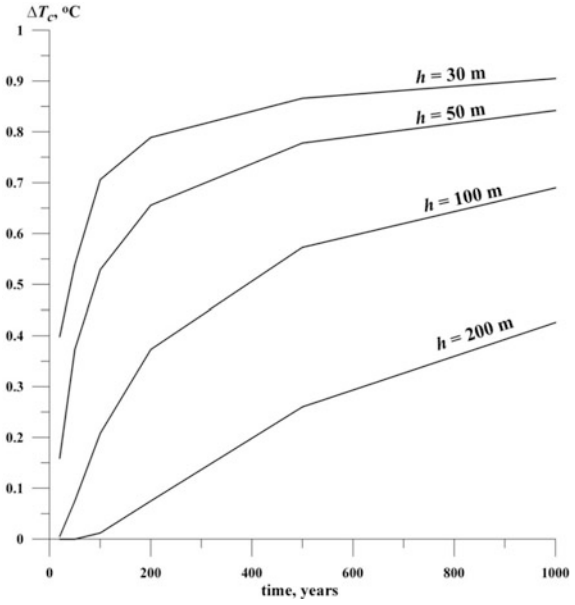

Fig. 11.19 Present perturbations versus the temperatures ΔT_c due to instantaneous surface temperature changes of 1 °C at various times prior to the present. Thermal diffusivity = 0.0036 m^2/h, ΔT in °C

from Tables 11.6 and 11.7 we can determine the values of shut-in times when the condition $\Delta T \leq 0.2$ °C is satisfied (Fig. 11.18). For a depth of 30 m reliable values of ΔT_c can obtained at shut-in times of $t_s \geq 350$ h (time interval 20–1,000 years). Similarly, for a depth of 100 m the value of $t_s \geq 245$ h (time interval 100–1,000 years), and for a depth of 200 m the value of $t_s \geq 19$ h (time interval 500–1,000 years).

For a depth of 182.9 m (Kugpik O-13 well, Table 11.6 and Fig. 11.15) the reliable values of ΔT_c can be obtained at shut-in times of more than 6 years (time interval 500–1,000 years). By using Tables 11.6 and 11.7 we can estimate that for a depth of 70.1 m (Drew Point No. 1) and a depth of 61.0 m (East Simpson well #1) the corresponding shut times are 2,000 and 1,750 days (time interval of 500–1,000 years). The values of t_s for six depths were estimated by the interpolation method. Thus we can conclude that:

1. Even for shorter wells (500–700 m) a lengthy shut-in period is required to observe the effect of climate changes on the subsurface formation temperature.
2. The best candidates for temperature observational wells are shallow wells (up to 100–200 m) as shown in the simulated well.
3. Extreme caution should be exercised when using abandoned deep wells (2,000–4,000 m) as temperature observational wells.

Thus, Slider's method can be applied to estimate the rate of temperature decline (or increase) during well shut-in and thereby help choose observational temperature wells. An analytical formula (γ-function) can be used to estimate the relative accuracy when calculating the formation temperature. This methodology can contribute to the selection of observational wells for wellbore climatology.

References

Abramowitz M, Stegun I (1965) Handbook of mathematical functions. Dover Publications Inc, New York

Allen MR, Gillett NP, Kettleborough JA, Hegerl G, Schnur R, Stott PA, Boer G, Covey C, Delworth TL, Jones GS, Mitchell JFB, Barnett TP (2006) Quantifying anthropogenic influence on recent near-surface temperature change. Survey Geophys 27:491–544

Baker DG, Ruschy DL (1993) The recent warning in eastern Minnesota shown by ground temperatures. Geophys. Res Lett 20:371–374

Balobaev VT, Kutasov IM, Eppelbaum LV (2008) Borehole paleoclimatology—the effect of deep lakes and "heat Islands" on temperature profiles. Climate Past 4(2):1–18

Balobaev VT, Skachkov YB, Shender NI (2009) Forecasting climate changes and the permafrost thickness for Central Yakutia into the year 2200. Geogr Nat Resourses 30:141–145

Balobayev VT, Shastkevich YG (1974) The estimation of the talik zones configuration and the steady temperature field of rocks beneath the lakes of arbitrary contour. Lakes of the Siberia Cryolithozone, Nauka, Novosibirsk, 116–127 (in Russian)

Beltrami H, Jessop AM, Mareschal J-C (1992) Ground temperature histories in eastern and central Canada from geothermal measurements: evidence of climate change. Palaeogeogr Palaeoclimatol Palaeoecol (Glob Planet Change Sect) 98:167–183

Birchfield GE (1977) A study of the stability of model continental ice sheet subject to periodic variations in heat input. J Geophys Res 82(31):4909–4913

Blackwell DD, Steele JL, Brott CA (1980) The terrain effect on terrestrial heat flow. J Geophys Res 85(B9):4757–4772

Bodri L, Cermak V (1997) Climate change of the last two millennia inferred from borehole temperatures: results from the Czech Republic—part II. Glob Planet Change 14:163–173

Bodri L, Cermak V (2005) Borehole temperatures, climate change and the pre-observational surface air temperature mean: allowance for hydraulic conditions. Glob Planet Change 45:265–276

Boreholes locations and permafrost depths (1998) Alaska, USA, from US Geological Survey http://nsidc.org/data/docs/fgdc/ggd223_boreholes_alaska

Carslow HS, Jaeger JC (1959) Conduction of heat in solids, 2nd edn. Oxford University Press, Oxford

Čermak V (1971) Underground temperature and inferred climatic temperature of the past millennium. Palaeogeogr Palaeoclimatol Palaeoecol 10:1–19

Chouinard C, Mareschal J-C (2007) Selection of borehole temperature depth profiles for regional climate reconstructions. Climate Past 3:297–313

Clauser C, Mareschal J-C (1995) Ground temperature history in central Europe from borehole temperature data. Geophys J Int 121:805–817

Covington WW (1981) Changes in the forest floor organic matter and nutrient content following clear cutting in northern hardwoods. Ecology 62:41–48

Dowdle WL, Cobb WM (1975) Static formation temperatures from well logs—an empirical method. J Pet Technol 27(11):1326–1330

Earlougher RC Jr (1977) Advances in well test analysis. SPE, New York

Eppelbaum LV (2013b) Non-stochastic long-term prediction model for US tornado level. Nat Hazards 69(3):1–10. doi:10.1007/s11069-013-0787-7

Eppelbaum LV, Kardashov VR (2001) Analysis of strongly nonlinear processes in geophysics. In: Moresi L, Müller D (eds) Proceedings of the chapman conference on exploration geodynamics, Dunsborough, Western Australia, pp 43–44

Eppelbaum LV, Kardashov VR (2003) On one strongly non-linear generalization of the Sturm-Liouville problem. In: Proceedings of the colloquium on the occasion of the 200th anniversary of Charles-François Sturm and workshop on Sturm-Liouville theory, Geneva, Switzerland, pp 25–26

Eppelbaum LV, Kutasov IM (2011) Estimation of the effect of thermal convection and casing on temperature regime of boreholes—a review. J Geophys Eng 8:R1–R10

Eppelbaum LV, Kutasov IM (2014) Advanced analysis of thermal data observed in subsurface wells unmasks the ancient climate. Transactions of the 10th EUG meeting, geophysical research abstracts, Vienna, Austria, vol 16, EGU2014-3261, pp 1–3

Eppelbaum LV, Kutasov IM, Barak G (2006) Ground surface temperature histories inferred from 15 boreholes temperature profiles: comparison of two approaches. Earth Sci Res J 10(1):25–34

González-Rouco JF, Beltrami H, Zorita E, Stevens MB (2008) Borehole climatology: a discussion based on contributions from climate modeling. Climate Past Discuss 4:1–80

Gosselin C, Mareschal J-C (2003) Variations in ground surface temperature histories in the Thompson Belt, Manitoba, Canada: environment and climate changes. Glob Planet Change 39:271–284

Gruber S, King L, Kohl T, Herz T, Haeberli W, Hoelzle M (2004) Interpretation of geothermal profiles perturbed by topography: the Alpine permafrost boreholes at Stockohorn plateau, Switzerland. Permafrost Periglac Process 15:349–357

Guillou-Frottier L, Mareschal J-C, Musset J (1998) Ground surface temperature history in central Canada inferred from 10 selected borehole temperature profiles. J Geophys Res 103(B4):7385–7397

Hamza VM, Cavalcanti ASB, Benyosef LCC (2007) Surface thermal perturbations of the recent past at low latitudes—inferences based on borehole temperature data from Eastern Brazil. Clim Past 3:513–526

Harris RN, Chapman SD (1995) Climate change on the Colorado Plateau of eastern Utah inferred from borehole temperatures. J Geophys Res 100:6367–6381

Hopcroft PO, Gallagher K, Pain CC (2007) Inference of past climate from borehole temperature data using Bayesian reversible jump Markov chain Monte Carlo. Geophys J Int 171:1430–1439

Huang S, Pollack HN (1998) Global borehole temperature database for climate reconstruction, IGBP PAGES/World data center-A for paleoclimatology data contribution series #1998-044. NOAA/NGDC paleoclimatology program, Boulder, CO, USA. http://www.geo.lsa.umich.edu/~climate)

Huang S, Shen PY, Pollack HN (1996) Deriving century—long trends of surface temperature change from borehole temperatures. Geophys Res Lett 23:257–260

Huang S, Pollack HN, Shen PY (2000) Temperature trends over past five centuries reconstructed from borehole temperatures. Nature 403(17):756–758

Jain S, Pulwarty RS (2006) Environmental and water decision-making in a changing climate. EOS 87(14):139

Judge AS, Taylor AE, Burgess M, Allen VS (1981) Canadian geothermal data collection—Northern Wells 1978–80. Geothermal series, vol 12. Earth Physics Branch, Energy, Mines and Resources, Ottawa

Kappelmeyer O, Hänel R (1974) Geothermics with special reference to application. Gebruder Borntrargen, Berlin

Kardashov VR (1993) Generalized eigenvalue problems, stationary regimes and regimes with aggravation of strongly nonlinear nonstationary processes. Diff Eqn 29(3):597–604

Kohl T (1999) Transient thermal effects below complex topographies. Tectonophysics 306(3–4):311–324

Kooi H (2008) Spatial variability in subsurface warming over the last three decades; insight from repeated borehole temperature measurements in The Netherlands. Earth Planet Sci Lett 270:86–94

Kostizyn VA (1984) Evolution of atmosphere biosphere and climate. Nauka, Moscow (in Russian)

Kukkonen IT, Cermak V, Safanda J (1994) Subsurface temperature—depth profiles, anomalies due to climatic ground surface temperature changes or groundwater flow effects. Glob Planet Change 9:221–232

Kutasov IM (1987) Dimensionless temperature, cumulative heat flow and heat flow rate for a well with a constant bore-face temperature. Geothermics 16(2):467–472
Kutasov IM (1989) Application of the Horner method for a well produced at a constant bottomhole pressure. Formation Eval 3:90–92
Kutasov IM (1999) Applied geothermics for petroleum engineers. Elsevier, Amsterdam
Kutasov IM, Devyatkin VN (1977) Experimental investigation of temperature regime of shallow convective holes. CRREL Draft Trans 589
Kutasov IM, Eppelbaum LV (2003) Prediction of formation temperatures in permafrost regions from temperature logs in deep wells—field cases. Permafrost Periglac Process 14(3):247–258
Kutasov IM, Eppelbaum LV (2007) Temperature well testing—utilization of the Slider's method. J Geophys Eng 4(1):1–6
Kutasov IM, Eppelbaum LV (2013) Optimisation of temperature observational well selection. Explor Geophys 44(3):192–198
Kutasov IM, Eppelbaum LV, Dorofeyeva RP (2000) Physical-mathematical problem of the recent climate reconstruction from subsurface temperature logs. Sci Isr 2(2):79–83
Lachenbruch AH (1965) Rapid estimation of the topographic disturbance to superficial thermal gradients. Rev Geophys 6:365–400
Lachenbruch AH, Brewer MC (1959) Dissipation of the temperature effect of drilling a well in Arctic Alaska. US Geol Surv Bull 1083-C:74–109
Lachenbruch AH, Marshall BV (1986) Changing climate: geothermal evidence from permafrost in the Alaskan Arctic. Science 234:689–696
Lachenbruch AH, Cladouhos TT, Saltus RW (1988) Permafrost temperature and the changing climate. In: Proceedings of the 5th international conference on permafrost, vol 3. Tapir Publication, Trondheim, Norway, pp 9–17
Lewis TJ, Wang K (1992) Influence of terrain on bedrock temperatures. Palaeogeogr Palaeoclimatol Palaeoecol 98:87–100
Lewis TJ, Wang K (1998) Geothermal evidence for deforestation induced warming: implications for the climatic impact of land development. Geophys Res Lett 25:535–538
Majorowicz JA, Safanda J (2005) Measured versus simulated transients of temperature logs—a test of borehole climatology. J Geophys Eng 2:1–8
Majorowicz JA, Skinner WP (1997) Potential causes of differences between ground and surface air temperature warming across different ecozones in Alberta, Canada. Glob Planet Change 15:79–91
Majorowicz JA, Skinner WP, Safanda J (2012) Western Canadian sedimentary basin—depth transients from repeated well logs: evidence of recent decade subsurface heat gain due to climatic warming. J Geophys Eng 9:127–137
Maple W (2001) Maple 7 learning guide. Waterloo Maple Inc, Waterloo
Mareschal J-C, Beltrami H (1992) Evidence for recent warming from perturbed geothermal gradients: examples from Eastern Canada. Clim Dyn 6(3–4):135–143
Milankovitch M (1941) Canon of insolation and the ice-age problem. Special Publication of the Royal Serbian Academy, Serbia, vol 132 (in German)
Moritz RE (1979) Nonlinear analysis of a simple sea ice—ocean temperature oscillator model. J Geophys Res 84(C8):4916–4920
Mottaghy D, Schellschmidt R, Popov YA, Clauser C, Kukkonen IT, Nover G, Milanovsky S, Romushkevich RA (2005) New heat flow data from the immediate vicinity of the Kola super-deep borehole: vertical variation in heat flow confirmed and attributed to advection. Tectonophysics 401:119–142
Mukhtarov AS, Kadirov FA, Mamedov VA (2010) Reconstruction of the surface temperature in the Kura depression (Azerbaijan) by the inversion of borehole data. Izv Russ Acad Sci Phys Earth 46(6):524–528
Muto A, Scambos TA, Steffen K, Slater AG, Clow DG (2011) Recent surface temperature trends in the interior of East Antarctica from borehole firn temperature measurements and geophysical inverse methods. Geophys Res Lett 38:L15502. doi:10.1029/2011GL048086

Nitoiu D, Beltrami H (2005) Subsurface thermal effects of land use changes. J Geophys Res 110:F01005. doi:10.1029/2004JF000151
Oh J, Reischmann E, Rial JA (2014) Polar synchronization and the synchronized climatic history of Greenland and Antarctica. Quat Sci Rev 83:129–142
Ort MH, Elson MD, Anderson KS, Duffield WA, Samples TL (2008) Variable effects of cinder-cone eruptions on prehistoric agrarian human populations. J Volcanol Geoth Res 176:363–376
Pimenov VP, Popov YA, Klimanov VA (1996) Vertical variations of thermal flow and paleoclimate. Isv Russ Acad Sci Phys Earth 6:84–92
Pollack HN, Huang S (2000) Climate reconstruction from subsurface temperatures. Ann Rev Earth Planet Sci 28:339–365
Pollack HN, Shauopeng H, Shen P-Y (2000) Climate change record in subsurface temperatures: a global perspective. Science 282:279–281
Powell WG, Chapman DS, Balling N, Beck AE (1988) Continental heat-flow density. In: Hänel R, Rybach L, Stegena L (eds) Handbook of terrestrial heat-flow density determination. Kluwer Academy Publication, Dordrecht, Boston, London, pp 167–222
Rath V, Mottaghy D (2007) Smooth inversion for ground surface temperature histories: estimating the optimum regularization parameter by generalized cross-validation. Geophys J Int 171:1440–1448
Roy S, Chapman DS (2012) Borehole temperatures and climate change: ground temperature change in south India over the past two centuries. J Geophys Res D Atmos 117(11):D11105
Safanda J (1994) Effects of topography and climatic changes on the temperature in borehole GFU-1, Prague. Tectonophysics 239:187–197
Safanda J (1999) Ground surface temperature as a function of slope angle and slope orientation and its effect on the subsurface temperature field. Tectonophysics 306(3–4):367–376
Safanda J, Rajver D, Correia A, Dedecek P (2007) Repeated temperature logs from Czech, Slovenian and Portuguese borehole climate observatories. Climate Past 3:453–462
Schmidt BE (1997) On a nonlinear eigenvalue problem arising from climate modeling. Nonlinear Anal 30(6):3645–3656
Sergin VY (1979) Numerical modeling of the glaciers-ocean-atmosphere global system. J Geophys Res 78(C6):3191–3204
Shen PY, Beck AE (1992) Paleoclimate change and heat flow density inferred from temperature data in the Superior Province of the Canadian shield. Palaeogeogr Palaeoclimatol Palaeoecol (Glob Planet Change Sect) 98:143–165
Shen PY, Wang K, Beltrami H, Mareschal J-C (1992) A comparative study of inverse methods for estimating climatic history from borehole temperature data. Glob Planet Change 98:113–127
Shen PY, Pollack HN, Huang S, Wang K (1995) Effects of subsurface heterogeneity on the inference of climate change from borehole temperature data: model studies and field examples from Canada. J Geophys Res 100:6383–6396
Taniguchi M (2006) Anthropogenic effects on subsurface temperature in Bangkok. Climate Past Discuss 2:832–846
Taylor AE, Burgess M, Judge AS, Allen VS (1982) Canadian geothermal data collection—Northern Wells 1981. Geothermal series, vol 13. Earth Physics Branch, Energy, Mines and Resources, Ottawa
Timko DJ, Fertl WH (1972) How downhole temperatures and pressures affect drilling. World Oil 175:73–78
Tsytovich NA (1975) The mechanics of frozen ground. Scripta Book Company, Washington, pp 8–250
Vernadsky VI (1945) The biosphere and the noosphere. Sci Am 33(1):1–12
Wang K (1992) Estimation of ground surface temperatures from borehole temperature data. J Geophys Res 97:2095–2106
Wang G, Schimel D (2003) Climate change, climatemodes, and climate impacts. Annu Rev Environ Resour 28:1–28
Weart S (2003) The discovery of rapid climate change. Phys Today 8:30–36

Chapter 12
Influence of Temperature Changes to Other Fields

12.1 Correlations Between Temperature and Other Physical Parameters

Identifying the mutual interrelations between different physical parameters of geological associations is highly important for correctly carrying out an integrated geophysical analysis, making the necessary corrections to observed physical values, the recognition of many geodynamic processes and solving various other problems. Since temperature is one of the fundamental physical properties, it is crucial to establish some correlations between temperature and other geophysical fields.

Obviously, studying the temperature changes in other physical parameters must begin by studying the combined physical properties of different targets and host media. Table 12.1 lists data on thermal conductivity, electric resistivity, polarizability, magnetic susceptibility, density and compressional velocity of some typical rocks, minerals and environmental features.

Note that the effects of temperature and pressure on thermal properties of rocks and minerals as well as fluid density are considered in detail in Sects. 2.6 and 2.7.

12.1.1 Correlations Between Various Geothermal Parameters and Environments

Numerous relationships and correlations have been computed between different thermal parameters. For instance, the dependence of the thermal conductivity of ice on temperature is shown in Fig. 12.1.

A variation of the thermal conductivity of salt on temperature is shown in Fig. 2.2. The relationship between conductivity λ and temperature T (K) for different rocks is shown in Fig. 12.2 (Yerofeyev et al. 2009). It shows three groups of rocks: (1) λ and T have a direct correlation (2) λ and T have an inverse correlation (3) λ practically does not depend on T. However, it should be noted that this

L. Eppelbaum et al., *Applied Geothermics*, Lecture Notes in Earth System Sciences,
DOI: 10.1007/978-3-642-34023-9_12,

Table 12.1 Physical properties of rocks, minerals and some environmental features (on the basis of Parasnis 1997; Kobranova 1986; Yerofeyev et al. 2009; Eppelbaum and Khesin 2012)

Type of matter	Thermal conductivity, W/(m °C)	Electric resistivity, Ohm m	Polarizability, %	Magnetic susceptibility, SI unit	Density, g/cm^3	Compressional velocity, km/s
Granite	1.9–3.2	5×10^3–10^6	0.5–2.5	(10–65) (without magnetite) 25–5 $\times$ 10^4 (with magnetite)	2.5–2.7	4.6–7.0
Basalt	1.5–2.2	10^3–10^8	0.2–3.8	1.5×10^3–2.5×10^4	2.7–3.3	2.5–6.4
Dunite	3.7–5.2	10^6–10^7	0.3–1.9	10–300	2.5–3.30	7.45–8.1
Gabbro	2.0–2.3	10^3–10^8	0.5–1.8	3.8×10^3–9×10^4	2.7–3.5	6.0–7.4
Diabase (dykes)	2.1–2.3	1,200–2,500	0.8–4.0	$(1.25–5) \times 10^3$	2.5 – 3.2	6.3–6.75
Gneiss	1.9–3.7	10^3–10^6	0.8–1.1	$0–3 \times 10^3$	2.6–2.9	5.2–6.3
Serpentinite	2.0–3.8	10^2–10^4	0.3–1	$(3–75) \times 10^3$	2.2–2.9	6.5–6.9
Shale	~7 (parallel) ~1 (perpend.)	1–10^4	0.3–2.0	10–50	2.3–2.75	3.1–3.8
Sandstone	2.5–3.2	$35–4 \times 10^3$	0.25–2.0	$25–5 \times 10^3$	1.8–2.7	1.5–4.0
Limestone (compact)	2.0–3.0	$120–4 \times 10^3$	1.3	$25–3 \times 10^3$	2.6–2.7	3.5–6.5
Sand	0.3–2.95	$1–1 \times 10^6$	0.1–1.0	$25–5 \times 10^3$	1.3–2.0	0.3–1.5
Clay	0.25–1.08	1–120	0.1–1.7	$25–1 \times 10^3$	1.2–2.4	1.2–2.5
Gypsum	0.5–1.5	10^5–10^6	Very low	−12.6	2.1–2.5	3.4–4.6
Rock salt	5.3–7.2	10^6–10^7	Very low	−10	2.1–2.4	4.0–5.5
Iron	18–20	1×10^8	18–20	1×10^6–1×10^7	7.8	4.6–5.9
Sulphide ore	5–6	1×10^{-4}–1×10^{-3}	12–60	10–40	3.3–3.7	6.0–6.4
Pyrrhotite	3.5	1×10^{-5}–1×10^{-3}	20–60	1×10^{-3}–1×10^{-1}	4.6	5.0
Chalcopyrite	10.7	1×10^{-4}–1×10^{-1}	10–25	10–30	4.2	4.85
Pyrite	9.5–15	1×10^{-4}–1×10^{-1}	50–90	35–60 (pure)	5.0	7.9–8.0
Magnetite (ore)	5.2	1×10^{-2}–1×10^1	10–40	7×10^4–14×10^6	5.2	7.0–7.4
Galena	2.0	1×10^{-2}–3×10^2	10–30	−4.3	7.5	3.7–3.77

(continued)

Table 12.1 (continued)

Type of matter	Thermal conductivity, W/(m °C)	Electric resistivity, Ohm m	Polarizability, %	Magnetic susceptibility, SI unit	Density, g/cm^3	Compressional velocity, km/s
Sphalerite	26.7	$>1 \times 10^4$	12–50	−3.3	4.0	5.3–5.6
Gold	318	2.4×10^{-8}	close to 0	−2.5	19.3	3.2
Graphite	1.15–17	1×10^{-4}–1×10^{-2}	30–90	−100 (diamagnetic)	2.2	4.1
Water	0.50 (25 °C)	0.1–1×10^5	Close to 0	~0	1.0	1.43–1.59
Oil	0.11–0.16	1×10^9–1×10^{14}	Close to 0	−10	0.9	1.15–1.3
Coal	0.13–2.2	1×10^2–1×10^4	3–15	10−20–1×10^4 (fired)	1.2–1.5	2.4–2.7
Air	0.023 (0°C)	1×10^{14}	0	~0	0.0012	0.33
Ice	2.2 (0 °C)	1×10^4–1×10^8	0.5–20	−9 (0°C)	0.92	3.0–4.0
Pine wood	0.4–1.2	0.8–2.5	low	≈0	0.5–0.8	1.4–1.7

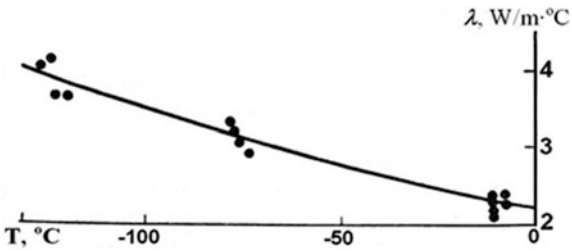

Fig. 12.1 Dependence of the thermal conductivity of ice on temperature (after Ivanov and Gavrilyev 1965)

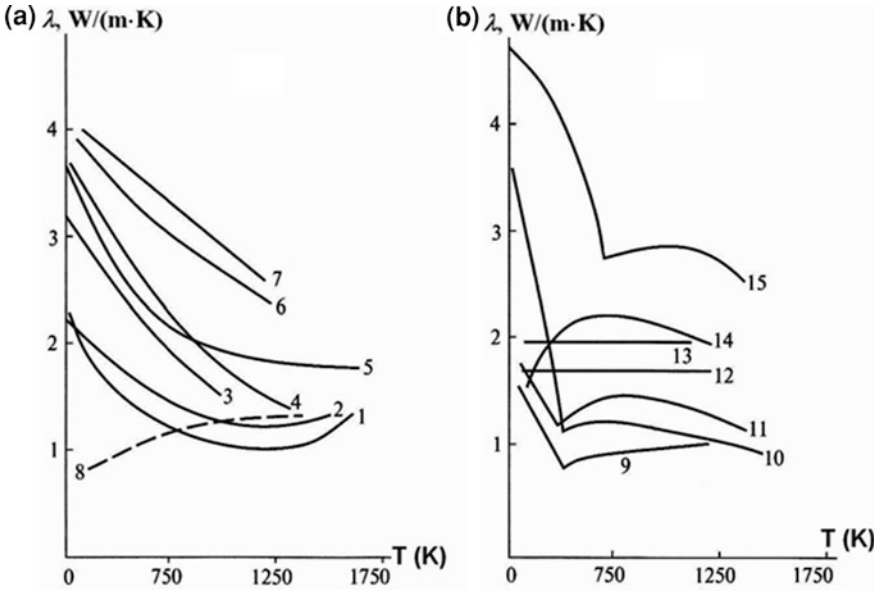

Fig. 12.2 Dependence of thermal conductivity of rocks on temperature [after Dortman (1976) and Yerofeyev et al. (2009)]. (*1*) leucocratic granite (*2*) diorite (*3*) limestone (organogenic) (*4*) harburgite (*5*) olivine (*6*) porhyrite (*7*) pumice tuff (*8*) obsidian (*9*) eclogite (*10*) dolerite (*11*) pyroxene gabbro (*12*) hornblende augite porphyrite (*13*) hornblende pyroxene porphyrite (*14*) diabase porphyrite (*15*) lherzolite

process is accompanied by others (dispersion of phonons of crystallic grains and defects in crystallic structure) which sometimes significantly complicate joint behavior. The first group of rocks is represented in Fig. 12.2a, for instance, by porhyrite and pumice tuff. Obsidian is a light representative of the second group (Fig. 12.2a). Finally, the third group is represented by hornblende augite porphyrite and hornblende pyroxene porphyrite in Fig. 12.2b.

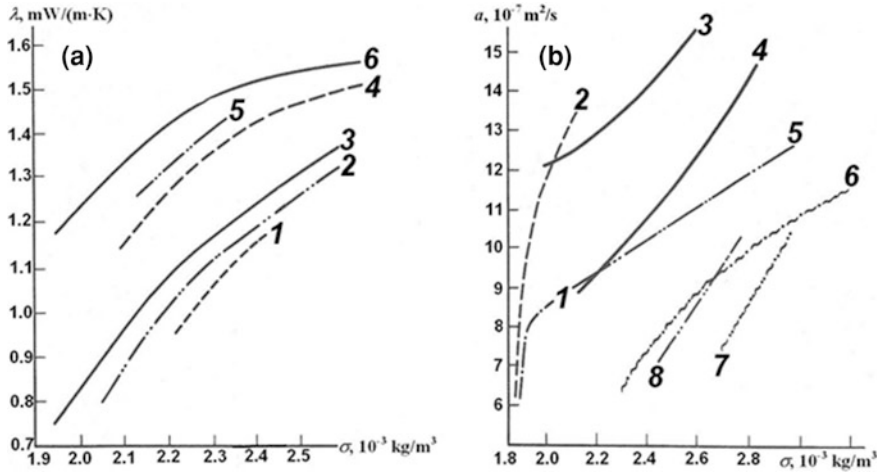

Fig. 12.3 **a** Relationship between thermal conductivity and density. (*1*) dry siltstone (*2*) dry argillite (*3*) dry sandstone (*4*) water-saturated siltstone (*5*) water-saturated argillite (*6*) water-saturated sandstone. **b** Relationship between thermal diffusivity and density. (*1*) (*3*) and (*4*) sandstone (*2*) water-saturated sandstone (*5*) and (*8*) limestone (*6*) siltstone (*7*) dolomite. (**a** and **b** after Babaev et al. 1987, with modifications)

12.1.2 Thermal and Density Properties

The relationship between different thermal factors and density properties is well known (i.e., Birch et al. 1942; Kutasov 1999; Aleinikov et al. 2001). An effective example of the inverse correlation between gravity and temperature observed over salt domes was described in Poley and Steveninck (1970). Figure 4.4 depicts the inverse correlation between the heat flow and Bouguer gravity over several mud volcanoes in Central Azerbaijan.

The thermal conductivity of rocks usually increases with increases in density and is especially characteristic of sedimentary rocks (Fig. 12.3a). An analysis of 330 samples (igneous, metamorphic and sedimentary rocks) found the following relationship between the logarithm of sedimentary rock thermal conductivity and density (Babaev et al. 1987):

$$\lg \lambda_{(T=293\mathrm{K})} = 0.36\sigma - 0.20, \tag{12.1.1}$$

with a correlation coefficient of 0.74.

The dependence between thermal diffusivity and density for some rocks is shown in Fig. 12.3b.

Reliable correlations were found between specific thermal capacity and density (Fig. 12.4).

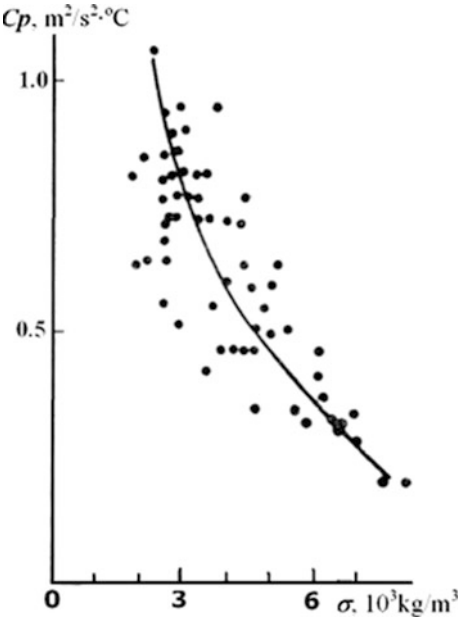

Fig. 12.4 Relationship between specific thermal capacity and density (after Rzhevsky and Novik 1964)

Vosteen and Schellschmidt (2003) presented the following equation showing the influence of temperature on thermal conductivity and thermal diffusivity of different Eastern Alpine rocks:

$$\lambda(T) = \frac{\lambda(0)}{0.99 + T\left(\frac{a-b}{\lambda(0)}\right)}, \tag{12.1.2}$$

$$\alpha = 0.45\lambda, \tag{12.1.3}$$

where λ is the thermal conductivity, $\lambda(0)$ is the thermal conductivity at 0 °C, α is the thermal diffusivity, T is the temperature, and a and b are coefficients ($a = 0.0030 \pm 0.0015$, $b = 0.0042 \pm 0.0006$ for crystalline rocks, and $a = 0.0034 \pm 0.0006$, $b = 0.0039 \pm 0.0014$ for sedimentary rocks).

Finally, temperature is known to have a significant influence on gravimeter data recording (e.g., Clewell 1942).

12.1.3 Temperature and Electric Properties

Laboratory measurements in high *P*-*T* conditions have shown a certain number of correlations between temperature and resistivity (Olhoeft 1982; Parkhomenko 1982). The relationship between water-saturated sandstone and temperatures up to

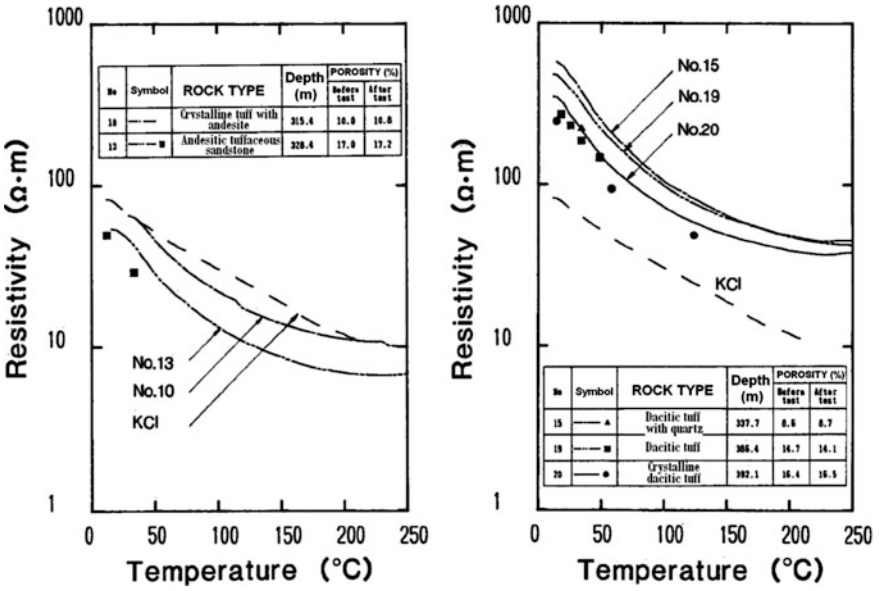

Fig. 12.5 Temperature dependence of the resistivity of some water saturated rocks (after Llera et al. 1990)

190 °C was studied in Dailey and Lin (1985). Llera et al. (1990) reported a reliable correlation between the temperature and resistivity of different kinds of water-saturated rock (dacitic tuff, sandstone, limestone, crystalline tuff, granite and andesite) and temperatures up to 250 °C. One example of this investigation is shown in Fig. 12.5.

Popov et al. (2003) carried out petrophysical investigations on more than 400 cores from the scientific well "Nördlingen 1973" (1,206 m in depth) drilled in the Ries impact structure (Germany) of lake sediments, suevite impact breccia, suevite intercalating with crystalline rocks, amphibolites, gneisses, granites, ultramafic rocks, and breccia dikes (Fig. 12.6). It was found that the regression line corresponds to all rocks excluding ultrabasites and high temperature suevites.

Shanov et al. (2000) correctly pointed out that in all cases, the change in the electrical conductivity of rocks with changes in the temperature can be analyzed as a function of the mineral composition, the structure and the quantity of highly electrically conductive minerals such as magnetite. Figure 12.7 illustrates this increasing electrical conductivity with increasing temperature. The jumps on the electrical conductivity curves can be explained by phase transitions of minerals in the rocks. Thus, the abrupt decrease in the electrical conductivity between 180–210 °C and 330–340 °C can be related to the transition at this temperature of magnetite.

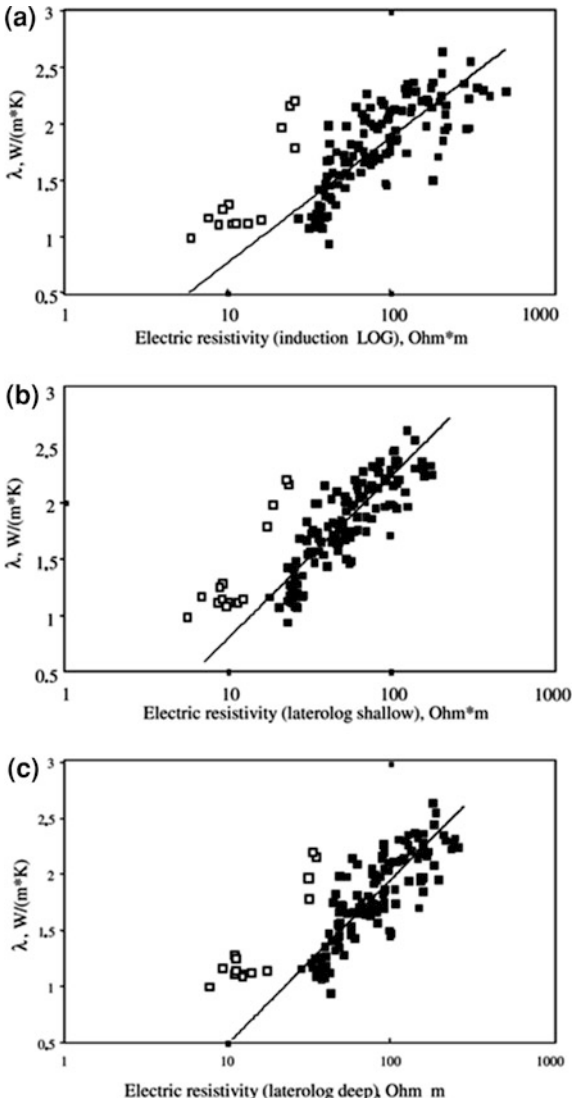

Fig. 12.6 Regressed correlations between the thermal conductivity of dry rocks and electric resistivity determined from the induction log (**a**) the laterlog shallow (**b**) and the laterolog deep (**c**). *Empty squares*—ultrabasites and high temperature suevites, *solid squares*—all other rocks (after Popov et al. 2003 with minor modifications)

12.1.4 Temperature and Seismic Velocities

Laboratory measurements of temperature-dependent seismic velocities of rocks at high pressures (up to 6,000 bars in 500 bar intervals) and temperatures (up to 1,000 °C at 100 °C intervals) were conducted by Kern (1978), Kern and Siegesmund (1989), Kern et al. (2001), Punturo et al. (2005), and Scheu et al. (2006).

The temperature dependence of seismic properties of geothermal rocks in reservoir conditions was investigated in Jaya et al. (2010). Figure 12.8 shows the

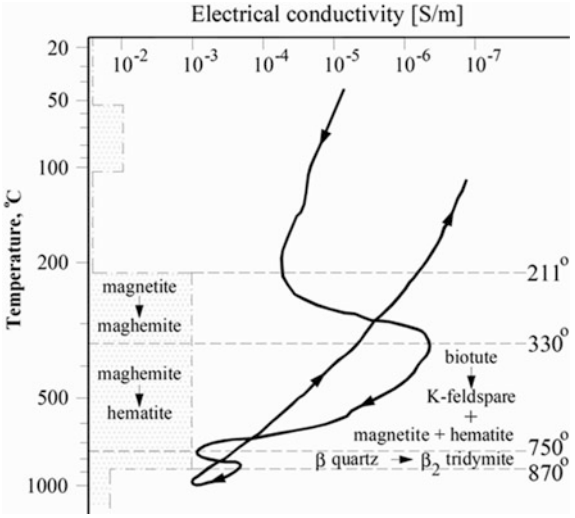

Fig. 12.7 Electrical conductivity curve versus temperature for Boshulia granite (Bulgaria) with possible mineral transitions. The grey area corresponds to the crustal conductivity model, according to the magnetotelluric sounding (after Shanov et al. 2000)

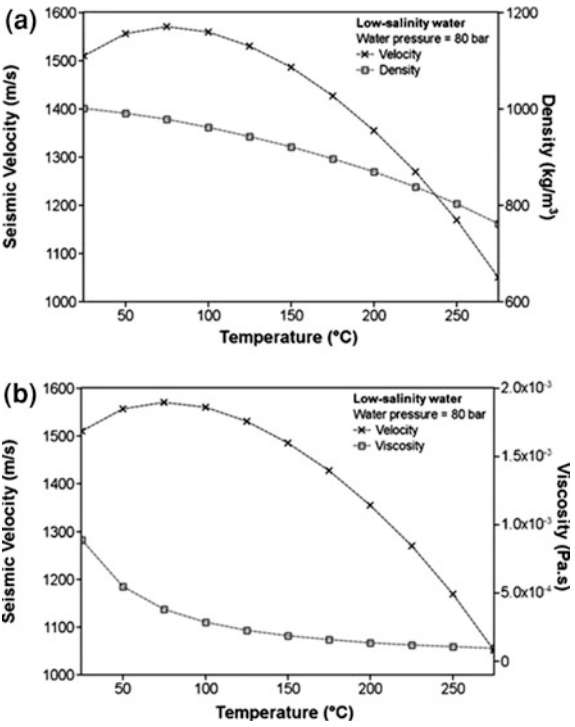

Fig. 12.8 **a** Seismic velocity and density of low-salinity water as a function of temperature at 80 bars fluid pressure. **b** Seismic velocity and viscosity of low-salinity water as a function of temperature at 80 bars fluid pressure (after Jaya et al. 2010)

relationship between temperature and compressional seismic velocities at comparatively low temperature and pressure. This figure indicates that the density, viscosity and P-wave velocity of water each vary in a seemingly unrelated manner with respect to temperature, at a constant pore fluid pressure.

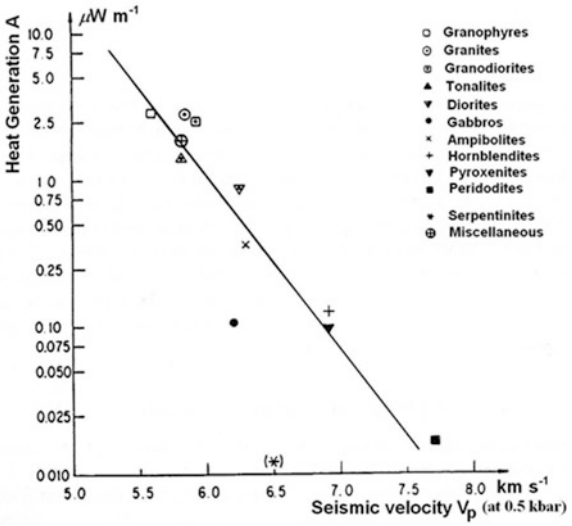

Fig. 12.9 Relationship between heat production A and seismic velocity: $\ln A = 16.5 - 2.74\ V_p$ (after Rybach 1988)

Some peculiarities of the correlations between the seismic velocity and heat production are considered in Sect. 1.7.1. Figure 12.9 illustrates the relationship between the heat production rate A and compressional seismic velocity v_p. This relationship derives from laboratory experiments at 50 MPa pressure (Rybach 1988).

The measured dependence of *P*- and *S*-waves in the Cold Lake area (Alberta, Canada) oil sands on temperature was compared to theoretical model predictions for seismic wave propagation in porous media. These experiments indicated that changes in fluid properties with temperature primarily affect the observed velocities (Eastwood 1993).

12.1.5 Temperature and Magnetic Properties

No significant relationship between temperature and magnetic properties has been found except for the well-known Curie point effect. This phenomenon is described in detail in Sect. 6.7. Features common to temperature and magnetic anomalies of several classes of objects are discussed in Sect. 7.5.

12.1.6 Temperature and Electromagnetic Properties

Spichak and Zakharova (2012) suggested that the subsurface temperature can be detected by an indirect electromagnetic (EM) geothermometer. This approach is based on an artificial neural network technique, which, unlike other available approaches, does not require prior knowledge of electrical conductivity

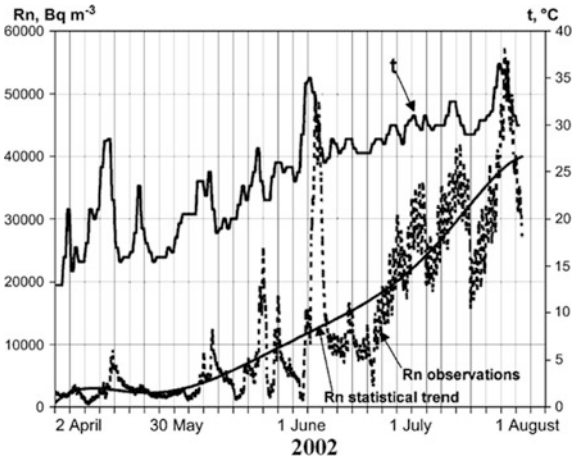

Fig. 12.10 Influence of temperature on radon (Rn) variations; observations in a deep tunnel in Eilat (southern Israel) (after Finkelstein et al. 2006)

mechanisms or rock properties. The relative accuracy of the temperature extrapolation to depths twice as deep as the borehole depth did not exceed 5 % on average (Spichak and Zakharova 2012). Using an indirect EM geothermometer, it was possible to reconstruct 2D and 3D temperature models of the areas from EM sounding data, which, in turn, served to draw important conclusions regarding dominant heat transfer mechanisms, fluid circulation paths, and better locations for drilling new boreholes. The temperature dependence of electrical conductivity can thus provide additional information that is especially useful in active crustal areas (Spichak and Manzella 2009).

12.1.7 Temperature and Radon Anomalies

The influence of temperature changes on radon anomalies observed in subsurface and deep tunnels was investigated in detail in Finkelstein et al. (1998, 2006). A reliable connection between temporary variations in radon observed in shallow wells and caves (several meters deep) and surface seasonal temperature variations was discussed in Finkelstein et al. (1998).

However, radon observations in comparatively deep tunnels are also subject to thermal influence (Fig. 12.10). The outward alternating heat flow can create surface dynamic lag effects with the alternating coefficient of viscosity in porous space. Periods of surface temperature fluctuations determine the periods of anomalous values of ventilation indices and, respectively, the variations in radon concentration (Finkelstein et al. 2006).

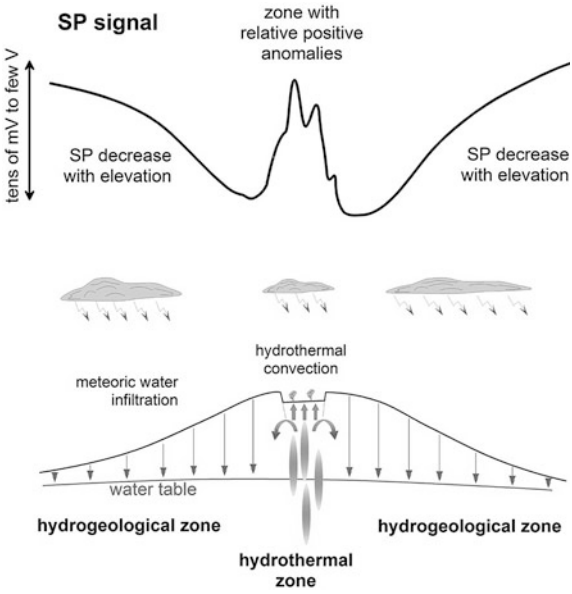

Fig. 12.11 Conceptual model of SP patterns on a volcano (after Lénat 2007)

12.1.8 Temperature and Induced Polarization

Bücker (2011) developed a methodology to predict spectral induced polarizations (SIP) at various temperatures. Bairlein et al. (2013) found that the SIP relationship with temperature exists both at the subsurface (within the heliothermozone) and at greater depths where temperature values increase due to the geothermal gradient. Bairlein et al. (2013) analyzed the temperature dependence by calculating the polarization parameters with an extended membrane polarization model, and by measuring the SIP-response of a limestone sample at a temperature range of 0 °C–60 °C. Both modeling and measurements indicated a complex electrical conductivity dependence on temperature. The small changes in this correlation were found to depend on the pore geometry of limestone.

12.1.9 Temperature and the Self-Potential Field

It is known that the groundwater flow is responsible for both thermal and self-potential anomalies (SP). It makes possible, for instance, the joint inversion of temperature and self-potential data (Jardani and Revil 2009). In field conditions SP anomalies usually depend on the temperature gradient (Semenov 1974; Revil and Jardani 2013).

SP anomalies are correlated with geothermal activity in many areas of the world. These anomalies often are associated with faults in which thermal fluids

propagate, or with areas of high heat flow (Corwin and Hoover 1979). Figure 12.11 presents a typical example of SP anomaly behavior over a model of a volcano. As can be seen from this figure, on the topographic slopes with meteoric water infiltration, there is an inverse correlation between SP and topography. This indicates (see also Sect. 10.3) that there is a direct correlation between the SP signal and temperature (both observed on the Earth's surface). It is obvious that this direct correlation exists and is over the hydrothermal zone.

The problems of the Dead Sea liquid stratification in conditions of extremely arid climate and water production in conditions of high humidity are considered in Appendices A and B, respectively.

References

Aleinikov AL, Belikov VT, Eppelbaum LV (2001) Some physical foundations of geodynamics. Kedem Printing-House, Tel Aviv in Russian, contents and summary in English

Babaev VV, Budymka VF, Sergeyeva TA, Dombrovsky MA (1987) Thermophysical properties of rocks. Nedra, Moscow

Bairlein K, Bücker M, Hördt A, Nordsiek S et al. (2013) Experimental and theoretical studies of the temperature dependence of spectral induced polarization (SIP). Trans Near Surf Geosci 19th European Meet Environ Eng Geophys, Bochum, Germany, p 12, 1–5

Birch F, Schairer JF Spicer HC (eds) (1942) Handbook of physical constants. Geol Soc Am, Special papers, 36:94–101

Bücker M (2011) Die membranpolarisation als ursache des IP-effekts in porösen medien. Master thesis, TU Braunschweig

Clewell DH (1942) Problems in temperature control of gravimeters. Geophysics 7(2):155–168

Corwin RF, Hoover DB (1979) The self-potential method in geothermal exploration. Geophysics 44:226–245

Dailey WD, Lin W (1985) Laboratory-determined transport properties of Berea sandstone. Geophysics 50:775–784

Dortman NB (ed) (1976) Physical properties of rocks and minerals (petrophysics): handbook of geophysicist. Nedra, Moscow in Russian

Eastwood J (1993) Temperature-dependent propagation of P-and S-waves in Cold Lake oil sands: Comparison of theory and experiment. Geophysics 58(6):863–872

Eppelbaum LV, Khesin BE (2012) Geophysical studies in the Caucasus. Springer, Berlin

Finkelstein M, Brenner S, Eppelbaum L, Ne'Eman E (1998) Identification of anomalous radon concentration due to geodynamic processes by elimination of *Rn* variations caused by other factors. Geophys J Int 133(2):407–412

Finkelstein M, Eppelbaum L, Price C (2006) Analysis of temperature influences on the amplitude-frequency of Rn gas concentration. J Environ Radioact 86(2):251–270

Ivanov NS, Gavrilyev RI (1965) Thermal physical properties of the frozen rocks. Nauka, Moscow in Russian

Jardani A, Revil A (2009) Stochastic joint inversion of temperature and self-potential data. Geophys J Int 179:640–654

Jaya MS, Shapiro SA, Kristinsdyttir LH, Bruhn D, Milsch H, Spangenberg E (2010) Temperature dependence of seismic properties in geothermal rocks at reservoir conditions. Geothermics 39:115–123

Kern H (1978) The effect of high temperature and high confining pressure on compressional wave velocities in quartz-bearing and quartz-free igneous and metamorphic rocks. Tectonophysics 44:185–203

Kern H, Siegesmund S (1989) A test of the relationship between seismic velocity and heat production for crustal rocks. Earth Plan Sci Lett 92(1):89–94

Kern H, Popp T, Gorbatsevich F, Zharikov A, Lobanov KV, Smirnov YP (2001) Pressure and temperature dependence v_P and v_S in rocks from the superdeep well and from the surface analogues at Kola and the nature of velocity anisotropy. Tectonophysics 338:113–134

Kobranova VN (1986) Petrophysics. Nedra, Moscow (in Russian)

Kutasov IM (1999) Applied geothermics for petroleum engineers. Elsevier, Amsterdam

Lénat J-F (2007) Retrieving self-potential anomalies in a complex volcanic environment: an SP/elevation gradient approach. Near Surf Geophys 5:161–170

Lera FJ, Sato M, Nakatsuka K, Yokoyama H (1990) Temperature dependence of the electrical resistivity of water-saturated rocks. Geophysics 55(5):576–585

Olhoeft GR (1982) Electrical properties of granite with implications for the lower crust. J Geophys Res 86:931–936

Parasnis DS (1997) Principles of applied geophysics, 5th edn. Chapman & Hall, London revised and supplemented

Parkhomenko GR (1982) Electrical resistivity of minerals and rocks at high temperature and pressure. Rev Geophys Space Phys 10:193–218

Poley JP, Steveninck JV (1970) Delineation of shallow salt domes and surface faults by temperature measurements at a depth of approximately 2 meters. Geophys Prospect 18:666–700

Popov Y, Tertychnyi V, Romushkevich R, Korobkov D, Pohl J (2003) Interrelations between thermal conductivity and other physical properties of rocks: experimental data. Pure Appl Geophys 160:1137–1161

Punturo R, Kern H, Cirrincione R, Mazzoleni P, Pezzino A (2005) P-and S-wave velocities and densities in silicate and calcite rocks from the Peloritani Mountains Sicily (Italy): the effect of pressure, temperature and the direction of wave propagation. Tectonophysics 409:55–72

Revil A, Jardani A (2013) The self-potential method: theory and applications in environmental geophysics. Camridge University Press, Cambridge

Rybach L (1988) Determination of heat production rate. Hänel R, Rybach L, Stegena L, Handbook of Terrestrial Heat-Flow Density Determination. Kluwer Academic Publishers, Dordrecht, pp 125–142

Rzhevsky VV, Novik GY (1964) Principles of physics of rocks. Mir, Moscow in Russian

Scheu B, Kern H, Spieler O, Dingwell DB (2006) Temperature dependence of elastic P-and S-wave velocities in porous Mt. Unzen dacite. J Volcanol Geoth Res 153:136–147

Semenov AS (1974) Electric prospecting by self-potential method, 3rd edn. Nedra, Leningrad revised and supplemented

Shanov S, Yanev Y, Lastovickova M (2000) Temperature dependence of the electrical conductivity of granite and quartz-monzonite from south Bulgaria: geodynamic inferences. J Balkan Geophys Soc 3(2):13–19

Spichak VV, Manzella A (2009) Electromagnetic sounding of geothermal zones. J Appl Geophys 68:459–478

Spichak V, Zakharova O (2012) Electromagnetic sounding of geothermal zones. Geophysics 77(4):WB179–WB190

Vosteen H-D, Schellschmidt R (2003) Influence of temperature on thermal conductivity, thermal capacity and thermal diffusivity for different types of rock. Phys Chem Earth 28:499–509

Yerofeyev LYa, Vakhromeyev GS, Zinchenko VS, Nomokonova GG (2009) Physics of Rocks. Tomsk Polytechnical University, Tomsk (in Russian)

Chapter 13
Integration of Thermal Observations with Other Geophysical Methods

13.1 Theoretical Preferences for Integration

Integrated interpretation errors mainly depend on the type of applied algorithm (Eppelbaum and Khesin 2012). For example, in the "linear solving function" algorithm (Fotiadi 1970) that uses unequal covariance matrices, the classification error depends on the value of d. The latter is an analog of the generalized distance between the compared images for identical covariance matrices. The probability of correct classification P is given by

$$P = \aleph(d),$$

where $\aleph(d)$ is a normal distribution function.

Theoretical errors in determining parameters on the basis of regression equations are characterized by argument variability and measurement errors (Akselrod and Putkaradze 1979). Theoretical errors can be estimated by analogy to integrated interpretation, if we test the hypothesis that a parameter can be classified in a certain class (or a group of similar values) of parameters. Integrated interpretation errors are the most damaging (Khesin et al. 1996) and can introduce highly incorrect data as regards the targets.

The high complexity of expert systems led to the development of a special approach known as fuzzy logic for the analysis of similar systems. Zadeh (1983), who revolutionized statistical methods by introducing the fuzzy logic approach to the analysis of complex systems, divided all systems into two types: technical ("type 1") which involves the implementation of equations, and expert ("type 2") where experience, knowledge and man-made solutions dominate. These systems do not only assume the usual quantitative variables, but also integrate qualitative, so-called linguistic variables, which may be words and expressions in natural or artificial languages. Geological–geophysical investigations are typical examples of an applied field where the greater part of most solutions depends on expert opinion.

All forms of geological–geophysical investigations take place in a definite sequence in time and space. In investigations, different geological methods are

L. Eppelbaum et al., *Applied Geothermics*, Lecture Notes in Earth System Sciences,
DOI: 10.1007/978-3-642-34023-9_13, © Springer-Verlag Berlin Heidelberg 2014

employed (geophysical investigations, geological mapping, geochemical analyses, mining works, drilling, etc.). The ultimate goal of a geological–geophysical examination is to find the most accurate identification of targets in a given area within given limitations (Eppelbaum and Khesin 2012).

In real conditions many random factors affect the results obtained by a set of geophysical tools (means). One of the essential problems is that it is impossible to obtain a satisfactory formalized description of factors influencing the results of local determinations. Similar situations are known to exist in decision making theory where a full mathematical formalization of a problem is complex. However using expert methods in many situations (a set of logical and math-statistical procedures) can contribute to greater effectiveness.

For purposes of illustration, take the reliability of geophysical prospecting at the level of local determination and the reliability of information obtained by separate means or a set of means. The main aim of such a study is a problem of determination of the set of means making up the notion of "geophysical prospecting" (relative to some fixed feature) by the assumed reliability of the means (in contrast to Khesin and Eppelbaum (1997), where mainly statistical criteria were analyzed). Solving this problem will yield the most optimal combinations of geological means for different physical–geological conditions. Assessment the reliability of individual means can be obtained through control observations or on the basis of expert methods (Eppelbaum et al. 2003).

13.2 Types of Integration Methodologies

There are different approaches to integrated interpretation, including those using traditional visual comparison of fields, and quantitative expression of the specificities of fields and media. The benefits of integrated interpretation become clearer when moving from qualitative integration to quantitative integration.

Quantitative integrated interpretation usually involves a quantitative estimation of parameters by a set of data. This concept appears to be more general; it primarily includes defining the type of target (quality) by a set of data employing quantitative criteria. There are different types of quantitative criteria used to evaluate the nature of the objects (Khesin et al. 1996; Borovko 1979).

Integrated interpretation can be deterministic, probabilistic and mixed (probabilistic–deterministic). The latter actually includes elements of both types, as in the case of single-method interpretation. An interesting sophisticated description of the probabilistic–deterministic approach for a typical case was presented in Malyshev (1981). Integrated interpretation based on the deterministic approach can be successful provided the researcher is certain that the anomalies identified by different methods are from the same sources. In this case Poisson's law is applied between the magnetic and gravity fields (Teldord et al. 1990) and the linear programming technique (e.g., Bulakh et al. 1976).

The most universal tool for deterministic interpretation is to select a geophysical field to model the medium obtained from data from another geophysical method, and compare the selected field with the observed one. This sequential integrated interpretation can yield results which cannot be derived from a separate study of data obtained through different methods.

In a rough analogy with electric engineering, interpretation can take place in series or in parallel (Khesin et al. 1996). However, a series of interpretations in which each of the stages employs the results of the preceding ones actually interprets individual fields. Hence we will basically confine ourselves to the parallel interpretation, which involves simultaneous utilization of data obtained by different geophysical methods. Another promising approach to integrated analysis of different geophysical fields involves a combination of advanced wavelet methodologies (Eppelbaum et al. 2011).

Certain additional information can be derived from parallel integrated interpretation (these may be tentative values of vertical and horizontal thickness and the dip angles), if different approximations of a source body are admissible when interpreting anomalies caused by diverse fields. This model is then used in an iterative process for direct problem solution. Such a process of deterministic integrated interpretation is characterized by many special features and primarily utilizes potential geophysical fields.

Regression-correlation integrated interpretation (e.g., drawing up structural maps from the gravity data on the basis of the correlation between these data and the position of seismic boundaries) is frequently used to solve problems in petroleum geology. This approach to interpretation became popular following a series of publications (e.g., Shraibman et al. 1977; Karatayev and Pashkevich 1986). This kind of interpretation has features characteristic of probabilistic–deterministic interpretation. That is why the techniques based on computation of the correlation coefficient between the results obtained by different methods do not fall into this category if they have no data on the seismic boundary locations or other information obtained by the deterministic method. Rather, these techniques should be classified as information-statistical methods.

13.2.1 Conventional Integration

The development of numerous disjunctive dislocations impeding geophysical data interpretation is typical of these deposits.

In the fields predicted by a typical Physical–Geological Model (*PGM*) of a polymetallic deposit of the Filizchay type (Greater Caucasus, Azerbaijan) different depths of occurrence of the upper orebody edge h (Table 13.1) were computed using the *GSFC* program. For SP, VLF, IP and thermal prospecting methods, the calculation of these effects took into account the results of physical and mathematical modeling, and field investigations (Eppelbaum and Khesin 1988). The resulting physical–geological model substantiated the interpretation criteria and

Table 13.1 Geophysical effects for a *PGM* of the Filizchay type

h value, m	Anomaly					
	Gravity, mGal	Magnetic, nT	*SP*, mV	*VLF*, %	*IP*, %	Temperature, °C
20	1.0 ÷ 2.2	150 ÷ 200	−(120 ÷ 300)	25 ÷ 50	7 ÷ 15	0.7 ÷ 2.0
60	0.6 ÷ 1.2	50 ÷ 70	−(60 ÷ 100)	10 ÷ 15	5 ÷ 9	0.2 ÷ 0.7
100	0.2 ÷ 0.6	25 ÷ 30	−(20 ÷ 40)	2 ÷ 4	2 ÷ 7	0.05 ÷ 0.10

Table 13.2 Geophysical effects for the *PGM* of the Lesser-Caucasian type

h value, m	Anomaly					
	Gravity, mGal	Magnetic, nT	*SP*, mV	*VLF*, %	*IP*, %	Temperature, °C
20	0.3 ÷ 0.5	−(70 ÷ 100)	−(20 ÷ 50)	15 ÷ 30	4 ÷ 12	0.5 ÷ 1.2
60	0.08 ÷ 0.15	−(20 ÷ 30)	−(15 ÷ 30)	5 ÷ 10	3 ÷ 6	0.1 ÷ 0.3
100	0.05 ÷ 0.08	−(5 ÷ 10)	−(5 ÷ 10)	1 ÷ 3	1 ÷ 4	0.03 ÷ 0.05

optimal geophysical sets for prospecting and estimates. For deposits of the Filizchay type this set comprised gravimetric and magnetic prospecting and the SP method. The IP method can also be a significant tool. If ore objects differ only slightly in terms of their magnetic properties from the host sandy-shale deposits, it is worth using the VLF technique in the set instead of magnetic prospecting. Near-surface thermal prospecting has also been employed as effective interpretation tool (Eppelbaum and Khesin 1988).

When comparing the two forms of *PGM* presentation, it should be noted that graphic *PGM* models (which are primarily quantitative) are easier to grasp. However, whereas the development of quantitative graphical *PGM* using computer-aided gravity and magnetic field computations presents no technical problems, quantitative computation of the temperature and self-potential fields using the same *PGM*, as well as fields from distant *VLF* transmitters leads to many mathematical and computational difficulties. This is why the combined application of these two approaches supplementing each other seems more promising.

A combination of gravity and magnetic prospecting, the VLF method and near-surface thermal prospecting has proved to be efficient for determining deposits of the Lesser-Caucasian type (Eppelbaum and Khesin 2012) (Table 13.2).

13.2.2 Integration on the Basis of Information Theory

It is well known that most inverse problem solutions in geophysics are ill-posed (e.g., Zhdanov 2002). In other words, a solution does not exist, or is not unique, or is not a continuous function of observed geophysical data (when small perturbations in the observations cause random errors in the solution). This in particular

calls for wider application of informational and probabilistic methodologies in applied geophysics.

Geophysical observations in hydrocarbon geology are notoriously complicated by numerous factors (Khesin et al. 1996). To eliminate many of these disturbances, numerous interpretational methodologies have been developed. However, at times the complexity of the geological environment (variability in lateral and vertical physical properties), large depth of hydrocarbon target (HT) occurrence and additional disturbances makes it impossible or unfeasible to apply this methodology. In such cases information-probabilistic methods are effective tools to recognize and classify targets, estimate the potential information value of geophysical methods and decide upon a workable solution. The objective of geophysical surveys is to obtain qualitative and quantitative information about the geometric and physical characteristics of buried HT; e.g., to develop physical–geological models (*PGM*) of target objects. *PGM*s of varying degrees of complexity (the simplest *PGM*s are simply target identification and complex *PGM*s can be 3D models of buried HT) can be used to justify direct excavation in defined areas (or prohibit industrial activity) and generate future strategies for hydrocarbon searches in sites where ancient remains are known to exist.

Here we give a very short description of some of the key features of the informational approach to geophysical methods applied in hydrocarbon geophysics. It shown that simple informational and probabilistic criteria can be applied to formalize the relative value of geophysical methods, geophysical information, cost, and time factors to generate integrated parameters.

All available geophysical–geological information can be represented in a classic three-level model composed of: (a) a syntactic component—the amount of information; (b) a semantic component—the nature of the information, and (c) a pragmatic component—the value of the information (Eppelbaum et al. 2003). This model is based on the fundamental terms of information theory combined with a structural (hierarchical) approach. This approach defines each geological indicator as a structure that reflects a set of typical situations. Next, depth of search is estimated and calculated using the informational approach. This strategy provides a quantitative calculation and effective control of geophysical–geological studies.

Estimating the information value of geophysical and other means can be formalized on the basis of the following criteria (after Eppelbaum et al. 2003) (Fig. 13.1):

(1) Informativeness of the application (informational criterion Γ);
(2) Cost of implementing the method (cost criterion C);
(3) Time required to carry out the method (time criterion T).

A simplified algorithm can be written as:

$$\Omega = \Gamma \cup C \cup T, \tag{13.2.1}$$

where $\cup$ is the symbol of unification.

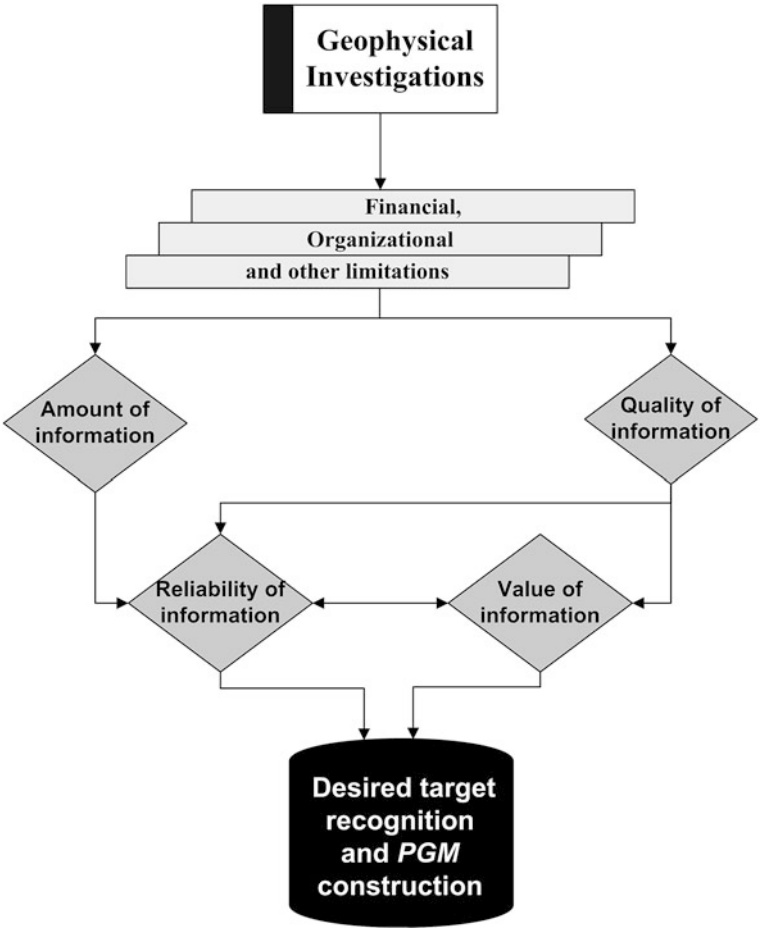

Fig. 13.1 A scheme of hydrocarbon target recognition and *PGM* construction with elements of information theory

Criteria C and T are easy to calculate directly, but criterion Γ is a non-trivial research problem.

All the available geological information can be represented as the classic three-level model (Fig. 13.1): (a) syntactic—quantity of information (b) semantic—content of information, and (c) pragmatic—value of information. The logical-heuristic model for describing geological–geophysical information thus takes the following form (Eppelbaum et al. 2003):

$$\Gamma = I \cup R \cup V, \tag{13.2.2}$$

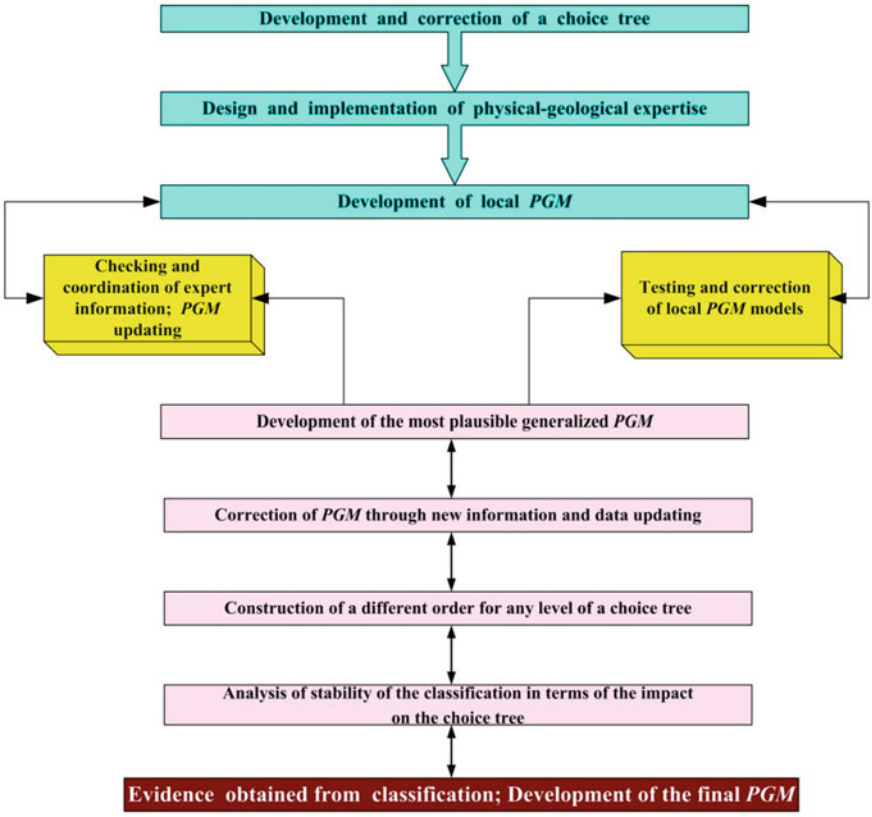

Fig. 13.2 Flow-chart of integrated geological–geophysical analysis using the comprehensive informational

where I is the quantitative estimate of information, R is the estimate of informational reliability corresponding to the semantic criterion, and V is the estimate of informational value in terms of feasibility according to the pragmatic criterion.

A variant (algorithm) of the possible analysis of geological information is presented in Fig. 13.2. Figure 13.2 is based on the fundamental terms of information theory and is combined with the structural (hierarchical) approach. This approach defines each indicator as a structure reflecting a set of typical situations and is then used to calculate the value of each estimator using the informational measure. Parameters V and R should be estimated geologically and geophysically, but this is beyond the scope of this book. Here parameters V and R will be neglected, and it is assumed that $\Gamma = I$.

13.2.2.1 Evaluating the Efficiency of Geophysical Methods with Informational-Statistical Procedures

Choosing the right method (or number of methods) can be based on a quantitative estimate (Figs. 13.1 and 13.2). For this purpose, reliable informational and statistical criteria are needed. The first issue is the quantity of information that can be obtained by a single method or a set of methods. The second is to define a criterion to express the decision-making risk as a function of the geophysical data. Nevertheless, informational criteria are preferable, because geophysical prospecting is a permanent process of acquisition and analysis of information.

The classic information theoretic works by Shannon (1948) and Brillouin (1962) prompted Khalfin (1958) to apply these criteria to geophysics. It has been shown (Khesin et al. 1996) that informational and statistical approaches represent two aspects of a shared approach. For instance, the solution to an identification problem using the criterion of minimal average risk or that of maximum information (minimal residual uncertainty) under certain conditions results in the same expressions (Nikitin 1993; Svetov 1992). An enhanced wavelet approach to integration of geophysical data under complex geological conditions was proposed by Eppelbaum et al. (2011).

This lays the groundwork for presenting some of the key elements of the theory of information and statistical-probabilistic approaches in hydrocarbon prospecting. Illustrating how these fairly straightforward methods can yield valuable results should highlight commonalities in HT localization and geophysical theory and hence optimize *PGM* development and successful HT discovery.

Let's assume that there is only one HT in the area. This area is divided into N equal cells. For simplicity each cell is assumed to have the same probability of containing the HT. Thus, the probability of finding the HT is equal to $P = 1/N$ in each cell. Hence, the entropy of experiment β (discovery of HT) is $\log_2 N$. The entropy is determined using following expression:

$$H(\beta) = -\sum_{i=1}^{N} P(B_i) \cdot \log_2 P(B_i), \tag{13.2.3}$$

where $P(B_i)$ is the probability of a B_i outcome (B is the range of outcomes of experiment β).

In this situation $H(\beta)$ value $(\log_2 N)$ is maximum possible uncertainty. Experiment α (geophysical observation) gives additional information. The A value is a range of outcomes for experiment α.

The difference between uncertainties in the β results before and after experiment α serves to estimate the information in α as related to β:

$$I(\alpha, \beta) = H(\beta) - H(\beta|\alpha), \tag{13.2.4}$$

where $H(\beta|\alpha)$ is the conditional entropy for experiment β (provided that experiment α has been conducted).

The conditional entropy is the average value of a random variable taking a $H(\beta_i|\alpha_i)$ value with a probability of $P(A_i)$:

$$H(\beta_i|\alpha_i) = \sum_{i=1}^{N} P(A_i)H(B_i|A_i). \tag{13.2.5}$$

13.2.2.2 Advantages of Geophysical Method Integration

What information do geophysical field measurements contain? We assume that a geophysical (gravity, thermal, magnetic, etc.) field is observed in a range D, and the measurement precision is given by τ. Let us fit an integer number of small intervals ξ into the intervals D and τ. Hence after measurement it is known that the value of the field in ξ units (with a precision up to ξ) fits into the interval τ. Using Eq. (13.2.4) and considering that the entropy in this expression before and after measurement is expressed by logarithms D/ξ and τ/ξ, respectively, one easily obtains (on the basis of Ventsel 1969):

$$I(\alpha, \beta)_{\xi} = \log_2\left(\frac{D}{\tau}\right). \tag{13.2.6}$$

With decreasing ξ, these entropies increase unlimitedly, but the information remains unchanged. With unrestricted increase in the measurement precision the information also increases unlimitedly, but slowly: an n-fold increase in the precision only yields an additional $\log_2 n$ of information units.

An essential property of composite experiments is as follows. If some tests Ψ, φ and θ are independent, experiments Ψ and θ can have zero information about φ. However, an integrated experiment Ψ and θ can completely determine the outcome of experiment φ. Consequently, whereas separate geophysical methods give no information on the presence (or absence) of ore or other targets, it is possible to obtain this by integrating these methods. Taking into account the conclusion which follows from Eq. (13.2.5), it is evident that the development of integrated investigations is more reasonable than an increase in the precision of separate methods.

13.2.2.3 Estimating the Efficiency of Individual Methods

When selecting methods for integration, it makes sense to evaluate the amount of information provided by each method.

Starting from a well-investigated site (with an equal distance between observation points) typical of the area under study, it is assumed that 1/50 of it contains an HT. It is a priori assumed that in the HT the temperature field is always negative, whereas in the empty part of the area it may be either negative or positive

with equal probability. In other words, it is known a priori that 2 and 98 % of the area are HT-containing and empty, respectively, and in 49 and 51 % of this area the temperature anomalies, respectively, are positive and negative. The results of experiment β can be designated as follows: B–HT occupying part of the area, $\bar{B}$—empty part of the area. Thus, $P(B) = 0.02,\ P(\bar{B}) = 0.98$. According to expression (13.2.3) $H(\beta) \cong 0.14$.

The results of experiment α are expressed as follows: A is a negative field, $\bar{A}$ is a positive field. The relative partial entropy (after recording the negative temperature) can be calculated in the following way: $P(A) = 0.51; P(\bar{A}) = 0.49; P(B|A) = 2/51, P(\bar{B}|A) = 1 - P(B|A) = 0.98$. Thus, $H(\beta|\alpha) \cong 0.24$. According to the recorded positive temperature, the area is certainly empty: $H(B|\bar{A}) = 0$. Consequently, the partial entropy for experiment β under the conditions of α, as stated in Eq. (13.2.5), is $H(\beta|\alpha) \cong 0.12$. Thus, the uncertainty of the HT determination decreased after the temperature field observation from 0.14 to 0.12.

By taking into account the cost of each measurement, the effectiveness of respective methods can be estimated (e.g., Eppelbaum et al. 2003). For this purpose it is sufficient to compare the values (costs) of the information units provided by each method. On this basis, a valid solution for a reasonable integration of the methods can be made.

13.2.2.4 Estimation of Information by Indicator (Field) Gradations

The geophysical fields applied in hydrocarbon geology usually have maximal and minimal intensity within the areas under investigation. The difference between the maximal and minimal intensities can be subdivided into intervals (gradations). Gradations of indicators can also be used to obtain information about the types of HT. Physical fields, geochemical analyses, HT features, etc. can serve as indicators. Let $P(A_i|B)$ denote the posterior probability of finding the i-th gradation of indicator A (e.g., magnetic field intensity) over target B, $P(A_i)$ is the prior probability of finding the same gradation in a survey area. Thus the partial information on the presence of target $I_{A_i \to B}$ contained in the recorded A_i gradation takes the following form:

$$I_{A_i \to B} = \log_2 \left[\frac{P(A_i|B)}{P(A_i)} \right], \tag{13.2.7a}$$

as the uncertainty in the recording of A_i before the survey was $\log_2 P(A_i)$ and after the survey—$\log_2 P(A_i|B)$.

Similarly,

$$I_{A_i \to \bar{B}} = \log_2 \left[\frac{P(A_i|\bar{B})}{P(A_i)} \right]. \tag{13.2.7b}$$

Statistically, the probabilities (or, to be more precise, relative frequencies) are expressed by the following ratios: S is the total number of values, S_i is the number of values occupied by the i-th interval of the A_i values, S_p is the total number of points reflecting the HT projections to the Earth's surface, and S_{pi} is the number of points common to interval A_i and the HT projections.

Hence:

$$P(A_i) = \frac{S_i}{S}, \quad P(A_i|B) = \frac{S_{pi}}{S_p}, \quad P(A_i|\bar{B}) = \frac{S_i - S_{pi}}{S - S_p}.$$

The increment in information about the presence of the object

$$\Delta I_i = I_{A_i \to B} - I_{A_i \to \bar{B}} = \log_2 \left[\frac{P(A_i|B)}{P(A_i|\bar{B})} \right]. \tag{13.2.8}$$

is summed up in each elementary cell of the geological site.

To estimate the informational significance, the following expression can be used:

$$I'_{A \to B} = \sum_i \lfloor P(A_i) \cdot I_{A_i \to B} \rfloor. \tag{13.2.9}$$

The estimates serve to substantiate the ratio between informational significance, cost and time (see Eq. 13.2.1). To normalize the results, the following semi-empirical expressions (obtained on the basis of the informational approach and long-term experience in the field of applied geophysics) can be used (one example of the thermal method (TM): geophysical method II):

$$\Omega_{TM} = \frac{I'_{A \to B(TM)}}{C_{(TM)}/C_{(II)} \cdot T_{(TM)}/T_{(II)}}, \tag{13.2.10a}$$

$$\Omega_{II} = \frac{I'_{A \to B(II)}}{C_{(II)}/C_{(TM)} \cdot T_{(II)}/T_{(TM)}}. \tag{13.2.10b}$$

Comparison of the corresponding factors is used to estimate the effectiveness of the geophysical method.

13.2.2.5 Estimates of the Efficiency of Geophysical Integration Based on the Probability of Type I and Type II Errors

Classification efficiency can be estimated quantitatively not only for separate methods, but also for geophysical integration by calculating the reliability of revealing a HT. Let's assume that in some region 20 anomalies have been contoured and localized by a set of geophysical methods. The revealed anomalies were divided into three groups with various degrees of desired HT discovery. Under the

assumption that the results of drilling are absolutely reliable, the classification reliability can be assessed by calculating the probability of type I and type II errors.

The probability of a type II error (M_2) is expressed as the relative frequency of an erroneous diagnosis for objects from sampling B (HT). The probability of a type I error (M_1) is expressed as the relative frequency of an erroneous diagnosis for objects from the sampling $\bar{B}$ (the remainder of the objects). These errors are used to determine the total unconditional error of separation q between classes B and $\bar{B}$ (i.e. the risk of an erroneous solution):

$$q = M_2 P(B) + M_1 P(\bar{B}), \tag{13.2.11}$$

where $P(B)$ and $P(\bar{B})$ are the prior probabilities of the appearance of objects of the first and second classes, respectively.

If $P(B) = P(\bar{B}) = 0.5$, then the q value corresponds to the intersection area of the distribution densities $P(X|B)$ and $P(X|\bar{B})$. Here X is the separation index. It can represent geophysical field amplitude or gradient, the value of integrated indicator, etc.

The separation reliability (γ) is:

$$\gamma = 1 - q. \tag{13.2.12}$$

The total empirical error should be compared to the theoretical error. The approximation of the errors can confirm a correct assumption and provide high reliability of identification. Using logical-informational methods (Khesin et al. 1996), the classification reliability is estimated solely from empirical errors.

The errors due to assigning observation results to a class (with or without the HT) can be determined as follows. The absence of anomalies for the complex indicator in a known target- containing area is a type II error, or "omission of target". The presence of these anomalies in the empty part of this area is a type I error, or a "false alarm".

Comparing these rapid results with those of a more complex integration can also be used to estimate the respective errors and the reliability of classification. Let's assume that the hydrocarbon nature of 14 out of 20 recognized geophysical anomalies was confirmed. New HT were not revealed in the areas where geophysical methods were applied. Thus, $M_1 = 0$, $M_2 = 14/20$. Assuming that $P = (B) = P(\bar{B}) = 0.5$, and taking into account Eqs. (13.2.11) and (13.2.12), then $q = 0.70$ and $\gamma = 0.30$.

13.2.2.6 Calculation of Information Parameters

Typically, the first step in qualitative interpretation involves visual inspection of profile observations or compiled maps. However, this simple analysis is often not sufficient to locate buried objects. Detecting geophysical anomalies caused by HT is often difficult because the effect may be masked by the influence of surrounding

inhomogeneities of different sizes and intensities. Various transformation and filtering procedures have been developed for more effective localization of finite objects (Telford et al. 1990; Parasnis 1997, etc.). We have shown elsewhere (Khesin et al. 1996; Khesin and Eppelbaum 1997) that applying information parameters often overcomes these problems. The method involves considering that the noise component—the combined effect of the surrounding inhomogeneities that are not associated with the target objects—is random. The amount of information (I_i) at each observation point by application of the i-th method is

$$I_i = -\log_2 P_j \tag{13.2.13a}$$

or

$$I_i \cong \log_2\left(\frac{H_i}{\Delta H_i}\right), \tag{13.2.13b}$$

where P_j is the frequency rate of the j-th interval of the i-th indicator (field) in the histogram (more precisely, Bayes' evaluation of the probability that the results will end up in the j-th interval) and H_i and ΔH_i are the amplitude and determination error of this indicator, respectively.

Eppelbaum et al. (2008) proposed the following expression:

$$I_i = U_i\left(\sum_i^n U_i\right)^{-1}\log_{10}\left[U_i\left(\sum_i^n U_i\right)^{-1}\right]K, \tag{13.2.13c}$$

where U_i is the geophysical observation at i-th point ($U_i > 0$) in the area under study, n is the total number of observations, and K is a coefficient.

After summing the information elements that suggest a priori that a target object is present, the random noise and components caused by dissimilar geological features are suppressed. In order to avoid singling out fictitious objects by the plot of $\frac{1}{n}\sum_{i=1}^{n} I_i$, which can occur when a large amount of information is contained in the data from only one or two methods, an additional complex criterion that depends on the number of significant indicators can be calculated while adjusting for their relative influence (Khesin and Eppelbaum 1997):

$$I_{\text{integr}} = \sum_{k=1}^{\frac{n(n-1)}{2}} \frac{(I_p)_k}{(I_p)_{\max}}, \tag{13.2.14}$$

where I_p is determined from the formula

$$I_p = (I_1 + I_2)\frac{I_1}{I_2}, \quad (I_1 \le I_2),$$

by using pairwise combinations of the n methods employed.

The results of the parameter calculation may be compiled as maps of I_i and I_{integr}. To avoid missing deeply embedded objects, in some cases it is better to use frequency rates of average values or average field estimates on a sliding scale instead of the P_j and H_i values, respectively. The correlation of I_{integr} with the sum of information elements makes it possible to avoid missing an object which for these or other reasons was not revealed by other indicators. The combination of indices permits certain interpretative conclusions.

In practice J_i is usually replaced by the relative amount of information, also known as the coefficient of informativity (Khesin et al. 1996):

$$K_i = \frac{J_i}{\bar{J}_i}. \tag{13.2.15}$$

The value of $\bar{J}_i$ determines the information obtained when the result of U_j falls into the x_j interval of the histogram with an equal probability of falling into any of the R intervals. According to probability principles (Ventsel 1969; Daston 1988), it is equal to the average (complete) information obtained when using a single method:

$$\bar{J}_i = \log_2 R. \tag{13.2.16}$$

The application of K_i takes differences in the ranges of different fields into account. However, the application of expressions (13.2.12) and (13.2.14)–(13.2.16) may not be effective for sparse sampling.

13.2.2.7 Estimating Integration Efficiency by Localization of Weak Anomalies

If a set of methods is focused on investigating independent indicators of equal value, the anomaly detection reliability γ can be described by an error function (probability integral) (Khesin and Eppelbaum 1997) as:

$$\gamma = \Phi\left(\frac{\sqrt{\sum_i \upsilon_i}}{2}\right), \tag{13.2.17}$$

where υ is the ratio of the anomaly squared to the noise dispersion for each i-th geophysical field, and F is the probability integral of type

$$\Phi(t) = \frac{1}{\sqrt{2\pi}} \int_{-\infty}^{t} e^{\left(\frac{-x^2}{2}\right)} dx.$$

Now let us assume that the anomaly is indicated by three points and that the mean square of the anomaly for each field is equal to the noise dispersion. For a single method, the reliability of the detection of an anomaly of a known form and intensity by Kotelnikov's criterion (e.g., Borda 2011) is expressed by $F(t)\left(\sqrt{v_i}/2\right)$. Hence the reliability for individual methods is 0.61 and 0.77 and 0.87 for a set of two or three methods respectively. This means that the q value (risk of an erroneous solution) when integrating two or three methods decreases by factors of 1.7 and 3.0, respectively (according to Eq. (13.2.12)). A comparison of the risk with costs C yields an optimum set of methods.

13.2.3 Multimodel Approach to Geophysical Data Analysis

Multimodel approach to geophysical data analysis may be illustrated on example of quantitative analysis of temperature anomalies. Quantitative interpretation of thermal anomalies (as and many other geophysical methods) was traditionally oriented to a single model for buried objects identification. In the case of the existence of several hypotheses relating to the parameters of the body causing the disturbance (i.e., the buried object) usually only one model was selected roughly presenting the object in the domain $\Re_x$ of k-dimensional space of the physical–geological factors. At the same time, many geological features are strongly disturbed by various geological processes (erosion, geodynamic activity, metamorphism, etc.).

Additional noise affecting interpretation includes rugged terrain relief, thermal anisotropy of geological objects and heterogeneous host medium. As a consequence, response function Ψ_i—geophysical field—may ambiguously represent the studied targets. Therefore, domain $\Re_x$ may be divided into several subdomains $\Re_1$, $\Re_2$, …, $\Re_m$ and in each of them a single model will dominate (Eppelbaum 1987). In such a way we could develop m physical–geological models of the same target, each corrected for separate subdomains $\Re_1$, $\Re_2$, …, $\Re_m$.

13.3 Case Histories

13.3.1 Integrated Geophysical Investigations of Areas of the Saatly Super-Deep Borehole

For many years, the dominant point of view in Azerbaijan was that in the Kura Depression separating the mega-anticlinoria of the Greater and the Lesser Caucasus, thick sedimentary deposits were present in the crystalline Pre-Alpine

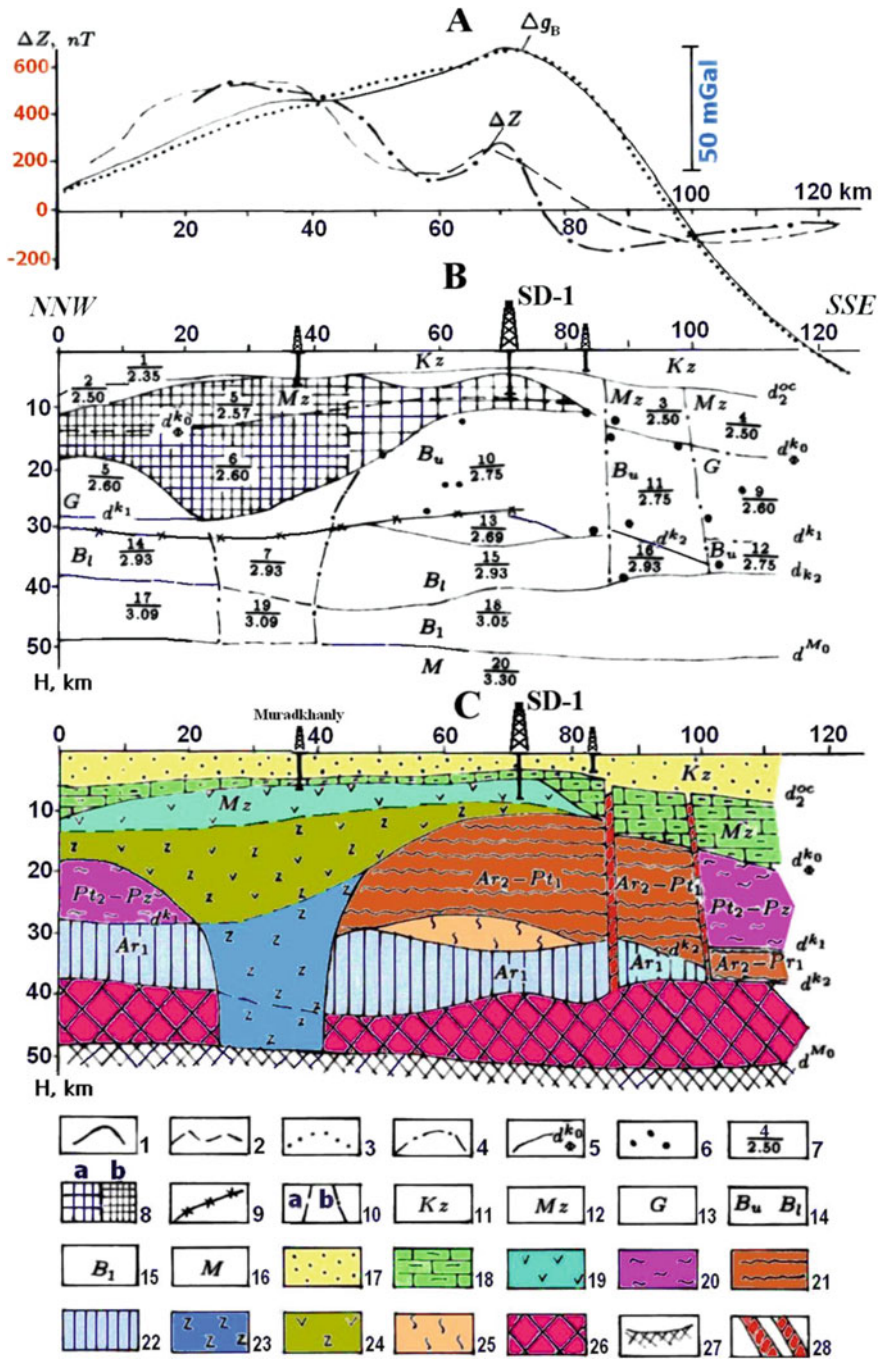
A
ΔZ, nT
600
400
200
0
-200
Δg_B
ΔZ
50 mGal
20
40
60
80
100
120 km
B
NNW
SSE
SD-1
0
20
40
60
80
100
120
Kz
Mz
G
Bu
Bl
B1
M
H, km
10
20
30
40
50
C
SD-1
Muradkhanly
Pt2 – Pz
Ar2 – Pt1
Ar1
H, km

◀ **Fig. 13.3** Deep geological section of the Earth's crust in the SD-1 area (after Eppelbaum and Khesin 2012) **a** gravitational and magnetic fields, observed and computed by the model **b**; **b** petrophysical model; **c** geological model. Observed *curves* (*1*) Δg (*2*) ΔZ; curves computed by the model **b** (*3*) Δg (*4*) ΔZ; (*5*) boundaries of the velocity and the density inhomogeneities and their indices; (*6*) diffraction points; (*7*) body number (numerator) and density value, g/cm^3 (denominator); (*8*) geological bodies with a magnetization of 2,500 mA/m (**a**) and 2,800 mA/m (**b**); (*9*) projection of the Curie surface on the basis of geothermal data; (*10*) subvertical boundaries of bodies on the basis of magnetic (**a**) and gravitational (**b**) fields; (*11*) Cenozoic; (*12*) Mesozoic; (*13*) *G* complex (velocity analog of the "granitic" layer); (*14*) B_u and B_l subcomplexes of *B* complex (complex *B* is the "basaltic" layer velocity analogue); (*15*) B_1 complex (presumably basite and eclogite composition); (*16*) *M* complex (presumed peridotite composition); (*17*) Cenozoic complex: mainly terrigeneous deposits; Mesozoic complex: (*18*) terrigeneous-carbonaceous formations (*19*) mainly effusive associations of basic and intermediate composition; (*20*) mainly Baikalian complex ($Pt_2 - Pz$): metamorphic (primarily terrigeneous) associations (the presence of younger deposits is possible in the upper part); (*21*) Pre-Baikalian complex ($Ar_2 - Pt_1$): mainly gneisses and marbles; (*22*) ancient complex (Ar_1): gneisses and amphibolites; (*23*) root of the basic magmatism; (*24*) undivided effusive-intrusive complex; (*25*) rock complex with low density (serpentinization zone ?); (*26*) complex of associations corresponding to crust-to-mantle transition; (*27*) upper mantle roof position; (*28*) large fault zones

basement, and these structures were divided by subvertical deep faults. On the buried uplift of the basement, hypothesized on the basis of high densities and velocities of elastic waves, the Saatly superdeep borehole SD-1 was designed in 1965. The drilling area was selected using the analysis of seismic profiles as well as regional gravity field analysis (Tzimelzon 1959).

However, analysis of the magnetic properties of rocks and the magnetic survey results showed that the basement was not magnetized, and a large part of the geological section of the Middle Kura Depression was occupied by Mesozoic magmatic associations of basic and intermediate composition with high magnetization (Khesin and Eppelbaum 1997). These mainly Jurassic associations are widely distributed in the north-eastern part of the Lesser Caucasus. They have a deep-seated gently sloping underthrust under the sand-shale thick series of the Greater Caucasus Jurassic. For such a complex model it was very important to compute the depth of the Curie surface (carried out by Pilchin in 1981 on the basis of thermal field analysis). On the basis of the data obtained, the lower edge of the magnetoactive zone was defined and the *PGM* of this area was elaborated (Fig. 13.3). Thus, the *PGM* presented in this figure is the result of combined analysis of four geophysical methods: seismic, gravity, magnetic and thermal.

13.3.2 Integrated Thermal-Gravity-VLF Investigations in Ore Geophysics

An impressive integration of gravity, temperature and VLF observations in the Katsdag pyrite-polymetallic deposit (Greater Caucasus, Azerbaijan) is presented in Fig. 13.4. Analysis of geophysical graph behavior in the lower part of this figure

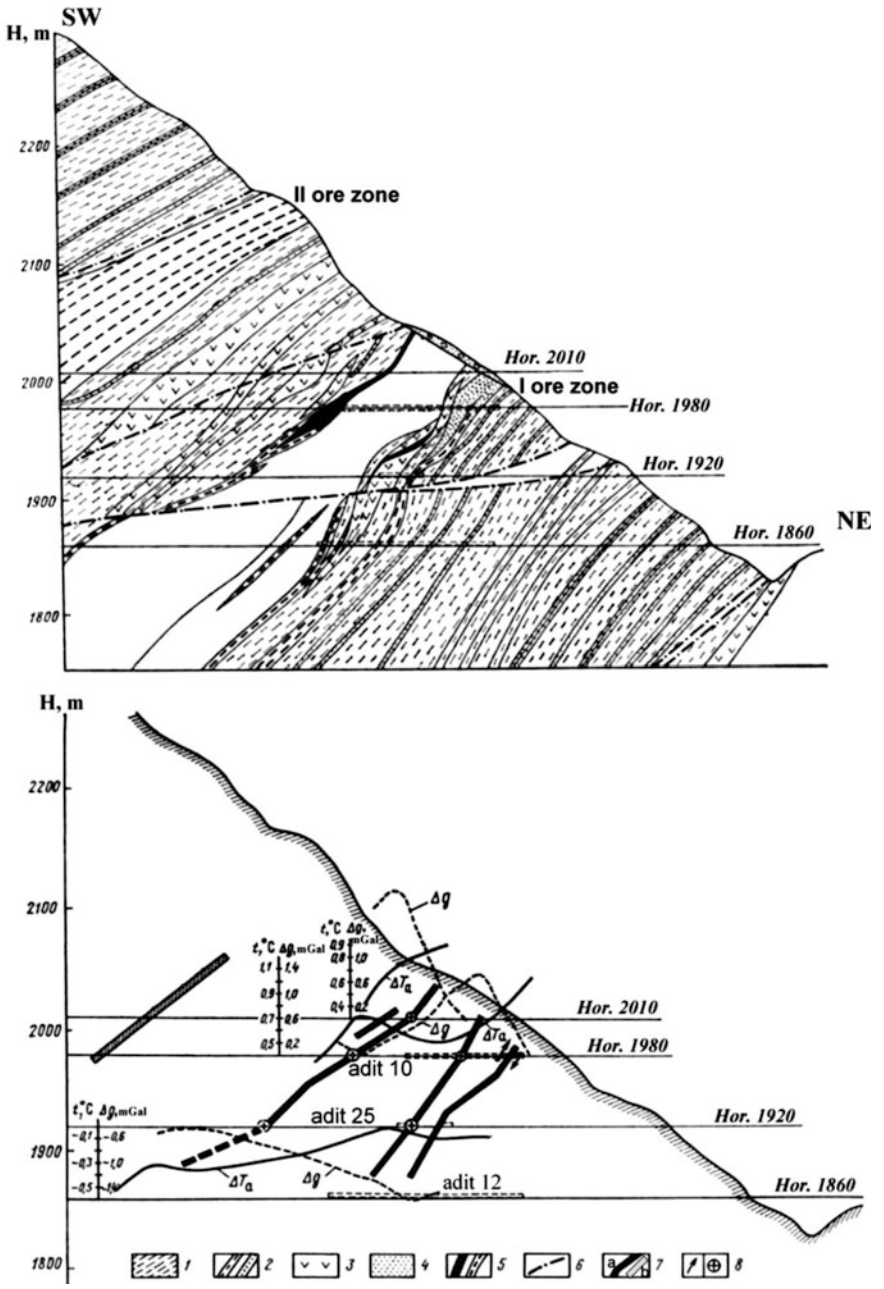

Fig. 13.4 Integrated geophysical investigations in mines of the Katsdag deposit (southern slope of the Greater Caucasus) (Poltoratsky and Ginzburg 1989) (*1*) shales (*2*) interbedding of shales, sandstones and siltstones (*3*) dioritic porphyry (*4*) oxidizing zone (*5*) polymetallic ores of I and II zones (*6*) faults (*7*) apparent beds of redundant: density (**a**) and thermal conductivity (**b**) (*8*) current axes revealed by the VLF method

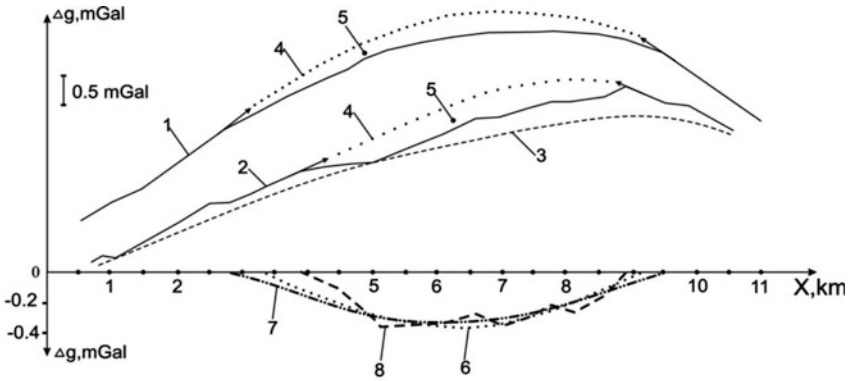
Δg,mGal
0.5 mGal
1
2
3
4
5
0
-0.2
-0.4
1
2
5
6
7
8
10
11
X,km
Δg,mGal
7
8
6

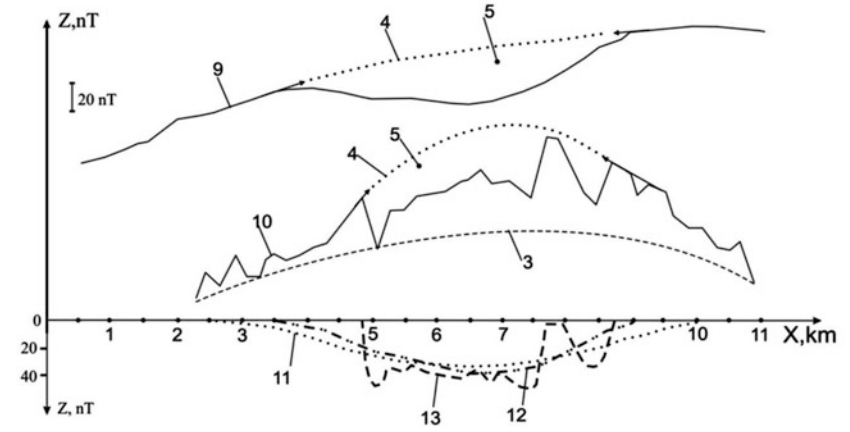
Z,nT
20 nT
9
4
5
10
3
0
20
40
1
2
3
5
6
7
10
11
X,km
Z, nT
11
13
12

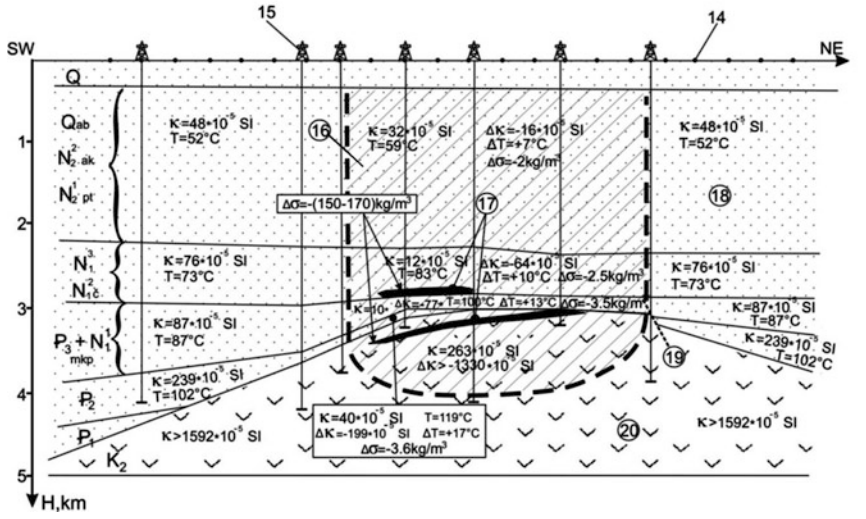
15
14
SW
NE
Q
Qab
N2 2 ak
N2 1 pt
N1 3
N1 2 c
P3 + N1 1 mkp
P2
P1
K2
κ=48•10-5 SI
T=52°C
16
κ=32•10-5 SI
T=59°C
ΔK=-16•10-5 SI
ΔT=+7°C
Δσ=-2kg/m3
Δσ=-(150-170)kg/m3
17
18
κ=76•10-5 SI
T=73°C
κ=12•10-5 SI
T=83°C
ΔK=-64•10-5 SI
ΔT=+10°C Δσ=-2.5kg/m3
κ=87•10-5 SI
T=87°C
κ=239•10-5 SI
T=102°C
κ=263•10-5 SI
ΔK>-1330•10-5 SI
19
κ>1592•10-5 SI
κ=40•10-5 SI T=119°C
ΔK=-199•10-5 SI ΔT=+17°C
Δσ=-3.6kg/m3
20
1
2
3
4
5
H,km

◀ **Fig. 13.5** Results of gravity-magnetic modeling in the Muradkhanly area (after Gadirov and Eppelbaum, 2012) (*1*) computed gravity effect from geological model; (*2*) observed field Δg_B; (*3*) regional trend; (*4*) restored maxima due to changes in the gradient zones; (*5*) local minima; (*6*) computed gravity effect from subvertical hydrocarbon zone; (*7*) and (*8*) local gravity anomalies extracted from graphs 1 and 2; (*9*) computed magnetic effect from the geological model; (*10*) observed magnetic field; (*11*) computed magnetic effect from subvertical oil zone; (*12*) and (*13*) local magnetic anomalies extracted from graphs (*9*) and (*10*), respectively; (*14*) points where gravity-magnetic effects were computed; (*15*) deep boreholes; (*16*) subvertical hydrocarbon zone; (*17*) oil pool; (*18*) sedimentary deposits; (*19*) fault; (*20*) effusive associations

and comparison of these data with the geological section provide rich data for integrated analysis and prospection. Certain geophysical graph distributions testify to the presence of previously unknown ore bodies.

13.3.3 Integrated Thermal-Gravity-Magnetic Investigations in Oil and Gas Geophysics

A quantitative estimation of changes in acquired magnetization, density and temperature data was applied to develop a detailed physical–geological model of the Muradkhanly deposit (Fig. 13.5) (Gadirov and Eppelbaum 2012). Geometry, stratigraphy, lithology and HD location (17) in the model were taken from the drilled deep well cores (15). Data on density, porosity and magnetization were utilized from the works. The density contrast within the subvertical zone over HD was calculated using the new approach.

As was shown in Fig. 13.5, the physical parameters of the zone over HD (16) differed considerably from the surrounding medium (18, 20). At increased depths there were increased contrast magnetization (up to 200×10^{-5} SI) and temperature (up to 17 °C) parameters, and a decreased density contrast (up to 3.6 kg/m^3) in the sedimentary deposits in the HD zone (Gadirov and Eppelbaum 2012). Analysis of selected cores also showed a sharp decrease in magnetization in effusive associations in the structure arch in the vicinity of the HD.

Computed gravity and magnetic anomalies (curves 6 and 11, Fig. 13.5) from subvertical zone (16) indicated ≈ -0.35 mGal and ≈ -35 nT. Comparison of the theoretical curves of the gravity and magnetic fields (graphs 1 and 9) with the observed curves (graphs 2 and 10) indicated that they had a similar form. Both in observed and theoretical graphs relative decreases in the gravity and magnetic fields over the HD were found. Retrieved maxima on gradient zone changes (4) clearly pinpointed local gravity and magnetic minima.

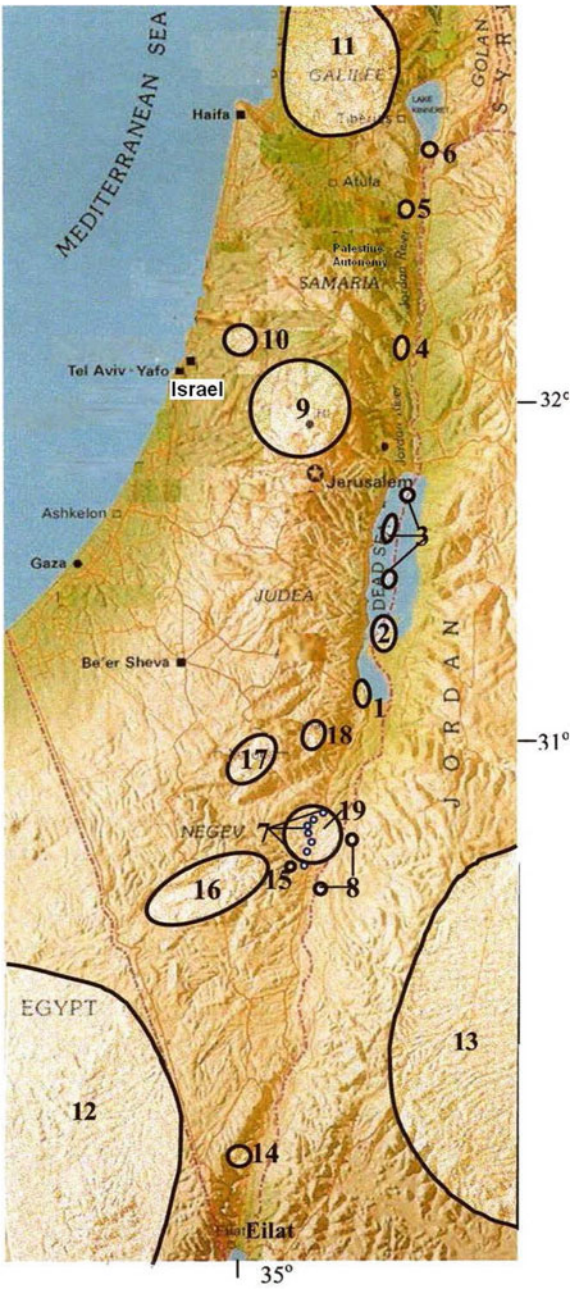

Fig. 13.6 Location of some ring structures in Israel and adjacent areas (after Eppelbaum et al. 1998). **a** Tectonic *RS*: salt diapirs (*1–6*): (*1*) Mt. Sedom (*2*) Lisan (*3*) north Dead Sea (*4*) Zahrat et Qurein (*5*) Bet-She'an (*6*) Zemah; (*7*) "Country of the Domes" (*8*) compressional domes; Highs (*9–11*): (*9*) Ramalla (*10*) Rosh-Ha'Ayin (*11*) Galilee; Basins (*12–13*): (*12*) Sinai (*13*) Jordan; **b** Magmatic *RS*: (*14*) Timna dome (*15*) Karkeshet caldera; **c** Erosional *RS*: (*16*) Makhtesh Ramon (*17*) Makhtesh Gadol (*18*) Makhtesh Katan; **d** Extraterrestrial (?) (*19*) *RS* Ein Yahav

13.3.4 Integrated Delineation of Ring Structures in Israel and the Easternmost Mediterranean

Structures of relatively ring form in the Earth are known sufficiently long time. The last decades a lot of Ring Structures (RS) have been recognized by space images and advanced geophysical field analysis. It is known that many of petroleum/mineral deposits are associated with RS. A number of RS (diameter from hundreds of meters to 150 km) in the Eastern Mediterranean (Israel, Sinai and Jordan) were recognized on the basis of gravity, magnetic, thermal and seismic data analysis as well as topography data utilization (Fig. 13.6) (Eppelbaum et al. 1998). A preliminary classification of the phenomenon showed that terrestrial RS are presented by tectonic, magmatic and erosional types. As for the extraterrestrial RS, Ein Yahav circular structure of 20–25 km diameter has been preliminary interpreted as having impact origin.

Eppelbaum et al. (1998) suggested to subdividing investigation of RS into three successive stages. (1) Recognition of targets; visual analysis of space images and geological data (including field searching meteorite signatures); application of statistic-probabilistic procedures based on revealing circular like anomalies (topography field and potential geophysical fields) against the noise background. It should be noted that some RS, which are clearly impressed in the space images, do not represented in the structure of sedimentary cover. Their origin may be caused by deep structure inhomogeneities reflected in geophysical fields. (2) Application of modern inverse problem solution for determination of geometrical and physical characteristics of RS; integrated quantitative interpretation of geophysical anomalies; cross-correlation and transformations. (3) 3-D combined modeling of potential fields (with utilization of seismic and other geophysical data) and development of 3-D models of RS.

The interpreting system have been effectively applied for studying several RS. The results of the integrated analysis are used for: (a) development of principles of the RS recognition in the Eastern Mediterranean. (b) morphogenetic and physical–geological classification of RS. (c) revealing possible connection between the RS and petroleum and mineral resources.

References

Akselrod SM, Putkaradze LA (1979) Integrated interpretation of logging with due account of variations in physical properties of the object under study. Review of VIEMS, Ser. Regional, Exploration, and Borehole Geophysics, Moscow (in Russian)

Borda M (2011) Fundamentals in information theory and coding. Springer, Berlin

Borovko NN (1979) Optimization of geophysical investigations in ore deposit prospecting. Nedra, Leningrad (in Russian)

Brillouin LN (1962) Science and information theory, 2nd edn. Academic Press, NY

Bulakh EG, Rzhanitsyn VA, Markova MN (1976) Application of minimization method for solution of structural geology problems using gravity data. Naukova Dumka, Kiev (in Russian)

Daston L (1988) Classical probability in the enlightenment. Princeton University Press, Princeton

Eppelbaum LV (1987) Multimodel approach to the study of geophysical targets (in Russian). Deposited by VINITI, USSR Academic of Science, No. 7842-87, pp 1–10

Eppelbaum LV, Alperovich L, Zheludev V, Pechersky A (2011) Application of informational and wavelet approaches for integrated processing of geophysical data in complex environments. In: Proceeding of the 2011 SAGEEP conference, vol 24. Charleston, South Carolina, USA, pp 24–60

Eppelbaum L, Eppelbaum V, Ben-Avraham Z (2003) Formalization and estimation of integrated geological investigations: informational approach. Geoinformatics 14(3):233–240

Eppelbaum LV, Ezersky MG, Al-Zoubi AS, Goldshmidt VI, Legchenko A (2008) Study of the factors affecting the karst volume assessment in the Dead Sea sinkhole problem using microgravity field analysis and 3D modeling. Adv GeoSci 19:97–115

Eppelbaum LV, Khesin BE (1988) Physical–geological models for pyrite deposits of the Filizchay and Lesser-Caucasian types. In: Transactions of all-union meeting "Multifactor ore deposit models as the basis for developing effective methods of search, evaluation and prospecting", Tbilisi, pp 126–127 (in Russian)

Eppelbaum LV, Khesin BE (2012) Geophysical studies in the caucasus. Springer, Berlin

Eppelbaum LV, Livshits Ya, Flexer A, Ben-Avraham Z (1998) Integrated geological–geophysical analysis of Ring Structures phenomenon in the Eastern Mediterranean. Transactions of the conference of Israel geological society annual meeting. Mizpe-Ramon, Israel, p 25

Fotiadi EE (ed) (1970) Geology and mathematics; problems of diagnosis and identification in geology, geochemistry and geophysics. Nauka, Novosibirsk (in Russian)

Gadirov VG, Eppelbaum LV (2012) Detailed gravity, magnetics successful in exploring Azerbaijan onshore areas. Oil Gas J 110(11):60–73

Karatayev GI, Pashkevich IK (1986) Integrated analysis of geological and geophysical data. Naukova Dumka, Kiev (in Russian)

Khalfin LA (1958) Information theory of geophysical interpretation. Doklady AN USSR 122(6):1007–1010 (in Russian)

Khesin BE, Alexeyev VV, Eppelbaum LV (1996) Interpretation of Geophysical Fields in Complicated Environments. Kluwer Academic Publishers, Springer, Ser: Modern Approaches in Geophysics, Boston, Dordrecht, London

Khesin BE, Eppelbaum LV (1997) The number of geophysical methods required for target classification: quantitative estimation. Geoinformatics 8(1):31–39

Malyshev VP (1981) Probabilistic–deterministic design of experiment. Nauka, Alma-Ata (in Russian)

Nikitin AA (1993) Statistical processing of geophysical data. Series of advanced geophysics, Russian experience, vol 22. Electromagnetic Research Centre, Moscow (in Russian)

Parasnis DS (1997) Principles of applied geophysics (revised and supplumented), 5th edn. Chapman & Hall, London

Pilchin AN (1981) Influence of additional pressure on seismic velocity and density of rocks in Middle-Kura depression. Explor Geophys (Razvedochnaya Geofizika) 91:122–127 (in Russian)

Poltoratsky VV, Ginzburg SN (1989) Gravity prospecting. In: Brodovoi VV (ed) Borehole and mining geophysics, vol II. Nedra, Moscow, pp 190–209 (in Russian)

Shannon CE (1948) A mathematical theory of communication. Bell Syst Tech J 27:3–4, 379–432, 623–656

Shraibman VI, Zhdanov MS, Vitvitsky OV (1977) Correlation methods for transformation and interpretation of geophysical anomalies. Nedra, Moscow (in Russian)

Svetov BS (1992) Information theory basis of geophysics. Electromagnetic Research Centre, Moscow

Telford WM, Geldart LP, Sheriff RE (1990) Applied geophysics. Cambridge University Press, Cambridge

Tzimelzon IO (1959) A problem of geological interpretation of Talysh-Vandam gravity maximum. Geol Oil-and-Gas (3):55–65 (in Russian)

Ventsel ES (1969) The probability theory (revised), 3rd edn. Nauka, Moscow (in Russian)

Zadeh LA (1983) The role of fuzzy logic in the management of uncertainty in expert systems. Fuzzy Sets Syst 11:199–227

Zhdanov MS (2002) Geophysical inverse theory and regularization problems. Methods in geochemistry and geophysics, vol 36, Elsevier, Amsterdam

Biographies of the Authors

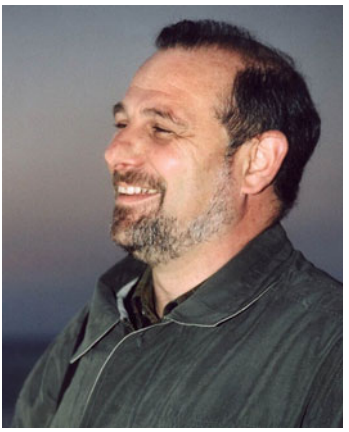

Lev V. Eppelbaum received M.Sc. from the Azerbaijan Oil Academy in 1982, and Ph.D. from the Geophysical Institute of Georgia in 1989. In 1982–1990 he worked as geophysicist, Researcher and Senior Researcher at the Institute of Geophysics in Baku (Azerbaijan). In 1991–1993 Eppelbaum completed postdoctoral studies in the Department of Geophysics and Planetary Sciences at Tel Aviv University; at present he occupies a position of Associate Professor at the same Department. He author of more than 300 publications including 5 books, 115 articles and 50 proceedings. His scientific interests cover potential and quasi-potential geophysical field analysis, integrated interpretation of geophysical fields, geodynamics and tectonics. Eppelbaum's research interests in geothermics include examination of temperature regime of boreholes, thermal interactions at a depth, near-surface temperature measurements, study of climate of the past and nonlinear analysis.

L. Eppelbaum et al., *Applied Geothermics*, Lecture Notes in Earth System Sciences,
DOI: 10.1007/978-3-642-34023-9, © Springer-Verlag Berlin Heidelberg 2014

Izzy M. Kutasov holds Ph.D. in Physics from O. Schmidt Earth Physics Institute in Moscow. He was a Senior Lecturer at the School of Petroleum Engineering, University of New South Wales, Sydney, and a graduate faculty member at the Department of Petroleum Engineering and Geosciences, Louisiana Tech University. He worked for Shell Development Co., Houston, as a Senior Research Physicist. Now Dr. I.M. Kutasov is a consultant with BYG Consulting Co., Boston, USA. His research interests include the temperature regime of deep wells, transient pressure/flow analysis, well drilling in permafrost areas as well as deriving climate of the past from subsurface temperature measurements. He is author of more than 250 publications including four books and more than 100 articles. Dr. Kutasov presented his scientific achievements at more than 60 International Conferences. His developments in the thermal data analysis in oil and gas wells received a wide recognition in the world scientific and engineering community.

Arkady N. Pilchin has been involved in geoscientific research since he received his M.Sc. in Physics in 1973. He participated in a number of geophysical and geological research endeavors including geothermal investigations in the Caucasus, Caspian Sea and Middle Asia, developing physical-geological models of the regions, earthquake prognosis, methods of prognosis for overpressure, analysis of the thermodynamic conditions of the Earth's crust, and those of oil and gas fields. He authored a number of geothermal methods including determining heat absorbing and heat releasing strata within a sedimentary layer. After leaving the former USSR in 1990, he worked on geoscientific problems of different regions of the world such as the Eastern Mediterranean, Alps, Baltic Shield and Canada. He is the author of over 150 publications, including 2 books, 3 book chapters, several geothermal maps and 15 patents. His current scientific interests are related to the formation, evolution and thermodynamic conditions of: the magma-ocean, early Earth atmosphere, earliest lithosphere, water-ocean, ore deposits, and different generations of sulfur.

Appendix A
Computing Water Flow Geodynamics in Stratified Liquids (An Example from the Dead Sea Basin)

The Dead Sea (DS), with a total area of 1,049 km^2 is located on the border between Israel and Jordan. It is the lowest place on Earth (in 2013 it was about 427 m below the Mediterranean Sea level) with an arid climate (in the summer the temperature can reach 45 °C). Thermal and pressure parameters in this area are characterized by a strong inhomogeneity (Eppelbaum et al. 1996). The density of water in the vertical direction varies from 1,150 kg/m^3 at the DS surface up to 1,430 kg/m^3 at a depth of 310–330 m. This density gradient exceeds the normal water density gradient in the Earth's oceans and seas by more than 10^2. Thus, the DS Basin may be considered a distinctive native polygon of vertically stratified liquid (the role of rock stratification in the magma-ocean was shown in Sect. 6.1). The most significant source of this are temperature and density gradients based on the constant inflow of a mineral substance from great depths (apparently, from the upper mantle). To analyze the water flows geodynamics in the DS Basin, solutions for the motion of stratified liquid with different initial boundary values can be used. Given the very high current rate of change of the physical, chemical and geological features of this unique basin, the development of a geodynamic predictable model of the area is extremely important. As was shown earlier, density practically always has a reliable correlation with temperature.

A.1 Nature of the Problem

At present, the distinctive DS water is intensively utilized for extracting useful components contained in the liquid. This industrial activity, combined with the extremely arid climate has caused a significant drop in the sea level and the development of hundreds of sinkholes on the DS coast (Eppelbaum et al. 2008). For the DS, the conventional mathematical model describing sea behavior consists of a set of algebraic and a system of differential equations (e.g., Asmar and Ergenzinger 2002). The state of the sea is found by solving a system of ordinary differential equations formed by writing a system of mass balance equations for the water and eight major chemicals in the sea. The law of conservation is accounted for implicitly through evaporation calculations. However, this approach is unable to calculate all the peculiarities of the unique DS Basin. Interesting results were

L. Eppelbaum et al., *Applied Geothermics*, Lecture Notes in Earth System Sciences,
DOI: 10.1007/978-3-642-34023-9,

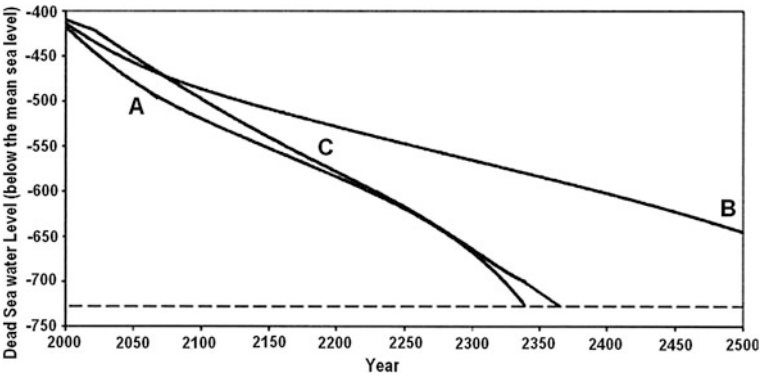

Fig. A.1 Predicted water levels in the Dead Sea up to the year 2500. **a** Scenario 1 shows a continuation of the current conditions. **b** Scenario 2 shows cessation of industrial extraction activity. **c** Scenario 3 shows simplified climate change (after Asmar and Erdenzinger 2004)

presented by Bubnov and Linden (1998) for a homogeneously rotating linear density-stratified fluid. However, this approach demands significant evaluation.

We suggested applying a more precise physical-mathematical model which has implications for forecasting environmental scenarios for the DS (three variants are presented in Fig. A.1) and in estimating the possible ecological impact of excavation of a channel between the Red and Dead Seas (the differences in chemical composition of water from these seas are shown in Table A.1).

A.2 Development of Mathematical-Physical Model

Let's consider the motion of stratified, rotating and compressible liquid (*SRCL*) in the Cartesian coordinates (x_1, x_2, x_3) which is rotating together with the *SRCL*. Let's assume that *SRCL* is rotating around axis Ox_3 and Coriolis vector $\mathbf{f} = (0, 0, f)$, where f is the double angle velocity of rotation. *SRCL* is stratified along the axis Ox_3; i.e., its density in undisturbed conditions depends on $x_3, \rho_0 = \rho_0(x_3)$. We assume below that $\rho_0(x_3) = Ae^{-2\beta x}, A > 0, \beta > 0$. Small *SRCL* motions under the influence of gravity acceleration without any external forces may be described as (Gabov and Sveshnikov 1986):

$$\begin{cases} \rho_0(x_3)\frac{\partial \mathbf{v}}{\partial t} + \rho_0(x_3)[\mathbf{f}, \mathbf{v}] + \nabla p + \mathbf{e}_3\rho_1 g = 0, \\ \frac{\partial \rho_1}{\partial t} + (\mathbf{e}_3 \cdot \mathbf{v})\rho_0'(x_3) + \rho_0(x_3)\mathrm{div}\ \mathbf{v} = 0, \\ \frac{\partial}{\partial t}\rho_1 = \frac{1}{c^2}\frac{\partial}{\partial t}p + \rho_0(x_3)\omega_0^2(x_3)\frac{(\mathbf{e}_3 \cdot \mathbf{v})}{g}, \end{cases} \tag{A.1}$$

where g is the gravity acceleration, $\mathbf{v} = (v_1, v_2, v_3)$ is the vector of *SRCL* particle motion, ρ_1 is the change in *SRCL* density caused by its motion, c is the acoustic velocity, p is the dynamic pressure and $\mathbf{e}_3$ is the ort of axis Ox_3 and $[\mathbf{f}, \mathbf{v}]$ denotes the vector product between two vectors. Value $\omega_0^2(x_3) \geq 0$ is the quadrate of

Table A.1 Some typical chemical analyses of the Dead Sea (*DS*) and the Red Sea (*RS*) (after Abu-Khader 2005; Ravizky and Nadav 2007, with supplements)

Element	*DS* concent-rations (mg/l)	*RS* concent-rations (mg/l)	Ratio, *DS*/*RS*
Chloride	224,000	23,000	9.74
Magnesium	44,000	1,500	29.33
Sodium	40,100	12,500	3.21
Calcium	17,650	500	35.3
Potassium	7,650	500	15.3
Bromide	5,300	70	75.71

Vyasyalay-Brent frequency. The condition $\omega_0^2(x_3) \geq 0$ indicates an absence of convective motion and stability of the density distribution $\rho_0(x_3)$ in the *SRCL*. It is known that physical parameters such as liquid density, acoustic velocity and pressure depend on temperature. Thus, the temperature is present in the formulas in an implicit form.

After several cumbersome transformations, Eq. (A.1) was reduced to the following type:

$$\frac{\partial^2}{\partial t^2}\left[\frac{\partial^2 u}{\partial t^2} - c^2\Delta_3 u + \left(f^2 + \beta^2 c^2\right)u\right] - \left[\omega_0^2 c^2 \Delta_2 u + f^2 c^2 \frac{\partial^2 u}{\partial x_3^2} - \beta^2 c^2 f^2 u\right] = 0, \tag{A.2}$$

where u is a scalar function on which unknown functions $\mathbf{v}$, ρ_1 and p depend.

A generalization of Eq. (A.2) was investigated in Yakubov (1989). Let's consider the following problem

$$\begin{cases} L(t, D_t, D_x)u(t,x) = \dfrac{\partial}{\partial t^2}\left[\dfrac{\partial^2 u(t,x)}{\partial t^2} - \displaystyle\sum_{i,j=1}^{3} \frac{\partial}{\partial x_i}\left(A_{ij}(t,x)\frac{\partial u(t,x)}{\partial x_j}\right)\right. \\ \qquad \left. + \displaystyle\sum_{i=1}^{3} B_i(t,x)\frac{\partial u(t,x)}{\partial x_i} + C(t,x)u(t,x)\right] + \displaystyle\sum_{i,j=1}^{3}\frac{\partial}{\partial x_i}\left(a_{ij}(t,x)\frac{\partial u(t,x)}{\partial x_j}\right) \\ \qquad + \displaystyle\sum_{i=1}^{3} b_i(t,x)\frac{\partial u(t,x)}{\partial x_i} + d(t,x)u(t,x) = f(t,x),\ (t,x) \in [0,T] \times \Omega, \end{cases} \tag{A.3}$$

where t is the time, A_{ij}, B_i, C, a_{ij}, b_i, d are sufficiently smooth functions (for an application, see Eq. (A.2), and depend on c, f, β and ω_0).

$$u(t,x)|_{x\in\partial\Omega} = 0, \quad t \in [0,T], \tag{A.4}$$

$$\frac{\partial^k u(t,x)}{\partial t^k}|_{t=0} = u_k(x), \quad k = 0,\ldots,3,\ x \in \Omega. \tag{A.5}$$

Equations (A.4) and (A.5) present the Dirichlet boundary condition and the Cauchy initial conditions, respectively. Thus, Eqs. (A.3)–(A.5) can be seen as a foundation for the development of a geodynamical model of *SRCL* in the DS Basin (Yakubov and Eppelbaum 2005).

A.3 Application of the Methodology

In the DS Basin (at the sea surface and at various depths) the following physical parameters were observed: temperature, gravity acceleration, water density, pressure, and acoustic velocity. Modern processing schemes can extend analytical continuations (downward, upward and sideward) of the physical observations to areas where we do not have these measurements. Thus, we can create a solvable system of differential equations and utilize this to create a precise physical-mathematical-geological model of the DS Basin. This model may be used not only for predictions, but also for the projected channel between the Red and Dead Seas, as well as to calculate the free electrochemical energy released from the unique DS Basin.

Appendix B
Water Production Using the Air-Cooling Method

The coastal regions in many regions of the world are characterized by their high moisture content—more than 15.0 g of water vapor per m^3 of air. This appendix is based on a phenomenon observed in the atmospheric boundary layer known as dew formation. At night, the boundary layer of air cools down considerably, which generally causes moisture saturation in the boundary layer and dew formation on the ground and plants. The ancient Greeks used this for water production (Zibold 1905). In more modern times, many investigations have been carried out to evaluate the quantitative potential of dew (Broza 1979; Kogan and Trahtman 2003; Nilsson 1996; Schemenauer and Cereceda 1992). However, all of these investigations have indicated that its potential is low.

To obtain fresh water by cooling humid air, we propose using a horizontal pipe. At the entrance to the pipe we will install a ventilator, which will introduce external humid air into the pipe. The outside wall of the pipe will be supplied with a special cooling system. A simplified scheme of this pipe is presented in Fig. B.1.

Let's consider the climatic conditions of Israel for illustrative purposes. According to Goldreich (2003) the average daily temperature, pressure and relative humidity in the coastal regions are $\bar{T} = 25\,^{\circ}\mathrm{C}$, $\bar{P} = 1{,}004\,\mathrm{mb}$ and $\bar{R}_H = 72\,\%$, respectively. Preliminary calculations using a relatively simplified thermodynamics method based on these average values show that if the air is cooled to 20 °C, 5.4 g of water can be obtained from 1.0 m^3 of air. If the radius of the pipe (cooling equipment) is 10 m and the velocity of the air inflow is 3.0 m/s, the air mass entering the pipe equals about 940 m^3/s. Therefore, the maximum amount of water obtainable from this system is 5.0 l/s; i.e., about 430 m^3 per day and 78,000 m^3 per summer period. These rough estimates indicate that the idea of producing considerable amounts of drinking water by air-cooling in the coastal regions of Israel is practical.

Let's make some preliminary calculations for conditions typical to Israel. Based on these data, one can compute the daily average specific saturating humidity by applying Teten's (1930) empirical formula:

$$\bar{Q}_S(\bar{P},\bar{T}) = \frac{3.8}{\bar{p}}\bar{E}\cdot\exp\left\{17.27\frac{\bar{T}-273.16}{\bar{T}-35.86}\right\}, \tag{B.1a}$$

where $\bar{T}$ is the absolute average temperature.

L. Eppelbaum et al., *Applied Geothermics*, Lecture Notes in Earth System Sciences,
DOI: 10.1007/978-3-642-34023-9, © Springer-Verlag Berlin Heidelberg 2014

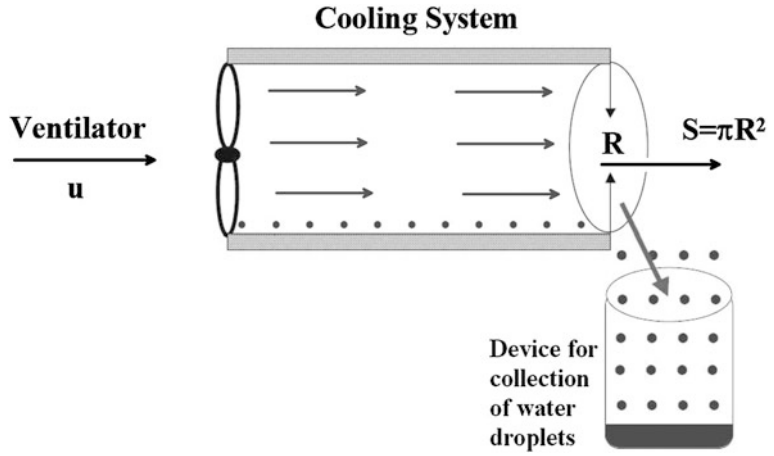

Fig. B.1 Schematic diagram of pipe for water production (after Tzivion and Eppelbaum 2004)

$$\bar{Q}_S(\bar{P} = 1{,}004\ \text{mb},\ \bar{T} = 298.16\ ^\circ\text{C}) = 19.63 \times 10^{-3}\ \text{g/g}. \tag{B.1b}$$

Thus, under these conditions, 1 kg of air contains 19.63 g of water vapor. Hence, we can calculate the daily average specific humidity in summer:

$$\bar{q}_v(\bar{P}, \bar{T}) = \bar{Q}_s(\bar{P}, \bar{T}) \cdot RH\,\% = 14.13\ \text{g/kg}.$$

If the air is cooled down to 20 °C, the specific moisture content will remain unchanged, and only $\bar{Q}_S$ will change, and its new value will be

$$\bar{Q}_S(\bar{p} = 1{,}004\ \text{mb},\ \bar{T} = 278.16) = 5.4\ \text{g/kg}. \tag{B.2}$$

Thus, we obtain the excessive water content—over saturation ΔS:

$$\Delta\bar{S} = \bar{q}_v - \bar{Q}_S = (14.13 - 5.4) = 8.73\ \text{g/kg}. \tag{B.3}$$

The average air density $\bar{\rho}$ for the above $\bar{p}$ and $\bar{T}$ values is roughly 1.2 kg/m^3. Hence, we obtain

$$\Delta\bar{S} = 10.5\ \text{g/m}^3.$$

Thus, 1 m^3 of air contains excess water of about 10.5 g.

Now we estimate the maximum amount of water that can be obtained from this excess water in humid air. During vapor condensation, the following values will change: $\bar{T}$, $\bar{q}_v$, $\bar{Q}_S(\bar{p}, \bar{T})$, $\Delta\bar{S}$.

We denote the new values of these functions as T^*, P^*, Q_S^* and ΔS^*. For simplification we assume that due to condensation the pressure remains unchanged and that after condensation the over-saturation becomes zero. Under such conditions, we calculate the maximum possible amount of condensed water

$\delta M_{cond}(\mathrm{g/kg})$. If δM_{cond} of the water is condensed, after condensation T^*, P^*, q_v^*, Q_S^* and ΔS^* take on new values:

$$P^* = \bar{P},\ T^* = \bar{T} + T',\quad q_v^* = \bar{q}_v - \delta M_{cond},\quad Q_S^* = Q_S^*(\bar{P}, T^*). \tag{B.4}$$

Here T' is the temperature disturbance due to condensation:

$$T' = \frac{L}{C_P}\delta M_{cond}, \tag{B.5}$$

where L is the specific heat condensation, and C_p is the specific heat capacity of the air at a constant pressure.

For purposes of simplification, we introduce the following notations:

$$A = 3.8/P,\quad b = 17.27,\quad T_0 = 273.16,\quad C = 35.86.$$

According to (B.2), we obtain:

$$Q_S^*(\bar{P}, T^*) = A \cdot \exp\left(b \cdot \frac{\bar{T} - T_0 + T'}{\bar{T} - C + T'}\right) \tag{B.6}$$

Given that $T' \ll \bar{T}$, we can rewrite (B.6) as follows:

$$Q_S^*(\bar{P}, T^*) = A \cdot \exp\left[b\frac{\bar{T} - T_0}{\bar{T} - C} + b\frac{T_0 - C}{(\bar{T} - C)^2}\right]T'. \tag{B.7}$$

Using (B.2) and (B.5), we can rewrite Q_S^* as follows:

$$Q_S^*(\bar{P}, T^*) = \bar{Q}_S(\bar{P}, \bar{T}) \cdot \exp\left[\frac{b(T_0 - C)}{(\bar{T} - C)^2}\frac{L}{C_P}\delta M_{cond}\right]. \tag{B.8}$$

Since the exponent is below unity, the final approximate value of Q_S^* is (Tzivion and Eppelbaum 2006):

$$Q_S^*(\bar{P}, T^*) \approx \bar{Q}_S(\bar{P}, \bar{T}) \cdot \exp\left[1 + \left(\frac{L}{C_P}b\right)\frac{T_0 - C}{(\bar{T} - C)^2}\delta M_{cond}\right]. \tag{B.9}$$

Differentiating (B.2) with respect to $\bar{T}$, we obtain:

$$\frac{d\bar{Q}_S(\bar{P}, \bar{T})}{dT} = \frac{b(T_0 - C)}{(\bar{T} - C)^2}\bar{Q}_S(\bar{P}, \bar{T}). \tag{B.10}$$

Substituting (B.10) into (B.9), we obtain:

$$Q_S^*(\bar{P}, T^*) = \bar{Q}_S(\bar{P}, \bar{T}) + \frac{L}{C_P} \cdot \delta M_{cond}\frac{d\bar{Q}_S(\bar{P}, \bar{T})}{d\bar{T}}. \tag{B.11}$$

Using (B.11) and taking into account that $\Delta S^* = q_v^* - Q_S^* = 0$ and $\bar{\Delta}\bar{S} = \bar{q}_v - \bar{Q}_S$, we obtain

$$\Delta\bar{S} - \left[1 + \frac{L}{C_P} \cdot \frac{d\bar{Q}_S(\bar{P},\bar{T})}{d\bar{T}}\right]\delta M_{cond} = 0.$$

Hence we finally derive a formula for determining the maximum possible amount of condensed water:

$$\delta M_{cond} = \frac{\Delta\bar{S}}{A(\bar{P},\bar{T})}, \tag{B.12}$$

where

$$A(\bar{P},\bar{T}) = \left[1 + \frac{L}{C_P} \cdot \frac{d\bar{Q}_S(\bar{P},\bar{T})}{d\bar{T}}\right]. \tag{B.13}$$

In the case of $\bar{Q}_S(\bar{P},\bar{T}) = 5.4\,\text{g/kg}$, $b = 17.27$, $\bar{T} = 278.16\,^{\circ}\text{C}$, $L = 600$ cal/g, $C_p = 0.24$ cal/g $\cdot$ grad we obtain:

$$A(\bar{p},\bar{T}) = 1.942. \tag{B.14}$$

Since $\Delta\bar{S} = 8.73\,\text{g/kg}$, we get that the maximum possible amount of condensed water will be about 4.5 g per 1 kg of air, i.e.

$$\delta M_{cond} \approx 4.5\,\text{g/kg} \quad \text{or} \quad \delta M_{cond} \approx 5.4\,\text{g/m}^3.$$

At $\delta M_{cond} \approx 4.5\,\text{g/kg}$ based on Eqs. (B.2)–(B.5) and (B.9) we get that new values of T^*, q_v^*, Q_S^* and $RH\,\%^*$ are equal to (Tzion and Eppelbaum 2006):

$$T^* = 289.4^{\circ}, \quad q_v{}^* = 9.63\,\text{g/kg}, \quad Q_S{}^* = 9.63\,\text{g/kg}, \quad RH\,\%^* = 100\,\%. \tag{B.15}$$

If we place a horizontal pipe with internal cooling in the vicinity of the sea coast perpendicularly to the latter, the amount of air entering the pipe will equal

$$M_{\text{air}} = U \cdot \rho_{\text{air}} \cdot S, \tag{B.16}$$

where M_{air} is the mass of the air entering the pipe with an area $S = \pi R_S$, U is the air velocity at the entrance to the pipe (m/s), ρ_{air} is the air density (kg/m^3).

If we assume that $R_S = 10$, $U = 3$ m/s, and $\rho = 1.2$ kg/m^3, then, according to (B.16), the mass of air entering the pipe in 1 s equals

$$M_{\text{air}} = 3.0(\text{m/s}) \cdot 1.2\left(\text{kg/m}^3\right) \cdot 3.14 \cdot 100\,\text{m}^2,$$
$$M_{\text{air}} \approx 1{,}130\,\text{kg/s} = 942\,\text{m}^3/\text{s},$$
$$M_{\text{air}} \approx 940\,\text{m}^3/\text{s}.$$

Since it is possible to obtain 5.4 g of water from 1 m^3 of air, the maximum amount of water obtainable from this system roughly amounts to 5,000 g of water in 1 s; i.e, about 18,000 kg of water per hour, or about 430 m^3 per day and 78,000 m^3 per summer period.

These rough estimates show that producing a considerable amount of water by air cooling is feasible. The obtained water can be used for drinking and other purposes. It should be noted that this methodology could be applied in Israel and in many regions of world at the sea coasts with high humidity.

References

Abu-Khader MM (2005) Viable engineering options to enhance the NaCl quality from the Dead Sea in Jordan. J Cleaner Prod 14(1):80–86

Asmar BN, Ergenzinger P (2002) Dynamic simulation of the Dead Sea. Adv Water Resour 25:263–277

Asmar BN, Ergenzinger P (2004) The Dead Sea is unlikely to dry up in 50 years. EOS 85(7):69–73

Broza M (1979) Dew, fog and hydroscopic food as a source of water for desert arthropods. J Arid Environ 2:43–49

Bubnov BM, Linden PF (1998) Diffusion stratification in a rotating linearly-stratified fluid. Fluids Dyn 33(2):201–208

Eppelbaum LV, Modelevsky MM, Pilchin AN (1996) Geothermal investigations in the Dead Sea rift zone, Israel: implications for petroleum geology. J Pet Geol 19(4):425–444

Eppelbaum LV, Ezersky MG, Al-Zoubi AS, Goldshmidt VI, Legchenko A (2008) Study of the factors affecting the karst volume assessment in the Dead Sea sinkhole problem using microgravity field analysis and 3D modeling. Adv GeoSci 19:97–115

Gabov SA, Sveshnikov AG (1986) Problems of stratified liquid dynamics. Nauka, Moscow

Goldreich Y (2003) The climate of Israel, observations, research and applications. Kluwer Academic Publication, NY

Kogan B, Trahtman A (2003) The moisture from the air as water resource in arid region: hopes, doubts and facts. J Arid Environ 53:231–240

Nilsson T (1996) Initial experiments on dew collection in Sweden and Tanzania. Solar Energy Math Solar Cells 40:23–32

Ravizky A, Nadav N (2007) Salt production by the evaporation of SWRO brine in Eilat: a success story. Desalination 205:374–379

Schemenauer RS, Cereceda P (1992) The quality of fog water collected for domestic and agricultural use in Chile. J Appl Meteorol 31:275–290

Tetens O (1930) Ober einige meteorologische Vegriffe. Z Geophys 6:297–309

Tzivion S, Eppelbaum L (2004) Water production using air cooling under the conditions of some coastal regions of world. In: Trans of the 2nd international scient conference organized by the World Congress of Georgian Jews. Bat Yam, Israel, pp 39–40

Tzivion S, Eppelbaum L (2006) Water production using air-cooling under the conditions of some coastal regions of world. In: Proceedings of the 1st international conference on from invitation and development to production, from research institute to the water industry, Sde Boqer, Israel, pp 139–144

Yakubov YS (1989) Correctness of one initial boundary value problem describing the motion of stratified liquid. Izv AN Azerb. SSR (Baku, Azerbaijan), No 4–5, 21–27

Yakubov YS, Eppelbaum LV (2005) Geodynamics of water flows in the Dead Sea basin: a proposed model for analysis of stratified, rotating and compressible liquid. In: Proceedings of the 2nd EUG meeting, vol 7(291), Vienna, Austria, pp 1–3

Zibold EI (1905) The role of underground dew in water supply of Feodosia. Trans of experimental forestries, No 111, Sankt-Petrsburg (in Russian)

Index

L. Eppelbaum et al., *Applied Geothermics*, Lecture Notes in Earth System Sciences,
DOI: 10.1007/978-3-642-34023-9,